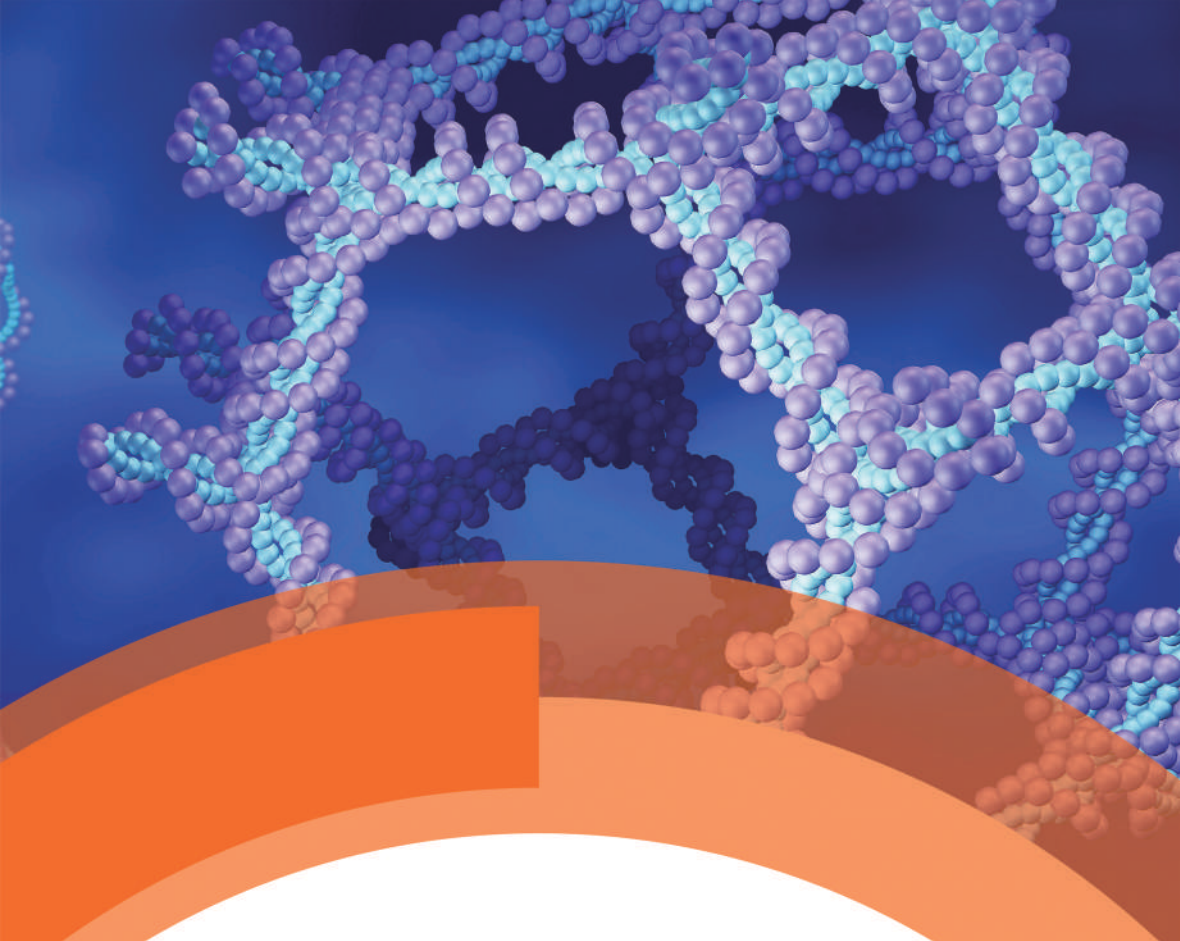

Nanoscience & Nanotechnology Series

Concepts and Design of Materials Nanoarchitectonics

Edited by Omar Azzaroni and Katsuhiko Ariga

ROYAL SOCIETY OF CHEMISTRY

Concepts and Design of Materials Nanoarchitectonics

Nanoscience & Nanotechnology Series

Editor-in-chief:
Nguyễn T. K. Thanh, *University College London, UK*

Series editors:
Gabriel Caruntu, *Central Michigan University, USA*
Shinya Maenosono, *Japan Advanced Institute of Science and Technology, Japan*
Neerish Revaprasadu, *University of Zululand, South Africa*

Titles in the series:
1: Nanotubes and Nanowires
2: Fullerenes: Principles and Applications
3: Nanocharacterisation
4: Atom Resolved Surface Reactions: Nanocatalysis
5: Biomimetic Nanoceramics in Clinical Use: From Materials to Applications
6: Nanofluidics: Nanoscience and Nanotechnology
7: Bionanodesign: Following Nature's Touch
8: Nano-society: Pushing the Boundaries of Technology
9: Polymer-based Nanostructures: Medical Applications
10: Metallic and Molecular Interactions in Nanometer Layers, Pores and Particles: New Findings at the Yoctolitre Level
11: Nanocasting: A Versatile Strategy for Creating Nanostructured Porous Materials
12: Titanate and Titania Nanotubes: Synthesis, Properties and Applications
13: Raman Spectroscopy, Fullerenes and Nanotechnology
14: Nanotechnologies in Food
15: Unravelling Single Cell Genomics: Micro and Nanotools
16: Polymer Nanocomposites by Emulsion and Suspension
17: Phage Nanobiotechnology
18: Nanotubes and Nanowires, 2nd Edition
19: Nanostructured Catalysts: Transition Metal Oxides
20: Fullerenes: Principles and Applications, 2nd Edition
21: Biological Interactions with Surface Charge Biomaterials
22: Nanoporous Gold: From an Ancient Technology to a High-tech Material
23: Nanoparticles in Anti-Microbial Materials: Use and Characterisation
24: Manipulation of Nanoscale Materials: An Introduction to Nanoarchitectonics
25: Towards Efficient Designing of Safe Nanomaterials: Innovative Merge of Computational Approaches and Experimental Techniques
26: Polymer–Graphene Nanocomposites
27: Carbon Nanotube-Polymer Composites
28: Nanoscience for the Conservation of Works of Art
29: Polymer Nanofibers: Building Blocks for Nanotechnology
30: Artificial Cilia

31: Nanodiamond
32: Nanofabrication and its Application in Renewable Energy
33: Semiconductor Quantum Dots: Organometallic and Inorganic Synthesis
34: Soft Nanoparticles for Biomedical Applications
35: Hierarchical Nanostructures for Energy Devices
36: Microfluidics for Medical Applications
37: Nanocharacterisation, 2nd Edition
38: Thermometry at the Nanoscale: Techniques and Selected Applications
39: Nanoceramics in Clinical Use: From Materials to Applications, 2nd Edition
40: Near-infrared Nanomaterials: Preparation, Bioimaging and Therapy Applications
41: Nanofluidics, 2nd Edition
42: Nanotechnologies in Food, 2nd Edition
43: ZnO Nanostructures: Fabrication and Applications
44: Diatom Nanotechnology: Progress and Emerging Applications
45: Nanostructured Materials for Type III Photovoltaics
46: Chemically Derived Graphene: Functionalization, Properties and Applications
47: Graphene-based Membranes for Mass Transport Applications
48: Carbon Nanostructures for Biomedical Applications
49: Surface Chemistry of Colloidal Nanocrystals
50: Reducing Agents in Colloidal Nanoparticle Synthesis
51: Carbon Nitride Nanostructures for Sustainable Energy Production and Environmental Remediation
52: Nanotubes and Nanowires, 3rd Edition
53: Bionanodesign: Old Forms for New Functions, 2nd Edition
54: Photothermal Nanomaterials
55: Concepts and Design of Materials Nanoarchitectonics

How to obtain future titles on publication:
A standing order plan is available for this series. A standing order will bring delivery of each new volume immediately on publication.

For further information please contact:
Book Sales Department, Royal Society of Chemistry, Thomas Graham House, Science Park, Milton Road, Cambridge, CB4 0WF, UK
Telephone: +44 (0)1223 420066, Fax: +44 (0)1223 420247
Email: booksales@rsc.org
Visit our website at www.rsc.org/books

Concepts and Design of Materials Nanoarchitectonics

Edited by

Omar Azzaroni
INIFTA-CONICET-Universidad Nacional de La Plata, Argentina
Email: azzaroni@inifta.unlp.edu.ar

and

Katsuhiko Ariga
National Institute for Materials Science, Japan
Email: ariga.katsuhiko@nims.go.jp

Nanoscience & Nanotechnology Series No. 55

Print ISBN: 978-1-78801-802-9
PDF ISBN: 978-1-78801-961-3
EPUB ISBN: 978-1-78801-962-0
Print ISSN: 1757-7136
Electronic ISSN: 1757-7144

A catalogue record for this book is available from the British Library

The Royal Society of Chemistry is a charity, registered in England and Wales, Number 207890, and a company incorporated in England by Royal Charter (Registered No. RC000524), registered office: Burlington House, Piccadilly, London W1J 0BA, UK, Telephone: +44 (0) 20 7437 8656.

For further information see our web site at www.rsc.org

Printed in the United Kingdom by CPI Group (UK) Ltd, Croydon, CR0 4YY, UK

Preface

The field of materials nanoarchitectonics has developed rapidly because of the continuous and ever-expanding practical needs of many technology-based sectors, including energy and healthcare among the most active areas.

There is currently a broad variety of medical devices, diagnostic products, and energy conversion and storage devices that rely on the operation of carefully designed nanostructured hybrid materials consisting of different, complementary building blocks with unique property combinations. This is the essence of materials nanoarchitectonics: *the integration of molecular components with strict control over the architecture and function*.

Conceptually speaking, materials production with nanoarchitectonics is generally accomplished through the concerted harmonization of multiple interactions. Thus, in order to reach such a goal, it is important to combine different techniques to manipulate building blocks and control materials organization. Methodologies based on chemical and physicochemical modification and organization upon application of external physical stimuli are among the strategies most frequently used.

One of the main targets of nanoarchitectonics is the reliable construction of functional nanosystems through the organization of nanoscale structures. Paradoxically, the main players are not the building blocks themselves, but their interactions causing a new emerging functionality.

From a historical perspective, materials nanoarchitectonics marks a departure from the traditional understanding of nanosystems construction, which is generally based on the criterion of "functional building block". Or, in other words, the building block is responsible for introducing a given functionality to the system. In this sense, nanoarchitectonics tries to offer a broader point of view to this issue by considering that different unexpected emergent functionalities can result from assembling or organizing the same building blocks under different configurations.

Nanoscience & Nanotechnology Series No. 55
Concepts and Design of Materials Nanoarchitectonics
Edited by Omar Azzaroni and Katsuhiko Ariga

Published by the Royal Society of Chemistry, www.rsc.org

This explains why one of the grand challenges in materials nanoarchitectonics is the synthetic control of chemical interactions at the supramolecular level. During the last decade, significant research efforts have been devoted to manipulating molecular materials at different levels of dimensionality, ranging from two-dimensional architectures, such as graphene, to complex three-dimensional crystalline structures, like metal–organic frameworks.

Expertise that we have gathered throughout these years has enabled us to exert extended control over chemical interactions in two and three dimensions with a concomitant effect on numerous key processes, namely electrocatalysis, photocatalysis, molecular separations, energy flow, optical effects, molecular recognition and so on. The magnitude of these processes relies on nanoscale interfacial phenomena in which the interplay between molecular interactions and the functional features of predefined building blocks plays a major part. Here is when materials nanoarchitectonics come into the picture as a valuable concept to engineer materials at the molecular level and customize the production of complex, hybrid materials displaying spatially-addressed chemical interactions.

On the other hand, we should bear in mind that nanorchitectonics operate like an incredibly well-synchronized orchestra of molecular interactions among different building blocks. Understanding this network of molecular interactions is essential not only to understand how nanoarchitected materials work but also to determine the molecular mechanisms responsible for an emergent functionality.

This book is written for a wide readership, including university students and researchers from diverse backgrounds such as chemistry and chemical engineering, materials science, nanotechnology, engineering, biomedical engineering, physics, life sciences, and biotechnology. It can be used not only as a textbook for undergraduate and graduate students but also as a review and reference book for researchers in the materials science, chemistry and nanotechnology arenas. We hope that the chapters of this book will provide the reader with valuable insight into functional materials with respect to the fundamentals of architecture, design, and applications.

Last, but not least, we would like to thank all those who have been helpful in the realization of this book and all colleagues who kindly devoted their time to contribute chapters.

Omar Azzaroni and Katsuhiko Ariga

Contents

Nanoscience & Nanotechnology Series No. 55
Concepts and Design of Materials Nanoarchitectonics
Edited by Omar Azzaroni and Katsuhiko Ariga

Published by the Royal Society of Chemistry, www.rsc.org

CHAPTER 1

What is Nanoarchitectonics: Origin and Task

KATSUHIKO ARIGA*[a,b] AND OMAR AZZARONI*[c]

[a]WPI Research Center for Materials Nanoarchitectonics (MANA), National Institute for Materials Science (NIMS), 1–1 Namiki, Tsukuba, Ibaraki 305-0044, Japan; [b]Graduate School of Frontier Sciences, The University of Tokyo, 5-1-5 Kashiwanoha, Kashiwa, Chiba 277-8561, Japan; [c]Instituto de Investigaciones Fisicoquímicas y Aplicadas (INIFTA), Departamento de Química, Facultad de Ciencias Exactas, Universidad Nacional de La Plata, CONICET, Diagonal 113 y 64 (1900), La Plata, Argentina
*E-mail: ARIGA.Katsuhiko@nims.go.jp, azzaroni@inifta.unlp.edu.ar

1.1 Nanotechnology Comes First

The progress of mankind has always been related to the construction of novel materials and devices. We can recall many examples from ancient times that indicate how important it is for our societies to design and fabricate functional materials. In this sense, the use and application of nanoarchitected materials and/or nanomaterials has proved very useful both at scientific and technological levels.

We are now aware that nanosized particles exist in nature and can be created from a variety of precursors. However, if we look across the history of materials science and chemistry, we realize that in ancient times craftsmen-turned-scientists often used a variety of nanomaterials for different purposes.

Nanoscience & Nanotechnology Series No. 55
Concepts and Design of Materials Nanoarchitectonics
Edited by Omar Azzaroni and Katsuhiko Ariga

Published by the Royal Society of Chemistry, www.rsc.org

But, in their primitive nanotechnology approach, these craftsmen were not able to exert control over the composition, morphology, and dimensions of these materials. Indeed, they were not even able to characterize them.

History offers revealing examples of "pre-modern nanotechnology". The Lycurgus cup – a 4th-century Roman glass cage cup – is a wonderful example of a dichroic glass containing gold and silver nanoparticles which exhibits an impressive change in colour depending on the illumination.[1] Another remarkable example is the 17th-century Persian-forged Damascus steel sword containing carbon nanotubes and cementite nanowires. The presence of these nanomaterials added strength and the ability to maintain the edge after cleaving through stone, metal, or even other swords.[2] Some investigations revealed that these carbon nanotubes originated in the use of biomass derived from trees as carburizing additives. We now know that conversion of iron to quality steel demands control over carburization in order to tune the carbon concentration in the material. In ancient times, control over these variables was very poor, and the production process relied exclusively on the craftsman's skills.

On the contrary, in modern times it is difficult if not impossible for chemists or materials scientists to create a new material without considering how to control its structure at the nanoscale or even molecular level. Contemporary science has made great strides in improving our capability to design and fabricate materials with impressive nanoscale structural precision, with a concomitant effect on their practical applications in diverse technological areas such as energy, environmental science, device technology, and healthcare.[3]

Chemists have long pursued the idea of creating materials from elemental building blocks. By the end of 19th century, the French chemist Pierre-Eugène-Marcellin Berthelot already had a long record in the quest for synthetic strategies to obtain all organic compounds, starting from inorganic elements and proceeding step by step from hydrocarbons to alcohols to esters and so forth.[4] According to Berthelot, all organic materials could be synthesized, and thus manufactured and manipulated in a laboratory. Half a century later, in the year 1956, Arthur von Hippel from MIT coined the term "molecular engineering" in an article published in *Science*.[5] In his paper on this topic, von Hippel emphasizes *"what is molecular engineering? It is a new mode of thinking about engineering problems. Instead of taking prefabricated materials and trying to devise engineering applications consistent with their macroscopic properties, one builds materials from their atoms and molecules for the purpose at hand."* What von Hippel was saying is that if we are able to control the relationships among structure, function, composition and processing, then we are able to design the properties and characteristics of a particular material.

Three years later, in 1959, Richard Feynman gave an enlightening talk entitled *"There's Plenty of Room at the Bottom"* at an American Physical Society meeting at Caltech,[6] outlining seminal ideas and concepts behind nanoscience and nanotechnology. It is no wonder that Feynman began his

presentation by saying "what I want to talk about is the problem of *manipulating and controlling things on a small scale*". This talk took place long before the term nanotechnology was widely used by the entire international scientific community. In his talk, Feynman highlighted *"at the atomic level, we have new kinds of forces and new kinds of possibilities, new kinds of effects".*

The very same Richard Feynman wrote on his blackboard, *"What I cannot create, I do not understand".* He was probably reminding himself and his students that creation and understanding are two factors closely intertwined. There is an old saying that you cannot manage what you do not understand. In this sense, the combination of practical and theoretical research approaches to improve our understanding of nanoscale systems has been decisive for the advancement of nanotechnology during the last decades.

The term "nanotechnology" was introduced by Prof. Norio Taniguchi during a conference in 1974.[7] At this stage, nanotechnology was slowly emerging from the attempts to create nanosized objects using optimized microfabrication techniques ("top-down" approach). However, the appearance of nanotechnology as a major area of research took place only after the invention of the scanning tunnelling microscope (STM) in 1981. Gerd Binnig and Heinrich Rohrer submitted their first publication on the STM in September 1981.[8] In 1986 they received the Nobel Prize. This instrument was able to scan a surface, yielding information with a finer resolution than ever before. This Nobel Prize in Physics was shared with Ernst Ruska who designed the first electron microscope, another key instrument in the history of nanoscience and nanotechnology. As time went by, the resolution of electron microscopes has been improving and nowadays these instruments are able to reach resolutions of 0.5 Å.

In 1987, K. Eric Drexler published the first book on nanotechnology *"Engines of Creation: The Coming Era of Nanotechnology"*, propelling nanotechnology into popular culture. It was in this context that the concept of "molecular nanotechnology" first came into the limelight. At this point we must say that this book has been a matter of some controversy, in which renowned scientists like Richard Smalley and George M. Whitesides were particularly critical. A few years later, Drexler published *"Nanosystems: Molecular Machinery, Manufacturing and Computation".*[9] This book describes the physical principles, components and systems and implementation strategies to accomplish functional architectures from bottom-up molecular organization. This concept was further supported by several advances in materials science regarding programmed organization of DNA origami[10] and enzyme-powered nanomotors,[11] among other examples.

Also in 1987, Charles J. Pedersen, Donald J. Cram, and Jean-Marie Lehn were awarded the Nobel Prize in Chemistry for their development and use of molecules with structure-specific interactions of high selectivity.[12] Throughout years of research these chemists demonstrated that cations, anions, or neutral molecules can enter the cavities of specifically designed compounds and be held there by intermolecular forces. Pedersen, Cram and Lehn are the founding fathers of "supramolecular chemistry", a term

coined by Jean-Marie Lehn. The focal point of supramolecular chemistry is dominating and understanding interactions between molecules in order to control their molecular recognition, assembly and concerted functions on a molecular scale, among other features.

During the past decades, supramolecular chemistry emerged as a new sub-field of chemistry offering a new dimension in the design of molecular systems with tailor-made properties. As we move further into the 21st century, we observe that supramolecular chemistry has come a long way and borne many fruits. In 2016, Pierre Sauvage, Sir J. Fraser Stoddart and Bernard L. Feringa were jointly awarded the Nobel Prize in Chemistry for the design and synthesis of molecular machines.[13] Built up over decades, these researchers introduced new and inspiring ideas to create nanosystems with unprecedented molecular precision. The use and application of mechanically bonded molecules and sterically crowded olefins brought about a bottom-up philosophy to create complex artificial molecular machineries that closely resemble the operations of macroscopic machineries.[14]

1.2 Nanoarchitectonics Initiated – Integrated Molecular Systems from Scratch

The notion of creating functional and integrated molecular systems from scratch has been around for decades. In fact, these notions and ideas evolved independently within the chemistry and materials science communities before Masakazu Aono introduced in 2000 the concept of "nanoarchitectonics" as a framework to unify potentially complementary scientific disciplines into one methodology.[15]

In 1994, Allen Bard published an insightful book *"Integrated Chemical Systems: A Chemical Approach to Nanotechnology"*. This book was based on the Baker Lectures that Allen Bard gave at Cornell University in 1987. Perhaps we could say that this is the first book to take a truly systematic approach to the study of nanotechnology from a chemist's perspective. In fact, the book begins with a discussion and some examples of integrated chemical systems and analogies between man-made systems and biological ones.[16] Contrary to the ambitious Drexlerian vision[17] aimed at improving biology by applying engineering principles, one of the important corollaries of Bard's book is that we can do better nanotechnology by using biological principles. The key to devising strategies and implementing principles of construction to create integrated chemical nanosystems is to learn how to deal with molecular assembly, self-organizing systems, assembly techniques, nanofabrication techniques, template synthesis, molecular recognition, supramolecular chemistry, and so on.

The 1990s was a decade in which nanotechnology activities proliferated around the world. Culturally, the decade was characterized by the rise of nanotechnology programs, the development of advanced large-scale equipment and the construction of nanofabrication facilities. The major focuses of these worldwide activities were the study of nanoscale properties, synthesis

of materials and characterization, and the application and development of useful devices and processes leading to potential economic benefits. During this decade the first "nanotech" companies began to operate, *e.g.*, Nanophase Technologies, Zyvex or Nano-Tex. During this time, advances in nanomaterials chemistry opened the door to a myriad of new opportunities for nanotechnology. Sumio Iijima was credited with the discovery of carbon nanotubes (CNT) in 1991. One year later, Charles T. Kresge and co-workers at Mobil Oil discovered the mesoporous materials,[18] now used and commercialized for different purposes including catalysis, drug delivery and water remediation. Contemporaneously, Moungi Bawendi and his collaborators[19] at MIT worked on the controlled synthesis of colloidal quantum dots (previously discovered by Louis Brus[20] at Bell Labs in the 1980s). Robert F. Curl Jr, Sir Harold W. Kroto and Richard E. Smalley received the Nobel Prize in Chemistry in 1996 for their discovery of fullerenes. Some years later, Andre Geim and Konstantin Novoselov received the Nobel Prize in Physics[21] for their ground-breaking experiments regarding the two-dimensional material graphene, another member of the carbon nanomaterials family.

In the early 1990s, Amit Kumar and George Whitesides at Harvard University developed the microcontact printing technique[22] (the birth of "soft lithography"[23]). This simple patterning method is based on the use of an elastomeric stamp inked with an organothiol or organosilane solution. Upon bringing the inked stamp into contact with gold or silicon substrate the molecules react with the surface, forming a highly self-assembled monolayer that replicates the stamp pattern. Later in that decade, Chad Mirkin and co-workers (Northwestern University) developed a patterning technique based on the use of a scanning probe microscope called dip-pen lithography.[24] In this technique an atomic force microscopy (AFM) tip is coated with thiol molecules and these molecules are then transferred to a gold substrate. Although dip-pen lithography is not easily implemented, this technique offers ample chemical flexibility to nanometre-scale patterning.

At the end of 20th century and the beginning of 21st century, the scientific community was completely aware of the importance of architectonics on the nanoscale. In 1999, Heath and co-workers (University of California Los Angeles, UCLA) published an article in Accounts of Chemical Research entitled Architectonic Quantum Dot Solids.[25] In this article, the term "architectonics" was suggested by Richard Stanley Williams from Hewlett-Packard Labs and refers to "having an organized and unified structure that suggests an architectural design", according to Merriam-Webster's WWW dictionary.[26] On the other hand, nanoarchitectonics as a concept was first used in title of scientific conference *"1st International Symposium on Nanoarchitectonics Using Suprainteractions"*, in 2000 at Tsukuba, Japan, led by Masakazu Aono.[27] This can be considered the beginning of the conceptual term within the scientific community: nanoarchitectonics (nano + architectonics). In 2001, the National Institute of Advanced Industrial Science and Technology (AIST) started a research centre under the name of Interfacial Nanoarchitectonics, led by Toshimi Shimizu, in the same city. The first paper including the term "nanoarchitectonics" in the title: "Welding, organizing, and planting organic

molecules on substrate surfaces – Promising approaches towards nanoarchitectonics from the bottom up", was published by Stefan Hecht (Freie Universität Berlin) in 2003.[28] Concomitantly, Aono re-named the World Premier International Research Center in the National Institute for Materials Science (NIMS) as the Research Center for Materials Nanoarchitectonics (WPI-MANA) in 2007. Roughly speaking, the nanoarchitectonics approach to the creation of functional materials and systems through the organization of nanoscale units into larger functional is analogous to the situation of a carpenter willing to assemble a furniture and put it together, piece by piece. Perhaps at this point, we should emphasize that even when nanotechnology provides tools to characterize nanoscale phenomena and manipulate nanoscale objects, it cannot be interpreted as a universal methodology for material production. There exists an evident need to architecturally manipulate functional materials and systems from nanosized functional units. Within this framework, nanoarchitectonics, seeks to realize this level of control over molecular systems through a set of different technologies.

1.3 How Nanoarchitectonics Works

At first sight, one may think that the elaboration of nanoscale objects is a logical consequence of the continuous miniaturization of fabrication techniques traditionally employed for the construction of microscale objects. However, strategies used in the microscale domain may not always be useful for the fabrication of specific nanostructures. Materials fabrication and structural construction in nanoscale or mesoscale domains cannot be extrapolated from microscale domains and, sometimes, they are difficult to be accomplished according to their original expectations. In nanoscale domains, uncontrollable and unexpected disturbances and fluctuations such as thermal fluctuations, statistic distributions, and quantum effects are unavoidable. Clear examples of this combination of phenomena are the ensemble properties emanating directly from ordering and confinement at different length scales. Chemical processes taking place in constrained spaces deserve particular attention for they are a fundamental part of nanoscience and nanotechnology. In a physically constrained environment, interfacial interactions, symmetry breaking, and confinement-induced entropy loss can play dominant roles in determining molecular organization or chemical reactivity.[29] In addition, mutual component interactions significantly affect the entire material system. Outputs such as materials structures and properties do not emerge from simple additive contributions of individual components.[30] In many cases, the outcome results from the harmonization of diverse controllable and uncontrollable interactions.

For instance, when a nanoarchitected system – held together by supramolecular forces (Figure 1.1) – is exposed to an external stimulus targeting a specific building block it is probable that there will be changes in the surrounding components of the nanoscale material due to changes in mutual interactions.[31] As a result, when we design nanostructured materials it is

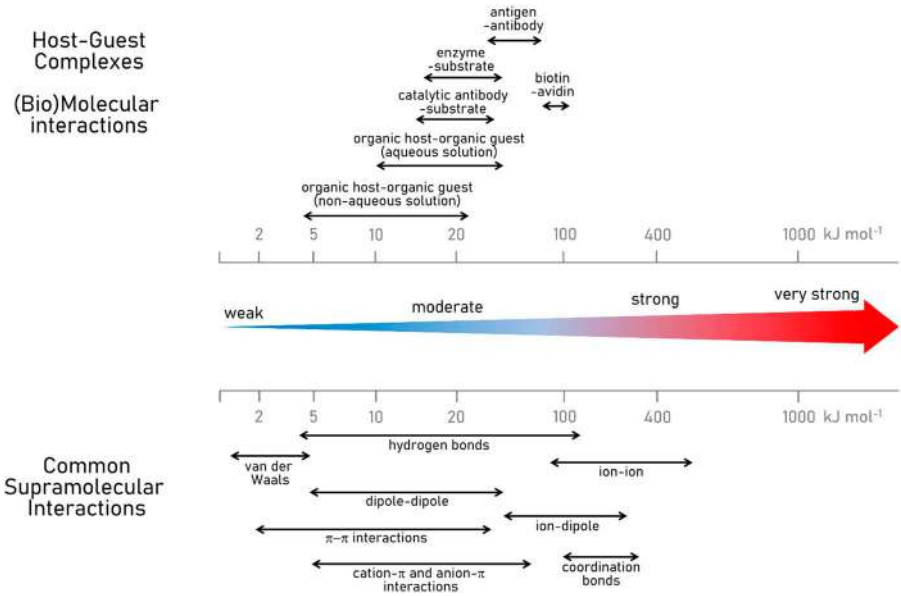

Figure 1.1 Summary of common (bio)supramolecular interactions. Data taken from ref. 32 and 33.

Figure 1.2 Materials nanoarchitectonics offers an integrated approach for the design and fabrication of nanomaterials and nanodevices. It is based on five pillars: self-organization, chemical manipulation, molecular manipulation, field-induced control, and theoretical modelling and design.

necessary to consider not only the compositions of nanosized components but also the strength of inter-component interactions.

Putting "materials nanoarchitectonics"[34] into practice to its full extent requires the combination of five "technologies" (Figure 1.2): self-organization, (bio)chemical nanomanipulation, field-induced interaction, new atom/

molecule manipulation, and theoretical modelling. Self-organization refers to the capacity of systems to reorganize its own structure, most often making its own structure more complex. Self-organization lies behind the formation of a wide variety of soft nanostructures, including liposomes, polymeric nanoparticles, polymersomes, and protein-only self-assembled nanoparticles. Regarding this latter, we should consider molecular biorecognition as a particular form of self-organization encompassing different biological processes. Field-induced interactions involve physical forces such as heat, light or redox potential, involved in the actuation or functioning of nanodevices. Chemical manipulations refer to reactions performed on functional groups present in the molecular system that allow precise engineering of the functional capabilities of the nanoarchitected system. New atom and molecular manipulations involve innovative treatments to regulate and manipulate the orientation and spatial arrangement of nanomaterials leading to well-defined nanosystems. For example, the use of dynamic bonds represents a plausible strategy to create macroscopically responsive structurally dynamic materials.[35] The dynamic nature of phenomena and properties in the nanoscale region caused by local disturbances and fluctuations often results in an advantageous situation for the creation of dynamically stable, flexible, self-adjustable, self-repairing, and harmonized outputs. Finally, theoretical modelling provides a framework for the interpretation of the molecular systems from multiple perspectives and evaluate causes and effects from a fundamental background.[36] Theoretical modelling can also play a decisive role as a predictive tool in different nanoarchitected systems. Computer simulations can prove essential in addressing important issues related to how nanoscale building blocks self-assemble and how to choose a pathway to engineer new advanced materials. The concatenation of these key five technologies is nicely exemplified in the remarkable work carried out by Müller and co-workers, depicted in Figure 1.3, involving the use of triblock terpolymers to create complex materials through hierarchical self-assembly.

1.4 Nanoarchitectonics at Work

De novo construction of nanoarchitected materials has great potential for the conversion of basic research into successful innovation, especially in the case of practical applications related to energy and healthcare. For example, the performance of energy devices is critically dependent on nanoscale interfacial phenomena.[38] From the viewpoint of materials design, it is essential to gain control over the complex interface between dissimilar materials. In this sense, nanoarchitectonics expresses a particular attitude in which materials are designed with pre-planned properties through the imaginative exploitation of a fundamental knowledge of the structure and chemistry of internal interfaces and free surfaces. It this way, 2D nanomaterials such as nanosheets and other molecular structures in thin film formats have been prepared by different techniques including the Langmuir–Blodgett (LB) method,[39]

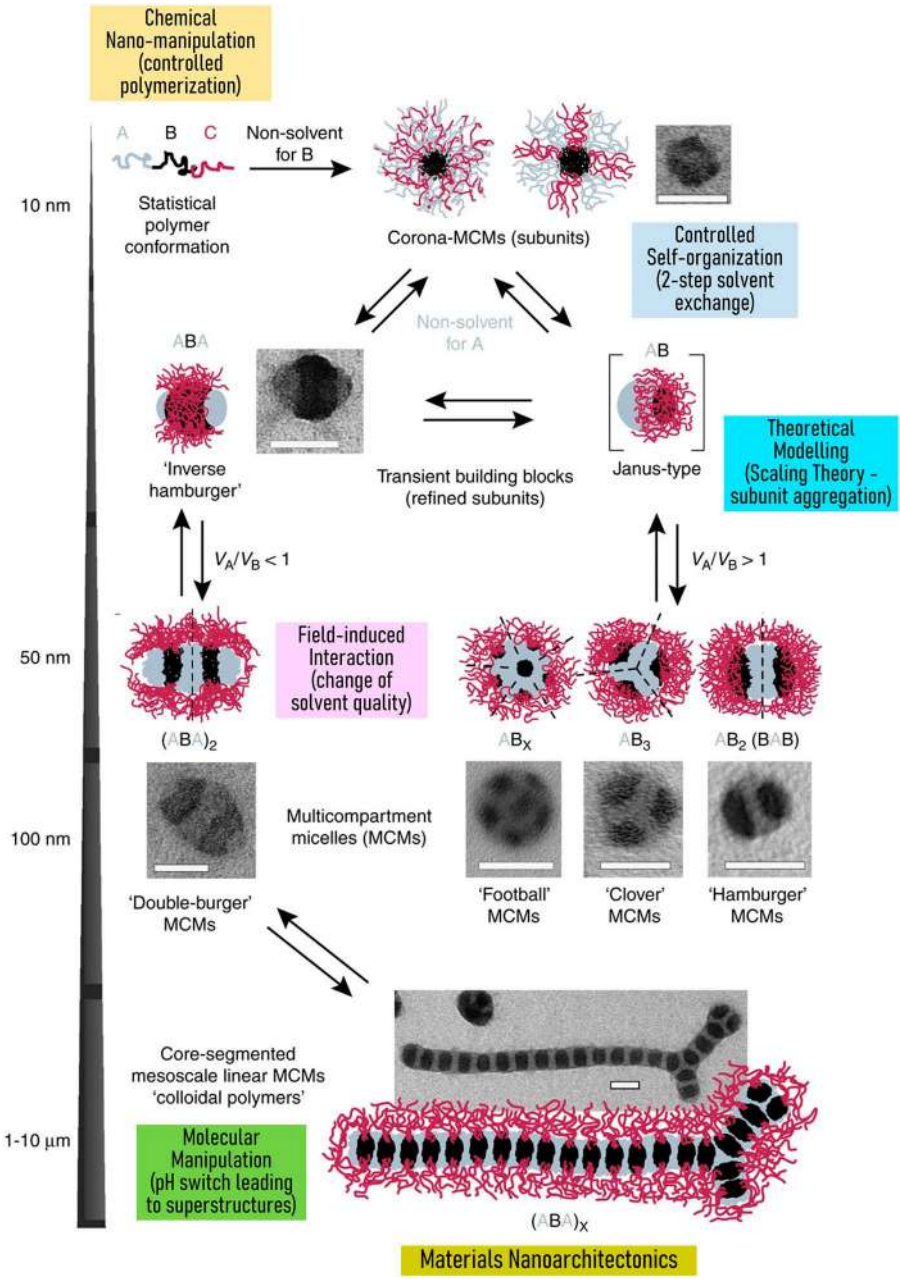

Figure 1.3 Example of the concatenation of the five technologies of materials nanoarchitectonics taking place in the hierarchical self-assembly of well-defined multicompartment micelles. Reproduced from ref. 37 with permission from Springer Nature, Copyright 2012.

layer-by-layer (LbL) assembly,[40] self-assembled monolayer (SAM)[41] and polymer brush[42] modifications. For example, the repeated LB transfer of oversized $Ti_{0.87}O_2$ nanosheets can provide the highly ordered multilayer films,[43] which are promising candidates for applications in high-*k* nanofilms and as seed layers for crystal film growth. In a similar way, the Langmuir technique has been employed to create 2D networks of metal-organic frameworks at the air–water interface (Figure 1.4). The LB method is a powerful strategy for preparing ultrathin films on both organic and inorganic substances by transferring a monolayer structure from water surface.[44] The concept of the LB technique can also be used to control the 2D structures and properties by dynamic motion, a concept often refer to "hand-operated nanotechnology".[45] This notion has been elegantly demonstrated by Yonamine *et al.* who prepared Langmuir films of DNA wheels[46] and rectangle DNA origami[47] at the air–water interface (Figure 1.5). In the latter case, supramolecular polymerization of the DNA origami pieces into a one-dimensional array was demonstrated upon two-dimensional mechanical stimulus motions.

In addition to this method, Langmuir monolayers are well known as suitable platforms for molecular recognition[48] and molecular patterning,[49] which are advantageous for the design of sensing devices.

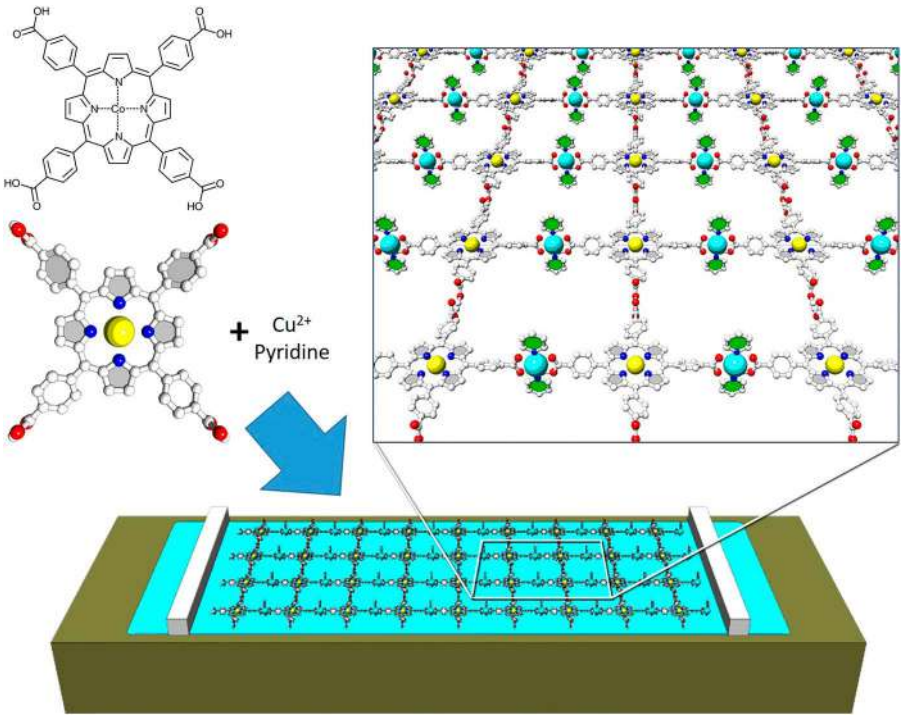

Figure 1.4 Two-dimensional assembly of metal-organic framework structures consisting of metalloporphyrin building units. Reproduced from ref. 50 with permission from Springer Nature, Copyright 2018.

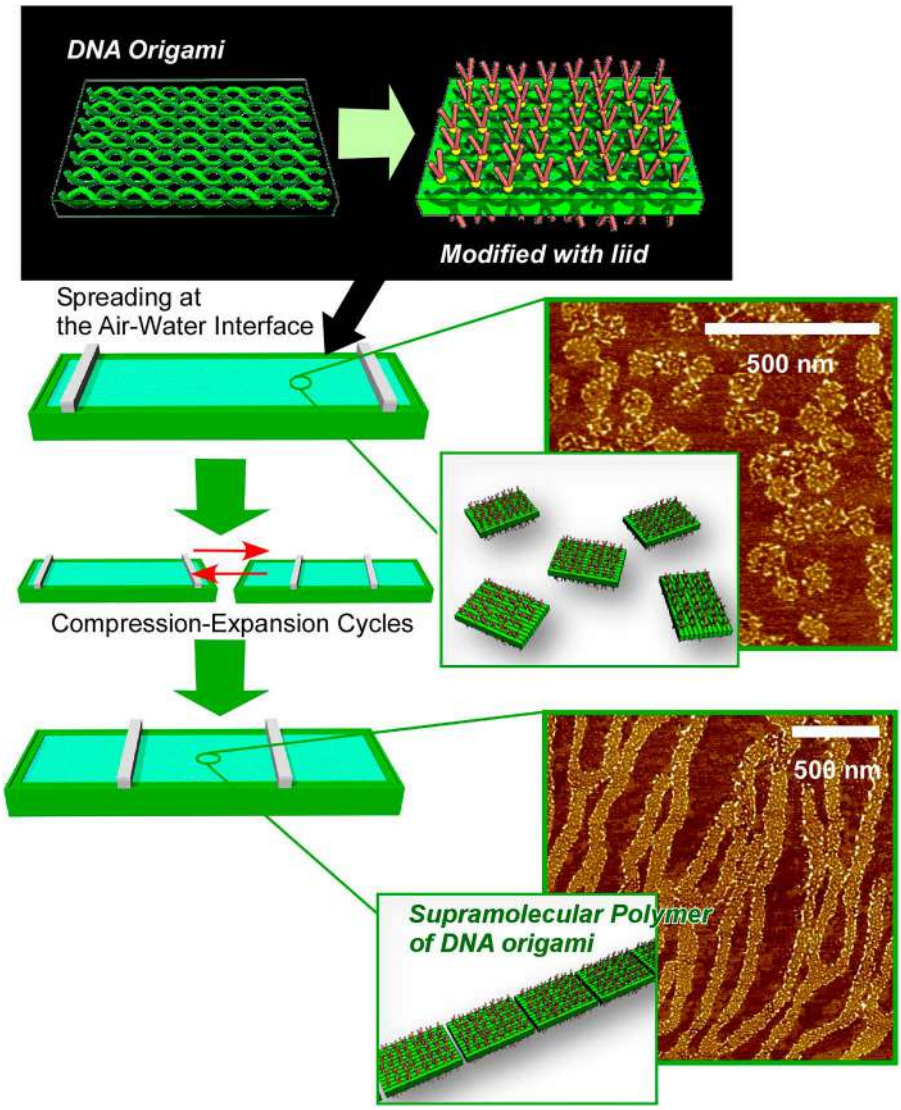

Figure 1.5 Supramolecular polymerization of the DNA origami pieces into one-dimensional upon two-dimensional mechanical stimulus motions. Reproduced from ref. 51, https://doi.org/10.1080/14686996.2018.1553108, under the terms of the CC BY 4.0 license http://creativecommons.org/licenses/by/4.0/.

LbL assembly is nowadays well-known as a versatile strategy for the controlled formation of layered structures,[52] that can be implemented on both flat substrates and spherical colloidal particles.[53] This rapidly advancing preparative technique has granted access to a wide range of hierarchical structures through the combination of different building blocks (Figure 1.6),[54]

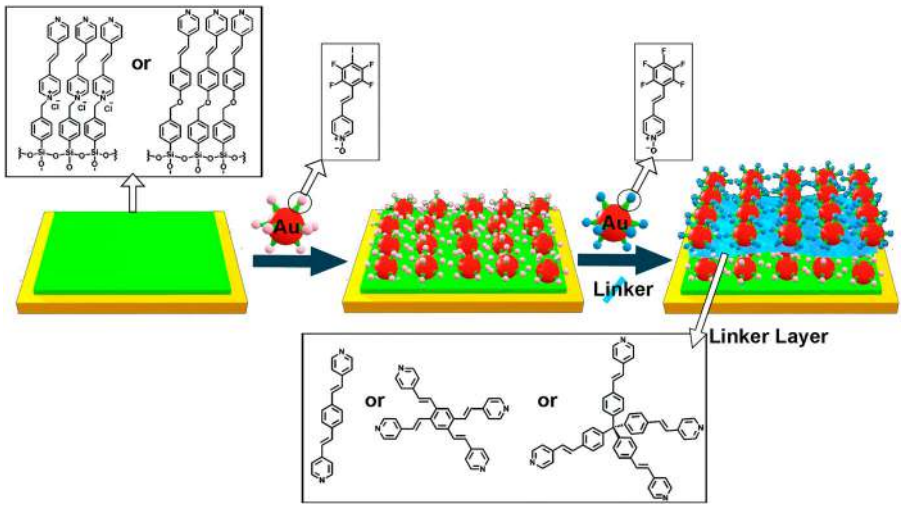

Figure 1.6 Schematic representation of halogen-bonding-mediated LbL assembly. Reproduced from ref. 59 with permission from Springer Nature, Copyright 2012.

the formation of stimuli-responsive films and the construction of responsive capsules, among other examples. On the other hand, the construction of multicomponent interfacial architectures through recognition-driven LbL assembly has also offered the opportunity to integrate molecular building blocks into well-defined organized assemblies for biosensing purposes.[55] A similar approach has also been extended to include ionic self-assemblies[56] bearing recognizable units.[57] Additionally, the synergistic combination of LbL assembly and nanoporous membrane templating has greatly facilitated the creation of complex and functional nanotubular structures.[58]

The use of SAMs has proved useful for preparing modified and patterned surfaces for various devices at the molecular level.[60] In this regard, microcontact printing has been a key enabling technology for the patterned functionalization of surfaces with specific functional groups.[61] SAMs constituted of chemisorbed species represent fundamental building blocks for creating complex structures by a "bottom-up approach".[62] The self-assembly of molecules into structurally organized thin films exploiting the flexibility of organic and supramolecular chemistry has led to the generation of synthetic surfaces with well-defined chemical and physical properties. Over the last decades, SAMs on solid surfaces have attracted widespread attention because of their potential applications in many fields, such as corrosion protection[63] of surfaces, molecular recognition,[64] molecular electronics,[65] nanofabrication[66] and biosensors,[67] among others.

Materials synthesis involving the combination of two or more existing materials is a powerful strategy for materials creation by nanoarchitectonics. Assembling different nanocomponents into an "integrated chemical system" can be an interesting method to create heterostructures with concerted

and/or novel functions.[68] Materials constructed through a nanoarchitectonics approach may exhibit unusual properties where the functionalities of the resulting materials cannot be predicted based on those of the original components. This characteristic feature very closely resembles what is to be found in biological systems, as they often operate based on cooperative action of assembled components. For example, it has been demonstrated that the modification of mesoporous silica with zwitterionic polymer brushes results in a hybrid system with proton-gated, cation-selective, ion transport properties that can be interpreted correctly only in terms of a synergy between the mesoporous scaffold and the hosted polymeric molecules.[69] In this way, the combination of porous materials with macromolecular or supramolecular units brings with it the possibility of creating phase separated regions (functional domains) within the pores that can behave as "reactive pockets" of nanoscale size, with highly controlled chemistry and interactions within restricted volumes.[70] By way of example, Zink and his collaborators have designed hybrid Janus nanoparticles for targeted chemo-photothermal therapy (Figure 1.7) in

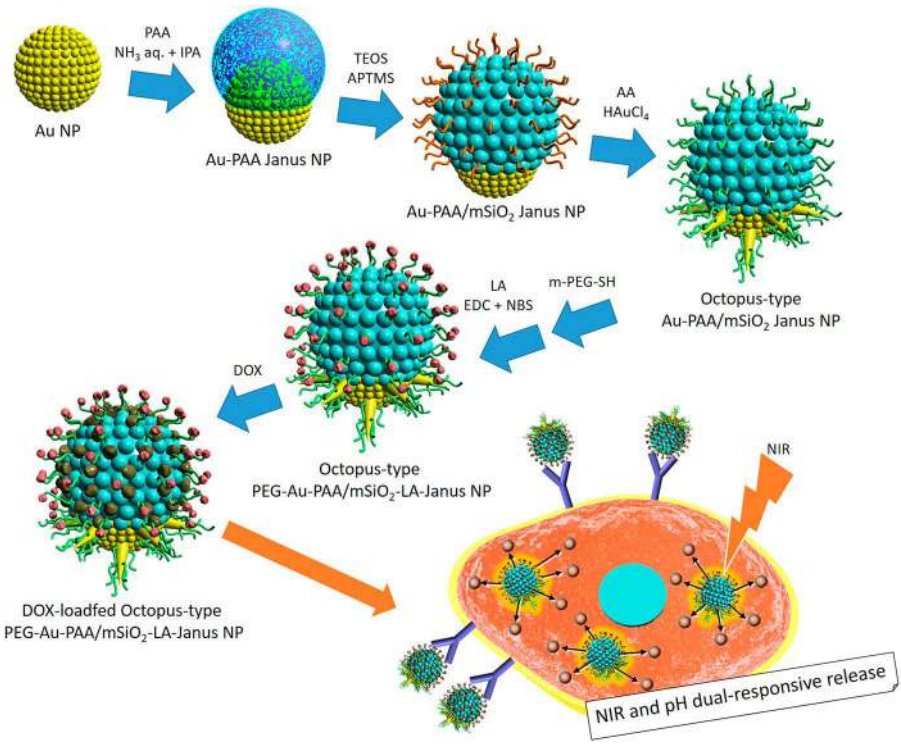

Figure 1.7 Fabrication of octopus-type PEG-Au-PAA/mSiO$_2$-LA Janus nanoparticles (NPs) (PEG-OJNP-LA) with pH and near-infrared (NIR) light dual-stimuli responsive cancer therapy: PEG, poly(ethylene glycol); PAA, poly(acrylic acid); and LA, lactobionic acid. Reproduced from ref. 72 with permission from John Wiley & Sons, Copyright 2017 Wiley-VCH Verlag GmbH & Co. KGaA.

which gold/poly(acrylic acid) hybrids were modified with mesoporous silica as octopus-type particles.[71] These particular nanoarchitectures exhibit several advantageous characteristics such as stability, biocompatibility, blood circulation time, and biospecificity to hepatocytes or hepatoma cells. After loading doxorubicin hydrochloride in the multifunctional Janus nanoparticles, a higher toxicity at the cellular and animal levels upon near-infrared light irradiation was confirmed, indicating the superiority of the combined chemotherapy and photothermal therapy over their single effects.

Materials created using the nanoarchitectonics concept can also exhibit dynamic properties and flexibility. Supramolecular assembly can be used to construct a wide variety of ordered structures by exploiting the cumulative effects of multiple noncovalent interactions. The programmed control of multiple assembly strategies led to the preparation of anisotropic fullerene-based nanostructures (Figure 8a) Time-programmed shape changes of

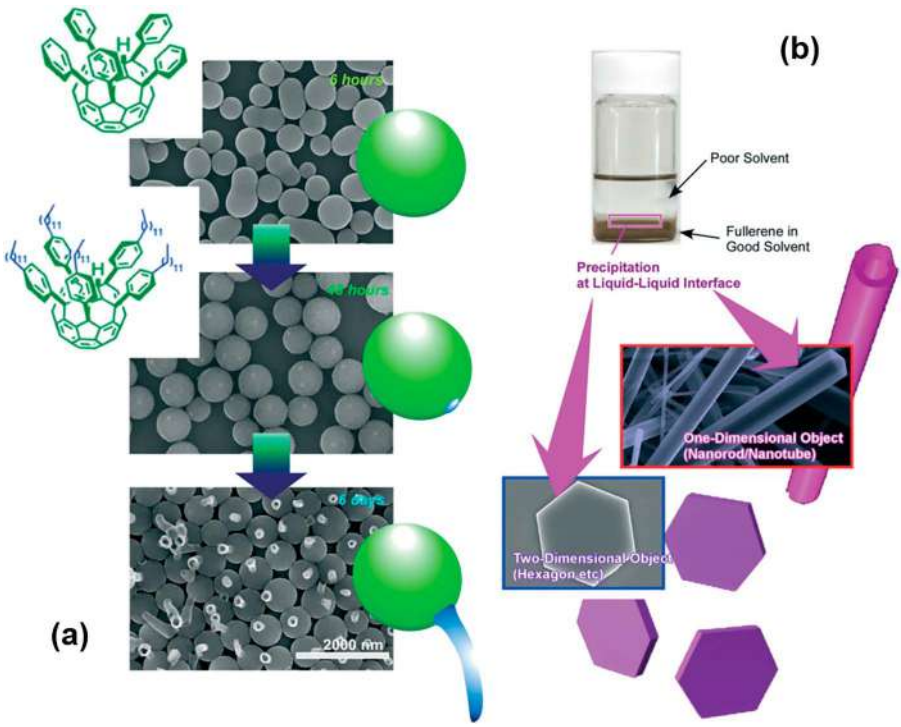

Figure 1.8 (a) Time-programmed shape changes of fullerene assemblies like the transformation from frogspawn to tadpoles were demonstrated in a liquid–liquid interfacial environment as supramolecular differentiation. (b) Various examples of nanoarchitectonics construction with fullerene (C_{60} and C_{70}) molecules using the liquid–liquid interfacial precipitation method. Reproduced from ref. 75 with permission from the Royal Society of Chemistry.

fullerene assemblies involving the transformation from eggs to tadpoles were demonstrated in liquid–liquid interfacial environments.[73]

Preparation of nano- and microstructures with predetermined morphologies through self-assembly is the key process of the bottom-up approaches to nanotechnology. In particular, construction of shape-defined nanomaterials of functional nanocarbons such as fullerenes could lead to development of highly versatile nanodevices. For example, at the interface between a good solvent and a poor solvent for derivatized fullerenes, supersaturation induces the formation of shape-defined nanostructures of fullerene molecules (Figure 1.8b). The shapes, dimensions, and sizes of the formed fullerene nanoarchitectures can be controlled by selection of combinations of good and poor solvents together with other physical parameters.[74]

On the other hand, and very recently, Ajayan and his collaborators[76] demonstrated that solvent-assisted ligand exchange (SALE) represents a powerful strategy for the design of multiple metal-organic frameworks with diverse and complex nanoarchitectures. By precisely adjusting the balance between the cleavage rate of old bonds and the formation rate of new bonds, many different metal-organic frameworks (MOF) materials displaying different types of MOF configurations ranging from 3D to 2D and 1D structures have been successfully created (Figure 1.9).

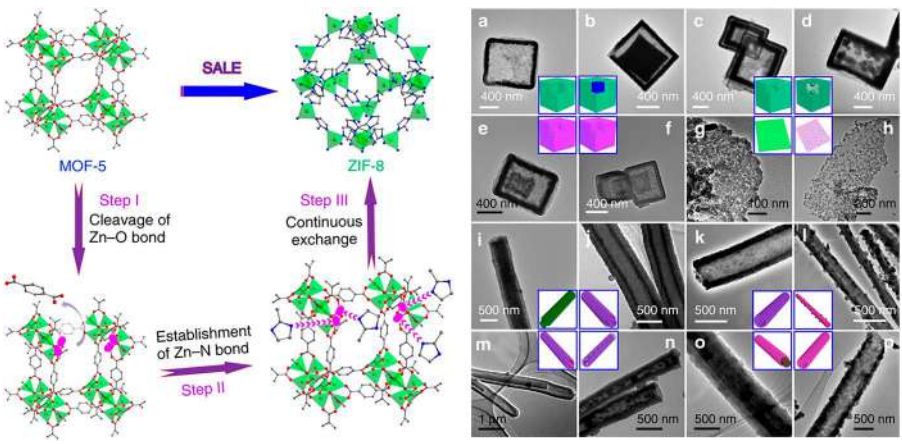

Figure 1.9 (Left panel) Schematic representation of a typical solvent-assisted ligand exchange (SALE) process with the transformation from MOF-5 to ZIF-8. (Right panel) Zeolitic imidazolate framework-based nanoarchitectures. TEM images of SH-ZIF-8 nanocube (a), yolk-shell MOF-5@ZIF-8 nanocube (b), DH-ZIF-8 nanocube (c), ball-in-box ZIF-8 nanocube (d), DH-ZnCo-ZIF nanocube (e), TH-ZnCo-ZIF nanocube (f), ZIF-8 nanosheet (g), sesame pancake-like Zn-HMT@ZIF-8 nanosheet (h), DT-ZIF-8 nanotube (i), DTZnCo- ZIF nanotube (j), ST-ZnCo-ZIF nanotube (k), bead-on-string hybrid structure (l), nanowire-nanotube hybrid structure (m), peapod-like structure (n), ZnCo-MOF-74@ZnCo-ZIF core–shell structure (o) and ZnCo-MOF-74-derived ZnCo-ZIF nanotube (p). Reproduced from ref. 75 with permission from Springer Nature, Copyright 2020.

The creation of dynamic molecular systems based on multicomponent assemblies is one of the main focuses of contemporary materials science. In these cases, the implementation of nanoarchitectonic concepts to attain control over multi-molecular organization at different hierarchic levels is essential to achieve specific functions. For example, Farha and co-workers at Northwestern University showed the controlled integration of enzymes and photosensitizers in a hierarchical mesoporous metal–organic framework in order to realize a highly efficient CO_2 fixation system.[77] Concomitantly, Feringa and co-workers[78] devised a strategy based on solvent-assisted solvent exchange to achieve spatial 3D organization of light-driven molecular motors in MOFs, thus opening the door to the use of molecular motors as tools for controlling dynamic functions in nanoarchitected crystalline materials (Figure 1.10).

Another key goal of nanoarchitectonics is to fill the gap between molecular sciences and device engineering in order to nurture the development of multiple technologies with their concomitant potential applications. Along these lines, after having made significant efforts in research the nanoscience community has managed to manipulate and integrate molecular systems into nano- and microsystems, thus creating bridge connecting nanostructures to the macroscopic world. Many recent advances in device engineering have been possible due to nanotechnological advancements together

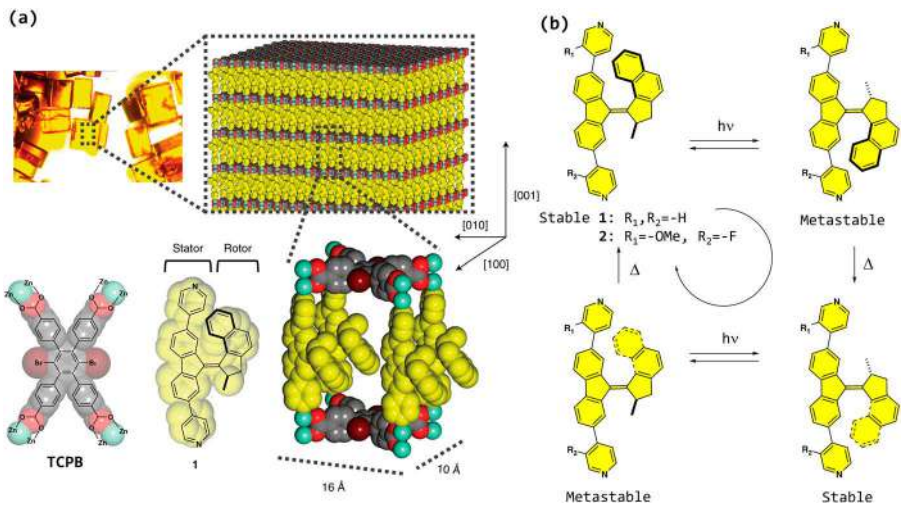

Figure 1.10 (a) Schematic representation of the 3D organization of molecular motor 1 in the moto-MOF. The fluorene unit is used to bridge the 2D layers constructed from Zn paddlewheel clusters and TCPB, while the naphthyl unit can rotate freely with respect to the other half. (b) Structures of motors and light-powered 360° unidirectional rotary cycle of the bipyridine motor. TCPB: 1,4-dibromo-2,3,5,6-tetrakis(4-carboxyph enyl)benzene. Reproduced from ref. 77 with permission from Springer Nature, Copyright 2019.

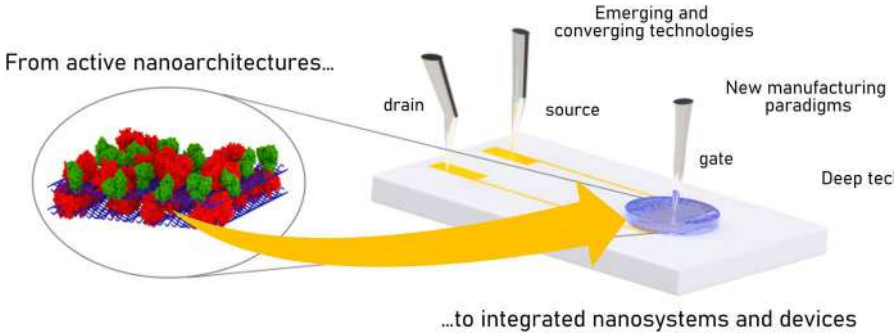

Figure 1.11 Integration of active nanoarchitectures and advanced molecular systems into nanodevices.

with the implementation of nanoarchitectonics concepts on nanodevice fabrication. By definition, a nanodevice is a device with at least one overall dimension in the nanoscale or comprising one or more nanoscale components essential to its operation.[79] The ultimate goal of these activities is to add nano-functionality to nanodevices in a standardized wafer-level production, at room-temperature, through a cost-effective process. In this context, a broad variety of materials such as organic semiconductor crystals, carbon nanotubes, conducting polymers, and graphene nanosheets were nanoarchitected by different means and integrated into non-volatile memories,[80] multi-valued logic circuits,[81] organic field-effect transistors,[82] organic photovoltaics,[83] fuel cells,[84] nanofluidic elements[85] biofuel cells,[86] and graphene field-effect transistors (Figure 1.11).[87]

1.5 Conclusions

Nanoarchitectonics embraces a concept for the development of materials with dynamic/adaptable functionalities based on the dynamic harmonization of atomic-/molecular-level manipulation and control, chemical nanofabrication, self-organization, and field-controlled organization. In some sense, the term "nanoarchitectonics" refers to a unified concept blending nanotechnology with supramolecular chemistry, self-assembly, and self-organization, with one goal in mind: *assembly of nanoscale objects into higher order functional materials.*

Looking at the literature over recent years, we observe that nanoarchitectonics concepts have pervaded many scientific and technological areas to a remarkable degree. Just to name a few examples, there are plenty of valuable nanoarchitectonic concepts and notions around supramolecular assemblies,[88] hybrid nanomaterials,[89] functional nanocomposites,[90] porous materials,[91] self-assembled supraparticles,[92] responsive nanoparticulate materials,[93] adaptive/responsive[94] and nanostructured surfaces,[95] nanocarbon science,[96] nanostructure fabrication,[97] (bio)sensing devices,[98]

biocompatible films,[99] batteries,[100] catalysis,[101] electrocatalysis,[102] capacitors,[103] and bio and medical science and technologies.[104]

Nanoarchitectonics shows us that the harmony between covalent and noncovalent interactions can lead to the emergence of large structures with unprecedented functions. Consequently, it seems plausible to stimulate possibilities for the transformation of nanoarchitectonics concepts into advanced nanoarchitected functional materials ready for integration in specific nanodevices. Viewed in this way, we anticipate that more wide-ranging developments of functional nanoscale materials and nanodevices are to be achieved through further advancement of nanoarchitectonics.

Acknowledgements

This work was supported by the Consejo Nacional de Investigaciones Científicas y Técnicas (CONICET, Argentina) (Grant No. PIP 0370), Agencia Nacional de Promoción Científica y Tecnológica (ANPCyT) (PICT 2016-1680, 2017-1523), the Austrian Institute of Technology GmbH (AIT-CONICET Partner Group: *"Exploratory Research for Advanced Technologies in Supramolecular Materials Science"*, Exp. 4947/11, Res. No. 3911, 28-12-2011), and Universidad Nacional de La Plata (UNLP). O.A. is a staff member of CONICET.

References

1. I. Freestone, N. Meeks, M. Saxs and C. Higgitt, *Gold Bull.*, 2007, **40**, 270.
2. E. Yong, *Carbon Nanotechnology in an 17th Century Damascus Sword*, National Geographic, 27 September, 2008, https://www.nationalgeographic.com/science/article/carbon-nanotechnology-in-an-17th-century-damascus-sword.
3. (a) J. M. Giussi, M. L. Cortez, W. A. Marmisollé and O. Azzaroni, *Chem. Soc. Rev.*, 2019, **48**, 814–849.
4. A. A. Ashdown, *J. Chem. Educ.*, 1927, **4**, 1217.
5. A. von Hippel, *Science*, 1956, **123**, 315–317.
6. http://calteches.library.caltech.edu/1976/.
7. N. Taniguchi, *On the Basic Concept of Nanotechnology*, Proceedings of the ICPE, Tokyo, 1974.
8. G. Binnig, H. Rohrer, C. h. Gerber and E. Weibel, *Appl. Phys. Lett.*, 1982, **40**, 178–180.
9. K. Eric Drexler, *Nanosystems: Molecular Machinery, Manufacturing, and Computation*, Wiley, New York, 1992.
10. (a) F. Wang, X. Zhang, X. Liu, C. Fan and Q. Li, *Small*, 2019, **15**, 1900013; (b) Y. Zhang, C. Wang, Y. Dong, D. Wang, T. Cao, S. Wang and D. Liu, *Adv. Funct. Mater.*, 2019, **29**, 1809097.
11. (a) X. Ma, A. C. Hortelão, T. Patiño and S. Sánchez, *ACS Nano*, 2016, **10**, 9111–9122; (b) A. C. Hortelão, T. Patiño, A. Perez-Jiménez, À. Blanco and S. Sánchez, *Adv. Funct. Mater.*, 2018, **2**, 1705086.

12. https://www.nobelprize.org/prizes/chemistry/1987/summary/.
13. https://www.nobelprize.org/prizes/chemistry/2016/summary/.
14. (a) J.-P. Sauvage, *Angew. Chem., Int. Ed.*, 2017, **56**, 11080–11093; (b) J. F. Stoddart, *Angew. Chem., Int. Ed.*, 2017, **56**, 11094–11125; (c) B. L. Feringa, *Angew. Chem., Int. Ed.*, 2017, **56**, 11060–11078.
15. (a) K. Ariga, Q. Ji, W. Nakanishi, J. P. Hill and M. Aono, *Mater. Horiz.*, 2015, **2**, 406; (b) M. Aono and K. Ariga, *Adv. Mater.*, 2016, **28**, 989.
16. A. J. Bard, *Integrated Chemical Systems: A Chemical Approach to Nanotechnology*, Wiley-Interscience, New York, 1994.
17. R. Jones, *Mater. Today*, 2005, **8**, 56.
18. C. T. Kresge, M. E. Leonowicz, W. J. Roth, J. C. Vartuli and J. S. Beck, *Nature*, 1992, **359**, 710.
19. C. B. Murray, D. J. Norris and M. G. Bawendi, *J. Am. Chem. Soc.*, 1993, **115**(19), 8706–8715.
20. L. E. Brus, *J. Chem. Phys.*, 1984, **80**, 4403.
21. https://www.nobelprize.org/prizes/physics/2010/summary/.
22. A. Kumar and G. M. Whitesides, *Appl. Phys. Lett.*, 1993, **63**, 2002.
23. Y. Xia and G. M. Whitesides, *Angew. Chem., Int. Ed.*, 1998, **37**, 550–575.
24. R. D. Piner, J. Zhu, F. Xu, S. Hong and C. A. Mirkin, *Science*, 1999, **283**, 661–663.
25. G. Markovich, C. P. Collier, S. E. Henrichs, F. Remacle, R. D. Levine and J. R. Heath, *Acc. Chem. Res.*, 1999, **32**, 415.
26. https://www.merriam-webster.com/dictionary/architectonic.
27. (a) K. Ariga, Q. Ji, J. P. Hill, Y. Bando and M. Aono, *NPG Asia Mater.*, 2012, **4**, e17; (b) K. Ariga and M. Aono, *Jpn. J. Appl. Phys.*, 2016, **55**, 1102A6.
28. S. Hecht, *Angew. Chem., Int. Ed.*, 2003, **42**, 24.
29. (a) F. Goettmann and C. Sanchez, *J. Mater. Chem.*, 2007, **17**, 24–30; (b) R. A. Schoonheydt and B. M. Weckhuysen, *Phys. Chem. Chem. Phys.*, 2009, **11**, 2794–2798; (c) Y. Wu, G. Cheng, K. Katsov, S. W. Sides, J. Wang, J. Tang, G. H. Frederickson, M. Moskovits and G. D. Stucky, *Nat. Mater.*, 2004, **3**, 816–822; (d) O. Azzaroni, B. Trappmann, P. van Rijn, F. Zhou, B. Kong and W. T. S. Huck, *Angew. Chem., Int. Ed.*, 2006, **45**, 7440–7443; (e) G. Laucirica, G. Pérez-Mitta, M. E. Toimil-Molares, C. Trautmann, W. Marmisollé and O. Azzaroni, *J. Phys. Chem. C*, 2019, **123**, 28997–29007; (f) F. M. Gilles, F. M. Boubeta, O. Azzaroni, I. Szleifer and M. Tagliazucchi, *J. Phys. Chem. C*, 2018, **122**, 6669–6677; (g) G. Pérez-Mitta, A. Albesa, F. M. Gilles, M. E. Toimil-Molares, C. Trautmann and O. Azzaroni, *J. Phys. Chem. C*, 2017, **121**, 9070–9076; (h) F. M. Gilles, M. Tagliazucchi, O. Azzaroni and I. Szleifer, *J. Phys. Chem. C*, 2016, **120**, 4789–4798; (i) M. Tagliazucchi, O. Azzaroni and I. Szleifer, *J. Am. Chem. Soc.*, 2010, **132**, 12404–12411.
30. P. Kujawa and F. M. Winnik, *Polym. Int.*, 2014, **63**, 377–380.
31. G. Laucirica, W. A. Marmisollé and O. Azzaroni, *Phys. Chem. Chem. Phys.*, 2017, **19**, 8612–8620.
32. J. W. Steed and J. L. Atwood, *Supramolecular Chemistry*, John Wiley & Sons, Ltd, Chichester, 2nd edn, 2009.

33. K. N. Houk, A. G. Leach, S. P. Kim and X. Zhang, *Angew. Chem., Int. Ed.*, 2003, **42**, 4872–4897.
34. (a) O. Azzaroni and K. Ariga, *Mol. Syst. Des. Eng.*, 2019, **4**, 9–10; (b) P. Kujawa and F. M. Winnik, *Langmuir*, 2013, **29**, 7354–7361.
35. R. J. Wojtecki, M. A. Meador and S. J. Rowan, *Nat. Mater.*, 2011, **10**, 14–27.
36. G. Pérez-Mitta, A. G. Albesa, M. E. Toimil Molares, C. Trautmann and O. Azzaroni, *ChemPhysChem*, 2016, **17**, 2718–2725.
37. A. H. Gröschel, F. H. Schacher, H. Schmalz, O. V. Borisov, E. B. Zhulina, A. Walther and A. H. E. Müller, *Nat. Commun.*, 2012, **3**, 710.
38. G. Laucirica, M. E. Toimil-Molares, C. Trautmann, W. Marmisollé and O. Azzaroni, *ACS Appl. Mater. Interfaces*, 2020, **12**, 28148–28157.
39. (a) S. Acharya, A. Shundo, J. P. Hill and K. Ariga, *J. Nanosci. Nanotechnol.*, 2009, **9**, 3; (b) S. Acharya, J. P. Hill and K. Ariga, *Adv. Mater.*, 2009, **21**, 2959.
40. (a) K. Ariga, J. P. Hill and Q. Ji, *Phys. Chem. Chem. Phys.*, 2007, **9**, 2319; (b) N. Fujii, K. Fujimoto, T. Michinobu, M. Akada, J. P. Hill, S. Shiratori, K. Ariga and K. Shigehara, *Macromolecules*, 2010, **43**, 3947.
41. (a) N. Shirahata, S. Furumi, Y. Masuda, A. Hozumi and Y. Sakka, *Thin Solid Films*, 2008, **516**, 2541; (b) N. Shirahata, A. Hozumi and Y. Sakka, *J. Nanosci. Nanotechnol.*, 2009, **9**, 666.
42. (a) B. Yameen, A. Kaltbeitzel, A. Langner, H. Duran, M. F. Müller, U. Gösele, O. Azzaroni and W. Knoll, *J. Am. Chem. Soc.*, 2008, **130**, 13140–13144; (b) B. Yameen, A. Kaltbeitzel, G. Glasser, A. Langner, F. Müller, U. Gösele, W. Knoll and O. Azzaroni, *ACS Appl. Mater. Interfaces*, 2010, **2**, 279–287; (c) B. Yameen, A. Kaltbeitzel, A. Langner, F. Müller, U. Gösele, W. Knoll and O. Azzaroni, *Angew. Chem., Int. Ed.*, 2009, **48**, 3124–3128; (d) S. E. Moya, O. Azzaroni, T. Kelby, E. Donath and W. T. S. Huck, *J. Phys. Chem. B*, 2007, **111**, 7034–7040; (e) O. Azzaroni, B. Trappmann, P. van Rijn, F. Zhou, B. Kong and W. T. S. Huck, *Angew. Chem., Int. Ed.*, 2006, **118**, 7600–7603; (f) O. Azzaroni, S. E. Moya, A. A. Brown, Z. Zheng, E. Donath and W. T. S. Huck, *Adv. Funct. Mater.*, 2006, **16**, 1037–1042; (g) O. Azzaroni, A. A. Brown and W. T. S. Huck, *Angew. Chem., Int. Ed.*, 2006, **118**, 1802–1806.
43. K. Akatsuka, M. Haga, Y. Ebina, M. Osada, K. Fukuda and T. Sasaki, *ACS Nano*, 2009, **3**, 1097.
44. P. C. Claro, M. E. Coustet, C. Diaz, E. Maza, M. S. Cortizo, F. G. Requejo, L. I. Pietrasanta, M. R. Ceolín and O. Azzaroni, *Soft Matter*, 2013, **9**, 10899.
45. K. Ariga, M. V. Lee, T. Mori, X.-Y. Yu and J. P. Hill, *Adv. Colloid Interface Sci.*, 2010, **154**, 20.
46. Y. Yonamine, K. Cervantes-Salguero, W. Nakanishi, I. Kawamata, K. Minami, H. Komatsu, S. Murata, J. P. Hill and K. Ariga, *Phys. Chem. Chem. Phys.*, 2015, **17**, 32122–32125.
47. Y. Yonamine, K. Cervantes-Salguero, K. Minami, I. Kawamata, W. Nakanishi, J. P. Hill, S. Murata and K. Ariga, *Phys. Chem. Chem. Phys.*, 2016, **18**, 12576–12581.

48. (a) K. Ariga and T. Kunitake, *Acc. Chem. Res.*, 1998, **31**, 371; (b) K. Ariga, T. Michinobu, T. Nakanishi and J. P. Hill, *Curr. Opin. Colloid Interface Sci.*, 2008, **13**, 23.
49. K. Ariga, *J. Photopolym. Sci. Technol.*, 2008, **21**, 553.
50. K. Ariga, S. Watanabe, T. Mori and J. Takeya, *NPG Asia Mater.*, 2018, **10**, 90–106.
51. K. Ariga, M. Nishikawa, T. Mori, J. Takeya, L. K. Shrestha and J. P. Hill, *Sci. Technol. Adv. Mater.*, 2019, **20**, 51–95.
52. (a) W. A. Marmisollé, E. Maza, S. Moya and O. Azzaroni, *Electrochim. Acta*, 2016, **210**, 435–444; (b) W. A. Marmisollé and O. Azzaroni, *Nanoscale*, 2016, **8**, 9890–9918; (c) E. Maza, J. S. Tuninetti, N. Politakos, W. Knoll, S. Moya and O. Azzaroni, *Phys. Chem. Chem. Phys.*, 2015, **17**, 29935–29948; (d) M. Coustet, J. Irigoyen, T. A. García, R. A. Murray, G. Romero, M. S. Cortizo, W. Knoll, O. Azzaroni and S. E. Moya, *J. Colloid Interface Sci.*, 2014, **421**, 132–140.
53. J. Irigoyen, S. E. Moya, J. J. Iturri, I. Llarena, O. Azzaroni and E. Donath, *Langmuir*, 2009, **25**, 3374–3380.
54. (a) K. Ariga, Q. Ji, J. P. Hill and A. Vinu, *Soft Matter*, 2009, **5**, 3562; (b) Q. Ji, M. Miyahara, J. P. Hill, S. Acharya, A. Vinu, S. B. Yoon, J.-S. Yu, K. Sakamoto and K. Ariga, *J. Am. Chem. Soc.*, 2008, **130**, 2376; (c) Q. Ji, S. Acharya, J. P. Hill, A. Vinu, S. B. Yoon, J.-S. Yu, K. Sakamoto and K. Ariga, *Adv. Funct. Mater.*, 2009, **19**, 1792; (d) E. Piccinini, M. Ceolín, F. Battaglini and O. Azzaroni, *ChemPlusChem*, 2020, **85**, 1616–1622.
55. (a) D. Pallarola, N. Queralto, W. Knoll, O. Azzaroni and F. Battaglini, *Chem. - Eur. J.*, 2010, **16**, 13970–13975; (b) D. Pallarola, C. von Bildering, L. I. Pietrasanta, N. Queralto, W. Knoll, F. Battaglini and O. Azzaroni, *Phys. Chem. Chem. Phys.*, 2012, **14**, 11027–11039; (c) L. D. Sappia, E. Piccinini, W. Marmisollé, N. Santilli, E. Maza, S. Moya, F. Battaglini, R. E. Madrid and O. Azzaroni, *Adv. Mater. Interfaces*, 2017, **4**, 1700502; (d) O. Azzaroni, M. Alvarez, A. I. Abou-Kandil, B. Yameen and W. Knoll, *Adv. Funct. Mater.*, 2008, **18**, 3487–3496.
56. (a) M. L. Cortez, A. Lorenzo, W. A. Marmisollé, C. von Bilderling, E. Maza, L. Pietrasanta, F. Battaglini, M. Ceolín and O. Azzaroni, *Soft Matter*, 2018, **14**, 1939; (b) M. L. Cortez, G. A. González, M. Ceolín, O. Azzaroni and F. Battaglini, *Electrochim. Acta*, 2014, **118**, 124; (c) M. L. Cortez, D. Pallarola, M. Ceolín, O. Azzaroni and F. Battaglini, *Anal. Chem.*, 2013, **85**, 2414; (d) M. L. Cortez, M. Ceolín, O. Azzaroni and F. Battaglini, *Bioelectrochemistry*, 2015, **105**, 117; (e) A. Lorenzo, W. A. Marmisollé, E. M. Maza, M. Ceolín and O. Azzaroni, *Phys. Chem. Chem. Phys.*, 2018, **20**, 7570–7578; (f) E. Piccinini, J. S. Tuninetti, J. I. Otamendi, S. E. Moya, M. Ceolín, F. Battaglini and O. Azzaroni, *Phys. Chem. Chem. Phys.*, 2018, **20**, 9298–9308; (g) M. L. Cortez, M. Ceolín, L. Cuellar Camacho, E. Donath, S. E. Moya, F. Battaglini and O. Azzaroni, *ACS Appl. Mater. Interfaces*, 2017, **9**, 1119–1128; (h) M. L. Cortez, N. De Matteis, M. Ceolín, W. Knoll, F. Battaglini and O. Azzaroni, *Phys. Chem. Chem. Phys.*, 2014, **16**, 20844–20855.

57. M. L. Cortez, D. Pallarola, M. Ceolín, O. Azzaroni and F. Battaglini, *Chem. Commun.*, 2012, **48**, 10868.
58. (a) O. Azzaroni and K. H. A. Lau, *Soft Matter*, 2011, **7**, 8709–8724; (b) M. Ali, B. Yameen, J. Cervera, P. Ramirez, R. Neumann, W. Ensinger, W. Knoll and O. Azzaroni, *J. Am. Chem. Soc.*, 2010, **132**, 8338–8348.
59. K. Ariga, Q. Ji, J. P. Hill, Y. Bando and M. Aono, *NPG Asia Mater.*, 2012, **4**, e17.
60. (a) O. Azzaroni, M. E. Vela, M. Fonticelli, G. Benitez, P. Carro, B. Blum and R. C. Salvarezza, *J. Phys. Chem. B*, 2003, **107**, 13446–13454; (b) M. Fonticelli, O. Azzaroni, G. Benitez, M. E. Martins, P. Carro and R. C. Salvarezza, *J. Phys. Chem. B*, 2004, **108**, 1898–1905; (c) O. Azzaroni, M. E. Vela, H. Martin, A. Hernández Creus, G. Andreasen and R. C. Salvarezza, *Langmuir*, 2001, **17**, 6647–6654.
61. (a) R. J. Jackman, J. L. Wilbur and G. M. Whitesides, *Science*, 1995, **269**, 664–666; (b) D. B. Wolfe, J. C. Love, K. E. Paul, M. L. Chabinyc and G. M. Whitesides, *Appl. Phys. Lett.*, 2002, **80**, 2222; (c) Y. Xia, M. Mrksich, E. Kim and G. M. Whitesides, *J. Am. Chem. Soc.*, 1995, **117**, 9576–9577.
62. (a) J. J. Gooding and S. Ciampi, *Chem. Soc. Rev.*, 2011, **40**, 2704–2718; (b) D. Samanta and A. Sarkar, *Chem. Soc. Rev.*, 2011, **40**, 2567–2592.
63. O. Azzaroni, M. Cipollone, M. E. Vela and R. C. Salvarezza, *Langmuir*, 2001, **17**, 1483–1487.
64. (a) K. D. Schierbaum, T. Weiss, E. U. T. van Veizen, J. F. J. Engbersen, D. N. Reinhoudt and W. Göpel, *Science*, 1994, **265**, 1413–1415; (b) J. Spinke, M. Liley, H. J. Guder, L. Angermaier and W. Knoll, *Langmuir*, 1993, **9**, 1821–1825; (c) B.-H. Huisman, R. P. H. Kooyman, F. C. J. M. van Veggel and D. N. Reinhoudt, *Adv. Mater.*, 1996, **8**, 561–564.
65. (a) S. Casalini, C. A. Bortolotti, F. Leonardi and F. Biscarini, *Chem. Soc. Rev.*, 2017, **46**, 40–71; (b) J.-R. Koo, S.-W. Pyo, J.-H. Kim, H.-K. Lee and Y. K. Kim, *Jpn. J. Appl. Phys.*, 2005, **44**, 566–569; (c) G. D. Kong, S. E. Byeon, S. Park, H. Song, S.-Y. Kim and H. J. Yoon, *Adv. Electron. Mater.*, 2020, **6**, 1901157.
66. (a) P. L. Schilardi, P. Dip, P. C. dos Santos Claro, G. A. Benítez, M. H. Fonticelli, O. Azzaroni and R. C. Salvarezza, *Chem. - Eur. J.*, 2006, **12**, 38–49; (b) O. Azzaroni, P. L. Schilardi, R. C. Salvarezza, J. Manuel-Herrero, C. Zaldo and L. Vásquez, *Appl. Phys. A*, 2005, **81**, 1113–1116; (c) M. A. Auger, P. L. Schilardi, I. Caretti, O. Sánchez, G. Benítez, J. M. Albella, R. Gago, M. Fonticelli, L. Vázquez, R. C. Salvarezza and O. Azzaroni, *Small*, 2004, **1**, 300–309; (d) O. Azzaroni, M. Fonticelli, P. L. Schilardi, G. Benitez, I. Caretti, J. M. Albella, R. Gago, L. Vázquez and R. C. Salvarezza, *Nanotechnology*, 2004, **15**, S197; (e) O. Azzaroni, P. L. Schilardi and R. C. Salvarezza, *Electrochim. Acta*, 2003, **48**, 3107–3114; (f) O. Azzaroni, P. L. Schilardi and R. C. Salvarezza, *Appl. Phys. Lett.*, 2002, **80**, 1061–1063; (g) O. Azzaroni, P. L. Schilardi and R. C. Salvarezza, *Nano Lett.*, 2001, **1**, 291–294.
67. (a) E. Katz and I. Willner, *Angew. Chem., Int. Ed.*, 2004, **43**, 6042–6108; (b) I. Willner and E. Katz, *Angew. Chem., Int. Ed.*, 2000, **39**, 1180–1218; (c) I. Willner, V. Heleg-Shabtai, R. Blonder, E. Katz, G. Tao, A. F. Bückmann and A. Heller, *J. Am. Chem. Soc.*, 1996, **118**, 10321–10322.

68. A. B. Descalzo, R. Martínez-Máñez, F. Sancenón, K. Hoffmann and K. Rurack, *Angew. Chem., Int. Ed.*, 2006, **45**, 5924–5948.
69. A. Calvo, B. Yameen, F. J. Williams, G. J. A. A. Soler-Illia and O. Azzaroni, *J. Am. Chem. Soc.*, 2009, **131**, 10866–10868.
70. (a) S. Schmidt, S. Alberti, P. Vana, G. J. A. A. Soler-Illia and O. Azzaroni, *Chem. - Eur. J.*, 2009, **23**(58), 14500–14506; (b) A. Andrieu-Brunsen, S. Micoureau, M. Tagliazucchi, I. Szleifer, O. Azzaroni and G. J. A. A. Soler-Illia, *Chem. Mater.*, 2015, **27**, 808–821; (c) S. Alberti, G. J. A. A. Soler-Illia and O. Azzaroni, *Chem. Commun.*, 2015, **51**, 6050–6075; (d) A. Brunsen, C. Díaz, L. I. Pietrasanta, B. Yameen, M. Ceolín, G. J. A. A. Soler-Illia and O. Azzaroni, *Langmuir*, 2012, **28**, 3583–3592; (e) A. Brunsen, J. Cui, M. Ceolín, A. del Campo, G. J. A. A. Soler-Illia and O. Azzaroni, *Chem. Commun.*, 2012, **48**, 1422–1424; (f) A. Brunsen, A. Calvo, F. J. Williams, G. J. A. A. Soler-Illia and O. Azzaroni, *Langmuir*, 2011, **27**, 4328–4333; (g) G. J. A. A. Soler-Illia and O. Azzaroni, *Chem. Soc. Rev.*, 2011, **40**, 1107–1150.
71. L. Zhang, Y. Chen, Z. Li, L. Li, P. Saint-Cricq, C. Li, J. Lin, C. Wang, Z. Su and J. I. Zink, *Angew. Chem., Int. Ed.*, 2016, **55**, 2118.
72. K. Ariga, D. T. Leong and T. Mori, *Adv. Funct. Mater.*, 2017, **28**, 1702905.
73. P. Bairi, K. Minami, J. P. Hill, W. Nakanishi, L. K. Shrestha, C. Liu, K. Harano, E. Nakamura and K. Ariga, *ACS Nano*, 2016, **10**, 8796–8802.
74. (a) M. Sathish, K. Miyazawa, J. P. Hill and K. Ariga, *J. Am. Chem. Soc.*, 2009, **131**, 6372; (b) L. K. Shrestha, R. G. Shrestha, J. P. Hill, T. Tsuruoka, Q. Ji, T. Nishimura and K. Ariga, *Langmuir*, 2016, **21**, 12511.
75. K. Ariga, X. Jia and L. K. Shrestha, *Mol. Syst. Des. Eng.*, 2019, **4**, 49.
76. D. Yu, Q. Shao, Q. Song, J. Cui, Y. Zhang, B. Wu, L. Ge, Y. Wang, Y. Zhang, Y. Qin, R. Vajtai, P. M. Ajayan, H. Wang, T. Xu and Y. Wu, *Nat. Commun.*, 2020, **11**, 927.
77. Y. Chen, P. Li, J. Zhou, C. T. Buru, L. Đorđević, P. Li, X. Zhang, M. M. Cetin, J. F. Stoddart, S. I. Stupp, M. R. Wasielewski and O. K. Farha, *J. Am. Chem. Soc.*, 2020, **142**, 1768–1773.
78. W. Danowski, T. van Leeuwen, S. Abdolahzadeh, D. Roke, W. R. Browne, S. J. Wezenberg and B. L. Feringa, *Nat. Nanotechnol.*, 2019, **14**, 488–494.
79. J. J. Ramsden, *Nanotechnology: An Introduction*, Elsevier, Amsterdam, 2011.
80. (a) D. Chaudhary, S. Munjal, N. Khare and V. D. Vankar, *Carbon*, 2018, **130**, 553–558; (b) L. Kou, F. Li, W. Chen and T. Guo, *Org. Electron.*, 2013, **14**, 1447–1451; (c) B. Cho, K. Kim, C.-L. Chen, A. M. Shen, Q. Truong and Y. Chen, *Small*, 2013, **9**, 2283–2287.
81. K. Kobashi, R. Hayakawa, T. Chikyow and Y. Wakayama, *Nano Lett.*, 2018, **18**(7), 4355–4359.
82. (a) L. Torsi, M. Magliulo, K. Manolia and G. Palazzo, *Chem. Soc. Rev.*, 2013, **42**, 8612–8628; (b) S. Yuvaraja, A. Nawaz, Q. Liu, D. Dubal, S. G. Surya, K. N. Salama and P. Sonar, *Chem. Soc. Rev.*, 2020, **49**, 3423–3460.
83. (a) X. Wan, C. Li, M. Zhang and Y. Chen, *Chem. Soc. Rev.*, 2020, **49**, 2828–2842; (b) A. Bessette and G. S. Hanan, *Chem. Soc. Rev.*, 2014, **43**, 3342–3405; (c) J. Li and A. C. Grimsdale, *Chem. Soc. Rev.*, 2010, **39**, 2399–2410.

84. (a) Y. Xiang, S. Lu and S. P. Jiang, *Chem. Soc. Rev.*, 2012, **41**, 7291–7321; (b) M. A. Z. G. Sial, M. A. U. Dina and X. Wang, *Chem. Soc. Rev.*, 2018, **47**, 6175–6200.
85. (a) G. Laucirica, V. Cayón, M. L. Cortez, Y. T. Terrones, M. E. Toimil-Molares, C. Trautmann, W. Marmisollé, O. Azzaroni, *Nanoscale*, 2020, **12**, 18390–18399; (b) G. Laucirica, V. M. Cayón, Y. T. Terrones, M. L. Cortez, M. E. Toimil-Molares, C. Trautmann, W. Marmisollé and O. Azzaroni, *Nanoscale*, 2020, **12**, 6002–6011; (c) G. Pérez-Mitta, M. E. Toimil-Molares, C. Trautmann, W. A. Marmisollé and O. Azzaroni, *Adv. Mater.*, 2019, **31**, 1901483; (d) G. Laucirica, W. A. Marmisollé, M. E. Toimil-Molares, C. Trautmann, W. Marmisollé and O. Azzaroni, *ACS Appl. Mater. Interfaces*, 2019, **11**, 30001–30009; (e) G. Pérez-Mitta, W. A. Marmisolle, L. Burr, M. E. Toimil-Molares, C. Trautmann, W. Marmisollé and O. Azzaroni, *Small*, 2018, **14**, 1703144; (f) G. Pérez-Mitta, W. A. Marmisollé, A. G. Albesa, M. E. Toimil-Molares, C. Trautmann and O. Azzaroni, *Small*, 2018, **14**, 1702131; (g) G. Pérez-Mitta, A. S. Peinetti, M. L. Cortez, M. E. Toimil-Molares, C. Trautmann and O. Azzaroni, *Nano Lett.*, 2018, **18**, 3303–3310; (h) G. Pérez-Mitta, W. A. Marmisollé, C. Trautmann, M. E. Toimil-Molares and O. Azzaroni, *Adv. Mater.*, 2017, **29**, 1700972; (i) G. Pérez-Mitta, A. G. Albesa, C. Trautmann, M. E. Toimil-Molares and O. Azzaroni, *Chem. Sci.*, 2017, **8**, 890–913; (j) G. Pérez-Mitta, L. Burr, J. S. Tuninetti, C. Trautmann, M. E. Toimil-Molares and O. Azzaroni, *Nanoscale*, 2016, **8**, 1470–1478; (k) G. Pérez-Mitta, W. A. Marmisollé, C. Trautmann, M. E. Toimil-Molares and O. Azzaroni, *J. Am. Chem. Soc.*, 2015, **137**, 15382–15385; (l) G. Pérez-Mitta, J. S. Tuninetti, W. Knoll, C. Trautmann, M. E. Toimil-Molares and O. Azzaroni, *J. Am. Chem. Soc.*, 2015, **137**, 6011–6017; (m) G. Pérez-Mitta, A. G. Albesa, W. Knoll, C. Trautmann, M. E. Toimil-Molares and O. Azzaroni, *Nanoscale*, 2015, **7**, 15594–15598; (n) B. Yameen, M. Ali, M. Álvarez, R. Neumann, W. Ensinger, W. Knoll and O. Azzaroni, *Polym. Chem.*, 2010, **1**, 183–192; (o) B. Yameen, M. Ali, R. Neumann, W. Ensinger, W. Knoll and O. Azzaroni, *Chem. Commun.*, 2010, **46**, 1908–1910; (p) B. Yameen, M. Ali, R. Neumann, W. Ensinger, W. Knoll and O. Azzaroni, *Nano Lett.*, 2009, **9**, 2788–2793; (q) B. Yameen, M. Ali, R. Neumann, W. Ensinger, W. Knoll and O. Azzaroni, *Small*, 2009, **5**, 1287–1291.
86. (a) T. Nöll and G. Nöll, *Chem. Soc. Rev.*, 2011, **40**, 3564–3576; (b) C.-e. Zhao, P. Gai, R. Song, Y. Chen, J. Zhang and J.-J. Zhu, *Chem. Soc. Rev.*, 2017, **46**, 1545–1564.
87. (a) G. E. Fenoy, W. A. Marmisollé, O. Azzaroni and W. Knoll, *Biosens. Bioelectron.*, 2020, **148**, 111796; (b) E. Piccinini, C. Bliem, J. M. Giussi, W. Knoll and O. Azzaroni, *Langmuir*, 2019, **35**, 8038–8044; (c) T. Berninger, C. Bliem, E. Piccinini, O. Azzaroni and W. Knoll, *Biosens. Bioelectron.*, 2018, **115**, 104–110; (d) E. Piccinini, S. Alberti, G. S. Longo, T. Berninger, J. Breu, J. Dostalek, O. Azzaroni and W. Knoll, *J. Phys. Chem. C*, 2018, **122**, 10181–10188; (e) E. Piccinini, C. Bliem, C. Reiner-Rozman, F. Battaglini, O. Azzaroni and W. Knoll, *Biosens. Bioelectron.*, 2017, **92**, 661–667.

88. (a) M. Ramanathan, L. K. Shrestha, T. Mori, Q. Ji, J. P. Hill and K. Ariga, *Phys. Chem. Chem. Phys.*, 2013, **15**, 10580; (b) M. Ramanathan, K. L. Hong, Q. Ji, Y. Yonamine, J. P. Hill and K. Ariga, *J. Nanosci. Nanotechnol.*, 2014, **14**, 390; (c) H. Hamoudi, *Nanoscale Res. Lett.*, 2014, **9**, 287; (d) M. Pandeeswar and T. Govindaraju, *J. Inorg. Organomet. Polym. Mater.*, 2015, **25**, 293; (e) S. E. Herrera, M. L. Agazzi, M. L. Cortez, W. A. Marmisollé, C. von Bilderling and O. Azzaroni, *Macromol. Chem. Phys.*, 2019, **220**, 1900094; (f) D. Zappi, L. L. Coria-Oriundo, E. Piccinini, M. Gramajo, C. von Bilderling, L. I. Pietrasanta, O. Azzaroni and F. Battaglini, *Phys. Chem. Chem. Phys.*, 2019, **21**, 22947–22954; (g) M. L. Agazzi, S. E. Herrera, M. L. Cortez, W. A. Marmisollé, C. von Bilderling and O. Azzaroni, *Soft Matter*, 2019, **15**, 1640–1650; (h) W. A. Marmisollé, J. Irigoyen, D. Gregurec, S. Moya and O. Azzaroni, *Adv. Funct. Mater.*, 2015, **25**, 4144–4152; (i) A. S. Picco, W. Knoll, M. Ceolín and O. Azzaroni, *ACS Macro Lett.*, 2015, **4**, 94–100; (j) A. S. Picco, E. Zelaya, O. Azzaroni and M. Ceolín, *J. Colloid Interface Sci.*, 2013, **397**, 206–209; (k) A. S. Picco, B. Yameen, O. Azzaroni and M. Ceolín, *Chem. Commun.*, 2011, **47**, 3802–3804; (l) O. Azzaroni, M. Alvarez, M. Mir, B. Yameen and W. Knoll, *J. Phys. Chem. C*, 2008, **112**, 15850–15859; (m) O. Azzaroni, M. Mir and W. Knoll, *J. Phys. Chem. B*, 2007, **111**, 13499–13503.
89. (a) K. Ariga, A. Vinu, Y. Yamauchi, Q. Ji and J. P. Hill, *Bull. Chem. Soc. Jpn.*, 2012, **85**, 1; (b) L. Zerkoune, A. Angelova and S. Lesieur, *Nanomaterials*, 2014, **4**, 741; (c) M. J. Penelas, C. B. Contreras, P. C. Angelomé, A. Wolosiuk, O. Azzaroni and G. J. A. A. Soler-Illia, *Langmuir*, 2020, **36**, 1965–1974; (d) R. E. Giménez, E. Piccinini, O. Azzaroni and M. Rafti, *ACS Omega*, 2019, **4**, 842–848; (e) G. M. Segovia, J. S. Tuninetti, S. Moya, A. S. Picco, M. R. Ceolín, O. Azzaroni and M. Rafti, *Mater. Today Chem.*, 2018, **8**, 29–35.
90. (a) M. I. Velasco, R. H. Acosta, W. A. Marmisollé, O. Azzaroni and M. Rafti, *J. Phys. Chem. C*, 2019, **123**, 21076–21082; (b) M. J. Penelas, C. B. Contreras, J. M. Giussi, A. Wolosiuk, O. Azzaroni and G. J. A. A. Soler-Illia, *Colloids Surf., A*, 2019, **574**, 12–20; (c) L. D. Sappia, J. S. Tuninetti, M. Ceolín, W. Knoll, M. Rafti and O. Azzaroni, *Global Challenges*, 2020, **4**, 1900076; (d) J. A. Allegretto, J. M. Giussi, S. E. Moya, O. Azzaroni and M. Rafti, *RSC Adv.*, 2020, **10**, 2453–2461; (e) J. Scotto, E. Piccinini, C. von Bilderling, L. L. Coria-Oriundo, F. Battaglini, W. Knoll, W. A. Marmisollé and O. Azzaroni, *Appl. Surf. Sci.*, 2020, **525**, 146440; (f) L. D. Sappia, E. Piccinini, C. von Binderling, W. Knoll, W. Marmisollé and O. Azzaroni, *Mater. Sci. Eng. C*, 2020, **109**, 110575.
91. J. S. Tuninetti, M. Rafti, A. Andrieu-Brunsen and O. Azzaroni, *Microporous Mesoporous Mater.*, 2016, **220**, 253–257.
92. (a) A. S. Picco, B. Yameen, W. Knoll, M. R. Ceolín and O. Azzaroni, *J. Colloid Interface Sci.*, 2016, **471**, 71–75; (b) E. Piccinini, D. Pallarola, F. Battaglini and O. Azzaroni, *Mol. Syst. Des. Eng.*, 2016, **1**, 155–162; (c) E. Piccinini, D. Pallarola, F. Battaglini and O. Azzaroni, *Chem. Commun.*, 2015, **51**, 14754–14757.

93. (a) S. E. Herrera, M. L. Agazzi, M. L. Cortez, W. A. Marmisollé, M. Tagliazucchi and O. Azzaroni, *Phys. Chem. Chem. Phys.*, 2020, **22**, 7440–7450; (b) J. M. Giussi, M. M. Moro, A. Iborra, M. L. Cortez, D. Di Silvio, I. L. Conde, I. Llarena Conde, G. S. Longo, O. Azzaroni and S. Moya, *Soft Matter*, 2020, **16**, 881–890; (c) A. Iborra, L. Salvatierra, J. M. Giussi and O. Azzaroni, *Eur. Polym. J.*, 2019, **116**, 117–125; (d) S. E. Herrera, M. L. Agazzi, M. L. Cortez, W. A. Marmisollé, M. Tagliazucchi and O. Azzaroni, *ChemPhysChem*, 2019, **20**, 1044–1053; (e) S. E. Herrera, M. L. Agazzi, M. L. Cortez, W. A. Marmisollé, M. Tagliazucchi and O. Azzaroni, *Chem. Commun.*, 2019, **55**, 14653–14656; (f) J. M. Giussi, M. I. Velasco, G. S. Longo, R. H. Acosta and O. Azzaroni, *Soft Matter*, 2015, **11**, 8879–8886.
94. (a) G. E. Fenoy, J. M. Giussi, C. von Bilderling, E. M. Maza, L. I. Pietrasanta, W. Knoll, W. Marmisollé and O. Azzaroni, *J. Colloid Interface Sci.*, 2018, **518**, 92–101; (b) T. Alonso-García, C. A. Gervasi, M. J. Rodríguez-Presa, E. Gutiérrez-Pineda, S. E. Moya and O. Azzaroni, *J. Phys. Chem. C*, 2013, **117**, 26680–26688; (c) O. Azzaroni, *J. Polym. Sci., Part A: Polym. Chem.*, 2012, **50**, 3225–3258; (d) J. Cui, T. H. Nguyen, M. Ceolín, R. Berger, O. Azzaroni and A. del Campo, *Macromolecules*, 2012, **45**, 3213–3220; (e) J. Cui, O. Azzaroni and A. del Campo, *Macromol. Rapid Commun.*, 2011, **32**, 1699–1703; (f) B. Yameen, M. Alvarez, O. Azzaroni, U. Jonas and W. Knoll, *Langmuir*, 2009, **25**, 6214–6220; (g) A. A. Brown, O. Azzaroni, L. M. Fidalgo and W. T. S. Huck, *Soft Matter*, 2009, **5**, 2738–2745.
95. (a) J. A. Allegretto, J. Dostalek, M. Rafti, B. Menges, O. Azzaroni and W. Knoll, *J. Phys. Chem. A*, 2018, **123**, 1100–1109; (b) E. Maza, C. von Bilderling, M. L. Cortez, G. Díaz, M. Bianchi, L. I. Pietrasanta, J. M. Giussi and O. Azzaroni, *Langmuir*, 2018, **34**, 3711–3719; (c) J. A. Allegretto, J. S. Tuninetti, A. Lorenzo, M. Ceolín, O. Azzaroni and M. Rafti, *Langmuir*, 2018, **34**, 425–431; (d) J. M. Giussi, C. von Bilderling, E. Alarcón, L. I. Pietrasanta, R. Hernandez, P. Rafael, M. Vázquez, C. Mijangos, M. L. Cortez and O. Azzaroni, *Nanoscale*, 2018, **10**, 1189–1195; (e) M. Rafti, J. A. Allegretto, G. M. Segovia, J. S. Tuninetti, J. M. Giussi, E. Bindini and O. Azzaroni, *Mater. Chem. Front.*, 2017, **1**, 2256–2260; (f) B. Sanz, C. Von Bilderling, J. S. Tuninetti, L. Pietrasanta, C. Mijangos, G. S. Longo, O. Azzaroni and J. M. Giussi, *Soft Matter*, 2017, **13**, 2453–2464; (g) J. S. Tuninetti, M. Rafti and O. Azzaroni, *RSC Adv.*, 2015, **5**, 73958–73962.
96. (a) L. K. Shrestha, Q. Ji, T. Mori, K. Miyazawa, Y. Yamauchi, J. P. Hill and K. Ariga, *Chem. - Asian J.*, 2013, **8**, 1662; (b) H. Hamoudi, *RSC Adv.*, 2014, **4**, 22035; (c) H. Pan, S. Zhu and L. Mao, *J. Inorg. Organomet. Polym. Mater.*, 2015, **25**, 179.
97. (a) K. Wang, K. Galatsis, R. Ostroumov, A. Khitun, Z. Zhao and S. Han, *Proc. IEEE*, 2008, **96**, 212; (b) K. Ariga, M. V. Lee, T. Mori, X.-X. Yu and J. P. Hill, *Adv. Colloid Interface Sci.*, 2010, **154**, 20; (c) K. Ariga, Q. Ji, J. P. Hill, Y. Bando and M. Aono, *NPG Asia Mater.*, 2012, **4**, e17; (d) T. Govindaraju and M. B. Avinash, *Nanoscale*, 2012, **4**, 6102; (e) T. Mori, K. Sakakibara,

H. Endo, M. Akada, K. Okamoto, A. Shundo, M. V. Lee, Q. Ji, T. Fujisawa, K. Oka, M. Matsumoto, H. Sakai, M. Abe, J. P. Hill and K. Ariga, *Langmuir*, 2013, **29**, 7239; (f) K. Ariga, T. Mori and J. P. Hill, *Langmuir*, 2013, **29**, 8459; (g) K. Ariga, Y. Yamauchi, G. Rydzek, Q. Ji, Y. Yonamine, K. C.-W. Wu and J. P. Hill, *Chem. Lett.*, 2014, **43**, 36; (h) S. Cordier, F. Grasset, Y. Molard, M. Amela-Cortes, R. Boukherroub, S. Ravaine, M. Mortier, N. Ohashi, N. Saito and H. Haneda, *J. Inorg. Organomet. Polym. Mater.*, 2015, **25**, 189.

98. (a) K. Ariga, Y. Yamauchi, Q. Ji, Y. Yonamine and J. P. Hill, *APL Mater.*, 2014, **2**, 030701; (b) S. Ishihara, J. Labuta, W. Van Rossom, D. Ishikawa, K. Minami, J. P. Hill and K. Ariga, *Phys. Chem. Chem. Phys.*, 2014, **16**, 9713; (c) M. Mir, P. J. Cameron, X. Zhong, O. Azzaroni, M. Álvarez and W. Knoll, *Talanta*, 2009, **78**, 1102–1106; (d) M. Ali, B. Yameen, R. Neumann, W. Ensinger, W. Knoll and O. Azzaroni, *J. Am. Chem. Soc.*, 2008, **130**, 16351–16357; (e) M. Mir, M. Álvarez, O. Azzaroni and W. Knoll, *Langmuir*, 2008, **24**, 13001–13006; (f) M. Mir, M. Álvarez, O. Azzaroni, L. Tiefenauer and W. Knoll, *Anal. Chem.*, 2008, **80**, 6554–6559; (g) O. Azzaroni, M. Mir, M. Álvarez, L. Tiefenauer and W. Knoll, *Langmuir*, 2008, **24**, 2878–2883.
99. (a) N. E. Muzzio, M. A. Pasquale, E. Diamanti, D. Gregurec, M. M. Moro, O. Azzaroni and S. Moya, *Mater. Sci. Eng., C*, 2017, **80**, 677; (b) E. Diamanti, N. Muzzio, D. Gregurec, J. Irigoyen, M. Pasquale, O. Azzaroni, M. Brinkmann and S. E. Moya, *Colloids Surf., B*, 2016, **145**, 328; (c) N. E. Muzzio, D. Gregurec, E. Diamanti, J. Irigoyen, M. A. Pasquale, O. Azzaroni and S. E. Moya, *Adv. Mater. Interfaces*, 2017, **4**, 1600126; (d) N. E. Muzzio, M. A. Pasquale, D. Gregurec, E. Diamanti, M. Kosutic, O. Azzaroni and S. E. Moya, *Macromol. Biosci.*, 2016, **16**, 482; (e) E. Diamanti, E. Gutiérrez-Pineda, N. Politakos, P. Andreozzi, M. J. Rodriguez-Presa, W. Knoll, O. Azzaroni, C. A. Gervasi and S. E. Moya, *Soft Matter*, 2017, **13**, 8922–8929; (f) E. Diamanti, D. Gregurec, M. J. Rodríguez-Presa, C. A. Gervasi, O. Azzaroni and S. E. Moya, *Langmuir*, 2016, **32**, 6263–6271.
100. (a) K. Takada, *Langmuir*, 2013, **29**, 7538; (b) K. Takada, N. Ohta and Y. Tateyama, *J. Inorg. Organomet. Polym. Mater.*, 2015, **25**, 205.
101. (a) C.-M. Puscasu, E. M. Seftel, M. Mertens, P. Cool and G. Carja, *J. Inorg. Organomet. Polym. Mater.*, 2015, **25**, 259; (b) M. Rafti, A. Brunsen, M. C. Fuertes, O. Azzaroni and G. J. A. A. Soler-Illia, *ACS Appl. Mater. Interfaces*, 2013, **5**, 8833–8840.
102. (a) A. P. Mártire, G. M. Segovia, O. Azzaroni, M. Rafti and W. Marmisollé, *Mol. Syst. Des. Eng.*, 2019, **4**, 893–900; (b) G. E. Fenoy, J. Scotto, J. Azcárate, M. Rafti, W. A. Marmisollé and O. Azzaroni, *ACS Appl. Energy Mater.*, 2018, **1**, 5428–5436; (c) G. E. Fenoy, E. Maza, E. Zelaya, W. A. Marmisollé and O. Azzaroni, *Appl. Surf. Sci.*, 2017, **416**, 24–32; (d) M. Rafti, W. A. Marmisollé and O. Azzaroni, *Adv. Mater. Interfaces*, 2016, **3**, 1600047.

103. (a) R. Rajendran, L. K. Shrestha, K. Minami, M. Subramanian, R. Jayavel and K. Ariga, *J. Mater. Chem. A*, 2014, **2**, 18480; (b) R. Rajendran, L. K. Shrestha, R. M. Kumar, R. Jayavel, J. P. Hill and K. Ariga, *J. Inorg. Organomet. Polym. Mater.*, 2015, **25**, 267; (c) G. E. Fenoy, B. Van der Schueren, J. Scotto, F. Boulmedais, M. R. Ceolín, S. Bégin-Colin, D. Bégin, W. A. Marmisollé and O. Azzaroni, *Electrochim. Acta*, 2018, **283**, 1178–1187.

104. (a) K. Ariga, Q. Ji, M. J. McShane, Y. M. Lvov, A. Vinu and J. P. Hill, *Chem. Mater.*, 2012, **24**, 728; (b) S. Howorka, *Langmuir*, 2013, **29**, 7344; (c) K. Ariga, Q. Ji, T. Mori, M. Naito, Y. Yamauchi, H. Abe and J. P. Hill, *Chem. Soc. Rev.*, 2013, **42**, 6322; (d) M. L. Agazzi, S. E. Herrera, M. L. Cortez, W. A. Marmisollé and O. Azzaroni, *Colloids Surf., B*, 2020, **190**, 110895; (e) M. L. Agazzi, S. E. Herrera, M. L. Cortez, W. A. Marmisollé, M. Tagliazucchi and O. Azzaroni, *Chem. - Eur. J.*, 2020, **26**, 2456–2463; (f) A. Escobar, N. E. Muzzio, P. Andreozzi, S. Libertone, E. Tasca, O. Azzaroni, M. Grzelczak and S. E. Moya, *Adv. Mater. Interfaces*, 2019, **6**, 1901373; (g) N. E. Muzzio, M. A. Pasquale, X. Rios, O. Azzaroni, J. Llop and S. E. Moya, *Adv. Mater. Interfaces*, 2019, **6**, 1900008; (h) N. E. Muzzio, M. A. Pasquale, W. A. Marmisollé, C. Von Bilderling, M. L. Cortez, L. I. Pietrasanta and O. Azzaroni, *Biomater. Sci.*, 2018, **6**, 2230–2247; (i) N. E. Muzzio, M. A. Pasquale, S. E. Moya and O. Azzaroni, *Biointerphases*, 2017, **12**, 04E403.

CHAPTER 2

Design of Halloysite Based Core–Shell Nanosystems

A. STAVITSKAYA*[a], A. VUTOLKINA[a,b], A. GLOTOV[a], V. VINOKUROV[a] AND Y. LVOV*[c]

[a]Gubkin University, 65/1, Leninsky Prospect, 119991 Moscow, Russian Federation; [b]Lomonosov Moscow State University, 3, 1 Leninskie Gory, 119991 Moscow, Russian Federation; [c]Louisiana Tech University, 505 Tech Dr, Ruston, LA 71270, USA
*E-mail: stavitsko@mail.ru, ylvov@latech.edu

2.1 Introduction

The world industrial focus is shifting from clay usage in traditional pottery production and the related study of their geology to developing novel functional materials with integrated nano or micro properties. Clay minerals have high specific surface areas and ion-exchange capacities, surface functional groups and diverse morphologies at the mesoscale, *e.g.*, nanorods, nanofibers, nanotubes, and nanosheets/nanoplates, all with developed internal porosity.[1] They exhibit excellent colloidal, adsorption, reinforcing, and carrier functions, as well as having nontoxic and eco-friendly advantages. Depending on chemical treatment one can adjust the surface chemistry, varying acidity and surface charge and, thus, strongly affect clay properties, making them favorable for more applications. Natural structured clay could be used for the design of hierarchical aluminosilicate systems as building nano-blocks or templates to form new classes of hybrid materials.[2]

Nanoscience & Nanotechnology Series No. 55
Concepts and Design of Materials Nanoarchitectonics
Edited by Omar Azzaroni and Katsuhiko Ariga

Published by the Royal Society of Chemistry, www.rsc.org

In the last years, one of the most innovative clays was 50 nm diameter tubular halloysite, demonstrating an exponential increase in the number of scientific papers and patents[3] (since 2005, the number of patents has virtually equaled the number of papers). By now halloysite is already applied in the production of polymer composites, color formulations and cosmetic creams, with perspectives in paints and coating, biomedicine and catalysis. With the evolution of nanotechnology, halloysite has become one of the most studied clay minerals due to a number of possible applications with perspectives for commercialization.

In this chapter, we want to attract attention to core–shell structures with halloysite tubes as a nanoscale template or structural agent. As a rule, observed core–shell materials were synthesized and tested as catalysts, bioactive agents, color agents or polymer fillers.

2.2 Structure and Physicochemical Properties of Halloysite

Halloysite is a natural clay mineral from the kaolin group with the chemical formula $Al_2Si_2O_5(OH)_4 \cdot nH_2O$. Naturally occurring halloysite appears as plates, spheres or tubes, with the domination of the last. Cylinders with 0.4–1.5 μm length form by the rolling of kaolin sheets in specific geological conditions.[4] The outer diameter of halloysite nanotubes is 50–100 nm (depending on the clay deposit) with 10–20 aluminosilicate layers comprising the walls and 10–20 nm inner lumen (Figure 2.1). There are two forms of halloysite nanotubes – hydrated and dehydrated. When water molecules are present between the aluminosilicate layers (hydrated halloysite), the spacing

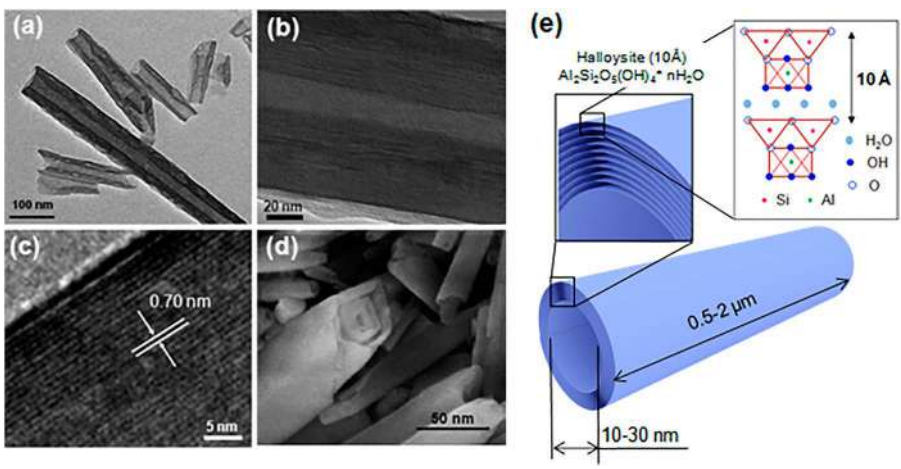

Figure 2.1 (a–c) TEM and (d) SEM images and (e) structure of natural halloysite nanotubes. Adapted from ref. 5 with permission from American Chemical Society, Copyright 2011.

(packing periodicity) is 1.0 nm. This form is called halloysite-(10 Å), where the "10 Å" designation indicates the periodicity in the wall. The dehydrated halloysite-(7 Å) may be obtained through the loss of interlayer water molecules under heating to more than 100 °C or in a vacuum (or just keeping the sample for a long time in a dry environment).[4,5] These two halloysite formations may be distinguished by X-ray diffraction.[6]

Halloysite pores vary in the range of meso (5–30 nm) sizes. The specific surface area of this tubular mineral is 50–70 $m^2\ g^{-1}$ with a 10–30% internal lumen volume. The mesoporous lumen provides a natural container for the loading of active substances and their sustained release. It is possible to enlarge the lumen space by selective etching with mineral acid. Halloysite nanotubes have a density, porosity, and cationic exchange capacity of 2.53 g cm^{-3}, 50–60 $cm^2\ g^{-1}$, and 3–5 nm ~10^{-2} mol kg^{-1}, respectively.[7]

The unique property of halloysite clay nanotubes is their side dependent chemistry. The external surface is composed of tetrahedral siloxane (Si–O–Si) groups, while the inner lumen consists of octahedral aluminol (Al–OH) groups. The electrical ζ-potential of halloysite is negative and about −30 mV at pH 5–8 due to its silica outer surface.[8] Meanwhile, the low density of hydroxyl groups on the outermost surface along with developed nanoroughness endows halloysite with good dispersion ability in low-polar polymers, offering advantages for the simple preparation of its composites with polyethylene.[9] Halloysite often contains impurities varying depending on deposits. Fe_2O_3 is the most common impurity, reaching 0.1–0.3 wt%,[10] and MgO and TiO_2 can also be present in smaller quantities. Traces of Na^+, Mg^{2+}, Ca^{2+} or K^+ in oxides or carbonate salts could also be found.[11]

2.3 Modification of Halloysite Nanotubes

The modification of halloysite clay surfaces is the most important step on the way to well-structured core–shell systems. The recommendation that should be followed is the pre-treatment of purchased halloysite, otherwise it is difficult to reach good results reproducibility due to small variations in the chemistry of different nanoclay supplies. Preparation procedures may include acid cleaning, hydrogen peroxide treatment and heating to different temperatures (depending on the following modification). This is especially important when chemical reactions take place on the surface.

2.3.1 Outer Surface or Non-selective Modification

Different inside/outside chemistry (outer SiO_2, inner $Al(OH)_3$) with positive/negative charges of surfaces allows the selective and non-selective modification of clay nanotubes. According to Yuan *et al.*, the Al–OH groups present in the halloysite lumen possess a high degree of chemical reactivity towards organosilanes.[12] On the contrary, the external surface of halloysite nanotubes consists of siloxane (Si–O–Si) groups and a few silanols (Si–OH). The quantity of the available hydroxyl groups, which determines the content of

the grafted molecules, is highly dependent on the morphological parameters (length, external and internal diameter, and wall thickness) of the halloysite tubes. Kaolinite is much less reactive for aminopropyltriethoxysilane modification due to its very low content of available hydroxyl groups.[12]

Acid or alkali etching helps to increase the surface area of clay and leads to Al^{3+} or Si^{4+} leaching and may result in surface recharge.[13] Pre-treated halloysite could be further used for modification.[14] Here, we focus on general conceptions of clay modification prior to core–shell nano and micro architecting.

The addition of functional groups may be achieved using one or multistep functionalization. Organosilanes like 3-aminopropyltriethoxysilane (APTES), *N*-2-aminoethyl-3-aminopropyltrimethoxysilane (AEAPTMS), (3-mercaptopropyl) trimethoxysilane (MPTMS), (3-bromopropyl)-trimethoxysilane (BrTMS), vinyltrimethoxysilane (VTMS), and phenyltriethoxysilane (PhTES) are commonly used to change the surface properties of halloysite clay.[15] The tubes' surface could be functionalized by $-HSO_3$ groups by different methodologies including one-pot organosilylation with (4-chlorosulfonylphenyl)-ethyltrimethoxysilaneorganosilane or sulfonation and two-step organosilylation using phenyl- and mercaptopropyl-organosilanes followed by sulfonation or oxidation to link the sulfonic acid groups.[16] A two-step modification was proposed in[17] where the halloysite clay nanotubes were modified with (3-aminopropyl)triethoxysilane (APTES) followed by treatment with HCl to obtain halloysite–NH_2•HCl.

Three step modification techniques are applied to insure metal particle grafting and enhanced stabilization on halloysite surfaces. As shown in[18] halloysite could be modified with (3-chloropropyl) trimethoxysilane to obtain Cl- on the surface, at first. After the incorporation of guanidine took place, a decoration of imine functionalized halloysite with the polymer poly(methyl methacrylate-*co*-maleic anhydride) was performed. Such a hybrid structure was used for Pd nanoparticle stabilization. A combination of polymer and macromolecule properties with halloysite surfaces as a carrier for metal particles were explored in;[19] combining the exceptional features of halloysite and starch, a unique hybrid was synthesized based on the conjugation of amine-functionalized starch with Cl–halloysite.

The modification of halloysite with amines is the most promising and simple way to design materials with controlled morphology (different metals, alloys, oxides nanoparticles) due to various ion hosting by amino groups. The amino-functionalized clay also serves as a scaffold to introduce organic molecules, like tartaric acid, by further covalent grafting.[20] Amino groups are linked *via* condensation between hydrolyzed aminosilane and the hydroxyl groups are located on the external surface as well as inside the nanotube.

Recently, it has been shown that calcination at 700 °C helps to optimize nanoclay properties to enhance the loading of silanes to the external surface.[21] The calcined sample with maximum Si–OH groups acting as reactive sites gives the silane loading of *ca.* 5.8 wt%. The loading efficiency depends on the activation of sites at the tube external surface, and the oligomerization of silane species (Figure 2.2). This could be extrapolated to other modification techniques.

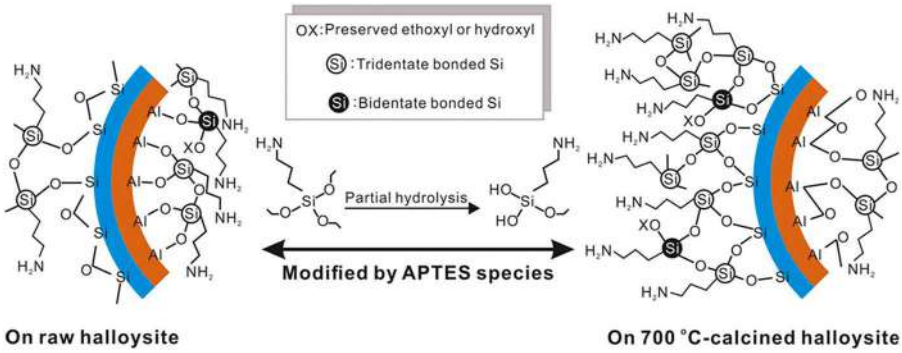

Figure 2.2 Mechanism of raw and calcined halloysite modification with (3-aminopropyl) triethoxysilane. Reproduced from ref. 21 with permission from Elsevier, Copyright 2019.

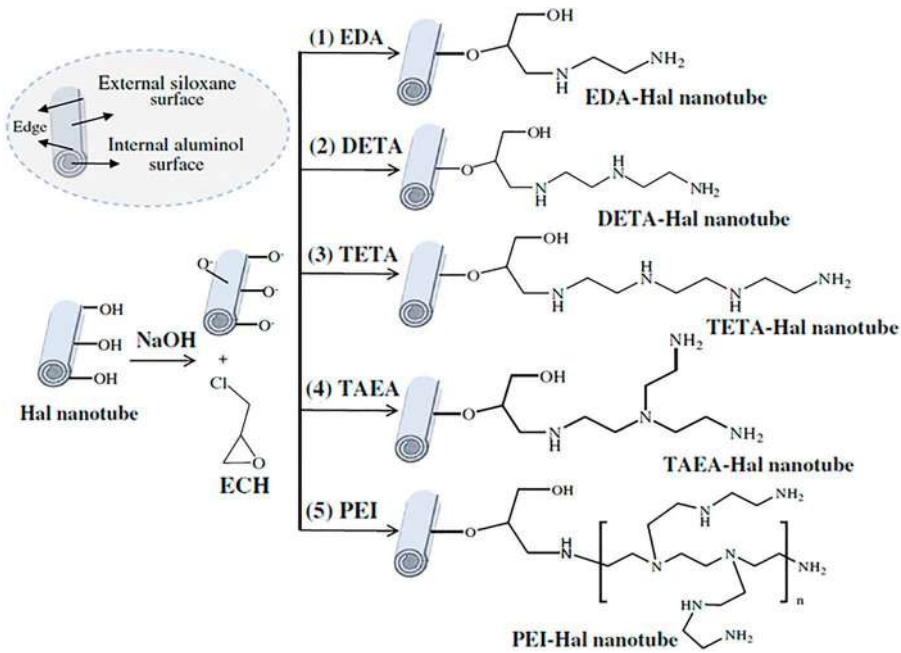

Figure 2.3 Modification of halloysite with ethylenediamine (EDA), diethylenetriamine (DETA), triethylenetetramine (TETA), and tris(2-aminoethyl) amine (TAEA), and polyethyleneimine (PEI). Adapted from ref. 22 with permission from Elsevier, Copyright 2017.

Amino groups could be grafted to the clay outer surface using organic precursors like ethylenediamine, diethylenetriamine, triethylenetetramine, tris(2-aminoethyl)amine (Figure 2.3), and polyethyleneimine.[22,23] Decoration by nanoparticles could be performed after amines grafting. It is also possible to use silane-modified halloysite for further modification with organic

molecules.[24,25] Such procedures add new chelating sites for binding ions or address surface hydrophobic properties.

Electrostatic interaction or the physical sorption of molecules may be considered the first modification step. For example, cethyltrimethylammonium salts are often used for the adjustment of halloysite outer surface properties due to the positively charged heads of the surfactant. Polycations are explored to form layered surface coverings for further medical applications and active coatings preparation.[26–28]

2.3.2 Selective Lumen Modification

The selective modification of the inner surface of halloysite tubes, including the utilization of alkyl phosphates (octadecylphosphonic acid), dopamine derivative, ionic liquids (1-(2-hydroxyethyl)-3-methylimidazolium), arylboronic acid, poly(vinyl alcohol) (PVA), poly(ethylene oxide) (PEO) and click chemistry was reviewed in.[29] The selective modification of halloysite could be made by loading of urea, hydrazine or negatively charged chemicals like ethylenediaminetetraacetic acid (EDTA).[30] To enhance loading efficiency, vacuum or sonication could be applied to the sample. Figure 2.4 demonstrates a possible mechanism of EDTA attaching to Al^{3+} located on the inner surface of a halloysite nanotube.

In our recent works, we proposed selective and non-selective modification of halloysite nanotubes with azines of various composition.[31–36] It has been found that morphology, catalytic activity and such properties as fluorescence, cytotoxicity of metal-containing halloysite may be varied depending on the molecules used to bind metal ions.

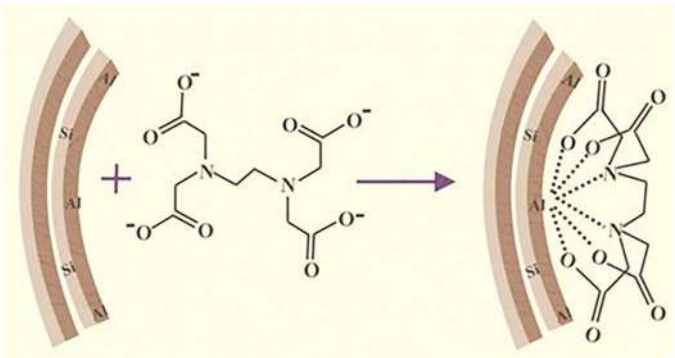

Figure 2.4 Schematic presentation of the selective modification of the halloysite lumen with ethylenediaminetetraacetic acid (EDTA). Reproduced from ref. 30 with permission from the Royal Society of Chemistry.

2.3.3 Intercalation

Halloysite can be intercalated with small molecules. For example, halloysite intercalated with Ca^{2+}, Na^{+}, NH^{4+}, or Pb^{2+} acetates was reported, and the adsorption capacity of copper ions was related to the intercalated fraction of acetate. This was partly attributed to cation exchange on the negative surface sites.[37,38] Another approach to fabricate intercalated halloysite with diethanolamine and triethanolamine molecules was proposed.[9,39] The tailored clay adsorption capacity in terms of Pb(II), Cd(II), Zn(II), and Cu(II) was significantly improved due to the two-step gradual diffusion of the metals into the interlayer space and subsequent binding to the amine nitrogen of the grafted amino alcohol.

The design of systems of sandwich-like structures with metals or organic macromolecules intercalated into the wall multilayers could be based on the works described above, though by now this has been poorly investigated.

2.4 Core–Shell Metal-containing Halloysite Systems

An accepted definition for core–shell type structures is as follows: an ordered bi- or multiphase material which has an inner core and an outer shell made of different components. There are many variations of halloysite based core–shell materials (realized and still not made). Halloysite clay nanotubes may serve as an aluminosilicate shell for metal-containing structures located inside the lumen (core structures) and also play a role of core material coated with various shells.

Several core–shell architectural strategies could be realized for halloysite clay nanotubes (Figure 2.5): (1) the outer surface coating; (2) core

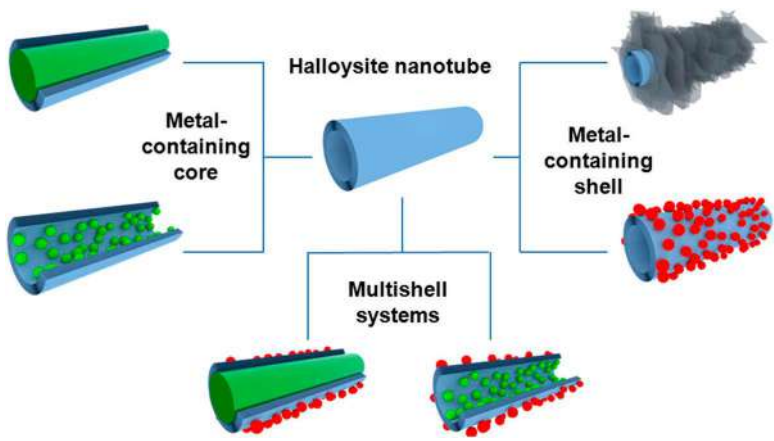

Figure 2.5 The design of halloysite nanotubes metal-containing core–shell systems. Reproduced from ref. 40 with permission from American Chemical Society, Copyright 2019.

formed in the tube's lumen; (3) multishell nanosystems.[40] Sandwich type systems with interlays spacing loaded with metal compounds are theoretically possible but have not been published yet due to very complex synthesis procedures.

Metal-containing structures could be synthesized using clay nanotubes as templates.[33,41–43] Coating halloysite with inorganic substrates usually gives morphologies such as nanohybrids or their aggregates. Nanoflakes or nanosheets could be obtained under favorable conditions when layers structures like metal sulfides are synthesized. The typical representatives of structures are depicted on Figure 2.6.

Figure 2.6 represents different methods of preparation: (a) formation of Ag nanoparticles on the outer surface *via* silver acetate thermal decomposition;[33] (b) pre-formed Au nanoparticles adsorption onto the surface of amino-modified halloysite;[44] (c) ultrathin NiO nanosheets assembling on pristine clay tubes through a simple precipitation reaction;[45] (d) In_2S_3 layers organization on azine-modified clay using microwave irradiation and PEO as a solvent; (e) cobalt oxide nanorod synthesis *via* ligand assisted loading of cobalt salt; (f) selective Ru nanoparticles formation inside the azine-modified lumen of clay tube;[46] (g) Au-halloysite peapod synthesis using surfactants;[47] (h) MoS_2 layer formation inside the clay lumen under hydrothermal conditions. Three out of eight TEM images show the formation of metal-containing structures on or inside pristine clay, but unmodified halloysite is rarely used for such synthesis. Due to the low outer surface chemical activity and positively charged inner lumen that repel most metal salts, such nanoclay composites usually have variegated morphology.

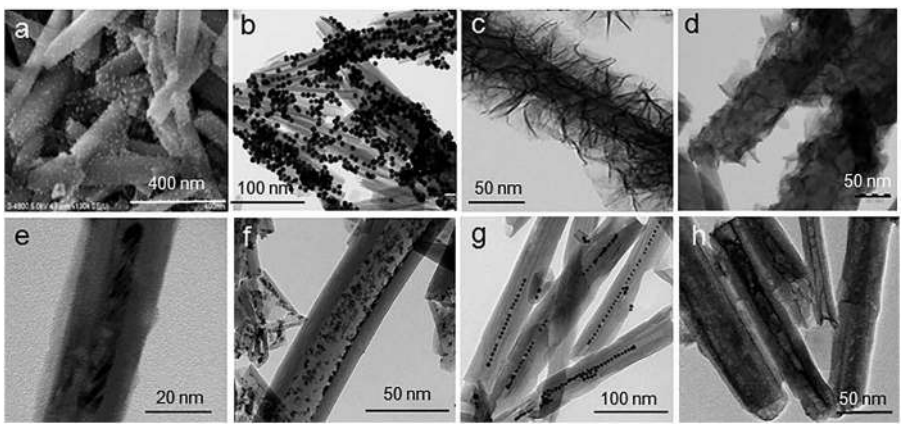

Figure 2.6 Outer surface of halloysite decorated with (a) Ag nanoparticles; (b) Au nanoparticles; (c) NiO nanosheets. Adapted from ref. 45 with permission from Elsevier, Copyright 2015; (d) In_2S_3 layers and inner surface of halloysite with (e) Co_3O_4 nanorod; (f) Ru nanoparticles; (g) Au nanoparticles; (h) MoS_2 layers.

2.4.1 External Surface Coating

External surface coating is the simplest way to form a core–shell nanosystem on a base of halloysite aluminosilicate tubes. Particles can be formed on the silica surface by metal salt precipitation from solutions and further reduction or thermal decomposition in the presence of pristine or modified mineral. Metal compounds may be attached to the surface using precipitation reactions. For better control of the morphology, capped nanoparticles may be synthesized by standard methods and grafted to clay surfaces.

2.4.1.1 Metallic Nanoparticles

Au, Ag, Ru, Pt, and Pd are the most often synthesized metal nanoparticles due to their unique optical or catalytic properties. As these particles are synthesized using a capping agent or due to low reactivity, they stay in the zero-valence state after formation. Metal nanoparticle coatings may be achieved by *in situ* formation *via* the reduction of metal precursors on the surface of modified halloysite or by the seeding of pre-formed nanoparticles. Metallic nanoparticles can also be obtained using electrochemical processes or microwave- and sonication-assisted treatments.[48] Microwave-assisted Ru-synthesis was performed with 1–2 nm size particles formed on the external surface of clay nanotubes.[46]

Animosilane modified clay was used to form silver through the immobilization of metal precursors followed by reduction, forming quite similar morphologies and different applications.[49–51] The typical procedure is shown in Figure 2.7 with an additional step for enzyme attachment[49] – amino-functionalization

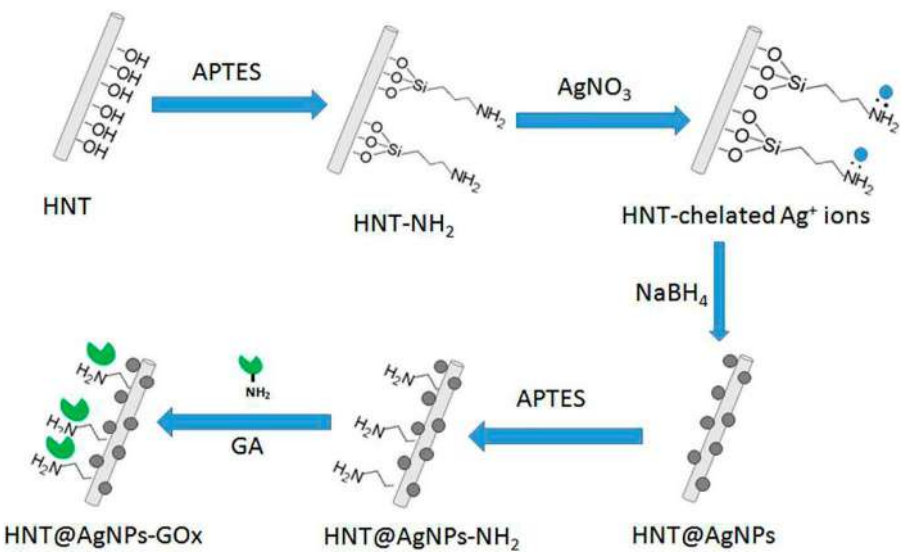

Figure 2.7 Schematic representation of Ag nanoparticles grafting to amino-modified halloysite following by glucoamylase attachment. Reproduced from ref. 49 with permission from the Royal Society of Chemistry.

followed by *in situ* metal deposition by ultrasonic dispersion of Rh, Pt and Pd from an aqueous solution of metal precursors. This allowed for noble metal particles with extremely small sizes (~1.5 nm) to be dispersed densely and uniformly on both the outside and inside surface of the halloysite.[52]

The gold particles were supported on thiol-functionalized halloysite: thiol-terminated organosilane was used as an anchoring group for Au nanoparticles due to the strong gold–thiol bonds.[53] The Au nanoparticles with uniform distribution and spherical shape were well dispersed and attached to the tubes' surface. The material was tested for 4-nitrophenol reduction by $NaBH_4$ and demonstrated high activity as expected due to the synergistic effect between the clay nanotubes and Au-particles. Moreover, halloysite can exert both transferring electrons from borohydride ions to 4-nitrophenol and modulating interfacial charge transfer dynamics. It is interesting to note that an apparent kinetic constant decreases with increasing amounts of catalyst. The authors highlighted that at higher catalyst concentrations the aggregation resulted in a greater particle sizes. It led to the reduction of the catalytic active sites and poorer catalytic performances. This type of core–shell mesocatalyst is very stable and does not lose its activity for at least ten cycles.

It is difficult to control the size and shape of *in situ* produced uncapped metal nanoparticles on modified halloysite (especially Ag), but this method is still applied when the morphology of particles is not crucial. It has been shown that uncapped nanoparticles give a better reaction activity due to the availability of reactant catalytic sites.[50] Ag-halloysite composites with uncapped nanoparticles are more active in killing bacteria in a short period of a few hours.

The morphology is important when properties such as size-dependent band gap, electron and phonon transport, and absorbing or emitting properties are a research goal. In this case, pre-formed nanoparticles could be combined with a clay tubule template to enhance stability and widen applications. It was shown in[54] that an amino-modified nanotube clay was seeded with gold to enhance plasmonic resonance. The electrostatic attraction between positively charged amine terminal groups and negatively charged Au nanoparticles, especially at low pH values, favored a suitable coating and good distribution of the pre-formed gold particles. In,[55] poly(vinyl pyrrolidone) was used as a capping agent for Pd nanoparticles grafted to APTES-modified halloysite. The results indicated that Pd particles with an average diameter of *ca.* 3 nm were densely immobilized onto NH_2-halloysite. The Pd distribution on the surface of silanized tubes was more uniform and the nanoparticle size became smaller compared with those directly deposited on the clay carrier without silanization.

In,[44] two approaches were combined. Pre-formed Au seeds were strongly grafted to APTES-modified clay and after this a gold shell with controlled morphology was grown with the addition of gold hydroxide solution. Authors claim that there is a direct correlation between the architecture of the

core–shell systems and their heating capacity. The conditions can be finely tuned to obtain plasmonic responses from the visible to the near-infrared (NIR) window.

They conclude that halloysite is a suitable dielectric core for plasmonic applications, inexpensive, eco-friendly and readily available. This allows for many possibilities for the halloysite nanotubes in NIR remote-triggered devices, SERS platforms, permselective membranes, sensors and catalysts.

2.4.1.2 Bimetallic Nanoparticles

Bimetallic Au–Ag or Pt–Ag nanocages loaded on halloysite nanotubes were generated on the basis of Ag@HNT, which was fabricated *via* a modified silver-mirror-reaction without halloysite pre-treatment (Figure 2.8). The morphology of Au–Ag or Pt–Ag nanostructures on the nanotubes was modulated by changing the ratio of $HAuCl_4$ (or H_2PtCl_6) to Ag in galvanic exchanges.[56] It is very interesting that monometallic catalysts had a limited exposure of the active facets of metallic nanoparticles and bimetallic catalysts showed enhanced exposure of the active facets of nanoparticles in the peroxidase-like catalytic oxidation.

Halloysite nanotubes were proposed as supports for dispersing FeNi and BFeNi alloy nanoparticles produced by the co-impregnation method.[57] Polydopamine (PDA) was used to synthesize AgPd/PDA-halloysite nanocatalysts.[58] It is believed that oxygen-containing functionalities, hydroxyl groups, are necessary for supporting metal ions, which thus helps to control the sizes and distributions of the formed particles on the halloysite. Poly(diallyldimethylammonium) chloride, a water-soluble quaternary ammonium polyelectrolyte, was used as a reducing agent and a stabilizer for the fabrication of nanostructured metals on halloysite producing Co–Cu mesocatalysts with ultrasmall particles.[59]

2.4.1.3 Metal Oxide Nanoparticles

Oxide nanoparticles can easily be obtained by metallic nanoparticle preparation methods followed by an oxidation step. Other methods are available, such as the precipitation of the oxo-hydroxide form of the metal precursor (*e.g.*, chloride or nitrate) in water as a result of the presence of a base. Following this approach, it is difficult to regulate nanoparticle size; moreover, in case of mixed oxides, chemical homogeneity of the sample is also difficult to control.[48] These rules are true for metal oxides templated on clay nanotubes.

The application of pristine halloysite with metal salts adsorption followed by the precipitation of solid aggregates is the simplest method of metal oxide structure formation, thought it has its negatives. Mixed oxides such as $CuFe_2O_4$[60] and Fe_3O_4[61,62] were synthesized using thermal decomposition of salts or precipitation with the formation of metal oxide nanoparticles on the surface of clay and also in the bulk.

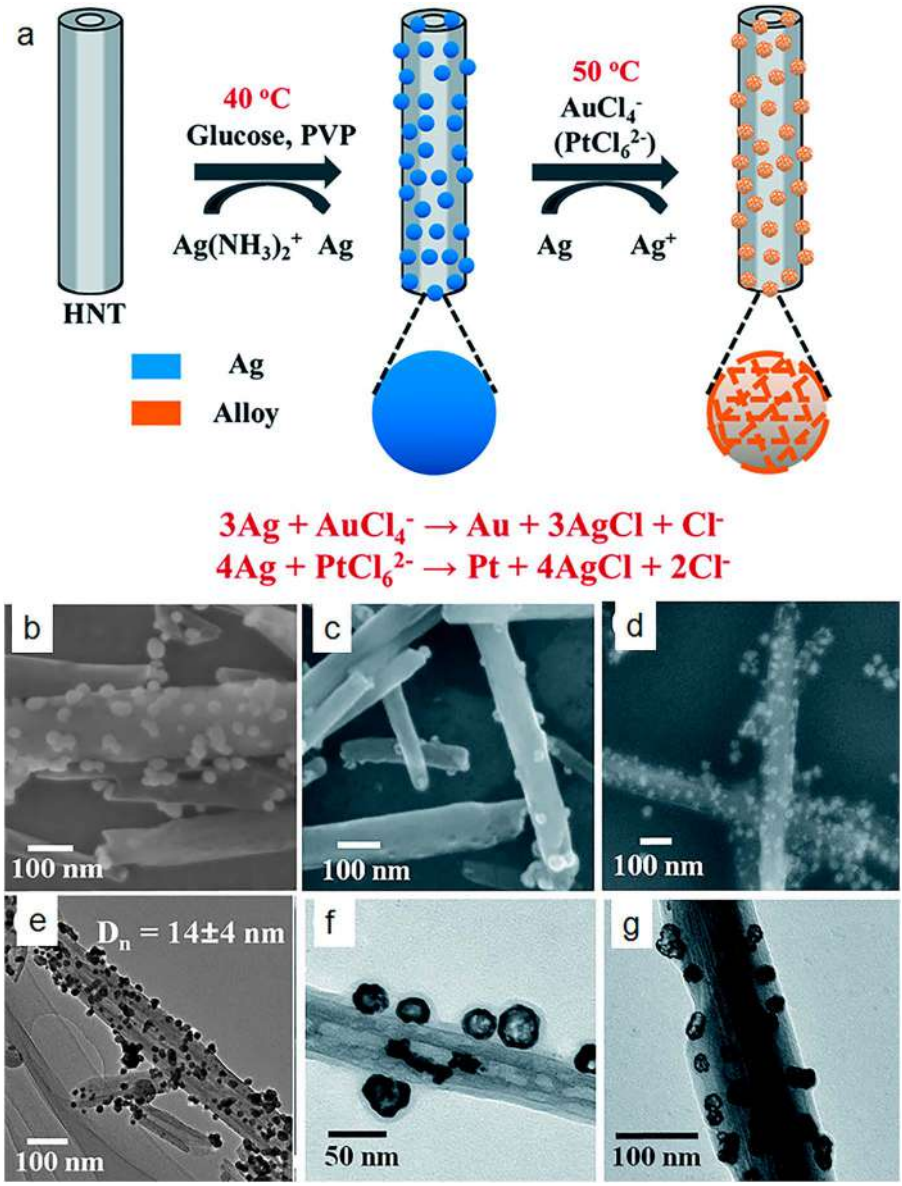

Figure 2.8 General scheme of bimetallic nanoparticles deposition on halloysite nanotubes (a) and TEM and SEM images of Ag (b, e), Au–Ag (c, f) and Pt–Ag (d, g) composites. Adapted from ref. 56 with permission from the Royal Society of Chemistry.

The formation of nanoparticles is mainly achieved when modified clay with additional active sites capable of adsorbing metal ions is used. The molten salt method could be successfully applied to treat the external surface of the halloysite for further nanoparticle formation.[63] A combination of several methods used to prepare nanoparticles could be successfully applied to achieve multimetal oxide structures as also shown in.[63] The formation of CeO_2–WO_3 on the activated surface of halloysite was achieved using wet impregnation of cesium and tungsten precursors, and Fe_2O_3 by iron nitrate reduction and rapid oxidation on the surface of the Ce/W-catalyst with about 5 nm Ce–W–Fe oxide nanoparticles. Hence, the composition of mixed oxides is hard to control by this method (Figure 2.9).

Semiconductor metal oxides stabilized on halloysite are extensively studied due to possible application in photocatalytic water purification, gas sensing, *etc.* A TiO_2 shell was synthesized on clay tubes using a hydrothermal method to enhance the available surface area of this oxide and as a consequence its photocatalytic activity.[64] In,[65] highly monodispersed ZnO nanoparticles were obtained by calcination of $ZnAc_2{\cdot}2H_2O$ seeded on halloysite at 500 °C. Compared with the individually dispersed ZnO nanoparticles, the as-prepared ZnO/halloysite nanocomposites showed a smaller band gap energy and relatively strong light absorption.

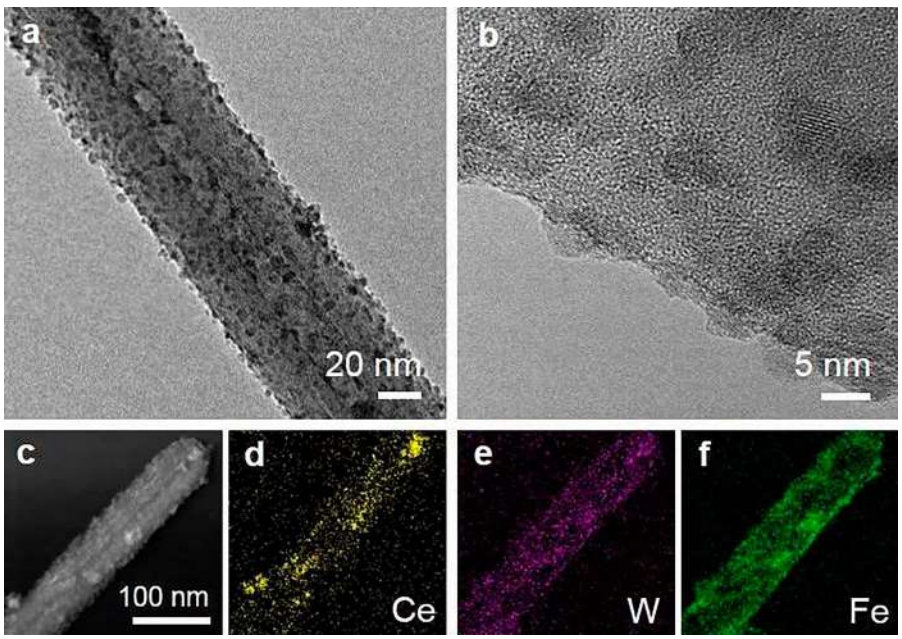

Figure 2.9 (a) TEM image, (b) HRTEM image and (c–f) the EDX mapping of the Fe(4)@CeW/H catalyst. Reproduced from ref. 63 with permission from American Chemical Society, Copyright 2018.

2.4.1.4 Ordered Metal Oxide Nanostructures

The unique ultrathin NiO nanosheets assembled on pristine clay tubes were obtained through a simple precipitation reaction.[45] Halloysite was well dispersed in deionized water by sonication, $Ni(NO_3)_2 \cdot 6H2O$, hexamethylenetetramine and citric acid trisodium salt dehydrate were dissolved into the above dispersion to form a light green solution. The resulting solution was then heated to 90 °C in an oil bath for 6 h. After cooling, washing and drying, α-Ni(OH)2 nanosheets were obtained on the clay. NiO nanosheets were prepared by annealing this material at 300 °C for about 3.5 h in air (Figure 2.6c).

The sol–gel method was used to obtain another hierarchic material with a clay core and structured mesoporous silica shell. The MCM-41 type phase was assembled on halloysite using cethyltrimethyl ammonium bromide as a template for mesoporous silica formation.[2] Novel nanocomposite design was reached *via* cethyltrimethyl ammonium bromide self-assembly onto halloysite clay nanotubes followed by silanization and calcination (Figure 2.10). The resulting inorganic mesoporous silica was grown concentrically around clay nanotubes. Moreover, unlike pristine mesoporous MCM-41 silica, this composite is characterized by enhanced thermal and mechanical stability up to 1100 °C and 500 MPa.

Together with structured amorphous aluminosilicates like MCM-41, zeolites are a very important class of ordered metal oxides. ZSM-5 type zeolites are often used as acid catalysts in organic and petroleum chemistry. The disadvantage of this material is its mircoporous structure and high diffusion limitations. In this regard, mesoporous aluminosilicate nanotubes may serve

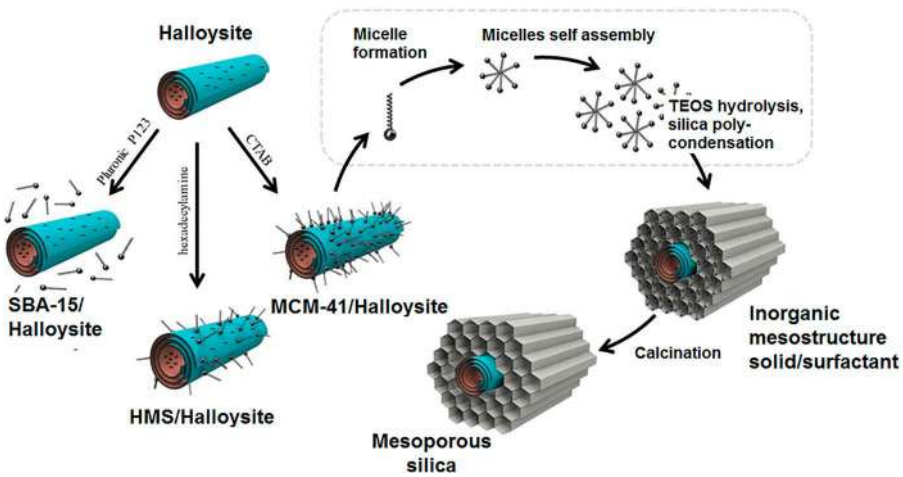

Figure 2.10 Scheme of the halloysite-silica mesomaterial synthesis (HMS hexadecylamine, CTAB-cethyltrimethylammonium). Adapted from ref. 2 with permission from the Royal Society of Chemistry.

as a template for ZSM-5 growth to form micro-mesoporous material with better properties. A type of ZSM-5/halloysite material was proposed in.[66] The specific structure of the Pt-catalysts template on it allowed both *m*-xylene isomerization and ethylbenzene dealkylation to be performed selectively in contrast to Pt/ZSM-5 catalyst.

2.4.1.5 Insoluble Metal Salts

The approaches for insoluble metal salt nanoparticle formation is generally similar to that described above. Still, there are some interesting modifications to be noted. For example, in[67] imine functionalization of halloysite through the introduction of aminosilanes followed by condensation with salicylaldehyde was applied for the immobilization of CuI on halloysite.

ZnS nanoparticles were also prepared in a halloysite suspension using zinc acetate dehydrate dissolved in ethanol with addition of acetic acid. Then HNTs were dispersed in this solution by ultrasound followed by the addition of thioacetamide to the mixture and a 24 h synthesis procedure.[68] Inspired by this work, very nice core–shell structures were obtained by authors and described in[32,34,69] with CdS or $Cd_{0.7}Zn_{0.3}S$ shell loaded on amino- or azine-functionalized halloysite nanotubes (Figure 2.11). The very dense metal sulfide nanoparticle shell was obtained using azine as a modification agent due to better loading on the outer halloysite surface by electrostatic interaction and van der Waals forces rather than covalent grafting as in case of APTES.

In,[70] tubular hierarchical core-sheath NiS2@Ni–Mn–O was achieved through halloysite-assisted hydrothermal reaction and sulfidation. This system was investigated for possible application as supercapacitor.

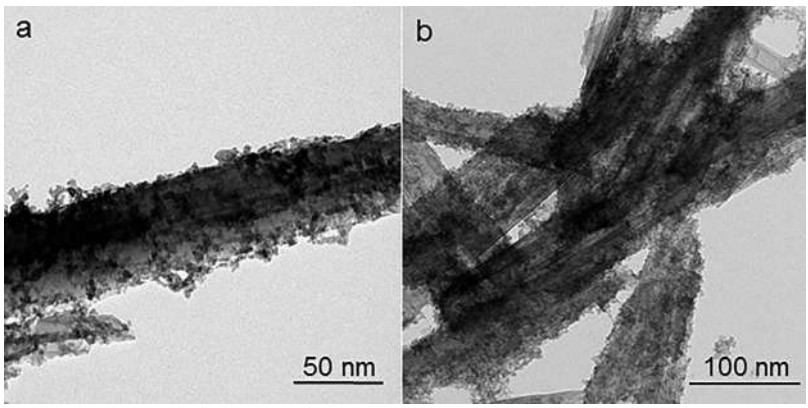

Figure 2.11 (a) CdS shell on the surface of amino-modified halloysite; (b) CdS shell on the surface of azine-modified halloysite.

2.4.2 Halloysite with a Metal-containing Core

A metal-containing core may be loaded inside aluminosilicate nanotubes using pre-formed nanoparticles or particles, cubes, rods or may be obtained *in situ*. The decoration of halloysite lumen with metal compounds opens great possibilities to construct selective, stable and long-lasting catalysts with the possibility to control the morphology of active sites and their composition, specific environment modulations that could be varied may change the activity, and the stability of produced systems.

2.4.2.1 Metallic Core

The unmodified halloysite was used to encapsulate Pd nanoparticles by the impregnation technique using pre-formed particles derived from $Pd(OAc)_2$.[71] The metal precursor was preliminarily reduced using sodium ascorbate and trisodium citrate. The Pd : HNTs molar ratio and content of reducing as well as capping agents strongly effects the mean size of Pd. The synthesis of selectively deposited palladium nanoparticles inside tubular halloysite lumens was directed by the selective modification of the aluminol surfaces using ionic liquid (1-(2-hydroxyethyl)-3-methylim idazolium).[72]

The selective loading of halloysite with Ag nanoparticles with a good loading efficiency and monodispersed ~2.6 nm particles formation was reported in.[73] *N*-acetyl-L-cysteine (NAC) was chosen as the capping agent for silver nanoparticles. Stabilized Ag particles were prepared by the UV-light reduction of NAC supramolecular gels containing $AgNO_3$. The obtained NAC-modified silver was deprotonated using acetic acid. After the dispersion of negatively charges particles in the clay tube suspension they readily entered the positive cavity and formed a core–shell structure.

Using surfactants (oleic acid, oleylamine) and $HAuCl_4 \cdot 3H_2O$ as a gold-nanoparticle precursors allows us to obtain Au@halloysite nano-peapods (Figure 2.6g) in ethanol toluene solution. The majority of the nanoparticles were formed inside the nanotubes due to the fast loading of the gold salt and other components into the wettable clay nanotube lumens pushed by strong capillary pressure. The particle size distribution of gold-nanoparticles depends on the synthesis conditions.[47]

Very interesting observations were made in.[74] It has been found that acid etching may not only increase the surface area but also make the selective loading of metals possible. Silver was selectively loaded in the lumen and the outer surface of halloysite nanotubes pre-treated through leaching by sulfuric acid. Selective loading was achieved using different metal salts. When nitrate was used as the raw source the silver NPs were loaded on both sides of the HNTs, while in the case of acetate Ag NPs were found only in the lumen cavity (Figure 2.12). It was established that the properties of the two sides of the tubes depend on the affordability of the acid treatment induced on the surface defects in the cavity. Meanwhile, the selective

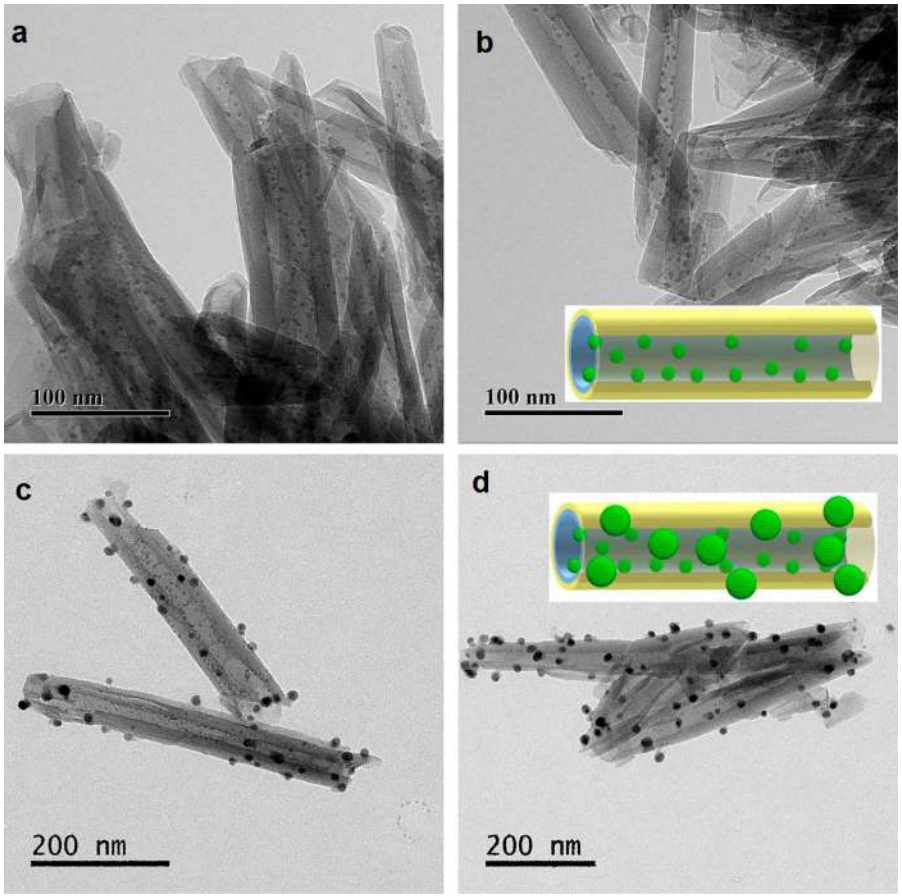

Figure 2.12 TEM image of Ag loaded halloysite prepared from silver acetate (a, b). Inset in (b) is a modulation that Ag NPs are located in the lumen of HNTs. TEM images of Ag-halloyste sample prepared from silver nitrate (c, d). Inset in (d) is the modulation that both sides of the HNTs are decorated by Ag NPs with different sizes. Adapted from ref. 74 with permission from Elsevier, Copyright 2016.

adhesion of metal cations is affected by electron affinity, ionization energy and steric configuration of the ionic radical of the raw sources. This leads to selective formation of Ag particles.

It is also possible to produce metal particles inside halloysite lumen by socking metal precursors into it with complexing agents covering the surface. Ligands formation by chemical reaction of hydrazine loaded inside halloysite with various aldehydes helped to form Ru nanoparticles within the tubes.[31,33] Loading of ruthenium salt was possible due to complex formation in the lumen followed by reduction. As a result, monodispersed nanoparticles were obtained (Figure 2.13, Figure 2.6f). It has been found that depending on the chemical composition of the ligand used the morphology of

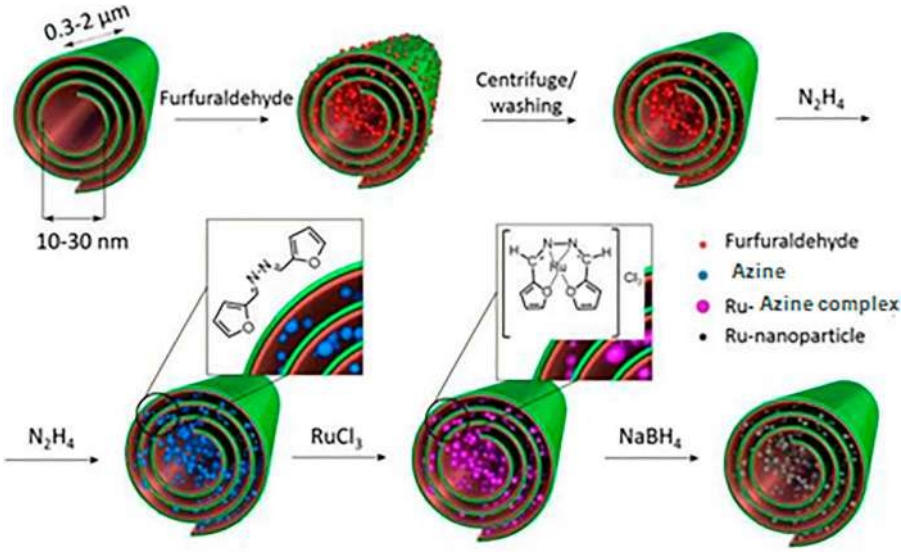

Figure 2.13 Synthesis scheme for selective Ru nanoparticles loading inside the halloysite nanotubes using azine as complexing agent. Reproduced from ref. 33 with permission from Taylor and Francis, Copyright 2017.

obtained nanoparticles may be varied. Such procedures also make it possible to load metal ions in more than one cycle. This opens the possibility of forming more than one type of metal ion inside the clay tube and also regulating metal content.

Following, nanotubes with ruthenium nanoparticles inside were obtained by prior tubes processing with ethylenediaminetetraacetic acid (EDTA), urea or acetone azine.[36] To achieve a ruthenium concentration of *ca.* 2%, a two-step ruthenium chloride loading technique was used. Materials were reduced in a flow of hydrogen at 400 °C. It has been found that the morphology of the materials as well as textural characteristics were quite similar. The main difference was observed in the total acidity of materials that has a significant impact on their catalytic activity in Fischer–Tropsch synthesis. It was assumed that the affinity of ligands towards alumina inner surfaces plays an important role in catalysts performance.

2.4.2.2 Bimetallic Nanoparticles

The selective loading of Pt–Cu bimetallic nanoparticles in the lumen was achieved by increasing the pH of metallic precursor solutions.[75] The pH enhances the dissociation of H_2PtCl_6, advancing the association of $[PtCl_6]^{2-}$ with the positively charged inner surface (Al–OH) of halloysite. Moreover, the pH-modulated ligand exchange leads to shrinkage of bond length from Pt–Cl in $[PtCl_6]^{2-}$ to Pt–O in $[PtCl_4(OH)_2]^{2-}$ followed by Pt(IV) trapping inside

the HNTs. Meanwhile, Cu(II) cations may complex with Pt(IV) anions *via* electrostatic force to form Pt–Cu bimetallic NPs inside the halloysite (Figure 2.14).

The resulted catalysts demonstrated excellent catalytic performance in the 4-nitrophenol reduction, over 20 times higher than that of Pt loaded halloysite and nearly 60 times higher than that of unloaded Pt NPs. It was concluded that the bimetallic active phase was protected by an aluminosilicate shell from leaching and deactivation, providing high catalytic activity of Pt or Pt–Cu bimetallic particles.

CuNi nanoparticles were successfully formed inside the lumen *via* citrate–metal complex formation.[76] It has been shown that CuNi particles are formed on the outer surface when citrate was not used. The loaded particles were much more stable at high temperature gas phase reaction than particles

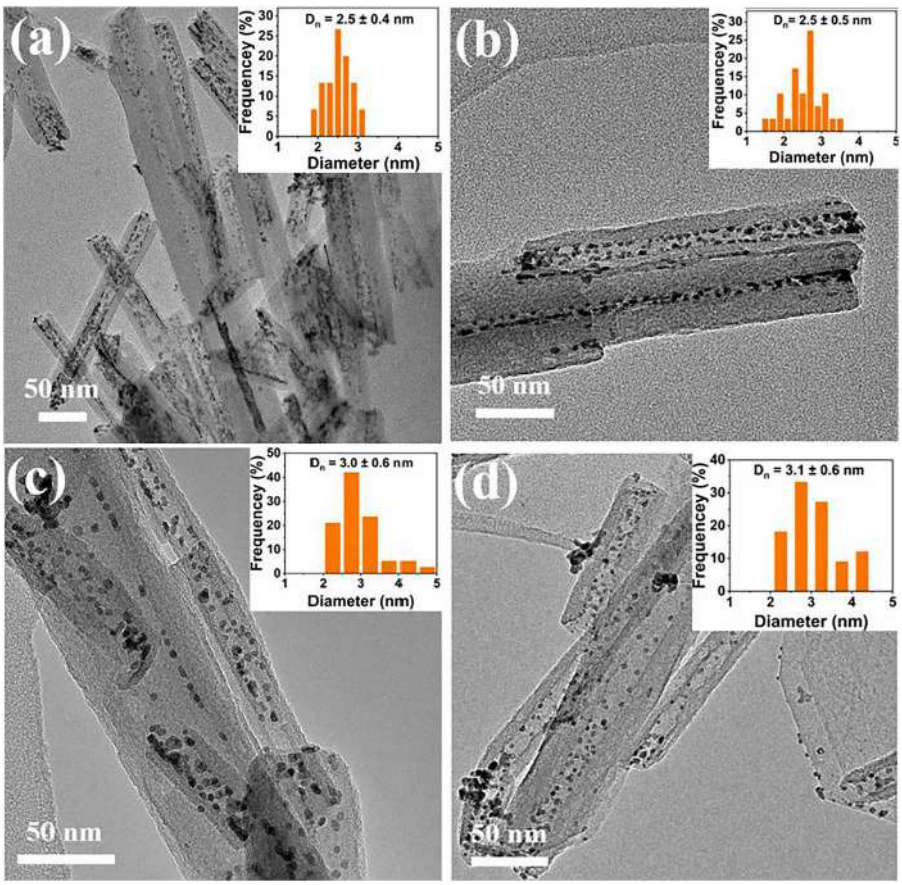

Figure 2.14 (a)–(d) TEM images of Pt@HNT, Pt_3Cu@HNT, PtCu@HNT, and $PtCu_3$@HNT. Adapted from ref. 75 with permission from American Chemical Society, Copyright 2019.

covering the silica surface of the halloysite. This work is an example of pristine halloysite properties utilization without complex methods of modification resulting in well organized and stable metal-containing shell.

It could be assumed that metallic nanoparticles loaded inside clay tubes are stable and can be selective catalysts for various types of chemical reactions with controlled morphology and surface chemistry. The efficient synthesis procedure results in almost 100% of the tubes being loaded with metal particles. Metallic nanorods could also be formed inside clay nanotubes as shown for silver rods.[5,33] Though the yield of loaded tubes was not high, this works and future investigations are very promising for nanorods formation. It is known that nanorods are more difficult to obtain than nanoparticles. In this case tubes may act as a sacrificial template for nanorod formation.

2.4.2.3 Metal Oxide Core

Exploiting the inner lumen of halloysite clays as nanoconfined reactors, the synthesis of nanoscale inorganic materials is possible. Halloysite lumen modification with ethylenediaminetetraacetic acid (EDTA) made the formation of Fe_2O_3 nanorods possible for catalytic application in water purification.[30] Selective modification of the clay lumen produces an inorganic micelle-like architecture, facilitating the formation of rod shaped nanoscale iron oxide inside the lumen of the clay nanotubes and finally giving rise to a nanocomposite having α-Fe2O3 core with a halloysite shell. The as-prepared α-Fe2O3/halloysite exhibited enhanced photocatalytic activity toward degradation of organic dyes in presence of sunlight.

CuO nanoparticles were loaded inside the halloysite lumen forming a peapod structure.[77] A solution of $Cu(NO_3)_2$ was mixed with urea and added dropwise to the hot halloysite powder taken from the oven until the surface of HNT powder was moist. The moist powder was transferred to an oven and treated at 120 °C; the procedure was repeated. Finally, the sample was calcined at 500 °C. In here urea served as a ligand to make loading possible.

In[78] a mesoporous silica was incorporated inside a clay cavity *via* an improved pseudomorphic transformation method. Prior to mesoporous silica formation, halloysite was etched with acid to enlarge the lumen and remove alumina from the surface. This material has an enhanced surface area, adsorption capacity and MCM-41 type structure and is thought to be promising for drug delivery and a catalyst template.

2.4.2.4 Insoluble Metal Salts

The hydrothermal method was utilized to load metal sulfides inside clay tubes. CdSe nanoparticles formed selectively inside clay tubes are shown in.[69] Recently, a new core–shell system was obtained by the authors. MoS_2 layers were successfully formed inside clay lumen by standard hydrothermal method, described in.[79] The presence of clay tubes resulted in the formation

of MoS_2 sheets in the lumen and also between multilayers in hydrothermal conditions with the temperature of reaction 140 °C. The morphology of MoS_2 layers synthesized in the aluminosilicate mesoporous clay is shown in Figure 2.6h.

2.4.3 Hybrid Core–Shell Nanostructures

Today inorganic/organic core–shell nanoparticles are of great interest due to the expected combination of properties of both inorganic nanoparticles and organic polymers or macromolecules. Combining the concepts of nanotechnology with powerful synthetic methodologies based on supramolecular chemistry and the principles of self-assembly/organization opens a possibility to access higher order functional materials for the construction of nanoscale devices and machines.[80] Accordingly, a number of different nanoparticles have so far been encapsulated into a polymer shell.[81] The halloysite clay nanotubes are not excluded. Halloysite clay tubes were grafted with various macromolecules or covered with polymers of different compositions. The possible field of application for such hybrid systems may start from polymer fillers of various functionalities to multifunctional catalysts and systems for drug delivery and medical tissue engineering.

One of the first works in hybrid nanoparticles formation on the base of halloysite clay was halloysite nanotubes/polystyrene inorganic/organic core–shell particles prepared *via* a convenient soap-less microemulsion polymerization.[81] The inorganic cores were pre-treated with allyl alcohol and the polymer shells were prepared successfully by the facile soap-less microemulsion polymerization of styrene with the allyl alcohol-modified/halloysite nanotube as seeds, and potassium persulfate as the initiator in water. Here allyl alcohol acted both as a co-monomer and an emulsifier. In this work it was shown that spherical hybrids could be obtained when two tubes are polymerized in one shell, though this process is hard to control this was the first work to show this for tubular coated hybrid material.

The polymer covering could be introduced in the systems with unique magnetic or optical properties in order to prevent nanoparticles from aggregation or decomposition as well as to adjust affinity to organic media or polymers matrix. For example, halloysite modified with dopamine was applied to form a core–shell halloysite-magnetite system with a polymer coating for application in water purification (Figure 2.15).[82] The nanohybrid consisted of a halloysite nanotube as a skeleton, an intermediate magnetic nanoparticle coating, resulting from metal salts precipitation on dopamine modified clay, and a polydopamine-(3-aminopropyl) triethoxysilane derivate layer outside that provided active adsorption sites for dye removal. Thanks to the polymeric coating organic dyes and organic pollutants could be adsorbed onto the surface of the material and collected by a magnetic field or decomposed on the surface of catalytically active nanoparticles covering tubes under irradiation.

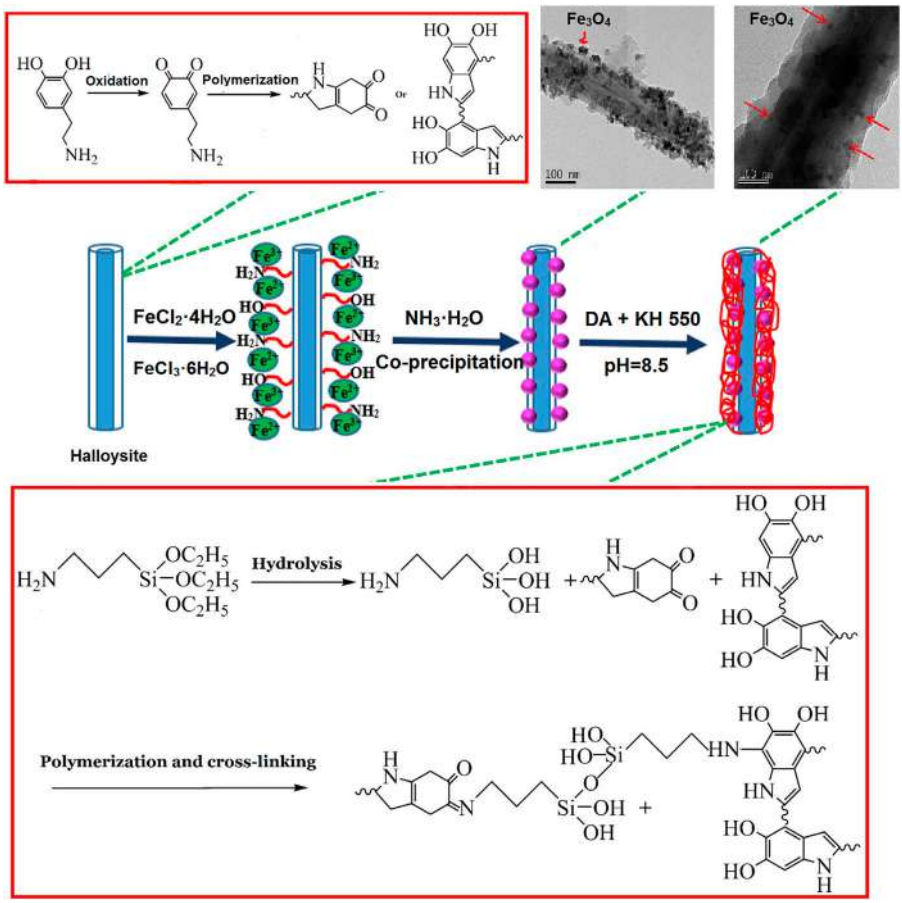

Figure 2.15 Multishell polymer/Fe_3O_4/halloysite hybrid preparation method. Adapted from ref. 82 with permission from Elsevier, Copyright 2017.

Polymers capable of binding ions may coat clay tubes. Mishra and Maity *et al.* fabricated a polypyrrole coated nanocomposite *via in situ* polymerization of pyrrole onto halloysite nanotubes.[83] Such materials may be applied in water purification technologies for heavy metal ion removal as was proposed by the authors. In addition, polypyrrole is a conductive polymer and its application could be extended. Polyaniline is the most used conductive polymer to form coatings on tubular clay surfaces. Polyaniline based materials are of great interest, first of all, due to the electroconductive properties of the proposed composites and secondly, their complexing properties.[84–86] By facilely tuning the dopant acid, pH, and apparent weight proportion for aniline and halloysite nanotubes in the synthesis process, polyaniline with a tuned oxidation state, doping extent, and content coats halloysite nanotubes. Conductive polymer coatings could be further used to prepare fillers

with multifunctional properties to prevent metal corrosion and also cap halloysite nanocontainers with active substrates, for example, for antifouling painting. Such material will also add stiffness and prevent crack formation.

The coating of halloysite is also performed when drugs or active agents are loaded into tubes. In this case, organic molecules could be trapped in an aluminosilicate tube using end-stoppers or coating.[87] The surface coating of halloysite significantly extends the release behavior of drugs over that of untreated nanotubes. For example, a benzotriazole–copper coating provided a more sustained release of brilliant green form clay lumen, extending it from 50 to 200 hours.[88] Essential oils encapsulation showed the same result. Thyme oil was encapsulated inside clay nanotubes and then caged inside using end-stoppers or surface coating.[89] Both ends of nanocapsules were capped with sodium alginate-calcium chloride complexing or coating the negatively charged surface of untreated clay nanotubes was performed using polyethyleneimine. It has been found that coating provides slower essential oil release compared to end-stoppers.

A similar approach was used to formulate nanocontainers coated with polyelectrolyte.[26,90] In[26] clay tubes were loaded with the corrosion inhibitor 2-mercaptobenzothiazole, which is partially soluble in water and very soluble in ethanol or acetone. To prevent undesirable leakage of the loaded inhibitor from the halloysite interior, the outer surface of the 2-mercaptobenzothiazole-loaded halloysite was modified by deposition of several alternating polyelectrolyte multilayers (poly(allylamine hydrochloride)/poly(styrene sulfonate)). Another functionality of the polyelectrolyte shell is to provide the release of the encapsulated inhibitor controlled by pH changes in the environment surrounding the halloysite nanotube, which will perform inhibitor release triggered by pH changes directly in the corrosion pit. Figure 2.16 shows the mechanism of polyelectrolyte shell assembly on nanocontainers surface and the zeta potential variations while layer-by-layer modification.

The hydrophilic nature and low chemical activity of halloysite play a negative role in catalysis, which is why various techniques are used to modify the surface. The Pd-containing material based on a halloysite-poly (ionic liquid) nanocomposite was studied in.[91] The interesting point was that the IL-polymer just covered the surface of halloysite and formed a shell. It should be noted as a disadvantage that upon IL polymerization, the specific surface area of bare halloysite considerably decreased and reached 10.37 $m^2 g^{-1}$, but the structure of the nanotubes was not destroyed. It was shown that the content of poly (ionic liquid) polymer coating significantly affected the catalytic activity of hybrid material.

In,[92] taking advantage of the synergistic effects between polymer and halloysite clay as well as the capability of heteroatom-containing polymers for anchoring nanoparticles and suppressing their leaching, a novel support composed of clay tubes and 2-amino pyrimidine functionalized polyglycidylmethacrylate was prepared through the initial functionalization of halloysite followed by polymerization with glycidylmethacrylate and functionalization

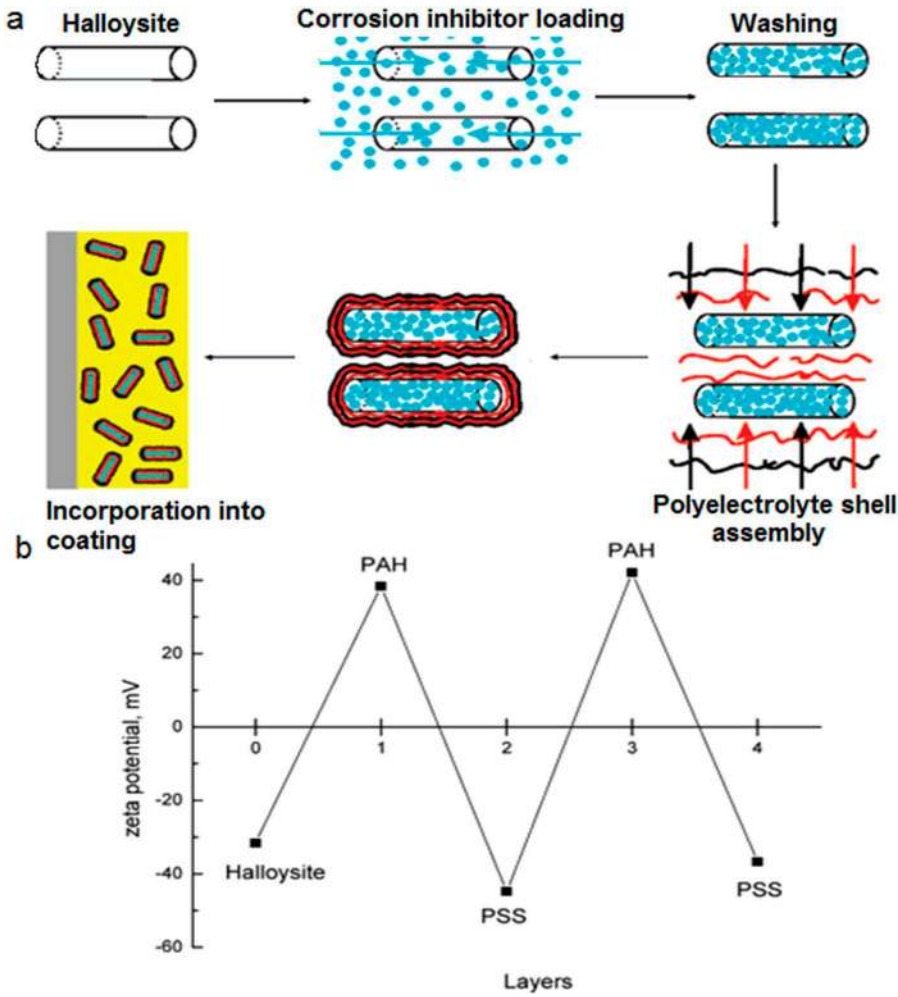

Figure 2.16 (a) schematic illustration of the fabrication of 2-mercaptobenzothiazole-loaded halloysite/polyelectrolyte nanocontainers; (b) zeta potential data for sequential deposition of PAH and PSS polyelectrolytes on halloysite nanotubes, pH = 7.5. Reproduced from ref. 26 with permission from American Chemical Society, Copyright 2008.

with 2-amino pyrimidine. The hybrid halloysite-polymer system with poly(methyl methacrylate-*co*-maleic anhydride) was shown in.[18]

One of the interesting types of 3-D macromolecules is dendrimers. They can be synthesized through various methodologies, like divergent and convergent methods. Dendrimers have diverse applications ranging from drug delivery and diagnosis to the synthesis of nanomaterials and catalysis.[93] The unique structure of dendrimers, in which a core is surrounded with repeating branches, forms an interior microenvironment, and access to it can be

controlled with the dendrimer periphery. This microenvironment can affect the reaction in terms of selectivity, conversion and reactivity. First attempts to graft this macromolecule to halloysite were performed in.[93] A novel magnetic heterogeneous material was synthesized through the growth of a dendrimer of generation 3 (G3) on the surface of clay tubes followed by the decoration of dendrimer terminal groups with ionic liquid and the incorporation of Fe species. The higher the generation of dendrimer, the higher Fe content that was achieved, which is favorable for applications.

Cyclodextrins are a biocompatible and bioavailable class of molecules.[94] They are often applied as phase transfer catalysts due to their specific geometry. An interesting approach was proposed by a group of authors, where cyclodextrin, together with a carbon coating, was used as a shell for clay tubes to address those enhanced catalytic properties. Considering the possible synergism between halloysite, cyclodextrins and carbon porous materials, the research group studied Pd-containing halloysite decorated with a cyclodextrin modified melamine-based polymer.[95] The schematic representation of the synthesis method is shown in Figure 2.17. The system was used as a catalyst for the hydrogenation of nitroarenes to the corresponding anilines. The results established that the incorporation of a melamine-based polymer could improve the anchoring of Pd species through electrostatic interactions while suppressing Pd leaching. The presence of cyclodextrin, on the other hand, could promote the formation of an inclusion complex with a hydrophobic substrate and transferring them into the aqueous media. Moreover, cyclodextrin could act as a capping agent and stabilize Pd nanoparticles. Following the results obtained, the next study was focused on functionalization of halloysite through the β-Cyclodextrin and glycidyl methacrylate polymerization to form a polymeric network.[96]

2.5 Halloysite Core–Shell Micro- and Macrosystems

Due to the tubular nanosized structure of halloysite and its high aspect ratio, it is a perfect Pickering emulsifier, especially after surface hydrophobization. The use of modified halloysite could be expended to the formation of micro- and even macroscale structures like microcapsules, or hollow or porous spheres. The interfacial energy principles allow hydrophobic particles to encapsulate individual droplets into a stable form as individual macroscopic objects, which have recently been called “liquid marbles”.[97] Reversing the organization of oil-in-water Pickering emulsion formed with halloysite nanoclay, liquid marbles were created with water droplets encapsulated by a layer of clay nanotubes.[98,99] The surface-modified halloysite formed pincushion agglomerates on the surface of the liquid droplets, which create a superhydrophobic surface similar to that of the plant gall surface prepared by aphids. As a result, the liquid marbles showed high mechanical strength upon impact without the use of low surface energy fluoroalkyl or fluorine-modified materials. It is interesting to note that the morphology of solid particles affects the dynamic behavior of liquid marbles.[100] Liquid marbles stabilized with

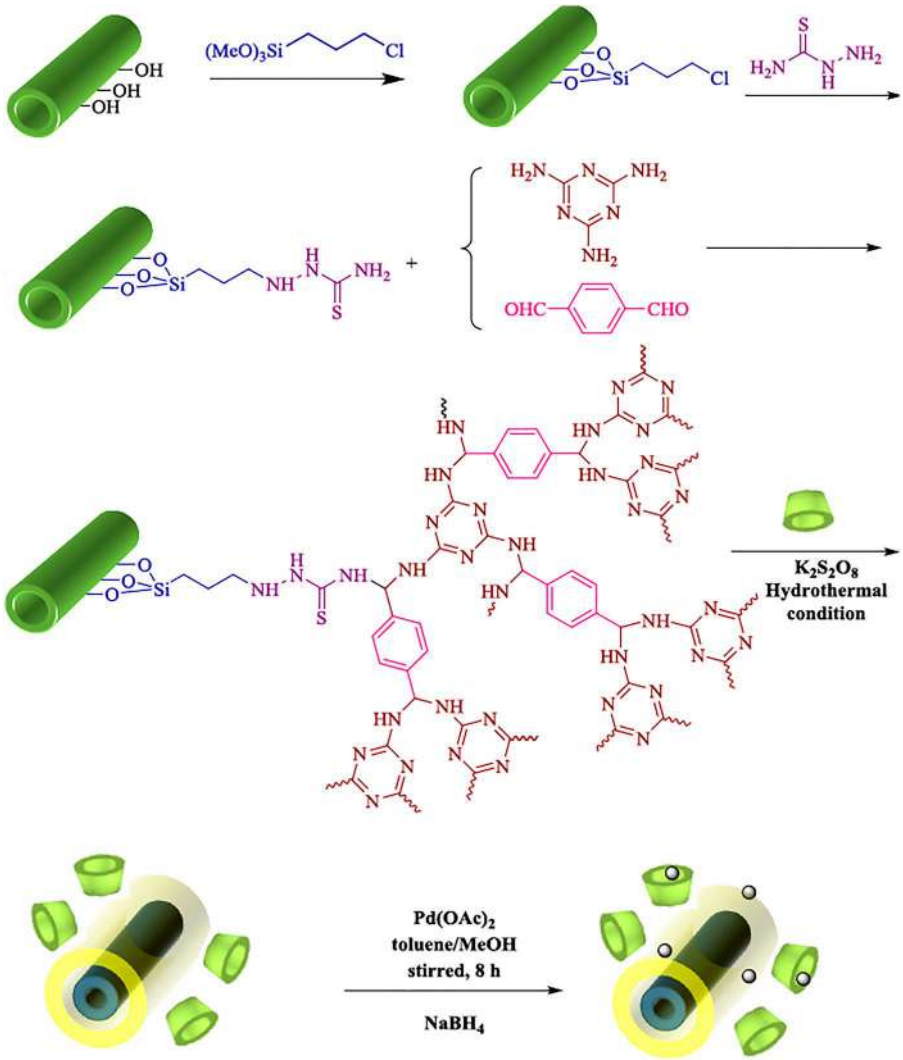

Figure 2.17 The schematic procedure of the synthesis of the halloysite decorated with a cyclodextrin modified melamine-based polymer catalyst. Reproduced from ref. 95 with permission from the Royal Society of Chemistry.

spherical $CaCO_3$ particles show an elastic response to mechanical deformation almost up to collapse. In contrast, liquid marbles prepared with rod-like particles exhibit a more plastic response to compression. The rod shaped particles form three dimensional network structure, and therefore, the liquid marbles stabilized with the particles show a higher resistance to deformation at low stress and more plastic deformation at higher stress.

Exploring the described approach, halloysite stabilized liquid marbles were proposed for the encapsulation and protection of bacteria (Figure 2.18).[98] Because of the water repellency, the nanotubes are able to trap water inside a

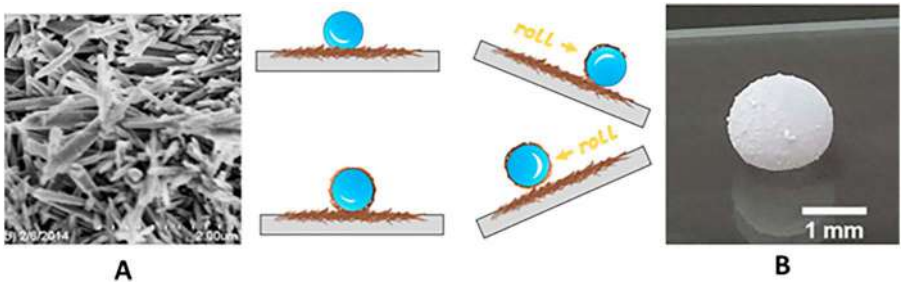

Figure 2.18 Clay nanotube liquid marbles enhanced with inner biofilm. Reproduced from ref. 98 with permission from American Chemical Society, Copyright 2019.

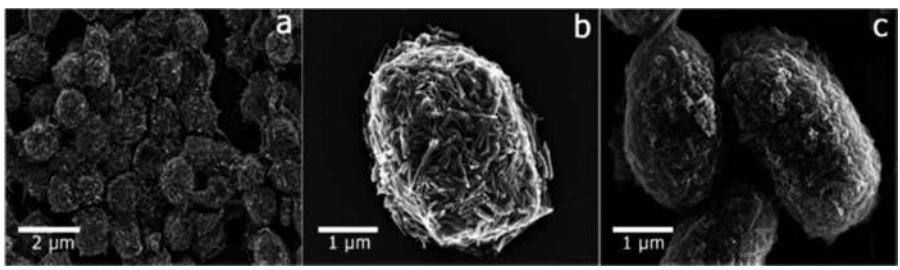

Figure 2.19 SEM images demonstrating the polyelectrolyte-mediated self-assembly of pristine halloysite nanotubes (a, b) with yeast cells/PAH/HNT/PAH/PSS architecture and the direct self-assembly of magnetite-modified halloysite (c) on *Saccharomyces cerevisiae* yeast cells. Reproduced from ref. 42 with permission from the Royal Society of Chemistry.

thin shell making a stable interface between inner liquid and air, thus forming marbles with reversed emulsion architecture. The halloysite with its alkane modifications encourages the growth of selected bacteria inside the marble. The biofilm produced at the inner walls of the halloysite shell by such bacteria strengthens the marbles' structure and reduced evaporation, keeping the bacteria viable for a period of up to 4 days after drying.

Microbial cells with protective coatings are been developed for biosensors design, cell delivery, tissue engineering and fabrication of cell-based inorganic microcapsules. An encapsulation of individual microbial cells, known as cell surface engineering, includes a layer-by-layer deposition of polyelectrolytes, direct deposition of nanoparticles or fabrication of biomimetic solid inorganic shells.[101] Anionic halloysite nanotubes were deposited on yeast cells modified with a polycation (poly(allylamine hydrochloride), PAH), providing mechanical protection and a nutrient surplus (halloysite was loaded with sucrose).[102] Importantly, clay nanotubes did not induce any toxic effects in yeast. The typical scanning electron microscopy images demonstrating the “hedgehog-like” architecture of polycation/halloysite shells are shown in Figure 2.19a and b.[40] An alteration

of this approach has also been demonstrated using magnetite-PAH-modified halloysite capable of one-step direct deposition onto yeast cells. The deposition of halloysite modified with Fe_3O_4 onto yeast cells was proposed in.[62] Such nanocoated cells are a step in the development of "cyborg" microorganisms that could be manipulated using a magnetic field (Figure 2.19c).

Halloysite may be also applied to guide core–shell structures formation. Core–shell thermally expandable microcapsules were prepared *via* Pickering suspension polymerization using halloysite nanotubes as the Pickering emulsifier.[103] Acrylonitrile and methyl methacrylate were used as the comonomers. When the halloysite concentration was 0.6 wt%, the microcapsules exhibited a core–shell morphology that contained approximately 35 wt% of the blowing agents (alkane) with an average particle size of 232.0 μm.

Recently, porous microspheres of Al/MCM-41/halloysite composite were synthesized (Figure 2.20).[104] Hierarchical composite materials based on ordered aluminosilicates of the Al–MCM-41 type and halloysite nanotubes with different Al–MCM-41/halloysite weight ratios were synthesized and studied as components of supports of platinum catalysts for the isomerization of the C8 aromatic fraction. A catalytic activity higher than that of the commercial catalyst was obtained. Hence, this new material could be perfect for active substrates encapsulation due to high porosity combined with microscopic volume and relatively strong frame. It should be noted that these microspheres do not form by the standard procedure for Al/MCM-41 preparation. The addition of halloysite clay tubes was a key factor in hollow material formation.

An extension of the self-assembly approach to core–shell macrostructures could be the coating of the hair surface with halloysite (Figure 2.21). Halloysite covers the hair surface in a 1–3 μm thick layer.[105] With their inherent ability to load molecules inside the lumen and release them in a sustained and controlled manner, surface engineering of hair with halloysite creates a novel approach to deliver active chemicals to the surface of hair.[106]

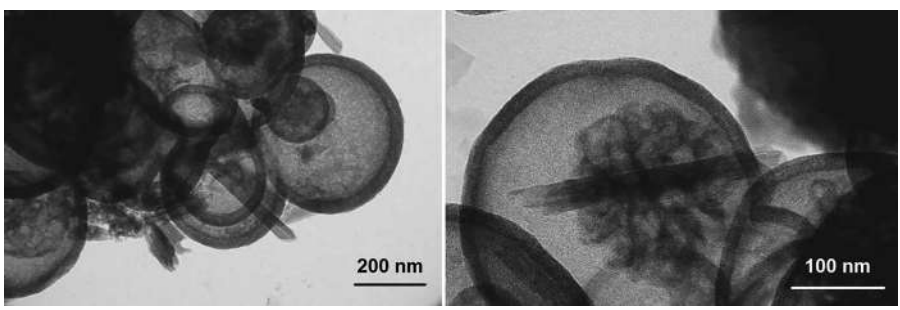

Figure 2.20 TEM images of Al/MCM-41/halloysite hollow microspheres. Adapted from ref. 104 with permission from Springer Nature, Copyright 2019.

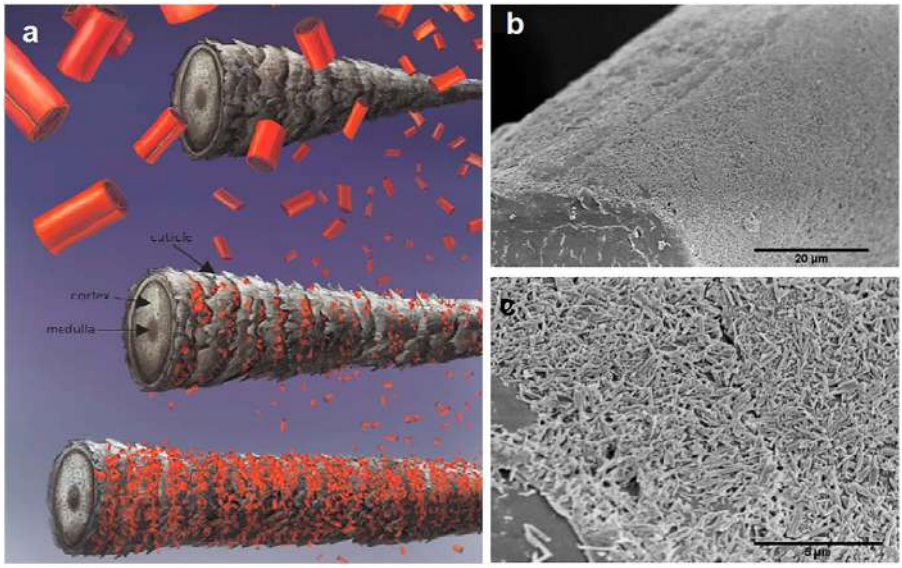

Figure 2.21 (a) Hair with applied clay nanotubes and development of the coating from anchoring in the cuticle to capillary force/drying driven surface assembly; (b and c) SEM images of hair with applied clay nanotubes shell. Adapted from ref. 106 with permission from the Royal Society of Chemistry.

2.6 Conclusion

We describe the nanoarchitectural design of core–shell clay-metal tubule systems allowing the selective placing of metals and their compounds inside or outside the aluminosilicate nanotubes. This approach allows the scale up of metal nanoparticles production by placing them on abundantly available clay nanotemplates, stabilizing them and maximizing their efficiency by the hierarchic construction of ceramic and multiple metal components. Hierarchical clay nanotube-ordered silica composites are also a perspective for mesocatalytic systems preparation. The formation of metal nanoparticle cores in the clay nanotubes makes this core–shell system safer and applicable in biotechnology for cell/bacteria encapsulation and tissue engineering.

Acknowledgements

This work was supported by the Ministry of Education and Science of the Russian Federation (Grant 14.Z50.31.0035) and as a part of the state task of Gubkin University, project number 0768-2020-0007 (A.S., A.G., V.V.).

References

1. A. Wang and W. Wang, in *Nanomaterials from Clay Minerals*, ed. A. Wang and W. Wang, Elsevier, 2019, pp. 1–20.
2. A. Glotov, N. Levshakov, A. Stavitskaya, M. Artemova, P. Gushchin, E. Ivanov, V. Vinokurov and Y. Lvov, *Chem. Commun.*, 2019, **55**, 5507–5510.
3. G. Jock Churchman, P. Pasbakhsh and S. Hillier, *Clay Miner.*, 2018, **51**, 303–308.
4. E. Joussein, S. Petit, J. Churchman, B. Theng, D. Righi and B. Delvaux, *Clay Miner.*, 2005, **40**, 383–426.
5. E. Abdullayev, K. Sakakibara, K. Okamoto, W. Wei, K. Ariga and Y. Lvov, *ACS Appl. Mater. Interfaces*, 2011, **3**, 4040–4046.
6. P. Pasbakhsh, J. Churchman and J. Keeling, *Appl. Clay Sci.*, 2013, **74**, 47–57.
7. Y. Lvov, W. Wang, L. Zhang and R. Fakhrullin, *Adv. Mater.*, 2016, **28**, 1227–1250.
8. J. Tully, R. Yendluri and Y. Lvov, *Biomacromolecules*, 2016, **17**, 615–621.
9. L. Yu, H. Wang, Y. Zhang, B. Zhang and J. Liu, *Environ. Sci.: Nano*, 2016, **3**, 28–44.
10. R. Liu, C. Yan, H. Wang, G. Xiao and D. Tu, *J. Nanosci. Nanotechnol.*, 2015, **15**, 7385–7390.
11. J. Keeling, Natural Mineral Nanotubes: Properties and Applications, 2015, pp. 96–115.
12. P. Yuan, P. D. Southon, Z. Liu, M. E. R. Green, J. M. Hook, S. J. Antill and C. J. Kepert, *J. Phys. Chem. C*, 2008, **112**, 15742–15751.
13. R. D. White, D. V. Bavykin and F. C. Walsh, *Nanotechnology*, 2012, **23**, 065705.
14. M. Massaro, G. Lazzara, S. Milioto, R. Noto and S. Riela, *J. Mater. Chem. B*, 2017, **5**, 2867–2882.
15. A. F. Peixoto, A. C. Fernandes, C. Pereira, J. Pires and C. Freire, *Microporous Mesoporous Mater.*, 2016, **219**, 145–154.
16. S. Silva, A. Peixoto and C. Freire, *Appl. Catal., A*, 2018, **568**, 221–230.
17. N. Sahiner and S. B. Sengel, *Fuel Process. Technol.*, 2017, **158**, 1–8.
18. S. Sadjadi, M. Malmir, N. Pourmohammad, S. Ahmadi and M. M. Heravi, *Res. Chem. Intermed.*, 2019, **45**, 4349–4366.
19. S. Sadjadi, M. Malmir, M. M. Heravi and F. G. Kahangi, *Int. J. Biol. Macromol.*, 2018, **118**, 1903–1911.
20. M. Massaro, G. Barone, G. Biddeci, G. Cavallaro, F. Di Blasi, G. Lazzara, G. Nicotra, C. Spinella, G. Spinelli and S. Riela, *J. Colloid Interface Sci.*, 2019, **552**, 236–246.
21. S. Jia and M. Fan, *Appl. Clay Sci.*, 2019, **180**, 105204.
22. N. Sahiner and S. B. Sengel, *Appl. Clay Sci.*, 2017, **146**, 517–525.
23. A. Philip, J. Lihavainen, M. Keinänen and T. Pakkanen, *Appl. Clay Sci.*, 2017, **143**, 80.
24. S. Sadjadi, M. M. Heravi, M. Malmir and F. Noritajer, *Mater. Chem. Phys.*, 2019, **223**, 380–390.
25. Y. Long, B. Yuan and J. Ma, *Chin. J. Catal.*, 2015, **36**, 348–354.

26. D. G. Shchukin, S. V. Lamaka, K. A. Yasakau, M. L. Zheludkevich, M. G. S. Ferreira and H. Möhwald, *J. Phys. Chem. C*, 2008, **112**, 958–964.
27. E. Abdullayev and Y. Lvov, *J. Mater. Chem. B*, 2013, **1**, 2894–2903.
28. Y. M. Lvov, D. G. Shchukin, H. Mohwald and R. R. Price, *ACS Nano*, 2008, **2**, 814–820.
29. Z. Hailei, *Nanotechnol. Rev.*, 2017, **6**, 573–581.
30. S. Das and S. Jana, *Environ. Sci.: Nano*, 2017, **4**, 596–603.
31. A. V. Vinokurov, V. A. Stavitskaya, A. Y. Chudakov, P. A. Glotov, V. E. Ivanov, A. P. Gushchin, M. Y. Lvov, L. A. Maximov, V. A. Muradov and A. E. Karakhanov, *Pure Appl. Chem.*, 2018, **90**, 825.
32. A. V. Stavitskaya, A. A. Novikov, M. S. Kotelev, D. S. Kopitsyn, E. V. Rozhina, I. R. Ishmukhametov, R. F. Fakhrullin, E. V. Ivanov, Y. M. Lvov and V. A. Vinokurov, *Nanomaterials*, 2018, **8**, 391.
33. V. A. Vinokurov, A. V. Stavitskaya, Y. A. Chudakov, E. V. Ivanov, L. K. Shrestha, K. Ariga, Y. A. Darrat and Y. M. Lvov, *Sci. Technol. Adv. Mater.*, 2017, **18**, 147–151.
34. V. A. Vinokurov, A. V. Stavitskaya, E. V. Ivanov, P. A. Gushchin, D. V. Kozlov, A. Y. Kurenkova, P. A. Kolinko, E. A. Kozlova and Y. M. Lvov, *ACS Sustainable Chem. Eng.*, 2017, **5**, 11316–11323.
35. V. Vinokurov, A. Stavitskaya, A. Glotov, A. Ostudin, M. Sosna, P. Gushchin, Y. Darrat and Y. Lvov, *J. Solid State Chem.*, 2018, **268**, 182–189.
36. A. Stavitskaya, K. Mazurova, M. Kotelev, O. Eliseev, P. Gushchin, A. Glotov, R. Kazantsev, V. Vinokurov and Y. Lvov, *Molecules*, 2020, **25**, 1764.
37. S. Mellouk, A. Belhakem, K. Marouf-Khelifa, J. Schott and A. Khelifa, *J. Colloid Interface Sci.*, 2011, **360**, 716–724.
38. S. Mellouk, S. Cherifi, M. Sassi, K. Marouf-Khelifa, A. Bengueddach, J. Schott and A. Khelifa, *Appl. Clay Sci.*, 2009, **44**, 230–236.
39. J. Matusik and A. Wścisło, *Appl. Clay Sci.*, 2014, **100**, 50–59.
40. Y. Lvov, A. Panchal, Y. Fu, R. Fakhrullin, M. Kryuchkova, S. Batasheva, A. Stavitskaya, A. Glotov and V. Vinokurov, *Langmuir*, 2019, **35**, 8646–8657.
41. M. Massaro, C. G. Colletti, G. Lazzara, S. Milioto, R. Noto and S. Riela, *J. Mater. Chem. A*, 2017, **5**, 13276–13293.
42. G. Lazzara, G. Cavallaro, A. Panchal, R. Fakhrullin, A. Stavitskaya, V. Vinokurov and Y. Lvov, *Curr. Opin. Colloid Interface Sci.*, 2018, **35**, 42–50.
43. A. Vinokurov Vladimir, V. Stavitskaya Anna, P. Glotov Aleksandr, A. Novikov Andrei, V. Zolotukhina Anna, S. Kotelev Mikhail, A. Gushchin Pawel, V. Ivanov Evgenii, Y. Darrat and M. Lvov Yuri, *Chem. Rec.*, 2018, **18**, 858–867.
44. M. Zieba, J. L. Hueso, M. Arruebo, G. Martinez and J. Santamaria, *New J. Chem.*, 2014, **38**, 2037–2042.
45. J. Liang, H. Tan, C. H. Xiao, G. J. Zhou, S. W. Guo and S. J. Ding, *J. Power Sources*, 2015, **285**, 210–216.
46. V. Vinokurov, A. Glotov, Y. Chudakov, A. Stavitskaya, E. Ivanov, P. Gushchin, A. Zolotukhina, A. Maximov, E. Karakhanov and Y. Lvov, *Ind. Eng. Chem. Res.*, 2017, **56**, 14043–14052.

47. T. Rostamzadeh, M. S. Islam Khan, K. Riche', Y. M. Lvov, A. V. Stavitskaya and J. B. Wiley, *Langmuir*, 2017, **33**, 13051–13059.
48. E. Lamouroux and Y. Fort, in *Spectroscopy of Polymer Nanocomposites*, ed. S. Thomas, D. Rouxel and D. Ponnamma, William Andrew Publishing, 2016, pp. 15–64.
49. S. Kumar-Krishnan, A. Hernandez-Rangel, U. Pal, O. Ceballos-Sanchez, F. J. Flores-Ruiz, E. Prokhorov, O. Arias de Fuentes, R. Esparza and M. Meyyappan, *J. Mater. Chem. B*, 2016, **4**, 2553–2560.
50. S. Das and S. Jana, *Dalton Trans.*, 2015, **44**, 8906–8916.
51. T. Barot, D. Rawtani and P. Kulkarni, *Heliyon*, 2020, **6**, e03601.
52. M. Zou, M. Du, M. Zhang, T. Yang, H. Zhu, P. Wang and S. Bao, *Mater. Res. Bull.*, 2015, **61**, 375–382.
53. M. Massaro, C. G. Colletti, B. Fiore, V. La Parola, G. Lazzara, S. Guernelli, N. Zaccheroni and S. Riela, *Appl. Organomet. Chem.*, 2019, **33**, e4665.
54. L. Gómez, J. L. Hueso, M. C. Ortega-Liébana, J. Santamaría and S. B. Cronin, *Catal. Commun.*, 2014, **56**, 115–118.
55. Y. Zhang, X. He, J. Ouyang and H. Yang, *Sci. Rep.*, 2013, **3**, 2948.
56. S. Li, F. Tang, H. Wang, J. Feng and Z. Jin, *RSC Adv.*, 2018, **8**, 10237–10245.
57. X. Tang, L. Li, B. Shen and C. Wang, *Chemosphere*, 2013, **91**, 1368–1373.
58. Y. Liu, H. Guan, J. Zhang, Y. Zhao, J.-H. Yang and B. Zhang, *Int. J. Hydrogen Energy*, 2018, **43**, 2754–2762.
59. Y. Liu, J. Zhang, H. Guan, Y. Zhao, J.-H. Yang and B. Zhang, *Appl. Surf. Sci.*, 2018, **427**, 106–113.
60. A. Maleki, Z. Hajizadeh and P. Salehi, *Sci. Rep.*, 2019, **9**, 5552.
61. T. Tsoufis, F. Katsaros, B. J. Kooi, E. Bletsa, S. Papageorgiou, Y. Deligiannakis and I. Panagiotopoulos, *Chem. Eng. J.*, 2017, **313**, 466–474.
62. S. A. Konnova, Y. M. Lvov and R. F. Fakhrullin, *Clay Miner.*, 2018, **51**, 429–433.
63. L. Kang, L. Han, J. He, H. Li, T. Yan, G. Chen, J. Zhang, L. Shi and D. Zhang, *Environ. Sci. Technol.*, 2019, **53**, 938–945.
64. R. Wang, G. Jiang, Y. Ding, Y. Wang, X. Sun, X. Wang and W. Chen, *ACS Appl. Mater. Interfaces*, 2011, **3**, 4154–4158.
65. H. Peng, X. Liu, W. Tang and R. Ma, *Sci. Rep.*, 2017, **7**, 2250.
66. A. P. Glotov, E. A. Roldugina, M. I. Artemova, E. M. Smirnova, N. R. Demikhova, V. D. Stytsenko, S. V. Egazar'yants, A. L. Maksimov and V. A. Vinokurov, *Russ. J. Appl. Chem.*, 2018, **91**, 1353–1362.
67. N. Bahri-Laleh, S. Sadjadi, M. M. Heravi and M. Malmir, *Appl. Organomet. Chem.*, 2018, **32**, e4283.
68. Y. I. Zhang and H. Yang, *Funct. Mater. Lett.*, 2013, **06**, 1350013.
69. B. Micó-Vicent, F. M. Martínez-Verdú, A. Novikov, A. Stavitskaya, V. Vinokurov, E. Rozhina, R. Fakhrullin, R. Yendluri and Y. Lvov, *Adv. Funct. Mater.*, 2018, **28**, 1703553.
70. N. Li, J. Zhou, J. Yu, Y. Liu, J. Tang and W. Tang, *Electrochim. Acta*, 2018, **273**, 349–357.
71. J. Hamdi, A. A. Blanco, B. Diehl, J. B. Wiley and M. L. Trudell, *Org. Lett.*, 2019, **21**, 3471–3475.

72. G. K. Dedzo, G. Ngnie and C. Detellier, *ACS Appl. Mater. Interfaces*, 2016, **8**, 4862–4869.
73. X. Zeng, Q. Wang and Y. Yang, *J. Mater. Sci.*, 2017, **52**(14), 8391–400.
74. J. Ouyang, B. Guo, L. Fu, H. Yang, Y. Hu, A. Tang, H. Long, Y. Jin, J. Chen and J. Jiang, *Mater. Des.*, 2016, **110**, 169–178.
75. X. Gao, F. Tang and Z. Jin, *Langmuir*, 2019, **35**, 14651–14658.
76. N. M. Sanchez-Ballester, G. V. Ramesh, T. Tanabe, E. Koudelkova, J. Liu, L. K. Shrestha, Y. Lvov, J. P. Hill, K. Ariga and H. Abe, *J. Mater. Chem. A*, 2015, **3**, 6614–6619.
77. Z. Cheng and W. Sun, *Chin. Chem. Lett.*, 2016, **27**, 81–84.
78. L. Fu, H. Yang, A. Tang and Y. Hu, *Nano Res.*, 2017, **10**, 2782–2799.
79. X. Zan, Z. Pan, Z. Wu, Z. Wang and Z. Liu, *J. Power Sources*, 2014, **264**, 229–234.
80. V. P. Ananikov, *Nanomaterials*, 2019, **9**, 1197.
81. M. Zhao and P. Liu, *J. Macromol. Sci., Part B*, 2007, **46**, 891–897.
82. X. Wan, Y. Zhan, Z. Long, G. Zeng and Y. He, *Chem. Eng. J.*, 2017, **330**, 491–504.
83. N. Ballav, H. J. Choi, S. B. Mishra and A. Maity, *Appl. Clay Sci.*, 2014, **102**, 60–70.
84. F. Hu, J. Xu, S. Zhang, J. Jiang, B. Yan, Y. Gu, M. Jiang, S. Lin and S. Chen, *J. Mater. Chem. C*, 2018, **6**, 5707–5715.
85. T. Zhou, C. Li, H. Jin, Y. Lian and W. Han, *ACS Appl. Mater. Interfaces*, 2017, **9**, 6030–6043.
86. L. Zhang, T. Wang and P. Liu, *Appl. Surf. Sci.*, 2008, **255**, 2091–2097.
87. A. Stavitskaya, S. Batasheva, V. Vinokurov, G. Fakhrullina, V. Sangarov, Y. Lvov and R. Fakhrullin, *Nanomaterials*, 2019, **9**, 708.
88. W. Wei, R. Minullina, E. Abdullayev, R. Fakhrullin, D. Mills and Y. Lvov, *RSC Adv.*, 2014, **4**, 488–494.
89. S. H. Jang, S. R. Jang, G. M. Lee, J. H. Ryu, S. I. Park and N. H. Park, *J. Food Sci.*, 2017, **82**, 2113–2120.
90. E. Abdullayev and Y. Lvov, *J. Nanosci. Nanotechnol.*, 2011, **11**, 10007–10026.
91. S. Sadjadi and M. Tavakolian, *ChemistrySelect*, 2019, **4**, 3369–3375.
92. S. Sadjadi, F. Koohestani, N. Bahri-Laleh and K. Didehban, *J. Solid State Chem.*, 2019, **271**, 59–66.
93. S. Sadjadi, M. Malmir and M. M. Heravi, *Appl. Clay Sci.*, 2019, **168**, 184–195.
94. J. Rousseau, S. Menuel, C. Rousseau, F. Hapiot and E. Monflier, in *Organic Nanoreactors*, ed. S. Sadjadi, Academic Press, Boston, 2016, pp. 15–42.
95. S. Sadjadi, M. Akbari, E. Monflier, M. M. Heravi and B. Leger, *New J. Chem.*, 2018, **42**, 15733–15742.
96. S. Sadjadi, F. Koohestani, B. Léger and E. Monflier, *Appl. Organomet. Chem.*, 2019, **33**, e5213.
97. G. Mchale and M. I. Newton, *Soft Matter*, 2015, **11**, 2530–2546.
98. A. Panchal, N. Rahman, S. Konnova, R. Fakhrullin, D. Zhang, D. Blake, V. John, E. Ivanov and Y. Lvov, *ACS Appl. Nano Mater.*, 2020, **3**, 1263–1271.

99. H. Wu, H. Watanabe, W. Ma, A. Fujimoto, T. Higuchi, K. Uesugi, A. Takeuchi, Y. Suzuki, H. Jinnai and A. Takahara, *Langmuir*, 2013, **29**, 14971–14975.
100. S. Azizian, S. Fujii, M. Kasahara, H.-J. Butt and M. Kappl, *Adv. Powder Technol.*, 2019, **30**, 330–335.
101. A. I. Zamaleeva, R. T. Minullina, J. R. Tully, M. R. Dzamukova, S. A. Konnova and E. A. Naumenko, in *Cell Surface Engineering: Fabrication of Functional Nanoshells*, The Royal Society of Chemistry, 2014, pp. 28–47.
102. Y. Lvov, W. C. Wang, L. Q. Zhang and R. Fakhrullin, *Adv. Mater.*, 2016, **28**, 1227–1250.
103. J. G. Kim, J. U. Ha, S. K. Jeoung, K. Lee, S.-H. Baeck and S. E. Shim, *Colloid Polym. Sci.*, 2015, **293**, 3595–3602.
104. A. P. Glotov, M. I. Artemova, N. R. Demikhova, E. M. Smirnova, E. V. Ivanov, P. A. Gushchin, S. V. Egazar'yants and V. A. Vinokurov, *Pet. Chem.*, 2019, **59**, 1226–1234.
105. M. Liu, R. Fakhrullin, A. Novikov, A. Panchal and Y. Lvov, *Macromol. Biosci.*, 2019, **19**, e1800419.
106. A. Panchal, G. Fakhrullina, R. Fakhrullin and Y. Lvov, *Nanoscale*, 2018, **10**, 18205–18216.

CHAPTER 3

Biomimetic Nanoarchitectonics: Natural Cellulose Based Nanocomposites as High Performance Catalysts

ZEHAO LIN[a] AND JIANGUO HUANG*[a]

[a]Department of Chemistry, Zhejiang University, Hangzhou, Zhejiang 310027, China
*E-mail: jghuang@zju.edu.cn

3.1 Introduction

The last decades have witnessed impressive developments in nanoscience and nanotechnology in both fundamental researches and practical applications. Aiming at creating specific materials by assembling the corresponding nanoscale building blocks, a new concept, namely nanoarchitectonics, was firstly proposed at a conference in 2000 by M. Aono and co-workers.[1] The concept was extended extensively and deepened systematically by K. Ariga and his colleagues recently.[2–5] The specific nanoarchitectures were fabricated by various functional units ranging from atoms and molecules to polymers, biomacromolecules and nanoscale objects through the harmonization of various methodologies including layer-by-layer (LbL) self-assembly, self-organization, chemical modification, field-controlled organization and so on.[6,7] In particular, the LbL self-assembly technique provides an effective pathway in the bottom-up fabrication of nanoarchitectured materials

Nanoscience & Nanotechnology Series No. 55
Concepts and Design of Materials Nanoarchitectonics
Edited by Omar Azzaroni and Katsuhiko Ariga

Published by the Royal Society of Chemistry, www.rsc.org

through the utilization of various molecular building blocks.[8,9] It is a versatile approach for the design and development of biomimetic nanoarchitectured materials through applying the LbL self-assembly technique on the surfaces of the specific natural substances.[10] In this way, the employed substances with naturally formed and hierarchically macro-to-nanoscale structures act as the scaffolds or templates for the assembling of the guest components with specific functionalities, leading to the fabrication of the corresponding functional materials.[11]

Among the various natural matters, cellulose substance arouses wide attentions because it is an almost inexhaustible polymeric raw material in bacteria and plants, exhibiting the hierarchically micro-to-nano morphology and three-dimensionally cross-linked porous structures.[12] Cellulose is a carbohydrate polymer comprised of β-D-glucopyranose units, abundant hydroxyl groups on the polymer chains, and hydrogen bonds among the polymer chains (see Figure 3.1a), making its hierarchically nanofibrous structure and unique properties of extensive chemical activity, degradability and hydrophilicity.[12] Ordinary laboratory filter paper is one of the ideal natural cellulose substances for the fabrication of functional nanoarchitectured materials due to its unique structures and excellent mechanical strength. The filter paper is composed of the randomly cross-linked cellulose microfibre assemblies (see Figure 3.1b), which are formed by numerous cellulose nanofibres with diameters varying from tens to thousands of nanometers (see Figure 3.1c). As shown in Figure 3.1d, due to the plentiful hydroxyl groups on the surfaces of the cellulose nanofibres, the filter paper is suitable for the deposition of the ultrathin metal oxide layer on the surfaces *via* the surface sol–gel processes through the LbL self-assembly method, giving the corresponding metal-oxide-thin-layer/cellulose-nanofibre composite. The as-prepared composites are calcined to give the metal oxide and relevant composite nanotubes or carbonized to give the metal-oxide/carbon and relevant composite nanofibres. Moreover, the metal-oxide-thin-layer/cellulose-nanofibre composite is convenient for the surface modification with other nanosized building blocks to give nanostructured paper based composites with good flexibilities and mechanical strengths. These natural cellulose derived composites display both the three-dimensionally hierarchical structure inherited from the cellulose substance and the specific properties of the guest components, which are employed in various applications,[13–17] such as electrode materials,[18,19] sensing matrices,[20,21] superhydrophobic matters,[22,23] and catalysts.[24–37]

Recently, we have developed a series of natural cellulose substance derived catalysts (especially photocatalysts) for environmental and energy issues, such as the degradation of organic pollutants, the production of hydrogen from water splitting, antibiosis, and so on. In recent years, environmental pollution and energy shortage problems have become increasingly more serious due to rapid industrialization and urbanization.[38] Photocatalysis is one of the most promising solutions because of its environmental friendliness and high efficiency.[39] Titania (TiO_2) is the most commonly investigated photocatalyst due to its sufficient photocatalytic activity, high chemical stability,

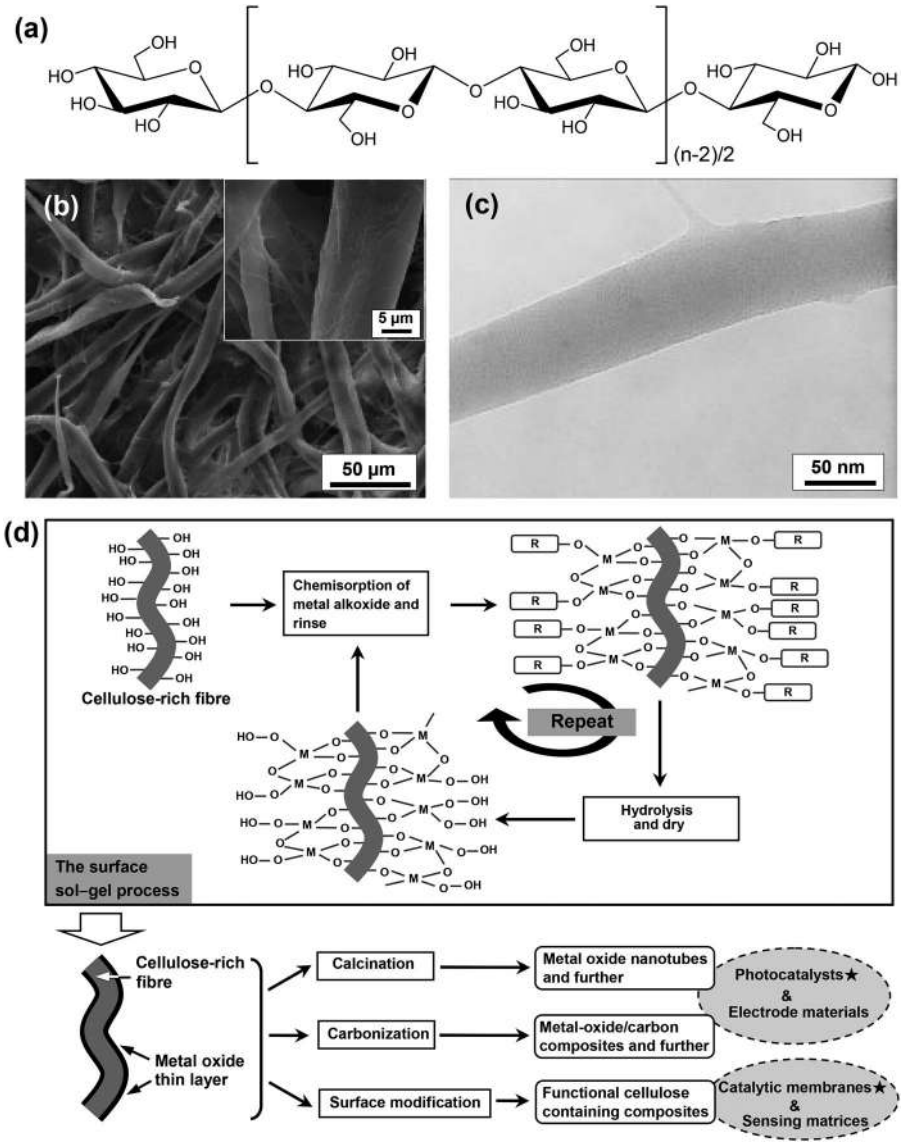

Figure 3.1 (a) Molecular structure of cellulose. (b) Field emission scanning electron microscopy (FE-SEM) image of laboratory filter paper. The inset displays an enlarged image of the microfibres. (c) Transmission electron microscopy (TEM) image of an individual nanofibre isolated from the microfibre. (d) Schematic illustrations of the deposition processes of the ultrathin metal oxide layer on the surfaces of the natural cellulose fibres *via* the surface sol–gel process through the LbL self-assembly technique, and different applications of the natural cellulose derived composites. Reproduced from ref. 16 with permission from John Wiley & Sons, Copyright © 2015 WILEY-VCH Verlag GmbH & Co. KGaA, Weinheim.

low cost, and nontoxicity.[40] However, the development and utilization of titania based photocatalysts were limited mainly owing to the low specific surface area of the bulk titania and the inconvenient cycling usage of the photocatalysts in powder form. In order to overcome these problems, fabricating nanoarchitectured photocatalysts with stable structures and high specific surface areas, building the heterostructures by combing titania and other semiconductors, as well as growing titania based photocatalysts *in situ* on the matrices have been demonstrated to be effective.[41]

Herein, we summarize various titania based powder catalysts and catalytic membranes derived from natural cellulose substances (*e.g.*, ordinary laboratory filter paper), which are fabricated by the surface sol–gel process through the LbL self-assembly technique. These natural cellulose substance derived catalysts in powder form displayed hierarchically porous network structures with improved specific surface areas and those in membrane form exhibited great mechanical strength, leading to the enhanced catalytic activities and stabilities.

3.2 Natural Cellulose Derived Catalytic Membranes

Due to severe water pollution in different factories, it is urgent to develop effective catalysts for the degradation of organic pollutants and antibiosis.[42] However, the practical applications of the catalysts for specific reactions in solution are limited because of the poor cycling stabilities of the catalysts in powder form. Many researches have been conducted to grow nanoarchitectured functional materials on solid matrices of glass and polymer substances to give the corresponding matrices based composites, leading to the easy recovery of the catalysts.[43] In order to increase the flexibilities, biodegradabilities, and sustainabilities of the matrices based composites, nanoarchitectures with catalytic active building blocks are fabricated on the nanofibre surfaces of the natural cellulose substances to give the catalytic membranes.

According to this point of view, we have developed a series of natural cellulose substance (*e.g.*, ordinary laboratory filter paper) supported catalysts for various applications.[24–27] For example, a nanofibrous anatase-titania–cellulose composite was fabricated by hydrothermal treatment of the titania-gel–cellulose composite, which was obtained through depositing ultrathin titania films on the surfaces of the cellulose nanofibres *via* the LbL sol–gel self-assembly process (see Figure 3.2a).[24] The resulting composite exhibited the hierarchical network structure derived from the natural cellulose substance, and each cellulose nanofibre was uniformly coated with anatase-titania nanoparticles with diameters varying from 20 to 50 nm. When the anatase-titania–cellulose membrane was applied as the photocatalyst for the degradation of methylene blue (MB) and methyl orange (MO) solutions (concentration 10.0 mg L^{-1} for both), it displayed excellent photocatalytic performances with the complete decomposition of the dyes after UV irradiation of 18 and 12 min, respectively. Moreover, the catalytic membrane was

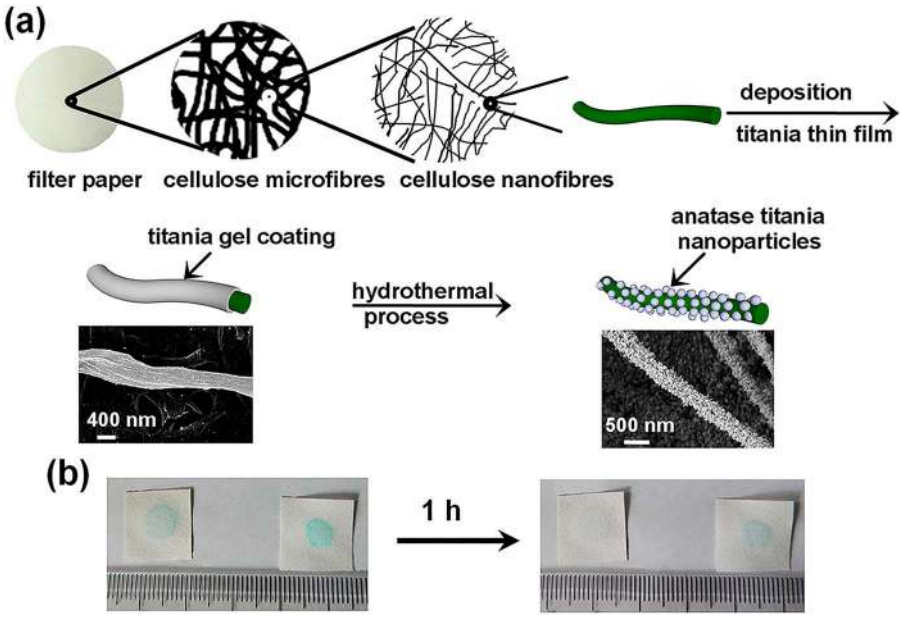

Figure 3.2 Hierarchical anatase-titania–cellulose composite based on the ordinary laboratory filter paper. (a) Schematic illustration of the fabrication process of the anatase-titania–cellulose composite sheet. (b) Degradation of methylene blue by using anatase-titania–cellulose A (left) and the pure filter paper (right) under sunlight irradiation. Reproduced from ref. 24 with permission from the Royal Society of Chemistry.

directly dropped with the MB solution under outdoor sunlight irradiation, and the MB molecule was found to be decomposed after 1 h, which was more obvious than the one dropped on the pure filter paper (see Figure 3.2b).

In order to increase the amount of catalytic active titania component on the cellulose, another anatase-titania/cellulose composite was obtained through subjecting the titania-gel/cellulose composite to a solvo-co-hydrothermal treatment.[25] The precursor of titanium butoxide was absorbed onto the cellulose nanofibres *via* the solvothermal process firstly, followed by the hydrothermal procedure to hydrolyze and crystallize it, leading to more anatase-titania nanoparticles (sizes *ca.* 2–5 nm) uniformly anchored on the surfaces of the cellulose nanofibres. As compared with the pure filter paper, the resultant anatase-titania/cellulose catalytic membrane delivered superior photocatalytic performances towards the degradation of MB solution (concentration 10.0 mg L^{-1}) under UV light, and the one prepared with more titanium butoxide precursor showed better photocatalytic activity of 30 min irradiation for the complete decomposition. Besides, small silver nanoparticles (weight ratio *ca.* 0.83 wt%) were coated onto the anatase-titania/cellulose composite sheet through the photocatalytic reduction approach, resulting in significant antibacterial activity against both *E. Coli* and *S. aureus*.

It is known that silver nanoparticles (Ag-NPs) display excellent antibacterial activities towards various microorganisms, but the serious aggregation behavior of the Ag-NPs results in a severe decrease in antibacterial performance.[44] Supporting Ag-NPs on the cellulose substance could provide an effective solution to this problem due to the hierarchically porous network structure and excellent properties of flexibility, edibility, and biocompatibility of the cellulose substance. Hence, an Ag-NPs/chitosan/titania/cellulose composite film was fabricated by employing a natural cellulose substance (*e.g.*, ordinary laboratory filter paper) as the matrix through the LbL self-assembly technique.[26] Due to the great chelating ability of chitosan for metal ions, uniform chitosan/titania composite layers were deposited on the microfibre surfaces of the cellulose substance, followed by the *in situ* photocatalytic reduction of silver ions into Ag-NPs (sizes *ca.* 4–20 nm) on the surface of the chitosan/titania composite layers. The obtained composite film replicated the hierarchically fibrous network structure of the initial cellulose substance, and a nanometer-thick Ag-NPs/titania/chitosan composite layer shell was coated tightly on the cellulose microfibre core, which showed a cable-like core–shell structure. It displayed excellent antibacterial activities towards both *E. Coli* and *S. aureus*, which were attributed to the synergistic effects among the high loading content of Ag-NPs with small sizes, the intrinsic antibacterial performance of the titania component, as well as the positively charged chitosan component.

Another harmful organic pollutant for the water environment is 4-nitrophenol (4-NP), and gold nanoparticles (Au-NPs) are demonstrated to be effective catalysts for the sufficient catalytic reduction of 4-NP to 4-aminophenol (4-AP).[45] Similarly, an cellulose/$(TiO_2)_5$/Au@$(PDDA/PSS)_n$ catalytic membrane with Au-NPs was fabricated based on the natural cellulose substance (see Figure 3.3a).[27] Positively charged poly(diallyl-dimethylammonium chloride) (PDDA) layers and negatively charged two-component layers composed of $KAuCl_4$ and poly(sodium-*p*-styrenesulfonate) (PSS) were deposited on the surface of the 5-cycle pre-coated titania-gel/cellulose composite for *n* times through the LbL self-assembly approach, followed by the reduction treatment of $KAuCl_4$ into Au-NPs with aqueous $NaBH_4$ solution. The resultant catalytic membrane exhibited a hierarchically fibrous network structure with lots of nanoparticles (sizes *ca.* 50 nm) anchored on the composite nanofibres, which were attributed to the Au@polyelectrolyte core–shell structures composed of Au-NPs (sizes *ca.* 3.5 nm) capped with the PDDA/PSS layers. When the catalytic membranes were applied to the sufficient catalytic reaction of 4-NP to 4-AP through the simple filtration of the mixed reaction solution (see Figure 3.3b and c), the cellulose/$(TiO_2)_5$/Au@$(PDDA/PSS)_{20}$ catalytic membrane prepared with 20 cycles of the polyelectrolyte and $KAuCl_4$ precursors showed better catalytic performances with the complete reduction after the second filtration, as compared with the one prepared with 10 cycles of precursors. The simple and effective filtration processes, the abundant source of filter paper, as well as the facile and controllable modification of Au-NPs, make the fabrication of such catalytic membranes possible on a large scale.

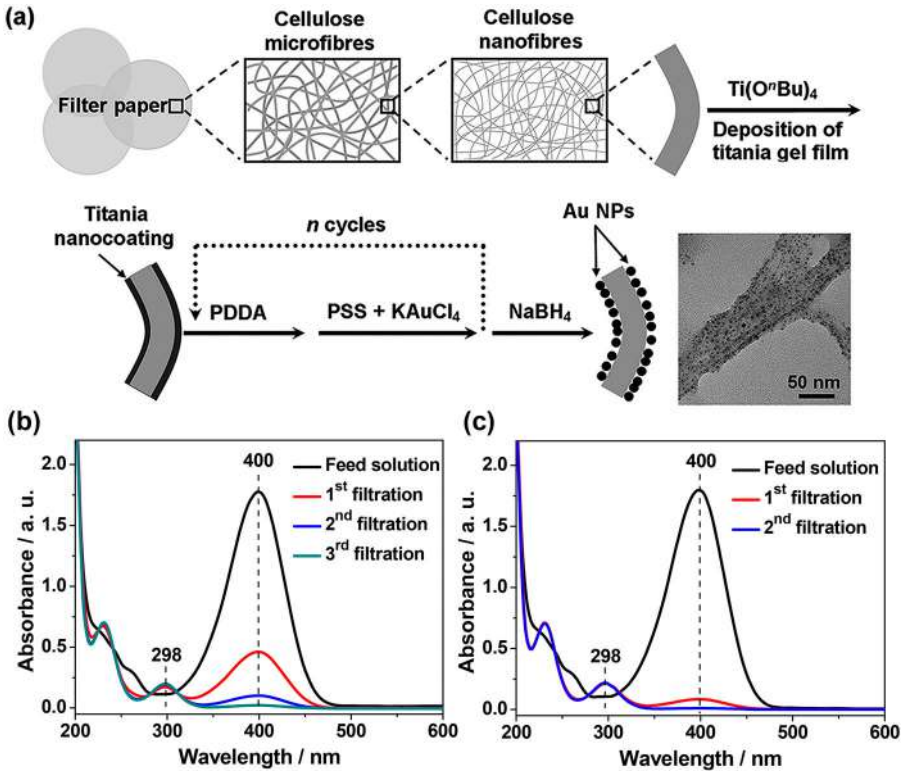

Figure 3.3 Hierarchical cellulose/Au-NP composite membrane based on the natural cellulose substance. (a) Schematic representation of the fabrication of the catalytic cellulose/Au-NP composite membranes. (b and c) UV-vis spectra of the initial aqueous feed solution containing 4-NP and $NaBH_4$, and the spectra of the filtrate after filtering the feed solution through the cellulose/$(TiO_2)_5$/Au@$(PDDA/PSS)_{10}$ paper (b) and the cellulose/$(TiO_2)_5$/Au@$(PDDA/PSS)_{20}$ paper (c) for single, double and triple cycles. Reproduced from ref. 27 with permission from the Royal Society of Chemistry.

3.3 Natural Cellulose Derived Nanomaterials as Photocatalysts for the Degradation of Dyes

Various kinds of dyes produced from the textile industries are another group of problematic organic pollutants in the water environment. Titania has been demonstrated to be effective in the photocatalytic degradation of various kinds of dyes under UV light.[46] However, the advances of the titania based photocatalysts are hindered due to the serious aggregation and low specific surface area of the bulk titania material. An efficient solution for this problem is the fabrication of nanostructured titania based materials by employing natural cellulose substances as the scaffolds or templates.

3.3.1 Titania Based Photocatalysts

Among the three main phases of titania, anatase phase titania is known to be a more effective photocatalyst, while rutile phase titania owns better chemical stability and a higher refractive index than the others. It is noted that the rutile phase titania materials also show good photocatalytic activities if they possess both high crystallinities and large specific surface areas.[47] However, the high-temperature treatment during the synthetic process results in the collapse of the fine structures and large sizes of the rutile crystallites of the rutile phase titania materials.[48] The facile flame burning technique was attempted to solve this problem. The ultrathin titania gels were deposited on the surfaces of the cellulose nanofibres *via* the surface sol–gel method, followed by the flame burning procedure of the titania-gel/cellulose composite to give the nanotubular rutile titania material (see Figure 3.4a).[28] The obtained rutile titania matter faithfully inherited the hierarchically nanotubular network structure of the filter paper, and the titania nanotubes were composed of rutile titania nanoparticles with particle sizes ranging from *ca.* 55 to 70 nm, which were controlled by the layers of the

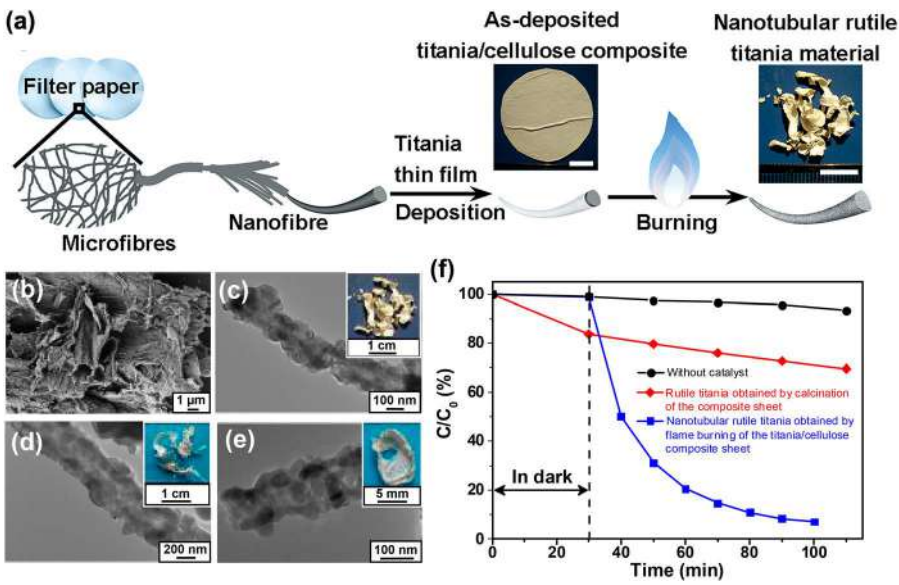

Figure 3.4 Hierarchically nanotubular rutile titania derived from natural cellulose substance. (a) Schematic illustration of the fabrication process of the nanotubular rutile titania material by means of flame burning of the titania/filter paper composite (Scale bars: 1 cm). (b–e) Electron micrographs of the nanotubular rutile titania material deposited with twenty cycles (b and c), ten cycles (d) and five cycles (e) of ultrathin titania gel films. (f) The photocatalytic degradation profiles by degrading MB under UV light of the titania materials. Reproduced from ref. 28 with permission from the Royal Society of Chemistry.

ultrathin titania gel (see Figure 3.4b–e). When the hierarchical rutile titania matter was applied to the photocatalytic degradation of MB solution (concentration 5.0 mg L^{-1}), it achieved a better performance of 90% degradation rate in 100 min under UV light compared with the rutile titania matter prepared by the calcination treatment (see Figure 3.4f). The excellent photocatalytic activity of the natural cellulose derived rutile titania matter was attributed to the unique hierarchically nanotubular structure, the small sizes of the titania nanocrystallites, and the large specific surface area.

Apart from ordinary laboratory filter paper, cotton is another natural cellulose substance as an ideal hard template for the fabrication of titania tubes. For instance, a hierarchically tubular structured mesoporous titania matter was prepared by employing cotton as a hard template and cetyltrimethylammonium bromide (CTAB) as a soft template through the one-pot sol–gel process, followed by calcination treatment at 500 °C to remove cotton and CTAB.[29] The obtained anatase-titania material consisted of hierarchically mesoporous titania tubes inherited from the overall morphology of cotton, which were composed of titania nanoparticles with sizes of *ca.* 12 nm. As compared with the titania matter prepared without the cotton template, it displayed a better photocatalytic degradation performance towards MB solution (concentration 5.0 mg L^{-1}) with a 90% degradation rate in 210 min under UV light, owing to the unique hierarchical structure, the large specific surface area, as well as the uniform formation of titania nanoparticles with smaller sizes without aggregation.

It is known that the photocatalytic activities of the titania based materials are largely affected by their morphological and structural properties, and those titania nanoarchitectures with hollow interiors possessed attractive advantages of low densities and high surface-to-volume ratios.[49] Herein, we developed a hollow sphere/nanotube hybrid structured anatase-titania material by applying natural cellulose substance (*e.g.*, laboratory ordinary filter paper) as the nanotube template while silica and polystyrene colloidal microspheres as the hollow sphere templates.[30] The ultrathin titania gel was deposited on the surfaces of the cellulose nanofibres, followed by the deposition of the colloidal microsphere layer *via* the LbL self-assembly technique to give the colloidal microspheres/titania-gel/cellulose composite. The as-prepared composite was calcined to remove the cellulose and polystyrene microsphere templates and subjected to an alkali treatment to remove the silica microsphere template. The resultant TiO_2 nanotube/hollow sphere hybrid material was composed of hierarchical anatase-titania nanotubes derived from the initial cellulose substance, which were anchored with titania hollow nanospheres (wall thicknesses *ca.* 7.5 nm, diameters *ca.* 100 nm). When it was employed as the photocatalyst for the degradation of MB (aqueous solution, concentration 10.0 mg L^{-1}), it showed a degradation rate of 90% under 60 min of UV light irradiation, which was superior to that of the nanotubular titania prepared without the microsphere templates. The excellent photocatalytic performance of the TiO_2 nanotube/hollow sphere hybrid material was due to the unique

cross-linked network structure that prevented the aggregation of titania and the large specific surface area that resulted from the tightly attached hollow microspheres on the surfaces of the nanotubes.

As illustrated above, the anatase phase titania displays excellent photocatalytic performance, and the rutile phase titania owns unique properties of great light scattering efficiency and thermodynamical stability. The formation of the heterogeneous nanostructure between the anatase and rutile phase titania promotes the transfer of photogenerated electrons from anatase to rutile titania, showing a synergistic effect between the two components.[50] For example, a heterogeneous nanotubular anatase/rutile titania composite was fabricated by employing a natural cellulose substance as the template.[31] The rutile phase titania nanoneedles were anchored on the hierarchical anatase phase titania nanotubes derived from the calcination of the as-prepared titania-gel/cellulose composite through a hydrothermal process, giving the nanotubular anatase/rutile titania composite. The obtained composite was composed of hierarchical anatase phase titania nanotubes coated with rutile phase titania nanoneedles (width *ca.* 50 nm, length *ca.* 100 nm), which exhibited a significant photocatalytic activity towards the degradation of MB solution (concentration 5.0 mg L^{-1}) with complete decomposition in 25 min under UV light and excellent stability after 5 cycles of reactions. The superior and stable photocatalytic performance of the nanotubular anatase/rutile titania composite was attributed to the unique hierarchically nanotubular structure derived from the initial cellulose substance, which improved the light absorption and adsorption of dye molecules, as well as the formation of the anatase/rutile titania heterostructure that promoted the charge transfer and hindered the recombination of the photogenerated electrons and holes.

3.3.2 Titania/Carbon Photocatalysts

It has been demonstrated that growing titania matter on an activated carbon support would greatly increase the corresponding photocatalytic performance of the nanoarchitectured titania based material, where the carbon component acts as an electron acceptor for the effective separation of the photogenerated charges on titania and a coadsorbent with better porous properties.[51,52] However, the uniform coating of titania on the nanofibrous carbon materials with effective photocatalytic activities remains a challenge. The application of natural cellulose substances in the fabrication process of materials provides an efficient solution for this problem because cellulose substances play a role as both the scaffolds and the carbon sources.

For instance, ultrathin titania gel layers were deposited on the surfaces of the cellulose nanofibres *via* the surface sol–gel method, followed by carbonization and calcination processes under a nitrogen atmosphere at 450 °C, giving a hierarchically nanofibrous titania/carbon composite.[32] The yielded composite was formed by hierarchical carbon nanofibres derived from the initial cellulose substance, which were coated with uniform titania layers on the nanofibre surfaces composed of anatase-titania nanocrystals (sizes *ca.* 4.5 nm) (see Figure 3.5a–c). As compared with the pure nanotubular titania and pure

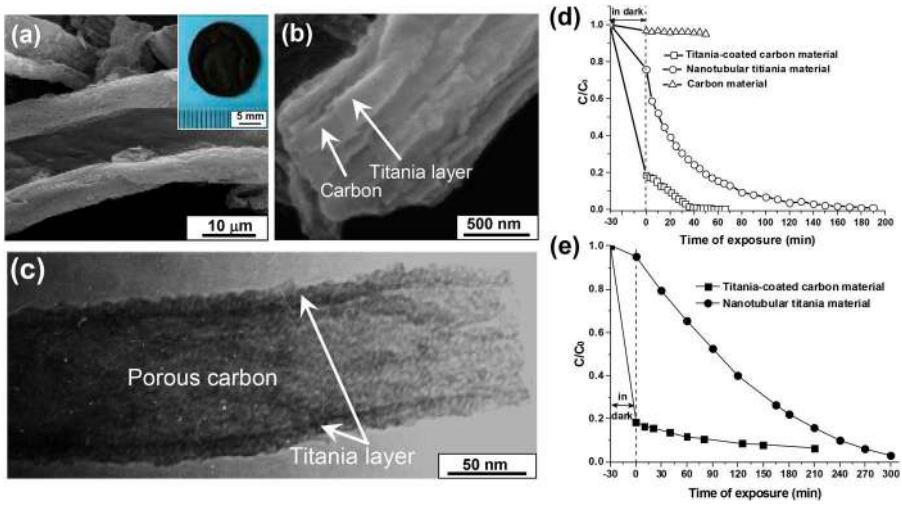

Figure 3.5 Hierarchically nanofibrous titania-coated carbon hybrid material fabricated by employing natural cellulose substances (ordinary laboratory filter paper) as a scaffold and carbon precursor. (a–c) Electron micrographs of the titania-coated, carbon nanofibrous material. (d and e) The photocatalytic degradation profiles for degrading MB (d) and RhB (e) under UV light by different materials. Reproduced from ref. 32 with permission from John Wiley & Sons, Copyright © 2010 WILEY-VCH Verlag GmbH & Co. KGaA, Weinheim.

nanofibrous carbon matters, the nanofibrous titania/carbon composite displayed improved photocatalytic performances towards the degradation of MB (concentration 0.03 mM) and RhB (concentration 0.01 mM) solution with degradation rates of 100% and 95% after 40 and 210 min irradiation under UV light, respectively (see Figure 3.5d and e). The enhanced photocatalytic activities of the nanofibrous titania/carbon composite were attributed to the rather large specific surface area and high adsorption capacities towards organic pollutants, as well as the effective transfer of the photogenerated electron–hole pairs, which were derived from the unique hierarchically porous structure of the composite, the uniform core–shell titania/carbon hybrid structure, and the synergistic effects between the carbon and titania components.

Similarly, a hierarchically nanofibrous rutile-titania/graphite composite was yielded from the calcination and carbonization treatment of the as-prepared titania-gel/cellulose composite at 1300 °C under argon atmosphere, where natural cellulose substance was employed as the scaffold and carbon source.[33] It was composed of core–shell structured carbon nanofibres with graphite phase carbon at the outer and amorphous carbon at the inner, which were anchored with rutile titania nanoparticles (sizes *ca.* 20–50 nm) on the surfaces of the carbon fibres. When the nanofibrous rutile-titania/graphite composite was applied as the photocatalyst for the degradation of MB solution (concentration 5.0 mg L^{-1}), it displayed an enhanced photocatalytic activity with a degradation rate of 90% in 260 min under UV light in

contrast with the nanotubular rutile-titania matter. Although this composite exhibited a worse photocatalytic performance than that of the nanofibrous anatase-titania/carbon composite[32] and the rutile titania matter prepared by the flame burning technique[28] mentioned previously due to the existence of the graphite phase carbon and the less amount of the active titania component, it provided a choice for the development of the composite material of rutile phase titania and carbon for the photocatalytic degradation of dyes.

3.3.3 Titania Based Composite Photocatalysts

Metal doping has been demonstrated to be an effective strategy for the improvement of the photocatalytic performances for the titania based materials because the doped metal ions are likely to increase the lifetime of the photogenerated electron–hole pairs, promote the transfer of the photogenerated charges, as well as extend the absorption edge to the visible light range of the corresponding photocatalysts.[53] Besides, the incorporation of certain kinds of metal ions into the lattice of titania is able to effectively reduce the temperature of phase transformation from anatase to rutile.[54] Among the doped metal elements, vanadium (V) is an ideal choice because of the formation of the $Ti_{1-x}V_xO_2$ solid-solution phase due to the close ionic radius of V^{4+} (0.72 Å) and Ti^{4+} (0.74 Å), the extended range of light absorption, and the decreased phase transformation temperature of titania from anatase to rutile.[55] As an example, a hierarchically nanofibrous V-doped rutile titania material was fabricated by the flame burning treatment of the as-prepared titania–vanadia/cellulose composite derived from the deposition of ultrathin titania–vanadia gels on the surfaces of the natural cellulose nanofibres.[34] The nanocomposite was composed of V-doped rutile titania nanofibres that consisted of titania nanoparticles with small and uniform sizes of *ca.* 15 nm, which was caused by the suppression of the titania crystal growth and the phase separation of vanadia and titania during the flame burning process. However, no obvious photocatalytic performance of the obtained nanofibrous V-doped rutile titania material was observed when it was applied as the photocatalyst for the degradation of MB solution under either UV or visible light. It was ascribed to the doped V atoms substituting Ti^{4+} in the crystal lattice of rutile phase titania, which acted as the center for the fast recombination of photogenerated electron–hole pairs, leading to the poor photocatalytic activity of the nanocomposite.

It is known that compositing TiO_2 with other components is an effective pathway for decreasing the recombination rate of the photogenerated electron–hole pairs of TiO_2 and inhibiting the growth of TiO_2 crystallinities, leading to the improvement of the photocatalytic performance.[52] Although the growth of rutile titania crystallites were suppressed through the flame burning technique by employing a natural cellulose substance as the template,[28] the precise and stepwise size control of the rutile titania nanocrystallites and the comparable photocatalytic activity of the anatase-titania matter have not been achieved. Hence, a hierarchically nanotubular silica/titania composite

was fabricated by depositing ultrathin titania-sandwiched silica layers onto the nanofibre surfaces of the natural cellulose substance, followed by the flame burning treatment in air (see Figure 3.6a).[35] This composite showed hierarchically network and tube-based bundling structures that were inherited from the initial natural cellulose substance and each nanotube was composed of silica-enwrapped ultrafine rutile titania nanocrystallites (see Figure 3.6b and c). The nano-precise size regulation of the embedded ultrafine rutile

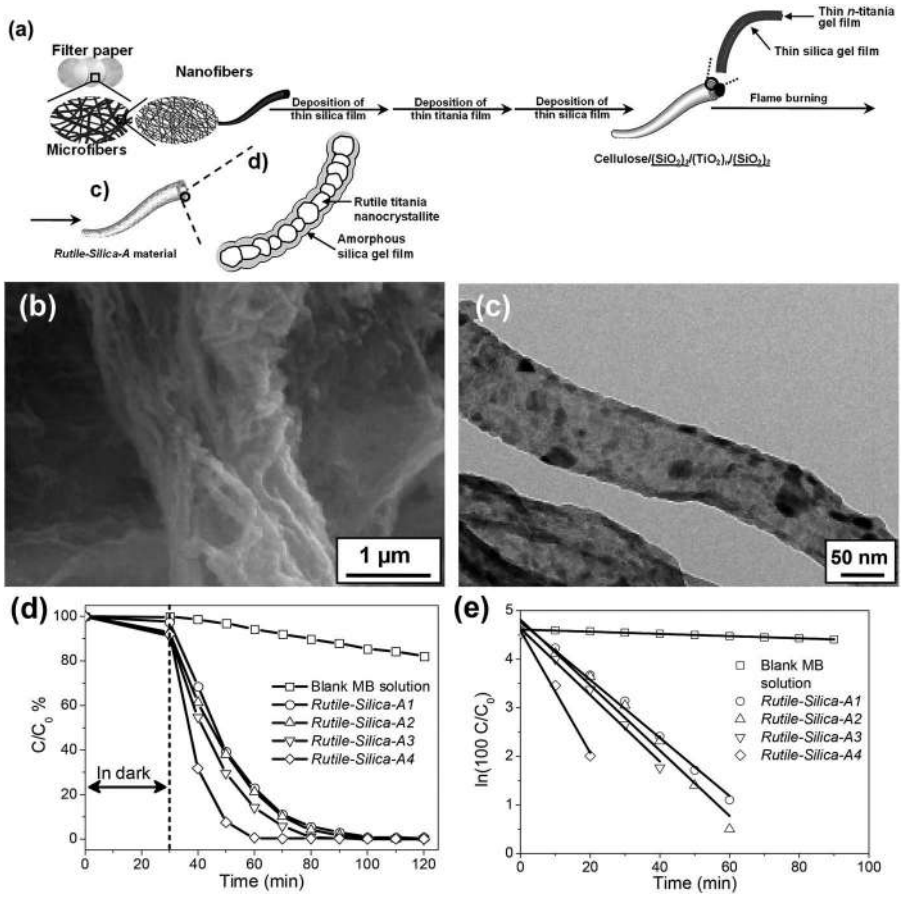

Figure 3.6 Hierarchical nanotubular silica/titania composite derived from a natural cellulose substance. (a) Schematic illustration of the fabrication process of the nanotubular silica/titania composite. (b) FE-SEM image of the tube-based bundling structures of the composite. (c) TEM micrograph of an isolated nanotube of the composite. (d and e) The degradation profiles and the corresponding pseudo-first-order simulations in degrading MB under UV light for a blank aqueous MB solution, with the rutile-silica-A materials prepared by the flame burning method containing titania nanocrystallites of varied sizes. Reproduced from ref. 35 with permission from John Wiley & Sons,

titania nanocrystallites was achieved due to the suppression effect of the silica gel films, and the average sizes of the nanocrystallites were finely tunable from *ca.* 3.3 to 16.0 nm through adjusting the deposition cycles of the initial titania gel layer. When being applied as the photocatalysts for the degradation of MB solution (concentration 5.0 mg L^{-1}), the nanotubular silica/titania composites showed excellent photocatalytic activities, while the one with the largest nanocrystallite size of *ca.* 16 nm delivered the optimal performance with complete decomposition in 60 min under UV light and an apparent rate of 0.126 min^{-1} (see Figure 3.6d and e). The hydroxyl and superoxide radicals were demonstrated to be active species during the photodegradation process of MB molecules. The superior photocatalytic performances of the nanotubular silica/titania composites were owing to the unique hierarchically network structures, the ultrafine rutile titania nanocrystallites, as well as the effective transfer of photogenerated electrons from the activated rutile phase titania to the silica matter.

Silver oxide (Ag_2O) is a p-type semiconductor with outstanding properties of narrow band gap (1.2 eV), low cost and facile preparation, which is suitable as the substrate for the fabrication of heterojunctions with titania, leading to the formation of a built-in electric field within the space charge region and further the promotion of the photocatalytic activity.[56] For example, we fabricated a series of hierarchical Ag_2O-nanoparticle/TiO_2-nanotube (Ag_2O-NP/TiO_2-NT) composites by employing natural cellulose substance (*e.g.*, laboratory ordinary filter paper) as the template.[36] Hierarchical anatase TiO_2 nanotubes were obtained by the calcination of the titania-gel/cellulose composite prepared by the deposition of ultrathin titania gel layers onto the surfaces of the cellulose nanofibres, and the Ag_2O nanoparticles were anchored on the surfaces of the TiO_2-NTs by a simple precipitation method, yielding the Ag_2O-NP/TiO_2-NT nanocomposites (see Figure 3.7a). The resultant composites possessed three-dimensionally porous network structures, which were composed of TiO_2 nanotubes coated with fine Ag_2O nanoparticles on the nanotube surfaces. When they were subjected as the photocatalysts towards the photocatalytic degradation of organic pollutants including MB, RhB and norfloxacin (NFCX), they all exhibited improved photocatalytic performance compared with the pure TiO_2 nanotubes and pure Ag_2O nanoparticles (see Figure 3.7b). The apparent rate constants of the optimal Ag_2O-NP/TiO_2-NT nanocomposite in the photocatalytic degradation of MB, RhB and NFCX are 0.62, 0.37, 0.39 min^{-1}, respectively, which were several times higher than those of the pure TiO_2 nanotubes and pure Ag_2O nanoparticles. The photocatalytic performance of the nanocomposite was demonstrated to be stable after three cycles of degradation reactions towards MB solution. The enhanced photocatalytic performances of the nanocomposites were ascribed to the increased adsorption capacities of organic pollutants, enhanced amount and lower recombination rate of the photogenerated electron–hole pairs, and the increased active sites of the photocatalysts, which were due to the hierarchical nanotubular structures and the effective formation of heterostructures between the TiO_2 and Ag_2O phases. It was revealed

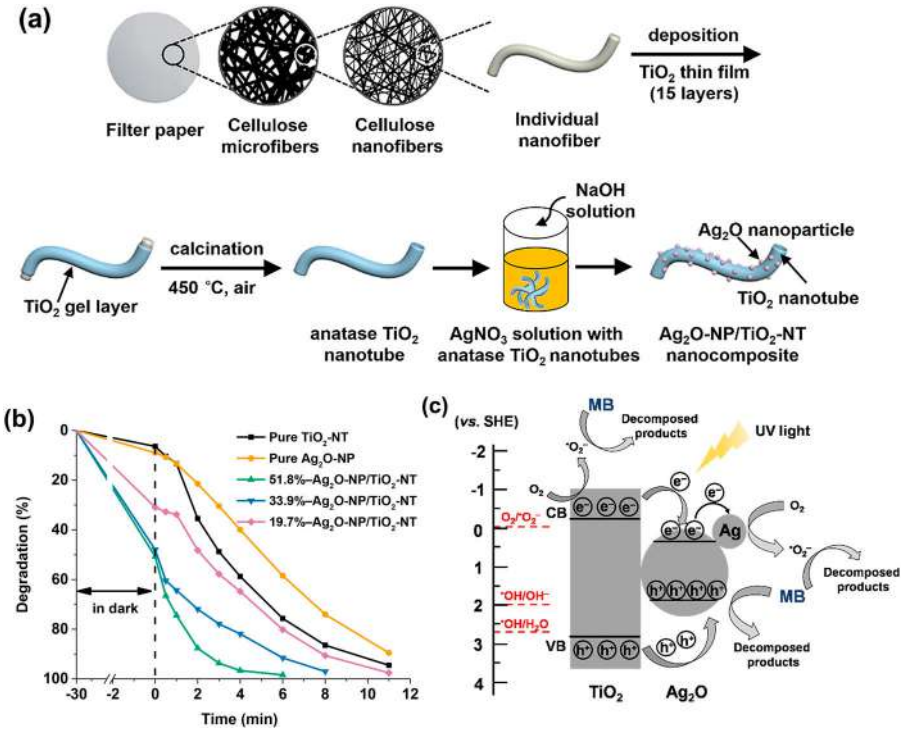

Figure 3.7 Hierarchical Ag_2O-nanoparticle/TiO_2-nanotube composite fabricated by employing commercial filter paper as a template. (a) Schematic illustration of the synthetic process of the hierarchical Ag_2O-NP/TiO_2-NT nanocomposites derived from natural cellulose substance. (b) The photocatalytic degradation profiles of the pure Ag_2O nanoparticles, the pure TiO_2 nanotubes, and the hierarchical Ag_2O-NP/TiO_2-NT nanocomposites in degrading MB under UV light irradiation. (c) The purposed photocatalytic mechanisms in degrading MB of the hierarchical 51.8%–Ag_2O-NP/TiO_2-NT nanocomposite under UV light irradiation. Reproduced from ref. 36 with permission from Springer Nature, Copyright 2019.

that the transfer of the photogenerated electron–hole pairs was promoted, while the reactive holes and superoxide radicals were the main active species during the photocatalytic degradation process (see Figure 3.7c).

3.4 Natural Cellulose Derived Nanomaterials as Photocatalysts for Hydrogen Production

The depletion of fossil fuel has made the photocatalytic hydrogen production from water splitting one of the most promising research areas in energy, and titania was still demonstrated to be effective in photocatalytic hydrogen

production.[57] In order to improve the photocatalytic activities of the titania based materials, loading a noble metal on the surface of titania accompanied with the addition of a sacrificial reagent in the reactive water was proven to be the most effective approach.[58] It was attributed to the fact that the loaded noble metal would decrease the large over-potential for hydrogen production and result in the formation of a Schottky barrier at the noble metal/titania interface, leading to the accelerated transfer of the photogenerated electrons. Besides, the added sacrificial reagents (*e.g.*, methanol) acted as the hole scavenger, and then hindered the recombination of the photogenerated electron–hole pairs. Among the various noble metals, platinum (Pt) is the most widely applied one due to its lowest over-potential and the formation of a relatively stronger Schottky barrier.[59]

As an example, a hierarchically nanotubular Pt/TiO_2 composite was fabricated by employing a natural cellulose substance (*e.g.*, ordinary laboratory filter paper) as the template.[37] The nanocomposite was prepared by depositing the ultrafine Pt nanoparticles using hydrogen hexachloroplatinate(IV) hexahydrate as the precursor *via* the photo-deposition method onto the surfaces of TiO_2 nanotubes obtained from the calcination process of the as-prepared titania-gel/cellulose composite through the LbL surface sol–gel self-assembly technique. It displayed a three-dimensionally porous network structure, and the ultrafine metallic Pt nanoparticles (sizes *ca.* 2 nm) were anchored on the surfaces of the hierarchical anatase TiO_2 nanotubes (see Figure 3.8a and b). As compared with the nanotubular Pt/TiO_2 composites with varied Pt loading contents, the optimal photocatalytic hydrogen production activity of 16.44 mmol h^{-1} g^{-1} was achieved by the one loaded with 1.06 wt% Pt content, while the less and excessive loading of Pt caused worse photocatalytic activities when they were employed as the photocatalysts under UV light (see Figure 3.8c). Besides, the photocatalytic performance of the optimal Pt/TiO_2 nanocomposite remained stable after five cycles of the hydrogen production reaction (see Figure 3.8d). The excellent photocatalytic water-splitting hydrogen production performance of the natural cellulose derived nanotubular Pt/TiO_2 composite was ascribed to the hierarchically nanotubular structure inherited from the initial cellulose substance and the uniform loading of Pt nanoparticles on such a composite.

3.5 Summary and Outlook

The fabrication of nanoarchitectured functional materials was achieved through the layer-by-layer (LbL) self-assembling of specific guest species by employing natural cellulose substances (*e.g.*, ordinary laboratory filter paper) as the structural templates or scaffolds, giving various nanomaterials that inherited the initial fine structures or/and physical properties of the cellulose substance, as well as the functionalities of the guest components. As reviewed in this chapter, a series of titania based catalytic membranes and powder photocatalysts derived from a natural cellulose substance were

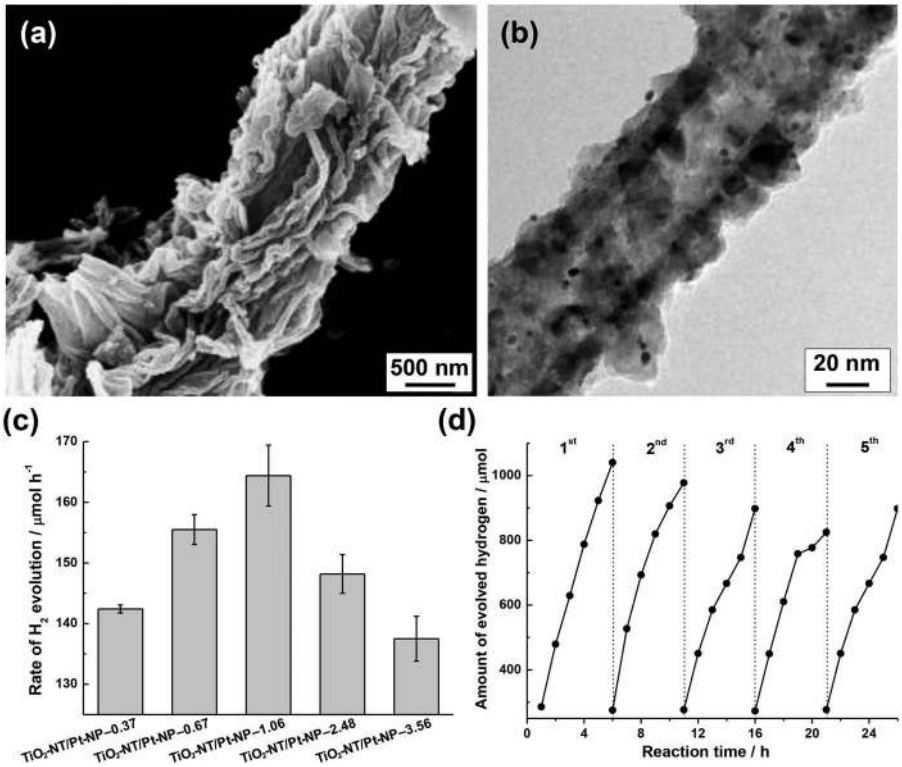

Figure 3.8 Hierarchical titania-nanotube/platinum-nanoparticle composite derived from natural cellulose substance. (a) FE-SEM micrograph of the TiO_2-NT/Pt-NP-1.06 composite. (b) TEM image of an isolated nanotube of the TiO_2-NT/Pt-NP-1.06 composite. (c) Effect of the platinum contents of the TiO_2-NT/Pt-NP composites on the photocatalytic hydrogen production rates. (d) Cyclic photocatalytic hydrogen evolution performance of sample TiO_2-NT/Pt-NP-1.06. Reproduced from ref. 37 with permission from John Wiley & Sons, © 2015 WILEY-VCH Verlag GmbH & Co. KGaA, Weinheim.

fabricated, which were employed for the catalytic degradation of organic pollutants, the photocatalytic production of hydrogen from water splitting, and antibiosis. The excellent catalytic performances of these nanoarchitectured materials were attributed to the mechanical strength of the cellulose matrices for the catalytic membranes or the hierarchically porous network structures of the powder photocatalysts, and the synergistic effects among the guest components contained therein. It provides an effective pathway for the design and fabrication of nanostructured catalysts for various specific reactions by taking the structural and physicochemical advantages of the natural cellulose substance. However, it remains plenty of room for the development and design of effective and facile synthetic strategies with good universalities for the fabrication of nanostructured functional materials.

References

1. K. Ariga and M. Aono, *Jpn. J. Appl. Phys.*, 2016, **55**, 1102A6.
2. K. Ariga, J. A. Jackman, N.-J. Cho, S. Hsu, L. K. Shrestha, T. NMori and J. Takeya, *Chem. Rec.*, 2018, **18**, 1.
3. K. Ariga, D. T. Leong and T. Mori, *Adv. Funct. Mater.*, 2018, **28**, 1702905.
4. K. Ariga, T. Mori and J. Li, *Langmuir*, 2018, **35**, 3585.
5. K. Ariga, T. Mori and L. K. Shrestha, *Chem. Rec.*, 2018, **18**, 676.
6. K. Ariga, J. Li, J. Fei, Q. Ji and J. P. Hill, *Adv. Mater.*, 2016, **28**, 1251.
7. K. Ariga, K. Minami and L. K. Shrestha, *Analyst*, 2016, **141**, 2629.
8. K. Ariga, M. Nishikawa, T. Mori, J. Takeya, L. K. Shrestha and J. P. Hill, *Sci. Technol. Adv. Mater.*, 2019, **20**, 51.
9. X. Jia, K. Minami, K. Uto, A. C. Chang, J. P. Hill, T. Ueki, J. Nakanishi and K. Ariga, *Small*, 2019, **15**, 1804640.
10. G. Li, J. Fei, Y. Xu, Y. Li and J. Li, *Adv. Funct. Mater.*, 2018, **28**, 1706557.
11. Y. Luo and J. Huang, *Sci. China: Chem.*, 2014, **57**, 1672.
12. D. Klemm, B. Heublein, H.-P. Fink and A. Bohn, *Angew. Chem., Int. Ed.*, 2005, **44**, 3358.
13. Z. Lin and J. Huang, *Dalton Trans.*, 2019, **48**, 14221.
14. Z. Lin, S. Li and J. Huang, *Chem. Rec.*, 2020, **20**, 187.
15. S. Li, D. Qi and J. Huang, *Curr. Opin. Colloid Interface Sci.*, 2018, **35**, 1.
16. S. Li and J. Huang, *Adv. Mater.*, 2016, **28**, 1143.
17. J. Huang and Y. Gu, *Curr. Opin. Colloid Interface Sci.*, 2011, **16**, 470.
18. S. Li, M. Wang, Y. Luo and J. Huang, *ACS Appl. Mater. Interfaces*, 2016, **8**, 17343.
19. S. Li and J. Huang, *J. Mater. Chem. A*, 2015, **3**, 4354.
20. Y. Lu, Y. Luo, Z. Lin and J. Huang, *Beilstein J. Nanotechnol.*, 2019, **10**, 1270.
21. W. Xiao, H. Hu and J. Huang, *Sens. Actuators, B*, 2012, **171–172**, 878.
22. S. Li, Y. Wei and J. Huang, *Chem. Lett.*, 2010, **39**, 20.
23. C. Jin, R. Yan and J. Huang, *J. Mater. Chem.*, 2011, **21**, 17519.
24. Y. Luo, J. Xu and J. Huang, *CrystEngComm*, 2014, **16**, 464.
25. Y. Luo and J. Huang, *Chem. - Eur. J.*, 2015, **21**, 2568.
26. W. Xiao, J. Xu, X. Liu, Q. Hu and J. Huang, *J. Mater. Chem. B*, 2013, **1**, 3477.
27. T. Niu, J. Xu, W. Xiao and J. Huang, *RSC Adv.*, 2014, **4**, 4901.
28. J. Zhao, Y. Gu and J. Huang, *Chem. Commun.*, 2011, **47**, 10551.
29. H. Huang, X. Liu and J. Huang, *Mater. Res. Bull.*, 2011, **46**, 1814.
30. Y. Gu, X. Liu, T. Niu and J. Huang, *Mater. Res. Bull.*, 2010, **45**, 536.
31. Y. Luo, X. Liu and J. Huang, *CrystEngComm*, 2013, **15**, 5586.
32. X. Liu, Y. Gu and J. Huang, *Chem. - Eur. J.*, 2010, **16**, 7730.
33. Y. Luo, X. Liu and J. Huang, *J. Nanosci. Nanotechnol.*, 2013, **13**, 582.
34. J. Li, J. Xu and J. Huang, *CrystEngComm*, 2014, **16**, 375.
35. Y. Gu and J. Huang, *Chem. - Eur. J.*, 2013, **19**, 10971.
36. Z. Lin, Y. Lu and J. Huang, *Cellulose*, 2019, **26**, 6683.
37. X. Liu, J. Li, Y. Zhang and J. Huang, *Chem. - Eur. J.*, 2015, **21**, 7345.
38. Y. Yang, C. Zhang, C. Lai, G. Zeng, D. Huang, M. Cheng, J. Wang, F. Chen, C. Zhou and W. Xiong, *Adv. Colloid Interface Sci.*, 2018, **254**, 76.

39. H. Wang, L. Zhang, Z. Chen, J. Hu, S. Li, Z. Wang, J. Liu and X. Wang, *Chem. Soc. Rev.*, 2014, **43**, 5234.
40. J. C. Colmenares, R. S. Varma and P. Lisowski, *Green Chem.*, 2016, **18**, 5736.
41. E. Bet-moushoul, Y. Mansourpanah, Kh. Farhadi and M. Tabatabaei, *Chem. Eng. J.*, 2016, **283**, 29.
42. H. Yi, L. Qi, D. Huang, G. Zeng, C. Lai, X. Liu, B. Li, H. Wang, C. Zhou, F. Huang, S. Liu and X. Guo, *Chem. Eng. J.*, 2019, **358**, 480.
43. Y. Jiang, I. Lawan, W. Zhou, M. Zhang, G. F. Fernando, L. Wang and Z. Yuan, *Cellulose*, 2020, **27**, 595.
44. J. Song, H. Kang, C. Lee, S. H. Hwang and J. Jang, *ACS Appl. Mater. Interfaces*, 2012, **4**, 460.
45. Y. Dai, Y. Li and S. Wang, *J. Catal.*, 2015, **329**, 425.
46. H. Dong, G. Zeng, L. Tang, C. Fan, C. Zhang, X. He and Y. He, *Water Res.*, 2015, **79**, 128.
47. J. T. Carneiro, T. J. Savenije, J. A. Moulijn and G. Mul, *J. Phys. Chem. C*, 2011, **115**, 2211.
48. A. Fujishima, X. Zhang and D. A. Tryk, *Surf. Sci. Rep.*, 2008, **63**, 515.
49. L. Wang, T. Sasaki, Y. Ebina, K. Kurashima and M. Watanabe, *Chem. Mater.*, 2002, **14**, 4827.
50. Y. Liao, W. Que, Q. Jia, Y. He, J. Zhang and P. Zhong, *J. Mater. Chem.*, 2012, **22**, 7937.
51. C. Moreno-Castilla, F. J. Maldonado-Hódar, F. Carrasco-Marín and E. Rodríguez-Castellón, *Langmuir*, 2002, **18**, 2295.
52. M. Dahl, Y. Liu and Y. Yin, *Chem. Rev.*, 2014, **114**, 9853.
53. J. Schneider, M. Matsuoka, M. Takeuchi, J. Zhang, Y. Horiuchi, M. Anpo and D. W. Bahnemann, *Chem. Rev.*, 2014, **114**, 9919.
54. F. Jia, W. Sun, J. Zhang, Y. Li and B. Yang, *J. Mater. Chem.*, 2012, **22**, 2435.
55. W. Choi, A. Termin and M. R. Hoffmann, *Angew. Chem., Int. Ed. Engl.*, 1994, **33**, 1091.
56. N. Wei, H. Cui, Q. Song, L. Zhang, X. Song, K. Wang, Y. Zhang, J. Li, J. Wen and J. Tian, *Appl. Catal., B*, 2016, **198**, 83.
57. D. Y. C. Leung, X. Fu, C. Wang, M. Ni, M. K. H. Leung, X. Wang and X. Fu, *ChemSusChem*, 2010, **3**, 681.
58. C.-H. Liao, C.-W. Huang and J. C. S. Wu, *Catalysts*, 2012, **2**, 490.
59. J. S. Jang, S. H. Choi, H. G. Kim and J. S. Lee, *J. Phys. Chem. C*, 2008, **112**, 17200.

CHAPTER 4

Nanoarchitectonics Based on S-layer Proteins: Design of Noble Metal Nanoparticle Arrangements and Nanostructured Materials

P. A. BOLLA*[a], M. A. SERRADELL[b], M. L. CASELLA[a] AND P. J. PERUZZO*[c]

[a]Centro de Investigación y Desarrollo en Ciencias Aplicadas "Dr Jorge J. Ronco"-CINDECA (UNLP – CONICET CCT La Plata – CIC), Calle 47 N 257, B1900AJK La Plata, Argentina; [b]Cátedra de Microbiología, Departamento de Ciencias Biológicas, Facultad de Ciencias Exactas, Universidad Nacional de La Plata – UNLP, 47 y 115 s/n, B1900AJK La Plata, Argentina; [c]Instituto de Investigaciones Fisicoquímicas Teóricas y Aplicadas – INIFTA (UNLP – CONICET CCT La Plata), Diag. 113 y 64 (B1904DPI), La Plata, Argentina
*E-mail: pbolla@quimica.unlp.edu.ar, pjperuzzo@inifta.unlp.edu.ar

4.1 Introduction: from the S-layer to Metal Nanoparticle Arrays

Technology focused on the preparation and study of materials with dimensions in the nanometer scale has great relevance in many fields of science; the manufacture of noble metal nanoparticles as one of the areas of most

Nanoscience & Nanotechnology Series No. 55
Concepts and Design of Materials Nanoarchitectonics
Edited by Omar Azzaroni and Katsuhiko Ariga

Published by the Royal Society of Chemistry, www.rsc.org

interest due to their applications, among which sensors,[1,2] catalysis,[3] *etc.* can be highlighted.[4,5]

Metal particle synthesis typically takes place following one of two different protocols: top-down or bottom-up.[6,7] In general, these methods require protecting agents to avoid the aggregation of the nanoparticles, which reduces the active surface of the metal. Nevertheless, conventional noble metal nanoparticles (MNPs) obtained by solution-phase methods still display difficulties, especially in terms of control over their properties (size, shape, composition, face exposition, *etc.*), and agglomeration.[8,9] So, new noble MNPs have to show high activity and stability, as well as to be prepared through a simple, low cost and ecofriendly procedure.[6,7]

In this respect, certain biomolecular systems offer some unique possibilities as they combine both self-organization and spatial patterning at the nanometer length scale. Because of this, a few years ago S-layer proteins (SLPs) have begun to be used as patterning elements for nanobiotechnological applications like noble MNPs synthesis.[10,11] The S-layer is a regular two-dimensional quasi-crystalline structure, consisting of proteins or glycoproteins, and it constitutes the outermost component of the cellular envelope of many *Bacteria* and *Archaea*. The S-layer is composed of identical subunits arranged periodically, leading to a precise spatial distribution of sites with particular physicochemical characteristics on the surface of the protein, which can be used to carry out a specific chemical reaction.[12] One of the most notable features of the S-layer is that, after isolation, its proteins are capable of forming self-assembled structures in solution, reassembling at solid supports, and covering liposomes, nanocapsules and nanoparticles.[13] These assembled structures (in solution or on different surfaces) can be used for the synthesis of MNPs and obtaining nanoparticle-based nanostructured systems.

There are different strategies reported in the literature, in which SLPs isolated from different microorganisms are used for the preparation of MNPs, MNP arrays or nanostructured materials. Table 4.1 shows some of the most representative examples of these alternatives which are highly related to the concept of nanoarchitectonics using bio-components.[14] In general, these can be divided into two groups: those in which structures of self-assembled SLPs in suspension, and those in which recrystallized SLPs on different surfaces are used. In both cases, once the patterns are obtained, they can be used to generate arrangements of MNPs by the deposition of preformed nanoparticles, or by *in situ* synthesis through a reduction procedure after an activation stage that consists of combining the SLP arrangements with metal complex solutions (Figure 4.1).

In this chapter, we present an overview of recent developments in the fabrication of MNP arrangements and nanostructured systems based on SLPs as a biotemplate. First, a brief introduction to the S-layer concept is discussed. As focus items, examples of the fabrication of hierarchical structures taking advantage of the properties of this bio-active component are described as successful products of the nanoarchitectonics strategy. Finally, further wide-ranging advanced possibilities of these strategies are described in the application and perspective section.

Table 4.1 Representative examples of the preparation of metal nanoparticle arrays or nanostructured materials using S-layer proteins isolated from different microorganisms.

Species	Strain	Characteristics	Metal nanoparticle/ nanostructure	Method	Reference
			Suspension		
Sporosarcina ureae			Pt (1.9 nm)	*in situ* chemical reduction (NaN_3)	Mertig *et al.*, 1999[15]
Bacillus sphaericus	NCTC 9602		Pt/Pd (2–3 nm)	*in situ* chemical reduction (NaN_3)	Mertig *et al.*, 2001[16]
Bacillus sphaericus	NCTC 9602	SLP in sheets and tubes in suspension	Pt/Pd 4–10 nm and 1–3 nm clusters	*in situ* chemical reduction (NaN_3)	Wahl *et al.*, 2001[17]
Sporosarcina ureae	ATCC 13881		Pd (1.2–1.5 nm)	*in situ* chemical reduction (NaN_3)	Wahl *et al.*, 2005[18]
Bacillus sphaericus	JG-A12		Au (0.5–0.6 nm)	*in situ* chemical reduction ($H_{2(g)}$)	Merroun *et al.*, 2007[19]
Bacillus sphaericus	JG-A12				Jankovski *et al.*, 2010[20]
Sulfolobus acidocaldarius			Au (2.5 nm)	*in situ* chemical reduction (boron hydride dimethylamine)	Selenska-Pobell *et al.*, 2011[21]
Lactobacillus kefiri	CIDCA 83111 CIDCA 8348		Pt	*in situ* chemical reduction ($H_{2(g)}$)	Bolla *et al.*, 2020[22]
Lactobacillus kefiri	CIDCA 83111 CIDCA 8348		Ag	*in situ* chemical reduction ($H_{2(g)}$ and $NaBH_4$)	Bolla *et al.*, 2020[23]
Supported Pre-synthesized					
Deinococcus radiodurans		Carbon-coated formvar-backed copper TEM grids	Au (5, 10, 20 nm)	pre-synthesized nanoparticles	Hall *et al.*, 2001[24]
Deinococcus radiodurans *Sulfolobus acidocaldarius*	Sark I DG6	Carbon-coated Formvar TEM grids	Pt (1.8 nm) dendrimer- encapsulated	pre-synthesized nanoparticles	Mark *et al.*, 2006[25]

Deinococcus radiodurans	Sark I	Carbon-coated Formvar TEM grids	Au (5 nm citrated-capped)	pre-synthesized nanoparticles	Mark *et al.*, 2006[26]
Sulfolobus acidocaldarius	DG6				
Deinococcus radiodurans	Sark I	Chemical modified (organosilane) silicon substrate	Au (5 nm citrated-capped)	pre-synthesized nanoparticles	Mark *et al.*, 2007[27]
Bacillus subtilis		Carbon-coated copper TEM grids	Au (5 nm) arrangement of NPs on 2D-SLP array	pre-synthesized nanoparticles	Puranik *et al.*, 2008[28]
***In situ* synthesized**					
Bacillus sphaericus	NCTC 9602	Carbon-coated copper TEM grids (pre-activated SLP arrays)	Pt/Pd (5–7 nm) arrangement of NPs on laying SLP tube	*in situ* (electron beam induction in TEM)	Wahl *et al.*, 2001[17]
Bacillus sphaericus	CCM 2177	Pioloform®-coated platinum TEM grids	Au (5 nm) arrangement of Au NPs on 2D-SLP array	*in situ* chemical reduction ($H_2S_{(g)}$)	Dieluweit *et al.*, 2005[29]
Bacillus subtilis		Carbon-coated copper TEM grids	Au (6 nm)/Ag (4 nm) arrangement of NPs on 2D-SLP array	*in situ* chemical reduction (N_2H_4 solution)	Puranik *et al.*, 2008[28]
Lactobacillus kefiri	CIDCA 83111 CIDCA 8348	Polyacryilic particles	Pt (3 nm) strawberry-like particles (around 100 nm): metal nanoparticles on SLP-polymer particles	*in situ* chemical reduction ($H_{2(g)}$ at environmental P and T)	Huggias *et al.*, 2020[30]
Lactobacillus kefiri	CIDCA 83111	Polyurethanic particles	Pt (5 nm)/Ag (8 nm) strawberry-like particles (around 100 nm): metal nanoparticles on SLP-polymer particles	*in situ* chemical reduction ($H_{2(g)}$ at environmental P and T)	Huggias *et al.*, 2020[31]

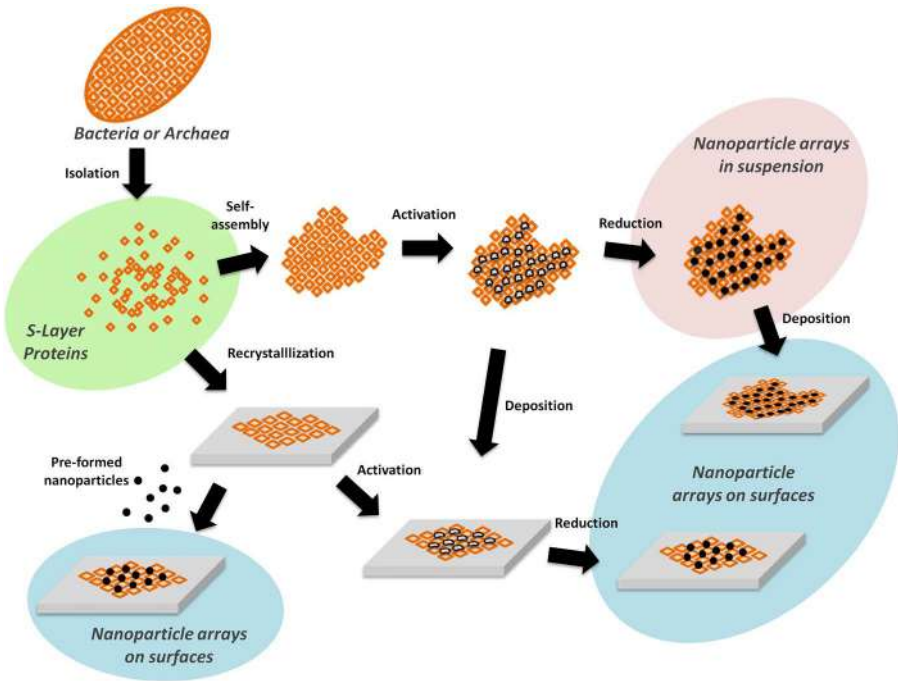

Figure 4.1 Schematic representation of possible ways for the fabrication of metal nanoparticles arrays using S-layer proteins.

4.2 S-layer and S-layer Proteins

Currently, several biomolecules that self-assemble into nanoscale three-dimensional (3D) or two-dimensional (2D) shapes serve as bricks for the building of complex functional nanostructures. So far, a variety of biomolecules such as proteins, nucleic acids and lipids are used in that way in different areas of nanotechnology. In this regard, a crystalline prokaryotic cell surface layer, known as the S-layer and ubiquitously found in *Bacteria* and *Archaea*, represents an excellent candidate with a high potential for nanobiotechnological applications.[12]

The S-layer is a rigid (glyco)-protein envelope considered the most ancient biological membrane, and it has been maintained throughout evolution in prokaryotes.[32] This multifunctional paracrystalline protein lattice fully covers the microbial surface, and electronic microscopy-based techniques are the methods of choice for detecting the presence of an S-layer on the microbial cell surface. S-layers are comprised of one or several protein or glycoprotein monomers with a molecular weight in a range of 40–200 kDa, which form a two-dimensional, regular, and highly porous array (unit cell sizes ranging from 3 to 30 nm, thicknesses of roughly 10 nm, and regularly arranged porous with sizes of 2–8 nm). Formed protein structures exhibit an oblique ($p1$, $p2$), square ($p4$) or hexagonal ($p3$, $p6$) symmetry (Figure 4.2).

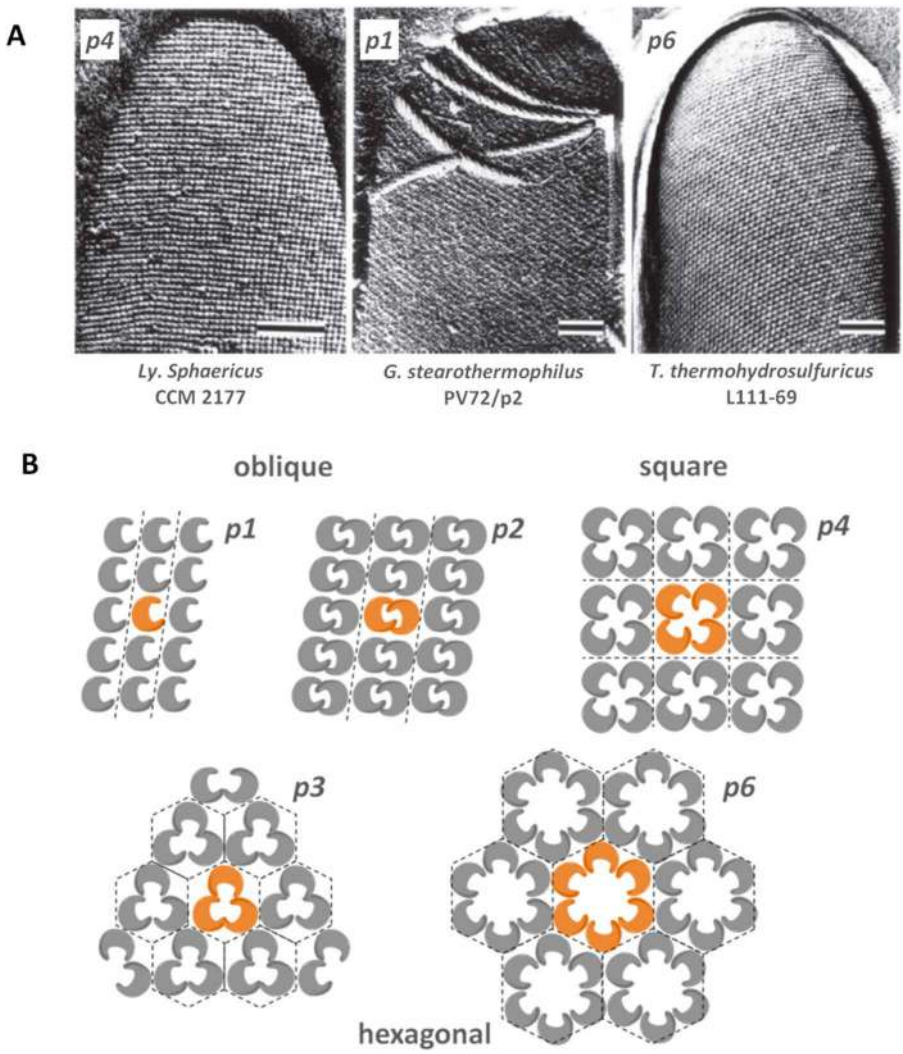

Figure 4.2 (A): Electron micrographs of freeze-etched preparations of intact cells from (*p*4) *Lysinibacillus sphaericus* CCM 2177 showing square lattice symmetry (bar, 150 nm), (*p*1) Geobacillus stearothermophilus PV72/*p*2 exhibiting an oblique lattice type (bar, 50 nm), and (*p*6) Thermoanaerobacter thermohydrosulfuricus L111-69 showing a hexagonal S-layer lattice (bar, 100 nm). Reproduced from ref. 10 with permission from Elsevier, Copyright 2011. (B): Schematic drawing of different S-layer lattice types. The regular S-layer arrays show either oblique (*p*1, *p*2), square (*p*4), or hexagonal lattice symmetry (*p*3, *p*6). The morphological units are composed of one, two, three, four, or six identical subunits.

Since the SLPs represent approximately 10–15% of total cellular proteins, its synthesis demands a great metabolic effort from the microorganism and, considering that the biomass of prokaryotic microorganisms surpasses the biomass of eukaryotic organisms, they can be considered one of the most abundant biopolymers on Earth.[33]

Despite no common function for all S-layers emerging, many different biological functions of the S-layer and SLPs have been proposed in the last decades. Thus far, they include the maintenance of cell shape, functions as a molecular sieve, a binding site for large molecules or ions, a mediator of microbial adhesion, protection of microbial cells from adverse environmental conditions, and modulation of immune responses (antigenic variation, protection from complement killing or phagocytosis, immunomodulation).[34]

Non-covalent interactions, including electrostatic and hydrophobic interactions, are responsible for holding the SLP subunits together within the lattice as well as attaching the S-layer to the underlying cell surface. Thus, SLPs can be easily extracted from the microbial cell surface. Most techniques for the isolation and purification of SLPs employ detergents (such as Triton X100 or sodium dodecyl sulfate) or chaotropic agents (such as urea, guanidine hydrochloride, or lithium chloride).[35]

After extraction, all SLPs share the intrinsic property to spontaneously self-assemble in suspension, at interfaces, or even on different surfaces. For instance, a closed protein monolayer can be completed on a suitable surface in less than 10 minutes.[36] This exceptional property makes them a unique organizational structure with a high application potential in the field of modern nanobiotechnology. It has been shown that SLPs are able to form different free-floating self-assembled products in solution (*e.g.* flat sheets, tubes, vesicles), to reassemble into mono- and double layers at solid supports, at the air–water interface, at lipid films, and to cover liposomes, nanocapsules, and nanoparticles completely (Figure 4.3).

In addition to providing a highly ordered structure, SLPs are a rich source of different functional groups. Due to their crystalline character, SLPs allow the reiterative arrangement of functional groups (*e.g.*, amino-, carboxyl-, hydroxyl-groups) with the periodicity of the protein lattice.[12] One of the hallmarks of the primary structure of these proteins is the high percentage of hydrophobic (40–60 mol%) and acidic amino acids such as glutamic and aspartic acid (15 mol%), threonine (8–12 mol%) and lysin (10 mol%).[42] Regarding sulfur-containing amino acids, they are only rarely found in bacterial SLPs, but are often found in *Archaea*. SLPs were the first glycoproteins detected in prokaryotes, and indeed, glycosylation is the most frequent posttranslational modification reported for these proteins which are among the best-studied examples of glycosylated proteins. Since *N*-glycosylation is a rare event in bacteria, bacterial SLPs were usually characterized as *O*-glycosylated,[37] however, the co-existence of *O*- and *N*-glycans have been described in some cases.[38,39] S-layers are anisotropic structures with an outer surface less corrugated than the inner surface, exhibiting different net charges and hydrophobicity in both faces.[12]

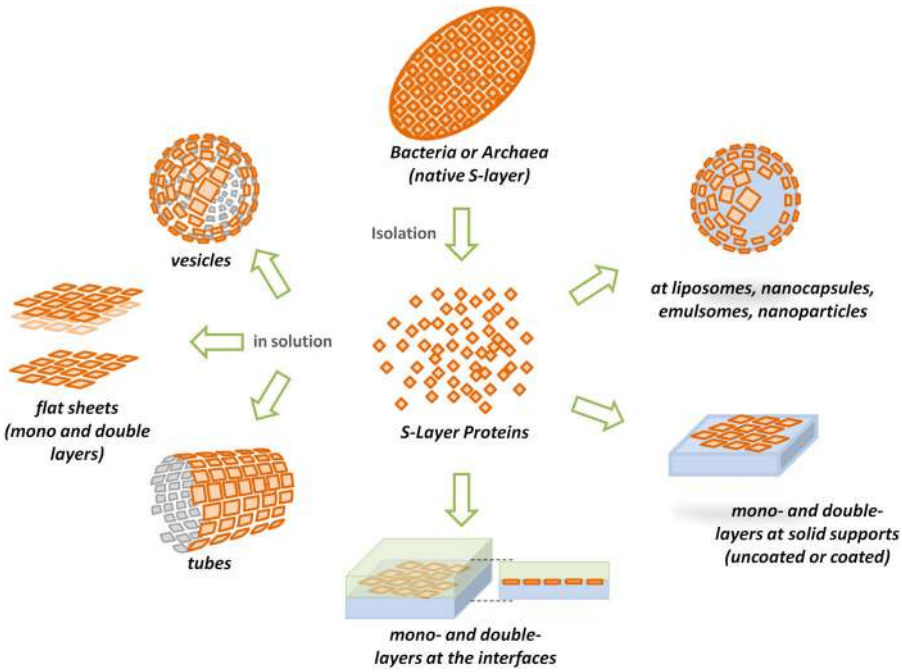

Figure 4.3 Schematic drawing of the reassembly of S-layer proteins in solution, at the interfaces, solid supports, and particles.

Despite efforts, conventional methods for high-resolution structural analysis such as X-ray crystallography cannot be easily applied to S-layers, thus the information available regarding the atomic structure of SLPs and the spatial arrangement of domains and secondary structure elements within the S-layer lattice is scarce. Most of the information about the 3D structure and surface topology of S-layer assemblies has been obtained by atomic force microscopy (AFM) and small-angle X-ray scattering (SAXS).[40]

Thus, considering the extraordinary ability of self-assembling, in combination with the precise repetitive exposition of functional groups and the possibility of genetic manipulation, SLPs are extremely valuable tools with high potential for the development of carriers for biomolecules, vaccines, ultrafiltration membranes, affinity structures, diagnostic devices, biosensors, biocatalysts, *etc*[41–43].

4.3 Metal Nanoparticles on S-layer Protein Assemblies in Suspension

The use of biological molecules with the ability to form regular structures constitutes a novel nanoarchitecture tool to obtain inorganic material with a periodical organization and nanometric dimension. The structural properties

of the SLPs make them ideal templates to direct the synthesis and organization of MNPs. Regular distribution of sites with physicochemical affinity in the S-layer surface allows the use of them as a matrix to obtain highly ordered arrangements of semiconductor nanocrystals or metallic nanoclusters. Thus, the capacity of SLPs to interact with inorganic complexes, MNPs and nanocrystals, has been widely used for the nucleation and ordering of two-dimensional arrays of MNPs (*e.g.*, Au, Pt or Pd), as well as CdS or CdSe nanocrystals.[17,44–46]

The most popular methods to obtain SLP assembling consist in the extraction of the protein with guanidium hydrochloride, followed by dialysis against a buffer containing $CaCl_2$ to remove the extracting agent and favor the self-assembly of SLPs. Then, the incubation with different metallic salts and the subsequent reduction of the metal cation, mainly with NaN_3 and in some cases with H_2 or electron beam, leads to the obtention of regular arrays of MNPs supported on SLP biotemplates.[15,17,19,21,22] The nanoarchitecture of the MNPs arrays is governed by the SLP structure template.

It has been reported that the SLPs of species such as *Sporosarcina ureae* and *Bacillus sphaericus* are able to link *ca.* 200–300 Pd or Pt complexes per protein monomer, suggesting an interaction with different amino acid residues found at specific metallization sites on the S-layer surface, where the amino acids with reducing capacity are not required.[17,18]

The S-layer of *Bacillus sphaericus* JG-A12 can complex Pd(II), which can be reduced with H_2 to obtain nanoparticles of 0.85 to 1 nm with a few atoms around a central one.[19] SLP carboxylic groups could be responsible for the binding of Pd(II).[47] In all the arrangements, nucleation sites of nanoparticles are the pores of the SLP. Due to this, the topography of the surface of the SLP and the specific interaction of the complex salts with some of its functional groups can contribute to direct the regular matrices of MNPs.

Regular arrays of Pt and Pd nanoparticles were obtained with the SLP of *Bacillus sphaericus* NCTC 9602 as a support. The directed synthesis of Pt and Pd nanoparticles using cavities as nucleation sites constituted a novel system. These cavities are obtained from facing two SLPs through the inner face, leading to the formation of a cylindrical hole in which the metallic salt is deposited and subsequently reduced with NaN_3. To this aim, the SLP of *Bacillus sphaericus* NCTC 9602 was crystallized in two different forms (sheets and tubes), which were then treated with chlorocomplex salts of Pt or Pd (K_2PtCl_4 or K_2PdCl_4, respectively). The SLP directed the formation of groups of metals as both clusters (4–10 nm in diameter) distributed on the protein surface and groups located in the pores (1–3 nm in diameter). Reduced nanoparticles are distributed periodically reproducing the *p*4 symmetry of *Bacillus sphaericus* NCTC 9602 S-layer and showing identical structural characteristics.[17]

It has been shown that SLPs are suitable for the directed manipulation of small metal clusters with a narrow size distribution. The chemical deposition of Pt as crystalline spherical particles onto the SLP of *Sporosarcina ureae* leads to the formation of highly ordered arrays of metal clusters, following the symmetry of the SLP template since the unit cell of the cluster lattice is quadratic with a size in good agreement with the S-layer lattice constants.

Mertig and co-workers could identify the central pores and gaps of the protein structure as specific Pt cluster deposition sites. The mean diameters of the MNPs are 1.2–1.9 nm, in good agreement with the apparent diameter of the SLP layer pores. Not only the position of Pt particles but also the cluster growth is controlled by the protein template. The metallic character of the nano-sized clusters deposited on the SLP surface was confirmed by high-resolution TEM (transmission electron microscopy), identifying a pure metallic Pt phase with a lattice constant of 0.39 nm.[15]

Recently, SLPs of *Lactobacillus kefiri* were extracted using 5M guanidium hydrochloride, and the dialyzed suspension was incubated with $(NH_4)_2PtCl_4$ or $AgNO_3$, which leads to obtaining MNPs with size, form, and distribution perfectly directed by the assembly of the SLP after reduction with H_2 (Figure 4.4).[22,23] In these experiments, as in all those studied so far, the pores of the

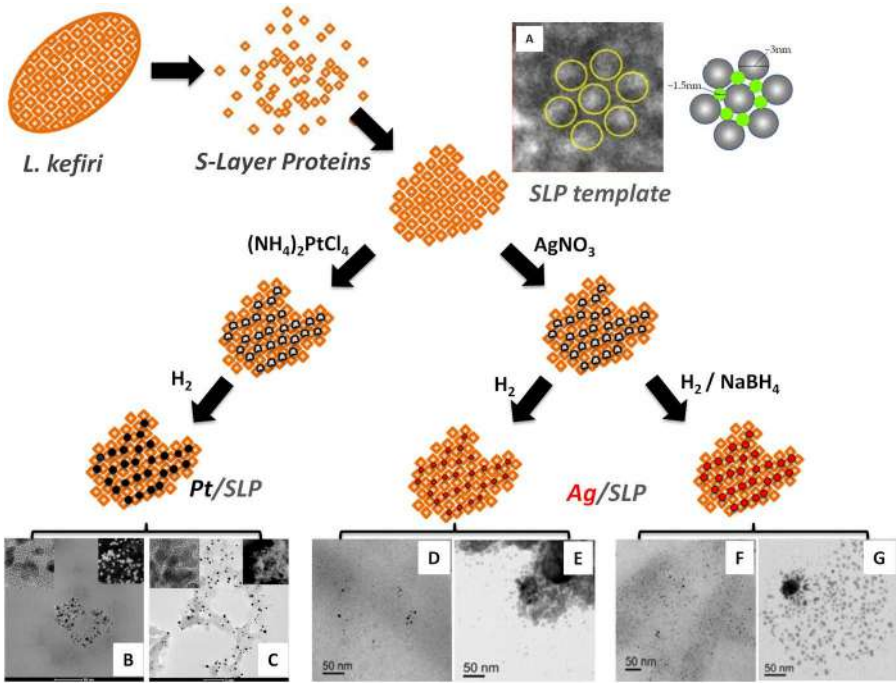

Figure 4.4 MNPs obtained on SLP arrays from *L. kefiri*. (A): TEM micrography of SLP48 and representation of *p*6 arrangement obtained by self-assembly for this protein. (B and C): TEM images of Pt nanoparticles obtained on SLP111 and SLP48, respectively. Adapted from ref. 22 with permission from Elsevier, Copyright 2011. (D and F): TEM images of Ag nanoparticles obtained on SLP48 after reduction with H_2 or $H_2/NaBH_4$, respectively. (E and G): TEM images of Ag nanoparticles obtained on SLP111 after reduction with H_2 or $H_2/NaBH_4$, respectively. (A), (D), (E), (F) and (G) adapted from ref. 23, https://doi.org/10.3390/nano10112322, under the terms of the CC BY 4.0 license https://creativecommons.org/licenses/by/4.0/.

SLP could play a special role in the orientation and growth of the nanoparticles. According to the results obtained in some experiments carried out with different platinum complexes,[48] it is quite probable that the electrostatic interactions with the charged sites of the SLP play an important role. The structural order of the SLPs of *Lactobacillus kefiri* 83111 (SLP111) y *Lactobacillus kefiri* 8348 (SLP48) guide the formation of the Pt nanoparticles with the presence of some small clusters constituted of a few Pt atoms.[22] Metallic particle sizes of Pt/SLP111 ranged from 0.67 to 5.99 nm in diameter, and Pt/SLP48 showed diameters ranging from 0.80 and 6.56 nm (Figure 4.4B and C). This is another contribution indicating that the SLP symmetry, as well as the experimental conditions, could influence the size of MNPs. Subnanometric Pt clusters as well as highly dispersed Pt single atoms were observed. The separation between the single atoms was 0.48 nm for the Pt supported on SLP48 while for the Pt/SLP111 systems this distance was 0.34 nm. This is novel evidence that the structure of the SLP directs how the platinum particles are structured on them, reinforcing the relevance of the SLP as a template. Also, the Pt/SLP48 presented a higher number of single atoms than Pt/SLP111, suggesting that the organization of the SLP used as support could have an important role in the stabilization of subnanometric Pt species. TEM images of Pt nanoparticles reveal that the most frequently observed interlattice plane distance was 0.227 nm, indicating that the exposed face of all Pt nanoparticles is the (111) plane, with a lattice constant of 0.39 nm. The importance of obtaining nano-, subnanoparticles, and single atoms lies in the direct correlation with their electronic properties, and consequently with their behavior.

The same SLPs were used to synthesize stable Ag nanoparticles.[23] These nanoparticles (NPs) were obtained at different reduction conditions showing different structural characteristics. Silver NPs exhibit different sizes and topography according to the nature of the SLP employed. Bolla and coworkers verified that SLP48 shows a *p*6 symmetry constituted by subunits of 3 nm with pores size of 1.5 nm (Figure 4.4A). TEM images showed that both SLPs employed as templates are decorated with Ag NPs mostly evenly distributed, although some small aggregates could also be observed. Nevertheless, SLP48-supported Ag NPs obtained using either H_2 (Figure 4.4D and E) or H_2 plus a small amount of $NaBH_4$ as reducing agents showed smaller particle sizes than their SLP111-supported counterparts (Figure 4.4F and G). For the same reduction condition, the symmetry of the SLP is responsible for directing the growth of the Ag MNPs. Conversely, a drastic reduction with $NaBH_4$ led to larger Ag NPs, indicating that the reduction method used is essential to determine the characteristics and sizes of the Ag NPs obtained. It is worth mentioning that the Ag NPs presented crystalline structures evidenced from crystalline planes observed in the diffraction patterns. All this evidence shows that the nanoarchitecture of the Ag NPs is influenced by both the type of the protein template and the experimental reduction conditions.

4.4 Metal Nanoparticles on Supported S-layer Protein Assemblies

As indicated above, after isolation, SLPs are capable of reassembling at solid supports and covering different particles.[13] Thus, it could be possible to achieve nanoparticle arrays or controlled MNP growth by combining the nanostructuring properties afforded by the SLP-based templates with the properties of the supports. This approach limits the stability problems of MNPs (aggregation, changes in shape) obtained by other methods.[49,50] In this section, several selected examples of recent developments exploring this alternative are briefly presented.

4.4.1 Preformed MNPs

One of the strategies used for the generation of supported MNP arrangements is the use of pre-synthesized particles, with well-defined sizes and properties. As a general methodology, a dispersion of MNPs is incubated on a surface (typically a TEM grid) on which the SLP template has been previously obtained. In this way, when interaction with the self-assembled SLP takes place on the surface, the MNPs are arranged following a pattern determined mainly by the spatial arrangement that the bio-component has acquired on the proposed surface (Figure 4.5A), avoiding the problems observed in metal precipitation procedures typically employed in protein-based *in situ* array bionanofabrication techniques such as to control the size and morphology of the particles.

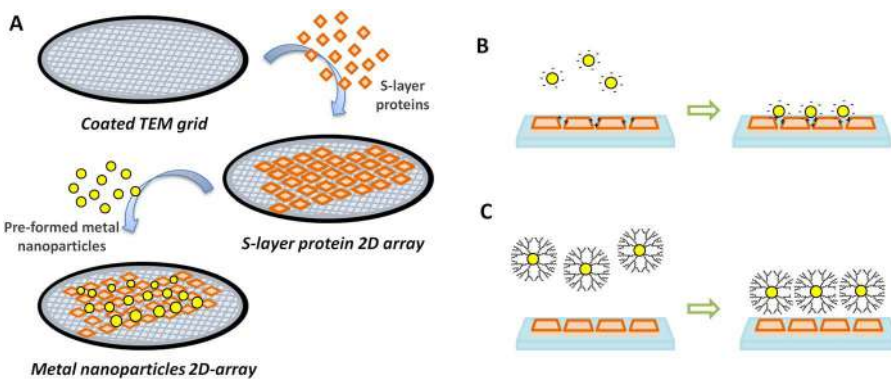

Figure 4.5 Schematic representation of the typical obtention of metal nanoparticle 2D arrays on solid supports using preformed nanoparticles (A). Interaction between preformed nanoparticles and supported SLP biotemplates can be allowed by electrostatic interaction (B) or non-covalent interactions (C).

Following this procedure, Hall and co-workers[24] obtained lattices of Au NPs by biomolecular templating using bacterial SLP membranes. They allowed a standing solution of SLPs isolated from *Deinococcus radiodurans* on a carbon-coated formvar-backed copper TEM grid, obtaining a hexagonally packed with a periodic structure of hexameric units in the form of a hollow cone-shaped with a positively charged central channel.[51] After that, they passed the grid through a dispersion of Au NPs with different mean diameters (5, 10, and 20 nm), which were negatively or positively charged due to surface citrate ions or surface capping with poly-L-lysine, respectively. For negatively charged Au NPs with mean diameters of 5 and 10 nm, they obtained micrometer-sized arrays of regularly spaced nanoparticles organized into a hexagonal superlattice. In the case of the biggest particles, no long-range periodicity was obtained, suggesting that the superlattices were not templated when the size of the particles is larger than the SLP membrane lattice parameters. Instead, particles were randomly distributed across the molecular templating. Similar results were obtained for the positively charged Au NPs regardless of their size, likely due to their surface charge is similar to that of the site for the specific interaction with the SLP surface. Thus, the spontaneous self-assembly of the preformed nanoparticles is controlled by electrostatic binding at the SLP layer in association with the size of the Au NPs (Figure 4.5B).

The electrostatic binding of citrate-stabilized Au NPs to self-assembled SLPs isolated from *Bacillus sphaericus* CCM 2177 on SiO_2-coated grids was also shown to depend on the size of MNPs.[46] When 5 nm nanoparticles (mean diameter) were used, regular nanoparticle arrangements resembling a square lattice symmetry were obtained, where the inner face of the SLP (positively charged) was exposed. However, incubation of the SLP layer with 10 nm Au NPs dispersion resulted in randomly distributed NPs on the crystalline surface of the SLP, whereas the smaller particles (2 nm) formed a tightly packed monolayer. Based on their experiments, the authors claim that the 5 nm Au NPs bind in the pore regions of the crystalline S-layer lattice. The binding seems to occur through electrostatic interactions between the negatively charged nanoparticles and the exposed cationic moieties in the pores and at the inner face of the S-layer.

Mark and co-workers explored the same strategy by the formation of self-assembled two-dimensional arrays of dendrimer-encapsulated Pt NPs (1.8 nm in diameter) using SLPs isolated from *Deinococcus radiodurans* (Sark I strain) and *Sulfolobus acidocaldarius* (DG6 strain) as biomacromolecular templates.[25] For the obtention of the biotemplates, the grid was floated on top of a drop of the SLP solution, and after that onto a drop of the dendrimer-encapsulated Pt NPs (at different pHs). As indicated above, it was reported that the *D. radiodurans* SLP template has a *p*6 symmetry, while the template based on SLP isolated from *S. acidocaldarius* displays *a p*3 symmetry.[52] The authors showed that using the SLPs as biomolecular templates, spatially ordered arrays of dendrimer-encapsulated metallic particles could be fabricated *via* non-covalent binding forces (Figure 4.5C). At neutral pH, individual particles as well as dimeric/trimeric clusters appear to form a regular

hexagonal pattern on the surface of the SLP from *S. acidocaldarius*. When the biotemplate is formed with SLP from *D. radiodurans* the metallic particles are arranged into a hexagonal pattern arising from an affinity between the dendrimer component of the particles and various polar/charged functional groups located within the vertex regions of the S-layer lattices. In acidic conditions, they observed an increase of the overall surface coverage and level of random (bulk aggregation) of bound nanoparticles for both types of S-layers compared to the experiments carried out at pH 7. Instead, at pH 9, the number of bounded nanoparticles decreased compared to the other conditions. The changes can be attributed to the effect of the pH on the ionization states of the proteins due to the functional groups that they contain, as well as to the influence of pH on the polymer's ability (dendrimeric component) to undergo hydrogen bond interactions. In other work, following the same procedure, the authors extend the results to the formation of self-assembled ordered arrays of Au NPs (5 nm, citrated-capped).[26]

Similarly, the production of arrays of Au and Ag NPs by assembling preformed MNPs on an SLP array deposited on a grid was reported.[28] In this case, Mark and co-workers used an SLP isolated from *Bacillus subtilis* and the protein biotemplate was produced on carbon-coated copper TEM microscopy grids. For this, the grids were placed on the liquid–air interface of a solution of the protein that had been incubated for a time to allow its self-assembly and were subsequently fixed with glutaraldehyde. Subsequently, the grid coated with the protein monolayer was exposed to a dispersion of Au and Ag NPs, thus obtaining a regular arrangement of the metallic particles.

These same authors also explored the strategy on a new support in a later work.[27] In this case, a biotemplate of SLP from *D. radiodurans* (Sark I strain) was formed on a chemically modified silicon surface to produce a hexagonally ordered array of gold nanoparticles (5 nm, citrated-capped), as can be observed in Figure 4.6. For the chemical modification of the substrate, two silane reagents, (3-aminopropyl) triethoxysilane (APTES) and dimethyldichlorosilane (DDS), were selected. Under the experimental conditions selected (pH 7), for the APTES-modified Si substrate, the adsorption of the SLP results from electrostatic interaction between the positively charged amino groups of the silane and acidic negatively charged sites on the protein. On the other hand, for the DDS-modified Si substrate, the adsorption of the SLP was mainly due to hydrophobic interactions. When the SLP-covered surfaces were used for the fabrication of Au NPs arrays, two distinct nanoparticle patterns were observed in both surfaces: a hexagonally ordered pattern with the lattice constant of the native protein, and another one with a low degree of spatial order. Interestingly, the ordered patterns were predominant on the biotemplate obtained on the DDS-modified surface, while most of the arrays observed on the APTES-based surface correspond to the less-ordered pattern. The generation of the higher portion of hexagonally ordered nanoparticle arrays corresponds to the adsorption of nanoparticles on the extracellular face of the protein.[26] Thus, the authors presume that the binding of the SLP to the DDS-modified Si supports can be attributed to an enhanced level of adsorption of

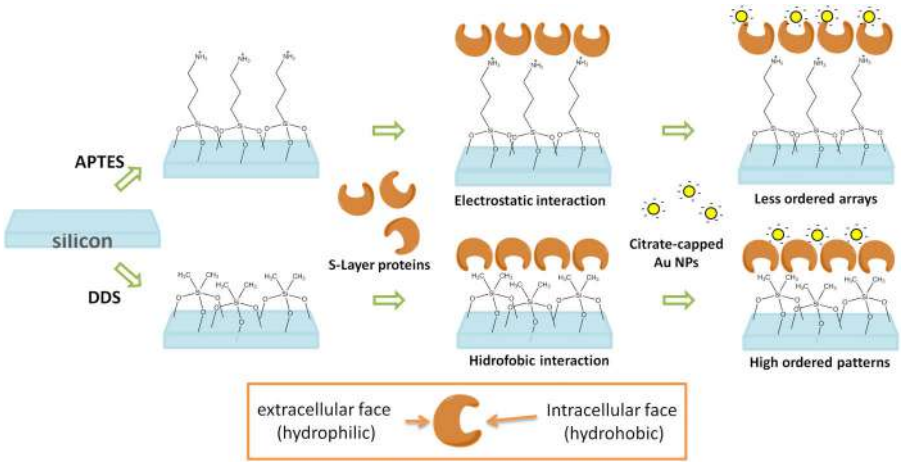

Figure 4.6 Adsorption of gold nanoparticles to an SLP-layer supported on a silicon substrate. The silicon substrate has been chemically modified with an organosilane (3-aminopropyl) triethoxysilane (APTES) or dimethyldichlorosilane (DDS) leading to the obtention of a hydrophilic or hydrophobic surface, respectively. SLP isolated from *D. radiodurans* interact with this surface according to their structure favoring the obtention of high ordered arrays of gold nanoparticles when the hydrophilic extracellular face was exposed.

the intracellular face (hydrophobic) of the SLP to the hydrophobic surface, which leads to the exposition of the SLP extracellular face to the nanoparticle dispersion. Conversely, on positively APTES-support the proteins tend to become adsorbed through their hydrophilic extracellular surface, leading to the prevalence of random-appearing nanoparticle patterns because the SLP mainly exposed their intracellular face to the metal nanoparticles.

4.4.2 MNPs Obtained on Supported SLP Assemblies

An interesting variant of the previous examples is to incubate the SLP biotemplates obtained on the selected support with a solution of a salt of the metal of interest. It is also possible to incubate the SLP biotemplates in suspension with the metal salt before depositing them on a support. After that, in both cases, it is necessary to use a reduction method for the *in situ* obtention of the metal nanoparticles. This method presents the advantage of avoiding the use of expensive and non-eco-friendly reagents. The experiments have demonstrated that this is a versatile strategy for the preparation of supported nanoparticles of different noble metals, avoiding the use of stabilizing agents.

Mertig and co-workers obtained Pt and Pd nanoparticles by *in situ* electron-beam induced cluster formation in a transmission electron microscope.[15] After an activation treatment with the metal complex solution

(K_2PtCl_4 or K_2PdCl_4), the SLP isolated from *Bacillus sphaericus* NCTC 9602 was placed on a carbon-coated copper TEM grid. By exposing the sample to the high-energy electron beam in a TEM, the formation of MNP clusters was clearly observed. In those samples, nanoparticles of 5–7 nm diameter size were periodically arranged, reproducing exactly both the *p*4 symmetry of the S-layer template and its lattice constant. On the other hand, when SLP was not used on the substrate, the authors observed the formation of non-regular agglomerates of MNPs with diameters higher than 20 nm, demonstrating that the nanoparticles array is directly determined by the protein template.

A gold nanoparticle array was also obtained using SLPs extracted from *Bacillus sphaericus* CCM 2177.[29] The SLPs were prepared as monolayers on TEM grids coated with a polyvinyl film (Pioloform®). For this, the grids were immersed in a solution of the protein and later they were fixed with glutaraldehyde. The grids were subsequently placed on drops of a $HAuCl_4{\cdot}_3H_2O$ solution and then put in a desiccator containing a Na_2S solution acidified with HCl. Thus, a slow reaction of the samples with the H_2S gas occurred in the desiccator. The gas treatment resulted in a surface decorated with gold nanoparticles of 5 nm regularly arranged in accordance with the lattice geometry of the protein template (Figure 4.7).

Arrangements of gold and silver nanoparticles were also obtained by *in situ* synthesis with an SLP isolated from *Bacillus subtilis*.[28] Self-assembled arrays of the proteins were deposited on carbon-coated copper TEM microscopy grids. To achieve this, the grids were placed in the liquid–air interface of a solution of the protein that had been incubated for a time to allow its self-assembly and they were subsequently fixed with glutaraldehyde. The grid coated with the protein monolayer was exposed to a chloroauric acid solution. The synthesis of Au NPs was achieved by exposing

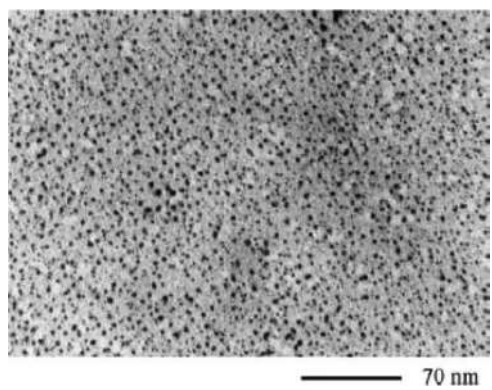

Figure 4.7 Transmission electron micrograph of Au clusters formed on a Pt grid coated with Pioloform® film and S-layer + glutaraldehyde fixation + H_2S treatment Reproduced from ref. 29 with permission from Elsevier, Copyright 2011.

the coated grid to hydrazine, obtaining an ordered assembly of spherical gold nanoparticles (around 6–7 nm) replicating the native geometry of the SLP biotemplate. A similar process was followed for the synthesis of Ag NPs, but in this case the SLP coated surface was incubated with a solution of silver nitrate. Again, the obtention of Ag NPs (4–5 nm) arranged in a periodic assembly confirmed the formation of the MNPs within the pores of the SLP template.

Recently, Huggias and co-workers extend the use of this strategy to other support as polymeric particles using SLP isolated from *Lactobacillus kefiri* (CIDCA 83111 and CIDCA 8348 strains).[30,31] In short, they obtained Pt or Ag nanoparticles on S-layer protein/polymeric particle systems, after the combination of the supports with a platinum or silver salt and its subsequent reduction with hydrogen at mild conditions (Figure 4.8). The experiments were carried out at pH 7.2, a value lower than the pI of proteins and higher than the pKa of the carboxylic groups of the polymer particles. After combining SLP solution and an acrylic or polyurethanic aqueous dispersion

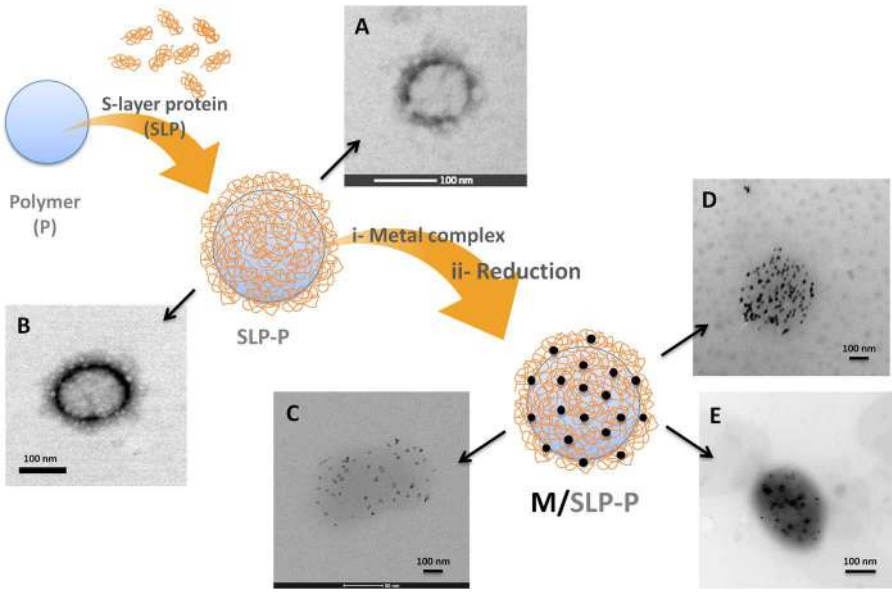

Figure 4.8 Schematic representation of the synthesis of MNPs supported on SLP-polymer particle. (A): TEM image of SLP-acrylic support (SLP-AC). (B): TEM image of SLP-polyurethane support (SLP-PU). Adapted from ref. 31 with permission from Elsevier, Copyright 2020. (C): Pt nanoparticles obtained on SLP-acrylic system. (D): Pt nanoparticles obtained on SLP-polyurethane system. (E): Ag nanoparticles obtained on SLP-PU. In all cases, SLP corresponds to a protein isolated from *L. kefiri* CIDCA 83111. In (A and B), samples were negatively stained. (A and C): Adapted from ref. 30 with permission from American Chemical Society, Copyright 2020.

(particles diameter of 80 nm and 115 nm, respectively) the formation of core–shell systems was observed by TEM (Figure 4.8A and B), with a protein cover of 20–30 nm on the polymeric particles in agreement with SAXS and dynamic light scattering (DLS) results.

After combining the SLP-acrylic supports with an adequate concentration of a platinum complex solution ($(NH_4)_2PtCl_4$) and a subsequent reduction with H_2 at 25 °C, strawberry-like particles were obtained with Pt NPs of around 3 nm in diameter located on the surface of the polymer-protein systems (Figure 4.8C).[30] Attempts to reduce the Pt complex in the presence of the polymer particles (without protein) did not lead to the production of Pt nanoparticles. Moreover, the supported SLPs maintained their ability to produce metal nanoparticles as it was also reported for these proteins in solution.[22] Similarly, protein-polymer systems consisting of SLP isolated proteins from *L. kefiri* CIDCA 83111 (SLP111) supported on polyurethane particles in aqueous dispersion were used for the *in situ* synthesis of nanosystems with strawberry morphology formed by Pt or Ag NPs of around 5 nm and 8 nm, respectively, decorating the protein-polymer core–shell particle (Figure 4.8D and E).[29] The experiments demonstrate that the synthesis method is versatile for the *in situ* preparation of nanoparticles of different noble metals, where the SLP-polymer tandem act as a template and support combining the nanostructuring properties of the SLP biotemplates with the properties of the polymeric particles-based supports, which provide the great advantage of obtaining well-dispersed metal clusters in aqueous dispersion and reveals a lot of opportunities in the design of metal-nanoparticle-based hierarchical structures.

4.5 Applications and Perspective

The application of MNPs synthesized by microorganisms or bio-components has been claimed as very promising in various scientific and technological areas, such as catalysis, energy storage, biomedical therapy, *etc.*[53,54] However, in the case of systems based on SLPs, not many deep studies related to their applications have been reported. For the case study of this chapter, where nanostructured systems constituted by MNPs obtained taking advantage of the SLPs' properties have been shown, we will present here their use as catalysts in the reduction of *p*-nitrophenol (*p*-NP) with $NaBH_4$ and the fabrication of silicon nanopillar structures.

4.5.1 Bionanocatalysts for the Reduction of *p*-Nitrophenol

The model reaction usually employed to evaluate the catalytic performance of MNPs is the hydrogenation of *p*-nitrophenol (*p*-PN). The reduction of *p*-PN is a simple reaction in which a single product, *p*-aminophenol (*p*-AN), is produced under mild reaction conditions ($NaBH_4$ as reducing agent, at room temperature and atmospheric pressure).[55] The treatment of nitro derivatives

such as *p*-PN represents a great challenge due to the contaminating and the low biodegradability nature of these compounds. Recently, the United States Environmental Protection Agency (EPA) has granted *p*-PN the classification of a priority organic pollutant due to its high toxicity and mutagenic effects on living beings. In this sense, obtaining catalysts based on MNPs with orientations and homogeneous distributions constitutes an advance in the catalytic area with environmental applications. The Pt or Ag nanoparticles obtained on SLP111 and SLP48, both in suspension[22,23] or supported on polymeric particles,[30,31] are interesting examples of applications of nanosystems prepared by this approach (Figure 4.9A).

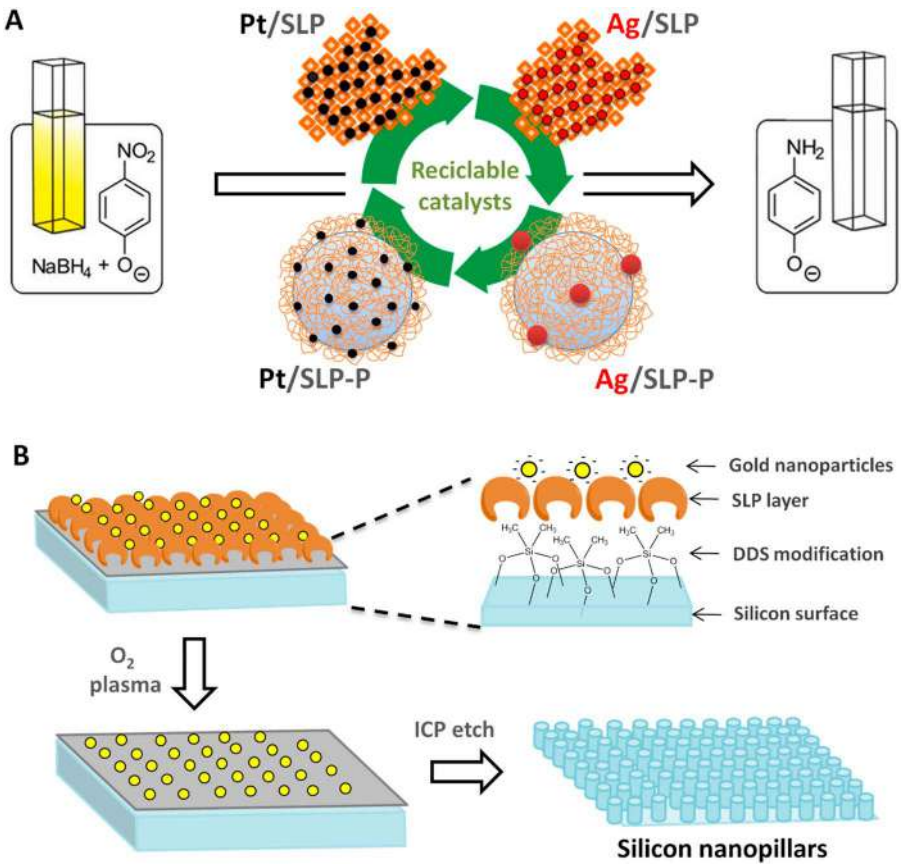

Figure 4.9 Application of systems obtained taking advantage of the SLP biotemplates. (A): Catalytic performance of bionanocatalysts based on Pt or Ag nanoparticles obtained and supported on SLP or SLP-polymeric particle in the reduction of *p*-nitrophenol with $NaBH_4$ (SLP isolated from *L. kefiri* 8348 and 83111). (B): Fabrication of a silicon nanopillar array using an inductively coupled plasma (ICP) etch process.

4.5.1.1 Platinum-based Nanobiocatalysts

Bolla and co-workers investigated the Pt nanoparticles obtained and supported on SLP assemblies isolated from two different strains of *L. kefiri* in the reduction of *p*-NP.[22] The studied catalysts had a very good performance, with more than 80% conversion and a high apparent reaction rate constant (K_{app}). The K_{app} values obtained were similar or even higher than those obtained with other nanocatalysts prepared through different methodologies,[32] showing the benefits of SLP as a template. The structure of Pt NPs with the (111) face exposed and the presence of single atoms allowed obtaining unique catalytic performance. In addition, one of the important characteristics concerning the use of a catalyst is its stability and reusability under reaction conditions. The studied Pt/SLP catalysts were submitted to several reaction cycles with conversion between 75 and 90% after nine cycles. In the case of Pt NPs obtained and supported on SLP/polyacrylic particle systems,[30,31] excellent performance in the p-NP catalytic reduction was also observed, reaching conversions of 100% at 60 min of reaction. The K_{app} values obtained with these catalysts were similar to those reported for the counterpart systems obtained on SLP in suspension under similar reaction conditions. While the SLP self-assembled on the polymeric particles maintained their ability to act as biotemplate for the synthesis of Pt nanoclusters, the resulting supports could direct and favor the exposure and accessibility of their active sites.

4.5.1.2 Silver-based Nanobiocatalysts

As previously shown, Ag NPs could be synthesized and stabilized on SLPs as bidimensional regularly arranged biotemplates.[23] Six different Ag/SLP systems with Ag NPs of variable sizes were obtained on two different SLPs isolated from *L. kefiri* (SLP111 and SLP48). They were tested in the reduction of *p*-NP to *p*-AP showing conversion values of *p*-NP around 75 and 80% with high reaction rates. In addition, *p*-NP interaction on the catalyst was studied using density functional theory (DFT). The calculations indicated that the adsorption of *p*-nitrophenolate species through the nitro group is the most favored mechanism, leading to *p*-AP as the only feasible product of the reaction, which was corroborated experimentally. Also, Huggias and co-workers reported that Ag NPs obtained on SLP-polyurethane support showed high catalytic activity, reaching a conversion to the desired product (*p*-AP) of 97%, with K_{app} slightly lower than that obtained for Pt-based counterpart.[31] Such excellent catalytic properties could be attributed mainly to the distinctive structural characteristics of the SLP-polymeric particle systems, where the support offers easy access routes for rapid transfer of reagents to the Ag NPs, and also provided an effective stabilizing shield for the metal nanoparticles. All synthesized MNPs, directed and oriented by SLP isolated of *L. kefiri*, were found to be very efficient regardless of the noble metal used. Both Pt and Ag nanoparticles supported either on SLP isolated of *L. kefiri* or on SLP/polymer showed the ability to be reused in the reduction of *p*-Np to *p*-AP, maintaining their catalytic performance.

4.5.2 Fabrication of Silicon Nanopillar Structures

An interesting procedure is the use of SLP biotemplates for the preparation of gold nanoparticles arrays able to act as masks for the fabrication of silicon nanopillar arrays, which was carried out by Mark and co-workers.[27] In this case, they use the hexagonally ordered array of gold nanoparticles obtained on a chemically modified silicon surface taking advantage of the properties of SLP isolated from *D. radiodurans* as we described previously in this chapter. The gold nanoparticle arrays were first cleaned by performing a process with an O_2-based plasma to avoid the deleterious effects of the organic SLP material during the etching processes. When utilized in an inductively coupled plasma etching process, the biotemplated nanoparticle arrays were shown to be efficient nanolithographic masks for the formation of a high surface density of silicon nanopillar structures (Figure 4.9B). The authors proposed that this biological-based route to nanostructure fabrication could be useful for achieving the monolithic integration of multifunctional optoelectronic/electroluminescent materials into current silicon-based device architectures.

4.6 Conclusions

An interesting application of SLPs isolated from *Bacteria* or *Archaea* in nanotechnology and nanoarchitectonics is their use as biotemplates for the synthesis of metal and semi-metal nanoclusters. The S-layers can act both in suspension and supported on different surfaces as a template directing the deposition or growing of crystals and noble metals in the nucleation sites on the surface of the SLP layer. This approach allows fabricating noble metal nanoparticle arrays and noble metal-based nanostructured materials avoiding the use of solvents and protecting agents. Thus, obtaining metal nanoparticles using bio-components as the SLP promises to be a powerful tool in nanotechnology, chemistry, and biochemistry area. Although there are few demonstrated applications for the MNPs and nanostructures obtained by using the nanoarchitecture of the S-layer, they present a promising horizon. There are still many applications to study such as antimicrobial and antitumoral activities, and magnetic and luminescent properties, as well as their use as biosensors, in molecular diagnostics and bio-detection. Also, the study of properties afforded by the combination of the properties of MNPs with the characteristics that other supports can offer is an emerging topic. In this way, the study of the SLPs is waiting for new contributions and opens a lot of opportunities in areas related to the design and creation of the hierarchic organization.

References

1. W. Deng and E. M. Goldys, *Analyst*, 2014, **139**, 5321.
2. M. Blanco-Loimil, A. Pardo-Montero, E. Villar-Alvarez, R. Martínez, A. Topete, S. Barbosa, P. Taboada and V. Mosquera, *RSC Adv.*, 2016, **6**, 60502.

3. T. S. Rodrigues, A. G. da Silva and P. H. Camargo, *J. Mater. Chem. A*, 2019, **7**, 5857.
4. Y. N. Slavin, J. Asnis, U. O. Häfeli and H. Bach, *J. Nanobiotechnol.*, 2017, **15**, 1.
5. M. Azharuddin, G. H. Zhu, D. Das, E. Ozgur, L. Uzun, A. P. Turner and H. K. Patra, *Chem. Commun.*, 2019, **55**, 6964.
6. P. G. Jamkhande, N. W. Ghule, A. H. Bamer and M. G. Kalaskar, *J. Drug Delivery Sci. Technol.*, 2019, **53**, 101174.
7. S. Iravani, in *Metal Nanoparticles: Synthesis and Applications in Pharmaceutical Sciences*, ed. S. Thota and D. C. Crans, Wiley-VCH, Weinheim, Germany, 2017, ch. 2, pp. 15–31.
8. A. L. Stepanov, A. N. Golubev, S. I. Nikitin and Y. N. Osin, *Rev. Adv. Mater. Sci.*, 2014, **38**, 160.
9. P. Mendis, R. M. de Silva, K. N. de Silva, L. A. Wijenayaka, K. Jayawardana and M. Yan, *RSC Adv.*, 2016, **6**, 48792.
10. U. B. Sleytr, B. Schuster, E. M. Egelseer, D. Pum, C. M. Horejs, R. Tscheliessnig and N. Ilk, *Prog. Mol. Biol. Transl. Sci.*, 2011, **103**, 277.
11. N. Creamer, I. Mikheenko, P. Yong, K. Deplanche, D. Sanyahumbi, J. Wood, K. Pollmann, M. Merroun, S. Selenska-Pobell and L. E. Macaskie, *Catal. Today*, 2007, **128**, 80.
12. B. Schuster and U. B. Sleytr, in Protein Nanotechnology, *Methods in Molecular Biology*, ed. J. Gerrard and L. Domigan, Humana, New York, NY, 2020, ch. 12, pp. 195–218.
13. D. Pum and U. B. Sleytr, *Nanotechnology*, 2014, **25**, 312001.
14. K. Ariga, X. Jia, J. Song, J. P. Hill, D. T. Leong, Y. Jia and J. Li, *Angew. Chem., Int. Ed.*, 2020, **59**, 15424.
15. M. Mertig, R. Kirsch, W. Pompe and H. Engelhardt, *Eur. Phys. J. D*, 1999, 45.
16. M. Mertig, R. Wahl, M. Lehmann, P. Simon and W. Pompe, *Eur. Phys. J. D*, 2001, **16**, 317.
17. R. Wahl, M. Mertig, J. Raff, S. Selenska-Pobell and W. Pompe, *Adv. Mater.*, 2001, **13**, 736.
18. R. Wahl, H. Engelhardt, W. Pompe and M. Mertig, *Chem. Mater.*, 2005, **17**, 1887.
19. M. Merroun, A. Rossberg, C. Hennig, A. C. Scheinost and S. Selenska-Pobell, *Mater. Sci. Eng. C*, 2007, **27**, 188.
20. U. Jankovski, M. Merroun, S. Selenska-Pobell and K. Fahmy, *Spectroscopy*, 2010, **24**, 177.
21. S. Selenska-Pobell, T. Reitz, R. Schönemann, T. Herrmansdörfer, M. Merroun, A. Geißler, J. Bartolomé, F. Bartolomé, L. M. García, F. Wilhelm and A. Rogalev, *Nanomater. Nanotechnol.*, 2011, **15**, 8.
22. P. A. Bolla, A. Sanz, S. Huggias, J. F. Ruggera, M. A. Serradell and M. L. Casella, *Mol. Catal.*, 2020, **481**, 110262.
23. P. A. Bolla, S. Huggias, M. A. Serradell, J. F. Ruggera and M. L. Casella, *Nanomaterials*, 2020, **10**, 2322.
24. S. R. Hall, W. Shenton, H. Engelhardt and S. Mann, *ChemPhysChem*, 2001, **16**(2), 184.

25. S. S. Mark, M. Bergkvist, X. Yang, E. R. Angert and C. A. Batt, *Biomacromolecules*, 2006, **7**, 1884.
26. S. S. Mark, M. Bergkvist, X. Yang, L. M. Teixeira, P. Bhatnagar, E. R. Angert and C. A. Batt, *Langmuir*, 2006, **22**, 3763.
27. S. SMark, M. Bergkvist, P. Bhatnagar, C. Welch, A. L. Goodyear, X. Yang, E. R. Angert and C. A. Batt, *Colloids Surf., B*, 2007, **57**, 161.
28. S. S. Puranik, H. M. Joshi, S. B. Ogale and K. M. Paknikar, *J. Nanosci. Nanotechnol.*, 2008, **8**, 3565.
29. S. Dieluweit, D. Pum, U. B. Sleytr and W. Kautek, *Mater. Sci. Eng. C*, 2005, **25**, 727.
30. S. Huggias, P. A. Bolla, M. A. Serradell, M. Casella and P. Peruzzo, *Langmuir*, 2020, **36**, 1201.
31. S. Huggias, P. A. Bolla, J. C. Azcarate, M. A. Serradell, M. L. Casella and P. J. Peruzzo, *Catal. Today*, 2021, **372**, 98.
32. H. Claus, E. Akça, T. Debaerdemaeker, C. Evrard, J. P. Declercq, J. R. Harris, B. Schlott and H. König, *Can. J. Microbiol.*, 2005, **51**, 731.
33. U. B. Sleytr, B. Schuster, E. M. Egelseer and D. Pum, *FEMS Microbiol. Rev.*, 2014, **38**, 823.
34. E. Gerbino, P. Carasi, P. Mobili, M. A. Serradell and A. Gómez-Zavaglia, *World J. Microbiol. Biotechnol.*, 2015, **31**, 1877.
35. M. Malamud, P. A. Bolla, P. Carasi, E. Gerbino,A. Gómez-Zavaglia, P. Mobili and M. A. Serradell, in *S-layer Proteins from Lactobacilli: Biogenesis, Structure, Functionality and Biotechnological Applications*, ed. S. Ruzal, Caister Academic Press, Poole, UK, 2019, ch. 6, pp. 105–130.
36. M. Suhr, N. Unger, K. E. Viacava, T. J. Günther, J. Raff and K. Pollmann, *BioMetals*, 2014, **27**, 1337.
37. P. Messner, C. Schäffer and P. Kosma P, *Adv. Carbohydr. Chem. Biochem.*, 2013, **69**, 209.
38. G. Cavallero, M. Malamud, A. C. Casabuono, M. A. Serradell and A. S. Couto, *J. Proteomics*, 2017, **162**, 20.
39. M. Malamud, G. J. Cavallero, A. C. Casabuono, B. Lepenies, M. A. Serradell and A. S. Couto, *J. Biol. Chem.*, 2020, **295**, 14430.
40. T. Pavkov-Keller, S. Howorka and W. Keller, *Prog. Mol. Biol. Transl. Sci.*, 2011, **103**, 73.
41. X. Y. Wang, D. B. Wang, A. P. Zhang, L. J. Bi, J. B. Zhang, W. Ding and X. E. Zhang, *Small*, 2015, **11**, 5826.
42. J. Raff, S. Matys, M. Suhr, M. Vogel, T. Günther and K. Pollmann, in Protein-based Engineered Nanostructures, *Advances in Experimental Medicine and Biology*, ed. A. L. Cortajarena and T. Z. Grove, Springer International Publishing Switzerland, 2016, ch. 11, pp. 245–279.
43. F. Li, D. Wang, J. Zhou, D. Men and X. E. Zhan, *Sci. China: Life Sci.*, 2020, **63**, 1142.
44. S. Dieluweit, D. Pum and U. B. Sleytr, *Supramol. Sci.*, 1998, **5**, 15.
45. W. Shenton, D. Pum, U. B. Sleytr and S. Mann, *Nature*, 1997, **389**, 585.
46. E. Györvary, A. Schroedter, D. V. Talapin, H. Weller, D. Pum and U. B. Sleytr, *J. Nanosci. Nanotechnol.*, 2004, **4**, 115–120.

47. K. Pollmann, J. Raff, M. Merroun, K. Fahmy and S. Selenska-Pobell, *Biotechnol. Adv.*, 2006, **24**, 58.
48. R. Wahl, PhD thesis, University of Technology, Dresden (Germany), 2003.
49. A. Alshammari, V. Narayana Kalevaru and A. Martin, in *Green Nanotechnology: Overview and Further Prospects*, ed. M. Larramendy and S. Soloneski, IntechOpen, London, UK, 2016, ch. 1, pp. 1–33.
50. H. J. Salavagione, C. Sanchís and E. Morallón, *J. Phys. Chem. C*, 2007, **111**, 12454.
51. H. Brim, S. C. McFarlan, J. K. Fredrickson, K. W. Minton, M. Zhai, L. P. Wackett and M. J. Daly, *Nat. Biotechnol.*, 2000, **18**, 85.
52. G. Devaud, P. S. Furcinitti, J. C. Fleming, M. K. Lyon and K. Douglas, *Biophys. J.*, 1992, **63**, 630.
53. F. Ahmad, N. Ashraf, T. Ashraf, R. B. Zhou and D. C. Yin, *Appl. Microbiol. Biotechnol.*, 2019, **103**, 2913.
54. G. Gahlawat and A. R. Choudhury, *RSC Adv.*, 2019, **9**, 12944.
55. P. Zhao, X. Feng, D. Huang, G. Yang and D. Astruc, *Coord. Chem. Rev.*, 2015, **287**, 114.

CHAPTER 5

Surface Engineering Towards Better Material Performance

YING WANG[a,b], ZILI PANG[a] AND JUNHUI HE[a,*]

[a]Functional Nanomaterials Laboratory, Center for Micro/Nanomaterials and Technology and Key Laboratory of Photochemical Conversion and Optoelectronic Materials, Technical Institute of Physics and Chemistry, Chinese Academy of Sciences, Zhongguancundonglu 29, Haidianqu, Beijing 100190, China; [b]University of Chinese Academy of Sciences, Beijing 100049, China
*E-mail: jhhe@mail.ipc.ac.cn

5.1 Introduction

A material can be defined as a solid substance that is processed by physical or chemical processing of raw materials. According to the chemical composition and microstructure characteristics, materials can be divided into metal materials, inorganic non-metal materials, organic polymer materials and composite materials. Materials are often used to fabricate useful components, devices, or other items such as ceramics, glass and plastic.

A metal material is a general term for a metal element or a metal material that is mainly composed of a metal element. Metal materials are widely used in various fields of social and economic construction, and their role and significance are beyond imagination. Taking the manufacture of mechanical products as an example, more than 90% of the materials of various mechanical products are made of metal materials. Metallic materials have the following advantages: good heat resistance, high mechanical strength, good

Nanoscience & Nanotechnology Series No. 55
Concepts and Design of Materials Nanoarchitectonics
Edited by Omar Azzaroni and Katsuhiko Ariga

Published by the Royal Society of Chemistry, www.rsc.org

durability, good dimensional stability, uneasy to be damaged, uneasy to be contaminated with dust and dirt. However, the surface of metal materials is susceptible to corrosion, rust and oxidation.

The concept of inorganic non-metallic materials originated in the 1940s, early represented by traditional silicate materials. Inorganic non-metallic materials are composed of oxides, carbides, nitrides, and silicates, aluminates, borates of certain elements, which are known for their dimensional stability, fire and water resistance, and durability. Common inorganic non-metallic materials including glass, ceramics, cement, *etc.* are usually relatively brittle.

Polymer materials are matters of high molecular weight (usually up to 10 ~ 10^6) that are repeatedly joined by covalent bonds from many identical, simple structural units. Natural products such as wood, leather, rubber, cotton, hemp, silk, starch and silicate are all polymer materials. Natural rubber is one of the first natural polymer materials discovered by humans. The fully synthetic polymer materials begin with phenolic resins. Other polymer materials contain plastics, fiber, and rubber. Despite many obvious advantages of polymer materials, like lightweight, aging resistant, and chemical resistant, for example – they are not without their problems. The mechanical properties of polymer materials are worse than metals, and most of them are easy to burn and have poor heat resistance.[1,2]

In general, pure materials cannot fully meet the requirements of actual applications due to poor mechanical robustness, low transmittance, and easy corrosion, *etc.* Pure materials are susceptible to the surrounding environment and exert some problems, such as rust, cracks, dirt. In recent years, there has been increasing interest in improving the performance of materials. A wide range of materials scientists, physicists, chemists, engineers, biochemists, medical researchers have been seeking different strategies towards better material performance. On one hand, based on the materials themselves, some methods are used to change the material ingredients. For example, the composite material's comprehensive performance is superior to the original composition material to meet various requirements.[3] Alloys from pure metals have higher hardnesses and lower melting points than pure metals, which own a more extensive application range.[4] Adding additives, reinforcing agents, stabilizers, or toughening agents is a common method to improve the mechanical properties of and prolong the service life of plastic, rubber, and resin. Surface engineering strategy is another pathway to design surface structure and surface composition for better performance.

Surface engineering is to design, manufacture, research, and utilize surface materials to tailor the properties of engineered surfaces and to eventually improve their functionality and performance, which encompasses physics, chemistry, medicine, engineering, multi-discipline. The ASM (American Society for Metals) handbook considers surface engineering performing a series of operations on the surface to make the surface distinct from the bulk of material.[5] Thus, surface engineering is to change the morphology, chemical composition, structure, and properties of a solid metal surface or nonmetal surface by surface modification, surface deposition, surface coating

or various surface techniques after pretreatment. The resultant materials demonstrate excellent properties such as antireflective, anticorrosion, self-cleaning, anti-fatigue, and anti-wear, *etc.*

This review aims to summarize surface engineering strategies towards better material performance. In the second section, we show surface engineering strategies, including surface pretreatment, surface modification, surface deposition, coating, surface structuring and electrochemical surface engineering. In the third section, we give some examples of surface engineering strategies to improve material properties, including optical, anticorrosion, self-cleaning, thermochromic properties, detection sensitivity and fog collection. Finally, a conclusion will be given and future challenges will be pointed out, and an outlook is also shown toward future prospects in surface engineering.

5.2 Surface Engineering Strategies

5.2.1 Surface Pretreatment

Surface pretreatment is an important part of the surface engineering of materials. The results directly affect the quality of the coating and even the performance of materials. Poor pretreatment will cause a series of problems such as coating shedding, foaming and rusting. Surface pretreatment covers surface cleaning, surface oxidation, surface roughness control, and the like. Usually, surface cleaning aims at removing surface organic matter, dust particles and any adsorbed impurities. The cleaning process is often accompanied by the occurrence of surface activation. Common methods include plasma, piranha acid (a mixture of concentrated H_2SO_4 and H_2O_2), ultrasonic cleaning, alkaline washing, and electrochemical degreasing.[6] For surface descaling processes, methods include polishing, shot blasting, pickling, and electrochemical technologies. Surface roughness can be tailored by polishing, grinding, grit blasting, shot peening, chemical etching.[7] The selection of a pretreatment method depends on the material characteristics and needs of the actual application. For example, a plastic substrate can be corona treated or flame treated to ensure an effective combination of the coating and the substrates.[8]

5.2.2 Surface Modification

Surface modification is a technology for processing the material itself that uses heat treatment, mechanical treatment, ion treatment and chemical treatment to change the composition and properties of materials' surface. After the material has been modified, it can not only exert high mechanical robustness, but also obtain various special properties such as wear resistance, corrosion resistance, high temperature resistance, and suitable radiation absorption. Surface modification techniques contain surface deformation strengthening,[9] surface heat treatment,[10] ion beam surface diffusion

treatment, high-energy beam surface treatment,[11] ion implantation surface modification,[12] *etc.*

Taking high-energy beam surface treatment technology as an example, the heat source for high-energy beam heat treatment generally refers to laser, electron beam, ion beam, solar energy, and synchrotron radiation. This method with a heat source such as a laser beam with a high power density heats the surface of the material in a non-contact manner, then the surface forms a treatment layer of a certain thickness.[13] Finally, the surface modification process is realized by means of conduction cooling of the surface of the material itself. The wear resistance and corrosion resistance of materials are improved to meet various usage requirements, and high-energy beam surface treatment technologies are widely used in aerospace vehicles.

5.2.3 Surface Deposition

5.2.3.1 Liquid Phase Deposition (LPD)

LPD is a method of preparing films in liquid phase in wet chemical method. The principle of LPD is that the films can be formed on a substrate by the action of atoms or molecules in the liquid phase or by adding certain substances that can react with the starting material. The raw material may be a soluble silicate, a nitrate or a metal fluoride and so on. The preparation process is relatively simple, low cost, highly reproducible, and be generally applied to deposit a wide variety of oxide films.[14,15] In addition, the method can also apply heat, light, or doping on the precursor film in various atmospheres to functionalize the film. However, researchers should improve the traditional preparation process, and make the finished film have a required surface topography.

5.2.3.2 Physical Vapor Deposition (PVD)

A film is formed by atoms directly transported from a source to the substrate through the gas phase during the PVD process. The PVD technique uses physical processes such as thermal evaporation, glow discharge, or arc discharge to achieve material migration. The process includes production, transport and deposition of the gas phase, which involves two physical changes, evaporation and condensation.[16] And the entire process must be carried out in a vacuum. The key to this technology is how to convert raw materials into gas phase particles. There are many types of PVD, such as evaporation deposition, sputtering deposition, ion plating, electron beam PVD, pulsed laser deposition, and cathodic arc deposition.[17–19] Evaporation and sputtering deposition can be shown in Figure 5.1. PVD technique has been widely used in aerospace, films, integrated circuits[20] and so on.

Due to the easily controllable operation process, with the PVD technique it is possible to control the structure and composition of the processed materials.[18] However, there are some general limitations of PVD.[21] For example,

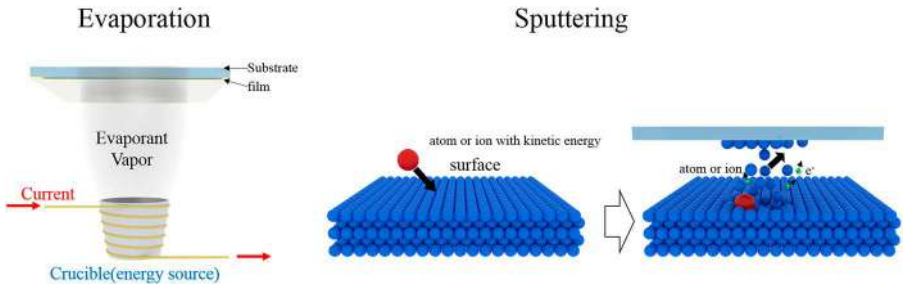

Figure 5.1 Schematic diagram of evaporation and sputtering deposition.

sophisticated reactor and vacuum systems need high capital cost, and complex shaped components are difficult to treat because the process is line-of-sight. Large-area deposition and research in chemometrics are still difficult points.

5.2.3.3 Chemical Vapor Deposition (CVD)

CVD is a deposition technique by means of a gas phase reaction under high temperature, plasma or laser assistance. A stable solid product, single crystal or film is formed on the surfaces of materials after homogeneous gas phase reactions occurring in the gas phase and/or heterogeneous chemicals reactions on or in the vicinity of the surface. The process is shown in Figure 5.2,[21] and CVD of thin films using some precursors, such as metals,[22] metal oxides,[23] metal nitrides[24] carbon materials[25] and polymer monomer(s)[26] have been researched, which are widely used in the fields of solar cells,[27,28] sensors,[29,30] and other functional coatings including corrosion-resistant, heat-resistant, anti-fouling, anti-icing[31] and so on. CVD technology is a very mature technology and, in addition to traditional thermal CVD, there are many other new technologies emerging, such as plasma-enhanced chemical vapor deposition (PECVD),[32] metal–organic CVD (MOCVD),[33] aerosol-assisted (AA) CVD,[34] initiated chemical vapor deposition (iCVD),[35,36] atmospheric pressure chemical vapor deposition (APCVD),[37] hot wire chemical vapor deposition (HWCVD),[38] laser chemical vapor deposition (LCVD),[39] and microwave hydrogen plasma chemical vapor deposition (RP-CVD).[40]

As a special mode of CVD, atomic layer deposition (ALD) is a method of applying thin films to various substrates with atomic scale precision.[41] By keeping the precursors separate throughout the coating process, atomic layer thickness control of film growth can be obtained. ALD film growth is self-limited and based on surface reactions.

Compared with PVD technology, CVD is an attractive way to prepare highly pure uniform films and coatings, and the stoichiometry in the deposition process may effectively be controlled. However, a limited range of materials

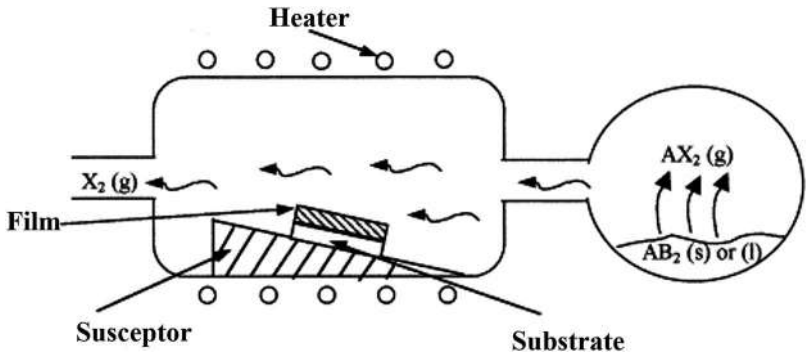

Figure 5.2 Schematic diagram of the CVD technology. Reproduced from ref. 21 with permission from Elsevier, Copyright 2003.

can be coated by CVD, and sharp edge coating is difficult because of thermal expansion mismatch stresses. In addition, complex chemistry and chemical processes generally run through the CVD process.[21]

5.2.4 Surface Coating

Coating technologies are to apply liquid material to the surface of the substrate by some means, which can control and alter material surface properties. Different areas have different requirements for material properties and processing methods, which has led to the development of many coating technologies. Examples include dip-coating, spray-coating, spin-coating, layer-by-layer assembly, *etc.*

5.2.4.1 Dip-coating

Dip-coating is an efficient coating preparation process involving simple immersion and withdrawal of the substrate. After the substrate is withdrawn from the precursor solution at a controlled rate, the partial solution is drained from the substrate. Then, the coated substrate is baked in an oven or dried at room temperature to achieve the finish. The whole process includes the following steps: immersion, start-up, deposition, drainage and evaporation,[42] as shown in Figure 5.3. The thickness of the coating can be controlled by the pulling speed and the viscosity of the solution. The dip-coating technique is suitable for preparing thin films on substrates of large areas. The process is automated and easy to control, and the coating materials utilization is relatively high. Despite the many obvious advantages of dip-coating technology, it is not without its problems. Air bubbles or pockets may be also associated with the formation of the film, especially when the solution is sticky. The thickness of film on the upper surface and lower surface may not be uniform.

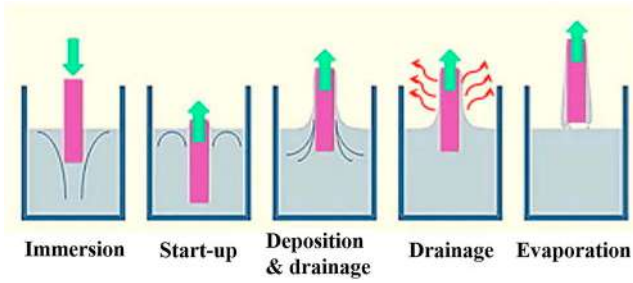

Figure 5.3 The whole process of dip-coating. Reproduced from ref. 42 with permission from Elsevier, Copyright 2014.

5.2.4.2 Spay-coating

Spay-coating is a technique that involves forcing the solution to disperse into uniform and tiny droplets followed by coating on the surface of different materials. The process is carried out under pressure or centrifugal force by means of a spray gun or a dish atomizer. Surface morphology is related to the spraying speed because spraying speed adjusts the balance of the spraying and solvent evaporation time.[43] Spray-coating can be divided into air spray, airless spray, electrostatic spray and various derivative methods of the above basic spray forms, such as high flow and low pressure atomization spray, thermal spray, cold spray, plasma spray, and automatic spray.[44–46] Among these methods, thermal spray is a key new technology and has been readily applied toward the preparation of a coating resistant to wear, corrosion, oxidation and heat.[47,48] The process heats a powdered or filamentous metal or non-metal material to a molten or semi-molten state through a heat source (such as electric arc, plasma spray or combustion flame, *etc.*) and then molten or semi-molten materials are sprayed onto the pretreated substrate surface at a certain speed by means of the flame itself or compressed air.

The spraying method has high work efficiency and strong adaptability. Crevices, holes, and inclined and curved planes can be sprayed. It is especially suitable for the construction of quick-drying coatings. The disadvantage is that tiny droplets will fly away and are lost, which results in a lower utilization rate of the raw material. The gun tip is easily blocked.

5.2.4.3 Spin-coating

Spin-coating technique is a commonly used preparation method in the fabrication of organic light-emitting diodes. The spin-on process has been developed for the so-called spin-on glasses in microelectronics and substrates with a rotational symmetry, *e.g.* optical lenses or eyeglass lenses. During the process, the substrate spins around an axis which should be perpendicular to the coating area. The process of rotation repels excess precursor solution and spreads the fluid by centrifugal force. A schematic diagram of spin-coating

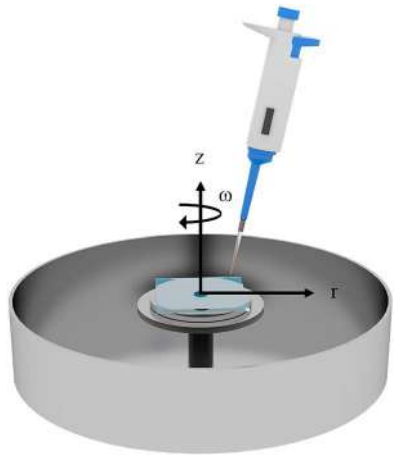

Figure 5.4 Schematic diagram of spin-coating technology.

technology is demonstrated in Figure 5.4. The process includes three steps: batching, high-speed rotation, and volatilization into a film. The final thickness of a spin-coated layer during the processing can be calculated by the semi-empirical formula,

$$d = k\omega^{\alpha}$$

The formula expresses the relationship between the thickness of the coating (d) and materials parameters like angular velocity, viscosity and solvent evaporation rate where ω is angular velocity, empirical constants k and α contain many materials parameters that demonstrate the physical properties of the solvent, solute and substrate. Typically, α has a value of around -0.5.[49] Therefore, the thickness of coatings could be tailored by controlling the rotational time and speed, the amount of liquid, and the concentration and viscosity of the solution.

The spin-coating process is also simple and easy to operate. Compared with dipping and spraying methods, the substrate suitable for spin-coating technology is small. The method is not suitable for large-area film preparation on large substrates, and the solution utilization rate is not very high.

5.2.4.4 Layer-by-layer (LbL) Assembly

Layer-by-layer (LbL) assembly is a popular method in which multilayer functional films are prepared by repeating immersion, spin, spray, electromagnetic, or fluidic technologies,[50] as shown in Figure 5.5. The basis of LbL assembly is multiple weak interactions between layers and layers, such as electrostatic interactions, hydrogen bonds, charge-transfer interactions, and/or cation–dipole interactions.[51] In LbL assembly, each technology has

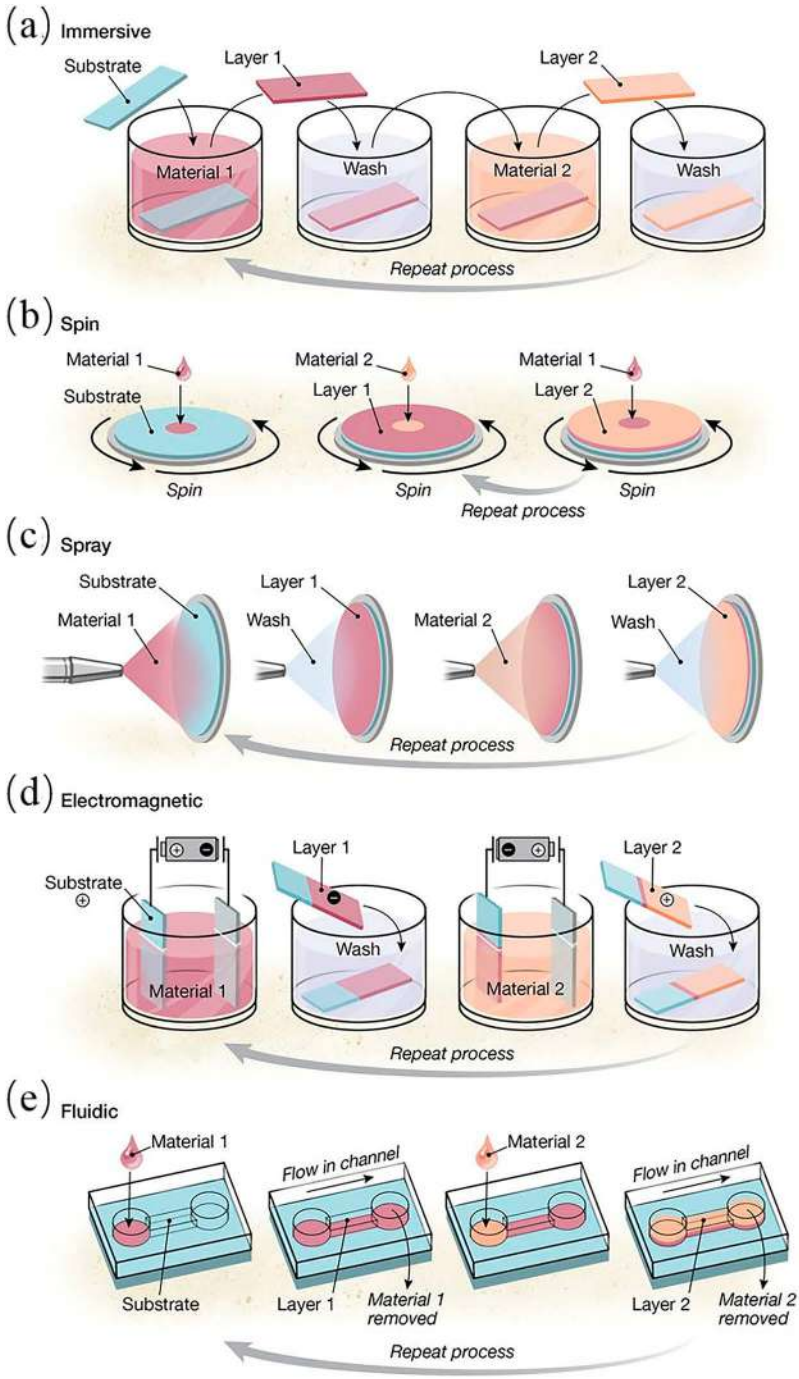

Figure 5.5 LbL assembly technologies by reusing immersion (a), spin-coating (b), spray-coating (c), electromagnetic technology (d), fluidic technology (e). Reproduced from ref. 50 with permission from Science, Copyright 2015.

its own advantages. With the development of these technologies, LbL assembly has become one of the most widely used methods for coating different materials in biomedicine, energy, optics, and catalysis. LbL assembly highlights advantages in terms of cost, operability, and controllability. It is very important to choose the assembly technology for film engineering towards tailor-made physicochemical properties.

5.2.5 Surface Structuring

5.2.5.1 Etching

Etching is defined as a process of selective dissolution and stripping of a material surface and a film coated on the surface. The etching process can be roughly classified into the following steps: "reactant close to surface", "surface reaction", and "product leaving the surface". So the entire etching process contains the diffusion effect of the reactants and the products, and the chemical reaction. Etching rate, selectivity, uniformity, directionality (isotropic or anisotropic), etched surface quality and reproducibility are several important factors in determining the quality of the etching process.[52] Etching can be divided into wet etching and dry etching based on whether solutions are used or not.

Wet etching is the most common etching method with a simple experimental procedure and the lowest equipment costs. There are three factors that affect the etching rate: the etching solution concentration, the etching solution temperature, and the stirring. By electrochemical/chemical etching, controllable surface micro-nano structures and patterned shapes of materials can be obtained. The dissolution of Si in alkaline solution and Al in HCl containing isopropyl alcohol (IPA)[53] and the electrochemical etching of silicon[54] are some examples of chemical etching and electrochemical etching. Chemical etching usually takes more time than electrochemical etching.

Dry etching that removes materials by using plasma-driven chemical reactions and/or energetic ion beams is a complex process. It covers four basic mechanisms: sputtering, purely chemical, ion-enhanced energy-driven mechanism, ion-enhanced inhibitor.[52] Dry etching is performed by rapid but isotropic chemical processes and slow but anisotropic physical processes. Therefore, coordinating the balance of chemical and physical processes is the key to the dry etching technique. Plasma etching, reactive ion etching (RIE), and reactive ion beam etching (RIBE) are commonly used in dry etching techniques.[55–58]

Compared with wet etching, the dry etching process reduces waste liquid production and it is easy to achieve in terms of automation and tool clustering. But generally speaking, this process is quite complicated and the used instruments are expensive. Whether it is wet etching or dry etching, the resulting surfaces are fragile or soft due to the removal of a part of the raw materials.[59]

5.2.5.2 Templating

The template method is a synthetic method in which the template is the main configuration to control, influence and modify the morphology and size of the material for better material properties. Based on the nature of the template used, the method is divided into that of hard template which maintains its specific structure by covalent bonds, and that of soft template which maintains its specific structure by means of intermolecular or intramolecular interaction forces.

Materials used as hard templates, like AAO, polymer microspheres, and carbon fiber, are usually rigid. The size and morphology of the obtained surface or sample greatly depend on the structure of the hard template. Among these hard templates, the AAO template has high pore density and uniform pore distribution, which can be fabricated by placing aluminum in an acid solution for an anodization reaction. It consists of a close-packed hexagonal array with parallel cylindrical nanopores which are perpendicular to the surface of aluminum substrate,[60] as shown in Figure 5.6. AAO is focused on surface and structural engineering applications.[61,62]

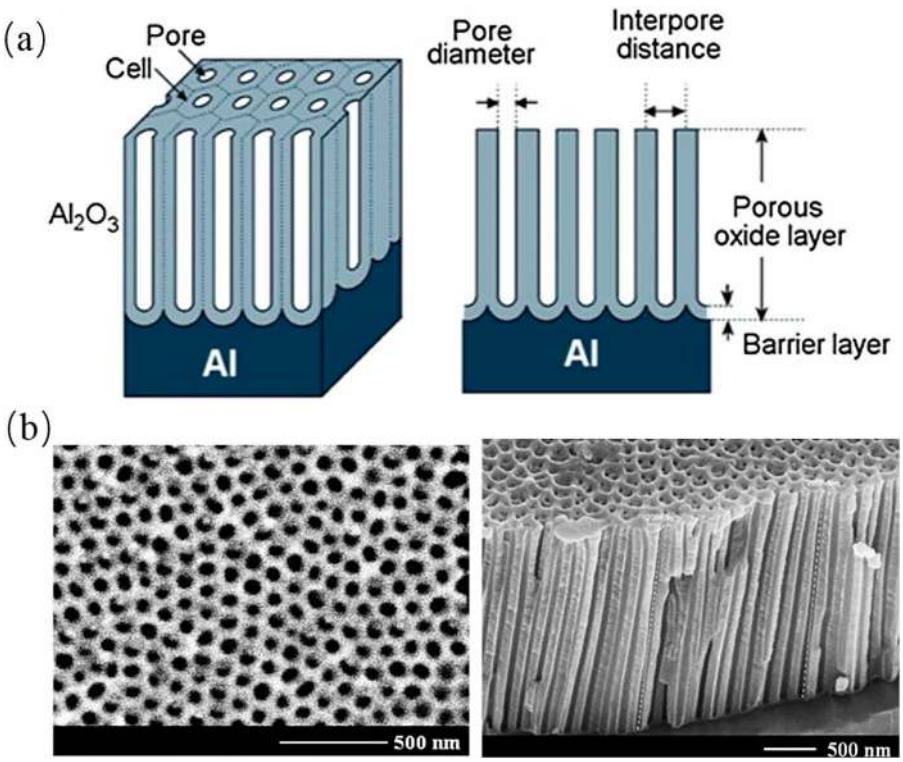

Figure 5.6 (a) Schematic of AAO structure prepared by electrochemical anodization of Al. Reproduced from ref. 60 with permission from Elsevier, Copyright 2013. (b) Top view and cross-sectional images of AAO template by SEM. Reproduced from ref. 61 with permission from Elsevier, Copyright 2010.

Aggregates formed through weak interaction forces (electrostatic, hydrogen bonding, van de Walls interaction) are used as soft templates, including those of surfactants, polymers and biopolymers.[63] The synthesis of nanostructured materials is the main example of the use of soft templates.[64,65] Normally, nanostructured materials can be obtained by using surfactants such as PAA, CTAB, or biopolymers such as F127 or P123.[66–72] Compared with a hard template, a soft template has its advantages such as its good repeatability, simplicity of the process.

Template selection and removal are very important steps in the fabrication of nanomaterials or structured surfaces. The type of template and selection of removal methods are mainly based on the physical and chemical properties of the material. Dissolution, calcination, and etching are the most common methods of removing templates.

5.2.5.3 Phase Separation

In the field of materials and chemistry, phase separation is defined as the phenomenon of an unstable tendency in which a change in environmental conditions occurs between phases and phases. There are some commonly used phase separation methods, such as non-solvent induced phase separation (NIPS), vapor induced phase separation (VIPS), evaporation induced phase separation (EIPS), and thermo-induced phase separation (TIPS).[73] These methods have often been employed to prepare polymer films with porous structures or rough surfaces.

Among these methods, the process of NIPS is carried out first by dissolving the polymer in a solvent to form a homogeneous solution. Following that, another solvent (called an extractant), which is more miscible with the solvent, slowly extracts the solvent, and there finally forms a two-phase structure of polymer as the continuous phase and the solvent as the dispersed phase. Polymer films with pore structures or rough surfaces are obtained after removal of the solvent.[74,75] VIPS belongs to a typical NIPS process. During the process, non-solvent vapor (usually moist air) slowly transfers water molecules from the gas phase to the coating solution before coatings solidification. By controlling air temperature, relative humidity and gas velocity of the humid air, and the exposure time of coatings, the VIPS process can obtain coatings with highly porous, ordered surface patterns or attractive surface properties.[76,77] However, compared with other phase separation processes, the VIPS process is very slow due to the slow mass transfer rate of a non-solvent vapor to a coating solution. Some examples that use NIPS and VIPS are illustrated in Figure 5.7.

In general, the properties of films or coatings *via* phase separation methods not only closely relate to the materials itself but also strongly depend on the morphology formed during phase separation and subsequent solidification.[78] The pore-size control and the surface geometry control in the phase separation process are difficult due to a variety of factors.

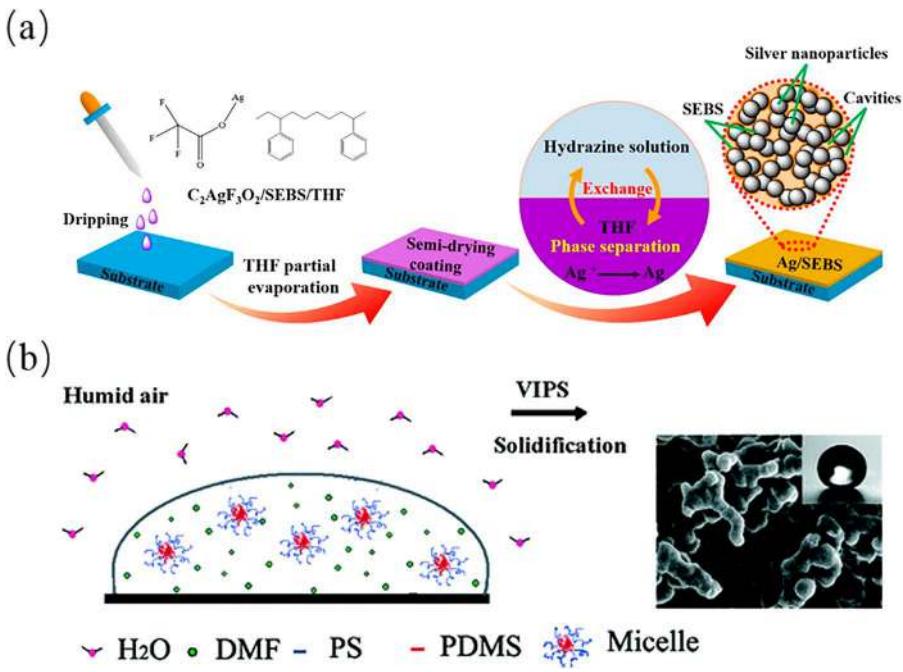

Figure 5.7 (a) Scheme for the preparation of superhydrophobic multifunctional coatings by NIPS. Reproduced from ref. 75 with permission from American Chemical Society, Copyright 2019 (b) Scheme for the preparation of superhydrophobic surface from VIPS of copolymer micellar solution. Reproduced from ref. 76 with permission from American Chemical Society, Copyright 2005.

5.2.6 Electrochemical Surface Engineering

Electrochemical surface engineering is often accompanied by the occurrence of electrochemical reactions. Electrochemical surface engineering strategies comprise electrochemical plating, electrochemical anodization, micro-arc oxidation, electrochemical etching, and deposition (Figure 5.8).[79,80] Electroplating is a common method for surface protection and decoration in which a plated substrate is used as a cathode to obtain a strongly bonded metal or alloy film on the substrate by electrolysis. Electrochemical anodization is devoted to generating an oxide layer, nanotubes, nanopores, or nanorods on the surface of metals and alloys, such as an AAO template. Micro-arc oxidation (MAO) employs high voltage plasma to fabricate films, and therefore, it is also named plasma electrolytic oxidation (PEO). Electrochemical parameters, including electrolyte composition, applied voltage, electrochemical reactive time, and temperature, strongly influence materials' performances. Electrochemical surface engineering has attracted widespread attention for researchers and engineers due to the advantages of simplicity, low cost, controllability, and easy preparation in large areas, *etc.*[80,81]

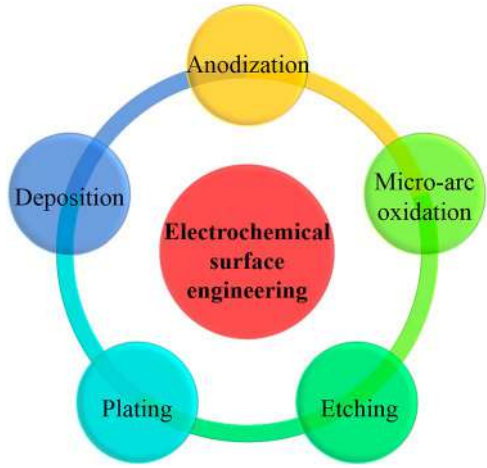

Figure 5.8 Electrochemical surface engineering.

5.3 Examples in Surface Engineering Strategies

5.3.1 Enhancement of Optical Properties

Light reflection and scattering generally occur on transparent substrates such as glass or plastics, which would result in low transmittance especially in the field of architectural glasses, optical lenses, display panels and solar cells. The phenomenon may have a negative impact on the operation and performance of instruments, such as reducing the photoelectric conversion efficiency of solar cells, reducing the sharpness and contrast of imaging on displays. Constructing antireflection coatings (ARCs) is a good strategy for overcoming these problems. According to the Fresnel equation, single-layer antireflective coatings to achieve zero reflection needs to meet two conditions: $n_c=(n_a n_s)^{1/2}$ and $d = \lambda/4n_c$, where n_a and n_c are the refractive indices of the air and substrate, respectively, and d is the thickness of ARCs, λ is the wavelength of incident light.[58,71] In general, it is difficult to obtain a lower refractive index for a single material because such materials in nature are few and expensive. Thus, constructing surfaces with special structures such as porous structures and multilayer structures will be a better strategy for better antireflective performance.

Dip-coating and template methods are commonly used for improving the optical property of surfaces. He's group[69] fabricated high-performance broadband antireflective thin films with mesoporous structures. The process contained two surface engineering strategies, dip-coating and soft template (CTAB), respectively. After removing the template at high temperature, the optimal thin film has a maximum transmittance of nearly 100% and an average

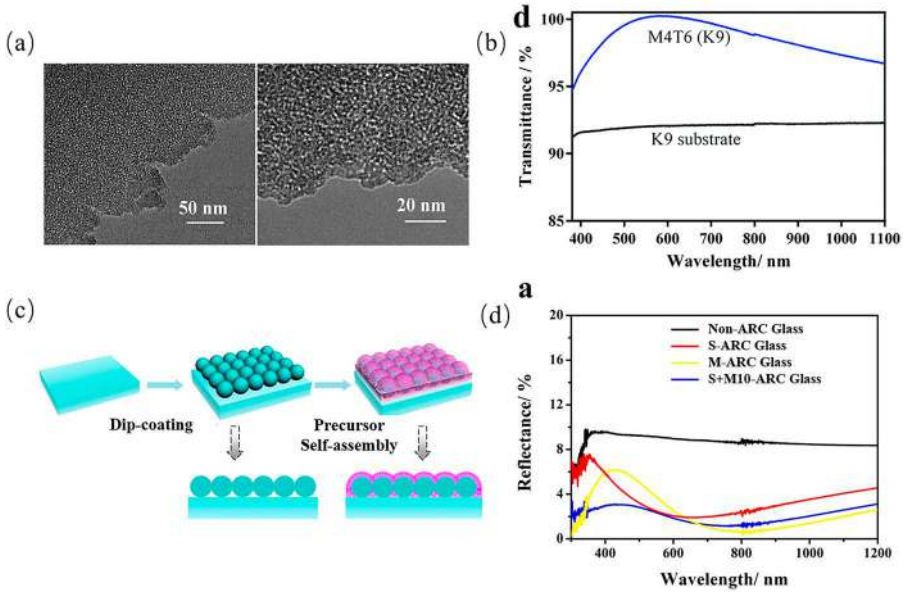

Figure 5.9 (a) TEM images of the hybrid thin film; (b) Transmittance spectra of thin film on K9 glass and blank K9 glass. Reproduced from ref. 69 with permission from the Royal Society of Chemistry. (c) Fabrication process of silica-based moth-eye-like nanostructures antireflective coatings; (d) Reflectance spectra of different coatings, S-ARC glass and M-ARC glass meant that glass was coated by dip-coating solid silica nanoparticles and precursor-derived self-assembly at 60 °C for 30 h, respectively. Reproduced from ref. 71 with permission from American Chemical Society, Copyright 2017.

transmittance of 99.3% in the visible light region on K9 glass (Figure 5.9a and b). Then, they designed robust silica-based moth-eye-like nanostructures anti-reflection coatings combining solid silica with mesoporous silica layer *via* dip-coating (Figure 5.9c).[71] The average reflective index was decreased to 1.88%, and coatings can maintain high transmittance when the light incidence angle is up to 40° in the wavelength range of 400–1200 nm (in Figure 5.9d).

Other methods like RIE, have been proved to effectively increase AR bandwidth. Ye and coworkers[57] obtained an ultra-broadband antireflective fused silica surface with subwavelength nanostructures by one step, self-masking reactive ion etching (RIE). As illustrated in Figure 5.10, a maximum transmittance of 99.5% and an AR bandwidth of 860 nm were achieved. And FDTD stimulation results demonstrated that light scattering was the main factor that affected the transmittance of the deep-ultraviolet region.

The recent developments in the fabrication of ARCs *via* some surface engineering strategies are listed in Table 5.1.

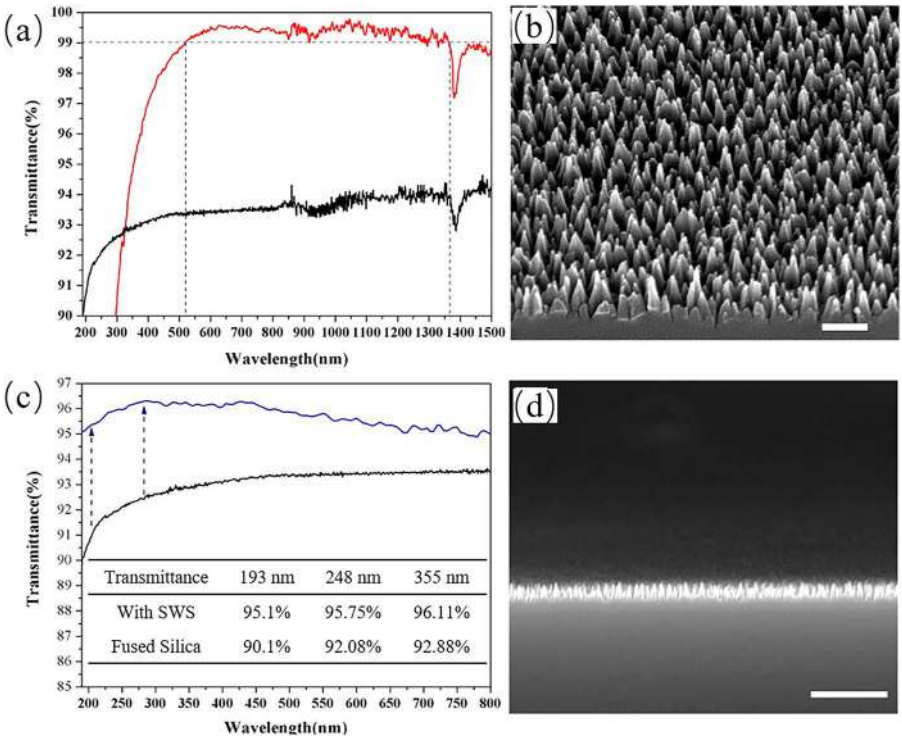

Figure 5.10 (a) Transmission spectra of fused silica surface with subwavelength nanostructures; (b) SEM image of subwavelength nanostructures; (c) Transmittance spectra and table for deep-UV antireflection; (d) Cross-section SEM image of subwavelength nanostructures for deep-UV antireflection. Reproduced from ref. 57 with permission from American Chemical Society, Copyright 2018.

Table 5.1 Summary of ARCs *via* some surface engineering strategies.

Substrate	Strategy	AR material	Max transmittance	Wavelength range	Reference
Glass	Dipping, CVD	Silica, TEOs	98.7%	300–2500	82
	Dipping, spraying	Silica	96%	300–2500	83
	Dipping, RIE	Polymer	98.9%	400–1100	58
Quartz	LbL assembly	TiO_2/SiO_2	99.2%	200–800	84
	Dipping, template	Silica	99.99%	300–1600	85
PMMA	Spinning, template	PMMA, PS	99.95%	400–800	86
PET	PECVD	SiO_2	95.8%	300–800	87

5.3.2 Anticorrosion

Corrosion is a universal phenomenon that occurs on various substrate surfaces such as Al, Fe, Cu, Zn, steel and alloys. This phenomenon causes serious problems in actual applications, including the premature invalidation of material, economic loss, and a negative impact on the environment and humans. In addition to the use of corrosion-resistant substrates, electrochemical protection and surface coating are often used to prevent corrosion of materials. Electrochemical protection methods include cathodic protection methods with impressed current[88] and cathodic protection methods for sacrificial anode.[89] Ravichandran *et al.*[90] deposited an iron–manganese phosphate composite coating on aluminum which offered good corrosion protection for aluminum in 3.5% NaCl. Birbilis *et al.* developed a lanthanum based coating system for the protection of commercial Mg-alloy AZ91D *via* radio frequency (RF) magnetron sputtering.[91] As shown in Figure 5.11a, a

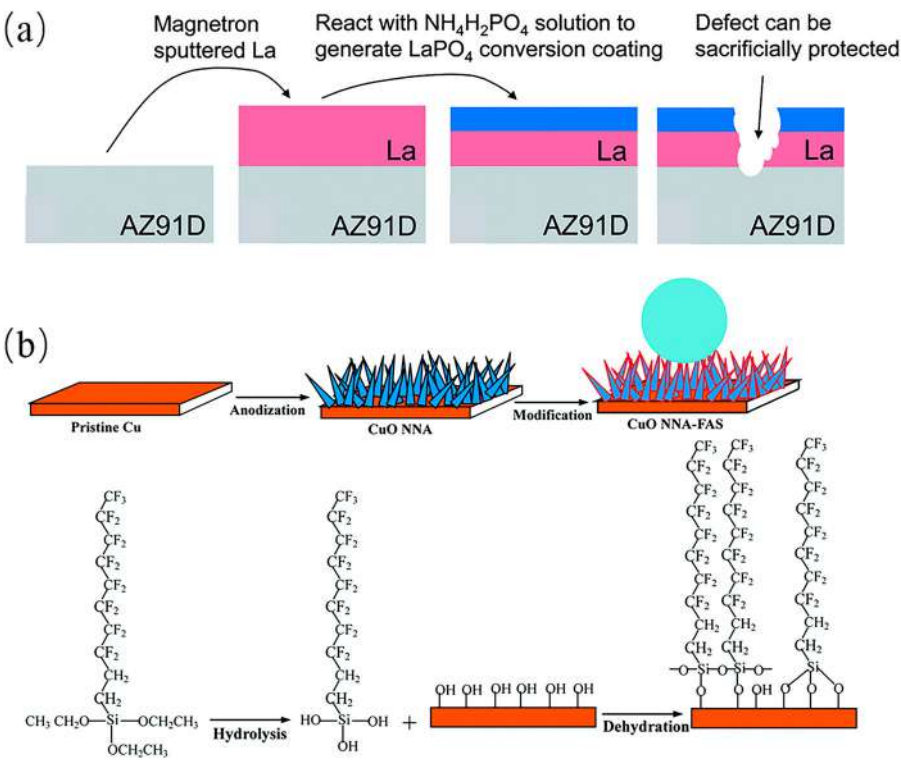

Figure 5.11 (a) Fabrication process of lanthanum based coating system. Reproduced from ref. 91 with permission from the Royal Society of Chemistry. (b) Fabrication process of superhydrophobic CuO nanoneedle array surfaces. Reproduced from ref. 96 with permission from the Royal Society of Chemistry.

lanthanum based coating consisted of La layer and $LaPO_4$ layer, $LaPO_4$ conversion coating was used to prevent the dissolution of La without the need to act as a sacrificial barrier. When a defect is present, the coating system sacrifices to protect the AZ91D substrate. The novel sacrificial anodic coating system effectively addresses the corrosion issue of Mg.

The coating method is to electroplate or chemically form a dense and corrosion-resistant oxide film on a metal surface, paint or fabricate superhydrophobic coatings.[92–94] Ishizaki *et al.*[95] fabricated a superhydrophobic film on magnesium alloy AZ31 through the microwave plasma-enhanced chemical vapor deposition.

(MPECVD) process. The introduction of superhydrophobic film decreased significantly both the anodic and cathodic current density, and improved anticorrosion resistance and chemical stability. Yuan's group[96] designed superhydrophobic CuO nanoneedle array films by electrochemical anodization followed by modification with fluoroalkylsilane (FAS-17) (Figure 5.11b), which effectively prevented copper substrate from corrosion and had an inhibition efficiency higher than 90% in an aqueous NaCl solution (3.5%).

5.3.3 Self-cleaning Properties

Self-cleaning materials are defined as materials that keep themselves clean under natural conditions. Usually, these materials also have multiple functions such as anti-fog and anti-fouling. Self-cleaning of materials may result from photocatalysis or special surface wetting. For the principle of photocatalytic self-cleaning, taking titanium dioxide as an example,[97] titanium dioxide generates photogenerated electrons and holes under ultraviolet light irradiation, thereby generating superoxide radicals and hydroxyl radicals, which oxidize organic pollutants, and effectively degrading organic pollutants. For example, Sun's group[98] developed self-cleaning coatings with ZnO@TiO_2 core–shell nanorod arrays *via* spin-coating on FTO glass substrate (Figure 5.12a). Heterojunctions between the ZnO nanorods and TiO_2 nanosheets efficiently facilitated the degradation of dye molecules (Figure 5.12b). After four cycles of experiments, the photocatalytic degradation rate is still the same as before (Figure 5.12c and d).

For self-cleaning due to special surface wettability, according to the Cassie-Baxter model, water droplets first absorb dust particles, and then carry the dust particles away from the surface when they roll off on the surface.[100,101] He's group[99] fabricated superhydrophobic self-cleaning coatings on different substrates by spraying 1*H*,1*H*,2*H*,2*H*-perfluorooctyltriethoxysilane modified silica nanoparticles and acid-catalyzed silica precursor at room temperature, as shown in Figure 5.12e. The introduction of acid-catalyzed silica precursors improved the robustness of the coatings, and spraying hydrophobic silica nanoparticles resulted in micro-nano roughness, which made the coatings become superhydrophobic and self-cleaning. Water droplets rolled off the surface of superhydrophobic coatings and carried contaminants away from the surface (Figure 5.12f).

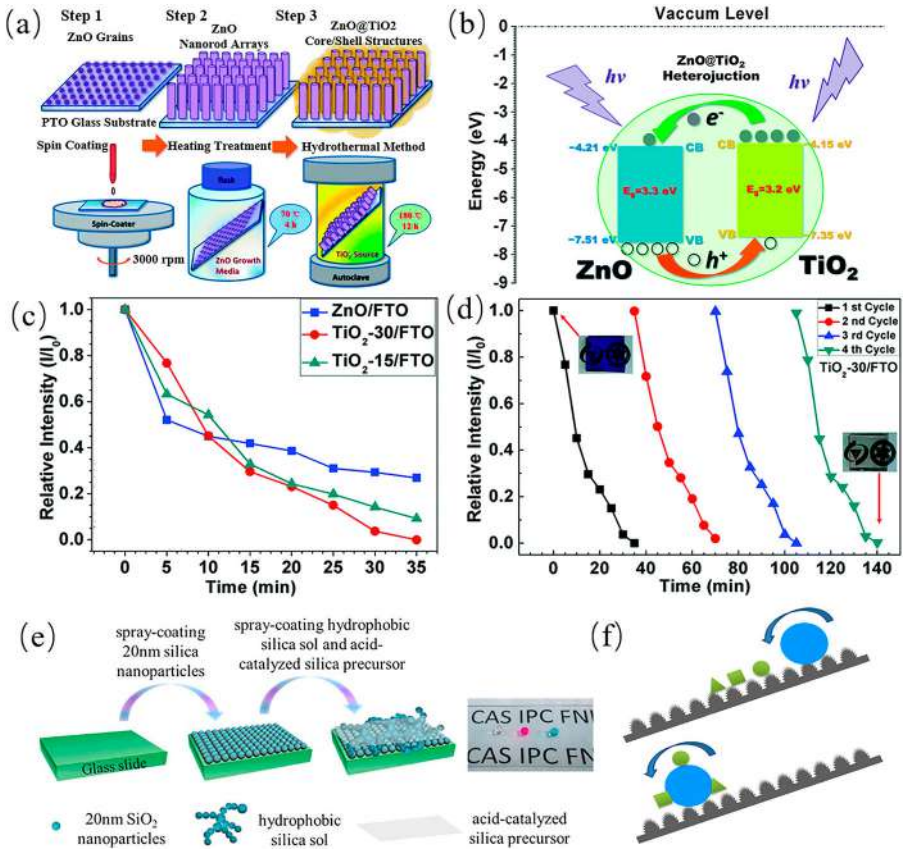

Figure 5.12 (a) Fabrication process of self-cleaning coatings with ZnO@TiO_2 core–shell nanorod arrays; (b) Heterojunction between the ZnO nanorods and TiO_2 nanosheets; (c) The photocatalytic degradation rates of rhodamine B (RhB) of the selected samples; (d) Four cycles of photocatalytic degradation experiments for the TiO_2-30 sample. Reproduced from ref. 98 with permission from the Royal Society of Chemistry. (e) Fabrication process of robust antireflective and superhydrophobic coatings. (f) Self-cleaning phenomenon of water on superhydrophobic coatings. Reproduced from ref. 99 with permission from American Chemical Society, Copyright 2017.

5.3.4 Thermochromic Properties

In today's world, due to global warming, the use of indoor air conditioners has become more and more widespread, which has led to an increase in energy consumption.[102] Smart windows, the most typical technique for energy-saving, can improve indoor energy comfort while improving building energy efficiency by dynamically adjusting the transmittance of solar irradiation according to weather conditions and personal preferences.[103]

Electrochromic, photochromic, and thermochromic materials have been widely used in smart windows. As commonly used thermochromic materials, VO_2-based materials coated glass window has been fabricated by physical vapor deposition (PVD), surfactant-assisted deposition,[104] phase separation,[105] LbL assembly.[106] Many investigations were devoted to increasing light transmission (T_{lum}) and surface plasmonic enhancement to obtain high solar switch efficiency (ΔT_{sol}) of thermochromic coatings.[107] He's group[108] designed $SiO_2/TiO_2/VO_2$ hollow nanospheres (TLHNs) coatings (Figure 5.13a). The thermochromic coatings not only have an ultrahigh luminous transmittance ($T_{lum\text{-}l}$ = 74%) and an improved solar modulation

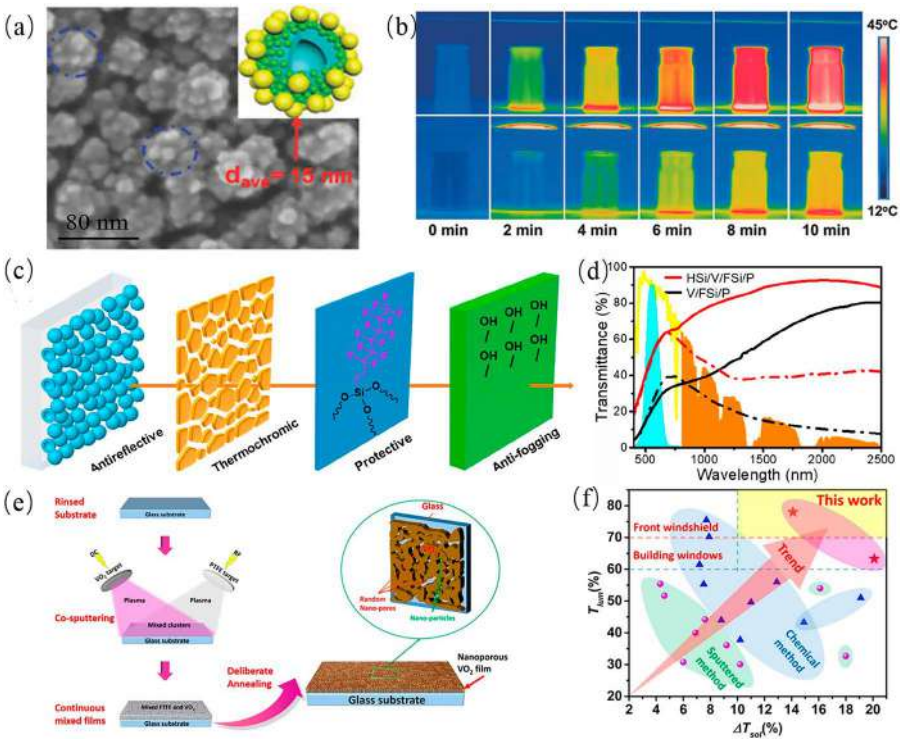

Figure 5.13 (a) SEM image of TLHNs coating; (b) Infrared thermal images of water in beakers irradiated through blank glass (up) and TLHNs coated glass (down), respectively. Reproduced from ref. 108 with permission from John Wiley & Sons, Copyright © 2018 WILEY-VCH Verlag GmbH & Co. KGaA, Weinheim. (c) Schematic illustration of four-layer thermochromic coating by LbL assembly; (d) Transmission spectra of coatings at both 20 °C (solid line) and 100 °C (dashed line). Reproduced from ref. 109 with permission from American Chemical Society, Copyright 2019. (e) The preparation process of nonporous VO_2 films. (f) Comparison of ΔT_{sol} and T_{lum} in recently reported VO_2-based coatings and this work. Reproduced from ref. 110 with permission from American Chemical Society, Copyright 2019.

ability (ΔT_{sol} = 12%), but have a self-cleaning function as well. And as shown in Figure 5.13b, water in the beaker under the TLHNs coated glass was not heated by infrared radiation. Very recently, the HSi/V/FSi/P four-layer coating composed of a hollow SiO_2 layer (HSi), a VO_2 layer (V), a fluorosilane-SiO_2 layer (FSi), and an antifogging layer (P) was fabricated by LbL assembly in the group,[109] which showed antifogging, and self-healing properties, and the solar regulation efficiency and luminous transmittance were up to ΔT_{sol} = 16.4% and $T_{lum\text{-}a}$ = 54.0%, respectively (Figure 5.13c and d). Cao *et al.*[110] prepared nonporous VO_2 films by self-template synthesis and a reactive magnetron sputtering method followed by post-annealing, as shown in Figure 5.13e. The luminous transmittance reached up to 78%, and the solar modulation ability was promoted to 14.1% after removing PTFE. The thermochromic performance in this work is better than previous works, and may meet the requirements of actual use in architectural glazing (Figure 5.13f).

5.3.5 Detection

Surface engineering has important applications in biomedical and environmental detections, which can be applied to improve detection sensitivity and reduce detection limits.[111–113]

He's group[114] showed a paper-based hydrophobic and lipophobic surface with a superior confining ability *via* dip-coating, which was used for sensitive heavy metal ions detection and bacteria assay. The control of wettability avoided the problem of poor reproducibility caused by surface liquid diffusion and droplet drift. The colorimetric quantitative detection limits of heavy metal ions Cr(VI) and Ni(II) by paper-based surface were reduced to 0.035 mg L^{-1} (0.7 ng) and 1 mg L^{-1} (10 ng), respectively, as illustrated in Figure 14a and b.

Another work[115] reported a surface-enhanced Raman spectroscopy (SERS) substrate with a hexagonal-packed lotus seedpod (LSP) like array of adjustable nanogaps. The fabrication process used the plasma etching procedure and Ag sputtering (Figure 14c and e). Due to the uniform distribution of the LSP array substrate and the high-density gap of less than 10 nm, the substrate achieved ultra-sensitive (10^{-12} M) and repeatable detection of rhodamine 6G (R6G) and provided a high sensitivity Raman signal for unlabeled detection of Aβ oligomers at a low concentration of 0.1×10^{-6} M (Figure 14d and f). It is a potential method for researching the dynamic and conformational changes of unlabeled amyloid.

5.3.6 Fog Collection

With population growth, water pollution intensification and climate change, the lack of fresh water resources is becoming a major problem worldwide. Fog collection is of great significance in sustainable development. Effective regulation of material surface structure and wettability would facilitate fog

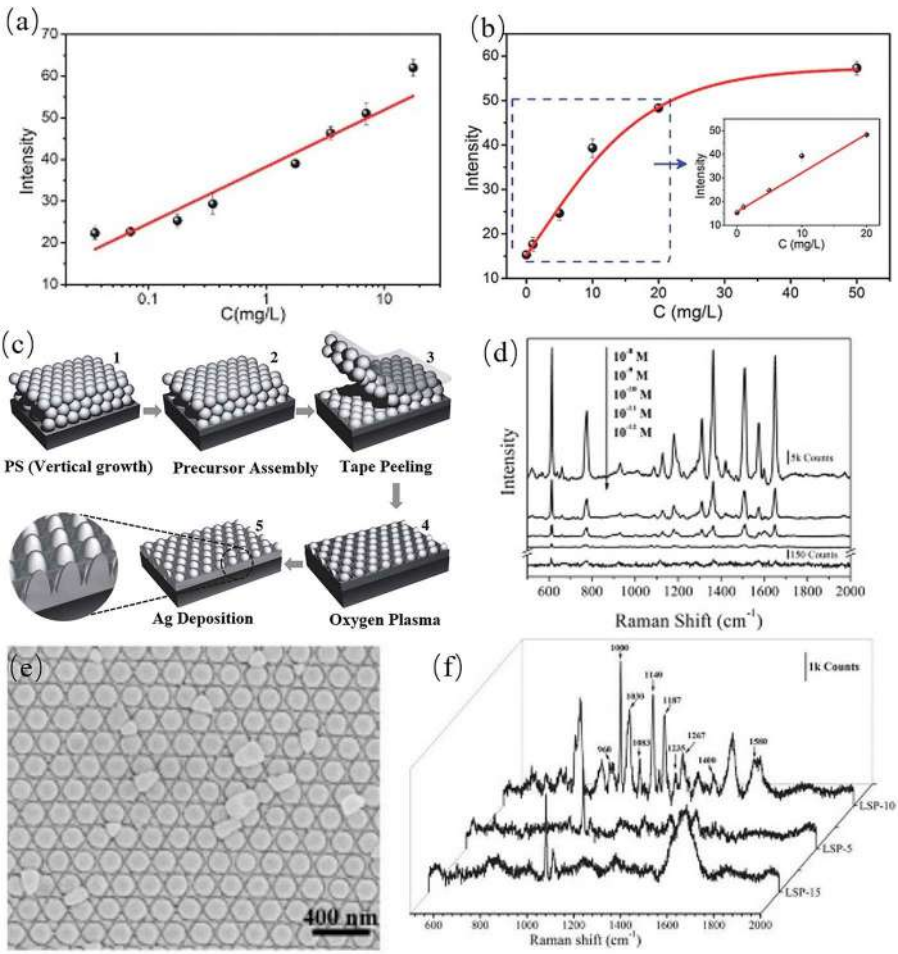

Figure 5.14 Quantitative calibrations for (a) Cr(VI) and (b) Ni(II) sensing, respectively. Reproduced from ref. 114 with permission from John Wiley & Sons, Copyright © 2016 WILEY-VCH Verlag GmbH & Co. KGaA, Weinheim. (c) Fabrication process of LSP; (d) Raman spectra of R6G with concentrations ranging from 10^{-8} M to 10^{-12} M; (e) SEM image of LSP-10; (f) Raman spectra of Aβ oligomers at a low concentration of 0.1×10^{-6} M on LSP with different magnetic sputtering time, 5 min, 10 min, and 15 min, respectively. Reproduced from ref. 115 with permission from John Wiley & Sons, Copyright © 2018 WILEY-VCH Verlag GmbH & Co. KGaA, Weinheim.

collection. Zheng *et al.*[116] designed a novel star-shaped surface. After depositing TiO_2 by spin-coating, the film was modified by heptadecafluorodecyltrimethoxysilane (FAS). Star-shaped patterns were fabricated by illuminating the FAS-modified film under UV light with a photomask (Figure 5.15a). Fog droplets were collected in the star-shaped region. As illustrated in Figure 5.15b, the weight of collected water by surfaces with star-shaped patterns

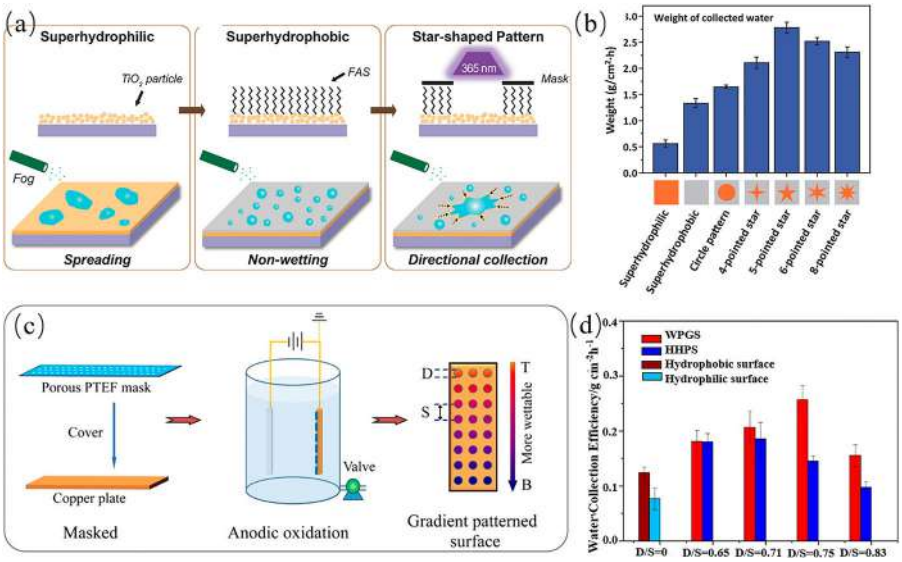

Figure 5.15 (a) Fabrication process of star-shaped surface; (b) Weight of collected water on surface with varied shapes of patterns. Reproduced from ref. 116 with permission from John Wiley & Sons, Copyright © 2014 WILEY-VCH Verlag GmbH & Co. KGaA, Weinheim. (c) Fabrication process of WPGS; (d) Water collection efficiency comparison of different surfaces. Reproduced from ref. 117 with permission from American Chemical Society, Copyright 2019.

reached up to 2.78 g cm^{-2} h^{-1}. Hou's group[117] proposed an integrative bio-inspired surface with wettable patterns and gradients for enhancement (WPGS) of fog collection. As shown in Figure 5.15c and d, anodic oxidation was carried out on a porous polytetrafluoroethylene mask. The highest water collection efficiency was about 0.2568 g cm^{-2} h^{-1}. Continuous water collecting circulation was achieved under the cooperation of multidriving forces.

5.4 Summary and Outlook

Materials with superior properties are needed in many applications. Surface engineering demonstrates its potential and superiority in this regard. In this review, we have accounted surface engineering methods for better materials performance. We divided these methods into surface pretreatment, surface modification, surface deposition, surface coating, surface structuring, and electrochemical surface engineering. The principles, preparation methods, strengths and weaknesses of various methods were discussed in detail. Then, we listed examples of surface engineering methods to improve the performance of materials, including the enhancement of optical, self-cleaning, anticorrosion, and thermochromic properties, detection sensitivity and fog

collection. This review provides a reference for various applications. However, which method should be used will depend on the actual needs and the characteristics of the material itself.

Although researchers have developed various strategies to improve material surface performance, most methods still confront some challenges. Thus, we believe that the following aspects require more attention and research in the future. First, the development of multifunctional surfaces would be an inevitable trend, which requires a combination of various surface engineering strategies. In this regard, how to effectively combine multiple methods would become a key yet challenging point. It is in fact quite difficult to use a variety of methods together, which either has an impact on surface properties or is technically demanding. Second, many methods are only suitable for the preparation of small areas of specific materials. It is urgent to develop methods for the large-area fabrication of various materials surfaces. For example, RIE can only prepare a 100 mm optical glass limited by its sample chamber size.[57] Therefore, the excellent surface properties given by RIE are difficult to be displayed in a large area. Third, although many works have been carried out to improve the strength and durability of surfaces, actual applications have higher function and performance requirements for the surfaces. Moreover, problems such as complex and time-consuming processes, expensive instruments, polluting the environment in some methods also restrict their practical applications. And such methods may not be suitable either for large-scale industrial production. Finally, to meet emerging requirements of applications, some brand-new surface engineering strategies may also be developed.

Acknowledgements

This work was supported by the National Natural Science Foundation of China (21571182), the National Key Research and Development Program of China (2017YFA0207102), the Science and Technology Commission of Beijing Municipality (Z151100003315018), and a Chinese Academy of Sciences Grant (CXJJ-14-M38).

References

1. E. H. Lee, M. B. Lewis, P. J. Blau and L. K. Mansur, *J. Mater. Res.*, 2011, **6**, 610–628.
2. H.-C. Yang, J. Luo, Y. Lv, P. Shen and Z.-K. Xu, *J. Membr. Sci.*, 2015, **483**, 42–59.
3. H.-C. Yang, J. Hou, V. Chen and Z.-K. Xu, *J. Mater. Chem. A*, 2016, **4**, 9716–9729.
4. C. Suryanarayana, *Prog. Mater. Sci.*, 2001, **46**, 1–184.
5. L.-S. Wan, Z.-M. Liu and Z.-K. Xu, *Soft Matter*, 2009, **5**, 1775–1785.

6. J. C. Hoogvliet, M. Dijksma, B. Kamp and W. P. van Bennekom, *Anal. Chem.*, 2000, **72**, 2016–2021.
7. M. Browne and P. J. Gregson, *Biomaterials*, 2000, **21**, 385–392.
8. L. Mazzola, E. Bemporad and F. Carassiti, *Appl. Surf. Sci.*, 2011, **257**, 2148–2158.
9. C. Cui, X. Cui, X. Li, K. Luo, J. Lu, X. Ren, J. Zhou, C. Fang, R. Farkouh and Y. Lu, *Int. J. Plast.*, 2018, **102**, 83–100.
10. S. V. Telrandhe, J. Bhagyaraj, S. Mishra and S. Karagadde, *J. Mater. Process. Technol.*, 2018, **262**, 492–502.
11. C. Dong, A. Wu, S. Hao, J. Zou, Z. Liu, P. Zhong, A. Zhang, T. Xu, J. Chen, J. Xu, Q. Liu and Z. Zhou, *Surf. Coat. Technol.*, 2003, **163–164**, 620–624.
12. J. P. Singh, W. C. Lim, J. Lee, J. Song, I.-J. Lee and K. H. Chae, *Appl. Surf. Sci.*, 2018, **432**, 132–139.
13. H. M. Meyer, A. S. Sabau and C. Daniel, *Appl. Surf. Sci.*, 2019, **489**, 893–904.
14. A. Yourdkhani, D. Caruntu, M. Vopson and G. Caruntu, *CrystEngComm*, 2017, **19**, 2079–2088.
15. Y.-S. Park, G. Kim and J. S. Lee, *Langmuir*, 2019, **35**, 12656–12664.
16. S. Shahidi, B. Moazzenchi and M. Ghoranneviss, *Eur. Phys. J. Appl. Phys.*, 2015, **71**, 31302.
17. U. Schulz, B. Saruhan, K. Fritscher and C. Leyens, *Int. J. Appl. Ceram. Technol.*, 2004, **1**, 302–315.
18. J. Singh and D. E. Wolfe, *J. Mater. Sci.*, 2005, **40**, 1–26.
19. A. Baptista, F. Silva, J. Porteiro, J. Miguez and G. Pinto, *Coatings*, 2018, **8**, 402.
20. Q. M. Mehran, M. A. Fazal, A. R. Bushroa and S. Rubaiee, *Crit. Rev. Solid State Mater. Sci.*, 2018, **43**, 158–175.
21. K. L. Choy, *Prog. Mater. Sci.*, 2003, **48**, 57–170.
22. N. Jin, Y. Q. Yang, X. Luo and Z. H. Xia, *Prog. Mater. Sci.*, 2013, **58**, 1490–1533.
23. N. Bahlawane and D. Lenoble, *Chem. Vap. Deposition*, 2014, **20**, 299–311.
24. A. Kafizas, C. J. Carmalt and I. P. Parkin, *Coord. Chem. Rev.*, 2013, **257**, 2073–2119.
25. X. D. Chen, Z. L. Chen, J. Y. Sun, Y. F. Zhang and Z. F. Liu, *Acta Phys.-Chim. Sin.*, 2016, **32**, 14–27.
26. A. Asatekin, M. C. Barr, S. H. Baxamusa, K. K. S. Lau, W. Tenhaeff, J. J. Xu and K. K. Gleason, *Mater. Today*, 2010, **13**, 26–33.
27. L. Gomez De Arco, Y. Zhang, C. W. Schlenker, K. Ryu, M. E. Thompson and C. Zhou, *ACS Nano*, 2010, **4**, 2865–2873.
28. P. Dutta, M. Rathi, D. Khatiwada, S. Sun, Y. Yao, B. Yu, S. Reed, M. Kacharia, J. Martinez, A. P. Litvinchuk, Z. Pasala, S. Pouladi, B. Eslami, J. H. Ryou, H. Ghasemi, P. Ahrenkiel, S. Hubbard and V. Selvamanickam, *Energy Environ. Sci.*, 2019, **12**, 756–766.
29. Y. Huang, X. Dong, Y. Shi, C. M. Li, L.-J. Li and P. Chen, *Nanoscale*, 2010, **2**, 1485–1488.

30. N. F. Santos, S. O. Pereira, A. J. S. Fernandes, T. L. Vasconcelos, C. M. Fung, B. S. Archanjo, C. A. Achete, S. R. Teixeira, R. F. Silva and F. M. Costa, *ACS Appl. Mater. Interfaces*, 2019, **11**, 8470–8482.
31. N. Chen, D. H. Kim, P. Kovacik, H. Sojoudi, M. H. Wang and K. K. Gleason, in *Annual Review of Chemical and Biomolecular Engineering*, ed. J. M. Prausnitz, 2016, vol. 7, pp. 373–393.
32. M. C. Vasudev, K. D. Anderson, T. J. Bunning, V. V. Tsukruk and R. R. Naik, *ACS Appl. Mater. Interfaces*, 2013, **5**, 3983–3994.
33. C. Thurier and P. Doppelt, *Coord. Chem. Rev.*, 2008, **252**, 155–169.
34. X. H. Hou and K. L. Choy, *Chem. Vap. Deposition*, 2006, **12**, 583–596.
35. R. Yang, J. Xu, G. Ozaydin-Ince, S. Y. Wong and K. K. Gleason, *Chem. Mater.*, 2011, **23**, 1263–1272.
36. A. M. Coclite, *Surf. Innovations*, 2013, **1**, 6–14.
37. C. Drosos and D. Vernardou, *Sol. Energy Mater. Sol. Cells*, 2015, **140**, 1–8.
38. Y. J. Shi, *Acc. Chem. Res.*, 2015, **48**, 163–173.
39. T. Goto, *J. Wuhan Univ. Technol.*, 2016, **31**, 1–5.
40. A. Walkiewicz-Pietrzykowska, P. Uznanski and A. M. Wrobel, *Curr. Org. Chem.*, 2017, **21**, 2229–2239.
41. B. S. Lim, A. Rahtu and R. G. Gordon, *Nat. Mater.*, 2003, **2**, 749–754.
42. L. Yao and J. He, *Prog. Mater. Sci.*, 2014, **61**, 94–143.
43. L. Li, Y. Bai, L. Li, S. Wang and T. Zhang, *Adv. Mater.*, 2017, **29**, 1702517.
44. P. Fauchais, M. Vardelle and S. Goutier, *Plasma Chem. Plasma Process.*, 2017, **37**, 601–626.
45. S. Pathak and G. C. Saha, *Coatings*, 2017, **7**, 122.
46. D. Tejero-Martin, M. R. Rad, A. McDonald and T. Hussain, *J. Therm. Spray Technol.*, 2019, **28**, 598–644.
47. Y. Kawahara, *J. Therm. Spray Technol.*, 2007, **16**, 202–213.
48. Y. Kawahara, *Coatings*, 2016, **6**, 34.
49. F. C. Krebs, *Sol. Energy Mater. Sol. Cells*, 2009, **93**, 394–412.
50. J. J. Richardson, M. Björnmalm and F. Caruso, *Science*, 2015, **348**, aaa2491.
51. Y. Li, X. Wang and J. Sun, *Chem. Soc. Rev.*, 2012, **41**, 5998–6009.
52. S. J. Pearton and D. P. Norton, *Plasma Processes Polym.*, 2005, **2**, 16–37.
53. J. J. Kelly and H. G. G. Philipsen, *Curr. Opin. Solid State Mater. Sci.*, 2005, **9**, 84–90.
54. D. B. Mawhinney, J. A. Glass and J. T. Yates, *J. Phys. Chem. B*, 1997, **101**, 1202–1206.
55. H. He, W. Cai, Y. Lin and Z. Dai, *Langmuir*, 2011, **27**, 1551–1555.
56. X. Xue, K. Zhou, J. Cai, Q. Wang and Z. Wang, *Microelectron. Eng.*, 2018, **191**, 1–9.
57. X. Ye, T. Shao, L. Sun, J. Wu, F. Wang, J. He, X. Jiang, W.-D. Wu and W. Zheng, *ACS Appl. Mater. Interfaces*, 2018, **10**, 13851–13859.
58. Y. Wang, X. Ye, B. Li, J. He and W. Zheng, *Langmuir*, 2019, **35**, 11351–11357.
59. T. Jiang, Z. Guo and W. Liu, *J. Mater. Chem. A*, 2015, **3**, 1811–1827.

60. A. M. Md Jani, D. Losic and N. H. Voelcker, *Prog. Mater. Sci.*, 2013, **58**, 636–704.
61. J.-T. Wu, S.-Y. Yang, W.-C. Deng and W.-Y. Chang, *Microelectron. Eng.*, 2010, **87**, 1951–1954.
62. C. Mu and J. He, *Mater. Lett.*, 2012, **70**, 101–104.
63. Y. Xie, D. Kocaefe, C. Chen and Y. Kocaefe, *J. Nanomater.*, 2016, **2016**, 11.
64. Y. Liu, J. Goebl and Y. Yin, *Chem. Soc. Rev.*, 2013, **42**, 2610–2653.
65. N. D. Petkovich and A. Stein, *Chem. Soc. Rev.*, 2013, **42**, 3721–3739.
66. Z. Geng and J. He, *J. Mater. Chem. A*, 2014, **2**, 16601–16607.
67. L. Yao, J. He, Z. Geng and T. Ren, *Nanoscale*, 2015, **7**, 13125–13134.
68. X. Du, Y. Xing, X. Li, H. Huang, Z. Geng, J. He, Y. Wen and X. Zhang, *RSC Adv.*, 2016, **6**, 7864–7871.
69. T. Li and J. He, *J. Mater. Chem. C*, 2016, **4**, 5342–5348.
70. T. Li and J. He, *Sol. Energy Mater. Sol. Cells*, 2017, **170**, 95–101.
71. B. Jin and J. He, *ACS Photonics*, 2017, **4**, 188–196.
72. K. Wang and J. He, *ACS Appl. Mater. Interfaces*, 2018, **10**, 11189–11196.
73. C. Yang, Y. Fang, K. Zhao, C. Li, X. Yang, H. Zhou, Y. Wang, Y. Zhu, H. Xu and Y. Liu, *J. Macromol. Sci., Part B: Phys.*, 2015, **54**, 907–926.
74. G. R. Guillen, Y. Pan, M. Li and E. M. V. Hoek, *Ind. Eng. Chem. Res.*, 2011, **50**, 3798–3817.
75. L. Wu, L. Wang, Z. Guo, J. Luo, H. Xue and J. Gao, *ACS Appl. Mater. Interfaces*, 2019, **11**, 34338–34347.
76. N. Zhao, Q. Xie, L. Weng, S. Wang, X. Zhang and J. Xu, *Macromolecules*, 2005, **38**, 8996–8999.
77. V. P. Khare, A. R. Greenberg and W. B. Krantz, *J. Membr. Sci.*, 2005, **258**, 140–156.
78. P. van de Witte, P. J. Dijkstra, J. W. A. van den Berg and J. Feijen, *J. Membr. Sci.*, 1996, **117**, 1–31.
79. M. B. Kannan, R. Walter, A. Yamamoto, H. Khakbaz and C. Blawert, *RSC Adv.*, 2018, **8**, 29189–29200.
80. A. Gao, R. Hang, L. Bai, B. Tang and P. K. Chu, *Electrochim. Acta*, 2018, **271**, 699–718.
81. E. Vazirinasab, R. Jafari and G. Momen, *Surf. Coat. Technol.*, 2018, **341**, 40–56.
82. Z. Geng and J. He, *J. Mater. Chem. A*, 2014, **2**, 16601–16607.
83. T. Ren, Z. Geng, J. He, X. Zhang and J. He, *J. Colloid Interface Sci.*, 2017, **486**, 1–7.
84. X. Zhang, A. Fujishima, M. Jin, A. V. Emeline and T. Murakami, *J. Phys. Chem. B*, 2006, **110**, 25142–25148.
85. J. Sun, C. Zhang, C. Zhang, R. Ding and Y. Xu, *RSC Adv.*, 2014, **4**, 50873–50881.
86. H. Jiang, W. Zhao, C. Li and Y. Wang, *Soft Matter*, 2011, **7**, 2817–2824.
87. J. Yun, T.-S. Bae, J.-D. Kwon, S. Lee and G.-H. Lee, *Nanoscale*, 2012, **4**, 7221–7230.
88. S. W. Cui, Y. B. Zheng, J. Liang and D. A. Wang, *Chem. Sci.*, 2016, **7**, 6477–6483.

89. S. L. Li and J. Zhao, *Appl. Mech. Mater.*, 2014, **556–562**, 973–976.
90. S. Shanmugam, K. Ravichandran, T. S. N. Sankara Narayanan and M. H. Lee, *RSC Adv.*, 2015, **5**, 988–1008.
91. Y. J. Wu, X. B. Chen, G. Williams, J. R. Scully, T. Gengenbach and N. Birbilis, *RSC Adv.*, 2016, **6**, 43408–43417.
92. J. T. Simpson, S. R. Hunter and T. Aytug, *Rep. Prog. Phys.*, 2015, **78**, 086501.
93. S. Das, S. Kumar, S. K. Samal, S. Mohanty and S. K. Nayak, *Ind. Eng. Chem. Res.*, 2018, **57**, 2727–2745.
94. X. Jing and Z. Guo, *J. Mater. Chem. A*, 2018, **6**, 16731–16768.
95. T. Ishizaki, J. Hieda, N. Saito, N. Saito and O. Takai, *Electrochim. Acta*, 2010, **55**, 7094–7101.
96. F. Xiao, S. Yuan, B. Liang, G. Li, S. O. Pehkonen and T. Zhang, *J. Mater. Chem. A*, 2015, **3**, 4374–4388.
97. A. Fujishima, X. Zhang and D. A. Tryk, *Surf. Sci. Rep.*, 2008, **63**, 515–582.
98. R. Wang, H. Tan, Z. Zhao, G. Zhang, L. Song, W. Dong and Z. Sun, *J. Mater. Chem. A*, 2014, **2**, 7313–7318.
99. T. Ren and J. He, *ACS Appl. Mater. Interfaces*, 2017, **9**, 34367–34376.
100. Y. Li, H. Shao, P. Lv, C. Tang, Z. He, Y. Zhou, M. Shuai, J. Mei and W.-M. Lau, *Chem. Eng. J.*, 2018, **338**, 440–449.
101. K. Feng, G.-Y. Hung, J. Liu, M. Li, C. Zhou and M. Liu, *Chem. Eng. J.*, 2018, **331**, 744–754.
102. Y. Gao, H. Luo, Z. Zhang, L. Kang, Z. Chen, J. Du, M. Kanehira and C. Cao, *Nano Energy*, 2012, **1**, 221–246.
103. Y. Wang, E. L. Runnerstrom and D. J. Milliron, *Annu. Rev. Chem. Biomol. Eng.*, 2016, **7**, 283–304.
104. Y. Xu, W. Huang, Q. Shi, Y. Zhang, L. Song and Y. Zhang, *J. Sol-Gel Sci. Technol.*, 2012, **64**, 493–499.
105. J. Du, Y. Gao, Z. Chen, L. Kang, Z. Zhang and H. Luo, *Sol. Energy Mater. Sol. Cells*, 2013, **110**, 1–7.
106. M. Kamalisarvestani, R. Saidur, S. Mekhilef and F. S. Javadi, *Renewable Sustainable Energy Rev.*, 2013, **26**, 353–364.
107. Z. Qu, L. Yao, Y. Zhang, B. Jin, J. He and J. Mi, *Mater. Res. Bull.*, 2019, **109**, 195–212.
108. L. Yao, Z. Qu, Z. Pang, J. Li, S. Tang, J. He and L. Feng, *Small*, 2018, **14**, 1801661.
109. L. Yao, Z. Qu, R. Sun, Z. Pang, Y. Wang, B. Jin and J. He, *ACS Appl. Energy Mater.*, 2019, **2**, 7467–7473.
110. S. Long, X. Cao, R. Huang, F. Xu, N. Li, A. Huang, G. Sun, S. Bao, H. Luo and P. Jin, *ACS Appl. Mater. Interfaces*, 2019, **11**, 22692–22702.
111. G. Hong, C. Li and L. Qi, *Adv. Funct. Mater.*, 2010, **20**, 3774–3783.
112. L.-P. Xu, Y. Chen, G. Yang, W. Shi, B. Dai, G. Li, Y. Cao, Y. Wen, X. Zhang and S. Wang, *Adv. Mater.*, 2015, **27**, 6878–6884.
113. J. Zhang, X. Li, J.-C. Zhang, J.-S. Yan, H. Zhu, J.-J. Liu, R. Li, S. Ramakrishna and Y.-Z. Long, *Chem. Eng. J.*, 2020, **382**, 122779.

114. Y. Zhang, T. Ren, T. Li, J. He and D. Fang, *Adv. Mater. Interfaces*, 2016, **3**, 1600672.
115. B. Jin, J. He, J. Li and Y. Zhang, *Adv. Opt. Mater.*, 2018, **6**, 1800056.
116. H. Bai, L. Wang, J. Ju, R. Sun, Y. Zheng and L. Jiang, *Adv. Mater.*, 2014, **26**, 5025–5030.
117. Y. Xing, W. Shang, Q. Wang, S. Feng, Y. Hou and Y. Zheng, *ACS Appl. Mater. Interfaces*, 2019, **11**, 10951–10958.

CHAPTER 6

Nanostructured Biocompatible Materials

V. KARTHICK*[a] AND KATSUHIKO ARIGA*[b,c]

[a]Centre for Ocean Research (DST-FIST Sponsored Centre), Sathyabama Institute of Science and Technology, Jeppiaar Nagar, Rajiv Gandhi Salai, Chennai – 600119, India; [b]International Center for Materials Nanoarchitectonics (MANA), National Institute for Materials Science (NIMS), Tsukuba, Ibaraki 305-0044, Japan; [c]Graduate School of Frontier Sciences, The University of Tokyo, Kashiwa, Chiba 277-8561, Japan
*E-mail: vkarthick.cor@sathyabama.ac.in, ARIGA.katsuhiko@nims.go.jp

6.1 Introduction

Biomaterials are of widespread interest as their relevance in improving clinical research is immense. The current challenge remains in developing biocompatible materials for improving the quality and efficiency of therapies. Materials science and bioengineering have combined to offer various approaches and nanostructured biomaterials play a huge role in the emergence of tissue engineering, regenerative medicine, and therapies. Biomaterials have helped in prolonging patients' health and relieving suffering in clinical settings. They also serve as an excellent tool for doctors, biomedical researchers, and scientists. Nanostructured biomaterials intended for human applications when implanted undergo cellular responses and the tolerable materials are often considered biocompatible materials. An ideal biocompatible material will have very little *in vivo* toxicity, minimal inflammatory response, site-specificity, cell support, and fewer graft rejections.

Nanoscience & Nanotechnology Series No. 55
Concepts and Design of Materials Nanoarchitectonics
Edited by Omar Azzaroni and Katsuhiko Ariga

Published by the Royal Society of Chemistry, www.rsc.org

Biocompatibility is defined as the ability of the material or device to perform a set of specific functions with appropriate host response and evaluation of adverse alterations in homeostatic conditions that determine the response. Simply put, it is the evaluation of the biological response to the material studied to check whether that material works as intended and presents no significant side effects to the patients or study organism. The ability to tune the size, shape and structure of materials led to the concept of nanoarchitectonics, where self-assembly is an important component.[1] In this chapter, we will discuss some of the nanostructured materials that have improved the efficiency of biomaterials in the field of medicine.

6.2 DNA Nanostructures

DNA nano constructs have amazing properties; based on the molecular conformations, and use of external triggers, they can be a potential game-changer in the field of drug delivery and imaging. Predictable base pairing, programmability, and size make them an excellent choice over other nanosystems. Live imaging is feasible for a broad range of cell types considering its exclusivity on interaction with biomolecules. They also have diverse sensing properties which can sense a range of analytes as well. DNA motifs such as aptamers are deployed for imaging analytes in living systems such as quantum dots, small interfering RNA, and other agents (Figure 6.1). More so, DNA based structures are assembled precisely to meet the precise function as they are homogenous by design and offer solutions with single-nucleotide resolution.[2] Tailoring the DNA as tetrahedron, icosahedron or polyhedron are some of the effective nanomachines created using canonical Watson–Crick base pairing. For instance, DNA tetrahedra can be reversed precisely in response to a specific signal. The added advantage is that they are synthesized rapidly for greater stability by controlling their asymmetric three-dimensional architecture. A variety of structures can be tailored using DNA, namely DNA origami, multi-arm junction, double crossover, and complex designs such as ss bricks, square lattice bundles, honeycomb and multistranded motifs, all considered 3D nanostructures.[3] Scaffolded DNA origami is a method by which long-stranded DNA is folded into precise shapes using several short-stranded

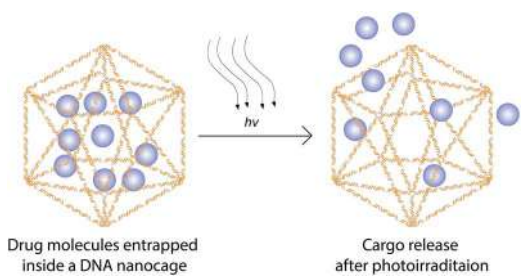

Figure 6.1 DNA nanostructures to deliver cargo (drug or fluorescence dyes) by photoirradiation.

DNA (called staple strands). The staple strands bind specifically to the long-stranded DNA and help in folding thereby giving stability to the overall structure. The branched junctions between double helices along with cytosine rich regions play a crucial role in the development of complex DNA nanomachines. Cytosine rich regions in oligonucleotides under acidic conditions form i-tetraplex structures which consist of intercalated double base-paired parallel-stranded duplexes in a relatively antiparallel orientation.[4] In another technique, an inorganic core (say, gold) is used as a template to immobilize oligonucleotides to form supramolecular structures. To form a more orderly structure, the core is usually tagged with a thiol moiety which will orient the oligonucleotides. In a typical DNA nanocage, conformational stability is offered by the single-stranded thymidine linkers by stacking hydrogen bonds between the bases. Supramolecular chemistry of nucleic acids, mainly DNA and its components, are used for target guided synthesis to achieve complex assembly.[5] Understanding the stability and lifetime of nanostructures is essential as unmodified oligonucleotides are often degraded by nucleases. In general, DNA nanomachines can withstand around 40 hours and DNA origami nanostructures are well known for maintaining their structural integrity in cellular conditions. When these structures are used as a carrier, the host system recognizes them as a foreign body and tries to eliminate them with the help of the immune system. Hence, researchers explored various measures to help protect these structures, which include lipid coatings, covalent linking of base pairs, chemical modification and covalently linking base pairs. The ability of DNA based carriers in internalization *via* various pathways is interesting and this is used for the diagnosis of certain disease types.[5] Yamuna and co-workers have developed a system in living systems that can be triggered with protons to act as a pH sensor based on the fluorescence resonance energy transfer (FRET) technique (Figure 6.2). They studied how low and high FRET can make an effective tool as a switch to map spatial

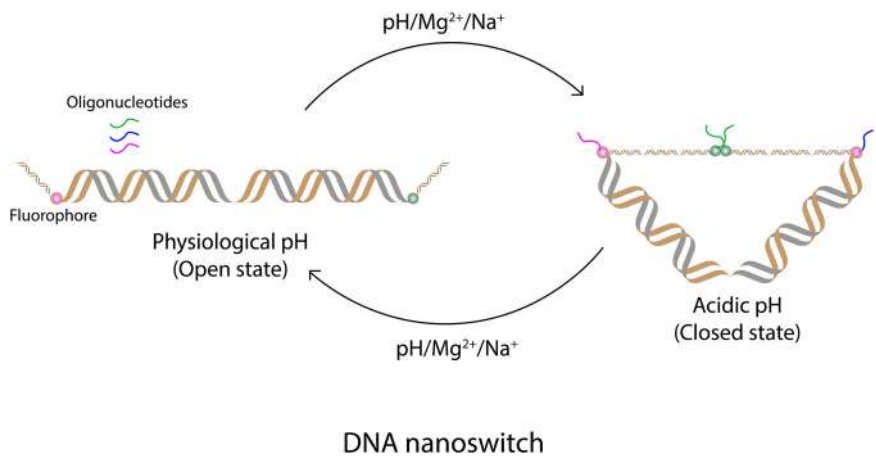

Figure 6.2 Mechanism on how low and high FRET could cause a conformational change in open and closed state DNA structures.

and temporal changes in living cells.[6] Deepanjan Panda and co-workers have developed target guided synthesis using a DNA nano template promoting Huisgen cycloaddition to selectively assemble a G-quadruplex binding c-MYC inhibitor and control duplex system.[7] Vindigni and co-workers have constructed a DNA octahedral cage for its selective interaction with the help of "oxidized low-density lipoprotein receptor-1", a scavenger associated with cardiovascular disease. The truncated octahedral DNA nanocage was tagged with biotin to observe the internalization *via* biotin-streptavidin assay. They found that the DNA nanocages were internalized at a higher range in oxidized low-density lipoprotein receptor-1 cells than the normal cells indicating its specificity.[8] Xiu Han and collaborators have developed a self-assembled system to encapsulate doxorubicin in a tetrahedral multivalent DNA nanocage by modifying mucin 1 aptamers. They found that the uptake of nanocages inside tumor cells was high and directly proportional to the number of modified mucin 1 aptamers in the nanocage.[9] DNA based nanostructures are also used in tumor specific immune responses for cancer therapy. Recently, Shaoli Liu and co-workers have developed a DNA nanodevice containing molecular adjuvants and antigenic peptides on tubular DNA nanostructures. Peptides containing propargylglycine at the C terminus were attached to azide-modified oligonucleotides *via* click chemistry. The conjugates were then assembled as origami by DNA hybridization along with switchable fluorescent beacons for quantification. They found that the built DNA nanodevice vaccines could be able to precisely assemble antigens and adjuvants for controlled immunogenicity for tumor inhibition and regression.[10] Similarly, a proton-driven nanotransformer-based vaccine, containing polymer and peptide was used to induce immune response for cancer therapy. The DNA vaccine undergoes structural transformation at various pH conditions, and this was utilized for the delivery of antigenic peptides to the cytoplasm by disrupting the endosomal membrane. It was found that the nanotransformer-based vaccine delivered antigenic peptide to lymph nodes that elicited cytotoxic lymphocyte response.[11] In another interesting study, Elena Ambrosetti and collaborators used DNA-nanoassemblies to map membrane protein nanoenvironments using the concept, nanoscale deciphering of membrane protein nanodomains.[12] These studies suggest that DNA based nanostructures plays a multifaceted role in biomedical applications.

6.3 Biodegradable Polymers

Biodegradable polymers have evolved into an important tool for biomedical scientists due to their biocompatibility with tissue types and targeting. Modern innovations like nanoarchitectonics help in achieving different shapes, including fibers, spheres, scaffolds, composites and so on. Specifically, poly(lactic-*co*-glycolic acid) (PLGA) is known for its tunable mechanical properties, pharmacokinetics and biodegradable nature. In this section, we will focus our review on the recent advancements in the use of PLGA as

a powerful biomaterial and its role in the field of nanomedicine. Based on the cargo, PLGA is prepared conveniently using emulsion techniques (single/double emulsion) or spun into various sizes. PLGA based nanoparticles are often functionalized with a variety of ligands or small molecules such as proteins, short peptides, and nucleic acids. An added advantage of PLGA is that it can be modified to transform its properties in response to extracellular, intracellular, or external stimuli. For better functionalization, PLGA is often PEGylated to increase the hydrophilic nature. Carbodiimide-assisted coupling, thiol–maleimide coupling, copper-catalyzed azide–alkyne cycloaddition and biotin/avidin ligation are some of the common ways to achieve functionalization.[13] In tissue engineering, scaffold architecture is pivotal for the comfortable growth of cells (Figure 6.3). Sacrificial templates are often used to achieve such supramolecular structures. To prevent necrotic core formation within a scaffold/hydrogel, researchers look for materials with perfusion networks for the long-term growth of cells.[14] Although the current review is focused on nanostructured biomaterials, it is imperative to see what happens when foreign material is implanted into our system. Hence, we also look at the first line of defence and adaptations made by cells. Whenever an implant is placed, the immediate reaction would be an inflammatory response, which is seen evident with elevated levels of interleukins, the tumor necrosis factor, interferons, *etc.* (Figure 6.4). S. Rahima Benhabbour *et al.* have developed a tunable biodegradable structure for the controlled release of multiple drugs by combining PLGA, water-miscible solvent and antiviral compounds. *In vitro* and *in vivo* pharmacokinetics showed sustained plasma concentrations with very little inflammation.[15] The use of PLGA in the field of cancer research is immense and several studies have shown that it can be a crucial biomaterial. In a recent study, Asmita Banstola and collaborators designed panitumumab-conjugated and temozolomide-loaded PLGA based nanoparticles for enhancing cellular uptake. They found that the cytotoxic effect of the conjugate depends on cellular models where the epidermal

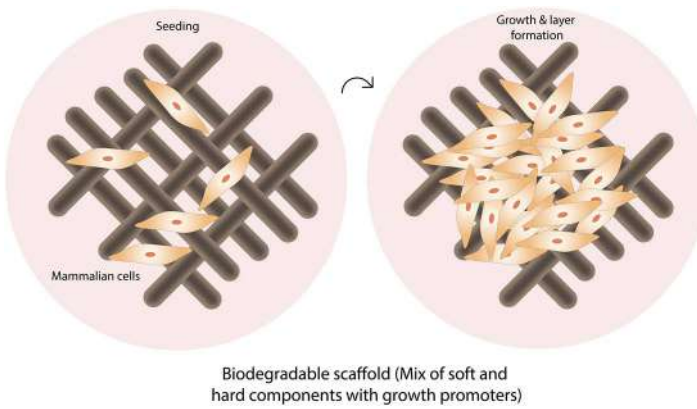

Figure 6.3 Biodegradable scaffold for cell proliferation and differentiation.

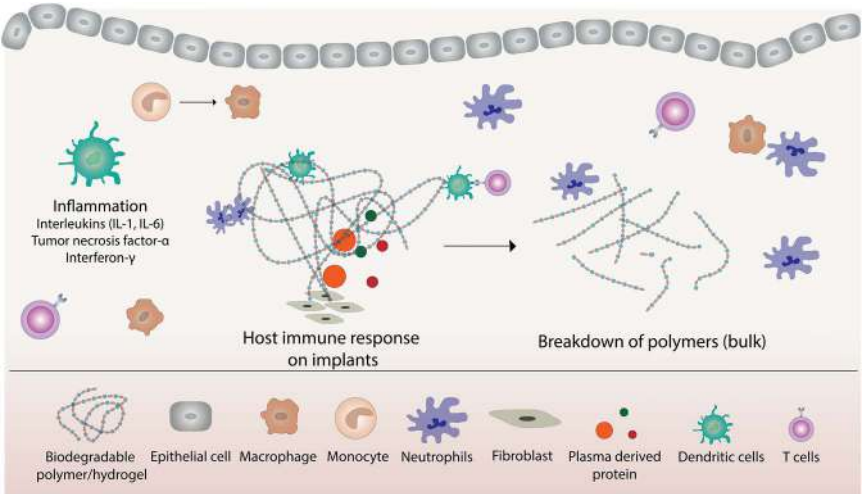

Figure 6.4 Defense mechanism to eliminate foreign substances by host immune system. Macrophages and other cells are recruited at the site inducing a cascade of inflammatory response.

growth factor receptor is high. The authors believed that the mode of action of the conjugate could be by the autophagy pathway as elevated levels of autophagy markers were observed.[16] Controlled release of nitric oxide is the biggest challenge in therapies as they have a very short lifetime and the diffusion radius is less. Hence, researchers are finding ways to prolong the release of nitric oxide using various biobased systems. To achieve that, Yoogyeong Oh and co-workers have created a PLGA based nitric oxide delivery system using branched polyethylenimine diazeniumdiolate and a pH-responsive nitric oxide donor. They found that the system can sustainably release nitric oxide to regulate the inflammatory response in *in vitro* conditions.[17]

6.4 Gold Nanoparticles (AuNPs)

Metal nanoparticles have been used for centuries, but recent studies have started to unravel the vast potential in frontiers of medicine. Particularly, AuNPs are identified as a key material and are widely used for biological applications. Several studies have shown its effective utilization as a drug carrier and in imaging and theranostics owing to its fascinating optical properties. When AuNPs are excited by light at a particular wavelength, the interaction between the electromagnetic field and the conduction electrons cause the electrons to oscillate (Figure 6.5), termed Surface Plasmon Resonance (SPR).[18] To deliver the drugs to specific cell/tissue types, carriers such as metal nanoparticles were tagged with a special type of ligand/molecules that recognize target cells. The binding is established by affinity/weak forces like van der Waal's interactions, *e.g.*, the interaction of nanomaterials

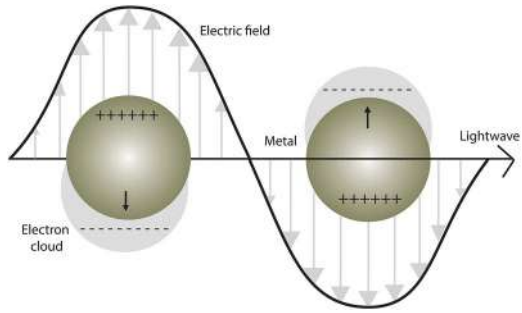

Figure 6.5 Collective oscillation of free electrons cause localized surface plasmon resonance (SPR), a unique characteristic of noble metal nanomaterials.

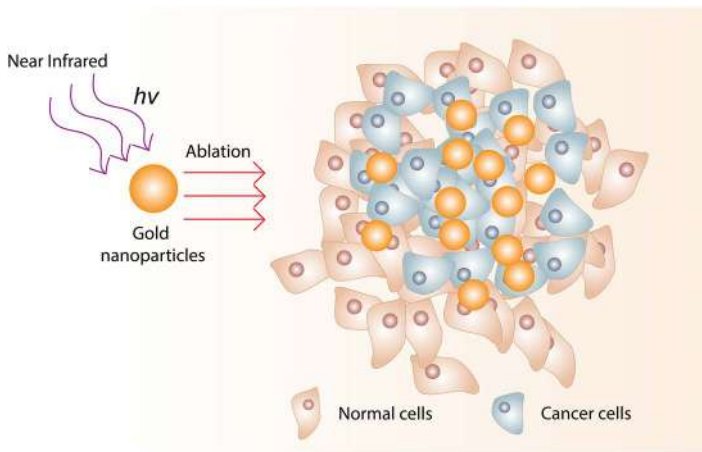

Figure 6.6 Photoirradiation of AuNPs cause ablation and destroys cells knows as plasmonic photothermal therapy (PPTT).

with thiol molecules. They can identify receptors and interact with them to deliver cargo, *i.e.*, anticancer drugs to the cancer microenvironment. This phenomenon is crucial for studies like imaging and the detection of molecules like proteins, drugs, small peptides, and nucleic acids. Mounting evidence indicates that engineering the surface of particles to attach a ligand can effectively deliver drugs to a specific site with sustained release.[5] The functionalization of metal nanoparticles say AuNPs, can be paramount when it comes to drug targeting and bioimaging. In general, AuNPs are tagged with a ligand molecule by means of affinity/binding (thiol group) which can be used to estimate the analyte. Plasmonic Photothermal Therapy (PPTT) is an approach by which AuNPs are injected into the system thereby accumulating them near the cancer environment and they destroy cancer cells by generating heat upon excitation by a laser source (Figure 6.6). In a recent study,

pifithrin-μ, a heat shock protein A5 inhibitor has been tagged to AuNPs along with polydopamine to maintain cancer homeostasis in the cellular microenvironment. The results suggest that the conjugate can effectively activate pro-apoptotic unfolded protein response cascades for enhanced radiotherapy and PPTT.[19] AuNPs can deliver anticancer drugs by establishing a binding/affinity using thiol moieties, the most common approach used by researchers. The process requires surface functionalization to attach to the cell surface *via* receptors. Mostafa A. El Sayed and team have developed AuNPs of various shapes and tagged them with short peptides which can target αβ integrins on the cell membrane of the cancer cells. The conjugate was tested on human oral squamous cell carcinoma 3 and human keratinocyte cancer cells, and they found that the uptake of AuNPs was achieved by receptor-mediated endocytosis for effective PPTT against tumors.[20] Arg-Gly-Asp (RGD) is an integrin-binding site in adhesive protein necessary for cell adhesion. In a study, AuNPs were coupled with RGD to create a nanoscale anisotropic presentation of cell-adhesive peptides for cell adhesion. The conjugates were able to promote cell spreading, basal cytoskeletal structural alignment and nanopodia attachment. In addition, β1 and β3 class integrins were recruited at the site in regulating the development of focal adhesion towards fibrillar adhesion.[21] These approaches denote the various role played by AuNPs in biomedical applications and it is noteworthy to say that AuNPs are the most explored metal nanoparticle system that offers great biocompatibility and desired results.

6.5 Dendrimers Nanosystems

Latest advancements like layer-by-layer, self-assembly, nanofabrication, 3D bioprinting, bioink are some of the breakthroughs seen recently.[22] Self-assembly is a facile technique to achieve complex 3D architectures by the development of multiple non-covalent interactions to form supramolecular structures such as dendritic nanosystems. Specifically, intra- and intermolecular interactions between cargo and the carrier form polyplexes and spontaneous micelles. Though the non-covalent bonds may seem to offer slight strength, collectively they can form forces strong enough to stabilize a supramolecular structure. From a biological perspective, it is pivotal to have a stable structure to perform a specific function. During equilibrium, disassembled and self-assembled states occur as a function of change of thermal and chemical conditions. Self-assembled dendrimer nanomiscelles are known for their profound drug loading capacity and fabrication approaches (Figure 6.7). They can act as biomimetic artificial proteins, nanoscale containers, for gene transfection, drug delivery agents, imaging agents and nanoscaffolds.[23] Donald A. Tomalia and Ling Peng have done pioneering works in the field of self-assembled dendrimers.[23,24] Dendrimers like poly(amidoamine) (PAMAM) can effectively reach the tumor microenvironment and are able to deliver anticancer drugs like doxorubicin.[25] Likewise, hydrophilic PAMAM dendrimers were used for the delivery

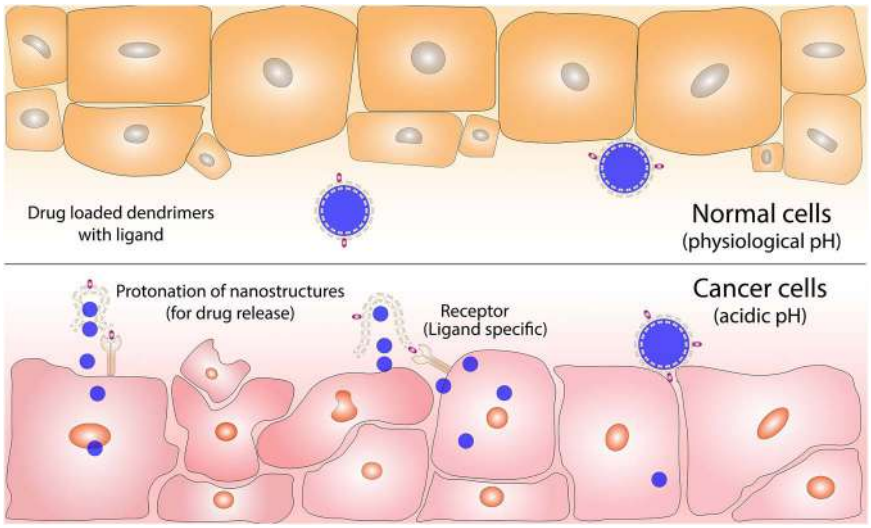

Figure 6.7 Dendrimers and their mode of release of cargo in the cancer microenvironment. Physiological and acidic pH affect the release of the drug, increases in hydrogen ion concentrations increase protonation and change the structural integrity of the whole assembly.

of small interfering RNAs (siRNAs) to achieve gene silencing in hematopoietic $CD34^{+}$ stem cells and heat shock protein 27 in prostate cancer xenografted nude mice model. These results suggest that PAMAM dendrimers are a versatile tool and have wide spectrum use in the delivery of small molecules.[26] Critical micelle concentration is an important aspect that controls the number of dendrimers in a dendrimiscelle conjugate. By maintaining the optimal conditions and electrostatic interactions, structural stability is maintained for the delivery of drugs. Tailoring hydrophilic and hydrophobic branched segments can yield various geometries of Janus dendrimers with astonishing fluorescent properties.[27] It is feasible to achieve monodisperse structures and the fluorescent nature of such dendrimersomes can be utilized for live-cell imaging. In this context, Shaodong Zhang and co-workers have developed onion-like vesicles by self-assembly of six single–single amphiphilic Janus minidendrimers. An increase in the concentration of Janus dendrimers resulted in the formation of double-bilayer vesicle to multibilayer onion-like vesicles.[28] The application of dendrimers is not limited to the delivery of drug molecules and imaging. A recent study was evaluated to assess the use of PAMAM dendrimers in CRISPR-Cas genome editing, a cutting-edge technology that won The Nobel Prize in Chemistry 2020. A generation 5 amine-terminated PAMAM dendrimer with 4-(bromomethyl)phenyl-boronic acid was used to deliver *Streptococcus pyogenes* Cas9 ribonucleoprotein for CRISPR-Cas based genome editing.[29] The delivery of siRNA into a cell system for gene silencing was conceptual until Ling Peng and co-workers developed a dendrimer-based nanostructure to

deliver siRNA. They used a hydrophilic PAMAM dendron head and a hydrophobic part containing variable-length linear hydrocarbon chains against a prostate cancer bearing animal model.[30] To create a more robust dendrimer system, amphiphilic dendrimer along with phospholipids can also be used. In another study interesting study, the same group used a dendrimer system by combining an amphiphilic dendrimer with oligo (glutamic acid) E_{16}, oligo(glycine) G_6, RGDK Warhead combined complex. They believed that the dendrimer system will be able to deliver siRNA to the cancer cells by binding with integrin and the neuropilin-1 receptors.[31]

6.6 Fullerene Nanostructures

Fullerenes are zero-dimensional structures that belong to a class of carbon. Through π-π stacking interactions of fullerene molecules, a variety of higher dimensional structures are prepared for enhanced optical, electrical, and magnetic properties.[32] These intriguing properties are very useful in the design and development of supramolecular fullerene nanostructures for potential applications in sensing devices, solar cells, superconductors and biomedical applications.[33] In this section, we focus on recent advances in the emergence of fullerenes as biocompatible material. Our group has extensively studied the use of fullerenes as functional scaffolds for the alignment and differentiation of various cell types (Figure 6.8). Fu-Yu Hsieh *et al.* have studied neural stem cells differentiation on highly aligned fullerene nanowhiskers. The alignment was performed at the air–water interface as opposed to Langmuir–Blodgett or vortex-aligned techniques.[34] Expression of neuronal markers such as nestin, b-tubulin, microtubule-associated protein 2, and glial fibrillary acidic protein revealed the maturation of neurons from stem cells.[35] These results are welcoming in tissue engineering as they can be used as potential scaffolds for the growth and differentiation

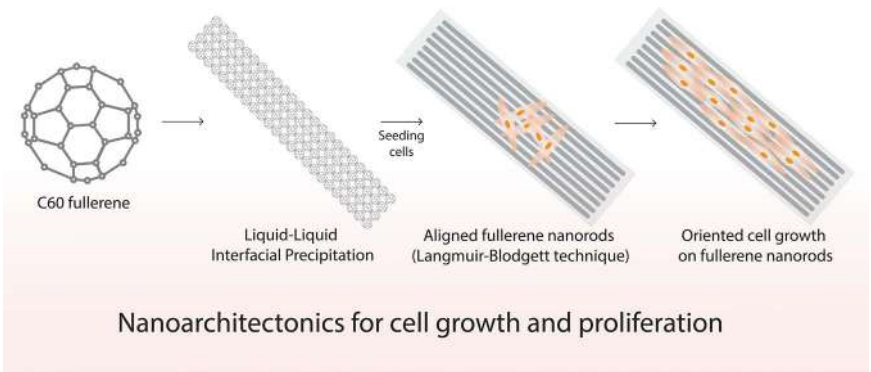

Figure 6.8 Oriented cell growth along the fullerene nanorods assembled using the Langmuir–Blodgett technique.

of sensitive cells such as neurons, cardiomyocytes, bone cells and so on. In another study, human osteosarcoma cells, MG-63 cells were cultured on vortex-flow-induced aligned C_{60} fullerene nanostructures. It was found that the cells adhere comfortably to the fullerene nanostructures and grow along the axis of the alignment of fullerene nanostructures.[36] Aligning of cells along a certain axis can be decisive for the mass culture of cells and artificial organ development as several other materials are also developed to achieve the same.[37] The retention of multipotency for a longer period remains a huge challenge for therapies that use mesenchymal stem cells. Very recently, Jingwen Song *et al.* have used aligned fullerene nanostructures for the long-term retention of self-renewal human mesenchymal stem cells. The self-renewal and multipotency of stem cells were evaluated by expressing specific markers such as octamer-binding transcription factor 4, SRY-box containing gene 2, and nanog homeobox. It was found that fullerene nanostructures helped in regulating the expression of these markers. Further, immunofluorescence imaging suggested that the fullerene nanostructures regulate stem cells behaviour that includes cell spreading, focal adhesion, cell cytoskeleton, and YAP translocation.[38] That no significant toxicity reported in these studies makes them a new class of biomaterial that needs attention in the field of biomedical engineering. These studies suggest that fullerene can be an alternative tool for the alignment and differentiation of cell types.

6.7 Hydroxyapatite

Hydroxyapatite (HAP) is a key mineral component of bones and helps in bone tissue regeneration. HAP possesses size- and shape-dependent physicochemical properties that are useful in the construction of useful bone-like material. The fabrication of HAP into various structures is applied to various fields like drug delivery, bioimaging and so on. The main direction of nanosized HAP is to promote osteoregeneration to improve bone strength and HAP is an excellent candidate that offers biocompatibility and osteoconductivity. Hiroki Tamagawa and co-workers have studied the effects of the addition of nano-hydroxyapatite to a collagen membrane recombinant human bone morphogenetic protein-2 on tissue formation and dentin resorption. They found that implanting the structure resulted in the formation of thin, cementum-like hard tissue on the dentin surface.[39] Bone is an interesting natural material with beautiful architecture. To mimic bone, an implant requires similar bone-like constituents and structure. Hong Jiang *et al.* have developed a scaffold made of nano-HAP/cellulose/chitosan with a spiral bone-like structure with similar structure and composition. After implantation, the authors observed that the newly formed bone tissue tended to grow in a longitudinal direction of the scaffold and formed a medullary cavity.[40] Hydrogels are another form of biomaterials that can fill places where irregularity is observed, bone for instance can make use of hydrogel for filling cracks or fractures. Combining biopolymers and HAP could also

serve as a potential coating for improving bone cell regeneration (Figure 6.9). Jazmín I. González Ocampo and co-workers have used carrageenan of the kappa family and mixed it with HAP to improve the osteoblast viability and adhesion of cells. Further, the material also enhanced the alkaline phosphatase levels and deposition of calcium in bones.[41] Zhaozhao Ding *et al.* have leveraged the use of injectable hydrogels made up of silk-HAP and used them for improving osteogenesis. They found that the prepared hydrogel offered good biocompatibility, mechanical strength and osteogenic differentiation capability.[42] The biggest challenge is to withhold the structure of the hydrogel when a higher percentage of HAP is used for making it. There is a threshold to the mix ratio as aggregation tend to occur when HAP content is higher. Our group developed a facile way to synthesize HAP plates using low molecular weight heparin. The prepared HAP plates were tested for their suitability as bone material using *in vitro* conditions by immersing it in simulated body fluid.[43] Dong Xu and co-workers have developed a micro/nano hierarchy and evaluated its efficiency in osteogenic differentiation. It was found that the HAP structures significantly upregulated the expression of the gene necessary for osteogenic differentiation *via* the extracellular-signal-regulated kinase/mitogen-activated protein kinase signaling pathway. The authors believed that the unique flake-like structure helps in the endocytosis with the adsorption of serum adhesion proteins.[44] Researchers find it very difficult to treat rotator cuff tears as the mobility of tendons in that region is limited. To overcome this problem, Yaying Sun *et al.* have

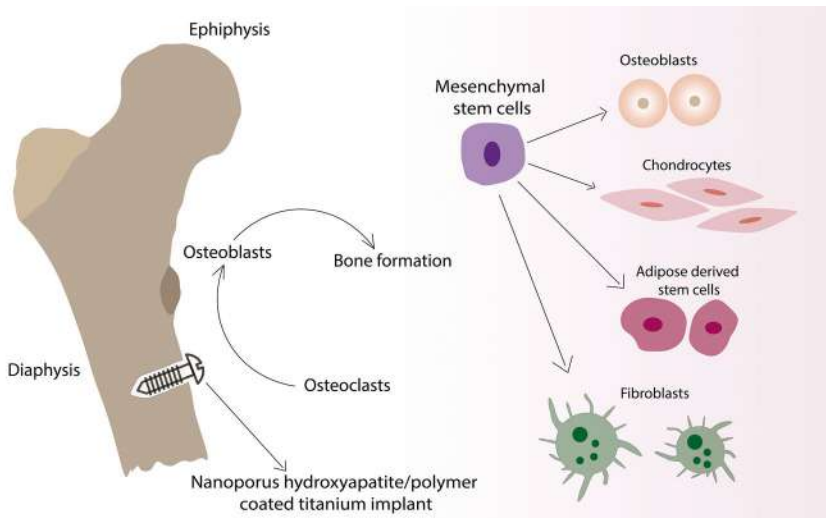

Figure 6.9 Hydroxyapatite coated titanium implant promotes osteogenic differentiation of bone cells and improved healing.

developed a nano-scaffold containing PLGA, type I collagen, polycaprolactone and nano-HAP. The authors used a combination of PLGA and PLGA/Collagen to connect the tendon stumps and a combination of polycaprolactone and polycaprolactone/nano-HAP was used as an insert in the bone tunnel of the infraspinatus tendon. They found that the fibroblast showed higher cell viability and collagen secretion whereas osteoblasts showed good mineralization. The overall mechanical strength of the bone was also found to be increased after the insertion of scaffold.[45] Postmenopausal osteoporosis is a condition that poses a serious threat to women which results in reduced bone mineral density and strength. To address this, Xian Liu and co-workers have developed a system involving HAP and osteoprotegerin gene-modified bone mesenchymal stem cells. When the modified HAP were introduced to an ovariectomized-induced osteoporotic animal model, they could observe the material enhances bone regeneration in critical-sized mandibular defects.[46] Similarly, regenerating enthesis is complicated due to the modular complexity of the tissue which is seen in between tendon and bone. Xiaoxi Li and co-workers have developed flexible bipolar nanofibrous membranes made of poly-L-lactic acid and nano-HAP to mimic non-mineralized fibrocartilage and mineralized fibrocartilage. They found that the membrane significantly increased the area of glycosaminoglycan staining at the tendon-bone interface and improved collagen organization in animal studies. The material also induces bone formation, fibrillogenesis and offered great mechanical strength to bone.[47]

6.8 Conclusion and Prospects

There has been tremendous growth in the field of nanobiomaterials, thanks to advanced studies involving *in vitro* and *in vivo* models. The growing need to develop nanoscale biomaterials for application-related aspects is well supported by engineerable materials, mainly nanoarchitectonics. Biocompatibility and structural conformation hold the key to promising biomaterials, which assist the growth of cells, destroying unwanted (cancer) cells and delivering cargo at specific sites. Realizing the characteristics of materials will help in the design and tailoring of nanostructured biomaterials. Recent advancements in nanostructured biomaterials discussed in this review will help researchers narrow down to suitable systems for their studies. The fate and long-term effects of such material are evenly poised as detailed *in vivo* studies can answer both.

Acknowledgements

V. Karthick would like to thank the Japan Society for the Promotion of Science (JSPS), Indian National Science Academy (INSA) and Department of Science and Technology (DST) for his research fellowship.

References

1. K. Ariga, M. Nishikawa, T. Mori, J. Takeya, L. K. Shrestha and J. P. Hill, Self-assembly as a key player for materials nanoarchitectonics, *Sci. Technol. Adv. Mater.*, 2019, **20**(1), 51–95.
2. A. T. Veetil, K. Chakraborty, K. Xiao, M. R. Minter, S. S. Sisodia and Y. Krishnan, Cell-targetable DNA nanocapsules for spatiotemporal release of caged bioactive small molecules, *Nat. Nanotechnol.*, 2017, **12**(12), 1183–1189.
3. Y. Wang, W. Ge, B. Lu, J.-J. Zhu and S.-J. Xiao, Two-layer stacked multi-arm junction tiles and nanostructures assembled with small circular DNA molecules serving as scaffolds, *Nanoscale*, 2020, **12**(38), 19597–19603.
4. K. Gehring, J.-L. Leroy and M. Guéron, A tetrameric DNA structure with protonated cytosine· cytosine base pairs, *Nature*, 1993, **363**, 561–565.
5. G. N. Pandian and H. Sugiyama, Nature-inspired design of smart biomaterials using the chemical biology of nucleic acids, *Bull. Chem. Soc. Jpn.*, 2016, **89**(8), 843–868.
6. S. Modi, M. G. Swetha, D. Goswami, G. D. Gupta, S. Mayor and Y. Krishnan, A DNA nanomachine that maps spatial and temporal pH changes inside living cells, *Nat. Nanotechnol.*, 2009, **4**(5), 325–330.
7. D. Panda, P. Saha, T. Das and J. Dash, Target guided synthesis using DNA nano-templates for selectively assembling a G-quadruplex binding c-MYC inhibitor, *Nat. Commun.*, 2017, **8**(May), 1–11.
8. G. Vindigni, S. Raniolo, A. Ottaviani, M. Falconi, O. Franch and B. R. Knudsen, *et al.*, Receptor-Mediated Entry of Pristine Octahedral DNA Nanocages in Mammalian Cells, *ACS Nano*, 2016, **10**(6), 5971–5979.
9. X. Han, Y. Jiang, S. Li, Y. Zhang, X. Ma and Z. Wu, *et al.*, Multivalent aptamer-modified tetrahedral DNA nanocage demonstrates high selectivity and safety for anti-tumor therapy, *Nanoscale*, 2019, **11**(1), 339–347.
10. S. Liu, Q. Jiang, X. Zhao, R. Zhao, Y. Wang and Y. Wang, *et al.*, A DNA nanodevice-based vaccine for cancer immunotherapy, *Nat. Mater.*, 2020, **20**, 421–430.
11. N. Gong, Y. Zhang, X. Teng, Y. Wang, S. Huo and G. Qing, *et al.*, Proton-driven transformable nanovaccine for cancer immunotherapy, *Nat. Nanotechnol.*, 2020, **15**, 1053–1064.
12. E. Ambrosetti, G. Bernardinelli, I. Hoffecker, L. Hartmanis, G. Kiriako and A. de Marco, *et al.*, A DNA-nanoassembly-based approach to map membrane protein nanoenvironments, *Nat. Nanotechnol.*, 2020, **16**, 85–95.
13. J. Nicolas, S. Mura, D. Brambilla, N. Mackiewicz and P. Couvreur, Design, functionalization strategies and biomedical applications of targeted biodegradable/biocompatible polymer-based nanocarriers for drug delivery, *Chem. Soc. Rev.*, 2013, **42**(3), 1147–1235.
14. J. S. Miller, K. R. Stevens, M. T. Yang, B. M. Baker, D. H. T. Nguyen and D. M. Cohen, *et al.*, Rapid casting of patterned vascular networks for perfusable engineered three-dimensional tissues, *Nat. Mater.*, 2012, **11**(9), 768–774.

15. S. R. Benhabbour, M. Kovarova, C. Jones, D. J. Copeland, R. Shrivastava and M. D. Swanson, *et al.*, Ultra-long-acting tunable biodegradable and removable controlled release implants for drug delivery, *Nat. Commun.*, 2019, **10**, 4324.
16. A. Banstola, R. Duwa, F. Emami, J. H. Jeong and S. Yook, Enhanced Caspase-Mediated Abrogation of Autophagy by Temozolomide-Loaded and Panitumumab-Conjugated Poly(lactic- co-glycolic acid) Nanoparticles in Epidermal Growth Factor Receptor Overexpressing Glioblastoma Cells, *Mol. Pharm.*, 2020, **17**(11), 4386–4400.
17. Y. Oh, H. Jeong, S. Lim and J. Hong, Controlled Nitric Oxide Release Using Poly(lactic-co-glycolic acid) Nanoparticles for Anti-Inflammatory Effects, *Biomacromolecules*, 2020, **21**(12), 4972–4979.
18. P. Mulvaney, Surface Plasmon Spectroscopy of Nanosized Metal Particles, *Langmuir*, 1996, **12**(3), 788–800.
19. H. Zhu, X. Cao, X. Cai, Y. Tian, D. Wang and J. Qi, *et al.*, Pifithrin-μ incorporated in gold nanoparticle amplifies pro-apoptotic unfolded protein response cascades to potentiate synergistic glioblastoma therapy, *Biomaterials*, 2020, **232**(December 2019), 119677.
20. S. R. Panikkanvalappil, N. Hooshmand and M. A. El-Sayed, Intracellular Assembly of Nuclear-Targeted Gold Nanosphere Enables Selective Plasmonic Photothermal Therapy of Cancer by Shifting Their Absorption Wavelength toward Near-Infrared Region, *Bioconjugate Chem.*, 2017, **28**(9), 2452–2460.
21. S. H. D. Wong, B. Yin, B. Yang, S. Lin, R. Li and Q. Feng, *et al.*, Anisotropic Nanoscale Presentation of Cell Adhesion Ligand Enhances the Recruitment of Diverse Integrins in Adhesion Structures and Mechanosensing-Dependent Differentiation of Stem Cells, *Adv. Funct. Mater.*, 2019, **29**(8), 1–12.
22. M. L. Cortez, A. Lorenzo, W. A. Marmisollé, C. Von Bilderling, E. Maza and L. Pietrasanta, *et al.*, Highly-organized stacked multilayers: *Via* layer-by-layer assembly of lipid-like surfactants and polyelectrolytes. Stratified supramolecular structures for (bio)electrochemical nanoarchitectonics, *Soft Matter*, 2018, **14**(10), 1939–1952.
23. S. Svenson and D. A. Tomalia, Dendrimers in biomedical applications-reflections on the field, *Adv. Drug Delivery Rev.*, 2012, **64**(SUPPL.), 102–115.
24. Z. Lyu, L. Ding, A. Tintaru and L. Peng, Self-Assembling Supramolecular Dendrimers For Biomedical Applications: Lessons Learned From Poly(Amidoamine) Dendrimers, *Acc. Chem. Res.*, 2020, **53**(12), 2936–2949.
25. T. Wei, C. Chen, J. Liu, C. Liu, P. Posocco and X. Liu, *et al.*, Anticancer drug nanomicelles formed by self-assembling amphiphilic dendrimer to combat cancer drug resistance, *Proc. Natl. Acad. Sci.*, 2015, **112**(10), 2978–2983.
26. C. Chen, P. Posocco, X. Liu, Q. Cheng, E. Laurini and J. Zhou, *et al.*, Mastering Dendrimer Self-Assembly for Efficient siRNA Delivery: From Conceptual Design to *In Vivo* Efficient Gene Silencing, *Small*, 2016, **12**(27), 3667–3676.

27. V. Percec, D. A. Wilson, P. Leowanawat, C. J. Wilson, A. D. Hughes and M. S. Kaucher, *et al.*, Self-Assembly of Janus Dendrimers into Uniform Dendrimersomes and Other Complex Architectures, *Science*, 2010, **328**(5981), 1009–1014.
28. S. Zhang, H.-J. Sun, A. D. Hughes, R.-O. Moussodia, A. Bertin and Y. Chen, *et al.*, Self-assembly of amphiphilic Janus dendrimers into uniform onion-like dendrimersomes with predictable size and number of bilayers, *Proc. Natl. Acad. Sci. U. S. A.*, 2014, **111**(25), 9058–9063.
29. C. Liu, T. Wan, H. Wang, S. Zhang, Y. Ping and Y. Cheng, A boronic acid–rich dendrimer with robust and unprecedented efficiency for cytosolic protein delivery and CRISPR-Cas9 gene editing, *Sci. Adv.*, 2019, **5**(6), 1–12.
30. C. Chen, P. Posocco, X. Liu, Q. Cheng, E. Laurini and J. Zhou, *et al.*, Mastering Dendrimer Self-Assembly for Efficient siRNA Delivery: From Conceptual Design to *In Vivo* Efficient Gene Silencing, *Small*, 2016, **12**(27), 3667–3676.
31. Y. Dong, T. Yu, L. Ding, E. Laurini, Y. Huang and M. Zhang, *et al.*, A Dual Targeting Dendrimer-Mediated siRNA Delivery System for Effective Gene Silencing in Cancer Therapy, *J. Am. Chem. Soc.*, 2018, **140**(47), 16264–16274.
32. Q. Tang, S. Maji, B. Jiang, J. Sun, W. Zhao and J. P. Hill, *et al.*, Manipulating the Structural Transformation of Fullerene Microtubes to Fullerene Microhorns Having Microscopic Recognition Properties, *ACS Nano*, 2019, **13**(12), 14005–14012.
33. G. S. Kumar, R. G. Shrestha, Q. Ji, J. P. Hill, K. Ariga and S. Acharya, *et al.*, Hierarchical heterostructure of Ag-nanoparticle decorated fullerene nanorods (Ag-FNRs) as an effective single particle freestanding SERS substrate, *Phys. Chem. Chem. Phys.*, 2018, **20**(27), 18873–18878.
34. K. Ariga, X. Jia, J. Song, J. P. Hill, D. T. Leong and Y. Jia, *et al.*, Nanoarchitectonics beyond Self-Assembly: Challenges to Create Bio-Like Hierarchic Organization, *Angew. Chem., Int. Ed.*, 2020, **59**(36), 15424–15446.
35. F. Y. Hsieh, L. K. Shrestha, K. Ariga and S. H. Hsu, Neural differentiation on aligned fullerene C60 nanowhiskers, *Chem. Commun.*, 2017, **53**(80), 11024–11027.
36. V. Krishnan, Y. Kasuya, Q. Ji, M. Sathish, L. K. Shrestha and S. Ishihara, *et al.*, Vortex-Aligned Fullerene Nanowhiskers as a Scaffold for Orienting Cell Growth, *ACS Appl. Mater. Interfaces*, 2015, **7**(28), 15667–15673.
37. N. E. Muzzio, M. A. Pasquale, W. A. Marmisollé, C. Von Bilderling, M. L. Cortez and L. I. Pietrasanta, *et al.*, Self-assembled phosphate-polyamine networks as biocompatible supramolecular platforms to modulate cell adhesion, *Biomater. Sci.*, 2018, **6**(8), 2230–2247.
38. J. Song, X. Jia, K. Minami, J. P. Hill, J. Nakanishi and L. K. Shrestha, *et al.*, Large-Area Aligned Fullerene Nanocrystal Scaffolds as Culture Substrates for Enhancing Mesenchymal Stem Cell Self-Renewal and Multipotency, *ACS Appl. Nano Mater.*, 2020, **3**(7), 6497–6506.

39. H. Tamagawa, T. Tenkumo, T. Sugaya and M. Kawanami, Effect of nano-hydroxyapatite on bone morphogenetic protein-2-induced hard tissue formation and dentin resorption on a dentin surface, *Appl. Surf. Sci.*, 2012, **262**, 140–145.
40. H. Jiang, Y. Zuo, Q. Zou, H. Wang, J. Du and Y. Li, *et al.*, Biomimetic spiral-cylindrical scaffold based on hybrid chitosan/cellulose/nano-hydroxyapatite membrane for bone regeneration, *ACS Appl. Mater. Interfaces*, 2013, **5**(22), 12036–12044.
41. J. I. González Ocampo, M. M. Machado de Paula, N. J. Bassous, A. O. Lobo, C. P. Ossa Orozco and T. J. Webster, Osteoblast responses to injectable bone substitutes of kappa-carrageenan and nano hydroxyapatite, *Acta Biomater.*, 2019, **83**, 425–434.
42. Z. Ding, H. Han, Z. Fan, H. Lu, Y. Sang and Y. Yao, *et al.*, Nanoscale Silk-Hydroxyapatite Hydrogels for Injectable Bone Biomaterials, *ACS Appl. Mater. Interfaces*, 2017, **9**(20), 16913–16921.
43. A. Rajeswari, V. G. Kumar, V. Karthick, T. S. Dhas and S. L. Potluri, Hydrothermal synthesis of hydroxyapatite plates prepared using low molecular weight heparin (LMWH), *Colloids Surf., B*, 2013, **111**, 764–768.
44. D. Xu, Y. Wan, Z. Li, C. Wang, Q. Zou and C. Du, *et al.*, Tailorable hierarchical structures of biomimetic hydroxyapatite micro/nano particles promoting endocytosis and osteogenic differentiation of stem cells, *Biomater. Sci.*, 2020, **8**(12), 3286–3300.
45. Y. Sun, F. Han, P. Zhang, Y. Zhi, J. Yang and X. Yao, *et al.*, A synthetic bridging patch of modified co-electrospun dual nano-scaffolds for massive rotator cuff tear, *J. Mater. Chem. B*, 2016, **4**(45), 7259–7269.
46. X. Liu, C. Bao, H. H. K. Xu, J. Pan, J. Hu and P. Wang, *et al.*, Osteoprotegerin gene-modified BMSCs with hydroxyapatite scaffold for treating critical-sized mandibular defects in ovariectomized osteoporotic rats, *Acta Biomater.*, 2016, **42**, 378–388.
47. X. Li, R. Cheng, Z. Sun, W. Su, G. Pan and S. Zhao, *et al.*, Flexible bipolar nanofibrous membranes for improving gradient microstructure in tendon-to-bone healing, *Acta Biomater.*, 2017, **61**, 204–216.

CHAPTER 7

Self-assembling Nanoarchitectonics for Oral Drug Delivery

K. KAWAKAMI*

Medical Soft Matter Group, National Institute for Materials Science, Tsukuba, Japan
*E-mail: kawakami.kohsaku@nims.go.jp

7.1 Introduction to the Oral Delivery of Poorly Soluble Drugs

Orally taken drugs are dissolved in the stomach and small intestine. Then, they are mainly absorbed from the small intestine. Thus, to achieve the desired therapeutic effect, the drug molecules must have sufficiently high solubility and membrane permeability. However, many drugs with low solubility and/or permeability are on the market and in pipelines. Special formulation technologies are thus required to deliver such compounds to the market.[1–3]

More than two decades ago, a paradigm shift from a phenotypic to a target-based approach occurred in drug discovery.[4] The phenotypic approach is a classical trial-and-error methodology where compounds are screened against cells, tissues, or whole bodies, containing different physicochemical and biological factors that may influence their efficacy, including solubility, protein binding, or metabolism, were simultaneously evaluated. However,

Nanoscience & Nanotechnology Series No. 55
Concepts and Design of Materials Nanoarchitectonics
Edited by Omar Azzaroni and Katsuhiko Ariga

Published by the Royal Society of Chemistry, www.rsc.org

compounds are tested against specific targets based on hypotheses on their action mechanisms in the recent target-based approach. Although it provides a clear idea for molecular design, the physicochemical and biological problems are frequently ignored in the screening stage. However, this is currently recognized as one of the major reasons for the increase in poorly soluble candidates.[5]

To overcome the low solubility problem of the drug candidates, extensive efforts have been made in academia and industry to derive effective formulation technologies. Simple methodologies include the addition of a surfactant to the formulation and reducing particle size. Current regulation does not allow the addition of enough surfactant for drug solubilization;[6] however, the addition of a small amount of surfactant could be performed as it can improve the wetting and disintegration process of the formulation. Milling of the drug to reduce the particle size is currently a common strategy in the pharmaceutical industry. The dissolution rate of the drug/formulation is proportional to the surface area, which is inversely proportional to the particle size. Therefore, the low solubility problem may be overcome by milling.

As a very simple approach to overcome the low solubility problem, drugs are occasionally taken in the form of an oil solution to skip the dissolution process. Long-chain or medium-chain triglycerides, including vegetable oils, are typically used for this purpose. If surfactants are added to the drug/oil solution, the emulsification behavior of the oil in the small intestine can be enhanced. This type of formulation is called a self-emulsifying drug delivery system and is believed to be more effective than the simple oil solutions.[2,7–9] Although oral formulations are usually developed using crystalline drugs, the amorphous state may also be employed to improve drug solubility.[1–3,10,11] The higher solubility of the amorphous solids relative to that of the crystal can be explained by their difference in the Gibbs energy of dissolution, ΔG:

$$\Delta G = RT \ln x, \tag{7.1}$$

where x is the molar solubility, and R and T are the gas constant and the temperature, respectively. Thus, the Gibbs energy difference between the crystalline and amorphous forms, ΔG_{AC}, can be expressed as

$$\Delta G_{AC} = -RT \frac{a_A}{a_C}, \tag{7.2}$$

where a_A and a_C are the activity of the solute relative to the amorphous and crystalline solids, respectively. This equation is based on the assumption that the solid form is unchanged during dissolution. The practical solubility ratio between the amorphous and crystalline solids is lower because of the interaction between the solid and solvent.[12] Moreover, the proportion of the ionized fraction is lowered because of the increase in the solubility of the amorphous solid, which also decreases the solubility advantage of the amorphous solids.[12] Figure 7.1 shows the typical dissolution profile of the amorphous solids, which is called "spring and parachute." Initially, the amorphous

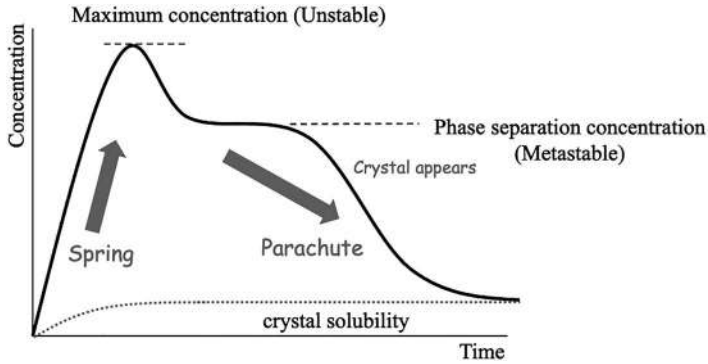

Figure 7.1 Typical dissolution profile of the amorphous solids.

Table 7.1 Theoretical and experimental solubility ratio between the amorphous and crystalline solids.[13]

Compound	Theoretical (a_A/a_C)	Experimental
Indomethacin	7.0	4.9
Iopanoic acid	5.7	1.5
Glipizide	11.1	9.2
Glybenclamide	17.1	22.6
Hydrochlorothiazide	33.9	4.9
Terfenadine	13.0	10
Griseofulvin	29.1	1.4
Spironolactone	110.3	2.1
Danazol	26.5	3.0

solids exhibit a much faster dissolution than the crystalline solids to reach maximum concentration, which is unstable and depends on different experimental conditions, including stirring rate, amount of solid, and even how the sample was added to the solution. The powder properties, such as particle size and surface area, also influence this process. After reaching the maximum concentration (supersaturated state), the concentration decreases to reach a metastable state where phase separation occurs (discussed later). Then, the concentration decreases again due to the appearance of the crystals to reach crystalline solubility. Table 7.1 shows an example of the solubility advantage of pharmaceutical glasses determined by both experiment and theoretical calculations when the water sorption and ionization are considered in addition to the energy difference as mentioned above.[13] The phase separation concentration presented in Figure 7.1 can be regarded as the amorphous concentration in ideal cases. However, in practical dissolution studies that begin with the addition of solids to the medium, the dissolution curve frequently fails to show the plateau period as the dissolution process consists of multiple non-equilibrium dynamic phenomena, including phase separation (spinodal decomposition) and nucleation/crystallization. Thus,

it is generally difficult to identify consistencies between the theoretical and experimental amorphous solubility values. Nevertheless, a relatively good agreement between the experimental and theoretical solubility values was found for indomethacin, glipizide, and terfenadine. For all the compounds, except glybenclamide, the experimental solubility ratio was lower than that obtained by the calculation, which indicates that crystallization was already initiated in the experiments.

Milling technology has allowed notable progress during the last two decades in the reduction of drug crystals to sizes below 500 nm.[2,11,14,15] Such small crystals are usually called nanocrystals in the pharmaceutical field, although nanomaterials are usually defined as those with a size below 100 nm. This is because the FDA (U.S. Food and Drug Administration) enables the use of the term "nano" if the material exerts a size effect due to its smallness. Under the assumption that the material volume is identical, the surface area is inversely proportional to the size of the particle. Thus, down-sizing to a few nanometers leads to a significant increase in the surface area, which has a linear relationship with dissolution rate. In addition, size reduction may lead to an increase in surface energy because of an increase in curvature. This effect is described by the following Ostwald–Freudlich equation.[2]

$$C(r) = C(\infty)\exp\left(\frac{2\gamma M}{r\rho RT}\right), \tag{7.3}$$

where γ, M, r, and ρ are interfacial tension at the particle surface, the molecular weight, the density of the particle, and the radius of the particle, respectively. $C(r)$ and $C(\infty)$ are the solubilities of a particle of radius r and infinite size, respectively. The nanocrystals are usually manufactured by either media milling or high-pressure homogenization. Such top-down processes break crystals to expose a high-energy surface, which can be another factor for the enhanced dissolution property.

It has been generally thought that the absorption-enhancing mechanism of the previously-mentioned technologies for poorly soluble drugs was the increase in the solubility in the gastrointestinal tract. However, how the molecules are dissolved is more important for improved absorption as proven in recent studies. Beig *et al.*[16] showed that the solubility of etoposide increased by adding polyethylene glycol 400, β-cyclodextrin, or sodium dodecyl sulfate. However, in all cases, the permeability of the drug across the semipermeable membrane was found to decrease. Because of this solubility-permeability interplay, the flux across the semipermeable membrane almost remain unchanged. In contrast, the use of an amorphous solid significantly increased the flux as a supersaturated state was established. Elkhabaz *et al.*[17] reported that the solubility of atazanavir and posaconazole was significantly enhanced by using simulated intestinal fluid compared to plain buffer. However, the transmembrane flux remained unchanged relative to that from the plain buffer, suggesting that the solubilized drug by the surface-active components did not contribute to the permeation. Hens *et al.*[18] investigated the

food effect on the oral absorption of fenofibrate nanosuspension in healthy volunteers by evaluating the drug concentration both in the gastrointestinal tract and blood. In the fed state, although the fenofibrate concentration in the gastrointestinal tract was observed to increase after food intake, its absorption was suppressed. This was explained by the solubilization by the food components, which was likely to inhibit transmembrane absorption.

Recent investigations on the oral absorption of poorly soluble drugs suggest that it is extremely important to control their dissolved state in the gastrointestinal tract for the control of absorption. As the equilibrium solubilization using additives is not effective as mentioned previously, new concepts are required to control non-equilibrium dissolution. In this chapter, a new concept, self-assembling nanoarchitectonics, is introduced which is beneficial for improving the oral absorption of poorly soluble drugs.

7.2 Concept of Self-assembling Nanoarchitectonics

7.2.1 Non-equilibrium Dynamics of the Supersaturated Solution

Amorphous solids create a supersaturated state during dissolution. Thereafter, two fates are available.[10] If the degree of supersaturation is very high and/or the compound has a high crystallization tendency, immediate crystallization occurs. Subsequently, the solute concentration quickly decreases to the equilibrium solubility of the compound. Another route is the liquid–liquid phase separation based on the mechanism of spinodal decomposition, where an energetically favorable state is achieved *via* phase separation into concentrated and diluted phases. The Gibbs energy of mixing, ΔG_m, can be expressed as follows:

$$\Delta G_m = xG_c + (1 - x)G_d \tag{7.4}$$

Here x is the fraction of the concentrated phase. G_c and G_d are the Gibbs energies of the concentrated and diluted phases, respectively. This is schematically explained in Figure 7.2, where the relationship between the mixing ratio and Gibbs energy is described. Two minima in the Gibbs energy can exist as a result of mixing the two phases. The most stable state is found on the adjustment line of the two minima. Thus, negative diffusion of the solutes from the diluted to the concentrated phase proceeds in the mechanism of spinodal decomposition to complete the phase separation.

The phase separation concentration is difficult to observe in practical dissolution studies in many cases. Thus, it is usually determined by adding an organic solution of the drug to the media, followed by observation of turbidity. The drug can dissolve if the concentration is lower than the phase separation concentration; the concentration where the turbidity starts to increase can be regarded as the phase separation concentration. Figure 7.3 shows an example of this analysis for ritonavir. In a phosphate buffer,

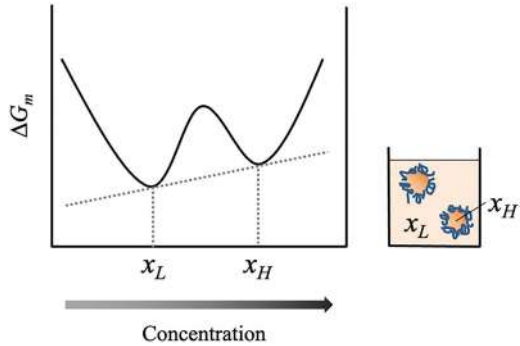

Figure 7.2 (Left) Gibbs energy of mixing, where x_L and x_H denote the concentrations of the diluted (continuum) and concentrated (dispersed) phases, respectively. (Right) Schematic representation of the phase separation. The amphiphilic polymer that stabilizes the interface is also presented.

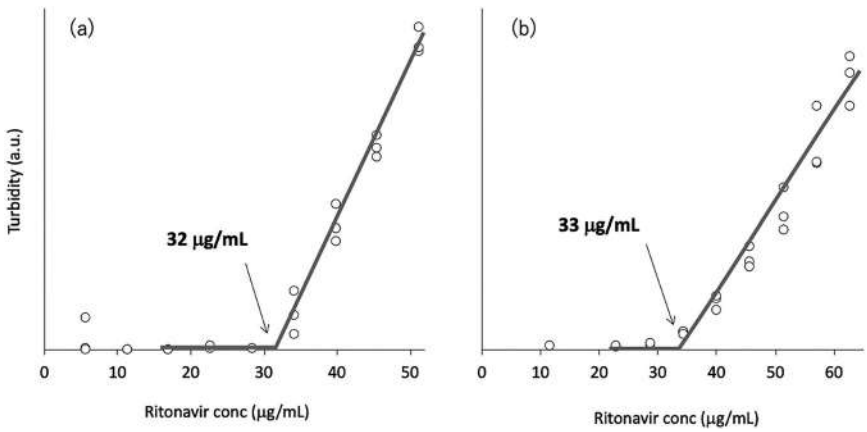

Figure 7.3 Turbidity of the ritonavir solution as a function of concentration. Ritonavir was added as the ethanol solution to 50 mM phosphate buffer (pH 7.0) at 25 °C. Turbidity was determined after 30 min of stirring. The phase separation concentrations were detected as break points as shown in the figures. (a) Phosphate buffer and (b) Phosphate buffer with 0.5% HPMCAS.

the phase separation concentration was identified as a break point at 32 μg mL^{-1}. The phase separation concentration is not influenced by the presence of the polymer. In the presence of hydroxypropyl methylcellulose acetate succinate (HPMCAS), almost the same phase separation concentration was observed. Table 7.2 shows the comparison of equilibrium solubility and the phase separation concentration determined by the turbidity for different drug molecules. Typically, the reported phase separation concentrations are approximately 5- to 25-fold that of the equilibrium solubilities.

Table 7.2 Comparison of the crystalline solubility and liquid–liquid phase separation (LLPS) concentration.

Compound	Temperature	pH	Crystal solubility (μg mL^{-1})	LLPS (μg mL^{-1})	LLPS/ Crystal solubility	Reference
Indomethacin	37	2.0	3.0	30.4	10	19
Ritonavir	37	6.8	1.3	18.8	14	19
Efavirenz	37	6.8	8.2	18.4	2.2	19
Loratadine	37	6.8	1.6	7.6	4.8	19
Ketoconazole	37	10.0	3.7	54.4	15	19
Felodipine	37	6.8	0.94	9.8	10	19
Clotrimazole	37	10.0	0.4	5.2	13	19
Clozapine	37	10.0	8.8	136	15	19
Felodipine	37	6.8	1.21	8.70	7.2	20
Nifedipine	37	6.8	10.0	58.3	5.8	20
Danazol	25	6.8	0.9	13	14	21
Fenofibrate	25	7.0	0.1	1.0	10	22
Ritonavir	25	7.0	1.3	32	25	—
Griseofulvin	37	7.0	12	38	3.2	23

Hydrophilic polymers are usually contained in amorphous solid dispersion (ASD). If such moderately surface-active compounds exist in the solutions, the concentrated phase may be kinetically stabilized in the form of colloidal dispersions. Thereafter, the dispersed phase is solidified in the form of (nano)particles, which may either exist as the crystal or amorphous phase. Occasionally, the size of the particles is as small as a few tens of nanometers as found for itraconazole[24] and ritonavir.[25] The charged polymers are usually effective for stably reducing the particle size because their adsorption on the particle surface causes electrostatic repulsion. Even when there are no charges, the adsorption of polymers can cause steric repulsion. The surfactants are frequently observed to immediately destroy the supersaturated state because they tend to assist the crystallization process of the drug.[22,23]

7.2.2 Stabilization of the Concentrated Phase as Nanoarchitectures

During the phase separation process mentioned previously, the size of the dispersed phase continues to grow to reach the metastable state. Figure 7.4 shows the evolution of the size of the fenofibrate/polymer particles produced from the supersaturated solutions as a function of time.[22] In the absence of a polymer and in the presence of vinylpyrrolidone-vinyl acetate copolymer (PVPVA), the particle size immediately became larger than one micrometer. However, the particles are stabilized by an association with charged polymers, including HPMCAS and Eudragit (Poly(methacrylic acid-*co*-methyl methacrylate)) L100, resulting in the formation of nanoparticles of *ca.* 200 nm in size. The zeta potential of the polymer-free fenofibrate particle was

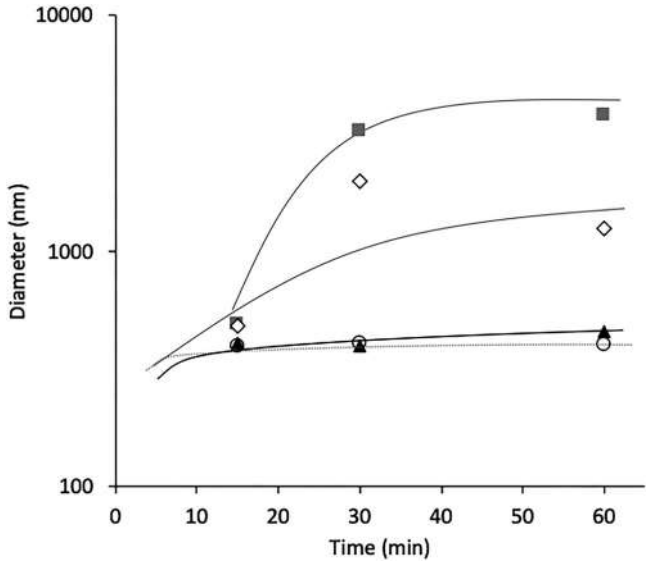

Figure 7.4 Size of the fenofibrate particles produced after the addition of its ethanol solution to 50 mM phosphate buffer (pH 7.0) at 25 °C. Symbols: no polymer added (■), 0.5% PVPVA (◇), 0.5% HPMCAS (▲), and 0.5% Eudragit L100 (○). Reproduced from ref. 22 with permission from Elsevier, Copyright 2018.

−1.6 mV. This value changed to 0.3, −8.8, and −34.3 mV, by adding PVPVA, HPMCAS, and Eudragit L100, respectively. Thus, the surface charge might play a dominant role in colloidal stability. For the ibuprofen nanoparticles, the colloidal stability was better improved by the addition of HPMC than PVPVA and Eudragit E.[26] In this case, the stabilization effect of HPMC can be explained by its strong interaction with the ibuprofen particle to provide steric repulsion between the particles as charges are not added. The detailed structure of each nanoparticle has not been well investigated; however, some studies have revealed that the nanoparticles might have a heterogeneous composition as revealed by the asymmetrical flow field-flow fractionation analysis.[27,28]

An important role of nanoparticles during oral absorption is the maintenance of a drug concentration in the continuum phase by acting as reservoirs.[20,29–31] Nanoparticles are also expected to behave as rapid-diffusing shuttles in the mucus layer.[32] Mucus is a hydrogel with a very complicated structure that consists of glycoproteins, lipids, salts, *etc.* It possesses a size-filtering effect,[33] which is one of the mechanisms to protect the cellular surface. The mesh size of the mucus layer was thought to be between a few tens of nanometers and a few hundreds of nanometers. However, Lai *et al.* reported that 500 nm styrene particles diffused as rapidly as water molecules if their surface was decorated with polyethylene glycol. Such a finding

indicates that larger pores were available for the permeation of nanoparticles than those that were general thought.[34] Polyethylene glycol is widely recognized to provide a stealth function to particulate injectable formulations.[35] This study revealed that it is also applicable to transmembrane drug delivery. The decoration of fenofibrate nanocrystals with *ca.* 150 nm in size with HPMC on their surface was also found to be advantageous for rapid diffusion in the mucus layer.[36] The oral absorption of fenofibrate was improved by the polymer decoration and the efficacy depended on the molecular weight of the polymer. Conversely, if the nanoparticles are coated by polyvinyl alcohol, the diffusion was significantly suppressed most likely because of a strong interaction between the polymer and the mucus.[37] Chitosan is also known as a polymer that has a strong interaction with mucus.[38,39] The diffusion rate of nanoparticles can be controlled by both their size and interaction with the mucus components.

To obtain nanoparticles after phase separation, the degree of the supersaturation (DS) must be moderate. If it is too large, crystallization promptly proceeds as the DS is the most important driving force of crystallization. Figure 7.5 presents the effect of the DS on the phase separation behavior of the griseofulvin solution.[23] Because griseofulvin has a high crystallization tendency, its metastable phase separation concentration is difficult to determine. Thus, the "apparent" phase separation concentration, which depends on the polymers added, is presented in the

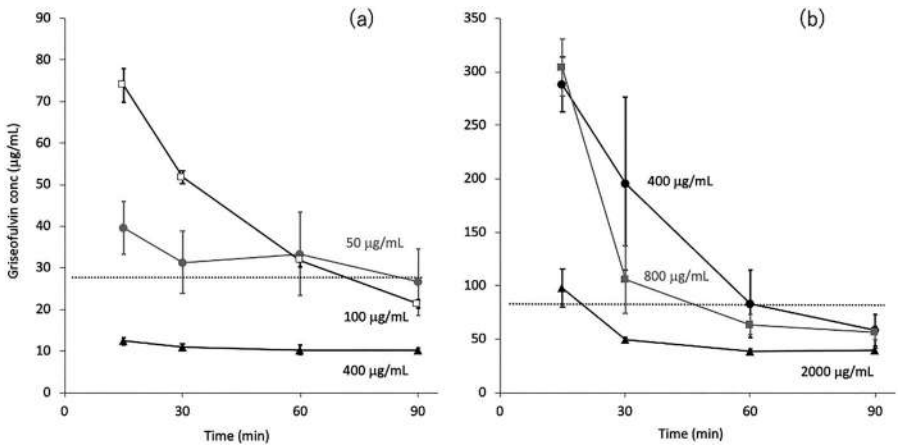

Figure 7.5 Effect of the degree of supersaturation on the precipitation behavior of griseofulvin. The acetone solution of griseofulvin was added to 50 mM phosphate buffer (pH 7.0) at the concentrations indicated in the figure. Each supersaturated suspension was filtered using syringe filters with pore sizes of 0.45 mm prior to quantification. The apparent phase separation concentrations are presented as dotted lines. (a) no polymer added. (b) in the presence of 0.5 wt% of PVPVA. Reproduced from ref. 23 with permission from Elsevier, Copyright 2020.

figure. In the absence of the polymer, a gradual approach to the phase separation concentration (25 μg mL^{-1}) was observed when DS was 4.3 (50 μg mL^{-1}) or 8.5 (100 μg mL^{-1}). When DS was too high (34.2, 400 μg mL^{-1}), the concentration immediately decreased to reach equilibrium crystalline solubility owing to direct crystallization. Thus, the order of the concentration after 90 min fully reversed to the order of the initial concentration. The same result was obtained in the presence of PVPVA. The larger the DS, the faster the decrease in concentration. Similar observations, that is, completely reversed concentration in the initial and final states for the supersaturated solutions, are frequently reported.[23,40] This observation indicates that the applied amount of the formulation is important for producing nanoparticles after their dissolution.

7.2.3 Nanoarchitectures as Drug Reservoirs

The role of the nanoparticle as a drug reservoir is schematically explained in Figure 7.6 which contains example data for felodipine.[29] The phase separation concentration of felodipine is 8.7 μg mL^{-1} at 37 °C. Thus, the concentrated nanophase appears above the concentration, which may initially exist as droplets, followed by transformation to solid nanoparticles. If the felodipine solutions/suspensions are in contact with another phase (acceptor phase) *via* a semipermeable membrane, felodipine molecules move to the acceptor phase. The flux is proportional to the monomer concentration; therefore, it is almost constant above the phase separation concentration. If the dissolution of felodipine from the nanoparticles is sufficiently fast, the

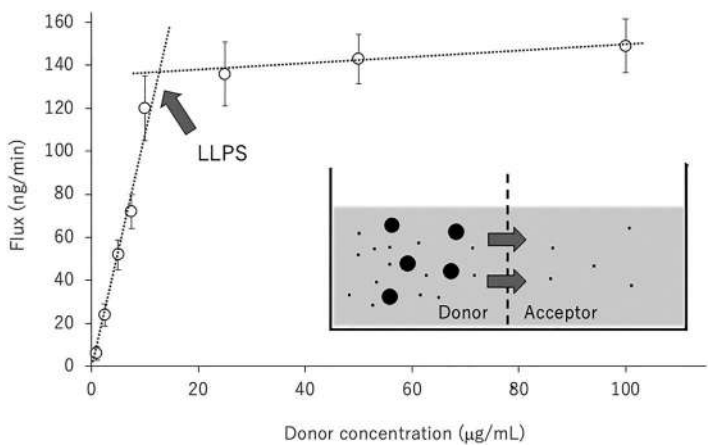

Figure 7.6 Relationship between felodipine concentration in the donor phase and transmembrane flux.[29] Inset shows the schematic representation of the experimental setup.

nanoparticles can act as reservoirs. As a result, a constant flux is expected until the nanoparticles are fully consumed. The ability of the nanoparticles to act as reservoirs may depend on the drug species.

The practical environment in the gastrointestinal tract is more complex. Poorly soluble drugs are dissolved by various intestinal colloids including bile salt micelles and lipid emulsions, and lipid vesicles under the fed condition.[41] Figure 7.7 depicts the absorption process of drug molecules from the amorphous dosage forms in the small intestine. After the supersaturated state is established, phase separation is expected to occur to form nanoparticles. Simultaneously, drug molecules are solubilized by intestinal colloids. Both aggregates are expected to release drug molecules for absorption. If the release rate (denoted as K_p in the figure) from the nanoparticles is sufficiently large, they act as reservoirs to enhance the absorption.

In some cases, oral absorption is remarkably enhanced by food intake, which is referred to as the positive food effect. For example, if the oral absorption is limited by the dissolution rate of the drug, the positive food effect might occur because of solubilization by bile salts.[42] On the other hand, a very small K_c may lead to the suppression of absorption by food ingredients, which is referred to as the negative food effect. Both the positive and negative food effects are not favorable properties if the effect is extreme. If K_p is markedly larger than K_c, such food effects may be reduced. Thus, supersaturating dosage forms function to eliminate the food effect as well as to improve oral absorption if K_p is sufficiently large.

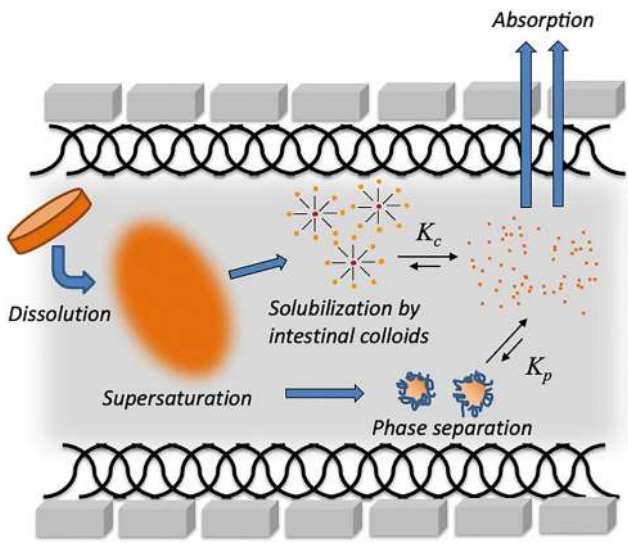

Figure 7.7 Schematic representation of the absorption process of the drug molecules from amorphous dosage forms.

7.2.4 Improvement of the Oral Absorption of Poorly Soluble Drugs

ASD has been utilized for more than half of a century as an efficient formulation technology to enhance the oral absorption of poorly soluble drugs. Although its mechanism has been explained by an increase in drug solubility, its dissolution behavior is not simple as explained in previous sections. For conventional dosage forms, oral absorption is predicted from dissolution studies.[3,43] However, such prediction is difficult for ASDs because of the complexity of the dissolution behavior.

Figure 7.8a shows the oral absorption of fenofibrate in rats after the administration of its solid dispersions.[22] Oral absorption was significantly improved relative to that of the crystalline drug when the ASD was prepared with Eudragit L100, followed by that with PVPVA. This absorption behavior was predictable from dissolution studies following extensive optimization trials. However, the phase separation concentration could provide a clearer idea regarding oral absorption. The order of the oral absorption exhibited good consistency with the apparent phase separation concentration as shown in Figure 7.8b, indicating that the phase separation really occurred in the gastrointestinal tract to allow the absorption of only the free drug. Presumably, the nanoparticles acted as drug reservoirs during the absorption process.

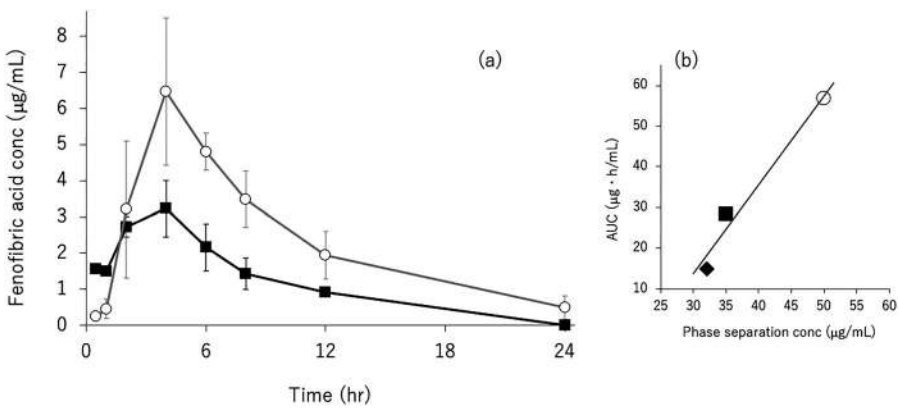

Figure 7.8 (a) Plasma fenofibric acid (an active metabolite of fenofibrate) concentration after the oral administration of the fenofibrate amorphous solid dispersions to rats at a dose of 7.5 mg kg^{-1}. Symbols: crystalline fenofibrate as a negative control (◆), PVPVA formulation(■), and Eudragit L100 formulation (○). (b) Relationship between area under concentration (AUC) of the oral administration study and apparent phase separation concentration of fenofibrate in the presence of 0.1% Tween 80. Reproduced from ref. 22 with permission from Elsevier, Copyright 2018.

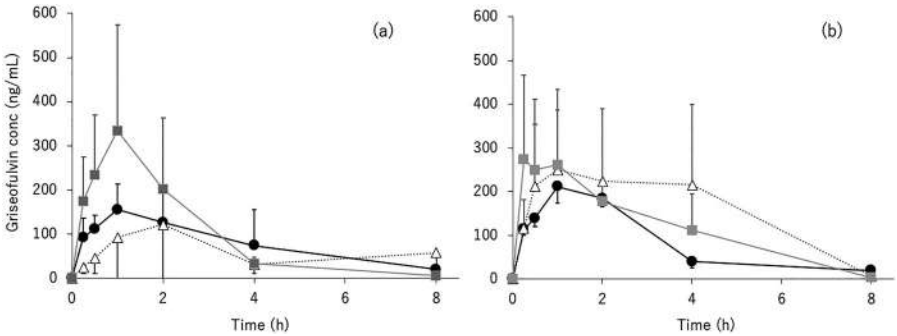

Figure 7.9 (a) Plasma griseofulvin acid concentration after the oral administration of its amorphous solid dispersions to rats at a dose of (a) 10 mg mL^{-1} or (b) 7.5 mg kg^{-1}. Symbols: crystalline griseofulvin as a negative control (●), PVPVA formulation (△), and HPMCAS formulation (■). Reproduced from ref. 23 with permission from Elsevier, Copyright 2019.

The development of ASD and prediction of oral absorption are quite challenging for drugs with a high crystallization tendency. Figure 7.9 presents another example of an oral administration study of ASD, where griseofulvin, which has a very high crystallization tendency, was used as a model compound.[23] In this study, the effect of the administration dose was also investigated. At a lower dose (7.5 mg kg^{-1}), the highest absorption was observed for PVPVA ASD, followed by HPMCAS ASD. However, at the higher dose (10 mg kg^{-1}), the absorption from PVPVA ASD was significantly suppressed, resulting in poorer absorption than that achieved with the crystalline drug. Such results might be due to the crystallization of the drug in the gastrointestinal tract for PVPVA ASD owing to the high concentration. In fact, the intra-individual deviation was significant for PVPVA ASD, with enhanced absorption for one rat but suppressed absorption was for the remaining two rats, indicating crystallization occurred in the gastrointestinal tract for one rat.

The crystallization tendency of the drug molecule[10,44–46] must be comprehended well to design ASDs based on the nanoarchitectonics concept. The crystallization tendency is influenced by many factors, including molecular weight, number of hydrogen bond donors/acceptors, number of aromatic rings, and number of rotatable bonds.[44,47,48] If the crystallization tendency of the drug is high, a large amount of excipients is required for the stabilization.[49,50] Many ASD products are presently available on the market, despite the lack of knowledge regarding the detailed mechanism for enhancement of oral absorption. More strategic formulation design based on self-assembling nanoarchitectonics should increase the value and usefulness of the ASD technology in the pharmaceutical industry.

7.3 Summary

This chapter described the oral drug delivery using nanoarchitectures spontaneously created following the supersaturated dissolution of the drug molecules in the gastrointestinal tract. Many researchers are actively working on nanoarchitectonics for use as injectable dosage forms; however, such attempts are important for oral drug delivery as well. Unlike the non-equilibrium nanoarchitectures used for the injectable dosage forms, a thermodynamic understanding is necessary for the nanoarchitectures for oral drug delivery. The self-assembling nanoarchitectonics for oral drug delivery are scientifically attractive and have practical importance in the maintenance of human health.

References

1. J. Brouwers, M. E. Brewster and P. Augustijns, *J. Pharm. Sci.*, 2009, **98**, 2549.
2. K. Kawakami, *Adv. Drug Delivery Rev.*, 2012, **64**, 480.
3. B. Hens, M. Kataoka, K. Ueda, P. Gao, Y. Tsume, P. Augustijns, K. Kawakami and S. Yamashita, *J. Drug Delivery Sci. Technol.*, 2020, **56**, 101275.
4. D. Brown, *Drug Discovery Today*, 2007, **12**, 1007.
5. K. Kawakami, *J. Pharm. Sci.*, 2009, **98**, 2875.
6. R. G. Strickley, *Pharm. Res.*, 2004, **21**, 201.
7. K. Kawakami, T. Yoshikawa, Y. Moroto, E. Kanaoka, K. Takahashi, Y. Nishihara and K. Masuda, *J. Controlled Release*, 2002, **81**, 65.
8. K. Kawakami, T. Yoshikawa, T. Hayashi, Y. Nishihara and K. Masuda, *J. Controlled Release*, 2002, **81**, 75.
9. C. J. H. Porter, C. W. Pouton, J. F. Curie and W. N. Charman, *Adv. Drug Delivery Rev.*, 2008, **60**, 673.
10. K. Kawakami, *Expert Opin. Drug Delivery*, 2017, **14**, 735.
11. S. V. Jermain, C. Brough and R. O. Williams III, *Int. J. Pharm.*, 2018, **535**, 379.
12. S. B. Murdande, M. J. Pikal, R. M. Shanker and R. H. Bogner, *J. Pharm. Sci.*, 2010, **99**, 1254.
13. S. B. Murdande, M. J. Pikal, R. M. Shanker and R. H. Bogner, *Pharm. Res.*, 2010, **27**, 2704.
14. Y. Wu, A. Loper, E. Landis, L. Hettrick, L. Novak, K. Lynn, C. Chen, K. Thompson, R. Higgins, U. Batra, S. Shelukar, G. Kwei and D. Storey, *Int. J. Pharm.*, 2004, **285**, 135.
15. D. A. Shah, S. B. Murdande and R. H. Dave, *J. Pharm. Sci.*, 2016, **105**, 10.
16. A. Beig, J. M. Miller, D. Lindley, R. A. Carr, P. Zocharski, R. Agbaria and A. Dahan, *J. Pharm. Sci.*, 2015, **104**, 2941.
17. A. Elkhabaz, D. E. Moseson, J. Brouwers, P. Augustijns and L. S. Taylor, *Mol. Pharmaceutics*, 2019, **16**, 5042.
18. B. Hens, J. Brouwers, M. Corsetti and P. Augustijns, *Eur. J. Pharm. Sci.*, 2015, **77**, 40.

19. G. A. Ilevbare and L. S. Taylor, *Cryst. Growth Des.*, 2013, **13**, 1497.
20. S. A. Raina, G. G. Z. Zhang, D. E. Alonzo, J. Wu, D. Zhu, N. D. Catron, Y. Gao and L. S. Taylor, *J. Pharm. Sci.*, 2014, **103**, 2736.
21. M. J. Jackson, S. J. Toth, U. S. Kestur, J. Huang, F. Qian, M. A. Hussain, G. J. Simpson and L. S. Taylor, *Mol. Pharmaceutics*, 2014, **11**, 3027.
22. K. Kawakami, K. Sato, M. Fukushima, A. Miyazaki, Y. Yamamura and S. Sakuma, *Eur. J. Pharm. Biopharm.*, 2018, **132**, 146.
23. K. Kawakami, K. Suzuki, M. Fukiage, M. Matsuda, Y. Nishida, M. Oikawa and T. Fujita, *J. Drug Delivery Sci. Technol.*, 2020, **56**, 101172.
24. R. Mellaerts, A. Aerts, T. P. Caremans, J. Vermant, G. Van den Mooter, J. A. Martens and P. Augustijns, *Mol. Pharmaceutics*, 2010, **7**, 905.
25. I. Tho, B. Liepold, J. Rosenberg, M. Maegerlein, M. Brandl and G. Fricker, *Eur. J. Pharm. Sci.*, 2010, **40**, 25.
26. K. Ueda and L. S. Taylor, *Mol. Pharmaceutics*, 2020, **17**, 1352.
27. J. Kanzer, S. Hupfeld, T. Vasskog, I. Tho, P. Hölig, M. Mägerlein, G. Fricker and M. Brandl, *J. Pharm. Biomed. Anal.*, 2010, **53**, 359.
28. K. J. Frank, U. Westedt, K. M. Rosenblatt, P. Hölig, J. Rosenberg, M. Mägerlein, G. Fricker and M. Brandl, *Int. J. Nanomed.*, 2012, **7**, 5757.
29. S. A. Raina, G. G. Z. Zhang, D. E. Alonzo, J. Wu, D. Zhu, N. D. Catron, Y. Gao and L. S. Taylor, *Pharm. Res.*, 2015, **32**, 3350.
30. A. S. Indulkar, Y. Gao, S. A. Raina, G. G. Z. Zhang and L. S. Taylor, *Mol. Pharmaceutics*, 2016, **13**, 2059.
31. A. S. Indulkar, J. E. Waters, H. Mo, Y. Gao, S. A. Raina, G. G. Z. Zhang and L. S. Taylor, *J. Pharm. Sci.*, 2017, **106**, 1998.
32. A. M. Stewart, M. E. Grass, T. J. Brodeur, A. K. Goodwin, M. M. Morgen, D. T. Friesen and D. T. Vodak, *Mol. Pharmaceutics*, 2017, **14**, 2437.
33. H. H. Sigurdsson, J. Kirch and C. M. Lehr, *Int. J. Pharm.*, 2013, **453**, 56.
34. S. K. Lai, D. E. O'Hanlon, S. Harrold, S. T. Man, Y. Y. Wang, R. Cone and J. Hanes, *Proc. Natl. Acad. Sci. U. S. A.*, 2007, **104**, 1482.
35. J. S. Suk, Q. Xu, N. Kim, J. Hanes and L. M. Ensign, *Adv. Drug Delivery Rev.*, 2016, **99**, 28.
36. K. Ueda, T. Iwai, Y. Sunazuka, Z. Chen, N. Kato, K. Higashi and K. Moribe, *Int. J. Pharm.*, 2019, **564**, 39.
37. M. Yang, S. K. Lai, T. Yu, Y. Y. Wang, C. Happe, W. Zhong, M. Zhang, A. Anonuevo, C. Fridley, A. Hung, j. Fu and J. Hanes, *J. Controlled Release*, 2014, **192**, 202.
38. Y. Daimon, N. Kamei, K. Kawakami, M. Takeda-Morishita, H. Izawa, Y. Takechi-Haraya, H. Saito, H. Sakai, M. Abe and K. Ariga, *Mol. Pharmaceutics*, 2016, **13**, 4034.
39. M. Collado-González, Y. G. Espinosa and F. M. Goycoolea, *Biomimetics*, 2019, **4**, 32.
40. J. Beverage, J. Brouwers, P. Annaert and P. Augustijns, *Eur. J. Pharm. Biopharm.*, 2012, **82**, 424.
41. D. Riethorst, A. Mitra, F. Kesisoglou, W. Xu, J. Tack, J. Brouwers and P. Augustijns, *Eur. J. Pharm. Biopharm.*, 2018, **129**, 104.

42. K. Sugano, M. Kataoka, C. da Costa Mathews and S. Yamashita, *Eur. J. Pharm. Sci.*, 2010, **40**, 118.
43. J. B. Dressman, G. L. Amidon, C. Reppas and V. Shah, *Pharm. Res.*, 1998, **15**, 11.
44. J. A. Baird, B. van Eerdenbrugh and L. S. Taylor, *J. Pharm. Sci.*, 2010, **99**, 3787.
45. L. I. Blaabjerg, E. Lindenberg, K. Löbmann, H. Grohganz and T. Rades, *Mol. Pharmaceutics*, 2016, **13**, 3318.
46. K. Kawakami, *Pharmaceutics*, 2019, **11**, 202.
47. T. Miyazaki, S. Yoshioka, Y. Aso and T. Kawanishi, *Int. J. Pharm.*, 2007, **336**, 191.
48. D. Mahlin, S. Ponnambalam, M. H. Hockerfeit and C. Bergstrom, *Mol. Pharmaceutics*, 2011, **8**, 498.
49. K. Kawakami, *Int. J. Pharm.*, 2012, **433**, 71.
50. K. Kawakami, Y. Bi, Y. Yoshihashi, K. Sugano and K. Terada, *J. Drug Delivery Sci. Technol.*, 2018, **46**, 197.

CHAPTER 8

Atomic-scale Characterization of Platinum Nanoparticles Deposited on C_{60} Fullerene Nanowhiskers and Related Carbon Nanomaterials

K. MIYAZAWA*[a], M. YOSHITAKE[a] AND Y. TANAKA*[a]

[a]Department of Industrial Chemistry, Tokyo University of Science, Tokyo, Japan
*E-mail: miyakuni@rs.tus.ac.jp, yutanaka@rs.tus.ac.jp

8.1 Introduction

Fullerene molecules possess closed cage-type structures composed of carbon atoms. C_{60} with 60 carbon atoms, is the best-known fullerene molecule and was discovered by Kroto *et al.* in 1985.[1] C_{60} fullerene nanowhiskers (C_{60}FNWs) are thin single-crystal fibers that are composed of C_{60} molecules and can be easily synthesized by the liquid–liquid interfacial precipitation (LLIP) method.[2–6] C_{60}FNWs are n-type semiconductors and have a diverse range of applications in field effect transistors (FETs),[7] solar cells,[8] photocatalysts,[9] chemical sensors,[10] photosensors,[11] and as scaffolds to grow human osteoblast cells,[12] myotubes[13] and neurons,[14] and so forth. Doping alkali metals in C_{60}FNWs results in lightweight superconducting fibers with

Nanoscience & Nanotechnology Series No. 55
Concepts and Design of Materials Nanoarchitectonics
Edited by Omar Azzaroni and Katsuhiko Ariga

Published by the Royal Society of Chemistry, www.rsc.org

a density of ~2 g cm^{-3}. The superconducting transition temperature (T_c) of alkali-doped C_{60}FNWs was 17, 25 and 26 K for $K_{3.3}C_{60}$FNWs, $Rb_{3.0}C_{60}$FNWs, and $Cs_{2.0}Rb_{1.0}C_{60}$FNWs, respectively.[15,16] Therefore, the liquid hydrogen cryogen, which has a boiling temperature of 20.27 K, will be useful to form superconducting $Cs_{2.0}Rb_{1.0}C_{60}$FNWs and $Rb_{3.0}C_{60}$FNWs in the future.[17] Tubular C_{60}FNWs are specially called C_{60} fullerene nanotubes (C_{60}FNTs).[3–6] Figure 8.1 shows the models of C_{60}FNW and C_{60}FNT.

The C_{60} molecules in the C_{60}FNWs are loosely bound *via* van der Waals bonding forces.[18] Graphite is made up of a stack of flat graphene layers.[19] Although the graphene layers are held *via* weak van der Waals forces,[20] the carbon atoms in each graphene sheet are strongly bonded to one another through σ bonds, formed by the overlap of sp^2 hybrid orbitals.[21] The Jenkins-Kawamura model[22,23] has shown that the glassy carbon (GC) is composed of randomly oriented graphitic ribbons and is very hard. GC is fabricated by heat treating polymers such as polyacrylonitrile under pressure in an inert atmosphere at 1000–3000 °C.[24] Carbon black (CB) particles are composed of concentric graphene layers.[25]

Fuel cells are "the electrochemical devices that directly convert the energy of a chemical reaction into electricity with water as its by-product".[26] As displayed in Figure 8.2, in polymer electrolyte fuel cells (PEFCs), the platinum nanoparticles (Pt NPs) supported on carbon particles attached to the polymer electrolyte membranes assist the reaction between hydrogen molecules and oxygen molecules to form water molecules.[27–29] Carbon materials are indispensable Pt catalyst supports for PEFCs. In practical PEFCs, CB particles are usually used for the supports of Pt NPs.

The hydrogen molecules (fuel) diffuse to the anode catalyst layer loaded with Pt NPs and dissociate into protons and electrons *via* the hydrogen oxidation reaction. The protons diffuse through the polymer electrolyte membrane to the cathode catalyst layer loaded with Pt NPs and the electrons pass through an external conductive circuit having a load resistance. The oxygen molecules supplied from the air adsorb onto the surface of the cathode catalyst layer; the oxygen molecules and the protons that pass through the membrane and the electrons that reach the cathode react together to produce water (H_2O) on the surface of Pt NPs.

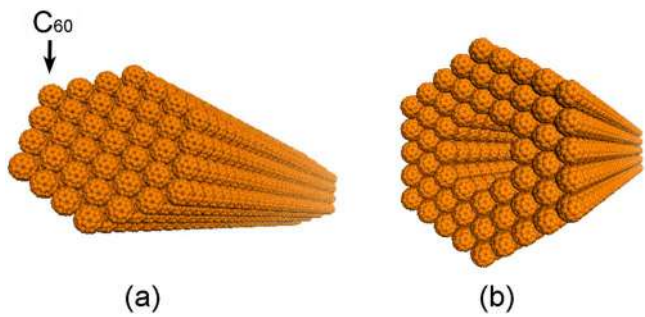

Figure 8.1 Model of (a) C_{60} fullerene nanowhisker, and (b) C_{60} fullerene nanotube.

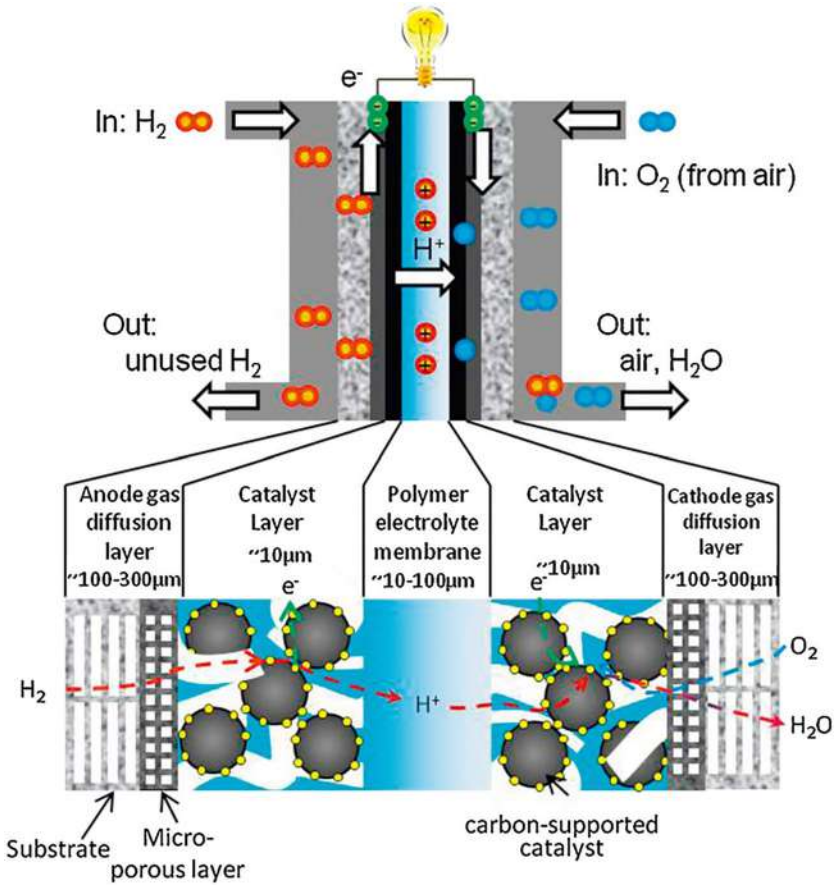

Figure 8.2 Schematic of a polymer electrolyte fuel cell. Reproduced from ref. 27 with permission from Elsevier, Copyright 2012.

The chemical reactions that occur in a typical PEFC are shown in eqn (8.1)–(8.3).[26]

At the anode, hydrogen molecules are oxidized to produce protons as charge carriers, and in the cathode, the protons transported through the electrode membrane form water molecules.

$$2H_2 \rightarrow 4H^+ + 4e^- \tag{8.1}$$

$$O_2 + 4H^+ + 4e^- \rightarrow 2H_2O \tag{8.2}$$

The overall reaction can be written as follows.

$$2H_2 + O_2 \rightarrow 2H_2O \tag{8.3}$$

It is reported that the oxygen reduction reaction (ORR) (Eqn (8.2)) is significantly slower than the hydrogen oxidation reaction at the anode.[30] The ORR is known to be the most important cathodic process in PEFCs,[31] and it has been reported that among all catalysts evaluated, Pt still remains the best catalyst to enhance the ORR.[31] However, efforts to enhance the catalytic activity of Pt are being pursued to reduce the usage of Pt, which is a scarce and expensive resource.

The lattice parameters of crystals are known to change depending on their size. As early as 1936, Finch *et al.*[32] reported the variation of lattice constant depending on the crystal size and showed that the lattice constants of ZnO and alkali halides (lithium, sodium and potassium halides) varied depending on their sizes by performing electron diffraction experiments. In 1951, Boswell showed by electron diffraction studies, that the lattice constants of alkali halide NPs (NaCl, KCl, NaBr, LiF) and gold NPs decrease with decreasing particle size, using electron diffraction. The decreasing behavior of the lattice constant was discussed in relation to the surface compressive layers in the NaCl crystals.[33] In 1928 Lennard-Jones *et al.* calculated the surface tension of NaCl type crystals that affects the interatomic distances of crystal surfaces.[34] In 1952, the reduction of lattice parameters with decreasing crystal size was reported for silver nanocrystals by Berry[35] from electron diffraction studies. The reduction of the lattice parameter of NPs is attributed to the surface tension that becomes more apparent with the decrease of crystal size.[35–37]

Bulk Pt crystals have a face-centered cubic structure (fcc) with a lattice constant a_0 = 0.39231 nm (JCPDS 00–004-0802). Recently, synchrotron XRD measurements of the Pt NPs prepared on carbon supports showed that their lattice constants decrease with decreasing particle diameter, and are smaller than the bulk Pt.[36]

Wang *et al.* reported that the ORR activity is enhanced in the contracted Pt surface layers.[38] DFT calculations on core–shell PtCu NPs catalysts showed a maximum ORR activity at a compressive strain of *ca.* −2.3% at the Pt shell.[39] Thus, it is of utmost importance to investigate the crystal structure of the Pt NPs for their catalytic applications in PEFCs.

Among a variety of preparation methods of metal NPs, a simple dry process named coaxial arc plasma deposition (CAPD) has been developed recently. In CAPD, high-energy metal ions ejected from a coaxial arc plasma gun are directly deposited on substrates in a vacuum.[40,41] Pulsed discharges are generated between a metal cathode and an anode in the coaxial arc plasma gun. Then, the surface of the metal cathode is vaporized and ionized, and the metal ions with high energies hit the target substrates, and metal NPs are deposited on the substrates. Various metal nanoparticles of Fe, Cu, Rh, Pd, Pt, Au, Ce, and so forth have been synthesized by CAPD.[40,41] The Pt NPs prepared on carbon black (CB) particles by CAPD were tested for their ORR catalytic activity, and they showed a higher catalytic performance than commercially available Pt catalysts.[40]

Through CAPD, it is possible to deposit metal nanoparticles on other carbon substrates as well as on CB particles. This chapter reviews our recent research on the atomic structure of Pt NPs produced on C_{60} fullerene

nanowhiskers (C_{60}FNWs), graphite particles, and glassy carbon (GC) substrate by CAPD, using high-resolution transmission electron microscopy (HRTEM). The results are compared to the atomic structure of commercial Pt NPs chemically prepared on CB particles.

8.2 Experimental

8.2.1 Synthesis of C_{60}FNWs

The LLIP method utilizes the diffusion of a poor solvent of fullerene such as isopropyl alcohol into a fullerene-saturated solution consisting of a good solvent of fullerene such as toluene. For synthesizing C_{60}FNWs, an aliquot of a C_{60}-saturated toluene solution is added to a glass bottle, followed by the gentle addition of an equal amount of isopropyl alcohol (IPA) to form the liquid–liquid interface.[2] The resulting is kept at a temperature below ~21 °C. During the slow mixing of toluene and IPA, the liquid–liquid interface becomes supersaturated with C_{60} and the nucleation and growth of C_{60}FNWs begin. This supersaturated state of C_{60} caused by the interdiffusion of toluene and IPA assists in the growth of the C_{60}FNWs.

The diameter of the C_{60}FNWs depends on the ratio of the good solvent to the poor solvent[42] and decreases with a decreasing amount of toluene in the solvent mixture toluene + IPA.[42] Here, the solubility of C_{60} in solution decreases with the addition of IPA, thus the solution becomes supersaturated with C_{60}.

Apart from the solvent ratio, the container size (glass bottle) is also found to influence the diameter of the C_{60}FNWs.[43] The length and the diameter of the C_{60}FNWs are found to decrease for a glass bottle size of a smaller size. The mean number density of C_{60}FNW nuclei is inversely proportional to the square root of the solution volume and this explains the relationship between the size of the C_{60}FNWs and the volume of the mixture (toluene solution and IPA).[4]

The C_{60}FNWs to be used with the Pt deposition step are synthesized using the LLIP method.[44] At first, C_{60} powder (99.5%, MTR Ltd, U.S.A.) is ground using an agate mortar and dissolved in benzene (99.5%, Kanto Chemical Co., Inc., Japan) at room temperature to form the C_{60}-saturated solution. This solution is stored at 5 °C in an incubator (Fine FLT-15W, TGK, Tokyo, Japan). To 14 mL of the C_{60}-saturated benzene solution taken in a glass bottle, 14 mL of IPA is gently added to form the liquid–liquid interface. The glass bottle is ultrasonicated for several seconds in an ultrasonic water bath (Ultrasonic Cleaner FU-16C, 75 W, 28 kHz, TGK, Tokyo, Japan) and then stored at 5 °C to grow the C_{60}FNWs.

8.2.2 Deposition of Pt NPs on Carbon Substrates Using CAPD

The synthesized C_{60}FNWs are sampled onto TEM carbon microgrids supported on copper grids using a pipette and dried in air at room temperature. The TEM microgrids are carefully placed on the sample holder in the vacuum chamber of a CAPD apparatus (APD-1P, ADVANCE RIKO, Inc., Yokohama, Japan). The Pt NPs are then deposited on the C_{60}FNWs with a condenser

capacity of 360 μF, and a discharge voltage of 70 V under vacuum using a turbomolecular pumping system.[44] The discharge energy is 0.88 J per pulse.

In addition, Pt NPs are deposited on as-received graphite particles (GNH-XZ, Graphene Platform Corp, Tokyo, Japan) using CAPD with a condenser capacity of 720 μF and a discharge voltage of 100 V in a vacuum and the discharge energy is 3.6 J per pulse.[45] Similarly, Pt NPs are deposited on glassy carbon (GC) substrates (4 mm in diameter, 4 mm in height). Here the condenser capacity, discharge voltage and the discharge energy are 300 μF, 300 V, and 13.5 J per pulse^{-1}, respectively.

8.2.3 Cross-sectional Sample Preparation for HRTEM Observations

The cross-sectional sample preparation of the Pt-deposited GC substrate is performed on a FIB apparatus (FIB-SEM, Hitachi NB5000) with a Ga ion beam of 40 keV. A thin layer of carbon is vacuum-deposited on the surface of Pt-deposited GC substrate to protect the GC surface from the bombardment of Ga ions, using a carbon coater (JEOL Carbon coater JEC-560).

A commercial Pt catalyst, herein referred to as "catalyst A" in this chapter is ultrasonically dispersed into a solution of 0.24 mL water and 0.76 mL IPA. The ultrasonicated catalyst A powder is then deposited on the flat surface of a glassy carbon electrode of 4 mm diameter and 4 mm height. Using the FIB, a thin layer (~500 nm thick) of tungsten (W) is coated on the deposited catalyst A powder; the W-coated catalyst A powder is milled to a thickness ≤100 nm with a Ga ion beam (40 keV) for the observation of Pt NP-CB particle adhesion interfaces.[46]

8.2.4 HRTEM Observations and the Measurement of Particle Diameters

The carbon samples with the Pt NPs are imaged using an HRTEM (JEOL JEM-2800) at an acceleration voltage of 200 kV.

The diameter of a Pt NP is estimated from the binary image area of the Pt NP using the image analysis software HALCON (MVTec Software GmbH, Munich, Germany) and Adobe Photoshop CS6.[45] The simulation of the HRTEM images is performed using the self-developed software based on the eigenvalue method.[47] The magnification of the HRTEM images is calibrated using high-purity silicon (Si) crystals (Optostar Ltd, Tsukuba, Japan).

8.3 Results and Discussion

8.3.1 Pt NPs Deposited on C_{60}FNWs by CAPD

The TEM image of the C_{60}FNWs synthesized by the LLIP method is shown in Figure 8.3a.[44] The C_{60}FNWs exist as bundles, and each C_{60}FNW has a constant diameter along the growth axis. Figure 8.3b shows the diameter distribution

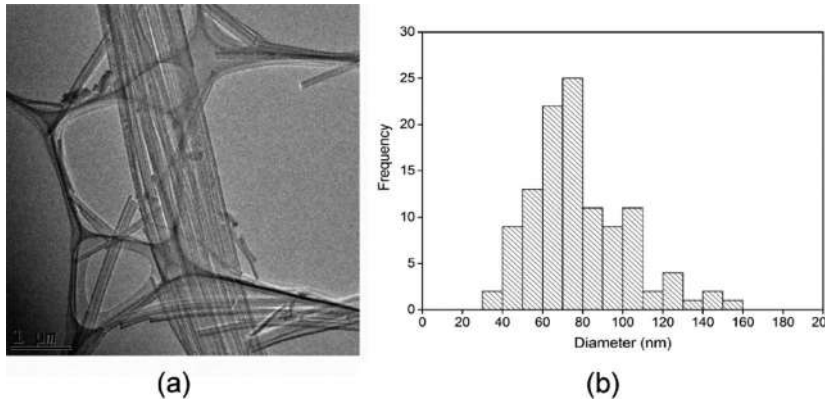

Figure 8.3 (a) Bright-field TEM image of C_{60}FNWs synthesized by the LLIP method using a C_{60}-saturated benzene solution and IPA. (b) Histogram showing the diameter distribution of 112 synthesized C_{60}FNWs. Reproduced from ref. 44 with permission from Taylor & Francis, Copyright 2017.

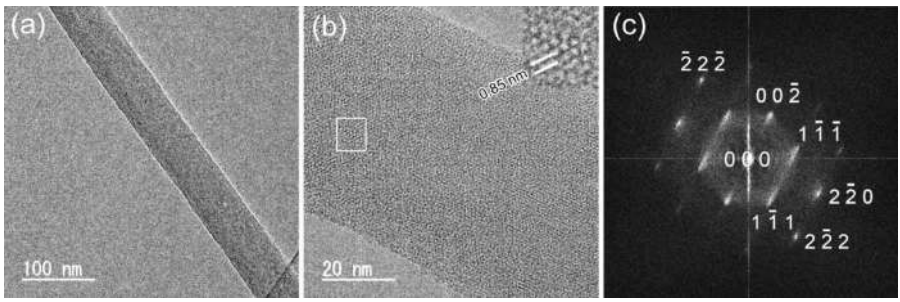

Figure 8.4 (a) Bright-field TEM image of an as-synthesized C_{60}FNW with a diameter of 64 nm, (b) HRTEM image of part of the C_{60}FNW in (a). An enlarged HRTEM image of the rectangular area in (b) is shown in the inset. (c) FFT pattern for the HRTEM image of (b). Reproduced from ref. 44 with permission from Taylor & Francis, Copyright 2017.

of the synthesized C_{60}FNWs, where the mean diameter of the 112 C_{60}FNWs is measured to be 79 ± 24 nm (mean ± standard deviation). A mixture of benzene and IPA is found to be very efficient to synthesize smaller sized C_{60}FNWs, whereas, a mixture of toluene and IPA results in C_{60}FNWs with diameters larger than 300 nm.[42] Thus, the diameter of C_{60}FNWs depends on the combination of the good solvent and the poor solvent of C_{60}.

Figure 8.4a shows the bright-field TEM image of a C_{60}FNW having a diameter of 64 nm. Figure 8.4b shows the HRTEM image of the C_{60}FNW, and Figure 8.4c shows the fast Fourier transform (FFT) pattern for the HRTEM image given in Figure 8.4b. The $00\bar{2}$, $1\bar{1}\,\bar{1}$ and $2\bar{2}0$ spots are indexed to the fcc structure

of C_{60}.[44] The inset is an enlarged image of Figure 8.4b and it shows the $(1\bar{1}1)$ lattice plane spacing of 0.85 nm measured from the $2\bar{2}2$ spot of Figure 8.4c. The FFT spots are streaked. The streaked FFT spots indicate that a high density of planar faults is introduced parallel to the growth axis of the C_{60}FNW.[44]

Figure 8.5 a shows an example of a bright-field TEM image for a C_{60}FNW deposited with Pt NPs. The HRTEM images of Pt NPs in the rectangles (Figure 8.5b) are shown in the enlarged images of Figure 8.5c, where Pt (111) or (200) lattice fringes are indicated.

The lattice constant, a (nm) of an fcc Pt crystal can be calculated using eqn (8.4).

$$a = d(hkl)(h^2 + k^2 + l^2)^{1/2} \tag{8.4}$$

where $d(hkl)$ denotes the interplanar spacing of $(h\ k\ l)$ lattice planes.

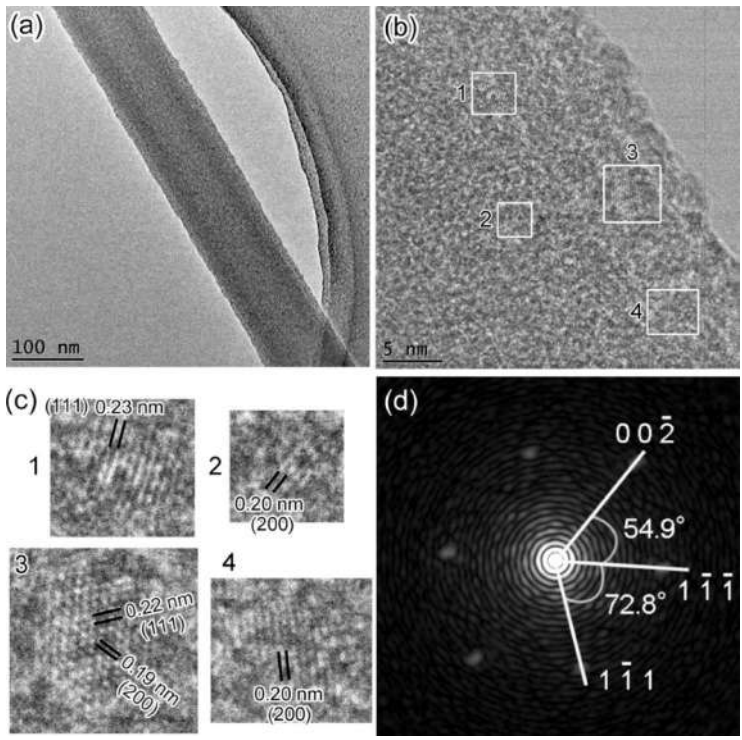

Figure 8.5 (a) Bright-field TEM image of a C_{60}FNW with a diameter of 114 nm with deposited Pt NPs. (b) HRTEM image of Pt NPs on the C_{60}FNW in (a). (c) Enlarged images of the Pt NPs labeled 1–4 in (b). (d) FFT pattern for Pt NP 3 in (c). Reproduced from ref. 44 with permission from Taylor & Francis, Copyright 2017.

Figure 8.5d shows the FFT pattern of the HRTEM image of Pt NP 3 of (c), indicating that the Pt NP is imaged along the [110] zone axis. In fcc crystals, the interplanar angle between $(1\bar{1}\,\bar{1})$ and $(00\bar{2})$ planes is 54.7° and that between $(11\bar{1})$ and $(1\bar{1}\,\bar{1})$ planes is 70.5°. However, the observed angles of 54.9° and 72.8° deviate from those values. This example shows that the Pt NP is anisotropically strained from the correct fcc lattice.

The lattice constant, a (fcc crystal), for each Pt NP is calculated from the {111} or {200} single lattice fringes of the Pt NP seen in the HRTEM images of 239 Pt NPs deposited on the C_{60}FNWs.

Figure 8.6a shows the distribution of the measured lattice constant, a, plotted as a function of the diameter of the 239 Pt NPs. The mean lattice constant of the 239 Pt NPs deposited on C_{60}FNWs is calculated to be $a = 0.391 \pm 0.013$ nm, which is smaller by 0.33% compared to the bulk Pt with $a_0 = 0.39231$ nm. No correlation is observed between a and the diameter of Pt NPs. The strong scattering in the lattice constants must be due to the anisotropic distortion of Pt NPs from the fcc structure. This will be discussed in the section on Pt NPs deposition on graphite particles. Figure 8.6b shows the size distribution of the 239 Pt NPs used in Figure 8.6a, where the mean diameter of the Pt NPs is measured to be 2.7 ± 0.8 nm.

Figure 8.7a shows the distribution of fcc lattice constants calculated using the data from Figure 8.6. Figure 8.7b shows the lattice strain distribution of the Pt NPs. The lattice strain, S, is defined as $100(a - a_0)/a_0$ (%). Among the 239 Pt NPs analyzed, 131 Pt NPs are compressed, and 108 Pt NPs are expanded, *i.e.*, 54.8% of the Pt NPs are compressed, and 45.2% of the Pt NPs are expanded. The mean compressive strain, S(compressive), and the mean expansive strain, S(expansive), are calculated to be -2.6 ± 1.7% and 2.6 ± 2.2%, respectively.

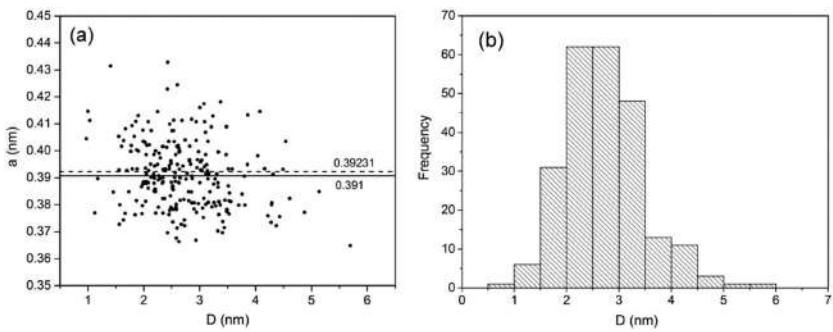

Figure 8.6 (a) Relationship between the diameter D (nm) of 239 Pt NPs deposited on C_{60}FNWs and their fcc lattice constant a (nm). (b) Histogram showing the distribution of D of the Pt NPs deposited on the C_{60}FNWs. Reproduced from ref. 44 with permission from Taylor & Francis, Copyright 2017.

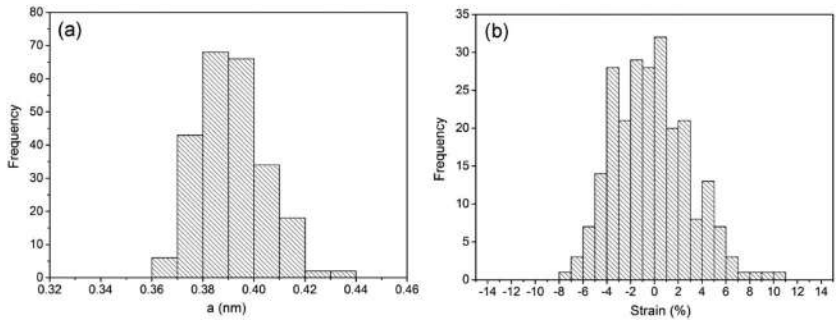

Figure 8.7 Distributions of the fcc lattice constant *a* (nm) of (a) 239 Pt NPs deposited on C_{60}FNWs. (b) Lattice strain distributions of the 239 Pt NPs deposited on C_{60}FNWs. Reproduced from ref. 44 with permission from Taylor & Francis, Copyright 2017.

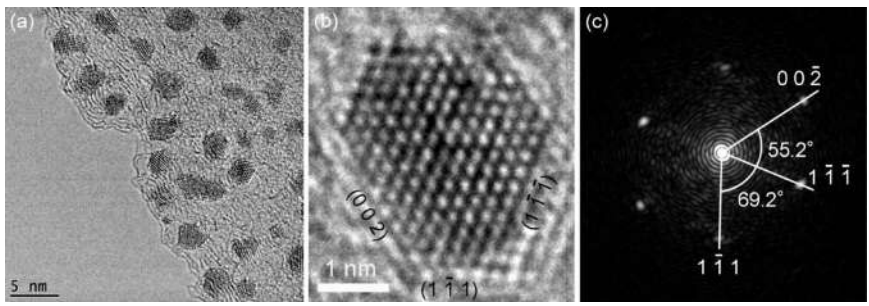

Figure 8.8 (a) HRTEM image of Pt particles deposited on a graphite particle. (b) HRTEM image of a Pt NP taken along [110] zone axis. (c) FFT pattern for the Pt NP image (a). Reproduced from ref. 45 with permission from Springer Nature, Copyright 2017.

8.3.2 Pt NPs Deposited on Graphite Particles by CAPD

Figure 8.8a shows the HRTEM image of the Pt NPs deposited on a graphite particle. Pt NPs with polygonal morphologies are seen. Figure 8.8b shows an example of the Pt NP prepared by CAPD that is surrounded by {111} and {100} facets.

The lattice constants of Pt NPs are measured from the HRTEM images of the Pt NPs deposited on the graphite particles. Two approaches are conducted for the measurement. One method assumes that the Pt NPs have fcc symmetry like the case of the Pt NPs deposited on C_{60}FNWs, and as a result, no correlation is observed between the fcc lattice constant and the particle diameter of the analyzed 285 Pt NPs. The mean *a* was calculated to be 0.388 ± 0.015 nm, which is smaller by ~1% than the Pt bulk *a* = 0.39231 nm.

The scattering of the lattice constant increases with a decrease in the particle diameter. The strong scattering in a implies that the crystal structure of Pt NPs is anisotropically distorted from the pristine fcc crystal structure. The *S*(compressive) is calculated to be −3.3 ± 2.4% and the *S*(expansive) is calculated to be 2.9 ± 2.3%, *i.e.*, 65.3% of the Pt NPs are compressed and 34.7% of the Pt NPs are expanded. The mean diameter of the 285 Pt NPs is 2.2 ± 0.7 nm. The Pt NPs with diameters between 2.0 and 2.5 nm are most frequently seen. Shao *et al.* reported that this size of 2.2 nm exhibited the maximum mass activity of ORR by the Pt NPs in a $HClO_4$ solution.[48]

The second method for the lattice constant of Pt NPs is as follows. An HRTEM image of the Pt NP with an electron beam incident direction [110] is shown in Figure 8.8b. The Pt NP is surrounded by {111} and {200} habit planes. The FFT pattern for the lattice image of the Pt NP shown in Figure 8.8c is observed to slightly deviate from the fcc structure like the case of the Pt NP on the C_{60}FNW. Taking into account of this anisotropic straining, the Pt NP is approximated to a monoclinic lattice, and the *a* for the monoclinic structure is calculated following the least square method (3.2), where $d_0(hkl)$ means the (*hkl*) interplanar spacing measured from the observed lattice image.

$$F(a,b,c,\beta) \equiv (d_0(1\bar{1}1) - d(1\bar{1}1))^2 + (d_0(1\bar{1}\bar{1}) - d(1\bar{1}\bar{1}))^2 + (d_0(002) - d(002))^2 \quad (8.5)$$

The optimized parameters for Figure 8.8c are a = 0.375 nm, b = 0.375 nm, c = 0.385 nm, and β = 90.0°. Eqn (8.5) is performed for 100 Pt NPs, and the results are shown in Figure 8.9.

The lattice parameters show the scattered data and no correlation is observed between the diameter of the Pt NPs and the lattice parameters. The wide variation of the lattice parameters implies that the Pt NPs are randomly distorted irrespective of their particle size. The parameter β is a measure for shear strain, and the values of c/a and c/b are measures for the anisotropic strain. Hence, the strong scattering in the values of β and c show the diversity of anisotropic strain in the Pt NPs. The mean diameter of the 100 Pt is measured to be 2.9 ± 0.7 nm and is slightly greater than the value of 2.2 ± 0.7 nm. The cube root of the unit cell volume ($V^{1/3}$) of the Pt NPs is plotted as a function of the particle diameter (D) in Figure 8.10a. The mean value of $V^{1/3}$ is 0.386 ± 0.008 nm and is ~1.6% smaller than bulk Pt. It is to be noted that the mean lattice constant a = 0.388 ± 0.015 nm is very close to the mean value of $V^{1/3}$ = 0.386 ± 0.008 nm.

The lattice strain is defined as $100(V^{1/3} - a_0)/a_0$ and the distribution of the lattice strain is shown in Figure 8.10b, where the lattice strain of the Pt NPs ranges from a compression of 5.9% to an expansion of 2.8% as compared to bulk Pt. The *S*(compressive) and *S*(expansive) of the Pt NPs are calculated to be −2.5 ± 1.3%, and 1.2 ± 0.8%, respectively.

Among the Pt NPs analyzed, 73% of the NPs are compressed, and 27% of the NPs are expanded. Since the lattice measurement is performed using a single FFT pattern for each Pt NP, the histogram for the strain distribution

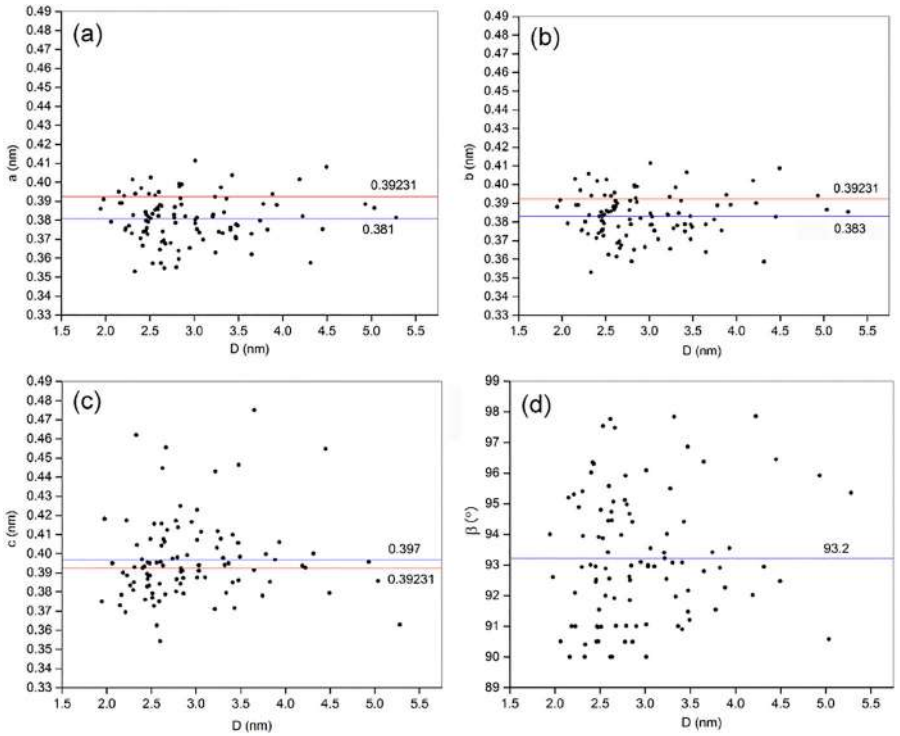

Figure 8.9 Distributions of the monoclinic lattice parameters *a* (a), *b* (b), *c* (c), and *β* (d) plotted as a function of the Pt NP diameter. Reproduced from ref. 45 with permission from Springer Nature, Copyright 2017.

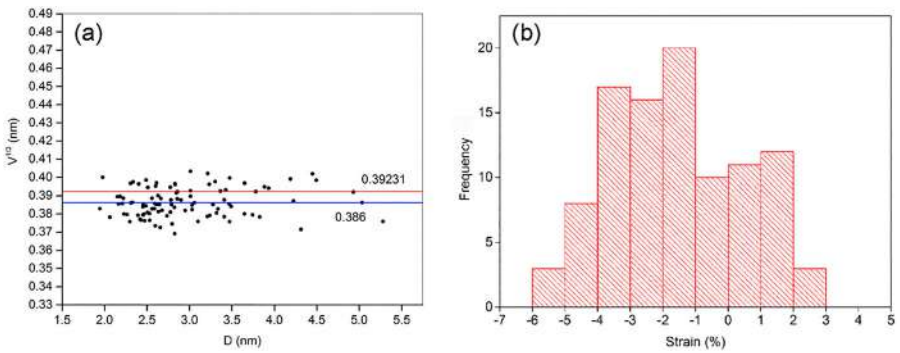

Figure 8.10 (a) Monoclinic unit cell volume of the Pt NPs plotted as a function of diameter *D* (nm). (b) Lattice strain distribution of the Pt NPs deposited on the graphite particles. Reproduced from ref. 45 with permission from Springer Nature, Copyright 2017.

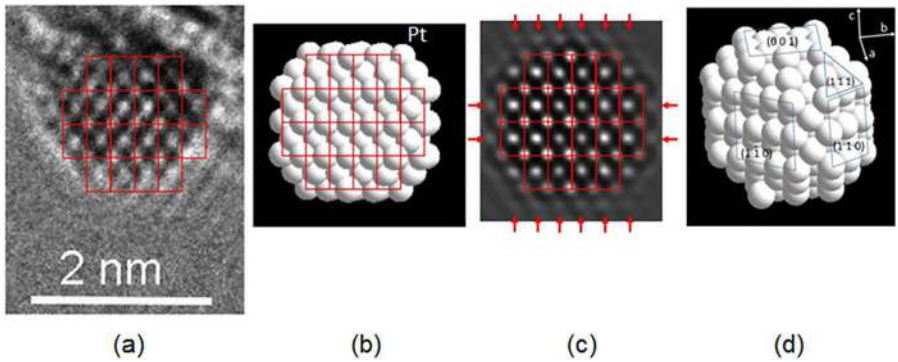

Figure 8.11 (a) HRTEM image of a Pt NP with a size close to 2 nm taken along *a* ⟨110⟩ zone axis. (b) Pt NP model with a size similar to (a). (c) Calculated HRTEM image using the model of (b). (d) Habit planes of the Pt NP model (b). The arrows in (c) show ghost images. Reproduced from ref. 45 with permission from Springer Nature, Copyright 2017.

must be statistically interpreted, *i.e.*, for a single Pt NP, the result implies that 73% of the volume is compressed and the rest is expanded.

Figure 8.11a shows the HRTEM image of a Pt NP with a size close to 2 nm. The optimized lattice constants for this particle are a = 0.386 nm, b = 0.388 nm, c = 0.375 nm and β = 94.0°. Figure 8.11b shows a model of the Pt particle composed of 206 atoms and has a size similar to Figure 8.11a. Figure 8.11c displays a calculated HRTEM image that closely resembles the image of Figure 8.11a. Assuming that the Pt NP in Figure 8.11a is composed of 206 Pt atoms, the volume of the Pt NP is calculated to be 2.89 nm^3. Hence by adopting a spherical model for the Pt NP its diameter is estimated to be 1.8 nm. On the other hand, the particle diameter deduced from the area of the HRTEM image is 1.9 nm. This good coincidence in the grain size estimation supports the appropriateness of the model.

As shown in Figure 8.11d, the surface of the Pt NP model is composed of four {110} planes, four {111} planes, and two {100} planes. The surface energies calculated for Pt are 1.68 J m^{-2} for (110), 1.84 J m^{-2} for (100), and 1.48 J m^{-2} for (111) faces.[49] Although the origin of the anisotropic strains in Pt NPs is not clear, one reason for the anisotropic distortion of the unit cell is due to the different surface energies that become more pronounced with decreasing the Pt particle size.

8.3.3 Pt NPs Deposited on the GC Substrate by CAPD

Figure 8.12a shows an example of the cross-sectional HRTEM image of the GC substrate with the Pt NPs deposited using CAPD. A vacuum-deposited carbon layer and randomly oriented graphitic ribbons with a layer spacing of 0.36 nm are observed along with the layer of the Pt NPs. Figure 8.12b shows the cross-sectional HRTEM image at higher magnification for the Pt NPs

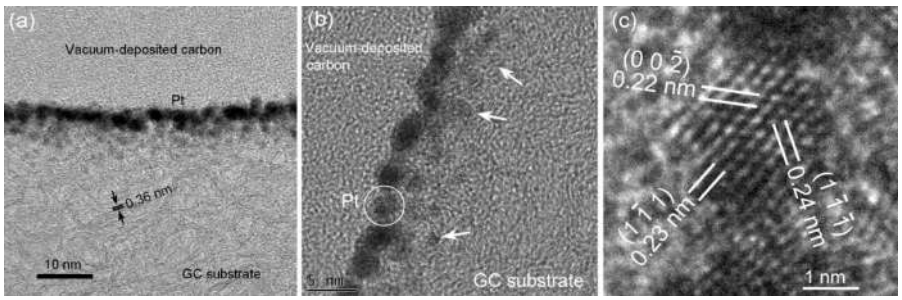

Figure 8.12 (a) Cross-sectional HRTEM image of the GC substrate with the Pt NPs deposited by CAPD. (b) Cross-sectional HRTEM image of the GC substrate with the Pt NPs deposited by CAPD. (b) Magnified image for the circled Pt NP in (c) that was observed along [110] zone axis.

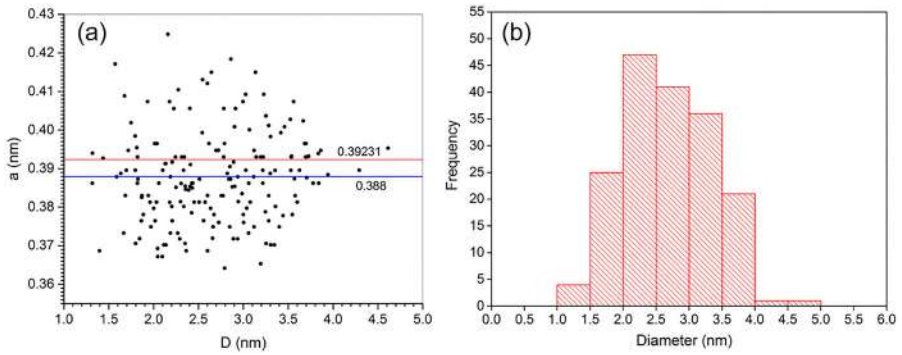

Figure 8.13 (a) fcc lattice constant *a* (nm) of 176 Pt NPs on the GC substrate plotted as a function of diameter *D*. (b) Histogram showing the diameter distribution of the 176 Pt NPs used for the lattice constant measurement (*a*).

deposited on the GC substrate. Nucleation of Pt NPs is observed in the GC substrate as indicated by arrows, showing that high-energy Pt atoms penetrate the GC substrate surface and nucleate inside the substrate. The deposited Pt NPs are shown to be embedded in the matrix of the GC substrate, which indicates that strong bonds are formed between the Pt NPs and the GC substrate.

Figure 8.13a shows the relationship between the diameter and the fcc lattice constant of the Pt NPs deposited on the GC substrate using CAPD, and Figure 8.13b shows the diameter distribution of the 176 Pt NPs analyzed in Figure 8.13a. The mean lattice constant of the analyzed 176 Pt NPs is $a = 0.388 \pm 0.012$ nm, which is very close to $a = 0.388 \pm 0.015$ nm for the Pt NPs deposited on graphite particles. The mean diameter of the 176 Pt NPs is obtained to be 2.7 ± 0.7 nm, which is very close to the values obtained for Pt NPs deposited on C_{60}FNWs (2.7 ± 0.8 nm) and Pt NPs deposited on graphite particles (2.9 ± 0.7 nm) using CAPD. The above observations show that it is

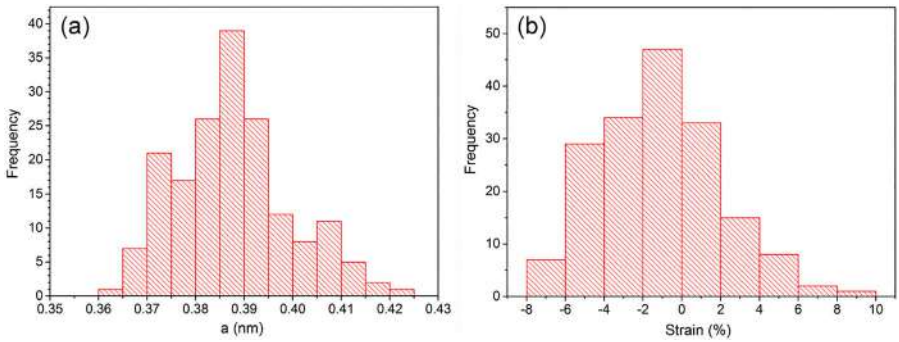

Figure 8.14 (a) Distribution of the fcc lattice constant a (nm) of the 176 Pt NPs. (b) Lattice strain (S) distribution of the 176 Pt NPs.

possible to deposit Pt NPs with mean diameters between 2 and 3 nm using CAPD and can result in mean fcc lattice parameters or $V^{1/3}$ values between 0.386 nm and 0.391 nm.

Figure 8.14 shows the distributions of a (nm) and lattice strain S for the 176 Pt NPs. In the 176 Pt NPs, the compressive strain is 117 and the expansive strain is 59, which means that 66.5% of the Pt NPs are compressed and 33.5% are expanded. The S(compressive) and S(expansive) of the Pt NPs are calculated to be $-2.9 \pm 1.8\%$, and $2.2 \pm 2.0\%$, respectively.

The relationship between the diameter D and the FCC lattice constant, a of the Pt NPs are reported to follow eqn (8.6).[36]

$$a(D) = a_0\left(1 - \frac{1}{1+\sqrt{\alpha GD/\gamma}}\right), \tag{8.6}$$

where γ is the surface energy, G is the shear modulus, and $\alpha = S_{pol}/S_{sph}$ is the shape factor that is defined as the ratio of the surface area of a nonspherical nanoparticle, S_{pol}, to that of a spherical nanoparticle, S_{sph}, where both nanoparticles have an identical volume.[36] Eqn (8.6) implies that the fcc lattice constant of Pt NPs decreases with decreasing particle diameter D, the shape factor α, and with increasing the surface energy γ. In Figure 8.15, the above three data points of mean fcc lattice constants and diameters of Pt NPs are plotted over Figure 2 of ref. 36, which are closely located to the curve of (eqn (8.6)). It is found that the mean values of diameter and fcc lattice constant of the Pt NPs obtained from HRTEM images give a result similar to XRD measurements, although no correlation is observed in the individual results obtained by the lattice image analysis.

8.3.4 Pt NPs Deposited on CB Particles

This section describes the atomic structure of the commercial Pt NPs deposited on CB particles. Figure 8.16a displays a part of the as-received catalyst A powder showing the CB particles with Pt NPs.[50] A Pt NP with cross-lattice

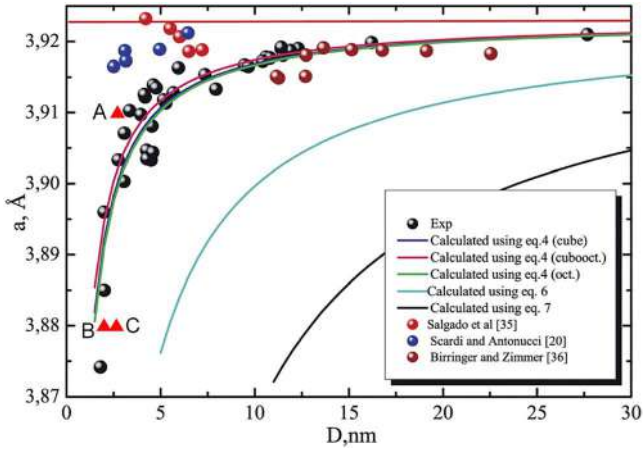

Figure 8.15 Data points of the mean diameter and mean lattice constant of the Pt NPs obtained in A: C_{60}FNWs, B: graphite particles and C: glassy carbon substrates that were plotted on Figure 2 of ref. 36. Reproduced from ref. 36 with permission from the Royal Society of Chemistry.

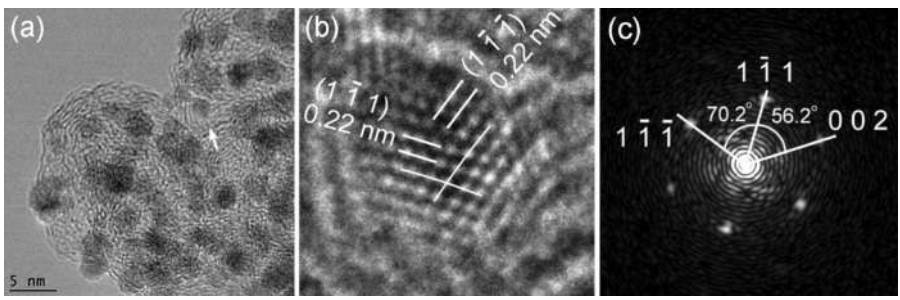

Figure 8.16 (a) HRTEM image of a part of the as-received catalyst A powder, (b) magnified image of the arrowed Pt NP of (a), and (c) FFT pattern for the Pt NP of (b).[50] Reproduced from ref. 50 with permission from IJERA.

fringes indicated by an arrow is displayed in the magnified image of Figure 8.16b. The lattice planes indicated by $(1\bar{1}\bar{1})$ and $(1\bar{1}1)$ are observed to be curved, showing that the Pt NP is inhomogeneously strained.

Figure 8.16c displays an FFT pattern of the strained Pt NP (Figure 8.16b) showing the incident electron beam direction parallel to the [110] zone axis, where the interplanar angles measured are indicated. The angles measured shown in Figure 8.16c are 56.2° between the (002) and $(1\bar{1}1)$ planes and 70.2° between the $(1\bar{1}1)$ and $(1\bar{1}\bar{1})$ planes, slightly deviating from the theoretical angles for an fcc Pt, indicating the anisotropic straining of the Pt NP.

HRTEM images with cross-lattice fringes taken along the [110] zone axes are obtained for 134 Pt NPs from the as-received catalyst A. The anisotropically strained lattices of the Pt NPs are approximated to a monoclinic

structure, and the monoclinic lattice parameters, a (nm), b (nm), c (nm), and β (°) are calculated. Figure 8.17 shows the results of fitting the monoclinic lattice parameters which are plotted as a function of particle diameter (D). The mean lattice parameters are $a = 0.373 \pm 0.016$ nm, $b = 0.377 \pm 0.015$ nm, $c = 0.406 \pm 0.035$ nm, and $\beta = 93.7 \pm 3.5°$. No correlation is observed between the lattice parameters and the particle diameters. The measured lattice parameters are widely scattered, which implies that the lattices are randomly strained irrespective of the particle diameter. The mean diameter of the 134 Pt NPs was measured to be 3.4 ± 0.9 nm.[50]

The cube root of the monoclinic unit cell volume ($V^{1/3}$) for the 134 Pt NPs was determined. Like the previous cases, no correlation is observed between $V^{1/3}$ and the particle diameter as displayed in Figure 8.18.

The mean value of $V^{1/3}$ is 0.384 ± 0.009 nm, which is approximately 2.1% smaller than the lattice parameter $a_0 = 0.39231$ nm of the bulk Pt and is smaller than the values of $V^{1/3}$ and a of the Pt NPs prepared by CAPD. The value of $V^{1/3}$ ranged from 0.356 nm to 0.405 nm. As shown in Figure 8.19, the lattice strain of the Pt NPs, defined as $100(V^{1/3} - a_0)/a_0$ (%), is found to range from −9.2% compression to 3.2% expansion. The 134 Pt NPs exhibit

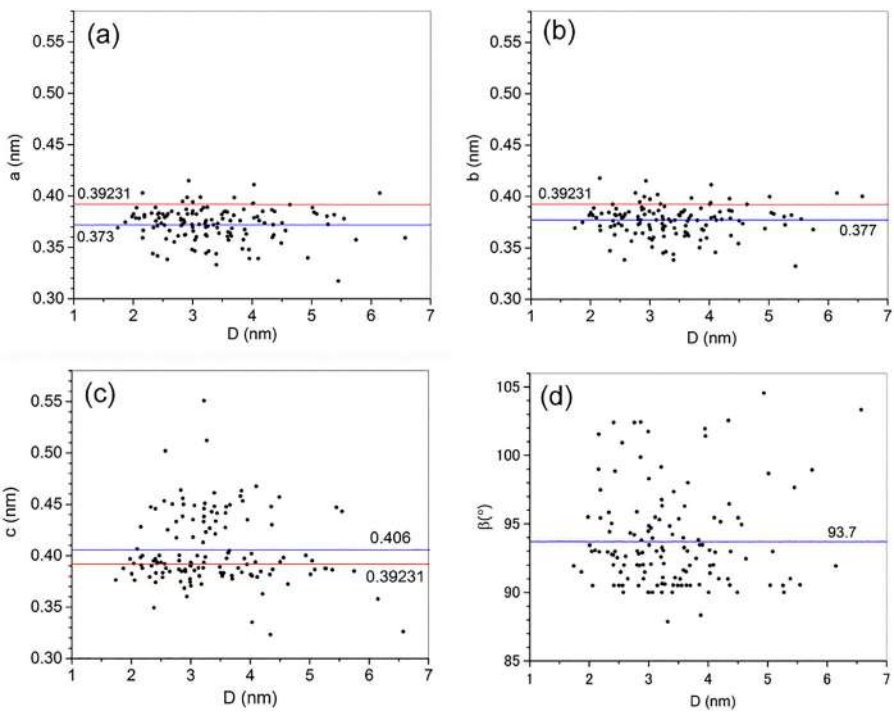

Figure 8.17 Monoclinic lattice parameters a (nm), b (nm), c (nm), and β (°) of the Pt NPs from the as-received catalyst A powder plotted as a function of diameter D (nm)[50]. Reproduced from ref. 50 with permission from IJERA.

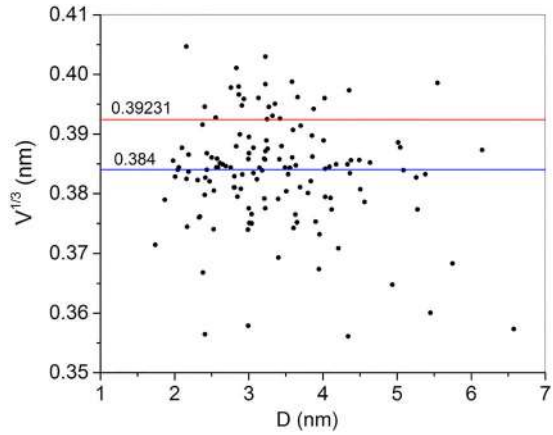

Figure 8.18 Cube root of unit cell volume $V^{1/3}$ (nm) of the Pt NPs from the as-received catalyst A powder plotted as a function of diameter D (nm).[50] Reproduced from ref. 50 with permission from IJERA.

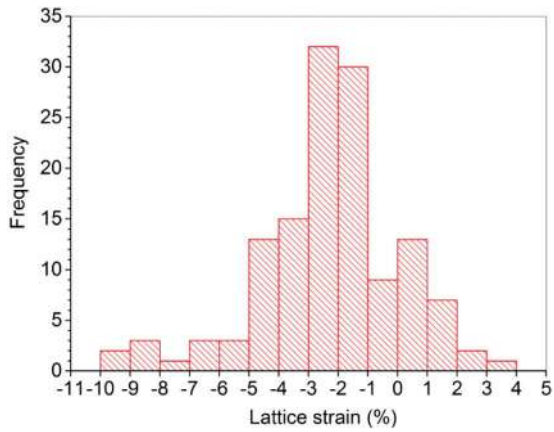

Figure 8.19 Lattice strain distribution of the Pt NPs from the as-received catalyst A powder[50]. Reproduced from ref. 50 with permission from IJERA.

S(compressive) and S(expansive) of $-2.9 \pm 1.9\%$ and $1.1 \pm 0.8\%$, respectively. The Pt NPs have compressive and expansive strains of 82.8% and 17.2%, respectively.

To know what facets of the Pt NPs appear in catalyst A, side view imaging of Pt NPs is conducted using the FIB-processed sample. A side view image of the Pt NP adhered to the surface of a CB particle is shown in Figure 8.20a. The magnified image in Figure 8.20b shows the $(1\bar{1}\bar{1})$, (001), and $(1\bar{1}1)$ facets of the Pt NP. The (001) facet of the Pt NP is shown to adhere to the CB particle. A simulated image is inserted to roughly estimate the thickness of the Pt NP, assuming a thickness of 4 nm and a defocus value of 10 nm over-focusing

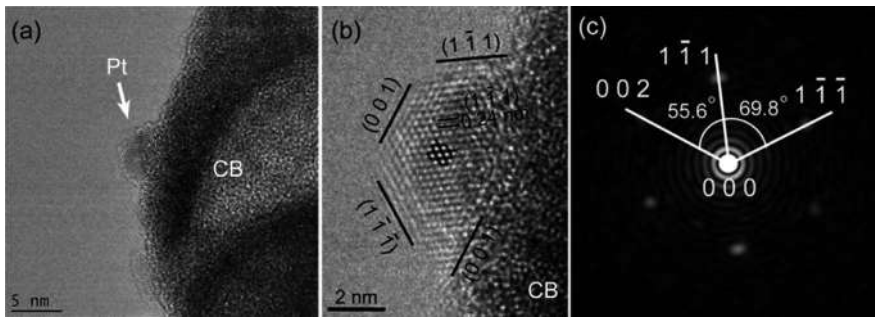

Figure 8.20 (a) HRTEM image of a Pt NP adhered to the surface of CB particle in the FIB-processed catalyst A powder. (b) Magnified image of (a) with an inserted simulated image. (c) FFT image of the Pt NP shown in (b)[50]. Reproduced from ref. 50 with permission from IJERA.

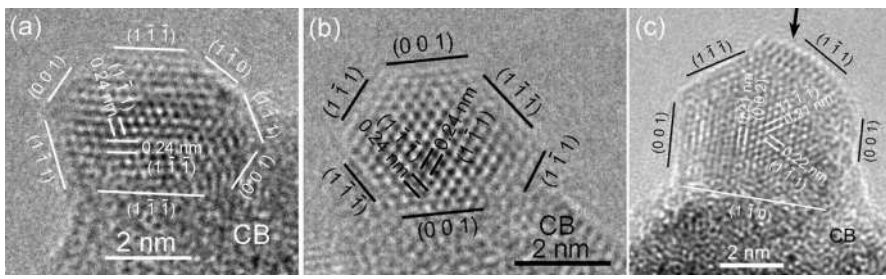

Figure 8.21 HRTEM images of the FIB-processed catalyst A powder. (a) Pt NP adhered to CB surface *via* $(1\bar{1}\bar{1})$ and (001) facets. (b) Pt NP adhered to CB surface *via* $(1\bar{1}\bar{1})$, (001), and $(1\bar{1}1)$ facets. (c) Pt NP adhered to the CB surface *via* $(1\bar{1}0)$ facet[50]. Reproduced from ref. 50 with permission from IJERA.

(spherical aberration coefficient C_s = 0.7 mm). The monoclinic lattice parameters of the Pt NP are determined from the FFT image shown in Figure 8.20c using the least squares method, where values of a = 0.407 nm, b = 0.408 nm, c = 0.423 nm, and β = 92.7° are obtained. The cube root of the unit cell volume is calculated to be 0.413 nm, showing an expansive strain of 5.2%.

Examples of the Pt NPs having the disordered structure are shown in Figure 8.21.[50] Figure 8.21a shows a Pt NP whose $(1\bar{1}\,\bar{1})$, $(1\bar{1}1)$, and (001) facets are adhered to the CB surface. The inside $(1\bar{1}\bar{1})$ lattice planes are heavily distorted and show wavy structures. The Pt NP is surrounded by other $(1\bar{1}1)$, $(1\bar{1}0)$, and $(1\bar{1}\bar{1})$ surface facets. Figure 8.21b shows a Pt NP whose $(1\bar{1}\bar{1})$, $(1\bar{1}1)$, and (001) facets adhere to the CB surface, and the Pt NP is also surrounded by other $(1\bar{1}1)$, (001), and $(1\bar{1}\bar{1})$ surface facets. Figure 8.21c shows a Pt NP whose $(1\bar{1}0)$ facet is adhered to the CB surface, and the Pt NP is also surrounded by (001), $(1\bar{1}\bar{1})$, and $(1\bar{1}1)$ surface facets. The curved facet indicated by the arrow is parallel to the $(1\bar{1}1)$ surface and expands outward.

Figure 8.22a shows the Pt NP with the surface facets indexed and having the joint interface. The $(1\bar{1}1)$ stacking faults are visible in the image, and the streaked FFT spots indicated by the small arrows denote the stacking faults.[46]

The previous examples show that the Pt NPs on CB particles are variously strained and locally deformed, and contain lattice defects such as stacking faults and dislocations. The various inhomogeneous distortions of Pt NPs give rise to the scattered lattice parameter data. Comparing the lattice images of the Pt NPs chemically deposited in solution and that deposited by CAPD, CAPD can produce the Pt NPs with better crystallinity and smaller size distributions.

As shown in the previous examples, the {111}, {100}, and {110} facets of Pt NPs are observed to adhere to the CB particles of catalyst A. Next, to know what facets are likely to adhere to CB particles and what facets of Pt NPs are likely to appear, 128 Pt NPs adhering to CB particles of the FIB-processed catalyst A powder are analyzed and the frequency of each facet is plotted as a function of the planar packing fraction of Pt crystals in Figure 8.23, where 462 facets of Pt NPs and 167 Pt NP-CB adhesion interfaces are analyzed.

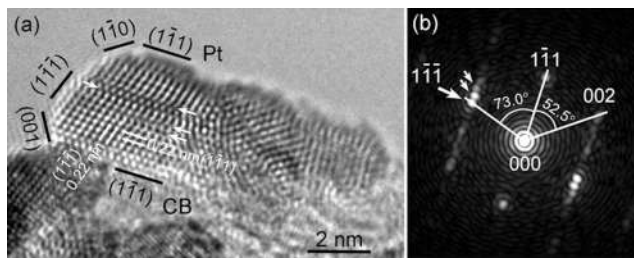

Figure 8.22 (a) Side view HRTEM image of a Pt NP adhered to a CB particle. The $(1\bar{1}1)$ planar faults are indicated by the arrows. (b) FFT image of the Pt NP in (a). Reproduced from ref. 46 with permission from Elsevier, Copyright 2018.

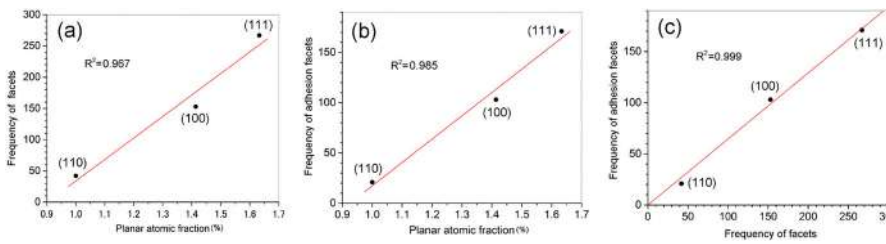

Figure 8.23 (a) Observed frequency of Pt NP facets plotted as a function of Pt planar packing fraction (%). (b) Observed frequency of Pt NP-CB adhesion facets plotted as a function of Pt planar packing fraction (%). (c) Observed frequency of Pt-CB adhesion facets plotted as a function of the observed frequency of Pt NP facets.[50] Reproduced from ref. 50 with permission from IJERA.

The ratio of planar packing fractions of Pt crystals is 1.633:1.414:1 in the (111), (100), and (110) lattice planes. Figure 8.23a and b show respectively the observed frequency for the Pt NP facets, and Pt NP-CB adhesion facets plotted as a function of planar packing fraction, where a good linear correlation is observed between the two parameters. The order of observed frequency of facets is consistent with the surface energy, σ, of the Pt crystals which decreases in the order of $\sigma(110)$, $\sigma(100)$, and $\sigma(111)$.[51] This result implies that the facets with the lower surface energy can appear more frequently. However, this result does not necessarily imply that the (111) facets of Pt NPs have a higher affinity for the CB surfaces, as the frequency of Pt NP-CB adhesion facets is strongly proportional to the frequency of Pt NP facets in Figure 8.23c. This suggests that the observed frequency order might have been brought about by a probabilistic factor. Besides, the strong correlation between the frequency of facets and the frequency of adhesion facets of Pt NPs suggests that the Pt NPs are randomly oriented to the surface of CB particles.

Next, to elucidate the influence of the CB surface energy on the strain of Pt NPs, the (111) interplanar spacing is measured as a function of the orientation relative to the Pt NP-CB adhesion interface for the 97 Pt NPs observed in the FIB-processed catalyst A powder.

The orientation of the (111) plane is defined as shown in Figure 8.24a, using the azimuth angle, θ (°). Figure 8.24b shows the strain distribution of the 175 (111) planes of Pt NPs measured as a function of the azimuth angle, θ, where the (111) interplanar strain (%) is defined as $100(d_{111}\text{-}0.2265)/0.2265$ for the spacing d_{111} of a (111) lattice plane. The mean strain is compressive and is calculated to be −1.6%. We note that no correlation can be observed between the (111) interplanar strain and the azimuth angle, indicating that the (111) interplanar strain does not depend on the orientation of the (111) planes. Reported surface energy values of CB particles range from 20.55 mJ m^{-2} to 96.20 mJ m^{-2},[52] while the mean surface energy of the (111), (100) and

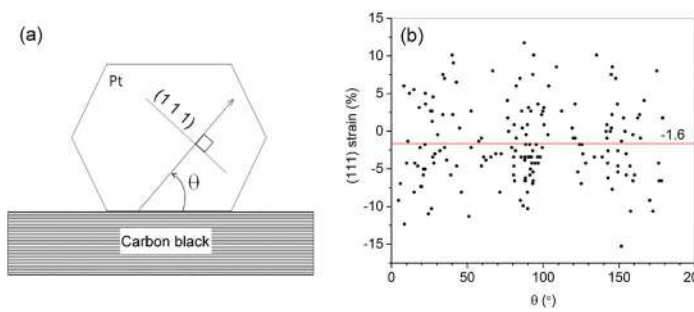

Figure 8.24 (a) Azimuth angle, θ (°), normal to the (111) plane of a Pt NP measured from the Pt NP-CB adhesion interface. (b) (111) interplanar strain (%) of Pt NPs from the FIB-processed catalyst A powder plotted as a function of azimuth, θ.[50] Reproduced from ref. 50 with permission from IJERA.

(110) facets of Pt crystals is 2.49 ± 0.26 J m^{-2}.[51] Hence, it is conjectured that the surface tension caused by CB particles must be negligibly small to induce anisotropic strains in Pt NPs and that the Pt NPs are spontaneously strained and hardly influenced by the surface tension of CB particles. However, further investigations are necessary to reveal the influence of the CB surface on the lattice parameter of Pt NPs by using clearly defined Pt-CB interfaces in the future.

8.4 Summary

The structure of the Pt NPs deposited on four different carbon substrates, C_{60}FNWs, graphite particles, GC substrate, and CB particles are analyzed on the atomic scale. Anisotropically strained Pt NPs are commonly observed in all the samples. This anisotropic straining causes the scattering of the lattice constants of the Pt NPs when measured as a function of diameter. Of the Pt NPs, ~55% (C_{60}FNW) and ~80% (catalyst A) were compressively strained and the other parts were expansively strained. The mean compressive strain ranged from −3.3% to −2.5%, and the mean expansive strain ranged from 1.1% to 2.9% in all the samples. As compared to the Pt NPs of commercial CB catalysts, CAPD can produce the Pt NPs of smaller sizes with narrow size distributions. No correlation was observed between the lattice constant and the Pt NP diameter in all the samples from the HRTEM observations. However, the mean fcc lattice constant or cube root of unit cell volume of the Pt NPs showed smaller values in all the samples than the fcc lattice constant of bulk Pt. Moreover, the data points of the mean fcc lattice constants and mean diameter of the Pt NPs deposited on the C_{60}FNWs, the graphite particles, and the GC substrate are closely located to the data points obtained by the synchrotron XRD measurements.

It was observed that the Pt NPs are randomly attached to the CB particles in catalyst A. The frequency of the adhesion interfaces decreased in the order of (111), (100), and (110) facets in catalyst A, which is consistent with the (111), (100), and (110) planar packing fractions of Pt, and is consistent with the surface energy, σ, of Pt crystals which decreases in the order of σ(110), σ(100), and σ(111). It is also conjectured that the Pt NPs are spontaneously strained and hardly influenced by the CB particle substrates. However, the Pt NPs deposited on the GC substrate by CAPD are embedded in the GC substrate, which suggests the formation of strong bonds of Pt NPs with the GC substrate by the anchoring effect. These are the outstanding characteristics of the Pt NPs prepared by CAPD and is quite different from the Pt NPs chemically deposited on CB particles.

Acknowledgements

A part of this study was conducted at the NIMS Microstructural Characterization Platform and the Advanced Characterization Nanotechnology Platform of the University of Tokyo. This study is based on the results obtained from a

project commissioned by NEDO. The authors are grateful to Mr Makoto Mori (TUS), Mr Yuta Nakajo (TUS), Mr Yorito Nishizawa (TUS), Mr Kazuki Kasahara (TUS), Ms. Yurie Inoue (TUS), and Mr Tomoki Shinohara (TUS) for their help in preparing the carbon samples with Pt NPs deposited using CAPD.

References

1. H. W. Kroto, J. R. Heath, S. C. O'Brien, R. F. Curl and R. E. Smalley, *Nature*, 1985, **318**, 162.
2. K. Miyazawa, Y. Kuwasaki, A. Obayashi and M. Kuwabara, *J. Mater. Res.*, 2002, **17**, 83.
3. K. Miyazawa, *J. Nanosci. Nanotechnol.*, 2009, **9**, 41.
4. K. Miyazawa, *Sci. Technol. Adv. Mater.*, 2015, **16**, 013502.
5. K. Miyazawa, *Fullerene Nanowhiskers*, Pan Stanford Publishing Pte Ltd, Singapore, 2011.
6. K. Miyazawa, Y. Ochiai, M. Tachibana, T. Kizuka and S. Nakamura, *Fullerene Nanowhiskers*, Pan Stanford Publishing Pte Ltd, Singapore, 2nd edn, 2019.
7. K. Ogawa, T. Kato, A. Ikegami, H. Tsuji, N. Aoki and Y. Ochiai, *Appl. Phys. Lett.*, 2006, **88**, 112109.
8. T. Wakahara, K. Miyazawa, O. Ito and N. Tanigaki, *J. Nanomater.*, 2016, **2016**, 2895850.
9. J. Won Ko and W. Bae Ko, *Fullerenes, Nanotubes, Carbon Nanostruct.*, 2018, **26**, 851.
10. X. Zhanga, Y. Qu, G. Piao, J. Zhao and K. Jiao, *Mater. Sci. Eng., B*, 2010, **175**, 159.
11. J. Yang, H. Lim, H. C. Choi and H. S. Shin, *Chem. Commun.*, 2010, **46**, 2575.
12. V. Krishnan, Y. Kasuya, Q. Ji, M. Sathish, L. K. Shrestha, S. Ishihara, K. Minami, H. Morita, T. Yamazaki, N. Hanagata, K. Miyazawa, S. Acharya, W. Nakanishi, J. P. Hill and K. Ariga, *ACS Appl. Mater. Interfaces*, 2015, **7**, 15667.
13. K. Minami, Y. Kasuya, T. Yamazaki, Q. Ji, W. Nakanishi, J. P. Hill, H. akai and K. Ariga, *Adv. Mater.*, 2015, **27**, 4020.
14. F.-Y. Hsieh, L. K. Shrestha, K. Ariga and S. Hsu, *Chem. Commun.*, 2017, **53**, 11024.
15. H. Takeya, K. Miyazawa, R. Kato, T. Wakahara, T. Ozaki, H. Okazaki, T. Yamaguchi and Y. Takano, *Molecules*, 2012, **17**, 4851.
16. H. Takeya, T. Konno, C. Hirata, T. Wakahara, K. Miyazawa, T. Yamaguchi, M. Tanaka and Y. Takano, *J. Phys.: Condens. Matter*, 2016, **28**, 354003.
17. K. R. Kunniyoor, T. Richter, P. Ghosh, R. Lietzow and H. Neumann, *IEEE Trans. Appl. Supercond.*, 2018, **28**, 9000111.
18. M. Tachibana, K. Kobayashi, T. Uchida, K. Kojima, M. Tanimura and K. Miyazawa, *Chem. Phys. Lett.*, 2003, **374**, 279.
19. A. K. Geim and K. S. Novoselov, *Nat. Mater.*, 2007, **6**, 183.
20. R. Heyrovska, *Graphene*, 2016, **5**, 35.

21. G. Yang, L. Li, W. B. Lee and M. C. Ng, *Sci. Technol. Adv. Mater.*, 2018, **19**, 613.
22. P. J. F. Harris, *Philos. Mag.*, 2004, **84**, 3159.
23. S. Sharma, *Materials*, 2018, **11**, 1857.
24. R. L. McCreery, *Chem. Rev.*, 2008, **108**, 2646.
25. J. S. Speck, *J. Appl. Phys.*, 1990, **67**, 495.
26. I. D. Gimba, A. S. Abdulkareem, A. Jimoh and A. S. Afolabi, *J. Appl. Chem.*, 2016, **2016**, 2684919.
27. J. Mishler, Y. Wang, R. Mukundan, J. Spendelow, D. S. Hussey, D. L. Jacobson and R. L. Borup, *Electrochim. Acta*, 2012, **75**, 1.
28. S. Sepp, K. Vaarmets, J. Nerut, I. Tallo, E. Tee, H. Kurig, J. Aruväli, R. Kanarbik and E. Lust, *Electrochim. Acta*, 2016, **203**, 221.
29. K. Miyabayashi and M. Miyake, *Electroanalysis*, 2016, **28**, 1.
30. R. Izumi, Y. Yao, T. Tsuda, T. Torimoto and S. Kuwabata, *J. Mater. Chem. A*, 2018, **6**, 11853.
31. L. Khotseng, *Electrocatalysts for Fuel Cells and Hydrogen Evolution*, Oxygen Reduction Reaction, IntechOpen Limited, London, 2018, ch. 2, DOI: 10.5772/intechopen.79098.
32. G. I. Finch and S. Fordham, *Proc. Phys. Soc.*, 1936, **48**, 85.
33. F. W. C. Boswell, *Proc. Phys. Soc., London, Sect. A*, 1951, **64**, 465.
34. J. E. Lennard-Jones and B. M. Dent, *Proc. R. Soc. London, Ser. A*, 1928, **121**, 247.
35. C. R. Berry, *Phys. Rev.*, 1952, **88**, 596.
36. I. N. Leontyev, A. B. Kuriganova, N. G. Leontyev, L. Hennet, A. Rakhmatullin, N. V. Smirnova and V. Dmitriev, *RSC Adv.*, 2014, **4**, 35959.
37. W. H. Qi, B. Y. Huang, M. P. Wang, Z. M. Yin and J. Li, *J. Nanopart. Res.*, 2009, **11**, 575.
38. J. X. Wang, H. Inada, L. Wu, Y. Zhu, Y. Choi, P. Liu, W.-P. Zhou and R. R. Adzic, *J. Am. Chem. Soc.*, 2009, **131**, 17298.
39. P. Strasser, S. Koh, T. Anniyev, J. Greeley, L. More, C. Yu, Z. Liu, S. Kaya, D. Nordlund, H. Ogasawara, M. F. Toney and A. Nilsson, *Nat. Chem.*, 2010, **2**, 454.
40. Y. Agawa, H. Tanaka, S. Torisu, S. Endo, A. Tsujimoto, N. Gonohe, V. Malgras, A. Aldalbahi, S. M. Alshehri, Y. Kamachi, C. Li and Y. Yamauchi, *Sci. Technol. Adv. Mater.*, 2015, **16**, 024804.
41. S. Hinokuma, S. Misumi, H. Yoshida and M. Machida, *Catal. Sci. Technol.*, 2015, **5**, 4249.
42. K. Miyazawa and K. Hotta, *J. Cryst. Growth*, 2010, **312**, 2764.
43. K. Miyazawa, C. Hirata and T. Wakahara, *J. Cryst. Growth*, 2014, **405**, 68.
44. K. Miyazawa, M. Yoshitake and Y. Tanaka, *Surf. Eng.*, 2018, **34**, 846.
45. K. Miyazawa, M. Yoshitake and Y. Tanaka, *J. Nanopart. Res.*, 2017, **19**, 191.
46. K. Miyazawa, S. Shimomura, M. Yoshitake and Y. Tanaka, *Mater. Lett.*, 2019, **237**, 96.
47. K. Miyazawa, H. Satsuki, M. Kuwabara and M. Akaishi, *J. Mater. Res.*, 2001, **16**, 1960.
48. M. Shao, A. Peles and K. Shoemaker, *Nano Lett.*, 2011, **11**, 3714.

49. R. Tran, Z. Xu, B. Radhakrishnan, D. Winston, W. Sun, K. A. Persson and S. P. Ong, *Sci. Data*, 2016, **3**, 160080.
50. K. Miyazawa, S. Shimomura, M. Yoshitake and Y. Tanaka, *Int. J. Eng. Res. Appl.*, 2018, **8**, 13.
51. A. Patra, J. E. Bates, J. Sun and J. P. Perdew, *Proc. Natl. Acad. Sci. U. S. A.*, 2017, **114**, E9188.
52. M. Mezgebe, Q. Shen, J.-Y. Zhang and Y.-W. Zhao, *Colloids Surf., A*, 2012, **403**, 25.

CHAPTER 9

Shedding a Light on the Colloidal Architectures of a Metal-free Polymeric Semiconductor Graphitic Carbon Nitride

BARIS KUMRU*

Max Planck Institute of Colloids and Interfaces, Department of Colloid Chemistry, Am Mühlenberg 1, 14424 Potsdam, Germany
*E-mail: baris.kumru@mpikg.mpg.de

9.1 Introduction

Nowadays, it is inevitable that humankind is facing many problems, one of the most significant is that the energy sources (fossil-based) that fuel our technology and lifestyle are rapidly depleting, as well as their consumption leading to global pollution. Increased consumption of any kind is leading to increased irreversible pollution by many means, molding an endless cycle that harms the health of the planet and therefore the health of humankind. The search for sustainable energy resources has brought about the idea to utilize natural sources, *i.e.* energy harvesting from the sun, wind and water. The idea to employ sunlight as an energy source has highlighted semiconductor materials to be integrated into energy

Nanoscience & Nanotechnology Series No. 55
Concepts and Design of Materials Nanoarchitectonics
Edited by Omar Azzaroni and Katsuhiko Ariga

Published by the Royal Society of Chemistry, www.rsc.org

generation devices as well as transform the chemistry to a light-assisted analog by semiconductor photocatalysis. To date, many semiconductor materials are available, *i.e.* TiO_2, CdS, ZnO, V_2O_5, Si, ZnS, perovskites and some conjugated polymers.[1] Comprehending the sustainability and toxicity problems of the aforementioned semiconductors (as well as restricted tunability) has led to the rise of an old polymeric material, namely polymeric graphitic carbon nitride (g-CN). The structure of the polymer has been discussed in the previous century,[2] but its photocatalytic activity was reported in 2009, which brought about the 'spring' for the material and intensive research has bloomed since then.[3]

g-CN is a metal-free semiconductor that shows activity in the visible light range, and reductive pathways through excited electrons or oxidative pathways through remaining holes are available through photoredox chemistry.[4] g-CN is composed of polymeric structures with the ideal C_3N_4 formula. g-CN is synthesized from nitrogen-rich and abundant precursors, such as melamine and urea, through thermal condensation. g-CN has pronounced stability in strong acidic and basic environments and exhibits high thermal stability up to 630 °C. Due to its conjugated structure, it is composed of stacked sheets (unless special morphologies are made) with a negative overall surface charge. g-CN is easy to handle and non-toxic and thus it is highly promising to be employed as a semiconductor, despite suffering from high recombination rates, low surface area, processability, low conductivity, *etc.* Even though the price of g-CN is estimated to be only a few euros per kilogram, very surprisingly it is not fully commercially available, and the ones on the market by BASF and TCI are significantly costly. It is very important to understand the properties of g-CN, its synthesis and its applications to widen its industrial viability.

Mother nature is the best architect when it comes to design functional and durable materials, and centuries of evolution have furnished advanced systems which we are realizing and being inspired by today. The concept of nanoarchitectonics offers a philosophical understanding at the atomic scale for a rational design of nano-mesoscale materials that are inspired from life,[5,6] and what is better than to merge the nanoarchitectonics concept with g-CN chemistry?

Throughout the literature survey of g-CN, it is quite easy to get lost due to the fact that g-CN is not a single material but represents a family of materials. Ease of tunability is a striking advantage of g-CN over other semiconductors, and this renders possibilities for the discovery of novel structures and functionalities. In this chapter, the synthesis of g-CN architectures will be summarized in a simplified version by the basis of the nanoarchitectonics concept. The first part will introduce the synthetic strategies of g-CN materials and their corresponding properties. Following that, g-CN composites will be briefly enclosed and as a final subchapter an overview of emerging g-CN applications will be presented.

9.2 Carbon Nitride Formation

To be introduced to carbon nitride chemistry, a fundamental understanding of the synthesis of g-CN materials is of vital importance. In the following section, a guide to g-CN synthesis and insights into colloidal engineering will be presented.[7] g-CN synthesis can simply be seen as 'condensation polymerization' that takes place at high temperatures. Its fundamentally facile synthesis has served a great purpose for the development of the field. Despite some recently developing methods such as hydrothermal synthesis, here a traditional oven-based synthesis will be stressed.

9.2.1 Carbon Nitride Synthesis – Simplified

As previously mentioned, ease of synthesis is an important factor; as a start, one needs an oven with a nitrogen atmosphere. In the presence of air, the product undergoes oxidation, which is not desired. Nitrogen-rich monomers such as melamine and urea can be put in an aluminum crucible, capped and placed in an oven with a nitrogen protected atmosphere. An important hint for the g-CN formation mechanism can be attained by a simple adjustment of this experiment – one can obtain very little product if the same reaction is conducted without capping. A conclusion from this simple experiment is that the carbon nitride fabrication does not proceed *via* condensation of the solid from solid-state, but the recondensation of the decomposed gas molecules (from the precursor) to form the thermodynamically stable solid species that is g-CN. The interplay of the gas and solid phases in a closed crucible at condensation temperatures is the key factor driving g-CN synthesis. Therefore, one can imagine g-CN as a high-temperature vitrimer-like polymer.

Typical g-CN formation is reported to occur around 550 °C, which is slightly below the ceiling temperature of g-CN (600 °C). This temperature slightly favors polymerization over depolymerization, which can be rephrased as the formation of g-CN solid from the gas condensates is favored. Temperature here plays a role in the degree of polymerization, such that in the literature many temperature based formattings can be found. Lower condensation temperatures (*i.e.* 450 °C) result in a 'polymer with low molecular weight', therefore oligomeric CN can be obtained (Figure 9.1).[8] As a result, a small sheet size can be achieved, and the edges of g-CN are decorated with non-condensed hydrophilic groups (*i.e.* $-NH_2$). Products from such temperature programming exhibit quantum-dot-like behavior thanks to their incomplete condensation, therefore they possess high water dispersibility and high photoluminescence. It is possible to encounter the utilization of oligomeric g-CN as imaging agents. On the contrary, due to their high defect structure, they possess none to extremely low photoactivity.

Additionally, simple synthesis can be tailored *via* a monomer choice.[9] A typical requirement for g-CN synthesis is to start from nitrogen-rich precursors. Melamine, dicyandiamide and urea are prime candidates for simple g-CN synthesis, in which the synthesis occurs through different pathways. When

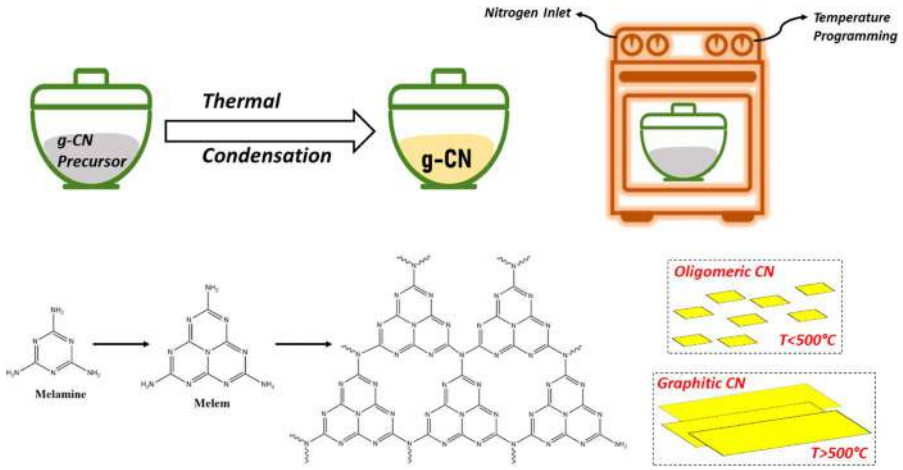

Figure 9.1 Brief schematic description of CN synthesis (tri-*s*-triazine repeating unit of g-CN is depicted).

a monomer contains a heteroatom, this heteroatom could be integrated into the final g-CN material, providing a feasible modification method is used. Heteroatoms can influence the electronic environment of CN heterocycles, thus tailored photophysical properties can be obtained by the utilization of heteroatom-containing precursors (*i.e.* thiourea).[10]

As a general drawback, g-CN suffers from a low surface area which hinders many potential applications due to restricted light absorption. In order to expand the surface area of g-CN, one can use templating methods at this stage.[11] Growth of g-CN around an inert template during condensation is the main approach, where the template can be removed subsequently. Hard templates such as silica nanoparticles and SBA-15 and soft surfactant templates such as Pluronic 123 and Triton X-100 can be of help at this stage. The high acidic stability of g-CN grants the usage of hard templates, however the removal of the template requires effort and hinders scalability. The main disadvantage of utilizing soft templates is the possible decomposition of the templates resulting in impurities in the g-CN structure.

As explained in this section, getting started with g-CN requires a fundamental understanding of the formation mechanism, simple experiments and a cheap setup. A combination of these results in feasible synthesis conditions that grasp the attention from laboratory to industry scale. From the nanoarchitectonics perspective, it is possible to obtain nanosheets, nanodots, porous sheets and nanocapsules *via* simple synthesis methodologies. In order to confirm the structure of the final g-CN products, typical analyses compromise UV-Vis absorption, photoluminescence (PL), infrared (FT-IR), combustive elemental analysis and X-ray diffraction (XRD). More advanced techniques such as transmission electron microscopy (TEM), scanning electron microscopy (SEM), X-ray photoelectron spectroscopy (XPS), ultraviolet

photoelectron spectroscopy (UPS), time-resolved fluorescence, electron paramagnetic resonance (EPR) and some electrochemical measurements (*i.e.* electrochemical impedance spectroscopy) can be performed in order to comprehend the properties of the synthesized g-CN.

9.2.2 Carbon Nitride Synthesis – Advanced

This chapter will present a journey through advanced tricks for g-CN synthesis. The high temperatures that are required for g-CN synthesis eliminate the possibility of employing solvents, which otherwise would induce more control on g-CN synthesis. The salt-melt method (also known as ionothermal) offers a great aid for this problem. Eutectic salt mixtures can melt and provide a solvent-like environment during g-CN synthesis, thus one can picture this process similar to a precipitation polymerization. A g-CN precursor can be ground with an eutectic salt mixture and polymerized subsequently. The resulting g-CN from ionothermal synthesis possesses an altered character compared to g-CN from simple synthesis. This type of g-CN typically consists of poly(triazine imide) or poly(heptazine imide) repeating units with a cation located in the pores (Figure 9.2). Furthermore, as the condensation takes place in a solvent-like media, resulting g-CNs are highly ordered, hexagonal packed and crystalline.[12] Not only the physical, but also photophysical properties vary by salt-melt synthesis, and the interest in recent years has forged ionothermal g-CNs as a new class of material, known as K or Na-PHI (potassium or sodium – poly(heptazine imide)), with a reduced bandgap and more

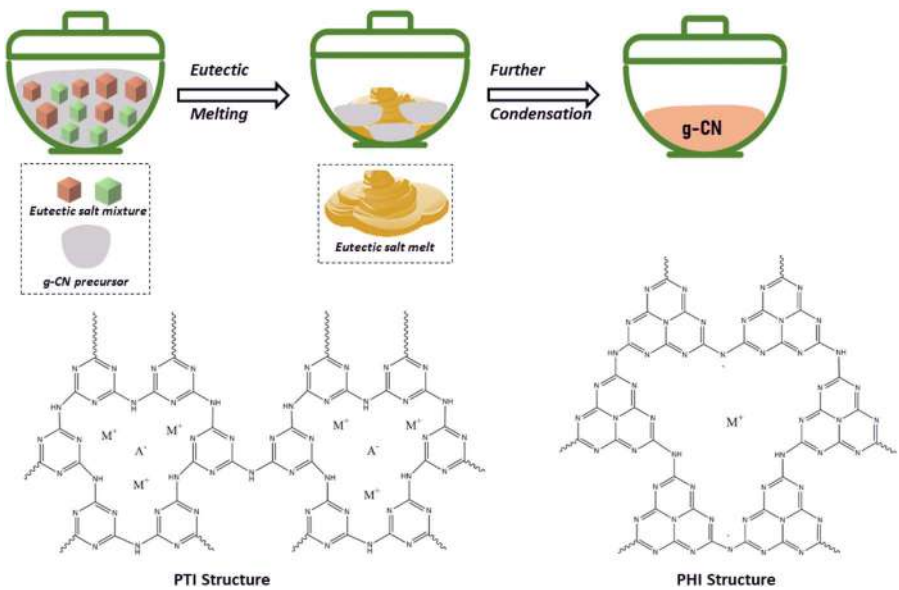

Figure 9.2 Synthetic route for the ionothermal synthesis of g-CN and resulting g-CN structures (poly(triazine imide) and poly(heptazine imide)).

oxidative power compared to simple g-CNs. At this stage, tunability parameters include the type of eutectic salt mixture, the composition of the eutectic salt mixture, monomer choice and temperature programming. Typical eutectic salt mixtures include LiCl–KCl, LiBr–KBr, NaCl–KCl in which the cation remains in the pores of g-CN and the anion can tune the gallery height of the final g-CN material.[13] In addition, great potential is revealed once the cation is exchanged with a hydrogen, forming a polaronic state of g-CN. One can encounter the utilization of monomers such as dicyandiamide, melamine, urea and guanazole in the literature.

Another strategy to attain advanced g-CN is a monomer supramolecular assembly method.[14] Employed monomers have a great potential to form supramolecular organization in suitable solvents owing to their hydrogen bonding capacity. This methodology allows comonomer utilization and serves a purpose for modifying g-CN structure, from repeating unit motifs to edge (boundary) modification (Figure 9.3). Herein, monomers can be guided to form intermolecular interactions by the means of hydrogen bonding and hydrogen-halogen interactions, or acid–base complexes can be constructed as well. Generally, monomers are mixed in a solvent overnight to form the supramolecular complex, and dried subsequently. It is highly important to characterize the supramolecular complex in such projects. Condensation of such ordered precursor results in g-CN materials with facile tunability. First of all, as the monomer structure is represented in the repeating units of g-CN, a choice of electronically diverse monomers will significantly influence the properties of the final g-CN. Another distinct advantage of this method is edge modification, it is depicted that the growth from trifunctional amine or hydroxy groups are the key for g-CN formation, so if one elects a bifunctional or monofunctional comonomer this will have a terminating property thus decorate the edge of the g-CN sheets.[15] The first illustration of the concept

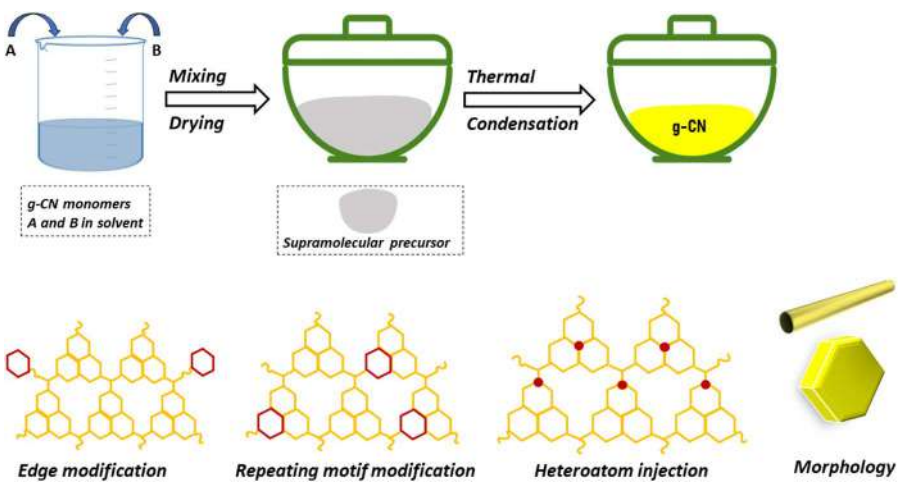

Figure 9.3 Schematic overview of supramolecular monomer assembly method and possible modifications rendered by this approach.

started with a cyanuric acid–melamine supramolecular complex.[16] Then many articles have followed the effect of complex formation in different solvents in varied pH values, which elucidated the influence on the final g-CN materials. Cyanuric acid–melamine–barbituric acid, melamine–3-amino-1,2,4-triazole, cyanuric acid–melamine–2,4,6-triaminopyrimidine assemblies are utilized in the literature. Melamine-boric acid complex is favored to synthesize boron carbon nitride (BCN) materials. Assembly of monomers in the presence of phosphoric acid has been a popular choice as resulting g-CNs are reported to possess hexagonal rod-like structure with phosphorus doping. The choice of monomers with heteroatoms at this level can be used to integrate heteroatoms on the repeating units of final g-CN. Edge modification of g-CN was reported from the supramolecular assemblies of cyanuric acid–melamine–2,4-diamino-6-phenyl-1,3,5-triazine, cyanuric acid–melamine–caffeine and cyanuric acid–melamine–polycyclic aromatic hydrocarbon substituted 1,3,5-triazine.

So far, the synthesis of powder g-CNs were revisited, nevertheless other physical forms are required for some target applications, such as photoelectrochemistry. However, solution-processing of g-CN is not straightforward as g-CN is composed of strongly π-stacked sheets which hinder dispersibility. Therefore, the formation of g-CN films generally relies on *in situ* condensation techniques. One common way is to place the active surface (FTO or ITO) inside the crucible cap, and during the condensation the gas phase from precursor will condense and form g-CN film on the active surface (thermal vapor deposition) (Figure 9.4a).[17] Alternatively, templates such as anodic aluminum oxide (AAO) can be employed, which leads to g-CN formation in the cavities and creating g-CN nanotubes, then can be utilized as membranes.[18]

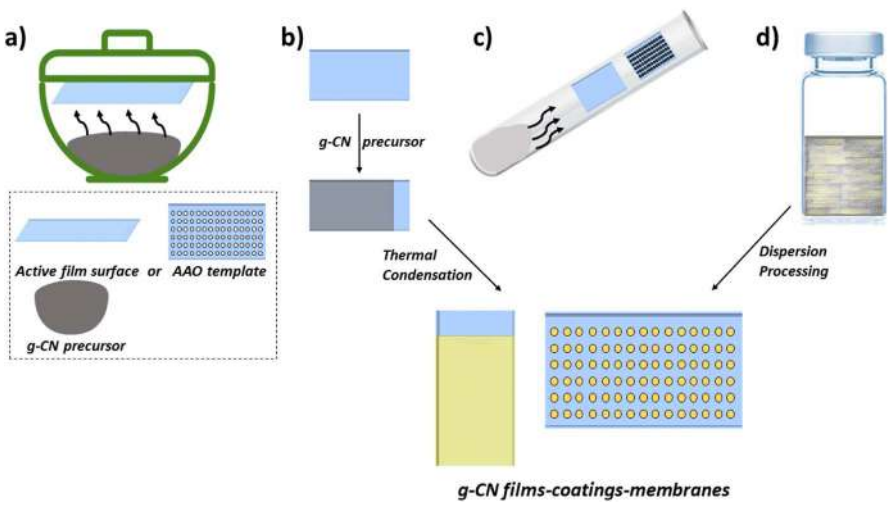

Figure 9.4 Common methods to prepare g-CN films-coatings and membranes: (a) active surface on the lid of a crucible during condensation, (b) condensation of the monomers directly on the active surface, (c) condensation in the tilted glass tube, which a similar concept was evolved to CVD process, (d) dispersion-oriented processing such as spray coating.

The active surface can be covered with the precursor and subsequent condensation exhibits g-CN films as well (Figure 9.4b). In these methods, g-CN films are non-transparent, thick and with a high defect structure, yet still active enough to be integrated into photoinduced applications such as photoelectrochemical cells.[19] Synthesis of peelable g-CN thin film was demonstrated from guanidinium carbonate precursor by vapor deposition in a tilted glass tube, which showed extreme sensitivity to moisture and irradiation thus presented as an actuator (Figure 9.4c).[20] Very recently, highly reproducible synthesis of g-CN thin films by chemical vapor deposition is described.[21] The synthesis relies on chambers at two different temperatures, first chamber vaporizes the monomer, then the vapor is dragged into a second chamber where the thin film formation on active surface takes place at 550 °C. Facile and reproducible synthesis of g-CN thin films hint towards industrial scalability, and films show high refractive index and retain photocatalytic activity.[22] Solution-processing is another approach to form g-CN coatings on surfaces (Figure 9.4d).[23] Organoprocessable g-CN was granted *via* covalent surface photomodification with vinyl thiazole groups which allow successful exfoliation in organic solvents, thus contributes for a scalable g-CN processing method for films and coatings.[24]

Post-modification of g-CN offers a versatile platform that welcomes organic chemistry techniques. First of all, it is quite common to apply acid digestion to g-CN in order to form defects and oxidized analog of g-CN that reaches better aqueous dispersibility. Acid digestion (typically with sulfuric acid or nitric acid at moderate temperatures) provides smaller sheet sizes with enhanced porosity (holey structure) and oxidized structure.[25] Base digestion results in similar material formation as well. The surface of g-CN can be oxidized *via* plasma treatment for the transformation to a hydrophilic g-CN. Edges of g-CN (–NH_2, –OH *etc.*) can be covalently modified *via* amidation, crosscoupling, halogenation and mesylation reactions.[26] Furthermore, the reaction of g-CN with allyl bonds under visible light irradiation is reported to form covalent attachment of allylic molecules to g-CN surface, which provides significant opportunities to tailor g-CN surface from hydrophilic to hydrophobic.[27]

As summarized in this chapter, g-CN consists of a big family with many photoactive members, and facile tunability is a striking advantage of g-CN over other semiconductors. Pre-modification (monomer engineering, ionothermal synthesis *etc.*) as well as post-modification techniques introduce a modular toolbox for g-CN chemistry.

9.3 Carbon Nitride Composites

Even though g-CN is a very appealing class of photocatalyst, the activity of the bulk is often not satisfactory for the target applications. The formation of nano-mesoscale composites grants access to the tailored architectures with advanced catalytic activities. Such composites can be divided into metal and organic composites of g-CN, which will be reviewed briefly.

9.3.1 g-CN Metal Composites

The formation of g-CN-metal composites holds great promise to enhance the activity of g-CN based photocatalysis. As introduced previously, g-CN has a negative surface charge and the repeating units of g-CN contain electron-rich nitrogen potholes which donate interesting surface properties.[28] In order to manufacture metal composites on the g-CN surface, common methods such as solvothermal processing, photodeposition and precipitation are employed, and metals such as Pt, Pd, Au and Ag can be introduced. The purpose of metal loading is to enhance charge separation after g-CN is photoexcited, so that the excited electrons and remaining holes can be accumulated far enough to conduct an efficient photoredox chemistry (Figure 9.5a).[29] However, the efficiency of the system significantly relies on understanding g-CN/metal interfacial properties, likewise the construction of nanoarchitectonic structures.[30] Interface-driven processes can be better understood by doping bimetallic and alloy-like systems on g-CN, and the role of g-CN is being photoexcited and electrons and holes migrate simultaneously to metal dopants. Metals can also be

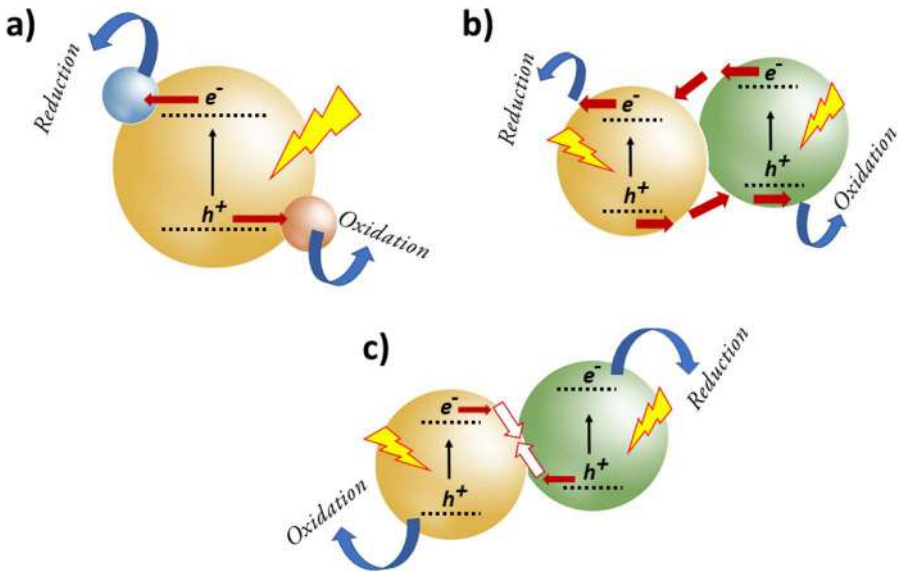

Figure 9.5 Schematic overview of g-CN/metal composites: (a) metal doping on g-CN surface for electron or hole transfer where g-CN is the only photoexcited component. (b) Type-II heterojunction which relies on photoexcitation of both semiconductors and corresponding electron and hole migration by suitable bandgap position matching. (c) Z-scheme which relies on photoexcitation of both semiconductors and recombination of an excited electron from the first semiconductor with the hole from the second semiconductor resulting in an enhanced overall charge separation.

introduced *via in situ* polymerization, which allows scalable and more precise composite synthesis. By this strategy, a metal precursor is mixed with g-CN precursor and polymerized subsequently which results in *in situ* composite formation. However, it is important to note that the metal salts can significantly alter the condensation mechanism and final product, thus this strategy relies on careful selection of precursors. The chemistry above 500 °C in the presence of metals and carbon nitride as a ligand can be very different, and it was recently shown that utilizing melamine-silicotungstic acid complex precursor results in the single-step formation of tungsten single atoms on the carbon nitride framework with positively improved photophysical properties.[31] A similar approach can be extended for Co metal as well.[32] This infant strategy is highly promising to form g-CN-metal composites with high precision, scalability and reproducibility, however coordination chemistry at such high temperatures should be considered.

Another interesting possibility is to form g-CN based heterojunctions. Previously, g-CN was the only photoexcited species and charge migration on metal particles was reported. However, g-CN can be coupled with semiconductors to form heterojunctions with staggered bandgap alignments (Figure 9.5b). Heterojunctions govern enhanced charge migration properties and a possible extended light utilization.[33] Type-II heterojunction of g-CN is based on the principle that both conduction band (CB) and valence band (VB) of g-CN are either higher or lower than the ones of a second semiconductor. This energy difference creates band bending and resulting in a built-in electric field at the interface. If the light is sufficient to excite only one semiconductor, then the second one could be applied as an electron/hole acceptor. These nanoarchitectonics are generally constructed *via* solvothermal processing, and to date many g-CN and metallic semiconductor composites are available for type-II heterojunctions, and their corresponding photocatalytic performances can be found.[34] However, interfacial charge migration in type-II heterojunctions causes energy loss as well as decreased redox activities. To overcome this problem, Z-scheme nanoarchitectures are becoming popular (Figure 9.5c). This strategy relies on utilizing two semiconductors with similar bandgap positions, where an excited electron of one recombines with the hole of the second one and thus inherent charge separation is achieved without restricted redox capacity.[35] There are three types of Z-scheme architectures that generally take place *via* solvothermal processing: (i) utilizing an aqueous redox mediator, (ii) utilizing a solid mediator, and (iii) direct Z-scheme, and the details of each architecture with g-CN can be found in the cited literature.[33] Colloidal processes determine the efficiency of the composite, also govern the interfacial properties. Furthermore, g-CN composites *via* MOFs and MXenes are of growing interest.

9.3.2 g-CN Organic Composites

The organic nature of g-CN with abundant aromatic interactions and hydrogen bonding is highly propitious, therefore the formation of g-CN/organic composites can be found in the literature. The first classification can be made on evolving

photocatalytic activity of g-CN by forming heterojunctions and Z-schemes using conjugated polymers such as poly(thiophene)s, poly(aniline)s, and poly(ethylenedioxythiophene)s. From a solution-processing perspective, both g-CN and conjugated polymers possess aromatic structures and thus can form highly stable composites in an easy fashion. Furthermore, such polymers can help to increase the conductivity of the system compared to bulk g-CN. Additionally, constructing dye-sensitized g-CN systems is also a part of g-CN/organic composites which target the enhanced light utilization and corresponding charge separation, and many systems can be found in the literature.[36]

Besides a combination with materials that directly aim to enhance photophysical properties, g-CN can be structured with other organic materials as well.[7] In the literature, there are some reports regarding self-assembly induced processes of exfoliated g-CN with carbon materials and poly(ionic liquid)s. Small aromatic molecules are prone to form π-interaction induced nanoarchitectonics with g-CN as well. Recent trend compromises the integration of g-CN in polymer networks through blending or covalent binding, where a mutual benefit for both materials is observed. Application of g-CN in heterophase systems harnesses the full potential of g-CN in a variety of environments, *i.e.* continuous phase, interface, dispersed phase. Based on the combination of these structures, many novel catalytic pathways are being proposed, and without a doubt that the organic composites of g-CN have a significant influence on the field. Organic composites of g-CN mainly rely on dispersion induced processing, thus it is important to attain knowledge on the colloidal properties of g-CN and enhance its processing in dispersive systems.

9.4 g-CN Applications at a Glance

Once the synthesis of g-CN nanoarchitectonics for nano-mesoscale composites is introduced, it is important to provide a library of applications. It is important to keep in mind that the applications rely on the state of the utilized g-CN (bulk powder, film, dispersion). In this subchapter, a brief survey of the emerging applications of g-CN will be staged.

9.4.1 Photocatalytic Water Splitting

Converting solar energy into hydrogen fuel *via* water splitting has brought attention to semiconductor materials.[37] Overall, water splitting is a complex multi electron-proton transfer reaction, and hydrogen from water reduction and oxygen from water oxidation can be attained. There are many parameters that a catalyst should possess, such as suitable light absorption, high surface area and matching bandgap positions, however the activity of the bulk g-CN is significantly low. Therefore, the addition of a cocatalyst and sacrificial agent is required to boost the activity. Many g-CN composites for hydrogen evolution, oxygen evolution and overall water splitting are available in the literature.[38]

9.4.2 CO_2 Photoreduction

Photocatalytic reduction of CO_2 has sparked significant interest; it would utilize the energy from the sun absorbed by a semiconductor to reduce the greenhouse effect by forming valuable products.[39] It is a multielectron process and CO_2 photoreduction can lead to the formation of products such as formic acid, carbon monoxide, methanol, methane and methanal. g-CN and corresponding composites are favored in such applications which mainly rely on efficient charge separation and matching redox potentials. However, high reduction capacity, high turnover number and product selectivity are strived for.[34] the formation of g-CN heterojunctions plays a critical role here.

9.4.3 Pollutant Degradation

Pollutants, which threaten the health of the planet and human beings, are one of the main dangers that we are facing recently. Pollutant classes include some dissolved organic dyes and heavy metals. As g-CN can form active radicals (such as •OH and $\bullet O_2^-$) under visible light irradiation, high concentrations of radicals can degrade dyes such as Rhodamine B and methyl orange.[40] There are some articles that exhibit the potential of g-CN based composites for antibiotic and pesticide removal as well.[41] Furthermore, toxic heavy metals can be removed through reductive or oxidative pathways.

9.4.4 Organic Synthesis

A plausible photoredox cycle allows reductive and oxidative routes once the charges are well-separated, which can be targeted for selective organic transformations.[42] In addition to selective oxidation–reduction reactions, more complex organic syntheses, such as C–C coupling, C–N crosscoupling, cycloaddition, click chemistry, halogenation, cyclodimerization are available *via* g-CN composite photocatalysts.[43] Coupling g-CN photocatalyst composites with flow chemistry allows the precise synthesis of valuable molecules for a much cheaper price.[44]

9.4.5 Sanitization

The application of semiconductor materials in healthcare has sparked interest, especially in the era of pandemics. The metal free and non-toxic nature of g-CN with a photoactivity under visible light has placed g-CN as a hot candidate to be employed in sanitization-disinfection.[45] Several strategies include forming bulk g-CN film[46] or g-CN based soft hydrogel materials[47] for antibacterial investigations. Furthermore, soluble g-CN oligomer nanoarchitectonics are favored for bioimaging, biosensors and photothermal therapy.[48]

9.4.6 Photovoltaic Devices

Semiconductors are the prime candidates for photovoltaic energy generation devices. The idea to implement g-CN into photovoltaics is therefore not a surprise. Energy generation properties of a bulk g-CN film in polymer based solar cells were reported.[49] Furthermore, integration of g-CN into perovskite based solar cells as a colloidal crystallization modifier[50] or as an electron transport layer[51] shows a great promise for bandgap alignment and enhancing the stability of the solar cell architectures as well as enhancing the overall energy generation efficiencies.

9.4.7 Batteries

A notable interest in constructing g-CN based anodes for battery systems can be encountered in literature. g-CN promises to lower the cost of batteries and enhance ion conductance at the interface preventing dendrimerization of ions. To date, g-CN chemistry for lithium ion batteries, vanadium redox flow batteries, zinc-air battery and supercapacitors are available.[52] From another perspective, g-CN can be a precursor for nitrogen-doped carbon materials.

9.4.8 Polymer Chemistry

Very recently, g-CN has become a popular member of polymer science.[53] It was employed as a heterogeneous photoinitiator for free radical, Fenton-type free radical and controlled radical (atom transfer radical polymerization and reversible addition-fragmentation chain transfer polymerization) polymerizations thanks to its capacity to form active radicals through photoredox chemistry. Furthermore, g-CN dispersions constitute a special interest for polymer chemistry, thus g-CN embedded or g-CN photoinitiated hydrogel synthesis is a hot topic in the soft materials section.[54] Thanks to the surface properties of g-CN, besides bulk polymerization, g-CN can be applied in heterophase polymerizations by the means of emulsion polymerization where g-CN is a stabilizer and photoinitiator. Following that, g-CN can be confined in a specific phase of suspension and emulsion type polymerizations. Additionally, embedding g-CN in polymer networks donates reinforced properties such as enhanced mechanical properties and thermal resistance, hence g-CN based polymer composites are becoming popular as well.[55]

9.4.9 Ion Transport

Special g-CN architectures such as nanorods and membranes possess a temporary change in the net surface charge *via* light illumination.[56] Despite it being a very recent concept, g-CN materials exhibit the potential to be employed as artificial ion pumps for energy generation and sensor technologies.[57]

9.5 Conclusion and Outlook

Eleven years of intense research on catalytic properties of g-CN has demonstrated it as a feasible candidate that can answer the needs as a sustainable semiconductor. Despite the main interest arising from a materials perspective which focuses on the applications, the development of g-CN materials by nanoarchitectonics concepts will have a direct influence on the final properties of the material. Ease of synthesis, the cheap price and non-toxicity render g-CN an attractive material to be investigated, thus many synthetic methodologies are available to date, *e.g.* bulk, ionothermal, and hydrothermal. Monomer engineering admits a synthesis of advanced g-CNs, and the recipes for g-CN films-thin films-membranes-coatings have been reported. Composites of g-CN hold a great promise for high-end applications. Ligand-like properties of g-CN can be profited to attach metals on the surface. Furthermore, organic composites of g-CN can be attained through dispersion-oriented chemistry.

Variation of g-CN materials constituted a shelter for photoinduced applications. Many appealing applications regarding environmental remediation such as water splitting, CO_2 reduction and pollutant degradation are available through g-CN chemistry. Non-toxicity places soluble CN oligomers as promising candidates for bioimaging, whereas g-CN materials are withdrawing attention for light induced sanitization. In addition, g-CN is becoming a milestone in organic synthesis, batteries, optoelectronics, photovoltaics, polymer chemistry as well as optics and photoelectrochemistry.

A positive breeze for the upcoming years is in the air, now there is a better understanding of the synthesis of g-CN materials *via* the nanoarchitectonics philosophy and more science is available for the applications. There are still some parameters that should be significantly enhanced (lowering inherent recombination, increasing conductivity, simple synthesis for enhanced surface area, commercial availability of g-CN, facile processing) but the creativity of scientists will overcome the hurdles. It is highly important to foster a collaborative field rather than a competitive approach to reach an ultimate goal. Additionally, it is important to grasp the interest of the industry and construct an industry-academia bridge to affirm the availability of g-CN materials worldwide and to propose ideas for real-life applications based on the nanoarchitectonics mentality. Therefore, it is anticipated that the g-CN family can answer the needs of society in a near future with the help of nanoarchitectonics concept.

References

1. A. Facchetti, *Mater. Today*, 2007, **10**, 28–37.
2. J. V. Liebig, *Ann. Pharm.*, 1834, **10**, 1–47.
3. X. Wang, K. Maeda, A. Thomas, K. Takanabe, G. Xin, J. M. Carlsson, K. Domen and M. Antonietti, *Nat. Mater.*, 2009, **8**, 76–80.

4. J. Liu, H. Wang and M. Antonietti, *Chem. Soc. Rev.*, 2016, **45**, 2308–2326.
5. K. Ariga and Y. Yamauchi, *Chem. - Asian J.*, 2020, **15**, 718–728.
6. O. Azzaroni and K. Ariga, *Mol. Syst. Des. Eng.*, 2019, **4**, 9–10.
7. B. Kumru and M. Antonietti, *Adv. Colloid Interface Sci.*, 2020, **283**, 102229.
8. H. Liu, X. Wang, H. Wang and R. Nie, *J. Mater. Chem. B*, 2019, **7**, 5432–5448.
9. Z. Zhou, Y. Zhang, Y. Shen, S. Liu and Y. Zhang, *Chem. Soc. Rev.*, 2018, **47**, 2298–2321.
10. L. Zhou, H. Zhang, H. Sun, S. Liu, M. O. Tade, S. Wang and W. Jin, *Catal. Sci. Technol.*, 2016, **6**, 7002–7023.
11. F. K. Kessler, Y. Zheng, D. Schwary, C. Merschjann, W. Schnick, X. Wang and M. J. Bojdys, *Nat. Rev. Mater.*, 2017, **2**, 17030.
12. H. Schlomberg, J. Kröger, G. K. Savasci, M. W. Terban, S. Bette, I. Moudrakovski, V. Duppel, F. Podjaski, R. E. Siegel, J. R. Senker, R. E. Dinnebier, C. Ochsenfeld and B. V. Lotsch, *Chem. Mater.*, 2019, **31**, 7478–7486.
13. S. Y. Chong, J. T. A. Jones, Y. Z. Khimyak, A. I. Cooper, A. Thomas, M. Antonietti and M. J. Bojdys, *J. Mater. Chem. A*, 2013, **1**, 1102–1107.
14. J. Barrio and M. Shalom, *ChemCatChem*, 2018, **10**, 5573–5586.
15. Q. Cui, J. Xu, X. Wang, L. Li, M. Antonietti and M. Shalom, *Angew. Chem., Int. Ed.*, 2016, **55**, 3672–3676.
16. Y.-S. Jun, E. Z. Lee, X. Wang, W. H. Hong, G. D. Stucky and A. Thomas, *Adv. Funct. Mater.*, 2013, **23**, 3661–3667.
17. W. Xiong, F. Huang and R.-Q. zhang, *Sustainable Energy Fuels*, 2020, **4**, 485–503.
18. K. Xiao, B. Tu, L. Chen, T. Heil, L. Wen, L. Jiang and M. Antonietti, *Angew. Chem., Int. Ed.*, 2019, **58**, 12574–12579.
19. G. Peng, L. Xing, J. Barrio, M. Volokh and M. Shalom, *Angew. Chem., Int. Ed.*, 2018, **57**, 1186–1192.
20. H. Arazoe, D. Miyajima, K. Akaike, F. Araoka, E. Sato, T. Hikima, M. Kawamoto and T. Aida, *Nat. Mater.*, 2016, **15**, 1084–1089.
21. P. Giusto, D. Cruz, T. Heil, H. Arazoe, P. Lova, T. Aida, D. Comoretto, M. Patrini and M. Antonietti, *Adv. Mater.*, 2020, **32**, 1908140.
22. P. Giusto, B. Kumru, J. Zhang, R. Rothe and M. Antonietti, *Chem. Mater.*, 2020, **32**, 7284–7291.
23. N. Karjule, R. Phatake, M. Volokh, I. Hod and M. Shalom, *Small Methods*, 2019, **3**, 1900401.
24. B. Kumru, D. Cruz, T. Heil, B. V. K. J. Schmidt and M. Antonietti, *J. Am. Chem. Soc.*, 2018, **140**, 17532–17537.
25. A. Wang, C. Wang, L. Fu, W. Wong-Ng and Y. Lan, *Nano-Micro Lett.*, 2017, **9**, 47.
26. M. Majdoub, Z. Anfar and A. Amedlous, *ACS Nano*, 2020, **14**, 12390–12469.
27. Q. Cao, B. Kumru, M. Antonietti and B. V. K. J. Schmidt, *Macromolecules*, 2019, **52**, 4989–4996.
28. L. Wang, C. Wang, X. Hu, H. Xue and H. Pang, *Chem. - Asian J.*, 2016, **11**, 3305–3328.
29. I. F. Teixeira, E. C. M. Barbosa, S. C. E. Tsang and P. H. C. Camargo, *Chem. Soc. Rev.*, 2018, **47**, 7783–7817.

30. M. Ismael, *J. Alloys Compd.*, 2020, **846**, 156446.
31. B. Kumru, D. Cruz, T. Heil and M. Antonietti, *Chem. Mater.*, 2020, **32**, 9435–9443.
32. Y. Yang, G. Zeng, D. Huang, C. Zhang, D. He, C. Zhou, W. Wang, W. Xiong, B. Song, H. Yi, S. Ye and X. Ren, *Small*, 2020, **16**, 2001634.
33. J. Yi, W. El-Alami, Y. Song, H. Li, P. M. Ajayan and H. Xu, *Chem. Eng. J.*, 2020, **382**, 122812.
34. S. Cao, J. Low, J. Yu and M. Jaroniec, *Adv. Mater.*, 2015, **27**, 2150–2176.
35. B.-J. Ng, L. K. Putri, X. Y. Kong, Y. W. Teh, P. Pasbakhsh and S.-P. Chai, *Adv. Mater.*, 2020, **7**, 1903171.
36. N. Zhang, L. Wen, J. Yan and Y. Liu, *Chem. Pap.*, 2020, **74**, 389–406.
37. G. Zhang, Z.-A. Lan and X. Wang, *Angew. Chem., Int. Ed.*, 2016, **55**, 15712–15727.
38. G. Zhang, Z.-A. Lan and X. Wang, *Chem. Sci.*, 2017, **8**, 5261–5274.
39. H. Shen, T. Peppel, J. Strunk and Z. Sun, *Sol. RRL*, 2020, **4**, 1900546.
40. X. Liu, R. Ma, L. Zhuang, B. Hu, J. Chen, X. Liu and X. Wang, *Crit. Rev. Environ. Sci. Technol.*, 2021, **51**, 751–790.
41. T. O. Ajiboye, A. T. Kuvarega and D. C. Onwudiwe, *Appl. Sci.*, 2020, **10**, 6286.
42. A. Savateev, I. Ghosh, B. König and M. Antonietti, *Angew. Chem., Int. Ed.*, 2018, **57**, 15936–15947.
43. A. Akhundi, A. Badiei, G. M. Ziarani, A. Habibi-Yangjeh, M. J. Munoz-Batista and R. Luque, *Mol. Catal.*, 2020, **488**, 110902.
44. S. Mazzanti, B. Kurpil, B. Pieber, M. Antonietti and A. Savateev, *Nat. Commun.*, 2020, **11**, 1387.
45. W. Wang, C. Zhou, Y. Yang, G. Zeng, C. Zhang, Y. Zhou, J. Yang, D. Huang, H. Wang, W. Xiong, X. Li, Y. Fu, Z. Wang, Q. He, M. Jia and H. Luo, *Chem. Eng. J.*, 2021, **404**, 126540.
46. J. H. Thurston, N. M. Hunter and K. A. Cornell, *RSC Adv.*, 2016, **6**, 42240–42248.
47. J. H. Thurston, A. J. Clifford, B. S. Henderson, T. R. Smith, D. Quintana, K. F. Cudworth, T. J. Lujan and K. A. Cornell, *ACS Appl. Bio Mater.*, 2020, **3**, 1681–1689.
48. G. Liao, F. He, Q. Li, L. Zhong, R. Zhao, H. Che, H. Gao and B. Fang, *Prog. Mater. Sci.*, 2020, **112**, 100666.
49. J. Xu, T. J. K. Brenner, L. Chabanne, D. Neher, M. Antonietti and M. Shalom, *J. Am. Chem. Soc.*, 2014, **136**, 13486–13489.
50. L.-L. Jiang, Z.-K. Wang, M. Li, C.-C. Zhang, Q.-Q. Ye, K.-H. Hu, D.-Z. Lu, P.-F. Fang and L.-S. Liao, *Adv. Funct. Mater.*, 2018, **28**, 1705875.
51. D. Cruz, J. G. Cerrillo, B. Kumru, N. Li, J. D. Perea, B. V. K. J. Schmidt, I. Lauermann, C. J. Brabec and M. Antonietti, *J. Am. Chem. Soc.*, 2019, **141**, 12322–12328.
52. Y. Luo, Y. Yan, S. Zheng, H. Xue and H. Pang, *J. Mater. Chem. A*, 2019, **7**, 901–924.
53. Q. Cao, B. Kumru, M. Antonietti and B. V. K. J. Schmidt, *Mater. Horiz.*, 2020, **7**, 762–786.

54. C. Hu, Y. R. Lin and H. C. Yang, *ChemSusChem*, 2018, **12**, 1794–1806.
55. S. K. Gaddam, R. Pothu and R. Boddula, *Polym. Compos.*, 2020, **41**, 430–442.
56. K. Xiao, L. Chen, R. Chen, T. Heil, S. D. C. Lemus, F. Fan, L. Wen, L. Jiang and M. Antonietti, *Nat. Commun.*, 2019, **10**, 74.
57. K. Xiao, C. Wan, L. Jiang, X. Chen and M. Antonietti, *Adv. Mater.*, 2020, **32**, 2000218.

CHAPTER 10

Crystalline Coordination Polymers Nanoarchitectonics by Epitaxial Growth and Etching

W. ZHANG[a,b], C. J. SHI[a,b] AND M. HU*[a,b]

[a]State Key Laboratory of Precision Spectroscopy, East China Normal University, Shanghai 200241, China; [b]Engineering Research Center for Nanophotonics and Advanced Instrument (MOE), School of Physics and Electronic Science, East China Normal University, Shanghai 200241, China
*E-mail: mhu@phy.ecnu.edu.cn

10.1 Introduction

Crystalline coordination polymers are promising inorganic–organic hybrid coordination materials, which offer incredible freedom for scientists to design advanced materials such as metal–organic frameworks (MOFs) or porous coordination polymers, metal–organic polyhedrons, porous liquids.[1–3] The properties of coordination polymers have been extensively alternated through molecular engineering which operates the assembly of molecular building blocks such as clusters, ligands, atoms, or ions, *etc.*[4] After several decades' academic research, academic and industrial researchers aim to use coordination polymers in applications such as molecules sieving, adsorption, catalysis, energy storage and conversion, and opt-electronics.[4,5] These applications require coordination polymers in the form of a membrane, thin film, colloidal crystal or heterostructures. These structures are simply beyond the molecular scale thus need to be realized

Nanoscience & Nanotechnology Series No. 55
Concepts and Design of Materials Nanoarchitectonics
Edited by Omar Azzaroni and Katsuhiko Ariga

Published by the Royal Society of Chemistry, www.rsc.org

via nanoarchitectonics. In semiconductor industries, epitaxial growth and etching are two main routes.[6,7] In this chapter, we would like to give a tutorial review about the fundamental points and progress of epitaxial growth and etching of the coordination polymers.

10.2 Epitaxial Growth

Epitaxial growth means deposition of crystals on the surface of substrates by atomically precise connection when the lattice structures of the substrate and deposited layer match with each other. Because coordination polymers are basically assembled arrays of nodes and ligands, their epitaxial growth can be realized either by layer-by-layer growth or continuous growth.[8]

10.2.1 Layer-by-layer Growth

Layer-by-layer assembly means sequential deposition of layers on the substrates, which permits the rational introduction of ligands and center nodes. Therefore, atomic control of the thickness of the thin film can be possible.[9,10] In 2010, Makiura *et al.* fabricated coordination polymers nanofilm *via* a layer-by-layer growth.[10] Figure 10.1 shows that copper ions, 5,10,15,20-tetrakis(4-carboxyphenyl)porphyrinato-cobalt(II) (CoTCPP) and pyridine molecules were assembled into a 2D array *via* Langmuir–Blodgett method. The 2D array, which was a single layer of the coordination polymer, was epitaxially deposited onto the silica substrate by the horizontal dipping method. Deionized water was used to remove the residual solution and then deposition of another monolayer onto the deposited single layer. Two layers of the 2D arrays could interact with each other *via* coordination interaction and converted into a bilayer film eventually. Through repeating this process, any film with a desired thickness could be obtained.

In addition to the Langmuir–Blodgett method, the atomic/molecular layer deposition (ALD/MLD) technique is another state-of-art route to fabricate coordination polymer film *via* epitaxial layer-by-layer growth.[11,12] The ALD technique employs gaseous precursors, thus can control the thickness more precisely during assembly. This is highly needed for growing high-quality films. In 2016, Ahvenniemi *et al.* demonstrated the gas-based layer-by-layer growth of coordination polymer film.[12] $Ca(thd)_2$ (thd: 2,2,6,6-tetramethyl-3,5-heptanedione) and terephthalic acid (TPA; 1,4-benzenedicarboxylic acid) were used as the gaseous precursors. The two kinds of molecules can be vaporized at more than 180 °C. A single layer of $Ca(thd)_2$ was firstly anchored on silica substrate as depicted in Figure 10.2. Then, the gaseous TPA interacted with the $Ca(thd)_2$ to form a monolayer of CaTP film as shown in section II of Figure 10.2. The metal-containing gas and the ligand gas were alternately deposited on the substrate in a layer-by-layer manner (section III). A well-crystallized coordination polymer film was obtained finally.

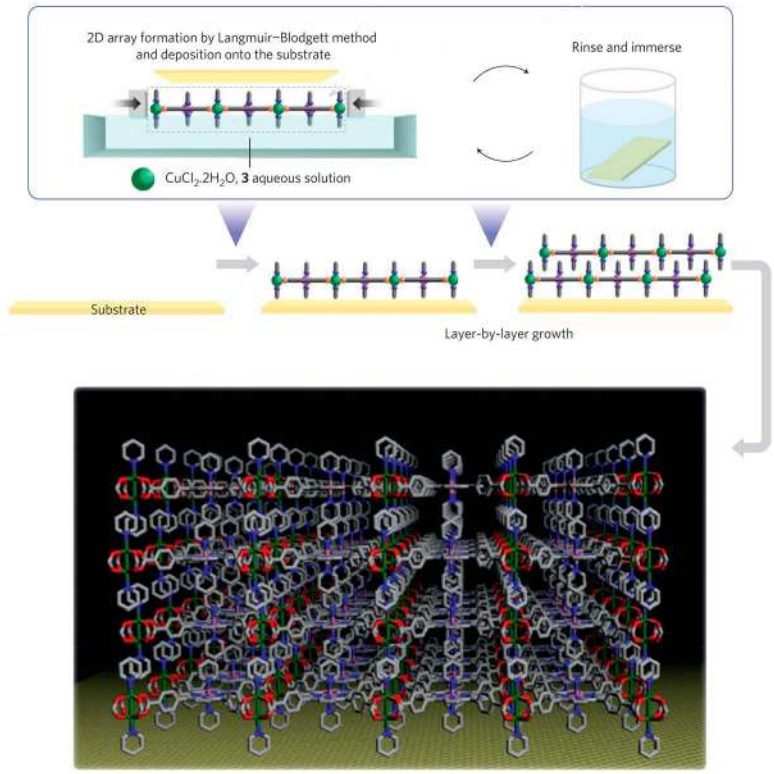

Figure 10.1 Schematic illustration of epitaxial growth of coordination polymer through a Langmuir–Blodgett method and layer-by-layer growth. Reproduced from ref. 10 with permission from Springer Nature, Copyright 2010.

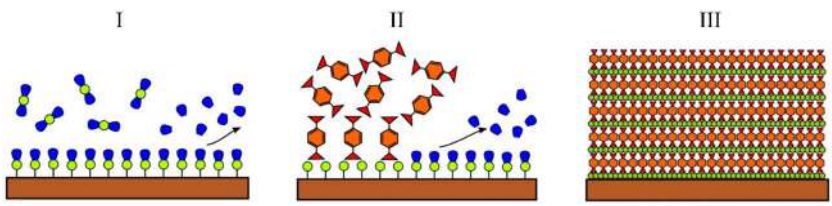

Figure 10.2 Schematic illustration for layer-by-layer epitaxial growth of coordination polymer through atomic/molecular layer deposition (ALD/MLD) technique. Reproduced from ref. 12 with permission from American Chemical Society, Copyright 2016.

The surface of the substrate plays a vital role in epitaxial growth of coordination polymer thin film. By deposition of self-assembled monolayers (SAMs) on the substrate, the substrates could be modified with various organic moieties such as –COOH, –OH, $–NH_2$, and –pyridine.[8,13–16] The terminated groups can be utilized to anchor metal ions or metal clusters, thus forming

a monolayer of the metal nodes. After that, the organic ligands and metal nodes were alternately fixed by subsequent layer-by-layer growth. Notably, in some cases, the type of functional group influenced the orientation of the thin film.[14,15] For instance, the substrate functionalized by –COOH groups was applied to fabricate $Cu_3(btc)_2$ films which oriented perpendicularly to the (100) planes.[14] In the bulk crystal of $Cu_3(btc)_2$, the (100) plane is terminated by the metal-binding btc units, thus the (100) planes could contact with the –COOH terminated surface growing along the perpendicular direction. Modifying the substrate with desired groups is an effective method to construct the highly oriented, crystalline coordination films. In some cases, the resulting highly oriented thin film could display a distinguishing characteristic compared to the intrinsic bulk crystals. For instance, gate-opening behavior during adsorption has been found when the bulk crystal downsized into the highly oriented thin film.[16]

10.2.2 Continuous Growth

Continuous growth on preformed seeds or substrates has been utilized both for colloidal crystals or thin films. The epitaxial growth relies on the surface lattice structure of the selected core crystals or substrates. The lattice mismatch in heteroepitaxial system is the key point to control and influence the epitaxial growth process.

The close lattice structure between substrate and deposited crystal could greatly decrease the required epitaxial growth energy *via* continuous assembly.[17–21] In many coordination polymer systems, the frameworks are constructed by different metal nodes but the same ligands. The frameworks exhibit similar or the same crystal structure. Hence, in these systems, epitaxial growth occurs at the interface as shown in Figure 10.3. The growth of a Co-based Prussian blue analog (purple) was done on the inner framework (green) consisted of the Fe nodes.[20] Lattice matching is the solid foundation for continuous epitaxial growth. The semblable phenomenon has also been reported by other works. For example, Lee *et al.* reported a typical strategy for the construction of sophisticated hetero-compositional coordination polymers (M-MIL-88b, M representing the metal nodes including Fe, In and Ga).[21] Fe-MIL-88b was used as the core crystal for the epitaxial growth of secondary coordination polymers. Owing to the lattice matching between the Ga-MIL-88b and Fe-MIL-88b, a controlled isotropic growth of Ga-MIL-88b on a core crystal of Fe-MIL-88b was observed. The obtained particles present uniform core–shell structures.

In addition to the three-dimensional lattice matching, lattice matching in two directions with the lattice mismatching in the remaining direction was also workable for continuous epitaxial growth.[21–23] In the M-MIL-88b series, the (002) plane of the In-MIL-88b is similar to its analogs such as Ga-MIL-88b and Fe-MIL-88b.[21] However, the corresponding d_{002} of Ga-MIL-88b is about 1.02 nm which is larger than that of In-MIL-88b and Fe-MIL-88b (0.96 nm), indicating a larger *c* parameter. The In-MIL-88b was found to anisotropically grow on the Fe-MIL-88b. The epitaxial growth occurred only along the *c*-direction.

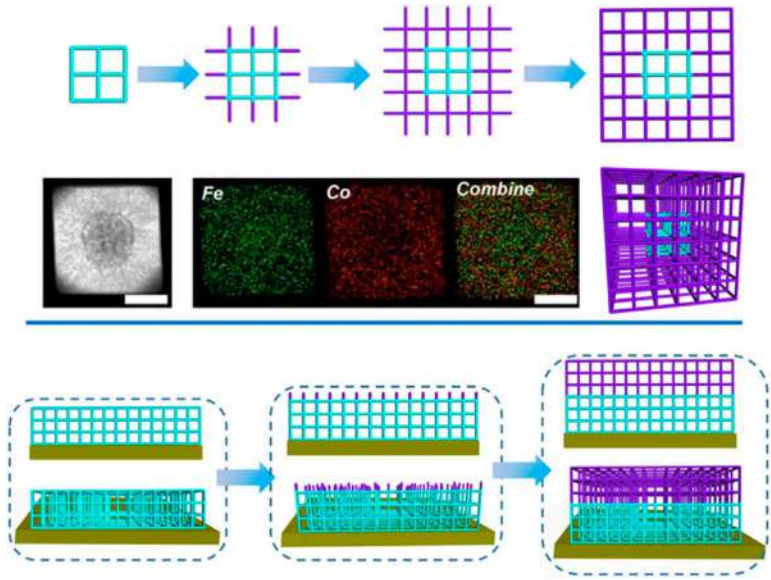

Figure 10.3 Schematic illustration of heteroepitaxial growth of Prussian blue analogs through continuous growth. Reproduced from ref. 20 with permission from John Wiley & Sons, Copyright © 2017 Wiley-VCH Verlag GmbH & Co. KGaA, Weinheim.

Anisotropic epitaxial growth of crystals with the same metal nodes but diverse organic ligands was also observed. A family of tetragonal frameworks, $[M_2(\text{dicarboxylate})_2\ (\text{N ligand})]_n$, has similar parameters along the *a* axis but different parameters along the *c* axis.[22] Epitaxial growth on exposed {001} facets of the inner frameworks along the *c*-direction could be achieved by using various pillar ligands.

The above results reveal that the coordination polymers can easily grow on their derivatives *via* epitaxial continuous growth owing to the lattice matching. Besides these examples, lattice matching also exists in different materials. For example, Falcaro *et al.* found that the crystalline coordination polymer films could be synthesized on inorganic substrates *via* heteroepitaxial growth.[24] In this case, the $Cu_2(BDC)_2$ (*P*4 space group) and copper hydroxide ($Cmc2_1$ space group) have different space groups, but lattice matching still can be found. The $Cu_2(BDC)_2$ has lattice parameters as a = 10.61 Å, b = 5.80 Å, c = 10.61 Å. The copper hydroxide has lattice parameters as a = 2.95 Å, b = 10.59 Å and c = 5.26 Å. Figure 10.4 indicates a comparison of the lattice parameters. The lattice distance in the *a* direction (10.61 Å) of the $Cu_2(BDC)_2$ is close to the lattice distance in the *b* direction (10.59 Å) of the copper hydroxide. Besides, the *b* (5.80 Å) of the $Cu_2(BDC)_2$ is about twice the *a* (2.95 Å) of the copper hydroxide. Therefore, epitaxial growth is permitted as shown in Figure 10.4. As a result, the orientation of the obtained $Cu_2(BDC)_2$ film depended on the orientation of the copper hydroxide. Through aligning

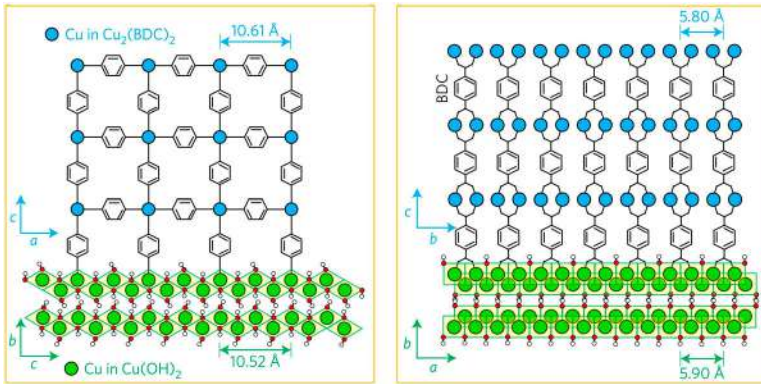

Figure 10.4 Schematic illustration of heteroepitaxial growth of coordination polymer on inorganic substrates based on lattice matching. Reproduced from ref. 24 with permission from Springer Nature, Copyright 2017.

the fluorescent dye into the oriented films, an anisotropic photoluminescent response was observed. The direction-based optical properties are of importance to develop optoelectronic devices in the future.

Epitaxial growth could be possible with a large lattice mismatch. The integration of functional groups such as –COOH, –OH and $–NH_2$ onto the substrate is workable for continuous assembly growth, even when the lattice mismatch is large. In 2017, Ono *et al.* deposited Prussian blue films on glass substrates.[25] Glass is known as disordered material. There is no lattice matching between the Prussian blue and the glass substrates. However, by treating the glass substrate with 3-aminopropyltrimethoxysilane, the surface of the substrates was terminated with $–NH_2$. The strong coordination interaction between the $–NH_2$ groups and the iron ions guaranteed growth of the Prussian blue on the glass substrates. It was always possible to find some $–NH_2$ groups with distances close to the lattice parameters of the Prussian blue in all the randomly distributed $–NH_2$ groups. Therefore, epitaxial growth of the Prussian blue became possible on the glass substrates.

As an extension of the concept of epitaxial growth, shape replicable growth of the coordination polymer is another important trend. In this concept, the coordination polymers replicate the micro/macrostructure of the sacrificing substrate by continuous growth on the substrate. This concept results in no lattice matching but micro/macrostructure matching between the substrate and the deposited coordination polymers. The most-used strategy is called coordination replication.[26,27] In 2012, Reboul *et al.* proposed this method to spatially control the formation of coordination polymers with mesoscopic architecture.[26] Alumina with processability and well-studied dissolving behavior was selected as both the metal source and architecture-directing agent for the growth of the coordination polymers. The alumina substrate gradually dissolved and released the metal precursor. The organic linkers interacted with the Al-containing clusters and formed coordination polymer

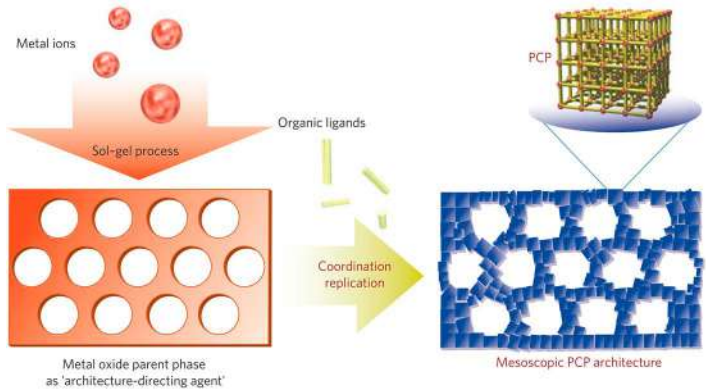

Figure 10.5 Schematic illustration of heteroepitaxial growth of coordination polymer through coordination replication. Reproduced from ref. 26 with permission from Springer Nature, Copyright 2012.

on the residual alumina substrate. Through the coordination replication protocol (Figure 10.5), mesoscopic coordination polymer architectures could be obtained by continuous growth. In addition to solution-based coordination replication, Stassen *et al.* reported a vapor deposition method to fabricate well-crystalized films of ZIF-8 through conversion of metal oxide substrate.[27] Instead of dissolving the sacrificial substrates and re-assembly of the coordination polymer in solution, the sacrificial ZnO_2 was directly reacted with the gas-phase ligands. The obtained ZIF-8 was directly deposited on the ZnO_2 substrates, and the produced water molecules were taken away by the gas flow.

10.3 Etching

Like in architectonics, it is possible to build up a house by attaching blocks. A reversed process can also be performed to remove the blocks. When the coordination polymers are under specific conditions where the coordination bonds are unstable, the nodes and ligands can disassemble by forming stronger bonds with other species.[28] Actually, partial disassembling of the coordination polymer has been utilized in coordination replication as well. This is the fundamental origin for the etching of the coordination polymers. Taking advantage of thermodynamic or kinetic differences in different parts of a crystal, nanoarchitectures could be realized by etching.

10.3.1 Thermodynamic Effects

Controlled removal of the building blocks including the metal nodes and the organic linker from the coordination polymer framework is an effective way to construct various architectures. For example, the spatially different

thermodynamic stability of the framework can result in different etching rates in one crystal. This is due to the fact that the coordination polymer crystals can be assembled with modified organic ligands or metal-containing nodes without changing their frameworks structure. Thus, it is possible to integrate diverse organic ligands and metal nodes into one crystal. The different ligands or nodes of course have different thermodynamic stability. Therefore, one crystal could have spatially different etching rates. By carefully removing the less stable parts in the controlled condition, various designed architectures could be obtained.

10.3.1.1 Diversity in Component Stability

Apparently, one particle with multiple compositions shows differences in etching rates in different parts. For instance, Choi *et al.* selected the ZIF-8/ZIF-67 as the targeted coordination polymer to synthesize multi-shelled hollow ZIF-8.[29] The as-synthesized rhombic dodecahedron is composed of ZIF-67 (Co^{2+} and 2-methylimidazole) and ZIF-8 (Zn^{2+} and 2-methylimidazole). The ZIF-67 is unstable in water, thus can be transformed into $Co(OH)_2$ after etching by H_2O. In contrast, the ZIF-8 is quite stable in water. Hence, after immersing the ZIF-8/ZIF-67 composite into the water, multi-shelled hollow ZIF-8 could be obtained.

10.3.1.2 Diversity in Linker Stability

Integration of various linkers into the coordination polymer could induce the spatial distribution of diverse linkers inside the framework. Selectively removing the unstable linker from multivariate coordination polymers through a controlled etching process was respected to create various architectures.[30,31] The diversity in the stability of organic linkers is essential for selectively releasing the building blocks. In 2018, Feng *et al.* demonstrated a general method to fabricate hierarchically porous coordination frameworks through controlled thermolysis of the linkers.[30] UiO-66 is a typical coordination polymer that consists of 1,4-benzenedicarboxylate (BDC) and a Zr-based cluster. This material exhibits high thermal stability before 480 °C. Interestingly, when the BDC molecules were modified with $–NH_2$, the coordination polymer (UiO-66-NH_2) became less stable. Using the BDC-NH_2 as a thermolabile linker (red line in Figure 10.6) could be easily eliminated under low temperature (300 °C) and transformed into defects as shown in Figure 10.6. Through this controlled thermolysis, the etching process could be regulated. It should be noted that the controlled etching process not only yield highly hierarchical pores but also produces massive open metal sites and metal oxide nanoparticles in the inner part of a crystal. A mount of diffusion channels and high-activity metal sites make the obtained framework a superior catalyst for many reactions. On the contrary to the diversity in thermostability, the organic linkers also show varied stability in various solvents. For instance, $Zn_4O(PyC)_3$ composed of Zn(II) and pyrazolecarboxylic acid is

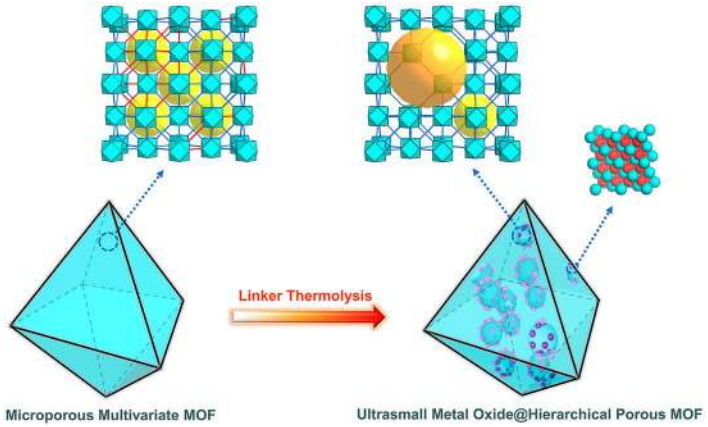

Figure 10.6 Scheme for synthesizing hierarchically porous coordination polymer through controlled thermolysis of the linkers. Reproduced from ref. 30 with permission from American Chemical Society, Copyright 2018.

unstable in water.[31] By immersing the frameworks into the water, two sets of octahedral SBUs were converted into two types of triangular SBUs after removing a quarter of the metal ions and half of the linkers, leading to a porous structure.

10.3.2 Kinetic Effects

For the crystal with a single component, kinetic effects are important for controlled etching. The etching rates could be influenced by many factors such as crystal facets, the distribution of etching agents or recrystallization, *etc.*[28] For instance, the atomic densities of the crystal facets varied from each other. The high density crystal facet can lead to a high erosion rate. Besides, defects inevitably exist in various crystals during the crystallization process. The parts with more defects are usually less stable and with high etching rate. In addition, it is also possible to regulate the etching rates by coating extra polymer macromolecules. Through adjusting the kinetics of the etching process, the building blocks will be selectively removed from the framework.

10.3.2.1 Surface Protection

Modification of the crystal surface with protective agents is expected to be a useful method. Macromolecules are typical protective agents during etching.[32–35] For instance, Hu *et al.* synthesized hollow Prussian blue and its analogs using poly(vinylpyrrolidone) (PVP) as the protective agent.[32] In the etching process, the PVP was adsorbed on the surface of particles and prevented the surface from serious attacking by the protons (Figure 10.7). Meanwhile, the protons had to diffuse into the inner part through channels and gradually

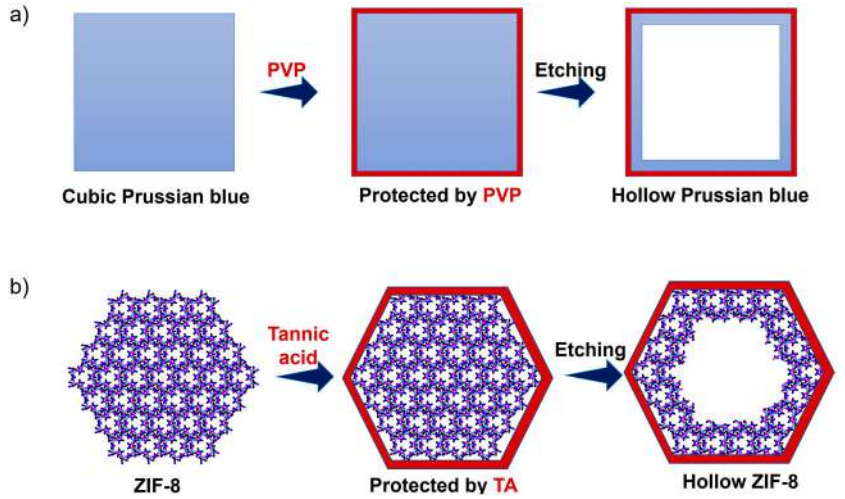

Figure 10.7 Schematic illustration for etching of the coordination polymers through selectivity protected surfaces. (a) Prussian blue. (b) ZIF-8.

removed the metal nodes and organic ligands. Therefore, etching of the inner part was faster than that of the outside part. Finally, the inner parts were totally removed, while the surfaces remained. A representative hollow Prussian blue particle was formed after controlled etching. Tannic acid can be used both as protective and etching agents to synthesize monocrystalline hollow ZIF-8.[34] The tannic acid molecules are absorbed on the surface of the ZIF-8 particles to act as the armor. It also modified the surface of the ZIF-8 crystals from hydrophobic to hydrophilic. The modified surface facilitated the protons to travel into the inner part, and dissolve the inner part of ZIF-8 particle.

10.3.2.2 Spatial Preferential Etching

Diverse orientations or facets of crystals usually show distinct characteristics. By utilizing the anisotropy of coordination polymer crystals, it is possible to control the etching kinetics in various parts of the crystals to construct different kinds of nanoarchitectures.

In 2013, Hu *et al.* reported a method to synthesize coordination polymers with shell-in-shell structure.[36] First, Prussian blue single crystals with non-uniformly distributed defects were fabricated (Figure 10.8). The parts with more defects could be etched faster in hydrochloric acid solution. The other parts with fewer defects were removed slower. By immersing the crystals in the etchants, several parts were removed faster, leading to shell-in-shell structures. Liu *et al.* demonstrated multi-shelled MIL-101 in a similar process (Figure 10.8b).[37] The parts with defects could be selectively etched.

Avci *et al.* demonstrated a strategy to regulate the anisotropic etching of ZIF-8 and ZIF-67 crystals.[38] Weak acid xylenol orange (XO) was applied to protonate

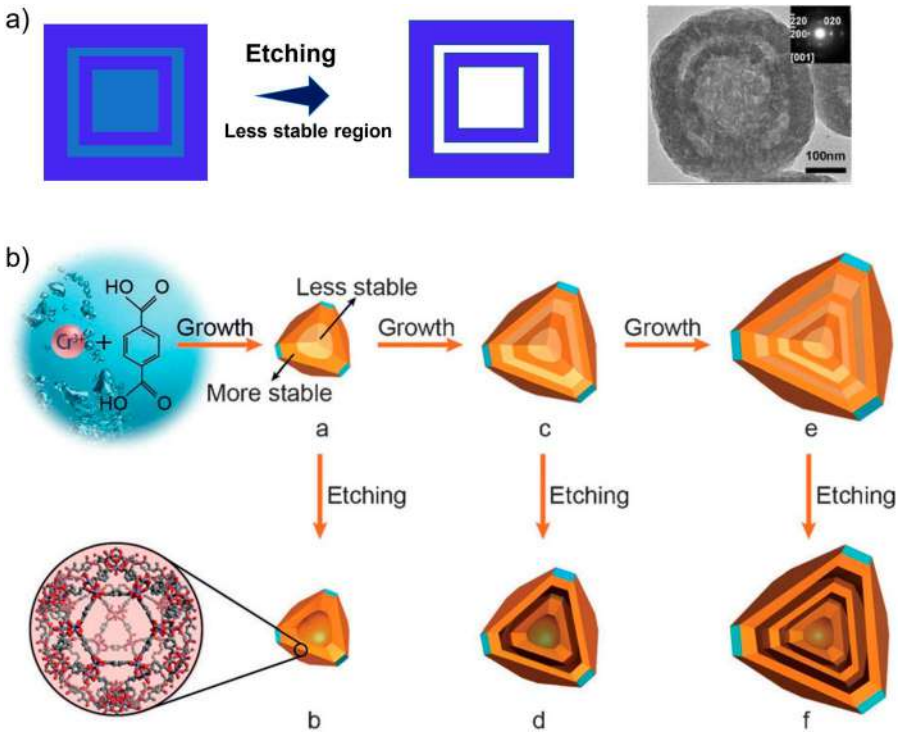

Figure 10.8 Schematic illustration of shell-in-shell particles through controlled etching. (a) Prussian blue. (b) MIL-101. Reproduced from ref. 36 with permission from American Chemical Society, Copyright 2013. Reproduced from ref. 37 with permission from John Wiley & Sons, Copyright © 2017 Wiley-VCH Verlag GmbH & Co. KGaA, Weinheim.

the 2-MIM (2-methylimidazole), breaking the Zn/Co-2-MIM bonds. The ZIF-8/ZIF-67 crystals with a high density of Zn/Co-2-MIM bonds could have a higher etching rate. Figure 10.9 shows that the rhombic dodecahedral crystals are gradually transformed into hollow boxes. The etching preferentially occurs along the ⟨211⟩ directions owing to the high packing density of the Zn/Co-2-MIM bonds along these directions. Preferential etching along different orientations could lead to diverse architectonics. If the etching rate of the centroid is higher than the edges, the cubes can be changed into nanoframes.[39] Otherwise, the cubes can be transformed into nanocages.[40] In a word, the anisotropic etching of the crystal can lead to different nanoarchitectures.[41]

10.3.2.3 Competitive Coordination Etching

The above-mentioned etching agents could break the bonds in coordination polymers. But they did not lead to the formation of any new crystals in the etching process. By using the coordination agents as the etching agent,

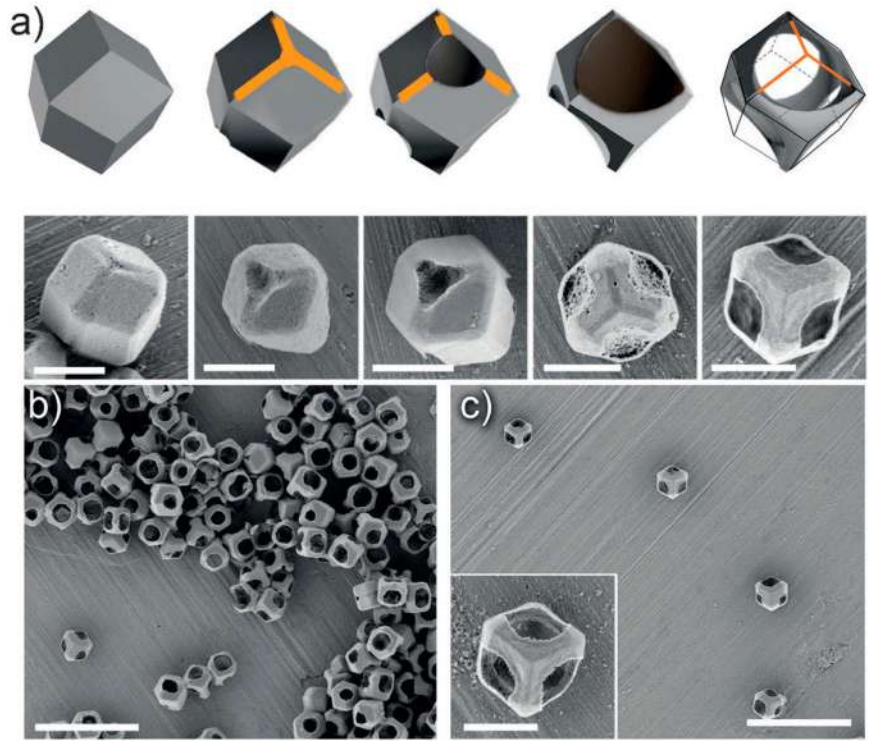

Figure 10.9 Schematic illustration of the change of the crystal morphology. (a) Etching preferentially occurred along the ⟨211⟩ directions. Scale bars represent 1 μm. (b and c) SEM images of the boxes. The scale bars represent 5 μm. The scale bar in the inset of (c) represents 1 μm. Reproduced from ref. 38 with permission from John Wiley & Sons, Copyright © 2015 WILEY-VCH Verlag GmbH & Co. KGaA, Weinheim.

regrowth of the initial crystal and formation of new crystals lead to competitive coordination etching.[42–46] For instance, Furukawa *et al.* reported a diffusion-coupled competitive coordination etching method to fabricate a superstructure of coordination polymers.[42] The as-synthesized MOF, $[Zn_2(ndc)_2(bpy)]_n$, (ndc = 1,4-Naphhalenedicarboxylate, bpy = 4,4′-bipyridyl) was successfully transformed into a hollow box using H_2bdc (1,4-benzenedicarboxylate) as the competitive coordination etching agents. The organic ligand, bdc, can coordinate to the metal clusters *via* diffusing from the outside to the inner part, replacing the initial linker of ndc and dissolving the Zn^{2+} (Figure 10.10). Then, the released Zn^{2+} and linkers diffuse outward. The bidirectional diffusion of the components triggers recrystallization at the surface, resulting in hollow superstructures. Besides, diverse metal ions and other organic ligands can also be used as competitive coordination etching agents to design coordination polymers nanoarchitectures.[43–46]

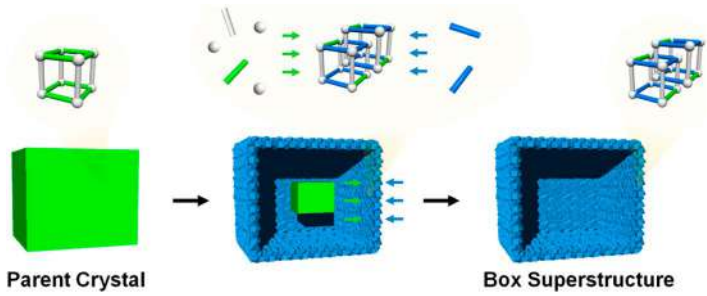

Figure 10.10 Schematic illustration of construction of hollow coordination polymer through competitive coordination etching. Reproduced from ref. 42 with permission from American Chemical Society, Copyright 2014.

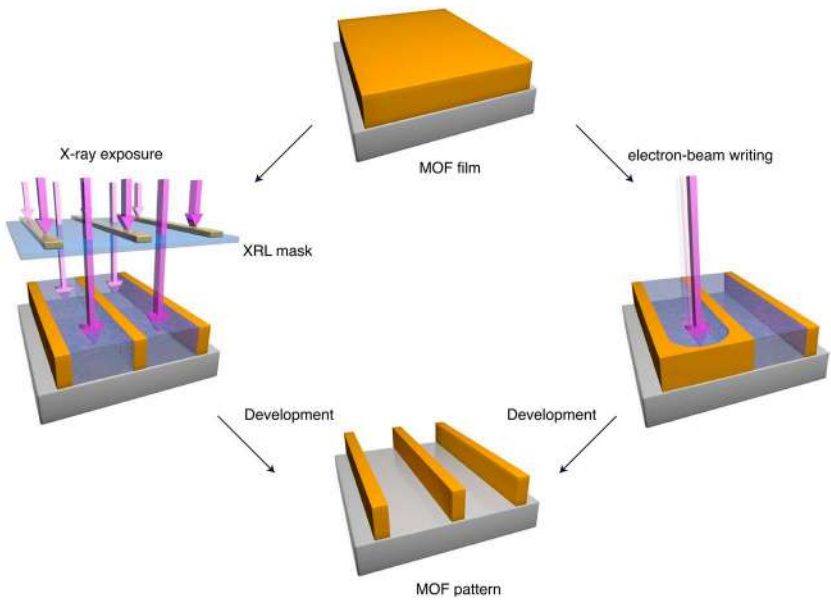

Figure 10.11 Schematic illustration of direct patterning of MOF films by X-ray and electron-beam lithography. Reproduced from ref. 47 with permission from Springer Nature, Copyright 2021.

10.3.2.4 X-ray and Electron-beam Etching

High energy laser and electron beams are important techniques for semiconductor processing. Ameloot *et al.* demonstrated a precise method to cave the coordination polymer films *via* using X-ray and electron-beam lithography (Figure 10.11).[47] This technique avoids damage and contamination of the uninterested parts, displaying sub-50 nm resolution which can promote the integration of MOFs in miniaturized systems. The MOF patterns are

impressive candidates for chemical sensors *via* direct transformation of the guest adsorption into an optical signal. The change of the phase and refractive index of MOF films occurs when the guest molecules are trapped in the pores. Therefore, the corresponding intensity of the diffraction spots will be changed, and the sensing data could be recorded.

10.4 Conclusion

In this chapter, we mainly focus on the fundamental analysis and technology for bottom-up epitaxial growth and top-down etching of coordination polymers. Layer-by-layer assembly and continuous assembly are the two most important strategies for epitaxial growth. Layer-by-layer assembly was used to atomically control epitaxial growth by the introduction of ligands and center nodes separately through the Langmuir–Blodgett method and ALD/MLD techniques. As for continuous assembly, the epitaxial growth mainly depends on the surface lattice structure of the substrates. The lattice matching, partially matching or modified with functional groups are regarded as useful methods to influence the epitaxial growth process. For top-down etching of coordination polymers, preferentially controlled etching occurs by making use of thermodynamic and kinetic etching differences. The diversity in component stability is the main factor in thermodynamic effects. The kinetic differences come from surface protection, distribution of defects, and recrystallization effects. Spatial preferential etching, competitive coordination etching and X-ray and electron-beam etching are utilized to realize the preferentially controlled. The nanoarchitectonics alternate the properties of the coordination polymers, thus is a promising way to improve the performance of coordination polymers in applications.

Although significant progress has been made in nanoarchitectonics of coordination polymers, the details about the structural evolution process are still unclear. It is highly needed to develop high-resolution *in situ* characterizations such as *in situ* XRD, Raman spectroscopy, and TEM, *etc.* In addition, to meet commercial demands, autonomous processing will be an impressive candidate. More attention should also be on fabricating commercial devices. We believe these devices will show great impacts in the future.

References

1. S. Kitagawa, *Chem. Soc. Rev.*, 2014, **43**, 5415.
2. H. Li, M. Eddaoudi, M. O'Keeffe and O. M. Yaghi, *Nature*, 1999, **402**, 276–279.
3. P. Horcajada, T. Chalati, C. Serre, B. Gillet, C. Sebrie, T. Baati, J. F. Eubank, D. Heurtaux, P. Clayette and C. Kreuz, *Nat. Mater.*, 2010, **9**, 172.
4. J. R. Long and O. M. Yaghi, *Chem. Soc. Rev.*, 2009, **38**, 1213.
5. O. K. Farha and J. T. Hupp, *Acc. Chem. Res.*, 2010, **43**, 1166.
6. D. Lee, *J. Appl. Phys.*, 1969, **40**, 4569.

7. T. Mårtensson, C. P. T. Svensson, B. A. Wacaser, M. W. Larsson, W. Seifert, K. Deppert, A. Gustafsson, L. R. Wallenberg and L. Samuelson, *Nano Lett.*, 2004, **4**, 1987.
8. J. Liu and C. Wöll, *Chem. Soc. Rev.*, 2017, **46**, 5730.
9. S. Motoyama, R. Makiura, O. Sakata and H. Kitagawa, *J. Am. Chem. Soc.*, 2011, **133**, 5640.
10. R. Makiura, S. Motoyama, Y. Umemura, H. Yamanaka, O. Sakata and H. Kitagawa, *Nat. Mater.*, 2010, **9**, 565.
11. J. Penttinen, M. Nisula and M. Karppinen, *Chem. - Eur. J.*, 2017, **23**, 18225.
12. E. Ahvenniemi and M. Karppinen, *Chem. Mater.*, 2016, **28**, 6260.
13. M. S. Yao, X. J. Lv, Z. H. Fu, W. H. Li, W. H. Deng, G. D. Wu and G. Xu, *Angew. Chem., Int. Ed.*, 2017, **129**, 16737.
14. O. Shekhah, H. Wang, D. Zacher, R. A. Fischer and C. Wöll, *Angew. Chem., Int. Ed.*, 2009, **48**, 5038.
15. E. Biemmi, C. Scherb and T. Bein, *J. Am. Chem. Soc.*, 2007, **129**, 8054.
16. S. Sakaida, K. Otsubo, O. Sakata, C. Song, A. Fujiwara, M. Takata and H. Kitagawa, *Nat. Chem.*, 2016, **8**, 377.
17. P. A. Gabrys, S. E. Seo, M. X. Wang, E. Oh, R. J. Macfarlane and C. A. Mirkin, *Nano Lett.*, 2018, **18**, 579.
18. Y. Kurihara and Y. Moritomo, *Jpn. J. Appl. Phys.*, 2011, **50**, 060210.
19. M. Itoi, T. Jike, D. Nishio-Hamane, S. Udagawa, T. Tsuda, S. Kuwabata, K. Boukheddaden, M. J. Andrus and D. R. Talham, *J. Am. Chem. Soc.*, 2015, **137**, 14686.
20. Y. Zhao, W. Zhang and M. Hu, *ChemNanoMat*, 2017, **3**, 780.
21. H. J. Lee, Y. J. Cho, W. Cho and M. Oh, *ACS Nano*, 2013, **7**, 491.
22. S. Furukawa, K. Hirai, K. Nakagawa, Y. Takashima, R. Matsuda, T. Tsuruoka, M. Kondo, R. Haruki, D. Tanaka and H. Sakamoto, *Angew. Chem., Int. Ed.*, 2009, **121**, 1798.
23. S. Furukawa, K. Hirai, Y. Takashima, K. Nakagawa, M. Kondo, T. Tsuruoka, O. Sakata and S. Kitagawa, *Chem. Commun.*, 2009, 5097.
24. P. Falcaro, K. Okada, T. Hara, K. Ikigaki, Y. Tokudome, A. W. Thornton, A. J. Hill, T. Williams, C. Doonan and M. Takahashi, *Nat. Mater.*, 2017, **16**, 342.
25. K. Ono, M. Ishizaki, K. Kanaizuka, T. Togashi, T. Yamada, H. Kitagawa and M. Kurihara, *Angew. Chem., Int. Ed.*, 2017, **129**, 5623.
26. J. Reboul, S. Furukawa, N. Horike, M. Tsotsalas, K. Hirai, H. Uehara, M. Kondo, N. Louvain, O. Sakata and S. Kitagawa, *Nat. Mater.*, 2012, **11**, 717.
27. I. Stassen, M. Styles, G. Grenci, H. Van Gorp, W. Vanderlinden, S. De Feyter, P. Falcaro, D. De Vos, P. Vereecken and R. Ameloot, *Nat. Mater.*, 2016, **15**, 304.
28. T. Qiu, S. Gao, Z. Liang, D.-G. Wang, H. Tabassum, R. Zhong and R. Zou, *Angew. Chem., Int. Ed.*, 2021, **60**, 17314.
29. W. H. Choi, B. C. Moon, D. G. Park, J. W. Choi, K. H. Kim, J. S. Shin, M. G. Kim, K. M. Choi and J. K. Kang, *Adv. Sci.*, 2020, **7**, 2000283.
30. L. Feng, S. Yuan, L.-L. Zhang, K. Tan, J.-L. Li, A. Kirchon, L.-M. Liu, P. Zhang, Y. Han and Y. J. Chabal, *J. Am. Chem. Soc.*, 2018, **140**, 2363.

31. B. Tu, Q. Pang, D. Wu, Y. Song, L. Weng and Q. Li, *J. Am. Chem. Soc.*, 2014, **136**, 14465.
32. M. Hu, N. L. Torad and Y. Yamauchi, *Eur. J. Inorg. Chem.*, 2012, **2012**, 4795.
33. M. Hu, S. Furukawa, R. Ohtani, H. Sukegawa, Y. Nemoto, J. Reboul, S. Kitagawa and Y. Yamauchi, *Angew. Chem., Int. Ed.*, 2012, **51**, 984.
34. W. Zhang, X. Jiang, Y. Zhao, A. Carné-Sánchez, V. Malgras, J. Kim, J. H. Kim, S. Wang, J. Liu and J.-S. Jiang, *Chem. Sci.*, 2017, **8**, 3538.
35. M. Hu, Y. Ju, K. Liang, T. Suma, J. Cui and F. Caruso, *Adv. Funct. Mater.*, 2016, **26**, 5827.
36. M. Hu, A. A. Belik, M. Imura and Y. Yamauchi, *J. Am. Chem. Soc.*, 2013, **135**, 384.
37. W. Liu, J. Huang, Q. Yang, S. Wang, X. Sun, W. Zhang, J. Liu and F. Huo, *Angew. Chem., Int. Ed.*, 2017, **56**, 5512.
38. C. Avci, J. Ariñez-Soriano, A. Carné-Sánchez, V. Guillerm, C. Carbonell, I. Imaz and D. Maspoch, *Angew. Chem., Int. Ed.*, 2015, **127**, 14625.
39. W. Zhang, Y. Zhao, V. Malgras, Q. Ji, D. Jiang, R. Qi, K. Ariga, Y. Yamauchi, J. Liu and J. S. Jiang, *Angew. Chem., Int. Ed.*, 2016, **55**, 8228.
40. J. Nai, Y. Lu, L. Yu, X. Wang and X. W. Lou, *Adv. Mater.*, 2017, **29**, 1703870.
41. J. Ye, G. Zhuang, Y. Wen, J. Wei, J. Chen, Z. Zhuang and Y. Yu, *Chem. Eng. J.*, 2019, **372**, 260.
42. K. Hirai, J. Reboul, N. Morone, J. E. Heuser, S. Furukawa and S. Kitagawa, *J. Am. Chem. Soc.*, 2014, **136**, 14966.
43. Z. Zhang, Y. Chen, S. He, J. Zhang, X. Xu, Y. Yang, F. Nosheen, F. Saleem, W. He and X. Wang, *Angew. Chem., Int. Ed.*, 2014, **53**, 12517.
44. T. He, X. Xu, B. Ni, H. Lin, C. Li, W. Hu and X. Wang, *Angew. Chem., Int. Ed.*, 2018, **130**, 10305.
45. L. Feng, J.-L. Li, G. S. Day, X.-L. Lv and H.-C. Zhou, *Chem*, 2019, **5**, 1265.
46. X. Xu, S. Chen, Y. Chen, H. Sun, L. Song, W. He and X. Wang, *Small*, 2016, **12**, 2982.
47. M. Tu, B. Xia, D. E. Kravchenko, M. L. Tietze, A. J. Cruz, I. Stassen, T. Hauffman, J. Teyssandier, S. De Feyter and Z. Wang, *Nat. Mater.*, 2021, **20**, 93.

CHAPTER 11

Structure–Function Relationship in Conjugated Porous Polymers

DOMINIC TAYLOR[a], SCOTT J. DALGARNO[a] AND FILIPE VILELA*[a]

[a]School of Engineering and Physical Sciences, Heriot-Watt University, Riccarton, Edinburgh, EH14 4AS, UK
*E-mail: f.vilela@hw.ac.uk

11.1 Introduction

Functional materials are becoming ever more ubiquitous and intertwined with our modern lifestyles: notable examples include wearable thermoelectrics, self-healing polymers and organic photovoltaics. Amongst the different types of materials that are being investigated for a myriad of applications, functional porous polymer networks, such as metal–organic frameworks (MOFs),[1] porous aromatic frameworks (PAFs),[2] covalent organic frameworks (COFs),[3] hypercross-linked polymers (HCPs),[4] polymers of intrinsic microporosity (PIMs),[5] and conjugated porous polymers (CPPs),[6,7] have recently been the subject of intense research. While each class of porous polymer network is linked by the overarching trait of porosity, they are each unique in the precise combination of synthetic conditions, tailorability towards key applications, physiochemical stability, ease of processing/modification, degree of crystallinity and extent of π-conjugation (see Figure 11.1).[5,8–11]

Among these examples of porous polymers, CPPs are particularly interesting because of the unique combination of properties they present. CPPs are a family of amorphous polymer networks that are designed to be fully

Nanoscience & Nanotechnology Series No. 55
Concepts and Design of Materials Nanoarchitectonics
Edited by Omar Azzaroni and Katsuhiko Ariga

Published by the Royal Society of Chemistry, www.rsc.org

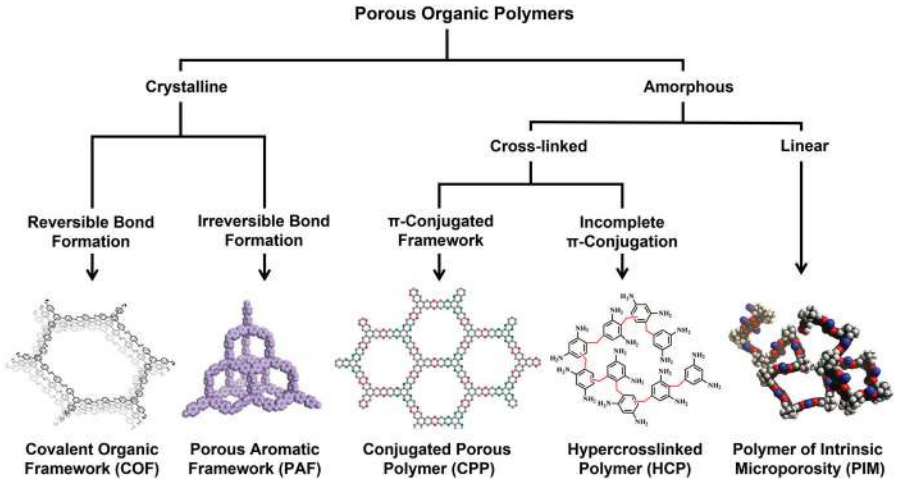

Figure 11.1 Different families of porous organic polymers identified by some of their defining characteristics. It should be noted that these classifications have been generalised and it is possible for polymers to sometimes be described as two different classes.[5,8–11] Reproduced from ref. 5, 8–10 and 11 with permission from the Royal Society of Chemistry.

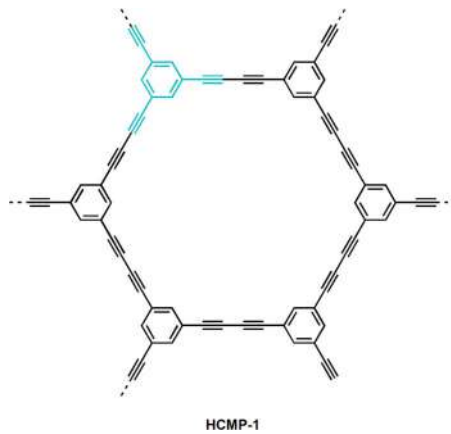

Figure 11.2 Structure of HCMP-1, the first CPP reported by Cooper and coworkers.[12] The repeating unit or monomer residue is highlighted in blue.

cross-linked and completely π-conjugated (see Figure 11.2).[12] The extensive cross-linking present in CPPs leads to permanent nanoscale porosity, high surface area and, for the most part, complete insolubility in common laboratory solvents.[13] Their porosity has led CPPs to be investigated for applications including pollutant removal, gas separation and storage as well as catalysis.[6,14–16] The complete conjugation is also beneficial for CPPs as this

permits the absorption of light (mainly in the ultraviolet to visible regions) for photocatalysis and also improves movement of electrons for sensing or energy storage.[15] The powerful combination of porosity and π-conjugation, as well as the diversity of building blocks available, has led to over 400 research articles since CPPs were first reported by Cooper and co-workers in 2007.[12]

This book chapter will discuss how the properties and applications of CPPs are heavily influenced not only by the choice of building blocks utilised in their construction, but also the synthetic conditions employed and any subsequent post synthetic modification. Significant discussion will be centred around methods to control the nanoscale structure of CPPs, namely their porosity, surface area and morphology, with special attention paid to examples where said control influences the properties and/or applications of the material. In addition to discussing ways to control the nanoscale structure, examples of CPPs where nanoscale organisation and non-covalent or supramolecular interactions play an important role will be highlighted. Discussion of CPPs in this chapter, in particular their applications, is not exhaustive and for more information the reader is directed towards two recent comprehensive reviews by Taylor *et al.* and Lee *et al.*[6,7]

11.1.1 Design and Synthesis of CPPs

11.1.1.1 Design Rules of CPPs

The basic design strategy for a CPP is to connect π-conjugated organic building blocks together in a way that simultaneously produces a polymer network and extends π-conjugation between each building unit. From a design viewpoint, CPPs are completely cross-linked and completely π-conjugated: in reality, defects such as unreacted functional groups can arise. To establish extensive cross-linking, it is necessary for a certain fraction of the building blocks to feature at least three reactive sites for connection. These building blocks can be described as A_3, A_4 *etc.* building blocks, where the subscript refers to the number of reactive sites. To generate a cross-linked polymer, these building blocks must then either undergo self-condensation or react with one or more comonomers that must themselves possess at least two reactive sites (B_2, B_3 *etc.*). This means that self-condensations such as A_3 or A_4, but not A_2, polymerisations and copolymerisations including A_3 + B_2 or A_4 + B_2 types are all suitable for CPP synthesis. To satisfy the second criteria and establish π-conjugation between the two building blocks, the constituent moieties must not have sp^3 hybridised carbon atoms that would fully disrupt the π-conjugation of the polymer backbone. An example of such a building block is tetra(4-bromophenyl)methane, which has been used to construct porous organic polymers (POPs) that have been incorrectly identified as being CPPs, despite not possessing complete π-conjugation, even from a purely design viewpoint (see Figure 11.3).

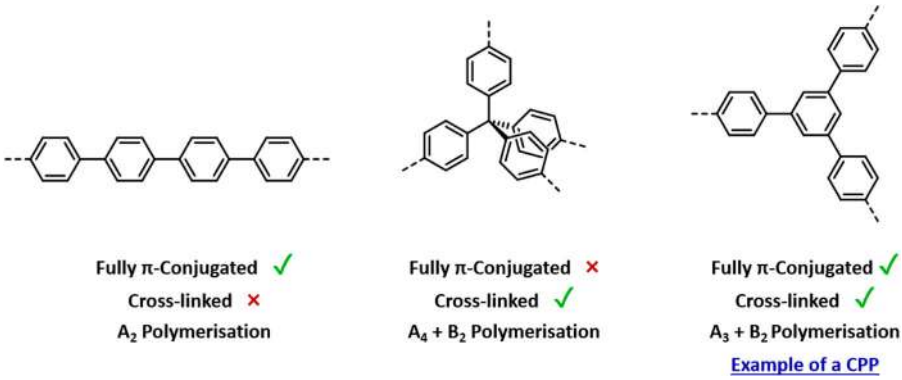

Figure 11.3 Examples of polymers with π-conjugation and/or complete cross-linking. Only the right most polymer is an example of a CPP as it exhibits both complete π-conjugation and cross-linking. Note, that in addition to these criteria, the polymer must also be amorphous to be accurately classified as a CPP.

11.1.1.2 Synthetic Reactions

The synthesis of CPPs normally relies upon reactions that establish strong covalent bonds between the constituent building blocks. For this reason, CPPs often exhibit superior chemical stability in comparison to COFs and MOFs, which normally rely on reversible reactions for synthesis. The most commonly utilised methods for synthesising CPPs rely on metal-mediated coupling reactions. This includes reactions involving palladium-based catalysts such as the Sonogashira–Hagihara and Suzuki–Miyaura couplings,[17,18] the two most commonly employed methods, as well as direct-arylation reactions.[19] Other synthetic methods that utilise catalysts derived from more naturally abundant metals include Friedel–Crafts type chemistry (aluminium or iron catalysts),[20] Yamamoto coupling (nickel catalysts),[21] and cyclotrimerisation (zinc or cobalt catalysts).[22]

A wide variety of building blocks can be successfully incorporated into a polymer framework through this array of metal-catalysed reactions. However, it is possible for some residual metal catalyst to be trapped within the pores of the material, potentially influencing the end application of the CPP. Considering this and the low natural abundance of some metal elements, routes that avoid the use of metals to synthesise CPPs have been the subject of significant research. Examples of such metal free polymerisations include Schiff-base chemistry,[23] pyrrole/aldehyde condensation,[24] cationic polymerisation,[25] the Knoevenagel condensation,[26] and the Aldol condensation.[27]

11.1.1.3 Post Synthetic Modification

An alternative approach to introducing functionality into CPPs besides the selection of suitable building blocks is to modify the material post synthesis *via* heterogeneous chemical reactions. As a representative example, Kiskan

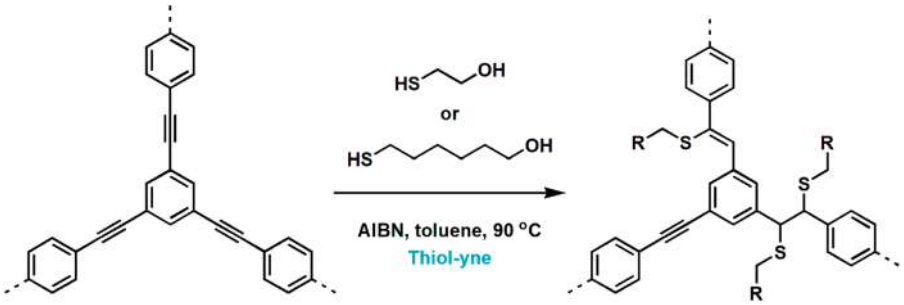

Figure 11.4 Example of CMP post synthetic modification of using thiol-yne type chemistry. Modification of the CMP by reaction with 1 and 2 equivalents of thiol shown on the same product polymer.

and Weber demonstrated that radical thiol-yne chemistry could be utilised to modify CPPs containing acetylene groups using thiols and azobisisobutyronitrile (AIBN) (see Figure 11.4).[28] The post synthetic introduction of side chains to the polymer network was accompanied by a slight reduction in the Brunauer–Emmett–Teller (BET) surface area and pore volume, which could be explained by the side groups occupying the pores as well as geometric changes upon converting from triple to double bonds. This approach was later utilised by Vilela and co-workers to improve the dispersibility of photoactive conjugated microporous polymers (CMPs) in water and increase the uptake of Ag(I) ions.[29,30]

An alternative method of post synthetic modification of CPPs is to use them as supports onto which metal particles can be loaded. An early example of this was demonstrated by Hasell *et al.*, who uniformly dispersed palladium nanoparticles through a CMP using supercritical CO_2 processing.[31] This was achieved by thermal decomposition of palladium(II) hexafluoroacetylacetonate to deposit palladium nanoparticles within the pores of the CPP (the fluorine atoms facilitated dissolution of the precursor in supercritical CO_2). The introduction of palladium nanoparticles was observed to increase the hydrogen adsorption by up to a factor of 12, despite a decrease in both the BET and micropore surface areas upon metal deposition.

11.2 Surface Area and Nanoscale Architectural Control

In accordance with recommendations by the International Union of Pure and Applied Chemistry (IUPAC), porous materials, including CPPs, can be classified based upon the diameter of their pores.[32] Pores that have a diameter of less than 2 nm can be classified as micropores, with CPPs with exclusively this type of pore accurately described as conjugated microporous polymers (CMPs). CPPs that feature pores with a diameter between 2 and 50 nm are referred to as conjugated mesoporous polymers while those with pores greater than 50 nm in diameter are conjugated macroporous polymers.

With CMPs, pores that have a diameter of less than 0.7 nm are often specifically referred to as ultramicropores.[33]

The porous structure of CPPs has a major influence on its properties and application, and as such, much effort has been directed towards establishing methods of controlling their porosity and surface area. For example, extensive research conducted into CMPs has demonstrated that the presence of micropores provides extremely high surface areas for catalytic reactions to occur on, or for the adsorption of gas molecules. However, the small diameter of these pores is a barrier to mass transport and thus the presence of additional meso- or macropores to facilitate diffusion to the micropores is highly beneficial. Such a material, possessing pores from multiple classifications is said to exhibit hierarchical porosity.

Research conducted into CPPs has revealed that their porous properties can be affected by a number of factors including the length of the cross-linkages, monomer geometry and reaction conditions (such as the catalyst/solvent used and presence of salts).[34–36] However, the first two approaches fundamentally change the identity of the CPP, including its optoelectronic properties, while the latter can be difficult to reliably predict or have narrow applicability. Another important feature of CPPs to consider is their morphology. Several different types of CPP morphology, which are elucidated *via* scanning electron microscopy (SEM) and/or transmission electron microscopy (TEM), are known to exist including tubes, spheres, platelets, rods and rings. This subsection discusses methods to control the structure that particles of CPPs adopt at the nanoscale level, namely their morphology, and also the surface area of the material.

11.2.1 Inorganic Templates

One approach that has been utilised to control the surface areas of CPPs is to utilise a templating agent. During synthesis, the CPP can grow around these templating agents, or porogens, which can then be subsequently removed post synthesis. An early example of this was reported by Vilela and co-workers, who utilised silica nanoparticles as templates for CMPs based on the benzo[*c*][1,2,5]thiadiazole group.[37] Following synthesis of the CMP the silica nanoparticles were removed by chemical etching with ammonium hydrogen difluoride (NH_4HF_2). Despite the harsh nature of these conditions, the overall structure of the CMPs remained intact. For the untemplated CMP, the BET surface area was measured to be 270 $m^2\ g^{-1}$: a positive correlation between the quantity of silica nanoparticle employed and the resultant surface area was observed, rising to a maximum of 660 $m^2\ g^{-1}$ when using 60 mg of silica per mL of reaction mixture. Subsequent application of these CMPs to the generation of the singlet oxygen, an electronically excited state of oxygen, for the photooxidation of α-terpinene showed that the rate of the reaction correlated with the surface area and quantity of silica nanoparticles used. However, it should be noted that while the surface area played a role in the rate of the reaction, it cannot be entirely decoupled from other effects such as its dispersibility. Materials with larger pore volumes and higher surface

areas can give rise to increased dispersibility that would also aid in the generation of singlet oxygen.

Zhang and co-workers have demonstrated another method for utilising mesoporous silica as a templating agent for CPP synthesis.[38] A mesoporous silica support, **SBA-15**, was first coated with the dicyanothiophene (DCT) monomer which upon exposure to triflic acid vapour underwent cyclotrimerisation through the cyano-groups. This formed a thiophene-triazine CPP coating on the silica, **CTF-Th@SBA-15**, which possessed a BET surface area of 548 $m^2\ g^{-1}$. Based on the pore size of the mesoporous silica template (5.7 nm) and the pore size of the CPP on the silica (3.8 nm), the authors deduced that the thickness of the polymer layer was approximately 1.9 nm. In contrast to the previous example that utilised silica as a template, the removal of the silica template from **CTF-Th@SBA-15** resulted in the pore structure collapsing and the BET surface area decreasing to 57 $m^2\ g^{-1}$.

This work by Zhang and co-workers can be reconciled with work performed by Nguyen and co-workers, who investigated the effect that different functional groups on the surface of a mesoporous silica template had on the porosity.[39] In the first instance, the authors employed unmodified silica, which possessed surface silanol groups, as the template. This led to an increase in the external surface area from 250 to 410 $m^2\ g^{-1}$, although the authors point out that this is much less than expected given the high mesoporosity of the template. The origin of this discrepancy was postulated to be the collapse in the mesoporous structure of the non-robust polymer when the silica template was removed. To improve the strength of the polymer network, the authors investigated modifying the surface of the silica template in order to increase its interaction with the CPP during synthesis. This would result in the formation of thicker coatings of polymer that are more robust towards chemical etching, thus better retaining the mesoporous features. The authors investigated two types of surface modification, installing either trimethylchlorosilane or phenyltriethoxysilane functional groups. Following removal of the modified silica nanoparticles, the external surface area of the CPPs increased to 890 and 760 $m^2\ g^{-1}$ respectively.

In addition to silica, other inorganic materials have been utilised as templates for CMP formation. This is exemplified by work performed by Son and co-workers, who investigated the use of Cu_2O nanocubes.[40] As the reaction selected for the formation of the CPP was an azide–alkyne Click reaction, the Cu_2O template also served as a catalyst for polymerisation. Once the Cu_2O template was removed by etching with hydrochloric acid, CMPs with a hollow cube morphology were obtained (see Figure 11.5). On average, the shells had a width of 210 nm and thickness of 35 nm.

11.2.2 Templating Using Polymers

A similar approach to utilising silica templates has also been explored using linear polymers as removable templates. For example, work by Chang and co-workers has demonstrated that electrospun poly(vinylpyrrolidone) (PVP) fibres could be used to fabricate a free standing CMP membrane with a tubular morphology.[41] By carrying out the Sonogashira–Hagihara cross coupling

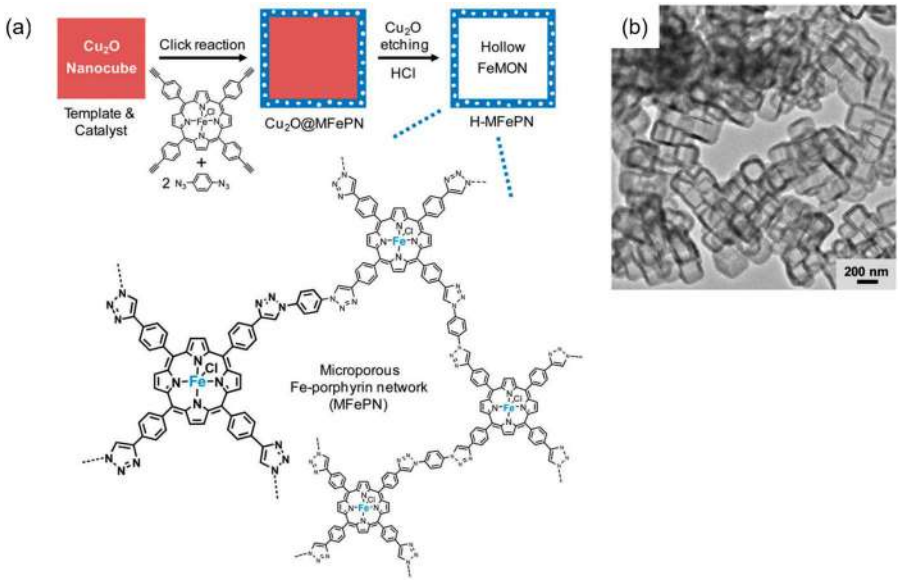

Figure 11.5 (a) Illustration of the templated CMP synthesis using Cu_2O nanocubes as both catalyst and template. (b) TEM image of **H-MFePN**. Adapted from ref. 40 with permission from the Royal Society of Chemistry.

of 1,3,5-triethynylbenzene and 1,4-diiodobenzene in the presence of the PVP template, a membrane (**PVP@CMP**) consisting of PVP nanofibres (average diameter 200 nm) coated in CMP (average diameter 50 nm) was obtained. Removal of the PVP by washing with DMF produced a **CMP** membrane featuring both macroporosity from the PVP template and microporosity intrinsic to the CMP (see Figure 11.6).

Wang and co-workers have also investigated using polymers as sacrificial templates for controlling the morphology of CMPs, by using cross-linked poly(methyacrylic acid) (PMAA) to template the formation of hollow CMP microspheres.[42] The authors utilised three different types of cross-linked PMAA (see Figure 11.7a) which each gave distinct shell structures upon removing the template. The carboxylate groups on each of the cross-linked PMAA templates provided a point at which to anchor the palladium and copper catalysts needed for the Sonogashira–Hagihara cross coupling. Concurrent with the formation of the CMP, the cross-linking unit also underwent cleavage, leading to disintegration of the template and formation of the hollow shell structure in a single step. When PMAA with a low cross-linked density was used, the microspheres of CMP that were obtained were smooth on the surface (see Figure 11.7b). As the cross-linking density increased, the surface of the PMAA template became rougher and this was reflected in the final CMP shell (see Figure 11.7c). The authors also demonstrated that by using Fe_3O_4 coated in the PMAA template, Fe_3O_4 could be trapped within the hollow CMP shell using the same methodology (see Figure 11.7d).

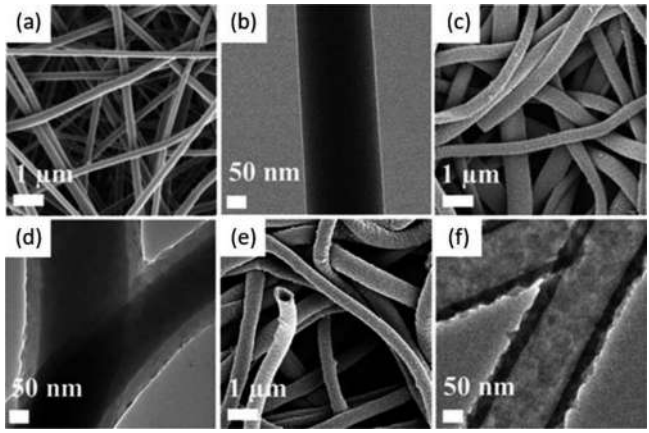

Figure 11.6 SEM (top) and TEM (bottom) images of (a and b) electrospun PVP membrane template, (c and d) **PVP@CMP** and (e and f) CMP membrane with PVP removed using DMF. Adapted from ref. 41, https://doi.org/10.1038/s41598-017-13827-w, under the terms of the CC BY 4.0 license https://creativecommons.org/licenses/by/4.0/.

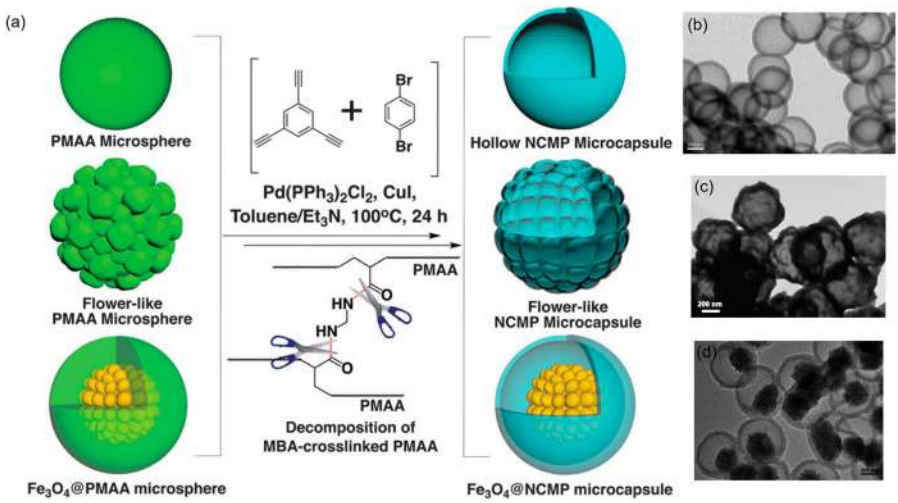

Figure 11.7 (a) Illustration of templating the structure of CMP microcapsules using cross-linked PMAA microspheres as templates. (b–d) TEM images of the hollow CMP microcapsule, flower-like microcapsule and Fe_3O_4-CMP composite microcapsule respectively. Adapted from ref. 42 with permission from the Royal Society of Chemistry.

11.2.3 Templating Using High Internal Phase Emulsions

High internal phase emulsions (HIPEs) are defined as emulsions where the internal (dispersed) phase constitutes more than 74.05% of the emulsions total volume.[43] This percentage corresponds to the maximum volume of space that can be filled by non-deformable spheres of uniform size. Vilela

and co-workers demonstrated a strategy to introduce hierarchical porosity to a CPP by polymerisation of monomers as a HIPE.[44] The authors prepared their conjugated porous polyHIPEs *via* Sonogashira–Hagihara cross coupling, using vigorous agitation to convert the reaction mixture into a HIPE and using a surfactant, Span 80, to stabilise the emulsion. This led to the formation of monolithic CPPs with BET surface areas in the range 35–50 $m^2 g^{-1}$. Formation of the benzo[*c*][1,2,5]thiadiazole/fluorene CPPs occurred around the water droplets present in the dispersed phase, leading to polymers with a combination of both micropores (due to the intrinsic microporosity of the CPP) and macropores (due to the water droplet templates).

11.2.4 Templating Using Removable Functional Groups

Zhang and co-workers have reported on a templating strategy that makes use of the cleavable *tert*-butyl carboxylate (Boc) groups attached to the CPP building blocks as spacer groups.[45] The Boc containing polymers were first prepared using the HIPE technique outlined above to produce CPPs with BET surface areas in the region of 26–45 $m^2 g^{-1}$ and a combination of macroporous and microporous features. Following synthesis, the Boc groups were removed by heating the CPPs under vacuum, resulting in an up to an 8-fold increase in the BET surface area and revealing new micropores with a diameter of *ca.* 1.5 nm. Furthermore, the authors note that removing the Boc groups did not compromise the macrostructure, indicating the compatibility of spacer groups techniques with other templating strategies.

11.2.5 Templating *via* Molecular Imprinting

A novel approach to template the porous features of CPPs towards a final application has been realised by Zhu and co-workers, who have utilised a molecular imprinting strategy to incorporate selective binding sites for uranyl ion adsorption.[46] Their strategy of molecular imprinting revolved around synthesising a CMP containing a UO_2^{2+} complex with salicylaldoxime, methacrylic acid and 4-vinylpyridine ligands (the vinyl group provided the point of attachment to the CMP *via* Heck coupling). Removing the UO_2^{2+} ions left vacant sites on the CMP that provided an ideal site for binding other UO_2^{2+} ions (see Figure 11.8). Through this approach, of nanoscale pre-organising the binding site towards a single target adsorbate, the authors were able to achieve selectivity coefficients for UO_2^{2+} over other ions (including alkali and transition metal ions) of over 746.

11.2.6 Nanoscale Architectural Control – Growing CPPs on Surfaces

Due to the insolubility of CPPs, solvent casting to form thin films or coatings is not a viable processing option although various strategies have been developed to synthesise CPPs as films with a reliably controllable thickness. One method

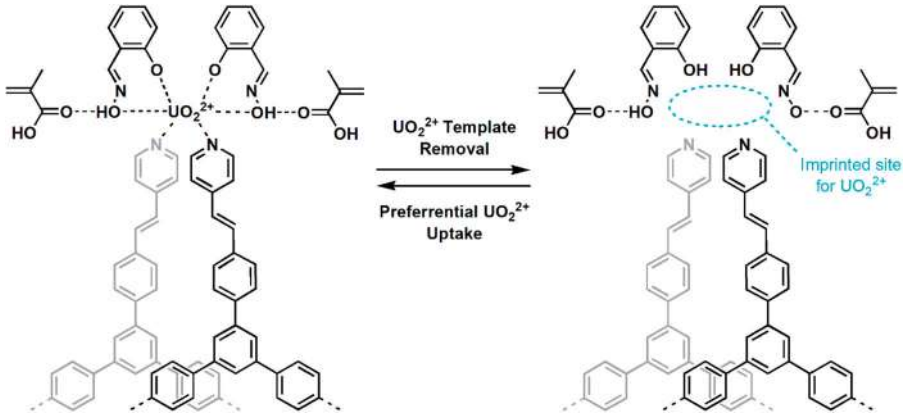

Figure 11.8 Molecular imprinting strategy using a complex with the UO_2^{2+} ion for subsequent binding of the same ion.

is to utilise electropolymerisation to grow thin films of CPP on the surface of an electrode. For example, Gu *et al.* have reported on the electropolymerisation of carbazole based monomers into emissive CMP films.[47] The authors reported that they were able to form microporous polymer films with micro- to nanometre thickness with sub-nanometre precision. This was achieved by changing the number of cyclic voltammetry cycles applied to the electrode on which the polymer was growing, with each subsequent cycle contributing approximately 1.7 nm to the overall thickness of the film. The thin polymer films, which were highly emissive, were applied to detecting various nitroaromatic compounds, including explosive compounds. When polymer films of different thicknesses were tested, an inversely proportional relationship between the film thickness and the degree of fluorescence quenching was observed. The authors attribute this to a lower luminescence produced by thinner films requiring fewer analyte molecules to quench the fluorescence.

Zhuang *et al.* have reported on the preparation of a CMP layered on a sheet of graphene oxide (see Figure 11.9). The graphene oxide, GO, was first functionalised by reduction with hydrazine hydrate to give **RGO**.[48] Subsequent reaction with the diazonium salt of bromobenzene introduced bromobenzene groups onto the graphene sheet (**RGBr**), providing points from which polymerisation of the building blocks could proceed. Carbonisation of this CMP-graphene material (**GMP**) yielded a sulfur and nitrogen doped porous carbon which the authors applied as an electrocatalyst for the oxygen reduction reaction under alkaline conditions. The same group have also expanded this approach by using carbon nanospheres and carbon nanotubes to synthesise 0-D and 1-D materials, in addition to the 2-D graphene material. Upon carbonisation, heteroatom doped porous carbons were obtained, with the authors noting that a correlation existed between the dimensionality of the nanocarbon and its electrochemical activity for the oxygen reduction reaction, such that 2-D > 1-D > 0-D.[49]

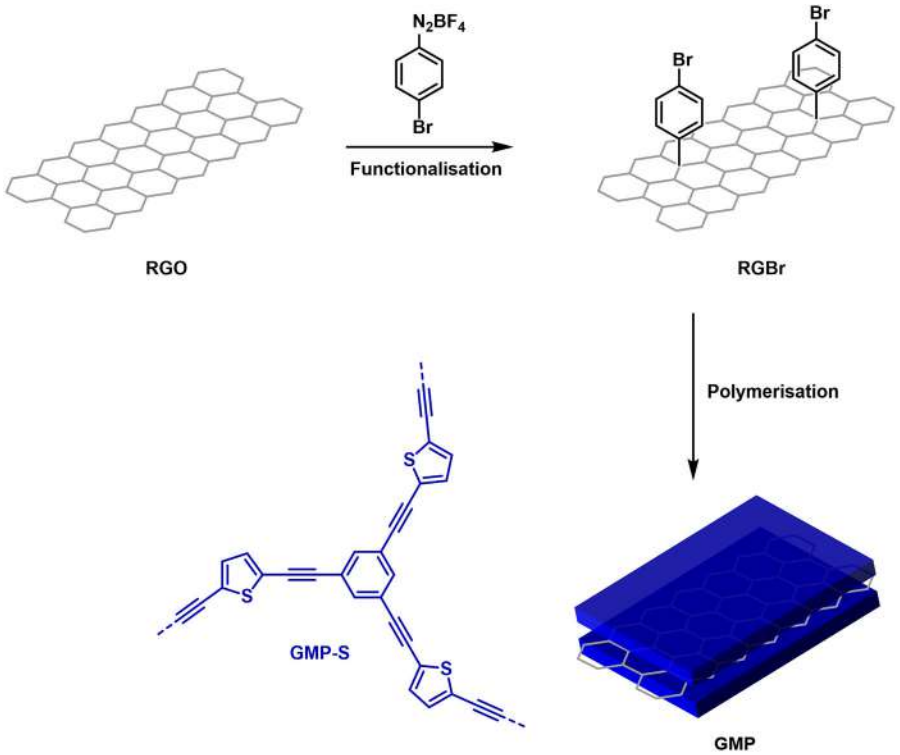

Figure 11.9 Illustration of the synthetic route from reduced graphene oxide to GMP (example structure of GMP-S is shown) which exhibits a 2D sandwich type structure.

11.3 Non-covalent Interactions Involving CPPs

This subsection will deal with applications of CPPs that involves their interaction with small molecules *via* non-covalent interactions. As has been discussed earlier in this chapter, one of the many benefits of CPPs is the plethora of building blocks available to construct the polymer, which permits the introduction of specific groups that can enhance non-covalent interactions with adsorbates. Specific separate discussion is allocated later in this chapter to discussion of CPPs featuring host–guest systems, although these systems still involve similar interactions.

11.3.1 Adsorption of Metal Ions and Organic Molecules

The nanoscale porosity of CPPs is highly conducive towards the adsorption and storage of various species including metal ions, organic molecules, and gases (mainly carbon dioxide and hydrogen). While increasing the surface area available for adsorption is one route to favour adsorption, it must be reconciled

with the classification of pore present as this is also a factor. In addition, the presence of intermolecular forces of electrostatic attraction between adsorbate and the sorbent material can also result in an increase in the heat of adsorption. A prime example of this is demonstrated in work by Zhu and co-workers, who studied the effect that polar groups on the surface of a CPP would have on the adsorption of the antibiotics tetracycline and doxycycline hydrochloride.[50] Both of these molecules possess polar groups but the latter molecule is also a hydrochloride salt. By synthesising a series of structurally similar CMPs decorated with different functional groups, the authors were able to control the polarity of the pores (see Figure 11.10). **PAF-79** possessed no polar groups and thus exhibited low uptake of both antibiotics (25 mg g^{-1} and 63 mg g^{-1}), despite **PAF-79** exhibiting a very high surface area (1964 m^2 g^{-1}). The addition of hydroxyl or sulfonate groups (forming **PAF-80** and **PAF-80-SO_3H** respectively) altered the polarity of the pores. In the case of doxycycline hydrochloride, electrostatic interactions with **PAF-80-SO_3H** (143 mg g^{-1}) led to greater adsorption in comparison to **PAF-80** (125 mg g^{-1}). In contrast, a higher adsorption of tetracycline was observed with **PAF-80** compared to **PAF-80-SO_3H** (111 mg g^{-1} *versus* 91 mg g^{-1}). The authors attribute this to the higher surface area of **PAF-80** over **PAF-80-SO_3H** favouring adsorption in the absence of strong ionic interactions.

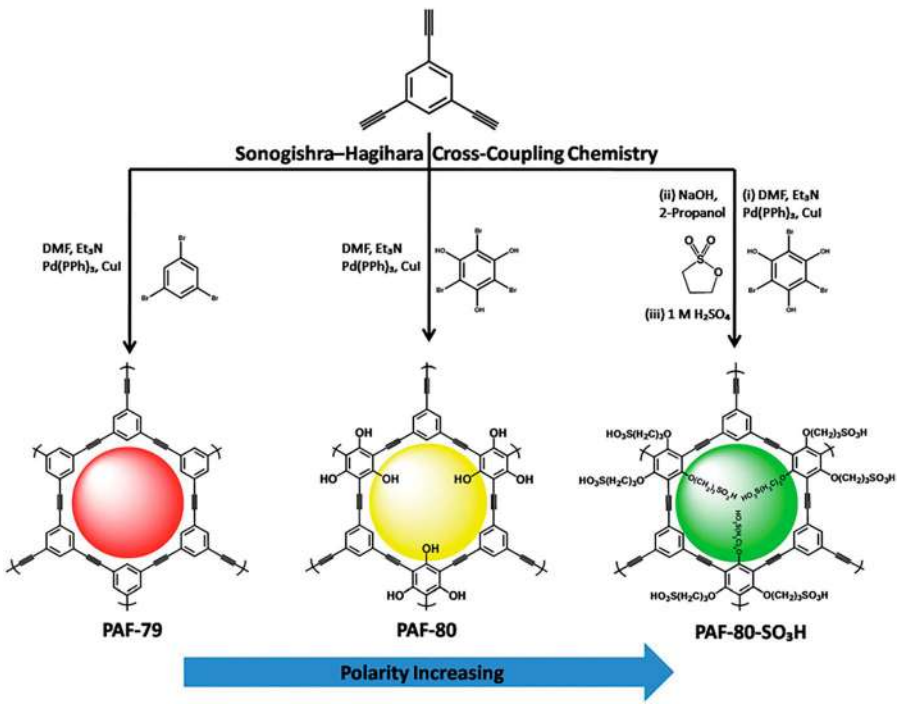

Figure 11.10 Synthesis and structure of **PAF-79**, **PAF-80** and **PAF-80-SO_3H**, bearing different functional groups on their surface. Adapted from ref. 50 with permission from the Royal Society of Chemistry.

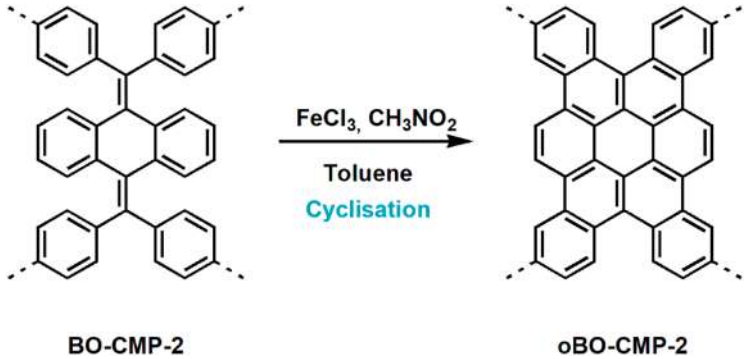

Figure 11.11 Post synthetic cyclisation of **BO-CMP-2** using $FeCl_3$ to form **oBO-CMP-2** and extend the π-conjugation.

The exploitation of much weaker π–π interactions between CMP and adsorbate have also been explored for adsorption of small organic molecules. Yang *et al.* have described a method for increasing the interaction between a tetrabenzocoronene based CMP and organic vapours by extending the π-conjugation of the material (see Figure 11.11).[51] Following a post synthetic oxidation reaction between **BO-CMP-2** and ferric chloride to yield **oBO-CMP-2**, an increase in the adsorption of benzene and toluene was observed, which the authors attribute to the interaction between adsorbate and the π-system. In comparison, **oBO-CMP-2** exhibited a low absorption of cyclohexane, which can be attributed to the lack of an aromatic π-system. Similar observations regarding the affinity of CPPs towards aromatic compounds over non-aromatic systems have been made by Ma and co-workers, who utilised a CMP containing naphthalene and carbazole groups to separate mixtures of similarly sized aromatic and alkane compounds.[52] Computational modelling demonstrated that the π-conjugated molecules benzene and 3-methylthiophene sat parallel to the planar naphthalene rings: by comparison the alkanes (cyclohexane and *n*-octane) occupied random positions.

11.3.2 Adsorption of Gases

11.3.2.1 Carbon Dioxide

The characteristic porosity and physiochemical stability of CPPs, as well as their high surface areas, makes them promising materials for CO_2 capture and storage, although it has been noted that the lack of crystallinity present in CPPs could be detrimental to CO_2 adsorption by limiting access to binding sites.[53,54] However, the diversity of available building blocks available for synthesising CPPs brings the prospect of introducing polar groups that could interact with the quadrupole moment of CO_2 and increase the heat of adsorption. An example of this is provided by work performed by Dawson *et al.*, which demonstrated that the addition of polar carboxylic acid, hydroxy- and

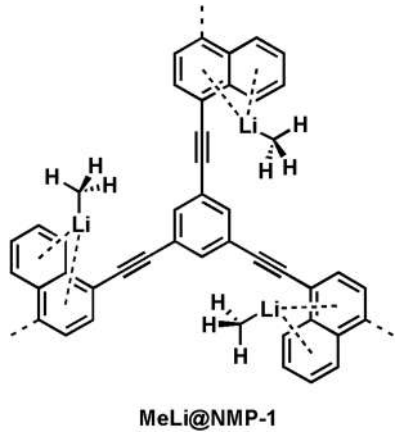

Figure 11.12 Structure of **MeLi@NMP-1** showing the postulated binding of methyl lithium molecules to the naphthalene rings.

amino-groups all resulted in an increase in the isosteric heat of adsorption and CO_2 uptake compared to an unmodified CMP consisting of only benzene rings.[55]

11.3.2.2 Hydrogen

Hydrogen gas is seen as an environmentally friendly fuel because it does not produce greenhouse gases upon combustion. In the context of hydrogen gas storage, CPPs benefit immensely from high surface areas and small pore sizes, particularly the availability of micropores and ultramicropores. Early research into CPPs for H_2 storage demonstrated that pores within these regimes contribute more to H_2 adsorption than other pore regimes.[12] Various studies have demonstrated that by changing the monomer units used to synthesise the CPP, the micropore volume could be adjusted and hydrogen adsorption improved.[56,57] Other studies that have been conducted into CPPs as storage media for H_2 gas have demonstrated that doping with lithium ions or organolithium molecules is an effective way to favour adsorption (see **MeLi@NMP-1** in Figure 11.12). Computational calculations demonstrated that the lithium dopants each possess a partial positive charge arising from charge transfer to the π-system of the CPP: this partial charge can then bind H_2 *via* a combination of ion-quadrupole and ion-induced dipole interactions.[58,59]

11.4 The Host–Guest Chemistry of CPPs

Supramolecular chemistry is the branch of chemistry that focuses on systems composed of discrete chemical species held together through intermolecular forces and as such was described by Nobel laureate Jehn-Marie Lehn

as "chemistry beyond the molecule". A common example of supramolecular chemistry in action is the formation of host–guest complexes, which involves the inclusion of at least one guest molecule within the cavity of larger hosts. Akin to the supramolecular chemistry observed with molecular hosts, there have been selected examples of CPPs hosting smaller molecules within their pores. For example, Zhao *et al.* have described the storage and release of small molecules within a CMP, where the size of the pores changed upon exposure to irradiation.[60] The CMP film, prepared by electropolymerisation, featured azo-benzene groups that underwent reversible *cis–trans* isomerisation when exposed to different wavelengths of light (355 nm produced the *cis*-configuration while 480 nm produced the *trans*-configuration). Using high resolution transmission electron microscopy, the authors discovered that the *trans*-to *cis*-isomerisation was accompanied by a change in the pore size from 1.47 nm to 0.87 nm. The larger pore size when the azo-benzene groups were in the *trans*-configuration allowed the guest molecule to diffuse into the CMP. Upon isomerisation of the azo-group, the reduction in pore size trapped the guest within the pores of the CMP.

There have been several reported examples of porous organic polymers that successfully incorporate common host molecules, such as calix[4] arenes, resorcin[4]arenes and pillar[5]arenes, which brings the prospect of selective guest binding.[61–63] A prime example of this has been demonstrated by Talapaneni *et al.*, who have reported that pillar[5]arene based CMPs, P5-CMPs, can selectively adsorb propane over methane (see Figure 11.13).[64] The authors determined that **P5-CMP-1** possessed an isosteric heat of adsorption for propane of 53 kJ mol^{-1} at zero coverage compared to 20 kJ mol^{-1} for methane. This can be attributed to the better match between the cavity diameter of the pillar[5]arene group (4.7 Å) and the kinetic diameter of propane (4.3 Å)

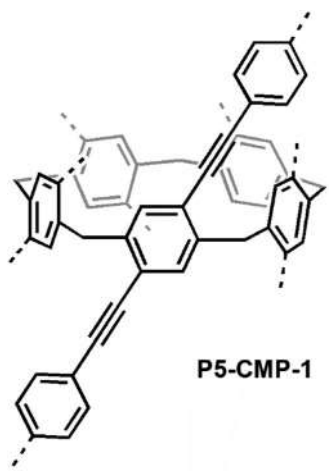

Figure 11.13 Structure of **P5-CMP-1**, which incorporates pillar[5]arene groups into a CMP.

over methane (3.8 Å). Furthermore, the isosteric heat of adsorption for propane was found to be significantly higher than other porous materials (33–37 kJ mol^{-1}), suggesting the presence of significant C–H···π interactions.

11.5 Conclusions

In recent years, CPPs have evolved from an emerging material to a truly versatile class of porous polymer networks. This success is, in part, underpinned by the plethora of building blocks that are available for their construction and permit functionality to be imparted on CPPs. This success is also underlain by the nanoscale structure of CPPs and the extensive research that has been directed towards controlling their pore structure and morphology. Despite this success, CPPs have yet to move beyond academic interest and gain industrial focus. This section will summarise some of the practical problems facing the use of CPPs outside of academic settings and provide a prospective outlook on the future direction of this field of research.

11.5.1 Limitations of CPPs

While CPPs have undoubtedly demonstrated their utility in various applications, their cross-linked nature presents a practical barrier that limits processing options and prevents widespread adoption of CPPs. The general insolubility of CPPs means that conventional plastic processing techniques such as 3D printing or solvent casting are currently impractical (there is one reported example of a soluble CMP allowing solvent casting).[13] This primarily restricts CPPs to use as either powders or films, although research has demonstrated that CPPs can be used to coat fibres or form composite materials. Recently, Liu *et al.* have also demonstrated a technique for making conjugated microporous thermosets from a processable melted precursor while Liao and co-workers have reported on a method to graft CMPs to flexible carbon fibres.[65,66]

Another major barrier to CPP synthesis is the cost of synthesis, which reflects the fact that the building blocks can be expensive and are used to form the bulk of the material, even though only the surface is freely accessible. An alternative to this could be to explore utilising CPPs as either thin coatings on cheap supports, such as graphene oxide, or with a shell type architecture as both strategies would minimise the ratio of bulk material to exposed surface with the obvious benefit of reducing cost.[41,49]

11.5.2 Technology Facilitated Design and Synthesis

Regardless of any limitations that CPPs may have, the extensive research that has been achieved in recent years has demonstrated that CPPs provide a pliant canvas that can be tailored to introduce specific types of functionality. In the future, the design of CPPs could be aided by computational modelling

as this would allow the properties to be investigated and the structure optimised, without the need for an iterative synthetic approach. Computational modelling of amorphous polymer networks represents a more challenging endeavour compared to crystalline materials, for which structural data can be provided by diffraction techniques. Approaches taken by both Trewin and co-workers and Jian and co-workers have separated the modelling of the bond forming reactions into a series of steps.[67,68] Broadly speaking these involved constructing an initial cell containing reagents, catalyst and solvent to simulate the reaction. An iterative search for new bonds to form and optimisation of the resultant structure was carried out until no new bonds could form. Additional consideration of how small molecules such as solvent, unreacted monomer and smaller oligomers were removed during desolvation and workup stages were taken by Trewin and co-workers.[67] Good approximation between the computed data and experimental measured properties such as surface area and bulk density were obtained, however, limitations on the computational calculations still existed. For example, Trewin and co-workers were unable to assess the pore size distribution above 20 Å, due to the limitations of the simulated cell size.

Computational modelling can also be used to explore the effect that different architectural features would have on the CPPs properties. Fan *et al.* have computationally modelled the electronic structure and adsorption of benzene for a series of single-walled CMP nanotubes.[69] Through density-functional theory (DFT) calculations, the authors showed that the nanotubes exhibited lower binding energies to benzene in comparison to films, despite the nanotube exhibiting larger pores and higher surface area. The reason for the lower adsorption with the nanotube CMP was attributed to the curvature of the tube exposing a smaller area of interaction between benzene and adsorbent. The diameter of rings that made up the nanotubes was also calculated to influence the properties of the CPP: larger diameters of rings led to a smaller area for physisorption, resulting in a lower binding energy.

11.5.3 Perspective Outlook

The research conducted into CPPs in recent years has demonstrated the suitability of this class of materials towards a plethora of applications. As has been discussed in this book chapter, the protean nature of CPPs is, in part, due to the wide range of building blocks at one's disposal when designing CPPs, as this allows for a diverse functionality to be imparted on the material. On top of this, the synthetic conditions employed, including the use of templating agents, and post synthetic modification processes, allows for even more complexity to be introduced to these materials, such as hierarchical porosity and specific morphologic features. To conclude, we predict that in the future, through a combination of judicious building block selection and innovative synthetic protocols, and potentially guided by computational modelling, researchers will continue to develop multifunctional CPPs that can help satisfy society's dynamic need for ever more advanced polymer materials.

References

1. J. Li, X. Wang, G. Zhao, C. Chen, Z. Chai, A. Alsaedi, T. Hayat and X. Wang, *Chem. Soc. Rev.*, 2018, **47**, 2322.
2. Y. Yuan and G. Zhu, *ACS Cent. Sci.*, 2019, **5**, 409.
3. H. V. Babu, M. G. M. Bai and M. R. Rao, *ACS Appl. Mater. Interfaces*, 2019, **11**, 11029.
4. L. Tan and B. Tan, *Chem. Soc. Rev.*, 2017, **46**, 3322.
5. N. B. McKeown and P. M. Budd, *Chem. Soc. Rev.*, 2006, **35**, 675.
6. D. Taylor, S. J. Dalgarno, Z. Xu and F. Vilela, *Chem. Soc. Rev.*, 2020, **49**, 3981.
7. J. S. M. Lee and A. I. Cooper, *Chem. Rev.*, 2020, **120**, 2171.
8. B. J. Smith, A. C. Overholts, N. Hwang and W. R. Dichtel, *Chem. Commun.*, 2016, **52**, 3690.
9. T. Ben and S. Qiu, *CrystEngComm*, 2013, **15**, 17.
10. R. Xiao, J. M. Tobin, M. Zha, Y.-L. Hou, J. He, F. Vilela and Z. Xu, *J. Mater. Chem. A*, 2017, **5**, 20180.
11. P. Su, X. Zhang, Z. Xu, G. Zhang, C. Shen and Q. Meng, *New J. Chem.*, 2019, **43**, 17267.
12. J. X. Jiang, F. Su, H. Niu, C. D. Wood, N. L. Campbell, Y. Z. Khimyak and A. I. Cooper, *Chem. Commun.*, 2008, **8**, 486.
13. G. Cheng, T. Hasell, A. Trewin, D. J. Adams and A. I. Cooper, *Angew. Chem., Int. Ed.*, 2012, **51**, 12727.
14. Y.-B. Zhou and Z.-P. Zhan, *Chem. - Asian J.*, 2018, **13**, 9.
15. Y.-L. Wong, J. M. Tobin, Z. Xu and F. Vilela, *J. Mater. Chem. A*, 2016, **4**, 18677.
16. F. Vilela, K. Zhang and M. Antonietti, *Energy Environ. Sci.*, 2012, **5**, 7819.
17. B. C. Ma, S. Ghasimi, K. Landfester, F. Vilela and K. A. I. Zhang, *J. Mater. Chem. A*, 2015, **3**, 16064–16071.
18. J. M. Tobin, J. Liu, H. Hayes, M. Demleitner, D. Ellis, V. Arrighi, Z. Xu and F. Vilela, *Polym. Chem.*, 2016, **7**, 6662.
19. H. Bohra, S. Y. Tan, J. Shao, C. Yang, A. Efrem, Y. Zhao and M. Wang, *Polym. Chem.*, 2016, **7**, 6413.
20. X. Jiang, Y. Liu, J. Liu, X. Fu, Y. Luo and Y. Lyu, *New J. Chem.*, 2017, **41**, 3915.
21. J. Schmidt, M. Werner and A. Thomas, *Macromolecules*, 2009, **42**, 4426.
22. L. Ma, M. M. Wanderley and W. Lin, *ACS Catal.*, 2011, **1**, 691.
23. X. Ding and B.-H. Han, *Angew. Chem., Int. Ed.*, 2015, **54**, 6536.
24. P. Ju, S. Wu, Q. Su, X. Li, Z. Liu, G. Li and Q. Wu, *J. Mater. Chem. A*, 2019, **7**, 2660.
25. H. Zhou, B. Zhao, C. Fu, Z. Wu, C. Wang, Y. Ding, B.-H. Han and A. Hu, *Macromolecules*, 2019, **52**, 3935.
26. Y. Wei, W. Chen, X. Zhao, S. Ding, S. Han and L. Chen, *Polym. Chem.*, 2016, **7**, 3983.
27. Z. H. Guo, C. Wang, Q. Zhang, S. Che, H. C. Zhou and L. Fang, *Mater. Chem. Front.*, 2018, **2**, 396.

28. B. Kiskan and J. Weber, *ACS Macro Lett.*, 2012, **1**, 37.
29. H. Urakami, K. Zhang and F. Vilela, *Chem. Commun.*, 2013, **49**, 2353.
30. J. Liu, J. M. Tobin, Z. Xu and F. Vilela, *Polym. Chem.*, 2015, **6**, 7251.
31. T. Hasell, C. D. Wood, R. Clowes, J. T. A. Jones, Y. Z. Khimyak, D. J. Adams and A. I. Cooper, *Chem. Mater.*, 2010, **22**, 557.
32. J. Rouquerol, D. Avnir, C. W. Fairbridge, D. H. Everett, J. M. Haynes, N. Pernicone, J. D. F. Ramsay, K. S. W. Sing and K. K. Unger, *Pure Appl. Chem.*, 1994, **66**, 1739.
33. B. D. Zdravkov, J. J. Čermák, M. Šefara and J. Janků, *Cent. Eur. J. Chem.*, 2007, **5**, 385.
34. B. Kim, N. Park, S. M. Lee, H. J. Kim and S. U. Son, *Polym. Chem.*, 2015, **6**, 7363.
35. J. Chen, T. Qiu, W. Yan and C. F. J. Faul, *J. Mater. Chem. A*, 2020, **8**, 22657.
36. J. Lee, O. Buyukcakir, T.-W. Kwon and A. Coskun, *J. Am. Chem. Soc.*, 2018, **140**, 10937.
37. K. Zhang, D. Kopetzki, P. H. Seeberger, M. Antonietti and F. Vilela, *Angew. Chem., Int. Ed.*, 2013, **52**, 1432.
38. W. Huang, B. C. Ma, H. Lu, R. Li, L. Wang, K. Landfester and K. A. I. Zhang, *ACS Catal.*, 2017, **7**, 5438.
39. S. Chakraborty, Y. J. Colón, R. Q. Snurr and S. T. Nguyen, *Chem. Sci.*, 2015, **6**, 384.
40. D. Kang, J. H. Ko, J. Choi, K. Cho, S. M. Lee, H. J. Kim, Y. J. Ko, K. H. Park and S. U. Son, *Chem. Commun.*, 2017, **53**, 2598.
41. J. Lee, J. G. Kim and J. Y. Chang, *Sci. Rep.*, 2017, **7**, 13568.
42. J. Tan, J. Wan, J. Guo and C. Wang, *Chem. Commun.*, 2015, **51**, 17394.
43. I. Pulko and P. Krajnc, *Macromol. Rapid Commun.*, 2012, **33**, 1731.
44. K. Zhang, Z. Vobecka, K. Tauer, M. Antonietti and F. Vilela, *Chem. Commun.*, 2013, **49**, 11158.
45. Z. J. Wang, S. Ghasimi, K. Landfester and K. A. I. Zhang, *Chem. Commun.*, 2014, **50**, 8177.
46. Y. Yuan, Y. Yang, X. Ma, Q. Meng, L. Wang, S. Zhao and G. Zhu, *Adv. Mater.*, 2018, **30**, 1.
47. C. Gu, N. Huang, Y. Wu, H. Xu and D. Jiang, *Angew. Chem., Int. Ed.*, 2015, **54**, 11540.
48. X. Zhuang, F. Zhang, D. Wu, N. Forler, H. Liang, M. Wagner, D. Gehrig, M. R. Hansen, F. Laquai and X. Feng, *Angew. Chem., Int. Ed.*, 2013, **52**, 9668.
49. X. Zhuang, D. Gehrig, N. Forler, H. Liang, M. Wagner, M. R. Hansen, F. Laquai, F. Zhang and X. Feng, *Adv. Mater.*, 2015, **27**, 3789.
50. X. Shen, M. Faheem, Y. Matsuo, S. Aziz, X. Zhang, Y. Li, J. Song, Y. Tian and G. Zhu, *J. Mater. Chem. A*, 2019, **7**, 2507.
51. S. J. Yang, X. Ding and B. H. Han, *Macromolecules*, 2018, **51**, 947.
52. T. Chen, W. Zhang, B. Li, W. Huang, C. Lin, Y. Wu, S. Chen and H. Ma, *ACS Appl. Mater. Interfaces*, 2020, **12**, 56385.
53. N. Huang, G. Day, X. Yang, H. Drake and H.-C. Zhou, *Sci. China: Chem.*, 2017, **60**, 1007.
54. L. Zou, Y. Sun, S. Che, X. Yang, X. Wang, M. Bosch, Q. Wang, H. Li, M. Smith, S. Yuan, Z. Perry and H. C. Zhou, *Adv. Mater.*, 2017, **29**, 1.

55. R. Dawson, A. Laybourn, R. Clowes, Y. Z. Khimyak, D. J. Adams and A. I. Cooper, *Macromolecules*, 2009, **42**, 8809.
56. D. Tan, W. Fan, W. Xiong, H. Sun, A. Li, W. Deng and C. Meng, *Eur. Polym. J.*, 2012, **48**, 705.
57. S. Yuan, B. Dorney, D. White, S. Kirklin, P. Zapol, L. Yu and D.-J. Liu, *Chem. Commun.*, 2010, **46**, 4547.
58. K. Srinivasu and S. K. Ghosh, *RSC Adv.*, 2014, **4**, 4170.
59. K. R. S. Chandrakumar and S. K. Ghosh, *Chem. Phys. Lett.*, 2007, **447**, 208.
60. R. Zhao, J. Han, M. Huang, F. Liu, L. Wang and Y. Ma, *Macromol. Rapid Commun.*, 2017, **38**, 1700274.
61. Z. Li, X. Li and Y.-W. Yang, *Small*, 2019, **15**, 1805509.
62. X. Li, Z. Li and Y.-W. Yang, *Adv. Mater.*, 2018, **30**, 1800177.
63. D. Shetty, S. Boutros, T. Skorjanc, B. Garai, Z. Asfari, J. Raya and A. Trabolsi, *J. Mater. Chem. A*, 2020, **8**, 13942.
64. S. N. Talapaneni, D. Kim, G. Barin, O. Buyukcakir, S. H. Je and A. Coskun, *Chem. Mater.*, 2016, **28**, 4460.
65. W. Liu, S. D. Jiang, Y. Yan, W. Wang, J. Li, K. Leng, S. Japip, J. Liu, H. Xu, Y. Liu, I. H. Park, Y. Bao, W. Yu, M. D. Guiver, S. Zhang and K. P. Loh, *Nat. Commun.*, 2020, **11**, 1.
66. W. Lyu, W. Zhang, H. Liu, Y. Liu, H. Zuo, C. Yan, C. F. J. Faul, A. Thomas, M. Zhu and Y. Liao, *Chem. Mater.*, 2020, **32**, 8276.
67. J. M. H. Thomas, C. Mollart, L. Turner, P. Heasman, P. Fayon and A. Trewin, *J. Phys. Chem. B*, 2020, **124**, 7318.
68. C. Song, F. Hu, Z. Meng, S. Li, W. Shao, T. Zhang, S. Liu and X. Jian, *RSC Adv.*, 2020, **10**, 4258.
69. W. J. Fan, Y. L. Zhao, Y. C. Hu, H. Shi, D. Z. Tan and R. Q. Zhang, *Int. J. Quantum Chem.*, 2018, **118**, 1.

CHAPTER 12

Polymer–Clay Hybrids; General Overviews and Recent Trends

KAMONNART (JAA) IMWISET[†a], ARANEE (PLENG) TEEPAKAKORN[†a], PLOYPAILIN (MILIN) SAENGDET[†b], CHALUNDA (BAITONG) TIRAYAPHANITCHKUL[†b] AND MAKOTO OGAWA*[b]

[a]School of Molecular Science and Engineering, Vidyasirimedhi Institute of Science and Technology (VISTEC), 555 Moo 1 Payupnai, Wangchan, Rayong 21210, Thailand; [b]School of Energy Science and Engineering, Vidyasirimedhi Institute of Science and Technology (VISTEC), 555 Moo 1 Payupnai, Wangchan, Rayong 21210, Thailand
*E-mail: makoto.ogawa@vistec.ac.th

12.1 Introduction

Numerous polymers/plastics are used for a wide range of applications owing to their materials' characteristics and versatile processing, while there are unlimited demands for the improved properties, environmentally friendly materials and preparation, emerging novel functions. One of the promising strategies for the improved materials' performances and characteristics is the use of polymer-based nanocomposites (hybrids) composed of filler. The addition/incorporation of various fillers with varied amounts has been done using different preparation/fabrication pathways. Among the fillers, clay minerals have been used extensively, since the pioneering work on nylon–clay

[†]Those authors contributed equally to the manuscript.

Nanoscience & Nanotechnology Series No. 55
Concepts and Design of Materials Nanoarchitectonics
Edited by Omar Azzaroni and Katsuhiko Ariga

Published by the Royal Society of Chemistry, www.rsc.org

nanocomposites (later on named NCH) developed in 1980.[1] Clay minerals are naturally occurring, chemically inert, environmentally friendly, and available with acceptable prices. The asymmetric shapes of fundamental particles, which are composed of their crystalline structures, as fibrous and platy nanoparticles with varied aspect ratio lead the functions of the resulting hybrid materials more versatile. In addition, the surface of individual particles of clay minerals can be modified chemically to manage the affinity at the interfaces between polymers and clay minerals for the controlled dispersion of the filler in polymer matrices, which is thought to be a parameter to affect the materials performance of the hybrids. Here, fundamentals of polymer–clay hybrids for each typical application will be introduced after the general background of structural and chemical characteristics of clay minerals and classification of possible interfacial design between polymer and filler.

12.2 General Background

12.2.1 Classification of Clay Minerals

The structural and compositional characteristics of the clay minerals are summarized in Table 12.1.

Mica-like 2 : 1 type layered clay minerals, composed of one gibbsite (or brucite) like sheet composed of edge-sharing $Mg(OH)_2$ or $Al(OH)_3$ octahedron sandwiched by two sheets of silicate formed by the edge-sharing SiO_2 tetrahedron, are the main component of bentonite. The mica type clay minerals are further classified into three groups of clay minerals (smectite, vermiculite, and mica) depending on the degree of isomorphous substitution. Among them, smectites have been used most extensively as polymer additives. Smectites are classified into several types by the structures; component of octahedral sheet (aluminum or magnesium) and the location of isomorphous substitution (in tetrahedral sheet or octahedral sheet) to montmorillonite, beidellite, saponite, hectorite and so on.[2,3] The most important characteristic of smectites is the expandable interlayer space to accommodate various kinds of guest species and well into the water.

Table 12.1 Examples of clay minerals.

Clay mineral	Type	Particle shape
Kaolinite Halloysite	1 : 1 Phyllosilicate	Hexagonal plate Tube
Montmorillonite Beidellite	2 : 1 Phyllosilicate (Dioctahedral smectites)	Stacked plate
Saponite Hectorite	2 : 1 Phyllosilicate (Trioctahedral smectites)	
Attapulgite Sepiolite Palygorskite	2 : 1 Inverted ribbons	Single lath or bundles of laths

Type 1:1 layered structures composed of one sheet of silicate formed by the edge-sharing SiO_2 tetrahedron and one gibbsite (or brucite) like sheet composed of edge-sharing $Mg(OH)_2$ or $Al(OH)_3$ octahedron and following two groups of clay minerals (kaolinite group (kaolinite, nacrite, *etc.*) and halloysite group) are also known. The well-crystallized kaolinite particles are hexagonal plate. The dimensions of platy particles of kaolinite group clay minerals range within sub microns to microns in the lateral size and the thickness below microns.[4] On the other hand, halloysite possesses a tubular structure and 1-D particle morphology. The outside and inside diameters of the tube are in the range of tens of nanometers to submicron, respectively.[5] The inherent hollow nanotube structure makes the materials application interesting.[6]

Chain-structured clay minerals (hornblende-like chains of silica tetrahedrons linked by oxygens and hydroxyls of octahedron containing $Mg(OH)_2$ or $Al(OH)_3$) such as attapulgite, sepiolite, and palygorskite are also known. The structure of attapulgite was determined by Bradley[7] where silica chains similar to those in amphibole (needle-like crystals composed of linked SiO_4 tetrahedra containing iron and/or magnesium in their structures). The structures of sepiolite and palygorskite are composed of ribbons of a 2:1 phyllosilicate structure, and each ribbon is linked to the next inversion of SiO_4 tetrahedra along with a set of Si–O bonds.[8] The morphology of attapulgite particle is single lath and bundles of the laths in the length of about 4 to 5 microns, with the thickness of 5 to 10 nm. The width is two or three times larger than the thickness. Sepiolite has elongated fibrous shapes like attapulgite with similar size.[9] In nature, fibrous clay minerals exist as aggregates of the fibers, often forming interwoven bundles and leading rigid particles. Thus, separation of fibrous clays to obtain fibrillated silicates to achieve high dispersion of fibrous particles in polymers is critical for the polymer–clay hybrids. Clay minerals of several structure types (tube, fiber, plate) have been used as fillers to modify the properties of polymers.[10–12]

12.2.2 Surface Modification of Clay Minerals

In order to make the clay surface compatible to various polymers, the surface of clay minerals, which is normally hydrophilic, is modified. Organophilic modification is done extensively and the reaction for the modification is based on the adsorption of surfactant.[13,14] When there is hydroxyl group on the surface of particles, grafting with silane coupling reagents is possible[15,16] (Figure 12.1).

12.2.3 Preparation of Polymer–Clay Hybrids

Polymer–clay hybrids have been prepared by polymer intercalation and *in situ* polymerization of monomers (Figure 12.2). For polymer intercalation, the common processing methods to produce polymer–clay hybrids are melt intercalation (mixing of clay with polymer melt) and solution blending

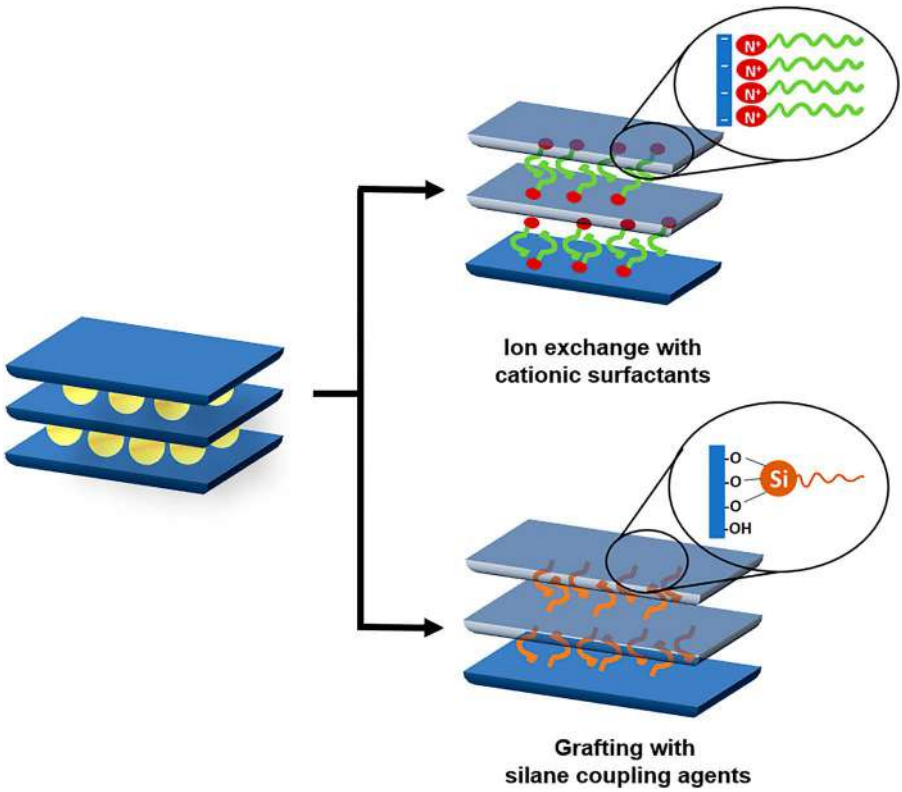

Figure 12.1 Schematic representation of organic modification of clay.

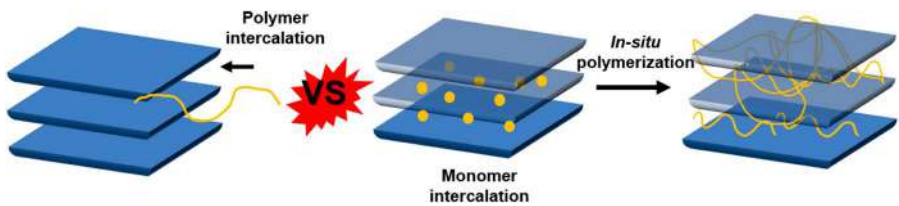

Figure 12.2 Schematic representation of the preparation of the types of polymer–clay hybrids.

(mixing of clay with polymer solution) using pre-synthesized polymers and clay. For the thermoplastics, masterbatch of polymer containing clay is prepared and is subsequently molded into the shapes for the desired application. Spontaneous swelling or dispersion of clay into polymers happens, while mechanochemical processing (sonication, intrusion, *etc.*) is required to obtain better dispersion in many cases.

Intercalation of monomers into the interlayer space and subsequent polymerization (*in situ* polymerization) is also commonly used. For the radical polymerization, initiator is mixed with monomer or is adsorbed on clay before the reaction with monomer.

12.2.4 Possible Structure Types of Polymer–Clay Hybrids

The possible structure types are classified into four as shown in Figure 12.3. The simplest structure is layered clay minerals containing polymers in the interlayer spaces (intercalation compounds, Figure 12.3A). Intercalation compounds are available as powders while they can be processed as oriented films on a substrate by simple casting or several coating methods (dip-coating, spin-coating, and spray-coating) and the coating film can be peeled off from the substrate to obtain a self-standing film. The second type (Figure 12.3B) is polymer containing filler as physical mixture. Thanks to the fine particles of clay minerals (after appropriate powder processing), the properties of polymers can be modified to some extent in this type even though the composite is not "nano" dimension. The third type (Figure 12.3C) is composed of polymer intercalated (but not exfoliated) layered clay minerals dispersed homogeneously in polymer (Figure 12.3C). The intrinsic dimension of clay minerals is the same after the hybridization, while the interlayer is expanded to some extent by the intercalation of polymer, which make the difference between 3B and 3C. The 4th type is exfoliation of layered clay minerals, where clay nanosheets are dispersed homogeneously in polymer as shown in Figure 12.3D. The classification is applicable when layered clay minerals are used to be hybridized, and 3A, 3C, and 3D are possible for smectites. For other layered clay minerals, 3B is common and 3C is possible, while 3D is difficult. X-Ray diffraction studies (the basal spacing) and TEM observations are used to clarify the structures of polymer/clay nanocomposites when layered clay minerals are used.

Similar classification (as shown in Figure 12.3) is applicable when fibrous and tubular clay minerals are used, however, the X-ray diffraction is not useful for structural determination for fibrous and tubular clay minerals.

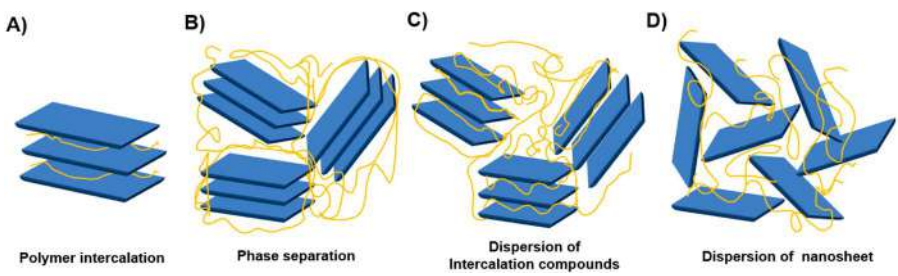

Figure 12.3 The structural variation of polymer–clay hybrids; (A) polymer intercalation, (B) phase separation (no intercalation), (C) dispersion of intercalation compounds, and (D) dispersion of nanosheet.

12.3 Applications

12.3.1 Gas Barrier

Gas barrier properties are required for several applications including food packaging, where product quality is expected to be maintained for long-term storage. Reduction of gas permeation of the packaging materials is the key to prevent permeation of gases – especially water vapor, oxygen and carbon dioxide, which cause food spoilage due to chemical, physical, or biological changes – from the external environment. Plastics are attractive for industrial production and transportation owing to low cost and lightweight products over glass and metal materials. Besides, transparency and flexibility of many plastics make their application more versatile. Accordingly, improvement of barrier properties of plastics is expected for such applications as vacuum insulation panel, hydrogen tank, gasket, solar module, and displays in such optoelectronics devices as Liquid Crystalline Display (LCD) or Organic Light Emitting Device (OLED), where higher barrier ability is demanded. For vacuum insulation panels used for the construction of building and household appliances, a gas barrier is needed to prevent heat transfer due to convection currents to reduce heat loss and improve energy efficiency. For storage applications, gaskets, and gas storage tanks, gas barrier properties are the main concerns to prevent leakage of the gases, especially small molecules such as H_2 gas. In the case of organic electronic devices, photovoltaic systems and electronic displays, oxygen and moisture are the main reasons for the degradation of organic parts. Oxygen and moisture also play a role on the luminescence quenching contributes to the performances of OLEDs. Taking these drawbacks into accounts, barrier properties are vital demand to achieve excellent efficiency and long lifetime of organic optoelectronic devices.

Incorporation of impermeable inorganic filler into polymer reduces mass transfer properties over the neat polymer because inorganic filler behaves as a barrier for the diffusion of gas molecules and increases path tortuosity across the polymer film. According to the tortuous path model, an ideal structure, in which fillers with high aspect ratios are homogeneously dispersed and regularly arranged perpendicular to the direction of gas diffusion as shown in Figure 12.4, was proposed to achieve superior barrier properties. The permeability of gas molecules in polymer–clay hybrids has been studied to highlight the key parameters and structure–barrier property relationship.[17]

12.3.1.1 Polymer–Layered Clay Mineral Hybrids

Based on the tortuous path model, mass transfer of gases is influenced by the aspect ratio and the volume fraction of filler, homogeneity of the filler dispersion and orientation of filler in a polymer film, which are the parameters to affect the gas barrier properties. As to the roles of filler shape on the barrier properties, platy particles are more efficient to decrease the relative permeability (P/P_0) as compared with iso-dimensional or simply 1-dimensionally elongated particles.[11] Among the possible platy particles used as fillers,

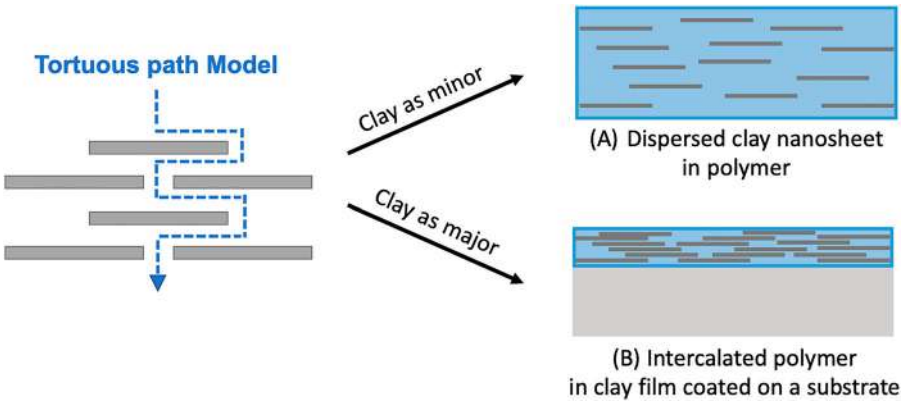

Figure 12.4 Schematic drawing to demonstrate two types of polymer–clay hybrid barrier flim; (A) dispersed clay nanosheet in polymer and (B) intercalated polymer in clay film coated on a substrate.

layered clay minerals, especially smectites, have attracted significant attention because of their natural abundance, low cost, high aspect ratio, particle size ranging from tens to thousands of nanometer, high mechanical strength and stiffness, and swelling ability.[12]

The degree of dispersion of clay minerals in polymer matrices depends on the preparation process and compatibility between clay minerals and polymers. The possible dispersion of clay minerals in polymer–clay hybrids can be classified into three types: phase-separated, intercalated, and the fully exfoliated system as shown in Figure 12.3D, and the latter is known as an "ideal" structure to achieve better barrier properties as demonstrated in Figure 12.4A. The smectite clay, which is originally hydrophilic, has good compatibility with hydrophilic systems such as water-soluble polymers. For such applications that required moisture resistance, polymers with high hydrophobicity are necessary to decrease the penetration of moisture. However, incompatibility between hydrophilic clay and hydrophobic polymer often causes the macroscopic phase separation (immiscible). Therefore, organic modification of smectites has been done to reduce the surface energy of smectites and promote efficient intercalation of hydrophobic polymers to achieve homogeneous exfoliation of smectites. Reduced permeability of polymer–clay hybrids can be explained as the result of the tortuosity effect induced by inorganic impermeable fillers which make the gas diffusion pathway longer. Moreover, dense packing of polymer confined in the interlayer space of smectites causes reduction in polymer free volume as well as increase in crystallinity of polymer chains. The resulting suppression of thermal vibration of polymer chains confined in the interlayer space is the main reason for decreasing permeability of moisture and gases in polymer–clay hybrids. Depending on the applications, the requirements of such physical properties are different, thus diverse types of clay minerals and polymers possibly used for such applications are summarized in Table 12.2. For the

Table 12.2 Examples of fillers, polymers used for gas barrier applications.

Applications	Requirements	Example of polymers	Example of fillers	Important role of filler
Food packaging	- Gas barrier (H_2O, O_2, CO_2) - Flexibility - Transparency	PE, PP, PS, PVC, PET, PLA, *etc.*	Syn-MMT, O-Syn-MMT, HAL, SEP, Mica	- Reduce permeation of moisture, oxygen, and carbon dioxide
Vacuum insulating panel	- Gas barrier (H_2O and O_2) - Thermal insulator - Heat durability - Flexibility	PU, PVA, PS, PI, EPS, *etc.*	MMT, O-MMT	- Reduce permeation of external gases resulting in heat transfer
Gasket	- Gas barrier (target gases) - Pressure resistant - Chemical resistant - Flexibility - Heat durability	Elastomers; NR, PTFE, *etc.*	MMT, O-MMT, Li-MMT	- Reduce diffusion of gases or leakage of liquids
Gas storage tank	- Gas barrier (H_2, He, or CO_2) - Heat durability	AR, MMN, GL, AQ nylon, *etc.*	MMT, Li-MMT	- Prevent permeation of storage gases
Inorganic solar cell	- Gas barrier (H_2O and O_2) - Transparency - UV resistance - Flexibility - Durability	PVA, PVB, EVA, EMA, TPU, PIB, PTFE, PFA, FEP, PET, *etc.*	Syn-MMT, O-Syn-MMT, Li-Syn-MMT	- Reduce oxygen and moisture permeation causing degradation of perovskite
Organic solar cell back sheet	- Gas barrier (H_2O and O_2) - Flexibility - UV resistance - Durability	PVF, PVDF, PEN, PET, EVA, ETFE, PTFE, TPU, PMMA, PP, PE, PI, PVA, PVB, PDMS, *etc.*	O-Syn-MMT, Li-Syn- MMT	- Reduce oxygen and moisture permeation causing degradation of organic substance
Display (OLED, LCD and LED)	- Gas barrier (H_2O and O_2) - Transparency - Flexibility	PET, PAS, PU, *etc.*	O-Syn-MMT, Li-Syn-MMT	- Reduce oxygen and moisture permeation causing fluorescence quenching and dye degradation

applications which required high transparency, synthetic smectite has been used to avoid color impurities such as iron and other transition metals in natural clay minerals.

Theoretically, the tortuous effect is more significant with increasing the content of inorganic platelets. However, homogeneous dispersion of exfoliated clay nanosheet in polymer matrix is difficult to achieve due to the possible particle agglomeration at high filler content. The content of fillers in the polymer is basically low (<10 wt%) to avoid particle agglomeration. Poor barrier properties have often been observed due to such defects as interfacial voids or cracking in the products. In addition, the incompatibility between clay and polymer also causes the interfacial voids and the cracks.

On the contrary to the exfoliated type polymer–clay hybrids (Figure 12.3D), intercalated types (Figure 12.3C) have attracted interest due to high gas barrier properties and heat resistance when fabricated as films.[18] The oriented clay platelets act as gas barriers where the polymer plays a role as a binder for the film formation.[19] The improved barrier properties of the film to moisture and other gases is caused by the dense packing of clay platelets as shown in Figure 12.4B. The gas barrier property was confirmed by the stability of the dye in the interlayer space of smectite.[20]

The hybrid film with high barrier properties to oxygen and moisture has been obtained even when the preparation of hybrid film has been done by waterborne formulation.[21,22] Recently, the effects of smectite contents in waterborne polymer/clay hybrids on the oxygen permeation were carefully examined.[22] The oxygen permeability was decreased when the volume fraction of smectite in waterborne polymer matrix increased. The limitation of oxygen permeation was attributed to the reduction of polymer segment motion by confining in the interlayer space of smectite. In addition to the gas barrier property, insoluble hybrid films were obtained by the hybridization of a waterborne polymer, poly(vinyl alcohol) (PVA), with a synthetic hectorite (HEC), which exhibited self-healing behavior in water.[23] The sedimentation during casting/drying induced the orientation of intercalated smectites platy particles parallel to the substrate. Superior barrier property has been achieved using reduced-charge smectites prepared by the Hoffmann–Klemen treatment, which is done by the thermal treatment of Li exchanged dioctahedral type smectites.[24] The improved barrier property was explained by the decrease of the interlayer water content, which led dense packing of the interlayer polymer.

The transportation of moisture, gases, and other solutes in the media containing clays has been studied to show the important roles of the preferential orientation of clay platelets, which have been shown by X-ray diffraction/scattering data.[25,26]

12.3.1.2 Polymer–Fibrous (and Tubular) Clay Mineral Hybrids

Fibrous clay minerals (sepiolite and palygorskite) have been used as a filler to improve mechanical properties, while scarcely applied for the improvement of gas barrier properties.[27] The introduction of fibrous clay minerals can increase

the crystallinity of polymer and act as an obstacle to introducing more torturous paths. However, tortuosity effect induced by layered clays is more efficient than fibrous clays as understood by simple geometrical consideration.[28]

12.3.2 Anticorrosion

There are several types of corrosion such as pitting, galvanic and uniform corrosion, depending on the types of materials and the environments. Concepts for corrosion prevention are environmental alteration, cathodic and anodic protection, material selection, structural design, coating and use of corrosion inhibitor. Polymer coatings have been used for protecting metals against corrosion due to their barrier property against such aggressive species as O_2 and H^+. However, the polymer coatings cannot be perfectly impenetrable so localized corrosion may occur through the cracks. The cracks of polymer coatings can occasionally develop during their service period, resulting in the failure of coatings. Layered clay minerals have been incorporated into many types of polymers in order to enhance the corrosion resistance of metallic substrates by improving barrier properties and increasing diffusion path length of corrosive media.[29] The concept of nanocontainer-based self-healing coating by adding nanocontainers loaded with corrosion inhibitors has been developed for preventing the corroded area and spontaneous leakage of corrosion inhibitor to the environment as schematically shown in Figure 12.5. Layered clay minerals and other inorganic nanomaterials have been used as nanocontainers of corrosion inhibitors.[30]

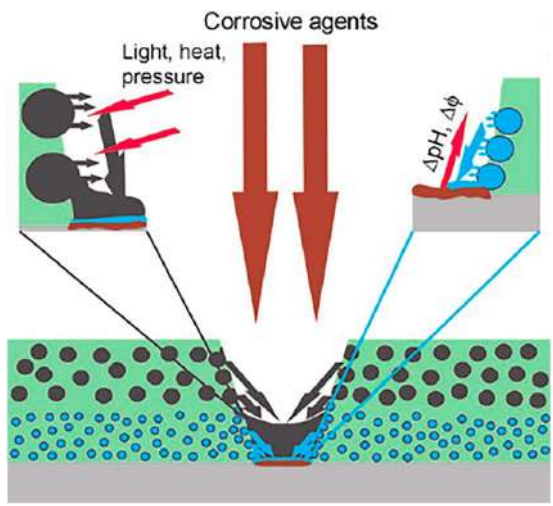

Figure 12.5 The concept of nanocontainer-based self-healing coating.[31] Adapted from ref. 31 with permission from John Wiley & Sons, Copyright © 2007 WILEY-VCH Verlag GmbH & Co. KGaA, Weinheim.

12.3.2.1 Polymer–Layered Clay Mineral Hybrids

Layered clay minerals are used as filler in anticorrosion polymer coating. The platy shape increases the length of diffusion path tortuosity for oxygen and moisture and decrease the permeability of the coating due to their high aspect ratio and large surface area as mentioned in the section on gas barrier properties (Section 12.3.1). The dispersion of fillers should be uniform to obtain significant improvement of the properties. Accordingly, the hydrophilic surface of clay minerals has been modified through ion-exchange with quaternary alkylammonium or alkylphosphonium cations to be compatible to hydrophobic polymer. Organically modified montmorillonite (O-MMT) has been widely used for the improvement of anticorrosion efficiency of polymers as summarized in Table 12.3.[29] For nanocontainer-based self-healing coatings concepts, both negatively charged and positively charged layered materials (smectite and layered double hydroxide, respectively) have been used. The release of the inhibitor can be triggered by the presence of metal cations, H^+, OH^-, Cl^-, *etc.* through ion-exchange reaction. By this concept, Na^+-montmorillonite (MMT) was exchanged with Ca^{2+} and Zn^{2+} and mixed with poly(vinyl butyral) (PVB), resulting in the reduction of the corrosion-driven coating cathodic disbondment, detachment between polymeric coating and

Table 12.3 Examples of fillers, corrosion inhibitors and polymers for anticorrosion applications.

Application	Polymer	Filler	Amount of filler (wt%)	Amount of corrosion inhibitor (wt%)
Anticorrosion	➢ 2D fillers – PANI – PEA – PMA – DBSA-doped PANI – PMMA – Acrylic latex paint – PPY – PHT – PI – PS – PSAN – PSF – EP	– MMT – O-MMT – O-SEP	0.1–10	—
Anticorrosion with corrosion inhibitor *i.e.* BTA, MBT, MBI, 8-HQ, and DDA	➢ 1D filler – Acrylic latex paint – PS latex paint – PU paint – EP paint	– HAL	5–10	5–20

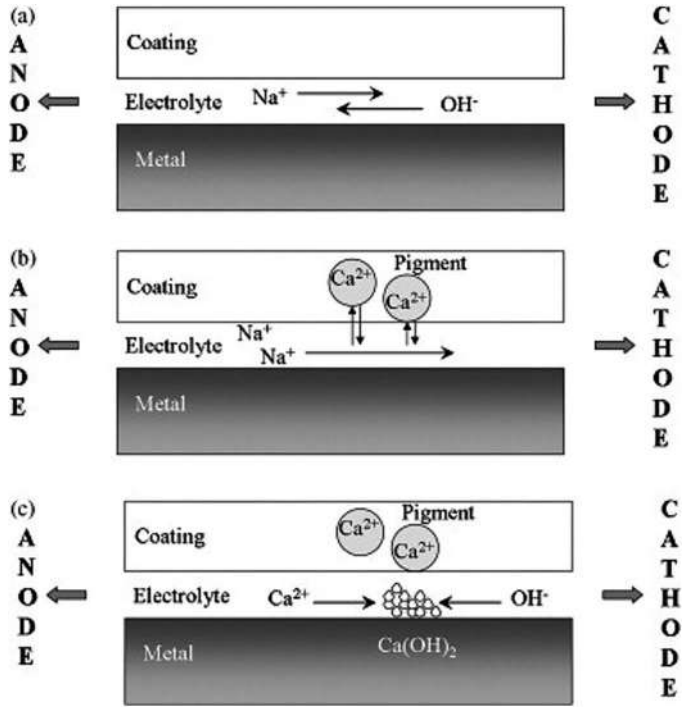

Figure 12.6 Schematic illustration of the inhibition mechanism of corrosion-driven cathodic coating disbondment. (a) Ion transport in the absent of MMT. (b) Cation exchanged of Ca^{2+}-MMT. (c) Cation hydrolysis at elevated pH.[33] Reproduced from ref. 33 with permission from Elsevier, Copyright 2010.

metal substrate (Figure 12.6). This phenomenon originates from the presence of the thin layer electrolyte in accessible defects of polymer coating, redox reaction occurring from cathodic oxygen reduction and anodic metal dissolution, disbondment at coating-metal interface, and eventually establishment of delaminated layer. The disbondment could be reduced by the exchange reaction of Zn^{2+}, Ce^{3+} and alkaline earth cations into the electrolyte solutions, which contributes the formation of hydroxides, reduction of ionic mobility and electrical conductivity, thus termination of disbondment and simultaneous facilitation of healing process were achieved.[30,32,33]

12.3.2.2 Polymer–Tubular Clay Mineral Hybrids

Tubular clay minerals have been doped into polymers, which provide sustained release of anticorrosion agents, resulting in long-term metal protection. The tubular clay mineral, halloysite (HAL), has the aspect ratio of 20 : 1 and the inner lumen, which may contain different functional chemicals for sustained release. HAL can be dispersed into single particles because the tubular clay mineral is not stacked together.[34] The processing

of polymer containing tubular clay minerals is similar to those with layered clay minerals, such as mixing with melted polymers by using double-screw extruders or by admixing HAL during the polymerization process. Corrosion inhibitors [benzotriazole (BTA), 2-mercaptobenzotriazole (MBT), 2-mercaptobenzimidazole (MBI), hydroxyquinoline (8-HQ), and dodecylamine (DDA)] have been encapsulated in the lumen of HAL to increase the protection time of coatings, where the release of the corrosion inhibitor occurred after the coating materials were cracked. The enlargement of the lumen of HAL by selective etching of alumina has been done to increase the loading capacity comparable to polymer capsules.[32,34,35] Hybridization of HAL with polymers resulted in not only sustained the release of corrosion inhibitors but also improved the mechanical strength. Additional modifications of the tubular clay minerals to slow down the release were achieved by coating the nanotube with thin polymer layers (layer-by-layer encapsulation) and by forming tube-end stoppers.[34]

12.3.3 Flame Retardancy

The combustion of polymers induced by the elevated temperature leads to the decomposition of polymers and the flammable volatile degradation products contact with oxygen and then combust.[36] Fire protection approaches must be considered from all aspects of the burning polymer *i.e.* heat release, smoke release, mechanical integrity under fire, and how that polymer behaves in a particular fire risk scenario. There are three main methods for improving the flame retardancy of polymeric materials: engineering approaches, use of inherently low flammable materials, and flame retardant additives. Flame retardant additives are widely used due to the cost-effectiveness over other methods. However, the problems are the leaching of the additives to the environment during usage and the difficulty of its recycling. There are several types of flame retardant additives: halogenated compounds, phosphorus-based compounds, and intumescent and inorganic flame retardants. The use of halogenated flame retardant compounds was prohibited because of the reasons of environmental contamination and their toxicity during the combustion. The mechanism of flame retardancy is classified into three: gas phase flame retardancy, endothermic flame retardancy, and char-forming flame retardancy. Depending on the application, polymer, and burning of polymer, suitable options should be applied among possible methods.

Gas phase flame retardance additives such as halogen and phosphate additives are slowdown the combustion process by the reducing of radical species such as decabromodiphenyl ether. Endothermic flame retardancy occurred by the degradation of the additive which degrade endothermically and release non-flammable gases. Metal hydroxide was classified in this mechanism. A carbonaceous char layer can form by using intumescent flame retardant additives or hybrids flame retardants. Intumescent flame retardant additives are composed of three components, *i.e.* an acid catalyst such as ammonium polyphosphate, a carbon source such as pentaerythritol and a gas source such as melamine. The carbon foam will form after the additive

is exposed to heat. Acid catalyst facilitates the crosslinking of the carbon source and, after the gas source was degraded and generated non-flammable gas, the gas will be released to form the carbon foam.

In this chapter, the improvement of flame retardancy by the hybridization of polymeric materials with clays and clay minerals will be discussed. Such inorganic flame retardants as metal hydroxides, metal oxides, and nanohybrids have been used so far. The expected roles of clay minerals are improving the physical properties of the polymer and reducing the mass loss rate of the polymer during the fire conditions through the formation of a nanoparticles-rich fire protection barrier, resulting in the reduction of peak heat release rate, hampering of polymer flow (melting/dripping) during a fire, less intense burning and spreading combustion period, while the total heat release of the fuel does not decrease.[36] Simple incorporation of clay minerals into polymers can reduce peak heat release rates, which is the important parameter for fire safety, but may not pass the regulatory fire tests. Many flame retardant additives have been combined with the incorporation of clay minerals for improving the flame retardancy to pass regulatory fire tests. The common tests of flame retardancy are the UL 94 vertical burning test, the limiting oxygen index (LOI) test, and cone calorimetry.[37]

12.3.3.1 Polymer–Layered Clay Mineral Hybrids

Layered clay minerals have been incorporated into such polymers as polymethyl methacrylate (PMMA), polystyrene (PS), polydimethylsiloxane (PDMS), polyetherimide (PEI), and nylon-6 (PA 6) in order to improve the thermal stability. Hybridization of polymers and layered clay minerals was done by *in situ* polymerization, melt blending and intercalation from polymer solution as summarized in Figure 12.2. Examples of fillers and polymers used for the application to flame retardancy are listed in Table 12.4. The improvement of the thermal stability of aliphatic PEI was reported by mixing with layered clay minerals. For the PEI–organically modified clay mineral hybrids, the exfoliated structure (Figure 12.3D) improved the thermal stability and the intercalated nanostructure (Figure 12.3C) showed higher thermal stability than the exfoliated structure, while the PEI–unmodified clay did not improve the thermal properties since the layered clay mineral and polymer were immiscible. The dispersion affected the thermal stability of polymer–clay hybrids, while the difference in the particle size of clay minerals did not affect the thermal properties as observed by using organically modified montmorillonite (O-MMT) and organically modified fluorohectorite (O-FHEC) mixed with PEI. The self-extinguish properties was also observed in PEI–clay mineral hybrids. The flame retardancy of polymer–clay hybrids was improved as observed by using cone calorimeter. Polyamide (PA), nylon-12 (PA 12), polystyrene (PS), polypropylene (PP), and epoxy (EP) hybridized with O-MMT showed both intercalated and exfoliated structures, resulting in the reduction of the peak and average heat release rate.[38] Hybridization of polymers and clay minerals resulted in the development

Table 12.4 Examples of fillers and polymers used for the application to flame retardancy.

Application	Polymer	Filler	Amount of filler (wt%)
Flame retardant	➢ 2D fillers		
	– PMMA	– MMT	0.1–10
	– PA 6	– O-MMT	
	– PA 12	– O-FHEC	
	– PA 66		
	– PS		
	– PU		
	– PP		
	– PEI		
	– PE		
	– PEMA		
	– PEMAAA		
	– EVA		
	– ABS		
	– Epoxy		
	➢ 1D filler		
	– LLDPE	– HAL	0.5–30
	– EP		
	– PS		
	– PP		
	– PA 6		
	– PA 12		
	– PVA		

of flame retardancy *via* carbonaceous char forming. This mechanism was improved by reducing the evaporation of flammable degradation products and catalyzing the charring and/or crosslinking reactions by the acidic sites of clay minerals, where clay minerals play an important role as the insulator and the barrier for mass transport as shown in Figure 12.7.[37] The surface modification of clay minerals using quaternary alkylammonium compounds and subsequent hybridization with polymer led to lower thermal stability if compared with the pristine polymer, because the decomposition of alkylammonium increases the heat of combustion and reduces the time to ignition.[38] Further improvements of flame retardancy were found for polyolefin, PA, acrylonitrile-butadiene-styrene copolymer (ABS), PS, and polyester by adding conventional flame retardants in addition to layered clay minerals, which was reviewed by Kiliaris and Papaspyrides.[37] Some of non-halogenated flame retardants combined with O-MMT showed the synergistic effect; intumescent flame retardants, phosphorus-based compounds such as tricresylphosphate and resorcinolbis(diphenylphosphate), were mixed with PS, and metal hydroxides such as aluminum hydroxide and magnesium hydroxide were mixed with poly(ethylene vinyl acetate) (PEVA).[37] For the combination of O-MMT with intumescent additive showed the improvement of barrier properties as a result of the increase of the rigidity of the intumescent shield, decreasing the formation of cracks and also

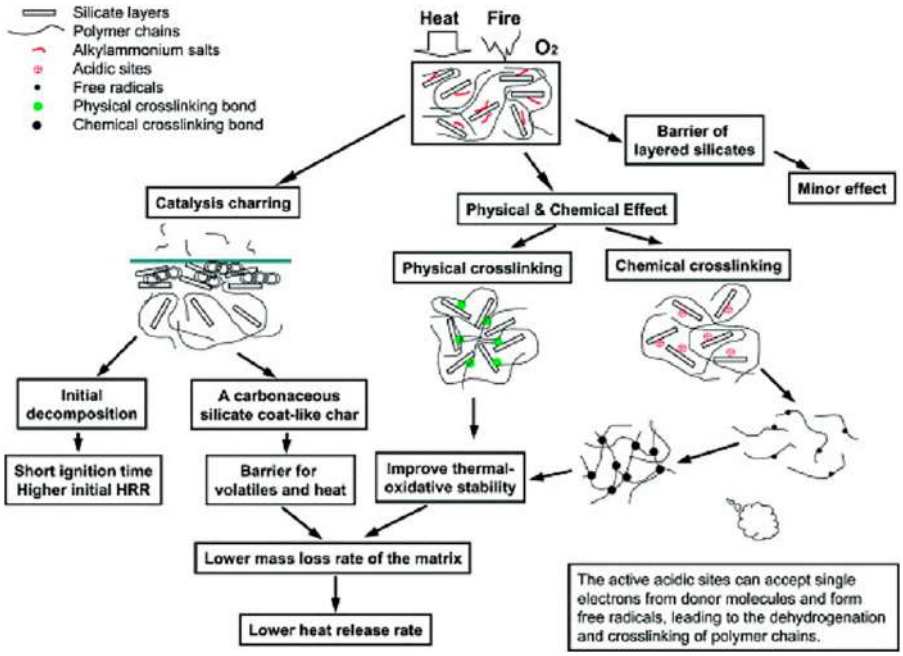

Figure 12.7 Proposed schematic mechanism of catalytic carbonaceous char formation of PP/clay nanocomposite during combustion.[40] Reproduced from ref. 40 with permission from Elsevier, Copyright 2005.

reducing heat and mass transfer, which improved the flame retardancy of polymer–clay hybrids.[39] The antagonism effect was also found for the complexation of layered clay minerals and conventional flame retardant additives *i.e.* hybridization of phosphorus-based compounds combined with layered clay minerals and epoxy resin decreased the fire retardant properties and caused an increase in heat release rate and total heat release. PA combined with melamine cyanurate and a clay mineral decreased flame retardancy since the melt viscosity of the polymer was increased by hybridizing with layered clay mineral, hindering the flame retardant mechanism of melamine cyanurate and releasing ammonia gas which induced the dripping of the polymer away from fire.[37] In order to improve the flame retardancy of a polymer, the mechanism of each additive should be considered.

12.3.3.2 Polymer–Tubular Clay Mineral Hybrids

Halloysite (HAL) has been used for the modification of flame retardancy of such polymers as polyethylene (PE), polystyrene (PS) and polypropylene (PP). Hybridization of polymer and HAL was done *via* melt blending and solution mixing methods. Char formation during the combustion was accelerated and the char layer acted as a thermal insulator and reduced the

evaporation of flammable degradation products. Moreover, the lumen of HAL can trap the degradation products, leading to higher thermal stability. The surface modification of HAL is required to obtain homogeneous dispersion of HAL in non-polar polymers, which enhances the performance of polymer hybrids. There are several methods for improving the dispersion of HAL in polymers using the modification of HAL by surfactants and silane coupling agents and functionalization of the polymers. The compatibilizer such as maleic anhydride has been grafted to polymers such as linear low density polyethylene (LLDPE) for increasing the dispersion of fillers, thus decreasing of heat release rate and mass loss rate have been achieved. Recently, phenyl phosphoric acid was used for the modification of both surfaces of HAL, which reduced peak heat release and heat release rate of PA 6 by 10 wt%. The loading of modified HAL showed higher CO evolved compared to unmodified halloysite, which reduced the amount of CO evolved.[41] HAL was modified selectively on its outer and inner surfaces. Phosphonic acid was attached to the inner alumina site and the outer silica site was modified with a silane coupling agent, *N*-(2-aminoethyl)-3-aminopropyltrimethoxysilane. After the modification, a flame retardant additive, bisphenol-bis(diphenyl phosphate) (BDP), was loaded in HAL lumen resulting in the loading amount higher by five times if compared with that achieved for unmodified HAL (Figure 12.8), which is useful for the sustained release of flame retardant additives.[33]

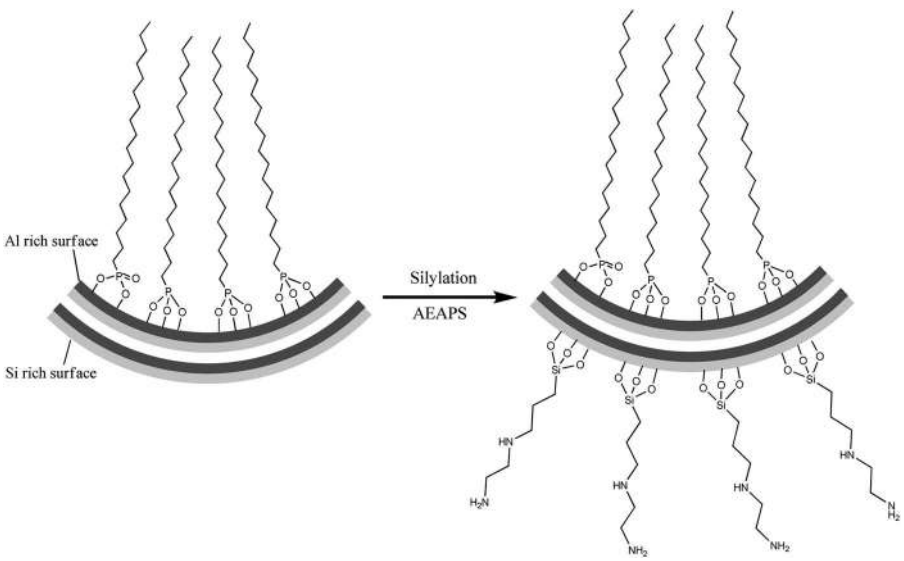

Figure 12.8 Schematic of HAL modifications for increasing loading efficiency of hydrophobic compounds by selective lumen modification and silylation of external surface of HAL.[42] Reproduced from ref. 42 with permission from American Chemical Society, Copyright 2012.

12.3.4 Mechanical Properties of Polymer–Clay Hybrids for Medical Applications

Numerous polymers are used in biomedical applications due to their properties including possible processing into complex shapes, while the demands for certain applications and usages are not satisfied, *e.g.* higher modulus materials to support their patients' weight are necessary for implants in orthopedic surgery. Polymer–clay hybrids have been expected to show not only for superior mechanical properties but also biological functions. For example, a polymer that appears to be non-cytotoxic *in vitro* is not necessarily biocompatible *in vivo*. Clay minerals are chemically inert and less toxic for patients, so that they have been used to enhance the mechanical properties of synthetic and natural polymers, leading to the synergistic combination of chemical and biological properties such as creating better treatment of diseases and long-term biocompatibility. Examples of polymer–clay hybrids for medical application are given in Table 12.5.

12.3.4.1 Polymer–Layered Clay Mineral Hybrids

Ethylene vinyl acetate and montmorillonite (MMT) modified with bis-(2-hydroxylethyl) methyl alkyl ammonium (Cloisite® 15A) were hybridized to exhibit such mechanical properties as compressive strength and compressive modulus, which were not achieved by polymer alone.[43] Such layered clay minerals as MMT and laponite (LAP) have the potential to induce the osteogenic function of stem cells in the absence of growth factors and also enhance proliferation of MC3T3 osteoblast cells on the materials surface.[44] Such biopolymers as chitosan, gelatin, collagen and synthetic bio-based polymers (*e.g.*, poly(lactic acid)) have been used instead of synthetic polymers because of the biocompatibility, cell interactive properties, cell signaling as well as biodegradability. MMT was used to improve mechanical properties of a bio-based polymer, poly L-lactic acid (PLLA) to achieve faster biodegradation than neat PLLA because MMT decreased the polymer crystallinity. The formation and repair of the bone was improved because MMT affected interfacial tension, making surface more hydrophilic.[45]

12.3.4.2 Polymer–Tubular Clay Mineral Hybrids

Halloysite (HAL) was also used to enhance mechanical properties when incorporated into polymers due to its high aspect ratio. The polymer–HAL hybrids exhibited enhancements in compressive strength and compressive modulus compared with neat polymers. For example, polyvinyl alcohol–halloysite hybrid (PVA-HAL) films supported cell growth. The addition of HAL enhanced compressive strength and compressive modulus, in addition to the effects on the pore structure and porosity of the polymers. The tensile strength and Young's modulus of polyamide 6 (PA6)

Table 12.5 Examples of polymer–clay hybrids for biomedical applications.

Applications	Fillers	Polymer	Important role of filler	Filler content
Drug and gene delivery	MMT, O-MMT, LAP, HAL, BN, HSCAS, APT, LiTN, VMT	PLG, PAM, P(AM-MA), PAM, PEO, Acryl-PEG, Pluronic® F127, ALG, P(MEOMA-OEGMA)	Sustained release profiles Non-cytotoxicity, enhance the dissolution resistant properties of the hydrogels, significant influence on the microstructure and swelling/deswelling behaviors, achieving high drug loading	HAL < 100 μg mL^{-1} 25–37 wt% MMT 0–20 wt% LAP
Bone cements	HAL, O-MMT	PMMA, PU, epoxy-based	Enhanced mechanical properties and release behavior of antibiotic	5–85 wt% HAL
Wound healing	MMT	PLA, PLLA, chitosan, GEL	Prolonged release of antimicrobial agent and accelerate wound healing	5–15 wt% MMT
Tissue regeneration	MMT, WL, HAL, IMO, LAP, APT	PLLA, PNIPA, PLA, PLC, PNIPAM, PLGA, PVA, LMWH, COL, CA, GEL-CTS, PEVA, Pluronic® F127, PCL-PEG-PCL	Enhanced cell adhesion and proliferation easily Improved mechanical properties, faster degradation, preferentially induce osteogenic differentiation, influence the polymer chain arrangement achieving thermal stability and mechanical toughness	2–3 w/v% LAP 5–7 w/v% HAL 5 wt% MMT
Cell sheet engineering	LAP	PNIPAM, PEO	Easily pull out of cell sheet	3–7 wt% LAP
Sealed medical devices	O-MMT	PU, PAA, PMA	Reduce water vapor permeability and enhance the mechanical properties while maintain good blood compatibility	6 v/v% MMT
Cosmetics (*e.g.* cleansing mask)	HAL	PAA	Releasing active component such as glycerol, personal care products	Up to 2.3 wt%

increased twice compared to pristine polymer by incorporating HAL, which was achieved at much lower filler concentration compared to the case when MMT was used as the filler.[46] The scaffolds thus obtained possessed a three-dimensional structure with interconnected pores for cell attachment and migration.

Orientation of HAL in polymer affected the properties.[47] By a spray-coating process, epoxy–HAL hybrid with vertically aligned nanotubes as shown in Figure 12.9 was fabricated. The hybrids showed improvements up to 50% in modulus and 100% in hardness as compared to pure epoxy resin, and the improvements in mechanical performance correlated with the alignment of HAL.

Polymer–clay hybrid hydrogels have become a popular material for biomedical applications especially for wound healing and tissue engineering. The details about polymer–clay hybrid hydrogel will be explained in Section 12.3.6. Layered clay minerals have been used to enhance the mechanical properties of polymer hydrogel. The applications of hybrid hydrogels are often restricted due to uncontrollable degradation and potential immunogenicity. In order to solve the issue, the designed hybrid has been changed by either combining a synthetic and natural polymer, such as a peptide functionalized poly(ethylene glycol)(P(PEG-*co*-peptides)) or poly(hydroxypropyl methacrylamide-*g*-peptide)(P(HPMA-*g*-peptide)), or modification of the clay's surface. These types of hybrid hydrogels can have new properties by sophisticated self-assembly over homopolymer hydrogels.[44]

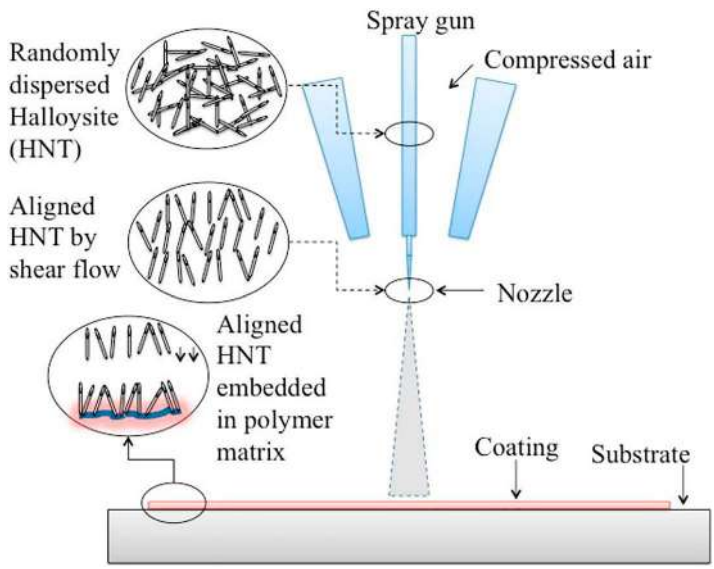

Figure 12.9 Spray-coating was utilized to prepare epoxy–HAL hybrids with vertically aligned nanotubes.[47] Reproduced from ref. 47 with permission from American Chemical Society, Copyright 2016.

12.3.5 Polymer–Clay Hybrids for Drug (Gene) Delivery

For drug delivery, polymers are expected to provide controlled release of therapeutic agents through the network of the polymer, while the drug release system which contains only polymer does not maintain drug levels within a therapeutic window over extended period. This often results in the drug level in the organism being lower than the minimum effective concentration. Moreover, the level may exceed the minimum toxic concentration, causing undesirable side effects for patients. From these limitations, the design of polymeric systems to satisfy the requirements and to have response to external stimuli is very important in smart implant and drug delivery systems as well as cell culture matrices. The main drawbacks in various drugs such as antibiotics, anticancer, anti-fungal and anti-inflammatory drugs are low bioavailability and poor water solubility. By designing new carriers to overcome the limitations about the burst release of entrapped drug, the release kinetics of drugs within a therapeutic window over extended periods has been controlled. Clay minerals offer barrier properties that suppress drug diffusion. Clay minerals can facilitate sustained release profile and increased drug loading capacities.[48]

12.3.5.1 Polymer–Layered Clay Mineral Hybrids

Due to the tortuous diffusion pathways, polymer–layered clay mineral hybrids exhibited superior slow-release properties for some drugs. The release characteristics are determined by surface area and ion-exchange capacity of the layered clay minerals, the types of interactions between host and guest, and clay/polymer ratio. For example, the release rate of vitamin B12 *via* electrostimulation was controlled by the hybridization of MMT and chitosan (CS), showing a stable release profile.[49,50] Hybridization of poly(lactic-*co*-glycolic acid) (PLGA), vitamin E derivative (TPGS) and MMT was reported for the release of docetaxel, a chemotherapeutic with low oral bioavailability.[51] The addition of clay mineral was justified by the gastroprotective effect to achieve sustained release of the drug, which provides a change in the frequency of administration of 22 hours to 3 weeks, avoiding fluctuation in plasma levels of the drug.[49] The organically modified MMT with cationic surfactant was employed. In addition, the chemical modification enlarged the distance between the adjacent platelets of layered clay minerals. Dimethyl dihydrogenated tallow ammonium modified Na^+-MMT (Cloisite® 20A) was added to poly(ethylene-*co*-vinyl acetate) (PEVA) to have attractive interactions between the negatively charged clay mineral surfaces and the drug resulting in slower release of dexamethasone. The drug release kinetics was suggested to be dependent on the aspect ratio and degree of dispersion of the layered silicate.[50]

12.3.5.2 Polymer–Tubular Clay Mineral Hybrids

Halloysite (HAL) has potential as a drug container due to its lower density than other clays, such as MMT and kaolinite, large aspect ratio and hollow tubular structures (empty lumen). HAL can be loaded with drugs, genes, proteins,

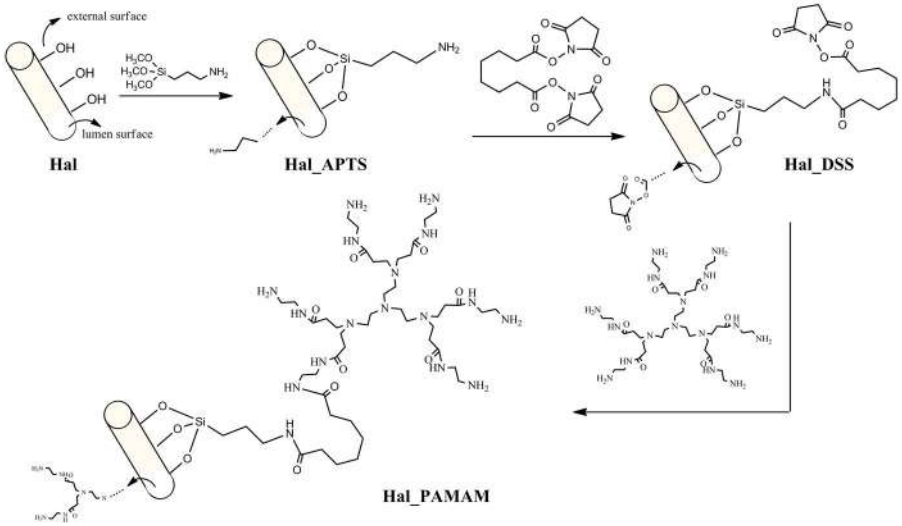

Figure 12.10 Scheme of synthesis of PAMAM functionalized HAL.[54] Reproduced from ref. 54 with permission from Elsevier, Copyright 2018.

antibacterial agents and others. The expected roles of HAL are a retardant effect to control the release and to protect the drug uptake by cells. The drug release from the HAL lasts 30–100 times longer than the drugs alone or other carriers.[6] The PMMA-HAL-gentamicin sulfate hybrids provided sustained release up to 12–16 days with enhanced release behavior at the cement cracks. HAL acted as container for antibiotic-gentamicin sulfate, they can survive in curing process of poly(methyl methacrylate) (PMMA) gel. Interestingly, their adhesion to bone was significantly increased. These clays have adsorption ability toward blood and tissue exudates when they are used in wound healing PMMA hybrid materials.[53]

Dendrimers (or hyper-branched polymers) are also studied for biomedical and biotechnological applications. Dendrimers have high reactivity and loading efficiency due to multiple functional groups on their highly branched structure. Therefore, the chemical functionalization of the HAL surface with a dendrimer should significantly affect both the adsorption of drug molecules and their release. PAMAM-dendrimer functionalized HAL (Figure 12.10) slowed the release rate of small molecules compared to unmodified HAL as a successful example.[52,54]

12.3.6 Polymer Hydrogel

A polymer hydrogel is a three dimensionally crosslinked polymer network containing water. In addition to the variety of common applications of hydrogel for sanitary, agricultural, medical and environmental uses, stimuli (external stimuli including temperature, light, pH, and electrical field) responsive volume change of polymer hydrogel[55,56] has motivated extensive

studies on polymer hydrogels for such applications as actuator, artificial muscle, drug delivery, tissue engineering, and wound/healing dressing applications. Mechanical strength, which is one of the drawbacks of hydrogels for the materials application, has been discussed.[57] The density of crosslinking in the polymer network is the key to modifying the mechanical properties, while higher crosslinking may result in the reduction in the degree of swelling. In order to overcome this drawback, hybridization of polymer hydrogels with clay minerals has been proposed by Haraguchi *et al.*[58]

12.3.6.1 Polymer–Layered Clay Mineral Hybrid Hydrogel

A polymer–clay hybrid hydrogel was reported by Haraguchi *et al.*,[58] where poly(*N*-isopropylacrylamide) (PNIPAM)-clay hydrogel was prepared by free radical polymerization of *N*-isopropyl acrylamide (NIPAM) monomers in the presence of laponite (LAP) (a synthetic hectorite ($Na_{0.66}Mg_{5.34}Li_{0.66}Si_8O_{20}(OH)_4$)), which is proposed to act as the crosslinking agent. Due to the hydrophilic surface, smectites have been incorporated into the hydrogel network and the methods were classified into three as summarized in Table 12.6.[59] The hydrogen bonding between the silanol groups at the edges of smectite with the functional group of the hydrophilic polymer was thought to be a possible crosslinking point. The uniform dispersion of smectites into the gel network significantly enhanced the mechanical and thermal properties of polymer hydrogels while the loading amount of smectites was limited. The transparency of polymer hydrogel was enhanced due to the uniform orientation of smectite and the restriction of polymer chain movement by the interactions with smectite. The superior swelling of the smectite containing hydrogels to the conventional polymer hydrogel was attributed to the ion-exchange of the cationic species at the smectite surface with water and proton and/or the swelling property of smectite itself. The polymer–clay hybrid

Table 12.6 Methods for the preparation of polymer–clay hybrid hydrogel and the typical composition.

	Monomer/polymer		Filler		Content of water (wt%)
Method	Type	Content (wt%)	Type	Content (wt%)	
***In situ* free radical polymerization**	AM, DMA, NIPAM, AA, SMA, SSNa, AMPS	0.04–40	HEC, MMT, LAP	0.5–20	20–90
Direct intercalation of hydrophilic polymer	PVA, PEG, PAAS, PVP	1–10	LAP, O-MMT	2.5–10	—
Freezing–thawing technique	PVA	15	MMT	2–10	75–85

gel has been shaped as sphere to be used as adsorbent,[57,60] which makes the application of hydrogel more versatile.

12.3.6.2 Polymer–Tubular Clay Mineral Hybrid Hydrogel

Halloysite (HAL) has been used as a cross-linker for polyacrylamide (PAM) hydrogel, which was prepared by *in situ* polymerization.[61] Similar to the smectite containing hydrogels, the hydrogel formation was attributed to the hydrogen bonding between the amide groups of PAM and the silanol group on the surface of HAL. The maximum loading of HAL was 30 w/v%, which was higher than the loading of LAP in PAM (10 w/v%).[58,61] In addition, HAL has been introduced into such natural polysaccharide as alginate, chitosan, carrageenan, starch and cellulose to form hydrogels.[62] The modification of HAL is necessary in order to increase the compatibility with the polysaccharides. Both chemical and physical methods for the surface modification have been applied. For example, the surface modification using silane coupling agents and the expansion of HAL by a cryogenic technique, where freezing water entrapped in the lumens and subsequent drying, has been done for the hybridization with polysaccharides.

12.3.7 Electrolytes

The ionic conduction along the polymer chains was generated by the rapid segment motion of polymer matrix and the interactions between cationic species and donor atom. The polymer electrolyte is classified into two types: gel electrolyte and solid polymer electrolyte. The superior properties of polymer electrolytes over the conventional liquid electrolyte are structural stability, low volatility and high electrochemical stability window. Therefore, polymer electrolytes have been applied for such electrochemical devices as solid-state batteries, solar cells, fuel cells, and dye-sensitized solar cells.[63] However, the ionic conductivity of solid/gel polymer electrolyte was still low when compared with those of liquid electrolytes. In order to solve this limitation, a combination of gel and solid polymer electrolytes, increasing the ionic salt or polymer concentration, and hybridization of metal oxides such as titania and alumina and layered material including layered double hydroxides, graphene oxides and clay minerals have been examined.[64]

12.3.7.1 Hybridization of Layered Clay Minerals with Polymer Electrolyte

The interactions between clay mineral and polymer electrolyte were investigated using montmorillonite and poly(ethylene oxide) (PEO).[65] Two arrangements of the intercalated PEO in the interlayer region (a planar zigzag conformation of PEO chains and a helical conformation) were proposed

to correlate the ionic conductivity as shown in Figure 12.11. Examples of polymer–clay hybrids for electrochemical applications are summarized in Table 12.7.[66,67] The roles of the clay minerals for the improvement of ionic conductivity have been proposed as the interference of the Lewis acid–base interactions between ions and polymer, reduction of polymer crystallinity, assistance the dissolution of salts to provide charge carriers. In addition to the electronic functions, the mechanical and thermal properties of solid/gel polymer electrolyte was modified by the addition of clay minerals. The alignment of clay nanosheets was proposed as a parameter affecting the ionic conductivity.[68] The vertically aligned clay sheets in the polymers were achieved by the vertical temperature gradient freezing using Teflon substrate, which was

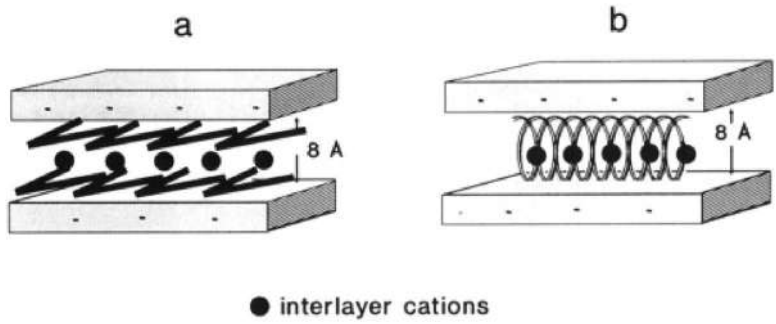

Figure 12.11 Schematic drawing of the structure models of PEO intercalation in smectites: (a) double layer planar zigzag; (b) helical conformation of PEO chains.[65] Reproduced from ref. 65 with permission from American Chemical Society, Copyright 1992.

Table 12.7 Summary of polymer–clay hybrids as electrolytes.

	Fillers		Polymer	
Applications	Type	Content (wt%)	Type	Content (wt%)
Li ion battery	O-MMT, MMT	4–6	PEO, PAN, PVDF, PVDF-HFP, PMMA, P(VDF-TrFE), HBPU	12–15
Li sulfur battery	O-MMT	10	PEG/LiTFSI, PVDF-HFP/PMMA	15
Fuel cells	MMT, Sulfonic acid-modified MMT, poly(styrene sulfonic acid)-modified MMT	0.15–20	Nafion, PVA	5–20
Supercapacitors	MMT	3–11	PEG/$TEABF_4$, PVDF-HFP, PAMPS	15–16

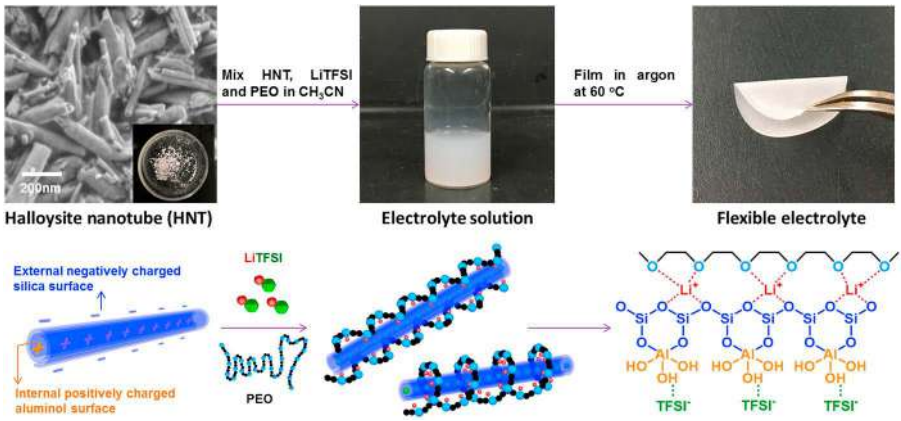

Figure 12.12 Preparation of solid electrolyte and mechanism of HAL for the enhancement of ionic conductivity. HAL, PEO and lithium bis(trifluoro-methanesulfonyl)imide (LiTFSI) were mixed in the solvent to form a uniform electrolyte solution. The solution was casted in an argon atmosphere to produce a flexible electrolyte thin film.[69] Reproduced from ref. 69 with permission from Elsevier, Copyright 2017.

placed on the top of liquid N_2 to induce the directional freezing casting. In addition to the ionic conductivity, the vertical alignment of clay nanosheets was reported to enhance the mechanical property and electrochemical stability of the polymer electrolyte.

12.3.7.2 Hybridization of Tubular Clay with Polymer Electrolyte

The modification of the ionic conductivity in the solid polymer electrolyte by the addition of HAL was reported, which is useful for the development of lithium sulfur batteries.[69] Due to the opposite charge of the external (negative) and inner (positive) surfaces of HAL, lithium ions were adsorbed at the external surface resulting in the charge separation. PEO was adsorbed on the external surface through the interactions with Li^+ ions, which is significantly shorten the distance of free Li^+ ions. The proposed structure is shown in Figure 12.12. Apart from the improvement of the ionic conductivity, the mechanical property and the homogeneity of the solid film were also improved by the addition of HAL.

12.4 Conclusions

Since the pioneering work of so-called "polymer–clay nanocomposites" based on nylon and montmorillonite in the 1980s, polymer–clay hybrids have been prepared using polymers of various kinds for many applications by applying different preparation pathways. In order to make the degree of

the complexation (separation of nanosheets, nanofibers and nanotubes) appropriately for each application, materials design at the interface (by the choice of clay minerals to be hybridized and the chemical modification of both polymers and the surface of clay minerals) as well as the process design for compounding have extensively been investigated. In order to satisfy the demands for many advanced and new applications, materials design is still worth investigating.[70–73] Aspect ratio of fillers, variation of aspect ratio (correspond to the particle size distribution of anisotropic particle), precise design of surface chemistry (charge strength, charge density and distribution), functional group and it density on the surface will further be more systematically designed to achieve desired degree of the complexation/separation for the materials performances. In addition to the common target application described here, un-expected new function may be found by the materials design,[74] inviting researchers to join the fascinating materials chemistry field. It should be noted here that the polymer–clay interactions can be applied for the collection of polymers from the environments, which is an important issue of concern.[75]

List of Abbreviations

AA	Acrylic acid
ABS	Acrylonitrile-butadiene-styrene copolymer
Acryl-PEG	Poly(ethylene glycol) methyl ether acrylate
AEAPS	*N*-(2-Aminoethyl)-3-aminopropyltrimethoxysilane
ALG	Alginate
AM	Acrylamide
AMPS	2-acrylamido-2-methylpropane sulfonic acid
APT	Attapulgite
AQ nylon	Water-soluble nylon (produced by Toray Industries, Inc., Tokyo, Japan)
AR	Acrylic resin
BDP	Bisphenol-bis(diphenyl phosphate)
BN	Bentonite
BTA	Benzotriazole
CA	Chondroitinsulfate
CH	Chitosan
COL	Collagen
CTS	Chitosan
DBSA-doped PANI	Dodecylbenzene sulfonic acid dope polyaniline
DDA	Dodecylamine
DMA	*N*,*N*-dimethylacrylamide
EL	Glycol lignin
EMA	Ethylene methyl acrylate
EP	Epoxy resin
EPS	Expanded polystyrene
ETFE	Ethylene tetrafluoroethylene

EVA	Poly(ethylene-*co*-vinyl acetate)
FEP	Fluorinated ethylene-propylene
GEL	Gelatin
HAL	Halloysite
HBPU	Hyper-branched polyurethane
HEC	Hectorite
HSCAS	Hydrated sodium calcium aluminosilicate
IMO	Imogolite
LAP	Laponite
Li-MMT	Lithium montmorillonite
Li-Syn-MMT	Lithium synthetic montmorillonite
LiTN	Fluoromica, Lithium taeniolite
LLDPE	Linear low density polyethylene
LMWH	Low molecular weight heparin
MBI	2-mercaptobenzimidazole
MBT	2-mercaptobenzotriazole
MEOMA	2-(2-methoxyethoxy) ethyl methacrylate
MMN	Methoxymethyl nylon
MMT	Montmorillonite
NIPAM	*N*-isopropyl acrylamide
NR	Natural rubber
OEGMA	Oligo(ethylene glycol) methacrylate
O-FHEC	Organically modified fluorohectorite
O-MMT	Organically modified montmorillonite
O-Syn-MMT	Organically modified synthetic montmorillonite
(P(AM-IA))	Poly(acrylamide-*co*-itaconic acid)
P(AM-MA)	Poly(acrylamide-*co*-maleic acid)
P(VDF-TrFE)	Poly(vinylidene fluoride-trifluorethylene)
PA	Polyamide
PA12	Nylon 12
PA6	Nylon 6
PA66	Nylon 66
PAA	Poly(acrylic acid)
PAAS	Sodium polyacrylate
PAM	Polyacrylamide
PAMPS	Poly(acrylamido-2-methyl-1-propanesulfonic acid)
PAN	Polyacrylonitrile
PANI	Polyaniline
PAS	Polyarylsulfone
PCEC	Poly(ε-caprolactone)-poly(ethylene glycol)–poly (ε-caprolactone) copolymer
PCL-PEG-PCL	Poly(ε-caprolactone)-poly(ethylene glycol)-poly(ε-caprolactone)
PDMS	Poly(dimethylsiloxane)
PE	Polyethylene

PEA	Poly(*o*-ethoxyaniline)
PEG	Poly(ethylene glycol)
PEI	Polyethylenimine
PEMA	Poly(ethylene-*co*-methyl acrylate)
PEMAAA	Poly(ethylene-*co*-methyl acrylate-*co*-acrylic acid)
PEN	Polyethylene naphthalate
PEO	Poly(ethylene oxide)
$PEO/TEABF_4$	PEG/tetraethylammoniumtetrafluoroborate
PET	Poly(ethylene terephthalate)
PEVA	Poly(ethylene vinyl acetate)
PFA	Perfluoroalkoxy
PHT	Poly(3-hexylthiophene)
PI	Polyimide
PIB	Polyisobutylene
PLA	Poly(lactic acid)
PLG	Poly(lactic-*co*-glycolide)
PLGA	Poly(lactic-*co*-glycolic acid)
PLLA	Poly(L-lactic acid)
PMA	Poly(*o*-methoxyaniline)
PMMA	Poly(methyl methacrylate)
PNIPAM	Poly(*N*-isopropylacrylamide)
PP	Polypropylene
PPY	Polypyrrole
PS	Polystyrene
PSAN	Poly(styrene-*co*-acrylonitrile)
PSF	Polysulfone
PTFE	Polytetrafluoroethylene
PU	Polyurethane
PVA	Poly(vinyl alcohol)
PVB	Poly(vinyl butyral)
PVC	Poly(vinyl chloride)
PVDF	Poly(vinylidene fluoride)
PVDF-HFP	Poly(vinylidene fluoride-*co*-hexafluoropropylene)
PVDF-HFP/PMMA	Poly(vinylidene fluoride-*co*-hexafluoropropylene)/ poly(methylmethacrylate)
PVF	Poly(vinyl fluoride)
PVF	Poly(vinyl fluoride)
PVP	Polyvinylpyrroridone
SEP	Sepiolite
SMA	Sodium methacrylate
SSNa	Sodium 4-styrene sulfonate
Syn-MMT	Synthetic montmorillonite
TPU	Thermoplastic polyurethane
VMT	Vermiculite
WL	Wollastonite

Acknowledgements

This work was supported by the Research Chair Grant 2017 (grant number FDA-CO-2560-5655) from the National Science and Technology Development Agency (NSTDA), and the Program Management Unit for Human Resources & Institutional Development, Research and Innovation, NXPO (Grant number B05F630117), Thailand. K.J.I., A.P.T., P.M.S., and C.B.T. acknowledge Vidyasirimedhi Institute of Science and Technology for the scholarship to their PhD study.

References

1. A. Usuki, Y. Kojima, M. Kawasumi, A. Okada, Y. Fukushima, T. Kurauchi and O. Kamigaito, *J. Mater. Res.*, 1993, **8**, 1179–1184.
2. *Crystal Structures of Clay Minerals and Their X-ray Identification*, ed. G. Brown and G. W. Brindley, Mineralogical Society, London, 1980.
3. *Handbook of Clay Science*, ed. F. Bergaya, B. K. G. Theng and G. Lagaly, Elsevier, Amsterdam, 2006.
4. T. Bate, *Am. Mineral.*, 1950, **35**, 463–484.
5. E. Joussein, S. Petit, J. Churchman, B. Theng, D. Righi and B. Delvaux, *Clay Miner.*, 2005, **40**, 383–426.
6. D. G. Shchukin, G. B. Sukhorukov, R. R. Price and Y. M. Lvov, *Small*, 2005, **1**, 510–513.
7. W. Bradley, *Am. Mineral.*, 1940, **25**, 405–410.
8. B. F. Jones and E. Galan, *Rev. Mineral. Geochem.*, 1988, **19**, 631–674.
9. R. E. Grim, *Clay Mineralogy*, McGraw-hill, New York, 2nd edn, 1968.
10. I. Uysal Unalan, G. Cerri, E. Marcuzzo, C. A. Cozzolino and S. Farris, *RSC Adv.*, 2014, **4**, 29393–29428.
11. C. Wolf, H. Angellier-Coussy, N. Gontard, F. Doghieri and V. Guillard, *J. Membr. Sci.*, 2018, **556**, 393–418.
12. Y. Cui, S. Kumar, B. Rao Kona and D. van Houcke, *RSC Adv.*, 2015, **5**, 63669–63690.
13. M. Ogawa and K. Kuroda, *Bull. Chem. Soc. Jpn.*, 1997, **70**, 2593–2618.
14. M. Ogawa, K. Saito and M. Sohmiya, *Dalton Trans.*, 2014, **43**, 10341–11054.
15. N. Takahashi and K. Kuroda, *J. Mater. Chem.*, 2011, **21**, 14336–14353.
16. C. B. Tirayaphanitchkul, K. J. Imwiset and M. M. Ogawa, *Bull. Chem. Soc. Jpn.*, 2021, **94**, 678–693.
17. G. Choudalakis and A. D. Gotsis, *Eur. Polym. J.*, 2009, **45**, 967–984.
18. T. Ebina and F. Mizukami, *Adv. Mater.*, 2007, **19**, 2450–2453.
19. T. Ebina, *Chem. Rec.*, 2018, **18**, 1020–1032.
20. M. Sohmiya, S. Omata and M. Ogawa, *Polym. Chem.*, 2012, **3**, 1069–1074.
21. E. S. Tsurko, P. Feicht, C. Habel, T. Schilling, M. Daab, S. Rosenfeldt and J. Breu, *J. Membr. Sci.*, 2017, **540**, 212–218.
22. T. Schilling, C. Habel, S. Rosenfeldt, M. Röhrl and J. Breu, *ACS Appl. Polym. Mater.*, 2020, **2**, 3010–3015.
23. A. P. Teepakakorn and M. Ogawa, *Mater. Adv.*, 2021, **2**, 3770–3776.

24. U. Hofmann and R. Klemen, *Z. Anorg. Allg. Chem.*, 1950, **262**, 95–99.
25. G. A. Martinez-Hermosilla, B. B. Mesic and J. E. Bronlund, *Packag. Technol. Sci.*, 2015, **28**, 565–578.
26. T. Dabat, F. Hubert, E. Paineau, P. Launois, C. Laforest, B. Grégoire, B. Dazas, E. Tertre, A. Delville and E. Ferrage, *Nat. Commun.*, 2019, **10**, 5456.
27. E. Ruiz-Hitzky, M. Darder, A. C. S. Alcântara, B. Wicklein and P. Aranda, Functional Nanocomposites Based on Fibrous Clays, in *Functional Polymer Composites with Nanoclays*, ed. Y. Lvov, B. Guo and R. F. Fakhrullin, The Royal Society of Chemistry, Cambridge, 2017.
28. A. C. S. Alcântara, M. Darder, P. Aranda and E. Ruiz-Hitzky, *Eur. J. Inorg. Chem.*, 2012, **2012**, 5216–5224.
29. J. M. Yeh and K. C. Chang, *J. Ind. Eng. Chem.*, 2008, **14**, 275–291.
30. E. Shchukina, H. Wang and D. G. Shchukin, *Chem. Commun.*, 2019, **55**, 3859–3867.
31. D. G. Shchukin and H. Möhwald, *Small*, 2007, **3**, 926–943.
32. H. Wei, Y. Wang, J. Guo, N. Z. Shen, D. Jiang, X. Zhang, X. Yan, J. Zhu, Q. Wang, L. Shao, H. Lin, S. Wei and Z. Guo, *J. Mater. Chem. A*, 2015, **3**, 469–480.
33. G. Williams, H. N. McMurray and M. J. Loveridge, *Electrochim. Acta*, 2010, **55**, 1740–1748.
34. Y. Lvov, W. Wang, L. Zhang and R. Fakhrullin, *Adv. Mater.*, 2016, **28**, 1227–1250.
35. S. A. Umoren and M. M. Solomon, *Prog. Mater. Sci.*, 2019, **104**, 380–450.
36. A. B. Morgan and J. W. Gilman, *Fire Mater.*, 2013, **37**, 259–279.
37. P. Kiliaris and C. D. Papaspyrides, *Prog. Polym. Sci.*, 2010, **35**, 902–958.
38. J. W. Gilman, *Appl. Clay Sci.*, 1999, **15**, 31–49.
39. S. Bourbigot and S. Duquesne, *J. Mater. Chem.*, 2007, **17**, 2283–2300.
40. H. Qin, S. Zhang, C. Zhao, G. Hu and M. Yang, *Polym. J.*, 2005, **46**, 8386–8395.
41. E. S. Goda, K. R. Yoon, S. H. El-Sayed and S. E. Hong, *Thermochim. Acta*, 2018, **669**, 173–184.
42. W. O. Yah, A. Takahara and Y. Lvov, *J. Am. Chem. Soc.*, 2012, **134**, 1853–1859.
43. H. M. Lewkowitz-Shpuntoff, M. C. Wen, A. Singh, N. Brenner, R. Gambino, N. Pernodet, R. Isseroff, M. Rafailovich and J. Sokolov, *Biomaterials*, 2009, **30**, 8–18.
44. F. Zhao, D. Yao, R. Guo, L. Deng, A. Dong and J. Zhang, *Nanomaterials*, 2015, **5**, 2054–2130.
45. C.-J. Wu, A. K. Gaharwar, P. J. Schexnailder and G. Schmidt, *Materials*, 2010, **3**, 2986–3005.
46. K. Prashantha, H. Schmitt, M. F. Lacrampe and P. Krawczak, *Compos. Sci. Technol.*, 2011, **71**, 1859–1866.
47. K. Song, R. Polak, D. Chen, M. F. Rubner, R. E. Cohen and K. A. Askar, *ACS Appl. Mater. Interfaces*, 2016, **8**, 20396–20406.
48. S. G. Intasa-Ard and M. Ogawa, *Enzymes*, 2018, **44**, 117–136.
49. L. M. A. Meirelles and F. N. Raffin, *J. Pharm. Pharm. Sci.*, 2017, **20**, 115–134.
50. E. Jamróz, P. Kulawik and P. Kopel, *Polymers*, 2019, **11**, 675.

51. S. S. Feng, L. Mei, P. Anitha, C. W. Gan and W. Zhou, *Biomaterials*, 2009, **30**, 3297–3306.
52. Z. Long, Y.-P. Wu, H.-Y. Gao, Y.-F. Li, R.-R. He and M. Liu, *Bioconjugate Chem.*, 2018, **29**, 2606–2618.
53. M. Liu, R. Fakhrullin, A. Novikov, A. Panchal and Y. Lvov, *Macromol. Biosci.*, 2019, **19**, 1800419.
54. J. Kurczewska, M. Cegłowski, B. Messyasz and G. Schroeder, *Appl. Clay Sci.*, 2018, **153**, 134–143.
55. A. Suzuki and T. Tanaka, *Nature*, 1990, **346**, 345–347.
56. E. S. Matsuo and T. Tanaka, *Nature*, 1992, **358**, 482–485.
57. S. Naficy, H. R. Brown, J. M. Razal, G. M. Spinks and P. G. Whitten, *Aust. J. Chem.*, 2011, **64**, 1007–1025.
58. K. Haraguchi and T. Takehisa, *Adv. Mater.*, 2002, **14**, 1120–1124.
59. L. Z. Zhao, C. H. Zhou, J. Wang, D. S. Tong, W. H. Yua and H. Wang, *Soft Matter*, 2015, **11**, 9229–9246.
60. T. Nakamura and M. Ogawa, *Appl. Clay Sci.*, 2013, **83–84**, 469–473.
61. M. Liu, W. Li, J. Rong and C. Zhou, *Colloid Polym. Sci.*, 2012, **290**, 895–905.
62. Y. Wu, Y. Zhang, J. Ju, H. Yan, X. Huang and Y. Tan, *Polymers*, 2019, **11**, 98.
63. K. S. Ngai, S. Ramesh, K. Ramesh and J. C. Juan, *Ionics*, 2016, **22**, 1259–1279.
64. S. Chua, R. Fang, Z. Sun, M. Wu, Z. Gu, Y. Wang, J. N. Hart, N. Sharma, F. Li and D. W. Wang, *Chem. - Eur. J.*, 2018, **24**, 18180–18203.
65. P. Aranda and E. Ruiz-Hitzky, *Chem. Mater.*, 1992, **4**, 1395–1403.
66. J. Nunes-Pereira, C. M. Costa and S. Lanceros-Méndez, *J. Power Sources*, 2015, **281**, 378–398.
67. S. Chua, R. Fang, Z. Sun, M. Wu, Z. Gu, Y. Wang, J. N. Hart, N. Sharma, F. Li and D. W. Wang, *Chem. - Eur. J.*, 2018, **24**, 18180–18203.
68. W. Tang, S. Tang, X. Guan, X. Zhang, Q. Xiang and J. Luo, *Adv. Funct. Mater.*, 2019, **29**, 1900648.
69. Y. Lin, X. Wang, J. Liu and J. D. Miller, *Nano Energy*, 2017, **31**, 478–485.
70. K. Isoda, K. Kuroda and M. Ogawa, *Chem. Mater.*, 2000, **12**, 1702–1707.
71. Y. Fuse, Y. Ide and M. Ogawa, *Polym. Chem.*, 2010, **1**, 849–853.
72. M. Minase, T. Hayakawa, M. Oya, K. Fujita and M. Ogawa, *Bull. Chem. Soc. Jpn.*, 2019, **92**, 1329–1334.
73. K. J. Imwiset, T. Hayakawa, Y. Fukushima, T. Yamada and M. Ogawa, *Langmuir*, 2019, **35**, 13977–13982.
74. A. C. S. Alcântara, N. Darder, P. Aranda, S. Tateyama, K. M. Okajima, T. Kaneko, M. Ogawa and E. Ruiz-Hitzky, *J. Mater. Chem. A*, 2014, **2**, 1391–1399.
75. A. P. Teepakakorn, T. Hayakawa, S. Bureekaew and M. Ogawa, *Clays Clay Miner.*, 2018, **66**, 96–103.

CHAPTER 13

Concepts and Design of Water Dispersive Hydrophobic Supracrystals: Specific Properties

MARIE PAULE PILENI*

Sorbonne Université, Department of Chemistry, 4 place Jussieu,
75005 Paris, France
*E-mail: mppileni@orange.fr

13.1 Introduction

Energy is a vital element for our modern society.[1] This explains the tremendous efforts, both in experimental and theoretical research, that have been made over these last three decades in this area. The topic of thermal energy storage and release has recently attracted increasing interest due to important potential applications not only in solar energy production and waste heat recycling but also in water heating, cooling or air-conditioning as well as in space research and in catalysis.

Self-assemblies of inorganic nanocrystals in 3D crystalline structures called super/supracrystals have attracted great interest in recent years because of the unusual mechanical, electrical, magnetic and optical properties endowed by confining the dimensions of such materials. The properties of these materials are neither those of the bulk phase nor those of the

Nanoscience & Nanotechnology Series No. 55
Concepts and Design of Materials Nanoarchitectonics
Edited by Omar Azzaroni and Katsuhiko Ariga

Published by the Royal Society of Chemistry, www.rsc.org

nanomaterials used as building blocks, but are dictated by their ordering in 3D superlattices.[2–5]

Several multidisciplinary researches also focus on innovative solutions involving hybrid and inorganic nanomaterials.[6,7] These approaches need a strong and broad range of competences in synthesis, characterization and modeling of organic and inorganic materials. The unique chemical and physical properties of these hybrid structures are needed to reach relevant applications.

In the last two decades nanomaterials have been designed for helping diagnostics and therapeutic applications in cancer, infectious diseases, cardiovascular disorders, regenerative medicine and others. The cornerstone of nanomedicine remains the tight control of nanomaterial interactions with the encountered biological environments.[8] Considering the process of cellular internalization of nanomaterials, a considerable effort is made to understand the effects of size, shape, material, charge, surface chemistry, chemical composition, flexibility, stiffness properties of nano-carriers, and the interplay among these, on the mechanisms of cellular uptake by immune cells or tumor cells.[9–15]

Here we develop new concepts to produce water dispersive hybrids structures of hydrophobic nanocrystals. Even though such hybrid structures are in their early stage, collective properties (optical and thermic) due to presence of aqueous solution are obtained. Furthermore, they are used as nanocarriers in model cancer cells.

13.2 Concept and Design of Water Dispersive Hydrophobic Supracrystals

13.2.1 "Clustered" Structures[16,17]

To produce Co and Au "clustered" structures, we need to build up an "organic molecular parachute" to disperse hydrophobic shaped supracrystals in aqueous solution. For this purpose, we use two steps:

(i) *Production of shaped supracrystals*: The control of colloidal crystal growth process produces shaped supracrystals. The addition of non-solvent traces to a colloidal solution subjected to solvent saturation induces a marked increase in the attractive interactions between nanocrystals and, consequently, favors a homogeneous growth process.[18] Either Co or Au nanocrystals dispersed in toluene precipitate when they are subjected to traces of isopropanol and ethanol respectively. The SEM images of the collected precipitates (Figure 13.1a) show formation of well-defined aggregates with various shapes and a rather large size distribution. Most of these shaped aggregates are characterized by a flat surface with well-defined facets in hexagonal symmetry while others present some defects. The Small Angle X-ray Scattering (SAXS) pattern of supracrystals and its profile (Figure 13.1d and g) show formation of fcc Co supracrystals. The edge-to-edge interparticle distance is 2.8 nm. Similar procedure is used to produce fcc Au "clustered" structures.

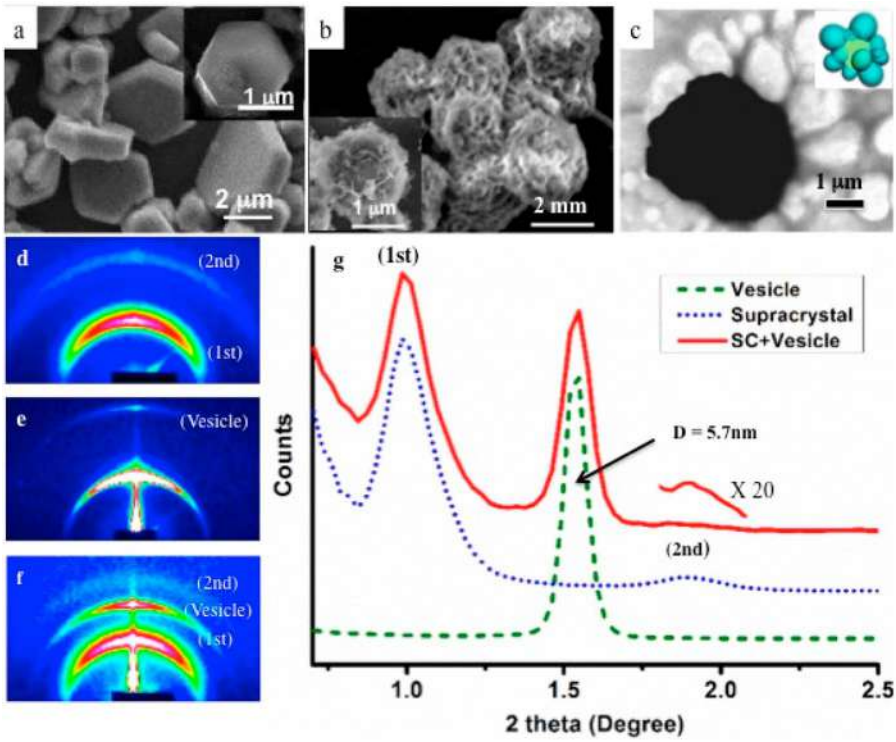

Figure 13.1 (a) and (b) are the SEM images of Co shaped nanocrystals before (a) and after (b) DPPC treatments. (c) TEM image corresponding to image of (b) showing that the vesicles are closely attached to the supracrystals forming cap-like structures. (d, e, f) SAXS patterns of the supracrystals (d) the vesicles (e) and the clustered structure(e), (g) profile the different SAXS patterns: The two red peaks in (f) can be attributed to the diffraction of the supracrystals and vesicles, respectively. Reproduced from ref. 16 with permission from American Chemical Society, Copyright 2016.

(ii) *Molecular parachute of supracrystals*: To disperse such hydrophobic supracrystals in aqueous solution we need to control the interdigitation processes and produce multi-walled structures. The coating agent of nanocrystals used as building blocks must interact strongly with the biological molecules. For this purpose, we use a concept, developed several years ago, to build up supra-aggregates thermodynamically stable:[19] The major parameters are the surfactant volume fraction, the volume of water, and the number of surfactant molecules. The surfactant parameter, σ, is given by $\sigma = \nu_s/a_s\, l_s$ where ν_s, a_s and l_s are the surfactant volume fraction, surface per head polar group and the surfactant tail length, respectively. Finally, the packing of multiwall structures depends on the radius of the vesicular water core, the thickness of the bilayer, and the volume of water in the core. According to the packing parameter, the

best interdigitation process is obtained with long tail surfactant molecules and large head group surface area.[20] Furthermore, we know that the energy gain, due to the addition of a $-CH_2-$ group into the alkyl chain is 8×10^{-21} J. The curvature of nanocrystals creates voids between two consecutive coating agent molecules at the nanocrystal surface. Because voids are energetically unfavorable, the dipalmitoylphosphatidylcholine (DPPC) alkyl chains and the C_{18} chains of PEG-2000-DOPE fill them up. This induces strong interactions between DPPC, PEG-2000-DOPE and nanocrystals coated with C_{18} $H_{37}X$, where X is either carboxylic group or thiol for Co and Au nanocrystals respectively. The PEG2000-DOPE, hydrophilic chain (C_{91}) makes bridges from one vesicle to another and consequently plays the role of "parachutes" preventing gravity processes. The SEM (Figure 13.1b) and the corresponding TEM (Figure 13.1c) images reveal the structure of individual composites, with presence of large vesicles attached to the supracrystal surface and drape-like structures linked to it. These draped-like structures are due to the drying process because during TEM sample preparation, water is released from vesicles and collapsed shells are left.

The SAXS pattern of structural studies acquired on shaped supracrystals after DPPC/PEG-DOPE treatment shows well-defined rings (Figure 13.1f). The new ring appearing in the diffraction pattern is attributed to the presence of vesicles. To support such a statement, a blank experiment is performed, in absence of supracrystals, with DPPC/PEG-DOPE molecules. After hydration, the solution is dried and the SAXS pattern (Figure 13.1e) shows a strong signal due to the diffraction of periodic vesicle bilayers. The calculated bilayer distance is 5.7 nm, which agrees with the thickness of the liposome shell.[21] The profile (Figure 13.1g) clearly shows that the diffraction peaks of the composite are a combination of the peaks of isolated Co-supracrystals and of vesicles indicating that the DPPC/PEG2000-PE vesicles strongly interact with Co-supracrystals. Similar data are obtained with Au instead of Co nanocrystals. From these data we conclude that "clustered" structures suspended in water retain their 3D crystalline ordering *i.e.* nanocrystals (Au/Co) used as build blocks remain in their metal form. With Co "clustered" structures, the magnetic properties of shaped supracrystals before and after biological treatment remain unchanged indicating that oxygen molecules do not diffuse inside the supracrystal. This is due to formation of CoO layers at the edges of the "clustered" structures preventing oxygen diffusion inside the crystalline structure. With Au "clustered" structures collective optical properties are pointed out (see below).

13.2.2 Colloidosomes and Supraballs[22]

More than century ago, Pickering originally proposed the concept of colloidosomes when they discovered that microsized solid particles stand at the interface between two immiscible fluids.[23] In the recent two decades much

diversified hollow capsules consisting of coagulated, fused or close-packed layers of colloidal particles with sizes ranging from micrometer to millimeter were produced and investigated.[24–27] Some of these new superstructures were produced *via* assembly into shells around water-in-oil emulsion of latex particles, large porous nanoparticles, and layer-by-layer assembly of multilayer shells consisting of alternating cationic and anionic polyelectrolytes. It was also demonstrated that solid microspheres in oil-water emulsion can be produced in the conditions of a weak nanoparticle confinement at the fluid interface affected by the thermal fluctuations.[27–29] On decreasing the particle size, the thermal energy fluctuations decrease the particle adhesion forces at the liquid–liquid interface. Consequently, it makes impossible to produce colloidosomes. This can be achieved *via* tuning surface properties using various ligand modifications such as chemical cross-linking, specific ligand interactions or other nanoparticles stabilizers at the fluid interface.[30,31] Recently, we developed a new concept to lock Fe_3O_4 nanocrystals at the liquid–liquid interface: a "Janus bilayer" shell for the nanocrystals coated with oleic acid (C_{18}–COOH) adsorbed at the liquid–liquid interface[22] inducing formation of colloidosomes. The inner shell of the bilayer is the tail part of oleic acid covalently bound to Fe_3O_4 nanocrystals whereas the outer shell is composed of DTAB (dodecyl trimethyl ammonium bromide, C_{12}–$NH_3^+Br^-$) in water phase and octadecene (ODE, $C_{18}H_{36}$) in chloroform. Specific interactions between aliphatic ODE and oleic acid, covalently bound at the nanocrystal surface, take place inducing the formation of a monolayer-nanocrystal-membrane. This favors the adsorption of nanocrystals at the oil/water interface and consequently locks them at liquid/liquid interface[32–34] and consequently colloidosomes are produced. They are composed either of one or a few layers of nanocrystals, (Figure 13.2a and b). This approach helps to avoid complicated procedures, such as those found in nanocrystal polymersomes.[35,36] Keeping the other conditions unchanged, in

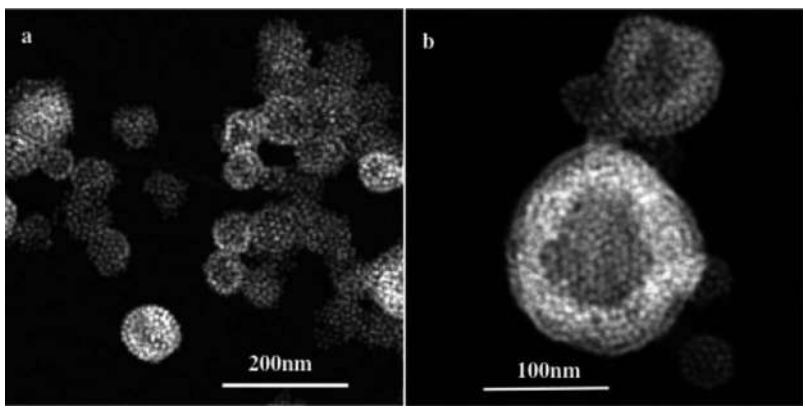

Figure 13.2 HAADF-STEM (High-Angle Annular Dark-Field Scanning Transmission Electron Microscopy) images of colloidosomes at various scales showing mon and multilayers of nanocrystals self-assembled and forming a shell (a,b).

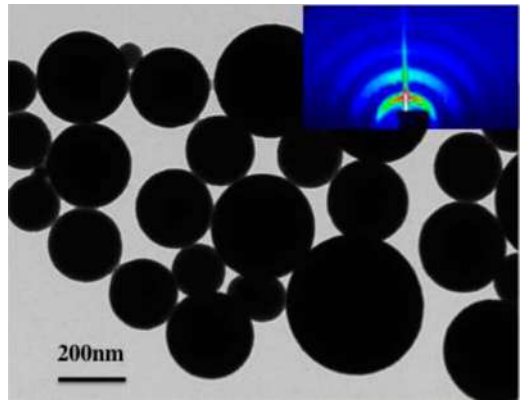

Figure 13.3 TEM image of supraballs inset small angle X-ray diffraction. Reproduced from ref. 22 with permission from American Chemical Society, Copyright 2016.

absence of ODE, the high mobility of the nanocrystals at the interface induces formation of large fcc spherical solid dense-packed assemblies of nanocrystals called supraballs (Figure 13.3). We deduce that ability to control the amphiphilic balance (Janus balance) of nanocrystals at the liquid–liquid interface is a key mechanism that drives the colloidosome formation. Note that similar fcc spherical supraballs have been previously obtained with either 6 nm cobalt iron oxide nanocrystals[37] or large colloidal silica particles.[38]

13.2.3 "Egg" Structures[22]

The concept developed for colloidosomes favors a new strategy for designing colloidosomes as a reservoir for fcc supracrystals of Fe_3O_4 nanocrystals. Consequently, semi-hollow suprastructures are obtained (Figure 13.4a). The average distance between nanocrystals is estimated at around 3 nm. The inner 3D superlattices are oriented along the outer monolayer nanocrystal shell indicating an epitaxial growth as already observed for heterostructures with matched lattices in atomic solids.[39] Therefore, we conclude that epitaxial overgrowth of 3D supracrystals colloidosome occurs yielding conformal semi-hollow suprastructure.

It is known that mixtures of hydrophobic nanocrystals, having two well-defined sizes, with a low size distribution, self-assemble into binary nanocrystal superlattices.[40–43] The key factor to produce such assemblies is the size ratio γ between large and small nanocrystals in the binary mixture. The ratio γ is given by $\gamma = d_{\text{eff(small)}}/d_{\text{eff(large)}}$, with ($d_{\text{eff}}$) being the effective diameter, defined as the center-to-center distance between nanocrystals (small or large) self-ordered in a compact hexagonal network. Using a hard sphere model based on the ratio γ, the structure of binary systems can be predicted.[44] To realize the growth of binary supracrystals inside the colloidosomes, 6.5 ± 0.3 nm Fe_3O_4 nanocrystals are

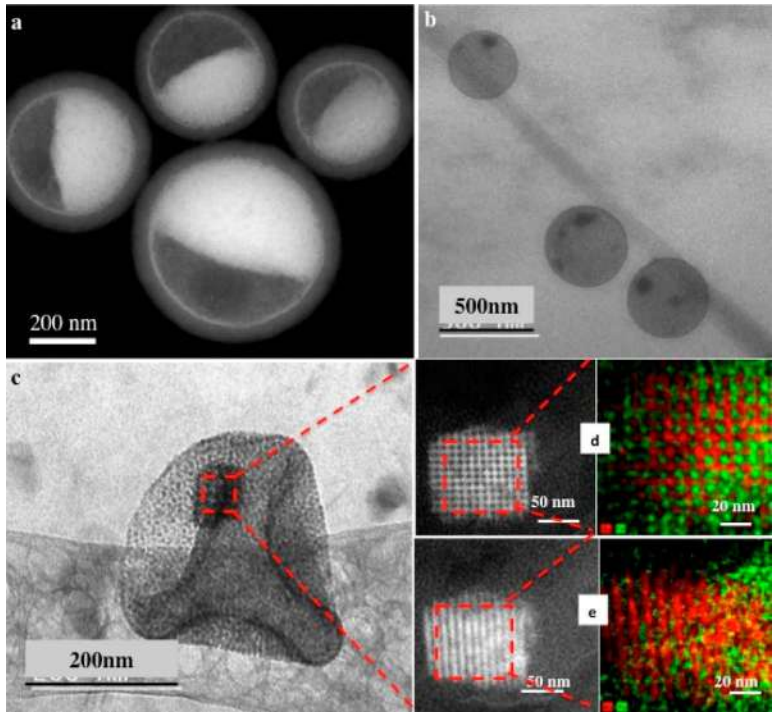

Figure 13.4 (a) HAADF-STEM overview image of the half-filled colloidosomes, (b, c) Cryo-TEM images of either an assembly (b) or one single (c) colloidosome filled by the Fe_3O_4/Au binary supracrystals. Enlarged HAADF-STEM images (d,e) of the binary supracrystals, tilted 45° with respect to each other with their corresponding STEM-EDS maps (d and e) Au and Fe are colored in red and green respectively. Reproduced from ref. 22 with permission from American Chemical Society, Copyright 2016.

combined with 3.5 ± 0.2 nm Au nanocrystals coated with oleic acid and dodecanethiol respectively, with γ = 0.54. From the hard sphere model and for this γ value, the expected crystalline structures correspond either to $NaZn_{13}$ or to AlB_2 -type structures. Figure 13.4b shows a cryo-TEM image of colloidosomes filled with a cubic shaped structure. The chemical maps (Figure 13.4d and e) assign these cubic assemblies to $(Fe_3O_4)Au_{13}$ structure corresponding to $NaZn_{13}$-type.

13.3 Specific Properties

13.3.1 Fingerprint of the Supracrystals Building Blocks and Collective Modes[17]

To control the size of "clustered" structures of 5.5 nm Au nanocrystals we need to control the nucleation (t_1) and growth (t_2) time processes. Figure 13.5 shows a progressive increase in the Au "clustered" structures. Supracrystals

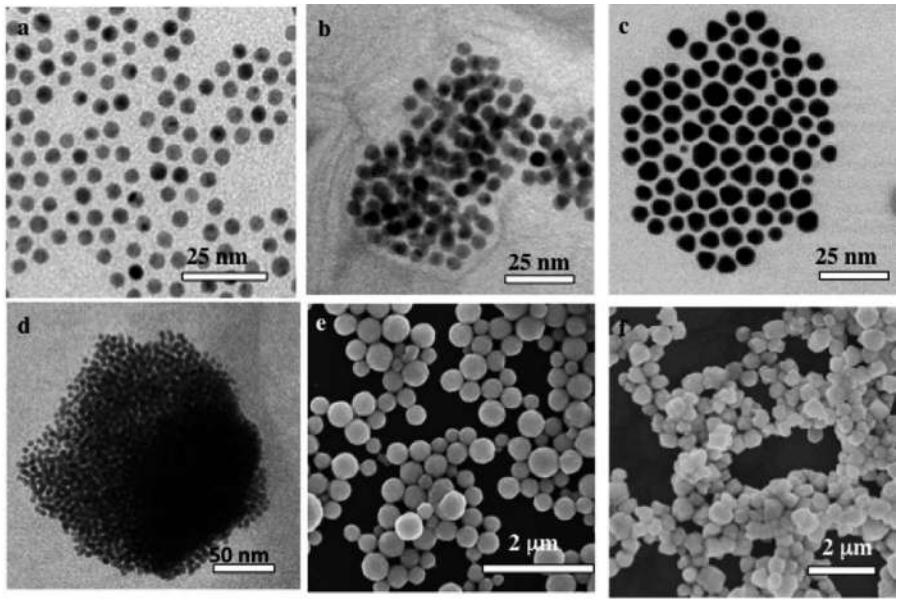

Figure 13.5 (a) TEM image of isolated water-soluble zwitterionic Au nanocrystals dispersed in vesicular solution and with a diameter of 5.5 ± 0.3 nm (b–f) aggregate of 5.5 nm Au nanocrystals having an average size of 52 nm, 125 nm, 198 nm, 413 nm and 611 nm respectively. Note that assemblies of 52 nm, 125 nm and 198 nm reveal a slight change in the interparticle distances indicating that the aggregates are disordered. However, we cannot neglect some nanocrystal ordering in the dark region as shown in (d). For 413 nm and 611 nm the nanocrystals used as building blocks are ordered in fcc crystalline structures. Reproduced from ref. 17 with permission from American Chemical Society, Copyright 2017.

are obtained for nucleation and growth times up to 6 and 10 hours respectively (Figure 13.5e,f). The size of the supracrystals increases with increasing these times. At 16 and 60 hours nucleation and growth process times respectively, the supracystals produced are too large to be stabilized for a long time by the "molecular parachute". Below these time values (6 and 10) the assemblies of Au nanocrystals are amorphous aggregates (Figure 13.5b–d).

The absorption spectrum of Au "clustered" is red shifted on increasing its average size (Figure 13.6) and a shoulder around 530 nm is observed.

To simulate the absorption spectra we first calculate the effective dielectric function of Au assemblies by using Maxwell-Garnett effective medium theory (EMT).[45] Then Mie theory is used to calculate the spectral response of Au assemblies dispersed in water. The distribution over the size of assemblies is deduced from SEM images (Figure 13.5) and accounted for in our calculations. Figure 13.6 shows a rather good agreement between experiments and calculated data. Note that the absorption spectra of the assemblies are the

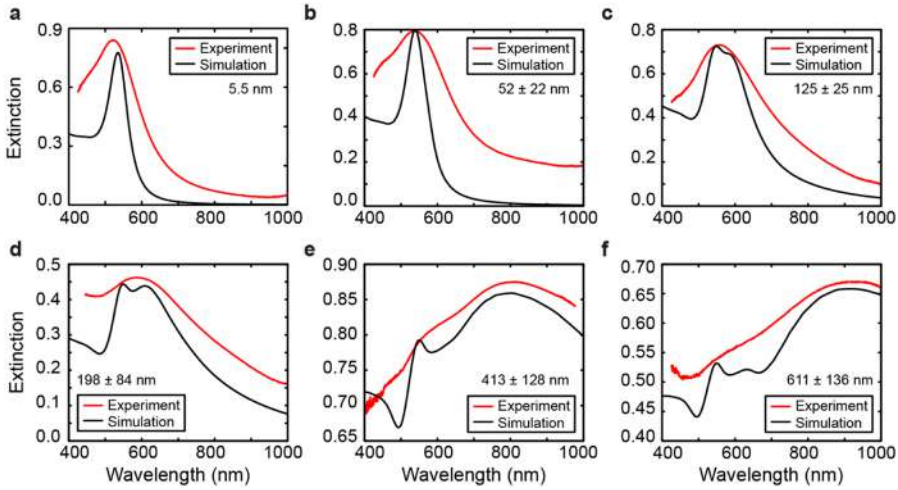

Figure 13.6 Extinction spectra for isolated Au nanocrystals and Au assemblies with various sizes. (a) 5.5 nm Au nanocrystals; Au aggregates with sizes of (b) 52 nm, (c) 125 nm, (d) 198 nm; Au supracrystals with sizes of (e) 413 nm and (f) 611 nm. The measured size distribution was also indicated. The following sizes were used to fit the measured data: 5.5 nm, 52 nm, 140 nm, 198 nm, 480 nm, and 611 nm. Reproduced from ref. 17 with permission from American Chemical Society, Copyright 2017.

sum of two spectra: At short wavelength one is found at fixed wavelength (530 nm) whereas the second one is red shifted with increasing the aggregate size. At shorter wavelength the peak fulfills the resonance condition of spherical Au nanocrystals in a ligands-based medium. The scattered spectra at larger wavelength are very broad and red shifted linearly with the wavelength as the assembly size increases (Figure 13.7). Such optical response at large wavelength is ascribable to a photonic (*i.e.* collective) mode of the assembly, since its spectral position scales linearly with the size of the supracrystal when the fingerprint of dispersed nanocrystals used as building blocks is retained.

13.3.2 Nanoheaters[46]

The energy flow upon light irradiation is investigated by pump-probe experiments. The differential transmission ($\Delta T/T$) spectra are recorded as a function of time and of the probe wavelength, λ. At the initial time scale of ten picoseconds, the typical $\Delta T/T$ map is due to the transient spectra of isolated nanocrystals at various probe wavelengths. They are dominated by shift and broadening of the plasmonic resonances as observed previously.[47] These spectra exhibit a decay constant of few picoseconds (Figure 13.8a), corresponding to the timescale of electron-phonon scattering in noble metals.[48,49] Both dynamic and static data confirm that Au "clustered" structures at room

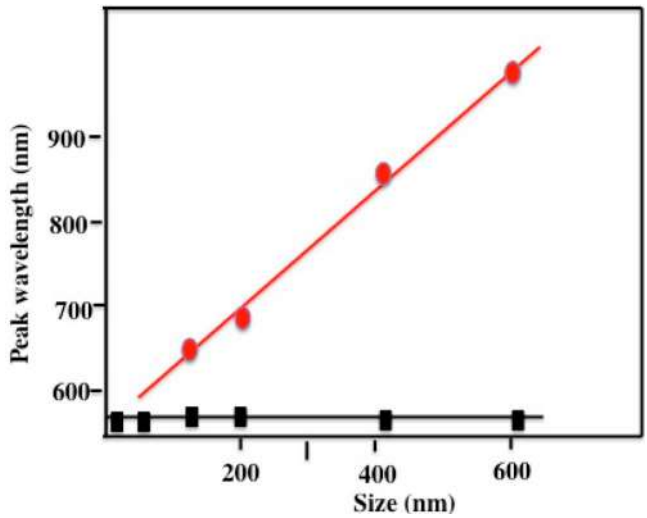

Figure 13.7 Variation of the peak wavelength as a function of the assembly size: The black curve illustrates the absorption peak of dispersed Au nanocrystals used as building blocks. The scattering peak represented in the red curve red shifts as the assembly size increases. Reproduced from ref. 17 with permission from American Chemical Society, Copyright 2017.

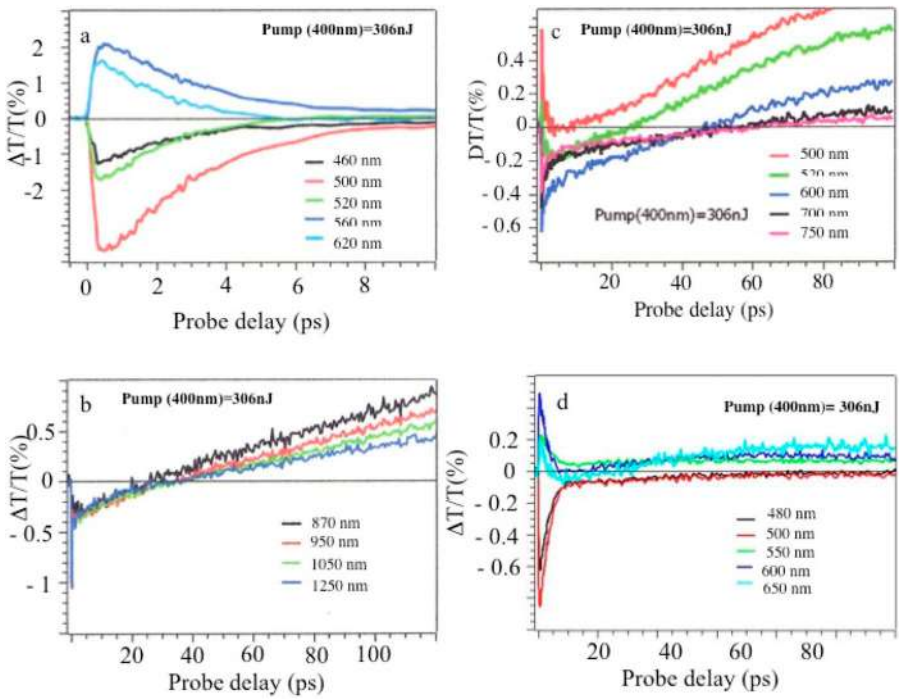

Figure 13.8 Dynamics of the $\Delta T/T$ at selected probe wavelengths, at the two different time scales of energy flow in the Au clustered structures (a,b) fcc Fe_3O_4 supraballs (c) and $Fe_30_4Au_{13}$ "egg" structure (d). Reproduced from ref. 52 with permission from National Academy of Sciences.

temperature keep the fingerprint of isolated nanocrystals used as building blocks. This was already observed in dried thick supracrystal by scanning tunneling microscopy/scanning tunneling spectroscopy (STM/STS) experiments at low temperature.[40,50,51]

At longer times scales, the $\Delta T/T$ map of Au "clustered" structures (Figure 13.8b) exhibit *very distinct features* which, to the best of our knowledge, have not been reported for any nanostructures: Instead of a monotonic decrease over time, we observe the build-up of a positive signal which is red shifted by about 100 nm compared to early spectra. This novel phenomenon cannot be ascribed to mechanical oscillations that, in Au nanocrystals, are well known to have a strong impact on the ultrafast optical response at suc time scale.[52] To explain the origin of such unexpected transient optical response at the 100 ps timescale, then remaining constant at the nanosecond time scale, a model to simulate the optical experiments was developed:[46] We have to remember how supracrystals are formed. The alkyl chains used to coat nanocrystals interdigitate and play a role in ordering nanocrystals in crystalline structure. The static optical response indicates that such supracrystals behave as metaparticles rather than finite arrays of nanocrystals and the collective effects are dominated by the onset of an effective medium. Due to higher penetration depth of light in the supracrystal structure (about 60 nm for Au nanocrystals), despite the thickness of the assembly, the power absorbs per unit volume is more uniform compared with that in a nanosphere of the same diameter. The pump pulse is absorbed by the metallic phase of the supracrystal and initiates a chain of energy transfer processes. According to this model, the delayed build-up of the $\Delta T/T$ signal on the few hundred picoseconds timescale is the signature of the final step in the light–heat conversion process that ultimately results in the heating of the matrix of organic ligands. The very good agreement between experiments and the model confirms a collective regime of photo-temperature generation enabled by the assembling. It is concluded that the coating agent, even though not directly absorbing, acts as an internal reservoir for efficient accumulation of energy within few hundreds of picoseconds. Such dynamical feature is expected to be an intrinsic property of any water dispersive hybrid assembly of hydrophobic nanocrystals, regardless of the peculiar nature (*i.e.*, plasmonic or not) of their building blocks. This is well demonstrated by the fact that similar behaviors in the transient optical responses (Figure 13.8c,d) are experimentally observed with both Fe_3O_4 supraballs (Figure 13.8c) and with binary supracrystals [$(Fe_3O_4)Au_{13}$] trapped in colloidosomes (Figure 13.8d). These results provide a clear indication that the water dispersive hybrid nanostructures can be operated as very efficient universal nanoheaters.

Interestingly, we observe a marked drop in the absorption spectra of colloidosomes and supraballs compared to dispersed Fe_3O_4 NCs (Figure 13.9). Such an effect remains an open question. It could be attributed to the fact these hybrids behave as metamaterials.[53]

Let compare the photothermal capacity of the colloidosomes and supraballs with dispersed Fe_3O_4 nanocrystals (at constant Fe concentration, 1 mg mL^{-1}). These three samples are irradiated with a near-infrared laser (808 nm) at 1 W cm^{-2}.

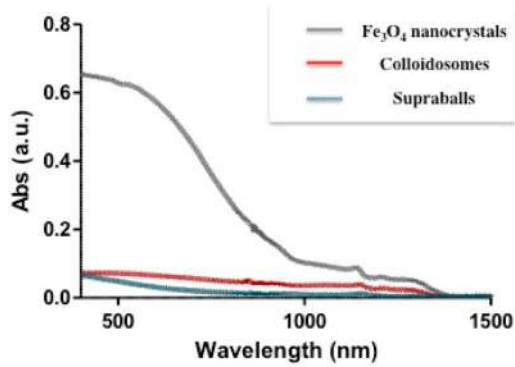

Figure 13.9 UV-vis-NIR absorption spectra of NCs, colloidosomes and supraballs.

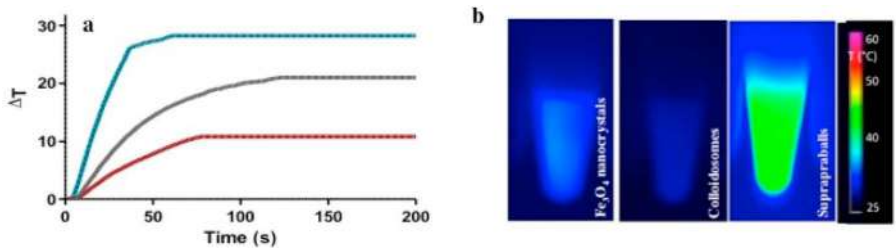

Figure 13.10 Photothermal properties of the water dispersive hybrids used with cells and described above ([Fe] = 1 mg mL^{-1}) in aqueous solution. (a) Temperature increment of dispersed Fe_3O_4 nanocrystals (gray) colloidosomes (red) and supraballs (blue) subjected to 808 nm laser light (1 W cm^{-2}). (b) Corresponding infrared thermal images of dispersed nanocrystals, colloidosomes and supraparticles aqueous dispersions (100 μL) after 5 min of 808 nm laser irradiation.

The surface temperature of the solution is monitored with an infrared camera over time. At such a wavelength the number of absorbed photons is larger for dispersed Fe_3O_4 nanocrystals than the two hybrid structures. The temperature increment (ΔT) of the solution increases with time exposure to reach plateau after few dozens of seconds (Figure 13.10). Even though the number of absorbed photons is less with supraballs compared to dispersed Fe_3O_4 nanocrystals, Figure 13.10a shows that the ΔT plateau reached for supraballs (25 °C) is higher than dispersed NCs (and 23 °C) and colloidosomes (10°).

Colloidosomes heating capacity is significantly lower than that of supraballs and its building blocks (Figure 13.10). The absorption of colloidosomes is similar to supraballs and consequently the difference in the ΔT cannot be attributed to the difference number of absorbed photons. Here we have to take into account the structural changes between colloidosomes and supraballs: From the data described above[46] we know that the coating agents of nanocrystals used to produce solid fcc supraballs act as an internal energy

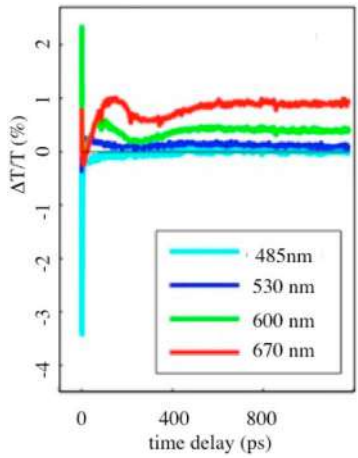

Figure 13.11 Dynamics of the $\Delta T/T$ at selected probe wavelengths, on nanometer time scales of energy flow in the Au clustered structures. Reproduced from ref. 52 with permission from National Academy of Sciences.

reservoir. With colloidosomes, the efficiency of the coating agents is lower because they are less densely packed with formation of one or few layers of nanocrystals. Figure 13.10a clearly shows, with supraballs, the ΔT slope to reach the plateau is larger than that of dispersed nanocrystals. This fast increase in ΔT is due to supraballs acting as nanoheaters.

Several years ago we demonstrated that, by subjecting supracrystals to light, inter-nanocrystal coherence inside fcc supracrystals takes place. Even though the forces involved between atoms in an atomic crystal and nanocrystals in a supracrystal are not the same, nanocrystals breath coherently in a supracrystal as atoms in a nanocrystal.[54] With water dispersive Au "clustered" structures Figure 13.11 shows an experimental oscillation period of 300 ps. We attribute this oscillation to the period of mechanical oscillation due to a breathing mode of the whole assembly. The calculated period, P, is given by $P = 2d/v_s$ where d is the average diameter of the assembly and v_s the speed of sound inside the supracrystal. With fcc supracrystals of 7.1 nm Co nanocrystals used as building blocks, at room temperature, the speed of sound is found equal to be 1235 ± 12 $m.s^{-1}$.[55] Assuming that the speed of sound in a supracrystal is independent of the type of metal used (Co or Au), the calculated period of the Au "clustered" structure with an average diameter of 198 nm ± 84 nm is 236 ± 77 ps. This calculated value is consistent with deduced from experiments (≠300 ps).

13.3.3 Magnetic Cells[56]

Colloidosomes and supraballs are used as a new generation of nano-carriers and compared to their building blocks considered as dispersed Fe_3O_4 nanocrystals (nanocrystals coated with dopamine) in A431 tumor cells intracellular

distribution. To do so, A431cells are exposed to the three different systems (dispersed Fe_3O_4 nanocrystals, colloidosomes and supraballs) at equivalent iron concentration ([Fe] = 28 μg mL^{-1}) in serum-complemented culture medium for 30 min to 1 day. The necrosis level induced by the nano-carriers does not exceed 7%. Using the magnetophoresis approach, in which cells in aqueous solution are subjected to a magnetic field, the average cell velocity increases with the hybrids compared to the same dispersed nanocrystals.

After 1 and 8 days tumor cell post-internalization with dispersed nanocrystals, colloidosomes and supraballs slices of tumor are imaged by TEM (Figure 13.12).

(i) With *dispersed nanocrystals*, after 30 min incubation, a prompt internalization into membrane-closed endosomes is observed. As the time increases, dispersed nanocrystals tend to aggregate into intracellular endosomes that mature and fuse with lysosomes to reach aggregation after 8 days incubation (Figure 13.12A,B). This data is fully in line with that already observed for water-soluble magnetic iron oxide nanoparticles (IONP) differing by shapes and coating agents. IONP undergo a more or less rapid degradation in lysosomes and Fe recycling into ferritin proteins.[57–59]

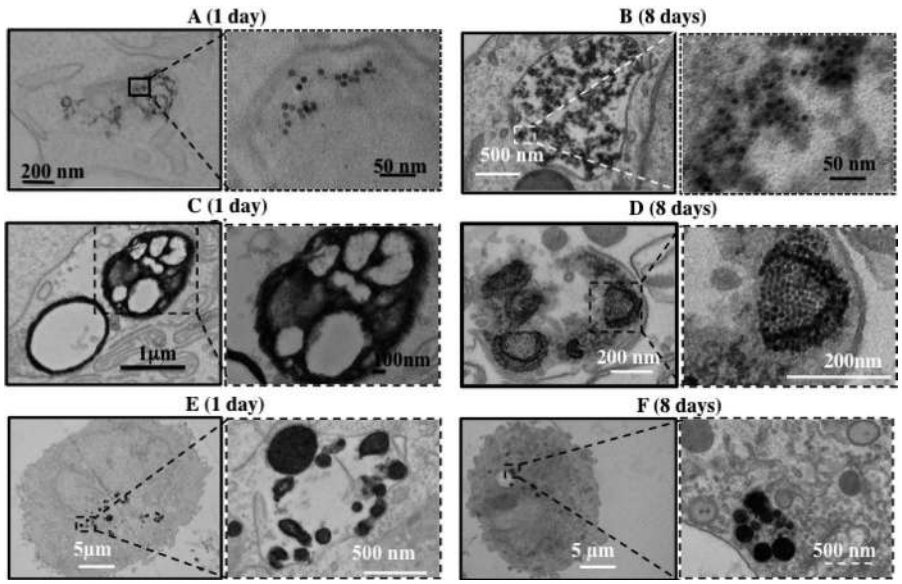

Figure 13.12 2D TEM slices images of ([Fe] = 28 μg mL^{-1}) nanocrystals at 1 day (A, C, E) and 8 days (B, D, F) post-internalization in A431 tumor cells of dispersed nanocrystals (A, B), colloidosomes (C, D) and supraballs (E, F). Reproduced from ref. 56 with permission from John Wiley & Sons, Copyright © 2020 Wiley-VCH GmbH.

(ii) *Colloidosomes* keep more or less similar shape with a marked increase in the size, morphology deformation and appearance of curved fragments (Figure 13.12C,D). As already mentioned, colloidosomes are closely stuck to the cell membranes, bending to the shape of the intracellular vesicles. Some curved fragments of colloidosomes are flattened to form anisotropic inclusions of several layers of nanocrystals along intracellular membranes. This flattening process increases over time as colloidosomes or fragments seem to condense into autophagosomes and lysosomes. Such organized layers of nanocrystals keep reminiscent of colloidosomes shell structure.

(iii) *Supraballs* more or less keep their spherical structures after entering the cell intracellular compartments. These compartments fuse with lysosomes over time, showing, at 8 days, an electron dense matrix surrounding well-preserved self-organized of nanocrystals, (Figure 13.12E,F).

Hence, colloidosomes and supraballs favor self-assemblies of nanocrystals within cell compartments up to 8 days, the final time-point of our experiment. Referring to dispersed nanocrystals, Figure 13.12 clearly shows a marked increase in Fe uptake by using these two hybrids as nano-carriers compared to their building blocks.

The major difference between the two hybrid structures concerns the evolution of their morphologies that must be related to their nanomechanical properties: Colloidosomes are softer, more flexible and provide more surface area contact with cells than supraballs.[60] Hence, colloidosomes because their ability to deform they maximize their cell interactions and a higher cell surface binding.

The average diameter of dispersed nanocrystals remains unchanged 1 day post-internalization whereas the nanocrystal size distribution slightly increases. In contrast, after one-day post incubation, the size of colloidosomes and supraballs increases by a factor between 2 and 10 and around 2–3 respectively compared to the one observed in absence of cells (160 nm and 210 nm in average). In both cases, the size distribution increases, being wider for the deformed colloidosomes and their fragments than for supraballs that remain mostly spherical. The independence of the increase in hybrid size with the incubation time (up to 1 day) indicates early interactions with cell membranes. The interactions between nanocrystals coated with the same coating agent (oleic acid) are stronger than those involving oleic acid and the biological membranes. This process is more efficient with colloidosomes than supraballs due to their differences in flexibility, stiffness and internal mobility of nanocrystals. This highlights the dynamical transformation of hybrids during the first incubation day upon contact with biological membranes. Such increases in size are independent of the incubation time (up to 1 day) indicating that they are involved early interactions with cell membranes.

The electronic contrast of the 2D TEM slices images shows significant differences on the lysosome morphology having various sizes and nanocrystal contents. The nanocrystal surface density is calculated from the ratio of the total nanocrystals area in lysosomes and the lysosome area (at 1 and 8 days post-internalization). Table 13.1 shows a marked increase in the nanocrystal surface density with both colloidosomes and supraballs compared to dispersed nanocrystals. This clearly shows that nanocrystals tend to condense into lysosomes. The increase in the nanocrystal surface density over time highlights the fusion process and maturation in a way that is modulated by the hybrid structures.

The lysosome circularity is more affected with colloidosome internalization than with supraballs or dispersed nanocrystals. It decreases when lysosomes are loaded with colloidosomes compared to dispersed nanocrystals (from 0.75 to 0.64 and from 0.59 to 0.53 after 1 and 8 incubation days respectively) and its distribution markedly increases. The dynamical change in size and circularity of intracellular compartments between colloidosomes and supracrystals shows the mutual adaptation of intracellular membranes.

According to others,[61–64] the distance from nanocrystals to lysosomal membrane remains a key parameter to induce cell death, mechanical stress, or activate heat-sensitive membrane channels *etc.* Therefore, we choose 100 nm as an arbitrary distance to quantify the density of nanocrystals close to the lysosome membrane. After 1 day post-internalization, the density of nanocrystals at the vicinity of the membrane is 10.6 and 12.4 times larger for colloidosomes and supraballs respectively than dispersed nanocrystals. This confirms membranes wrapping at the early stage of internalization. After 8 days, the local density is still 5.3 and 2.2 times higher than that of the building blocks. This reflects that lysosome maturation tends to push aside the supraballs from the cell membrane whereas colloidosomes remain close to it what can be associated to the dense packing and high elastic moduli and stiffness of supraballs compared to colloidosomes. Both hybrids maximize this fraction after 8 days by a factor close to 2 in comparison to dispersed nanocrystals. We conclude that both hybrids are valuable nano-carriers to affect the lysosome membrane, particularly on late lysosomes a few days after uptake. As observed by studying shape fluctuations of lipid membranes,[65] the coupling of membrane fluctuations to the colloidosome shell could give rise

Table 13.1 Surface density of nanocrystals (SD): percentage of area covered by nanocrystals in the lysosome surface at 1 and 8 days post-internalization.

	System dispersed nanocrystal	Colloidosomes	Supraballs
SD 1 day	4%	34%	52%
SD 8 days	11%	48%	32%

to the so-called Helfrich entropic repulsion which might favor colloidosomes flattening and concentration into the much smaller, still more undulated, lysosomes observed at 8 days. Hence, the size, morphology and membrane undulations of intracellular host vesicles clearly adapt to their loading, with striking differences between rigid and deformable hybrids. These data are based on local observations. At the macroscopic scale, SAXS experiments give an overview on the internalization processes. The SAXS scattering intensities are recorded for cells incubated in absence (control) and in presence of the dispersed nanocrystals, colloidosomes and supraballs, at various incubation times (from 4 hours to 2 days) and same experimental conditions. By subtracting the scattered intensity of the cells, Figure 13.13a,c,e show that the shapes of the SAXS scattering curves remain independent to the incubation time and their intensities increase indicating invariance behavior of the local structures and a progressive up take respectively. In other words, the structure of the aggregates is not modified at various internalization

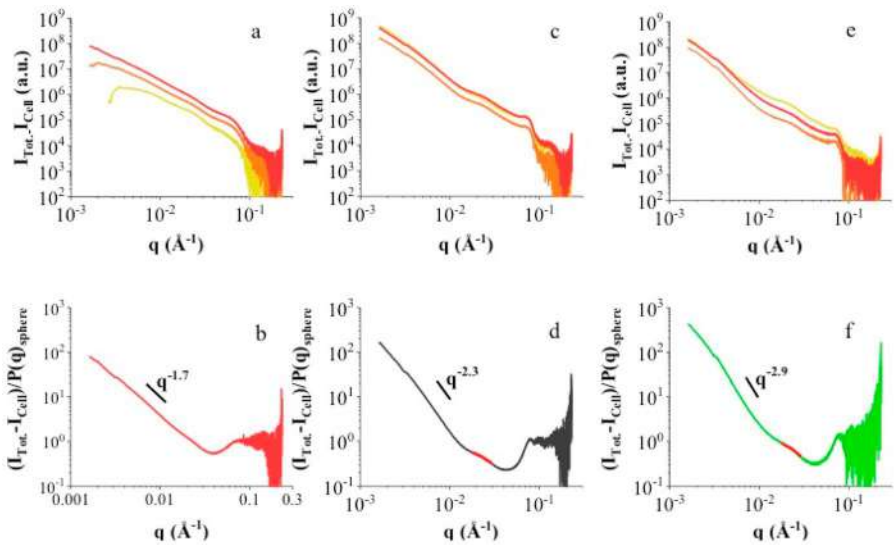

Figure 13.13 SAXS patterns of the total scattered intensity after subtraction of the cell contribution, $I_{total}(q) - I_{Cell}(q)$, (a, c, e) of cells after incubation for periods of 30 min (green), 4 hours (yellow), 1 day (orange) and 2 days (red) with (a, b) dispersed nanocrystals, (c, d) colloidosomes, (e, f) supracrystals. By dividing $I_{total}(q) - I_{cell}(q)$ in all the measured q range by $P(q)$, we obtain the structure factor, $S(q)$, of nanocrystals embedded in cells incubated with nanocrystals (b), colloidosomes (d) and supraballs (f) for 2 days. The red line (d and f) corresponds to simulation of hard spheres structure. This reflects loose fractal aggregates of nanocrystals (b) and denser structures of colloidosomes (d) and supraballs (f). Reproduced from ref. 56 with permission from John Wiley & Sons, Copyright © 2020 Wiley-VCH GmbH.

times (from 4 hours to 2 days). At a low q value, the structure factor decay follows a power law and its exponent is −1.7 with nanocrystals dispersed aqueous solution. This corresponds to elongated and branched clusters of nanocrystals (Figure 13.13b). With hybrid structures, the power law exponent markedly increases from −2.3 to −2.9 for colloidosomes and supraballs respectively (Figure 13.13b,d,f). This reflects a progressive increase in the nanocrystal packing from colloidosomes to supraballs. This confirms the fact that supraballs and colloidosomes tend to remain at very close distance once internalized by cells demonstrating the enduring assemblies of nanocrystals within intracellular compartments. With both colloidosomes and supraballs a broad peak with a small amplitude can be detected around $q = 0.02$ Å^{-1} whereas it is not with dispersed nanocrystals. This peak could correspond to a characteristic distance estimated by fitting with a hard sphere structure factor to an effective radius around 27 nm and 26 nm for colloidosomes (Figure 13.13d) and supraballs (Figure 13.13f) respectively. Such a peak, inexistent within dispersed nanocrystals, is a signature of hard sphere interactions in the internalized hybrid structures. It cannot be attributed to a characteristic dimension of the aggregates such as the average distance between adjacent nanocrystals. We can assume that it could be due to "nanocrystal clusters" belonging to various hybrids sitting inside a cell. In contrast, dispersed nanocrystals are aggregated into disordered structures similar to those obtained by diffusion-limited aggregation.

According to these data, we pose the following question: Does formation of such assemblies of nanocrystals favor magnetic manipulation? To answer this question, cells loaded with dispersed nanocrystals at day 1 post-internalization are subjected to a uniform magnetic field (1 Tesla) for 4 hours. The 2D slide TEM image (Figure 13.14) and the optical microscope (not presented here) do not show any anisotropic structures as well as to non-labeled cells. Keeping the same experimental conditions and replacing dispersed nanocrystals by colloidosomes dark rods (with length from 1 to 20 μm) in cells, observed through the optical microscope, are all aligned along the direction of the applied magnetic field and follow the field direction. The corresponding high magnification TEM image confirms formation of colloidosomes chains aligned along the field direction. Some of them are fully intracellular consisting of lysosome alignments whereas others are surrounded by a cell membrane and anchored to the cell but partly in the extracellular space (Figure 13.14II). With supraballs, hybrid chains are embedded in cytoplasm and entangled into membranes with intra and extracellular alignments (Figure 13.14III). This markedly contrasts with the absence of any anisotropic structures with dispersed nanocrystals (Figure 13.14I). Formation of such long chains is explained by the large magnetic dipolar interactions induced by the self-assemblies of nanocrystals both inside and close to the lysosome membrane. We attributed such high percentages of nanocrystals and their close vicinity internalized inside the cells to the hydrophobic coating agents bound covalently to surface atoms of nanocrystals.

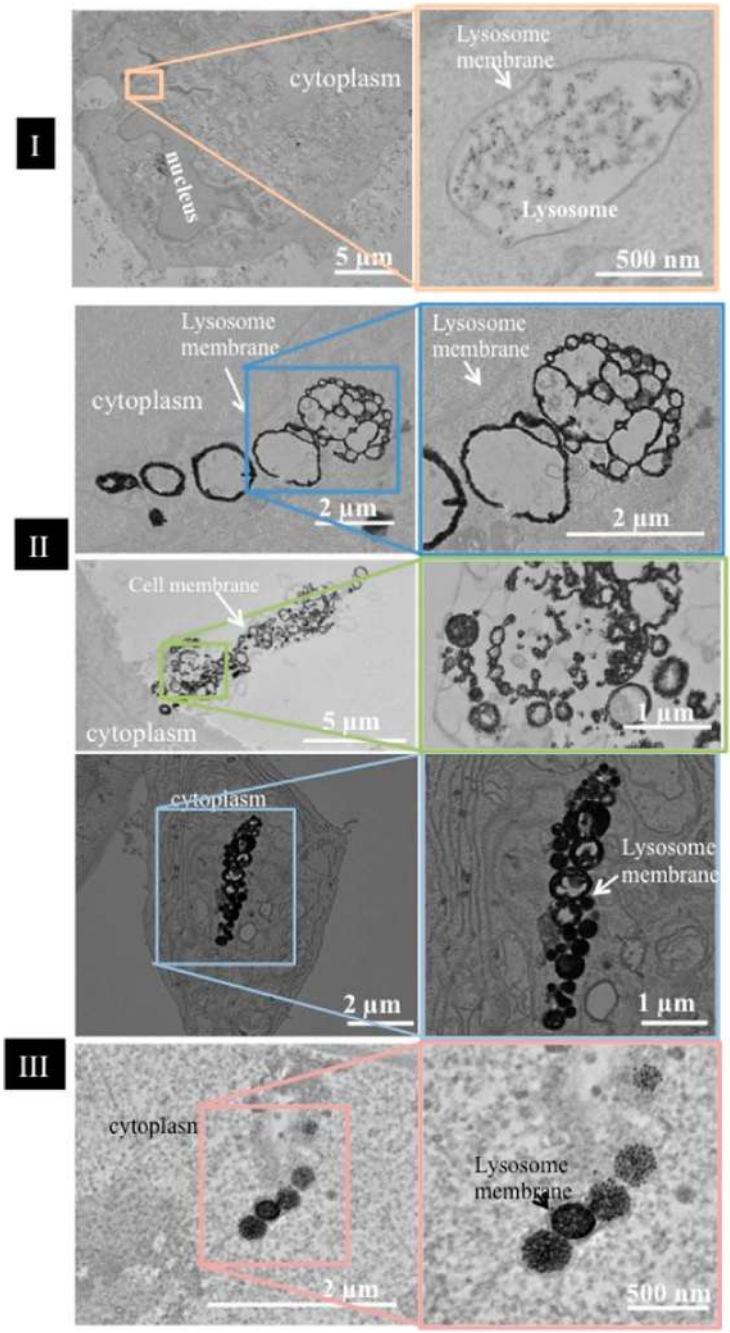

Figure 13.14 2D TEM slices images at various enhancements of A431 cells at 1 day post-internalization of nanocrystals in various samples upon exposure to a magnetic field around 1 Tesla, during 4 hours with dispersed nanocrystals (I) with colloidosomes (II) and with supraballs (III). Here we point out extracellular and intracellular nanocrystals alignments.

Regardless of their location we could expect to be able to manipulate such assemblies. Over one minute of field exposure, the internalized cells with colloidosomes or supraballs align along the field direction (Figure 13.15a,c). Once the hybrids are aligned, the magnetic field is rotated by 90° and we observe reorientation of the chains. A careful observation (see arrows in Figure 13.15b,c) shows that, with colloidosomes, some of the chains are

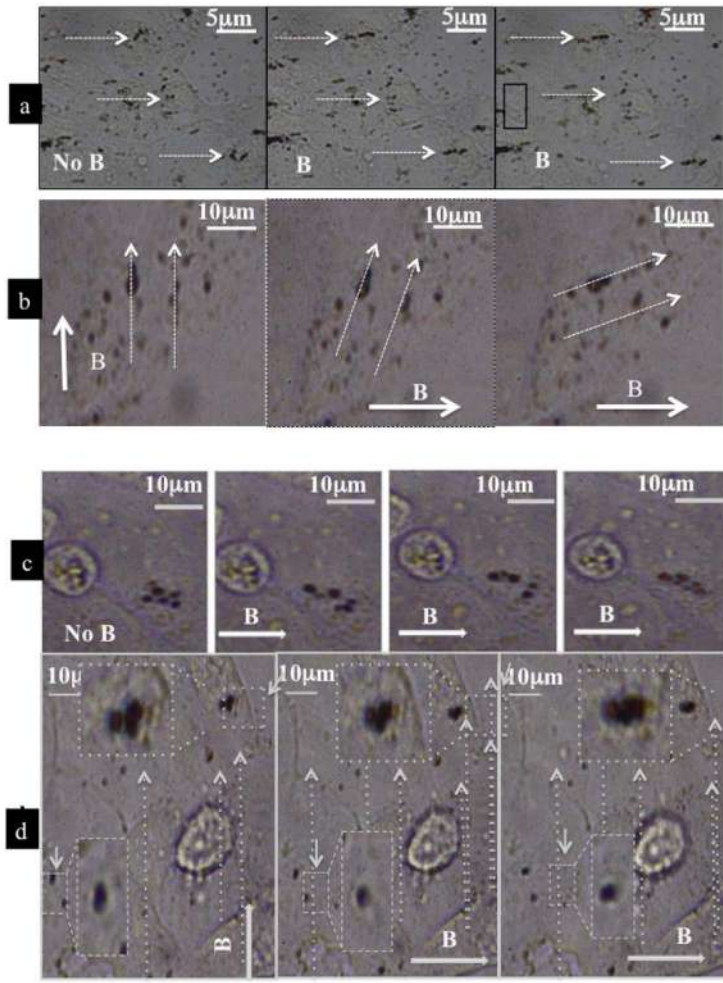

Figure 13.15 Bright field images of colloidosomes (a, b) and supraballs (c and d) internalized in cells during 1 day. Pictures are registered at various times from zero to 1 minute. (a and c) Progressive alignment of internalized colloidosomes (b) and supraballs (d) subjected to a magnetic field. (b and d) Effect on pre-aligned internalized colloidosomes (b) suparparticles (d) due to changing the orientation of the applied field by 90°. Reproduced from ref. 56 with permission from John Wiley & Sons, Copyright © 2020 Wiley-VCH GmbH.

more easily manipulated than others. Furthermore, due to the fact that supraballs are embedded in cytoplasm and entangled into membranes, their alignment rotation seems slower than with colloidosomes under the same conditions. Again, these differences between colloidosomes and supraballs can be related to their high plasticity, adaptability due to a softer and more flexible structure compared to supraballs.

13.4 Conclusions

Here we used several concepts to disperse self-assemblies of hydrophobic nanocrystals in aqueous solution. Various types of hybrids are produced: "clustered" structures, colloidosomes (shell of self-assembled nanocrystals), supraballs (spherical solid particles of nanocrystals in fcc structures) and "egg" structures (colloidosomes filled by supracrystals). It is shown that Au "clustered" structures present collective optical modes keeping the fingerprint of dispersed nanocrystals used as building blocks. Furthermore, these hybrids act as nanoheaters. With colloidosomes and supraballs are used as nano-carriers sensed by tumor cells keep their high proximity, triggering distinct intracellular fate. The density in lysosomes of nanocrystals and their amounts close to the membrane reach, in the best conditions, a factor up to 8 and 12 respectively, compared to their building blocks forming uncontrolled aggregates. This opens a new route to generate local effects, targeting lysosomal membrane such as magnetic manipulation or others.

Acknowledgements

MPP would like to special thanks to Prs. S. Bals, G. Cerullo, P. M. Claesson, G. Della Valle, F. Gazeau, D. Polli, N. Yang and Z. Yang. Thanks are also due to Drs A. Mazzanti, C. Manzoni, A.Nicolas-Boluda, A. M. de Paula, J. L. Pelouard, G. Rizza, M. G. Silvan, N. Winckelmans.

References

1. S. Koohi-Fayegh and M. A. Rosen, A review of energy storage types, applications and recent developments, *J. Energy Storage*, 2020, **27**, 101047.
2. M. P. Pileni, Nanocrystals self assemblies: fabrication and collective properties, *J. Phys. Chem.*, 2001, **105**, 3358–3372.
3. M. P. Pileni, Self-assembly of inorganic nanocrystals: Fabrication and collective intrinsic properties, *Acc. Chem. Res.*, 2007, **40**, 685–693.
4. M. P. Pileni, Supra and Nano crystallinity: Specific properties related to crystal growth mechanisms and nanocrystallinity, *Acc. Chem. Res.*, 2012, **45**, 1965–1972.
5. M. P. Pileni, Impact of the metallic crystalline structure on the properties of nanocrystals and their mesoscopic assemblies, *Acc. Chem. Res.*, 2017, **50**, 1946–1955.

6. C. Altavilla and E. Ciliberto, in *Inorganic Nanoparticles: Synthesis, Applications, and Perspectives*, ed. C. Altavilla and E. Ciliberto, CRC Press (an imprint of Taylor & Francis Group), 2010.
7. J. Park, J. Joo, Y. Jang and T. Hyeon, Synthesis of monodisperse spherical nanocrystals, *Angew. Chem., Int. Ed.*, 2007, **46**, 4630–4660.
8. S. Wilhelm, A. J. Tavares, Q. Dai, S. Ohta, J. Audet, H. F. Dvorak and W. C. Chan, Analysis of nanoparticle delivery to tumours, *Nat. Rev. Mater.*, 2016, **1**, 16014.
9. A. C. Anselmo, M. Zhang, S. Kumar, D. R. Vogus, S. Menegatti, M. E. Helgeson and S. Mitragotri, Elasticity of Nanoparticles Influences Their Blood Circulation, Phagocytosis, Endocytosis, and Targeting, *ACS Nano*, 2015, **9**, 3169–3177.
10. A. C. Anselmo and S. Mitragotri, Impact of Particle Elasticity on Particle-Based Drug Delivery Systems, *Adv. Drug Delivery Rev.*, 2017, **108**, 51–67.
11. N. Benne, J. Van Duijn, J. Kuiper, W. Jiskoot and B. Stütter, Orchestrating immune responses: How size, shape and rigidity affect the immunogenicity of particulate vaccines, *J. Controlled Release*, 2016, **234**, 124–134.
12. H. Sun, E. H. Wong, Y. Yan, J. Cui, Q. Dai, J. Guo, G. C. Qiao and F. Caruso, The role of capsule stiffness on cellular processing, *Chem. Sci.*, 2015, **6**, 3505–3514.
13. Z. Teng, C. Wang, Y. Tang, W. Li, L. Bao, X. Zhang, X. Su, F. Zhang, J. Zhang, S. Wang, D. Zhao and G. Lu, Deformable Hollow Periodic Mesoporous Organosilica Nanocapsules for Significantly Improved Cellular Uptake, *J. Am. Chem. Soc.*, 2018, **140**, 1385–1393.
14. X. Yi and H. Gao, Cell membrane wrapping of a spherical thin elastic shell, *Soft Matter*, 2015, **11**, 1107–1115.
15. Y. Hui, D. Wibowo, Y. Liu, R. Ran, H. F. Wang, A. Seth, A. P. J. Middelberg and C. X. Zhao, Understanding the Effects of Nanocapsular Mechanical Property on Passive and Active Tumor Targeting, *ACS Nano*, 2018, **12**, 2846–2857.
16. N. Yang, Z. Yang, M. Held, P. Bonville, P. A. Albouy, R. Lévy and M. P. Pileni, Dispersion of Hydrophobic Co Supracrystal in Aqueous Solution, *ACS Nano*, 2016, **10**, 2277–2286.
17. N. Yang, C. Deeb, J. L. Pelouard, N. Felidj and M. P. Pileni, Water-Dispersed Hydrophobic Au Nanocrystal Assemblies with a Plasmon Fingerprint, *ACS Nano*, 2017, **11**, 7797–7806.
18. M. A. Boles, M. Engel and D. V. Talapin, Self-Assembly of Colloidal Nanocrystals: From Intricate Structures to Functional Materials, *Chem. Rev.*, 2016, **116**, 11220–11289.
19. I. Lisiecki, P. André, A. Filankembo, C. Petit, J. Tanori, T. Gulik-Krzywicki, B. W. Ninham and M. P. Pileni, Mesostructured Fluids, *J. Phys. Chem.*, 1999, **103**, 9176–9189 and 9168 –9175.
20. M. Kranenburg, M. Veturoli and B. Smit, Phase Behavior and Induced Interdigitation in Bilayers Studied with Dissipative Particle Dynamics, *J. Phys. Chem. B*, 2003, **107**, 11491–11501.

21. J. F. Nagle and S. Tristram-Nagle, Structure of Lipid Bilayers, *Biochim. Biophys. Acta, Rev. Biomembr.*, 2000, **1469**, 159–195.
22. Z. Yang, T. Altantzis, D. Zanaga, S. Bals, G. Van Tendeloo and M. P. Pileni, Supracrystalline Colloidal Eggs: Epitaxial Growth and Freestanding Three-Dimensional Supracrystals in Nanoscaled Colloidosome, *J. Am. Chem. Soc.*, 2016, **138**, 3493–3500.
23. S. U. Pickering, Emulsions, *J. Chem. Soc., Trans.*, 1907, **91**, 2001–2021.
24. O. D. Velev, K. Furusawa and K. Nagayama, Assembly of Latex Particles by Using Emulsion Droplets as Templates. 1. Microstructured Hollow Spheres, *Langmuir*, 1996, **12**, 2374.
25. O. D. Velev, K. Furusawa and K. Nagayama, Assembly of Latex Particles by Using Emulsion Droplets as Templates. 2. Ball-like and Composite Aggregates, *Langmuir*, 1996, **12**, 2385–2391.
26. A. D. Dinsmore, F. Mink, M. G. Hsu, M. G. Nikolades, M. Marques, A. R. Bausch and D. A. Weitz, Colloidosomes: Selectively Permeable Capsules Composed of Colloidal Particles, *Science*, 2002, **298**, 1006–1009.
27. G. R. Yi, V. N. Manoharan, S. Klein, K. R. Brzezinska, D. J. Pine, F. F. Lange and S. M. Yang, Monodisperse Micrometer-Scale Spherical Assemblies of Polymer Particles, *Adv. Matter.*, 2002, **14**, 1137.
28. F. A. Montanarella, *Self-Assembly Tale Collective Structural and Optical Phenomena in Supraparticles of Nanocrystals*, PhD thesis, Universiteit Utrecht, 2019.
29. R. G. Harrison, A. L. Washburn, T. Ammon, A. T. Pickett and D. M. Call, Assembly of CdSe nanoparticles into microspheres by a liquid droplet emulsion process, *J. Mater. Chem.*, 2008, **18**, 3718–3722.
30. Y. Lin, H. Skaff, T. Emrick, A. D. Dinsmore and T. P. Russell, Nanoparticle Assembly and Transport at Liquid-Liquid Interfaces, *Science*, 2003, **299**, 226–229.
31. H. Duan, D. Wang, N. S. Sobal, M. Giersig, D. G. Kurth and H. Möhwald, Magnetic Colloidosomes Derived from Nanoparticle Interfacial Self-Assembly, *Nano Lett.*, 2005, **5**, 949–952.
32. J. Lacava, P. Born and T. Kraus, Nanoparticle Clusters with Lennard-Jones Geometries, *Nano Lett.*, 2012, **12**, 3279–3282.
33. X. Zhang, Y. Zhu and S. Granick, Hydrophobicity at a Janus Interface, *Science*, 2002, **295**, 663–666.
34. N. Glaser, D. J. Adams, A. Boeker and G. Krausch, Janus Particles at Liquid–Liquid Interfaces, *Langmuir*, 2006, **22**, 5227–5229.
35. J. R. Howse, R. A. L. Jones, G. Battaglia, R. E. Ducker, G. J. Leggett and A. J. Ryan, *Nat. Mater.*, 2009, **8**, 507–511.
36. R. J. Hickey, J. Koski, X. Meng, R. A. Riggleman, P. Zhang and S. J. Park, Size-Controlled Self-Assembly of Superparamagnetic Polymersomes, *ACS Nano*, 2014, **8**, 495–502.
37. B. de Nijs, S. Dussi, F. Smallenburg, J. D. Meeldijk, D. J. Groenendijk, L. Filion, A. Imhof, A. van Blaaderen and M. Dijkstra, Entropy-driven formation of large icosahedral colloidal clusters by spherical confinement, *Nat. Mater.*, 2015, **14**, 56–60.

38. L. Rossi, V. Soni, D. J. Ashton, D. J. Pine, A. P. Philipse, P. M. Chaikin, M. Dijkstra, S. Sacanna and W. T. M. Irvine, *Proc. Natl. Acad. Sci. U. S. A.*, 2015, **112**, 5286–5290.
39. S. E. Habas, H. Lee, V. Radmilovic, G. A. Somorjai and P. Yang, Shaping Binary Metal Nanocrystals Through Epitaxial Seeded Growth, *Nat. Mater.*, 2007, **6**, 692–697.
40. E. V. Shevchenko, D. V. Talapin, S. O'brien and C. B. Murray, Polymorphism In AB_{13} Nanoparticle Superlattices:An Example Of Semiconductor–Metal Metamaterials, *J. Am. Chem. Soc.*, 2005, **127**, 8741–8747.
41. E. V. Shevchenko, D. V. Talapin, N. A. Kotov, S. O'brien and C. B. Murray, *Nature*, 2006, **439**, 55.
42. Z. Yang, J. Wei, P. Bonville and M. P. Pileni, Engineering the Magnetic Dipolar Interactions in 3D Binary Supracrystals *Via* Mesoscale Alloying, *Adv. Funct. Mater.*, 2015, **25**, 4908–4915.
43. Z. Yang, J. Wei and M. P. Pileni, Metal–Metal Binary Nanoparticle Superlattices: A Case Study of Mixing Co and Ag Nanoparticles, *Chem. Mater.*, 2015, **27**, 2152–2157.
44. A. Travesset, Binary nanoparticle superlattices of soft-particle systems, *Proc. Natl. Acad. Sci. U. S. A.*, 2015, **112**, 9563–9567.
45. D. E. Aspnes, Local-Field Effects and Effective-Medium Theory: A Microscopic Perspective, *Am. J. Phys.*, 1982, **50**, 704–709.
46. M. G. Silva, D. C. Teles-Ferreira, L. Siman, C. R. Chaves, O. Luiz, S. Ladeira, S. Longhi, G. Cerullo, C. Manzoni, A. M. de Paula and G. Della Valle, Universal saturation behavior in the transient optical response of plasmonic structures, *Phys. Rev. B*, 2018, **98**, 115407.
47. C. K. Sun, F. Vallée, L. Acioli, E. Ippen and J. Fujimoto, Femtosecond-tunable measurement of electron thermalization in gold, *Phys. Rev. B*, 1994, **50**, 15337.
48. D. Polli, I. Lisiecki, H. Portalès, G. Cerullo and M. P. Pileni, Low Sensitivity of Acoustic Breathing Mode Frequency in Co Nanocrystals upon Change in Nanocrystallinity, *ACS Nano*, 2011, **5**, 5785–5791.
49. N. Goubet, C. Yan, D. Polli, H. Portalès, I. Arfaoui, G. Cerullo and M. P. Pileni, Modulating the Physical Properties of Isolated and Self-Assembled Nanocrystals by Change in Their Nanocrystallinity, *Nano Lett.*, 2013, **13**, 504–508.
50. P. Yang, I. Arfaoui, T. Cren, N. Goubet and M. P. Pileni, Unexpected electronic properties of micrometer-thick supracrystals of Au nanocrystals, *Nano Lett.*, 2012, **12**, 2051–2055.
51. G. V. Hartland, Optical Studies of Dynamics in Noble Metal Nanostructures, *Chem. Rev.*, 2011, **111**, 3858–3887.
52. A. Mazzanti, Z. Yang, M. G. Silva, N. Yang, G. Rizza, P.-E. Coulon, C. Manzoni, A. M. de Paula, G. Cerullo, G. Della Valle and M. P. Pileni, *Proc. Natl. Acad. Sci. U. S. A.*, 2019, **116**, 8161–8166.
53. M. Ravnik, G. P. Alexander, J. M. Yeomans and S. Žumer, Three-dimensional colloidal crystals in liquid crystalline blue phases, *Proc. Natl. Acad. Sci. U. S. A.*, 2011, **108**, 5188.

54. A. Courty, A. Mermet, P. A. Albouy, E. Duval and M. P. Pileni, Self-organized Ag-nanocrystals in fcc "supra" crystals: Vibrational Coherence, *Nat. Mater.*, 2005, **4**, 395–398.
55. I. Lisiecki, D. Polli, C. Yan, G. Soavi, E. Duval, G. Cerullo and M. P. Pileni, Coherent Longitudinal Acoustic Phonons in Three-Dimensional Supracrystals of Cobalt Nanocrystals, *Nano Lett.*, 2013, **13**, 4914–4919.
56. A. Nicolas-Boluda, Z. Yang, I. Dobryden, F. Carn, N. Winckelmans, Ch. Péchoux, P. Bonville, S. Bals, P. M. Claesson, F. Gazeau and M. P. Pileni, Intracellular Fate of Hydrophobic Nanocrystals Self-Asssembled in Tumor Cells, *Adv. Funct. Mater.*, 2020, (1–15), 2004274.
57. L. Lartigue, D. Alloyeau, J. Kolosnjaj-Tabi, Y. Javed, P. Guardia, A. Riedinger, C. Péchoux, T. Pellegrino, C. Wilhem and F. Gazeau, Biodegradation of iron oxide nanocubes: high-resolution *in situ* monitoring, *ACS Nano*, 2013, **7**, 3939–3952.
58. K. Kolosnjaj-Tabi, J. Just, K. B. Hartman, Y. Laoudi, S. Boudjemaa, D. Alloyeau, H. Swarc and L. J. Wilson, Anthropogenic carbon nanotubes found in the airways of Parisian children, *Biomedicine*, 2015, **2**, 1697–1704.
59. C. Monzel and K. Sengupta, Measuring shape fluctuations in biological membranes, *J. Phys. D: Appl. Phys.*, 2016, **49**, 243002.
60. I. Dobryden, Z. Yang, P. M. Claesson and M. P. Pileni, Water dispersive suprastructure: An Organizational Impact on Nanomechanical Properties, *Adv. Mater. Interfaces*, 2020, (1–10), 2001687.
61. I. T. Mak and W. B. Weglicki, Characterization of iron-mediated peroxidative injury in isolated hepatic lysosomes, *J. Clin. Invest.*, 1985, **75**, 58–63.
62. P. Boya and G. Kroemer, Lysosomal membrane permeabilization in cell death, *Oncogene*, 2008, **27**, 6434–6451.
63. M. Moros, A. Ambrosone, G. Stepiens, F. Fabozzi, V. Marchesano, A. Casaldi and J. M. Tinoand de la Fuette, *et al.*, Deciphering intracellular events triggered by mild magnetic hyperthermia *in vitro* and *in vivo*, *Nanomedicine*, 2015, **10**, 2167–2183.
64. P. Clerc, P. Jeanjean, N. Hallali, M. Gougeon, B. Pipy, J. Carrey, D. Fourmy and V. Gigoux, Targeted magnetic intra-lysosomal hyperthermia produces lysosomal reactive oxygen species and causes caspase-1 dependent cell death, *J. Controlled Release*, 2018, **270**, 120–134.
65. C. Monzel and K. Sengupta, Measuring shape fluctuations in biological membranes, *J. Phys. D: Appl. Phys.*, 2016, **49**, 243002.

CHAPTER 14

Developments on Supramolecular Thin Films to Sensing Applications

C. S. MARTIN[a], H. S. KAVAZOI[a], L. N. FURINI[b] AND P. ALESSIO*[a]

[a]School of Technology and Applied Sciences, São Paulo State University (UNESP), Presidente Prudente, 19060–900, SP, Brazil; [b]Departamento de Física, Universidade Federal de Santa Catarina, Florianópolis, SC, 88040-900, Brazil
*E-mail: priscila.alessio@unesp.br

14.1 Introduction – Supramolecular Thin Films

Supramolecular chemistry is described as a part of chemistry dedicated to studying the ionic and molecular aggregates united by non-covalent interactions. So, supramolecular chemistry provides one of the most important strategies toward molecular nanotechnology.[1] When working with nanostructured thin films, the way the molecules or molecular aggregates interact themselves offers an infinity of possibilities to create nanostructures or supramolecular arrangements. The structures based on supramolecular arrangements benefit from the non-covalent interaction of distinct functional units and the ability to manipulate the molecular environment to access functional materials with unique properties and performance. The emerging, growing concept of nanoarchitectonics encompasses[2] the supramolecular arrangement concepts that gather information regarding the molecular organization, thickness, morphology, and crystallinity of the films.[3,4]

Nanoscience & Nanotechnology Series No. 55
Concepts and Design of Materials Nanoarchitectonics
Edited by Omar Azzaroni and Katsuhiko Ariga

Published by the Royal Society of Chemistry, www.rsc.org

Since the supramolecular organization is a crucial factor in achieving excellent device performance, it has become one of the challenges for materials science.[4] Indeed, the development of novel sensor systems is one of the most promising fields of supramolecular chemistry.[5] In this chapter, we focus on the developments in supramolecular thin films applied to sense applications. We bring a brief overview of three different techniques for thin film deposition and some examples of tuning the supramolecular arrangements and the effects on the sensor's performance.

The first part reports the Langmuir films based Langmuir–Blodgett (LB) and Langmuir–Schaefer (LS) techniques. Although they require the Langmuir trough equipment, both LS and LB techniques provide the best control in molecular manipulation. The method can be applied to materials soluble in volatile organic solution or water-soluble and colloidal materials using some strategies as adsorption onto a preformed amphiphile monolayer by electrostatic interaction. The second part of the chapter brings electrochemical deposition techniques. The main advantage is that the same equipment for film fabrication is utilized for the sensor's application experiments. Yet, the method can be applied to water or soluble organic materials but is limited to deposition only onto conductive substrates. The last part deals with the Layer-by-Layer technique that has as main advantage the simplicity. The technique does not require equipment for the fabrication of the film and provides exciting features that allow obtaining supramolecular films using a wide range of materials as building blocks through different types of interactions (electrostatic, hydrogen bonds, acid-base or coordination interactions, or even covalent bonds). The technique can indeed be applied to water-soluble molecules and exceptionally in organic solvents and different shapes and material substrates.

14.2 Langmuir–Blodgett and Langmuir–Schaefer

The formation of a Langmuir film can be described as the spreading of a water-insoluble material over a gas–liquid interface, or specifically at the air–water interface. This scattered material forms a film on the water that alters its surface tension. Benjamin Franklin made the first observation of this phenomenon in 1773. In the 19th century, Agnes Pockles also studied the influence of impurities on water surface tension.[6] Only in the 20th century was the system formed by a film on the water surface systematically by Irving Langmuir. In Langmuir's work published in 1917[7] he makes a long-standing consideration of chemical and physical forces acting on solids and liquids, the relationship between solids and liquids, and oil films in water. In 1934 and 1935, Langmuir's assistant, Katharine Blodgett, published two works in which she reports a step forward in the study of films on the water surface. In these articles, she reports on the method developed to deposit Langmuir films on solid surfaces in the form of mono or multilayers.[8,9] From this, Langmuir–Blodgett (LB) films emerged, named both researchers. The Langmuir–Schaefer (LS) is a variant of Langmuir–Blodgett deposition in the

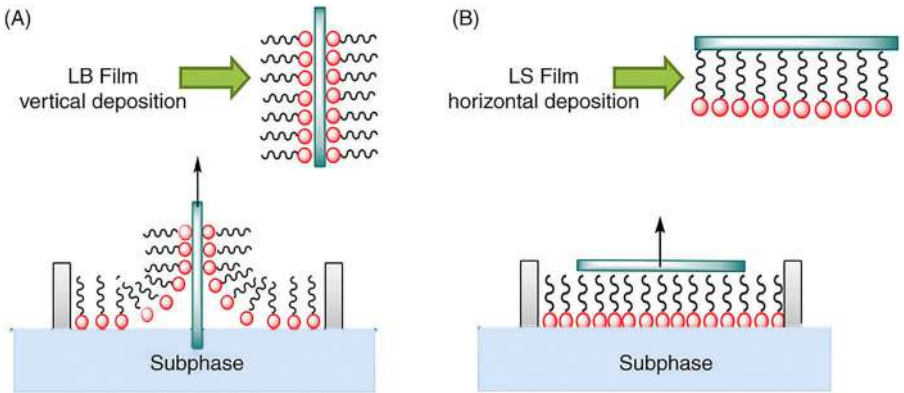

Figure 14.1 Illustration for the (A) LB (vertical) and (B) LS (horizontal) deposition from the monolayer at the air–water interface procedure. Reproduced from ref. 17 with permission from Elsevier, Copyright 2020.

case of horizontal deposition. Figure 14.1 illustrates the procedure of film deposition for the (A) LB (vertical) and (B) LS (horizontal) methods onto a solid substrate from the monolayer at the air–water interface.

From these studies and with the evolution of the technique, many works centered on films by Langmuir, LB, and LS were and continue to be developed. Other classes of molecules, other than fatty acids used by Langmuir, were tested and showed adequate behavior for such studies. Today it is known that Langmuir films, and consequently LB and LS films, can be applied to dyes,[5] organometallic complexes,[10] polymers,[11,12] biomolecules,[13,14] and even ceramic hybrids,[15] among others.

The LB technique is a unique way of making supramolecular assembly in ultrathin films with a highly controlled layered structure. Thus, the LB technique is probably the best method to manipulate materials at the molecular level and provides different designed supramolecular architectures.[16]

Another important point on Langmuir based LB and LS solid films is the facility to change the supramolecular architecture of the films changing, for instance, the subphase content, the subphase pH, the surface pressure of the deposition, among other experimental parameters. Because the LB and LS techniques can be applied to a variety of materials as cited before, allied to the possibility of change the supramolecular architecture of the films, making them versatile and useful techniques to develop new devices, in special, sensors and biosensors.

Langmuir film based solid LB and LS films bring the possibility of incorporate nanomaterials at the supramolecular arrangement to promote new properties to distinguish the sensors in relation to sensitivity and specificity. Recently, Wu *et al.*[18] reported the fabrication of homogeneous and controlled films of Nafion-nitrogen doped carbon nanotubes (Nafion-NCNTs) using the LB technique for the determination of caffeine in tea. At first, they studied

the stability of the Langmuir films. It is known from the literature that carbon nanotubes themselves cannot form stable LB film, but Nafion can in the presence of Na^+. Then, they presented a methodology to fabricate LB films of Nafion-NCNTs in the presence of K^+. Nafion was used to anchor and increase the LB film stability of NCNTs due to its excellent film-forming ability. The monolayers were deposited onto glassy carbon electrodes (GCE) for electrochemical measurements and into mica for atomic force microscopy (AFM) measurements at a surface pressure of 20 mN m^{-1}. From the AFM images (Figure 14.2), a uniform and dense surface of Nafion was observed. When the NCNTs were introduced, orderly arranged and snake-like structures without aggregation were well-dispersed on the surface of the film.

At the electrochemical characterization, the author first compared the performance of the sensors composed by bare GCE, Nafion-LB/GCE, and Nafion NCNTs LB/GCE at the fixed concentration of 2.0×10^{-6} mol L^{-1} caffeine in 0.1 mol L^{-1} H_2SO_4 (pH = 0.94) at a scan rate of 0.05 V s^{-1} (Figure 14.3A). The bare GCE presented a weak oxidation peak current for caffeine at 1.45 V while Nafion-LB/GCE shown a higher oxidation peak current response at 1.44 V. The results confirm that the homogeneous LB film of Nafion can attract the positively charged caffeine to the electrode surface. Indeed, the best performance was achieved at the Nafion NCNTs LB/GCE, which reached the maximum current response for caffeine at 1.42 V. The differences can be explained in consideration of both the increased surface area of the electrode and the enhanced conductivity due to the addition of NCNTs into LB films of Nafion. In the caffeine detection experiments, square wave voltammetry (SWV) was used to obtain a higher oxidation peak current response. The author also optimized the experimental conditions studying the number of LB layers: 3 layers; accumulation time (t_{acc}): 180 s; accumulation

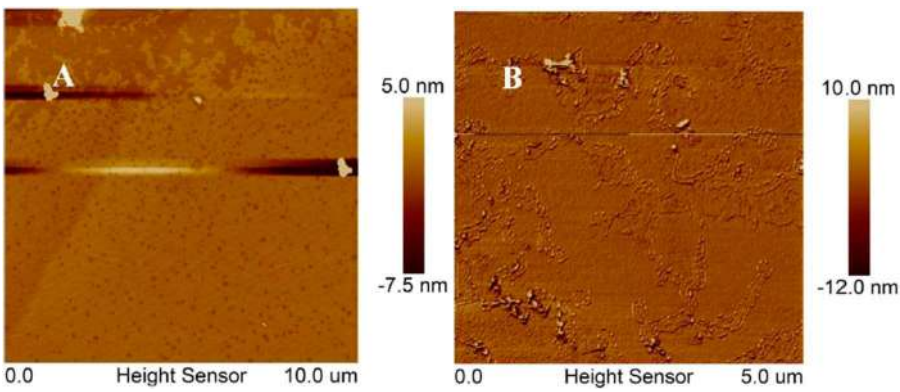

Figure 14.2 AFM 2D morphology images of the freshly cleaned mica covered with 1 layer of LB film of Nafion (A) and Nafion-NCNTs (under transfer surface pressures of 20 mN m^{-1}). Reproduced from ref. 18, doi: 10.20964/2019.12.50, under the terms of the CC BY 4.0 license https://creativecommons.org/licenses/by/4.0/.

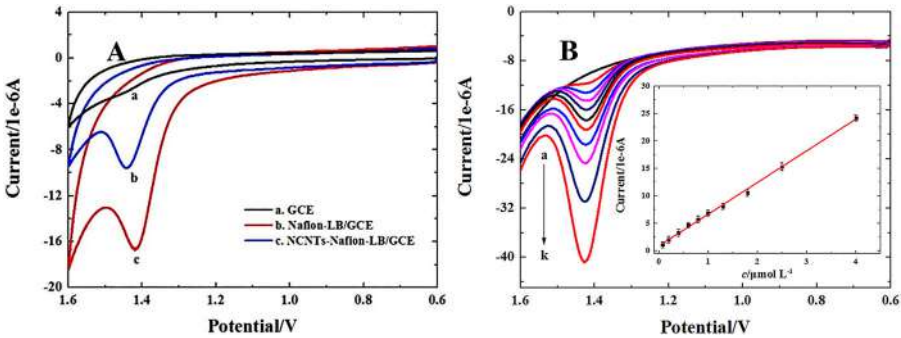

Figure 14.3 (A) CVs of 2.0×10^{-6} mol L^{-1} caffeine at bare GCE (curve a), Nafion-LB/GCE (curve b) and Nafion NCNTs LB/GCE (curve c) in 0.1 mol L^{-1} H_2SO_4 (pH = 0.94), $\nu = 0.05$ V s^{-1}; (B) SWASVs and their associated calibration plot (insert) for increasing concentrations of caffeine at Nafion NCNTs LB/GCE under optimum conditions. Adapted from ref. 18, doi: 10.20964/2019.12.50, under the terms of the CC BY 4.0 license https://creativecommons.org/licenses/by/4.0/.

potential (E_{acc}): open circuit. The parameters of SWV were selected as: scan increment: 4 mV; pulse amplitude: 25 mV; frequency: 30 Hz. The results for different caffeine concentrations are shown in Figure 14.3b. The described method provides a lower detection limit (2.0×10^{-8}) and a wider linear range ($8.0 \times 10^{-8} \sim 4.0 \times 10^{-6}$) than similar works. The authors attribute the performance to the uniform and dense LB films of Nafion-NCNTs.

Another possibility to improve the performance of a given sensor is changing the supramolecular arrangement by using different deposition techniques instead of adding compounds to the film. An excellent example of that is the work reported by Martin *et al.*[19] In that work, the authors report the influence of the supramolecular arrangement of iron phthalocyanine (FePc) thin films on catecholamine oxidation using LS and electrodeposition (ED) techniques. An extensive spectroscopic and morphological characterization for both films was reported in previous work.[20] Briefly, the morphological characterization has shown that the surface morphology of electrodeposited films is considerably more homogeneous than LS films at micro and nanometer scales. Infrared spectroscopy (FTIR) indicated FePc molecules are oriented preferentially with the macrocycle parallel to the substrate surface (flat-on) in the electrodeposited films. At the same time, a slight tilt is suggested in LS films, being both films crystalline.[20] Figure 14.4 summarizes the differences in the films. The differences in the supramolecular arrangement cited before strongly influenced the electrochemical behavior on catecholamines detection, as shown in Figure 14.8.

From Figure 14.5, it is observed that the deposition method influences not only the kinetics of the FePc redox process in KCl solution but also the catecholamine oxidation. The authors attribute the differences in the oxidation potential of dopamine at ED, and LS films may be explained through their

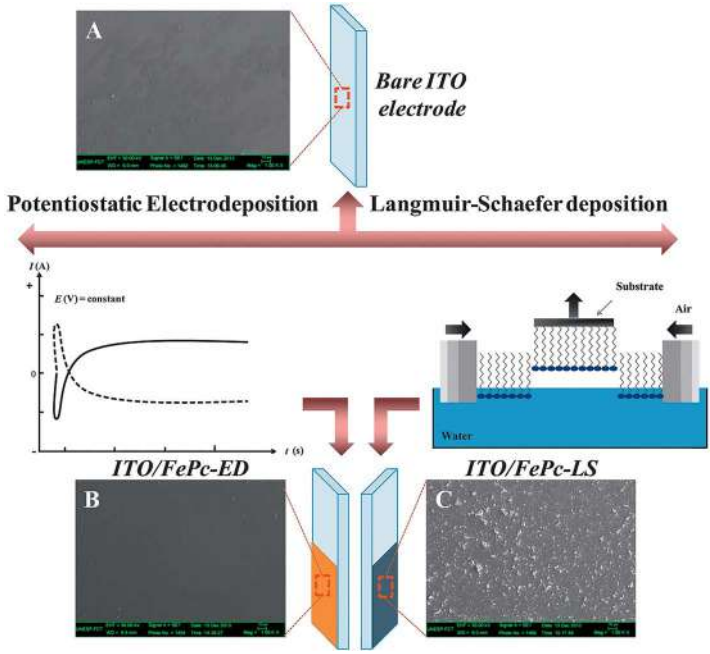

Figure 14.4 Representation of FePc deposition onto an ITO electrode surface. SEM micrographs for bare ITO electrode (A), ITO electrode covered with FePc/ED (B) and FePc/LS films (C). Adapted from ref. 19 with permission from Elsevier, Copyright 2020.

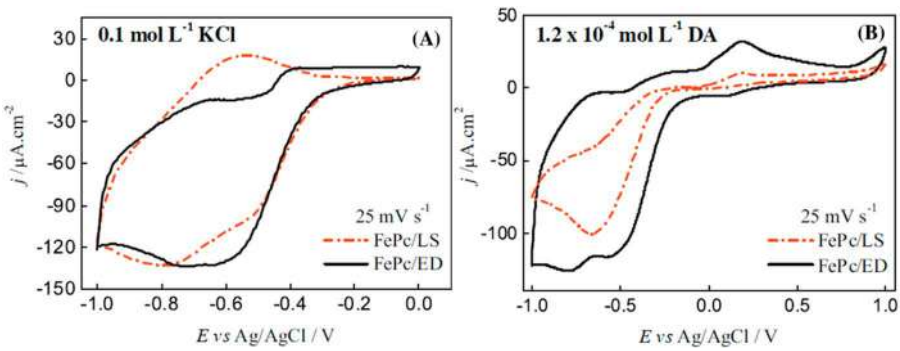

Figure 14.5 Cyclic voltammograms for ITO modified electrodes with FePc/ED and FePc/LS films in (A) 0.1 mol L^{-1} KCl and (B) 1.2×10^{-4} mol L^{-1} DA+ 0.1 mol L^{-1} KCl solution at 25 mV s^{-1}. Adapted from ref. 19 with permission from Elsevier, Copyright 2020.

surface morphology. The ED film is compact, with lower surface roughness (11.6 nm), while the LS film has aggregates, leading to higher roughness (22.4 nm) and, consequently, to the higher surface area. Thus, the difference in the electrooxidation potentials of catecholamines can indicate a difference in the interactions of catecholamine molecules with the film/electrode

interface.[19,20] As a consequence, the analytical parameters for dopamine (DA) and L-dopa were different. For instance, using LS films the linear response range was 2–80 μmol L^{-1} for DA and 40–120 μmol L^{-1} for L-dopa and the limit of detection was 0.024 μmol L^{-1} for DA and 0.168 μmol L^{-1} for L-dopa. However, using ED films the linear response range was 2–20 μmol L^{-1} for both DA and L-dopa and the limit of detection was 0.288 μ mol L^{-1} for DA, and 0.564 μ mol L^{-1} for L-dopa.[19] The performance of LS films were about 5–10 times better for both catecholamines compared to the ED films. The important information to highlight here is that both films were produced with the same composition. Still, the supramolecular arrangement provided by the different deposition techniques plays a determining role in the device performance.

Organo-clay hybrid films have also been studied and produced by LS and LB techniques following sensors applications.[21–23] The interest in these techniques refers to getting uniform films with a good organization of elementary clay mineral layers and surfactants. Another critical point is that the organization of molecules, as well as clay sheets in Langmuir films, can be controlled by changing several experimental parameters.[21] For instance, the work of De Barros *et al.* reported the combination of organic and hybrid materials of low cost by the LB technique for metal ions sensors fabrication.[23] The sensors were composed of LB films made with emeraldine salt polyaniline (PAni-ES) and organophilic montmorillonite clay mineral (OMt). To obtain the nanocomposite, OMt and PAni-ES were co-spread at the air–water interface. The characterization showed that mixed PAni-ES/OMt Langmuir films presented molecular-level interactions that led to changes in the PAni-ES conformation chains, which may be enveloping OMt layers. These interactions resulted in a synergy between the materials enhancing the performance of the sensor in detecting trace levels of cadmium (Cd^{2+}), lead (Pb^{2+}), and copper (Cu^{2+}). For the electrochemistry measurements, the authors used square wave anodic stripping voltammograms for simultaneous detection of the metals in HCl 0.1 mol L^{-1} with a deposition potential of −1.0 V, an accumulation time of 300 s, an amplitude of 50 mV, and a frequency of 15 Hz. They conclude that the PAni-ES/OMt sensor was the most efficient in detecting simultaneously the three metal ions based on the separation of the redox processes.

A step forward was the incorporation of gold nanoparticles (AuNPs) into LB films of PAni-ES/OMt for enhanced detection of metallic ions.[22] For that, De Barros *et al.*[22] co-spread PAni-ES solution and/or OMt dispersion with different concentrations of AuNPs on aqueous subphases containing purified water. As an example, the LOD for the detection of Cd^{2+} in the previously PAni-ES/OMt was 0.2 mg L^{-1}, while for the OMt/AuNPs/PAni-ES was 0.005 mg L^{-1}; for Pb^{2+} the LOD was 0.2 and 0.006 mg L^{-1} and for Cu^{2+} were 0.2 and 0.006 mg L^{-1}, for PAni-ES/OMt and OMt/AuNPs/PAni-ES respectively.[22,23] Square wave anodic stripping voltammograms were obtained in HCl 0.1 mol L^{-1} with deposition potential of −0.05 V, accumulation time 180 s, amplitude 50 mV, and frequency of 25 Hz. Figure 14.6 shows the idealized supramolecular architectures for the Langmuir films and their respective LB films.

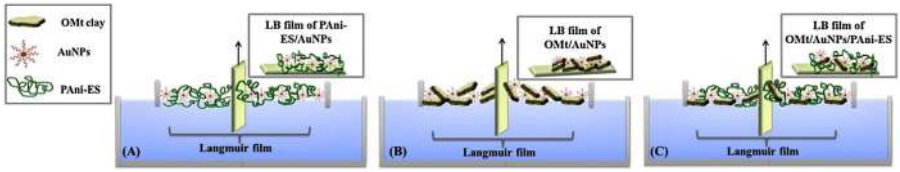

Figure 14.6 Idealized supramolecular architectures of Langmuir films and their respective LB films deposited as (A) PAni-ES/AuNPs, (B) OMt/AuNPs and (C) OMt/AuNPs/PAni-ES. Reproduced from ref. 22 with permission from Elsevier, Copyright 2020.

An exciting feature of LB and LS films is although they both originate from Langmuir films, they can present different supramolecular arrangements mainly because of the vertical or horizontal deposition. Alessio *et al.*[24] studied the direct relationship between the LB and LS deposition techniques and the supramolecular arrangement as well as the consequent effects on the sensor performance using ultrathin films of the bis[2,3,9,10,16,17,23,24-octachlorophthalocyaninate] lutetium(III) complex ($LuPc_2Cl_{32}$).[24] The LB and LS films presented no preferential molecular organization besides similar absorption at UV-Vis spectra, indicating similar molecular aggregation. The main difference relies on the thickness of each deposited monolayer. Despite the thickness difference be compensated by the number of layers in each sensor, the electrochemical behavior of the films preserves small variations. For instance, the oxidation and the polymerization of catechol, the analyte studied in that work, are favored at the surface of LS films, whereas LB films are more stable. LB films are stabilized after three cycles of CV, whereas LS films are not stabilized until 15 cycles are run.

The work of Furini *et al.*[25] has also studied the influence of supramolecular arrangement in LB and LS films on the sensor performance.[25] In that work, they used nickel phthalocyanine (NiPc) and tetrasulfonated nickel phthalocyanine (NiTsPc) to produce thin films using the techniques of LS, LB, physical vapor deposition (PVD), dipping- and spray-Layer-by-Layer (LbL). The objective was to evaluate the supramolecular arrangement and sensor performance for dopamine detection. All films were extensively characterized in terms of spectroscopic and morphological properties. In brief, the NiPc and NiTsPc films do not show preferential molecular organization, which is independent of both deposition technique and chemical structures. Comparing LS and LB films, both presented preferential crystalline α-phase (obtained by X-ray diffraction) but there are differences in terms of RMS roughness and thickness per step of deposition (nm) (obtained by AFM). The LB layers present RMS of 5.4 nm and the LS 11.8 nm. The LB layers had 2.3 nm of thickness in average and the LS had 5.12 nm. Besides, the relation RMS/thickness ratio in % was the same for both, 9%, which can be explained by the high homogeneity of these deposition techniques. Therefore, these little differences in supramolecular arrangement slight interfere in electrochemical behavior of

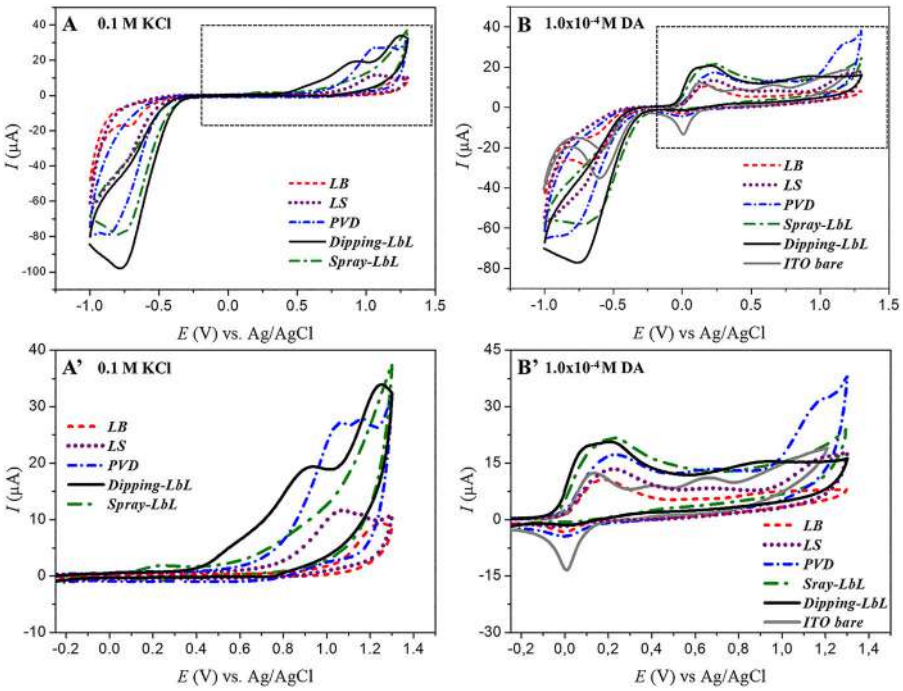

Figure 14.7 Cyclic voltammogram for all films in (A) 0.1 M KCl and in (B) 1.0×10^{-4} M dopamine solution. $\nu = 25$ mV s^{-1}. (A′) and (B′) represent a zoom. Reproduced from ref. 25 with permission from Elsevier, Copyright 2020.

LB and LS films in dopamine detection. Figure 14.7 shows the electrochemical behavior for all thin films studied.

The first papers on Langmuir and LB films were obtained using lipid or lipid-like molecules.[7–9] Some studies subsequently were reported developing methodologies to produce more complex monolayers, including proteins, cholesterol, antigens, *etc.*[26] Once all the natural cell membranes contain both lipids and proteins as components, the Langmuir, LB or LS films based on floating lipids or lipid-protein mixtures may form the basis of artificial biological systems or mimetic membrane models which find applications in biosensing devices.[27] Indeed, articles citing LB films composed of lipids and proteins for biosensors application date back in the 1980s.[27–29] The biomolecule immobilization method is shown to represent an important parameter that affects the biosensor performances, mainly in terms of sensitivity, selectivity, and stability, by influencing enzyme orientation, loading, mobility, stability, structure and biological activity.[30] In this way, the main advantage of using LB methods is that the order of biological molecules can be controlled, and then countless possibilities of well-designed interfaces can be designed.[31] Among the bioreceptors frequently used in the biosensor's construction are the nucleic acids, cells, antibodies, and enzymes, enzymes being the most common. The enzyme-based biosensors provide some

advantages such as high stability, sensitivity and specificity, portability, low cost, and the possibilities for miniaturization and point-of-care diagnostic. All these advantages make them suitable for research on several applications as clinical analysis, food safety control, or disease monitoring purposes.[32]

In the work of Wang *et al.*,[33] poly(3-hexylthiophene) (P3HT) was used to enhance the glucose sensing performance of glucose oxidase (GOx) LB films. The authors studied the changes in the supramolecular architecture of the P3HT films. Precisely, they explore the influence of adding different proportions of octadecylamine (ODA) on P3HT Langmuir films in its aggregation and glucose oxidase (GOx) adsorption following to fabricate a glucose biosensor. The results show that P3HT molecules tend to aggregate at the air-liquid interface, and the P3HT monolayer has a weak ability to adsorb GOx from the subphase. By using a mixed P3HT/ODA monolayer, the presence of ODA not only inhibits the aggregation of P3HT but also increases the adsorption ability of the monolayer to GOx. Figure 14.8A shows the adsorption behaviors of GOx carried out on mixed P3HT/ODA monolayers prepared using stock solutions of various concentrations. The monolayer with the highest homogeneity (200 ppm, curve b) achieves the highest surface pressures both in the initial adsorption stage and at the final step after eight hours adsorption, indicating better enzyme adsorption. Indeed, the circular dichroism spectroscopy shows the α-helix conformation for the enzyme independent of the template monolayers. Glucose sensing performance experiments were carried out with five layers of GOx LB films prepared using various template monolayers. The results in Figure 14.8B show the sensibility increases with increasing extensibility of P3HT molecules. The best sensitivity achieved for

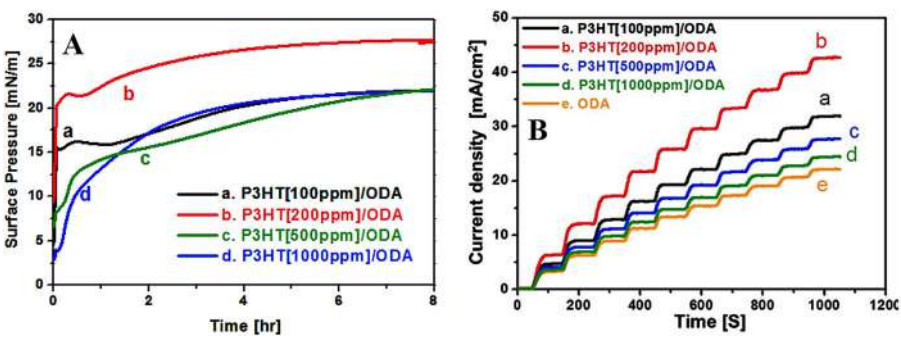

Figure 14.8 (A) Variation of surface pressure during GOx adsorption from an aqueous solution onto mixed P3HT/ODA(1/1) template monolayers prepared using various stock solutions. The adsorption was performed at 25 °C, and the concentration of GOx is 10 ppm. (B) Glucose sensing responses of 5 layers GOx LB films prepared using various template monolayers. The deposition was performed after 8 h GOx adsorption at π = 30 mN m^{-1}. The current response to a gradual injection of glucose was recorded at 0.6 V *vs.* Ag/AgCl (1 mM increment per injection). Adapted from ref. 33 with permission from Elsevier, Copyright 2020.

the P3HT/ODA/GOx film is 5.4 μA mmol L^{-1} $cm^{-2,}$ which is over two times the value obtained by the ODA/GOx film (2.3 μAmM^{-1} cm^{-2}).[33]

On the other hand, the ODA itself has also been applied as a platform to the bioreceptors immobilization. For instance, in the work of Gür *et al.*,[34] is presented high enzymatic activity preservation of malate dehydrogenase (MDH) immobilized in an LB film of ODA for malic acid detection. In this work, the immobilization of the enzyme occurs by physical adsorption to the monolayer and subsequently deposition to a solid substrate. In the used methodology, the monolayer material is spread at the air/water interface, compressed until the desired surface pressure, and then the enzyme is injected into the subphase. It takes 20 min before the interaction occurs entirely. The authors affirm that the high selectivity of the MDH–ODA/ITO electrode was due to malic acid being electrochemically transformed into oxalic acid through catalysis by the MDH immobilized on the ODA monolayer. Finally, the sensing performance data of the MDH–ODA/ITO electrode revealed that there was a good correlation between current response and malic acid concentration in the range of 2.2 to 50 mmol L^{-1}, which suggest that the method provides a new tool for enzymatic studies and opens the way to biomolecular diagnostic applications.[34] Similar work was also reported by Gür *et al.*,[35] which described the immobilization of polyphenol oxidase (PPO) on ODA monolayer and subsequent deposition to a solid substrate. However, some parameters were adjusted to achieve immobilization of PPO to ODA Langmuir film. For instance, after enzyme injection into the subphase solution waited for 45 min. PPO-ODA/ITO biosensors prepared by the presented immobilization method are easy to prepare, recyclable and have long storage stability. Immobilized PPO enzyme demonstrated an electrostatically strong interaction with ODA verified by stability test in which 96.9% catalytic activity was preserved at +4 °C after 7 days of storage. Furthermore, the loss of catalytic activity for PPO at +4 °C after one month of storage was only 11.8% and the electrode stability was 94.83% after two weeks.

The work of Pavinatto *et al.*[36] reported the optimization of the architecture for tyrosinase (tyr)-containing LB films to the detection of polyphenols. The methodology is also based on the physical adsorption of the enzyme to the monolayer. However, in this work, the authors utilize a mixed arachidic acid (AA) and a lutetium bis-phthalocyanine ($LuPc_2$) monolayer as a platform. Significantly, the activity of the immobilized Tyr was considerably higher than in previous work in the literature, which allowed Tyr-containing LB films to be used as highly sensitive voltammetric biosensors. The linear responses for the standard pyrogallol have been found up to 400 μmol L^{-1}, with a detection limit of 4.87×10^{-2} μmol L^{-1} and a sensitivity of 1.54 μA μmol^{-1} cm^{-2}. Also, the Hill coefficient ($h = 1.27$) indicates cooperation with $LuPc_2$ that also acts as a catalyst. The main point was to combine the preserved activity of Tyr and the catalytic activity of $LuPc_2$ to enhance the biosensor performance. The authors affirm that the strategy can be extended to other enzymes and analytes upon varying the LB film architecture.[36]

Peng *et al.*[37] take advantage of the supramolecular organization in Langmuir and LB films to propose a new method of bioreceptors immobilization

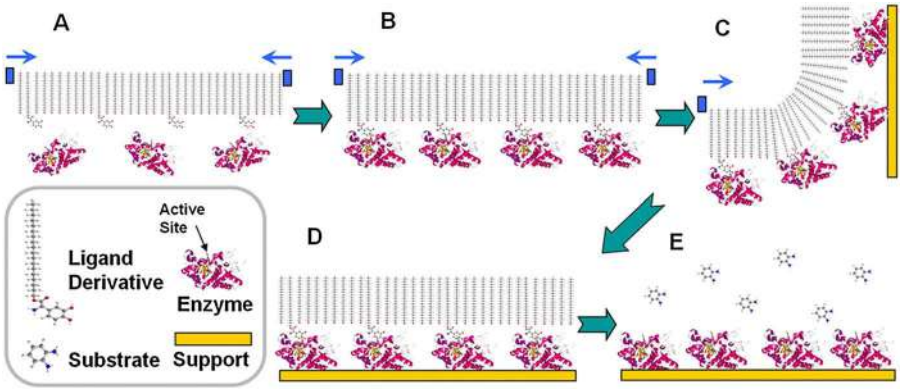

Figure 14.9 The schematic diagram of the oriented immobilization enzyme by the affinity LB method: (A) to form a monolayer of surfactant on the water–air surface; (B) to form the affinity interaction between the ligand derivative and the active site of the enzyme; (C) to deposit the affinity LB film with the enzyme onto the support; (D) to obtain the oriented immobilized enzyme; (E) to replace the ligand derivative with the substrate of the enzyme. Reproduced from ref. 37 with permission from Elsevier, Copyright 2020.

based on the affinity between a long carbon chain and the bioreceptor. Figure 14.9 illustrates the immobilization procedure that consists basically: (i) a long carbon chain is bonded to a ligand of the enzyme of interest, which has a similar molecular structure with the enzyme-substrate; (ii) the ligand forms affinity interaction with the active site of the enzyme; (iii) due to the long carbon chain the ligand derivative presents surface activity, which can assemble on the water–air surface The long carbon chain keeps oriented to air and the ligand faced to water; (iv) the Langmuir films is formed and deposited to the substrate producing LB films. The final structure is the oriented immobilized enzyme, with the active site faced to air; (v) the immobilized enzyme is immersed into a substrate solution, and the substrate readily replaces the ligand derivative. The authors used the Horseradish Peroxidase (HRP) as the proof-of-principle enzyme. The specific activity of HRP immobilized by affinity LB (182.1 ± 14 U mg^{-1}) was higher than that by adsorption (40.5 ± 5 U mg^{-1}). The authors attribute the higher activity to the HRP immobilized by affinity LB due to the new methodology maintain a more native conformation, compared to that by adsorption.[37]

14.3 Electrodeposition – General Aspects

Electrodeposition is another technique that can be applied to the formation of films from a monomeric species present in a solution. The formation of a supramolecular structure can be controlled or tuned by the experimental parameters applied during the potentiodynamic (*e.g.*, cyclic voltammetry) or

potentiostatic electrodeposition (*e.g.*, chronoamperometry) modes.[38] In general, the supramolecular arrangement of thin films depends on the chemical structure of the monomer, solvent, supporting electrolyte, and substrate (working electrode) used during the electrodeposition. However, using the potentiodynamic electrodeposition, the supramolecular arrangement can also be altered by the scan rate, potential range, and a number of potential cycles applied. Although, the potentiostatic electrodeposition can be affected by fixed potential and the time applied.

Previously to the sensorial application, the electrical properties of the supramolecular thin films formed by electrodeposition are often evaluated in an inert (salt or buffer solution) or electroactive electrolyte ($K_3[Fe(CN)_6]$/$K_4[Fe(CN)_6]$), by voltammetric techniques or also by using impedance electrochemical spectroscopy (IES).[39–41] The electrical characterization can be combined with morphologic and structural characterization promoting important information about the supramolecular arrangement and the consequences on the electrical properties.[42] Besides, due to solid–liquid interface in the electrochemical measurements, the supramolecular structure can switch with the redox transitions, intermolecular interaction, and self-organization.[43] After the previous electrochemical characterization, the supramolecular thin films chosen for the sensorial application are evaluated in the presence of the specific analyte (a target). Thus, in this topic, we describe some examples of electrochemical sensors and biosensors based on electrodeposited supramolecular films, and their principal results in sensorial application.

The electrodeposition technique has been widely applied in the development of supramolecular modified electrodes (substrate). The electrodeposition can be used for modification of electrode surface for direct application as a sensor[44] and also to the development of a molecularly imprinted sensor (MISen) (formation of the template of target molecule).[39–41,45–48] Based on this, the supramolecular structure on the electrode surface can be tuned, and the electrochemical sensing properties enhanced. The electrodeposition can be applied to the (i) deposition of one or more film layers on the electrode surface as support to supramolecular architecture construction for another technique (example: drop cast);[47] (ii) deposition of more than two different materials in the independent electrodeposition step (using only electrodeposition);[47] (iii) one-step electrodeposition of the film from a single molecule (monomer) solution or from using a supramolecular mixture of two or more molecules (different materials, composites, assemblies, *etc.*) in solution.[44] In this section, we gave examples of supramolecular electrodeposited film applied as an electrochemical sensor and biosensor.

Mohanan *et al.*[46] used the electrodeposition in two steps to fabricate the supramolecular template for MISen application. First, the GCE was modified with reduced graphene oxide (rGO) from graphene oxide (GO) dispersion. The rGO was electrodeposited on the GCE surface by ten potential cycles in a potential range from 0.5 to −1.5 V at 10 mV s^{-1}. After, the GC/rGO was modified by electropolymerization of 5-amino-8-hydroxyquinoline(AHQ) in the presence of DA. In this stage, the supramolecular structure was obtained

using 20 potential cycles in a potential range from −0.50 to +2.00 V at 100 mV s^{-1}. It is important to note, the DA is the target molecule, which was removed by washing the modified electrode with 0.5 mol L^{-1} H_2SO_4 for 2 hours. The author described the electropolymerization cycles and template concentration directly influence the sensing application. Besides, the sensor performance can be tuned by the immersion time, scan rate, and monomer concentration used during the electrochemical measurements. The MISen based on GCE/rGO/MIP showed an enhancement of the 2.83-fold of the current signal than GCE/MIP sensor, indicating an improvement of electrodeposited rGO layer. The GCE/rGO/MIP applied for DA quantification by differential pulse voltammetry (DPV), showing a small range of concentration (1×10^{-7} M to 14×10^{-7} M) with a limit of detection of 32.70 nmol L^{-1} and sensitivity of 13.3 A M^{-1} cm^{-2}. In plasma blood, the sensor showed a recovery of 101–105%.

MIP-based electrochemical sensor for DA detection was also reported by Kan *et al.*[41] However, the supramolecular structure of MIP template was formed by the electrodeposition of carboxyl functionalized multi-walled carbon nanotubes (MWNTs–COOH) as the first layer, following by electropolymerization of pyrrole in the presence of DA onto a GC electrode surface. The sensor (MIPs/MWNTs/GCE) showed a linear concentration range of 6.25×10^{-7} to 1.0×10^{-4} mol L^{-1} with a limit of detection of 6.0×10^{-8} mol L^{-1}, with no substantial changes in the current responses in the presence of interfering (epinephrine, ascorbic acid, and uric acid) and a relative standard deviation of 1.1% in the reproducibility.

Another electrochemical sensor for not only DA detection but also L-dopa detection, both classified as a neurotransmitter, was reported by Martin *et al.*[19] However, the sensor was fabricated by one-step electrodeposition of the film from the FePc organic solution. The thin film was electrodeposited using a fixed potential at −1.5 V during the 3600 s on the ITO electrode surface. An interesting point to note is that both potentiostatic or potentiodynamic electrodeposition mode, besides the electrode substrate material, does not affect the supramolecular arrangement of the FePc electrodeposited films.[38] However, increases of the electrodeposition time at a fixed potential increase the film thickness and charge-transfer resistance,[38] which indicates that the electrical properties of the FePc film can be tuned by electrodeposition parameters.[19,38] Indeed, the variation of the electrodeposition parameters can improve the electrical properties of organic films applied as sensors.[49,50] The FePc electrodeposited film evaluated for DA and L-dopa detection showed respectively a limit of detection of 0.288 μmol L^{-1} and 0.564 μmol L^{-1}, with reproducibility and repeatability below 4.9% (standard deviation).[19]

A MIP electrode based on electrodeposited polymethylene blue (PMB) and polyaniline (PANI) on functionalized multi-walled carbon nanotubes (f-MWCNTs) for the cardiac troponin T (cTnT) detection was described by Phonklam *et al.*[47] In this work, the PMB was used as the redox probe layer and the PANI as protection of target (cTnT). The screen-printed carbon electrode (SPCE) was firstly modified with f-MWCNTs by casting. After, the electropolymerization of PMB was carried out at a fixed potential of 1.5 V

for 900 s, washed with PBS, and dried with nitrogen gas forming the PMB/f-MWCNTs/SPCE. A PANI layer was built at the PMB/f-MWCNTs/SPCE surface by ten potential cycles between −0.20 and 1.0 V at 50 mV s^{-1}. This layer was activated with 2.0% glutaraldehyde at room temperature for 30 min, washed several times with water, and the target cTnT was added at the surface by drop cast. The MIP template was formed using the electrodeposition of one more PANI layer applying 20 potential cycles (cTnT/PANI/PMB/f-MWCNTs/SPCE) and the target removed using acetic acid, forming the MIP/PMB/f-MWCNTs/SPCE. This sensor construction is an example of sensor fabrication based on electrodeposition in the sequence of another deposition technique, showing a significant tool to tune the supramolecular structure of thin films. In the Phonklam *et al.*[47] results, all stages of electropolymerization showed an influence on electrochemical sensing response. Due to redox probe properties, the thickness of the PMB electrodeposited layer showed an important role in the current signal. A decrease of electron transfers and the current signal was observed for electrodes modified with electrodeposition of PMB up to 40 potential cycles. The thickness of the PANI layer was also crucial to increases the sensitivity of the modified electrode. The first PANI layer needs to be thin to not decreases the PMB signal, but sufficiently to provide amino groups for glutaraldehyde crosslinking. The second PANI needs to be thick enough to template formation. Thus, the sensitivity and selectivity of MISen can be easily tuned by variation of the electrodeposition parameters. The MIP/PMB/f-MWCNTs/SPCE was applied for cTnT detection showing a high low concentration range 0.10–8.0 pg mL^{-1} with a limit of detection of 0.040 pg mL^{-1}. The cTnT detection in human blood plasmas showed a recovery of 91–112%. Figure 14.10 showed the schematic representation of the composition of MIP/PMB/f-MWCNTs/SPCE for nTnT detection using PMB as a redox probe.

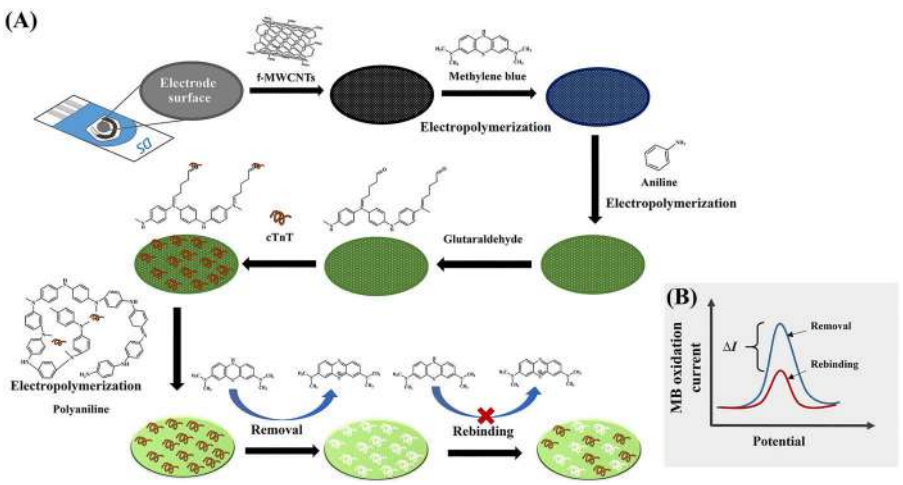

Figure 14.10 Schematic representation of the composition of MIP/PMB/f-MWCNTs/SPCE for nTnT detection using PMB as a redox probe (A). Schematic of binding detection by voltammetry (B). Reproduced from ref. 47 with permission from Elsevier, Copyright 2020.

The development of a supramolecular film for the electrochemical sensor using an electrodeposited PMB film as a redox probe was also reported by Li *et al.*[40] However, in this case, the supramolecular imprinted sensor for carbofuran (CBF) detection, a toxic carbamate pesticide, was carried out using a complex modification of the electrode surface. First, the GCE was modified with MWCNT + Nafion by drop cast follow the electrodeposition of the Pd–Ir layer applying 20 potential cycles from 0.6 to −1.5 V at 50 mV s^{-1}. After, the supramolecular film was finalized by electrodeposition from a mixture of MB, *o*-phenylenediamine, and 4-ter-butylcalix (4TB[8]A) + CBF using cyclic voltammetry (25 cycles) in a potential range of 0 to 1 V. The target was removed with a formic acid/ethanol solution. Indeed, the MB layer showed a catalytic effect, and the addition of the MWCNT/Pd–Ir layer enhanced the sensitivity and selective for CBF detection, indicating a dual catalytic effect. The sensor was applied for CBF detection in vegetables such as cowpea, Chinese cabbage, tomato, and apple, showing a recoveries range between 87.5 and 107%. A similar supramolecular imprinted sensor for CBF detection was also reported by Amatatongchai *et al.*[48] The electrodeposition from using a supramolecular solution of *o*-phenylenediamine, and 4-ter-butylcalix + arene-CBF was carried out on the modified carbon paste electrode (CPE) (carbon paste electrode modified with carbon nanotubes and gold-coated magnetite, CNTs-Fe_3O_4@Au/CPE) as substrate.[48] The electrodeposited film was obtained using similar electrodeposition conditions as described in Li *et al.*,[40] but in the absence of MB. The electrochemical results using the MIP-CNTs-Fe_3O_4@Au/CPE showed that the incorporation of the electrodeposited film of 4 TB[8]A-CBF assembly on the electrode surface improves the electrochemical catalytic and selectivity for the CBF detection, which as ascribed to the increases of specific sites for the CBF binding. The imprinted sensor showed a linear concentration range for CBF from 0.1 to 100 μmol L^{-1} with a limit of detection of 3.8 nmol L^{-1} through amperometric detection using the flow-injection analysis (FIA). The application for CBF detection in vegetables (cabbage, celery, chili, onion, and peppermint) showed a recovery variation of 95.3 to 109%.

Ebrahimi *et al.*[39] report the development of a sensor based on β-cyclodextrin (β-CD)+rGO electrodeposited on the GCE surface in a simple one-step procedure. The supramolecular structure was obtained by electropolymerization, applying five potential cycles in a potential range from −2.5 to 2.0 V at 50 mV s^{-1} in a β-cyclodextrin + rGO mixture solution. All electrical properties of the GCE/rGO/β-CD in aqueous solution was evaluated by the authors, which also observed an influence of the number of potential cycle of electropolymerization stage on the sensing efficiency. The GCE/rGO/β-CD was applied for the simultaneous detection of sulphasalazine (SSLZ) and its metabolite-5-aminosalicylic acid (5-ASA) by using DPV. In standard solution, the GCE/rGO/β-CD showed an enhancement of electrochemical responses in comparison with GCE/β-CD, which can be ascribed to an improvement of the electrodeposited rGO layer. The electrochemical sensor showed a linear range of concentrations of 0.2–12.0 μmol L^{-1} and 0.04–13.0 μmol L^{-1} and with a limit of detection of 0.05 μmol L^{-1} and 8.8 nmol L^{-1} for sulphasalazine and 5-aminosalicylic, respectively (Figure 14.11). In human serum, 89–102% and 97–105% of the recovery, respectively.

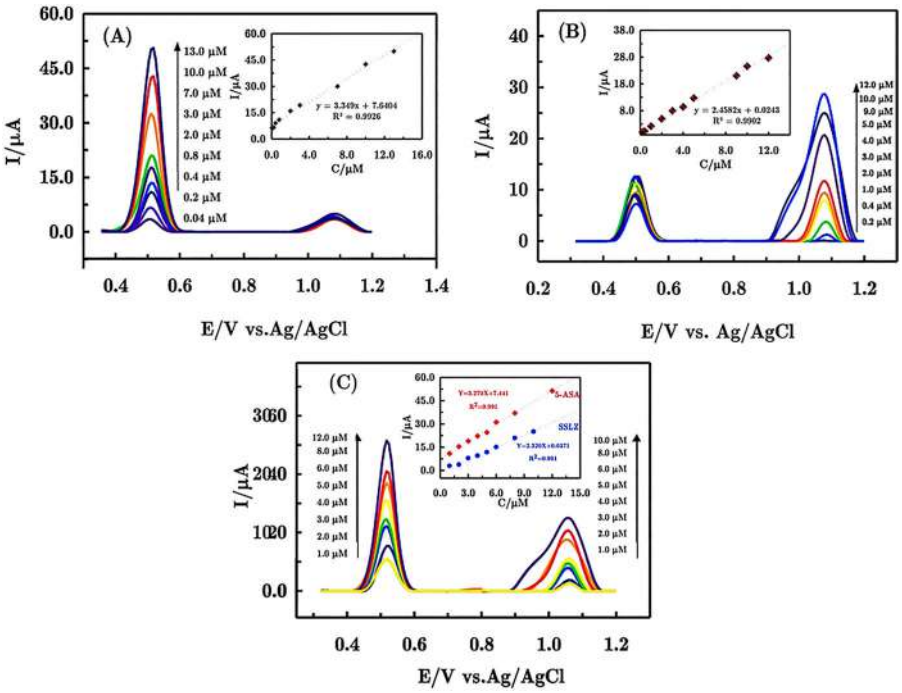

Figure 14.11 DPV responses using GCE/rGO/β-CD for individual detection of 5-ASA at a fixed SSLZ concentration (A); individual detection of SSLZ at a fixed 5-ASA concentration (B); and for simultaneous addition of 5-ASA and SSLZ (C). Reproduced from ref. 39 with permission from Elsevier, Copyright 2020.

The development of an electrochemical sensor based on the supramolecular modified electrode surface by one step of electrodeposition was also reported by Zhou *et al.*[44] The Thiolated β-cyclodextrin functionalized gold nanoparticles (Au-β-CDs) electrostatically combined with protonated aminated graphene quantum dots (NH_2-GQDs) was electrodeposited on the GC electrode surface. The GCE/NH_2-GQDs/Au-β-CD fabrication was carried out by 25 potential cycles using a potential range of −1.0 to −2.0 V at 100 mV s^{-1}. The GCE/NH_2-GQDs/Au-β-CD fabrication was compared with GCE/NH_2-GQDs and GCE/Au-β-CD fabrication, which showed a 2-fold higher current signal. The increases in the current signal were ascribed to the supramolecular arrangement, which provides better recognition sites and increases the specificity of the surface area. The number of electrodeposition cycles, as well as the parameters of sensing evaluation (which include accumulation potential, accumulation time, pH, and scan rate), was described by the authors. Using the optimized parameters, the GCE/NH_2-GQDs/Au-β-CD was applied to the detection of quercetin by using DPV. The sensor showed a linear concentration range from 0.001 to 0.21 μmol L^{-1} with a limit of detection

of 285 pM. Quercetin is a flavonoid common in the human diet, present in beverages, fruits, and vegetables[44] Thus, the GCE/NH_2-GQDs/Au-β-CD stable film was successfully applied for quercetin detection in honey, tea, and also in human serum, showing a recovery below 106.2%.

One of the methods widely applied for developing a biosensor is the modification with enzymes of a given transducer, classified as second-generation biosensors. The development of a second-generation biosensor is based on the immobilization of biological material (bioreceptor) onto a redox mediator in order to generate an improvement in the electron transfer. However, it is still a challenge to guarantee the biological activity of the enzyme and the electron transfer through this transducer (Figure 14.12). In this context, the electrodeposition technique has been used to form supramolecular structures through the formation of thin films on the electrode surface for subsequent immobilization of biological material. These supramolecular arrangements show significant improvement in the application of electrochemical biosensors.[51–54] Almeida *et al.*[51] described the development of a biosensor fabricated by one-step electrodeposition onto two different electrodes, GCE and graphite. In this biosensor, the laccase enzyme was immobilized during the electrodeposition of the thin polydopamine film (ePDA). Electrodeposition on both electrodes was performed at a fixed potential of 0.3 V for 120 seconds using 5 mmol L^{-1} dopamine solution in the presence of laccase enzyme. The electrodeposition with constant oxidative potential (potentiostatic) generated a high concentration of quinone groups in the ePDA film, which are known to play a key role in protein binding, including covalent amine bonding through the Michael-type addition or Schiff base reaction, enabling robust laccase immobilization. The procedure was adopted to developed a low-cost modification, disposable graphite electrodes, aiming at the detection of phenolic compounds such as caffeic, rosmarinic, and gallic acids. A linear range of concentration from 1.0 μmol L^{-1} to 150 μmol L^{-1} with a detection limit equal to 0.29 μmol L^{-1} and sensitivity of 19.3 ± 0.2 μA mM^{-1} cm^2 were obtained for the gallic acid detection. Thus, the biosensor was applied to estimate the amount of gallic acid on an aqueous extract of chestnut shell waste, obtaining a value close to that achieved by HPLC quantification.

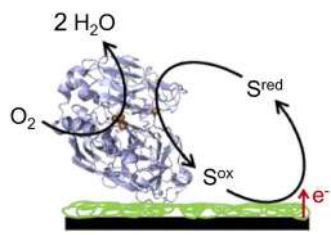

Figure 14.12 Schematic representation of second-generation biosensor composed by immobilized laccase, in the presence of oxygen, and electrochemical regeneration of the oxidized substrate. Adapted from ref. 51 with permission from Elsevier, Copyright 2020.

Also making use of the GCE, but now producing a label-based biosensor, Xu *et al.*[52] developed a sandwiched electrochemiluminescence (ECL) immunosensor (primary antibody-antigen-secondary antibody) for the carcinoembryonic antigen (CEA). CEA is a protein produced early in fetal life, and during the rapid multiplication of the digestive system cells, so it can be used as a marker of colorectal cancer. The immunosensor construction was initially performed by the potentiostatic electrodeposition of an AuNPs film on the GCE surface. This electrodeposition was carried out at the fixed potential of −0.2 V for 200 seconds. In the AuNPs film, there is an abundance of active sites that are important for the immobilization of the primary antibody (carcinoembryonic antigen–antibody (anti-CEA) or Ab_1), used as a CEA receptor. The capture of CEA by the Ab_1 does not generate a measurable signal. Since the label-based biosensor needs a second molecule/aggregate to generate a signal, the researchers developed an ECL nanomaterial using perylenetetracarboxylic acid (PTCA) and carbon quantum dots (CQDs) as luminophores, and graphene as a nanocarrier. They added Cu^{2+} ions and AuNPs to that hybrid material, the latter to immobilize the secondary antibody (Ab_2)-CEA receptor. The generation of a measurable signal was given by a sandwich experiment, as shown in Figure 14.13, in which the Ab_1 that was immobilized

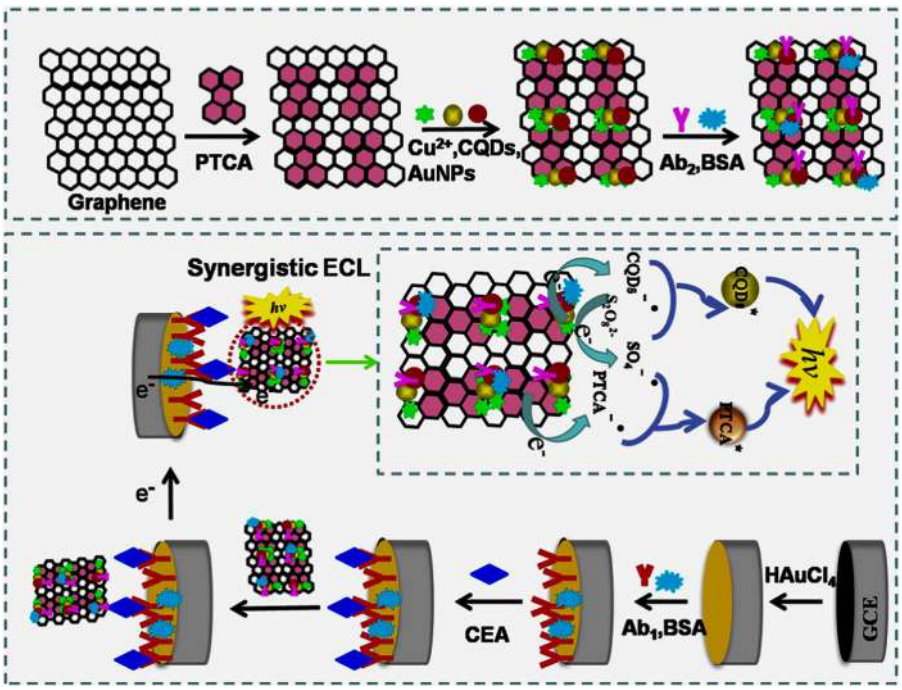

Figure 14.13 Schematic representation of LbL assemble graphene modification, ECL immunosensor fabrication, as well as the synergistic ECL principle in detection. Reproduced from ref. 52 with permission from Elsevier, Copyright 2020.

on the AuNPs/GCE captured the CEA. Subsequently, the Ab_2 immobilized on the graphene-PTCA-Cu^{2+}-CQDs/AuNPs nanohybrid, bound to the captured CEA. Thus, the authors demonstrated that the developed supramolecular structure showed excellent application as an immunosensor, obtaining a linear response range from 0.0001 fg mL^{-1} to 1 ng mL^{-1} and a limit of detection of 0.00026 fg mL^{-1} in a CEA standard sample.

Taking advantage of the AuNPs electrical conductivity property, Hejun Tang *et al.*[53] also performed the potentiostatic electrodeposition of an AuNPs film on the GCE surface for the construction of a biosensor. The potential was maintained at −0.2 V for 30 seconds for the electrodeposition of an AuNP layer. The researchers carried out the sandwich hybridization assay to detect the *Helicobacter pylori* DNA, an important bacterium in the diagnosis of gastric diseases. The sandwich hybridization principle consists in identifying hybridization events between two specific probes – capture probe (CP) and signal probe (SP) – and the target nucleic acid. Thus, the authors added the CP to the AuNPs/GCE, obtaining the bioconjugate material: CP/AuNPs/GCE. This modification occurred *via* the Au–S bond. Finally, to eliminate any non-specific binding effect, the CP/AuNPs/GCE was kept in an incubator at room temperature in the presence of 10 μL of a 1 mM mercaptoethanol (MCH) solution for 40 minutes, generating the MCH/CP/AuNPs/GCE. In addition, Tang *et al.* prepared a ternary ECL nanosphere containing luminol (Lum), polyethyleneimine (PEI), and amino-terminated perylene (PTC-NH_2). Afterward, they added to this material the SP, obtaining the bioconjugate PTC-PEI-lum/SP. The detection of *Helicobacter pylori* DNA was performed *via* ECL responses. The proposed biosensor presented a linear response range from 10 fmol L^{-1} to 10 nmol L^{-1} and a detection limit down to 2.4 fmol L^{-1}. Thus, this work shows the possibility of an enzyme-free bioassay to be applied in the clinical molecular diagnosis of gastric diseases.

In both works mentioned above,[52,53] the AuNPs films were electrodeposited at a fixed potential of −0.2 V. However, the variation of the applied electrodeposition time is directly related to the thickness and structure of the AuNPs films on the electrode surface, which can directly affect the supramolecular structure of the developed biosensor. These works demonstrate the possibility of tuning the supramolecular structure using the electrodeposition technique. Thus, the electrodeposition technique can be applied for manufacturing supramolecular films for application as non-enzymatic sensors.

Sun *et al.*[54] developed a non-enzymatic biosensor. However, the electrodeposition technique was applied to the formation of MnO_2 nanowires on the inner and outer surface of a hybrid material scaffold of graphene and polyacrylic acid (PAA-GG). The PAA-GG has a supramolecular self-assembly formation mechanism and a well-defined porous internal structure. For the electrodeposition of MnO_2 nanowires, the PAA-GG was cut into small and thin pieces and used as a working electrode in an electrochemical cell. The MnO_2 nanowires were electrodeposited *via* cyclic voltammetry, in a potential range between 1.4 V and −1.5 V at 250 mV s^{-1}. The biosensor supramolecular structure takes advantage of the characteristics of a large specific surface

area, the abundance of reactive sites, and the channel structure of the MnO_2 nanowires. Since the MnO_2 nanostructures have electrocatalytic activity in H_2O_2 oxidation, the researchers used MnO_2/PAA-GG as an electrochemical biosensor for the *in vitro* and *in vivo* detection of H_2O_2. The biosensor exhibited a linear range response from 0.05 mmol L^{-1} to 50 mmol L^{-1} and a detection limit down to 10 μmol L^{-1}, using the amperometric technique. The authors also performed measurements with potential interferents: nitric oxide and nitrite, and according to the amperometric results, the response to H_2O_2 reached its maximum value, showing that the biosensor is selective for this analyte. Finally, MnO_2/PAA-GG was used to track H_2O_2 generated by live macrophages cells. The measurements carried out in an *in vitro* system showed that after 2 h of incubation with MnO_2/PAA-GG, the macrophages cells maintain 89% of viability, which indicates good biocompatibility and low cytotoxicity.

Films from chitosan, a non-toxic biopolymer that can form a supramolecular structure by potentiostatic electrodeposition,[45] is another example of application as a non-enzymatic biosensor. The MIP sensor based on chitosan film for bisphenol-A (BPA) detection was described by Galai *et al.*[45] The sensor was fabricated from one-step electrodeposition of chitosan/BPA applying a −1.2 V fixed potential for 300 s (chronoamperometry) using the gold electrode. After electrodeposition, the surface was cross-linked by glutaraldehyde. The MIP template was formed from target removal using acetic acid. The MIP sensor showed a linear response in a concentration range from 10^{-21} to 10^{-3} mol L^{-1} BPA with a limit of detection of 0.67×10^{-21} mol L^{-1} by using SWV. The measurements were carried out in a plastic bottle for drinking water with a BPA concentration of 5.82 μmol g^{-1}.

14.4 Introduction to the Layer-by-Layer Technique

Thin films from alternative layers of distinct materials were proposed by Iler,[55] working with colloidal nanoparticles of silica and aluminum oxide. Posteriorly, Netzer, Sagavi, and group[56,57] working with functionalized surfactants developed a methodology based on the adsorption of one layer in which, through chemical activation (covalent bond), allows the adsorption of a new layer. By this procedure became possible through the fabrication of thin films with multilayers by chemical interaction. In the 1990s, Decher *et al.*[58,59] extended the fabrication of multilayer thin films to polyelectrolytes whose adsorption process occurs by electrostatic interaction between positively and negatively charged polyelectrolytes deposited alternatively onto a solid substrate. Based on this approach, the technique was extended to conjugated[60] and conductors polymers.[61]

The method to grow thin films with multilayers from the alternative deposition of monolayers is called Layer-by-Layer (LbL) or self-assembly. It presents considerable advantages related to operating costs, time, and efficiency, besides providing great control over the molecular architecture of the film. There are several adsorption mechanisms responsible for the growth of

films such as hydrogen bonds, van der Waals, and electrostatic interactions, the latter being the most common.[62] The films are grown in bilayers from the immersion of the substrate in alternative cationic and anionic aqueous solutions, making possible the manufacturing films in alternative layers by electrostatic attraction. It can also highlight the growth of LbL films in a non-aqueous medium, with FePc dissolved in chloroform and PAH in ultrapure water.[63] The LbL assembly is summarized in Figure 14.14.

Due to the physical–chemical properties (versatility and water-soluble), the polymers are widely applied to fabricate LbL films. PANI deposited onto gold interdigitated electrodes (IDE) or in printed graphite interdigitated electrodes (PGIE)[64] were applied as a gas sensor to detect aromas from grape, apple, and strawberry. Different architectures of films in which PANI was deposited by polymerization, or by LbL assembly with poly(sodium 4-styrene sulfonate) (PSS) with 7 bilayers, denoted by $(PANI/PSS)_7$. LbL films showed bigger aggregates than deposited by polymerization (in the order of nanometers), which was attributed to the already formed nuclei in solutions. Also, the films deposited onto IDE presented lower response time and recovery than PGIE substrates. The response is dependent on the methodology and electrode employed.

The technique also allows a wide variety of substrates. Based on the same concept but now, using a single-yarn as a substrate covered with an LbL film, it was fabricated a gas sensor applied to detect NH_3 and able to be incorporated into clothes for real-time monitoring.[65] First, a bilayer of poly(allylamine hydrochloride) – PAH – and PSS was deposited. Then, one, two, or three bilayers of PAH/GO were deposited and evaluated the sensor performance. In terms of electrical characteristics, all films present a linear *I–V* response in the −5 to 5 V range. Also, the current increases follow the number

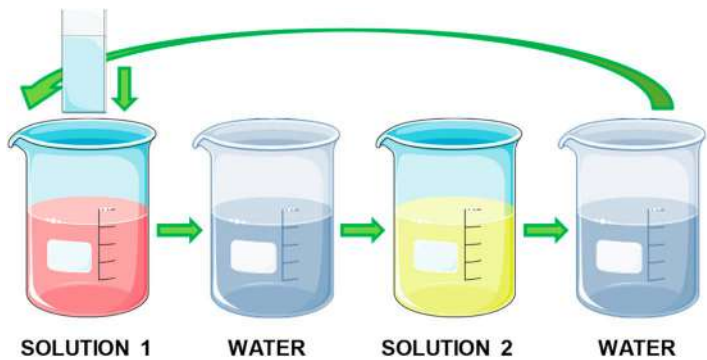

Figure 14.14 Methodology used for the growth of a bilayer film of cationic and anionic solutions. The substrate is initially immersed in a cationic solution (solution 1) waiting for a time, followed by washing in ultrapure water. Later it is immersed in an anionic solution (solution 2) waiting for a specific time followed by washing again. Of this mode, the first bilayer is formed. This procedure is repeated to form multilayers.

of assembled $(PAH/GO)_n$ bilayers. While, at the range of 5–10 ppm of NH_3, the better response was achieved to films $(PAH/GO)_2$ and $(PAH/GO)_3$, to 10–100 ppm range the sensor $(PAH/GO)_1$ presented better response. This effect was attributed to the adsorption of NH_3 onto the surface. The presence of irregularities as wrinkles and ripples on the surface increase with the number of assembled (PAH/GO) layers and, as a consequence, decrease the available sites to NH_3 adsorption. Then, subsequent experiments were carried out with $(PAH/GO)_1$ film. It was observed that the presence of humidity improves the response of the sensor, and the response to NH_3 was higher than NO_2 and H_2S gases, showing the selectivity toward NH_3. The mechanism proposed for good performance to NH_3 was the presence of polar oxygen from PAH and GO. In this case, it favors the adsorption of water molecules at the sensor surface, and as NH_3 is highly soluble in water, induce the formation of NH_4^+ and OH^- decreasing the electrical resistance of the sensor.

Also, GO can be deposited in an S fiber taper (SFT) as a substrate to determine the relative humidity (RH).[66] In this approach, the surface of STF was covered with GO by LbL procedure in a different step by step functionalization of the surface. After cleaning with acetone, the fiber was immersed into NaOH (1.0 mol L^{-1}) for 2 h to add –OH groups over the fiber surface. Then, it was immersed into 5% of (3-aminopropyl)triethoxysilane, and when the silanization was completed, the NH_2 groups positively charged are formed on the fiber surface. Thus, GO nanosheets adsorb by electrostatic interaction onto the fiber surface. This procedure is repeated as much as necessary to fabricate multilayers of GO. The humidity tests using the interference principle *via* optical spectrum analyzer were performed in three different waist diameters of fibers: 41, 33, and 27 μm. It was observed that as the waist diameter decrease, the transmission intensity within fiber loss became more substantial. If the diameter is too large, little light was coupled to the cladding. Thus, the subsequent experiments were carried out using fibers with 27 μm. Once determined the waist diameter, the next step was evaluating the number of LbL cycles to coating the fibers, being 4, 12, and 20 times. It was observed that when the film thickness is too thin (4 cycles), there is no sensitivity, and when it is too thick (20 cycles), the film absorbs light resulting in spectral disorder. Thus, in the best configuration (12 t cycles), the water molecules can penetrate the film resulting in good sensitivity, and the temperature fluctuations have a low impact (less than 2%).

One of the advantages of LbL films is exploring different architectures. For instance, Rodrigues *et al.*[67] report two architectures of poly(diallyl dimethylammonium chloride) (PDDA) and PSS assembled with graphene nanoplatelets and Au nanoparticles (AuNPs) to detect methyl parathion pesticide. The versatility of the technique allows the deposition of hydrophobic materials once solubilized with the assistance of another one. In this case, graphene nanoplatelets, which are hydrophobic, were stabilized by polar groups of PDDA or PSS. The substrates ITO were modified by immersing in the cationic and anionic solutions, as follow: aqueous dispersions of graphene nanoplatelets dispersed into PDDA (giving GPDDA) positively charged;

aqueous dispersions of PSS with graphene nanoplatelets (giving GPSS) negatively charged. Two architectures were tested: $(GPDDA/GPSS)_{10}$ and $(GPDDA/GPSS)_1(AuNP/GPSS)_{10}$. The characterization shows that according to Fourier-transform infrared data, the films were growth governed by electrostatic interactions. Also, Raman spectroscopy shows the presence of D′ band only in LbL films related to the structural disorder (associated with the carbon sp hybridization), a piece of evidence that graphene layers are sandwiched. The performance of the films to detect methyl parathion was evaluated by differential pulse voltammetry. While ITO/$(GPDDA/GPSS)_{10}$ films presented a lower limit of detection, the ITO/$(GPDDA/GPSS)_1(AuNP/GPSS)_{10}$ presents a wider linear range. In the first case, the absence of AuNP improves the current because the PAH is a nonconductive polymer. PAH was added to improve the colloid stability. However, the sensor ITO/$(GPDDA/GPSS)_1(AuNP/GPSS)_{10}$ showed better methyl parathion distribution over all the electrode surfaces giving a larger linear response. Also, the modified electrodes were able to detect the pesticide in real samples as tap water, soil, and cabbage. The architecture dependence allows tuning the performance of sensors.

Distinct architectures of AuNPs and CNT were utilized to immobilize the enzyme cholesterol oxidase to detect cholesterol *via* amperometry.[68] Previously, two bilayers of PAH and poly(vinyl sulfate) potassium salt (PVS) was deposited as a cushion layer to standardize the surfaces. AuNPs were functionalized whit PAH to provide cationic solutions while CNT provides negatively charged solutions. Subsequently, alternative layers of AuNP and CNT were assembled. Three architectures of films were tested being PAH/CNT, AuNP-PAH/PVS, and AuNP-PAH/CNT. In electrochemical behavior, although the PAH hinders electron transport, the presence of CNT leaves an increase of peak current showing the higher capacity of electron transfer in comparison with other architectures. The film architecture chosen to immobilize the enzyme was AuNP-PAH/CNT. The LOD for cholesterol was 14.8 μmol L^{-1} with a response time of ~200 s. The determination in real samples was performed using egg yolk.

The challenge to work with graphene is to adsorb into the substrate and keep its properties. Thus, LbL assembly can be a suitable technique for this purpose. Perez *et al.*[69] have explored the advantages of using 'bio-interfactants' attached to graphene as double-sided tapes in several substrates. The bio-interfactants applied were bovine serum albumin (BSA) and the mixture of laccase and maltodextrin (LAC). Four different film architectures were tested: (i) single layer of GO deposited onto the substrate; (ii) one layer of GO and one layer of BSA $(GO/BSA)_1$; (iii) one layer of GO and one layer of LAC (GO/LAC), and (iv) n bilayers $(GO/BSA)_n$ or $(GO/LAC)_n$. The effective deposition of bio-interfactants was confirmed by UV-Vis absorbance and X-ray photoelectron spectroscopy (XPS). The results show that when just one layer of GO was deposited, the absorbance increase slightly while when GO was deposited onto BSA or LAC, the absorbance increased significantly, being higher for BSA. The reason for effective anchoring of bio-interfactants can be related to the presence of arginine, lysine, and histidine amino acids, which has strong adsorption

forces for both GO and quartz. In the case of BSA, these three amino acids are distributed uniformly around the molecule, whereas to LAC, they are concentrated on one side of the molecule. By elemental composition obtained from XPS, the authors conclude that the choice of bio-interfactants is essential because they are responsible for the dynamic process of reduction GO, which is associated with electrical properties. All the films were placed in an ultrasound bath to promote the destabilization or destruction by cavitation to test the robustness of effective coatings. The best results were obtained with BSA revealing the stronger attachment. Also, $(BSA/GO)_1$ presents higher electrical conductivity due to the absence of contrasting regions, instead $(rGO)_1$ and $(LAC/rGO)_1$, which exhibits high contrasting regions, analyzed by AFM. Permanent electrical conductivity was acquired by placing all films under 250 °C to reduced GO (rGO) without compromising the BSA and LAC stability.

Using the LbL technique is also possible to immobilize GOx encapsulated by liposome to prevent their activity, as shown in Figure 14.15.[70] The liposomes are negatively charged. So, the positively charged chitosan solution (CS) was applied as alternative layers to fabricate LbL films onto a GCE. The liposomes successfully encapsulated the GOx, and the peak current *via* amperometric response increases with the film growth, achieving the maximum current for seven bilayers and decreasing for more layers. This effect was attributed to the difficulty of the diffusion of glucose into the bilayers. The electrodes show good reproducibility and stability, with a limit of detection of 1.31 μmol L^{-1}, also.

In another work, the LbL technique was applied to modify a solid-state substrate whose composition was ITO/PET with several layers of GO deposited *via* electrophoretic deposition, forming an ITO/PET/GO substrate.[71] Subsequently, Mg–Al layered double hydroxides (LDHs, giving Mg–Al LDHs) was electrodeposited under a pH range (acetate/carbonate buffer) to study the effect of pH on adsorption. Finally, *N*-ferrocenyl-1,8-naphthalimide (FC-NAPH) was electrodeposited. The process was repeated as much as necessary to obtain multilayers of Mg–Al LDH and FC-NAPH. The sensor was applied to detect dopamine *via* cyclic voltammetric with a limit of detection of 0.06 nmol L^{-1}.

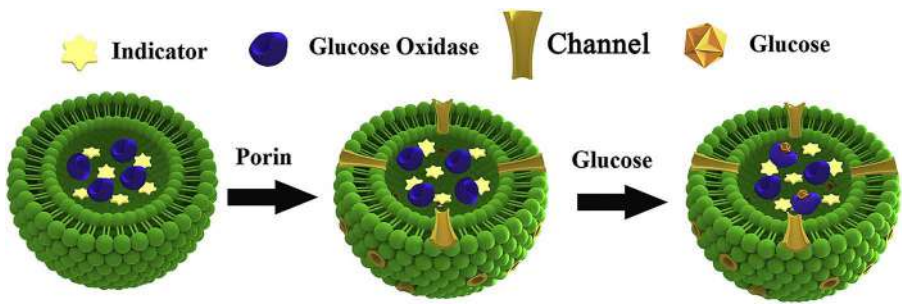

Figure 14.15 Schematic representation of glucose oxidase (GOx) encapsulated by liposome. Adapted from ref. 70 with permission from Elsevier, Copyright 2020.

In the work of Hernandez-Aldave *et al.*,[72] a different strategy was adopted for the fabrication of LbL films. Instead of immersing the substrate into the solutions, alternatively, both compounds were mixed in a vessel. Thus, LbL films of Nafion and graphite nanoplatelets (GNPs) were fabricated to be applied in the detection of caffeine in beverages *via* cyclic voltammetry. LbL films were grown with an automatic dip coater by immersing the substrate into the mixed solution with washing steps and dried process for 2 min. The speed selected was 50 mm min^{-1} to immersion and withdraw, achieving the desired number of layers. This methodology avoided the GNPs aggregation and allowed a faster assembly. The mechanism responsible for film growth was hydrophobic interactions and hydrogen bonds *via* carboxylate and epoxy groups of GNPs and sulfonic groups of Nafion. It was found that the film fabrication is GNP concentration-dependent. At concentrations higher than 0.8 wt%, the film growth is not linear. This effect was attributed to electrostatic repulsion between GNP molecules in solution. The morphology of the films do not present agglomerations for lower concentrations (0.1, 0.2 and 0.5 wt%) although at 0.8 wt% the film present aggregates and it starts to break down. The subsequent work was performed with 0.5 wt% of GNPs. Also, the Nafion concentration was evaluated from 0 to 1.5 wt%. No film growth was observed for 0 wt% of Nafion, revealing the importance of Nafion in the fabrication. In this case, it was speculated that the sulfonic groups of Nafion are responsible for hydrogen bonds with hydroxylic groups of the quartz substrate, driven by the LbL assembly. However, at higher Nafion concentrations, the film growth is hampered (similar to observed to higher GNP concentrations), and the optimal concentration determined was 1.0 wt%. In this way, the best condition was 1.0 wt% of Nafion and 0.5 wt% of GNP for LbL assembly. The electrochemical performance of LbL films was tested *via* cyclic voltammetry, with hexammineruthenium(III) chloride as a probe. It was observed the peak current increased as the number of bilayers increased, and it was chosen five bilayers for caffeine detection. The active surface, determined by chronocoulometry, was 1.645 cm^2, and the caffeine concentration determined was 0.453 mmol L^{-1}.

The versatility of technique allows conciliating the properties of distinct materials to develop a specific device. Li *et al.*[73] prepared LbL films to detect dopamine *via* cyclic voltammetry combining GO (high specific surface area, fast electron transport) and ferrocene (high redox activity and good catalytic activity towards dopamine). GO was functionalized with sulfo-group (SGO) to improve the poor dispersibility. Also, ferrocene was functionalized with poly(ethyleneimine), giving PEI-Fc, to avoid the diffuse away in the solution. Thus, by modifying and combining these materials, it was possible to fabricate LbL films to the desired application. The films were fabricated by immersing GCE (substrate) in each solution for 20 min with the solutions at pH 7.25. The characterization by UV-Vis absorption performed in a quartz substrate shows a linear growth of up to 8 bilayers. The electrochemical behavior was then evaluated by cyclic voltammetry. The modified electrode $(PEI\text{-}Fc/SGO)_8$/GCE presented a higher peak current than the bare electrode. The limit of detection was 2.55×10^{-7} mol L^{-1}. Besides, the electrode presents selectivity toward interfering compounds such as uric acid, glucose, and ascorbic acid in concentrations 1000-fold higher than the dopamine.

A sensor of adrenaline based in the molecularly imprinted polymer (MIP) was proposed by Dhanjai *et al.*[74] In this approach, one layer of cellulose nanocrystals/carbon nanotube (CNC/CNT) was deposited by casting in polydimethylsiloxane (PDMS) substrate. Subsequently, one layer of LbL poly(aniline/phenylboronic acid) (PANI/PBA)[74] with adrenaline was deposited onto (CNC/CNT) and polymerized at 80 °C. After polymerization, the adrenaline was removed by electrochemical cleaning. The electrode presents a highly ordered CNC/CNT network due to hydrogen bonds. The presence of polyaniline increases the redox current. The cavity left by adrenaline in the polymer structure plays a role as a template with interaction sites to act as a sensor. The LOD was 0.001 μmol L^{-1}, and there is no response to common interferents such as ascorbic acid, glucose, and urea. Finally, the sensor was applied in the detection of adrenaline in samples, previously prepared from extraction process, of zebrafish brain, quantifying 120 μmol L^{-1}.

The detection of volatile organic compounds was proposed using Localized Surface Plasmon Resonance (LSPR).[75] The sensor was composed of alternative layers of Au nanoparticles and SiO_2 coating fabricated as follows: glass slide was immersed in 3-aminopropyl triethoxysilane (APTMS) to creating sites allowing the bind of AuNP. Then the substrate was immersed into tetraethyl orthosilicate (TEOS), and a thin layer of SiO_2 is formed. This procedure was repeated as much as necessary, giving (Au@SiO_2) multilayers, as described in Figure 14.16. The sensor works measuring the difference

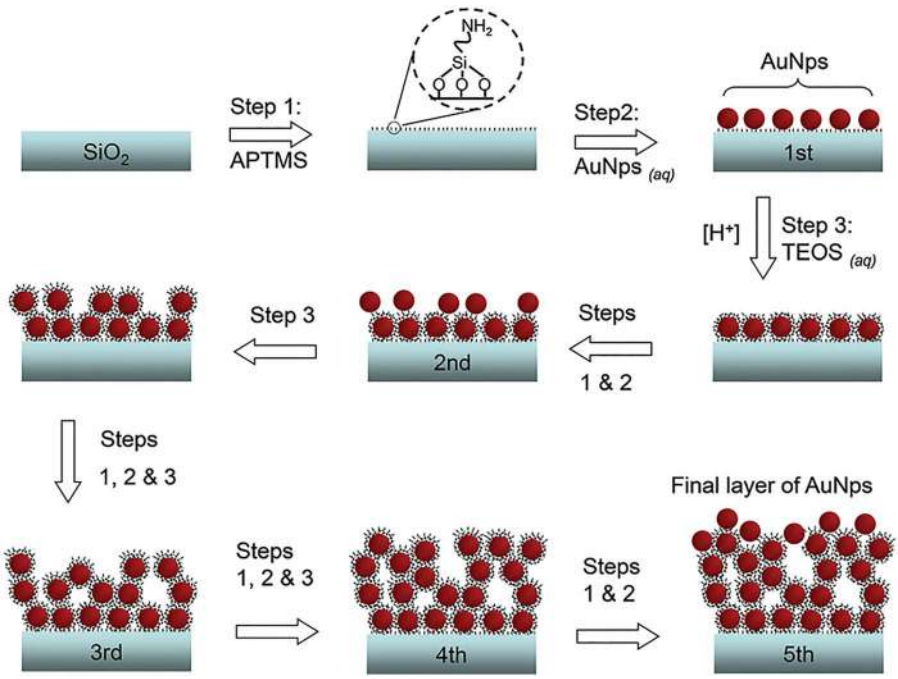

Figure 14.16 Fabrication of Au@SiO_2sensor. Reproduced from ref. 75 with permission from the Royal Society of Chemistry.

between the absorbance in clean air and the sample spectrum. The sensor response is instantly and without hysteresis. The gases tested were toluene, octane, among others. For instance, the limit of detection for cyclohexanone was 0.018 μg.

List of Abbreviations

4TB[8]A	4-Ter-butylcalix
5-ASA	5-Aminosalicylic acid
AA	Arachidic acid
AFM	Atomic force microscopy
anti-CEA	Carcinoembryonic antigen–antibody
APTMS	3-Aminopropyl triethoxysilane
AuNPs	Gold nanoparticles
Au-β-CDs	Thiolated β-cyclodextrin functionalized gold nanoparticles
BPA	Bisphenol-A
BSA	Bovine serum albumin
CBF	Carbofuran
CEA	Carcinoembryonic antigen
CNC	Cellulose nanocrystals
CP	Capture probe
CPE	Carbon paste electrode
CQDs	Carbon quantum dots
CS	Chitosan solution
cTnT	Cardiac troponin T
DA	Dopamine
DPV	Differential pulse voltammetry
E_{acc}	Accumulation potential
ECL	Electrochemiluminescence
ED	Electrodeposition
FC-NAPH	*N*-ferrocenyl-1,8-naphthalimide
Fe_3O_4@Au	Gold-coated magnetite
FePc	Iron phthalocyanine
FIA	Flow-injection analysis
f-MWCNTs	Functionalized multi-walled carbon nanotubes
GCE	Glassy carbon electrodes
GO	Graphene oxide
GOx	Glucose oxidase
IDE	Interdigitated Electrodes
IES	Impedance electrochemical spectroscopy
ITO	Indium-Thin Oxide electrode
LAC	Laccase and maltodextrin
LB	Langmuir–Blodgett
LbL	Layer-by-Layer
LDHs	Layered double hydroxides
LS	Langmuir–Schaefer

LSPR	Localized Surface Plasmon Resonance
Lum	Luminol
$LuPc_2$	Lutetium bisphthalocyanine
$LuPc_2Cl_{32}$	Bis[2,3,9,10,16,17,23,24-octachlorophthalocyaninate] lutetium(III) complex
MCH	Mercaptoethanol
MDH	Malate dehydrogenase
MIP	Molecular imprinted polymer
MISen	Molecularly imprinted sensor
MWNTs-COOH	Carboxyl functionalized multi-walled carbon nanotubes
NCNTs	Nitrogen doped carbon nanotubes
NH_2-GQDs	Protonated aminated graphene quantum dots
NiPc	Nickel phthalocyanine
NiTsPc	Tetrasulfonated nickel phthalocyanine
ODA	Octadecylamine
OMt	Organophilic montmorillonite clay mineral
P3HT	Poly(3-hexylthiophene)
PAA-GG	Polyacrylic acid
PAH	Poly(allylamine hydrochloride)
PANI	Polyaniline
PAni-ES	Emeraldine salt polyaniline
PBA	Phenylboronic acid
PDDA	Poly(diallyldimethylammonium chloride)
PDMS	Polydimethylsiloxane
PEI	Polyethyleneimine
PEI-Fc	Poly(ethyleneimine) functionalized with ferrocene
PGIE	Printed graphite interdigitated electrodes
PMB	Polymethylene blue
PSS	Poly(sodium 4- styrenesulfonate)
PTCA	Perylenetetracarboxylic acid
PTC-NH_2	Amino-terminated perylene
PVD	Physical vapor deposition
PVS	Poly(vinyl sulfate) potassium salt
rGO	Reduced graphene oxide
RH	Relative humidity
SFT	S fiber taper
SGO	Graphene oxide functionalized with sulfo-group
SP	Signal probe
SPCE	Screen-printed carbon electrode
SSLZ	Sulphasalazine
SWV	Square wave voltammetry
t_{acc}	Accumulation time
TEOS	Tetraethyl orthosilicate
tyr	Tyrosinase
XPS	X-ray photoelectron spectroscopy
β-CD	β-Cyclodextrin

Acknowledgements

The authors thank FAPESP (2017/15019-0, 2017/06534-8), CAPES, CNPq (422163/2018-0, 304836/2018-4), and INEO.

References

1. H. E. Toma, *J. Braz. Chem. Soc.*, 2003, **14**, 845–869.
2. K. Ariga, *Beilstein J. Nanotechnol.*, 2020, **11**, 450–452.
3. D. Volpati, P. Alessio, A. A. Zanfolim, F. C. Storti, A. E. Job, M. Ferreira, A. Riul, O. N. Oliveira and C. J. L. Constantino, *J. Phys. Chem. B*, 2008, **112**, 15275–15282.
4. M. A. Loi, E. da Como, F. Dinelli, M. Murgia, R. Zamboni, F. Biscarini and M. Muccini, *Nat. Mater.*, 2004, **4**, 81–85.
5. A. V. Shokurov, M. A. Shcherbina, A. V. Bakirov, A. V. Alexandrova, O. A. Raitman, V. V. Arslanov, S. N. Chvalun and S. L. Selektor, *Langmuir*, 2018, **34**, 7690–7697.
6. RAYLEIGH, Surface Tension, *Nature*, 1891, **43**, 437–439.
7. I. Langmuir, *J. Am. Chem. Soc.*, 1917, **39**, 1848–1906.
8. K. B. Blodgett, *J. Am. Chem. Soc.*, 1934, **56**, 495.
9. K. B. Blodgett, *J. Am. Chem. Soc.*, 1935, **57**, 1007–1022.
10. S. Bettini, R. Pagano, V. Borovkov, G. Giancane and L. Valli, *J. Colloid Interface Sci.*, 2019, **533**, 762–770.
11. V. J. R. Oliveira, L. V. L. Citolino, S. A. Camacho, P. Alessio and C. A. Olivati, *Mater. Chem. Phys.*, 2018, **217**, 421–426.
12. K. Ariga, M. Matsumoto, T. Mori and L. K. Shrestha, *Beilstein J. Nanotechnol.*, 2019, **10**, 1559–1587.
13. F. A. Scholl, P. V. Morais, R. C. Gabriel, M. J. Schöning, J. R. Siqueira and L. Caseli, *ACS Appl. Mater. Interfaces*, 2017, **9**, 31054–31066.
14. J. R. Siqueira, L. Caseli, F. N. Crespilho, V. Zucolotto and O. N. Oliveira, *Biosens. Bioelectron.*, 2010, **25**, 1254–1263.
15. M. Oswald, V. Hessel and R. Riedel, *Thin Solid Films*, 1999, **339**, 284–289.
16. S. A. Hussain, B. Dey, D. Bhattacharjee and N. Mehta, *Heliyon*, 2018, **4**, e01038.
17. R. F. de Oliveira, A. de Barros and M. Ferreira, *Nanostructures*, Elsevier, 2017.pp. 105–123.
18. Y. Wu, *Int. J. Electrochem. Sci.*, 2019, 11166–11177.
19. C. S. Martin, P. Alessio, F. N. Crespilho, C. M. A. Brett and C. J. L. Constantino, *J. Electroanal. Chem.*, 2019, **836**, 7–15.
20. C. S. Martin, P. Alessio, F. N. Crespilho and C. J. L. Constantino, *J. Nanosci. Nanotechnol.*, 2018, **18**, 3206–3217.
21. S. A. Hussain, S. Chakraborty, D. Bhattacharjee and R. A. Schoonheydt, *Thin Solid Films*, 2013, **536**, 261–268.
22. A. De Barros, C. J. L. Constantino, J. R. R. Bortoleto, N. C. Da Cruz and M. Ferreira, *Sens. Actuators, B*, 2016, **236**, 408–417.
23. A. de Barros, M. Ferreira, C. J. L. Constantino, J. R. R. Bortoleto and M. Ferreira, *ACS Appl. Mater. Interfaces*, 2015, **7**, 6828–6834.

24. P. Alessio, C. Apetrei, R. J. G. Rubira, C. J. L. Constantino, C. Medina-Plaza, J. A. De Saja and M. L. Rodríguez-Méndez, *J. Nanosci. Nanotechnol.*, 2014, **14**, 6754–6763.
25. L. N. Furini, C. S. Martin, S. A. Camacho, R. J. G. Rubira, J. D. Fernandes, E. A. Silva, T. C. Gomes, G. M. Stunges, C. J. L. Constantino and P. Alessio, *Thin Solid Films*, 2020, **699**, 137897.
26. P. Fromherz, *Biochim. Biophys. Acta, Biomembr.*, 1971, **225**, 382–387.
27. D. G. Zhu, M. C. Petty, H. Ancelin and J. Yarwood, *Thin Solid Films*, 1989, **176**, 151–156.
28. T. Moriizumi, *Thin Solid Films*, 1988, **160**, 413–429.
29. M. Sriyudthsak, H. Yamagishi and T. Moriizumi, *Thin Solid Films*, 1988, **160**, 463–469.
30. A. Sassolas, L. J. Blum and B. D. Leca-Bouvier, *Biotechnol. Adv.*, 2012, **30**, 489–511.
31. W. Schuhmann, S.-P. Heyn and H. E. Gaub, *Adv. Mater.*, 1991, **3**, 388–391.
32. H. H. Nguyen, S. H. Lee, U. J. Lee, C. D. Fermin and M. Kim, *Materials*, 2019, **12**, 121.
33. K.-H. Wang, W.-P. Hsu, L.-H. Chen, W.-D. Lin and Y.-L. Lee, *Colloids Surf., B Colloids Surf., B*, 2017, **155**, 104–110.
34. B. Gür, M. Işık, K. D. Kıranşan, M. Alanyalıoğlu, Ş. Beydemir and K. Meral, *RSC Adv.*, 2016, **6**, 79792–79797.
35. F. Gür, E. D. Kaya, B. Gür, A. Türkhan and Y. Onganer, *Colloids Surf., A Colloids Surf., A*, 2019, **583**, 124005.
36. F. J. Pavinatto, E. G. R. Fernandes, P. Alessio, C. J. L. Constantino, J. A. de Saja, V. Zucolotto, C. Apetrei, O. N. Oliveira Jr and M. L. Rodriguez-Mendez, *J. Mater. Chem.*, 2011, **21**, 4995.
37. Y. Peng, H. Ling-Ling, D. Yu-Zhi, X. Yong-Juan, N. Hua-Gang, C. Cong, L. Xiao-Lin and H. Xiao-Jun, *Appl. Surf. Sci.*, 2017, **403**, 89–94.
38. C. S. Martin, C. Gouveia-Caridade, F. N. Crespilho, C. J. L. Constantino and C. M. A. Brett, *J. Phys. Chem. C*, 2016, **120**, 15698–15706.
39. S. Ebrahimi, A. Afkhami and T. Madrakian, *J. Electroanal. Chem.*, 2019, **838**, 186–194.
40. S. Li, G. Yin, X. Wu, C. Liu and J. Luo, *Electrochim. Acta*, 2016, **188**, 294–300.
41. X. Kan, H. Zhou, C. Li, A. Zhu, Z. Xing and Z. Zhao, *Electrochim. Acta*, 2012, **63**, 69–75.
42. M. D. Maximino, C. S. Martin, M. S. Pereira and P. Alessio, *An. Acad. Bras. Cienc.*, 2019, **91**, 1–14.
43. K. Cui, I. Dorner and S. F. L. Mertens, *Curr. Opin. Electrochem.*, 2018, **8**, 156–163.
44. Z. Zhou, P. Zhao, C. Wang, P. Yang, Y. Xie and J. Fei, *Microchim. Acta*, 2020, **187**, 130.
45. H. Chakroun Galai, P. Namour, A. Bonhomme, F. Bessueille, S. Besbes Hentati and N. Jaffrezic-Renault, *J. Electrochem. Soc.*, 2020, **167**, 027507.

46. V. M. A. Mohanan, A. K. Kunnummal and V. M. N. Biju, *J. Mater. Sci.*, 2018, **53**, 10627–10639.
47. K. Phonklam, R. Wannapob, W. Sriwimol, P. Thavarungkul and T. Phairatana, *Sens. Actuators, B*, 2020, **308**, 127630.
48. M. Amatatongchai, W. Sroysee, P. Jarujamrus, D. Nacapricha and P. A. Lieberzeit, *Talanta*, 2018, **179**, 700–709.
49. T. Patois, J.-B. Sanchez, F. Berger, J.-Y. Rauch, P. Fievet and B. Lakard, *Sens. Actuators, B*, 2012, **171–172**, 431–439.
50. T. Patois, J.-B. Sanchez, F. Berger, P. Fievet, O. Segut, V. Moutarlier, M. Bouvet and B. Lakard, *Talanta*, 2013, **117**, 45–54.
51. L. C. Almeida, R. D. Correia, G. Squillaci, A. Morana, F. La Cara, J. P. Correia and A. S. Viana, *Electrochim. Acta*, 2019, **319**, 462–471.
52. L. Xu, W. Zhang, L. Shang, R. Ma, L. Jia, W. Jia, H. Wang and L. Niu, *Biosens. Bioelectron.*, 2018, **103**, 6–11.
53. H. Tang, W. Chen, D. Li, X. Duan, S. Ding, M. Zhao and J. Zhang, *Sens. Actuators, B*, 2019, **293**, 304–311.
54. Y. Sun, W. Zeng, H. Sun, S. Luo, D. Chen, V. Chan and K. Liao, *Carbon*, 2018, **132**, 589–597.
55. R. K. Iler, *J. Colloid Interface Sci.*, 1966, **21**, 569–594.
56. L. Netzer, R. Iscovici and J. Sagiv, *Mol. Cryst. Liq. Cryst.*, 1983, **93**, 415–417.
57. L. Netzer and J. Sagiv, *J. Am. Chem. Soc.*, 1983, **105**, 674–676.
58. G. Decher, J. D. Hong and J. Schmitt, *Thin Solid Films*, 1992, **210–211**, 831–835.
59. G. Decher, *Science*, 1997, **277**, 1232–1237.
60. M. Ferreira, J. H. Cheung and M. F. Rubner, *Thin Solid Films*, 1994, **244**, 806–809.
61. J. H. Cheng, A. F. Fou and M. F. Rubner, *Thin Solid Films*, 1994, **244**, 985–989.
62. M. Raposo and O. N. Oliveira Jr, *Braz. J. Phys.*, 1998, **28**, 392–404.
63. P. Alessio, M. L. Rodríguez-Méndez, J. A. De Saja Saez and C. J. L. Constantino, *Phys. Chem. Chem. Phys.*, 2010, **12**, 3972–3983.
64. A. M. Graboski, S. C. Ballen, E. Galvagni, T. Lazzari, A. Manzoli, F. M. Shimizu, J. Steffens and C. Steffens, *Anal. Methods*, 2019, **11**, 654–660.
65. P.-G. Su and Z.-H. Liao, *Mater. Chem. Phys.*, 2019, **224**, 349–356.
66. Y. Zhao, A.-W. Li, Q. Guo, X.-Y. Ming, Y.-Q. Zhu, X.-C. Sun, P. Li and Y.-S. Yu, *Opt. Commun.*, 2019, **450**, 147–154.
67. G. H. S. Rodrigues, C. M. Miyazaki, R. J. G. Rubira, C. J. L. Constantino and M. Ferreira, *ACS Appl. Nano Mater.*, 2019, **2**, 1082–1091.
68. D. P. B. Silva, C. M. Miyazaki, D. B. T. Mascagni and M. Ferreira, *J. Nanosci. Nanotechnol.*, 2019, **19**, 5483–5488.
69. F. M. U. Perez, Y. R. Corrales Ureña, K. Rischka, W. L. Cavalcanti, P. L. M. Noeske, A. A. Safari, G. Wei and L. C. Ciacchi, *Nanoscale*, 2019, **11**, 4236–4247.

70. H. Guan, D. Gong, Y. Song, B. Han and N. Zhang, *Colloids Surf., A Colloids Surf., A*, 2019, **574**, 260–267.
71. S. L. Esfahani, S. Rouhani and Z. Ranjbar, *Electrochim. Acta*, 2019, **299**, 1011–1023.
72. S. Hernandez-Aldave, A. Tarat, J. D. McGettrick and P. Bertoncello, *Nanomaterials*, 2019, **9**, 221.
73. N. Li, L. Zheng, F. Liao, H. Zheng and S. Suye, *Ionics*, 2019, **25**, 2823–2833.
74. N. Y. Dhanjai and S. M. Mugo, *Talanta*, 2019, **204**, 602–606.
75. P.-Y. Lin, G.-Y. Le, W.-I. Chiu, R.-S. Jian and C.-J. Lu, *Analyst*, 2019, **144**, 698–706.

CHAPTER 15

Biomolecules-guided Molecular Architectonics to Nanoarchitectonics

BAPPADITYA ROY[a] AND THIMMAIAH GOVINDARAJU*[a]

[a]Bioorganic Chemistry Laboratory, New Chemistry Unit and School of Advanced Materials (SAMat) Jawaharlal Nehru Centre for Advanced Scientific Research (JNCASR), Jakkur P. O., Bengaluru 560064, Karnataka, India
*E-mail: tgraju@jncasr.ac.in

15.1 Introduction

Molecular architectonics is defined as the controlled engineering of molecular assembly of functional molecules to generate novel molecular and material architectures with emergent properties and functions.[1,2] Architectonics is referred to the process of planning and construction of buildings, *i.e.*, pertaining to architecture, with its origin in the 1600s and has been philosophically related to systematization of knowledge around 1800.[3] At the molecular level, the architectonics can be best described by the DNA double helix, which involved the magnificent organization of two polynucleotides strands through balanced noncovalent forces. The elegance of DNA structure is an archetypal example of nature's molecular architectonics. Similarly, diverse structural and functional architectures of proteins exemplify the power and enormity of molecular and material architectures of nature.[4] In recent times, the reductionistic approach to producing such biomimetic molecular and

Nanoscience & Nanotechnology Series No. 55
Concepts and Design of Materials Nanoarchitectonics
Edited by Omar Azzaroni and Katsuhiko Ariga

Published by the Royal Society of Chemistry, www.rsc.org

materials architectures has become an attractive tool owing to its simplicity, robustness, modularity and economic viability to harvest novel properties and functions. In this context, we established the concept of molecular architectonics[1,2,5–8] to engineer the molecular assembly of designer small functional molecules with biomolecular characteristics by engaging meticulous and balanced noncovalent interactions to produce biomimetic molecular and material architectures with emergent properties and functional applications. The scheme of molecular architectonics is inspired by the helical, co-helical, self-sorted, β-sheets (parallel and antiparallel) and α-helices, 3D protein folding and DNA hybridization to form canonical and nonconical structures, and the derived molecular architectures. As per Anfinsen's hypothesis, information (molecular recognition) required for the protein folding is built in the primary sequence (amino acid units) of the protein which is responsible for acquiring a unique 3D functional structure out of myriad possibilities.[9] As a proof of principle, tailor-made functional aromatic modules (pyrene, naphthalene diimide: NDI, perylene diimide: PDI) have been designed with amino acids, peptides, nucleotides or sugar auxiliaries to enable the controlled molecular assembly to create well-defined nano-, micro-, and macroarchitectures of well-defined molecular ordering (0D, 1D, 2D or 3D). In particular, the generation of molecular architectures of nanoscale dimensions plays an important role in the field of nanoarchitectonics.[7,10–15] These efforts are in anticipation of gaining control over the complex molecular interactions and towards mastering the programmed and ordered molecular assemblies.[1,2,16] The tailor-made molecular and material architectures with emergent properties are expected to cater to potential applications in fields related to energy, environment and health.

Some of the greatest scientific and technological developments in modern times have made it possible to visualize atoms, molecules and their assemblies.[17] The sophisticated instrumentation related to various microscopy and spectroscopy techniques have aided in establishing deeper understanding of molecular interactions in terms of their physicochemical behaviour and energetics in solution or solid state. Thus, construction of diverse molecular architectures in various dimensions by manipulating the noncovalent interactions (van der Waals, hydrophobic, aromatic, hydrogen bonding, metal-coordination, and electrostatic interactions) and their free energies at the molecular level is possible to monitor and modulate using sophisticated spectroscopy and microscopy techniques. The structure–property-function relationship of the molecular assembly architectures on foundations of structural chemistry and biology guide the design of superior functional building blocks and their assembly architectures. Therefore, this chapter provides an overview of structural paradigms and guiding principles for interpretation and manipulation of molecular interactions to pave the way for development of the concept of molecular architectonics for the benefit of constructing biomimetic functional material architectures. Researchers are accustomed to mimicking nature, especially biological systems and materials, which reiterates the importance of biological systems and events that can be used

to design biomimetic analogues with emergent properties. In this context, molecular architectonics emphasizes the need to work towards mastering the complex molecular interactions and assemblies with novel properties and functions. The complex molecular interactions and assemblies involving self-assembly, coassembly and hetero-assembly to create emergent and life-like biomimetic systems and material architectures are underscored. The state-of-the-art is the engineering of homo or hetero-molecular organization with the balanced noncovalent interactions to mimic biomolecular events, systems and material architectures.[1,2,5,10]

15.1.1 Biomolecules as Functional Auxiliaries

Biological structures and functions are guided by specific biomolecular interactions, which inspired us to use them as auxiliaries to engineer molecular organization of functional organic units or modules.[1,2,5,10,15,18–26] Biomolecules that are evolved over billion years of molecular evolution possess in-built information for molecular recognition and can serve as potential functional components or auxiliaries to drive the assembly of synthetic aromatic modules through balanced noncovalent interactions.[1,2,5,10] The process of biomolecular auxiliary guided molecular organization provides mechanistic insights into diverse and distinct assemblies found in nature.[27,28] Biomolecules such as amino acids, peptides, nucleobases, nucleotides, deoxyribonucleic acids, sugars and lipids can serve as guiding auxiliaries in the scheme of molecular architectonics.[1,2,5,10] Amino acids are the molecular building units of peptides and proteins, and their inherent molecular recognition property control the molecular interactions to define the structure–function of protein in living organisms.[29] The basic structure with amine ($-NH_2$) and acid (–COOH) functional groups along with variable α-side chains (R) across diverse amino acids is shown in Figure 15.1a. The variable α-functionality (R) across the amino acids is termed as minute structural mutations, which also impart characteristic chirality (D/L) to individual amino acids. These structural mutations have a remarkable influence on their physicochemical properties which helps to choose a suitable amino acid as an auxiliary in the design of functional modules. In addition, short peptides, nucleotides, sugars and lipids are also considered with their diverse modes of interaction that govern the molecular organization (Figure 15.1b–d). These potential auxiliaries are covalently conjugated to arylenediimides (NDI/PDI) to harvest emergent properties and functionalities.[1,2,5,8,10,15,30,31] Molecular architectonics of functional modules are guided by the various properties of auxiliaries (amino acids, peptides, nucleobases, sugars or lipids) along with the structure and properties of core functional unit (*viz.*, extended aromatic chromophoric units with their unique self-assembly properties). Experimental parameters, *viz.*, solvent, temperature, pH, ionic strength or external agents also contribute to achieving control on the molecular organization.[28,32–35] All these factors (*vide supra*) serve as guiding tools towards the design of functional modules

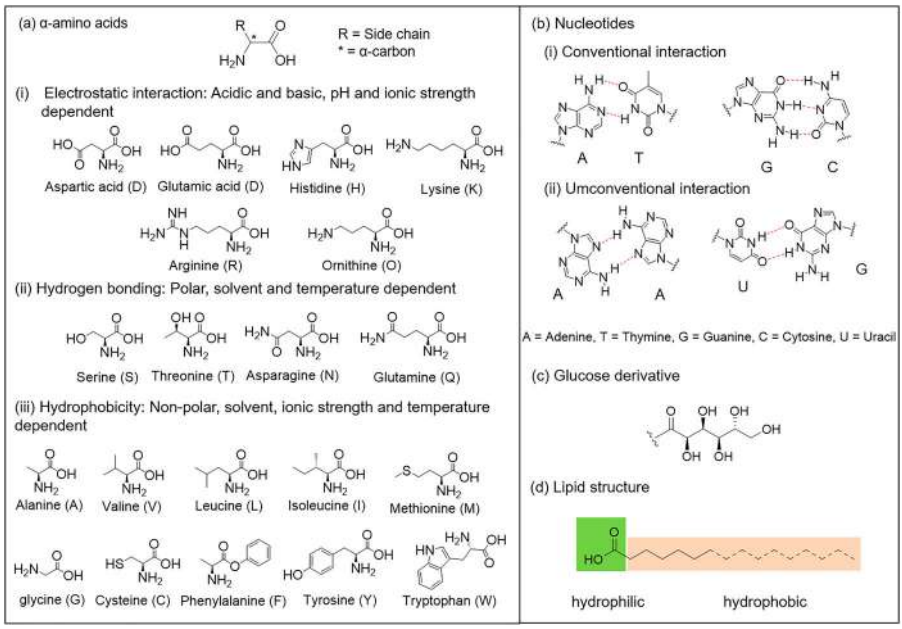

Figure 15.1 General structure and interactions of different biomolecules. (a) Amino acid structures are classified based on their α-functionality. (b) Conventional and nonconventional interactions among nucleobases. (c) Glucose-open structure. (d) Lipid structure comprises of hydrophilic head and hydrophobic tail. Reproduced from ref. 2, https://doi.org/10.1246/bcsj.20190215, under the terms of the CC BY 4.0 license https://creativecommons.org/licenses/by/4.0/.

with appropriate biomolecular or biomimetic auxiliary in the scheme of molecular architectonics to construct well-defined molecular and materials architectures with novel properties and functions.

15.2 Modular Building Blocks

NDI and PDI scaffolds are chosen as functional cores that are functionalized with biomolecular auxiliaries to impart the information required for molecular recognition. NDI and PDI units are extended π-aromatics with interesting optical and electronic properties. Biomolecular auxiliaries provide balanced noncovalent interactions to NDI/PDI, in a single functional module core, necessary for controlled molecular organization. Noncovalent forces are mainly including hydrophobic (van der Waals and aromatic π–π), hydrophilic (hydrogen bonding and electrostatic), hydrophobic–hydrophilic balance and metal-coordination interactions that work in a cooperative manner aid the process of controlled molecular organization. The intermolecular interactions and assembly characteristics of these biomolecular auxiliaries

appended modular building blocks are expected to unravel some of the mysterious secrets of complex biological systems. The experimental parameters also play a key role in attaining the right balance of various noncovalent forces among the designer modular units and solvent molecules, which ultimately decide on the outcome of the process of engineering molecular organization. The resulting molecular and material architectures are subsequently characterized by a diverse range of instrumental tools to determine their defined structures and properties. Our research group has worked extensively on developing such functional modules with the aim to establish fundamental understanding of molecular architectures and exploit the utility of the derived architectures for diverse applications ranging from materials science to biomedical applications. In this chapter, we demonstrate few representative examples of molecular architectonics based on NDI and PDI π-systems as functional cores and employing several biomolecules as auxiliaries.[5–7,10–12,15,18,27,28,30,31,33,36–50]

15.3 C_α-functionality in Amino Acids

Amino acids with variable functionalities at the α-carbon as aliphatic (alanine, **2**,**3**), aromatic (phenylalanine, **4**,**5**), heterocyclic/hetroaromatic (tryptophan, **6**,**7**) were introduced to planar NDI core to understand their effect on engineering molecular organization.[36] For the first time, minute structural mutations in amino acids guided the molecular organization of NDI into all possible crystal packing modes *viz.* cofacial, brickwork, herringbone and slipped stacks (Figure 15.2a). The distinct structural characteristics of individual amino acids depending on the chirality (D/L) and substituents at α-carbon drive the molecular organization of **2**–**7** into chiral architectures compared to achiral organization of **1**, a control with achiral ethylamine substituent. Achiral substituent led molecular organization which showed coexistence of both left and right-handed helical (racemic mixture) arrangements. In addition, transcription of the chiral information from amino acids (D/L) to achiral NDI core was confirmed by spectroscopy studies and single-crystal X-ray diffraction (XRD) data. Such biomolecule-guided assembly offers a fundamental understanding of molecular architectonics which aids the production of novel molecular materials with functional properties like optical (*e.g.*, solid state emission, charge transfer), viscoelastic (*e.g.*, gelation and mechanical strength) and nanoscale ordering (distinct crystal packing) as shown in Figure 15.2a.

Strategic engineering of 0D (spheres), 1D (fibres), and 2D (sheets) architectures have been established by the meticulous manipulation of different types of NDI–NDI molecular interactions through the help of minute structural mutations in the form of α-substituents of amino acids (Figure 15.2b, **8**–**12**).[7] The minute structural mutations of auxiliaries in the functional module led to defined variation in the molecular ordering, crystallinity and their optical, electronic and viscoelastic properties. For example, benzyl functionality in **8** and **9** bestowed additional aromatic interactions in a direction orthogonal to that of NDI–NDI stacking and thereby guiding the formation

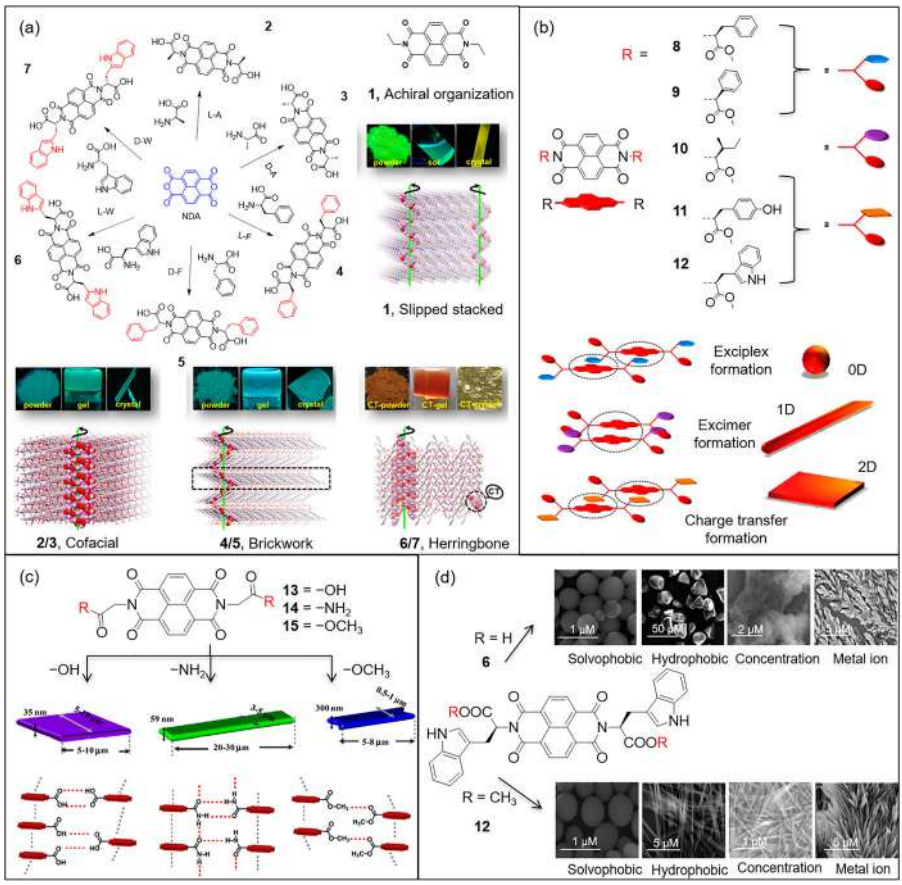

Figure 15.2 NDI derivatives with different auxiliary units (**1–15**). (a) Auxiliary led molecular organization of the modules (**1–7**) in all possible crystal packing modes and their differential gelation, solid-state emission and charge transfer (CT) properties are presented. (b) Illustration of different modes of molecular organization induced by π–π interactions in **8–12**. (c) Mutation in 2D sheets obtained from **13–15** with minute change in G derivatives. (d) The nano- and micro-architectures of **6** and **12** induced by various experimental conditions are presented. Panels (a)–(d) are adapted from ref. 7, 11, 36 and 39 with permission from the Royal Society of Chemistry; American Chemical Society, Copyright 2016; Springer Nature, Copyright 2015; and the Royal Society of Chemistry, respectively.

of 2D architectures with exciplex formation. Appropriate interaction between NDI chromophores led to excimer formation with I as the auxiliary (**10**). Similarly, charge–transfer (CT) complex formation was observed for Y (**11**) and W (**12**) functionalized NDIs. These findings have reiterated the fact that structural mutation facilitated well-defined molecular assembly with exceptional correlation in terms of molecular assembly structure, ordering, morphologies and functional properties.

Essentially, molecular architectonics deals with a delicate balance of structural and environmental factors to control the noncovalent interactions at the molecular level. For example, the presence of a α-methyl group in alanine (A) compared to glycine (G) can make a huge impact on the molecular organization to produce diverse structural and functional variation.[36,39] The planar NDI core functionalized with A (**2**) and G (**13**) showed distinct molecular architectures which reflected in their spectroscopic behaviour (Figure 15.2a and c). In terms of molecular organization, functional module **2** exhibited cofacial helical columnar stacks with a twist. Whereas, **13** with G auxiliary formed a large laterally extended smooth 2D architecture. The critical observation hints at the methyl group ($-CH_3$) directed steric hindrance being responsible for the helical twist and the potential hydrogen bonding of –COOH group has a significant role in controlling the molecular organization. Modulation of functional group, for example, G (**13**) and its methylester (**14**) and amide (**15**) derivatives as imide substituents on NDI core can significantly change the intermolecular hydrogen bonding modes leading to differential molecular assembly.[39] In fact, differential molecular assemblies can lead to the formation of laterally extended 2D architectures of variable dimensions (Figure 15.2c).

The modulation of hydrogen bonding interactions was understood from another study wherein an NDI unit is appended with tryptophan (W) (**6**) and its methyl ester (**12**) (Figure 15.2d).[11] The amino acid W with polar –COOH and aromatic indole heterocycle functionality offers balanced hydrophilic and hydrophobic properties within a single moiety. The weak π–π interaction between the aromatic cores in acetonitrile resulted in 0D nanospherical architectures for both **6** and **12**, while water–acetonitrile induce strong solvation to reduce the total surface area of the aromatic units that led to the formation of microparticles and nanofibres, respectively (Figure 15.2d). Further, deprotonation of –COOH in **6** using sodium hydroxide (base) produced fractals through H-type aggregation *via* cation–π interaction in coordination polymerization (Figure 15.2d).[11] Another parameter, *i.e.*, the concentration of molecular modules in solution was found to be important in the molecular organization. At high concentrations in 10% water–acetonitrile, **6** forms agglomerates, while assembly structure of **12** transforms from fibre to 1D nanobelt architectures (Figure 15.2d). The reduced solubility and enhanced solvophobic forces are believed to control the differential molecular assembly of **6** and **12**. All the discussed structural and experimental parameters (*vide supra*) can be exploited to realize diverse and well-defined *architectures through* the meticulous manipulation of intermolecular interactions at the molecular level.

Solution processing is considered a robust and scalable technique to modulate the assembly parameters to achieve controlled molecular ordering. NDI derivatives **8** and **16** with L- and D-chirality, respectively, of phenylalanine (F) methyl ester auxiliaries were designed to control the strong NDI–NDI interaction in high water–acetonitrile (90% *v*/*v*) solvent system (Figure 15.3a).[7,37] The cofacial staking of NDI core initiates the molecular assembly process while the phenyl ring facilitated lateral organization. The solvent-dependent

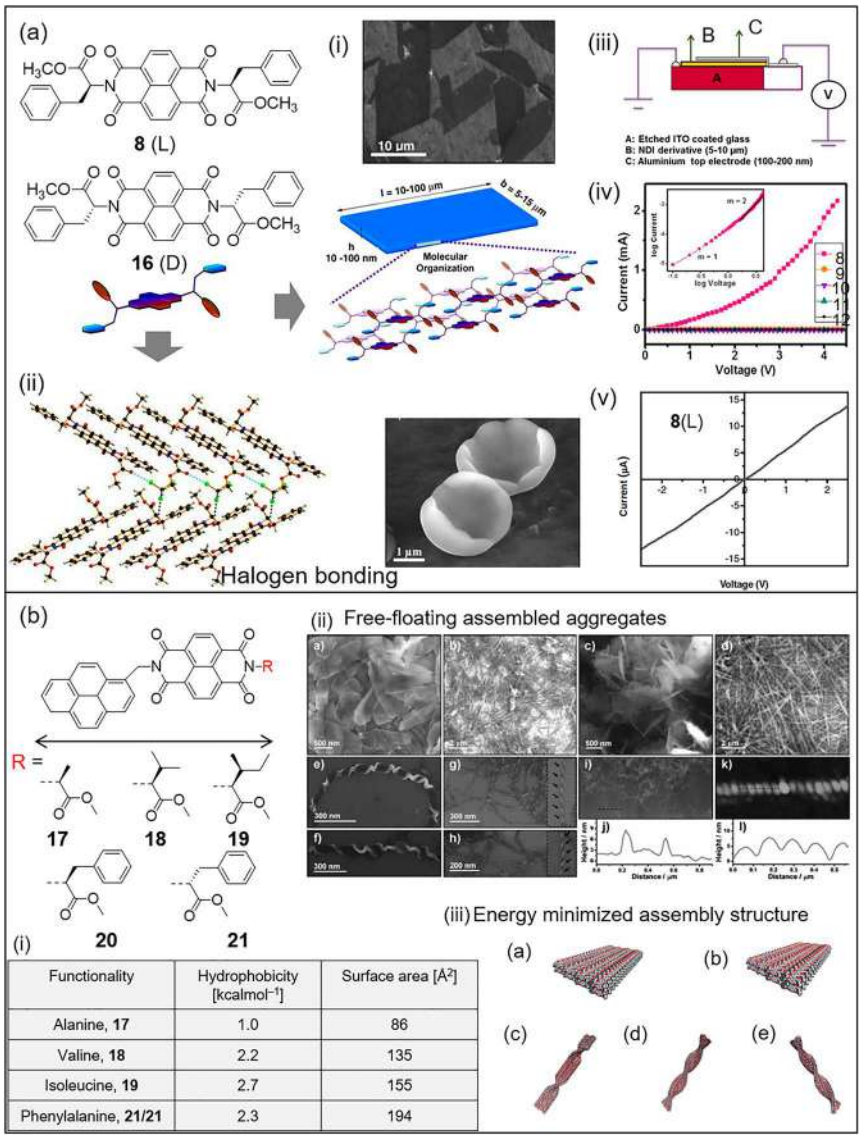

(i)

Functionality	Hydrophobicity [kcalmol^{-1}]	Surface area [Å^2]
Alanine, **17**	1.0	86
Valine, **18**	2.2	135
Isoleucine, **19**	2.7	155
Phenylalanine, **21/21**	2.3	194

Figure 15.3 (a) Solution processing technique applied to achieve controlled molecular ordering for **8** and **16**. Proposed molecular modelling for the self-assembled nanosheet (i) and nanocup (ii). (iii) Schematic representation of space charge limited current (SCLC) device structure, (iv) corresponding *I–V* plots of the nanosheets. The inset shows the slope (*m*) fitted to Mott–Gurney relation, and (v) *I–V* characteristics obtained by C-AFM on the nanosheet. (b) Asymmetric dyads, **17–21**: (i) physical parameters of the derivatives, (ii) Energy optimized assembly structures for **17** (nanosheet), **18** (nanoflakes), **19** (twisted nanoribbon), **20** and **21** (supercoiled helixes of opposite rotation). Field emission scanning electron microscopy (FESEM) images of **17** (a and b); **18** (c and d); **19** (e and f) and **20,21** (g and h) left- and

engineering of the molecular ordering produced free floating nanosheets with large lateral dimensions of 40–100 μM. Single-crystal XRD data showed crystalline molecular ordering along with *d* spacing of 3.68 Å corresponding NDI–NDI stacking (Figure 15.3a,i). L- and D-derivatives showed opposite chiral organization of the NDI core chromophore as revealed by the CD spectra. Remarkably, nanosheets of **8** showed metallic conductivity of 1.6 S cm^{-1}, as measured using conductive AFM (C-AFM) (Figure 15.3a,v),[37] which is similar to heavily doped conducting polymers and small molecules. Further, two probe conductivity measurements on the materials architectures of NDI derivatives (**8–12**) confirmed the long range electron mobility with the highest mobility of 1 $cm^2\ V^{-1}\ s^{-1}$ for **8** compared to others (Figure 15.3a,iv).[7] The observed low mobility of **9–12** is attributed to architectural orientation disorder influenced by the minute structural mutations of the amino acid auxiliaries which resulted in low crystalline order in their corresponding architectures. The utility of solvent processing technique has been also demonstrated to prepare nanocups, mesocups, and bowl-like complex architectures by employing chlorinated co-solvent that provide specific halogen bonding interactions between the functional molecular unit and solvent molecules (Figure 15.3a,ii).

The α-substituents in amino acid auxiliaries serve as powerful structural elements to control the molecular interactions in the field of molecular architectonics. Therefore, the effect of amino acids on the constrained chromophoric systems such as conjugated NDI–pyrene units was studied.[6] The NDI and pyrene chromophores are well–known donor–acceptor pair with topological complementarity in terms of molecular shape and structure. Asymmetrical dyads **17–21**, with pyrene on one side and methyl ester derivatives of L-alanine, L-valine, L-isoleucine, L- and D-phenylalanine on the other side of the NDI core was used to understand the amino acid-guided molecular architectonics (Figure 15.3b).[6] In spite of topological and π-complementarity (π-acidic and π-basic, respectively), individual NDI and pyrene chromorphores undergo self-sorting instead of charge–transfer (CT) interactions. Interestingly, their conjugation as in NDI–pyrene dyads facilitated the intermolecular CT interaction (functional property). The experimental result showed the formation of well-defined 1D and 2D nanoarchitectures (Figure 15.3b,ii). The architectural outcome of the molecular assembly of dyads **17–21** (nanosheets, nanoflakes, twisted nanoribbons, supercoiled helices, respectively) was correlated to varying hydrophobicity and nonpolar

right-handed supercoiled helices, respectively. (i and k) Atomic force microscopy (AFM) images, and (j and l) height profiles of the supercoiled helices. Panels (a) and (b) are adapted from ref. 37, 7 and 6 with permission from John Wiley & Sons, Copyright © 2011 WILEY-VCH Verlag GmbH & Co. KGaA, Weinheim; American Chemical Society, Copyright 2016; and Copyright © 2013 WILEY-VCH Verlag GmbH & Co. KGaA, Weinheim, respectively.

surface area of the α-substituent in amino acid auxiliaries. The surface areas of A, V, I, and F are determined to be around 86 to 194 Å^2, respectively, as shown in Figure 15.3b,i (the table). Notably, auxiliary units with methyl ester derivatives were used to eliminate any possible counter hydrophilic interactions in aqueous solution. The dyads containing less bulky side chains of A and V with surface area of 86 and 135 Å^2 formed planar 2D architectures like nanosheets and comb-edged nanoflakes, respectively (Figure 15.3b,ii). Dyads with I and F with higher surface areas of 155 and 194 Å^2 exhibit greater steric repulsions of side chains that led to twisted assembly to form nanoribbon and supercoiled helical nanoarchitectures, respectively. The 1D or 2D architectures formed by the successful tailoring of the molecular assemblies of NDI–pyrene dyads exemplify the role of minute structural mutations of the amino acid auxiliaries. The amino acid-guided controlled engineering of the molecular organization of NDI–pyrene dyads perfectly demonstrates the design principles of molecular architectonics.

The various examples described above support the notion that bioinspired design strategy is successful in effective implementation and practice of molecular architectonics. Protein folding is one of the complex and poorly understood biomolecular processes involving expeditious folding of the primary amino acid sequence of protein to adopt a unique 3D conformation.[51,52] The biomimetic systems designed to envision the principles of molecular architectonics are capable of serving as modular systems to understand the process of protein folding. In this context, PDI core was conjugated with selected amino acid auxiliaries, *viz.*, I (**22**), F (**23**) and A (**24**), and their molecular assembly was studied to gain insights into biochemical assembly (Figure 15.4).[27] The molecular self-assembly of **22** showed extremely slow dynamics to form helical assembly over a day. The experimental results also showed unusual correlation of the abiotic helical assembly or reassembly of

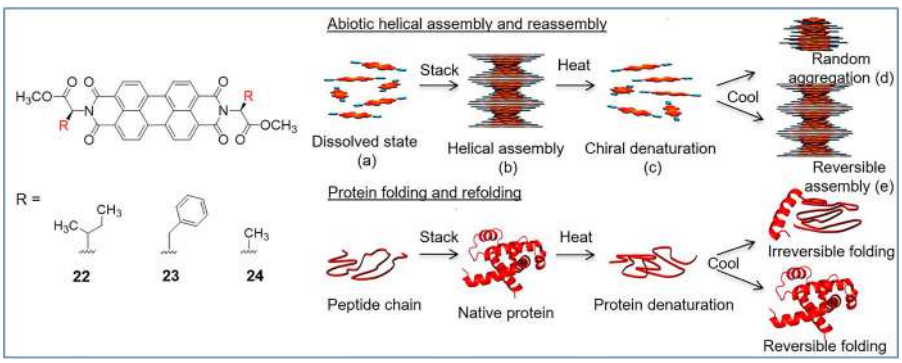

Figure 15.4 PDIs with nonpolar auxiliaries (22-24): Principles of molecular architectonics is demonstrated with different representative structures (a-e) to correlate with the process of protein folding–unfolding equilibrium. Panel is adapted from ref. 27 with permission from American Chemical Society, Copyright 2013.

22 with the protein folding process. Abiotic helical assembly or reassembly of **22** was mainly driven by solvatophobic forces and the unique hydrophobic interaction of α-substituent of the nonpolar amino acid (I). Further, the heat-induced irreversible chiral denaturation (c), subsequent formation of random aggregates upon cooling (d) and seeding induced reversible assembly (e) of **22** are fascinating examples of emergent behaviour. Such designer abiotic assembly behaviour mimics the biological protein folding (with some trivial limitations) and may be useful in understanding the complex protein folding problem.

Transcription of chiral information from amino acid auxiliary to achiral aromatic chromophores (*ca.* NDI, PDI, *etc.*) is one of the significant contributions of employing biomolecules in the scheme of molecular architectonics. The chirality of α-carbon (D/L) controls the handedness of molecular organization and the resulting architectures. In an interesting strategy, three-component modular systems, pyrene–NDI–amino acid triads (**25–30**) with minute structural variations were used to study complex structure–property interplay in molecular architectonics (Figure 15.5a,i).[38] The structural interplay among the synthetic triads led to complex interactions driven emergent behaviours. NDI–pyrene formed complementary pair with matching π-character that helps to engineer the molecular assemblies. The hydrophobic interactions are greatly influenced by solvent polarity, and therefore the self-assembly kinetics was followed to identify different molecular aggregation states under the experimental conditions. The chiral triads LL, DD, LD, and racemic triad RAC exhibited distinct morphological outcomes and the spectroscopy data suggested transcription of the chiral information of the amino acid auxiliaries to the molecular assembly of the triads (Figure 15.5a,ii). An important observation worth mentioning is that the fidelity of molecular assembly of the enantiomeric triad was found to show linearity behaviour, as revealed by the characteristic CD spectra. However, mixed stacked major and minor enantiomers showed nonlinear behaviour under the majority rules. The study revealed anomalous behaviour as a special case of emergent property in a molecularly assembled system and has been specifically termed as super-nonlinearity. These experimentally controlled emergent behaviours of synthetic triads are likely to provide novel insights into complex molecular interactions that may help in solving the prebiotic paradox of chemical evolution.

Asymmetrically functionalized NDIs **31** and **32** with ethyl group and alanine methyl ester (D and L, respectively) auxiliaries were designed to understand the chiral transcription process (Figure 15.5b).[40] Amino acid auxiliary was found to transfer the chiral information to the achiral NDI core, while the ethyl group enhances intermolecular hydrophobic interactions. Detailed study confirmed the formation of chiral supramolecular helices within 2D nanosheet architecture of both **31** and **32**.

The schematic proposed for the molecular arrangement through noncovalent interactions is shown in Figure 15.5 which is in close agreement with the experimental observations and explain the mechanism of the molecular assembly to form chiral supramolecular helices and their subsequent

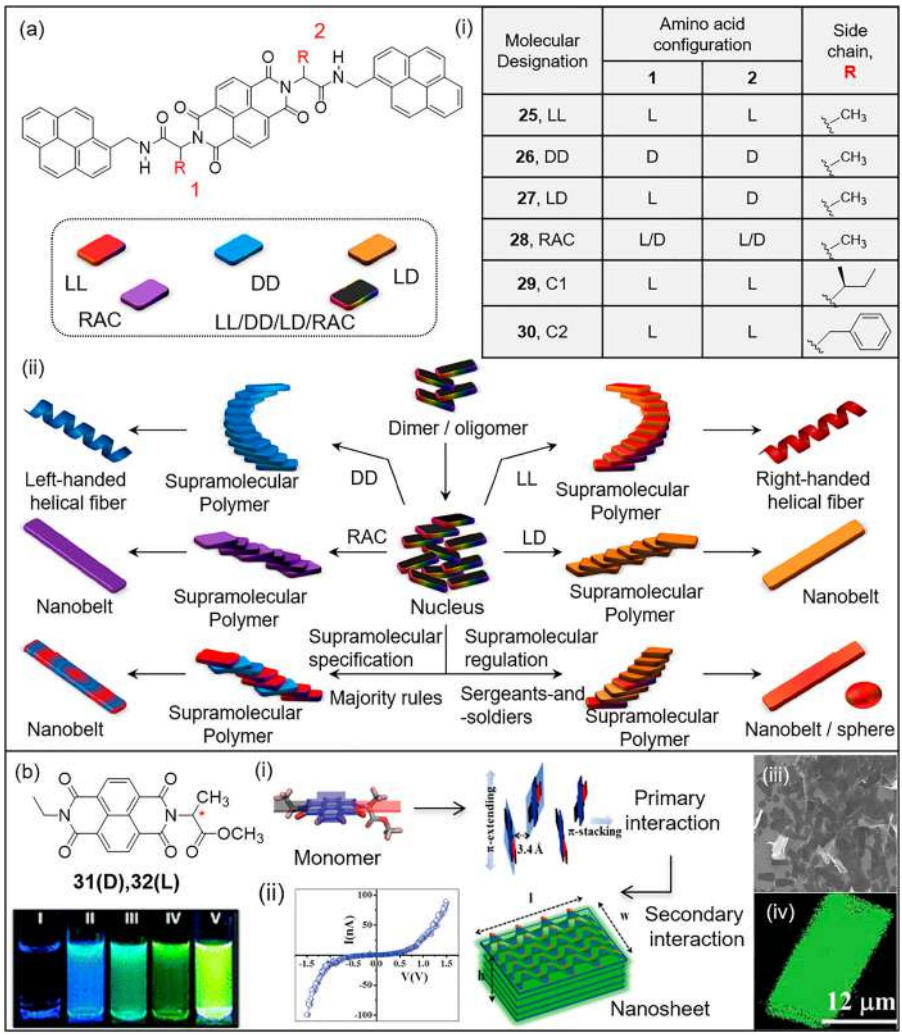

Molecular Designation	Amino acid configuration		Side chain, R
	1	2	
25, LL	L	L	CH_3
26, DD	D	D	CH_3
27, LD	L	D	CH_3
28, RAC	L/D	L/D	CH_3
29, C1	L	L	
30, C2	L	L	

Figure 15.5 (a) Chiral transcription in pyrene–NDI–amino acid triads, **25–30**. (i and ii) Different α-Substituents (25-30) and the emerging molecular organizations governed by the handedness (D/L). (b) Solution phase fluorescent colour of **31**/**32** in different solutions (I: DMSO, II: benzene, III: toluene, IV: xylene, and V: aqueous solution). Schematic representation of molecular organization (i), FESEM and confocal images of 2D nanosheets (iii and iv), and Characteristic *I–V* plot in STM experiment measured on a 2D nanosheet (ii). Panels (a) and (b) are adapted from ref. 38 and 40 with permission from American Chemical Society, Copyright 2016; and the Royal Society of Chemistry, respectively.

organization into hierarchical 2D nanosheet architectures. Further, the conductivity measurements revealed semiconducting nature of the 2D molecular architectures. Thus, minute alterations in the structure of molecular components can potentially influence the organization which in turn reflects in their functional properties and possible applications.

Artificial chirogenesis and chiral amplification can significantly influence the structural and functional evolution in molecular architectonics.[53,54] Various factors such as noncovalent interactions, host–guest steric interactions, equilibrium and thermodynamic parameters, and experimental conditions have been found to influence the artificial chirogenesis. Molecular systems **33–37** with small peptide auxiliaries of homo- and heterochirality (DD/LL and DL/LD, respectively, of F units) were designed to study the chirality transfer, induction, memory and amplification (Figure 15.6a).[28]

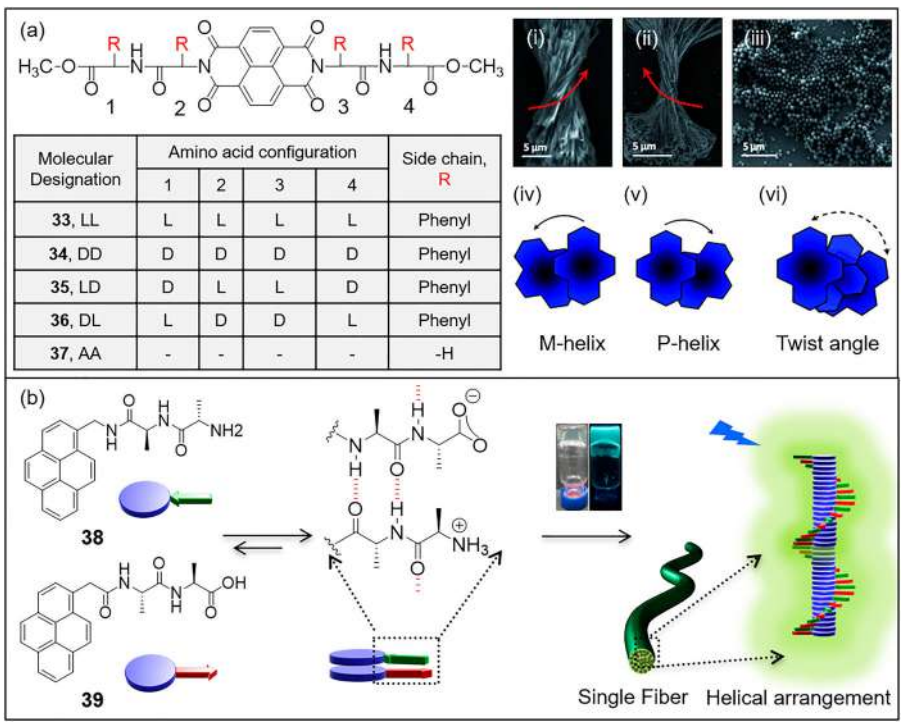

Molecular Designation	Amino acid configuration				Side chain, R
	1	2	3	4	
33, LL	L	L	L	L	Phenyl
34, DD	D	D	D	D	Phenyl
35, LD	D	L	L	D	Phenyl
36, DL	L	D	D	L	Phenyl
37, AA	-	-	-	-	-H

Figure 15.6 (a) Chiral transcription NDI–peptide conjugates (**33–37**). FESEM images of self-assembled structures; (i) LL, (ii) DD, (iii) LD in water/DMSO (85 : 15). (iv–vi) Proposed left-handed (LL and LD) and right-handed (DD and DL) twist in aromatic core. (b) Pyrene-conjugated dipeptide amphiphiles, **38** and **39**. Bicomponent assembly supported by antiparallel β-sheet formation *via* non-covalent interactions. Panels (a) and (b) are adapted from ref. 28 and 47 with permission from John Wiley & Sons, Copyright © 2012 WILEY-VCH Verlag GmbH & Co. KGaA, Weinheim; and the Royal Society of Chemistry, respectively.

Homochirality-driven molecular organization of the probe produced 1D helical architecture (extended assembly structures), while heterochirality of the probe produced 0D mesospheres (Figure 15.6a,i–iii). Sergeants-and-soldiers effect was tested in the case of homochiral probes LL and DD by mixing with achiral AA in different proportions. A strong chiral amplification was observed for the achiral "soldier" induced by the minor Sergeant (LL/DD). Further, morphological studies confirmed the formation 1D single-handed helical fibre bundles by homochiral (LL/DD) probes compared to heterochiral (DL/LD) probes. Detailed study confirmed that the helicity is determined by the first stereocenter adjacent to NDI core, whereas the second regulates the chiral enhancement and amplification, which is termed as retentive helical memory (remembering stereochemical information in chirogenesis in the presence of neighbours of opposite chirality) and in principle support the dominance of homochirality observed in nature.

The dipeptide auxiliary (Ala–Ala) conjugated to pyrene unit at the C-terminus (**38**) and N-terminus (**39**) were designed to construct novel molecular architectures with functional properties (Figure 15.6b).[47] Aromatic π–π interaction among the pyrene unit along with the hydrogen bonding and ionic (among the carboxylate: $-COO^-$ and ammonium: $-NH_3^+$ terminals) interactions of peptide auxiliaries contributed to unique molecular organization of **38** and **39**. The coassembly of **38** and **39** (1 : 1) created antiparallel β-sheet promoted helical organization of pyrene chromophores resulting in the excimer formation. The resultant fibre architecture was fluorescent and provide a suitable microenvironment to intercalate guest molecules (mainly electron acceptors). A sandwich-like donor–acceptor–donor complex formation was confirmed with trinitrotoluene (TNT) with appreciable change in the fluorescence property of the coassembly fibres.[47] Such novel design strategies with controlled molecular organization have practical implications in protecting human health, environment and security-related issues.

Proteinogenic auxiliary with in-built structural information drives the formation of highly ordered sequence–specific molecular architectures. A modular synthetic approach was followed to harvest the in-built information of proteinogenic auxiliaries together with functional core components as well as to understand the specific ordering during the molecular organization. A solid-state crystallographic study was undertaken with peptides containing non-proteinogenic achiral amino acids (α-aminoisobutyric acid: Aib, **40**) and proteinogenic amino acid (Ala, **41**) (Figure 15.7).[41] The designed modular units differ in just one additional methyl group at the C_α-position in the case of Aib, and are capable of forming unique secondary structures. Functional modules **40** and **41** were found to undergo molecular assembly to form achiral 1D nanotapes and chiral 2D nanosheets architectures, respectively, which is determined by the methyl groups at the α-carbon of amino acid units (Figure 15.7c and d). The formation of 1D architecture is guided by the H-type NDI–NDI cofacial arrangement, while edge-to-edge J-type chiral molecular organization was found responsible for the 2D architecture formation (Figure 15.7b). Further, spectroscopic studies revealed that the chiral (D/L) Ala–Ala dipeptide of **41**

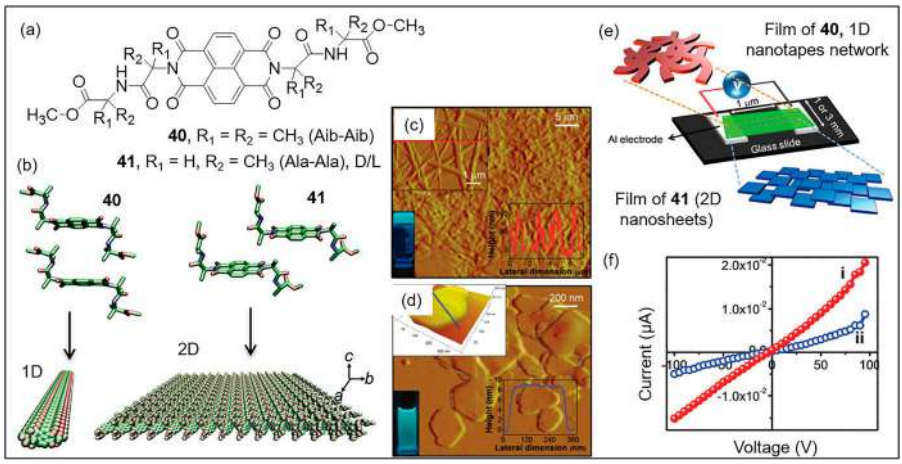

Figure 15.7 (a) Proteinogenic auxiliary conjugated **40** (Aib–Aib) and **41** (Ala–Ala). (b and c) Molecular organization to form 1D and 2D nanostructures in solid state. (d and f) Device fabrication and characteristics *I–V* plot of 1D nanotape network of **40** (i) and 2D nanosheets of **41** (ii). Panels are adapted from ref. 41 with permission from the Royal Society of Chemistry.

is more likely to form an antiparallel β-sheet structure, while the achiral Aib–Aib dipeptide backbone of **40** forms a random structure. Notably, in the case of spider silk protein mimics, Aib-rich peptides are known to promote helix conformation, while the Ala-rich peptides assist β-sheet formation.[55] The minute structural mutations of peptide auxiliaries were found to have significant influence on the conductivity property in the solid state. Superior conductivity was observed for a 1D nanotape network of **40** compared to 2D nanosheets of **41** (Figure 15.7e and f). The observed conductivity difference is attributed to the strong electronic coupling through NDI–NDI face-to-face cofacial arrangement of **40** in 1D nanotape architecture compared edge-to-edge organization of **41** in 2D nanosheet architecture.

15.4 Multicomponent Architectonics

Multicomponent design principles can be integrated and exploited through complex coassembly driven molecular architectonics to generate smart molecular and materials architectures with novel functional properties and applications. In particular, chromophore units with strong dipole moments can be synergistically organized into distinct stacks by the judicious harvesting of noncovalent interactions. In this context, a two-component system consisting of tweezer-sandwich molecular organization of NDI and pyrene pair has been successfully demonstrated (Figure 15.8).[31] a flexible dipyrene tweezer-like molecular system (**44**, π-electron donor) was designed which can appropriately accommodate aromatic guests (NDI, **42** and **43**, π-electron

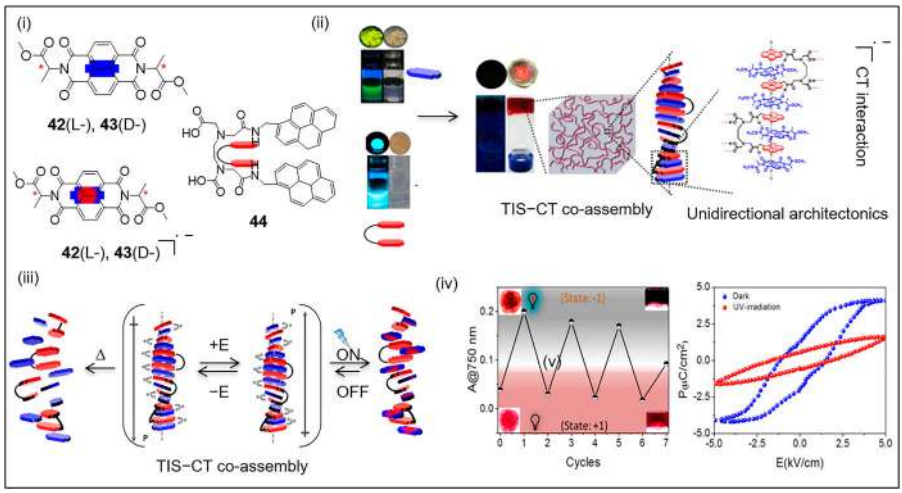

Figure 15.8 (i) Multicomponent systems comprising guests (**42** and **43**) and host **44** (tweezer). (ii) Photographs of different assembly and coassembly in aqueous, hydrogel and solid states under UV and visible light. (iii) Illustration of multi-stimuli responsiveness of CT complex. Electric field (E) induced polarization (P) switching, temperature (Δ) driven disassembly, and UV (365 nm) responsive photoinduced single-electron transformation reaction within the TIS-CT coassembly. (iv) Ferroelectric switching measurements under dark and light at 100 K of xerogel thin film. Panels are adapted from ref. 31 with permission from American Chemical Society, Copyright 2016.

acceptor) to form extended tweezer-inclusion-sandwich (TIS) CT coassembly (Figure 15.8b). The two carboxylic acid functionalities were incorporated in the backbone of **44** to aid the aqueous solubility and lateral extension of assemblies through intermolecular hydrogen bonding. Nonpolar alanine methyl ester also modulates the solubility of **41**/**42** in aqueous solvent, and α-functionality in the amino acid auxiliary determine the chirality (L/D) of the TIS-CT assembly architecture. Hydrogen bonding and chiral interactions play active roles in assuring the unidirectional non-centrosymmetric alignment of molecular electric dipoles. This results in the formation nanofibres with unidirectional polarization. The coassembly formation led to gelation in the aqueous solution and form chiral (non-centrosymmetric) supramolecular CT coassemblies through TIS-CT coassembly. For the first time, the coassembly was further exploited for the fabrication of a solution-processable multi-stimuli responsive supramolecular thin-film ferroelectric capacitor with Ps ~4 μC cm^{-2} at room temperature (Figure 15.8e). The TIS-CT coassembly was further utilized for colour tunability as a prospective optical memory device. The light responsive reversibility was demonstrated through the formation of $NDI^{\bullet-}$ and NDI in the coassembly by keeping the solution under UV-light and in dark conditions, (Figure 15.8e). Such multicomponent molecular architectonics and the exceptional emergent properties and

functions are expected to influence the processable optoelectronic and ferroelectric smart memory devices.

Experimental conditions play a key role in controlling the mode of molecular organization. Perturbation of hydrogen bonding interaction is one such approach and can be realized by changing the pH of the solution. Histidine (H, IP = 7.59, pK_a = 6.00), a basic amino acid was used as a potential pH-responsive auxiliary (Figure 15.1). H was conjugated to PDI unit (**45**) to modulate the variable molecular organization at different pH conditions depending on the protonation–deprotonation of –COOH (pK_a = 4.1) and imidazole (pK_a = 7.3) functionalities using acid or base, respectively (Figure 15.9a,i).[43] The PDI **45**

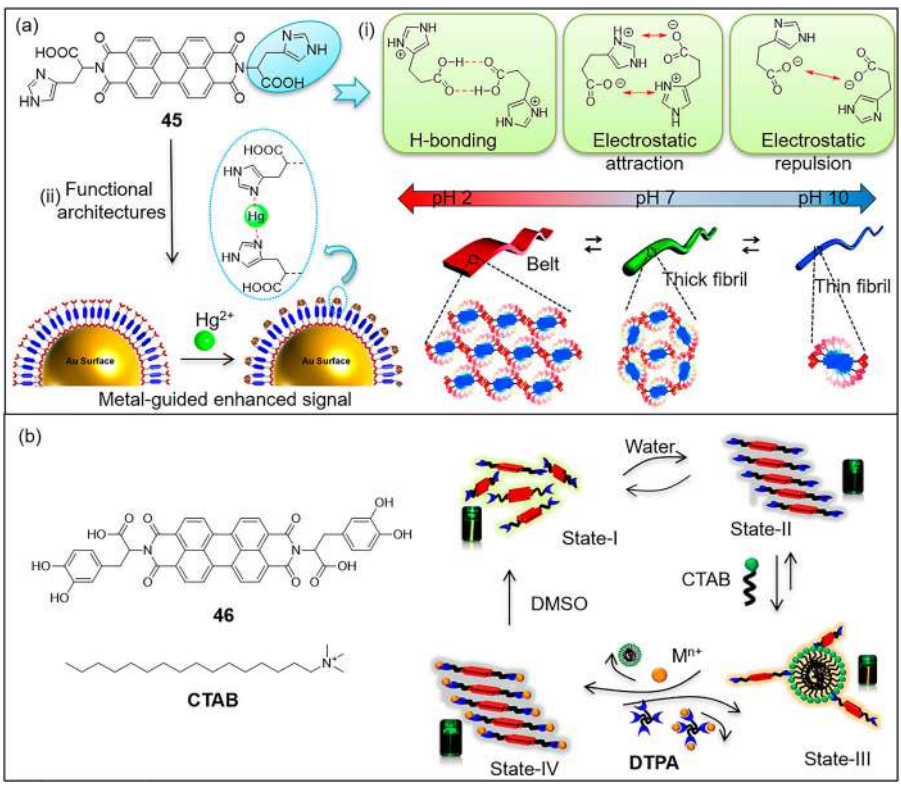

Figure 15.9 (a) Molecular structure of H appended PDI, **45**. (i) Illustration of pH-dependent supramolecular interactions in H residue and subsequent morphology developments. (ii) Metal ion (Hg^{II})-guided signal enhancement in functional architecture. (b) Schematic representation of surfactant (CTAB) modulated different self-assembly states (I–IV) of **46**, and transformation of State III to State IV *via* metal ion induced reorganization of **46** in the presence of CTAB micelles. Panels (a) and (b) are adapted from ref. 43, 46 and 48 with permission from the Royal Society of Chemistry; Elsevier, Copyright 2018; and American Chemical Society, Copyright 2014, respectively.

with imidazole α-functionality showed reversible supramolecular chiroptical switching at different pH. At pH 2 (acidic), inter-fibrilar hydrogen bonding interaction was observed in the form of interconnected belt structures that produced larger aggregates of a mean size distribution of 2–6.4 μm. At pH 10 (basic), **45** showed a uniformly distributed micrometre long thin nanofibre network with a mean size distribution of 80–140 nm. However, at pH 7 (neutral solution), coexistence of both the smaller and larger aggregates with a mean size distribution of 80–6400 nm was observed. The pH-responsive helical molecular organization and reversible chiroptical inversion were interesting observations from this study. The spectroscopy investigation showed a switching between *M*- to *P*-type organization of PDI chromophore units, within the experimental limitations. Then the multicomponent architectonics was achieved with the prior understanding of the imidazole functional group of H which chelates metal ions in many metalloproteins. Imidazole of H was established as a strong Hg^{II} chelator that formed ordered metallosupramolecular architectures (Figure 15.9a,ii).[46] The molecular organization of **45** (J and H-type) was found dependent on the concentration gradient of Hg^{II} in aqueous solution. This observation was successfully used to develop a highly selective and sensitive sensor platform with sol-to-gel transformation (visible), fluorescence and surface-enhanced Raman spectroscopy (SERS) methods. Remarkably, in the molecular architectonics approach, PDI **45** was used as a SERS marker for the selective and highly sensitive detection of Hg^{II} in water. Through this innovative approach, we accomplished the best ever reported attomolar (10^{-18} M) sensitivity for Hg^{II} with the detection limit of 0.01 parts per quadrillion.[46]

In another study, L-3,4-dihydroxyphenylalanine (L-DOPA) auxiliary conjugated PDI **46** was designed wherein PDI functional core served as the fluorophore unit (Figure 15.9b).[48] PDI **46** formed assembled aggregates in aqueous solution with very weak fluorescence properties compared to a highly fluorescent molecular state (State I). Therefore, aggregated **46** (State II) was used as a host to establish an assembly-disassembly platform with fluorescence "switching off-on" modulation protocol. Surfactant, cetyltrimethylammonium bromide (CTAB) was used as a complementary unit for ionic interaction between the cation and anion to modulate the assembly architectures of **46** into smaller aggregates (State III) with characteristic properties (Figure 15.9b). Furthermore, metal-assisted assembly of **46** (State IV) provided a sensitive detection platform for Fe^{3+} and Cu^{2+} by means of transforming into fluorescence switch ON disassembly state. The molecular assembly and disassembly process of **46** was found to be reversible with the addition of diethylenetriaminepentaacetic acid (DTPA), which is visualized by the significant spectroscopic changes. Therefore, careful component selection (chromophore and amino acid auxiliary) and experimental conditions (solvent, temperature, pH, ionic strength, *etc.*) play significant roles in harvesting novel properties and functional applications through the scheme of molecular architectonics.

Nucleobase, sugar and lipid molecules are also considered as potential auxiliaries in the scheme of molecular architectonics (Figure 15.1). We summarized molecular architectonics of functional molecules using biomolecular auxiliaries other than amino acids and small peptides in Figure 15.10. Nucleobases (Figure 15.10a–c), sugars (Figure 15.10d) and lipids (Figure 15.10e) are explored as potential auxiliaries to broaden the scope of molecular architectonics. For example, adenine (A)-tethered PDI derivative **47** was used to template ssDNA (dT_{10}) to generate novel DNA nanoarchitectures (Figure 15.10a).[44] Spectroscopy study confirmed the formation of [dT_{10}:**47**$_{10}$:dT_{10}] type hybrid DNA ensemble and was visualized by AFM. These bicomponent ensembles are formed through mutually templated ordered chiral architectonics and chiral imprinting through "double zipper" helical assembly, *i.e.*, dT_n:**47**$_n$:dT_n. ssDNA sequences or oligonucleotides (dB_n, n = 20) assemble with **47** with defined helicity in the assembly architectures. The result showed the formation of an ordered left-handed helix (M-helix) with dT_n and dG_{20}, however, a stable right-handed helix (P-helix) was observed with dA_n. These studies revealed the judicial exploitation of conventional or Watson–Crick (WC, A–T and G–C) and unconventional (A–A, A–G, *etc.*) hydrogen bonding to design small molecule-templated hybrid DNA molecular nanoarchitectures through the principles of molecular architectonics. Another A-appended NDI derivative **48** was designed to develop a conducting DNA device with an ordered NDI chromophore that would help to transport electrons through the assembly architectures (Figure 15.10b).[15] The mutually templated **48**$_n$–dT_n ensemble self-assembled to form 2D sheets with variable lateral dimensions (w and l) that depend on the dT_n sequence length. This small molecule-templated DNA architectonics demonstrated the tunability of the 2D nanostructures and allowed the modulation of chiroptical, morphological, and conductivity properties of **48**$_n$–dT_n. Furthermore, the semiconducting property of NDI units in the hybrid **48**$_n$–dT_n assembly architectures was used to construct a field-effect transistor (FET) device. Similarly, we designed nucleobase-appended NDI derivatives (**49** and **50**) and peptide nucleic acid dimers (**51** and **52**) as small molecule templates and molecular clamps, respectively (Figure 15.10c).[30] In this study, WC and Hoogsteen type hydrogen bonding of the A was explored to achieve unique structural transformation through bicomponent ensembles. The ensemble generation was controlled by shuffling the combination of components (**49–50**). The molecular architectonics exercise resulted in well-defined 2D microstructures, porous spheres, tapes and petal-like 2D sheets. This study revealed that molecular recognition of nucleobases through conventional and unconventional hydrogen bonding can be used for the design and development of diverse templated functional architectures.

The use of sugar as a functional auxiliary in the scheme of molecular architectonics is showcased in the form of D-gluconamide amphiphiles (**53**) containing a hydrophobic pyrene as the functional core unit (Figure 15.10d).[50] The structure–property is solely dependent on the environment

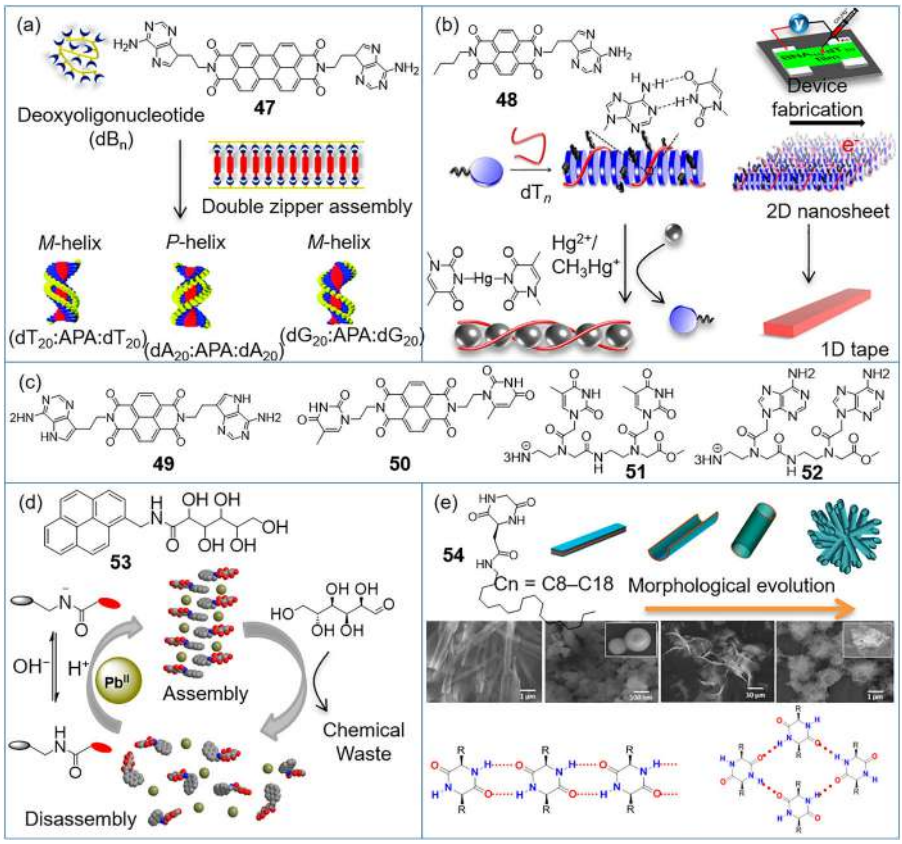

Figure 15.10 Additional biomolecules such as nucleobase, glucose and lipid. (a) Illustration of mutually templated 1D molecular arrangement of **47** and deoxyribonuclotide. Different helicities (*P*- or *M*-) were imprinted with different deoxyribonuclotide in the "double zipper" assembly depending on the types of interactions, canonical or non-canonical. (b) Structural insight of **48** and dT_{10} assembly to form 2D sheet-like structure. Mercury-mediated disassembly and transformation of $\mathbf{49}_n$–dT_n 2D structure into a metallo-DNA duplex $[dT–Hg–dT]_n$. A prototype device structure for CH_3Hg^+ detection. (c) Chemical structures of NDI derivatives (**49**,**50**) with nucleobase auxiliary used for the molecular interaction study with peptide nucleic acids (**51**,**52**). (d) Construction of functional architectonics with D-gluconamide amphiphiles (**53**) and metal ion (Pb^{2+}) to influence the kinetics of glucose hydrolysis. (e) A lipid-like peptide amphiphile with a CDP head group and long alkyl chain of variable length. Illustration of morphological evolution along with the increasing chain length and different modes of inter CDP unit hydrogen bonding, linear and cyclic. Panels (a)–(e) are adapted from ref. 15, 30, 44, 49 and 50 with permission from the Royal Society of Chemistry; American Chemical Society, Copyright 2016; the Royal Society of Chemistry; American Chemical Society, Copyright 2020; American Chemical Society, Copyright 2020, respectively.

of the molecular systems. We reported that the functional organic ligands with active –NH centres are capable of coordinating with metal centres (Pb^{II}) and forming a well-defined dynamic molecular assembly in alkaline conditions. The pH-dependent reversible ligand–metal ion interaction was used to enhance the catalytic efficiency (*ca.* glucose hydrolysis) by employing the principles of molecular architectonics. The catalytic efficiency was found very much dependent on the hydrophobic unit (aromatic/alkyl), while the metal coordination was supported by the sugar auxiliary. Together, D-gluconamide amphiphiles undergo well-defined assembly architecture to create the second coordination sphere necessary for the observed catalytic efficiency at room temperature. Different hydrophobic units produced secondary coordination spheres with varying assembly architectures and thereby variations in the catalytic efficiency. A comparative study between molecular assembly architecture and dispersed state or metal ion alone provided detailed understanding to guide the design of future advanced catalytic systems.[50]

In addition, cyclic dipeptide amphiphiles (CDPAs) with lipid-like long alkyl chains were introduced in the scheme of molecular architectonics to highlight the importance of lipid molecules as auxiliaries.[49] Cyclic dipeptide (CDP) with multiple hydrogen bond donors and accepters is considered as a versatile functional unit to engineer the molecular assembly employing the principles of molecular architectonics.[33,56–60] CDP with multiple hydrogen bonding capabilities was conjugated to alkyl chains of varying chain lengths of C8–C18 (**54**, Figure 15.10e). The multiple hydrogen bonding patterns of CDP units and variable hydrophobicity of the alkyl chains were considered in the design strategy. The CDP (hydrogen bonding) and alkyl chain (hydrophobic interactions) driven noncovalent interactions leads to evolution in morphology and produced well-defined and diverse nanoarchitectures such as nanotubes, nanospheres, nano/microsheets, and flowers. The coassembly of the peptide amphiphiles with biomolecules such as nucleosides was studied to ascertain their utility as potential drug (BrdU) delivery vehicles. Overall, the scheme of molecular architectonics to engineer the molecular assembly of functional molecules employing different biomolecules as auxiliaries through controlled noncovalent interactions is discussed to generate nano-, micro- and macro-scale architectures with functional properties and applications.

15.5 Conclusion

In summary, we discussed the power of molecular architectonics to engineer the molecular organization through meticulously controlled noncovalent interactions. The detailed structure–property correlation is demonstrated with applications across the areas of optoelectronics, chiroptical, homochirality, protein folding, nanoelectronics, molecular electronics, memory devices, energy or light harvesting and storage, (bio)sensing, (bio)imaging, targeted diagnostics and therapeutics to solve the problems related health, energy and environment. The contribution of different biomolecules such

as amino acids, small peptides, nucleobases, glucose and lipids as auxiliaries to guide the molecular organization of functional molecules into well-defined molecular and materials architectures has been established. These basic principles of molecular architectonics have huge implications towards the art of mastering the programmed molecular assemblies with tailor-made structure–property and function. In the field of molecular architectonics, apart from molecular component design, meticulously balanced experimental conditions such as solvent polarity, ionic strength, pH, temperature and external stimuli among other parameters control the outcome of smart architectures. Overall, appreciation for the subtle molecular and experimental factors that govern the outcome of molecular architectonics has been underlined in a rational and systematic fashion. While the understanding of noncovalent interactions or recognition forces at the molecular level is still in its infancy, tailoring the molecular units from the viewpoint of structure–function relationship under the skilful experimental conditions has great potential for the design and construction of minimalistic, dynamic, and functional molecular and material architectures.

Acknowledgements

We thank Prof. C. N. R. Rao FRS for his constant support and encouragement and JNCASR, BRICS Multilateral R&D Projects grant (DST/IMRCD/BRIC/PilotCAll2/EPNAPT/2018(G)), SwarnaJayanti Fellowship Grant (grant: DST/SJF/CSA-02/2015–2016), DST Nano Mission (Grant: SR/NM/TP-25/2016) the Department of Science and Technology (DST), Govt. of India and Sheikh Saqr Laboratory (SSL), ICMS-JNCASR for financial support.

References

1. M. B. Avinash and T. Govindaraju, *Acc. Chem. Res.*, 2018, **51**, 414.
2. B. Roy and T. Govindaraju, *Bull. Chem. Soc. Jpn.*, 2019, **92**, 1883.
3. I. Kant, *Moscow: Mysl*, 1964, p. 68.
4. L. P. Datta, S. Manchineella and T. Govindaraju, *Biomaterials*, 2020, **230**, 119633.
5. D. Ghosh, L. P. Datta and T. Govindaraju, *Beilstein J. Nanotechnol.*, 2020, **11**, 124.
6. M. B. Avinash, P. K. Samanta, K. V. Sandeepa, S. K. Pati and T. Govindaraju, *Eur. J. Org. Chem.*, 2013, **2013**, 5838.
7. M. B. Avinash, K. Swathi, K. S. Narayan and T. Govindaraju, *ACS Appl. Mater. Interfaces*, 2016, **8**, 8678.
8. B. Roy, S. Pal and T. Govindaraju, *ACS Appl. Mater. Interfaces*, 2020, 14057–14063.
9. C. B. Anfinsen, *Science*, 1973, **181**, 223.
10. M. B. Avinash and T. Govindaraju, *Nanoscale*, 2014, **6**, 13348.
11. M. B. Avinash and T. Govindaraju, *Nanoscale*, 2011, **3**, 2536.

12. M. Avinash and T. Govindaraju, *Adv. Mater.*, 2012, **24**, 3905.
13. M. Aono and K. Ariga, *Adv. Mater.*, 2016, **28**, 989.
14. K. Ariga, *Mater. Chem. Front.*, 2017, **1**, 208.
15. M. Pandeeswar, S. P. Senanayak and T. Govindaraju, *ACS Appl. Mater. Interfaces*, 2016, **8**, 30362.
16. J. V. Barth, *Annu. Rev. Phys. Chem.*, 2007, **58**, 375.
17. A. J. Olson, *J. Mol. Biol.*, 2018, **430**, 3997.
18. T. Govindaraju and M. B. Avinash, *Nanoscale*, 2012, **4**, 6102.
19. Y. Tu, F. Peng, A. Adawy, Y. Men, L. K. E. A. Abdelmohsen and D. A. Wilson, *Chem. Rev.*, 2016, **116**, 2023.
20. X. Yan, P. Zhu and J. Li, *Chem. Soc. Rev.*, 2010, **39**, 1877.
21. R. Bischoff and H. Schlüter, *J. Proteomics*, 2012, **75**, 2275.
22. S. Govindarajan and R. A. Goldstein, *Proc. Natl. Acad. Sci. U. S. A.*, 1998, **95**, 5545.
23. E. Haber and C. B. Anfinsen, *J. Biol. Chem.*, 1962, **237**, 1839.
24. R. J. Mart, R. D. Osborne, M. M. Stevens and R. V. Ulijn, *Soft Matter*, 2006, **2**, 822.
25. S. Fleming and R. V. Ulijn, *Chem. Soc. Rev.*, 2014, **43**, 8150.
26. G. M. Whitesides, J. P. Mathias and C. T. Seto, *Science*, 1991, **254**, 1312.
27. M. B. Avinash and T. Govindaraju, *J. Phys. Chem. Lett.*, 2013, **4**, 583.
28. M. Pandeeswar, M. B. Avinash and T. Govindaraju, *Chem. - Eur. J.*, 2012, **18**, 4818.
29. S. E. Paramonov, H.-W. Jun and J. D. Hartgerink, *J. Am. Chem. Soc.*, 2006, **128**, 7291.
30. N. Narayanaswamy, M. B. Avinash and T. Govindaraju, *New J. Chem.*, 2013, **37**, 1302.
31. M. Pandeeswar, S. P. Senanayak, K. Narayan and T. Govindaraju, *J. Am. Chem. Soc.*, 2016, **138**, 8259.
32. H. Cui, A. G. Cheetham, E. T. Pashuck and S. I. Stupp, *J. Am. Chem. Soc.*, 2014, **136**, 12461.
33. S. Manchineella, V. Prathyusha, U. D. Priyakumar and T. Govindaraju, *Chem. - Eur. J.*, 2013, **19**, 16615.
34. D. M. Ryan and B. L. Nilsson, *Polym. Chem.*, 2012, **3**, 18.
35. Q. Zou and X. Yan, *Chem. - Eur. J.*, 2018, **24**, 755.
36. M. Pandeeswar, H. Khare, S. Ramakumar and T. Govindaraju, *RSC Adv.*, 2014, **4**, 20154.
37. M. B. Avinash and T. Govindaraju, *Adv. Funct. Mater.*, 2011, **21**, 3875.
38. M. B. Avinash, K. V. Sandeepa and T. Govindaraju, *ACS Omega*, 2016, **1**, 378.
39. M. Pandeeswar and T. Govindaraju, *J. Inorg. Organomet. Polym. Mater.*, 2015, **25**, 293.
40. M. Pandeeswar and T. Govindaraju, *RSC Adv.*, 2013, **3**, 11459.
41. M. Pandeeswar, H. Khare, S. Ramakumar and T. Govindaraju, *Chem. Commun.*, 2015, **51**, 8315.
42. M. B. Avinash, K. V. Sandeepa and T. Govindaraju, *Beilstein J. Org. Chem.*, 2013, **9**, 1565.

43. M. Pandeeswar and T. Govindaraju, *Mol. Syst. Des. Eng.*, 2016, **1**, 202.
44. N. Narayanaswamy, G. Suresh, U. D. Priyakumar and T. Govindaraju, *Chem. Commun.*, 2015, **51**, 5493.
45. M. B. Avinash, D. Raut, M. K. Mishra, U. Ramamurty and T. Govindaraju, *Sci. Rep.*, 2015, **5**, 16070.
46. P. Makam, R. Shilpa, A. E. Kandjani, S. R. Periasamy, Y. M. Sabri, C. Madhu, S. K. Bhargava and T. Govindaraju, *Biosens. Bioelectron.*, 2018, **100**, 556.
47. C. Madhu, B. Roy, P. Makam and T. Govindaraju, *Chem. Commun.*, 2018, **54**, 2280.
48. A. K. Dwivedi, M. Pandeeswar and T. Govindaraju, *ACS Appl. Mater. Interfaces*, 2014, **6**, 21369.
49. K. Pandurangan, B. Roy, K. Rajasekhar, Y. V. Suseela, P. Nagendra, A. Chaturvedi, U. R. Satwik, N. A. Murugan, U. Ramamurty and T. Govindaraju, *ACS Appl. Bio Mater.*, 2020, 3413–3422.
50. B. Roy, S. Pal and T. Govindaraju, *ACS Appl. Mater. Interfaces*, 2020, **12**, 14057.
51. S. E. Radford, *Trends Biochem. Sci.*, 2000, **25**, 611.
52. C. M. Dobson, *Nature*, 2003, **426**, 884.
53. M. V. Escárcega-Bobadilla and A. W. Kleij, *Chem. Sci.*, 2012, **3**, 2421.
54. V. V. Borovkov, G. A. Hembury and Y. Inoue, *Acc. Chem. Res.*, 2004, **37**, 449.
55. P. Calvert, *Nature*, 1998, **393**, 309.
56. S. Manchineella and T. Govindaraju, *ChemPlusChem*, 2017, **82**, 88.
57. T. Govindaraju, *Supramol. Chem.*, 2011, **23**, 759.
58. T. Govindaraju, M. Pandeeswar, K. Jayaramulu, G. Jaipuria and H. S. Atreya, *Supramol. Chem.*, 2011, **23**, 487.
59. S. Manchineella, N. A. Murugan and T. Govindaraju, *Biomacromolecules*, 2017, **18**, 3581.
60. S. Manchineella and T. Govindaraju, *RSC Adv.*, 2012, **2**, 5539–5542.

CHAPTER 16

Designed Amphiphiles for Cell Membrane Mimetic Nanoarchitecture

K. YASUHARA*[a,b], K. OMOTO[a], T. NISHINO[a] AND G. RAPENNE[a,c]

[a]Division of Materials Science, Graduate School of Science and Technology, Nara Institute of Science and Technology, 8916-5 Takayama, Ikoma, Nara 6300192, Japan; [b]Centre for Digital Green-innovation, Nara Institute of Science and Technology, Ikoma, Japan; [c]CEMES, Université de Toulouse, CNRS, 29, rue Marvig, 31055 Toulouse, France
*E-mail: yasuhara@ms.naist.jp

16.1 Introduction

In any kind of living organism, biomembranes or cell membranes constitute the outermost layer of the cell that contact with the external environments.[1] Biomembranes provide a cross-wall to compartmentalise the cytoplasmic components as the most crucial function. Intracellular organelles such as the endoplasmic reticulum, Golgi apparatus, mitochondria are also enclosed by a membrane. Biomembranes promote the localisation of necessary molecules in specific locations of the cell and organise them hierarchically to achieve biological functions. Although the cross-wall is the most important role, biomembranes also mediate various important functions such

Nanoscience & Nanotechnology Series No. 55
Concepts and Design of Materials Nanoarchitectonics
Edited by Omar Azzaroni and Katsuhiko Ariga

Published by the Royal Society of Chemistry, www.rsc.org

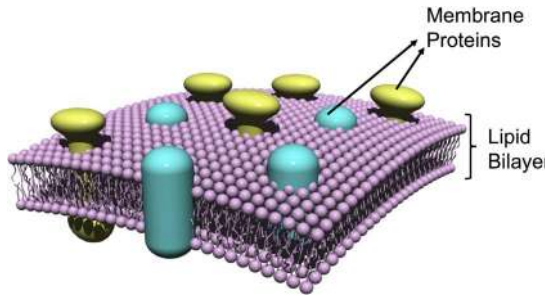

Figure 16.1 Schematic image of a biomembrane.

as material transport, signal transduction, and energy production. Thus, we can regard biomembranes as an essential biologic nanoarchitecture to understand the origin of life.

Biomembranes are complex molecular assemblies consisting of lipids and membrane proteins working as a matrix and functional module, respectively (Figure 16.1). Lipid molecules spontaneously assemble each other to form a bilayer structure in an aqueous environment. The lipid bilayer is a fluidic layer with a thickness of 5 nm assembled by a hydrophobic effect between lipid molecules. The impermeability of the lipid bilayer produces the gradient of chemical potential across the membrane that contributes to performing various biological functions. For instance, the synthesis of ATP to store energy in a cell or its hydrolysis back to ADP to release this energy, utilises the proton ion gradient across the membrane.[2] The hydrophobic interior of the lipid bilayer provides a unique environment for the organisation of membrane proteins as well as their biochemical reactions. Inspired by the complex and sophisticated functions of natural biomembranes, many attempts have been previously made to synthesise materials that mimic their structures and functions. In this chapter, we will introduce the molecular design of membrane-forming lipids and the characteristics of the lipid-based molecular assembly toward the creation of supramolecular materials that behave like natural biological membranes.

16.2 Molecular Design of Membrane-forming Lipid

Membrane-forming lipid molecules are always amphiphilic or amphipathic where polar head groups are conjugated with hydrophobic (nonpolar) tails. Natural lipids are classified as phospholipids, glycolipids, and neutral lipids. The lipid composition of cell membrane differs depending on living species, type of cells, and organelles.[3] The most abundant lipid in nature is phospholipids, which have a hydrophilic phosphate moiety in a head group and two long fatty acid chains as hydrophobic tails. The lipid molecules tend to associate in an aqueous solution through the hydrophobic effect between tails. Amphiphilic molecules, including lipids and surfactants, are known to

form a variety of molecular assemblies depending on their chemical structure. Israelachvili *et al.* proposed the concept of critical packing parameter (CPP) to describe the correlation between the geometry of amphiphilic molecules and the morphology of the molecular assemblies formed in water.[4] The critical packing parameter P can be expressed as $P = v/(a_0 \cdot l_c)$, where a_0, v, and l_c correspond to the cross-sectional area of the lipid molecule, the volume of the hydrocarbon chain, and the extended effective length of the hydrophobic chain, respectively. Figure 16.2 summarises the relationship between the shape of the amphiphilic molecule, the critical packing parameter, and the structure of the molecular assembly. As the CPP of the amphiphile increases, the spontaneous curvature of their assembly decreases. Natural bilayer-forming phospholipids are known to have a CPP in the range of 1/2 to 1 due to the presence of relatively bulky hydrophilic groups such as phosphocholine groups and two hydrophobic chains on the same molecule.

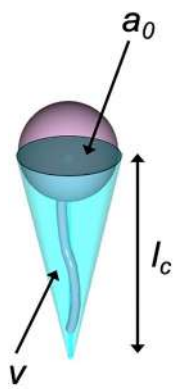

Critical packing parameter $v/(a_0 \cdot l_c)$	Critical packing shape	Structures formed
< 1/3	Cone	Spherical micelle
1/3 – 1/2	Truncated cone	Cylindrical micelle
1/2 – 1	Truncated cone	Vesicle, Flexible bilayer
~ 1	Cylinder	Planar bilayer
> 1	Inverted truncated cone	Inverted micelle

Figure 16.2 Effect of critical packing parameter on the aggregates formed by amphiphiles.

The formation of the lipid bilayer in water is not limited to natural phospholipids, but there are also synthetic lipid molecules, which satisfy the bilayer-forming CPP. In this section, we introduce some of the molecular designs of synthetic lipids (Figure 16.3).

Kunitake and Okahata have done pioneering work on the synthetic lipid bilayer. They first found that lipid bilayer vesicles are spontaneously formed by the simple dispersion of didodecyldimethylammoniumbromide (**1**),

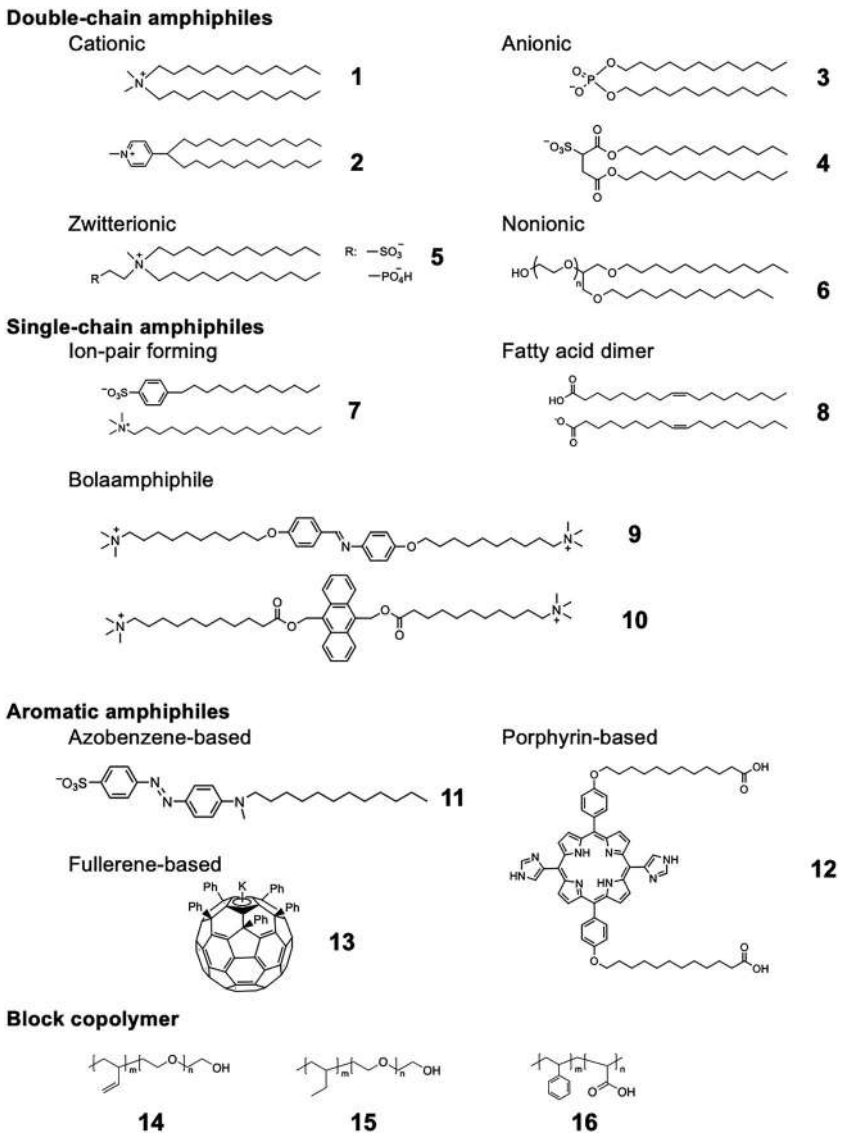

Figure 16.3 Chemical structures of membrane-forming amphiphiles.

a synthetic amphiphile, in water.[5] Following their discovery, a considerable number of amphiphilic molecules with two long alkyl chains have been synthesised to form lipid bilayers spontaneously.[6] A wide variety of functional groups can be introduced as hydrophilic groups of membrane-forming lipids: cationic ammonium and pyridinium (**2**) groups, anionic phosphate (**3**) and sulfate (**4**) groups, zwitterionic phosphobetaine and sulfobetaine groups (**5**), and nonionic polyoxyethylene (**6**). Also, some amphiphiles without two hydrophobic chains have been found to form lipid bilayers. The mixture of a long-chain cationic surfactant and an anionic surfactant, the so-called catanionic mixture, is known to form membranes in water by forming an ion pair, which possesses a structure similar to that of double-chain lipids.[7] For example, the mixture of cationic sodium dodecylbenzenesulfonate (SDBS) and cetyl trimethylammonium tosylate (CTAT) (**7**) is found to form vesicles.[8] The formation of lipid bilayers by molecular dimerisation is not limited to the formation of ion pairs; aqueous solution solely containing long-chain fatty acid also forms membrane under limited conditions.[9] Dimerisation of the non-ionised neutral form and the ionised form of fatty acid (**8**) coexisting in a specific range of pH results in the formation of lipid bilayer. Due to its simple chemical composition, the lipid bilayer formed by fatty acid dimers is considered to be one of the primitive membrane structures. There are several examples of single-chain amphiphiles, which are known to organise membranes without the formation of their dimers. Bolaamphiphiles (**9, 10**), which have a hydrophilic head at both ends of a hydrophobic centre part,[10] sometimes form a membrane consisting of a monolayer, resulting in thinner films than other membranes produced by bilayer-forming lipids.[11] Although the hydrophobic chains in natural lipids are mainly long fatty acid chains or sterols, a variety of other hydrophobic moieties are known to be introduced to synthetic membrane-forming lipids. For example, single-chain surfactants with rigid aromatic hydrophobic groups, such as azobenzene (**11**)[12] and porphyrin (**12**),[13] spontaneously form vesicles instead of spherical micelles due to their strong interaction and tight packing. Lipid molecules with fluorocarbon chains show unique features different from hydrocarbon lipids, such as the formation of bilayers in organic solvents.[14] Noteworthy, the presence of long and linear hydrophobic moieties is not even a minimum requirement for the formation of membranes. Nakamura *et al.* reported the formation of vesicles by amphiphilic fullerene derivatives (**13**).[15] Compared to phospholipid vesicles, fullerene vesicles are highly uniform in the aggregate size with lower water permeability and higher thermal stability, because fullerenes are tightly packed in the membrane.

Macromolecular frameworks including synthetic polymers can be also used to produce membranes in water through the precise tuning of their molecular structure.[16] The most common polymers that form vesicles are amphiphilic A–B type diblock copolymers (**14–16**) or triblock A–B–A type copolymers that have hydrophilic (A) and hydrophobic segments (B) on the same polymer chain. Various combinations of hydrophobic monomers such as polystyrene, polybutadiene, polyethyl ethylene, and polydimethylsiloxane and hydrophilic

monomers including polyethylene glycol, poly(2-methyloxazoline), and polyacrylic acid have been introduced to obtain membrane-forming amphiphilic polymers. To synthesise membrane-forming polymers, a living polymerisation technique such as reversible addition-fragmentation chain transfer (RAFT) polymerisation or atom transfer radical polymerisation (ATRP) is generally employed to tune the length of hydrophilic and hydrophobic segments precisely. The topology of the polymer aggregate can be also predicted by the CPP as demonstrated in the case of conventional small amphiphiles.[17] In particular, the block polymer with a small hydrophobic segment and a large hydrophilic segment will be assembled into a spherical micelle. The polymer having a similar size of hydrophobic and hydrophilic segments will form vesicles. In recent years, the formation of polymer vesicles other than amphiphilic block copolymers has also been demonstrated. Kataoka *et al.* reported the formation of vesicles by the mixture of polyanions and polycations without hydrophobic domains where stable polyionic complexes are formed between oppositely charged polymers in water.[18]

In the design of lipids employing a synthetic molecular framework, various functional groups can be introduced to develop membranes behaving differently from natural phospholipid membranes (Figure 16.4). Regen *et al.* developed a series of membrane-forming amphiphiles having polymerisable methacryloyl groups at the ends of the hydrophobic chains (**17**).[19] Formation of intermolecular cross-linking through polymerisation significantly improved the stability of vesicles that can maintain their hollow structure even in the presence of organic solvents. Furthermore, styryl (**18**), acryloyl (**19**), dienoyl (**20**), and lipoyl (**21**) monomers have been also introduced into either lipid head groups or hydrophobic chains to produce polymerised membrane.[20] Phospholipid with diacetylene groups in the hydrophobic chain (**22**) can be polymerised by the irradiation of UV light where the progress of the polymerisation reaction can be monitored by the colour change.[21] A phospholipid analogue with a thiol headgroup (**23**) provides a method for the quantitative evaluation of the interaction between nearest-neighbour lipid molecules by forming a disulfide dimer. This technique is expected to contribute to clarifying the nature of lipid rafts, functional phase-separated domains in the membrane.[22] Kikuchi *et al.* have developed an organic–inorganic hybrid vesicle so-called "Cerasome", which is formed by a lipid molecule with a triethoxysilyl group on the head group (**24**).[23,24] A thin cross-linked ceramic-like siloxane layer will be produced on the surface of the membrane through the sol–gel reaction. Compared to conventional phospholipid vesicles, Cerasomes displayed extremely high morphological stability that enables the construction of artificial multicellular models by layer-by-layer assembly of vesicles.[25] Stimuli-responsive vesicles can be also constructed by synthetic functional lipids. Amphiphiles conjugated with a supramolecular host have been developed for the recognition of small guest molecules on the surface of the membrane. Sasaki *et al.* demonstrated that, by using the lipid having a crown ether moiety (**25**), the clustering of lipid molecules in membranes can be controlled in response to the addition of external metal ions.[26]

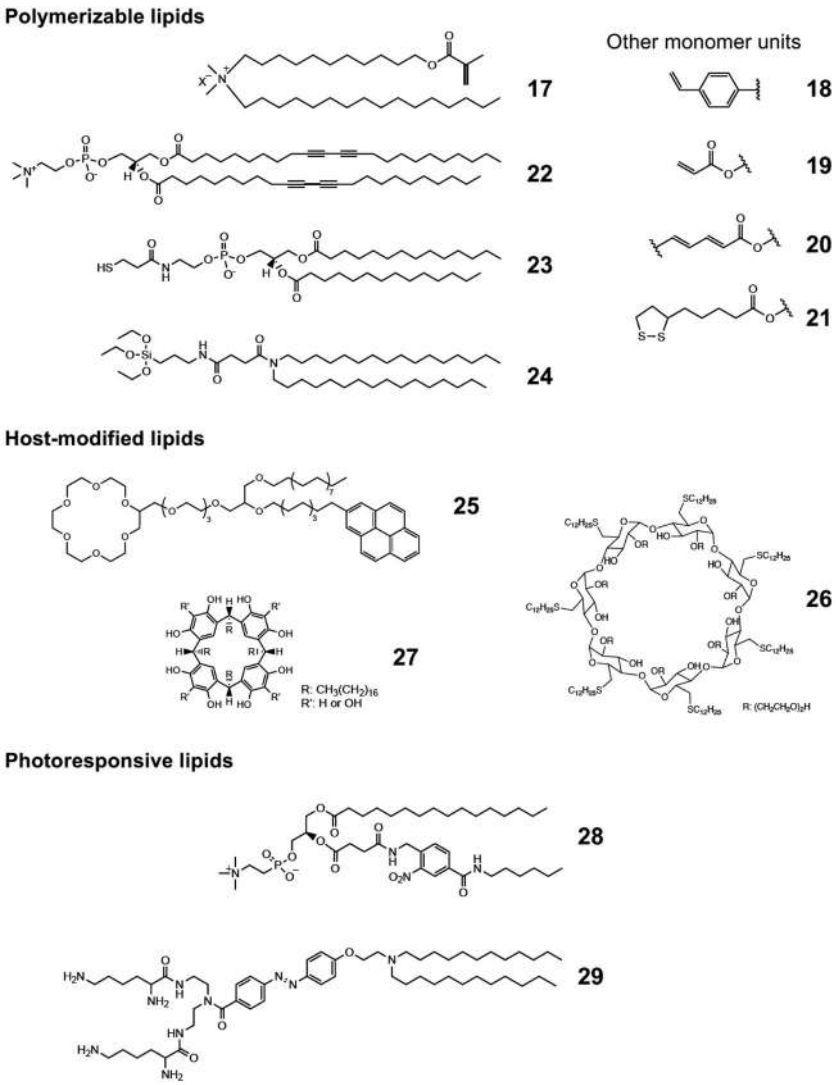

Figure 16.4 Chemical structures of functional lipids.

As other examples of host molecules, cyclodextrins (**26**)[27] and calixarenes (**27**)[28] have been also introduced to design the functional lipids for the recognition of guest molecules. Functional membranes responding to light irradiation have been also developed. Vesicles containing phospholipid analogues with nitrobenzyl group (**28**) in the hydrophobic chain can release the encapsulated molecules in response to light irradiation.[29] The photo-induced cleavage of the nitrobenzyl group produces bilayer-deforming lysolipid with a single hydrophobic chain, resulting in the destabilisation of the lipid membrane.

An azobenzene-modified lipid molecule (**29**) dynamically changes the morphology of the lipid membrane in response to light irradiation due to *trans*-to-*cis* conformational transition. The azobenzene-incorporated lipids achieved dynamic deformation of membrane morphology such as the opening and closing of a vesicle can be reversibly triggered by the irradiation of light.[30]

To date, a large number of amphiphilic molecules have been developed that are capable of mimicking not only the structures but also the functions of biological membranes in nature. Such a family of synthetic lipids can be utilised as a molecular platform of functional materials for desired purposes.

16.3 Architecture and Features of Membrane Mimetic Supramolecular Assembly

Natural and synthetic lipid molecules are known to adopt a variety of assembled structures depending on their molecular structure, composition, and preparation method. In this section, we will introduce the major architectures of molecular assemblies formed by lipids such as vesicle, nanodisc, and lipid cubic phase. Here, we describe the structural features, preparation procedure and applications of each lipid-based molecular assembly.

16.3.1 Vesicles

Vesicle is a general term for a hollow structure formed by membranes of amphiphilic molecules (Figure 16.5). The history of vesicle research began with Bangham's study on the electron microscopy of liposomes formed by egg yolk phospholipids.[31] After his finding, vesicles have been widely studied as the most common molecular assembly consisting of a lipid bilayer.[32] Vesicles can be classified according to the difference in their morphology. Specifically, vesicles having onion-like stacked multiple layers are named multilamellar vesicles (MLV). On the other hand, vesicles formed by a single membrane are called small unilamellar vesicles (SUV) or large unilamellar vesicles (LUV) depending on their size. Cell-sized giant vesicles (GV) that enable the direct observation of membrane morphology and phase-separated domains by an optical microscope have been also extensively investigated recently.[33]

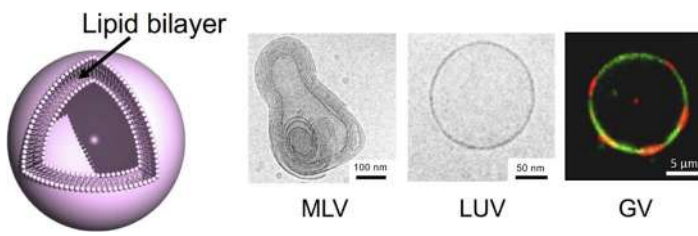

Figure 16.5 Schematic image of a vesicle and microscopic images of MLV, LUV and GV.

Since membrane-forming amphiphiles are generally difficult to be dissolved in water, appropriate methods are available to form the dispersion of vesicles. The essential method for vesicle formation is the hydration of lipid films.[34] First of all, lipid molecule is dissolved in an organic solvent such as chloroform and methanol and dried to form a thin lipid film in a sample tube. The suspension of MLVs is produced by the addition of aqueous solution to the obtained dry film of lipid and subsequent mechanical agitation. Since as-prepared MLVs have a large distribution in terms of membrane lamellarity and particle size, the uniform LUVs are prepared by multiple cycles of the freeze-thawing process that increases the size of vesicles and the following extrusion through a polycarbonate filter with defined pores. As an alternative method, irradiation of ultrasonic to MLV suspension produces SUVs with a diameter of several tens of nanometres. Other than the hydration of lipid films, several methods are also available for the preparation of vesicles. The reversed-phase evaporation method produces vesicles by the evaporation of the organic solvent from the water-in-oil emulsion containing lipids.[35] Also, SUVs are formed by the injection of the lipid dissolved in polar water-miscible organic solvents such as ethanol.[36] For the encapsulation of water-soluble molecules inside the vesicles, an aqueous solution of the entrapping molecules is employed to hydrate the lipid film. The untrapped excess molecules in the outer aqueous phase are further removed by gel filtration. Since cell-sized GVs are more fragile compared to MLVs and LUVs, their preparation requires a special technique. The simplest method of GVs preparation is the gentle and slow hydration of a lipid film by an aqueous solution without any mechanical stimulation.[37] This method generally takes several hours to overnight to produce GVs and yields various sizes of giant vesicles with multiple layers. The electroformation method became a common technique for the preparation of uniform GVs.[38] In this method, a dry thin film of lipid deposited on an indium tin oxide (ITO) electrode or platinum wire is swollen by applying an AC electric field in the water. The electroformation method has several advantages compared to the conventional gentle hydration method. This technique can form large, relatively monodisperse giant vesicles in a short time. In addition, the vesicles formed by the electroformation are immobilised on the surface of the electrode, enabling easy subsequent manipulation. The GVs can be also prepared by an inverted emulsion method or droplet transfer method that produces GVs by the sedimentation of the water droplet surrounded by a layer of lipid formed in oil into an aqueous phase across the oil-water interface.[39] This method efficiently entraps hydrophilic molecules in GV and does not require the untrapped molecule. Also, GVs with an asymmetric membrane, which is frequently seen in natural cell membranes, can be produced by this method.[40]

By utilising the impermeable property of lipid bilayers, many applications of vesicles as nanometre-sized capsules such as drug delivery[41] and bio-nanoreactors[42] have been explored, and some of them have become available for practical use. In addition, molecular recognition on the surface of the vesicle can be utilised for analytical applications like sensors.[43] Next,

we introduce several examples of the use of vesicles as model cell membranes to analyse biomimetic synthetic molecules that function by the integration in lipid membranes.[44]

In natural cell membranes, water-soluble small molecules and ions are selectively transported across the membrane through the membrane transporters such as channels and pumps. To artificially simulate the membrane permeation mechanism mediated by channels, various efforts have been made to design synthetic molecules from the approach of supramolecular chemistry.[45] Various molecular frameworks have been employed for the synthesis of artificial channels so far. Several artificial channels were constructed on the linear and rigid molecular backbones such as the dimer of cholic acid[46] and oligo(*p*-phenylene).[47] Alternatively, cyclic host molecules such as crown ethers[48] and calixarenes[49] have been also employed to design a channel that mediates the penetration of guest molecules or ions. Recently, Muraoka and Kinbara *et al.* developed an artificial channel with multiple transmembrane domains by alternating hydrophobic and hydrophilic groups.[36] This artificial channel can control ion transport by recognising the binding of 2-phenylethylamine, a neurotransmitter. Vesicles are a suitable model membrane system for the quantitative evaluation of channel-mediated permeation of ions across the membrane. Ion permeation across the membrane can be evaluated using fluorescent probes entrapped in vesicles. 8-Hydroxypyrene-1,3,6-trisulphonic acid (HPTS) is a pH-responsive probe that is widely used to characterise ion permeation.[50] The HPTS entrapped vesicles were prepared with a pH gradient between inside and outside the vesicle. The efflux and influx of ions through the channel collapses the pH gradient, reflecting the change in the fluorescence spectrum of HPTS. The formation of large permeation pores or the disruption of the membrane can be monitored in a similar method by measuring the leakage of the fluorescent marker. For this leakage assay, fluorescent markers such as carboxyfluorescein and calcein are entrapped in vesicles at a high enough concentration to induce the quenching of their fluorescence.[51] When the permeability of the membrane is increased by pore formation or other perturbation of the membrane, the fluorescent marker is released from the vesicles. This leakage behaviour can be quantitatively monitored as a recovery of fluorescence intensity due to the dilution of the leaked marker in an outer aqueous phase. This technique has been applied to evaluate the action mechanism of antimicrobial peptides[52] and their synthetic mimics,[53] which act through the disruption of the cell membrane. The size of the membrane opening formed by the pore-forming agent can be estimated by using the macromolecular marker with a variety of molecular weights (*e.g.* fluorescein-conjugated dextran).[54]

In the signal transduction across the natural cell membrane, there is a pathway that does not accompany the transport of molecules. Receptor tyrosine kinase, a transmembrane receptor, associates into dimer in response to the binding of ligand molecules, resulting in the activation of enzymes inside the cell.[55] Artificial signal transduction systems by synthetic molecules have been developed to mimic such oligomerisation of

transmembrane receptors in the membrane. An artificial transmembrane receptor has been designed by employing cholesterol dimer as its rigid molecular framework.[56] This transmembrane receptor displays a thiol group on the outer surface of the membrane as a sensor unit. In the signalling pathway, the oxidative reaction outside the vesicle leads to the formation of disulfide bonds and dimerisation of the receptor molecule. The formation of the receptor dimer triggered by this oxidation reaction is transmitted to the inner leaflet of the membrane as the formation of another disulfide bond at the other terminal of the receptor molecule, resulting in the production of the output molecule as a leaving group. Similar transmembrane artificial receptors have been developed to recognise adrenaline[57] and diethylenetriamine[58] as external signals.

Membrane fusion and fission is a dynamic rearrangement of membrane structure that plays an important role in cell function. The fusion of lipid membrane can be assessed by fluorescence spectroscopy for lipid mixing and content mixing. Lipid mixing is commonly assessed by utilising the energy transfer between a pair of fluorescent lipids.[59] In this method, membranes incorporating a pair of energy donor and acceptor fluorophores are mixed with non-labelled vesicles. Upon the membrane fusion event, the average distance between the donor and the acceptor increases, resulting in the recovery of the donor fluorescence. For the evaluation of the mixing of the inner aqueous phase, a pair of the fluorescent probe and quencher such as 8-aminonapthalene-1,3,6-trisulfonicacid(ANTS)/*p*-xylene-bis-pyridiniumbromide (DPX) can be employed.[60] In this assay, vesicles entrapping each kind of molecule are separately prepared. Membrane fusion of two vesicles with different content results in the quenching of fluorescence due to the collision of the fluorophore with the quencher. The induction of membrane fusion has been also investigated by designed artificial molecules. The SNARE protein is a molecular machinery involved in vesicle transport that mechanically attracts two lipid bilayers by forming a bundle of alpha-helices to induce membrane fusion.[61] Inspired by the mechanism of SNARE protein, Hook *et al.* constructed an artificial membrane fusion system based on DNA hybridisation.[62] They designed a DNA molecule conjugated with a cholesteryl group at the terminal for immobilisation in lipid membranes. The formation of a double-strand between DNAs with complementary sequences presented on the vesicular surface mechanically attracts the two lipid membranes and induces membrane fusion. For the evaluation of membrane fission events, the direct observation of GVs by microscopy is a promising approach. Sugawara *et al.* reported a unique artificial cell system that shows autonomous membrane division and proliferation.[63] In this system, the growth and subsequent division of the lipid bilayer can be induced in conjunction with DNA replication by polymerase chain reaction in vesicles, realising a primitive cell division by completely artificial molecular components. The water-soluble lipid precursor is hydrolysed by the catalyst bound to the DNA surface to produce membrane-forming lipids. The obtained lipid molecules are spontaneously incorporated into the membrane to increase its surface area.

The time-dependent morphological change of the GVs was visualised by phase-contrast microscopy to discuss the dynamic process of membrane division.

Membrane-incorporated synthetic molecular machinery featured here is expected to provide a functional element for the development of an artificial cell system that simulates the sophisticated and complex functions of living cells. We expect vesicles would continuously attract attention due to their potential as a platform for the integration of complex molecular systems.

16.3.2 Lipid Nanodiscs

Lipid nanodiscs are the smallest molecular assemblies with a lipid bilayer structure (Figure 16.6). Lipid nanodiscs have been used as model membranes for the analysis of various membrane-associated molecules, including membrane proteins because of their homogeneity and stability in aqueous solutions. Nanodiscs provide a particularly useful platform for spectroscopy, where vesicle systems have a limitation by their particle size and heterogeneity. Here, we introduce several approaches for the formation of lipid nanodiscs.

Bicelles or bilayered micelles are discoidal lipid membranes that are formed by a mixture of two lipids with significantly different hydrophobic chain lengths.[64] Among the various bicelle-forming compositions of lipids, the binary mixture of 1,2-dimyristoyl-*sn*-glycero-3-phosphorylcholine (DMPC) and 1,2-dihexaoyl-*sn*-glycero-3-phosphorylcholine (DHPC) have been well investigated. DMPC, a long-chain phospholipid, forms the planar part of the bicelle, while DHPC, a short-chain phospholipid, forms the edge. Several approaches have been reported to form bicelles using artificial lipids other than natural phospholipids. Zemb *et al.* reported the formation

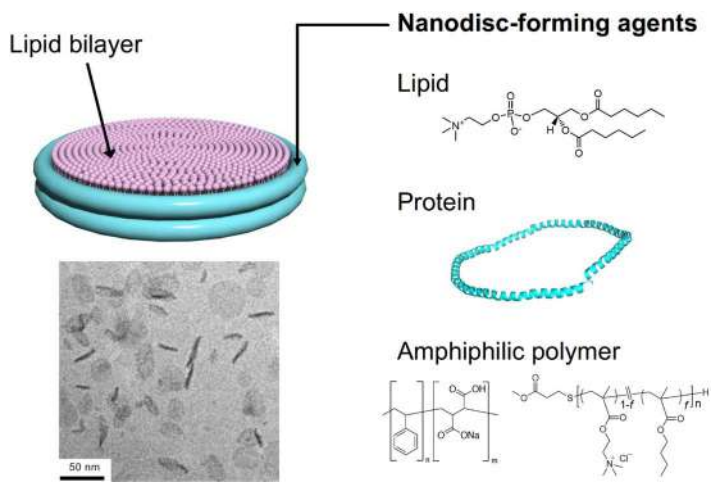

Figure 16.6 Nanodisc formation by various agents and TEM image of nanodisc.

of bicelles by a catanionic binary mixture of myristic acid and cetyltrimethylammonium bromide.[65] It has also been reported that bicelles can be formed using PEG-modified phospholipids[66] and 3-[(3-cholamidopropyl) dimethylammonio]-2-hydroxy-1-propanesulfonate (CHAPSO),[67] a derivative of cholic acid, instead of short-chain DHPC. Several attempts have been previously made to functionalise bicelles using synthetic lipids. Yasuhara and Kikuchi *et al.* reported that bicelles with ceramic-like cross-linked surfaces can be formed by using synthetic lipid with triethoxysilyl groups.[68] By introducing a ceramic layer, the discoidal structure of the bicelles can be stably maintained even under dry conditions and in the presence of surfactants, whereas conventional phospholipid bicelles hardly maintained their structure. In addition, the introduction of the cross-linked structure suppresses the collapse of the discoidal assembly due to the gel-to-liquid crystalline phase transition of the lipid bilayer, enabling the nanodiscs with high thermal stability.[69] Contribution of the cross-linked structure to enhance the thermal stability was also reported in the bicelles formed with methacrylate group-modified cholic acid derivatives.[70] Bicelles are known to respond to external magnetic fields in a size-dependent manner. Specifically, large bicelles are oriented to the magnetic field, whereas small bicelles are known to be isotropic to the field due to fast tumbling in solution. Taking advantage of this feature, membrane proteins and bioactive molecules have been extensively analysed using solid-state NMR. The incorporation of biphenyl-modified phospholipid[71] and metal-chelating lipid[72] in a bicelle modulates the response against a magnetic field that provides a suitable tool for NMR measurements. The application of bicelles is not only for the analysis of membrane proteins but also as drug carriers[73] and templates for the synthesis of anisotropic nanomaterials.[74]

Some membrane-binding proteins are known to be able to form nanodiscs when assembled with lipid bilayers. High-density lipoprotein (HDL) is a complex formed by lipid molecules and apolipoproteins that transport cholesterol *in vivo* system. HDLs are known to form disc-like molecular aggregates in the initial stages of their pathway.[75] By the structural modification of HDL-forming apolipoprotein A–I, Sligar *et al.* developed a membrane scaffolding protein (MSP) that produces nanodiscs with lipid molecules.[76] MSP is a protein composed of multiple amphipathic α-helices where hydrophobic amino acid residues are aligned on the lipid-facing side and hydrophilic amino acid residues are localised on the water-facing side. These amphipathic α-helices cover the hydrophobic edge of the lipid bilayer to stabilise nanodiscs. The size of the nanodiscs formed by MSPs can be controlled by changing the number of amphiphilic α-helices in a protein.[77] Several MSP mutants capable of forming discs with diameters of 9.8–12.9 nm have been developed. It is also found that nanodiscs can be formed not only by the full-length MSPs but also by shorter fragment peptides of Apo A–I and their oligomers.[78] These studies suggested that the amphiphilic α-helix is an essential structure in the design of proteins that form nanodiscs by interacting with lipid molecules.

Previously, several synthetic polymer-based attempts have been made for the preparation of nanodiscs. Watts *et al.* developed membrane-active styrene-maleic acid copolymer (SMA), which can form nanodiscs with a variety of lipid compositions including intact cell membranes.[79] A similar polymer with a diisobutylene group as hydrophobic moiety (DIBMA) is also known to be capable of forming nanodiscs like SMA.[80] DIBMA does not show strong absorption in the UV region whereas SMA has an absorption band (280 nm) originated in styrene. Ramamoorthy *et al.* have designed several SMA derivatives with different hydrophilic groups, which can provide nanodiscs with different surface charges that can minimise the unexpected interaction with incorporated membrane proteins.[81] SMA-based nanodiscs have been extensively applied to the analysis of various membrane proteins.[82] As another nanodisc-forming polymer, Yasuhara *et al.* have designed amphiphilic polymethacrylate random copolymers with ammonium terminals on the hydrophilic side chains and butyl groups as hydrophobic side chains.[83] This polymer spontaneously forms uniform lipid nanodiscs through the fragmentation of the lipid membrane. There are several advantages with the polymethacrylate nanodisc-forming polymer; (1) Since the methacrylate molecular framework does not show significant absorption in the UV-visible region, a variety of spectroscopies including absorption, fluorescence, and circular dichroism (CD) can be used for the analysis of membrane-associated molecules. (2) The size of nanodisc is tunable in a range of 8–20 nm by changing the ratio between lipid and polymer (3) It is easy to modify the degree of polymerisation, monomer structure, and composition. (4) A variety of functional groups can be quantitatively introduced to the polymer terminal using a chain transfer agent. Using nanodiscs formed by polymethacrylate derivatives, membrane-associated amyloid proteins such as islet amyloid polypeptide[83] and amyloid-β[84] were analysed by CD and fluorescence spectroscopy. These polymer-based synthetic techniques spontaneously produce uniform nanodiscs by simply mixing the polymer with natural or artificial cell membranes. This feature eliminates the use of detergents, which sometimes cause the denaturation of membrane proteins in contrast to the conventional techniques for the reconstitution of membrane proteins.

As described above, lipid nanodiscs have attracted much attention as a tool for exploring the functions of biological membranes, including reconstitution platform for the analysis of membrane proteins. In the future, further progress is expected not only in the field of biology but also in materials and energy applications.

16.3.3 Lipid Cubic Phase

The lipid cubic phase is a porous lyotropic liquid crystal with a specific regular nano-structure consisting of a three-dimensionally curved lipid bilayer and interpenetrated water nano-channels. Three major types of bicontinuous structures with different degrees of branching of water channels have

been found, which are known as double gyroid, double diamond, and double primitive cubic structures possessing water nano-channels with 3, 4 or 6-way junctions (Figure 16.7).

The structure of bicontinuous lipid cubic phases was firstly investigated by X-ray diffraction by Luzzati *et al.* in the 1960s.[85] After their finding, structural analyses of lipid cubic phase have been carried out for various natural or synthetic lipids such as monoolein (MO), glycolipids, and cationic lipids.[86] Considering the curvature of lipid membranes, the lipid cubic phase consists of saddle-shaped bilayers, showing zero mean curvature and negative Gaussian curvature at any points.[87] The lipid cubic phase is known to be formed in limited conditions because the organisation of lipids is strongly affected by the temperature and water content. Specifically, the lipid cubic phase exists between lamellar and inverse hexagonal phases which possess flat or negatively curved lipid membranes, respectively. Among various lipid cubic phase-forming amphiphiles, MO is the most well-studied lipid that forms lamellar, gyroid and diamond structures depending on the conditions of preparation.[88] The phase complexity is one of the essential characteristics of lipid lyotropic liquid crystals systems that contribute to providing unique functionalities.

As the most major application, the lipid cubic phase has been employed as a crystallisation medium for membrane proteins. Rosenbusch *et al.* firstly succeeded in crystallising bacteriorhodopsin (bR) incorporated in a lipid cubic phase.[89] This *meso*-crystallisation method induced a breakthrough in the structural analysis of membrane proteins. Since the lipid cubic phase can crystallise a variety of membrane proteins by choosing an appropriate lipid, more than 10% of membrane protein registered in the Protein Data Bank was crystallised by this method. Recently, Mezzenga *et al.* designed a cubic phase with a larger water channel than that of the conventional MO

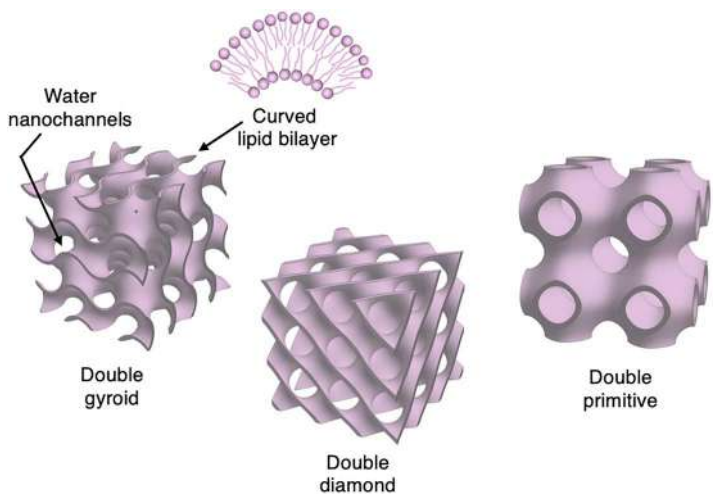

Figure 16.7 Structure of lipid cubic phases classified by their geometry.

cubic phase by the mixture of distearoyl phosphatidylglycerol and monopalmitolein. This system enabled the crystallisation of the Gloeobacter ligand-gated ion channel with a large extracellular domain that is difficult to fit into the nano-channels of the conventional cubic phase.[90]

The lipid cubic phase provides an excellent medium for the encapsulation of proteins to fabricate functional materials such as immobilised enzymes. Mezzenga *et al.* reported the immobilisation of fructose dehydratase (FDH) to the lipid cubic phase consisting of monolinoolein.[91] After immobilisation, the membrane-bound FDH fully maintained its enzymatic activity for 5 days, suggesting that the lipid cubic phase provides an ideal local environment for the membrane-bound enzyme. The lipid cubic phase can encapsulate not only membrane proteins but also hydrophilic water-soluble proteins. The incorporation of D-fructose-6-phosphate aldolase, a class-I aldolase, into the lipid cubic phase enhances its enzymatic activity and stability.[92] This improved enzymatic performance in the lipid cubic phase is thought to be originated in the increased accessibility of the catalytic reaction centre to substrates. Another example is the immobilisation of composite of lipid cubic phase and redox enzymes such as glucose and pyranose oxidases on electrodes.[93] This system allows the electrochemical switching of the redox reaction of the enzyme on the electrode surface, enabling sensing and biofuel applications.

The cubic phase is also widely used as a template for the fabrication of porous materials. Porous organic zeolite-like materials have been constructed by the polymerisation of synthetic lipids in the cubic phase.[20] Other porous materials, such as mesoporous metallic materials, have been developed through redox reactions of metal ions in regular nanochannels.[94] The lipid cubic phase can be also applied to biological or medicinal applications. The lipid cubic phase can efficiently entrap hydrophilic and hydrophobic molecules in the water channel and bilayer, respectively. Moreover, a stimuli-responsive structural transition of the lipid cubic phase opens its application as cargo for drug delivery systems. Mezzenga *et al.* reported the controlled drug transport and release utilising pH-induced phase transition of cubic phase.[95] They demonstrated that a double primitive cubic phase composed of the mixture of monolinoline-linolenic acid undergoes a pH-induced phase transition upon acidification to form an inverse hexagonal structure, resulting in the inhibition of the spontaneous release of incorporated hydrophobic molecules. For the injection and delivery of lipid cubic phases *in vivo*, it is important to formulate the stable dispersion of the lipid cubic phase in diluted conditions. Cubosome, which is a nanoparticle encompassing lipid cubic phase,[96] is a promising material for delivery application.[97] Colloidal stability of the cubosome is achieved by the addition of amphiphilic polymers or proteins that work as dispersing agents.[98]

The lipid cubic phase provides soft material with a specific biomembrane-like regular nanoarchitecture. Their unique structure-originated functions, in particular porosity, softness, and affinity to biological molecules, expect to create promising materials that can be applied to versatile fields such as biology, material engineering, analytical chemistry, pharmacy, medicine, and food science.

16.4 Conclusion

In this chapter, we have described the molecular design, properties, and applications of amphiphiles that can produce cell membrane mimetic nanoarchitecture. Since this research field has been extensively investigated in the last five decades, a significant number of molecular components were designed and utilised to simulate the characteristics of biomembranes. As an ultimate goal of this field, large efforts have been recently made to establish a completely artificial cell system by the integration of complex molecular machinery into a membrane.[99] The supramolecular chemistry-based approach for the creation of an artificial cell system expects to provide a deeper understanding of the origin of life. Furthermore, cell membrane mimetic materials would provide a foundation for novel environmentally-friendly technologies.

Acknowledgements

The authors are grateful to Ms Sakiko Fujita and Ms Tomoko Ohno of Nara Institute of Science and Technology for the cryo-TEM observation. The authors also thank Ms Kanako Hirata and Mr Shohei Miki, alumni of Nara Institute of Science and Technology for providing the microscopic images of the giant vesicle and lipid nanodiscs, respectively.

References

1. R. B. Gennis, *Biomembranes: Molecular Structure and Function*, Springer-Verlag, New York, 1989.
2. J. Weber and A. E. Senior, *Biochim. Biophys. Acta, Bioenerg.*, 1997, **1319**, 19.
3. T. Harayama and H. Riezman, *Nat. Rev. Mol. Cell Biol.*, 2018, **19**, 281.
4. J. N. Israelachvili, *Intermolecular and Surface Forces*, Elsevier Academic Press, Amsterdam, 3rd edn, 2017.
5. T. Kunitake and Y. Okahata, *J. Am. Chem. Soc.*, 1977, **99**, 3860.
6. T. Kunitake, *Angew. Chem., Int. Ed. Engl.*, 1992, **31**, 709.
7. S. Segota and D. Tezak, *Adv. Colloid Interface Sci.*, 2006, **121**, 51.
8. E. W. Kaler, K. L. Herrington, A. K. Murthy and J. A. N. Zasadzinski, *J. Phys. Chem.*, 1992, **96**, 6698.
9. K. Morigaki and P. Walde, *Curr. Opin. Colloid Interface Sci.*, 2007, **12**, 75.
10. A. Fuhrhop and T. Wang, *Chem. Rev.*, 2004, **104**, 2901.
11. G. H. Escamilla and G. R. Newkome, *Angew. Chem., Int. Ed. Engl.*, 1994, **33**, 1937.
12. T. Kunitake, Y. Okahata, M. Shimomura, S. Yasunami and K. Takarabe, *J. Am. Chem. Soc.*, 1981, **103**, 5401.
13. N. Nagata, S. Kugimiya and Y. Kobuke, *Chem. Commun.*, 2001, 689.
14. Y. Ishikawa, H. Kuwahara and T. Kunitake, *J. Am. Chem. Soc.*, 1994, **116**, 5579.
15. S. Zhou, C. Burger, B. Chu, M. Sawamura, N. Nagahama, M. Toganoh, U. Hackler, H. Isobe and E. Nakamura, *Science*, 2001, **291**, 1944.
16. J. Lefley, C. Waldron and C. R. Becer, *Polym. Chem.*, 2020, **11**, 7124.

17. N. Warren and S. Armes, *J. Am. Chem. Soc.*, 2014, **136**, 10174.
18. A. Koide, A. Kishimura, K. Osada, W. Jang, Y. Yamasaki and K. Kataoka, *J. Am. Chem. Soc.*, 2006, **128**, 5988.
19. S. Regen, B. Czech and A. Singh, *J. Am. Chem. Soc.*, 1980, **102**, 6638.
20. A. Mueller and D. F. O'Brien, *Chem. Rev.*, 2002, **102**, 727.
21. D. S. Johnston, S. Sanghera, M. Pons and D. Chapman, *Biochim. Biophys. Acta*, 1980, **602**, 57.
22. S. L. Regen, *Biochemistry*, 2020, **59**, 4617.
23. K. Katagiri, M. Hashizume, K. Ariga, T. Terashima and J. Kikuchi, *Chem. - Eur. J.*, 2007, **13**, 5272.
24. J. Kikuchi and K. Yasuhara, *Advances in Biomimetics*, ed. A. George, IntechOpen, Rijeka, 2011, p. 231.
25. K. Katagiri, R. Hamasaki, K. Ariga and J. Kikuchi, *J. Am. Chem. Soc.*, 2002, **124**, 7892.
26. D. Y. Sasaki, T. A. Waggoner, J. A. Last and T. M. Alam, *Langmuir*, 2002, **18**, 3714.
27. B. Ravoo, J. Jacquier and G. Wenz, *Angew. Chem., Int. Ed.*, 2003, **42**, 2066.
28. Y. Tanaka, M. Miyachi and Y. Kobuke, *Angew. Chem., Int. Ed.*, 1999, **38**, 504.
29. A. Bayer, S. Alam, S. Mattern-Schain and M. Best, *Chem. - Eur. J.*, 2014, **20**, 3350.
30. T. Hamada, R. Sugimoto, M. Vestergaard, T. Nagasaki and M. Takagi, *J. Am. Chem. Soc.*, 2010, **132**, 10528.
31. A. D. Bangham and R. W. Horne, *J. Mol. Biol.*, 1964, **8**, 660.
32. A. Akbarzadeh, R. Rezaei-Sadabady, S. Davaran, S. W. Joo, N. Zarghami, Y. Hanifehpour, M. Samiei, M. Kouhi and K. Nejati-Koshki, *Nanoscale Res. Lett.*, 2013, **8**, 102.
33. R. Dimova and C. M. Marques, *The Giant Vesicle Book*, CRC Press, Boca Raton, 2020.
34. H. Zhang, *Methods Mol. Biol.*, 2017, **1522**, 17.
35. F. Szoka and D. Papahadjopoulos, *Proc. Natl. Acad. Sci. U. S. A.*, 1978, **75**, 4194.
36. C. Jaafar-Maalej, R. Diab, V. Andrieu, A. Elaissari and H. Fessi, *J. Liposome Res.*, 2010, **20**, 228.
37. P. Mueller, T. F. Chien and B. Rudy, *Biophys. J.*, 1983, **44**, 375.
38. M. Angelova and D. Dimitrov, *Faraday Discuss.*, 1986, **81**, 303.
39. S. Pautot, B. Frisken and D. Weitz, *Langmuir*, 2003, **19**, 2870.
40. S. Pautot, B. Frisken and D. Weitz, *Proc. Natl. Acad. Sci. U. S. A.*, 2003, **100**, 10718.
41. T. M. Allen and P. R. Cullis, *Adv. Drug Delivery Rev.*, 2013, **65**, 36.
42. P. Walde and S. Ichikawa, *Biomol. Eng.*, 2001, **18**, 143.
43. F. Mazur, M. Bally, B. Stadler and R. Chandrawati, *Adv. Colloid Interface Sci.*, 2017, **249**, 88.
44. A. Barba-Bon, M. Nilam and A. Hennig, *ChemBioChem*, 2020, **21**, 886.
45. T. M. Fyles, *Chem. Soc. Rev.*, 2007, **36**, 335.
46. Y. Kobuke and T. Nagatani, *J. Org. Chem.*, 2001, **66**, 5094.

47. M. M. Tedesco, B. Ghebremariam, N. Sakai and S. Matile, *Angew. Chem., Int. Ed.*, 1999, **38**, 540.
48. A. Nakano, Q. S. Xie, J. V. Mallen, L. Echegoyen and G. W. Gokel, *J. Am. Chem. Soc.*, 1990, **112**, 1287.
49. V. Sidorov, F. W. Kotch, G. Abdrakhmanova, R. Mizani, J. C. Fettinger and J. T. Davis, *J. Am. Chem. Soc.*, 2002, **124**, 2267.
50. N. Clement and J. Gould, *Biochemistry*, 1981, **20**, 1534.
51. Y. Nagawa and S. L. Regen, *J. Am. Chem. Soc.*, 1992, **114**, 1668.
52. K. Matsuzaki, O. Murase and K. Miyajima, *Biochemistry*, 1995, **34**, 12553.
53. S. G. Hovakeemian, R. H. Liu, S. H. Gellman and H. Heerklotz, *Soft Matter*, 2015, **11**, 6840.
54. A. S. Ladokhin, M. E. Selsted and S. H. White, *Biophys. J.*, 1997, **72**, 1762.
55. J. Schlessinger, *Cell*, 2000, **103**, 211.
56. P. Barton, C. A. Hunter, T. J. Potter, S. J. Webb and N. H. Williams, *Angew. Chem., Int. Ed.*, 2002, **41**, 3878.
57. T. Schrader, M. Maue and M. Ellermann, *J. Recept. Signal Transduction*, 2006, **26**, 473.
58. K. Bernitzki, M. Maue and T. Schrader, *Chem. - Eur. J.*, 2012, **18**, 13412.
59. D. K. Struck, D. Hoekstra and R. E. Pagano, *Biochemistry*, 1981, **20**, 4093.
60. H. Ellens, J. Bentz and F. C. Szoka, *Biochemistry*, 1985, **24**, 3099.
61. T. Weber, B. V. Zemelman, J. A. McNew, B. Westermann, M. Gmachl, F. Parlati, T. H. Sollner and J. E. Rothman, *Cell*, 1998, **92**, 759.
62. G. Stengel, R. Zahn and F. Hook, *J. Am. Chem. Soc.*, 2007, **129**, 9584.
63. K. Kurihara, M. Tamura, K. Shohda, T. Toyota, K. Suzuki and T. Sugawara, *Nat. Chem.*, 2011, **3**, 775.
64. U. H. N. Durr, M. Gildenberg and A. Ramamoorthy, *Chem. Rev.*, 2012, **112**, 6054.
65. T. Zemb, M. Dubois, B. Deme and T. Gulik-Krzywicki, *Science*, 1999, **283**, 816.
66. E. Johansson, C. Engvall, M. Arfvidsson, P. Lundahl and K. Edwards, *Biophys. Chem.*, 2005, **113**, 183.
67. M. Li, H. Morales, J. Katsaras, N. Kucerka, Y. Yang, P. Macdonad and M. Nieh, *Langmuir*, 2013, **29**, 15943.
68. K. Yasuhara, S. Miki, H. Nakazono, A. Ohta and J. Kikuchi, *Chem. Commun.*, 2011, **47**, 4691.
69. K. Yasuhara, H. Hayashi and J. Kikuchi, *Chem. Lett.*, 2012, **41**, 1223.
70. R. Matsui, M. Ohtani, K. Yamada, T. Hikima, M. Takata, T. Nakamura, H. Koshino, Y. Ishida and T. Aida, *Angew. Chem., Int. Ed.*, 2015, **54**, 13284.
71. C. Loudet, A. Diller, A. Grelard, R. Oda and E. J. Dufourc, *Prog. Lipid Res.*, 2010, **49**, 289.
72. K. Yamamoto, J. D. Xu, K. E. Kawulka, J. C. Vederas and A. Ramamoorthy, *J. Am. Chem. Soc.*, 2010, **132**, 6929.
73. L. Barbosa-Barros, G. Rodriguez, C. Barba, M. Cocera, L. Rubio, J. Estelrich, C. Lopez-Iglesias, A. de la Maza and O. Lopez, *Small*, 2012, **8**, 807.
74. S. Tekobo and E. Pinkhassik, *Chem. Commun.*, 2009, 1112.

75. T. M. Forte, A. V. Nichols, E. L. Gong, S. Lux and R. I. Levy, *Biochim. Biophys. Acta, Lipids Lipid Metab.*, 1971, **248**, 381.
76. I. G. Denisov and S. G. Sligar, *Chem. Rev.*, 2017, **117**, 4669.
77. I. G. Denisov, Y. V. Grinkova, A. A. Lazarides and S. G. Sligar, *J. Am. Chem. Soc.*, 2004, **126**, 3477.
78. Y. N. Zhao, T. Imura, L. J. Leman, L. K. Curtiss, B. E. Maryanoff and M. R. Ghadiri, *J. Am. Chem. Soc.*, 2013, **135**, 13414.
79. M. C. Orwick, P. J. Judge, J. Procek, L. Lindholm, A. Graziadei, A. Engel, G. Grobner and A. Watts, *Angew. Chem., Int. Ed.*, 2012, **51**, 4653.
80. A. O. Oluwole, B. Danielczak, A. Meister, J. O. Babalola, C. Vargas and S. Keller, *Angew. Chem., Int. Ed.*, 2017, **56**, 1919.
81. T. Ravula, N. Z. Hardin, G. M. Di Mauro and A. Ramamoorthy, *Eur. Polym. J.*, 2018, **108**, 597.
82. J. M. Dorr, S. Scheidelaar, M. C. Koorengevel, J. J. Dominguez, M. Schafer, C. A. van Walree and J. A. Killian, *Eur. Biophys. J. Biophys. Lett.*, 2016, **45**, 3.
83. K. Yasuhara, J. Arakida, T. Ravula, S. Ramadugu, B. Sahoo, J. Kikuchi and A. Ramamoorthy, *J. Am. Chem. Soc.*, 2017, **139**, 18657.
84. B. R. Sahoo, T. Genjo, M. Bekier, S. J. Cox, A. K. Stoddard, M. Ivanova, K. Yasuhara, C. A. Fierke, Y. Z. Wang and A. Ramamoorthy, *Chem. Commun.*, 2018, **54**, 12883.
85. V. Luzzati, A. Tardieu, T. Gulik-Krzywicki, E. Rivas and F. Reiss-Husson, *Nature*, 1968, **220**, 485.
86. K. Fontell, *Colloid Polym. Sci.*, 1990, **268**, 264.
87. S. M. Gruner, *J. Phys. Chem.*, 1989, **93**, 7562.
88. H. Qiu and M. Caffrey, *Biomaterials*, 2000, **21**, 223.
89. E. M. Landau and J. P. Rosenbusch, *Proc. Natl. Acad. Sci. U. S. A.*, 1996, **93**, 14532.
90. A. Zabara, J. T. Y. Chong, I. Martiel, L. Stark, B. A. Cromer, C. Speziale, C. J. Drummond and R. Mezzenga, *Nat. Commun.*, 2018, **9**, 544.
91. W. Sun, J. J. Vallooran, W. K. Fong and R. Mezzenga, *J. Phys. Chem. Lett.*, 2016, **7**, 1507.
92. T. Zhou, J. J. Vallooran, S. Assenza, A. Szekrenyi, P. Clapés and R. Mezzenga, *ACS Catal.*, 2018, **8**, 5810.
93. E. Nazaruk and R. Bilewicz, *Bioelectrochemistry*, 2007, **71**, 8.
94. S. Akbar, J. M. Elliott, M. Rittman and A. M. Squires, *Adv. Mater.*, 2013, **25**, 1160.
95. R. Negrini and R. Mezzenga, *Langmuir*, 2011, **27**, 5296.
96. J. Gustafsson, H. Ljusberg-Wahren, M. Almgren and K. Larsson, *Langmuir*, 1997, **13**, 6964.
97. J. Zhai, C. Fong, N. Tran and C. J. Drummond, *ACS Nano*, 2019, **13**, 6178.
98. D. Yang, B. Armitage and S. R. Marder, *Angew. Chem., Int. Ed.*, 2004, **43**, 4402.
99. B. C. Buddingh and J. C. M. van Hest, *Acc. Chem. Res.*, 2017, **50**, 769.

CHAPTER 17

Design of Nanostructured Lipid Carriers and Hybrid Lipid Nanoparticles

IGNACIO RIVERO BERTI[a], TANYA SINGH[b], TUGCE BOZTEPE[a], IGNACIO E. LEON[c], ASHOK KUMAR NADDA*[b] AND GUILLERMO R. CASTRO*[d]

[a]Laboratorio de Nanobiomateriales, CINDEFI, Departamento de Química, Facultad de Ciencias Exactas, Universidad Nacional de La Plata (UNLP) – CONICET (CCT La Plata), Calle 47 y 115, (B1900AJI), La Plata, Buenos Aires, Argentina; [b]Department of Biotechnology and Bioinformatics, Jaypee University of Information Technology, Waknaghat, Solan – 173 234, India; [c]Chemical Inorganic Center (CEQUINOR, UNLP, CONICET), School of Sciences, Universidad Nacional de La Plata (UNLP), Calle 47 y 115, (1900) La Plata, Argentina; [d]Max Planck Laboratory for Structural Biology, Chemistry and Molecular Biophysics of Rosario (MPLbioR, UNR-MPIbpC), Partner Laboratory of the Max Planck Institute for Biophysical Chemistry (MPIbpC, MPG), Centro de Estudios Interdisciplinarios (CEI), Universidad Nacional de Rosario, Maipú 1065, S2000 Rosario, Santa Fe, Argentina
*E-mail: grcastro@gmail.com, ashok.nadda09@gmail.com

17.1 Introduction

Hybrid lipid nanoparticles have become an attractive tool for drug delivery and various medical applications. The unique properties of these particles, such as physical stability, easier templating with biological molecules,

Nanoscience & Nanotechnology Series No. 55
Concepts and Design of Materials Nanoarchitectonics
Edited by Omar Azzaroni and Katsuhiko Ariga

Published by the Royal Society of Chemistry, www.rsc.org

enzymes, DNA, RNA, peptides, and compatibility under a wide range of physicochemical conditions, have made them a suitable tool for various pharmacological applications. Liposomes or polymeric structures, including particles, membranes, are not very much efficient to deliver the therapeutic molecules as compared to hybrid lipid nanoparticles since they are thermodynamically unstable. The design and development of antibiotic-conjugated lipid nanoparticles have been reported for the efficient distribution of many biocides at a cellular level.[1] Lipids and other hybrid lipid nanoparticles promise a great deal of accuracy whether they are administered orally or given as drugs. Lipid-based drugs control their release and reduce the absorption variation. Lipid nanoparticle-based drugs given for many diseases showed better efficacy, drug delivery speed, and visible effects in comparison to the free drugs.[2] Because of the biocompatibility of constituent materials and simple methods of formulation, they have an emerging impact on nanomedicine and research. Like all other prevalent systems, they also have the capability for focused drug delivery, triggered drug release, and improved drug efficacy. Yet, these nanoparticles also are less toxic and are an easy tool for large-scale production methods.[2]

Also, two widely used antibiotics, penicillin and levofloxacin, were conjugated with lipid nanoparticles, as reported in a previous paper. They showed various striking differences as the lipid-based antibiotics were able to eliminate up to 99.9% of the intracellular bacteria. This remarkable property proves the potential of solid lipid nanoparticles for *in vivo* applications.[1] Thus antibiotic-loaded lipid nanoparticles are comparatively more efficient in terms of their administration and reduced to a nonexistent relapse frequency level. These are also effective vehicles to fight against multidrug resistance in cancer cells.[3] For instance, edelfosine belongs to the class of alkyl phospholipids that were reported to display antitumor properties. The lipid nanoparticles containing edelfosine are more effective than their free counterparts. These hybrid lipid nanoparticles also prevent the numerous side effects that are generally caused by free drug administration.[4] This gives us a valuable insight into the detoxification capability of lipid nanostructures for various drugs. Edelfosine lipid nanoparticles given as conjugate drugs are more effective and can tame the drug resistance in leukemia and cancer cells.[3] The lipid-based nanoparticles have also proven to be effective in the treatment of nasopharyngeal carcinoma with significant recovery rates.[5] The treatment of nasal carcinoma using lipid nanoparticles and fusion peptides has proven to be effective to extend life with better quality in cancer patients.[5] The effectiveness of a certain drug is directly associated with the mode of drug administration. The use of smart polymers, hydrogels, and lipid particles has enabled the pharma industry to conclude that the potency of drugs remains unaffected. In the last decades, the development of advanced drug delivery systems, new targeted devices for various cancers, and experimental gene delivery models using solid lipid nanostructures, micelles, lipids, liposomes, which are entirely composed of biodegradable substances were reported.[6] In this

book chapter, the design, synthesis properties, and applications of various hybrid lipid nanoparticles have been elaborated in detail.

17.2 Solid Lipid Nanoparticles

In the pharmaceutical industry, solid lipid nanoparticles (SLNs) have been widely used to formulate products such as lotions, ointments, emulsions, *etc.* The high affinity of these materials for the lipid-rich intercellular space of the stratum corneum makes them ideal candidates for topical applications. Moreover, they are also being used as regular constituents of formulations such as soft or hard capsules or parenteral emulsions.[7] These SLNs are perfect crystal lipid matrices that are tiny, spherical particles used for accommodating the drugs or other molecules between fatty acid chains (see Figure 17.1a).[8] However, recent studies indicated that these particles also exist as disc-like or flat ellipsoidal shapes and can be used for other applications.[9,10]

Methods and techniques for the synthesis of SLNs can be summarized as follows: The dimension of SLNs ranges from 10 to 1000 nm.[11] They can be easily synthesized using nontoxic solvents under high-pressure homogenization or agitation under high speed. Several methods for their synthesis have been reported in the literature. These nanoparticles can be easily prepared in the absence of toxic organic solvents using techniques such as high-pressure homogenization or high-speed stirring.[12,13]

The nanoemulsions of SLNs have been widely prepared by using homogenization under high pressure. This technique was generally employed for large-scale synthesis of SLNs in which the lipid and matrix emulsion is purged through a homogenizer under high pressure.[14,15] A preheated surfactant emulsion has been homogenized simultaneously to get the final preparation of SLNs.[16,17]

Another cost-effective method for the preparation of SLNs is ultrasonication and agitation under high speed, which provides the mechanical forces to convert the lipid emulsion containing drug molecules into different-sized particles.[18] In the 1990s a microemulsion-based method was developed,[19] which has been applied by various researchers.[10,20] In this technique, the drug

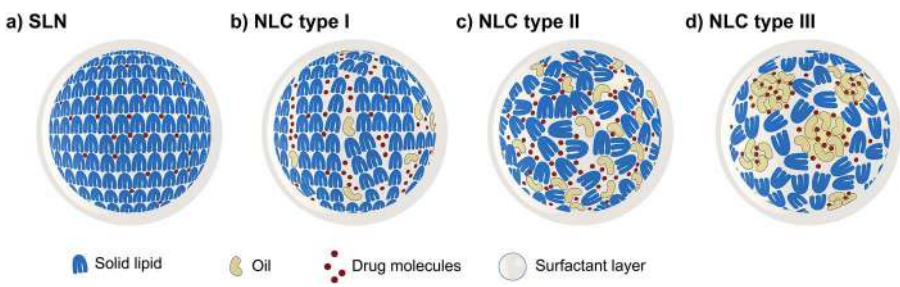

Figure 17.1 Types of SLNs.

is mixed with lipid in a molten state at a higher temperature than its melting temperature. The reaction mixture is subjected to continuous stirring that results in the formation of microemulsion.[21,22] A solvent-based emulsion diffusion method has also been used to prepare polymeric lipid nanoparticles.[23] In this technique, nonpolar solvents such as isopropyl acetate, ethyl acetate, benzyl alcohol, methyl acetate, and butyl lactate have been reported to dissolve the lipid and drug mixture.[24] The mixture is subjected to continuous stirring under controlled conditions, resulting in lipid precipitation. The solvent can be removed by freeze-drying techniques to yield the solid lipid nanocarriers with a molecule of our interest.

Similarly, a solvent-based emulsification evaporation method has also been employed to prepare SLNs using chloroform or cyclohexane.[25,26] In this method, a nanodispersion is prepared by mixing drug and lipid components in selected solvent on a rotary evaporator.[26,27] The solvent eventually evaporates, which results in the formation of solid lipid particle residues.

Another strategy was developed to encapsulate hydrophilic drugs and sensitive biomolecules such as protein, peptides, and antibodies with a double emulsion method.[28] In this method, a stabilizer and biomolecules are dissolved in water or an aqueous system, followed by mixing in lipid-containing organic solvent.[29–32] A temperature-induced phase inversion method using nonionic polyoxyethylene surfactants to prepare the SLNs has also been reported in previous studies.[33,34] A previous paper reported on a membrane contractor method to synthesize the solid lipid nanostructure by pressing the drug-lipid nanoemulsion against the porous membrane, leading to the formation of a small droplet, and these emulsion droplets were precipitated at low temperature in the solvent system.[35] SLNs were also produced using supercritical CO_2.[36] The particles formed using this method are quite uniform in shape and size and can be employed for therapeutic applications.[37] Besides, this coacervation method and the solvent extraction method have been used to synthesize the polymeric particles of lipid and drug molecules.[38,39] Thus, depending upon the type of drug, biomolecule, enzyme, or therapeutic agent, different methods can be employed for the synthesis of SLNs.

17.2.1 Application of SLNs

A relatively new field in nanotechnology is the application of lipid nanoparticles for the treatment of atherosclerosis. In this context, the nucleoside lipids were incorporated in SLNs and used for the treatment of atherosclerosis.[40] Also, the lipid particles modified using cations were utilized as nonviral vectors. The use of such nonviral vectors has not led to predisposing factors such as immunogenetics.[41] In a previous study cation-influenced solid lipid nanoparticle were used as a carrier for drug delivery. Several advantages of these SLNs, including easy production, relatively superior storage capability and large-scale production in pharmaceuticals, were reported.[42] The particles exhibited a lipid core with cationic lipids on their surface. These cationic

structures have been used to incorporate RNA and find their eminence within the range of nanotechnologies and drug-based gene delivery.

SLNs also have applications in the field of cancer therapy, which is the most frequent area of research using SLNs.[43] Another application of solid lipid nanoparticle was reported for the treatment of intracellular *Staphylococcus aureus*. Moreover, previous studies stated that instead of lipids, phospholipids help more efficiently to anchor the antibiotic to the bacterial membrane through its lipid part. For example, in a recent study penicillin G–phospholipid conjugated nanoparticles showed stronger and more effective antimicrobial activity against *S. aureus* than the penicillin G-lipid conjugate nanoparticles.[1] PEGylated lipid nanoparticles (polyethylene glycol covalently attached to lipid nanoparticles) were used to restrict the pathological effects of rheumatoid arthritis as they show a very good anti-inflammatory effect and reduce swelling by downgrading the levels of TNF-α and IL-1β.[42]

Furthermore, SLNs play a major role in the pharmaceutical industry. The reasons for their popularity are their biocompatibility, environment-friendly nature, methods of preparation, green synthesis, and low toxicity.[43] Lipid nanoparticles are amphipathic and act as a suitable carrier for both hydrophilic and lipophilic drugs that can be directed through different routes such as oral, ocular, brain drug delivery, parenteral, *etc.*[44] The current results of the pharmacological application have demonstrated that they are a very good drug delivery system. These SLNs are a safe and versatile system that can enhance drug efficacy along with the pharmacokinetic profile. Despite various advantages, the use of SLNs is still facing numerous challenges. At present, the commercial use of these SLNs has not been approved for several drugs due to insufficient loading of drugs for human dosage. Also, manufacturing SLNs at a large scale is not so easy. The physicochemical and microbiological stability of SLNs is another major challenge along with sterilization and tailoring strategies.[43] Overall, more in-depth research is needed to ensure the use of SLNs at a commercial scale.

17.3 Nanostructured Lipid Carriers

Nanostructured lipid carriers (NLCs) as a new system for drug delivery were developed in the 2000s and called the second generation of lipid nanoparticles. NLCs were the consequent evolution of SLNs to optimize lipid molecular delivery systems. Since SLNs are constituted by only solid lipids at room temperature, the process of incorporating active pharmaceutical ingredients (APIs) into de nanoparticles involves melting and mixing within the lipid, followed by the suspension cooldown and later dispersive techniques. Initially, the APIs are located in amorphous areas of the SLN such as in between the lipid layers and/or interacting directly with the fatty acid chains and the imperfections of the crystalline structure. However, the lipid nanoparticles start to form crystals and consequently, because of the high differences between free energies of lipid crystallization and the API-lipid interactions, the cargo molecule is squeezed out of the crystalline lipid structure. So, the

drug encapsulation efficiency for most of the SLNs is generally low because of cargo extrusion produced by the rearrangement of the crystalline lipid structure to move forward to a perfect lattice (*i.e.*, β-modification) over time. Additional drawbacks of SLNs are gelation during storage in the dispersed phase, and high-water content along with the synthesis, which could cause aggregation of a hydrophobic drug over the surface of the nanostructure, altering the profile of kinetic controlled release, and undesirable side effects. In the case of hydrophilic molecules, the presence of water surrounding the SLN can produce a partitioning effect, extracting the molecule from the lipid structure. Additionally, the chemical composition of lipid nanoparticles is very relevant since it directly affects the API interaction with the cells. SLNs are modifying the adsorption and/or triggering or not the membrane mechanism to incorporate the molecules within the cell. Typical examples of NLC administration are nasal, ocular, cutaneous, oral, and anal drug deliveries.[45–47]

The main components of NLCs are solid (*i.e.*, fats) and liquid (*i.e.*, oils) lipids stabilized with surface-active molecules and water. In the NLC, mixtures of lipid blends with different molecular structures, melting points involving liquid (*i.e.*, oils) and solid (*i.e.*, fatty acids, glycerides, steroids, and waxes) lipids at room temperature dislocate the rigid crystalline properties of SLNs. The amorphous liquid structure and solid–liquid interfaces inside the lipid nanoparticles are where generally most of the drugs can be located. Based on the physicochemical properties and concentrations of the lipids selected to synthesize the NLC, it can be classified as imperfect, amorphous, and multiple types (Figure 17.1). The classification is broadly generic and based on the amount of liquid lipid used for the synthesis of NLC. The imperfect type could contain more than one liquid lipid with dissimilar chemical composition (*i.e.*, glycerides with fatty acids of different chain lengths) but only in a small amount just to break the crystalline trend of the solid lipid. In such cases, the drugs could be found in the liquid lipids but also at the liquid–solid lipid interface.

The amorphous NLC contains a high concentration of drugs, and accordingly a high liquid lipid amount. The third one, called multiple NLC, contains the maximum concentration of liquid lipid allowed by the structural stability of the nanoparticle and determined by the solid lipid and the interactions of both lipid types. The multiple NLC contains the maximum API concentration in the nanostructure compatible with nanoparticle stability. Besides, multiple NLC types are more susceptible to environmental conditions.

Liquid lipids are generally esters or alcohols of fatty acids that are hydrophobic and excellent solvents for hydrophobic drugs.[48] However, there are three basic parameters to analyze before proceeding to the nanoparticle synthesis: the melting point and solubility of the oils in organic solvents, and the interaction between the oily molecule and the drug, which is generally done by spectroscopic methods. The most common liquid lipids used for NLC synthesis are oleic acid (*cis*-9-octadecenoic acid; C18 : 1) and medium-chain triglycerides, a saturated fatty acid mixture composed of hexanoic (C6 : 0, ≤ 2%),

octanoic (C8:0, 50–80%), decanoic (C10:0, 20–50%), dodecanoic (C12:0, ≤ 3%) and tetradecanoic (C14:0, ≤ 1%) acids, the latter two considered GRAS (generally regarded as safe) by the Food and Drug Administration (FDA, USA) and safe by the European Medicine Agency (EMA, EU). However, other liquid lipids were also reported for the synthesis of NLC such as isopropyl tetradecanoate, oleic oil ((9*Z*)-octadec-9-enoic acid), olive oil (99% triacylglycerols), and palm oil (approximately 50% saturated fatty acids, 40% oleic acid, and 10% polyunsaturated fatty acids), 2-octyl dodecanol, paraffin oil, and squalene, among others. Also, some liquid lipids are marketed such as decyl (*Z*)-octadec-9-enoate (Cetiol V®), 2-octanoylpropyl octanoate (Miglyol 840®), a mixture of MCT composed of octanoic and decanoic acids (Labrafac® lipophile WL 1349), lauroyl polyoxylglycerides (Gelucire® 44 or 14 Lipofen®), monoacylglycerol (Myverol 18–99 K), and soy lecithin (Epikuron™ 200 and Baycip®), for example.[49]

The choice of liquid lipid for the synthesis of NLC depends on the application. Particularly, decanoic, linoleic, and oleic acids showed improved penetration in topical and transdermal drug delivery uses.[50]

Additionally, as well as in SLN, other relevant components of NLCs are emulsifiers, which stabilize the nanoparticles dispersed in the aqueous phase, avoid coalescence, and protect structures against interfacial stresses. In general, emulsifiers are used in the range of 0.5% to 5.0% for lipid nanoparticle synthesis. Emulsifiers are a wide family of compounds with diverse physicochemical structures from charge, functional groups, chemical structure, molecular weight, and single molecules or complex blends, *etc.* A particular criterion to select emulsifiers is the hydrophile-lipophile balance (HLB). The HLB was defined considering the molecular weight and the ratio between hydrophilic and hydrophobic residues in the molecule.[51] Emulsifiers can be divided according to their sources into natural such as soy lecithin and bile acids, semisynthetic such as sodium cocoamphoacetate, or synthetic ones. Among the synthetic emulsifiers employed in lipid nanoparticle synthesis are poloxamers, a family of chemicals composed of triblock copolymers of hydrophobic polyoxypropylene (PPO) edged by two polyoxyethylene (PEO) hydrophilic groups (see Figure 17.2). The structure of PEO*x*–PPO*y*–PEO*x* with *x* and *y* number of monomers determines their HLB and different physicochemical properties such as cloud point, critical micelle concentrations, physical state (liquids, solids, and pastes at room temperature), *etc.* Poloxamers are currently available with different properties and brand names from BASF, Croda, Rhodia, *etc.* Many poloxamers were FDA approved for use in cosmetics, pharmaceutical applications, and tissue engineering.[52]

Poloxamines are a recent family of emulsifiers with a chemical composition made up of four PPO-PEO blocks bonded X designed of EDTA (*i.e.*, ethylenediamine) core. The physicochemical properties of poloxamines can be modified by changing the ratio of PPO/PEO, making emulsifiers in the range of highly hydrophilic to highly hydrophobic.

Polysorbates (PSs) are another family of commercial nonionic emulsifiers frequently used in the preparation of pharmaceuticals. PSs are frequently

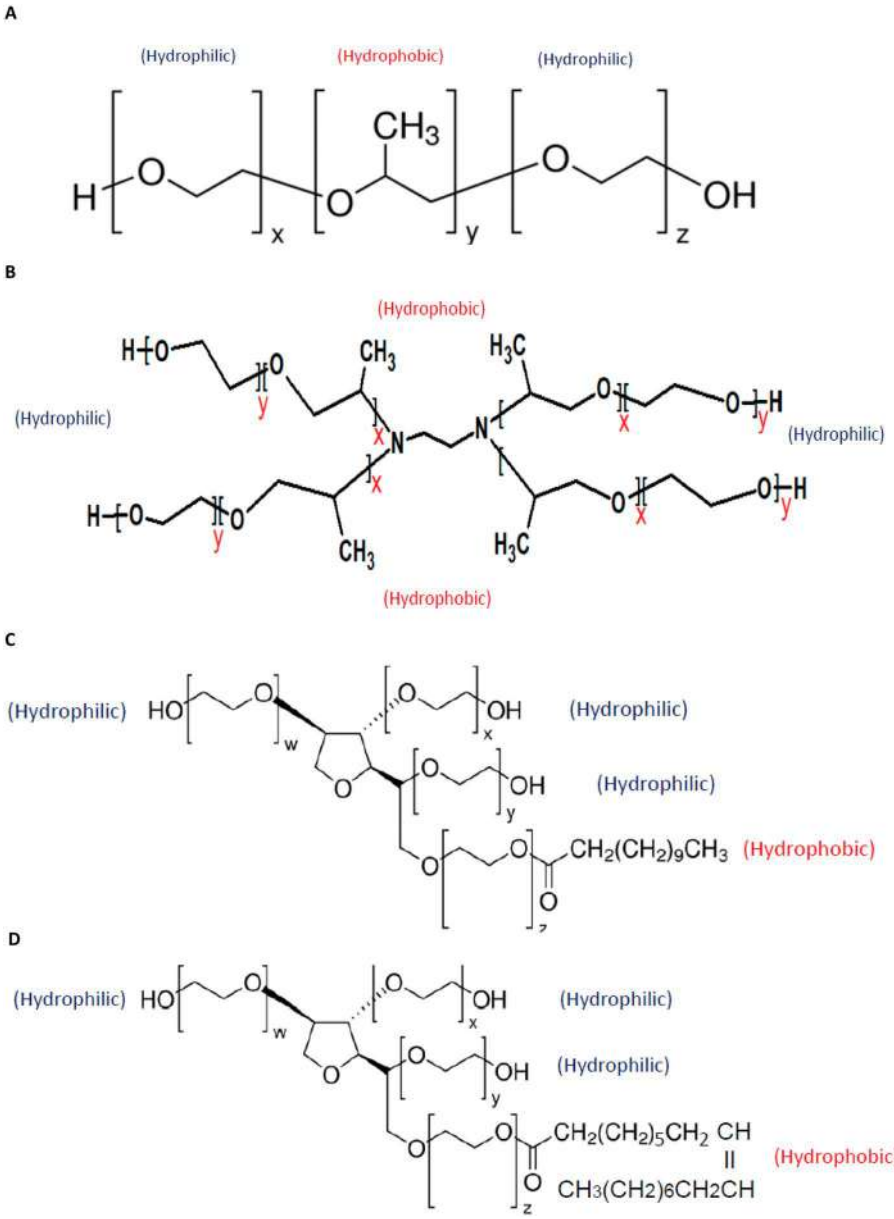

Figure 17.2 Cartoons of common emulsifiers used in the pharmaceutical industry: A, poloxamers; B, poloxamines; C, polysorbate 20; D, polysorbate 80. Symbols: x, y, w, and z represent chain lengths.

used in pharmaceutical formulations to protect labile structures from harsh environmental conditions.[53] The core of PSs is composed of the polyol sorbitan and isosorbide molecules linked to PEO (*e.g.*, hydrophilic moiety) through four hydroxyl groups and fatty acids (*e.g.*, hydrophobic moiety) that determine the main properties of the emulsifier. The most used are PS20 (Tween® 20) and PS80 (Tween® 80) that mainly contain lauric (C_{12}) and oleic ($C_{18:1}$) acids, respectively. However, commercial PSs showed heterogeneity in their structures based on the different chain lengths of PEO and, in general, poorly purified fatty acids.[54] Different strategies are in process of development to obtain lipids of high purity and were recently published elsewhere.[55] Besides, the FDA, EMA, and the Japanese agency approved PS20 and PS80 for pharmacological applications, but the pharmacopeias of China, EU, Japan, and USA (*i.e.*, EP, JP, and USP) impose some restrictions regarding the dispersity of fatty acids for different medicinal applications.[56]

17.3.1 Applications of Nanostructured Lipid Carriers

There are many pharmaceutical products made of NLC produced by several laboratories and approved by national regulatory agencies in the world and reviewed.[45] At experimental levels, many publications and reviews were published lately showing the high impact of this novel technology on several applications.[47,57–59]

Particularly, the promising major impacts of NLC development are severe chronic and acute pathologies such as tuberculosis, cancer, Parkinson's and other neurodegenerative illnesses, epilepsy, neglected diseases, *etc.*

One of the main problems of cancer chemotherapy is the high cytotoxicity of the available drugs in the market. Besides, most of the current anticancer drug formulations lack specificity for cancer cells and metastatic cancers, reaching many untargeted tissues with severe damage to other cells and tissues.[49] Also, most anticancer drugs are unstable under physiological environments with consequent loss of effectivity, and in such cases, the high drug concentration is required to obtain some treatment efficacy but with the resultant toxic effects. These characteristics of chemotherapeutic drugs could also create a multidrug resistance (MDR) to the treatment.[61] NLCs could bring a solution by reducing drug concentration and thus concomitantly decrease cell toxicity and increase the effectivity of the treatments just by modifying the cell surface with specific molecules to target markers of cancer cells.[62] Another potential strategy can be the use of encapsulated prodrugs in the nanoparticles that can be activated on-site by the biological mechanism of the tumoral cells that otherwise free prodrug could activate everywhere in the organism.[63] An example of treating cancer cells with NLC is related to the delivery of Metvan, a promising anticancer vanadium complex that shows high anticancer activity as well as high cellular toxicity. The Metvan encapsulation yield in the NLC was approximately 80% and showed sustained drug release for more than 2.5 days. Studies on osteosarcoma

MG-63 cells with Metvan-NLC showed not only a high cytotoxic effect of the loaded nanoparticles compared to free Metvan but also increased early and late cell apoptosis and cell death.[64]

Another relevant problem in drug administration is to reach the brain by circumventing the blood–brain barrier (BBB), a semipermeable membrane that prevents the access of many molecules including drugs to the brain. The typical example that combines MDR and exclusion by the BBB is epilepsy, and particularly refractory epilepsy is dramatic in children who, in some cases, suffer more than 100 episodes per day. In a preliminary recent study, encapsulation of oxcarbazepine (OXL) in NLC was explored. The OXL-loaded nanoparticles showed an encapsulation efficiency of 97–98% with an established controlled kinetic release. *In vitro* permeability studies carried out in MDR1-transfected Madin–Darby canine kidney (MDCK) expressing P-gp, known as ATP-binding cassette subfamily B member 1 or multidrug resistance protein 1, showed enhanced permeability of OXL-NLC compared to the free drug, which will be advantageous for the treatment of epilepsy.[65]

Diabetes is a chronic disease associated with the deficiency of glucose regulation and metabolism that accounted for the death of 414 million people in 2014 and is rising year to year with 1.6 million deaths yearly (WHO, 2020). Drugs such as pioglitazone (PZ), a thiazolidinedione-class drug, help to enhance the sensitivity of insulin in the liver and inhibit gluconeogenesis, among other beneficial effects. However, administration of PZ could be metabolically more efficient if the drug can be entrapped in a drug delivery system associated with an established mechanism of controlled release. In recent work, *in vivo* experiments developed with PZ loaded in NLC showed 2.17 times higher bioavailability than marketed tablets with a sustained release for 48 h and kept glycemic level stable for 24 h.[66]

An active ingredient of the herb *Tripterygium wilfordii*, triptolide (TPL), belongs to traditional Chinese medicine and is currently used to treat rheumatoid arthritis and autoimmune pathologies. However, oral TPL administration showed the disadvantage of reaching the maximum concentration in the body after 10 min with a $t_{1/2}$ of approximately 38 min. Besides, the chronic conditions of rheumatoid arthritis and autoimmune diseases require reiterative TPL administrations that cause undesirable toxic effects in the spleen and liver. A practical strategy to overcome TPL oral administration is by the development of a transdermal delivery system able to control local drug release. In this sense, a transdermal formulation of TPL-NLC was developed and analyzed *in vitro* and in rats as an *in vivo* model.[67] The TPL-NLC showed an encapsulation efficiency higher than 97% and drug loading greater than 10%, and the TPL concentration in the skin was approximately 18% higher than in blood. Topical administration of TPL-NLC significantly reduced the knee edema in the rat by diminishing the concentrations of ILs 1β and 6, as well as the TNF-α, and no signs of toxicity were detected in the liver and spleen after the treatment.

All these examples demonstrated the potential advantages of NLC for the treatment of different pathologies regardless of the type of therapy, administration mode, and properties of the drug.

17.4 Hybrid NLC Systems

There are two main strategies to produce hybrid NLC models by external or internal modifications, and by combining both techniques. The first one is by changing the NLC surface, decorating the surface with exogenous molecules and/or complexes to improve the properties of nanoparticles. The second one involves internal changes in the structure of the NLC, obtaining different properties.

The seminal approach to developing hybrid lipid systems was a liposome decorated with polyethylene glycol (PEG) to give "stealth condition" enhancing the circulation time of the cancer drug doxorubicin in the body, Doxil®, preliminarily approved by FDA and EMA in 1995.[68] Doxil® is considered as the first nanodrug using the technique denominated PEGylation. PEGylation of lipid nanoparticles avoids the detection and binding of NLC by macrophages and their elimination by the mononuclear phagocyte system, which reduces the therapeutic effectivity of the administered drug. A similar PEGylation strategy was developed for many drugs using SLNs. Particularly, a novel innovation was to introduce covalently attached PEG-stearate to the lipid nanoparticle and covalently attach folic acid to stearate.[69] to deliver paclitaxel to A549, a lung adenocarcinoma human alveolar basal epithelial cell line. This strategy to tailor the surface of lipid nanoparticles not only extended the circulation time in the bloodstream but also enhanced endocytosis by the enhanced expression of the folate receptor in A549 cancer cells. Similar strategies were developed by several authors using PEGylation procedures to deliver therapeutic molecules with different physicochemical properties.[70–72] Besides, there are some controversies about the PEGylation of molecules used in drug delivery since anti-PEG antibodies were found in many patients but also in healthy people, which is attributed to the extensive presence of PEG in foods and cosmetics.[73]

One of the most relevant and challenging areas for the use of lipid structures is nonviral gene delivery for the treatment of genetic diseases. Recently, the development of an NLC based on stearate and containing cholesteryl oleate to improve transfection effectivity, and octadecylamine to increase the cell binding was reported. After NLC formation, a plasmid-containing luciferase gene condensed with protamine for lipoplexes was used to decorate the nanoparticle surface.[74] The presence of protamine in the lipid formulation was included not only because it can protect DNA by lipoplex formation, but it is also considered as a lipid nanoparticle transfection enhancer by switching the endocytosis mechanism of cell internalization mediated by raft-caveolae to clathrin.[75] The displayed results indicate strong binding of the NLC to the cells and a high expression of luciferase.

For targeting cancer cells, a common strategy is to decorate the nanoparticle surface with folic acid (FA) and their derivatives, or transferrin.[76,77] The major advantage of FA or FA-derivatives is the fast uptake and internalization by the cancer cells. Other strategies to target cancer cells involve the binding of αvβ3 integrin by designed peptides, such as RGD (*i.e.*, the tripeptide-arginyl-glycyl aspartic acid).[78]

Another extensive tool to decorate particle surfaces but with more broad applications is positively charged polymers such as chitosan or polylysine that provide a residual positive charge to the particle to avoid coalescence during

storage.[79,80] Importantly, cationic polymers tend to bind to cellular membranes with a residual negative charge, which is relevant for the attachment of the drug devices to the cell surface. Besides, the opsonization of chitosan-covered nanoparticles by macrophages diminished probably because of the high polymer hydrophilicity.[81] Environmentally sensitive NLC systems can be obtained by the development of carboxymethyl chitosan-coated NLC to deliver quercetin, a flavonoid with anti-inflammatory and antioxidant properties, for ophthalmological therapy.[82]

17.4.1 Structural Hybrid NLC

In recent years research in the area of hybrid lipid carriers for drug delivery has attracted more attention because of the success of NLC in the controlled release of many therapeutic molecules with different biological and physicochemical properties (see Figure 17.3).[58,59,83] A summary of the current strategies to make hybrid NLC (H-NLC) is given below.

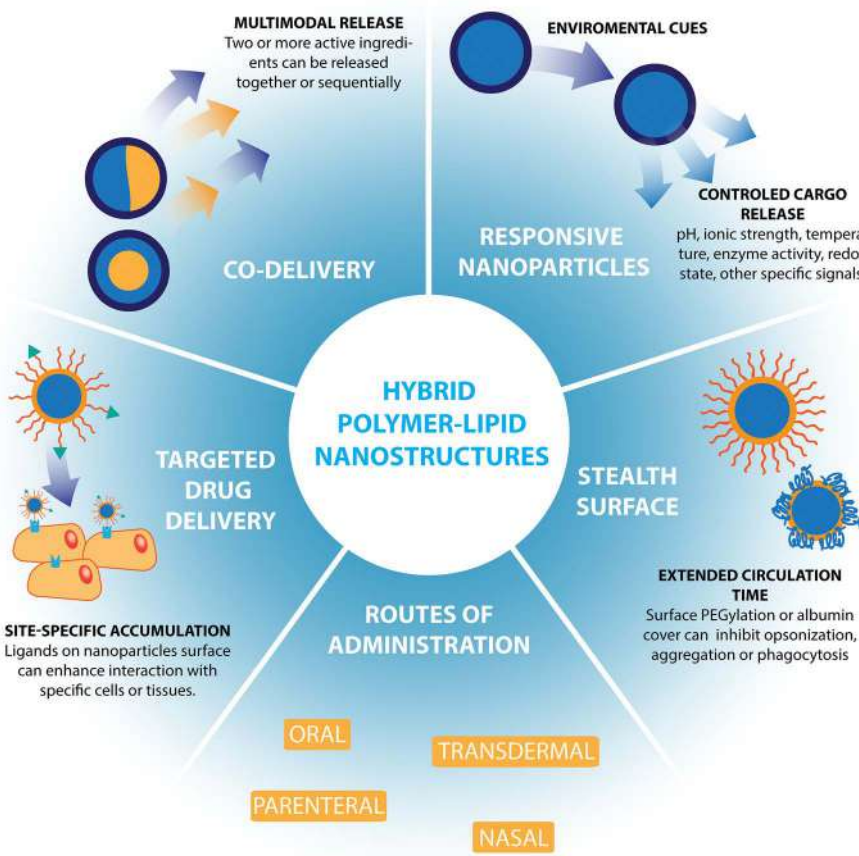

Figure 17.3 Main advantages of hybrid polymer–hybrid nanoparticles.

17.4.1.1 Essential Oil Compounds in NLC

Natural bioactive compounds showed plenty of activities to treat many pathologies, but most of them are hydrophobic, which limits their applications. Besides, the development of lipid nanoparticles, particularly NLC, opens a new door for the effective delivery of many natural molecules.[84]

Essential oils (EOs) extracted from plants showed interesting biological activities such as antifungal, antimicrobial, anti-inflammatory, antioxidant, and immunomodulatory activities that they can exert in plenty of therapeutic applications.[55,85] Also, under the frame of drug delivery, EOs could help to reduce the therapeutic drug concentration. Particularly, EOs can be successfully used with hydrophobic drugs since they can provide enhanced bioavailability. Considering the physicochemical properties of lipid nanoparticles, EO alters the internal crystalline or pseudo-crystalline structure of the nanoparticle.

An interesting application of EO loaded in NLC is the treatment of wound healing. Wound healing accounts for the death of 8.2 million people worldwide, and microbial infections are the prevalent condition for the development of chronic pathology that, in some cases, ends in septicemias with the potential death of the patients (Sen, 2019). In recent work, eucalyptus or rosemary essential oils were loaded in NLC, tested *in vivo* in a rat model with skin wound and assayed against *Staphylococcus aureus*, and *Streptococcus pyogenes*. The results confirmed the antimicrobial activity of the EO, positive cell proliferation in the wounded rats.[86]

A similar strategy was developed using eugenol as EO in NLC containing ofloxacin, a wide spectrum fluoroquinolone antibiotic with low solubility in physiological media associated with some toxicity. The antimicrobial activity of NLC containing eugenol and ofloxacin tested against *Staphylococcus aureus* and *Pseudomonas aeruginosa* and determined by their MICs (minimal inhibitory concentration) decreased 16.1 and 6.0 times compared to the free antibiotic, respectively. Administration of dry HNLC containing eugenol-ofloxacin by inhalation demonstrated effective delivery to the lungs without signs of toxicity.[87]

Natural extracts of *Lavandula and Rosmarinus* contain several EOs with relevant antioxidant and antiproliferative bioactivity.[88,89] For these reasons, *Lavandula* and *Rosmarinus* extracts were tested in the formulation of NLC as co-adjuvants of clotrimazole for the topical treatment of dermal pathologies caused by *Candida* spp. The main advantage of clotrimazole encapsulation is relevant since it is therapeutically used at high concentrations with potential toxicity to the liver and possesses low solubility under physiological conditions. The encapsulation of clotrimazole in HNLC containing EOs with antiproliferative activity against *Candida* spp. has the advantage of using a lower drug concentration with similar or higher activity than free drug and provides sustained drug release.[90]

Another group of bioactive compounds employed to formulate hybrid lipid nanodevices are terpenes and terpenoids for therapeutic purposes in dermal pathologies and also mucosal administration.[91] Linalool, an acyclic bioactive monoterpenoid involved in the mevalonate pathway, displays

antiproliferative activity in cancer cells. NLC containing linalool was tested *in vitro* in cultures of lung adenocarcinoma (A549) and hepatocarcinoma (HepG2) cell lines. The results showed high antiproliferative activity of linalool-LNC compared to free linalool and in a dose-dependent way.[92] Similar antiproliferative results were found by the same research group using 1,8 cineole, a terpene, encapsulated in a magnetic NLC system.[93]

17.4.1.2 NLC – Polymers

A recent trend in the controlled release of therapeutic molecules is the development of hybrid structures of polymers combined with lipids. Many polymers, natural, semisynthetic, and synthetic, can provide hydrophilic/hydrophobic support for different types of drugs but also for lipids. The hydrophilic/hydrophobic content can be altered, tailored, based on the type of drug, interactions with lipids and surfactants, and finally to the administration mode. Many polymers now have the status of GRAS by the FDA and have been approved by EMA of the EU. Polymers such as alginate, PGLA, PLA, carrageenans, cellulose and derivatives, dextrans, starch, and starch-derived molecules, casein, PEG, *etc.*, could be used for the development of new hybrid NLCs formulations. An extensive list of different degradable and nondegradable polymers used for different applications of drug delivery is shown in Table 17.1.[94,95]

Table 17.1 Polymers employed in the formulation of drug delivery devices.

Polymers used in molecular controlled release	
Biodegradable	Non-biodegradable
Albumins	Poly *N*-acrylamides
Alginates	Polyamidoamines
Carrageenans	Polyalkyl cyanoacrylates
Caseins	Poly(dimethylsiloxane)
Cellulose	Poly(ethylene glycol) (PEG)
Chitosan	Poly(ethylene imine) (LPEI)
Collagen	Polymethyl methacrylates (Eudragit®)
Dextrans	Poly(2-oxazoline)
Gelatin	Poly(propylene glycol) (PPG)
Hyaluronic acid	Polystyrene
Pectins	Poly(methyl vinyl ether/maleic anhydride) - Gantrez®
Polyanhydride	
Poly-ε-caprolactone	
Poly(γ-glutamate) (PGlu)	
Poly(ethyleneimine)	
Polylactic acid	
Poly(Lactide-coglycolide) acids	
Polyglycolic acid	
Poly(lactide-ε-caprolactone)	
Poly(oxalate) (PO)	
Poly(phosphate) (PP)	
Polyurethanes	
Poly(vinyl alcohol) (PVA)	

Also, polymer tailoring can be performed using any chemical or enzymatic reaction, providing a novel entire platform for drug delivery.[96] In general, it is assumed that the polymer is in charge of the drug loading, while the lipids are related to cell attachment. However, the polymer-drug relationship depends on their physicochemical and chemical composition. Besides, the stability of the hybrid polymer–NLC will depend on the interaction of the components, which means the polymer must contain a hydrophobic region in the molecule or the net charges of the polymer must be neutralized before synthesis of the hybrid polymer–NLC. Otherwise, the charged polymer will be extruded from the NLC structure. Based on these considerations, the hybrid polymer–NLC can be classified into three main different types: monolith type with polymer and lipids well distributed along the nanoparticle; core–shell structure with a polymer imbricated with the lipid core and covering all the nanoparticle surface, and with a polymer core covered with lipids, but they are not strictly NLCs (see Figure 17.4). Some examples are described below.

One example is the formulation of mitoxantrone hydrochloride in the presence of carrageenan. Carrageenans are linear and helical polymer composed of 1,3-linked β-D-galactose and 1,4-linked α-D-galactose with sulfate pending groups. Mitoxantrone is an anticancer drug and is used for the treatment of multiple sclerosis, with many undesirable secondary effects. The strategy was to neutralize the charges of carrageenan with the mitoxantrone, followed

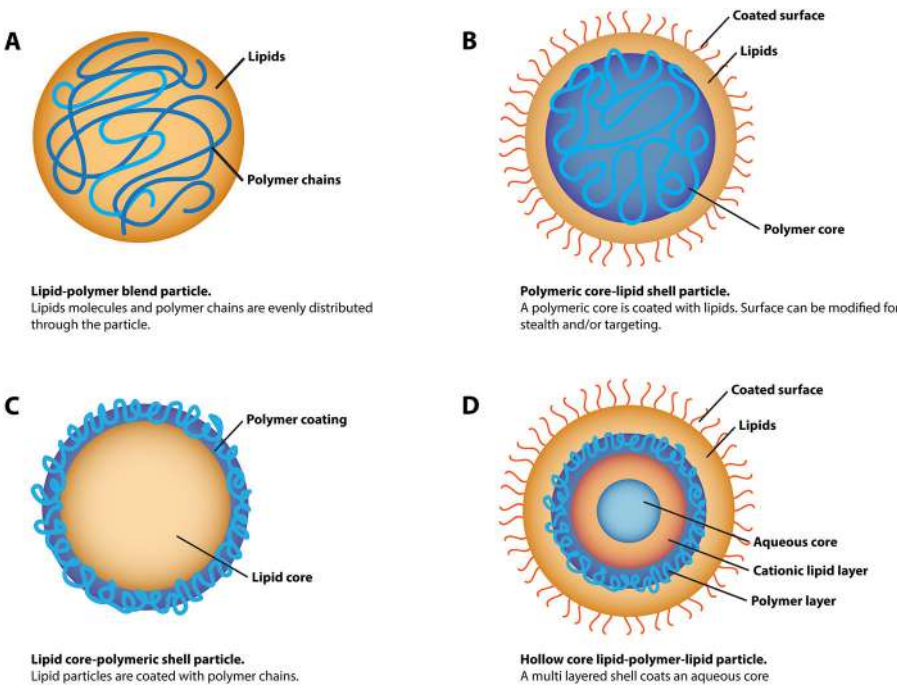

Figure 17.4 Cartoon of different models of hybrid polymer nanostructured lipid carriers.

by the synthesis of LNP. The hybrid mitoxantrone–carrageenan NLC displays a monolith structure with 134 nm diameter, and drug-controlled release for 48 h and with the advantage of bypass the breast cancer resistance protein (BCRP) transporters increasing the drug efficiency concomitantly with a toxicity decrease.[97]

Like the previously mentioned strategy, the oral delivery of vinpocetine (VP) was developed in a hybrid polymer–NLC. VP is an alkaloid with low solubility in aqueous media used for the treatment of dementia, cognitive dysfunction, and importantly, in ischemic stroke. The VP was complexed with three different modified β-cyclodextrins (CD) with hydroxypropyl and sulfobutylether groups to enhance the drug loading and added to the lipids for the NLC synthesis. The VP release from the hybrid VP-CD-NLC showed controlled release profiles and a strong pH dependence, with high release at pH values higher than 6.8, which is optimum for oral administration.[98]

Mitoxantrone hydrochloride (MTO) is a widely used anticancer drug with the advantage of high solubility in physiological media. However, the main obstacle to treat cancer with MTO is tumor multidrug resistance (MDR). A research group developed the encapsulation of MTO in a dextran sulfate-NLC. As a result of the interaction of the anionic dextran sulfate and positively charged MTO, both components were included in the NLC formulation. Analysis of the MTO hybrid NLC formulation *in vivo* showed lower distribution in different organs compared to soluble MTO with an enhanced uptake by the tumor and avoiding MDR. The hybrid nanoparticles displayed a sustained release, appropriate pharmacokinetics, and biodistribution.[99] An identical approach was developed for the encapsulation of verapamil, a cationic calcium blocker, using dextran sulfate and solid–liquid lipids. The uptake of verapamil by the cell was improved by the hybrid lipid formulation compared to non-lipid ones.[100]

Another strategy was developed for the formulation of bupivacaine (BVC), an anesthetic drug with low lipid solubility. The BVC was entrapped in NLC at high temperature and later incubated in an aqueous alginate solution. *In vivo* studies in wounded rats showed a modulated controlled release of the BVC with the formation of gels at the site of application. The anesthetic activity of the BVC alginate-NLC was extended more than five times compared to the commercial drug.[101]

17.4.1.3 NLC – Peptides and Proteins

Proteins are very sensitive molecules because of their complex supramolecular structure. In this sense, some proteins were encapsulated in complex systems to be used as a tool for drug delivery.

Transferrin (Tf) is a multitasking protein that consists of 679 amino acid residues and has a molecular weight of ≈79 kD.[102] The main biological function of Tf is serum iron transportation.[103] Upregulation of transferrin receptor (TfR) was reported in various cancer types, which makes transferrin an efficient molecule to be utilized in targeted cancer therapies.[104]

Paclitaxel and DNA-loaded NLCs were decorated with Tf-conjugated ligands and tested on human non-small cell lung carcinoma cell line (NC1-H460) and mice bearing NC1-H460 cells. Polyethylene glycol-phosphatidylethanolamine (PEG-PE) was used to generate a Tf-PEG-PE-conjugated ligand. PTX-DNA-NLCs were synthesized by microemulsion technique, and electrostatic attraction and lipophilic interaction were utilized to decorate the NLCs with the Tf-PEG-PE ligand. The results demonstrated that Tf decoration in NLC improved the controlled drug release and gene loading in NC1-H460 cells, and enhanced *in vivo* gene transfection efficiency and antitumor efficacy. Tf-mediated active tumor targeting delivery can be shown as a promising design for the treatment of lung cancer.[105]

Another research group investigated the delivery of plasmid-containing enhanced green fluorescence protein (pEGFP)[106] and co-delivery of doxorubicin and pEGFP *via* Tf-conjugated NLC for lung cancer gene therapy. These systems kept drug stability, high loading capacity, and both drug and gene therapeutic effects against A549 human lung adenocarcinoma cells.

Tf and hyaluronic acid (HA) dual ligand decorated NLCs (see Figure 17.5) were prepared for targeted lung cancer gene delivery. Ligands were synthesized with polyethylene glycol-di-stearoyl phosphatidylethanolamine

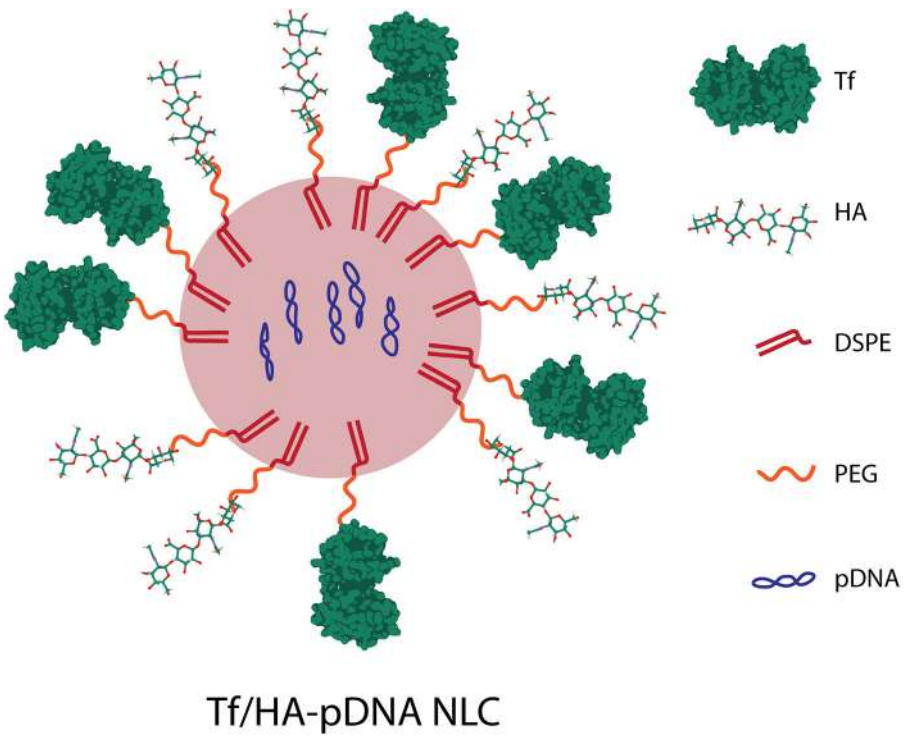

Figure 17.5 Scheme of Tf/HA-pDNA NLC.

(Tf-PEG-DSPE and HA-PEG-DSPE). The pEGFP loaded NLCs (Tf/HA-pDNA NLC) were evaluated in the human lung adenocarcinoma A549 cell-bearing mouse model. NLC decoration with Tf and HA provided slower pDNA release than nondecorated NLCs, thus the sustained release prevented the degradation of pDNA. Whereas Tf/HA-pDNA NLC exhibited high cell viability, *in vitro* and *in vivo* an efficient gene delivery occurred.[107]

Recently, a new strategy was developed based on Tf-decorated PTX-loaded NLC to treat brain cancer. It is aimed to increase the therapeutic effect of PTX by overcoming the problem of penetration of the blood–brain barrier (BBB). Nanoparticles were synthesized by emulsification-solvent evaporation and then, Tf conjugation was performed. The *in vitro* cytotoxicity assay demonstrated that the anticancer effect of Tf-PTX-NLC was higher than that of nontargeted NLC and free drugs.[108] In another study by Emami *et al.*, brain delivery of artemisinin (ART) from Tf-NLCs was investigated against U-87MG brain cancer cell line and was proven to overexpress TfR. ART was released faster at a very early stage but continued with a controlled release profile. It was observed that ART-Tf-NLC showed more toxicity than free ART and ART-NLC.[109]

Poorly soluble quercetin reduces protein oxidation, lipid peroxidation, neuronal cell death, and inhibits fibril formation that results from amyloid-beta peptide aggregation in Alzheimer's disease. TfRs are overexpressed on the luminal side of brain capillary endothelial cells of the BBB. Quercetin-loaded Tf-NLC is a good candidate for Alzheimer's disease treatment. Tf-NLCs loaded with 80–90% quercetin encapsulation efficiency did not show cytotoxicity to human cerebral microvascular endothelial cells (hCMEC/D3). Tf modification did not influence the permeability capacity of the NLCs. This result can be attributed to the saturation of TfRs. However, quercetin-loaded Tf-NLCs were better at inhibiting fibril formation in comparison to free quercetin and nonmodified NLCs.[110]

Lactoferrin (Lf) is an 80 kDa iron-binding glycoprotein that is included in the transferrin family. Besides its immunological properties such as antibacterial, antiviral, antifungal, and anti-inflammatory, Lf also shows anticancer activity.[111] Lactoferrin receptors (LfR) are characterized in many types of mammalian cells and tissues, small intestine, liver, monocyte, lymphocyte, platelet, fibroblast, bone, and brain.[112]

Nimodipine (NMD) is a neuroprotective agent that is investigated for ischemic stroke. However, low bioavailability and aqueous solubility, and BBB are the NMD's drawbacks to treat cerebrovascular disorders. The delivery of NMD *via* Lf-NLC to the brain tissue was performed by LfR-mediated endocytosis. PC12 based stroke cell line was utilized to evaluate *in vitro* cytotoxicity, cell uptake, and apoptosis-protection effect, and *in vivo* biodistribution. Sodium nitroprusside (SNP) is an inorganic compound that activates the apoptosis cascade *in vitro*. The cell uptake and protective effect of NMD against SNP-containing PC12 cells increased with Lf-NLC. *In vivo* study exhibited that the presence of Lf on the surface of nanoparticles enhanced the NMD accumulation into brain tissue.[113]

Curcumin (Cur)-loaded Lf decorated low–density lipoprotein (LDL)-based NLC was designed for the treatment of Alzheimer's disease. LDL-based NLC provides an advantage for brain-targeted delivery since it includes LDL receptors in the brain capillary endothelial cells (BCECs). *In vitro* cell uptake assay demonstrated the uptake of Lf-NLC was 1.4-fold greater than that of nondecorated NLC. *Ex vivo* imaging study revealed Lf-NLC could penetrate BBB and that its accumulation in the brain tissue was 2.8-fold higher than in nondecorated NLC.[114]

Temozolomide (TMZ) and vincristine-coloaded Lf- and arginine-glycine-aspartic acid (RGD) dual ligand-co-modified NLCs (L/R-T/V-NLCs) (see Figure 17.6) were fabricated to treat glioblastoma multiforme (GBM), which is the most frequent malignant brain tumor. In the clinic treatments, TMZ and radiotherapy are administrated to patients, but BBB limits the TMZ delivery to the brain tissue. *In vitro* cytotoxicity study showed that the highest cell inhibition effect was observed in the presence of L/R-T/V-NLCs against U87 MG cells and T98G cells in comparison to single-RGD-ligand-modified, no-ligand-modified, single-drug-loaded NLCs, and free drugs. Correspondingly, due to the synergistic effect of the two drugs and the presence of dual ligands, the uptake of NLCs and drug accumulation in the tissue increased. *In vivo* study exhibited that tumor inhibition was better achieved with L/R-T/V-NLCs.[115]

Epidermal growth factor receptor variant III (EGFRvIII) is an EGF receptor variant that is commonly expressed only in tumor cells such as GBM,

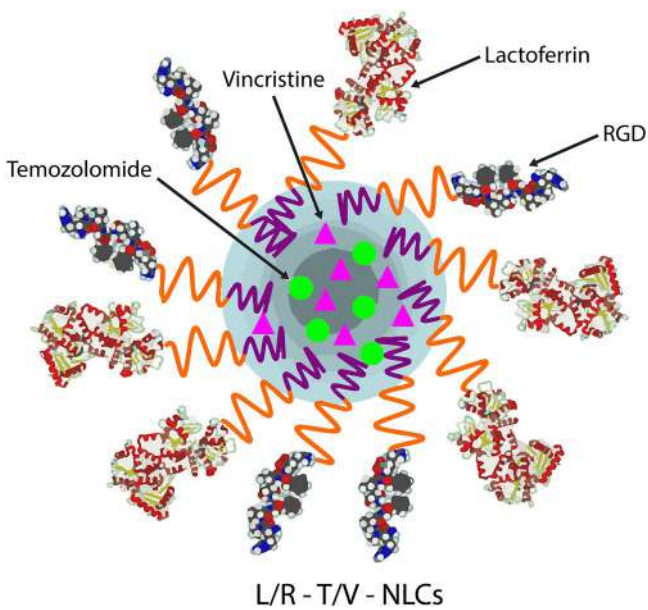

Figure 17.6 Scheme of L/R-T/V-NLCs. Reproduced from ref. 115 with permission from Dovepress, Copyright 2018.

medulloblastoma, prostate and lung carcinoma, breast, and ovarian adenocarcinoma, and can be used as a target. Anti-EGFRvIII monoclonal antibody (MAb) decorated doxorubicin (Dox)-loaded NLCs (MAb-Dox-NLC) were prepared to enhance the cell uptake of Dox *via* EGFRvIII. *In vitro* cytotoxicity assay showed that MAb-Dox-NLC induced greater toxicity than nontargeted Dox-NLC and free Dox against HC2 20d2/c also in comparison with the NIH-3T3 cells. Whereas the cellular uptake of targeted-NLC did not differ from nontargeted NLC in NIH-3T3 cells, the Dox accumulation by MAb-Dox-NLC was higher in HC2 20d2/c cells due to ligand-receptor recognition.[116]

Vascular endothelial growth factor receptors (VEGFRs) are more expressed in various solid tumors such as melanoma, breast, gastric, non-small-cell lung cancer, and cervix than in normal tissue and in tumor neovasculature *in situ*, which brings the prospective double targeting tumor therapy (tumor and vascular targeting). Anti-VEGFR-2 antibody decorated docetaxel (DTX)-loaded NLC was synthesized to observe the double targeting strategy. The IC50 values of tNLC were significantly lower than in nontargeted NLC and free DTX in hepatocellular liver carcinoma (HepG2), lung carcinoma (A549), and murine malignant melanoma (B16). Also, *in vitro* proliferation inhibition of tNLC was higher for tumor vessel endothelial cells (HUVEC). The greatest therapeutic effect and reduction in tumor volume occurred in the presence of tNLC due to its ability to bind and internalize in both tumor cells and tumor neovasculature by the interaction of ligand and receptor.[117]

The protective effects of the water-soluble phenolic acid, salvianolic acid B (Sal B), and the flavonoids baicalin (BA) have been proven in the treatment of ischemic stroke and neuron injury. TfR monoclonal antibody OX26-modified BA and Sal B-loaded NLC (OX26-BA/Sal B- NLC) was produced to improve BBB permeability and brain targeting. To observe the cellular uptake in brain microvascular endothelial cells, nanoparticles were prepared with coumarin-6 (cou-6) as a fluorescent probe, and the fluorescence intensity of nanoparticles was measured. OX26-cou-6-NLC integrated to the bEnd.3 cells was significantly better than other groups. When the formulations were injected into BALB/c-nude mice, the fluorescence signal was detected in the brain region at 4 h and 24 h in the OX26-modified group.[118]

The anti-intercellular adhesion molecule 1 (anti-ICAM- 1) is a transmembrane glycoprotein that is upregulated in pulmonary endothelial cells under inflammation states. Lung-targeted anti-ICAM-1-conjugated simvastatin (SV)-loaded NLCs (anti-ICAM/SV/NLCs) were synthesized. The anti-ICAM/SV/NLCs presented a sustained release during 36 h with low toxicity and higher uptake to EAhy926 cells.[119] Combined delivery of SV and angiopoietin-1 gene (Ang-1) from anti-ICAM-1-conjugated NLC (ICAM-NLC/Pro/Ang) was performed to treat acute lung injury (ALI). *In vivo* study revealed that ICAM-NLC/Pro/Ang treated ALI mice showed very effective suppression in the pulmonary TNF-α and IL-6 levels also, it can control the cytokine levels.[120]

Erythropoietin (EPO) is a 34 kDa glycoprotein secreted from the kidney and stimulates the bone marrow to produce erythrocytes. Besides, erythropoietin receptor (EpoR) is expressed in cancer cells and is responsible for

their proliferation and migration. Tamoxifen (TAM)-loaded EPO-modified NLC (EPO-TAMNLC) was developed to treat breast cancer. Antitumor activity of EPO-TAMNLC was analyzed *via* MTT assay against HDFa (primary human dermal fibroblast) and MCF-7 (mammary adenocarcinoma) cell lines. EPO-TAMNLC showed 10-fold more cytotoxicity against MCF-7 cells than HDFa cells. While EPO-TAMNLC minimized its toxicity towards normal cells, its high efficiency in cancer cells was revealed.[121] Another study of EPO-TAMNLC was conducted against the LA7 cells and LA7 cell-induced rat mammary gland tumor. It was proven that EPO-TAMNLC induced *in vitro* apoptosis and cancer cell cycle arrest, and decreased cancer cell proliferation. *In vivo* study indicated that EPO-TAMNLC was more effective than free TAM and tumor size decreased in the presence of both EPO-TAMNLC and TAMNLC.[122]

Platelets (PLTs) are anuclear fragments that are responsible for the generation of clot and hemostasis and thrombosis processes. Also, PLTs are associated with angiogenesis and keep the interaction with the tumor cells in the circulation system. Tumor metastasis is accepted to be correlated with the aggregation between tumor cells and PLTs. PLT membrane proteins can be used as biomimicry in tumor-specific targeting delivery. PLT-coated paclitaxel-loaded NLC (P-PT-NLC) was manufactured against the SK-OV-3 ovarian cancer cell line. Unlike PT-NLC, CD41 rat PLT membrane glycoprotein was detected as a marker in P-PT-NLC by confocal laser scanning microscopy, which indicates that P-PT-NLC has a greater tumor-cell affinity. *In vitro* cytotoxicity assay demonstrated that P-PT-NLC and PT-NLC systems were more toxic than free PT for SK-OV-3 cells.[123]

17.4.1.4 NLC-Organic Compounds

Folate (also known as folic acid) is one of the B vitamins with a low molecular weight (441 Da) and recognized by folate receptor (FR) (see Figure 17.7).[124] Also, folate is characterized as water-soluble, non-immunogenic, and has a crucial role in DNA synthesis, methylation, and repair. FR is a glycosylphosphatidylinositol-anchored cell surface receptor whose expression level increases mainly in epithelial, breast, colorectal, brain, ovarian, cervical, kidney, and lung tumor tissues, whereas it shows limited expression level in healthy tissues.[125] Therefore, folate-decorated nanocarriers can

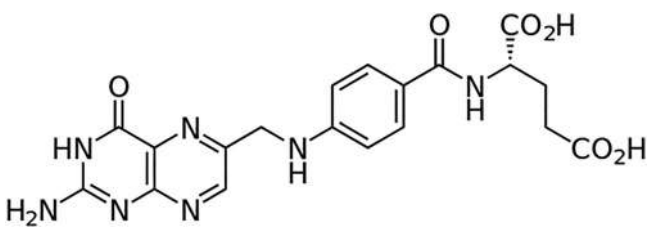

Figure 17.7 The chemical structure of folate.

facilitate the cellular uptake of anticancer compounds into tumor tissue *via* folate receptor-mediated endocytosis.[126]

Cisplatin (CIS)-loaded folate (FA)-modified NLCs were synthesized to decrease the severe side effects and rise the chemotherapeutic efficiency in the treatment of cervical cancer. As targeting ligand FA containing polyethylene glycol (PEG)-di-stearoyl phosphatidylethanolamine (DSPE) (FA-PEG-DSPE) was prepared, then conjugated with the loaded nanoparticles (FA-CIS-NLC). FA-CIS-NLC demonstrated greater cytotoxicity than CIS-NLC and free CIS against HeLa cervical carcinoma cell line (2.8-fold and 8.8-fold, respectively). Also, the *in vivo* tumor inhibition rate of FA-CIS-NLC was 79.3%, whereas it was 64.4% for CIS-NLC, and 18.5% for free CIS.[127] In another study for the treatment of cervical cancer, docetaxel (DTX)-loaded FA-functionalized NLCs were evaluated *in vitro* and *in vivo*. The effective tumor inhibition, superior tumor targetability, and notable biosafety profile of ultrasmall (30 nm) FA-DTX-NLC was proven.[128]

Cisplatin (DDP) and paclitaxel (PTX) were co-delivered by FA-conjugated NLCs against head and neck cancer. FA-PEG-DSPE ligand was used to decorate DDP/PTX NLCs. The anticancer effect of FA-DDP/PTX-NLC against neck and head cancer FaDu cells was higher due to the presence of FA and the synergic effect of DDP and PTX in comparison to DDP/PTX-NLC, DDP-NLC, PTX-NLC, free DDP, and free PTX. Likewise, *in vivo* tumor inhibition efficiency of FA-DDP/PTX-NLCs was better than in the other formulations without obvious toxicity.[129]

Letrozole (LTZ) is the third generation of nonsteroidal aromatase blockage that is utilized against hormone receptor-positive breast cancer. To increase its therapeutic efficiency, LTZ-loaded FA-modified NLCs were tested in the MCF-7 breast cancer cell line. While FA-LTZ-NLC showed more cytotoxicity than LTZ-NLC and free LTZ in MTT assay, FA-LTZ-NLC also enhanced the apoptotic cells from 24.6% to 42.2% in comparison to free LTZ.[130]

Resveratrol (RSV) is a natural phytoalexin that has anti-inflammatory, antioxidant, antiproliferative, and antimutagenic effects. Besides, RSV shows chemotherapeutic activities by inducing apoptosis *via* interacting with target molecules such as P53, P21, MMPs-2, 7, 9, caspases-9, 8, 7, 3, MAPK, VEGF, *etc.* To overcome some limitations of PSV (low solubility and poor absorption *in vivo*), FA-targeted RSV-loaded NLCs were designed to be investigated on MCF-7 breast cancer cell line (FR+) and A549 lung cancer cell line (FR-). MTT assay revealed that FA-RSV-NLCs were cytotoxic in both cancer lines compared to RSV-NLC and free RSV.[131]

Photodynamic therapy (PDT) involves a photosensitizer (PS) that is a photoactive compound. The PS absorbs photon energy with light of an appropriate wavelength and results in the production of reactive oxygen species (ROS) that induce apoptosis and necrosis. PS is nontoxic in the absence of light in comparison to chemotherapy. However, PS is low soluble and has limited tumor target ability. To eliminate its disadvantages, one of the

second generation of PS, such as phthalocyanine-loaded FA-functionalized NLCs were fabricated and investigated for the potential treatment of breast cancer. In MTT assay, three different concentrations of FA-PS-NLCs were tested against MCF-7 cells and until 0.91 μM concentration, they were found to be nontoxic. Then, FA-PS-NLC at 0.91 μM was exposed to light at four different times. FA-PS-NLC at 0.91 μM for 120 s exposure to light significantly decreased the cell viability to 57%.[132] Another PDT study was conducted with chlorin e6 (Ce6) as PS and PTX-loaded FA-modified NLCs against MDA-MB-231 human breast cancer cells. First, the conjugation of DSPE-PEG_{2000}-Ce6 was performed and then, the preparation of PTX@FA-NLC-PEG-Ce6 using emulsion evaporation-solidification method. Cellular uptake of PTX@FA-NLC-PEG-Ce6 was greater than PTX@NLC-PEG-Ce6 and free-Ce6 due to FR-mediated endocytosis.[133]

Recent work was conducted on a drug delivery system by a combination of both tumor microenvironment-sensitive polypeptides (TMSP) and FA-modified nanoparticles. TMSP is composed of polyanionic inhibitory peptides, polycationic cell-penetrating peptides, and the MMP-2/9-sensitive cleavable peptide. Whereas the level of MMP-2/9 protease increases, TMSP promotes specific cellular uptake *via* polyanionic inhibitory peptides in tumor tissue. The dual targeting system was designed to enhance selective delivery to tumor cells and diminish the toxicity in healthy tissues. FA and TMSP were conjugated with DSPE-PEG5000-amine and DSPE-PEG2000-maleimide to generate DSPE-PEG5000-FA and DSPE-PEG2000-TMSP, respectively. Next, these ligands were used to decorate the surface of DTX-loaded NLCs (F/TMSP-DTX-NLC) (see Figure 17.8). While F/TMSP-DTX-NLC exhibited a superior antiproliferation effect against KB month epidermoid and HT-1080 fibrosarcoma carcinoma cells, it showed less effect against MCF-7 breast and A549 pulmonary adenocarcinoma cells. This result was attributed to its occurrence at a different level of FR. Due to the ability of cell-penetrating peptides, F/TMSP-DTX-NLC significantly demonstrated penetration into multicellular tumor spheroids.[134]

Epigallocatechin-3-gallate (EGCG) is the main polyphenolic compound found in green tea. EGCG shows therapeutic benefits in inflammatory, obesity, infectious, and cancer diseases. EGCG is administrated orally, which brings some drawbacks such as poor oral bioavailability, low stability, and intestinal permeability. To overcome those problems, Granja *et al.* developed and characterized FA-modified EGCG-loaded NLCs (FA-EGCG-NLC) and observed the *in vitro* release profile of EGCG in simulated gastrointestinal conditions. In comparison with unmodified-EGCG-NLCs, both exhibited controlled and sustained release; however, the cumulative EGCG release from FA-EGCG-NLCs was higher, which indicates more absorption in the intestine and passage to the bloodstream.[135] When FA-EGCG-NLC was tested on CaCo-2 cells to detect *in vitro* intestinal permeability, the FA-modified NLC system 1.8-fold increased the permeability when compared to free EGCG and EGCG-NLC.[136]

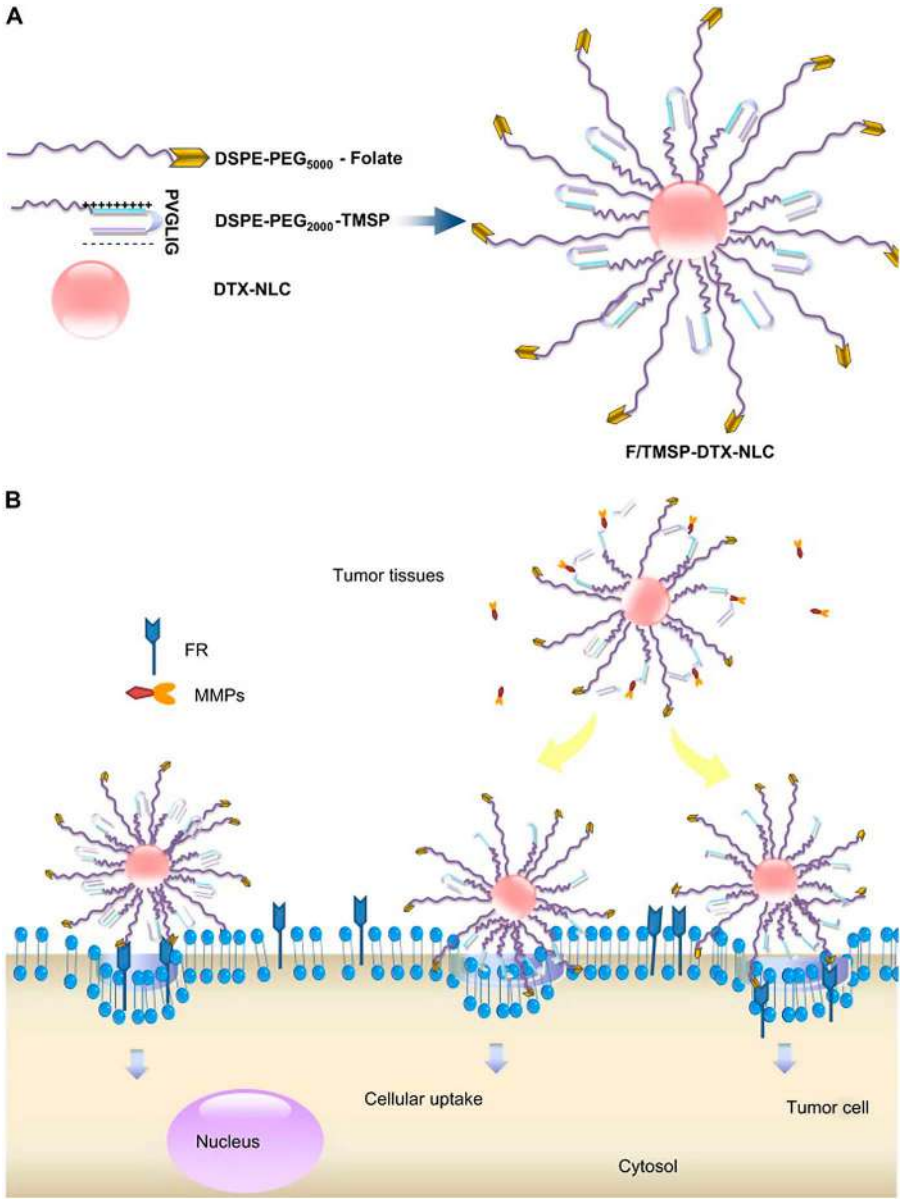

Figure 17.8 Scheme of F/TMSP-DTX-NLC (A), Scheme of the multivalent interactions of F/TMSP-DTX-NLC with cancer cell (B). Reproduced from ref. 134 with permission from Elsevier, Copyright 2013.

Biotin (also known as vitamin H or B7) is essential for normal human health and development. B7 plays a role in cell growth and significant metabolic pathways such as gluconeogenesis and the synthesis of fatty acids (see Figure 17.9). Cellular uptake of biotin occurs by receptor-mediated endocytosis, *i.e.*, Na^+-dependent transport pathway.[137,138] It has been proven that the

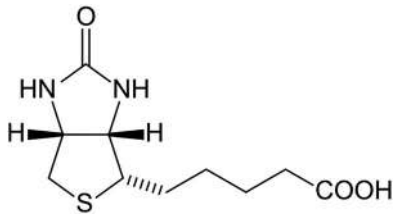

Figure 17.9 The chemical structure of biotin.

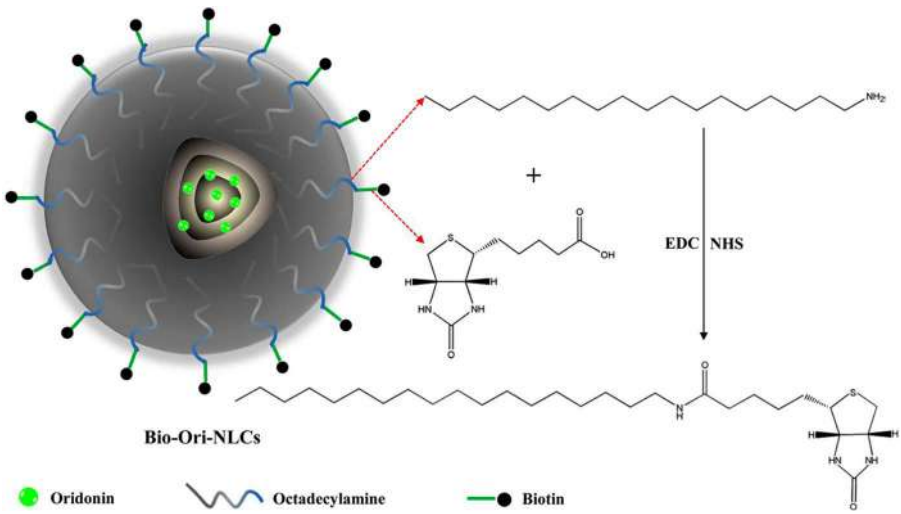

Figure 17.10 Scheme of Bio-Ori-NLC. Reproduced from ref. 138 with permission from Elsevier, Copyright 2015.

biotin receptor is overexpressed in numerous cancer tissues, whereas the healthy tissue shows a limited expression level.[139]

Oridonin is a natural compound derived from *Rabdosia rubescens* and presents an antiproliferation effect in pancreatic, liver, and esophagus cancer. Biotin as a functional ligand was utilized to modify oridonin-loaded NLC (Bio-Ori-NLC) for oral delivery (see Figure 17.10). *N*-Hydroxysuccinimide (NHS) and *N*-(3-dimethylaminopropyl)-*N*0-ethyl carbodiimide hydrochloride (EDC) were used as coupling agents to conjugate the biotin to the surface of NLC. While no significant difference was observed in the release profile of Ori-NLC and Bio-Ori-NLC, lipolysis assay revealed that biotin surface modification protects NLCs from enzymatic degradation. Bioavailability of Ori in rats improved by Bio-Ori-NLC and Ori-NLC in comparison to free Ori, 171% and 143% respectively.[138]

Chrysin (CHN) is a flavonoid that occurs naturally in several plants, mushrooms, propolis, and honey. Its extract can be used in the treatment of cancer, diabetes, bacterial and viral infections, arthritis, and depression. The antineoplastic effect of CHN was tested in various cell lines such as colon,

pancreatic, breast, cervical, lung, liver, leukemia, and glioblastoma. The limitations of CHN, including low aqueous solubility capacity and bioavailability, fast first-pass metabolism, and systemic elimination, constitute problems for its potential treatments. Sharma *et al.* developed biotin-functionalized CHN-loaded NLC for oral delivery. To measure cellular uptake affinity, NLCs were prepared with a fluorescence probe coumarin-6 (C_6) and tested on CaCo-2 cells. The highest fluorescence signal was detected with Bio–CHN–NLC due to its efficient endocytosis across the cellular membrane. IC50 values against MCF-7 cells were 66, 42, 30 μM for free CHN, CHN-NLC, and Bio–CHN–NLC, respectively, and for MDAMB-231 cells 74, 48, 36 μM, respectively.[140]

N-Acetyl-D-galactosamine (GalNAc) and galactose (Gal) are recognized by the asialoglycoprotein receptor (ASGPR), which is a C-type lectin receptor that principally exhibits expression on the surface of hepatic cells. GalNAc stearic acid (SA) PEG derivative (SA-PEG_{100}-GalNAc) ligand was prepared to decorate the NLC surface to target the ASGPR (see Figure 17.11).[141] Hepatocyte uptake of GalNAc-NLCs occurred rapidly without bounding plasma membranes after 1 h exposure to the hepatocarcinoma cell line HepG2 and its derivative HepG2/C3a. The study showed that a high density of GalNAc was required for specific liver targeting and internalization through the ASGPR pathway.[142]

Stearyl-2-amino-2-deoxyglucose (2-DG), a glucosamine derivative ligand, has been commonly used as components of contrast agents for diagnostic tumor monitoring. The 2-DG-conjugated fluorescein and cypate-loaded NLCs (2-DG-fluorescein-NLand 2-DG-cypate-NLC) were investigated. When their release profile was compared, the higher lipid-soluble drug model cypate exhibited a slower and linear release than fluorescein. The 2-DG-cypate-NLC and free cypate with fluorescence labels were injected into a healthy mouse model to monitor dynamic behavior. Whereas 2-DG-cypate-NLC was detected in the liver 5 min after injection and the signal disappeared after 36 h, the

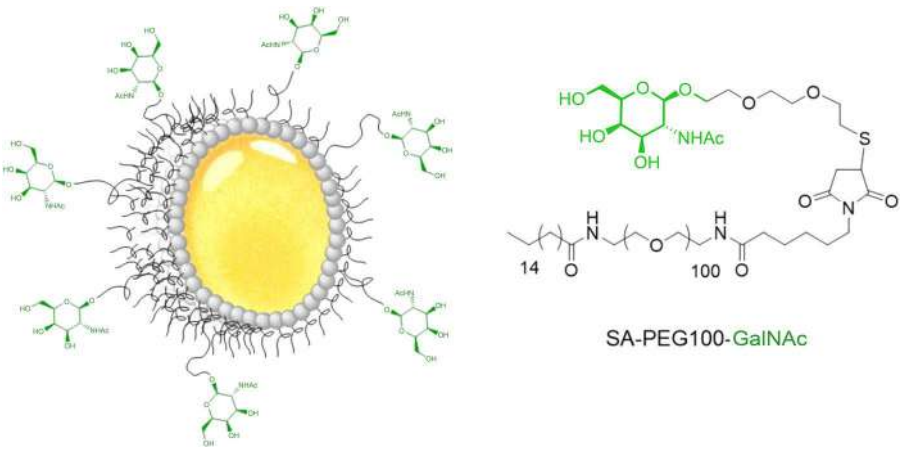

Figure 17.11 Scheme of GalNAc-NLC. Reproduced from ref. 142 with permission from Taylor & Francis, Copyright 2020.

signal of free cypate appeared in the liver in 3 min and disappeared from the liver 8 h later. Modified NLC extended the circulation time of the drug. Also, the therapeutic effect of 2-DG-PTX-NLC was compared with PTX-NLC and free PTX in the MCF-7 tumor-bearing mice model. The 2-DG-PTX-NLC demonstrated a better tumor inhibition profile and lower body weight decreasing rates than the other groups.[143]

17.4.1.5 Inorganic Hybrid Lipid Nanoparticles

The conjugation of NLC with inorganic materials is a relatively unexplored field, and only a few materials have been explored either as cargo or to provide new properties to the nanosystem. The cosmetic industry entered this type of system relatively early. Due to their size and composition NLCs have good cosmetic qualities, and they remain on the skin longer than traditional emulsions.[144]

NLCs can be used for sun protection applications as they have an intrinsic ability to scatter light, the addition of titanium dioxide and zinc oxide improves the UV protection (Sun Protection Factor – SPF) synergistically.[145] Moreover, the preparation method can be modified to increase oxide particles on the NLC surface, further enhancing SPF (Cengiz *et al.*, 2006). Hybrid silica-lipid nanoparticles carrying organic sun-blocking agents have been reported. NLC improved the capacity of the organic blocker, while the silica hydrogel provided considerable bioadhesion.[146]

Colloidal silica can be added to the aqueous phase, forming a shell around the NLC or added to the lipid phase, integrating into the volume of the NLC.[147,148] On the other hand, silica shells can be obtained by mineralization of the NLC surface by adding a silica precursor such as TMOS.[149] This type of hybrid can improve the antioxidant capacity of NLCs, protect them from the gastric environment, improving their oral bioavailability while preserving the high loading capacity for hydrophobic drugs and the preferential cellular uptake of non-hybrid NLCs.[149] Additionally, combinations with inorganic materials, either by adsorption or inclusion, may increase dispersions' stability and prolongs their shelf life.[150]

The combination of NLC with magnetic particles is fairly simple and can have different objectives.[151] The inclusion of iron magnetic nanoparticles (IMNs) can help to target a delivery system based on NLC, with the aid of an external magnetic field, even helping encapsulated drugs to reach the central nervous system by increasing BBB permeability.[152] If the magnetic field applied to these systems is pulsatile, IMN movement dissipates heat and raises the temperature in its surroundings, an effect normally called hyperthermia. The hyperthermic treatment uses this effect to induce apoptosis in cancer cells, on the rationale that it is more sensitive to temperature.[153] The inclusion of IMNs in lipid delivery systems can mitigate the drawbacks normally associated with hemotoxicity and aggregation while conserving the magnetic properties.[154] However, hyperthermia can be further taken advantage of; if a drug is co-loaded with IMNs in NLCs, a rise in local temperature

can melt or disrupt lipid structure, greatly increasing drug release, thus creating a magnetic responsive delivery system.[155,156] Furthermore, IMNs can enhance resolution and function as contrast agents in magnetic resonance agents. A combination of these diagnostic and therapeutic tools can result in true theragnostic devices in complex pathologies such as cancer or atherosclerosis.[157]

17.5 Concluding Remarks

The introduction of bionanotechnologies has transformed the landscape in the drug delivery field. Many new molecular sustained devices provide novel opportunities for the therapeutic use of drugs to overcome administration problems such as high toxicity, low bioavailability, fast opsonization and elimination, broad distribution in the body, *etc.* In particular, the development of SLNs and their further evolution to NLC demonstrated the advantages of a versatile structure for molecules with different physicochemical and biological properties and the possibility of targeting almost all organs in the body. A synthesis of the main properties of NLC devices is listed below.

Among the main advantages of SLNs are:

a. Chemical lipid composition with GRAS status by FDA (USA) and EMA (EU), which is relevant for drug administration to avoid acute and chronic toxicities compared to other drug delivery systems.
b. Lipid nanoparticles also increase the half-life of compounds sensitive to harsh environments such as UV-light, redox compounds, shear stress, and chemical and biological degradation proper of the oral, epidermic, and gastrointestinal tract.
c. Lipophilic drugs with low solubility and bioavailability are recommended to be formulated in lipid systems showing increasing effectivity and activity with low doses. Also, hydrophilic drugs can be administrated in hybrid NLC systems.
d. Lack of organic solvents along with the formulation and easy scale-up, highly reproducible formulation techniques, high yields, and low material costs.
e. The solid lipid matrices are, in general, very stable for many years, and concomitantly display constant kinetic controlled drug release, unlike nanoemulsions and nanoliposomes, which are thermodynamically unstable, and the kinetics of drug release is unpredictable.
f. Solid lipid nanostructures, in general, show a high payload compared to polymeric nanoparticles.
g. SLNs can be administered by many clinical routes such as anal, dermic, nasal, oral, parenteral, sublingual without losing stability and loading.
h. Tailoring and development of hybrid NLC systems is straightforward and with many options.
i. Thermodynamic stability of SLN, NLC, and their hybrid nanoparticles.

Despite the great advantages of lipid formulations, there are some disadvantages such as:

a. Low loading, particularly in SLNs because of their crystalline structure. In the case of NLC it is a tradeoff between loading and stability because of unstructured characteristics.
b. Impurities of the starting materials, which change the properties of the lipid configuration and physicochemical properties.
c. The water content of SLN could reduce the viability of the nanoparticles in shelf life.
d. Physicochemical exposure to redox chemicals, UV-light, or enzymes.

All the characteristics of NLCs mentioned in the present work show some of the major properties of the carriers with high structural diversity and complexity that can be developed for many pharmaceutical applications during the next decades.

Acknowledgements

The present work was supported by Argentine grants from the *Universidad Nacional de* La Plata (14/X041, 14/X701), *Agencia Nacional de Promocion Cientifica y Tecnologica* (PICT 2016-1574, PICT2016-4596, PICT2017-0359, PICT 2019-02322) to IEL and GRC, and PIP 0340 (CONICET) to IEL. GRC and IEL are members of the *Carrera del Investigador* CONICET. TB and IRB are fellows of CONICET.

References

1. C. Zhang, W. Zhao, C. Bian, X. Hou, B. Deng, D. W. McComb, X. Chen and Y. Dong, *ACS Appl. Bio Mater.*, 2019, **2**, 1270–1277.
2. A. A. Attama, M. A. Momoh and P. F. Builders, in *Recent Advances in Novel Drug Carrier Systems*, ed. A. D. Sezer, InTech, 2012, pp. 106–124.
3. M. Á. Aznar, B. Lasa-Saracíbar and M. J. Blanco-Prieto, *Mol. Pharm.*, 2014, **11**, 2650–2658.
4. G. A. Islan, M. L. Cacicedo, B. Rodenak-Kladniew, N. Duran and G. R. Castro, *Curr. Pharm. Des.*, 2018, **23**, 6643–6658.
5. H. Luo, L. Lu, F. Yang, L. Wang, X. Yang, Q. Luo and Z. Zhang, *ACS Nano*, 2014, **8**, 4334–4347.
6. H. Reza Rezaie, M. Esnaashary, A. Aref arjmand, A. Öchsner, H. R. Rezaie and M. Esnaashary, *A Review of Biomaterials and Their Applications in Drug Delivery*, Springer Singapore, 2018.
7. O. M. Feeney, M. F. Crum, C. L. McEvoy, N. L. Trevaskis, H. D. Williams, C. W. Pouton, W. N. Charman, C. A. S. Bergström and C. J. H. Porter, *Adv. Drug Delivery Rev.*, 2016, **101**, 167–194.
8. A. Puri, K. Loomis, B. Smith, J. H. Lee, A. Yavlovich, E. Heldman and R. Blumenthal, *Crit. Rev. Ther. Drug Carrier Syst.*, 2009, **26**, 523–580.

9. J. Mazuryk, T. Deptuła, A. Polchi, J. Gapiński, S. Giovagnoli, A. Magini, C. Emiliani, J. Kohlbrecher and A. Patkowski, *Colloids Surf., A*, 2016, **502**, 54–65.
10. R. M. Shah, D. S. Eldridge, E. A. Palombo and I. H. Harding, *Eur. J. Pharm. Biopharm.*, 2017, **117**, 141–150.
11. W. Mehnert and K. Mäder, *Adv. Drug Delivery Rev.*, 2012, **64**, 83–101.
12. R. H. Müller, K. Mäder and S. Gohla, *Eur. J. Pharm. Biopharm.*, 2000, **50**, 161–177.
13. S. A. Wissing, O. Kayser and R. H. Müller, *Adv. Drug Delivery Rev.*, 2004, **56**, 1257–1272.
14. S. de J. Calva-Estrada, O. García, M. R. Mendoza and M. Jiménez, *J. Dispersion Sci. Technol.*, 2018, **39**, 181–189.
15. K. C. S. Galvão, A. A. Vicente and P. J. A. Sobral, *Food Bioprocess Technol.*, 2018, **11**, 355–367.
16. J. Štecová, W. Mehnert, T. Blaschke, B. Kleuser, R. Sivaramakrishnan, C. C. Zouboulis, H. Seltmann, H. C. Korting, K. D. Kramer and M. Schäfer-Korting, *Pharm. Res.*, 2007, **24**, 991–1000.
17. F. Suter, D. Schmid, F. Wandrey and F. Zülli, *Eur. J. Pharm. Biopharm.*, 2016, **108**, 304–309.
18. S. Das and A. Chaudhury, *AAPS PharmSciTech*, 2011, **12**, 62–76.
19. M. Gasco, *US Pat.*, US5250236A, 1993.
20. R. Cortesi, E. Esposito, G. Luca and C. Nastruzzi, *Biomaterials*, 2002, **23**, 2283–2294.
21. M. Yasir, P. K. Gaur, D. Puri, S. Preeti and S. S. Kumar, *Curr. Drug Delivery*, 2018, **15**, 818–828.
22. W. L. Masiiwa and L. L. Gadaga, *J. Drug Delivery*, 2018, **2018**, 1–9.
23. M. Trotta, F. Debernardi and O. Caputo, *Int. J. Pharm.*, 2003, **257**, 153–160.
24. F. Q. Hu, H. Yuan, H. H. Zhang and M. Fang, *Int. J. Pharm.*, 2002, **239**, 121–128.
25. B. Sjöström, A. Kaplun, Y. Talmon and B. Cabane, *Pharm. Res.*, 1995, **12**, 39–48.
26. D. Pooja, H. Kulhari, L. Tunki, S. Chinde, M. Kuncha, P. Grover, S. S. Rachamalla and R. Sistla, *RSC Adv.*, 2015, **5**, 49122–49131.
27. K. K. Patel, S. Gade, M. M. Anjum, S. K. Singh, P. Maiti, A. K. Agrawal and S. Singh, *Appl. Nanosci.*, 2019, **9**, 1383–1394.
28. Z. Li, L. Yu, L. Zheng and F. Geng, *J. Therm. Anal. Calorim.*, 2010, **99**, 689–693.
29. S. Singh, A. K. Dobhal, A. Jain, J. K. Pandit and S. Chakraborty, *Chem. Pharm. Bull.*, 2010, **58**, 650–655.
30. P. Fonte, T. Nogueira, C. Gehm, D. Ferreira and B. Sarmento, *Drug Delivery Transl. Res.*, 2011, **1**, 299–308.
31. L. Becker Peres, L. Becker Peres, P. H. H. de Araújo and C. Sayer, *Colloids Surf., B*, 2016, **140**, 317–323.
32. K. L. Mazur, P. E. Feuser, A. Valério, A. Poester Cordeiro, C. I. de Oliveira, J. P. Assolini, W. R. Pavanelli, C. Sayer and P. H. H. Araújo, *Colloids Surf., B*, 2019, **176**, 507–512.

33. L. Montenegro, M. G. Sarpietro, S. Ottimo, G. Puglisi and F. Castelli, *Int. J. Pharm.*, 2011, **415**, 301–306.
34. L. Montenegro, C. Sinico, I. Castangia, C. Carbone and G. Puglisi, *Int. J. Pharm.*, 2012, **434**, 169–174.
35. C. Charcosset, A. El-Harati and H. Fessi, *J. Controlled Release*, 2005, **108**, 112–120.
36. P. Chattopadhyay, B. Y. Shekunov, D. Yim, D. Cipolla, B. Boyd and S. Farr, *Adv. Drug Delivery Rev.*, 2007, **59**, 444–453.
37. L. N. Andrade, D. M. L. Oliveira, M. V. Chaud, T. F. R. Alves, M. Nery, C. F. da Silva, J. K. C. Gonsalves, R. S. Nunes, C. B. Corrêa, R. G. Amaral, E. Sanchez-Lopez, E. B. Souto and P. Severino, *Molecules*, 2019, 3881.
38. D. Chirio, M. Gallarate, E. Peira, L. Battaglia, E. Muntoni, C. Riganti, E. Biasibetti, M. T. Capucchio, A. Valazza, P. Panciani, M. Lanotte, L. Annovazzi, V. Caldera, M. Mellai, G. Filice, S. Corona and D. Schiffer, *Eur. J. Pharm. Biopharm.*, 2014, **88**, 746–758.
39. L. Battaglia, E. Muntoni, D. Chirio, E. Peira, L. Annovazzi, D. Schiffer, M. Mellai, C. Riganti, I. C. Salaroglio, M. Lanotte, P. Panciani, M. T. Capucchio, A. Valazza, E. Biasibetti and M. Gallarate, *Nanomedicine*, 2017, **12**, 639–656.
40. K. Oumzil, M. A. Ramin, C. Lorenzato, A. Hémadou, J. Laroche, M. J. Jacobin-Valat, S. Mornet, C. E. Roy, T. Kauss, K. Gaudin, G. Clofent-Sanchez and P. Barthélémy, *Bioconjugate Chem.*, 2016, **27**, 569–575.
41. J. Chang, X. Chen, Z. Glass, F. Gao, L. Mao, M. Wang and Q. Xu, *Acc. Chem. Res.*, 2019, **52**, 665–675.
42. L. He, D. Fan, W. Liang, Q. Wang and J. Fang, *ACS Appl. Bio Mater.*, 2020, **3**, 3276–3284.
43. S. Scioli Montoto, G. Muraca and M. E. Ruiz, *Front. Mol. Biosci.*, 2020, **7**, 319.
44. P. Ghasemiyeh and S. Mohammadi-Samani, *Results Pharma Sci.*, 2018, **13**, 288–303.
45. A. Beloqui, M. Á. Solinís, A. Rodríguez-Gascón, A. J. Almeida and V. Préat, *Nanomedicine*, 2016, **12**, 143–161.
46. A. Garcês, M. H. Amaral, J. M. Sousa Lobo and A. C. Silva, *Eur. J. Pharm. Sci.*, 2018, **112**, 159–167.
47. A. Khosa, S. Reddi and R. N. Saha, *Biomed. Pharmacother.*, 2018, **103**, 598–613.
48. M. Rehman, A. Madni, A. Ihsan, W. S. Khan, M. I. Khan, M. A. Mahmood, M. Ashfaq, S. Z. Bajwa and I. Shakir, *Int. J. Nanomed.*, 2015, **10**, 2805–2814.
49. M. Rizwanullah, J. Ahmad and S. Amin, *Curr. Drug Delivery*, 2016, **13**, 4–26.
50. P. P. Constantinides, A. Tustian and D. R. Kessler, *Adv. Drug Delivery Rev.*, 2004, **56**, 1243–1255.
51. W. C. Griffin, *J. Soc. Cosmet. Chem.*, 1949, **1**, 311–326.
52. M. Almeida, M. Magalhães, F. Veiga and A. Figueiras, *J. Polym. Res.*, 2018, **25**, 1–14.

53. E. V. Brovč, J. Mravljak, R. Šink and S. Pajk, *Int. J. Pharm.*, 2020, **581**, 119285.
54. A. Martos, W. Koch, W. Jiskoot, K. Wuchner, G. Winter, W. Friess and A. Hawe, *J. Pharm. Sci.*, 2017, **106**, 1722–1735.
55. C. Cimino, O. M. Maurel, T. Musumeci, A. Bonaccorso, F. Drago, E. M. B. Souto, R. Pignatello and C. Carbone, *Pharmaceutics*, 2021, **13**, 1–35.
56. M. T. Jones, H. C. Mahler, S. Yadav, D. Bindra, V. Corvari, R. M. Fesinmeyer, K. Gupta, A. M. Harmon, K. D. Hinds, A. Koulov, W. Liu, K. Maloney, J. Wang, P. Y. Yeh and S. K. Singh, *Pharm. Res.*, 2018, 148.
57. S. Weber, A. Zimmer and J. Pardeike, *Eur. J. Pharm. Biopharm.*, 2014, **86**, 7–22.
58. S. Khan, S. Baboota, J. Ali, S. Khan, R. S. Narang and J. K. Narang, *Int. J. Pharm. Invest.*, 2015, **5**, 182–191.
59. G. A. Islan, M. E. Ruiz, J. F. Morales, M. L. Sbaraglini, A. V. Enrique, G. Burton, A. Talevi, L. E. Bruno-Blanch and G. R. Castro, *J. Mater. Chem. B*, 2017, **5**, 3132–3144.
60. T. S. Patil and A. S. Deshpande, *Int. J. Pharm.*, 2018, **547**, 209–225.
61. D. S. Spencer, A. S. Puranik and N. A. Peppas, *Curr. Opin. Chem. Eng.*, 2015, **7**, 84–92.
62. M. Majidinia, M. Mirza-Aghazadeh-Attari, M. Rahimi, A. Mihanfar, A. Karimian, A. Safa and B. Yousefi, *IUBMB Life*, 2020, **72**, 855–871.
63. S. Rawal and M. M. Patel, *J. Controlled Release*, 2019, **301**, 76–109.
64. M. L. Cacicedo, M. C. Ruiz, S. Scioli-Montoto, M. E. Ruiz, M. A. Fernández, R. M. Torres-Sanchez, E. J. Baran, G. R. Castro and I. E. León, *New J. Chem.*, 2019, **43**, 17726–17734.
65. S. Scioli Montoto, G. Muraca, M. Di Ianni, M. Couyoupetrou, G. Pesce, G. A. Islan, C. Y. Chain, M. E. Vela, M. E. Ruiz, A. Talevi and G. R. Castro, *J. Drug Delivery Sci. Technol.*, 2021, **63**, 102470.
66. S. Alam, M. Aslam, A. Khan, S. S. Imam, M. Aqil, Y. Sultana and A. Ali, *Drug Delivery*, 2016, **23**, 601–609.
67. Y. Gu, X. Tang, M. Yang, D. Yang and J. Liu, *Int. J. Pharm.*, 2019, **554**, 235–244.
68. Y. Barenholz, *J. Controlled Release*, 2012, **160**, 117–134.
69. H. Yuan, J. Miao, Y. Z. Du, J. You, F. Q. Hu and S. Zeng, *Int. J. Pharm.*, 2008, **348**, 137–145.
70. J. Luan, X. Yang, L. Chu, Y. Xi and G. Zhai, *J. Colloid Interface Sci.*, 2014, **428**, 49–56.
71. P. Nahak, R. L. Gajbhiye, G. Karmakar, P. Guha, B. Roy, S. E. Besra, A. G. Bikov, A. V. Akentiev, B. A. Noskov, K. Nag, P. Jaisankar and A. K. Panda, *Pharm. Res.*, 2018, 198.
72. P. Lakhani, A. Patil, K. W. Wu, C. Sweeney, S. Tripathi, B. Avula, P. Taskar, S. Khan and S. Majumdar, *Int. J. Pharm.*, 2019, 118771.
73. K. Shiraishi and M. Yokoyama, *Sci. Technol. Adv. Mater.*, 2019, **20**, 324–336.

74. M. J. Limeres, M. Suñé-Pou, S. Prieto-Sánchez, C. Moreno-Castro, A. D. Nusblat, C. Hernández-Munain, G. R. Castro, C. Suñé, J. M. Suñé-Negre and M. L. Cuetsas, *Colloids Surf., B*, 2019, 110533.
75. D. Delgado, A. Del Pozo-Rodríguez, M. Á. Solinís and A. Rodríguez-Gascón, *Eur. J. Pharm. Biopharm.*, 2011, **79**, 495–502.
76. H. O. Ammar, M. M. Ghorab, D. M. Mostafa, S. H. Abd El-Alim, A. A. Kassem, S. Salah and E. S. Shalaby, *J. Microencapsulation*, 2020, **37**, 366–383.
77. Y. Han, Y. Zhang, D. Li, Y. Chen, J. Sun and F. Kong, *Int. J. Nanomed.*, 2014, **9**, 4107–4116.
78. D. Kebebe, Y. Wu, B. Zhang, J. Yang, Y. Liu, X. Li, Z. Ma, P. Lu, Z. Liu and J. Li, *Int. J. Nanomed.*, 2019, **14**, 6179–6195.
79. S. Das, S. Ghosh, A. K. De and T. Bera, *Int. J. Biol. Macromol.*, 2017, **102**, 996–1008.
80. G. H. Shin and J. T. Kim, *Food Hydrocolloids*, 2018, **84**, 146–153.
81. J. A. Champion, A. Walker and S. Mitragotri, *Pharm. Res.*, 2008, **25**, 1815–1821.
82. Y. Yu, R. Feng, S. Yu, J. Li, Y. Wang, Y. Song, X. Yang, W. Pan and S. Li, *Int. J. Biol. Macromol.*, 2018, **114**, 462–469.
83. M. Haider, S. M. Abdin, L. Kamal and G. Orive, *Pharmaceutics*, 2020, **12**, 288.
84. C. Li, J. Zhang, Y. J. Zu, S. F. Nie, J. Cao, Q. Wang, S. P. Nie, Z. Y. Deng, M. Y. Xie and S. Wang, *Chin. J. Nat. Med.*, 2015, **13**, 641–652.
85. P. Tongnuanchan and S. Benjakul, *J. Food Sci.*, 2014, R1231–R1249.
86. F. Saporito, G. Sandri, M. C. Bonferoni, S. Rossi, C. Boselli, A. Icaro Cornaglia, B. Mannucci, P. Grisoli, B. Vigani and F. Ferrari, *Int. J. Nanomed.*, 2017, **13**, 175–186.
87. B. Rodenak-Kladniew, S. Scioli Montoto, M. L. Sbaraglini, M. Di Ianni, M. E. Ruiz, A. Talevi, V. A. Alvarez, N. Durán, G. R. Castro and G. A. Islan, *Int. J. Pharm.*, 2019, 118575.
88. A. Tarakemeh, V. Rowshan and S. Najafian, *Anal. Chem. Lett.*, 2012, **2**, 244–249.
89. C. Takayama, F. M. de-Faria, A. C. A. de Almeida, R. J. Dunder, L. P. Manzo, E. A. R. Socca, L. M. Batista, M. J. Salvador, A. R. M. Souza-Brito and A. Luiz-Ferreira, *Asian Pac. J. Trop. Biomed.*, 2016, **6**, 677–681.
90. C. Carbone, M. D. C. Teixeira, M. D. C. Sousa, C. Martins-Gomes, A. M. Silva, E. M. B. Souto and T. Musumeci, *Pharmaceutics*, 2019, 231.
91. E. Lasoń, *Molecules*, 2020, **25**, 5758.
92. B. Rodenak-Kladniew, G. A. Islan, M. G. de Bravo, N. Durán and G. R. Castro, *Colloids Surf., B*, 2017, **154**, 123–132.
93. B. Rodenak-Kladniew, N. Noacco, I. Pérez de Berti, S. J. Stewart, A. F. Cabrera, V. A. Alvarez, M. García de Bravo, N. Durán, G. R. Castro and G. A. Islan, *Colloids Surf., B*, 2021, **202**, 111710.
94. S. Maiti and S. Jana, *Polysaccharide Carriers for Drug Delivery*, Elsevier, 2019.
95. C. Englert, J. C. Brendel, T. C. Majdanski, T. Yildirim, S. Schubert, M. Gottschaldt, N. Windhab and U. S. Schubert, *Prog. Polym. Sci.*, 2018, **87**, 107–164.

96. D. C. Ferreira Soares, S. C. Domingues, D. B. Viana and M. L. Tebaldi, *Biomed. Pharmacother.*, 2020, **131**, 110695.
97. G. Ling, T. Zhang, P. Zhang, J. Sun and Z. He, *Drug Dev. Ind. Pharm.*, 2016, **42**, 1351–1359.
98. C. Lin, F. Chen, T. Ye, L. Zhang, W. Zhang, D. Liu, W. Xiong, X. Yang and W. Pan, *Int. J. Pharm.*, 2014, **465**, 90–96.
99. P. Zhang, G. Ling, X. Pan, J. Sun, T. Zhang, X. Pu, S. Yin and Z. He, *Nanomedicine*, 2012, **8**, 185–193.
100. A. A. Khan, I. M. Abdulbaqi, R. Abou Assi, V. Murugaiyah and Y. Darwis, *Nanoscale Res. Lett.*, 2018, 323.
101. G. H. Rodrigues da Silva, G. Geronimo, L. N. M. Ribeiro, V. A. Guilherme, L. D. de Moura, A. L. Bombeiro, J. D. Oliveira, M. C. Breitkreitz and E. de Paula, *Mater. Sci. Eng. C*, 2020, **109**, 110608.
102. P. T. Gomme and K. B. McCann, *Drug Discovery Today*, 2005, **10**, 267–273.
103. S. Tortorella and T. C. Karagiannis, *J. Membr. Biol.*, 2014, **247**, 291–307.
104. T. R. Daniels, E. Bernabeu, J. A. Rodríguez, S. Patel, M. Kozman, D. A. Chiappetta, E. Holler, J. Y. Ljubimova, G. Helguera and M. L. Penichet, *Biochim. Biophys. Acta, Gen. Subj.*, 2012, **1820**, 291–317.
105. Z. Shao, J. Shao, B. Tan, S. Guan, Z. Liu, Z. Zhao, F. He and J. Zhao, *Int. J. Nanomed.*, 2015, **10**, 1223–1233.
106. Y. Han, Y. Li, P. Zhang, J. Sun, X. Li, X. Sun and F. Kong, *Pharm. Dev. Technol.*, 2016, **21**, 277–281.
107. Z. Bin, Z. Yueying and D. Yu, *Oncol. Rep.*, 2017, **37**, 937–944.
108. J. Emami, M. Rezazadeh, H. Sadeghi and K. Khadivar, *Pharm. Dev. Technol.*, 2017, **22**, 370–382.
109. J. Emami, H. Yousefian and H. Sadeghi, *J. Pharm. Pharm. Sci.*, 2018, **21**, 225s–241s.
110. R. G. R. Pinheiro, A. Granja, J. A. Loureiro, M. C. Pereira, M. Pinheiro, A. R. Neves and S. Reis, *Eur. J. Pharm. Sci.*, 2020, 105314.
111. S. A. González-Chávez, S. Arévalo-Gallegos and Q. Rascón-Cruz, *Int. J. Antimicrob. Agents*, 2009, **33**, 301.e1–301.e8.
112. Y. A. Suzuki, V. Lopez and B. Lönnerdal, *Cell. Mol. Life Sci.*, 2005, **62**, 2560–2575.
113. C. Zhao, J. Zhang, H. Hu, M. Qiao, D. Chen, X. Zhao and C. Yang, *Mater. Sci. Eng. C*, 2018, **92**, 1031–1040.
114. F. Meng, S. Asghar, S. Gao, Z. Su, J. Song, M. Huo, W. Meng, Q. Ping and Y. Xiao, *Colloids Surf., B*, 2015, **134**, 88–97.
115. J. Zhang, X. Xiao, J. Zhu, Z. Gao, X. Lai, X. Zhu and G. Mao, *Int. J. Nanomed.*, 2018, **13**, 3039–3051.
116. S. Abdolahpour, T. Toliyat, K. Omidfar, H. Modjtahedi, A. J. Wong, M. J. Rasaee, S. Kashanian and M. Paknejad, *Artif. Cells, Nanomed., Biotechnol.*, 2018, **46**, 89–94.
117. D. Liu, F. Liu, Z. Liu, L. Wang and N. Zhang, *Mol. Pharm.*, 2011, **8**, 2291–2301.
118. Y. Wu, X. Song, D. Kebebe, X. Li, Z. Xue, J. Li, S. Du, J. Pi and Z. Liu, *Int. J. Pharm.*, 2019, 118754.

119. S. J. Li, X. J. Wang, J. B. Hu, X. Q. Kang, L. Chen, X. L. Xu, X. Y. Ying, S. P. Jiang and Y. Z. Du, *Drug Delivery*, 2017, **24**, 402–413.
120. S. Jiang, S. Li, J. Hu, X. Xu, X. Wang, X. Kang, J. Qi, X. Lu, J. Wu, Y. Du and Y. Xiao, *Nanomedicine*, 2019, **15**, 25–36.
121. C. Y. Beh, C. W. How, J. B. Foo, J. N. Foong, G. T. Selvarajah and A. Rasedee, *Drug Des., Dev. Ther.*, 2017, **11**, 771–782.
122. C. Y. Beh, A. Rasedee, G. T. Selvarajah, L. S. Yazan, A. R. Omar, J. N. Foong, C. W. How and J. B. Foo, *PLoS One*, 2019, **14**, e0219285.
123. K. H. Bang, Y. G. Na, H. W. Huh, S. J. Hwang, M. S. Kim, M. Kim, H. K. Lee and C. W. Cho, *Cancers*, 2019, **11**, 11.
124. F. Salahpour Anarjan, *Nano-Struct. Nano-Objects*, 2019, **19**, 100370.
125. G. L. Zwicke, G. Ali Mansoori and C. J. Jeffery, *Nano Rev.*, 2012, **3**, 18496.
126. Q. Tu, Y. Zhang, R. Liu, J.-C. Wang, L. Li, N. Nie, A. Liu, L. Wang, W. Liu, L. Ren, X. Wang and J. Wang, *Curr. Med. Chem.*, 2012, **19**, 3152–3162.
127. G. Zhang, F. Liu, E. Jia, L. Jia and Y. Zhang, *Drug Delivery*, 2016, **23**, 1393–1397.
128. M. Li, J. Pei, Z. Ma, J. Fu, F. Chen and S. Du, *Cancer Chemother. Pharmacol.*, 2020, **85**, 731–739.
129. J. Yang, Z. Ju and S. Dong, *Drug Delivery*, 2017, **24**, 792–799.
130. M. Sabzichi, J. Mohammadian, A. Yari Khosroushahi, R. Bazzaz and H. Hamishehkar, *Asian Pac. J. Cancer Prev.*, 2016, **17**, 5185–5188.
131. N. Poonia, J. Kaur Narang, V. Lather, S. Beg, T. Sharma, B. Singh and D. Pandita, *Colloids Surf., B*, 2019, **181**, 756–766.
132. J. A. Oshiro-Junior, M. R. Sato, F. I. Boni, K. L. M. Santos, K. T. de Oliveira, L. M. de Freitas, C. R. Fontana, D. Nicholas, A. McHale, J. F. Callan and M. Chorilli, *Mater. Sci. Eng. C*, 2020, **108**, 110462.
133. Q. Zhang, J. Zhao, H. Hu, Y. Yan, X. Hu, K. Zhou, S. Xiao, Y. Zhang and N. Feng, *Int. J. Pharm.*, 2019, 118595.
134. W. Gao, B. Xiang, T. T. Meng, F. Liu and X. R. Qi, *Biomaterials*, 2013, **34**, 4137–4149.
135. A. Granja, A. C. Vieira, L. L. Chaves, C. Nunes, A. R. Neves, M. Pinheiro and S. Reis, *Food Chem.*, 2017, **237**, 803–810.
136. A. Granja, A. R. Neves, C. T. Sousa, M. Pinheiro and S. Reis, *Heliyon*, 2019, e02020.
137. H. M. Said, *Subcell. Biochem.*, 2012, **56**, 1–19.
138. X. Zhou, X. Zhang, Y. Ye, T. Zhang, H. Wang, Z. Ma and B. Wu, *Int. J. Pharm.*, 2015, **479**, 391–398.
139. M. Mehdizadeh, H. Rouhani, N. Sepehri, R. Varshochian, M. H. Ghahremani, M. Amini, M. Gharghabi, S. N. Ostad, F. Atyabi, A. Baharian and R. Dinarvand, *Artif. Cells, Nanomed., Biotechnol.*, 2017, **45**, 495–504.
140. T. Sharma, O. P. Katare, A. Jain, S. Jain, D. Chaudhari, B. Borges and B. Singh, *Colloids Surf., B*, 2021, 111429.
141. L. Gauthier, M. Varache, A. C. Couffin, C. Lebrun, P. Delangle, C. Gateau and I. Texier, *Int. J. Mol. Sci.*, 2019, 5669.

142. L. Gauthier, M. Chevallet, F. Bulteau, M. Thépaut, P. Delangle, F. Fieschi, C. Vivès, I. Texier, A. Deniaud and C. Gateau, *J. Drug Targeting*, 2021, **29**, 99–107.
143. J. Chen, H. Chen, S. Cui, B. Xue, J. Tian, S. Achilefu and Y. Gu, *J. Mater. Chem.*, 2012, **22**, 5770–5783.
144. K. Morabito, N. C. Shapley, K. G. Steeley and A. Tripathi, *Int. J. Cosmet. Sci.*, 2011, **33**, 385–390.
145. D. Nesseem, *Int. J. Cosmet. Sci.*, 2011, **33**, 70–79.
146. T. Andreani, J. Dias-Ferreira, J. F. Fangueiro, A. L. R. Souza, C. P. Kiill, M. P. D. Gremião, M. L. García, A. M. Silva and E. B. Souto, *Heliyon*, 2020, **6**, e03831.
147. J. Shaji and D. Varkey, *J. Pharm. Invest.*, 2013, **43**, 405–416.
148. R. Yasmin, S. Rao, K. Bremmell and C. Prestidge, *Eur. J. Pharm. Sci.*, 2017, **96**, 508–514.
149. S. Kim, R. Diab, O. Joubert, N. Canilho and A. Pasc, *Colloids Surf., B*, 2016, **140**, 161–168.
150. M. Koroleva, O. Gorbachevski and E. Yurtov, *Mater. Chem. Phys.*, 2017, **202**, 1–6.
151. J. A. Kulkarni, Y. Y. C. Tam, S. Chen, Y. K. Tam, J. Zaifman, P. R. Cullis and S. Biswas, *Nanoscale*, 2017, **9**, 13600–13609.
152. A. Grillone, M. Battaglini, S. Moscato, L. Mattii, C. De Julián Fernández, A. Scarpellini, M. Giorgi, E. Sinibaldi and G. Ciofani, *Nanomedicine*, 2019, **14**, 727–752.
153. C. J. Gomer, M. Luna, A. Ferrario, N. Rucker and S. Wong, in *Photodynamic Medicine: From Bench to Clinic*, ed. H. Kostron and T. Hasan, Royal Society of Chemistry, London, 2016, vol. 5, pp. 87–99.
154. M. Muñoz de Escalona, E. Sáez-Fernández, J. C. Prados, C. Melguizo and J. L. Arias, *Int. J. Pharm.*, 2016, **504**, 11–19.
155. A. Grillone, E. R. Riva, A. Mondini, C. Forte, L. Calucci, C. Innocenti, C. de Julian Fernandez, V. Cappello, M. Gemmi, S. Moscato, F. Ronca, R. Sacco, V. Mattoli and G. Ciofani, *Adv. Healthcare Mater.*, 2015, **4**, 1681–1690.
156. R. R. Oliveira, M. S. Carrião, M. T. Pacheco, L. C. Branquinho, A. L. R. de Souza, A. F. Bakuzis and E. M. Lima, *Mater. Sci. Eng. C*, 2018, **92**, 547–553.
157. K. Oumzil, M. A. Ramin, C. Lorenzato, A. Hémadou, J. Laroche, M. J. Jacobin-Valat, S. Mornet, C. E. Roy, T. Kauss, K. Gaudin, G. Clofent-Sanchez and P. Barthélémy, *Bioconjugate Chem.*, 2016, **27**, 569–575.

CHAPTER 18

Transition Metal Dichalcogenides: Properties, Synthetic Routes and Applications

J. LUXA[a], V. MAZÁNEK[a] AND Z. SOFER*[a]

[a]Department of Inorganic Chemistry, University of Chemistry and Technology Prague, Technická 5, 166 28 Prague 6, Czech Republic
*E-mail: zdenek.sofer@vscht.cz

18.1 Introduction

Transition metal dichalcogenides (TMDs) belong to a family of materials that counts about 60 members, approximately 40 of which possess layered structure. The general formula is MX_2 (M = transition metal, X = chalcogen) and the possible combinations of metals and chalcogens are schematically shown in Figure 18.1. Despite being known for decades, TMDs have not regained the interest of scientists until the discovery of unique properties of graphene by Geim and Novoselov. Given the relatively large amount of representatives, the family of TMDs covers a wide range of properties including insulators, semiconductors, metals, superconductors or Weyl semimetals. The origin of such variations can be found in the existence of d-bands at the Fermi level and differences in their occupation with electrons.[1]

Nanoscience & Nanotechnology Series No. 55
Concepts and Design of Materials Nanoarchitectonics
Edited by Omar Azzaroni and Katsuhiko Ariga

Published by the Royal Society of Chemistry, www.rsc.org

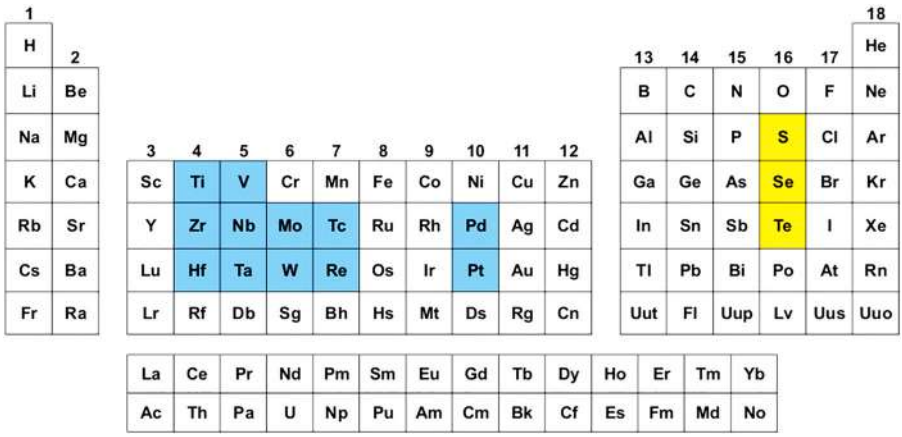

Figure 18.1 Possible combinations of metals and chalcogens that form TMDs with layered structure. Reproduced from ref. 2 with permission from the Royal Society of Chemistry.

Unlike graphene, which is a true 2D nanomaterial, single layers of these materials consist of "triple layers" composed of metal atoms sandwiched between two layers of chalcogens. Nevertheless, weak van der Waals forces between individual layers allow them to be exfoliated down to a single layer. A plethora of new unique properties often emerges as a consequence of quantum confinement effects. A stellar example is the transition from indirect to direct band gap and its opening in single layer MoS_2. Additionally, the band gap values of semiconducting TMDs is within the range of 0 to ~2 eV, which cannot be rivaled by pure graphene, a gapless semimetal. Such a variety predetermines these compounds for use in various fields including electronics, optoelectronics, biosensors, gas sensors or energy storage.[3]

The goal of this chapter is to introduce the reader to the vast field of TMDs. The following chapters cover some of the basic properties of TMDs including structure, electronic structure and optical properties. Further chapters deal with synthetic methods and applications of TMDs.

18.2 Properties of TMDs

18.2.1 Structure

The structure of TMDs is typically formed by a metal sandwiched between two layers of chalcogens. The thickness of such "triple-layer" commonly falls within the range of 6–7 Å and the hexagonal coordination of metal atoms results in trigonal prismatic or octahedral units. The presence of weak van der Waals forces between individual layers and strong covalent bonds within

the layers results in a highly anisotropic environment. Moreover, as discussed in further paragraphs, different orders of layer stacking also means that TMDs crystallize as various polytypes.

Typical coordination of metal atoms is displayed in Figure 18.2.[4] Within the group of TMDs, the coordination of central atoms is predominantly determined by the count of *d*-electrons, however, relative sizes of metal atoms also play a role. Group 4 TMDs all adopt octahedral coordination. In group 5, most metals are also octahedrally coordinated with some of them in trigonal prismatic coordinations. The opposite is true for group 6, where trigonal prismatic coordination is the most dominant. For groups 7 and 10, octahedral coordination is dominant again, however, in group 7 the structures are distorted. The explanation lies within the number of electrons and relative energy shifts within the band structure. For trigonal prismatic and octahedral coordinations, there are pronounced differences at the Γ and K points of the Brillouin zone.[5] The differences are negligible for d^0 configuration, however, as the bands slowly start to fill up, first the trigonal prismatic coordination is more stable. This effect reaches a maximum around d^2 configuration, where the octahedral coordination starts to be more stable. Interestingly enough, alkali metal intercalation can result in a phase transformation, where the coordination is changed from trigonal prismatic to octahedral (*e.g.* MoS_2) and *vice versa* (*e.g.* TaS_2).

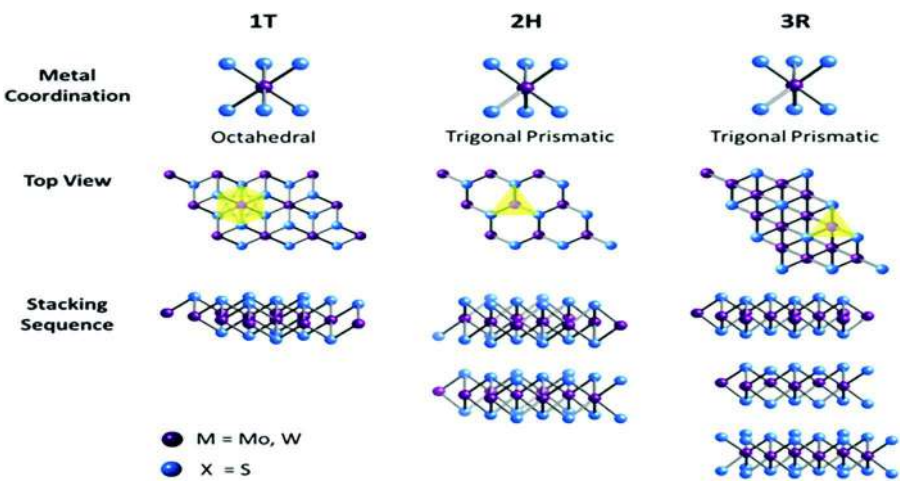

Figure 18.2 Various coordinations of metal atoms (upper row), top view of the structure and a stacking sequence in 1T, 2H and 3R polytypes. An example of MoS_2 is shown. Reproduced from ref. 4 with permission from the Royal Society of Chemistry.

The stacking order of individual layers gives rise to three of the most common polytypes. These are called 1T, 2H and 3R. Here, the number stands for number of layers in the unit cell and the letter represents the symmetry (T – trigonal, H – hexagonal, R – rhombohedral). Schematically, the polytypes are shown in Figure 18.2. It is also apparent that in both 2H and 3R polytypes, the coordination of metal atoms is trigonal prismatic. Apart from these, there are also other polytypes (4H or 6R), but they are not found quite as often. Additionally, there are multiple types of 2H stacking with $2H_a$ and $2H_c$ as the most common. $2H_c$ stacking can be found in the most known example from the TMDs family – MoS_2. In this polytype, the metals from one layer are on top of chalcogens from the surrounding layers.

Some TMDs also adopt distorted structures with examples being WTe_2, $ReSe_2$ or $NbTe_2$. Such a distortion is realized *via* the formation of chains of metal atoms. As a consequence, these TMDs crystallize in less symmetrical triclinic space groups. These distortions are related to Peierls or Jahn-Teller distortions.[6] Another distortion found in TMDs is the so-called charge density waves (CDWs). This is a relatively old scientific topic, however, one of the most challenging. Within this phenomenon, the electrons in a CDW form a standing wave pattern that can act in a collective manner. One of the most famous TMDs with CDW behavior is 1T-TaS_2.[7]

18.2.2 Electronic Structure

In terms of their electronic structure, TMDs cover metals (*e.g.* $ZrTe_2$, $HfTe_2$), semimetals (*e.g.* TiS_2 $TiTe_2$), semiconductors (*e.g.* MoS_2, WS_2) as well as superconductors (*e.g.* $NbSe_2$, $TaSe_2$). The overview of electronic band structure, together with band gap values and critical temperatures of superconducting TMDs can be found for example in[8] or.[9] Band gap values of TMDs lie within the range from 0 to ~2 eV. Due to that, TMDs find numerous applications in electronic devices such as field effect transistors. In their bulk form, TMDs semiconductors possess an indirect band gap. However, when exfoliated down to a single layer, an intriguing transition from indirect to direct band gap takes place for some TMDs. Additionally, the band gap value increases as the number of layers goes down. This has been described both theoretically and experimentally. This phenomenon further opens up the application potential of TMDs in optoelectronic devices. To describe this feature, an example of MoS_2 was chosen, since it is the most studied case. For the number of layers n = 1–7, the band gap value decreases monotonically with the increasing number of layers and converges to the bulk value thereafter.[10] This band gap opening, related to quantum confinement effects, can be described in the following manner. At the Γ-point of the Brillouin zone (see Figure 18.3) the states originate from a linear combination of d_{z2} and p_z of Mo and S atoms, respectively. Due to their orientation along the z axis, these states are influenced by the layer–layer interactions. As the material is exfoliated and the layer–layer interactions are weakened, the

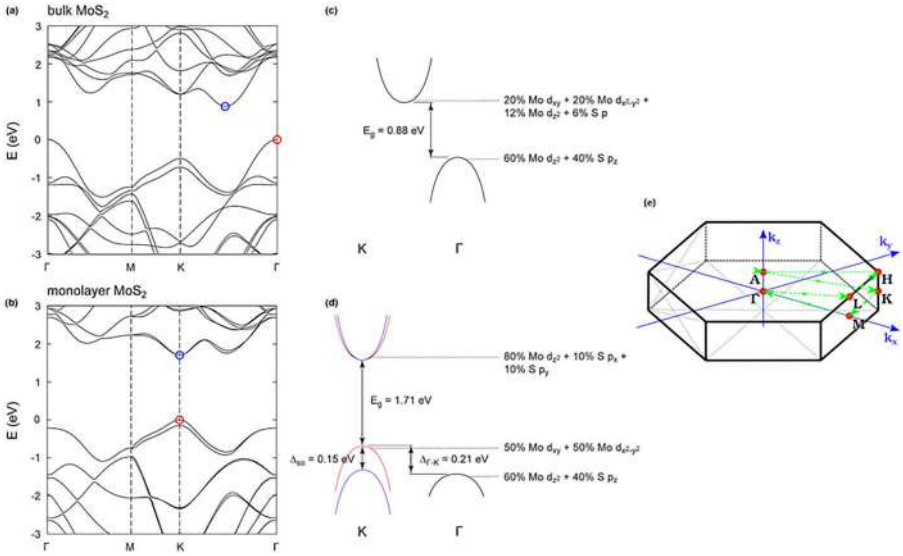

Figure 18.3 Electronic band structure of (a) bulk MoS_2 and (b) monolayer MoS_2. Illustration of band gap energy and band alignment in (c) bulk MoS_2 and (d) monolayer MoS_2. Reproduced from ref. 13 with permission from Elsevier, Copyright 2015. (e) Brillouin zone of MoS_2. Reproduced from ref. 14 with permission from AIP Publishing, Copyright 2016.

states at the Γ-point are separated farther away from one another. On the other hand, the states located at the K-point are composed of orbitals in the *xy* plane. Therefore, the change of distance along the *z* axis affects them minimally. As a result, the band gap in monolayer MoS_2 is direct and has a value of ~1.71 eV, almost twice as much as bulk material. It is important to note, however, that various calculations methods can result in different results. Another intriguing property of TMDs is the possibility to induce phase transition. As already mentioned, the phase transition occurs during alkali metal intercalation. Generally, it is believed that electron transfer from an alkali metal (*e.g.* Li) takes place and results in a change in electron configuration. In group 6 TMDs, the configuration changes from d^2 to d^3, which destabilizes the trigonal prismatic coordination (2H phase) in favor of octahedral coordination (1T phase). The mechanism of intercalation has been discussed more than 40 years ago.[11] The researchers conducted experiments with *n*-butyllithium intercalation of MoS_2. They proposed a mechanism involving several steps: (a) solution pre-equilibria generating the active species; (b) surface adsorption and activation of the adsorbent; (c) electron transfer from the alkali metal–carbon bond to the solid; (d) diffusion of the alkali metal into the lattice and dimerization and diffusion of the alkane into solution. Recently, there has been discussion about the stabilization of negative charge transferred from the alkali metal. Chowalla *et al.*

proposed that the charge is stabilized by protons in adsorbed water molecules.[12] Importantly, not only is the metal coordination changed but the electronic structure as well. The original 2H phase is semiconducting and the resulting 1T phase is metallic. This substantially enhances the conductivity of the material and has strong implications for various applications including catalysis or photoluminescence.

18.2.3 Optical Properties

The optical properties of TMDs have been studied intensively and a thorough description of their absorption can be found for example in ref. 15–17. For group IV, all TMDs exhibit an indirect absorption edge, the position of which is dependent on the composition of the particular TMD. Within this group, the absorption edge shifts to higher energies with heavier metal atoms, while the opposite is true for chalcogens. In groups V and VI, the absorption spectra are dominated by two excitons denoted as A and B and even C in some cases. Interestingly enough, the excitons are confined within individual layers even in bulk materials, pointing out the highly anisotropic character of these compounds. This confinement originates in the interlayer distance which is too high in comparison with the wavelength of the excitons, thus confining them within individual layers.

A recent work dealing with the optical properties of group VI monolayers showed that the reflectance spectra are still dominated by A and B excitons. These spectral features are associated with the interband transitions at the K (K′) point in the Brillouin zone.[18] As shown in Figure 18.4, there is also a broad feature at higher photon energies from higher-laying interband transitions.[15] The authors further analyzed the imaginary and real parts of the dielectric function and compared it with the values of bulk materials. It can be seen from Figure 18.4 that the differences for bulk materials and the monolayers are quite small. However, a certain degree of peak broadening could be observed for bulk materials. This was discussed to originate from additional optical transitions and carrier relaxation arising from interlayer coupling. Apart from that, the authors also evaluated the shifts in resonance energies in the dielectric function. They observed a blueshift in the energies of all excitons related to the quantum confinement effects.

The same group of compounds was also investigated in terms of their refractive indices and extinction coefficients using spectroscopic ellipsometry.[20,21] For all monolayers, the refractive indices show an increasing trend in the spectral region from 193 to 550 nm. Of particular interest is the MoS_2 monolayer, which exhibits an extraordinarily high refractive index of 6.5 at 450 nm.[22] Such a high value of refractive index predetermines this material for use in *e.g.* antireflection coatings for photonics and optoelectronics or optical encapsulants for enhancement of photovoltaic cell response. Apart from that, all of the investigated materials have a nearly constant refractive index of 3.5–4.0 in the infrared region.

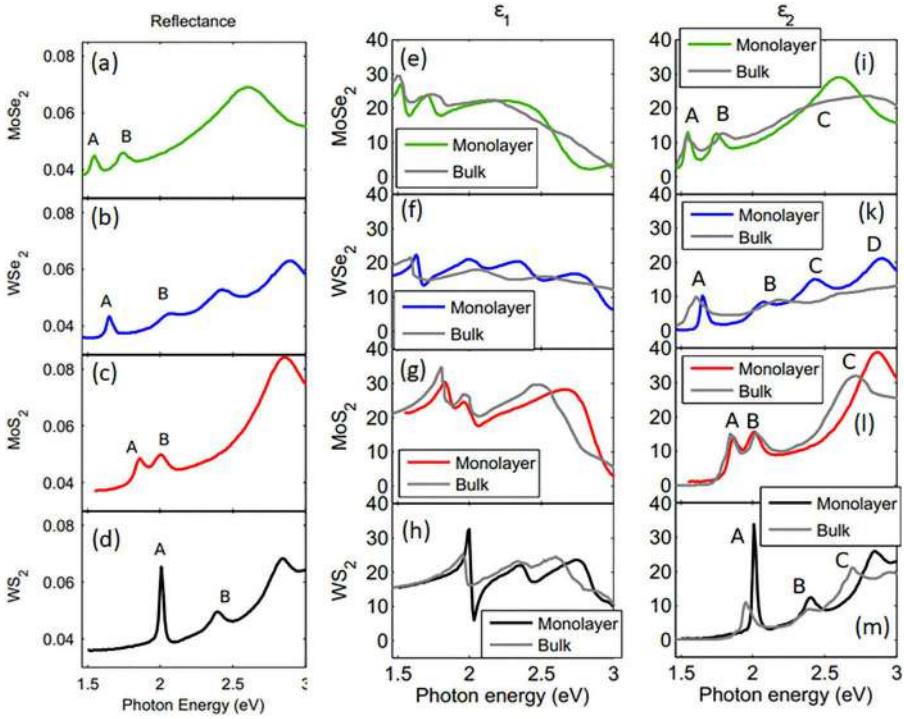

Figure 18.4 Reflectance spectra of group VI monolayers (a)–(d). The real part of the dielectric function (e)–(h) and imaginary part of the dielectric function (i)–(m) of monolayer and bulk group VI TMDs. Reproduced from ref. 19 with permission from American Physical Society, Copyright 2014.

18.3 Synthesis Methods

For the synthesis of TMDs, several approaches have been published including both "top-down" and "bottom-up" approaches. In general, the "top-down" methods are based on the use of starting bulk powder, which is downsized or nanostructured by mechanical or chemical exfoliation methods. Bulk powders are commercially available on a large scale only for molybdenum and tungsten disulfides. These materials are important lubricants and also MoS_2 is the main natural source of molybdenum. The other layered TMDs are typically prepared by direct synthesis from elements, however, at a significantly smaller scale.

18.3.1 Top-down Methods – Exfoliation

18.3.1.1 Mechanical Exfoliation

Mechanical exfoliation methods are the most commonly used procedures for the preparation of 2D nanomaterials by the "top-down" approach. Weak van der Waals interlayer interactions facilitate mechanical exfoliation.

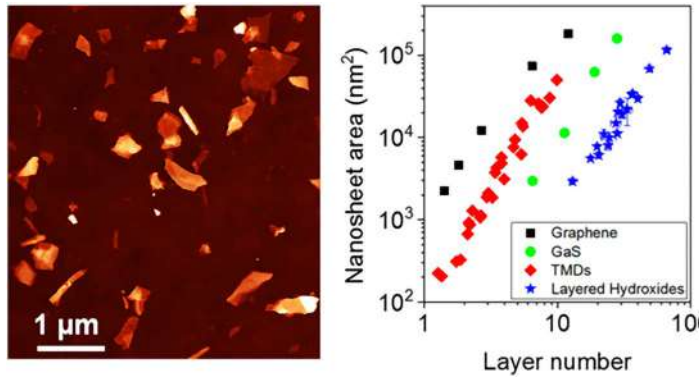

Figure 18.5 Atomic force microscopy image of exfoliated TMDs and an extracted correlation between the number of layers and lateral size of individual sheets. Reproduced from ref. 23 with permission from American Chemical Society, Copyright 2019.

The mechanical energy absorbed by the material leads to layer splitting and thus, the reduction of the material thickness (number of layers). However, this process is also accompanied by a reduction in the lateral size of individual sheets. Typically, individual mono- to few-layer sheets obtained by mechanical exfoliation have lateral sizes below one micron. The process of exfoliation was recently studied in detail showing correlations between the number of layers and lateral size of 2D materials (see Figure 18.5).[23] The most common method of mechanical exfoliation is ultrasonication, where the cavitation effect forms local hot spots with high temperature and high pressure. The absorption of this energy then results in exfoliation. Another approach is to use high speed shear force milling. In this case, shear forces are present between the stator and a fast rotating rotor. These act on individual sheets and induce their exfoliation. Recently, methods combining these two procedures were published, where the material transfer is provided by the pump for circulation of suspension between two exfoliation vessels. Besides these methods, there are also more exotic methods, for example the expansion of supercritical CO_2 within suspensions of 2D materials or transport of 2D material dispersion in various solvents through small orifices. Moreover, ball milling methods are broadly used for the exfoliation of TMDs due to their easy scalability. Significant disadvantages of this method are associated with the formation of defects induced by high energy ball impacts.

18.3.1.2 Chemical Exfoliation

Chemical exfoliation methods are based on intercalation of TMDs with alkali metals. This results in an increased interlayer distance and weakening of van der Waals forces. Apart from its use in exfoliation of TMDs, the intercalation reaction also plays a critical role in lithium and sodium batteries. Furthermore, intercalation can be also performed by Lewis bases such as various

organic compounds (pyridine) as well as small inorganic molecules (hydrazine). The use of hydrazine for the pre-expansion of MoS_2 crystals was demonstrated quite recently.[24] In this case, the intercalation leads to an increase of interlayer spacing, which significantly weakens the interlayer van der Waals interactions and makes the subsequent exfoliation much easier. The most common sources of alkali metals are organometallic compounds of alkali metals *e.g. n*-butyllithium and *tert*-butyllithium. Solutions of alkali metals formed in liquid ammonia or compounds with aromatic molecules such as naphthalene can also serve as efficient intercalation compounds. The mentioned group of alkali metal naphthalenides are particularly effective and capable of exfoliating not only TMDs in the form of powder but also large bulky crystals. The exfoliation of alkali metal-intercalated TMDs can proceed without mechanical exfoliation since intercalated metals rapidly react with water or another proton source. This reaction results in rapid hydrogen evolution in between layers of TMDs, which tears them apart. Such exfoliation is a relatively harsh process and the flakes of few/single-layer thickness are typically below micron size. The exfoliation process of MoS_2 is schematically shown in Figure 18.6. An important aspect of chemical exfoliation is a phase transition induced by the intercalation of alkali metals. During the process

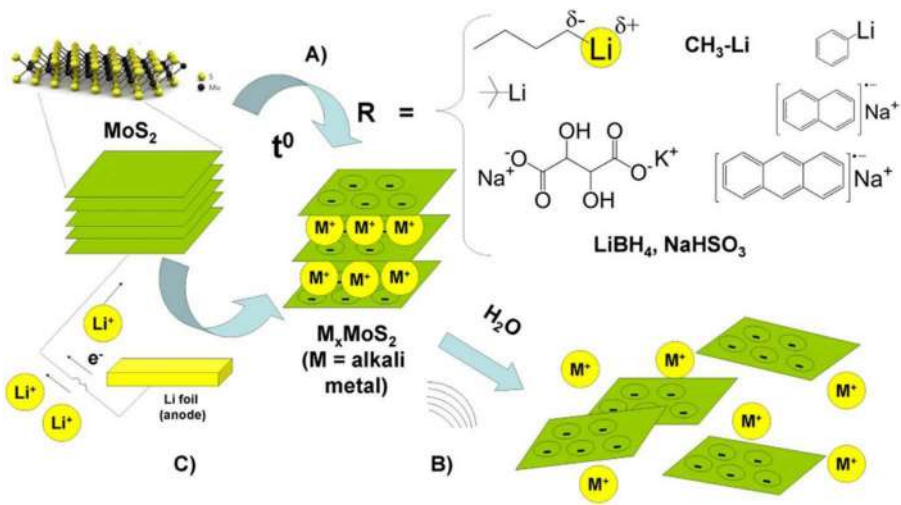

Figure 18.6 Intercalation-exfoliation route towards colloidal nanosheets of MoS_2 and related transition metal dichalcogenides: (A) Interaction with *n*-butyllithium or other reagents labeled as R, to produce an intercalated precursor M_XMoS_2 (M = Li, Na, K, depending on the intercalating agent R). The reaction is conducted under heating and/or sonication, or under microwave irradiation; (B) Exfoliation of the M_XMoS_2 in water into single and few-layer nanosheets, bearing some negative charge; (C) Electrochemical intercalation of MoS_2 (or WS_2, TiS_2, TaS_2, ZrS_2) with lithium as an alternative method, which allows better control over the process. Reproduced from ref. 25 with permission from Elsevier, Copyright 2017.

there is a charge transfer from the alkali metals to the host structure of TMDs which results in a stabilization of the metallic 1T' phase. This transition has a significant impact on the electrocatalytic properties of materials, especially the hydrogen evolution reaction.

18.3.2 Bottom-up Methods

For "bottom-up" methods, several different approaches exist. In general, these methods can be divided into synthesis in liquids (including solvothermal), thermal synthesis and chemical vapor deposition methods.

18.3.2.1 Synthesis in Liquids

For the synthesis in liquids, various precursors of transition metals and chalcogenides can be used. Most broadly studied TMDs of Mo and W can be effectively synthesized by decomposition of their thiocompounds – tetrathiomolybdate and tetrathiotungstate. Their decomposition leads to the formation of amorphous M^{VI} sulfide with the subsequent formation of more stable crystalline TMDs (MoS_2 and WS_2) at elevated temperatures. This method can be effectively used for the synthesis of TMDs on a surface of various substrates such as carbon foam or graphene. Typically, a substrate covered with a thiocompound precursor is treated at temperatures exceeding 400 °C in an inert (Ar) or reducing (H_2) atmosphere resulting in a surface covered by TMDs with low crystallinity.

These precursors can also serve for electrochemical deposition of TMDs on conductive substrates. The application of negative potentials decomposes soluble tetrathiosalts which results in the formation of disulfides. A slightly different approach has to be taken for selenides and tellurides. In this case, the salts are not readily available. For this reason, molybdate/tungstate together with soluble $Se^{IV/VI}$ or $Te^{IV/VI}$ compounds are commonly used to prepare TMDs nanostructures. In this case, the application of electrochemical potential can be substituted by strong reducing agents (*e.g.* complex hydrides or hydrazine and hydroxylamine) under solvothermal conditions. An interesting alternative for low temperature synthesis is direct precipitation using an appropriate chalcogen source. Trimethylsilyl chalcogenides can react at low temperature with transition metal halogens leading to precipitation of corresponding chalcogenides. This reaction proceeds at low temperature giving nanoparticles of the corresponding chalcogenide. Since there is a direct precipitation reaction without redox change, transition metals in oxidation state $^{4+}$ have to be used. Another alternative can be thermal post-treatment of transition metal chalcogenides with metal at a higher oxidation state. Especially, bis(trimethylsilyl) chalcogenides are highly reactive and are capable of precipitating nanocrystalline transition metal chalcogenides. Other methods use direct reactions with hydrogen sulfide or hydrogen selenide, which can proceed either in an aqueous or non-aqueous environment. The main disadvantage is the handling of highly toxic gases.

18.3.2.2 Chemical Vapor Deposition

Chemical vapor deposition (CVD) methods are well known from the electronic industry as well as many other applications like hard-coating of tools, low-friction-layer coating and many others. Compared to the well established industrial procedures for semiconductors, the CVD methods of TMDs are much less established. However, due to their huge application potential, thousands of works covering this topic have been published in the last decade. Unlike the CVD technology in the semiconductor industry which uses volatile organometallic precursors, TMDs deposition is typically based on short distance precursor transport in multizone tube furnaces. In these methods, elemental chalcogens are placed in the low temperature zone of the furnace and the transition metal source in a form of oxide (or its mixture with alkali metal halogens) is placed in the high temperature zone. Substrates are placed over the source of the transition metal or downstream of the furnace behind the metal element source. A schematic drawing of CVD deposition of TMDs is shown in Figure 18.7.[26] This method is capable of growing TMDs monolayers in a form of isolated islands with sizes typically below 0.1 mm. To the best of our knowledge, larger size or even homogeneous large-scale growth have not been reported up to this date. This originates especially from limited control possibilities over the deposition procedure, since precursors are evaporated directly in the CVD reactor. Only a limited number of works used the classical CVD approach based on the transport of gaseous precursors to the deposition chamber. Since most of the transition metal precursors have low volatility, heated lines are mandatory for such a deposition system. Up to now, depositions were reported mainly for Mo and W chalcogenides including dedicated commercial deposition systems.

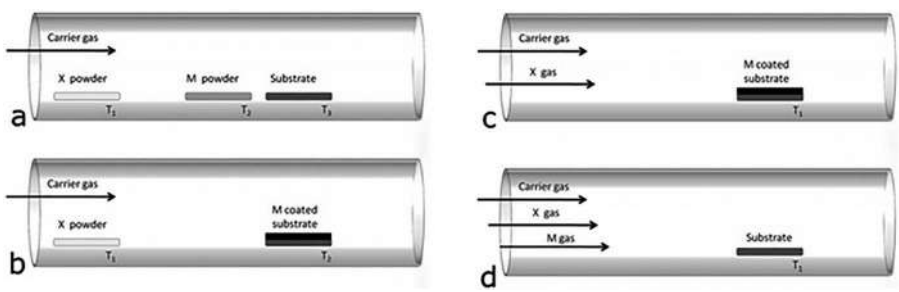

Figure 18.7 Schematics of common deposition techniques from the vapor phase. (a) metal (M) and chalcogen (X) powder; (b) metal or metal oxide coated substrate with chalcogen powder; (c) metal or metal oxide coated substrate with chalcogen in the form of gaseous precursor; (d) metal and chalcogen precursors in the form of gaseous precursors. Reproduced from ref. 26 with permission from the Royal Society of Chemistry.

18.3.2.3 Atomic Layer Deposition

Atomic layer deposition (ALD) is a highly prospective method for deposition of TMDs on a variety of substrates including planar as well as highly complex and porous 3D ones. This method gives excellent control about the material thickness down to monolayers. ALD is based on the separate injection of individual precursors and their self-limiting reactions. The scheme of the ALD reaction mechanism is shown in Figure 18.8.[27] Chalcogen precursors include hydrides (hydrogen sulfide, hydrogen selenide), alkyl chalcogens (*e.g.* dibutylsulfide, diethylselenide) and recently also bis(trimethylsilyl) chalcogens. The transition metal chalcogenide precursors are also highly variable, including metal carbonyls, halogens, beta-diketonates and alkylamides/alkylimides. The main advantage of ALD is the self-limiting growth and the possibility of using low volatile precursors since the precursor source as well as precursor delivery lines can be heated to temperatures exceeding 200 °C, depending on the system construction. Another advantage is relatively low deposition temperature which is related to the reactivity of precursors and temperature of sources necessary for precursor transport to the deposition reactor. The main disadvantage of ALD is the amorphous or nanocrystalline character of the deposited layer. Low crystallinity degree is suitable for applications in energy storage, catalysis and sensing, but nanoelectronic applications need high quality single-crystalline material. This can be partially overcome by an increased deposition temperature. Depositions using ALD methods have been reported for WS_2, MoS_2 as well as their selenides and a few other TMDs. Recently, ALD using metal substrates such as gold and

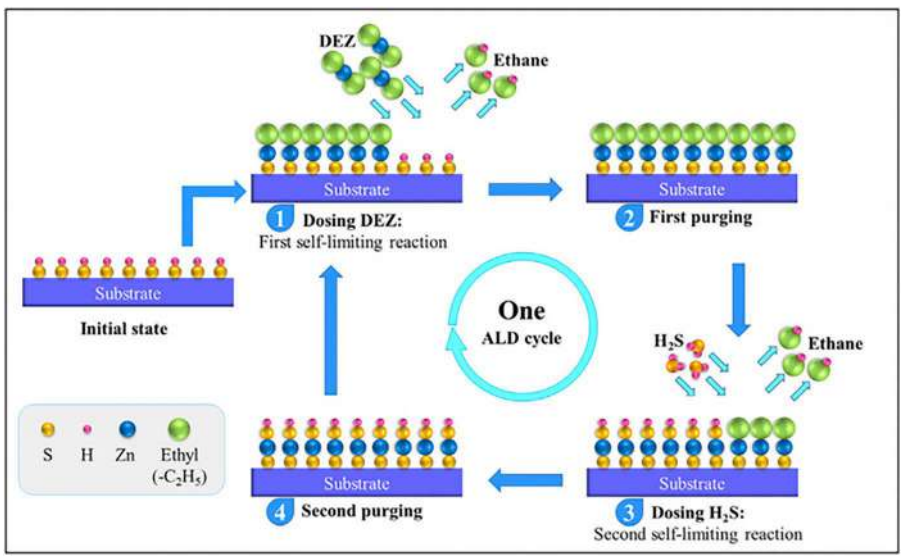

Figure 18.8 Schematic illustration of ALD shown on an example of ZnS. Reproduced from ref. 27 with permission from Elsevier, Copyright 2020.

underlayers of transition metals were also reported. Slow diffusion of metal through gold allowed limited growth and formation of monolayers. Gold can be subsequently removed by etching and deposited monolayers can be transferred using PMMA method.[28]

18.3.2.4 Molecular Beam Epitaxy

Molecular beam epitaxy (MBE) is a method of CVD proceeding in an ultra-high vacuum environment. Thanks to its nature, this method can be used for the synthesis of high quality TMDs monolayers. In an UHV environment, a sophisticated *in situ* monitoring method including reflection of high energy electron diffraction (RHEED) used for growth process monitoring can be used. On the other hand, there are disadvantages such as extreme complexity of the deposition system and its high cost. Recently, several TMDs growth by MBE was reported including molybdenum and tungsten disulfide and diselenide.

18.3.2.5 Physical Vapor Deposition

The deposition of TMDs was also performed using physical vapor deposition (PVD). The sputtering typically proceeds in an inert or slightly reducing atmosphere under low pressure. The reactive atmosphere based on chalcogen hydride (*e.g.* H_2Se) is typically not used due to the toxicity and reactivity of these gases. Unlike metal sputtering, where a simple high voltage DC source can be applied, methods like pulse DC, RF or HiPIMS sputtering techniques must be used because of the low conductivity of TMDs. Since the surface conformation effect is minor in this case, PVD can be performed only on a planar or at least flat surface. Sputtering methods typically provide polycrystalline or nanocrystalline surfaces with higher roughness compared to CVD methods, but sputtering can proceed at low temperatures. Therefore, the deposition can be performed on temperature-sensitive substrates like polymer foils and others. The use of non-reactive atmospheres for sputtering can lead to changes in stoichiometry and chalcogen deficiency in the layers. This can be a significant problem for some electronic applications; however, the presence of defects can enhance the catalytic properties of synthesized TMDs. Although, this method was primarily developed for the deposition of films with tribological properties, TMDs films prepared by sputtering methods have been recently tested for applications covering electronics and optoelectronics.[29]

18.4 Applications

The oldest application of TMD is their utilization as dry lubricants, similar to graphite or fluorographite. Since their individual layers hold together only by weak van der Waals forces, one can easily slide over another layer

which leads to a reduction of friction. MoS_2 and WS_2 are the most widely used materials to decrease friction mainly in fasteners or bearings. The most extensive studies were performed on MoS_2, which have found that its shear strength increases with increasing friction and that its wear resistance can be increased by Cr doping. Detailed study of MoS_2 cleavage has revealed that its mechanism is strongly dependent on the number of layers. While few-layered flakes are homogeneously rippled or bent, flakes with more than 10 layers exhibit interlayer sliding or kinking. After the discovery of graphene and expansion of exfoliation, TMDs have attracted great attention especially for applications in microelectronics, optics or catalysis.

18.4.1 Microelectronics

With the development in nanoarchitecture, various advanced technologies have been invented in microelectronics, optics, sensors or energetic applications. One of the biggest milestones in nanotechnology was the discovery of graphene which has a lot of fascinating properties; however, the lack of band gap has forced scientists to look for other 2D alternatives. One of the alternatives was found among TMDs which also possess an intrinsic band gap, good mobility of carriers and current on/off ratio (see Figure 18.9).

Field effective transistors (FETs) are considered as the elementary component in electronics; however, silicon semiconductor technology is approaching its limits in miniaturization. Ultrathin silicon suffers from surface roughness which can cause scattering of charge carriers. This can decrease their mobility by almost two orders of magnitude. Fortunately, TMDs do not suffer from such a thing. However, MoS_2 nanosheets have been shown to

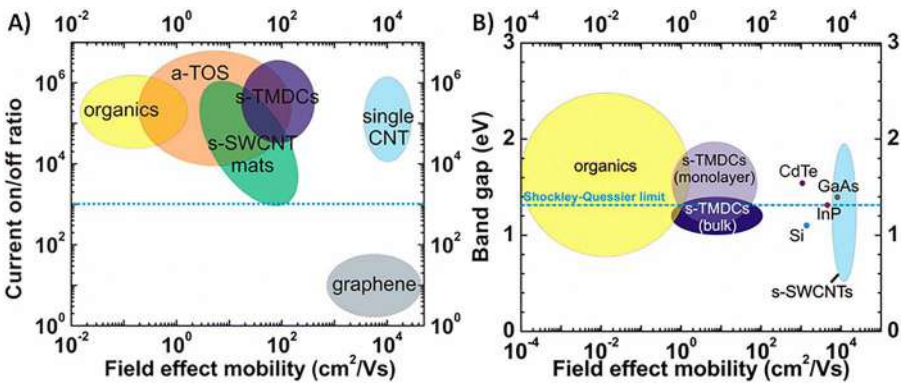

Figure 18.9 Comparison of field effect mobility with: (A) on/off ratios, blue dotted line (>10^3) marks the limit for microelectronic application; (B) band gap energies with marked Shockley–Quessier limit which is considered to provide the most effective solar cell based on single p–n junction. Reproduced from ref. 30 with permission from American Chemical Society, Copyright 2014.

have quite low mobility of charge carriers (0.5 to 3 $cm^2\ V^{-1}\ s^{-1}$).[31] Although, such low mobility limits its practical application, it has been predicted by theoretical calculations that deposition of high-κ dielectric could suppress columbic scattering in TMDs. Thus, dielectric engineering can improve mobility of carriers in TMDs. Lately, HfO_2 was tested as the high-κ dielectric which improved mobility of carriers in MoS_2 up to 217 $cm^2\ V^{-1}\ s^{-1}$ for top-gated configuration with on/off ratio exceeding 10^8.[31] These results are comparable with silicon based technology. However, only 0.1–10 $cm^2\ V^{-1}\ s^{-1}$ was achieved with a back-gated configuration. Fine tuning of electronic structure can be achieved by preparation of mixed-chalcogen alloys such as $WS_{2(1-x)}Se_{2x}$ in which the mobility of carriers was around 46.5 $cm^2\ V^{-1}\ s^{-1}$ with a top-gated configuration; in contrast, the back-gated configuration exhibited two orders of magnitude lower. In comparison with monoelemental 2D nanomaterials, TMDs still show low mobility of carriers which limits their high-performance application. Despite that, intrinsic band gaps with large scales of tailoring possibilities make TMDs suitable for low-power applications.

Contact resistance between TMD and source/drain electrode still remains a key issue that limits FET performance. A metal-TMD contact interface suffers from the Schottky barrier. To overcome this issue, the metallic phase of TMD (*e.g.* 1T MoS_2) can be used for the creation of contacts on the semiconducting one (*e.g.* 2H MoS_2).[32] Since these phases possess similar work functions, such a device exhibited ohmic-like behavior and one order in magnitude lower resistance in comparison with direct Au contacts. Similar results were also observed with WSe_2, where the 1T phase improved mobility, on/off ratio and subthreshold swing.[33]

Besides FETs, metallic TMDs can be also used in phase-transition-based memristive devices which are based on voltage dependent resistance. While devices based on 2H-MoS_2 exhibited linear ohmic response, the one based on 1T-phase showed memristive behavior. An applied electric field can cause lattice distortion in 1T phase which then causes the change in resistivity.[34] Recently, ionic modulation of MoS_2 was used for local and reversible 2H – 1T' phase transition. This modulation was based on a Li_xMoS_2 system, where $x \approx 0.28$ was the critical value needed to induce the phase transition.[35] The phase transition can be induced by local migration of Li^+ ions which is controled by an applied electric field. Such devices exhibited exceptional memristive behavior and enabled efficient integration into complex neural network systems.

18.4.2 Optoelectronics

In general, optoelectronic devices can be employed to generate, detect or control light. Such devices include lasers, LEDs, displays, solar cells, optical switches or photodetectors. For this application field, TMDs offers a wide range of tailorable bandgap (from IR to UV) with the type of transition directly dependent on the number of layers as well as high exciton binding energies. The electronic band structure of TMDs directly influences their ability to

absorb or emit photons. Due to their direct transition, single-layered TMDs are more favorable over their multilayer counterparts for light-emitting devices. However, multi-layered TMDs have also shown light-emitting abilities in high electric fields which are based on injection of hot electrons in metal-TMD heterojunction or redistribution of carriers from indirect to direct valleys.[36]

The light-emitting devices utilize electroluminescence which is a radiative recombination of electron–hole pairs that usually takes place in a p–n junction. In the case of TMDs, the p–n junction can be created in two ways – either within one layer (lateral) or by vertical stacking of layers. The lateral type of junction can be prepared by areal doping of TMD sheet, thus, by creating two regions with different semiconducting nature. Several types of chemical doping have been reported such as chemical p-type doping by $AuCl_3$ of n-type MoS_2.[37] However, lateral junction usually suffers from structural issues and high contact resistance that lead to low efficiency. Ambipolar semiconductors also enable p–n junction to be constructed and controled by electrostatic gating as shown in Figure 18.10A.[38,39] Such a device offers high efficiency of charge carries injection and thus several orders lower current for comparable performance with classical device.

Another possibility to create p–n junctions is vertical stacking which eliminates the structural issues of their lateral counterparts because the surface of

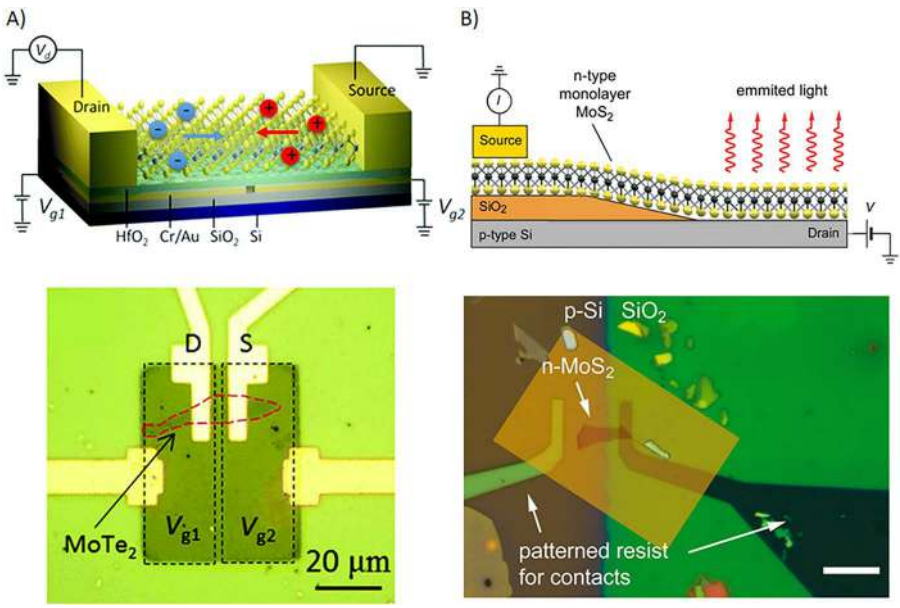

Figure 18.10 Schematic illustrations and optical pictures of (A) lateral junction based on electrostatic gating (B) vertical junction based on 2D/3D stacking. (A) Reproduced from ref. 40 with permission from the Royal Society of Chemistry. (B) Reproduced from ref. 41 with permission from American Chemical Society, Copyright 2014.

the TMDs is free of any dangling bonds and van der Waals heterostructures are not limited by any lattice matching conditions. Vertical stacking can be achieved either by placing 2D nanomaterial on the top of bulk semiconductor (2D/3D stacking) or by stacking several 2D nanomaterials on top of each other (2D/2D stacking). In the case of 2D/3D stacking, intrinsically doped TMD is typically placed on bulk silicon with opposite doping (see Figure 18.10B) and the entire surface of this junction is active for light emission. 2D/2D heterostructures can be made of single- or multi-layered nanomaterials with conducting (graphene), semiconducting (typically TMDs) or insulating properties (*e.g.* hexagonal boron nitride – hBN). Graphene is placed on the top and bottom layers and serves as a transparent electrode that injects charge carriers to TMDs while hBN is placed in between the graphene and TMD layers to prevent carriers from direct tunneling between the electrodes. A schematic structure as well as a constructed device are shown in Figure 18.11. The external quantum efficiency of such device with a single layer of MoS_2, WS_2 or WSe_2 (1–8.4% at room temperature) was more than one order

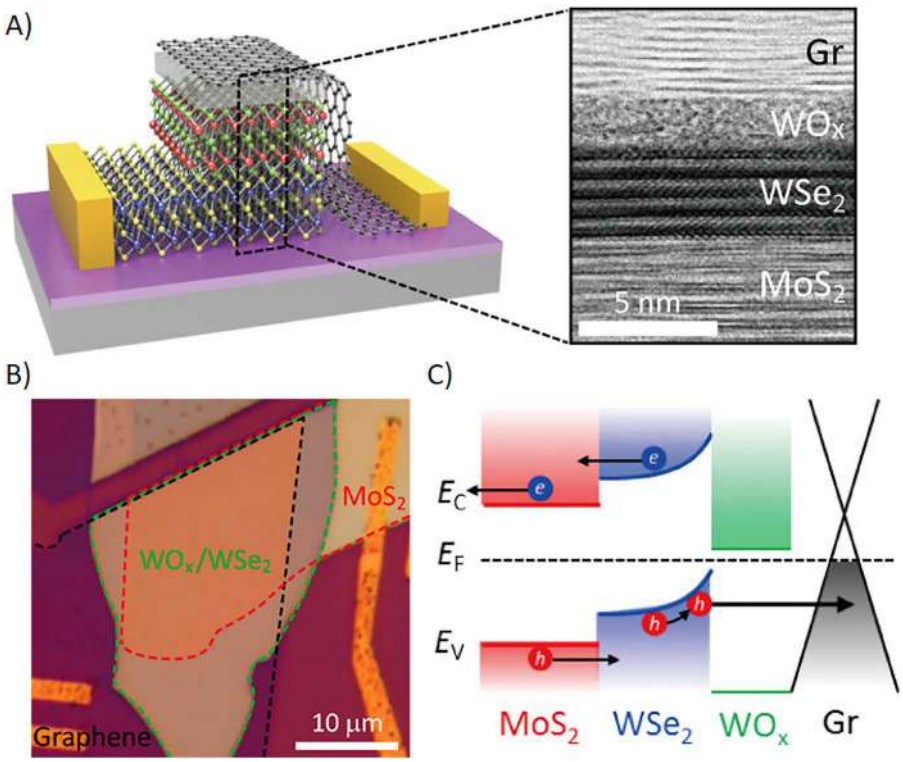

Figure 18.11 Vertical MoS_2 – WSe_2 heterostructure with WO_x reducing Schottky barrier between WSe_2 and graphene (A) schematic illustration with cross-sectional HR-TEM image, (B) optical image of the device and (C) schematic energy-band arrangement. Reproduced from ref. 42 with permission from American Chemical Society, Copyright 2020.

higher in magnitude in comparison with their lateral junction.[36] Coupling of TMDs with resonance cavity can further enhance their spontaneous emission which is given by the Purcell effect.

Photodetectors convert absorbed irradiation into an electrical signal. They are usually based on p–n junctions or the Schottky barrier where the absorption of photons can generate either free electron–hole pairs or excitons. This pair can be separated by an applied external or built-in electrical field. In comparison with graphene, TMDs have shown lower dark currents due to their semiconducting nature. Moreover, they also exhibit high photon absorption and photoresponsivity (ratio of output current to input optical power) which were attributed to stronger light–matter interaction. A monolayer of TMD (MoS_2 or WS_2) can absorb up to 5–10% of incoming irradiation which is one order higher in magnitude compared to bulk Si or GaAs.[43] Photoresponsivity of TMD falls within the range from 10^{-1} to 10^4 A W^{-1} [36] and is strongly dependent on the specific type of TMD and its number of layers. While mono- or bi-layer MoS_2 are most efficient in the green region of a spectrum, a shift towards the red region can be observed in the case of an increasing number of layers. However, TMDs based photodetector usually suffers from slow response speed (10^{-4}–10 s) which is caused by trapping of photo-generated carriers. Thus, TMDs possess application potential in fields where very high sensitivity can compensate for sluggish response. Owing to their physical properties, TMDs can be used for semitransparent and flexible electronics with easily tailored properties for desired application.

18.5 Gas Sensing Devices

Over the past decades, extensive research has been conducted on the gas sensing properties of transition metal chalcogenides. TMDs can be used as an active part of resistive gas sensors. Their sensing capabilities are strongly dependent on their electronic properties which can vary from metallic up to insulating. The electronic properties of TMDs are strongly dependent on their composition and number of layers. Thus, we can easily tailor their sensing capabilities by composition, doping, chemical surface modification and number of layers. This wide range of tailoring options represents a great advantage of TMDs. However, resistive gas sensors usually suffer from very limited selectivity as well as sensitivity. The most widely used materials for sensors are oxidic materials which excel especially in stability and longevity. Although TMDs exhibit lower stability, they show higher sensitivity than oxides. Low stability of TMD is caused by rapid oxidation of the top layer, but it can be increased by chemical modifications as well as by their shape engineering. A great example of this is flower-like MoS_2, which showed long term stability in comparison with MoS_2 films. Moreover, the porous structure of flower-like MoS_2 can also lead to higher sensitivity (see Table 18.1) in comparison with other morphologies.[44]

Table 18.1 Comparison of sensitivity (S) of MoS_2 with different structures. Sensitivity is defined as the ratio of sensor resistance in NO_2 and resistance in air.[45]

	Nanoflower	Nanofiber	Nanofilm	Flakes	Monolayer
NO_2 (ppm)	50	50	1.2	5	0.4
S (%)	78	60	10	4	0.4

Table 18.2 Comparison of gas adsorption energy (E_{Ad}) and subsequent charge transfer (ΔQ) obtained by DFT calculations. Positive and negative energies represent endothermic and exothermic reactions, respectively. Charge transfer from gas to the materials is represented by a negative value of charge and *vice versa*.[47]

		NH_3	NO	NO_2	CO	O_2
Graphene	E_{Ad} (meV)	31	29	67	14	—
	ΔQ (me)	27	18	99	12	—
MoS_2	E_{Ad} (meV)	−250	−195	276	−128	−106
	ΔQ (me)	−69	11	100	20	34
WS_2	E_{Ad} (meV)	—	—	—	140	−110
	ΔQ (me)	—	9.6	—	7.8	13
$MoTe_2$	E_{Ad} (meV)	130	—	200	—	—
	ΔQ (me)	—	—	—	—	—

The gas sensing mechanism of TMDs is based on adsorption of gaseous species on their surface, followed by charge transfer either from gaseous species to TMDs or *vice versa*. The direction of charge transfer is dependent on the semiconducting nature of TMD (p- or n-type) as well as on the redox nature of gaseous species. For example, we can observe an increment in resistivity of n-type TMD after exposure to oxidizing gas. Table 18.2 summarizes calculated adsorption energies as well as charge transfer for most studied chalcogenides. Interestingly, listed adsorption energies on TMDs have been shown to be negative, while they are positive in the case of graphene. Since the negative value of adsorption energy suggests a spontaneous process, TMDs should be a more favorable material for gas sensing applications from a theoretical point of view. The gas sensing mechanism based on electron transfer was confirmed by the measurement of PL spectra. To show gas sensing ability, TMDs have been most often tested for the detection of NO_x and NH_3, which are representatives of the oxidizing and reducing environment respectively. Theoretical calculations have found that adsorption preferentially occurs at the edges rather than at the basal surface of TMDs. This was further experimentally confirmed on sensors with different sheet orientations (see Figure 18.12).[46] In addition, gas adsorption can be also increased by the introduction of sulfur vacancies on the basal plane, which can act as adsorption sites.

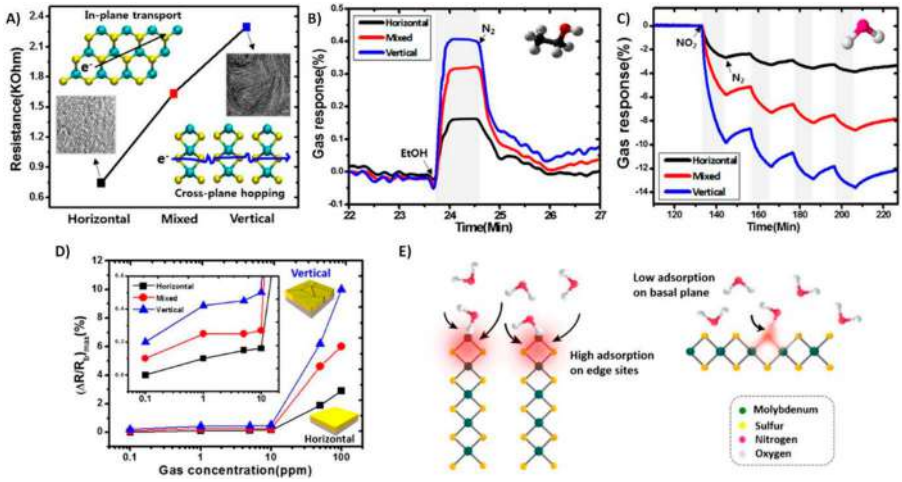

Figure 18.12 Gas sensing ability of MoS_2 was tested with three different sheet orientations: (1) horizontal – exposed basal planes, (2) vertical – exposed edges and (3) a mixture of both previously mentioned. (A) resistance of vertically aligned film exhibited higher resistance because of depicted cross-plane hopping. Response of sensor (ΔR/initial R) after the exposure of (B) ethanol (1000 ppm) and (C) NO_2 (100 ppm). (D) Summarization of response at different levels of NO_2 concentration. (E) Schematic illustration of preferential NO_2 adsorption on MoS_2 edges. Reproduced from ref. 46 with permission from American Chemical Society, Copyright 2014.

Overall, TMDs represent an interesting family of materials for gas sensing applications mainly due to the higher carrier mobility and sensitivity (up to tens of ppb) in comparison with oxidic materials. The low stability of TMDs, especially at higher operating temperatures, still represents a serious issue that limits their real-life applications. Recently, several works have been focused on heterostructures of TMD with oxides.[47] Their junctions can create new active sites for gas-sensing reactions or enhance gas adsorption so they can exceed the gas sensing ability of individual counterparts. However, the exact mechanism of gas sensing ability on this type of heterojunction has not been described yet. Most of these works ascribe the enhancement to the altered flow of charge carriers based on the Fermi energy difference or the formation of depletion areas. More experimental and theoretical results should be introduced for a better explanation in this area.

18.6 Electrochemical Water Splitting

Renewable energy sources have the potential to prevent the environmental crisis associated with burning fossil fuels. However, their productivity is highly dependent on the unpredictable weather, which considerably

complicates time-stable supplies of electric energy. Thus, energy from these sources needs to be stored during lower consumption. One option is to store this energy in the form of hydrogen, which can be prepared by electrocatalytic water splitting. For a long time, the most preferred catalyst was platinum due to its high efficiency; however, platinum is one of the most expensive metals. Although bulk TMDs show very low hydrogen evolution activity, their exfoliation dramatically enhances this activity. This enhancement is mainly caused by an increment of the specific surface area, but also other properties must be considered based on the reaction mechanism.

The hydrogen evolution mechanism consists of three steps: H^+ adsorption, its reduction and subsequent desorption of H_2. The key is the hydrogen adsorption strength on the TMD surface. According to the Sabatier principle, the adsorption must be strong enough to enable electrochemical reduction. However, too strong adsorption would complicate the desorption of H_2; thus, poisoning of catalyst would occur. Gibbs free energy of adsorption (ΔG_H) was calculated by the first principal method on the metal- or chalcogen-terminated edges (M-edge and C-edge, respectively) as well as on their basal plane (see Figure 18.13). With the assumption that the ideal value of ΔG_H is 0 eV, we can conclude that reactions primarily take place on the edges of TMDs.

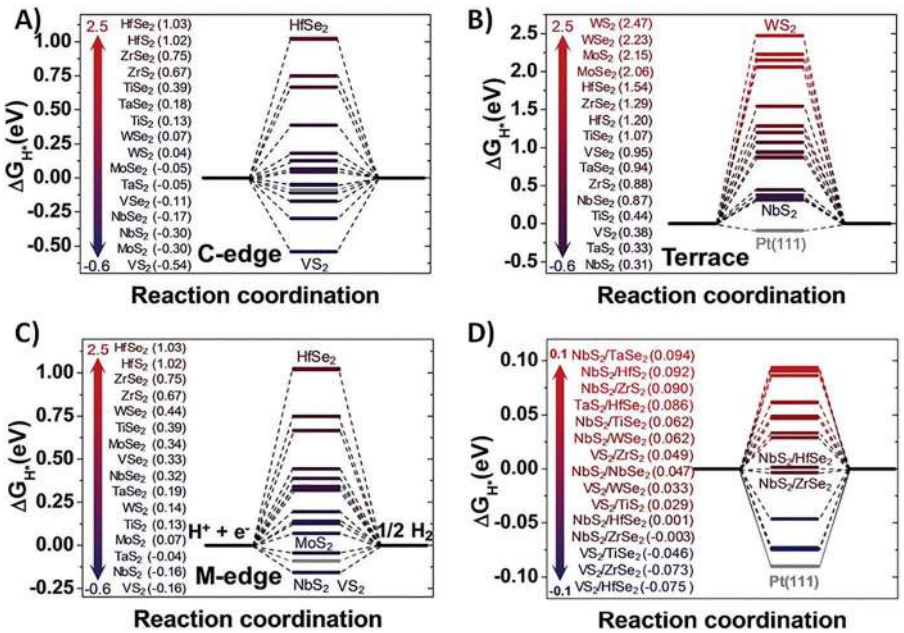

Figure 18.13 Gibbs free energy of hydrogen absorption calculated for (A) chalcogen- and (C) metal-terminated edges (both 0.5 monolayer coverage), (B) basal plane (0.06 monolayer coverage) and (D) the basal plane of optimized TMDs heterostructures. Reproduced from ref. 48 with permission from the Royal Society of Chemistry.

Therefore, the orientation of TMD flakes plays a crucial role in their catalytic activity. Moreover, Gibbs energy is associated with the density of states (DoS) near to the Fermi level and it can be reduced by increments of these DoS. Thus, the tailoring of TMD band structure can be one of the main strategies towards the fabrication of optimal catalysts. Band structure can be tailored *e.g.* by composition or phase engineering.

Although theoretical calculations suggested that the basal plane of 2H MoX_2 and WX_2 (X = S, Se, Te) should be catalytically inert, their 1T counterpart exhibited ΔG_H approaching 0 eV. Interestingly, opposite behavior has been observed for dichalcogenides of Ti, Zr and Hf, whose 1T phase exhibited higher energy of adsorption than their 2H counterparts.[49] Phase transition can be performed by intercalation of alkali metals, from which Li and Na have shown the best performance in the case of MoS_2 and WS_2, respectively.[50] These intercalations lead to the highest concentration of 1T phase, around 40%, as well as the best HER performance of exfoliated material. Moreover, Li-exfoliated MoS_2 showed comparable overpotential (0.24 V *vs.* SHE) as commercial Pt/C catalyst (0.12 V *vs.* SHE) at 10 mA cm^{-2}.

Further optimization of ΔG_H can be obtained by heteroatom doping. DFT calculation predicted that ΔG_H on the MoS_2 edges can be optimized by cation dopants such as Mn, Cr, Cu, Ni or Fe and these predictions were also experimentally confirmed.[51,52] The HER performance of MoS_2 can be also improved by low-level doping on anion site for example by C, N or O, which are able to reduce ΔG_H and they can also improve H coverage near the defect sites.[49] Moreover, such incorporation can increase the amount of charge carriers, and thus, the conductivity of catalysts. Fine tuning of the electronic structure was also achieved by the preparation of mixed chalcogen alloys $MS_{2-2x}Se_{2x}$ (M = Mo and W).[53] In contrast with their pure MS_2 counterparts, the metal exhibited a lower oxidation state which led to a lower adsorption energy. In addition, chalcogens can be also incorporated by ion implantation. During this treatment, defects and vacancies can be introduced on the basal planes, thus increasing the concentration of HER active sites. Moreover, this treatment can introduce strain into TMD flakes, which was shown to further enhance catalytic activity.[54] However, large amounts of defects can greatly reduce the conductivity of TMDs which may significantly reduce charge transfer. One way to increase the conductivity of TMD is phase engineering. Another possibility is the preparation of composite materials where the active low dimensional TMDs are combined with a conductive substrate such as graphene.

18.7 Conclusion

In conclusion, TMDs offer a low-priced alternative for Pt-based catalysts for water splitting applications. Due to enormous scientific effort, plenty of possible improvements were introduced for tailoring of TMDs catalytic activity. The latest approaches are based on theoretical calculations with a focus on ΔG_H optimization. Recent theoretical studies have shown that placing a TMD on 2D nanostructures (including other TMDs) could lead towards

optimal catalytic performance from a ΔG_H point of view.[48] However, there are still some unexplored TMDs as well as heterostructures yet to be prepared experimentally.

References

1. M. Chhowalla, H. S. Shin, G. Eda, L.-J. Li, K. P. Loh and H. Zhang, *Nat. Chem.*, 2013, **5**, 263–275.
2. A. Kuc, *Chemical Modelling: Volume 11*, The Royal Society of Chemistry, 2015, vol. 11.pp. 1–29.
3. W. Choi, N. Choudhary, G. H. Han, J. Park, D. Akinwande and Y. H. Lee, *Mater. Today*, 2017, **20**, 116–130.
4. R. J. Toh, Z. Sofer, J. Luxa, D. Sedmidubský and M. Pumera, *Chem. Commun.*, 2017, **53**, 3054–3057.
5. M. Kertesz and R. Hoffmann, *J. Am. Chem. Soc.*, 1984, **106**, 3453–3460.
6. C. Fang, G. Wiegers, C. Haas and R. De Groot, *J. Phys.: Condens. Matter*, 1997, **9**, 4411.
7. W. Wang, D. Dietzel and A. Schirmeisen, *Sci. Rep.*, 2019, **9**, 7066.
8. Z. Sofer, D. Sedmidubský, J. Luxa, D. Bouša, Š. Huber, P. Lazar, M. Veselý and M. Pumera, *Chem. - Eur. J.*, 2017, **23**, 10177–10186.
9. J. Silva-Guillén, P. San-Jose and R. Roldán, *Appl. Sci.*, 2016, **6**, 284.
10. J. Padilha, H. Peelaers, A. Janotti and C. Van de Walle, *Phys. Rev. B*, 2014, **90**, 205420.
11. M. B. Dines, *Mater. Res. Bull.*, 1975, **10**, 287–291.
12. M. Chhowalla, Z. Liu and H. Zhang, *Chem. Soc. Rev.*, 2015, **44**, 2584–2586.
13. O. V. Yazyev and A. Kis, *Mater. Today*, 2015, **18**, 20–30.
14. J. Kopaczek, M. P. Polak, P. Scharoch, K. Wu, B. Chen, S. Tongay and R. Kudrawiec, *J. Appl. Phys.*, 2016, **119**, 235705.
15. J. A. Wilson and A. Yoffe, *Adv. Phys.*, 1969, **18**, 193–335.
16. A. R. Beal, J. C. Knights and W. Y. Liang, *J. Phys. C: Solid State Phys.*, 1972, **5**, 3540–3551.
17. A. R. Beal, J. C. Knights and W. Y. Liang, *J. Phys. C: Solid State Phys.*, 1972, **5**, 3531–3539.
18. Y. Li, A. Chernikov, X. Zhang, A. Rigosi, H. M. Hill, A. M. Van Der Zande, D. A. Chenet, E.-M. Shih, J. Hone and T. F. Heinz, *Phys. Rev. B*, 2014, **90**, 205422.
19. Y. Li, A. Chernikov, X. Zhang, A. Rigosi, H. M. Hill, A. M. van der Zande, D. A. Chenet, E.-M. Shih, J. Hone and T. F. Heinz, *Phys. Rev. B*, 2014, **90**, 205422.
20. C. Yim, M. O'Brien, N. McEvoy, S. Winters, I. Mirza, J. G. Lunney and G. S. Duesberg, *Appl. Phys. Lett.*, 2014, **104**, 103114.
21. C.-C. Shen, Y.-T. Hsu, L.-J. Li and H.-L. Liu, *Appl. Phys. Express*, 2013, **6**, 125801.
22. H.-L. Liu, C.-C. Shen, S.-H. Su, C.-L. Hsu, M.-Y. Li and L.-J. Li, *Appl. Phys. Lett.*, 2014, **105**, 201905.

23. C. Backes, D. Campi, B. M. Szydlowska, K. Synnatschke, E. Ojala, F. Rashvand, A. Harvey, A. Griffin, Z. Sofer, N. Marzari, J. N. Coleman and D. D. O'Regan, *ACS Nano*, 2019, **13**, 7050–7061.
24. J. Zheng, H. Zhang, S. Dong, Y. Liu, C. Tai Nai, H. Suk Shin, H. Young Jeong, B. Liu and K. Ping Loh, *Nat. Commun.*, 2014, **5**, 2995.
25. E. D. Grayfer, M. N. Kozlova and V. E. Fedorov, *Adv. Colloid Interface Sci.*, 2017, **245**, 40–61.
26. M. Bosi, *RSC Adv.*, 2015, **5**, 75500–75518.
27. J. Cai, X. Han, X. Wang and X. Meng, *Matter*, 2020, **2**, 587–630.
28. A. Shivayogimath, J. D. Thomsen, D. M. A. Mackenzie, M. Geisler, R.-M. Stan, A. J. Holt, M. Bianchi, A. Crovetto, P. R. Whelan, A. Carvalho, A. H. C. Neto, P. Hofmann, N. Stenger, P. Bøggild and T. J. Booth, *Nat. Commun.*, 2019, **10**, 2957.
29. H.-S. Kim, M. D. Kumar, J. Kim and D. Lim, *Sens. Actuators, A*, 2018, **269**, 355–362.
30. D. Jariwala, V. K. Sangwan, L. J. Lauhon, T. J. Marks and M. C. Hersam, *ACS Nano*, 2014, **8**, 1102–1120.
31. B. Radisavljevic, A. Radenovic, J. Brivio, V. Giacometti and A. Kis, *Nat. Nanotechnol.*, 2011, **6**, 147.
32. S. Das, H.-Y. Chen, A. V. Penumatcha and J. Appenzeller, *Nano Lett.*, 2013, **13**, 100–105.
33. Y. Ma, B. Liu, A. Zhang, L. Chen, M. Fathi, C. Shen, A. N. Abbas, M. Ge, M. Mecklenburg and C. Zhou, *ACS Nano*, 2015, **9**, 7383–7391.
34. P. Cheng, K. Sun and Y. H. Hu, *Nano Lett.*, 2016, **16**, 572–576.
35. X. Zhu, D. Li, X. Liang and W. D. Lu, *Nat. Mater.*, 2019, **18**, 141–148.
36. A. Pospischil and T. Mueller, *Appl. Sci.*, 2016, **6**, 78.
37. M. S. Choi, D. Qu, D. Lee, X. Liu, K. Watanabe, T. Taniguchi and W. J. Yoo, *ACS Nano*, 2014, **8**, 9332–9340.
38. B. W. Baugher, H. O. Churchill, Y. Yang and P. Jarillo-Herrero, *Nat. Nanotechnol.*, 2014, **9**, 262–267.
39. J. S. Ross, P. Klement, A. M. Jones, N. J. Ghimire, J. Yan, D. Mandrus, T. Taniguchi, K. Watanabe, K. Kitamura and W. Yao, *Nat. Nanotechnol.*, 2014, **9**, 268.
40. Z. Wang, F. Wang, L. Yin, Y. Huang, K. Xu, F. Wang, X. Zhan and J. He, *Nanoscale*, 2016, **8**, 13245–13250.
41. O. Lopez-Sanchez, E. Alarcon Llado, V. Koman, A. Fontcuberta i Morral, A. Radenovic and A. Kis, *ACS Nano*, 2014, **8**, 3042–3048.
42. S. Yang, J. Cha, J. C. Kim, D. Lee, W. Huh, Y. Kim, S. W. Lee, H.-G. Park, H. Y. Jeong and S. Hong, *Nano Lett.*, 2020, **20**, 2443–2451.
43. M. Bernardi, M. Palummo and J. C. Grossman, *Nano Lett.*, 2013, **13**, 3664–3670.
44. S. Kumar, V. Pavelyev, P. Mishra, N. Tripathi, P. Sharma and F. Calle, *Mater. Sci. Semicond. Process.*, 2020, **107**, 104865.
45. L. Yu, F. Guo, S. Liu, J. Qi, M. Yin, B. Yang, Z. Liu and X. H. Fan, *Mater. Lett.*, 2016, **183**, 122–126.

46. S.-Y. Cho, S. J. Kim, Y. Lee, J.-S. Kim, W.-B. Jung, H.-W. Yoo, J. Kim and H.-T. Jung, *ACS Nano*, 2015, **9**, 9314–9321.
47. E. Lee, Y. S. Yoon and D.-J. Kim, *ACS Sens.*, 2018, **3**, 2045–2060.
48. S. H. Noh, J. Hwang, J. Kang, M. H. Seo, D. Choi and B. Han, *J. Mater. Chem. A*, 2018, **6**, 20005–20014.
49. M. Pandey, A. Vojvodic, K. S. Thygesen and K. W. Jacobsen, *J. Phys. Chem. Lett.*, 2015, **6**, 1577–1585.
50. J. Luxa, P. Vosecký, V. Mazánek, D. Sedmidubský, M. Pumera and Z. k. Sofer, *ACS Catal.*, 2018, **8**, 2774–2781.
51. K. Zhu, C. Li, Z. Jing, X. Liu, Y. He, X. Lv, Y. Wang and K. Liu, *FlatChem*, 2019, 100140.
52. H. Wang, C. Tsai, D. Kong, K. Chan, F. Abild-Pedersen, J. K. Nørskov and Y. Cui, *Nano Res.*, 2015, **8**, 566–575.
53. Q. Fu, L. Yang, W. Wang, A. Han, J. Huang, P. Du, Z. Fan, J. Zhang and B. Xiang, *Adv. Mater.*, 2015, **27**, 4732–4738.
54. J. Luxa, V. Mazánek, A. Mackova, P. Malinsky, S. Akhmadaliev and Z. Sofer, *Appl. Mater. Today*, 2019, **14**, 216–223.

CHAPTER 19

Optimal Silicon-based Nanomaterials for Biological Applications

M. L. DELL'ARCIPRETE[a], PAULA CAREGNATO[a], HERNÁN B. RODRÍGUEZ[a], E. GONIK[a], D. RODRÍGUEZ SARTORI[a] AND MÓNICA C. GONZALEZ*[a]

[a]Instituto de Investigaciones Fisicoquímicas Teóricas y Aplicadas (INIFTA), CCT La Plata, CONICET, Facultad de Ciencias Exactas, Universidad Nacional de La Plata, Diagonal 113 y 64 S/N, B1904DPI La Plata, Argentina
*E-mail: gonzalez@inifta.unlp.edu.ar

19.1 Semiconductor Silicon Nanostructures – Their Importance

Reducing the size of silicon semiconductor from bulk to nanoscale level brings about new properties and functionalities of significant interest to the optoelectronic and biological areas.[1] Freestanding semiconductor silicon nanoparticles below 4–5 nm size (herein denoted as SiNPs) and porous silicon particles containing nanopores in their microstructure (denoted as PSi) have attracted scientific interest for more than thirty years due to their optoelectronic properties, ease of surface functionalization, facile synthesis, high natural abundance and intrinsic nontoxicity of elemental silicon, among others. TEM images of SiNPs and PSi are shown in Figure 19.1, depicting the main differences between both silicon nanomaterials (SiNMs).

Nanoscience & Nanotechnology Series No. 55
Concepts and Design of Materials Nanoarchitectonics
Edited by Omar Azzaroni and Katsuhiko Ariga

Published by the Royal Society of Chemistry, www.rsc.org

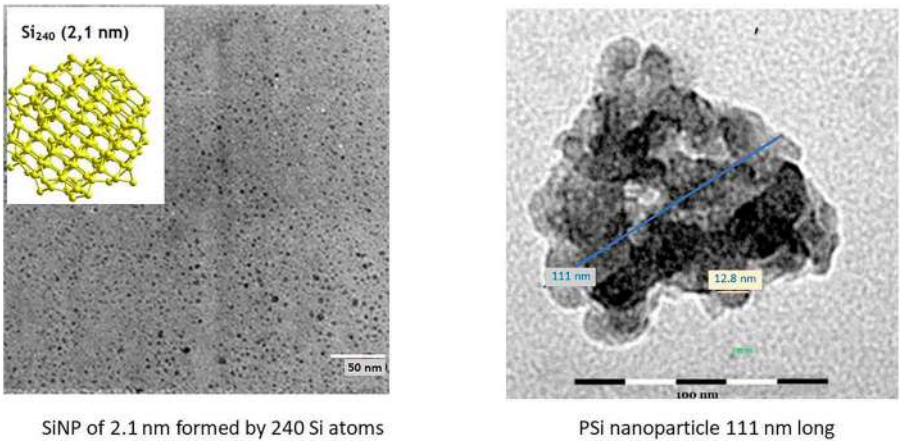

Figure 19.1 Transmission electron microscopy (TEM) images of SiNPs and PSi particles.

SiNPs are composed of 70–200 atoms depending on size, they are almost crystalline, show quantum confinement photoluminescence, and may form well dispersed solutions when they are conveniently surface derivatized. On the other hand, PSi nanoparticles sizes range from 50 nm to several micrometers, they may be formed by silicon crystallites of diverse sizes, present nanopores in their structure and, depending on size, surface derivatization does not always lead to stable dispersions. These differences in structure bring about important differences in their photoluminescence (PL) characteristics and origin. Despite the differences, both SiNP and PSi have been investigated for several technological uses including solar energy conversion,[2,3] sensors,[4,5] light-emitting diodes,[6,7] photo-pumped tunable lasers,[8] anode active materials for lithium-ion batteries,[9,10] and as diagnosis and therapeutic agents in nanomedicine.[11–14] Among the several technological uses of these materials, SiNPs with sizes below 4–5 nm and bright visible PL are effective for applications in bioimaging, while PSi provides tailored pore sizes and volumes and large specific surface area that makes them attractive for use in drug delivery.

Nanosized silicon offers many important properties necessary for biological applications such as high drug-loading potential, long blood circulation time, and specific clearance pathways from the body. Elemental silicon is the second most abundant element in the earth's crust after oxygen, is ecologically safe, biodegradable to orthosilicic acid, which is the bioavailable form of silicon in the human body and which can be excreted in urine.[15,16] Based on all these properties and through innovative fabrication of well controlled SiNMs of homogeneous size, defined morphology, easy coating with specific biomolecules, they have been tested as promising nanoplatforms for biological applications in bioimaging, photodynamic therapy, drug delivery, combination therapy, and theragnostic. Conveniently designed SiNMs can provide effective photosensitizers for photodynamic therapy by producing

photo-induced reactive oxygen species (ROS). Together with the action of light, these efficient therapeutic agents may target specific sites and favor the treatment of diseases, safely and effectively. These or similar silicon nanostructures can also be developed for bioimaging technologies. As SiNMs do not present induced toxicity due to long-term accumulation and incomplete excretion from the body, they overcome one of the most critical issues for clinical translation of nanomaterials for theragnosis.[17]

Silicon nanomaterials offer the potential to significantly improve existing methods of fluorescent labeling and cancer diagnosis and treatment, as well as alternative materials for organic dyes and toxic cadmium-based quantum dots.[18,19]

In view of the growing importance of SiNMs in the progress of nanomedicine for disease diagnosis and therapy, this contribution reviews some relevant properties of these materials to be taken into consideration when developing silicon-based nanomaterials for biological applications. The intrinsic biodegradability of SiNMs is generally advantageous for the design of biocompatible formulations for *in vivo* applications. However, bare SiNMs are prone to oxidation and degradation to silicic acid in air-saturated water, which is an important limitation for biological applications. In turn, PSi properties such as luminescence and medical biodegradability are direct consequences of nanoscale pores.

Therefore, desired SiNMs for biological uses should have the ability to withstand a physiological environment and maintain their optical and electronic properties long enough to serve their intended purpose, but should still be biodegradable and cleared from the organism.[1,20]

In general, the requirements for nanomaterials uses in biomedical applications are water stability, solubility or dispersibility, biocompatibility, increased circulation time in biological media, substantial photoluminescence quantum yield and tissue specific targeting.[1] In that sense, surface functionalization of SiNMs with polar groups provides the ability to disperse in aqueous medium. Among the molecules used for surface coating, amine containing moieties,[21–26] polyethylene glycol[25,27,28] and folic acid[25,29] moieties stand out for satisfying several of the above requirements. Moreover, several of the above-mentioned works have shown that chemical processes used to terminate the surfaces of the SiNMs, modify the internal electronic structure and thus plays an important role in the resultant emission wavelength and radiative lifetime of the nanomaterial. Then, we describe here how the nature of the surface coating of SiNMs affects the optical properties and reactive oxygen species production and reaction.

For those not familiar with SiNMs, needing more basic information, in preceding book chapters[1,20] we discussed the properties that make SiNMs potential photo and radiosensitizers for biological uses as a guide for researchers aiming to find new applications based on these particles. Herein, we discuss some successful SiNMs synthesis strategies stabilizing the particles for biological uses, as well as a state of the art on the still highly debated origin of the observed PL and the effect of surface derivatization on the optical

properties. Optical and magnetic multifunctionality achievable by combination with iron oxides will also be discussed. Despite SiNMs as nanowires[30] and nanotubes[31,32] have been developed as sensing materials, bioseparation, drug delivery, imaging, and other biomedical applications, herein we mainly focus on SiNPs and PSi because of their wide use and their easy and scalable synthesis for technological uses. In fact, these SiNM properties may be tuned according to the desired application by manipulating their structural parameters, altering their surface chemistry, or impregnating other materials.

19.2 SiNM Synthesis

Various preparation strategies have been proposed to fabricate different types of SiNPs.[11] Bottom-up methods involve condensation reactions of silicon compounds which use physical and chemical means to control nucleation and growth of SiNPs with uniform morphology. Among such methods are solution-phase reduction of: chlorosilanes,[25,33,34] sol–gel polymeric silsesquioxanes of empirical formula $RSiO_{1.5}$ with R representing either H, alkyl, silyl and aromatic groups[35] and polysiloxanes; laser pyrolysis of silane;[36] thermal processing of hydrogen silesquioxane;[37] solution-phase oxidation of Zintl salts as Mg_2Si and Na_4Si_4 with either NH_4Cl or NH_4Br.[38,39] Synthesis of SiNPs by top-down methods normally involve electrochemical etching of silicon wafers in hydrofluoric acid to obtain porous silicon films[40] followed by mechanical grinding, sonication, or acid solution treatment to break the nanoporous film into SiNPs.[41–43] Another top-down method involves femtosecond laser ablation of bulk silicon to produce nanosilicon by the rapid heating and vaporization effect of pulsed laser radiation.[44] When performed in a liquid, the latter method produces nanoclusters that form stable colloidal dispersions, as their surfaces are charged.

PSi preparation has been performed by rather simple and inexpensive methods depending on the desired structure and surface chemistry, as different pore dimensions and morphologies lead to different physicochemical properties, thus resulting in different biological behavior. Preparation of microscale PSi may be performed by both top-down and bottom-up approaches. In top-down methods, monocrystalline silicon wafers are treated to generate a porous structure by electrochemically etching[45] and electroless wet chemical etching involving hydrofluoric acid and concentrated nitric acid solution mixtures, Pt-assisted in a solution of HF, H_2O_2, and methanol,[46] among other types of etching as vapor, reactive ions, plasma, *etc.* The publication by Karbassian[47] summarizes and discuss the different methods. On the other hand, bottom-up approaches as electron-beam evaporation[48] and laser-induced silane decomposition[49] have not attracted much attention for biological uses, mainly because they involve more complex procedures than top-down approaches.

It should be noted that "as obtained" SiNPs and PSi from the mentioned synthesis procedures all present reactive surfaces either containing Si–H, Si–Cl or Si–OH terminal groups, which, in the presence of water and molecular

oxygen are readily oxidized to silica and finally degraded to silicates. To avoid the easy degradation of SiNMs, it is very important to functionalize the "as obtained" nanomaterials with water-friendly surface groups stabilizing the nanostructures in air-saturated aqueous suspensions.

19.3 SiNM Functionalization for Biological Uses

Surface coating with organic molecules containing pending polar groups is one of the most widely used strategies to obtain stable colloidal suspensions in aqueous solution. Among these polar groups, coating with terminal amine groups not only provides the nanomaterials with positive surface charges capable of stabilizing them in aqueous suspensions but provides a platform for further functionalization with target molecules like ligands or inhibitors of specific receptors. There are several easy strategies to obtain amine-coated SiNPs (NH_2SiNPs). Freshly obtained SiNPs can be superficially modified by activating Si–H surface groups either thermally, photochemically, or with metallic catalysts[1,21,22] and further reaction with unsaturated molecules containing terminal –NH_2 groups (see Scheme 19.1). Tilley group firstly describe a simple room-temperature synthesis for producing water soluble 1–2 nm SiNPs with strong blue photoluminescence with a rapid rate of recombination.[21,50] They reported the treatment of reactive Si–H surface group with C=C moieties containing terminal –NH_2, and a metallic catalyst.

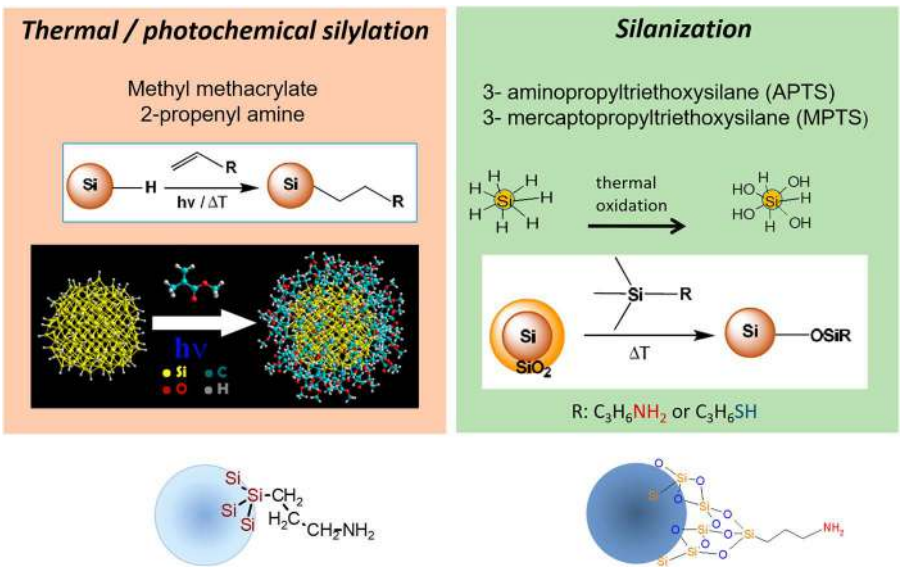

Scheme 19.1 Schematic representation of the two most widely used methods for SiNP and PSi surface derivatization: Silylation and silanization. The examples are specific for propylamine and propyl thiol pending groups.

The authors obtained water dispersible NH_2SiNPs which present an absorption maximum at 320 nm. Upon excitation in the 300–400 nm range, the NH_2SiNPs suspensions produce 480 nm maximum emission with good photoluminescence quantum yields of up to 10%. Moreover, they reported excellent stability and negligible photobleaching under UV illumination.[21]

Click-chemistry and one-pot methods have also been reported to obtain corrosion-stable and water soluble NH_2SiNPs with enhanced PL quantum yields.[51] Experimentally, amine groups anchorage may be corroborated by several commercially accessible techniques like zeta potential measurements, gel electrophoresis, IR spectroscopy by observing characteristic peaks at 3400, 1650, 1580 cm^{-1} ($-NH_2$), 1020–1100 cm^{-1} (–C–N) and 1030 and 997 cm^{-1} (–CO– deformation in amine bonds), and surface techniques as XPS which allows the determination of the presence and particular environment of N, C, and Si elements.

The study of NH_2SiNPs interaction with cell cultures has been undertaken by several research groups which probed internalization of NH_2SiNPs by different cell lines while the nanoparticles PL was observed to be stable without leading to cell toxicity.[21] Cytotoxicity of NH_2SiNPs is lower than that of other particles of identical synthesis procedure but different surface groups, also the photoproduction of $^1O_2$ is attenuated by the presence of the amine group.[52] However, as an advantage, it should be recalled that NH_2-capped SiNPs present a strong selective interaction with several molecules of biological interest, of potential use in the field of diagnostic medicine in PAGE assays[53] allowing the detection and subsequent purification and characterization of serum proteins with high sensitivity. Other applications of interest involve the non-enzymatic fluorescence quenching detection of glucose.[54]

Polyethylene glycol (PEG) became the most successful approach to produce surfaces that are able to resist protein adhesion and biological attack.[55] PEG coated surfaces provide SiNPs of good affinity for aqueous media and do not exhibit immunogenicity and antigenicity. Furthermore, several studies describe PEG capacity to inhibit biofilm adhesion over coated surfaces.[27,56,57] The formation of a permanent chemical bond, and not only the physical adsorption, between a material surface and PEG promotes the biocompatibility of the material. PEG coatings or "PEGylation" on nanoparticles protect the surface from aggregation, opsonization, and phagocytosis, also extending systemic circulation times.[58]

In order to provide water solubility, previous works focused on the formation of micelles as lipid-based transport vehicles with PEG endings, with the encapsulation of SiNPs but without intrinsic modification of the SiNP surface.[59,60] More recently, a few reports on PEGylation of SiNPs were found.

Zhang and co-workers evaluated the grafting of polymer brushes of poly(poly(ethylene glycol)monomethacrylate) (P(PEGMA)) on the surface of SiNPs attached to Si wafers (Si/SiNPs).[61] The protocol involved the hydrosilylation of Si/SiNPs with 10-undecen-1-ol(Si/SiNPs-UO) followed by esterification with 2-bromo-2-methylpropyl bromide. Then a radical polymerization with PEGMA and Cu^{2+}/Cu^{+}/2,2′-bipyridine as catalysts yielded the PEG-terminated brushes, Si/SiNPs-UO-BMPB-*g*-P(PEGMA). The SiNPs obtained

were crystalline and with a diameter of about 5 nm. The emission of the slices Si/SiNPs and the detached SiNPs in water showed a maximum of around 610 nm under UV irradiation. The detached SiNPs-UO-BMPB-g-P(PEGMA) displayed a 30 nm blue shift from that of SiNPs-UO which authors ascribed to the denser grafted polymer brushes on the SiNPs surface expanding the energy level difference between excited and ground states.

Our group has extensively studied the effect of direct PEG coating on SiNPs. Scheme 19.2 schematizes the synthetic routes as will be discussed here. Firstly, we proposed the surface attachment of PEG onto 2-propen-1

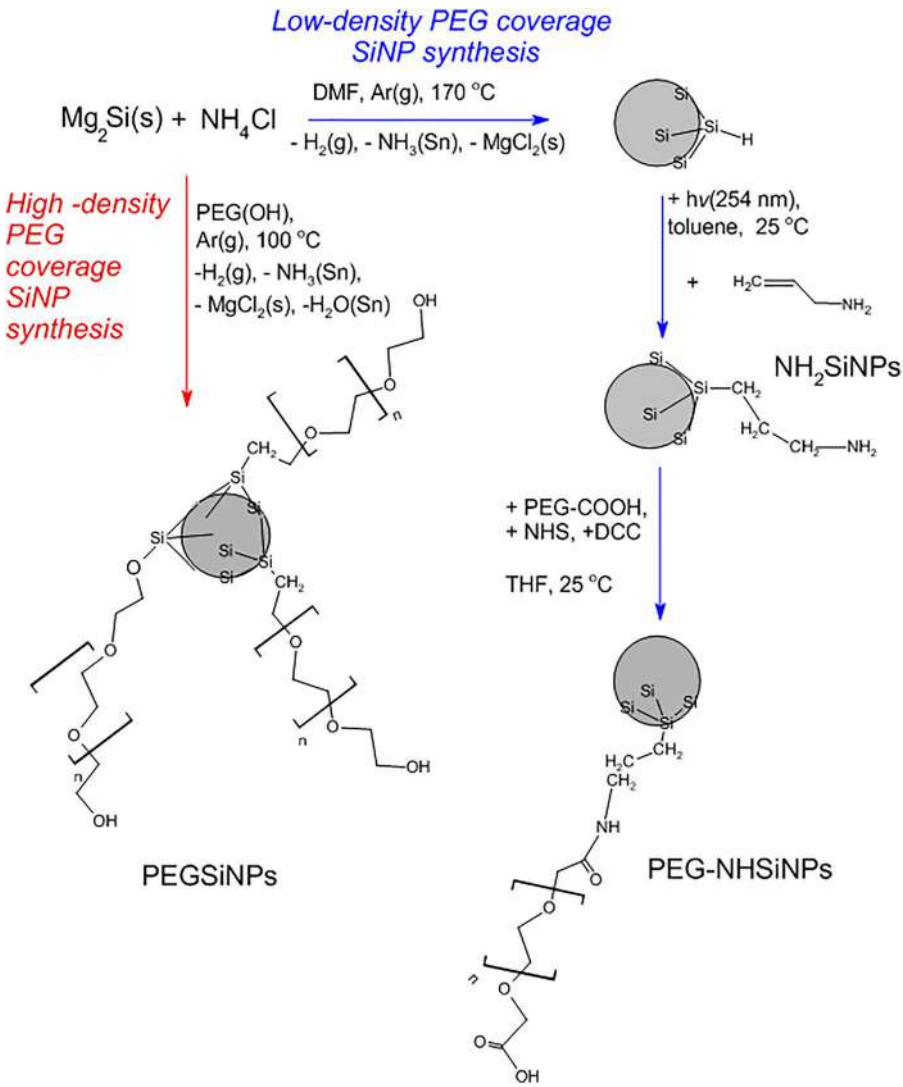

Scheme 19.2 Synthesis pathways of low- and high-density PEG-coated SiNPs.

amine functionalized SiNPs.[25] The water soluble 1–2 nm NH_2SiNPs were obtained upon photo-initiated silylation route of the highly reactive Si–H and Si–Cl nanoparticle surface. The synthetic route involved the coupling of carboxyl PEG conjugate (PEG-COOH) with NH_2SiNPs through a peptide bond to obtain PEG-NHSiNPs with <10% coverage of NH_2SiNPs with PEG chains, henceforth called low-density PEG covered SiNPs. Moreover, we proposed, in light of time-resolved anisotropy results, that this low attachment allows the grafted PEG chains to lie almost parallel to the particle's surface.

The particles mentioned above, NH_2SiNPs and PEG-NHSiNPs, present two coincident excitation and emission species with different relative contributions associated with PEG-NHSiNPs aggregation, being responsible for increased emission around 500 nm. Although a clear modification of particle surface charge and particle agglomeration were obtained, we showed that the PEG attachment does not modify NH_2SiNPs electronic states, though glycol molecules effectively increase by 25% the emission quantum yield in aqueous suspensions. Moreover, both NH_2SiNPs and PEG-NHSiNPs display a reversible dependence of the luminescence emission with dissolved oxygen concentration, being 10% higher in Ar-saturated suspension and reverting upon oxygen saturation of the solution. Concerning the interaction of SiNPs with proteins, it was demonstrated that the occurrence of resonance energy transfer (RET) between tryptophan residue of Bovine Serum Albumin (donor) and SiNPs (acceptor) is strongly dependent on the SiNP's surface coverage.[25] In that sense, the occurrence of RET between BSA tryptophan residues and NH_2SiNPs is strongly supported and oppositely, we concluded that PEG-NHSiNPs are not located within the RET distance. The binding constant (K_{SV}) between BSA and NH_2SiNP resulted in one order of magnitude higher than that with PEG-NHSiNP, also accounting for the protective character of only 10% coverage PEG chains.

Xu and co-workers synthesized core–shell SiNPs with a covalently attached PEG shell by a multi-step route involving the "click" reaction of copper-catalyzed azide–alkyne cycloaddition.[28] To that purpose, a 3.3 ± 1.5 nm size SiNPs suspension was obtained after milling of an undoped 111 Si wafer and further dispersion in dichloromethane. The suspension showed broad absorption at ≈600 nm and an excitation-dependant emission band in the range from 300 to 700 nm assigned to the polydispersity in the SiNPs size. To obtain PEGylated SiNPs, x-azido-pentenyl–SiNPs and monoalkynyl-PEG of different sizes (1.0, 2.0, and 4.6 kDa) in THF were conjugated using CuBr as a catalyst. TEM images of the obtained material evidenced the formation of 8–20 nm size aggregates with a distinctive dark core of Si and a lighter shell of PEG chains. The features of the absorption and PL spectra of the PEGylated SiNPs were coincident with those of the starting SiNPs in dichloromethane. Based on the aggregates porous structure and their strong PL, the authors proposed them as good candidates in drug delivery and bioimaging applications.

Later, our group proposed a one-pot synthetic pathway to obtain high-density coated amorphous PEGSiNPs of (3.3 ± 0.5) nm diameter and a Si core of 1.3–1.7 nm, involving the oxidation of magnesium silicide with NH_4Cl in

PEG (MW = 600 ± 30) as the reaction media.[27] Thermogravimetric analysis demonstrated >90% of PEG in a brush-type conformation in PEGSiNPs, in contrast with our previous work. The excitation and emission matrix for the PEGSiNPs was analyzed and compared with those of NH_2SiNPs and PEG-NHSiNPs (≈10% PEG chain coverage) obtained from magnesium silicide, but functionalized with a multi-step pathway as described above .[25] For all the above nanoparticles, two contributing species to the PL spectra were obtained from these analyses with an energy gap of 2.5–2.6 eV and 3.0 eV. Although this supports similar transitions involved in the PL spectra, the air-saturated aqueous suspension quantum yield for PEGSiNPs emission is ten times higher than for PEG-NHSiNPs. The last observation was explained by the protective effect given by the thick PEG shell on the PEGSiNPs silicon core where all surface silicon atoms are bonded to PEG chains.

Recently, our group immobilized the described high-density coated PEG-SiNPs on silica glass substrates through a sol–gel strategy to obtain porous films named fSiO_x-PEGSiNP, aiming to develop a self-cleaning surface.[57] These films displayed water wettability, strong photoluminescence and $^1O_2$ photosensitization capability, also demonstrating inhibition of *S. aureus* bacterial adhesion and biofilm growth, as well as killing action under UVA irradiation. The coating of the glass slide with PEGSiNPs was confirmed by fluorescence microscopy images, FTIR spectroscopy, EDX measurements, N_2 adsorption isotherm and contact angles determination. Concerning the optical properties, the fSiO_x-PEGSiNP showed absorption below 360 nm (EG = (3.09 ± 0.05) eV), coincident with that of PEGSiNPs.

PSi silanization and silylation chemistry have also been applied for the stabilization and functionalization of these materials for specific technological applications.[62–64] PSi surface was also chemically modified through a silanization process leading to the formation of pendant thiol groups.[65] PL studies showed the presence of new emission bands at 410–400 nm observed only after silanization, which were assigned to the presence of new emitting centers originated in the surface layer network of Si–O–Si formed after silanization. Simultaneously to the presence of the mentioned emission band, the characteristic visible band of PSi decreases in intensity after silanization.

19.4 Reactive Oxygen Species Generation by Surface Modified SiNPs

Singlet oxygen ($^1O_2$) production upon 350 nm irradiation of NH_2SiNPs and PEG–NH–SiNPs[25] was suggested by continuous illumination experiments. In addition, negligible chemical reaction between $^1O_2$ and NH_2SiNPs and PEG-NHSiNPs was demonstrated, though $^1O_2$ physical quenching by the particles is important. In fact, $^1O_2$ physical quenching rate constants calculated per propylamine group in the nanoparticle were k(NH_2SiNPs) = (2.0 ± 0.2)×10^9 M^{-1} s^{-1} and k(PEG-NHSiNPs) = (2.1 ± 0.5)×10^8 M^{-1} s^{-1} in toluene, supporting an important $^1O_2$ deactivation pathway by both nanoparticles. Propylamine

groups attached to SiNPs are responsible for the observed quenching, in line with the known $^1O_2$ quenching efficiency of propylamine isolated molecules. A quenching mechanism involving a stabilized charge transfer intermediate by chemical bonding to silicon was suggested. The one order of magnitude difference observed for PEG coated SiNPs compared to propylamine coated SiNPs, also support the protective effect of the glycol groups on particle reactivity towards $^1O_2$.

Highly-density coated PEGSiNPs[27] showed the formation of $^1O_2$ upon 355 nm irradiation of acetonitrile suspensions with singlet oxygen formation quantum yields in aqueous suspensions of ϕ_Δ (PEGSiNP) = (0.03 ± 0.01) in line with those reported for SiNPs of different origin in aqueous suspensions. Within the experimental error, PEGSiNPs were not able to generate superoxide radicals (O_2·–).

PEGSiNPs included on silica films (altogether denoted as fSiO_x-PEGSiNP) immersed in acetonitrile were able to generate $^1O_2$ upon 355 nm irradiation with ϕ_Δ(fSiO_x-PEGSiNP) = (1.1 ± 0.2) considering that $\phi_\Delta \approx 1$ for the reference molecule (phelanenone) also embedded in silica films, as determined by time-resolved phosphorescence of singlet oxygen experiments.[57] Furthermore, experiments in aqueous solution also demonstrated the $^1O_2$ production by fSiO_x-PEGSiNP under 350 nm continuous irradiation by reaction with the singlet oxygen sensor green (SOSG) probe. Taking as reference photosensitizer the molecule Rose Bengal, ϕ_Δ(fSiO_x-PEGSiNP) = (0.70 ± 0.15) in aqueous solution. The differences between the two determined quantum yields might be explained considering that SOSG sense preferentially the $^1O_2$ on the film interface and phosphorescence measurements monitors the $^1O_2$ produced at the surface and the films micropores. Noticeably, the inclusion of PEGSiNP in SiO_x films increase the ϕ_Δ of PEGSiNP one order of magnitude (from ϕ_Δ = (0.12 ± 0.04) to (1.1 ± 0.2)) probably due to the relaxation of nonradiative deactivation pathways of PEGSiNPs excited states when incorporated in the SiO_x solid matrix.

In summary, PEG chains confer SiNPs with water dispersibility, protect SiNPs $^1O_2$ self-deactivation, increment the emission quantum yield and reduce the interaction with proteins as BSA. These properties suggest that the PEG surface modification of SiNPs is a strategy that improves the optical properties of silicon nanoparticles and promotes their use in biological applications.

PSi is also well known as a photosensitizer for $^1O_2$ in organic and aqueous media. Size, porosity and oxidation grade of prepared PSi strongly determine the quantum yield of $^1O_2$ production. The singlet oxygen generation efficiency increases strongly for porous silicon with high (>80%) porosity.[66] PSi nanoparticles 146 ± 7 nm in diameter with 12 ± 4 nm pore sizes were capable of photosensitizing $^1O_2$ with quantum yield ϕ_Δ of (0.10 ± 0.02) and (0.17 ± 0.01) in ethanol and aqueous solutions, respectively.[67] Other authors[41] reported ϕ_Δ = (0.26 ± 0.01) for surface oxidized PSi in acetonitrile, though no specification on pore size was given. Early experimental results evidenced that the interaction of photogenerated $^1O_2$ with the H-terminated surface of

PSi lead to the photo-oxidation of the SiNM.[68] Moreover, the authors demonstrated that the formation of surface oxides on PSi reduced $^1O_2$ photosensitizing efficiency while resulted in a strong enhancement of the PL quantum yield. More recently, Caregnato *et al.*[41] reported that smaller $^1O_2$ lifetimes, τ_Δ, in mildly oxidized PSi suspensions in acetonitrile were smaller than those of the references in the same solvent.[69] These results strongly suggest the reaction between $^1O_2$ and mildly oxidized PSi. Silanol groups in PSi might contribute to the reduced τ_Δ as alcohols are known to support $^1O_2$ relaxation to the ground state.[70]

19.5 Photoluminescence in Silicon Nanostructures

Bulk crystalline silicon is an indirect bandgap semiconductor, *i.e.* the energy edges of the conduction and valence bands (energy gap ≈1.1 eV) do not fall in the same wavevector (large momentum mismatch between electrons and holes), thus bandgap radiative transitions are forbidden, requiring the coupling with phonons for an optical recombination process. Therefore, nonradiative transitions (such as Auger recombination or defects recombination at materials bulk, surface or interfaces) dominate the recombination process in bulk crystalline silicon, leading to very weak photoluminescence efficiencies.[71]

The situation is different when dealing with nm-length scales in silicon nanostructures, particularly when sizes are comparable to the Bohr radius of the exciton in bulk silicon (≈4 nm). In those cases, quantum confinement effects are expected to govern the photophysics, not only due to changes in the band structure of crystalline silicon leading to size-dependent band gaps, but also related to relaxation of the wavevector conservation law in indirect bandgap transitions, leading to higher radiative recombination rates with decreasing size. Thus, compared to bulk silicon, higher blue-shifted and size-dependent photoluminescence yields are expected for silicon nanostructures.

Starting from the pioneering work of Canham in 1990,[72] where the author reported efficient red light emission from PSi under UV light illumination, many researchers in the last 30 years focused their efforts on unraveling the origin of photoluminescence in silicon nanostructures. Even when many researchers provided evidence of the quantum confinement origin of photoluminescence in silicon nanostructures, an important number of works reported photoluminescence results and properties that cannot be explained by this model, thus leading to alternative models and theories pointing to surface phenomena. In those cases, photoluminescence properties appear to depend on surface chemistry, and were ascribed to radiative transitions from surface defects, bonds or molecular entities. Surface phenomena are expected to have a major role in nanostructures, particularly with decreasing size.

Two types of photoluminescence in the visible were observed in silicon nanostructures: the S-band (slow-band), characterized by a red-yellow emission with decay times in the order of microseconds; and the F-band

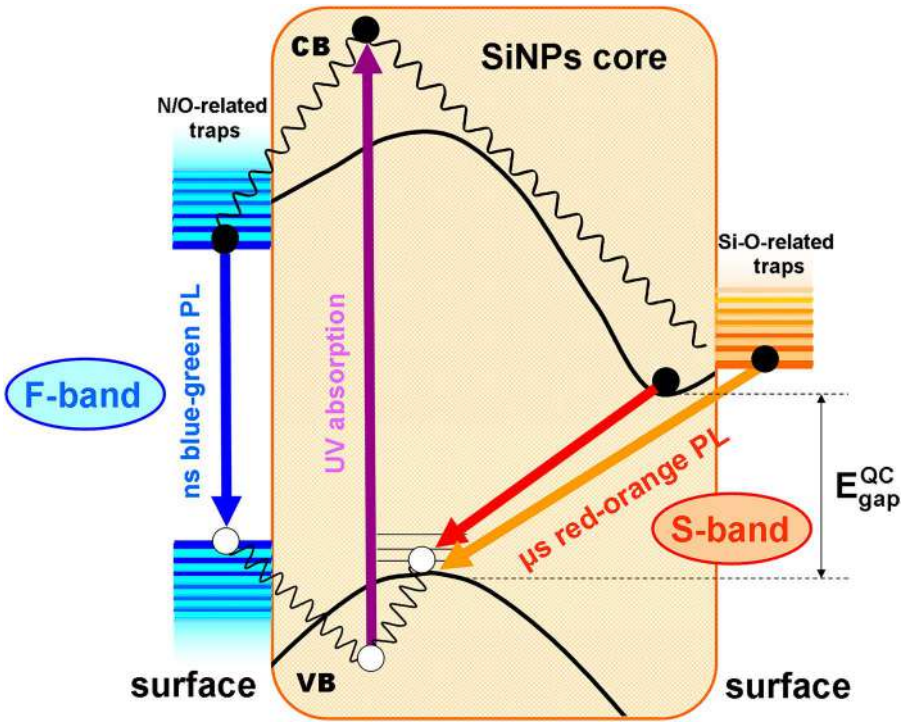

Scheme 19.3 Schematic representation of the proposed mechanisms of photoluminescence in SiNPs. For the sake of clarity, nonradiative recombination pathways (such as Auger recombination or defects recombination at materials bulk, surface or interfaces) were not explicitly included in the scheme.

(fast-band) with emission in the blue-green spectral range and fast nanosecond decays. In most cases, one or the other is dominant, but both can be present simultaneously in a given sample or even switched through surface passivation/modification. The possible origin of these photoluminescence regimes in silicon nanostructures is still a matter of intense debate in the scientific community,[73] and will be briefly summarized in the following sub-sections. Scheme 19.3 schematizes the mechanisms controlling PL, as will be discussed in the text.

19.5.1 Origin of the S-band Emission

The S-band emission is generally (but not exclusively) found in PSi structures, but it was also reported in freestanding silicon nanocrystals (herein denoted as SiNPs) prepared from high-purity reagents at high temperatures or using gas-phase methods, and in SiNPs embedded in a silica matrix prepared by Si ion implantation on SiO_2 films followed by high-temperature thermal annealing.[74]

There is a general consensus about the complex origin of the S-band emission, arising from the competition between bandgap radiative transitions in silicon nanocrystallites (contained within the porous matrix in the case of PSi), favored by quantum confinement effects (QC, leading to bandgap radiative recombination), and the emission from surface or interface defects. Thus, the origin of S-band emission in a particular silicon nanostructure depends on the relative energy levels of the electronic bands and defect states, and on the density and nature of the surface trap states.

Wolkin *et al.* proposed a theoretical model to explain the dependence of emission on the size of silicon crystallites within oxidized PSi.[75] Based on computational calculations of electronic energy levels of conduction and valence bands and Si=O trapping centers, they described three different regimes of emission: emission governed by indirect bandgap radiative transitions in bigger nanocrystals (>3 nm), and by surface traps recombination in the smaller ones (<1.5 nm), while in the intermediate cases (between 1.5 and 3 nm) emission may arise from recombination between bound electrons and free holes. Even when the experimental evidence apparently support the predictions of this model,[76] other works reported contrary conclusions. In that sense, Qin & Li proposed a different theoretical model based on calculations of charge-carriers dynamics in the presence of trapping luminescent centers.[77] Emission arising from the QC process or luminescent centers depends on the rates of both competitive processes, which are determined by the size of the silicon crystallites and the capture cross section, luminescence efficiency, and density of luminescent centers. According to this model, the higher the density of luminescent centers and the larger the size of silicon crystallites traps emission is beneficed over QC process, in contradiction with predictions of Wolkin model.

Irrespective of the mentioned discrepancies, S-band emission results from two competitive radiative recombination processes, QC bandgap transitions and defect-related PL (particularly in oxidized nanostructures). It is important to stress that defects-related PL associated with S-band emissions, due to their long lifetimes, are expected to be also of forbidden character.

19.5.2 Origin of the F-band Emission

The F-band emission is generally found in SiNPs prepared by bottom-up solution methods, such as those involving direct reduction of silicon halides or reaction of Zintl salts at low temperatures (*i.e.* <400 °C), but was also observed in top-down methods including contact with solvents (in the presence of oxygen), such as electrochemical etching followed by sonication and chemical etching (HF), and laser ablation of silicon wafers. This blue-green emission band with short lifetimes (in the order of nanoseconds) is typically size-independent and generally associated with allowed radiative recombination involving localized surface or interface trapping centers. Therefore, the emission of the F-band is critically dependent on the surface chemical composition in silicon nanostructures.

It has been recognized that partial surface oxidation of SiNPs (associated with wet oxidation at ambient conditions) leading to a silicon sub-oxide layer (SiO_x, with $0 < x < 2$) is crucial for F-band emission. Yang *et al.*[78] studied SiNPs obtained from laser ablation of clean Si wafers in solvents and evaluated the evolution of its blue photoluminescence during different treatments (aging at ambient conditions, thermal annealing, chemical etching). Their results point to radiative recombination of excitons, originally photogenerated in direct transitions in the SiNPs and subsequently trapped in near-interface traps between Si and SiO_x ($0 < x < 2$), as the origin of the blue photoluminescence.

Silicon nanostructures showing dual emission (F- and S-band) and the possibility of switching between both emission regimes *via* surface passivation/modification offers the possibility to get insight into the origin of blue PL. DeBenedetti *et al.*[79] studied the visible emission of decane-terminated SiNPs in colloidal suspensions of alcohols. On decreasing the chain length of the alcohols (bellow a critical length), emission was gradually switched from S-band emission (red) in hexane to F-band emission (blue) in ethanol, with clear dual emission in intermediate cases. The experimental evidence supported that the gradual switching of emission regimes is associated with oxidation of the SiNPs surfaces by alcohols small enough to surpass the alkyl-passivation layer. Therefore, the authors proposed that surface oxidation creates Si–O-related surface trap states and that blue emission arises from allowed radiative transitions between those traps and either the valence band or another trap state. Moreover, the observed higher intensity of the F-band compared to the S-band was associated with a decrease in nonradiative surface traps density (such as dangling bonds) due to surface oxidation (passivation). Dual emission in SiNPs was also reported in several works,[80,81] where size-dependent slow red emission (S-band) was associated with QC bandgap transitions and size-independent fast blue emission (F-band) was ascribed to allowed radiative transitions from Si–O-related traps within the conduction band.

Romero *et al.*[81] studied 1–2 nm size SiNPs obtained from different wet synthesis procedures (top-down electrochemical etching and bottom-up chemical reduction) and different surface compositions and capping, including alkyl, SiO_x and alkyl amine coverages. All nanoparticles showed mild surface oxidation (probably associated with wet oxidation during synthesis) and quite similar (but not equal) F-band emissions, independent of the synthesis procedure and surface derivatization. Results are compatible with blue emission originated in surface Si–O-related structures from wet synthesis procedures.

Dasog *et al.*[82] evaluated the photoluminescence properties of SiNPs prepared by three different syntheses methods: (a) thermally-induced disproportion of high-purity hydrogen silsesquioxane, followed by chemical etching to release hydrogen-terminated SiNPs (H-SiNPs), with subsequent dodecyl surface functionalization achieved *via* thermally-induced hydrosilylation; (b) Na_4Si_4/NH_4Br reaction in solution; and (c) direct solution reduction of $SiCl_4$.

In the last cases H-SiNPs could not be isolated from the reaction mixture and intermediate nanoparticles were directly dodecyl surface-functionalized *via* thermal hydrosilylation. While thermal synthesis method (a) renders excitation-independent red-emitting particles with microsecond lifetimes, compatible with QC bandgap transitions in the SiNPs, solution methods (b and c) produce excitation-dependent blue-emitting particles with nanosecond lifetimes. In the last case traces of Si–O and Si–N bonds were confirmed by XPS analysis. Moreover, switching from red to blue emission was obtained after exposing H-SiNPs (a) to nitrogen-containing reagents in solution, in the presence of oxygen. Therefore, the blue emission was ascribed to nitrogen defect or impurity sites (in the presence of oxygen impurities or partial surface oxidation). Experiments of solvatochromism reveal the charge-transfer character of the emitting states. Other works reported F-band emissions associated with the presence of surface oxygen and nitrogen impurities (silicon oxynitride surface structures, SiO_xN_y) constituting emitting traps with charge-transfer state character.[83,84]

In line with the proposed emission mechanisms in SiNPs, surface engineering appears as a plausible strategy to tune photoluminescence in silicon nanostructures. Dasog *et al.*[85] reported the synthesis of 3–4 nm size SiNPs with surface passivation using different surface groups (alkyl, SiO_x, phosphine oxide, aryl amine, acetal, alkyl amine). Starting from H-SiNPs obtained *via* thermally-induced disproportion of high-purity hydrogen silsesquioxane followed by chemical etching, through this strategy the authors were able to tune the photoluminescence across the visible spectrum without changing the particle size, with shorter lifetimes (nanoseconds) and higher quantum yields than those of silicon nanocrystals emitting from QC bandgap transitions. Other reports demonstrate that surface passivation with aryl amines (with N-linking phenyl rings) creates uniform emitting surface states, rendering PL in the nanosecond time-scale with narrow bandwidths and elevated quantum yields, with tunable peaks depending on the structure and chemical properties of the ligands.[86,87] Experimental evidence suggests that the emitting state has ligand-to-metal-charge-transfer (LMCT) character.[88]

In summary, silicon nanostructures prepared by thermal methods with highly pure reagents and in conditions preventing surface oxidation, whether hydrogen-terminated or alkyl-capped, generally show size-dependent (red-orange) S-band emissions associated with QC bandgap transitions. When surface oxidation in those SiNPs leads to a SiO_2 layer or when they are embedded in a silica matrix, QC processes compete with near-interface O-related trapping centers, but whose radiative recombination processes still have a forbidden character leading to slow (microsecond) lifetimes. However, when silicon nanostructures are prepared by wet chemical methods at low temperatures, size-independent (blue-green) F-band emissions are generally observed. In those cases, the creation of surface N/O-related trapping centers governs radiative transitions, completely quenching in most cases the S-band (partially-forbidden) transitions. These localized exciton estates with charge-transfer character recombine with radiative allowed transitions, leading to fast (nanosecond) lifetimes. Even when the exact chemical nature

of these surface traps is still unknown, surface passivation with N-containing ligands (particularly aryl amines) creates luminescent surface traps with properties associated with their chemical structure. Therefore, surface engineering appears mandatory to design and tune the fast-emission component in silicon nanostructures.

19.6 Metal–Si Nanocomposites

Silicon nanocomposites combine silicon-based fluorescent materials with other types of elements or nanostructures, such as transition metals or oxides of metals. The synthesis of these nanostructures displays unique fluorescent properties, allowing a wide range of uses: bioimaging, biological/chemical sensors, disease diagnosis, catalysts, and solar cells, among others.

Several authors have published a shift in the excitation and emission PL wavelength and a decrease in the PL quantum yield, depending on the dopant quantities. Doping introduces optical traps localized within the bandgap of photoluminescence silicon nanomaterials, changing the emission spectrum. Nevertheless, new properties such as magnetism show the promising advantages of the new nanostructures. Several interesting materials arise from the doping of Si-based nanostructures.

19.6.1 Silicon Nanoparticles

Doped silicon nanoparticles with 5% Mn and an average diameter of 4.2 nm showed a red shift in emission wavelengths from 430 to 520 nm when compared with bare silicon.[89] Song *et al.* investigated the effect of Mn concentration on the emission red shifts in 4.5 nm size Mn-doped Si nanoparticles, observing red shifts of 35 nm for the 1% Mn and of 100 nm for the 5% ones.[90] Also, McVey *et al.* reported that Mn-, Ni-, and Cu-doped Si nanoparticles show emission peaks at 483, 489, and 476 nm, giving a red shift of over 40 nm, pushing the emission from blue (corresponding to that of the undoped SiNPs) towards green, but with the particularity that emission quantum yields are similar.[91]

Paramagnetic iron-doped silicon nanoparticles with Fe^{3+} incorporated in the core of the nanoparticles as isolated iron centers showed not only a red-shifted emission wavelength with the increase of dopant, but also a quenching of emission intensity with increasing Fe concentrations. High concentrations of the iron dopant in the initial mixture led to extreme loss of photoluminescence.[92] On the other hand, SiNPs prepared in the presence of iron ions during the synthesis process involving Zintl salts showed the inhomogeneous incorporation of Fe leading to the formation of two distinct types of SiNPs in a given synthesis batch: iron-free and iron-containing SiNPs.[93] In addition, the partial reduction of Fe(III) to Fe(II) during synthesis takes place, thus suggesting that crystallization of Fe-containing SiNPs with high Fe contents are favored. These particles show an emission band centered at 450 nm with no observable shift due to the presence of iron though PL intensity as well as emission decay times strongly indicate an efficient emission quenching mechanism by iron which involves both, dynamic and

static processes. The nanoparticles were shown to generate $^1O_2$ upon 355 nm irradiation, though they were able to quench $^1O_2$. Analysis of cytotoxicity using MTT assay on rat glioma C6 cells showed a strong dependence not only on the presence of iron, but on the nature of the surface groups, as 100 μg ml^{-1} of propylamine-terminated iron-containing SiNPs leads to an 85% decrease in cell viability while equal amounts of surface oxidized particles induced 35% cell death.

19.6.2 Porous Silicon

As discussed before, PSi emission depicts a characteristic broad visible band with the maximum in the 550–700 nm range related to the S-band already described. Several literature publications report an enhancement of the S-band intensity of PSi, when metals, oxides and ions are incorporated into the silicon nanomaterial surface. Examples of the above PSi incorporated metals are iron ion impregnation;[94] Fe_3O_4 nanoparticles infiltration;[95] ultrathin metal film passivation with Ag, Au, and Al;[96] ferromagnetic Ni by electrodeposition;[97] colloidal Au nanoparticles;[98] Cr^{3+} ions incorporated by electrochemical process[99] and Zn doping using the photoelectrochemical etching process.[100] In these PSi nanocomposites, Cr^{+3}, Zn and iron have been incorporated at the surface of porous structure forming the oxide complex, while Au, Ag and Al formed a metal film on the PSi surface. These systems lead not only to an enhancement of the PL intensity with respect to undoped PSi, but also to a red shift with increasing the doping level in the samples. The red shift in the PSi containing Zn is in line with the decrease in the number of pores and porosity.[99]

In contrast, the PSi films doped with Cr^{+3} showed a blue shift effect of PL compared with bare PSi films.[100] In addition, a blue shift is observed with ferromagnetic metal (Ni) deposition time[97] and with decreasing particle size of Au nanoparticles which are deposited within the porous silicon.[101] Such shifts were proposed to be associated with an appreciable change in the size of the emissive Si nanoparticles within the PSi matrix.[95] On the other hand, some authors argued that, in most cases, the incorporation processes of metals in PSi surface is accompanied by partial oxidation of the PSi layer, with a consequent enhancement of PSi PL.[102] In other cases, the concentration of nonradiative recombination centers such as surface states and oxide charges decrease with the deposition of metal films, as discussed below.

Also, the incorporation of Au and Ni nanoparticles on the PSi surface create new luminescent centers with improved PL enhancement. The resulting high optical density of states was attributed to the coupling of a PSi emitter in the vicinity of a metal-dielectric interface with a plasmon mode.[97] Porosity is another parameter affecting the optical behavior of luminescent PSi,[98] as the increase in the surface concentration of metal is reported to be coupled with the decrease in the number of pores.[99]

On the other hand, other authors reported a decrease of PL intensity without a shift in the PSi S-band emission. Formation of a disordered network of ZnO nanowires which cover the surface of PSi in a dense layer[103] and CdS

nanoparticles embedded in PSi by a dip coating method[104] are examples where the intensity of low-energy PL band is significantly reduced.

In studies with suspensions of irregular shaped, 50–130 nm size, PSi showing visible PL with excitation–emission maximum at (λ_{exc}/nm, λ_{em}/nm): (285, 580), the particles emission intensity was observed to diminish after addition of magnetite nanoparticles of 15 nm size.[41] Scheme 19.4 depicts a schematic representation of how magnetite nanoparticles were proposed to interact with PSi by either filling the PSi and remaining attached to the surface. No shift of the emission band with the addition of the magnetic particles was observed. Also, time-resolved experiments performed exciting with light of 373 nm, which showed a mono-exponential PL decay with lifetimes increasing in a monotonic manner with increasing wavelength (40 μs at 650 nm to 10 μs at 500 nm), did not show variations due to the presence of magnetite. Therefore, a static quenching by magnetite of PSi PL was strongly suggested, probably due to the presence of nonradiative surface states raised by magnetite interaction with PSi, as the authors demonstrated that magnetite nanoparticles were either physically adsorbed or chemically bonded through Si–O–Fe bonds to the surface of the silicon structure. In line with these observations, the lower $^1O_2$ photosensitizing efficiency ($\phi_\Delta = 0.08 \pm 0.01$) and singlet oxygen lifetime τ_Δ, observed for magnetite-loaded PSi in acetonitrile suspensions, compared to those observed for unloaded PSi ($\phi_\Delta = 0.26 \pm 0.01$), strongly suggest a dynamic $^1O_2$ quenching by Si–O–Fe surface groups.[41]

Further silanization of magnetic PSi with 3-mercaptopropyl triethoxysilane lead to the appearance of a new band at 400–410 nm, assigned to the formation of a Si(O-)$_x$ environment, in line with literature reports on the effect of SiNPs mild oxidation.

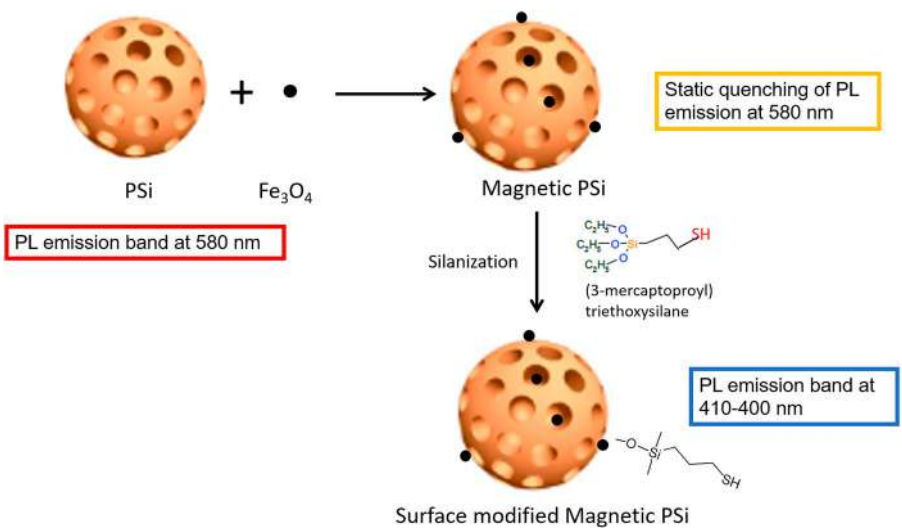

Scheme 19.4 Schematic representation of magnetic porous silicon showing the inclusion of magnetite within the pores and attached to the surface and further silanization with 3-mercaptopropyl triethoxysilane. The effect of these processes on PL is also shown.

19.7 Conclusions

Silicon-based nanomaterials, particularly freestanding SiNPs or PSi nanoparticles, are potentially useful as photoluminescent biomarkers and theragnostic agents, whether photochemically active for photodynamic therapy or as platforms for drug delivery. However, low PL yields and poor stability are expected for bare nanomaterials in biological media, while extended systemic circulation times and cell-targeting properties are mandatory for biological applications. Considering that their properties depend fundamentally on its surface chemistry, it was demonstrated that surface engineering of these SiNMs is essential to reach high PL and/or ROS generation quantum yields with tuned properties, meanwhile exerting cell-targeting properties and reducing aggregation, opsonization and phagocytosis, thus increasing nanoparticles stability in biological media. Furthermore, metal-silicon nanocomposites are also a plausible strategy to adjust their optical properties or to bring new ones, such as magnetism.

Silicon-based nanomaterials, conveniently surface derivatized and/or combined with other types of elements or nanostructures such as transition metals or oxides of metals, constitute a versatile platform for a new generation of bioimaging and theragnostic agents in biological applications.

In particular, PEG chains confer SiNPs water dispersibility, protects SiNPs $^1O_2$ self-deactivation, increments the emission quantum yield and reduces the interaction with proteins as BSA. These properties suggest that the PEG surface modification of SiNPs is a strategy that improves the optical properties of silicon nanoparticles and promotes their use in biological applications.

List of Abbreviations

SiNPs	Freestanding < 4 nm size silicon nanoparticles
PSi	Porous silicon particles
SiNMs	All silicon nanomaterials including SiNPs and PSi.
PL	Photoluminescence
$^1O_2$	Singlet oxygen
ϕ_Δ	Singlet oxygen quantum yield
τ_Δ	Singlet oxygen lifetime

References

1. P. Caregnato, M. L. Dell'Arciprete and M. C. Gonzalez, *et al.*, in *Versatile Silicon Nanoparticles with Potential Uses as Photoluminescent Sensors and Photosensitizers*, ed. A. Albini and E. Fasani, The Royal Society of Chemistry, 2017, vol. 44, pp. 322–345.
2. S. Wippermann, Y. He, M. Vörös and G. Galli, Novel silicon phases and nanostructures for solar energy conversion, *Appl. Phys. Rev.*, 2016, **3**(4), 040807.

3. A. Ramizy, W. J. Aziz, Z. Hassan, K. Omar and K. Ibrahim, Improved performance of solar cell based on porous silicon surfaces, *Optik*, 2011, **122**(23), 2075–2077.
4. B. Chu, H. Wang, B. Song, F. Peng, Y. Su and Y. He, Fluorescent and Photostable Silicon Nanoparticles Sensors for Real-Time and Long-Term Intracellular pH Measurement in Live Cells, *Anal. Chem.*, 2016, **88**(18), 9235–9242.
5. S. Ozdemir and J. Gole, The potential of porous silicon gas sensors, *Curr. Opin. Solid State Mater. Sci.*, 2007, **11**(5–6), 92–100.
6. F. Maier-Flaig, J. Rinck and M. Stephan, *et al.*, Multicolor Silicon Light-Emitting Diodes (SiLEDs), *Nano Lett.*, 2013, **13**(2), 475–480.
7. J. Linnros and N. Lalic, High quantum efficiency for a porous silicon light emitting diode under pulsed operation, *Appl. Phys. Lett.*, 1995, **66**(22), 3048–3050.
8. D.-C. Wang, C. Zhang and P. Zeng, *et al.*, *An Silicon Nanocrystal Laser*, 2017, http://arxiv.org/abs/1710.00215.
9. N. Liu, J. Liu and D. Jia, *et al.*, Multi-core yolk-shell like mesoporous double carbon-coated silicon nanoparticles as anode materials for lithium-ion batteries, *Energy Storage Mater.*, 2019, **18**, 165–173.
10. J. Entwistle, A. Rennie and S. Patwardhan, A review of magnesiothermic reduction of silica to porous silicon for lithium-ion battery applications and beyond, *J. Mater. Chem. A*, 2018, **6**(38), 18344–18356.
11. M. Qiu, A. Singh and D. Wang, *et al.*, Biocompatible and biodegradable inorganic nanostructures for nanomedicine: Silicon and black phosphorus, *Nano Today*, 2019, **25**, 135–155.
12. N. O'Farrell, A. Houlton and B. R. Horrocks, Silicon nanoparticles: applications in cell biology and medicine, *Int. J. Nanomed.*, 2006, **1**(4), 451–472, http://www.ncbi.nlm.nih.gov/pmc/articles/PMC2676646/.
13. M. L. Dell´Arciprete, M. C. Gonzalez, R. M. Gorojod and M. L. Kotler, Silicon dots in radiotherapy, in *Silicon Nanomaterials Sourcebook Hybrid Materials, Arrays, Networks, and Devices, Volume Two*, ed. K. D. Sattler, Taylor and Francis Group, 2018, DOI: 10.1039/9781782626954-00324.
14. H. A. Santos, E. Mäkilä, A. J. Airaksinen, L. M. Bimbo and J. Hirvonen, Porous silicon nanoparticles for nanomedicine: preparation and biomedical applications, *Nanomedicine*, 2014, **9**(4), 535–554.
15. C. Magnusson, R. Jugdaohsingh, L. Hulthen, A. Westerlund, J. J. Powell and M. Ransjö, Urinary Excretion of Silicon in Men, Non-pregnant Women, and Pregnant Women: a Cross-sectional Study, *Biol. Trace Elem. Res.*, 2020, **194**(2), 321–327.
16. A. A. Burns, J. Vider and H. Ow, *et al.*, Fluorescent Silica Nanoparticles with Efficient Urinary Excretion for Nanomedicine, *Nano Lett.*, 2009, **9**(1), 442–448.
17. D.-E. Lee, H. Koo, I.-C. Sun, J. H. Ryu, K. Kim and I. C. Kwon, Multifunctional nanoparticles for multimodal imaging and theragnosis, *Chem. Soc. Rev.*, 2012, **41**(7), 2656–2672.
18. R. Hardman, A Toxicologic Review of Quantum Dots: Toxicity Depends on Physicochemical and Environmental Factors, *Environ. Health Perspect.*, 2006, **114**(2), 165–172.

19. Y.-W. Huang, C. Wu and R. S. Aronstam, Toxicity of Transition Metal Oxide Nanoparticles: Recent Insights from *in vitro* Studies, *Materials*, 2010, **3**(10), 4842–4859.
20. M. L. Dell'Arciprete, M. C. Gonzalez, R. M. Gorojod and M. L. Kotler, in *Silicon Nanomaterials Sourcebook*, ed. K. D. Sattler, CRC Press, 2017, DOI: 10.4324/9781315153551.
21. J. H. Warner, A. Hoshino, K. Yamamoto and R. D. Tilley, Water-Soluble Photoluminescent Silicon Quantum Dots, *Angew. Chem., Int. Ed.*, 2005, **44**(29), 4550–4554.
22. J. H. Warner and R. D. T. Halina Rubinsztein-Dunlop, Surface Morphology Dependent Photoluminescence from Colloidal Silicon Nanocrystals, *J. Phys. Chem. B*, 2005, **109**, 19064–19067.
23. J. GJ, One-Pot Synthesis of Colloidal Silicon Quantum Dots and Surface Functionalization *via* Thiol-Ene Click Chemistry, *Chem. Commun.*, 2012, **48**, 11874.
24. S. Klein, M. L. Dell'Arciprete and M. Wegmann, *et al.*, Oxidized silicon nanoparticles for radiosensitization of cancer and tissue cells, *Biochem. Biophys. Res. Commun.*, 2013, **434**(2), 217–222.
25. C. R. Lillo, J. J. Romero, M. L. Portolés, R. P. Diez, P. Caregnato and M. C. Gonzalez, Organic coating of 1–2-nm-size silicon nanoparticles: Effect on particle properties, *Nano Res.*, 2015, **8**(6), 2047–2062.
26. A. Chaix, E. Cueto-diaz and A. Delalande, *et al.*, Amino-acid functionalized porous silicon nanoparticles for the delivery of pDNA †, *RSC Adv.*, 2019, **9**, 31895–31899.
27. D. Rodríguez Sartori, C. R. Lillo and J. J. Romero, *et al.*, Polyethylene glycol-coated blue-emitting silicon dots with improved properties for uses in aqueous and biological environments, *Nanotechnology*, 2016, **27**(47), 475704.
28. Z. Xu, Y. Li and B. Zhang, *et al.*, Water-soluble PEGylated silicon nanoparticles and their assembly into swellable nanoparticle aggregates, *J. Nanopart. Res.*, 2015, **17**(1), 1–16.
29. F. Erogbogbo, C.-A. Tien and C.-W. Chang, *et al.*, Bioconjugation of Luminescent Silicon Quantum Dots for Selective Uptake by Cancer Cells, *Bioconjugate Chem.*, 2011, **22**(6), 1081–1088.
30. J. I. Abdul Rashid, J. Abdullah, N. A. Yusof and R. Hajian, The Development of Silicon Nanowire as Sensing Material and Its Applications, *J. Nanomater.*, 2013, **2013**, 1–16.
31. P. Castrucci, M. Scarselli and M. De Crescenzi, *et al.*, Silicon nanotubes: Synthesis and characterization, *Thin Solid Films*, 2006, **508**(1–2), 226–230.
32. Y. Dahman, T. Truong, M. Jawaid and S. Widjaja, Nanomedicine, in *Nanotechnology and Functional Materials for Engineers*, ed. Y. Dahman, Elsevier, 2017th edn, 2017, pp. 229–249, DOI: 10.1016/B978-0-323-51256-5.00011-3.
33. M. J. Llansola Portolés, R. Pis Diez and M. L. Dell'Arciprete, *et al.*, Understanding the parameters affecting the photoluminescence of silicon nanoparticles, *J. Phys. Chem. C*, 2012, **116**(20), 11315–11325.

34. J. J. Romero, M. J. Llansola-Portolés, M. L. Dell'Arciprete, H. B. Rodríguez, A. L. Moore and M. C. Gonzalez, Photoluminescent 1–2 nm Sized Silicon Nanoparticles: A Surface-Dependent System, *Chem. Mater.*, 2013, **25**(17), 3488–3498.
35. K. Tokarska, Q. Shi and L. Otulakowski, *et al.*, Facile production of ultrafine silicon nanoparticles, *R. Soc. Open Sci.*, 2020, **7**(9), 200736.
36. X. Li, Y. He, S. S. Talukdar and M. T. Swihart, Process for Preparing Macroscopic Quantities of Brightly Photoluminescent Silicon Nanoparticles with Emission Spanning the Visible Spectrum, *Langmuir*, 2003, **19**(20), 8490–8496.
37. C. M. Hessel, E. J. Henderson and J. G. C. Veinot, Hydrogen Silsesquioxane: A Molecular Precursor for Nanocrystalline Si−SiO 2 Composites and Freestanding Hydride-Surface-Terminated Silicon Nanoparticles, *Chem. Mater.*, 2006, **18**(26), 6139–6146.
38. J. J. Romero, M. Wegmann, C. Lillo, A. Rubert, S. Klein and C. Kryschi, *Impact of Iron Incorporation on 2 − 4 nm Size Silicon Nanoparticles Properties*, 2015, DOI: 10.1021/acs.jpcc.5b00172.
39. B. M. Nolan, T. Henneberger, M. Waibel, T. F. Fässler and S. M. Kauzlarich, Silicon Nanoparticles by the Oxidation of [Si 4]4- and [Si 9]4-Containing Zintl Phases and Their Corresponding Yield, *Inorg. Chem.*, 2015, **54**(1), 396–401.
40. A. Halimaoui, C. Oules and G. Bomchil, *et al.*, Electroluminescence in the visible range during anodic oxidation of porous silicon films, *Appl. Phys. Lett.*, 1991, **59**(3), 304–306.
41. P. Caregnato, P. M. David Gara, E. D. Prieto and M. C. Gonzalez, Luminescence properties and ROS generation of magnetic porous silicon nanoparticles, *Colloids Surf., A*, 2020, **592**, 124577.
42. Y. H. Xie, W. L. Wilson and F. M. Ross, *et al.*, Luminescence and structural study of porous silicon films, *J. Appl. Phys.*, 1992, **71**(5), 2403–2407.
43. L. Canham, *Handbook of Porous Silicon*, Springer International Publishing, 2014, DOI: 10.1007/978-3-319-05744-6.
44. N. G. Semaltianos, S. Logothetidis and W. Perrie, *et al.*, Silicon nanoparticles generated by femtosecond laser ablation in a liquid environment, *J. Nanopart. Res.*, 2010, **12**(2), 573–580.
45. L. T. Canham, Properties of porous silicon, in *EMIS Data reviews Series No 18*, ed. L. T.Canham, INSPEC/IEE, 1997.
46. S. Chattopadhyay, X. Li and P. W. Bohn, In-plane control of morphology and tunable photoluminescence in porous silicon produced by metal-assisted electroless chemical etching, *J. Appl. Phys.*, 2002, **91**(9), 6134–6140.
47. F. Karbassian, Porous Silicon, in *Porosity – Process, Technologies and Applications*, ed. T. H. Ghrib, InTech, 2018, DOI: 10.5772/intechopen.72910.
48. L. Wei-Li, D. Xin-Zhong and W. Lian-Wei, *et al.*, Silicon-on-Insulator Structure Fabricated by Electron Beam Evaporation of Si on Porous Si and Epitaxial Layer Transfer, *Chin. Phys. Lett.*, 2001, **18**(5), 662–664.
49. F. Voigt, R. Brüggemann, T. Unold, F. Huisken and G. H. Bauer, Porous thin films grown from size-selected silicon nanocrystals, *Mater. Sci. Eng., C*, 2005, **25**(5–8), 584–589.

50. J. H. Warner, H. Rubinsztein-Dunlop and R. D. Tilley, Surface morphology dependent photoluminescence from colloidal silicon nanocrystals, *J. Phys. Chem. B*, 2005, **109**(41), 19064–19067.
51. Q. S. Li, R. Q. Zhang, S. T. Lee, T. A. Niehaus and T. Frauenheim, Amine-capped silicon quantum dots, *Appl. Phys. Lett.*, 2008, **92**(5), 053107.
52. C. R. Lillo, M. Natalia Calienni and R. M. Gorojod, *et al.*, Toward biomedical application of amino-functionalized silicon nanoparticles, *Nanomedicine*, 2018, **13**(11), 1349–1370.
53. P. Liu, N. Na, L. Huang, D. He, C. Huang and J. Ouyang, The Application of Amine-Terminated Silicon Quantum Dots on the Imaging of Human Serum Proteins after Polyacrylamide Gel Electrophoresis (PAGE), *Chem. - Eur. J.*, 2012, **18**(5), 1438–1443.
54. L. Du, Z. Li, J. Yao, G. Wen, C. Dong and H. Li, Enzyme free glucose sensing by amino-functionalized silicon quantum dot, *Spectrochim. Acta, Part A*, 2019, **216**, 303–309.
55. N. A. Alcantar, E. S. Aydil and J. N. Israelachvili, Polyethylene glycol – coated biocompatible surfaces, *J. Biomed. Mater. Res.*, 2000, **51**(3), 343–351.
56. J. Buxadera-Palomero, C. Canal, S. Torrent-Camarero, B. Garrido, F. Javier Gil and D. Rodríguez, Antifouling coatings for dental implants: Polyethylene glycol-like coatings on titanium by plasma polymerization, *Biointerphases*, 2015, **10**(2), 029505.
57. E. Gonik, D. R. Sartori, P. D. Gara, A. Miñán, M. Fernández and L. De Mele, Staphylococcus aureus biofilm eradication by the synergistic effect exerted by PEG- coated silicon dots immobilized in silica films and light irradiation, *Nanotechnology*, 2021, **32**(9), 95105.
58. J. S. Suk, Q. Xu and N. Kim, *et al.*, PEGylation as a strategy for improving nanoparticle-based drug and gene delivery, *Adv. Drug Delivery Rev.*, 2016, **99**(A), 28–51.
59. F. Erogbogbo, K. Yong, I. Roy, G. Xu, P. N. Prasad and M. T. Swihart, Biocompatible Luminescent Silicon Quantum Dots for Imaging of Cancer Cells, *ACS Nano*, 2008, **2**(5), 873–878.
60. F. Erogbogbo, K. Yong and R. Hu, *et al.*, Biocompatible Magnetofluorescent Probes: Luminescent Silicon Quantum Dots Coupled with Superparamagnetic, *ACS Nano*, 2010, **4**(9), 5131–5138.
61. C. Zhang, Y. Kuai, H. Cheng, X. Liu and L. Ma, Covalent bonding of grafted polymer brushes of poly (poly (ethylene glycol) monomethacrylate) on surface of silicon quantum dots and the activation of the end hydroxyls, *Arabian J. Chem.*, 2019, **12**(8), 5260–5267.
62. S. A. Trauger, E. P. Go and Z. Shen, *et al.*, High Sensitivity and Analyte Capture with Desorption/Ionization Mass Spectrometry on Silylated Porous Silicon, *Anal. Chem.*, 2004, **76**(15), 4484–4489.
63. M. P. Stewart, E. G. Robins, T. W. Geders, M. J. Allen, H. C. Choi and J. M. Buriak, Three methods for stabilization and functionalization of porous silicon surfaces *via* hydrosilylation and electrografting reactions, *Phys. Status Solidi A*, 2000, **182**(1), 109–115.

64. C. Smith, D. Mueller, P. Matz and R. Reidy, Topographical and chemical surface modification of porous MSQ using silylating agents with different numbers of methoxy groups, *MRS Proc.*, 2006, **914**, 0914-F04-04.
65. P. Caregnato, M. L. Dell'Arciprete and M. C. Gonzalez, Silanization effect on the photoluminescence characteristics of crystalline and amorphous silicon nanoparticles, *Photochem. Photobiol. Sci.*, 2013, **12**(9), 1658–1665.
66. Y. V. Ryabchikov, I. A. Belogorokhov, A. S. Vorontsov, L. A. Osminkina, V. Y. Timoshenko and P. K. Kashkarov, Dependence of the singlet oxygen photosensitization efficiency on morphology of porous silicon, *Phys. Status Solidi*, 2007, **204**(5), 1271–1275.
67. L. Xiao, L. Gu, S. B. Howell and M. J. Sailor, Porous Silicon Nanoparticle Photosensitizers for Singlet Oxygen and Their Phototoxicity against Cancer Cells, *ACS Nano*, 2011, **5**(5), 3651–3659.
68. M. Fujii, N. Nishimura and H. Fumon, *et al.*, Dynamics of photosensitized formation of singlet oxygen by porous silicon in aqueous solution, *J. Appl. Phys.*, 2006, **100**(12), 124302.
69. M. DeRosa, Photosensitized singlet oxygen and its applications, *Coord. Chem. Rev.*, 2002, **233–234**, 351–371.
70. J. R. Hurst and G. B. Schuster, Nonradiative relaxation of singlet oxygen in solution, *J. Am. Chem. Soc.*, 1983, **105**(18), 5756–5760.
71. J. R. Haynes and W. C. Westphal, Radiation Resulting from Recombination of Holes and Electrons in Silicon, *Phys. Rev.*, 1956, **101**(6), 1676–1678.
72. L. Canham, Introductory lecture: origins and applications of efficient visible photoluminescence from silicon-based nanostructures, *Faraday Discuss.*, 2020, **222**, 10–81.
73. P. Galář, T. Popelář and J. Khun, *et al.*, The red and blue luminescence in silicon nanocrystals with an oxidized, nitrogen-containing shell, *Faraday Discuss.*, 2020, **222**, 240–257.
74. D. Kovalev, H. Heckler, G. Polisski, J. Diener and F. Koch, Optical properties of silicon nanocrystals, *Opt. Mater*, 2001, **17**(1–2), 35–40.
75. M. V. Wolkin, J. Jorne, P. M. Fauchet, G. Allan and C. Delerue, Electronic States and Luminescence in Porous Silicon Quantum Dots: The Role of Oxygen, *Phys. Rev. Lett.*, 1999, **82**(1), 197–200.
76. J. S. Biteen, A. L. Tchebotareva, A. Polman, N. S. Lewis and H. A. Atwater, Controlled Passivation and Luminescence Blue Shifts of Isolated Silicon Nanocrystals, *MRS Proc.*, 2003, **770**, I6.2.
77. G. G. Qin and Y. J. Li, Photoluminescence mechanism model for oxidized porous silicon and nanoscale-silicon-particle-embedded silicon oxide, *Phys. Rev. B*, 2003, **68**(8), 085309.
78. S. Yang, W. Li, B. Cao, H. Zeng and W. Cai, Origin of blue emission from silicon nanoparticles: Direct transition and interface recombination, *J. Phys. Chem. C*, 2011, **115**, 21056–21062.
79. W. J. I. DeBenedetti, S.-K. Chiu and C. M. Radlinger, *et al.*, Conversion from Red to Blue Photoluminescence in Alcohol Dispersions of

Alkyl-Capped Silicon Nanoparticles: Insight into the Origins of Visible Photoluminescence in Colloidal Nanocrystalline Silicon, *J. Phys. Chem. C*, 2015, **119**(17), 9595–9608.

80. W. D. A. M. de Boer, D. Timmerman and K. Dohnalová, *et al.*, Red spectral shift and enhanced quantum efficiency in phonon-free photoluminescence from silicon nanocrystals, *Nat. Nanotechnol.*, 2010, **5**(12), 878–884.
81. J. J. Romero, M. J. Llansola-Portolés, M. L. Dell'Arciprete, H. B. Rodríguez, A. L. Moore and M. C. Gonzalez, Photoluminescent 1-2 nm sized silicon nanoparticles: A surface-dependent system, *Chem. Mater.*, 2013, **25**(17), 3488–3498.
82. M. Dasog, Z. Yang and S. Regli, *et al.*, Chemical insight into the origin of red and blue photoluminescence arising from freestanding silicon nanocrystals, *ACS Nano*, 2013, **7**, 2676–2685.
83. G. B. De los Reyes, M. Dasog, M. Na, L. V. Titova, J. G. C. Veinot and F. A. Hegmann, Charge transfer state emission dynamics in blue-emitting functionalized silicon nanocrystals, *Phys. Chem. Chem. Phys.*, 2015, **17**(44), 30125–30133.
84. R. Sinelnikov, M. Dasog, J. Beamish, A. Meldrum and J. G. C. Veinot, Revisiting an Ongoing Debate: What Role Do Surface Groups Play in Silicon Nanocrystal Photoluminescence?, *ACS Photonics*, 2017, **4**(8), 1920–1929.
85. M. Dasog, G. B. De Los Reyes, L. V. Titova, F. A. Hegmann and J. G. C. Veinot, Size *vs* Surface: Tuning the Photoluminescence of Freestanding Silicon Nanocrystals Across the Visible Spectrum *via* Surface Groups, *ACS Nano*, 2014, **8**(9), 9636–9648.
86. L. Wang, Q. Li and H.-Y. Wang, *et al.*, Ultrafast optical spectroscopy of surface-modified silicon quantum dots: unraveling the underlying mechanism of the ultrabright and color-tunable photoluminescence, *Light: Sci. Appl.*, 2015, **4**(1), e245.
87. Q. Li, T.-Y. Luo and M. Zhou, *et al.*, Silicon Nanoparticles with Surface Nitrogen: 90% Quantum Yield with Narrow Luminescence Bandwidth and the Ligand Structure Based Energy Law, *ACS Nano*, 2016, **10**(9), 8385–8393.
88. W. Y. So, Q. Li and C. M. Legaspi, *et al.*, Mechanism of Ligand-Controlled Emission in Silicon Nanoparticles, *ACS Nano*, 2018, **12**(7), 7232–7238.
89. X. Zhang, M. Brynda and R. D. Britt, *et al.*, Synthesis and Characterization of Manganese-Doped Silicon Nanoparticles: Bifunctional Paramagnetic-Optical Nanomaterial, *J. Am. Chem. Soc.*, 2007, **129**(35), 10668–10669.
90. B. Song and Y. He, Fluorescent silicon nanomaterials: from synthesis to functionalization and application, *Nano Today*, 2019, **26**, 149–163.
91. B. F. P. McVey, J. Butkus, J. E. Halpert, J. M. Hodgkiss and R. D. Tilley, Solution Synthesis and Optical Properties of Transition-Metal-Doped Silicon Nanocrystals, *J. Phys. Chem. Lett.*, 2015, **6**(9), 1573–1576.

92. M. P. Singh, T. M. Atkins and E. Muthuswamy, *et al.*, Development of Iron-Doped Silicon Nanoparticles As Bimodal Imaging Agents, *ACS Nano*, 2012, **6**(6), 5596–5604.
93. J. J. Romero, M. Wegmann and H. B. Rodríguez, *et al.*, Impact of iron incorporation on 2-4 nm size silicon nanoparticles properties, *J. Phys. Chem. C*, 2015, **119**(10), 5739–5746.
94. M. Rahmani, A. Moadhen, M.-A. Zaïbi, H. Elhouichet and M. Oueslati, Photoluminescence enhancement and stabilisation of porous silicon passivated by iron, *J. Lumin.*, 2008, **128**(11), 1763–1766.
95. F. A. Harraz, Synthesis and surface properties of magnetite (Fe3O4) nanoparticles infiltrated into porous silicon template, *Appl. Surf. Sci.*, 2013, **287**, 203–210.
96. C. Hong, H. Kim, H. W. Kim and C. Lee, Enhancement of the photoluminescence of porous silicon by sputter deposition of semitransparent metal films, *Met. Mater. Int.*, 2010, **16**(2), 311–315.
97. P. Granitzer, K. Rumpf, P. Poelt and M. Reissner, Magnetic Characteristics of Ni-Filled Luminescent Porous Silicon, *Front. Chem.*, 2019, **7**, 41.
98. M. B. de la Mora, J. Bornacelli, R. Nava, R. Zanella and J. A. Reyes-Esqueda, Porous silicon photoluminescence modification by colloidal gold nanoparticles: Plasmonic, surface and porosity roles, *J. Lumin.*, 2014, **146**, 247–255.
99. M. S. Almomani, N. M. Ahmed, M. Rashid, M. A. Almessiere and A. S. Altowyan, Broadband visible emission from photoelectrochemical etched porous silicon quantum dots containing zinc, *Mater. Chem. Phys.*, 2021, **258**, 123935.
100. W. J. Salcedo, M. S. Braga and R. F. V. V. Jaimes, Huge enhancement of photoluminescence emission from porous silicon film doped with Cr(III) ions, *J. Lumin.*, 2018, **199**, 109–111.
101. T. S. T. Amran, M. R. Hashim, N. K. A. Al-Obaidi, H. Yazid and R. Adnan, Optical absorption and photoluminescence studies of gold nanoparticles deposited on porous silicon, *Nanoscale Res. Lett.*, 2013, **8**(1), 35.
102. R. Boukherroub, D. D. M. Wayner, G. I. Sproule, D. J. Lockwood and L. T. Canham, Stability Enhancement of Partially-Oxidized Porous Silicon Nanostructures Modified with Ethyl Undecylenate 1, *Nano Lett.*, 2001, **1**(12), 713–717.
103. I. B. Olenych, L. S. Monastyrskii and A. P. Luchechko, Photoluminescence of Porous Silicon–Zinc Oxide Hybrid structures, *J. Appl. Spectrosc.*, 2017, **84**(1), 66–70.
104. N. V. Deshmukh, T. M. Bhave and A. S. Ethiraj, *et al.*, Photoluminescence and *I–V* characteristics of a CdS-nanoparticles-porous-silicon heterojunction, *Nanotechnology*, 2001, **12**(3), 290–294.

CHAPTER 20

Synergic Properties in Crystals: Implication of Motion at the Molecular Level

JESSICA I. VASQUEZ-MATÍAS[a], ERNESTO A. HERNÁNDEZ-MORALES[a], ABRAHAM COLIN-MOLINA[a], SALVADOR PÉREZ-ESTRADA[b] AND BRAULIO RODRÍGUEZ-MOLINA*[a]

[a]Instituto de Química, Universidad Nacional Autónoma de México, Circuito Exterior, Ciudad Universitaria, 04510, Ciudad de México, Mexico; [b]Área Académica de Química, Universidad Autónoma del Estado de Hidalgo, Carretera Pachuca-Tulancingo km 4.5, Mineral de la Reforma, 42184, Hidalgo, Mexico
*E-mail: brodriguez@iquimica.unam.mx

20.1 Introduction

Nanoarchitectonics has been intensely investigated in recent years, evoking the development of nanosized materials for technology applications.[1] The scope of this notion also includes the precise bottom-up organization of atoms and molecules into multifaceted supramolecular systems in solution and in the solid state, which may show emergent properties.[2] It seems likely that the complex functions of these new systems result from an amalgamation (product properties) of those of the starting materials, rather than a linear combination of them (sum properties). Thus, the

Nanoscience & Nanotechnology Series No. 55
Concepts and Design of Materials Nanoarchitectonics
Edited by Omar Azzaroni and Katsuhiko Ariga

Published by the Royal Society of Chemistry, www.rsc.org

word synergy (from the Greek *synergos*, working together), is used here to describe the advantageous association of motion with other functions to produce a combined effect.

It is therefore conceivable that our work on crystalline molecular rotors[3] could fit into the nanoarchitectonics perspective, as we try to understand how the molecular motion correlates with other properties in the solid state. The design of these crystalline materials is not a trivial task, given that their crystal arrays experience numerous intermolecular interactions that may hinder the internal dynamics. However, it seems possible to control the crystal array by taking advantage of the crystal engineering tools,[4] and supramolecular chemistry.[5] Therefore, the goal of this contribution is to describe crystalline materials with a response modulated by an external stimulus that also presents changes in their inner dynamics.

With this in mind, this chapter is divided into four sections, each one highlights the effect of molecular dynamics on four measurable properties of crystals. Section I draws a correlation between the optical properties of the crystals with the mobility of their components. Subsequently, section II associates the dielectric response of crystals with the angular motions of its constituents. Afterwards, section III describes selected examples where macroscopic motion of crystals may result from an amplification of the motion at the molecular scale. Finally, section IV highlights how the porosity of crystals can be correlated with intramolecular dynamics.

20.2 Molecular Motion and Optical Properties

One of the most exciting and promising avenues of studying molecular motion in crystals is the modulation of their optical properties controlling the conformational states of their constituents. The dynamic behavior in these materials could be a decisive factor, since fast molecular motions may interfere with their optical properties. For this reason, it is envisioned that exerting control over the intramolecular motion by using an appropriate external stimulus can allow tuning of properties such as fluorescence, phosphorescence, birefringence, and nonlinear optical phenomena. Although this field is still under development, several relevant examples have been reported in recent years.

20.2.1 Fluorescence, Phosphorescence, and Birefringence in Crystals with Moving Elements

A type of molecule that can show several properties are crystalline molecular rotors. They are advanced functional materials that contain large groups (stator) linked to smaller reorienting parts (rotators), which overcome an activation barrier to rotation (E_a). If the two components are highly conjugated, in addition to the envisioned internal dynamics these molecules may exhibit interesting optical properties in the solid state.

In 2016, our group reported a linearly conjugated molecular rotor with carbazole as the stator (**1**) (Figure 20.1a). This compound was obtained in two crystalline phases (termed I and II), where the stable solvent-free crystal (form II) showed fast motion of the central aromatic rotator.[6] The dynamics of this rotor was investigated by quadrupolar echo ^{2}H NMR in the solid state. These experiments demonstrated that the central phenylene undergoes 180° rotations in the MHz frequency at room temperature, with an activation energy to rotation of E_a = 8.5 kcal mol^{-1}.

Despite the fast rotation of the phenylene rotator in the solid state, this crystalline molecular rotor exhibits enhanced emission relative to that observed in solution, with quantum yields of Φ_F = 0.28 and Φ_F = 0.06, respectively. These interesting results suggested that this type of compound can be used in optical devices. To test this hypothesis, compound **1** was later used as the emissive layer in an organic light-emitting diode (OLED) with good performance.[7]

More recently, the coexistence of molecular motion and emission in the solid state in other compounds with heterocyclic stators was reported (Figure 20.1b).[8] Two tetrahydrocarbazole-based molecular rotors with minor structural differences (**2** and **3**) were crystallized with the same crystal array. Solid state NMR experiments and density functional theory (DFT) computations indicated that their central phenylenes can show fast angular oscillations

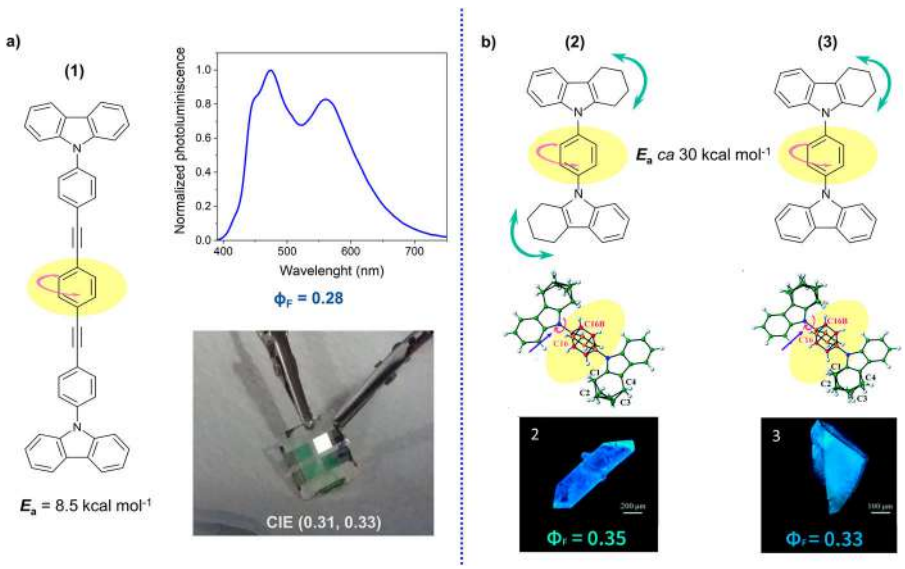

Figure 20.1 (a) Molecular structure and photoluminescence of carbazole based molecular rotor **1** used as an emissive layer in an OLED. (b) Molecular structures of molecular rotors **2** and **3** and photographs of single crystals under UV-light irradiation. Adapted from ref. 8 with permission from the Royal Society of Chemistry.

but with high barriers of rotation, E_a = *ca.* 30 kcal mol^{-1}. It is interesting to note that the exchange of the rigid carbazole moiety found in **1** by tetrahydrocarbazole (TCz) introduced additional conformational mobility of the framework that influenced the motion of the aromatic rotators. Despite this motion, both crystalline compounds showed emission with quantum yields of Φ_F = 0.35 and 0.33, respectively.

The coexistence of rotation and emission can also be observed in organometallic compounds. In 2017 Jin *et al.* reported a molecular rotor with a 1,4-phenylene rotator linked to two gold(I) triphenylphosphane complexes.[9] The resulting coordination complexes were responsive to changes in temperature, with important variations in their emission properties, *i.e.* green-emitting crystals showed reversible luminescent changes between 298 and 193 K. The authors correlated these optical fluctuations with changes in the rotational motion of the central phenylene by using variable temperature solid state NMR experiments. The aromatic ring experienced fast 180° rotations at room temperature with an E_a = 5.21 kcal mol^{-1} and becomes static below 193 K. In this case the temperature dependant phosphorescence was attributed to changes in the electronic communication that occurs when the central phenylene vibrates and rotates within the crystal.

Similarly, Thompson *et al.* reported a series of (diamidocarbene)Au(aryl) and (monoamido-aminocarbene)Au(aryl) complexes without the typical molecular rotor design with changes in the emission associated with the molecular motion.[10] The authors postulated that rotation around the coordinating Au–C_{aryl} and C–N single bonds of the arylamine moiety could be an effective non-radiative decay route in this luminescent material. To corroborate their hypothesis, complexes with different aryl donor ligands were prepared to reduce the aryl dynamics. The inclusion of the substituents prevented the rotation around the Au–C_{aryl} bond, increasing the quantum yield from Φ_F = 0.28 to Φ_F = 0.77. Although the motion was not explicitly addressed, the authors demonstrated that the modulation of the molecular rotation could improve the emission.

A strong correlation between emission and motion can also be found in compounds showing the Aggregation-Induced Emission (AIE) phenomenon,[11] where the restriction of the reorientation of the molecular components produces emissive aggregates. In 2020, Tang *et al.* reported the design of two chiral AIE-active isomers with a flexible diphenyl-ethane moiety selected to achieve AIE and a pentafluorophenyl (C_6F_5)–Au end to form strong aurophilic interactions.[12] A mechanical stimulus changed the initially randomly oriented powder into well-defined microcrystals with a turned-on photoluminescence. This off/on switching was attributed to the motion of molecules that might occur due to the mechanical process.

In this topic, Tian *et al.* recently reported the fine-tuning of the phosphorescence in three luminescent and crystalline stimuli-responsive phenothiazine derivatives: CzS-o-py (**4**), CzS-m-py, and CzS-p-py.[13] In these compounds, the phenothiazine was used as a room temperature phosphorescent portion and the pyridine as an acid-responsive rotary group. Although no rotational

frequencies were reported, computational studies showed that the intermolecular charge transfer deriving from orderly molecular motion in the crystals is mainly responsible for the room temperature phosphorescence behavior (Figure 20.2)

Birefringence is another optical property of crystals that can be modulated by the internal molecular dynamics. In 2012 Setaka and co-workers reported the thermal modulation of the birefringence in a phenylene based molecular gyroscope (**5**) as the first application of dynamical states in a crystal causing this change.[14] The temperature dependant rate of rotation of the phenylene ring was demonstrated using solid state NMR and spin-lattice relaxation experiments. At 230 K, the phenylene rotator experiences slow 180° flips, but above 270 K there is a continuous rotation of the ring, with an estimated activation energy of E_a = 10.3 kcal mol^{-1}. The observed changes in the birefringence of the crystals upon heating above 260 K were attributed to the fast dynamics and disorder of the phenylene moiety (Figure 20.3b)

This group has also prepared various molecular rotors using thiophene,[15] furan, selenophene,[16] and biphenylene[17] as rotators (**6-9**) (Figure 20.3a). In these cases, the birefringence of the crystals was unambiguously proven

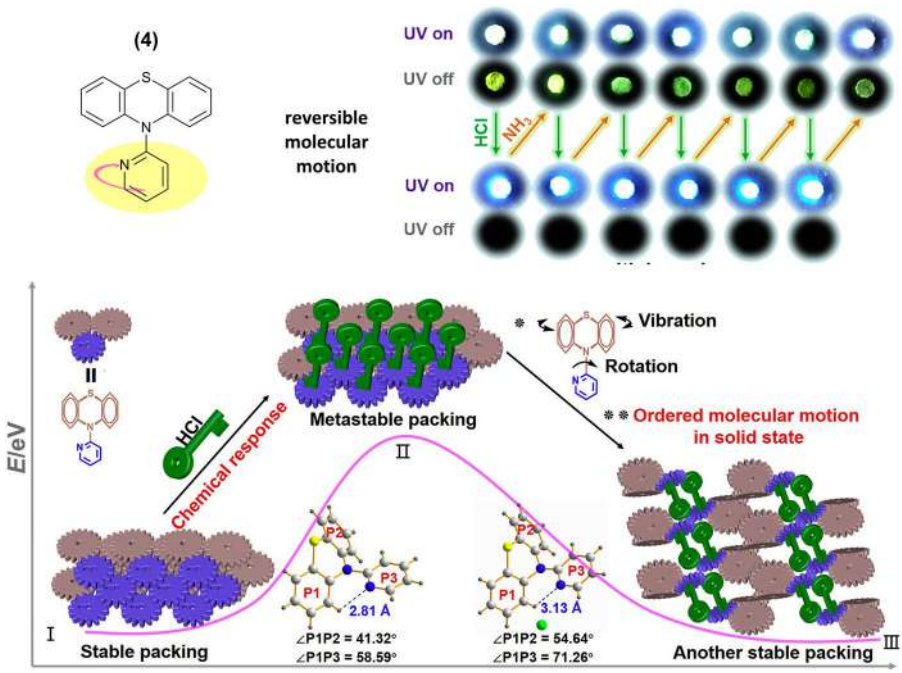

Figure 20.2 Molecular structure of CzS-o-py (**4**). Proposed diagram of the molecular motion mechanism in the solid state for **4** and reversible cycle diagram for the stimulus-responsive behavior. Adapted from ref. 13 with permission from Elsevier, Copyright 2020.

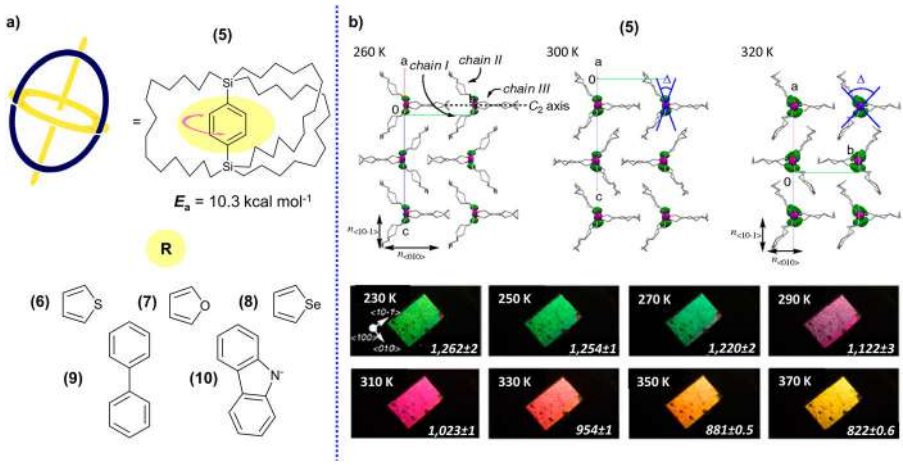

Figure 20.3 (a) Molecular structures of molecular gyroscopes reported by Setaka *et al.* (**5–10**) and (b) Changes in the crystal packing along with photographs of the single crystals of **5** under polarized white light. Adapted from ref. 14 with permission from National Academy of Sciences.

to depend on the reorientation of the dipolar rotators. Analogously, the recent use of a carbazole derivative (**10**)[18] as a rotating unit allowed them to show polarized fluorescence due to the unidirectional orientation of such heterocycle inside the gyroscope.

Other crystalline materials with molecular motion and interesting properties are plastic crystals. These unique materials simultaneously show short-range orientational disorder and long-range crystalline order. The plastic state can be reversibly converted to the ordered crystalline phase under an external electric field, which is closely associated with the rotational and orientational motions discussed above.

In 2015 Sun *et al.* reported the switch of nonlinear optical (NLO) behavior of the plastic crystal 2-(hydroxymethyl)-2-nitro-1,3-propanediol exhibiting a high contrast response ratio of ~150.[19] This record-high value exceeded all the known NLO switches and was attributed to the slowing down of highly isotropic molecular motions during a transition from plastic to rigid phase. Even though no activation energies were reported, solid state NMR analyses and theoretical computations were used to describe the switchable NLO behavior. Below the Curie temperature T_c (295–340 K), the molecular motions were highly restricted in an orientationally ordered state (SHG-on state), with large NLO effects. Above the T_c, significant molecular reorientations and a translational motion were allowed within the flexible architecture of the plastic state. The latter mode corresponds to an optic SHG-off state, in which NLO effects are suppressed.

20.3 Molecular Motion in Polarizable Crystals

20.3.1 Ferroelectricity and Molecular Motion

Ferroelectric crystals are another class of materials where molecular motion could have a strong influence. These crystalline materials present a spontaneous electrical polarization (P_s) caused by the imbalance of their positive and negative charges. This polarization can be regulated by an appropriate electric field (E) which leads to the observation of a typical hysteresis loop in the *P-E* plot. Ferroelectrics have been classified into two main types, displacive and order-disorder, and representative examples are discussed below.

20.3.1.1 Molecular Motion in Perovskite-type Ferroelectrics

In 2015, Zhang *et al.*[20] reported a double perovskite structure (**11**) with organic imidazolium $(HIm)^+$ and cobalt(III) cations. Thermal and structural characterization indicated that this material undergoes two phase transitions (*ca.* 112 K and 198 K) that gave rise to three crystalline phases at low, intermediate, and high temperatures, labeled LTP, ITP and HTP, respectively. In these three phases, the organic cation was perpendicularly oriented to the diagonal of the inorganic cubic frame and when the transition from ITP to LTP took place, the whole framework contracted causing a reduction in the organic cation mobility.

Permittivity (ε') experiments of this compound showed two significant anomalies in the dielectric constant value in the crystallographic direction [101]. To explain this anisotropic behavior, the motion of HIm^+ was studied by variable temperature solid state ^{2}H-NMR spectroscopy, indicating that the mobility of cations caused the large jump in the ε' *vs.* T plot. It was determined that the internal dynamics of the imidazolium ion required an activation energy of E_a = 2.63 kcal mol^{-1}, which is surpassed when the crystalline structure changes from the LTP to the ITP (first transition). Subsequently, the exchange frequency (k_{rot}) of Him+ increased as a function of temperature up to 198 K and higher. Above this temperature, the rotation coexists with *out-of-plane* oscillations which disturbs the balance of the centers of charge in the structure, causing the second anomaly in the dielectric constant (Figure 20.4a).

The fundamental role of the molecular dynamics of other heterocyclic cations such as pyrazolium[21] and pyrrolidinium[22] in order-disorder transitions of ferroelectrics has also been explored. Interestingly, in most studied perovskite-type solids, the second transition (typically at high temperature) has been attributed to polarization caused by *out-of plane* oscillatory motions experienced by organic cations.[23]

20.3.1.2 Molecular Motion in Ionic Ferroelectrics

Molecular cationic-anionic solids with ferroelectric properties have been developed pursuing the modulation of the switching temperature (T_s) between high and low dielectric states and the control over the direction of

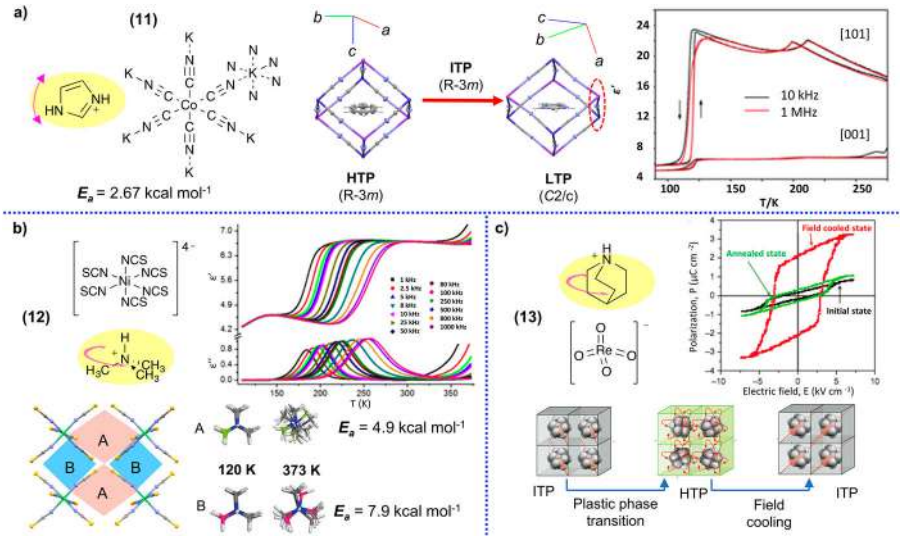

Figure 20.4 (a) Dielectric response **11** with the imidazolium ion as the mobile fragment. Reproduced from ref. 20 with permission from the Royal Society of Chemistry. (b) Cavities in the crystal structure of **12** allowing different mobility of the guest molecules. Adapted from ref. 25 with permission from John Wiley & Sons, Copyright © 2018 WILEY-VCH Verlag GmbH & Co. KGaA, Weinheim. (c) Controlled polarization in **13** using a plastic phase transition and a field cooling process. Adapted from ref. 26 with permission from Springer Nature, Copyright 2016.

polarization. These two characteristics can trigger the application of these crystalline materials in data storage, signal processing, sensors, and others.[24]

As an example of the regulation of the switching temperature, Liu *et al.*[25] prepared an ionic solid (**12**) with the general formula $(Me_3NH)_4[Ni(NCS)]_6$ in which two different cavities (A and B) were occupied by the trimethylammonium ions. The different crystallographic environments around the organic cations resulted in different molecular motions, with an activation energy to rotation of E_a = 4.9 kcal mol^{-1} for cations located in the cavity A, and an E_a = 7.9 kcal mol^{-1} for those in B, according to computational studies. This difference led to a strong dependence of temperature for the dielectric constant (ε'), producing a material with tunable T_s, as shown in Figure 20.4b.

The reorientation of dipoles can also be influenced during the crystallization process, so that control over the direction of polarization could be strongly correlated to the nucleation and growth mechanism of these materials. In 2016 Inabe and co-workers[26] reported the polarizable ionic crystal quinuclidinium perrhenate (**13**). The investigation showed that below 367 K, the solid displayed a ferroelectric behavior that was quenched above that temperature due to the formation of a paraelectric phase. The cooling process in the presence of an electric field (*field cooling*) gave rise to a ferroelectric material with a controlled polarization direction, indicating that globular molecules can be used in the construction of ferroelectric crystals with directional polarization (Figure 20.4c).

20.3.1.3 Molecular Motion in Hydrogen-bonded Ferroelectrics

Besides quinuclidine, other globular molecules that form plastic crystals as tetramethylammonium or 1,4-diazabicyclo[2.2.2]octane (DABCO) have been used.[27,28] The latter is frequently used to develop hydrogen-bond ferroelectrics (HBF). An interesting example of HBF was reported in 2009 by Akutagawa and Nakamura,[29] as a novel strategy to modify the dielectric response through the assembly of supramolecules with polar ammonium ions ($R–NH_3^+$) and crown ethers, in which the molecular rotations were facilitated to allow changes in the polarization of the material.

The crystal structure of (mFAni)(DB[18]crown-6)[Ni(dmit)$_2$] (**14**) showed alternating cation–anion layers where the proximity between ionic molecules creates steric hindrance restricting the reorientation of the organic cations. After the phase transition around 346 K, the cation experienced rotation around its C–N bond (k_{rot} < 100 kHz). The application of an electric field during the paraelectric–ferroelectric transition (field cooling), resulted in the creation of ferroelectric domains with a controlled orientation of the fluorine atoms in the organic cation (Figure 20.5a).

Recent works have demonstrated the key role of the counterion mobility and polarity on hydrogen-bonded ferroelectrics. For example, Zhang *et al.*[30] reported the synthesis and characterization of the solid [(CyNH$_3$)

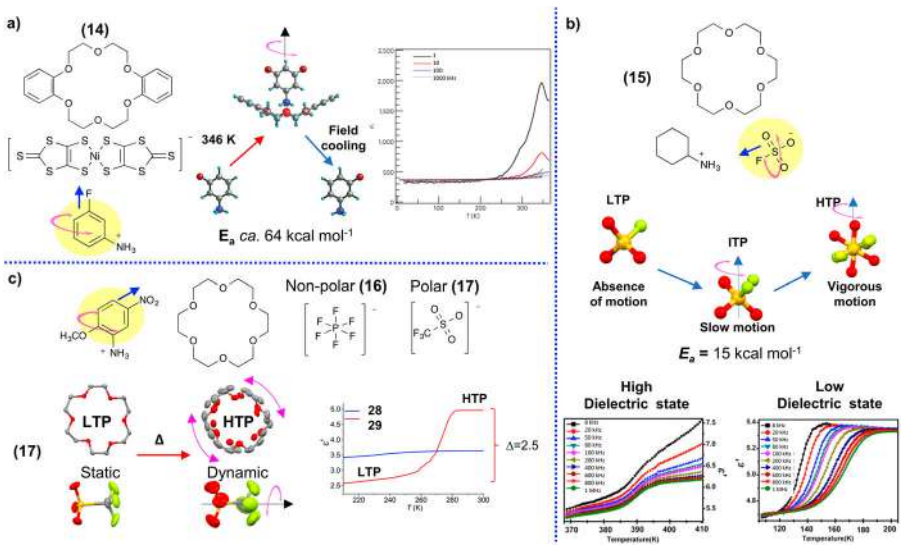

Figure 20.5 (a) Switchable direction of polarization from a field cooling process in **14**. Adapted from ref. 29 with permission from Springer Nature, Copyright 2009. (b) Effect of anion motion over dielectric response in **15**. Adapted from ref. 30 with permission from American Chemical Society, Copyright 2019. (c) Enhancing of dielectric gap between low and high dielectric states for introduction of polar counterions in **17**. Reproduced from ref. 31 with permission from the Royal Society of Chemistry.

(18-crown-6)]FSO_3 (**15**) where the cation is a non-polar molecule and the anion has a permanent dipole in the S–F bond direction. In this example, a severe crystallographic disorder was noticed in the crown ethers and sulfonate anions at room temperature. Despite the spherical shape of anions, the atomic positions of the fluorine atom strongly suggested that anions have a dynamic behavior in the intermediate phase (ITP), with a unique rotational axis. DFT computations allowed to determine a rotational potential with three global minima (3-fold motion) and activation energy *ca.* E_a = 15 kcal mol^{-1}, indicating a slow motion in the ITP. The corresponding permittivity experiments indicated that the thermal-induced variations due to the rotation allowed the three dielectric states, with ε' showing a direct dependence with temperature (Figure 20.5b).

Subsequently, Zhang and co-workers[31] demonstrated that increasing the polarity of the counterion could improve the dielectric response. To this end, they prepared two supramolecular rotors formed with the cation [(HMNA)(18-crown-6)]$^+$ and either the non-polar PF_6^- (**16**) or the polar $SO_3CF_3^-$ (**17**) counterions. When the solid **16** was analyzed by single crystal X-ray diffraction, it was found that the low temperature conditions only reduced the motion of the crown ether. Conversely, crystals of **17** showed a reduction in the dynamics of both the cyclic ether and the counterion, due to the strengthening of the intermolecular interactions. The change in the dynamics of the two components in **17** was reflected in a significant gap between high and low dielectric states, indicating that the dielectric switching can be enhanced by changing their molecular motion (Figure 20.5c).

20.3.1.4 Molecular Motion in Charge-transfer Ferroelectrics

Other systems that have received attention for the development of ferroelectrics are the charge-transfer (CT) complexes. In 2015, Inabe and co-workers[32] reported a family of cocrystals with a donor–acceptor architecture using the polar molecule tetrabromonaphtalic anhydride (TBPA) with a dipole moment of μ = 2.5 *D* as the acceptor and different disk-shape donor molecules: hexamethylbenzene (**18**), perylene (**19**) and coronene (**20**). Single crystal X-ray diffraction corroborated their sandwich structures with a disordered phase at *ca.* 300 K in cocrystals **19** and **20** indicating an *in-plane* rotation of TBPA above that temperature. The motions in these compounds have calculated activation energies to rotation of E_a = 13.3 kcal mol^{-1} and E_a = 11.4 kcal mol^{-1}, respectively (Figure 20.6a).

In 2018, a complementary work using tetrachlorophtalonitrile (TCPN) as acceptor was reported.[33] Similar to the previous complexes, a disordered phase at high temperature suggested the rapid in-plane reorientation of TCPN molecules. In these examples, it was possible to estimate the activation energies to rotation of E_a = 10.2 kcal mol^{-1}, 11.2 kcal mol^{-1}, 13.3 kcal mol^{-1} for coronene, pyrene and perylene complexes (**21–23**), respectively, which correlates well with a reduction of the energy barrier with larger donors (Figure 20.6b).

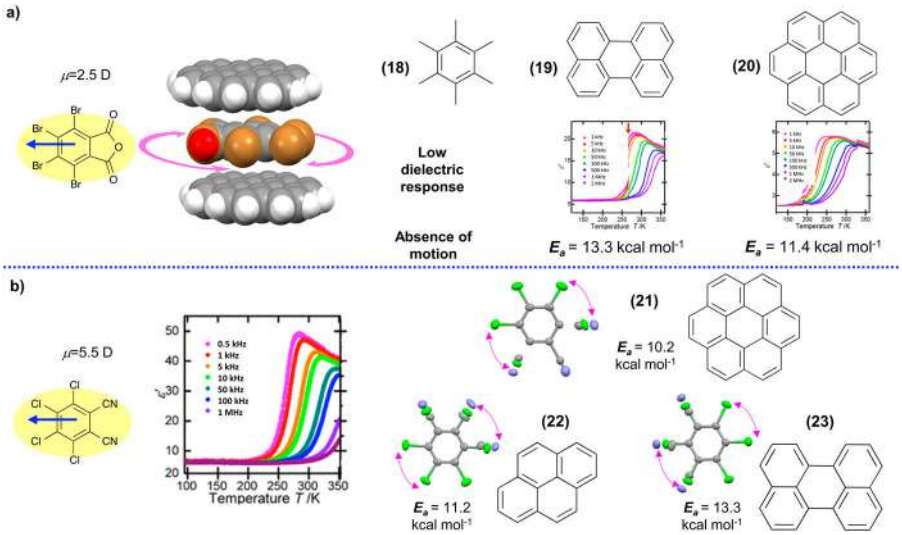

Figure 20.6 (a) Dielectric response as a function of the in-plane rotation of TBPA and (b) TCPN in charge-transfer complexes (**18–23**). The dielectric curves were adapted from ref. 32 with permission from American Chemical Society, Copyright 2015, and from ref. 33 with permission from American Chemical Society, Copyright 2019.

20.4 Salient Crystals with Molecular Motion

Dynamic crystals are another type of material that experience drastic structural changes with significant macroscopic motion: jumping, swirling, curling, *etc.*, where molecular motion plays an important role. These crystals can respond to an external stimulus with macro-, nano-, and microscopic mechanical motion. In the case of salient crystals, they can propel themselves over distances hundreds of times larger than their own size.[34] One classification of these materials is based on the stimulus that triggers the transition, and they can be thermosalient (responsive to temperature) or photosalient (responsive to the irradiated light).[35] In this section, only representative examples of compounds that experience thermal response and molecular motion are included.

20.4.1 Salient Crystals Involving Rotational Components

An early example where the rotation was determined to play a relevant role in macroscopic crystal changes was reported in 2014 by Sato and co-workers.[36] The thermosalient coordination compound $[Ni^{II}(en)_3](ox)$ (**24**) crystallized as bar-shaped prisms exhibiting a macroscopic and anisotropic contraction of the unit cell of *ca.* 5% when cooling below 253 K, giving rise to a low temperature phase (LTP) and high temperature phase (HTP). Thermal analyses

and variable temperature single crystal X-ray diffraction indicated that the oxalate ion experienced two types of rotation. In the HTP, the oxalate rotates vertically oriented over the nitrogen atoms of the coordinating ethylendiamine. Conversely, in the LTP the oxalate adopts a new orientation, with the anion experiencing a reorientation of 90° from the original position, creating new hydrogen bonds that restrict the previous rotation. DFT computations indicated that the reorientation of oxalate occurs in a two-step process, with corresponding barriers of 7.6 kcal mol^{-1} and 8.6 kcal mol^{-1}. This collective motion is aligned uniaxially through the crystal, inducing the macroscopic change (Figure 20.7a).

In 2019, work from the Naumov, Garcia-Garibay and Rodríguez-Molina groups described a supramolecular rotor with thermosalient effect (**25**).[37] This is a bicomponent crystal (cocrystal) that is held together through hydrogen bonds between carbazole and DABCO in a 2 : 1 ratio. Single crystal X-ray diffraction was used to determine that four carbazole molecules surrounded the rotator, creating a rhombohedral cavity where the rotation of DABCO occurs. When this cocrystal was placed on a heating plate and the temperature reached 316 K, a significant macroscopic displacement (jumping) was observed. This cocrystal reversibly interconverted between a low temperature phase (LTP) and a high temperature phase (HTP) between

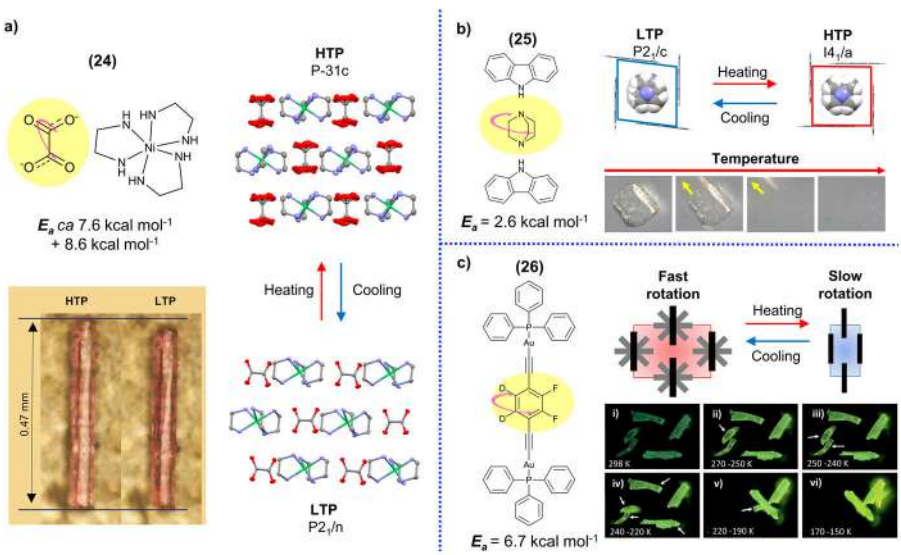

Figure 20.7 (a) Effect of the temperature on the crystal structure of **24** and dynamics of the oxalate ion. Adapted from ref. 36 with permission from Springer Nature, Copyright 2014 (b) Molecular structure of **25**, change in the symmetry and thermosalient effect. (c) Schematic representation of rotor **26** and proposed mechanism for the thermosalient effect. Adapted from ref. 40 with permission from John Wiley & Sons, Copyright © 2019 WILEY-VCH Verlag GmbH & Co. KGaA, Weinheim.

316 K and 322 K. NMR studies found that DABCO shows rapid motion in the LTP, with an activation energy to rotation of E_a = 2.6 kcal mol^{-1}.

Interestingly, after the phase transition, the rotational frequency was significantly reduced, due to changes in shape of the inner cavity and the length of hydrogen bonds that form the cocrystal. These changes occurred concomitantly with the thermosalient effect, giving rise to the first crystal where the dynamics at molecular and macroscopic scale was rigorously studied (Figure 20.7b). Recent studies indicate that this compound may be used as actuators for future technological applications.[38] It is important to note that rotors with similar architecture have shown that the salient effect cannot be directly extrapolated, although other uncommon displacive phase transitions have been found.[39]

Similarly, in 2019 the groups of Ito and Garcia-Garibay reported an organometallic gold-based molecular rotor (**26**) in which the rotation of a phenylene group was associated with the observed thermosalient effect of the crystal.[40] In this compound, a significant anisotropic expansion and compression of the lattice as a function of temperature was identified (Figure 20.7c). Solid state NMR experiments revealed that the rotational dynamics is a thermally activated process, with an activation barrier to rotation of E_a = 6.7 kcal mol^{-1}.

In addition to the previous dumbbell-like structures, there are interesting examples of crystals where the motion of the aliphatic groups is connected to their macroscopic motion. For example, in 2018, Diao *et al.* reported a crystalline semiconductor 6-13-bis(triisopropylsilylethynyl)pentacene (TIPS-pentacene) (**27**). When the crystal was heated to 400 K, it underwent a reversible structural deformation with changes in the dimensions of the axis of a single crystal as large as 10–12%.[41] These significant changes in the size of the crystal were accompanied by a change of color, and important variations in the charge carrier mobility. A close analysis of the crystallographic forms revealed a reversible order-disorder transition of the crystal, with changes in the bulky triisopropyl chains suggesting that the repulsions between these rotating chains could be the main driving force inducing the macroscopic motion (Figure 20.8a).

Similarly, the motion in aliphatic groups has been reported in the compound *N*,*N*-Bis [4-(*N*,*N*-diethylamino)benzylidene]-diaminomalononitrile (**28**),[42] which experiences a reversible phase transition at 443 K, creating two solid forms with different distances in the stacking of the molecules. In the high temperature form (HTP), there is an important contraction of the lattice along the stacking axis. The centroid–centroid distance in these molecules in the crystal phase at room temperature is up to 6% larger than the corresponding distance at high temperature. Single crystal X-ray analyses revealed that the centroid–centroid distances were anisotropically modified during phase change. This macroscopic crystalline deformation occurred due to the slight rearrangement of the molecules. The authors conclude that the thermal motion of the alkyl substituents at high temperature is correlated with the observed macroscopic deformation of the crystal (Figure 20.8b).

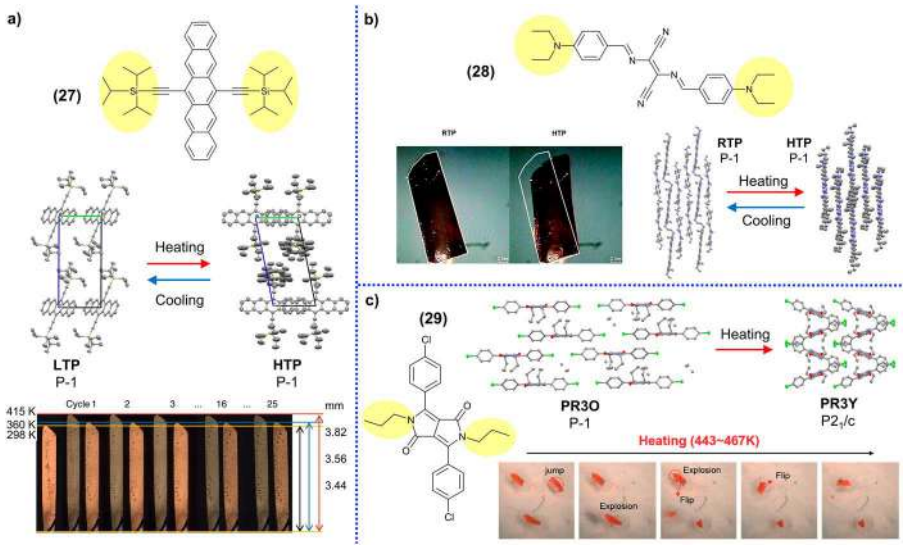

Figure 20.8 (a) Rotational disorder of triisopropyl side chains in **27** and accompanying changes in the dimensions of the crystal. Adapted from ref. 41 with permission from Springer Nature, Copyright 2018. (b) Structural deformation of **28** and dynamic effect of crystal. Adapted from ref. 42 with permission from the Royal Society of Chemistry. (c) Both PR3Y and PR3O polymorphs of **29** and salient effect. Adapted from ref. 43 with permission from the Royal Society of Chemistry.

Another related example is the propylated diketopyrrolopyrrole compound (**29**).[43] This compound crystallizes in two colored polymorphs (PR3Y and PR3O), yellow and orange, respectively. In the PR3Y polymorph, the propyl group have a significant crystallographic disorder even at low temperatures. This polymorph showed a marked thermosalient effect when heated, presenting a phase transition that occurs between 443 and 446 K, with a simultaneous transformation to the orange PR3O polymorph. The observed thermosalient effect was attributed to the stress accumulated by the aliphatic chain which was suddenly released as a macroscopic response. Unlike previously described thermosalient crystals, the irreversible transition in this crystal was attributed to greater thermal stability of the orange crystal (Figure 20.8c).

Dynamic crystals have also been obtained starting from components that are known to experience a change in their spatial disposition. For example, it is known that double bonds can show geometric isomerization under the appropriate temperature or incident light wavelength. When this functional group is incorporated within a crystal, a dynamic behavior known as pedal motion takes place.[44] In 2019, the work led by Hutchins *et al.* reported three isostructural cocrystals with halobenzenes linked to bipyridines (**30–32**).[45] Those bipyridines were distinguished from each other by the nature of the

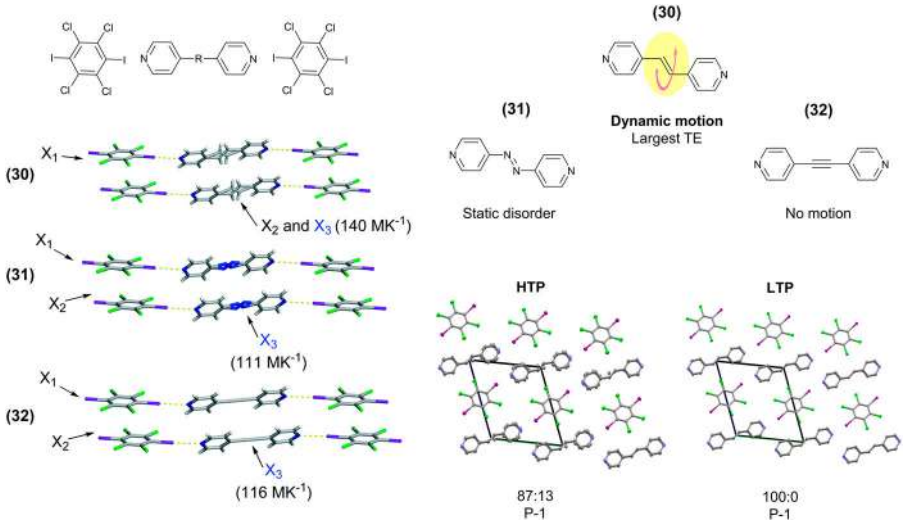

Figure 20.9 Effect of pedal motion in thermal expansion on cocrystals **30–32**. Adapted from ref. 45 with permission from the Royal Society of Chemistry.

inner bonds: C=C, N=N or ethynyl groups. The idea behind their approach was to determine the role of the pedal motion in thermal expansion by means of single crystal X-ray diffraction studies (Figure 20.9).

From these experiments, the *azo* and ethynyl derivatives **31** and **32** did not show dynamic disorder, associated with the lack of motion and minimal thermal expansion. On the other hand, the crystal with the *alkene* group **30** showed a severe crystallographic disorder that varied with the temperature, indisputable evidence of molecular motion. These findings were associated with the largest thermal expansion coefficients of this cocrystal. Recent studies from the same group have expanded this research fine-tuning the thermal expansion using a mixed cocrystal strategy, obtaining different thermal expansion coefficients in excellent agreement with the gradual inclusion of groups with pedal motion.[46]

From the examples presented here, it is possible to observe that the internal motion in dynamic crystals may involve the reorientation of molecules or some portions of them. Although at this time it seems difficult to definitively attribute any macroscopic motion in crystals to specific molecular displacements, it is possible to consider the two properties highly correlated.

20.5 The Influence of Molecular Motion on the Porosity of Crystals

One additional kind of material where molecular motion is expected to provide a vantage point is in the development of smart porous crystals. This section starts with the description of molecular crystals with adsorption

properties and then it evolves to extended porous lattices, particularly metal-organic frameworks (MOFs), resulting in a modulated porosity through changes in their inner dynamics.

In 2017, our group reported the intriguing properties of the elongated molecular rotor **1**.[47] The intramolecular rotation of this compound was previously determined using solid state ^{2}H NMR, with an activation energy of E_a = 8.5 kcal mol^{-1}.[6] Interestingly, when dry crystals of this rotor were exposed to vapors of several solvents, their appearance under the microscope changed. Further experiments showed that exposing the crystals to iodine vapors at room temperature brought about a reduction of the internal rotation from 6.0 MHz to 1.5 MHz, along with an increase of the initial activation energy E_a = 10.6 kcal mol^{-1} suggesting that the iodine molecules may diffuse within the crystal. Such a result was intriguing because no voids in the lattice were observed in the packing array. To explore this further, sorption experiments using a thermally activated sample revealed a large and selective CO_2 sorption (Figure 20.10a). It is important to note that the carbon dioxide did not diffuse within the crystal at room temperature when the rotation of the central phenylene is fast. The maximum CO_2 uptake of 201.6 cm^3 g^{-1} was achieved at low temperatures, which matched well with the temperature where the rotor becomes static (150 K). Such temporary accommodation of guest molecules within the crystal gave rise to the term of transient porosity, with the crystal lattice returning to the original parameters after the CO_2 atmosphere is removed (Figure 20.10b).

A similar correlation was reported by Bracco *et al.* also in 2017.[48] A porous molecular crystal formed by benzylamine (BA) and a strut-like molecular rotor exhibited fast rotation and selective CO_2 absorption that was later

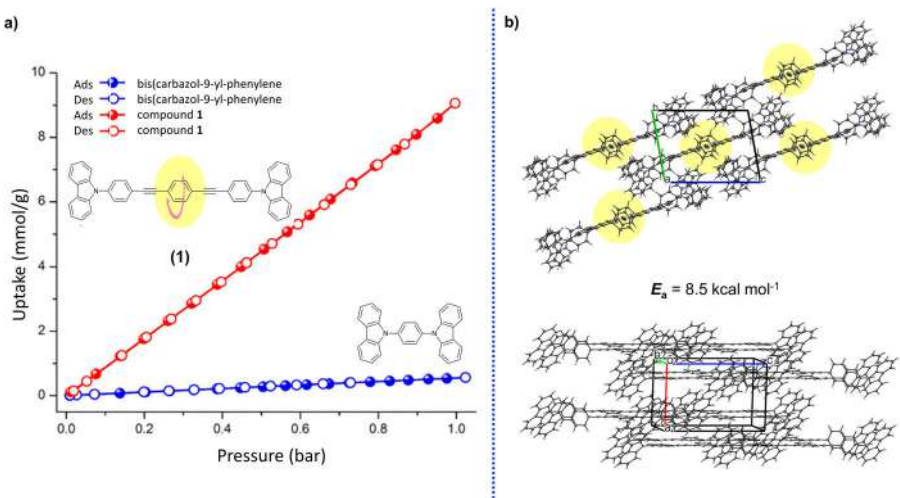

Figure 20.10 (a) CO_2 adsorption and desorption isotherms of **1** compared to those of the analog bis(carbazol-9-yl-phenylene) at 196 K. Adapted from ref. 47 with permission from American Chemical Society, Copyright 2017. (b) Molecular packing of **1**.

demonstrated to regulate the dynamics. The 4,4′-bis(sulfophenylethynyl)benzene (SPEB) molecular rotor structure consists of a phenylene rotator, linked through ethynylene groups to two *p*-phenylenesulfonate stators. Single crystal X-ray diffraction of a solvent-free crystal revealed a crystal structure where layers of molecular rotors are separated by stacks of benzylamonium ions, creating 1D channels.

Deuterium NMR experiments with solvent-free samples and deuterium labeled phenylene molecular rotor indicated that at 155 K the rotators are static and at 216 K they reach the fast exchange regime. The solid state ^{2}H NMR spectra of samples sealed under CO_2 pressure recorded at 200 K reflected a reduction in the dynamics in two orders of magnitude (k_{rot} = 6.3×10^4 Hz) compared to the empty crystals ($k_{rot} = 1.8 \times 10^6$ Hz). This clearly showed that the CO_2 molecules enter the channel of the crystal and obstruct the rotation of the central phenylene group. The barrier to rotation in crystals loaded with CO_2 is E_a = 7.0 kcal mol^{-1}, which is higher than that found in the empty crystals, with E_a = 5.7 kcal mol^{-1}.

Very recently, Mittleman *et al.* demonstrated that the gas capture process in clathrates is mediated by a single terahertz vibrational motion involving the guest molecules and that can be used to track the gas uptake.[49] In their work, they used experimental measurements and computational studies to provide a description of hydroquinone clathrate in the presence of high-pressure CO_2. The authors identified a specific vibrational mode directly linked to the gas uptake and proposed the possibility of using terahertz radiation to promote the phase change process.

The modulation of gas uptake is one of the long-standing challenges in porous materials. To this end, Feringa *et al.*[50] reported a porous covalent organic framework whose structure features a chiral overcrowded alkene (**33**) as a bistable chiroptical switch that allowed for switchable porosity (Figure 20.11a). Because of this, the material is referred to as a porous switchable framework (PSF). The photoisomerization of the double bond in the alkene inverts the helical chirality and generates a metastable isomer that can be reverted back by light irradiation (Figure 20.11a). This photoisomerization is responsible for the change in the cavity size and thus the variable gas uptake. The large porosity of the PSF material ensures the unhindered photoisomerization of the overcrowded alkene. They prepared two PSF materials denoted as **PSF-1** and **PSF-2** (**34**) with a molar content of 9.1% and 25% of **33**, respectively.

Changes in porosity through the isomerization cycle stable-metastable-stable were investigated by the N_2 absorption isotherms at 77 K. The irradiated sample at 365 nm of **PSF-2** showed a considerable reduction in the pore volume of 20% at a relative pressure (P/P_0) of 0.6 with respect to the pristine sample. When the irradiated sample was exposed to 470 nm radiation, only a partial recovery of the initial surface area is obtained (approximately 40% of the initial value); however, heating the irradiated sample allowed a complete recovery of the initial surface area. The CO_2 absorption isotherms at 195 K of irradiated samples of **PSF-2** confirmed a 20% reduction in pore volume. In line with a lower content of photoswitch **33**, the observed reduction in pore

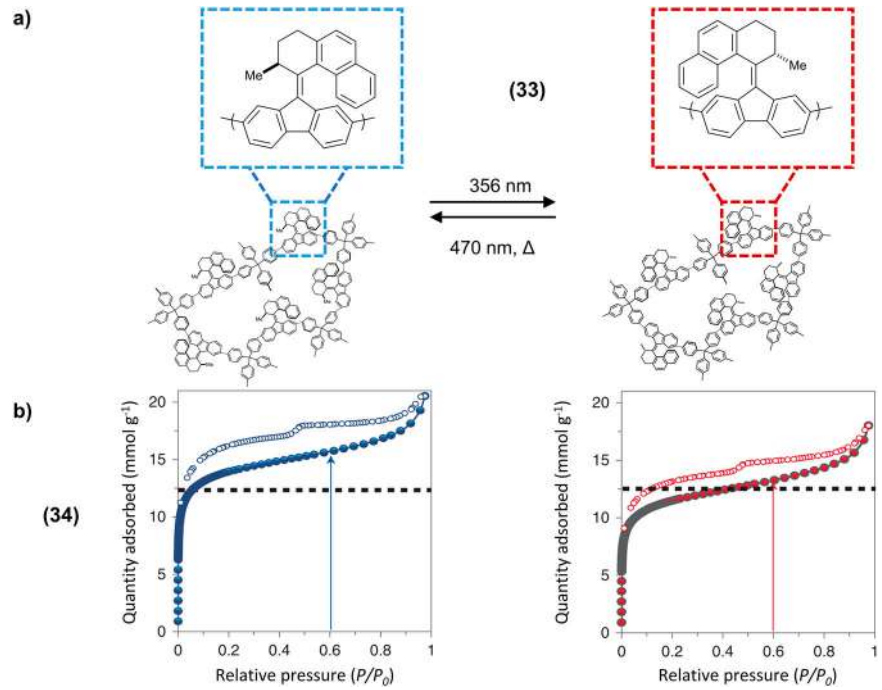

Figure 20.11 (a) Schematic representation of the photoisomerization of photoswitch (**33**) in **PSF-1** and **PSF-2** frameworks. (b) Nitrogen adsorption isotherms of **PSF-2** at 77 K for the pristine material (left) and after irradiation at 365 nm for 54 h (right). Adapted from ref. 50 with permission from Springer Nature, Copyright 2020.

size in the 365 nm irradiated sample of **PSF-1** was smaller than in **PSF-2** samples. Like this example, the *E* to *Z* photoisomerization of pending azobenzene groups in star-shaped azobenzene tetramer molecular crystal produces the modulation in the porosity.[51]

The internal dynamics could also be strongly associated to the adsorption properties of permanently porous materials such as Metal-Organic Frameworks (MOFs). It is important to note that this is a very broad subject described in recent reviews that address dynamical changes in the linkers, metallic clusters and/or the whole framework.[52] For the sake of brevity, only representative examples that involve the motion of the linkers will be described here.

In 2017, Yong Yan and co-workers[53] reported the methane adsorption properties of a family of isostructural MOFs with different linkers: MFM-112a (**35**), MFM-115a (**36**), and MFM-132a with high, moderate, and relatively low porosity, respectively. Distinctively, **36** displayed higher CH_4 storage at room temperature, outperforming **35**. Based on these results, it was hypothesized that the pore environment created by the rotating phenylene rings in the linker could affect the gas adsorption properties (Figure 20.12a).

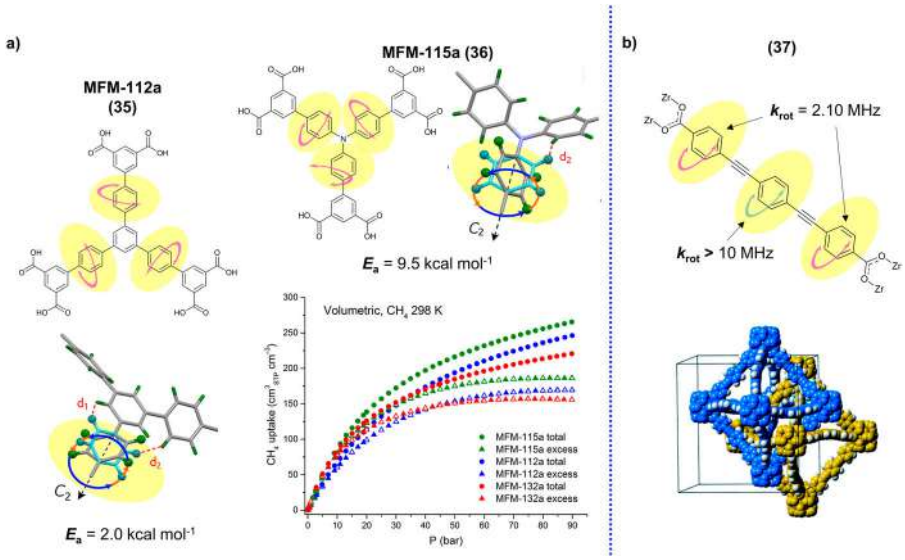

Figure 20.12 (a) Molecular structures and rotational models probed by solid state ^{2}H NMR spectroscopy of the ligands of (**35**) and (**36**), and comparison of high-pressure volumetric CH_4 adsorption isotherms for MFM-115a, MFM-112a, and MFM-132a in the pressure range 0–90 bar at 298 K. Adapted from ref. 53 with permission from American Chemical Society, Copyright 2017. (b) Molecular structure of the PEPEP linker and crystal structure of the double interweaved MOF PIZOF-2. Adapted from ref. 55 with permission from the Royal Society of Chemistry.

In situ solid state ^{2}H NMR spectroscopy using deuterium-enriched samples was used to investigate the rotational dynamics of the rotating rings in these MOFs. The results revealed that the phenylene ring rotation in **36**-d_{12} with an activation barrier to rotation of E_a = 9.5 kcal mol^{-1}, is almost five times higher than **35**-d_{12}. E_a = 2.0 kcal mol^{-1}. The authors concluded that the exceptional and different methane uptakes resulted from a combination of optimal molecular rotation, pore geometry, and favorable binding sites.

In contrast to the previous examples, the motion in the linkers of the MOFs can also be used to explore the diffusive processes within their crystals. In this field, our group has recently reported the dynamics of a highly porous material known as PIZOF-2 (**37**).[54] This MOF is made of a linear *p*-phenylene-ethynyl-phenylene dicarboxylate linker (PEPEP) coordinated to a zirconia cluster, with its gas sorption and fluorescent properties previously reported by Forgan *et al.*[55] Solid state NMR studies carried out using selectively deuterated samples demonstrated that the large pores in the lattice allow two types of motion in the aromatic rings with distinct frequencies. At room temperature, the central ring surrounded by two ethynylene groups can rotate in the megahertz regime (>12 MHz), while the peripheral ring, adjacent to the metal cluster, rotates at a much lower frequency (*ca.* 2 MHz). This difference

may arise from the electronic conjugation between the phenylene ring with the carboxylate group and/or affected by the interactions with the metal oxide clusters (Figure 20.12b).

This double dynamic behavior allowed us to gather insights about the diffusion of tetracyanoquinodimethane (TCNQ), an electron-deficient compound that 'sticks' within the pores. Interestingly, even when the initial solid state fluorescence of the MOF was quenched due to the presence of the guest, only the internal dynamics of the peripheral ring was affected. These findings indicate that the guest allocates preferentially near the metallic cluster, leaving the fast motion of the central ring intact. Although more experiments in this direction need to be performed, it seems clear that the motion in metal organic frameworks is a very useful tool to determine the adsorption mechanisms within these porous materials.

20.6 Final Remarks

From the examples contained in this chapter, the readers may identify some guidelines to obtain crystalline materials where the internal dynamics can be associated with one or more observables:

- The internal motion can modulate the optical response if the rotation is fast enough to enable non-radiative mechanisms. Otherwise, both properties can coexist in crystalline materials.
- The rapid reorientations of internal fragments within ordered lattices can be used to fine-tune the dielectric response in hybrid compounds, charge-transfer complexes, or hydrogen-bonded materials.
- The rotation of globular molecules or flexible fragments in the molecules or the isomerization of double bonds can contribute to abrupt phase transitions provoking salient effects.
- The motion of the internal components can regulate the sorption processes of crystalline materials. Furthermore, the study of the dynamics can shed light on diffusional processes of these materials.

It is considered that further developments of crystals with dynamics would be of great interest for a wide variety of applications in nanoarchitechtonics, including but not limited to sensors,[56] switches,[57] optical devices,[58] artificial muscles,[59] soft robotics,[60] among others.

Acknowledgements

Jessica I. Vasquez and Ernesto A. Hernández would like to acknowledge CONACyT for their MSc fellowships (1074502 and 1078913). Moreover, the financial support of PAPIIT (IN209119) and CONACyT Ciencia de Frontera (1715644) is acknowledged. The authors would like to thank the wonderful collaborators for the group developments included in this chapter.

References

1. K. Ariga, *Small Sci.*, 2021, **1**, 2000032.
2. (a) D. B. Amabilino, D. K. Smith and J. W. Steed, *Chem. Soc. Rev.*, 2017, **46**, 2404; (b) K. Ariga, *Mater. Chem. Front.*, 2017, **1**, 208.
3. (a) A. Colin-Molina, S. Pérez-Estrada, A. E. Roa, A. Villagrana-Garcia, S. Hernández-Ortega, M. Rodríguez, S. E. Brown and B. Rodríguez-Molina, *Chem. Commun.*, 2016, **52**, 12833; (b) M. C. Mayorquín-Torres, A. Colin-Molina, S. Pérez-Estrada, A. Galano, B. Rodríguez-Molina and M. A. Iglesias-Arteaga, *J. Org. Chem.*, 2018, **83**, 3768; (c) A. Aguilar-Granda, A. Colin-Molina, M. J. Jellen, A. Núñez-Pineda, M. E. Cifuentes-Quintal, R. A. Toscano, G. Merino and B. Rodríguez-Molina, *Chem. Commun.*, 2019, **55**, 14054; (d) K. Vargas-Romero, F. C. Martínez-Torres, A. Aguilar-Granda, S. Pérez-Estrada, M. Flores-Alamo, B. Rodríguez-Molina and M. A. Iglesias-Arteaga, *J. Org. Chem.*, 2020, **85**(13), 8501.
4. A. Comotti, S. Bracco, A. Yamamoto, M. Beretta, T. Hirukawa, N. Tohnai, M. Miyata and P. Sozzani, *J. Am. Chem. Soc.*, 2014, **136**, 618.
5. C. S. Vogelsberg and M. A. Garcia-Garibay, *Chem. Soc. Rev.*, 2012, **41**, 1892.
6. A. Aguilar-Granda, S. Pérez-Estrada, A. E. Roa, J. Rodríguez-Hernández, S. Hernández-Ortega, M. Rodriguez and B. Rodríguez-Molina, *Cryst. Growth Des.*, 2016, **16**, 3435.
7. W. Bernal, O. Barbosa-García, A. Aguilar-Granda, E. Pérez-Gutiérrez, J. L. Maldonado, M. J. Percino and B. Rodríguez-Molina, *Dyes Pigm.*, 2019, **163**, 754.
8. A. Colin-Molina, D. Velázquez-Chávez, M. J. Jellen, L. A. Rodríguez-Cortés, M. E. Cifuentes-Quintal, G. Merino and B. Rodríguez-Molina, *CrystEngComm*, 2020, **22**, 3789.
9. M. Jin, T. S. Chung, T. Seki, H. Ito and M. A. Garcia-Garibay, *J. Am. Chem. Soc.*, 2017, **139**, 18115.
10. T. Y. Li, D. S. Muthiah Ravinson, R. Haiges, P. I. Djurovich and M. E. Thompson, *J. Am. Chem. Soc.*, 2020, **142**, 6158.
11. (a) Y. Hong, J. W. Y. Lam and B. Z. Tang, *Chem. Soc. Rev.*, 2011, **40**, 5361; (b) S. Liu, Y. Li, H. Zhang, Z. Zhao, X. Lu, J. W. Y. Lam and B. Z. Tang, *ACS Mater. Lett.*, 2019, **1**, 425.
12. J. Zhang, B. He, W. Wu, P. Alam, H. Zhang, J. Gong, F. Song, Z. Wang, H. H. Y. Sung, I. D. Williams, Z. Wang, J. W. Y. Lam and B. Z. Tang, *J. Am. Chem. Soc.*, 2020, **142**, 14608.
13. Y. Tian, Y. Gong, Q. Liao, Y. Wang, J. Ren, M. Fang, J. Yang and Z. Li, *Cell Rep. Phys. Sci.*, 2020, **1**, 100052.
14. W. Setaka and K. Yamaguchi, *Proc. Natl. Acad. Sci. U. S. A.*, 2012, **109**, 9271.
15. W. Setaka and K. Yamaguchi, *J. Am. Chem. Soc.*, 2013, **135**, 14560.
16. T. Masuda, J. Arase, Y. Inagaki, M. Kawahata, K. Yamaguchi, T. Ohhara, A. Nakao, H. Momma, E. Kwon and W. Setaka, *Cryst. Growth Des.*, 2016, **16**, 4392.

17. A. Fujiwara, Y. Inagaki, H. Momma, E. Kwon, K. Yamaguchi, M. Kanno, H. Kono and W. Setaka, *CrystEngComm*, 2017, **19**, 6049.
18. H. Hashimoto, Y. Inagaki, H. Momma, E. Kwon, K. Yamaguchi and W. Setaka, *CrystEngComm*, 2019, **21**, 3910.
19. Z. Sun, T. Chen, X. Liu, M. Hong and J. Luo, *J. Am. Chem. Soc.*, 2015, **137**, 15660.
20. X. Zhang, X.-D. Shao, S.-C. Li, Y. Cai, Y.-F. Yao, R.-G. Xiong and W. Zhang, *Chem. Commun.*, 2015, **51**, 4568.
21. A. Piecha-Bisiorek, K. Mencel, V. Kinzhybalo, A. Szota, R. Jakubas, W. Medycki and W. Zawrocki, *CrystEngComm*, 2018, **20**, 2112.
22. M. Trzebiatowska, M. Maczka, A. Gagor and A. Sieradski, *Inorg. Chem.*, 2020, **59**, 8855.
23. W.-J. Xu, K. P. Xie, Z.-F. Xiao, W.-X. Zhang and X.-M. Chen, *Cryst. Growth Des.*, 2016, **16**, 7212.
24. (a) Y. Zhang, X.-J. Song, Z.-X. Zhang, D.-W. Fu and R.-G. Xiong, *Matter*, 2020, **2**, 697; (b) H.-Y. Liu, H.-Y. Zhang, X.-G. Chen and R.-G. Xiong, *J. Am. Chem. Soc.*, 2020, **142**, 15205.
25. J.-L. Liu, S.-Y. Zhang, Y. Zeng, X. Shu, Z. Y. Du, C.-T. He, W.-X. Zhang and X.-M. Chen, *Angew. Chem., Int. Ed.*, 2018, **57**, 8032.
26. J. Harada, T. Shimojo, H. Oyamaguchi, H. Hasegawa, Y. Takahashi, K. Satomi, Y. Suzuki, J. Kawamata and T. Inabe, *Nat. Chem.*, 2016, **8**, 946.
27. J. Walker, R. Miranti, S. Linn-Skjarvo, T. Rojac, T. Grande and M. Ann-Einarsrud, *J. Mater. Chem. C*, 2020, **8**, 3206.
28. Z.-S. Yao, K. Yamamoto, H. L. Cai, K. Takahashi and O. Sato, *J. Am. Chem. Soc.*, 2016, **138**, 12005.
29. T. Akutagawa, H. Koshinaka, D. Sato, S. Takeda, S.-I. Noro, H. Takahashi, R. Kumai, Y. Tokura and T. Nakamura, *Nat. Mater.*, 2009, **8**, 342.
30. Z.-X. Zhang, T. Zhang, P.-P. Shi, W.-Y. Zhang, Q. Ye and D. W. Fu, *J. Phys. Chem. Lett.*, 2019, **10**, 4237.
31. R.-K. Huang, X.-X. Chen, Z.-F. Xiao, D.-X. Liu, W.-X. Zhang and X.-M. Chen, *Chem. Commun.*, 2020, **56**, 4114.
32. J. Harada, M. Ohtani, Y. Takahashi and T. Inabe, *J. Am. Chem. Soc.*, 2015, **137**, 4477.
33. J. Harada, N. Yoneyama, S. Sato, Y. Takahashi and T. Inabe, *Cryst. Growth Des.*, 2019, **19**, 291.
34. P. Commins, I. T. Desta, D. P. Karothu, M. K. Panda and P. Naumov, *Chem. Commun.*, 2016, **52**, 13941.
35. S. H. Cheng, C. H. Wang, Y. C. Lin, Y. Tsuchido, Y. Suzaki, Y. Sei, T. S Kuo and M. Horie, *ACS Appl. Mater. Interfaces*, 2020, **12**, 50002.
36. Z. S. Yao, M. Mito, T. Kamachi, Y. Shiota, K. Yoshizawa, N. Azuma, Y. Miyazaki, K. Takahashi, K. Zhang, T. Nakanishi, S. Kang, S. Kanegawa and O. Sato, *Nat. Chem.*, 2014, **6**, 1079.
37. A. Colin-Molina, D. P. Karothu, M. J. Jellen, R. A. Toscano, M. A. Garcia-Garibay, P. Naumov and B. Rodrıguez-Molina, *Matter*, 2019, **1**, 1033.
38. D. P. Karothu, J. M. Halabi, L. Li, A. Colin-Molina, B. Rodríguez-Molina and P. Naumov, *Adv. Mater.*, 2020, **32**, 1906216.

39. A. Colin-Molina, M. J. Jellen, J. Rodríguez-Hernández, M. E. Cifuentes-Quintal, J. Barroso, R. A. Toscano, G. Merino and B. Rodríguez-Molina, *Chem. - Eur. J.*, 2020, **26**, 11727.
40. M. Jin, S. Yamamoto, T. Seki, H. Ito and M. A. Garcia-Garibay, *Angew. Chem.*, 2019, **131**, 18171.
41. H. Chung, D. Dudenko, F. Zhang, G. D. Avino, C. Ruzié, A. Richard, G. Schweicher, J. Cornil, D. Beljonne, Y. Geerts and Y. Diao, *Nat. Commun.*, 2018, **9**, 278.
42. T. Minami, H. Sato and S. Matsumoto, *CrystEngComm*, 2018, **20**, 2644.
43. H. S. So, T. Minami, T. Jindo and S. Matsumoto, *CrystEngComm*, 2018, **20**, 5317.
44. J. Harada and K. Ogawa, *Chem. Soc. Rev.*, 2009, **38**, 2244.
45. N. Juneja, D. K. Unruh, E. Bosch, R. H. Groeneman and K. M. Hutchins, *New J. Chem.*, 2019, **43**, 18433.
46. X. Ding, D. K. Unruh, R. H. Groeneman and K. M. Hutchins, *Chem. Sci.*, 2020, **11**, 7701.
47. A. Aguilar-Granda, S. Pérez-Estrada, E. Sánchez-González, J. R. Álvarez, J. Rodríguez-Hernández, M. Rodríguez, A. E. Roa, S. Hernández-Ortega, I. A. Ibarra and B. Rodríguez-Molina, *J. Am. Chem. Soc.*, 2017, **139**, 7549.
48. S. Bracco, T. Miyano, M. Negroni, I. Bassanetti, L. Marchiò, P. Sozzani, N. Tohnai and A. Comotti, *Chem. Commun.*, 2017, **53**, 7776.
49. W. Zhang, Z. Song, M. T. Ruggiero and D. M. Mittleman, *Cryst. Growth Des.*, 2020, **20**, 5638.
50. F. Castiglioni, W. Danowski, J. Perego, F. K.-C. Leung, P. Sozzani, S. Bracco, S. J. Wezernberg, A. Comotti and B. L. Feringa, *Nat. Chem.*, 2020, **12**, 595.
51. M. Baranconi, S. d'Agostino, G. Bergamini, P. Ceroni, A. Comotti, P. Sozzani, I. Bassanetti, F. Grepioni, T. M. Hernandez, S. Silvi, M. Venturi and A. Credi, *Nat. Chem.*, 2015, **7**, 634.
52. R. J. Marshall, Y. Kalinovskyy, S. L. Griffin, C. Wilson, B. A. Blight and R. S. Forgan, *J. Am. Chem. Soc.*, 2017, **139**, 6253.
53. Y. Yan, D. I. Kolokolov, I. Da Silva, A. G. Stepanov, A. J. Blake, A. Dailly, P. Manuel, C. C. Tang, S. Yang and M. Schröder, *J. Am. Chem. Soc.*, 2017, **139**, 13349.
54. A. Torres-Huerta, D. Galicia-Badillo, A. Aguilar-Granda, J. T. Bryant, F. J. Uribe-Romo and B. Rodríguez-Molina, *Chem. Sci.*, 2020, **11**, 11579.
55. R. J. Marshall, Y. Kalinovskyy, S. L. Griffin, C. Wilson, B. A. Blight and R. S. Forgan, *J. Am. Chem. Soc.*, 2017, **139**, 6253.
56. A. Comotti, S. Bracco, P. Valsesia, M. Beretta and P. Sozzani, *Angew. Chem., Int. Ed.*, 2010, **49**, 1760.
57. (a) C. Lemouchi, C. Mézière, L. Zorina, S. Simonov, A. Rodríguez-Fortea, E. Canadell, P. Wzietek, P. Auban-Senzier, C. Pasquier, T. Giamarchi, M. A. Garcia-Garibay and P. Batail, *J. Am. Chem. Soc.*, 2012, **134**, 7880; (b) W. Zhang, H. Y. Ye, R. Graf, H. W. Spiess, Y. F. Yao, R. Q. Zhu and R. G. Xiong, *J. Am. Chem. Soc.*, 2013, **135**, 5230.

58. (a) S. Liu, Y. Li, H. Zhang, Z. Zhao, X. Lu, J. W. Y. Lam and B. Z. Tang, *ACS Mater. Lett.*, 2019, **1**, 425; (b) R. Liao, S. Gu, X. Wang, X. Zhang, X. Xie, H. Sun and W. Huang, *J. Mater. Chem. C*, 2020, **8**, 8430.
59. (a) L. Fang, M. Hmadeh, J. Wu, M. A. Olson, J. M. Spruell, A. Trabolsl, Y. W. Yang, M. Elhablrl, A. M. Albrecht-Gary and J. F. Stoddart, *J. Am. Chem. Soc.*, 2009, **131**, 7126; (b) S. Ikejiri, Y. Takashima, M. Osaki, H. Yamaguchi and A. Harada, *J. Am. Chem. Soc.*, 2018, **140**, 17308.
60. (a) J. Berná, D. A. Leigh, M. Lubomska, S. M. Mendoza, E. M. Pérez, P. Rudolf, G. Teobaldi and F. Zerbetto, *Nat. Mater.*, 2005, **4**, 704; (b) J. Chen, S. J. Wezenberg and B. L. Feringa, *Chem. Commun.*, 2016, **52**, 6765; (c) S. Kassem, A. T. L. Lee, D. A. Leigh, A. Markevicius, D. J. Tetlow and N. Toriumi, *Chem. Sci.*, 2021, **12**, 2065.

CHAPTER 21

Tailoring Colloidal Core–Shell Quantum Dots for Optoelectronics

ALI IMRAN CHANNA[a], YIMIN YOU[a], XIN TONG*[a,b] AND ZHIMING M. WANG*[a]

[a]Institute of Fundamental and Frontier Sciences, University of Electronic Science and Technology of China, Chengdu 610054, PR China; [b]Yangtze Delta Region Institute (Huzhou), University of Electronic Science and Technology of China, Huzhou 313001, PR China
*E-mail: xin.tong@uestc.edu.cn, zhmwang@uestc.edu.cn

21.1 Introduction

Colloidal quantum dots (QDs) are tiny crystals of semiconductor materials with dimensions in the nano-meter scale.[1] Owing to their small size, comparable to the exciton Bohr radius, QDs exhibit novel properties such as size-dependent optical band gaps for tunable absorption and emission spectra, which are very promising for various optoelectronic applications.[2,3] The small size also results in high surface-to-volume ratio of QDs,[4] and changes in surface conditions of QDs (such as oxygen, light, temperature *etc.*) may deteriorate their optical properties,[5] which is unfavorable for QDs-based optoelectronics.[6] Generally, during the synthesis of QDs, organic ligands from the solvent can assemble on their surface for passivation, keeping them stabilized and provide a monodispersed colloidal suspension of QDs.[7,8] However, the interaction between the QD and surface organic ligand is weak and during

Nanoscience & Nanotechnology Series No. 55
Concepts and Design of Materials Nanoarchitectonics
Edited by Omar Azzaroni and Katsuhiko Ariga

Published by the Royal Society of Chemistry, www.rsc.org

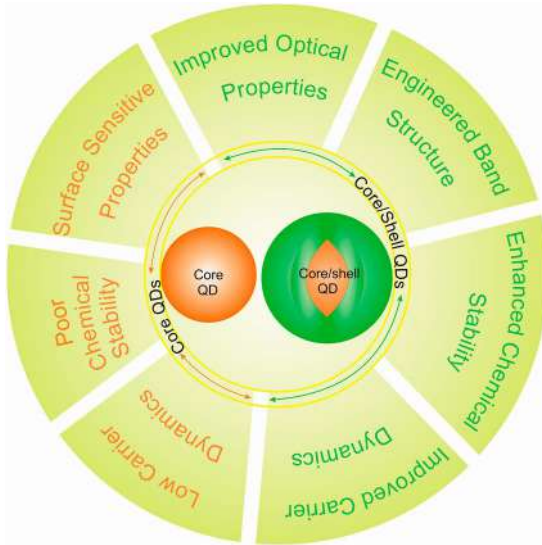

Figure 21.1 Properties of bare QDs *versus* core–shell QDs.

the solution-processed fabrication of QDs-devices, the organic ligands may damage and provide insufficient protection to QDs against the surrounding environment, thus promoting the formation of new surface defects/traps.

The effective way to protect QDs' surface is to coat a secondary semiconductor shell on core QDs to form a core–shell structure. Figure 21.1 demonstrates the superior features of core–shell QDs compared to bare QDs, which exhibit enhanced optical properties and photo-/chemical stability against various environmental factors. More importantly, the size and composition of core and shell materials in core–shell QDs can be tailored to achieve various band alignments that suit different QDs-based optoelectronic applications, for example, high photoluminescence quantum yield (PLQY) and/or efficient spatial charge separation. A suitable shell material can provide minimum lattice mismatch to core QDs and form proper band alignment to exhibit improved optical properties, which is essential for the growth of desirable core–shell QDs. A considerably large lattice mismatch between the core and shell may influence the properties of the core–shell due to strain effects. However, it is still feasible for the shell to form the crystal structure that matches with the core QDs during the growth process, thus minimizing the lattice mismatch for reduced interfacial defects.[9]

21.2 Classification of Core–Shell QDs

Colloidal core–shell QDs are generally categorized into type I, type II and quasi-type II on the basis of different band alignments between core and shell materials, as shown in Figure 21.2. The type I core–shell system consists of a

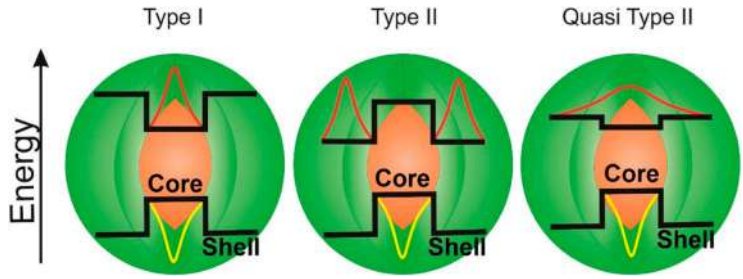

Figure 21.2 Schematic diagrams of type I, type II and quasi-type II band alignments for core–shell QDs.

shell with wider valence band (VB) and conduction band (CB) edges than the core, confining both the electrons and holes into the core region. This is beneficial to the radiative recombination of electrons and holes for enhanced PLQY and photo-stability. In the type II core–shell system, either the VB or CB edge of the shell resides within the bandgap of the core to form a staggered band alignment.[10] This type of core–shell structure exhibits long-lived recombination lifetimes of excitons owing to spatial separation of charge carriers (electrons and holes) upon excitation.[11,12]

In the quasi-type II core–shell structure, a small band offset exists between the CB or VB edges of core and shell, expanding the wave function of one type of carrier (generally for electrons) into both the core and shell region. Therefore, one type of charge carrier exists in the entire core–shell structure and the other type of carrier is confined in the core region.[13]

21.3 Synthesis and Optical Properties of Core–Shell QDs

Core–shell QDs can be synthesized either by one-step or two-step growth techniques. One-step growth techniques involve all the synthetic processes of core–shell QDs in the same pot.[14] Typically, after the growth of core QDs, the precursors for shell growth are directly injected into the core QDs reaction flask without stopping the reaction. While in a two-step growth technique, the core QDs are first grown and purified to remove the bulk and unreacted precursor. As-grown core QDs are then diluted in a suitable organic solvent for another reaction, in which the shell is grown at a suitable reaction temperature by injecting shell precursors.[9] Generally, all the semiconductors having smaller lattice mismatches with core are considered suitable materials for shell growth. In particular, shell thickness plays an important role in the optical properties of the core–shell QDs. An optimized shell thickness is required to realize efficient passivation for enhanced optical properties and improved charge transfer from QDs to other coupled semiconductor media.

21.3.1 Type I Core–Shell QDs

Type I core–shell structures (Figure 21.3a) have been developed to demonstrate enhanced PLQY and photo-/chemical stability. The examples of type I core–shell QDs include CdSe/ZnS, CdSe/ZnSe, CdS/ZnS,[15] InP/ZnS[16] and ZnSe/ZnS,[17] *etc.* Hines *et al.* have reported the growth of type I CdSe/ZnS core–shell QDs, in which a ZnS shell with a thickness of 1–2 monolayers was grown on CdSe core QDs.[18] The growth of the ZnS shell was carried out on pre-grown CdSe core QDs *via* sequentially injecting Zn and S shell precursors at a temperature of 300 °C.[18] The stock solutions for Zn and S were prepared by dissolving diethylzinc (Me_2Zn) and hexamethyldisilathiane [$S(TMS)_2$] into trioctylphosphine (TOP). Hao *et al.* also reported the synthesis of CdSe/ZnS core–shell QDs *via* a successive ionic layer adsorption and reaction (SILAR) technique.[19] The role of TOP solvent was highlighted for alleviating the strain effects during the growth of a thick ZnS shell, *i.e.* high-quality CdSe/ZnS core–shell QDs can be obtained by employing TOP solvent despite their higher lattice mismatch of ~10.6%.[20] Figure 21.3b,c exhibits the transmission electron microscope (TEM) images of CdSe core and CdSe/ZnS core–shell QDs, displaying controlled morphology and uniform particle size distribution.

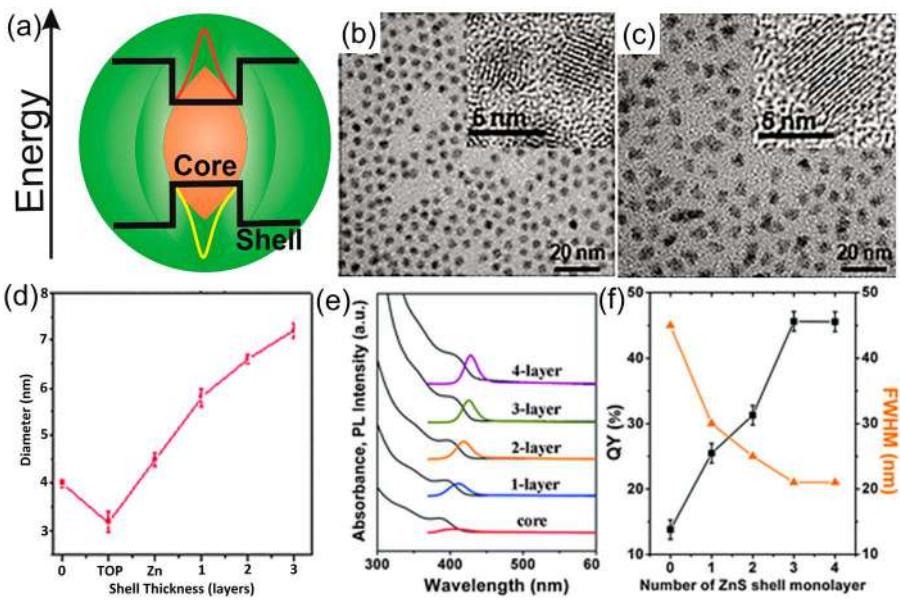

Figure 21.3 (a) Schematic diagram of type I core–shell structure. TEM images of (b) CdSe core and (c) CdSe/ZnS core–shell QDs. (d) Particle size *versus* shell thickness of CdSe/ZnS core–shell QDs. Adapted from ref. 19 with permission from the Royal Society of Chemistry. (e) Absorption and emission spectra of type I ZnSe/ZnS core–shell QDs. (f) QYs and FWHM of ZnSe/ZnS core–shell QDs with variable ZnS shell thickness. Adapted from ref. 21 with permission from the Royal Society of Chemistry.

A quick indication for the successful growth of shell on core QDs is the increasing average sizes of the QDs after the shell growth, as shown in Figure 21.3d. The decreased size of the CdSe core QDs after the introduction of TOP solvent was ascribed to the etching of CdSe core by the removal of excess Se from the surface *via* TOP.[19]

Low-temperature growth is often used to attain fine control on the particle size as well as to avoid the diffusion of shell material into core QDs. Bawendi *et al.* developed a low-temperature (140–220 °C) growth technique for the synthesis of CdSe/ZnS core–shell QDs.[22] Weller *et al.* used hexadecylamine (HDA) into trioctylphosphine oxide (TOPO)/TOP to tune particle size distribution.[23] Kudera *et al.* tailored the optical properties of CdSe/ZnS core–shell QDs to attain blue emission by lowering the particle size of QDs *via* using low growth temperature (80 °C).[24] The decreased particle size can lead to a strong quantum confinement effect in QDs, thus exhibiting enlarged band gaps for blue emission.

In type I core–shell QDs, the shell can passivate the defects and improve the original optical properties of the core QDs.[16,18] Figure 21.3e presents the ZnS shell thickness-dependent absorption and emission spectra of type I CdSe/ZnS core–shell QDs. The PL spectrum of CdSe core QDs exhibits a weak emission which showed considerable improvement (increased intensity) with increasing ZnS shell thickness, as shown in Figure 21.3e.[21] The increased ZnS shell also resulted in the enhanced PLQY (Figure 21.3f), that is, as-synthesized CdSe/ZnS core–shell QDs demonstrated suppressed surface defects and exhibited improved PLQY from 10% (bare CdSe QDs) to over 40%.[25]

21.3.2 Type II Core–Shell QDs

Bawendi *et al.* have developed type II core–shell QDs such as CdTe/CdSe and CdSe/ZnTe core–shell QDs.[11] As an example, CdTe/CdSe core–shell QDs were synthesized using CdO and TOP-Te precursors for the growth of CdTe core and CdO and TOP-Se for the growth of CdSe shell, respectively.[26] Wang *et al.* reported the synthesis of CdSe shell on CdTe core QDs *via* SILAR technique.[27] The CdTe core QDs mixed with TOP, tetradecylphosphonic acid (TDPA), and ODE were loaded into a round-bottom flask. The flask was heated at 170 °C after degassing and purging in an argon atmosphere. Cd and Se precursor solutions with equal molarity ratios were added alternately into the reaction flask at 30 min intervals. This technique yielded high-quality and homogenous CdTe/CdSe core–shell QDs, as depicted in Figure 21.4b,c. Xie and co-workers developed a variety of core–shell QDs employing ZnTe QDs as cores and CdTe, CdSe, CdS as shells.[28] The stock solutions for shell growth were prepared by dissolving cadmium oleate, TOP-Te, TOP-Se, and sulfur in 1-octadecane (ODE). The core–shell QDs were then obtained by injecting shell precursors into ZnTe core QDs, the variation in the morphology by lowering the shell growth temperature has been observed.[29,30] Highly luminescent type II CdS/ZnSe core–shell QDs were developed by Klimov's group.[31] The CdS core QDs were synthesized and dispersed in octadecylamine and

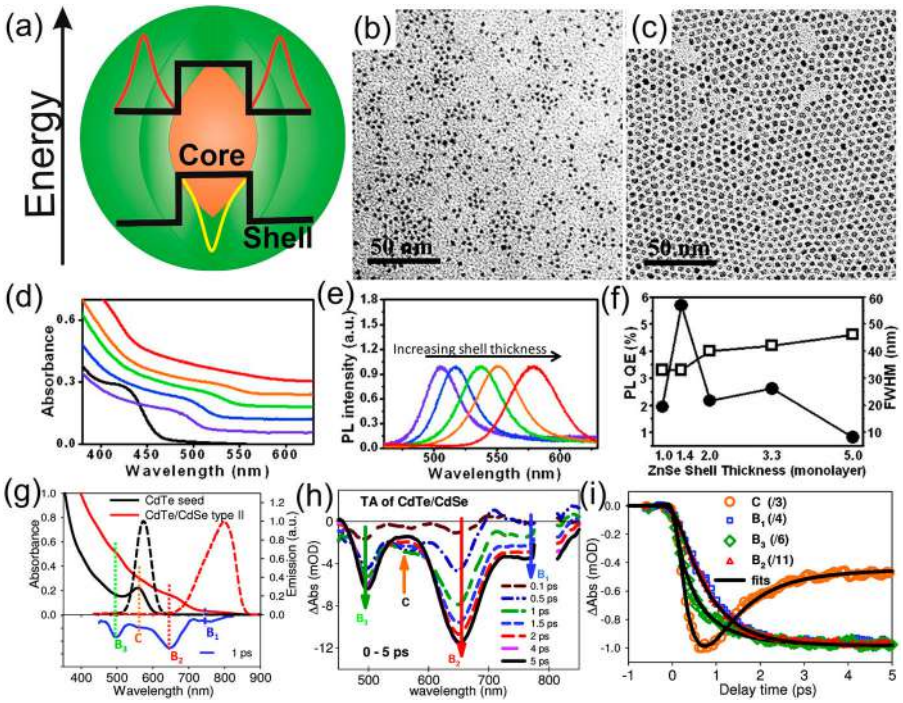

Figure 21.4 (a) Schematic diagram of type II core–shell QDs. TEM images of (b) CdTe core QDs and (c) CdTe/CdSe core–shell QDs. Adapted from ref. 27 with permission from American Chemical Society, Copyright 2013. (d) Absorption and (e) emission spectra of type II ZnTe/ZnSe core–shell QDs with increasing ZnSe shell thickness (black curve belongs to bare ZnTe QDs). (f) PLQE spectrum (circles) and FWHM trend (squares) for ZnTe/ZnSe core–shell QDs with variable ZnSe shell thickness. Adapted from ref. 33 with permission from American Chemical Society, Copyright 2010. (g) Absorption and emission spectra of CdTe core and CdTe/CdSe core–shell QDs. (h) TA spectra of CdTe/CdSe core–shell QDs. (i) Transient decay kinetics of transitions indicated in (h). Adapted from ref. 12 with permission from American Chemical Society, Copyright 2011.

ODE. Afterwards, ZnSe shell was grown by injecting zinc oleate and TOP-Se shell precursors into core QDs solution. Smith and co-workers have synthesized type II core–shell QDs with the existence of lattice strain.[32] Different shells with huge lattice mismatch (*e.g.* ZnS, ZnSe, ZnTe, CdS and CdSe) were grown on CdTe core QDs and as-prepared core–shell QDs exhibited a transition from type I to type II band structure.[32]

In contrast to the type I core–shell QDs, the optical properties of the type II core–shell QDs can exhibit red-shifted absorption and emission spectra with respect to the core QDs.[33] Figure 21.4d and e show the absorption and emission spectra of ZnTe core and ZnTe/ZnSe core–shell QDs with tunable optical properties by varying the shell thickness indicating a type II nature.

Figure 21.4f shows the shell thickness-dependent PL quantum efficiency (QE) and full width at half maxima (FWHM) of PL peaks. Over the course of ZnSe passivation the PLQE initially increased due to reduced surface defects and reached a PLQE of 6%. Further increase in ZnSe shell thickness leads to decreased PLQE due to enhanced type II spatial separation of electrons and holes.[11] The PL peak broadness showed gradual consistent increase with increasing shell thickness (Figure 21.4f). In type II core–shell QDs, the particle size inhomogeneity is defined as the convolution of core size and shell thickness distributions, which makes the PL bandwidth sensitive to the shell thickness.[33] CdTe/CdSe core–shell QDs also exhibited absorption spectrum extended to near-infrared (NIR) region compared to CdTe core QDs. Likewise, the emission spectrum of CdTe/CdSe core–shell QDs was red-shifted as compared to the CdTe core QDs due to the existence of type II band alignment (Figure 21.4g).[12]

The results indicated that tunable optical properties can be achieved by varying the shell thickness in type II core–shell QDs.[11,34] Moreover, the type II core–shell structures involve the transition of charge carriers between core and shell materials owing to the staggered band alignment. Figure 21.4g shows the absorption and emission spectra of CdTe/CdSe core–shell QDs with four absorption bands labeled as B1, B2, B3, and C at 770, 650, 500, and 560 nm, respectively (blue line spectrum in Figure 21.4g). These bands are more clearly observable in the transient absorption (TA) spectrum (Figure 21.4h) exhibiting bleaches at these bands due to the filling of CB electron levels.[12] The formation of bleach at the C band and its subsequent decay gives birth to the bleach signals of B1, B2, and B3 transitions. These transitions showed electron transfer from the CdTe (core) to CdSe (shell) CB. Moreover, B1, B2, and B3 transitions demonstrated identical bleach formation processes and decay kinetics, inferring that these transitions involve the same 1s electron level in the CdSe shell. This leads to the existence of an electron and hole in different regions of the core–shell structure, such as electrons in the shell and holes in the core, as exhibited by the bleach formation at B1, B2, and B3 (Figure 21.4h and i).[35–37] In this manner, the type II core–shell QDs exhibit prolonged PL lifetime with respect to the bare core QDs.[35]

21.3.3 Quasi-type II Core–Shell QDs

A typical quasi-type II band alignment (Figure 21.5a) is formed due to the small offset between CB and large offset between VB of the core and shell materials. In this way, the holes are localized in the core region and electrons are localized in both core and shell regions.[38] Various core–shell QDs have been developed with quasi-type II band alignment such as $CuInS_2$/CdS,[39] InP/CdS,[40] CdSe/CdS,[41] CdSe/ZnSe,[42] PbSe/CdSe,[43] $CuInSe_2$/$CuInS_2$,[44] $CuInSe_xS_{2-x}$/CdSeS/CdS[45] *etc.* CdSe/CdS core–shell QDs are interesting and among widely investigated quasi-type II core–shell systems due to their transition from type I to quasi-type II *via* tuning CdSe core size or CdS

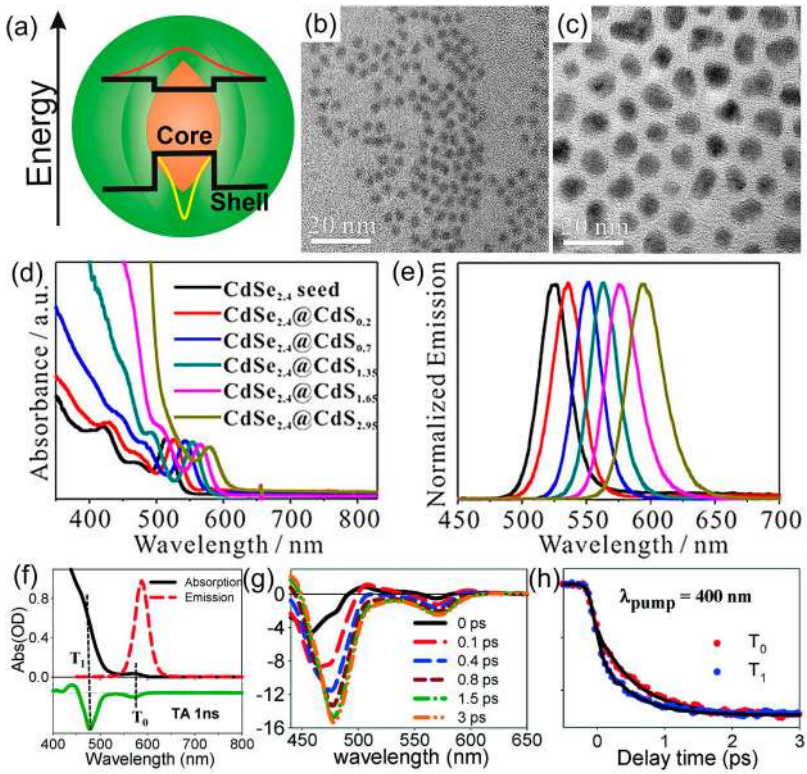

Figure 21.5 (a) Schematic diagram of quasi-type II core–shell structure. Representative TEM images of (b) CdSe core (c) CdSe/CdS (shell thickness ~2.95 nm) core–shell QDs. Absorption and emission spectra of (d) CdSe core and (e) CdSe/CdS core–shell QDs with variable shell thicknesses. Adapted from ref. 48 with permission from American Chemical Society, Copyright 2018. (f) Absorption and emission spectra with transient absorption spectrum (at 1 ns, green line) spectra of CdSe/CdS core–shell QDs. (g) TA spectra and (h) bleach formation kinetics CdSe/CdS QDs at indicated delay times. Adapted from ref. 50 with permission from American Chemical Society, Copyright 2012.

shell thickness.[46–48] Kong *et al.* have reported the synthesis of CdSe/CdS core–shell QDs in which the core QDs were synthesized *via* a hot injection approach.[48] CdS shell was grown on these CdSe core QDs by using SILAR process.[49] For this synthesis, cadmium precursor was prepared in advance by dissolving the calculated amount of CdO in oleylamine (OLA) and ODE at 300 °C and sulfur solution was prepared by dissolving sulfur in ODE *via* sonication. The shell precursor was then injected into core QDs at 200 °C after conventional degassing process. The core–shell QDs were further heated at 230 °C for improved crystallinity. Figure 21.5b and c show the

TEM images of CdSe core and CdSe/CdS core–shell QDs with CdS shell thickness of 2.95 nm, which is much obvious from the apparently large size of core–shell QDs compared to core QDs.

Figure 21.5d and e exhibit the absorption and emission spectra of CdSe core and CdSe/CdS core–shell QDs with variable shell thicknesses, which demonstrate the consistent red shifting of the first excitonic peak in absorption spectra and PL peaks.[48] In quasi-type II core–shell QDs, the FWHM of PL peaks with variable shell thickness showed no significant change as compared to that of the type II core–shell QDs, which indicates that the peak broadness is not sensitive to the shell thickness inhomogeneity (Figures 21.4e and 21.5e).

Figure 21.5f presents the absorption spectrum of CdSe/CdS core–shell QDs with a weak excitonic peak at ~575 nm (denoted as T_0) and strong absorption band at ~475 nm (denoted as T_1), which are clearer in TA spectrum (green line spectrum in Figure 21.5f). The T_0 band originated from the transition between the CB electron ($1s_e$) and VB hole ($1s_h$) levels in the core–shell structure. In the TA spectrum, the bleaches at T_1 and T_0 transitions exhibit identical $1s_e$ levels. The T_1 band hence appeared due to the transition between the delocalized $1s_e$ CB level and the VB edge level ($1s_h$) of the CdS shell.[50] After excitation *via* 400 nm laser, hot electrons and holes are generated at CB and VB edges. The relaxation of these excited hot carriers to the $1s_e$ and $1s_h$ levels leads to the continuous red-shift of the T_1 bleach and growth of T_0 bleach with a long lifetime, as shown in Figure 21.5g,h.[50]

21.4 Applications of Core–Shell QDs

Core–shell QDs offer a variety of applications owing to their excellent features compared to the bare QDs including engineered band structure, tunable optical properties (such as higher PLQY, narrow-band emission, and prolonged exciton lifetime), and robust photo-/chemical stability. Moreover, the facile and flexible solution-processed device fabrication steps make them highly desirable in optoelectronics. Herein, we present various core–shell QDs-based optoelectronic applications including solar cells, photoelectrochemical (PEC) cells, luminescent solar concentrators (LSCs), photodetectors, light emitting diodes (LEDs) and lasers.

21.4.1 Solar Cells

A solar cell is a photovoltaic (PV) device that converts solar energy into electricity. A typical QD-sensitized solar cell (QDSC) consists of three main elements including a photoanode, a counter electrode and electrolyte, as shown in Figure 21.6a.[51] Specifically, the photoanode is fabricated by using QDs as light absorbers and a wide band gap semiconductor (*e.g.* TiO_2 deposited on fluorine-doped tin oxide or indium-doped tin oxide glass) for electrons

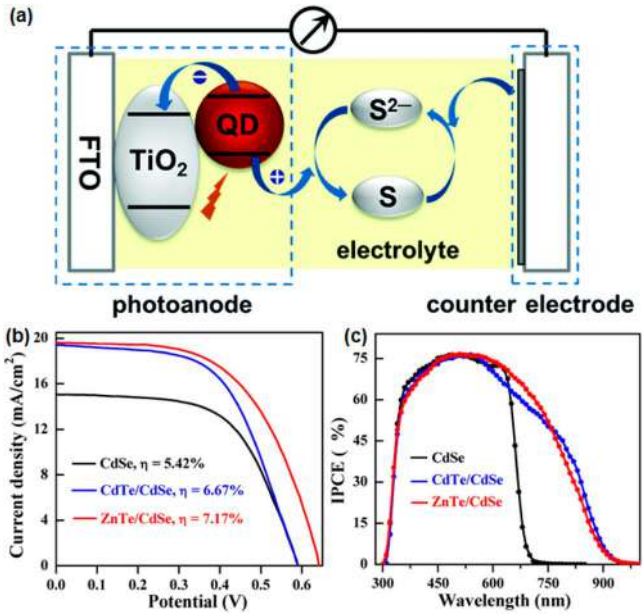

Figure 21.6 (a) Schematic diagram of a typical QD-sensitized solar cell. Adapted from ref. 51 with permission from the Royal Society of Chemistry. PV performance of bare CdSe QDs, CdTe/CdSe and ZnTe/CdSe core–shell QDs-based QDSCs: (b) J-V curves (c) IPCE curves. Adapted from ref. 52 with permission from American Chemical Society, Copyright 2015.

extraction. In this configuration, the photogenerated electrons in CB of QDs can be subsequently transferred to CB of TiO_2, FTO and the counter electrode.[51]

CdSe/ZnS core–shell QDs have been employed for the fabrication of QDSC and exhibited significantly enhanced stability compared to the bare CdSe QDs-based QDSC.[17] Ågren *et al.* synthesized ZnSe/CdS core–shell QDs for assembly of QDSC, yielding higher incident photon to current conversion efficiency (IPCE) due to efficient electron–hole separation derived from type II band structure.[53] Type II CdTe/CdS and CdTe/CdSeS core–shell QDs were also sensitized into TiO_2-based photoelectrode to fabricate the QDSCs, which demonstrated a power conversion efficiency (PCE) of 5.96% and 6.6%, respectively, under 1 sun illumination. The PCEs of core–shell QDs-based QDSCs are much higher than that of the CdTe core QDs-based QDSC (4.87%).[54] Such enhanced performance was ascribed to the extended absorption spectra and suppressed charge recombination of type II CdTe/CdS and CdTe/CdSeS core–shell QDs compared to the CdTe core QDs. Meng *et al.* employed $CdSe_xTe_{1-x}$/CdS core–shell QDs for the solar cell fabrication and reported a higher PCE than that of the bare $CdSe_xTe_{1-x}$ QDs with poor chemical stability.[55] A higher

PCE of 6.76% was obtained from CdTe/CdSe core–shell QDs-based QDSCs as compared to bare CdTe QDs, which was attributed to the broad light absorption of CdTe/CdSe core–shell QDs.[27] CdSeTe/CdS core–shell QDs were developed for the fabrication of QDSCs, as compared to the bare CdSeTe QDs-based device, the core–shell QDs-based device demonstrated a much higher PCE of 9.48% due to the suppressed surface defects by CdS shell passivation.[56]

QDSCs often suffer from low performance due to lower V_{oc} values, which suggests that increasing the V_{oc} is a prerequisite for further improvement in QDSC performance. In this regard, Bisquert *et al.* reported the synthesis of high-quality ZnTe/CdSe core–shell QDs with absorption in NIR region.[52] As-fabricated QDSCs exhibited a PCE of 7.17% and a certified efficiency of 6.82% under one sun illumination. The *J–V* curves and IPCE results for bare CdSe, CdTe/CdSe core–shell and ZnTe/CdSe core–shell QDs-based solar cells are displayed in Figure 21.6b and c, demonstrating PCEs of 5.43%, 6.67% and 7.17%, respectively. In addition, the V_{oc} values for these QDSCs are listed as 0.595 V, 0.597 V and 0.642 V, respectively. In these core–shell QDSCs, there exists a larger CB offset of ZnTe/CdSe core–shell QDs-TiO_2 (~1.22 eV) as compared to CdTe/CdSe core–shell QDs-TiO_2 (~0.27 eV), thus causing charge accumulation at QDs/TiO_2 interface and producing strong dipole effect.[57] This dipole effect delivered an upward shift of the TiO_2 CB, enabling higher performance in ZnTe/CdSe core–shell QDs-based QDSC than that of the CdTe/CdSe core–shell QDs.[58]

21.4.2 Photoelectrochemical Cells

A PEC cell is a water splitting system that enables the H_2 generation by utilizing solar energy, which mainly consists of a working electrode, a reference electrode and a counter electrode (Figure 21.7a). The working electrode is basically a photoelectrode made up of light sensitive semiconductor materials (such as QDs) which can generate electron–hole pairs upon exposure to sunlight.[59] QDs-based PEC cells have become a hot topic owing to the high absorption coefficient, multiple exciton generation and tunable optical properties of QDs, especially the core–shell QDs that demonstrate shell-engineered optical properties and improved photo-/chemical stability compared to bare QDs. Figure 21.7a illustrates the basic operation principle of a QD-PEC cell. After illumination by sunlight, electron–hole pairs are generated in the QDs. The electrons are transferred to the counter electrode by the applied external electric field where they take part in the targeted reaction such as water reduction reaction for hydrogen production whereas holes are consumed by the scavengers present in electrolyte.[9,44]

The bare QDs generally possess abundant surface defects and demonstrate poor PEC performance[44,45] Jin *et al.* have reported the synthesis of PbS/CdS core–shell QDs *via* cation exchange method for the fabrication of QDs-based PEC cells.[60] The PbS/CdS core–shell QDs decorated TiO_2 photoelectrode with further CdS SILAR coating exhibited a photocurrent density of ~11 mA cm^{-2} with decent stability.[60]

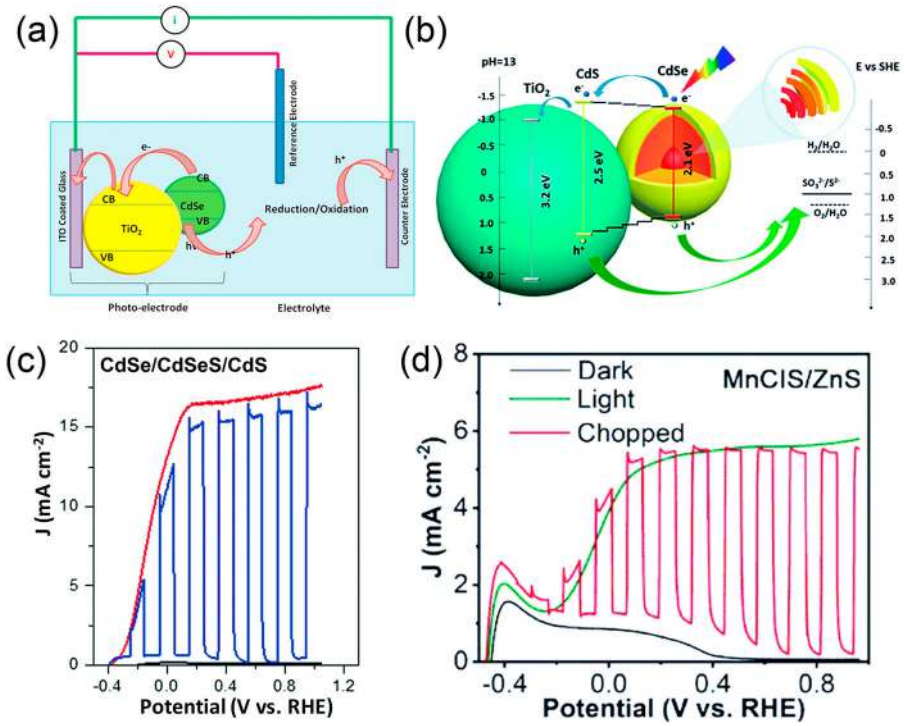

Figure 21.7 (a) Schematic illustration of a typical QDs/TiO_2-based PEC cell. Adapted from ref. 59 with permission from Elsevier, Copyright 2017. (b) Schematic diagram of the band structure and carrier transition of the CdSe/CdSeS/CdS core-alloyed–shell-shell QDs-based photoanode and corresponding (c) PEC performance. Adapted from ref. 61 with permission from the Royal Society of Chemistry. (d) PEC performance of heavy metal-free MnCIS/ZnS core–shell QDs-based photoanode. Adapted from ref. 62 with permission from the Royal Society of Chemistry.

Channa *et al.* developed $CuGaS_2$/CdS core–shell QDs for the fabrication of PEC photoelectrodes, which exhibited a higher photocurrent density of ~6.5 mA cm^{-2} than that of the $CuGaS_2$ core QDs (~0.83 mA cm^{-2}) under standard one sun illumination.[9] The higher performance in their case was ascribed to the enhanced absorption and prolonged exciton lifetime of the $CuGaS_2$/CdS core–shell QDs compared to bare CGS QDs. Wang *et al.* proposed and synthesized a novel type of interfacial engineered CdSe/CdSeS/CdS core–shell QDs with gradient CdSeS shell to establish stepped band alignment with optimized charge dynamics (Figure 21.7b) for obtaining high-performance PEC cells.[61] Figure 21.7c represents the PEC performance of the CdSe/CdSeS/CdS core/multi-shell QDs-based photoelectrode, which demonstrated a

maximum photocurrent density of 17.5 mA cm^{-2} under one sun illumination (AM 1.5 G, 100 mW cm^{-2}) with a retention of 70% photocurrent density after 2 hours.

However, despite the high efficiency of devices, the utilization of toxic heavy metals (*i.e.*, Pb, Cd *etc.*) based QDs for the application in PEC cells are deleterious for the environment and to human health. Environmentally friendly core–shell QDs are therefore highly demanded for practical applications. In this regard, Tong *et al.* reported pioneer work for the synthesis of heavy metal-free CuInSeS/ZnS core–shell QDs for the fabrication of heavy metal-free QDs-PEC cells.[63] The bare CuInSeS QDs-based photoelectrode only unveiled a photocurrent density of ~2.57 mA cm^{-2}. On the contrary, the CuInSeS/ZnS core–shell QD-incorporated photoelectrode revealed a significantly increased photocurrent density of ~4.3 mA cm^{-2} with retention of about ~77% photocurrent density after 2 hours. The enhanced performance of CuInSeS/ZnS core–shell QDs-based photoelectrode is attributed to the effective surface passivation of CuInSeS core QDs by ZnS shell, which leads to the suppressed non-radiative recombination and enhanced photo-/chemical stability, thus exhibiting much higher photocurrent density and enhanced device stability. Wang's group recently developed a heavy metal-free Mn-alloyed $CuInS_2$/ZnS core–shell QDs for the fabrication of environment friendly PEC cell.[62] Such Mn–$CuInS_2$/ZnS core–shell QDs-based PEC cell showed a photocurrent density as high as 5.7 mA cm^{-2} (Figure 21.7d) with outstanding retention of 73% of initial photocurrent density after 2 hours illumination. It was unveiled that the Mn-alloyed $CuInS_2$ core QDs possessed a larger band gap than the unalloyed $CuInS_2$, which formed a favorable band alignment (*i.e.* smaller conduction band offset) with ZnS shell for electron delocalization, which leads to efficient spatial charge separation of such core–shell QDs, thus consequently resulting in enhanced PEC performance. In addition, the ZnS shell can effectively protect the core QDs for improved photo-/chemical stability, giving rise to the excellent device durability.[62]

21.4.3 Luminescent Solar Concentrators

Luminescent solar concentrators (LSCs) have gained much interest for indoor building integrated PVs.[64–66] The motivation behind the fabrication of LSCs is to collect and concentrate solar radiation for application in low cost and high-performance PVs.[67,68] QDs-based LSCs are designed by embedding fluorescent QDs in transparent or semi-transparent materials (such as glass or polymer) as waveguide.[69,70] The incident light can be absorbed by the LSC and re-emitted/propagated to the waveguide edges *via* total internal reflection (TIR). The PV cells are attached to the lateral edges of the waveguide which collect the re-emitted light and convert it into electricity, as depicted in Figure 21.8.[71] Highly luminescent materials are very promising for the fabrication of LSCs such as organic dyes with high PLQY have been used as fluorophores for the fabrication of LSCs.[72] However, the poor photo-/chemical

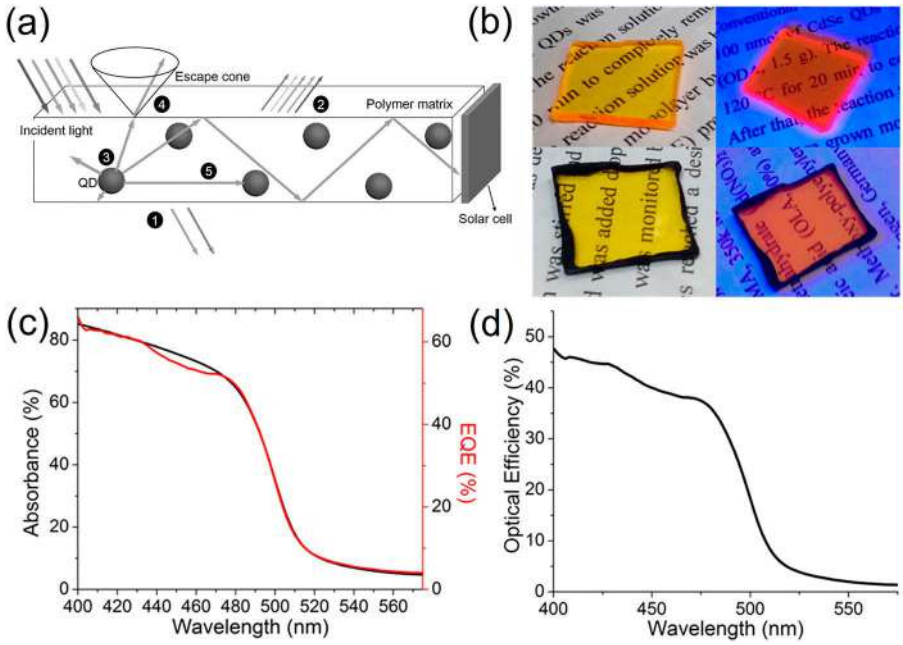

Figure 21.8 (a) Schematic diagram of a QDs-based LSC. Adapted from ref. 71 with permission from John Wiley & Sons, Copyright © 2016 WILEY-VCH Verlag GmbH & Co. KGaA, Weinheim. (b) CdSe/CdS core–shell QDs-based LSCs under ambient light (left panel) and UV light (right panel) with the edges clear (top) and blocked by carbon paint (bottom). (c) EQE spectrum of the prototype LSC. (d) Optical efficiency of the LSC. Adapted from ref. 79 with permission from American Chemical Society, Copyright 2014.

stability and overlapped absorption and emission spectra of such organic dyes limit the performance of corresponding LSCs.[73,74] Higher Stokes shift (difference in the energy between first exciton peak in the absorption spectrum and emission peak) is an important factor to realize high efficiency LSCs owing to reduced re-absorption losses. Colloidal core–shell QDs exhibit higher PLQY, shell thickness-dependent Stokes shift and improved photo-/chemical stability compared to organic dyes and bare QDs.[75,76] Numerous core–shell QDs, such as PbS/CdS, CdSe/CdS and $CuInS_2$/ZnS core–shell QDs have been employed for the fabrication of LSCs. Zhou *et al.* have reported NIR PbS/CdS core–shell QDs-based LSC.[77] They tuned the absorption and emission spectra by varying the size of the core and tailoring the thickness of the shell to exhibit large Stokes shift and higher PLQY.[77,78] Such PbS/CdS core–shell QDs with high PLQY and large Stokes shift can significantly reduce re-absorption losses for high efficiency, large-area LSCs. Furthermore, the PbS/CdS core–shell QDs-based LSC exhibited an optical efficiency (η_{opt}) of 6.1%,

which is much higher than that of bare PbS QDs-based LSC.[77] Bawendi *et al.* have developed LSCs from CdSe/CdS core–shell QDs with thick CdS shell (Figure 21.8b), demonstrating a very high QY of 86%.[79]

The EQE and absorbance spectra of LSC were in excellent agreement due to the minimal energy dependence of the QY (Figure 21.8c). The LSC fabricated using CdSe/CdS core–shell QDs exhibited an optical efficiency of 48% at a wavelength of 400 nm due to a higher magnitude of absorption at 400 nm (Figure 21.8d). However, at longer wavelengths, there is a reduction in the LSCs optical efficiency due to reduced light absorption (Figure 21.8c and d).

Li and the co-workers have reported heavy metal-free $CuInS_2$/ZnS core–shell QDs with a PLQY of 81% and large Stokes shift of 150 nm for the fabrication of LSCs, which exhibited an optical efficiency of 26.5%.[80] The $CuInS_2$/ZnS core–shell QDs were designed to absorb light of short wavelength (<450 nm) and re-emit as long wavelength light (~550 nm), which can be waveguided to the coupled crystalline-silicon (c-Si) PV cells. Such $CuInS_2$/ZnS core–shell QDs-LSC coupled PV device demonstrated an enhanced PCE of 8.71% compared to PV device without QDs-LSC (2.73%), *i.e.* Poly(methyl methacrylate) (PMMA) coupled PV device. The investigations related to QDs-based LSC infer that the cost of electricity production from PV cells can be reduced by employing QDs-based LSC technology.

21.4.4 Photodetectors

Photodetectors convert incident light into electrical signal and have attracted tremendous interest for their enormous applications in commercial and military fields.[81,82] Solution-processed device fabrication *via* colloidal QDs is an attractive approach to considerably lower the device fabrication cost.[83,84] In addition to the low fabrication cost, QDs also present size-dependent optical properties which can be utilized in photodetection to achieve diverse photodetection regimes.[85] However, compared to bare QDs, the core–shell QDs present improved photochemical stability and charge transfer characteristics due to the formation of type II or quasi-type II band structures which are vital for durable and high-performance photodetectors.[86] Chu's group has reported ZnCdSe/ZnS core–shell QDs-based photodetector fabricated on a thin layer of MoS_2.[87] The ZnCdSe/ZnS core–shell QDs act as light absorbers whereas the MoS_2 layer acts as the charge transporting channel. The schematic design of the ZnCdSe/ZnS core–shell QDs coupled with a MoS_2 layer-based photodetector is shown in Figure 21.9a. After illumination, the electron–hole pairs generated into QDs tunnel from QDs to MoS_2 channel and generate a photocurrent. Figure 21.9a shows QDs/MoS_2 photodetector device illuminated by incident wavelength of $\lambda = 450$ nm and $P = 400$ nW. The QDs/MoS_2 photodetector generated a considerably high photocurrent compared to only MoS_2-photodetector, as exhibited in Figure 21.9b.

Moreover, the ZnCdSe/ZnS core–shell QDs-based photodetector demonstrated faster rise/decay times as shown in Figure 21.9c and d which are ascribed to efficient injection of charge carrier from QDs to MoS_2 layer.[88]

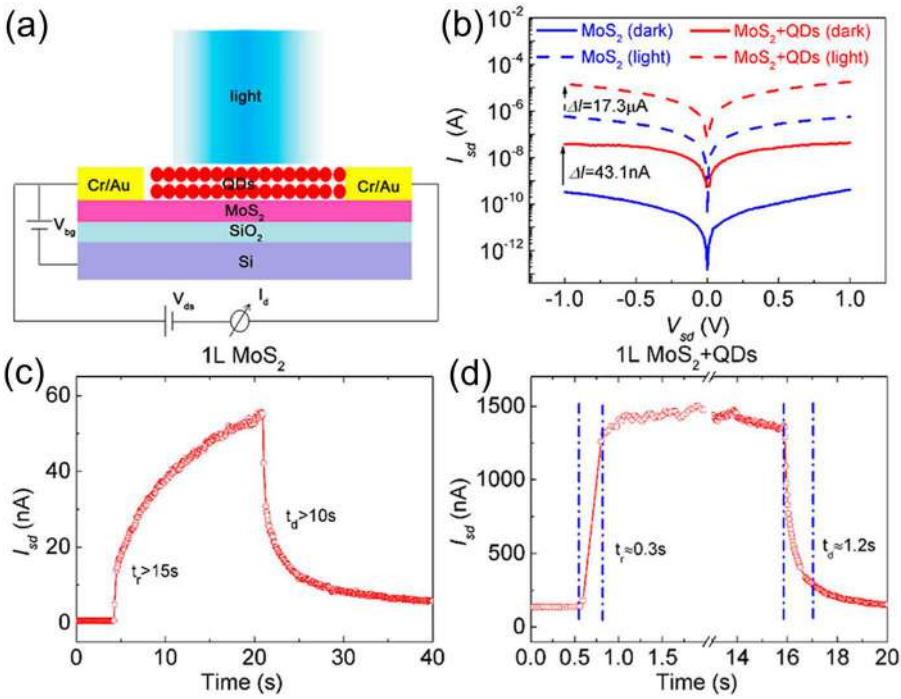

Figure 21.9 (a) Cross-sectional view of the schematic QDs/MoS_2 photodetector operated under illumination. (b) I–V curves of the MoS_2 photodetector device and QDs/MoS_2 hybrid device with and without 450 nm illumination keeping gate voltage (V_{bg}) = 0 V. (c, d) Time-dependent photoresponse of the pristine MoS_2 device and hybrid QD/MoS_2 devices. Adapted from ref. 87 with permission from American Chemical Society, Copyright 2019.

The faster rise/decay times are highly required for ultrafast responsive photodetectors and efficient carrier separation is the key to sensitive photodetectors.[89] The bare QDs are prone to the formation of charge trapping centers due to long term exposure in harsh environmental conditions which can lower the photodetector performance over time.[4,90] Moreover, the ZnCdSe/ZnS core–shell QDs-based photodetector exhibited much higher responsivity (~10^4 A W^{-1}) compared to photodetector without QDs (~10 A W^{-1}) and enhanced detectivity of 1.0×10^{12} Jones (about three orders of magnitude higher) compared to photodetector without QDs (4.6×10^9 Jones).[87]

21.4.5 Light Emitting Diodes

A light emitting diode (LED) is a device made up of semiconductors, which can emit light upon current injection. QDs-based LEDs (QLEDs) have gained much attention owing to their incredible features such as high brightness and color purity, low operating voltage and easy fabrication technologies.[91,92]

A QLED generally consists of a cathode, electron transport layer (ETL), QD layer for light emission, hole transport layer (HTL) and an anode as shown in Figure 21.10a.[93] Briefly, in QLEDs an external voltage is applied across the electrodes which causes the electrons and holes to transfer to ETL and HTL, respectively. The charges are then captured by QDs where they recombine and produce electroluminescence (EL).[94] Core–shell QDs have shown promising results for high-performance QLEDs owing to their higher photo-/chemical stability and PLQY.[95,96] Peng's group have developed red QLEDs employing CdSe/CdS core–shell QDs.[97] The CdSe/CdS core–shell QLED exhibited an external quantum efficiency (EQE) of 20.5% and a brightness of 1200 cd m^{-2}. However, by increasing the operating voltage up to 8 V the brightness can be reached as high as 42 000 cd m^{-2} with a simultaneous reduction in EQE. A similar decreasing trend in the EQE with increasing luminance was observed by Kazlas *et al.*[98] The performance of QLEDs is sensitive to the non-radiative Förster resonant energy transfer (FRET) process due to the closed packing of QDs, as a result of thin shell in core–shell QDs

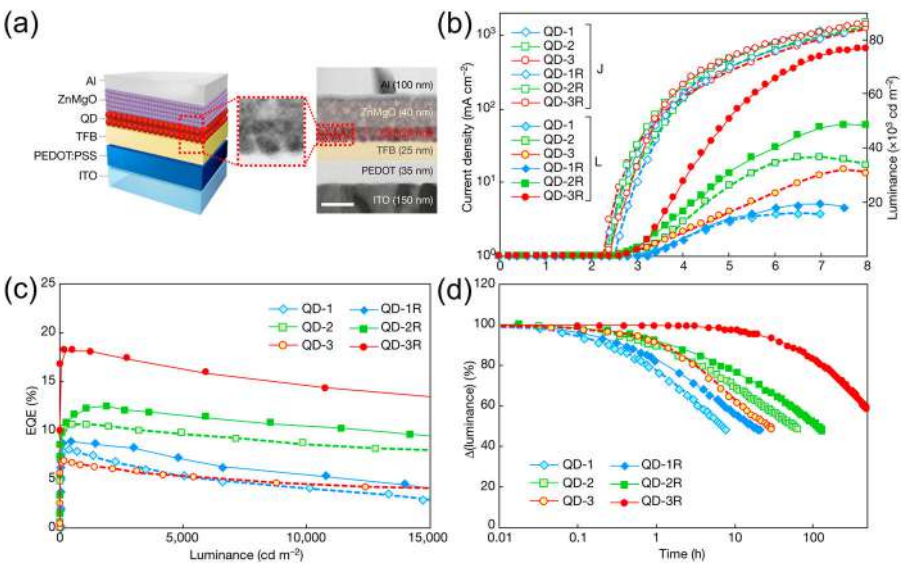

Figure 21.10 (a) Schematic illustration and cross-sectional TEM image of QLED device structure (scale bar, 50 nm). (b) Current density (left axis) and luminance (right axis) *versus* voltage profiles. (c) EQE-luminance profiles. (d) Lifetime measurements (at the initial luminance of 4500 cd m^{-2}) of the QLEDs with QD-1, QD-1R, QD-2, QD-2R, QD-3 and QD-3R. Note: QD-1, QD-2 and QD-3 refer to InP/ZnSe/ZnS (pod shaped) core/multi-shell QDs with variable ZnSe/ZnS shell thickness grown at 320 °C, whereas QD-1R, QD-2R and QD-3R represent InP/ZnSe/ZnS (spherical) core-multi-shell QDs with variable ZnSe/ZnS shell thickness grown at 340 °C. Adapted from ref. 106 with permission from Springer Nature, Copyright 2019.

and Auger recombination (AR).[99,100] Growth of thick multiple shells on core QDs has demonstrated a reduction of FRET and improved EQE compared to thin shell case.[101] Peng *et al.* optimized the performance of InP/ZnSe/ZnS core–shell–shell QDs-based LEDs to show an EQE of 12.2% and a brightness of over 10 000 cd m^{-2} by growing a thick shell and controlling the stoichiometry of the core–shell QDs.[102] The recent developments in QLED technologies have shown to exhibit either high EQE with low luminance or *vice versa*.[97,103–105] For instance, red light emitting CdSe/CdS core–shell QDs-based LEDs have reached an EQE in the range 18–20.5% with luminance limited in the range 100–2000 cd m^{-2}.[97,98]

Green QLEDs fabricated using CdSe/ZnS core–shell QDs have obtained high luminances of ~460 000 cd m^{-2} with EQE of 6%.[107] Blue QLEDs fabricated employing ZnCdS/ZnS core–shell QDs have reached an EQE of 10%, with a brightness of ~7600 cd m^{-2}.[108] Therefore, strategies are required to develop the enhancement of both EQE and the luminance of QLEDs.

Recently, Jang *et al.* have reported a tremendous improvement in the performance of red QLEDs by simultaneously enhancing both EQE and luminance.[106] They employed InP QDs over-coated by multiple thick shells of ZnSe and ZnS. However, prior to the shell growth on InP QDs, they performed surface treatment of InP core QDs during synthesis to alleviate the surface defects.[106] The surface treatment involved an *in situ* etching of InP core QDs for the removal of surface oxide which was conducted using hydrofluoric acid (HF). Multiple thick shells of ZnSe and ZnS were grown to eradicate non-radiative processes such as AR and FRET. However, the InP/ZnSe/ZnS core–shell/shell QDs obtained were observed to be pod shaped (termed QD-1, QD-2 and QD-3) with QYs of 98%, 92% and 75%, respectively. To obtain spherical shaped InP/ZnSe/ZnS core–shell–shell QDs (termed QD-1R, QD-2R and QD-3R) with enhanced QY (up to 100%) the shell growth temperature was increased to 340 °C. All the InP/ZnSe/ZnS core–shell–shell QDs-based LEDs exhibited a very low turn-on voltage in the range 1.8–2.0 V, which is close to the bandgap of InP QDs (~1.97 eV). The *I–V* curves for all the QLEDs devices with different ZnSe/ZnS shell thicknesses (both pod and spherical shaped) indicated identical charge transport as shown in Figure 21.10b. However, despite the similar transport behavior, the enhanced EQE and luminance was observed only for thicker ZnSe interlayer thicknesses (QD-3R). A maximum EQE of 18.0% and maximum luminance of 70 718 cd m^{-2} were observed for QLEDs fabricated from InP/ZnSe/ZnS (QD-3R, spherical shaped) core–shell–shell QDs with very thick ZnSe interlayer, as represented in Figure 21.10c. The QLED fabricated employing InP/ZnSe/ZnS QDs (QD-3, pod shaped) exhibited lower EQE and luminance due to its low PLQY (~75%) compared to the InP/ZnSe/ZnS (QD-3R, spherical shaped) core–shell–shell QDs. The low performance of InP/ZnSe/ZnS core-thin-shell QDs (both pod and spherical shaped) can be ascribed to the dominant FRET process.[106] In addition to the high-performance, the QLEDs with thicker ZnSe/ZnS shell (QD-3R, spherical shaped) demonstrated much enhanced durability compared to InP/ZnSe/ZnS core-thin-shell (both pod and spherical shaped) QDs-based LEDs, as shown in Figure 21.10d.

The QLED fabricated using InP/ZnSe/ZnS (QD-3R, spherical shaped) core//shell/shell QDs exhibited a remarkable predicted lifetime of about ~3000 h at a brightness of 1000 cd m^{-2}. The results infer that the spherical morphology of core–shell QDs with over-thick shells and much higher QY is promising for high-performance QLEDs.

21.4.6 Laser

In lasers, colloidal QDs have demonstrated advantageous features including tunable emission wavelength over a wide spectral range by the variation of QDs size with a low lasing threshold.[109] However, the bare QDs possess defects such as AR affecting the lifetime and bandwidth of optical gain and causes blinked emission from QDs, hindering the advanced development of QDs-based lasers.[110] Growth of thick shell on bare QDs can suppress the AR, making the core–shell QDs promising for laser application with continuous-wave operation and low-threshold amplification due to alleviated defects compared to bare QDs.[111–115]

Liao's group has reported the laser fabricated from a pure phase CdSe/CdS core–shell QDs and achieved single mode lasing with low thresholds of 16 μJ cm^{-2} and 2 μJ cm^{-2}.[112] These features were attributed to the suppressed AR in pure phase CdSe/CdS core–shell QDs. Dang *et al.* have reported type I CdSe/ZnCdS core–shell QDs with a PLQY of 80% for the fabrication of vertical-cavity surface-emitting lasers (VCSELs).[116] The schematic diagram of a VCSEL setup is shown in Figure 21.11a which is equipped with a long pass filter to wipe out residual pump excitation beam. Figure 21.11b shows pump energy dependent emission spectra, where sharp and coherent laser lines seem to appear above threshold energy. The lasing action triggered at a pumping threshold of ~60 μJ cm^{-2} for red light emitting laser. The QD-VCSEL exhibited an overall efficiency of 0.4% for red laser at an excitation energy density of 140 μJ cm^{-2}.

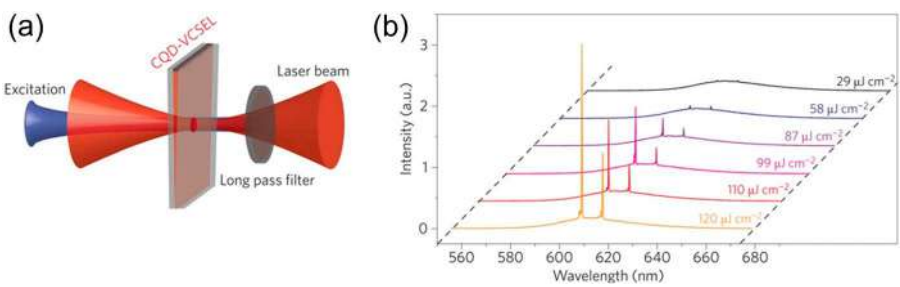

Figure 21.11 (a) Schematic diagram of a vertically pump CQD-VCSEL. (b) Emerging laser modes from spontaneous emission in a QD-VCSEL at increasing pump power. Adapted from ref. 116 with permission from Springer Nature, Copyright 2012.

Thick shell on QDs can further enable color switching in QDs-based lasers, *i.e.* the lasing can be switched from the core to shell.[117] Norris *et al.* have reported such color-tunable QDs-based lasers, they fabricated ring lasers with active color control *via* high-quality resonators through QD template stripping.[117] For lasing action, the as-fabricated QDs ring was illuminated by ultrafast laser pulses which demonstrated various features as a function of incident pulse energy: (i) Below the lasing threshold of 22 μJ cm^{-2}, only spontaneous emission was observed and a significant biexciton population can be expected to occur at an average exciton occupancy per QD $\langle N \rangle = 1.6$. (ii) Above the threshold energy, series of sharp laser peaks at a wavelength of ~610 nm appeared in the emission spectrum combined with ultrafast components (<100 ps) in the decay curve, which is the typical signature of stimulated emission. Further increase of excitation power resulted in the increased intensity of these laser peaks and the amplitude of the fast decay component followed by the beginning of red lasing, which saturated at around 80 μJ cm^{-2} ($\langle N \rangle = 5.9$). At 110 μJ cm^{-2} ($\langle N \rangle = 8.4$), the laser peaks switched to green lasing peaks emerging at 530 nm. (iii) Red lasing peaks and the fast decay components begin to diminish at higher pulse power. (iv) Finally, the green lasing peaks eventually grow stronger and dominate the device output.[117] These findings demonstrated that color switchable lasers can be fabricated by employing core–shell QDs as demonstrated by Norris and co-workers.

21.5 Conclusions

This chapter is dedicated to the chemical synthesis, optical properties and optoelectronic applications of various core–shell QDs. Recent progress for the development of different types of colloidal core–shell QDs (*e.g.*, type I, type II and quasi-type II) and their promising applications in light conversion (QDSCs, PEC cells and LSCs), light detection (photodetectors) and light emission (LEDs and lasers) have been presented. In particular, we highlighted the band alignment tuning *via* core–shell structures for achieving specific optoelectronic properties of QDs. It was revealed that the core–shell QDs with type II and quasi-type II band alignment are more beneficial to the PV applications owing to their intrinsic charge separation capability, while type I core–shell QDs with PLQY close to unity are the potential candidates for the light emitting devices. Moreover, the non-radiative process such as AR and FRET can be alleviated and charge-localization rates can be tuned by engineering the shell volume and the core–shell interface geometry, which can aid further development of QDs-based light emitting and PV devices.

To date, despite all the favorable conditions such as type II band alignment of core–shell QDs, which facilitates intrinsic charge separation and broad light absorption capabilities, the QDSCs suffer limited PCE and low V_{oc} values. In the case of QDs-based PEC cells, the PEC performance has covered a milestone, while the device stability is still a major problem owing to QDs degradation. Various strategies for improving device stability have been

employed and the obtained results showed that there is a trade-off between stability and performance. The LSC technology is a major breakthrough for low cost, high-performance building integrated PV devices, however, current QDs-based LSCs are prototypes with small dimensions. Besides the dimension issue, the PCEs of solar cells coupled with LSCs are still low. For ultrafast responsive photodetectors, the QDs-based photodetectors still require a major breakthrough to reach improved rise/decay time, responsivity and detectivity, which are dependent on the efficient charge extraction from the QDs and their transport properties. For QLEDs and lasers, the device performance is greatly affected by the non-radiative phenomena such as AR and FRET processes owing to the large surface area of QDs.

Besides, the major issue among state-of-the-art QDs-based optoelectronic devices is the use of QDs with heavy metals (such as Pb, Cd *etc.*), which are harmful to the environment and human health and hinder their practical usages. Therefore, it is suggested that developing heavy metal-free core–shell QDs (typically, I-III-VI group QDs) with excellent optical properties are essential and promising for prospective high-performance QDs-based optoelectronics. Unfortunately, due to their complex optical properties (*e.g.*, defect-related emission), current heavy metal-free core–shell QDs-based solar energy conversion devices suffer lower performance challenges despite their intrinsic broad light absorption as compared to heavy metals-based core–shell QDs. More effective approaches for enhancing the optical properties of heavy metal-free core–shell QDs and optimizing the performance of corresponding QD-devices should be explored in terms of future commercialization.

References

1. G. H. Carey, A. L. Abdelhady, Z. Ning, S. M. Thon, O. M. Bakr and E. H. Sargent, *Chem. Rev.*, 2015, **115**, 12732.
2. R. Ghosh Chaudhuri and S. Paria, *Chem. Rev.*, 2012, **112**, 2373.
3. A. M. Smith and S. Nie, *Acc. Chem. Res.*, 2010, **43**, 190.
4. H. Zhao and F. Rosei, *Chem*, 2017, **3**, 229.
5. C. Giansante and I. Infante, *J. Phys. Chem. Lett.*, 2017, **8**, 5209.
6. H. Moon, C. Lee, W. Lee, J. Kim and H. Chae, *Adv. Mater.*, 2019, **31**, 1804294.
7. C. B. Murray, C. R. Kagan and M. G. Bawendi, *Science*, 1995, **270**, 1335.
8. M. Green, *J. Mater. Chem.*, 2010, **20**, 5797.
9. A. I. Channa, X. Tong, J.-Y. Xu, Y. Liu, C. Wang, M. N. Sial, P. Yu, H. Ji, X. Niu and Z. M. Wang, *J. Mater. Chem. A*, 2019, **7**, 10225.
10. A. Piryatinski, S. A. Ivanov, S. Tretiak and V. I. Klimov, *Nano Lett.*, 2007, **7**, 108.
11. S. Kim, B. Fisher, H.-J. Eisler and M. Bawendi, *J. Am. Chem. Soc.*, 2003, **125**, 11466.
12. H. Zhu, N. Song and T. Lian, *J. Am. Chem. Soc.*, 2011, **133**, 8762.

13. Y. Jia, J. Chen, K. Wu, A. Kaledin, D. G. Musaev, Z. Xie and T. Lian, *Chem. Sci.*, 2016, **7**, 4125.
14. M. Jalalah, M. S. Al-Assiri and J.-G. Park, *Adv. Energy Mater.*, 2018, **8**, 1703418.
15. J. S. Steckel, J. P. Zimmer, S. Coe-Sullivan, N. E. Stott, V. Bulović and M. G. Bawendi, *Angew. Chem., Int. Ed.*, 2004, **43**, 2154.
16. L. Li and P. Reiss, *J. Am. Chem. Soc.*, 2008, **130**, 11588.
17. J. B. Sambur and B. A. Parkinson, *J. Am. Chem. Soc.*, 2010, **132**, 2130.
18. M. A. Hines and P. Guyot-Sionnest, *J. Phys. Chem.*, 1996, **100**, 468.
19. J.-J. Hao, J. Zhou and C.-Y. Zhang, *Chem. Commun.*, 2013, **49**, 6346.
20. B. Chon, S. J. Lim, W. Kim, J. Seo, H. Kang, T. Joo, J. Hwang and S. K. Shin, *Phys. Chem. Chem. Phys.*, 2010, **12**, 9312.
21. B. Dong, L. Cao, G. Su and W. Liu, *Chem. Commun.*, 2010, **46**, 7331.
22. B. O. Dabbousi, J. Rodriguez-Viejo, F. V. Mikulec, J. R. Heine, H. Mattoussi, R. Ober, K. F. Jensen and M. G. Bawendi, *J. Phys. Chem. B*, 1997, **101**, 9463.
23. D. V. Talapin, A. L. Rogach, A. Kornowski, M. Haase and H. Weller, *Nano Lett.*, 2001, **1**, 207.
24. S. Kudera, M. Zanella, C. Giannini, A. Rizzo, Y. Li, G. Gigli, R. Cingolani, G. Ciccarella, W. Spahl, W. J. Parak and L. Manna, *Adv. Mater.*, 2007, **19**, 548.
25. H. Zhu, N. Song and T. Lian, *J. Am. Chem. Soc.*, 2010, **132**, 15038.
26. K. Yu, B. Zaman, S. Romanova, D.-s. Wang and J. A. Ripmeester, *Small*, 2005, **1**, 332.
27. J. Wang, I. Mora-Seró, Z. Pan, K. Zhao, H. Zhang, Y. Feng, G. Yang, X. Zhong and J. Bisquert, *J. Am. Chem. Soc.*, 2013, **135**, 15913.
28. R. Xie, X. Zhong and T. Basché, *Adv. Mater.*, 2005, **17**, 2741.
29. R. Xie, U. Kolb and T. Basché, *Small*, 2006, **2**, 1454.
30. D. J. Milliron, S. M. Hughes, Y. Cui, L. Manna, J. Li, L.-W. Wang and A. Paul Alivisatos, *Nature*, 2004, **430**, 190.
31. S. A. Ivanov, A. Piryatinski, J. Nanda, S. Tretiak, K. R. Zavadil, W. O. Wallace, D. Werder and V. I. Klimov, *J. Am. Chem. Soc.*, 2007, **129**, 11708.
32. A. M. Smith, A. M. Mohs and S. Nie, *Nat. Nanotechnol.*, 2009, **4**, 56.
33. J. Bang, J. Park, J. H. Lee, N. Won, J. Nam, J. Lim, B. Y. Chang, H. J. Lee, B. Chon, J. Shin, J. B. Park, J. H. Choi, K. Cho, S. M. Park, T. Joo and S. Kim, *Chem. Mater.*, 2010, **22**, 233.
34. S. Kim, Y. T. Lim, E. G. Soltesz, A. M. De Grand, J. Lee, A. Nakayama, J. A. Parker, T. Mihaljevic, R. G. Laurence, D. M. Dor, L. H. Cohn, M. G. Bawendi and J. V. Frangioni, *Nat. Biotechnol.*, 2004, **22**, 93.
35. X. Tong, X. Li, A. I. Channa, R. Liu, J.-Y. Xu, P. Yu, L. Chang, H. Ji, Q. Wang and Z. M. Wang, *Sol. RRL*, 2019, **3**, 1900186.
36. C.-Y. Chen, C.-T. Cheng, J.-K. Yu, S.-C. Pu, Y.-M. Cheng, P.-T. Chou, Y.-H. Chou and H.-T. Chiu, *J. Phys. Chem. B*, 2004, **108**, 10687.
37. N. N. Hewa-Kasakarage, M. Kirsanova, A. Nemchinov, N. Schmall, P. Z. El-Khoury, A. N. Tarnovsky and M. Zamkov, *J. Am. Chem. Soc.*, 2009, **131**, 1328.

38. S. Brovelli, R. D. Schaller, S. A. Crooker, F. García-Santamaría, Y. Chen, R. Viswanatha, J. A. Hollingsworth, H. Htoon and V. I. Klimov, *Nat. Commun.*, 2011, **2**, 280.
39. C. Wang, X. Tong, W. Wang, J.-Y. Xu, L. V. Besteiro, A. I. Channa, F. Lin, J. Wu, Q. Wang, A. O. Govorov, A. Vomiero and Z. M. Wang, *ACS Appl. Mater. Interfaces*, 2020, **12**, 36277.
40. K. Wu, N. Song, Z. Liu, H. Zhu, W. Rodríguez-Córdoba and T. Lian, *J. Phys. Chem. A*, 2013, **117**, 7561.
41. F. García-Santamaría, S. Brovelli, R. Viswanatha, J. A. Hollingsworth, H. Htoon, S. A. Crooker and V. I. Klimov, *Nano Lett.*, 2011, **11**, 687.
42. A. Pandey and P. Guyot-Sionnest, *Science*, 2008, **322**, 929.
43. B. De Geyter, Y. Justo, I. Moreels, K. Lambert, P. F. Smet, D. Van Thourhout, A. J. Houtepen, D. Grodzinska, C. de Mello Donega, A. Meijerink, D. Vanmaekelbergh and Z. Hens, *ACS Nano*, 2011, **5**, 58.
44. X. Tong, X.-T. Kong, Y. Zhou, F. Navarro-Pardo, G. S. Selopal, S. Sun, A. O. Govorov, H. Zhao, Z. M. Wang and F. Rosei, *Adv. Energy Mater.*, 2018, **8**, 1701432.
45. X. Tong, X.-T. Kong, C. Wang, Y. Zhou, F. Navarro-Pardo, D. Barba, D. Ma, S. Sun, A. O. Govorov, H. Zhao, Z. M. Wang and F. Rosei, *Adv. Sci.*, 2018, **5**, 1800656.
46. X. Wen, A. Sitt, P. Yu, Y.-R. Toh and J. Tang, *Phys. Chem. Chem. Phys.*, 2012, **14**, 3505.
47. B. N. Pal, Y. Ghosh, S. Brovelli, R. Laocharoensuk, V. I. Klimov, J. A. Hollingsworth and H. Htoon, *Nano Lett.*, 2012, **12**, 331.
48. D. Kong, Y. Jia, Y. Ren, Z. Xie, K. Wu and T. Lian, *J. Phys. Chem. C*, 2018, **122**, 14091.
49. D. Yu, C. Wang and P. Guyot-Sionnest, *Science*, 2003, **300**, 1277.
50. H. Zhu, N. Song, W. Rodríguez-Córdoba and T. Lian, *J. Am. Chem. Soc.*, 2012, **134**, 4250.
51. Z. Pan, H. Rao, I. Mora-Seró, J. Bisquert and X. Zhong, *Chem. Soc. Rev.*, 2018, **47**, 7659.
52. S. Jiao, Q. Shen, I. Mora-Seró, J. Wang, Z. Pan, K. Zhao, Y. Kuga, X. Zhong and J. Bisquert, *ACS Nano*, 2015, **9**, 908.
53. Z. Ning, H. Tian, C. Yuan, Y. Fu, H. Qin, L. Sun and H. Ågren, *Chem. Commun.*, 2011, **47**, 1536.
54. J. Yang and X. Zhong, *J. Mater. Chem. A*, 2016, **4**, 16553–16561.
55. J. Luo, H. Wei, F. Li, Q. Huang, D. Li, Y. Luo and Q. Meng, *Chem. Commun.*, 2014, **50**, 3464.
56. J. Yang, J. Wang, K. Zhao, T. Izuishi, Y. Li, Q. Shen and X. Zhong, *J. Phys. Chem. C*, 2015, **119**, 28800–28808.
57. S. Buhbut, S. Itzhakov, I. Hod, D. Oron and A. Zaban, *Nano Lett.*, 2013, **13**, 4456.
58. M. Kazes, S. Buhbut, S. Itzhakov, O. Lahad, A. Zaban and D. Oron, *J. Phys. Chem. Lett.*, 2014, **5**, 2717.
59. S. Sahai, A. Ikram, S. Rai, R. Shrivastav, S. Dass and V. R. Satsangi, *Renewable Sustainable Energy Rev.*, 2017, **68**, 19.

60. L. Jin, B. AlOtaibi, D. Benetti, S. Li, H. Zhao, Z. Mi, A. Vomiero and F. Rosei, *Adv. Sci.*, 2016, **3**, 1500345.
61. K. Wang, X. Tong, Y. Zhou, H. Zhang, F. Navarro-Pardo, G. S. Selopal, G. Liu, J. Tang, Y. Wang, S. Sun, D. Ma, Z. M. Wang, F. Vidal, H. Zhao, X. Sun and F. Rosei, *J. Mater. Chem. A*, 2019, **7**, 14079.
62. R. Wang, X. Tong, A. I. Channa, Q. Zeng, J. Sun, C. Liu, X. Li, J. Xu, F. Lin, G. S. Selopal, F. Rosei, Y. Zhang, J. Wu, H. Zhao, A. Vomiero, X. Sun and Z. M. Wang, *J. Mater. Chem. A*, 2020, **8**, 10736.
63. X. Tong, Y. Zhou, L. Jin, K. Basu, R. Adhikari, G. S. Selopal, X. Tong, H. Zhao, S. Sun, A. Vomiero, Z. M. Wang and F. Rosei, *Nano Energy*, 2017, **31**, 441.
64. N. D. Bronstein, Y. Yao, L. Xu, E. O'Brien, A. S. Powers, V. E. Ferry, A. P. Alivisatos and R. G. Nuzzo, *ACS Photonics*, 2015, **2**, 1576–1583.
65. Y. You, X. Tong, W. Wang, J. Sun, P. Yu, H. Ji, X. Niu and Z. M. Wang, *Adv. Sci.*, 2019, **6**, 1801967.
66. F. Purcell-Milton and Y. K. Gun'ko, *J. Mater. Chem.*, 2012, **22**, 16687.
67. K. Wu, H. Li and V. I. Klimov, *Nat. Photonics*, 2018, **12**, 105.
68. Y. Zhou, H. Zhao, D. Ma and F. Rosei, *Chem. Soc. Rev.*, 2018, **47**, 5866.
69. S. Sadeghi, H. Bahmani Jalali, R. Melikov, B. Ganesh Kumar, M. Mohammadi Aria, C. W. Ow-Yang and S. Nizamoglu, *ACS Appl. Mater. Interfaces*, 2018, **10**, 12975.
70. M. Sharma, K. Gungor, A. Yeltik, M. Olutas, B. Guzelturk, Y. Kelestemur, T. Erdem, S. Delikanli, J. R. McBride and H. V. Demir, *Adv. Mater.*, 2017, **29**, 1700821.
71. H. Zhao, D. Benetti, L. Jin, Y. Zhou, F. Rosei and A. Vomiero, *Small*, 2016, **12**, 5354.
72. M. J. Currie, J. K. Mapel, T. D. Heidel, S. Goffri and M. A. Baldo, *Science*, 2008, **321**, 226.
73. R. Mazzaro and A. Vomiero, *Adv. Energy Mater.*, 2018, **8**, 1801903.
74. U. Resch-Genger, M. Grabolle, S. Cavaliere-Jaricot, R. Nitschke and T. Nann, *Nat. Methods*, 2008, **5**, 763.
75. L. Xu, Y. Yao, N. D. Bronstein, L. Li, A. P. Alivisatos and R. G. Nuzzo, *ACS Photonics*, 2016, **3**, 278.
76. F. Meinardi, A. Colombo, K. A. Velizhanin, R. Simonutti, M. Lorenzon, L. Beverina, R. Viswanatha, V. I. Klimov and S. Brovelli, *Nat. Photonics*, 2014, **8**, 392.
77. Y. Zhou, D. Benetti, Z. Fan, H. Zhao, D. Ma, A. O. Govorov, A. Vomiero and F. Rosei, *Adv. Energy Mater.*, 2016, **6**, 1501913.
78. H. Zhao, M. Chaker and D. Ma, *J. Mater. Chem.*, 2011, **21**, 17483.
79. I. Coropceanu and M. G. Bawendi, *Nano Lett.*, 2014, **14**, 4097.
80. C. Li, W. Chen, D. Wu, D. Quan, Z. Zhou, J. Hao, J. Qin, Y. Li, Z. He and K. Wang, *Sci. Rep.*, 2015, **5**, 17777.
81. L. Peng, L. Hu and X. Fang, *Adv. Mater.*, 2013, **25**, 5321.
82. S. Liu, M.-Y. Li, D. Su, M. Yu, H. Kan, H. Liu, X. Wang and S. Jiang, *ACS Appl. Mater. Interfaces*, 2018, **10**, 32516.

83. G. Konstantatos, I. Howard, A. Fischer, S. Hoogland, J. Clifford, E. Klem, L. Levina and E. H. Sargent, *Nature*, 2006, **442**, 180.
84. S. A. McDonald, G. Konstantatos, S. Zhang, P. W. Cyr, E. J. D. Klem, L. Levina and E. H. Sargent, *Nat. Mater.*, 2005, **4**, 138.
85. L. Gao, C. Chen, K. Zeng, C. Ge, D. Yang, H. Song and J. Tang, *Light: Sci. Appl.*, 2016, **5**, e16126.
86. W. Ouyang, F. Teng, J.-H. He and X. Fang, *Adv. Funct. Mater.*, 2019, **29**, 1807672.
87. S. Zhang, X. Wang, Y. Chen, G. Wu, Y. Tang, L. Zhu, H. Wang, W. Jiang, L. Sun, T. Lin, H. Shen, W. Hu, J. Ge, J. Wang, X. Meng and J. Chu, *ACS Appl. Mater. Interfaces*, 2019, **11**, 23667.
88. Y.-H. Chang, W. Zhang, Y. Zhu, Y. Han, J. Pu, J.-K. Chang, W.-T. Hsu, J.-K. Huang, C.-L. Hsu, M.-H. Chiu, T. Takenobu, H. Li, C.-I. Wu, W.-H. Chang, A. T. S. Wee and L.-J. Li, *ACS Nano*, 2014, **8**, 8582.
89. S. Pak, Y. Cho, J. Hong, J. Lee, S. Lee, B. Hou, G.-H. An, Y.-W. Lee, J. E. Jang, H. Im, S. M. Morris, J. I. Sohn, S. Cha and J. M. Kim, *ACS Appl. Mater. Interfaces*, 2018, **10**, 38264–38271.
90. C. Bi, S. V. Kershaw, A. L. Rogach and J. Tian, *Adv. Funct. Mater.*, 2019, **29**, 1902446.
91. X. Dai, Y. Deng, X. Peng and Y. Jin, *Adv. Mater.*, 2017, **29**, 1607022.
92. S. Pimputkar, J. S. Speck, S. P. DenBaars and S. Nakamura, *Nat. Photonics*, 2009, **3**, 180.
93. P. O. Anikeeva, J. E. Halpert, M. G. Bawendi and V. Bulović, *Nano Lett.*, 2009, **9**, 2532.
94. Z. Yang, M. Gao, W. Wu, X. Yang, X. W. Sun, J. Zhang, H.-C. Wang, R.-S. Liu, C.-Y. Han, H. Yang and W. Li, *Mater. Today*, 2019, **24**, 69.
95. Y.-C. Pu and Y.-J. Hsu, *Nanoscale*, 2014, **6**, 3881.
96. J. Lim, B. G. Jeong, M. Park, J. K. Kim, J. M. Pietryga, Y.-S. Park, V. I. Klimov, C. Lee, D. C. Lee and W. K. Bae, *Adv. Mater.*, 2014, **26**, 8034.
97. X. Dai, Z. Zhang, Y. Jin, Y. Niu, H. Cao, X. Liang, L. Chen, J. Wang and X. Peng, *Nature*, 2014, **515**, 96.
98. B. S. Mashford, M. Stevenson, Z. Popovic, C. Hamilton, Z. Zhou, C. Breen, J. Steckel, V. Bulovic, M. Bawendi, S. Coe-Sullivan and P. T. Kazlas, *Nat. Photonics*, 2013, **7**, 407.
99. D. Bozyigit, O. Yarema and V. Wood, *Adv. Funct. Mater.*, 2013, **23**, 3024.
100. Y. Shirasaki, G. J. Supran, W. A. Tisdale and V. Bulović, *Phys. Rev. Lett.*, 2013, **110**, 217403.
101. H. Zhang, N. Hu, Z. Zeng, Q. Lin, F. Zhang, A. Tang, Y. Jia, L. S. Li, H. Shen, F. Teng and Z. Du, *Adv. Opt. Mater.*, 2019, **7**, 1801602.
102. Y. Li, X. Hou, X. Dai, Z. Yao, L. Lv, Y. Jin and X. Peng, *J. Am. Chem. Soc.*, 2019, **141**, 6448.
103. H. Zhang, S. Chen and X. W. Sun, *ACS Nano*, 2018, **12**, 697–704.
104. Y. Shirasaki, G. J. Supran, M. G. Bawendi and V. Bulović, *Nat. Photonics*, 2013, **7**, 13.
105. H. Shen, Q. Gao, Y. Zhang, Y. Lin, Q. Lin, Z. Li, L. Chen, Z. Zeng, X. Li, Y. Jia, S. Wang, Z. Du, L. S. Li and Z. Zhang, *Nat. Photonics*, 2019, **13**, 192.

106. Y.-H. Won, O. Cho, T. Kim, D.-Y. Chung, T. Kim, H. Chung, H. Jang, J. Lee, D. Kim and E. Jang, *Nature*, 2019, **575**, 634.
107. X. Li, Y.-B. Zhao, F. Fan, L. Levina, M. Liu, R. Quintero-Bermudez, X. Gong, L. N. Quan, J. Fan, Z. Yang, S. Hoogland, O. Voznyy, Z.-H. Lu and E. H. Sargent, *Nat. Photonics*, 2018, **12**, 159.
108. H. Shen, W. Cao, N. T. Shewmon, C. Yang, L. S. Li and J. Xue, *Nano Lett.*, 2015, **15**, 1211.
109. V. I. Klimov, A. A. Mikhailovsky, S. Xu, A. Malko, J. A. Hollingsworth, C. A. Leatherdale, H. J. Eisler and M. G. Bawendi, *Science*, 2000, **290**, 314.
110. V. I. Klimov, A. A. Mikhailovsky, D. W. McBranch, C. A. Leatherdale and M. G. Bawendi, *Science*, 2000, **287**, 1011.
111. F. Fan, O. Voznyy, R. P. Sabatini, K. T. Bicanic, M. M. Adachi, J. R. McBride, K. R. Reid, Y.-S. Park, X. Li, A. Jain, R. Quintero-Bermudez, M. Saravanapavanantham, M. Liu, M. Korkusinski, P. Hawrylak, V. I. Klimov, S. J. Rosenthal, S. Hoogland and E. H. Sargent, *Nature*, 2017, **544**, 75.
112. C. Liao, R. Xu, Y. Xu, C. Zhang, M. Xiao, L. Zhang, C. Lu, Y. Cui and J. Zhang, *J. Phys. Chem. Lett.*, 2016, **7**, 4968.
113. Y.-S. Park, W. K. Bae, T. Baker, J. Lim and V. I. Klimov, *Nano Lett.*, 2015, **15**, 7319.
114. M. Zavelani-Rossi, M. G. Lupo, R. Krahne, L. Manna and G. Lanzani, *Nanoscale*, 2010, **2**, 931.
115. F. García-Santamaría, Y. Chen, J. Vela, R. D. Schaller, J. A. Hollingsworth and V. I. Klimov, *Nano Lett.*, 2009, **9**, 3482.
116. C. Dang, J. Lee, C. Breen, J. S. Steckel, S. Coe-Sullivan and A. Nurmikko, *Nat. Nanotechnol.*, 2012, **7**, 335.
117. B. le Feber, F. Prins, E. De Leo, F. T. Rabouw and D. J. Norris, *Nano Lett.*, 2018, **18**, 1028.

CHAPTER 22

Nanoarchitectonics of Stretchable Organic Electronics Materials

DING ZHANG[a], WEN HE[a] AND RUJUN MA*[a]

[a]School of Materials Science and Engineering, National Institute for Advanced Materials, Tianjin Key Lab for Rare Earth Materials and Applications, Nankai University, Tongyan Road 38, Tianjin, 300350, P. R. China
*E-mail: malab@nankai.edu.cn

22.1 Introduction

With the improvement of human material demand, as well as the continuous development of science and technology, flexible and stretchable organic electronic materials have obtained great development and attracted extensive attention in academia.[1–5] Nowadays, intrinsically stretchable electronic materials are widely used in different fields including electronic skin (e-skin),[6–8] stretchable strain sensors,[9–12] health monitoring,[13–15] soft robotics,[16–18] artificial muscles,[19–22] *etc.* As the basis and core of stretchable electronics, the mechanical and electrical properties of stretchable electronic materials can directly affect the output performance and practical application. To better realize the potential and feasible applications, it is important for intrinsically stretchable electronic materials and devices to achieve the best performance by reasonable materials selection and structure optimization.

Nanoscience & Nanotechnology Series No. 55
Concepts and Design of Materials Nanoarchitectonics
Edited by Omar Azzaroni and Katsuhiko Ariga

Published by the Royal Society of Chemistry, www.rsc.org

The traditional block inorganic conducting materials, such as metal and single crystal silicon, usually exhibit weak stretchability, or that these materials will break or occur plastic deformation under a small stretchable strain, which is not suitable for the preparation of stretchable electronics.[23–25] The stretchability of inorganic electronic materials can be obtained by means of stretchable organic polymer elastomers. Through depositing or embedding the active materials with specific geometric morphology or thin-layer structure on the surface of a pre-stretched matrix, researchers have successfully fabricated extrinsically stretchable inorganic electronic materials with curved or wave shapes after removing the applied pre-strain.[26–28] In addition, by using the kirigami-inspired technology, a freestanding polymer nanosheet with a hollow structure can achieve a superhigh stretchable strain and a constant electrical conductivity during strain ranging from 0% to 2000%.[29] Additionally, by mixing nanostructured conducting materials with stretchable organic elastomer, an interpenetrating percolation network can be formed inside the elastomer substrate, which will realize the preparation of intrinsically stretchable organic conducting materials.[30,31] For example, researchers successfully designed stretchable silver nanowires (AgNWs)/PDMS and carbon nanotubes (CNTs)/PDMS conducting composites, and the percolation network formed between one-dimensional AgNWs or CNTs will allow electrons to transfer easier across conducting polymer composites, showing excellent electrical property.[32,33]

The fabricated extrinsically and intrinsically stretchable conducting materials based on the two methods above can maintain good electrical conductivity within a certain strain range. However, the two methods still possess their shortcomings and face many restrictions. For example, the fabricated extrinsically stretchable electronic materials with meandering or wavy structure based on a pre-stretched elastomer can only be stretched along with the direction of pre-stretched direction under normal working conditions, and the stretchability of electronic materials entirely depends on the degree of pre-stretch, which limit and impede the development and application of stretchable organic electronic materials.[27–29] For intrinsically stretchable composite materials prepared by mixing electronic materials with organic elastomer, the preparation process may cause uneven materials with a large error of mechanical and electrical properties. In order to overcome these shortcomings, by introducing an appropriate crosslinking network and π–π stacking into organic electronic materials, the prepared intrinsically conducting polymers can obtain greater stretchable strain in different stretching directions including traditional conducting polymers, polymer hydrogels and ionic conducting elastomers.[34–36] This kind of intrinsically conducting elastomers can keep excellent electrical performance, realize high-density integration of small devices at the same time. Besides, owing to simple preparation, mass production, excellent biocompatibility and self-healing performance, these stretchable organic electronic materials show great application prospects in the field of wearable electronics and health monitoring.

In this chapter, some typical intrinsically stretchable organic conducting electronic materials were selected as research objects, including stretchable conducting organic composites and intrinsically stretchable conducting polymers. Then, we systematically analyzed the effect of micromorphology on mechanical and electrical properties of organic electronic materials, then discussed the structure engineering and output performance of corresponding electronic devices. Furthermore, the practical and potential applications of these typical materials were explored and analyzed. Finally, we discussed the development directions, possible challenges and opportunities of intrinsically stretchable organic electronic materials in the future.

22.2 Stretchable Organic Conducting Material-polymer Composites

It is one of the most common methods to design intrinsically stretchable electronic composite materials by mixing active materials with a soft matrix based on morphological control. Owing to the easy preparation process and lost cost, a large number of stretchable conducting inorganic-organic composites have been fabricated and widely used in different fields, such as flexible and wearable strain sensors, electronic skin, triboelectric nanogenerators and flexible heaters. The common inorganic-organic composites are composed of conductive materials (such as metal nanowires and carbon nanomaterials, *etc.*) and polymer matrix (such as polydimethylsiloxane (PDMS), Ecoflex, polyurethane).[26,37–41] In this section, we choose several representative conductive materials as research objects including metal nanomaterials (silver nanowires (AgNWs), copper nanowires, *etc.*),[42–46] carbon nanomaterials (carbon nanotube (CNTs) and graphene)[47,48] and liquid metals,[49–51] and discuss and overview the strategies of nanostructure engineering and performance optimization of intrinsically stretchable conducting electronic materials.

22.2.1 Metal Nanomaterial-based Composites

AgNWs have shown broad application potential in transparent devices, solar cells, and flexible heaters owing to excellent electrical, optical, and mechanical properties. Based on AgNWs networks and PDMS elastomer, researchers designed a highly flexible and stretchable strain sensor with a sandwich structure.[32] Figure 22.1a$_1$ shows the surface SEM image of the AgNWs embedded onto PDMS forming AgNWs/PDMS composite, indicating that all AgNWs are evenly distributed on the surface of PDMS, which attributes to the appropriate viscosity of PDMS and excellent adhesion between AgNWs and PDMS. The sandwich-structured strain sensor was fabricated by pouring liquid PDMS onto the surface of AgNWs/PDMS composite, Figure 22.1a$_2$ gives the corresponding cross-sectional morphology. We can see that the

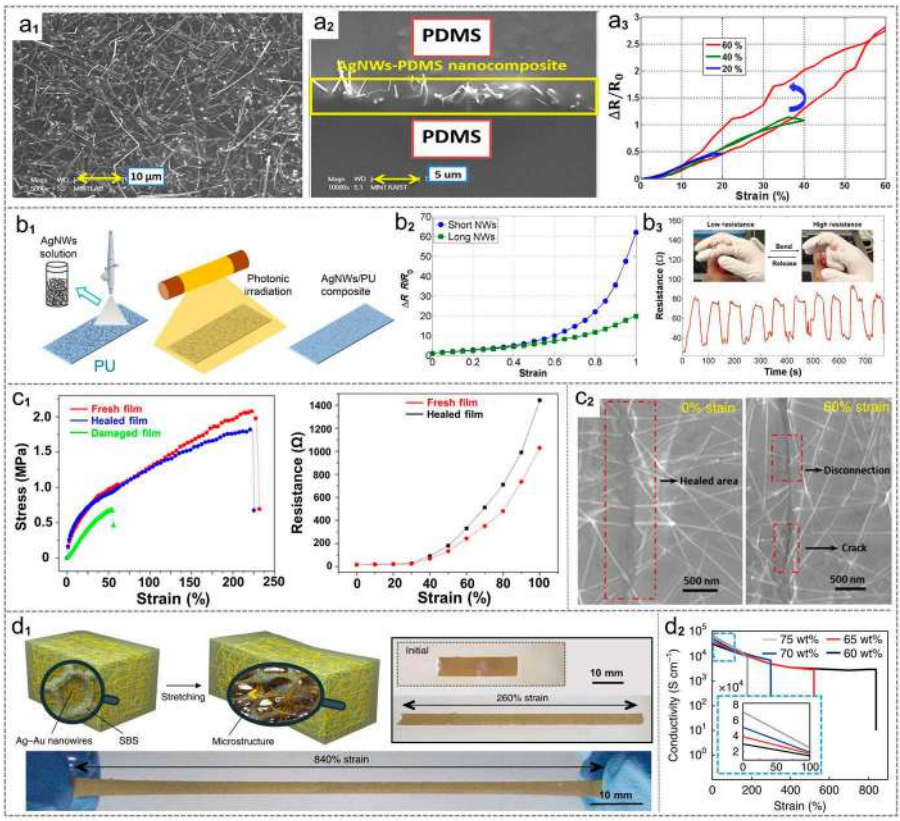

Figure 22.1 (a_1) Surface SEM image of AgNWs embedded onto PDMS matrix. (a_2 and a_3) Cross-sectional SEM image (a_2) and hysteresis curves (a_3) of PDMS/AgNWs/PDMS strain sensor. Reproduced from ref. 32 with permission from American Chemical Society, Copyright 2014. (b_1) Preparation process of AgNWs/PU composite. (b_2) Resistance change curves of the AgNWs/PU strain sensors corresponding to the AgNWs with different lengths during the strain from 0% to 100%. (b_3) Detection of a finger motion by a PDMS/AgNWs/PDMS strain sensor. Reproduced from ref. 37 with permission from Springer Nature, Copyright 2016. (c_1) Stretchability comparison of fresh and healed AgNW/PEDOT composite electrodes. (c_2) SEM images of a healed AgNW/PEDOT composite film at 0% strain and 60% strain. Reproduced from ref. 53 with permission from American Chemical Society, Copyright 2015. (d_1) Microstructure diagram of the Ag–Au–SBS nanocomposite and optical images of the nanocomposite at different stretchable strains (d_2) Electrical conductivity variation of stretchable nanocomposites with different Ag–Au content. Reproduced from ref. 54 with permission from Springer Nature, Copyright 2018.

liquid PDMS precursor completely enters the pores of the three-dimensional (3D) AgNWs network to form a robust organic conducting composite with outstanding mechanical properties. During the stretchable strain from 0% to 70%, the sandwich-structured strain sensor still maintains outstanding stability.[32] As shown in Figure 22.1a$_3$, there is no conspicuous hysteresis of strain response of the sandwich-structured strain sensor under repetitive stretch/release strain from 0% to 40%. When the stretchable strain increases up to 60%, the hysteresis phenomenon occurs due to the hysteresis effect of the PDMS matrix.[52] Whereas, when the applied strain is released to 0%, the initial resistance can be fully recovered. Based on AgNWs solution and high-intensity pulsed light (HIPL) technique, a highly stretchable AgNWs/PU composite electrode was fabricated by spray-depositing the AgNWs/ethanol solution onto PU matrix and then being treated by HIPL technique, as seen from Figure 22.1b$_1$.[37] After 1000 repetitive cyclic strain from 0% to 100%, the resistance of AgNWs/PU composite still retains a small value about 10 Ω/sq. In order to explore the effect of AgNWs length on the electrical property of AgNWs/PU composite at different strains, two different PU composites were fabricated by using long NWs and short NWs respectively. The comparison as displayed in Figure 22.1b$_2$,[37] demonstrating that there is no obvious difference between long and short NWs during the strain ranging from 0% to 50%, while the resistance variation of short NWs is larger than that of long NWs during 50% to 100% strain. It can be explained that the increase of strain will cause the displacement of AgNWs, and the long nanowires can still maintain relatively good interconnection of AgNWs network, leading to a smaller change in resistance compared with short AgNWs. The fabricated AgNWs/PU composite electrode can be capable of monitoring human motion as a wearable strain sensor. According to Figure 22.1b$_3$, different degrees of finger bend can be precisely detected through measuring and analyzing corresponding resistance change.[37] Additionally, the stretchable AgNWs/PU composite can act as a flexible electrode substrate for integrating light emitting diodes (LEDs) as smart windows owing to the high transparency of the composite electrode.

To improve the service life and maintain good performance of stretchable devices, designing self-healable devices has become one of the most important strategies. Pei *et al.* fabricated a healable stretchable composite film based on AgNWs and poly(3,4-ethylenedioxythiophene):polystyrene sulfonate (PEDOT:PSS) composite as conductive composite network, and a Diels–Alder (DA) elastomer as stretchable substrate.[53] The damaged film can be healed with high temperature treatment owing to the reversible cycloaddition reaction in DA elastomer. As shown in Figure 22.1c$_1$, the healed film retains good stretchability and electrical properties close to the initial performance of the fresh film. Figure 22.1c$_2$ shows a healed AgNWs/PEDOT/DA composite film at 0% strain and 60% strain, and it is observed that AgNWs network and PEDOT layer can reconnect by the healing process of DA elastomer.[53] At 60% strain, some disconnected AgNWs and cracks can be seen, suggesting the incomplete healing of AgNWs. However, the healed film still maintains a low resistance of about 310 Ω, slightly larger than that

of fresh film at 60% strain. During the process of preparation and application of AgNWs, partial AgNWs may be oxidized. To overcome this drawback, researchers designed a highly stretchable Ag–Au nanocomposite consisting of ultralong gold-coated silver nanowires and poly(styrene-butadiene-styrene) (SBS) block-copolymeric elastomer.[54] The thick gold layer coated on AgNWs surface can prevent the oxidation of AgNWs and make the stretchable composite biocompatible and highly conductive. Figure 22.1d$_1$ displays the microstructure diagram of the Ag–Au–SBS nanocomposite, showing a high stretchability up to 260% of the nanocomposite with 60% Ag–Au content. When the freestanding Ag–Au–SBS nanocomposite was covered with two VHB films with a sandwich structure, the stretchability greatly increased up to 840%. With the increase of Ag–Au NWs content from 60% to 75%, the nanocomposite has an increasing electrical conductivity but a decreased breaking strain from 840% to 180%, as observed in Figure 22.1d$_2$.[54]

Except for acting as a strain sensing and flexible electrode, the stretchable composite consisting of conductive active materials and organic elastomer can also act as a flexible heater for temperature regulation. By embedding AgNWs conductive network onto PDMS elastomer, a highly transparent and stretchable heater was designed with excellent electrical and thermal stability at an increasing strain from 0% to 60% owing to unique morphology and interconnection of AgNWs network and PDMS elastomer.[1] This stretchable heater can maintain a stable temperature (50 °C) at a 0–40% tensile strain by regulating applied external voltage (2.8–6.2 V). To better meet the requirement of wearable electronics, researchers fabricated a stretchable heating fabric based on hierarchical structural fibers for realizing personal heating regulation.[42] Figure 22.2a$_1$ shows the hierarchical structure of heating fiber consisting of CuNWs as active material, polyester (PE) as yarn and an elastic

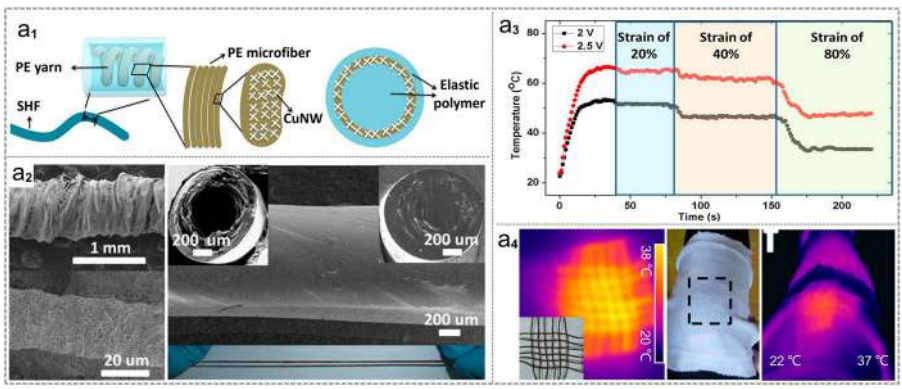

Figure 22.2 (a_1) Hierarchical structure diagram of stretchable heating fiber. (a_2) Surface and cross-sectional SEM images of stretchable heating fiber. (a_3) Temperature variation of stretchable heating fiber at different strains. (a_4) Wearable fabric for temperature regulation of knee. Reproduced from ref. 42 with permission from American Chemical Society, Copyright 2016.

polymer as elastomer matrix. The microstructures of PE yarn coated with CuNWs and single PE fiber, morphology comparison between a hollow-core fiber and a solid-core fiber, are all observed in Figure 22.2a$_2$. Figure 22.2a$_3$ displays the Joule heating performance of the stretchable heating fiber, and we can see that at a certain external voltage, the heating fiber shows excellent thermal stability with fast response induced by an increasing strain. Figure 22.2a$_4$ demonstrates a heating fabric for wearable application, the fabric can realize thermal therapy of knee by integrating the heating fabric with clothes.

22.2.2 Carbon Nanomaterial-based Composites

As another important one-dimensional nanomaterial, CNTs also exhibit huge application potential in stretchable electronics. Through using overlapped CNT bundles embedded onto an Ecoflex elastomer, a highly sensitive strain sensor was fabricated as shown in Figure 22.3a$_1$.[55] As observed in Figure 22.3a$_2$, at a strain ranging from 125% to 145%, an ultrahigh sensitivity of the strain sensor can reach 42 300. In addition, the detection ability of small strain was also demonstrated by increasing the applied small strain from 0.1% to 0.5%, and the different resistance change rates were obtained, which indicate that strain resolution is no more than 0.1%. The high sensing performance including high sensitivity and strain resolution attribute to strain induced sliding or disconnection between overlapped CNTs bundle. As a wearable device, it can precisely monitor health conditions according to wrist pulse, as shown in Figure 22.3a$_3$.[55] By using a facile one-step coaxial wet-spinning method, a highly stretchable CNTs-polymer composite fiber with a core-sheath structure was successfully prepared as a fiber-shaped strain sensor for monitoring human movement.[56] In Figure 22.3b$_1$, the optical image shows excellent flexibility of the as-prepared coaxial fiber. From the cross-sectional SEM image, the core-sheath structure can be clearly observed. The outer diameter of the sheath layer (pure silicone elastomer) is about 1.7 mm and the inner diameter of the core (CNT-silicone elastomer) is about 1.0 mm. Figure 22.3b$_2$ gives the increasing electrical conductivity of the CNTs composite fiber with the increase of CNTs contents, and the fitting result based on percolation theory in inset confirms that the conductive network in fiber is formed by contact among CNTs.[56,57] Relative resistance variation of the core-sheath fiber (CSF) with different MWCNTs contents, 2 wt% and 3 wt% (marked as CSF-2 and CSF-3) as exhibited in Figure 22.3b$_3$. Both the resistances of CSF-2 and CSF-3 increase slowly at first, then increases rapidly once the stretchable strain up to a threshold value when the percolating network begins to break down under a condition of electrical depercolation. Figure 22.3b$_4$ displays the time-dependent relative resistance change with different peak strains, suggesting good cyclic stability.

As important carbon nanomaterials, graphene and graphite nanomaterials are also widely used in the preparation of stretchable conducting composites for strain sensing and wearable electronics. Wu *et al.* reported a high-efficiency fabrication method to produce a large mass of graphite

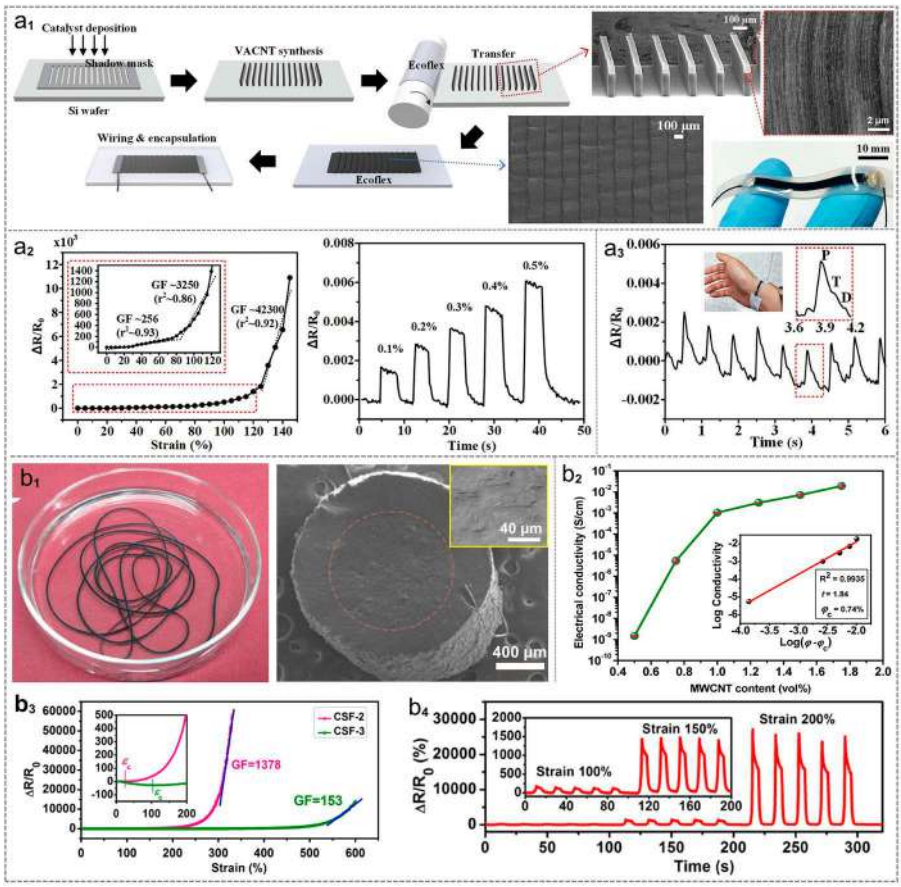

Figure 22.3 (a_1) The schematic diagram of the fabrication process of stretchable strain sensor. (a_2) Strain sensing property of the fabricated strain sensor. (a_3) Application for monitoring pulse. (a_4) Wearable fabric for temperature regulation of knee. Reproduced from ref. 55 with permission from American Chemical Society, Copyright 2019. (b_1) Optical image of the stretchable fiber and corresponding cross-sectional morphology. (b_2) Electrical conductivity variation of the conductive fiber with increasing MWCNT content. (b_3) Relative resistance change of the strain senor with different MWCNT contents. (b_4) Resistance change stability of the strain senor at different strains. Reproduced from ref. 56 with permission from American Chemical Society, Copyright 2018.

(GNP) and PU composite film, as shown in Figure 22.4a_1,[39] the length of GNP/PU film is up to 3.0 m. According to the SEM images of GNPs and GNP/PU composites, it is found that every initial GNP nanoplate has a sharp edge, and with the addition of PU, there are no obvious sharp GNP edges observed in the GNP/PU composite. As a wearable e-skin, it can detect bending and stretching motion with high sensitivity. As seen from Figure 22.4a_2 and a_3,

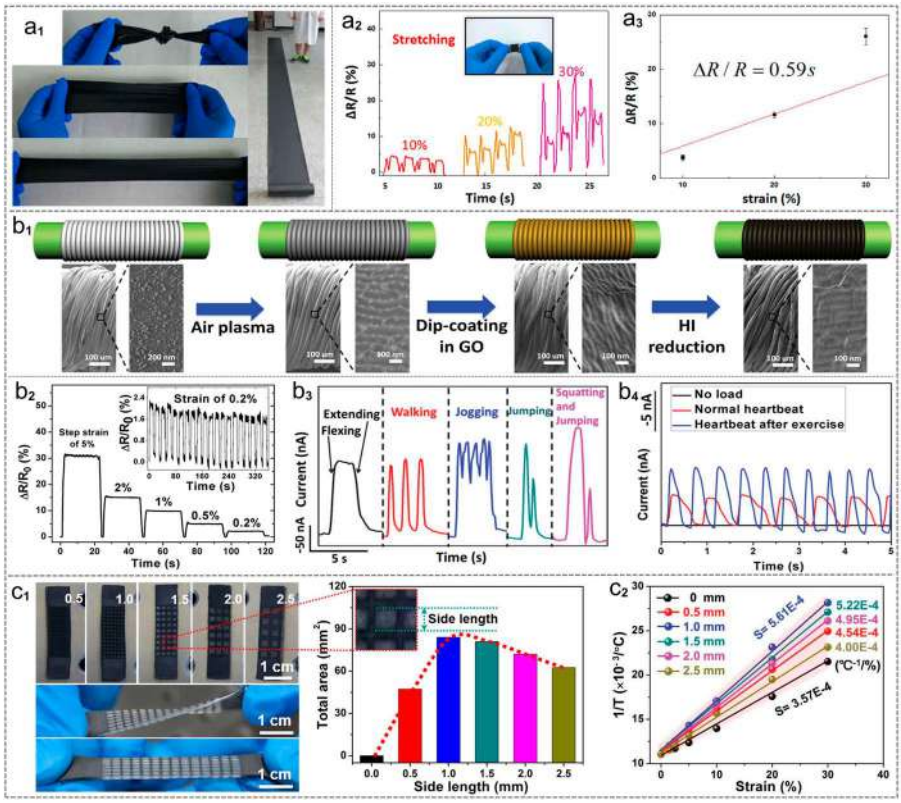

Figure 22.4 (a_1) Optical images of GNP/PU nanocomposite films. (a_2) Relative resistance variation of GNP/PU e-skin at different strains. (a_3) The fitting curve between relative resistance change rate and applied strain. Reproduced from ref. 39 with permission from American Chemical Society, Copyright 2017. (b_1) Schematic illustration of the fabrication process. (b_2) Relative resistance variation of the composite fiber at different stretchable strains. (b_3 and b_4) Responsive curves of a wearable sensor for monitoring knee motions (b_3) and heart-beat (b_4). Reproduced from ref. 58 with permission from John Wiley & Sons, Copyright © 2015 WILEY-VCH Verlag GmbH & Co. KGaA, Weinheim. (c_1) Optical images of graphene-Ecoflex film with various engraving morphologies and corresponding total engraving areas. (c_2) Linear fitting curves between $1/T$ and strain. Reproduced from ref. 66 with permission from John Wiley & Sons, Copyright © 2020 WILEY-VCH Verlag GmbH & Co. KGaA, Weinheim.

the GNP/PU film shows different resistance change responses to different stretchable strains with a strain sensitivity of about 0.59.[39] Based on high-performance two-dimensional graphene, researchers designed stretchable graphene/PE/PU composite fibers with 'compression spring' structure; the fabrication process as shown in Figure 22.4b_1.[58] The fabricated composite fiber exhibits ultrahigh sensitivity with a fast response (<100 ms), high strain

sensing range up to 100% and high cyclic stability over 10 000 cycles. In addition, the composite fiber also has excellent response to bending and torsion owing to special hierarchical microstructure. Figure 22.4b_2 exhibits relative resistance variation of the fiber at different stretchable strains, and the strain resolution is no more than 0.2%. As seen from Figure 22.4b_3 and b_4, the wearable sensor can monitor knee motion under different conditions including walking, jogging, jumping, and squatting-jumping. Through being attached to the wrist, the sensor can precisely monitor heart-beat with various motion conditions.[58]

There is no doubt that graphene is the most important two-dimensional material in recent decades owing to excellent thermal and electrical conductivity.[59–61] Likewise, graphene-polymer composites with good mechanical and electrical properties have showed huge application potential in self-powered strain sensing. Additionally, the preparation technology is relatively mature by depositing a graphene layer on a flexible matrix based on vacuum filtration.[62–65] Based on the above consideration and preparation method, Zhang *et al.* fabricated a graphene-Ecoflex nanocomposite for wireless small strain detection based on the Joule heating effect.[66] By engineering the surface structure of nanocomposite, the fabricated wireless strain sensor exhibited good cyclic stability and high strain sensitivity at the strain range from 0% to 30%. In order to obtain high sensitivity of the strain sensor, the surfaces of six strain sensors were engraved with different areas by a laser engraving machine, as shown in Figure 22.4c_1. The total graphene-free area of the strain sensor (engraving side length of 1.0 mm) is about 84 mm^2 larger than others. By controlling applied voltage, the initial stable temperatures of six specimens were about 90.5 °C. Then the temperatures of six strain sensors were recorded at the strain range from 0% to 30%. Figure 22.4c_2 displays the linear fitting curves between $1/T$ and strain, and the slope of the fitting line is the sensitivity of the stretchable strain sensor. We can see that the specimen has the highest sensitivity of 5.61×10^{-4} $°C^{-1}$ $\%^{-1}$ corresponding to the optimized engraving size of 1.0 mm of the strain sensor. Through using an infrared camera to detect temperature, a wearable and wireless strain sensor can realize wireless monitor strains with a high strain resolution of ≈0.1%.

22.2.3 Liquid Metal-based Composites

In recent years, liquid metals have exhibited huge application potential in stretchable electronics owing to low toxicity, good liquidity, no vapor pressure and high electrical conductivity.[51,67,68] Based on Galinstan alloy liquid metal and flexible polymer microchannel, researchers fabricated a flexible liquid metal coil–polymer composite for designing a stretchable acoustic device (SAD).[69] As demonstrated in Figure 22.5a_1 and a_2, the flexible liquid metal–polymer was stretched at a uniaxial strain range (0–50%) and a biaxial strain range (0–30%). The resistance increased gradually by 6% compared with the initial resistance. Both in the strain-releasing process of uniaxial

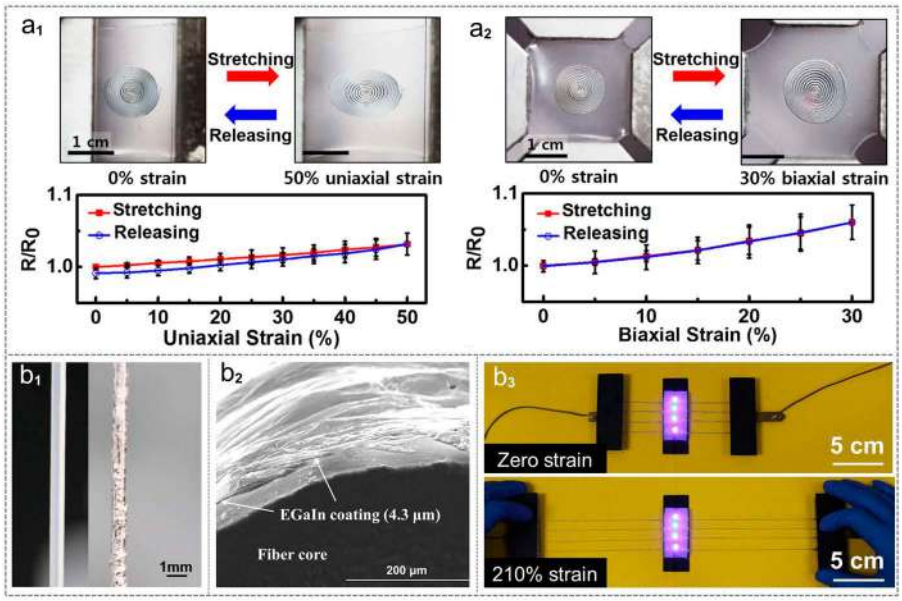

Figure 22.5 (a_1 and a_2) Optical images of the liquid metal microchannel at uniaxial (a_1) and (a_2) stretching strain, and corresponding normalized resistance change. Reproduced from ref. 69 with permission from Springer Nature, Copyright 2015. (b_1) Photographs of uncoated fiber and the coated one. (b_2) Microstructure of the interface between silicone fiber and EGaIn coating. (b_3) Photographs of stretchable fiber as conductive wire for powering LEDs. Reproduced from ref. 70 with permission from IOP Publishing Ltd, Copyright 2018.

and biaxial strain, the resistance varied without obvious hysteresis. In addition, after 2000 cycles of stretching strain (0–50%), there is no significant reduction.[69] Through dip-coating EGaIn liquid metal on a silicone elastomer, a highly stretchable and conductive fiber was prepared.[70] Figure 22.5b_1 shows the optical images of an uncoated silicone elastomer fiber and a liquid metal-coated fiber, and we can see that the surface of the uncoated fiber is smooth compared with the coated one. Combining with the cross-sectional SEM image of the coated fiber in Figure 22.5b_2, the core-sheath structure can be obviously observed and the thickness of the EGaIn coating is about 4.3 μm. By replacing traditional conductive wires with weak stretchability, the fabricated EGaIn-elastomer composite fiber was used as a stretchable conductive circuit. As demonstrated in Figure 22.5b_3, the brightness of the LED is almost unchanged, suggesting excellent electrical property of the stretchable fiber with almost constant conductivity.[70]

Owing to the high electrical properties of liquid metal (LM), liquid metal–polymer elastomer composites can be fabricated as flexible heaters with dynamic stability for wearable thermotherapy. Researchers designed a

sinusoidal structural LM/PDMS composite heater, as shown in Figure 22.6a$_1$,[50] both the period length and amplitude height can be easily regulated. Figure 22.6a$_2$ displays the cross-section SEM image of the composite heater with a semicircular shape, and there are many small holes inside the composite. The inset shows that the liquid metal with a continuous 3D network microstructure is distributed in the PDMS matrix, and the 3D network structure is similar to 3D calabash bunch shape, which can promote the dynamic stability of the composite.[50] By changing the ratio of amplitude height to period length, the initial resistance (R_0) and relative resistance variation ($\Delta R/R_0$) at 100% strain of the sinusoidal structural heaters were systematically studied, as seen from Figure 22.6a$_3$. Owing to the sinusoidal structure of the heater, the increase of the ratio of amplitude height to period length will decrease the relative resistance variation at the same 100% strain.

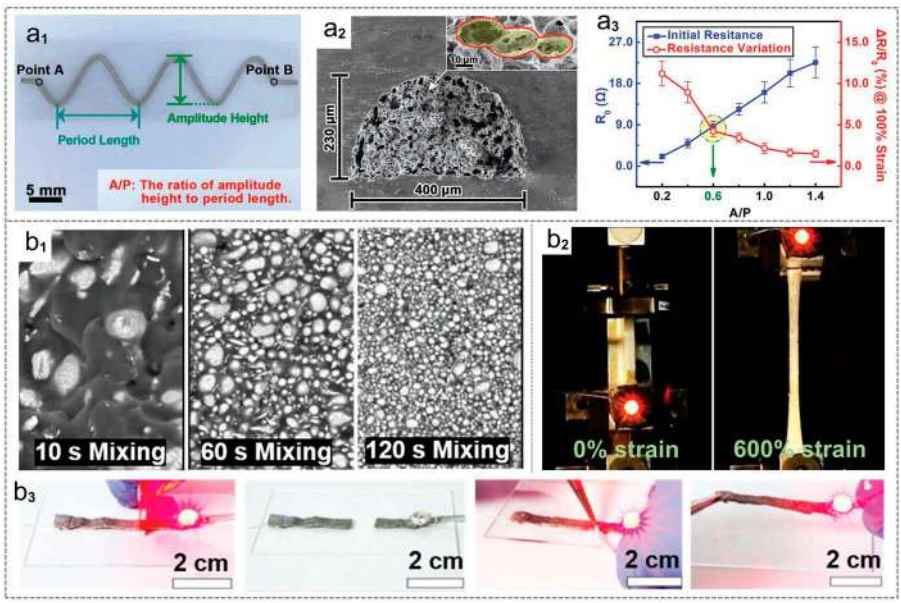

Figure 22.6 (a_1) Optical image of sinusoidal structural LM/PDMS heater. (a_2) Cross-sectional microstructure of the stretchable LM/PDMS heater. The inset shows the enlarged morphology of 3D calabash bunch network. (a_3) Initial resistance (R_0) and relative resistance variation at 100% strain of the sinusoidal structural specimen with the increase of the ratio of amplitude height to period length. Reproduced from ref. 50 with permission from John Wiley & Sons, Copyright © 2018 WILEY-VCH Verlag GmbH & Co. KGaA, Weinheim. (b_1) Microscopy images of the composite consisting of liquid metal and Sylgard 184 elastomer. (b_2) Optical images of LM–Ecoflex 00–30 composite for powering an LED at different stretchable strains. (b_3) Photographs of liquid metal–polycaprolactone composite from damaged to healed conditions. Reproduced from ref. 41 with permission from John Wiley & Sons, Copyright © 2020 Wiley-VCH GmbH.

In addition to common PDMS elastomer as a composite matrix, other matrix materials were studied for exploring the universality of LM-based stretchable composites. Researchers researched and compared the performance difference of Ga-based liquid metal and different polymer elastomers including Sylgard 184, Ecoflex 00-30 and polycaprolactone elastomer.[41] It is found that the assembly of LM droplets plays an important role in mechanical and electrical properties. Figure 22.6b$_1$ shows the microscopy images of LM/Sylgard 184 elastomer, and the LM droplet size decreases gradually with an increasing mixing time. The small droplet size will promote the stability of LM composite with high electrical conductivity. As seen from Figure 22.6b$_2$, stretchable LM–Ecoflex 00-30 composite remains almost unchanged electrical conductivity at the strain range of 0–600%. In addition, as compared with Sylgard matrix, low amounts of LM dispersed in the Ecoflex matrix will induce small particle size and increase the activation force between LM and matrix, and then increase the electrical conductivity of the LM–Ecoflex composite.[41] For stiff polycaprolactone polymer as matrix, the LM–polycaprolactone composite shows excellent electrical property when the volume content of LM exceeds a percolation threshold of about 65%. As displayed in Figure 22.6b$_3$, the damaged composite can recover original electrical conductivity after being heated, suggesting superior self-healing performance.

22.3 Stretchable Organic Conducting Polymers

Owing to more excellent stretchability, electrical property and uniformity compared with stretchable conducting nanomaterials-polymer composites, stretchable organic conducting polymers have broader application prospects and greater advantages in stretchable electronics. This section will review the design and optimization of traditional conducting polymers, ion-conducting elastomers, and polymer hydrogels by introducing a series of represented stretchable conductive materials.

22.3.1 Traditional Conducting Polymers

PEDOT:PSS is widely reported in stretchable electronics with high conductivity, whereas, solution-processed PEDOT:PSS has a low fracture strain of about 5%.[71] Much effort was made to improve the stretchability and electrical conductivity of PEDOT:PSS; it is often difficult to obtain optimal performance at the same time.[71,72] By incorporating ionic additives-assisted stretchability and electrical conductivity (STEC) enhancers, Bao's research group reported a highly stretchable and conductive PEDOT film with a high conductivity of 4000 S cm^{-1} under 100% strain.[73] High electrical conductivity depends on the excellent connection between PEDOT-rich domains, and the addition of STEC enhancers can soften PSS-rich domains to promote the formation of PEDOT conductive network. According to the conductivity variation of PEDOT with three common STECs, it can be illustrated that the

conductivity along the stretching direction increases by about 300% when 100% strain is applied, while it decreases quickly under >100% strain that the substrate was ruptured.[73]

Stretchable conductive textiles are an ideal choice for potential application in wearable electronics, so many kinds of highly stretchable conductive fibers and nonwovens have been reported. By electrospinning and drop-casting techniques, Ding *et al.* fabricated a stretchable PEDOT:PSS@PU fibrous nonwoven for wearable textile applications.[74] Figure 22.7a$_1$ shows the

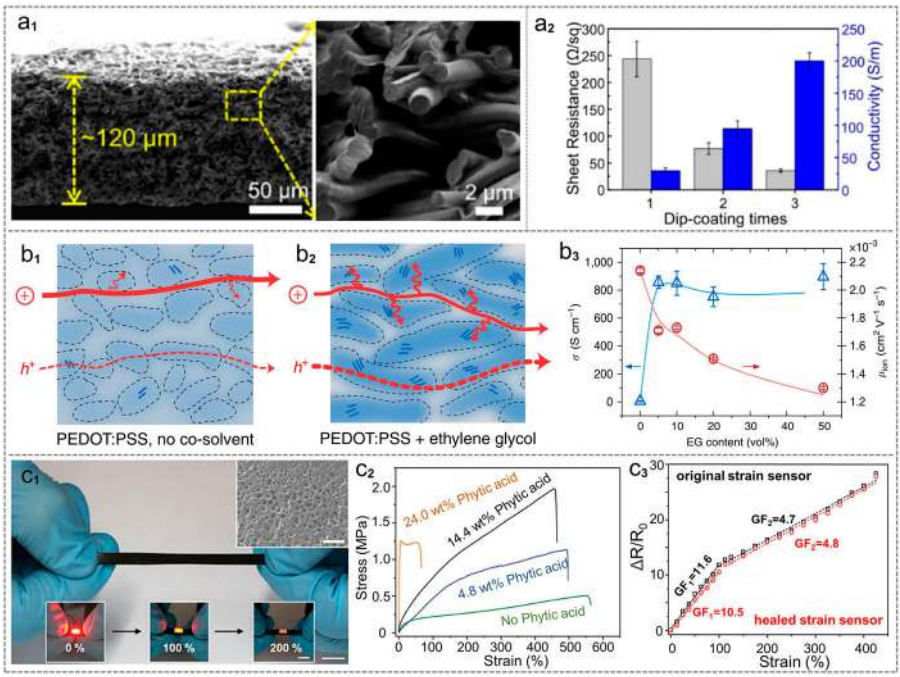

Figure 22.7 (a_1) Cross-sectional SEM images of PEDOT:PSS@PU. (a_2) Sheet resistance and electrical conductivity of PEDOT:PSS@PU nonwovens. Reproduced from ref. 74 with permission from American Chemical Society, Copyright 2017. (b_1 and b_2) Schematic diagram of morphologies and ions/holes transport in the bulk film of PEDOT:PSS without (b_1) and with (b_2) ethylene glycol. (b_3) Electrical conductivity (blue) and ion mobility (red) variation at increasing contents of ethylene glycol. Reproduced from ref. 75 with permission from Springer Nature, Copyright 2016. (c_1) Optical images of self-healable polymer showing high stretchability and electrical conductivity (scale bar = 1 cm). The inset is the SEM image of the surface of a self-healable polymer (scale bar = 200 μm). (c_2) Stress variation of the self-healable polymer with different phytic acid contents. (c_3) Relative resistance change of original and healed strain sensor at increasing strains. Reproduced from ref. 11 with permission from John Wiley & Sons, Copyright © 2017 WILEY-VCH Verlag GmbH & Co. KGaA, Weinheim.

cross-sectional SEM images, the thickness of the PEDOT:PSS@PU nonwoven is about 120 μm. The PU fibers are randomly distributed and overlapped with an average diameter of 1.2 μm, and PEDOT:PSS are uniformly coated on the surface of PU fibers without obvious aggregation. Moreover, researchers further researched the effect of dip-coating time on mechanical property and electrical property. It is found that the increase of dip-costing time will decrease the fracture strain. As displayed in Figure 22.7a_2, the sheet resistance of PEDOT:PSS@PU nonwovens also decreases gradually with a corresponding increase in electrical conductivity. Through pre-stretch treatment, the PEDOT:PSS@PU fiber and nonwoven in electric circuits can power a LED as conductors. And the PEDOT:PSS@PU nonwoven and fiber exhibit high stability under stretched and bent conditions.[74]

Through using polar solvents and ionic liquids, the morphology and conductivity of conductive polymers can be regulated and improved.[23] As a common, solution-processable hole conductor, PEDOT:PSS polymer and its composites have been utilized over twenty years, while few studies have been reported on ionic or mixed ionic/electronic transport in PEDOT:PSS polymer. Rivnay *et al.* firstly reported a high-performance PEDOT:PSS film with mixed ionic/electronic transport property by employing ethylene glycol (EG) as a co-solvent dispersion additive.[75] It is found that the variation of EG content will affect the nano-/meso-scale structure and morphology of PEDOT:PSS films, then affect ionic and electronic mobilities in bulk PEDOT:PSS. Figure 22.7b_1 and b_2 show the schematic diagram of morphologies and ions/holes transport in the bulk film of PEDOT:PSS, and the addition of EG will increase the aggregation degree of PEDOT with slightly tighter π-stacking, then affect transport property of ions and holes.[75] The small volume content of EG (<5%) will greatly increase electronic conductivity and ensure ion transport with a relative high ion mobility, as illustrated in Figure 22.7b_3, and electronic conductivity is almost unchanged when the EG content exceeds 10%. Whereas ion mobility decreases gradually with the increase of EG content, which may be caused by changes in the meso-scale arrangements.[75]

As another important conducting polymer, polyaniline (PANI) has obtained many applications in solar cells, bio/chemical sensors and organic light emitting diodes (OLEDs).[76] However, pure PANI is stiff owing to its rigid aromatic backbone structure. Therefore, it is necessary to modify PANI to obtain high flexibility for meeting practical applications. To overcome this drawback above, researchers prepared a highly stretchable PANI-based conducting polymer film based on polyacrylic acid (PAA) and phytic acid (PA) through a simple, solution-processable method.[11] The conductive film possesses a high stretchability of 500% and electrical conductivity (0.12 S cm^{-1}) with excellent self-healing properties. Figure 22.7c_1 shows optical images of the conductive film at a large stretching strain and powering an LED as a conductive wire, suggesting high stretchability and conductivity. In this conductive film, the PAA as soft counterpart crosslinks with the stiff PANI chains based on supramolecular interaction, and form a flexible and robust material.[77] Meanwhile, as the dopant, PA molecules can offer physical crosslinking

points to promote the crosslinking between PANI and PAA, and significantly increase the electrical conductivity of the PANI-based conductive film.[78] As seen from Figure 22.7c_2, the increase of PAA content can greatly enhance tensile strength of the polymer film while slightly decreasing the stretchability. When the content is up to 24.0 wt%, the conductive film almost completely loses its stretchability. Owing to the hydrogen bonding and electrostatic interactions between PANI and PAA chains, the damaged film can be self-healed and retain relatively good stretchability and conductivity. According to Figure 22.7c_3, we can see that the trend of resistance change of healed strain sensor is almost the same as that of the original device, indicating excellent self-healing properties and stability.[11] Additionally, the fabricated strain sensor shows a monotonic increase in resistance during the strain range of 0–425% with a relatively high gauge factor (GF) of 11.6 in <100% strain and 4.7 in >100% strain.

22.3.2 Polymer Hydrogels

As a kind of new intrinsically stretchable organic conducting material, polymer hydrogels have adjustable conductivity, excellent self-healing performance, ultrahigh stretchability, and show great potential applications in soft robots, biomimetic prostheses, wearable electronics.

Polyvinyl alcohol (PVA), one kind of common water-soluble material, is often used to prepare polymer hydrogels and is widely used in biomedical fields owing to the advantages of PVA-based hydrogels including high elastic modulus and mechanical strength, non-toxic and good biocompatibility, *etc.* Through dispersing acrylamide (AAm) monomer in PVA solution, *N*, *N*-methylenebisacrylamide (MBAA) as a chemical crosslinker and ammonium persulfate (APS) as initiator, Dong *et al.* reported a transparent, stretchable conductive PVA-PAAm hydrogel with binary networked structure.[79] Furthermore, potassium chloride (KCl) was used to enhance the electrical conductivity of stretchable hydrogel. As shown in Figure 22.8a_1, with the increase of PVA content from 0 wt% to 5 wt%, the fracture strain increases greatly from 318% to 470% while the tensile stress is almost unchanged. The content of PVA continues to increase to 15 wt%, compared with 5 wt%, the tensile stress is enhanced from 88 kPa to 184 kPa while there is no obvious difference in fracture strain. Figure 22.8a_2 illustrates the piezoresistive performance of the hydrogel pressure sensor, it is found that the relative current variation increases monotonously with the increase of pressure. In the pressure range of 0–3.27 and 3.27–6.83 kPa, corresponding sensitivities of the pressure sensor are 0.05 and 0.02 kPa^{-1}, respectively. In addition, owing to covalent crosslinking between PAAm chains, and the interconnections and hydrogen bonds between PAAm and PVA chains, the as-prepared hydrogel with a tough network exhibits excellent stretchability and reversibility.[79] Figure 22.8b_1 shows another PVA-based conductive, self-healing poly(vinylpyrrolidone) PVP-PVA hydrogel with hybrid networks, and Fe^{3+} cross-linked cellulose nanocrystals (CNCs) as "hard" parts and PVP cross-linked PVA chains as "soft" parts will

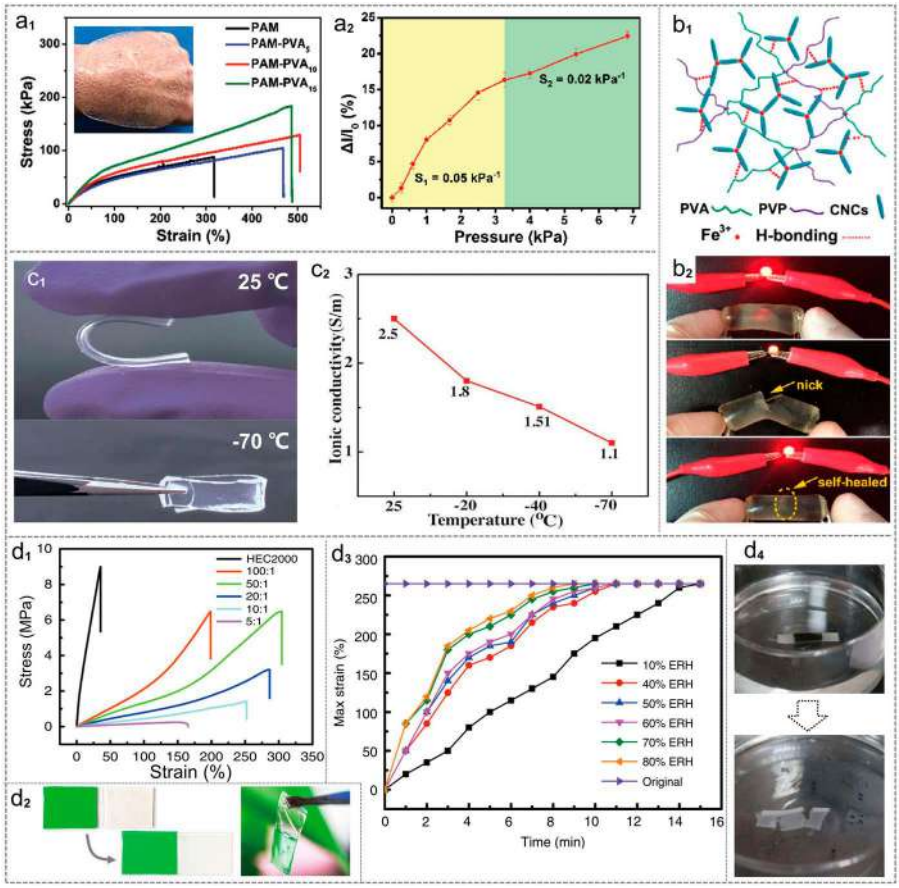

Figure 22.8 (a_1) Stress–strain curves of the PVA-PAAm hydrogel with different PVA contents. The inset is the photograph of a large-area hydrogel. (a_2) Relative current variation of the hydrogel-based strain sensor at different pressure. Reproduced from ref. 79 with permission from John Wiley & Sons, Copyright © 2018 WILEY-VCH Verlag GmbH & Co. KGaA, Weinheim. (b_1) Hierarchical network structure diagram of PVA-PVP hydrogel. (b_2) The optical images of the hydrogel before and after self-healing for powering a LED in an electric circuit. Reproduced from ref. 35 with permission from American Chemical Society, Copyright 2017. (c_1) Photographs of PVA-CNF organohydrogel at 25 °C and −70 °C. (c_2) Ionic conductivity variation of the PVA-1 wt% CNF organohydrogel at different temperatures. Reproduced from ref. 80 with permission from John Wiley & Sons, Copyright © 2020 WILEY-VCH Verlag GmbH & Co. KGaA, Weinheim. (d_1) Stress–strain curves of the elastomeric hydrogel films with different mass ratios of glycerol to HEC2000. (d_2) Optical images of the self-healing process of the hydrogel film. (d_3) Time-dependent self-healed degree of the film under various ambient humidities. (d_4) The degradation process of the stretchable electronic skin based on a self-healing hydrogel. Reproduced from ref. 82 with permission from Springer Nature, Copyright 2019.

form a synergistic "hard and soft" hybrid network.[35] In addition, the hierarchical network makes a PVP–PVA hydrogel possess ultrasensitive and stable resistance variation as a flexible strain sensor. Based on reversible coordination bonds and smooth stress-transfer, the hydrogel strain sensor exhibits superior mechanical strength, robust toughness, and self-healing performance. As seen from Figure 22.8b_2, the self-healed hydrogel retains excellent electrical conductivity similar to that of the initial hydrogel, which attributes to the reorganization of Fe^{3+} and CNCs through ionic coordination at fracture position.[35]

Stretchable conductive hydrogel attracts huge attention in flexible devices owing to intrinsically mechanical and electrical characteristics. However, it is still a challenge for synthesizing stretchable and highly conductive hydrogel with excellent freezing tolerance and biodegradability.[80–82] To expand the application field and environment of stretchable hydrogel, researchers prepared a high-performance PVA-CNF (cellulose nanofibril, CNF) organohydrogel with superior freezing tolerance by employing mixed solvent consisting of dimethyl sulfoxide (DMSO) and water.[80] The CNF can enhance the tensile strength of organohydrogel, and the DMSO acts as a anti-freezing agent. As displayed in Figure 22.8c_1, the PVA organohydrogel with 1 wt% CNF still maintains a flexible and transparent shape at −70 °C, showing excellent freezing tolerance. The corresponding ionic conductivity decreases gradually from 2.5 to 1.1 S cm^{-1} at a decreasing temperature ranging from 25 to −70 °C owing to the low ion transport rate in the organohydrogel at low temperatures, as seen from Figure 22.8c_2.[80]

Biodegradable hydrogels exhibit huge application prospects in the biomedical field, especially implantable electronics. Biodegradable properties can enable the implantable devices to self-degrade *in vivo* after failure and avoid the second pain caused by the extra medical operation.[83] Through using a mixed solution of hydroxyethylcellulose (HEC) and glycerol, Zhang *et al.* reported a stretchable, self-healing macromolecular hydrogel with excellent biodegradability.[82] Figure 22.8d_1 shows the stress–strain curves of the hydrogel with different mass ratios of glycerol to HEC. Pure HEC hydrogel has the lowest fracture strain of about 25% and the highest tensile stress of about 9 MPa. With the increase of glycerol content, the stretchability increases gradually and up to the best stretchability of 304% fracture strain when the mass ratio is 50 : 1. At a higher mass ratio (>50 : 1), the stretchability gradually decreases owing to the occurrence of hydrogen bonds between the glycerol molecules with weak intermolecular forces, which preferentially break before the HEC chains completely spread out.[81,84] The dynamic hydrogen bonds between glycerol molecules and HEC chains can enable the hydrogel to possess remarkable self-healing performance, as displayed in Figure 22.8d_2. In addition, the effect of ambient humidity on the self-healed performance of hydrogel was studied, as shown in Figure 22.8d_3. It is found that the increase of ambient humidity will decrease the self-healing time for the hydrogel to restore to the initial max strain. Figure 22.8d_4 shows the

degradation ability of glycerol-HEC hydrogel in water. In the degradation process, the CNTs electrode will fall off the hydrogel substrate and disintegrate into small fragments until completely disappear. The hydrogel substrate will absorb water and ultimately form a fluid flocculation in water.[82]

As a natural protein, silk fibroin (SF) shows excellent biocompatibility and mechanical toughness and strength, which make it widely used in flexible electronics and energy harvesters.[85,86] By using silk fibroin (SF) solution prepared from natural silkworm cocoon, combining graphene oxide, PEDOT:PSS and PAAm, researchers designed a stretchable, multifunctional, biocompatible SF hydrogel for strain and pressure sensing with a wide sensing range of 2–600% strain and 0.5–119.4 kPa respectively.[85] Figure 22.9a$_1$ displays the schematic diagram of the fabrication process of SF hydrogel. As observed in Figure 22.9a$_2$, the as-prepared SF hydrogel shows remarkable stretchability and the superior deformation ability to be fabricated into any

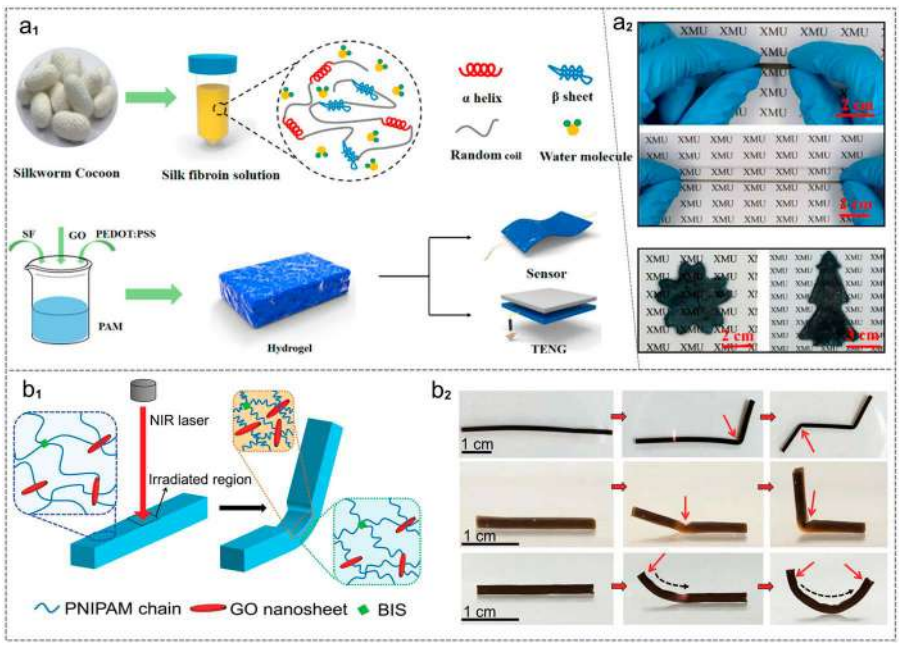

Figure 22.9 (a$_1$) Schematic diagram of the fabrication process of SF hydrogel for sensor and TENG. (a$_2$) Optical images of the SF hydrogel at a large tensile strain and fabricated into different shapes. Reproduced from ref. 85 with permission from American Chemical Society, Copyright 2020. (b$_1$) Schematic diagram of NIR laser induced folding deformation of the PNIPAAm/GO hydrogels. (b$_2$) Optical images of folding or bending deformation of hydrogel strip and sheet. The red arrows indicate the NIR laser irradiated direction. Reproduced from ref. 87 with permission from the Royal Society of Chemistry.

shape. Except for strain/pressure sensing, the SF conductive hydrogel can be fabricated as a single-electrode triboelectric nanogenerator (TENG) with excellent positive polarity response when it works. The SF hydrogel-based TENG can drive 20 commercial LEDs by a linear motor at a frequency of 1 Hz.[85] The stretchable conductive SF hydrogel will obtain increasing attention and exhibit huge application potential in self-powered systems and wearable electronics for health and exercise monitoring.

In artificial intelligent and biomedical therapy, for example smart robot and drug release, it is important for practical applications that wireless and remote operation can precisely control the shapes, sizes and specific directions of functional materials.[87,88] Shape-controllable hydrogels with excellent external stimuli response ability have a large number of potential applications in many fields. Through a novel and facile preparation method, Wang *et al.* reported a flexible poly(*N*-isopropylacrylamide)/graphene oxide (PNIPAAm/GO) nanocomposite hydrogel with controllable deformation performance.[87] Figure 22.9b$_1$ illustrates the schematic diagram of the deformation principle of this hydrogel induced by near infrared (NIR) laser irradiation. Under NIR irradiation, GO nanosheets can absorb NIR light energy and transform it into heat, and the accumulated heat will drive the phase transition of PNIPAAm hydrogel. Owing to the slow heat transfer property of the hydrogels, inducing higher temperatures at the irradiated region, there is a larger shrink in the irradiated region than that of the un-irradiated region of the PNIPAAm hydrogel, which leads to folding or bending toward the irradiated region.[87] Figure 22.9b$_2$ demonstrates the deformation property of the hydrogel strip and sheet; the desirable deformation can be controlled by changing the NIR laser irradiated direction and region of the hydrogel, suggesting a potential application in remote light-controlled robots and artificial muscles.

22.3.3 Ionic Conducting Elastomers

As described above, polymer hydrogels are playing important role in soft robots, wearable electronics, biomimetic prostheses owing to ultrahigh stretchability and conductivity, excellent self-healing property, and biocompatibility. However, the mechanical and electrical properties of these hydrogels will severely degrade in air due to the dehydration or evaporation of the liquid solvent in hydrogels.[79,89] Therefore, it is vital to develop highly stable conductive polymer materials without solvent dehydration or evaporation in practical application. Ding *et al.* firstly reported highly and transparent ionic conducting elastomers (ICE) by salt in polymer strategy.[34] Figure 22.10a$_1$ shows the molecular structures of ICE precursors, the butyl acrylate (BA) was used as the monomer, polyethyleneglycol diacrylate (PEGDA) as the crosslinker, photo-initiator 184 as photo-initiator, and the lithium bis(trifluoromethane sulfonimide) (LiTFSI) as electrolyte salt. The prepared ICEs show excellent stretchability up to 1200% strain, and the ICE exhibits

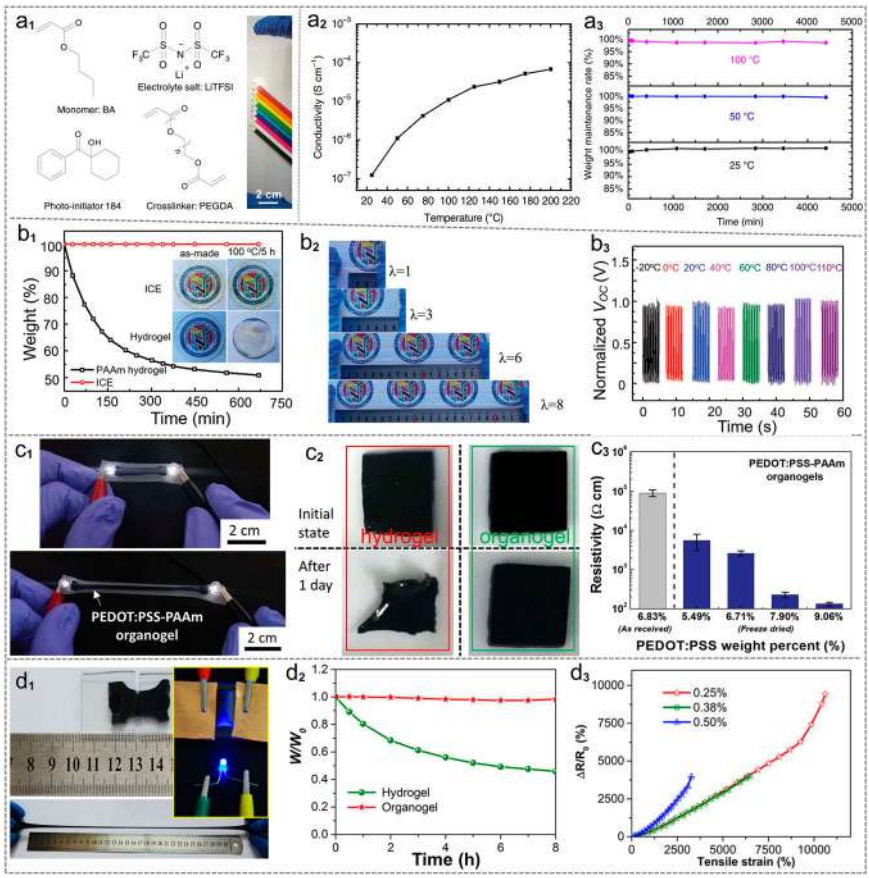

Figure 22.10 (a_1) Molecular structures of ICE precursor. (a_2) Temperature induced ionic conductivity variation. (a_3) Weight maintenance variation of the ICE at different temperatures. Reproduced from ref. 34 with permission from Springer Nature, Copyright 2018. (b_1) Weight variation of the PAAm hydrogel and ICE in an oven at 100 °C. The inset pictures were the ICE and PAAm hydrogel at the initial state and at 100 °C for 5 h. (b_2) Optical images of the ICE-iTENG at different strains. (b_3) The V_{oc} variation of the ICE-iTENG measured at different temperatures (normalized to V_{oc} at 20 °C). Reproduced from ref. 90 with permission from John Wiley & Sons, Copyright © 2020 WILEY-VCH Verlag GmbH & Co. KGaA, Weinheim. (c_1) Optical images of PEDOT:PSS-PAAm organogel at 0% strain and 200% strain for powering a white LED. (c_2) Optical images of the PEDOT:PSS-PAAm hydrogel and organogel films (side length = 1.0 cm) at the initial state and after 1 day. (c_3) Resistance variation of the organogel with different PEDOT:PSS weight. Reproduced from ref. 91 with permission from John Wiley & Sons, Copyright © 2015 WILEY-VCH Verlag GmbH & Co. KGaA, Weinheim. (d_1) Optical images of graphene filled PAAm/PVP/EG organogel at different strains, showing high stretchability and electrical conductivity. (d_2) Relative weight change of PAAm/PVP hydrogel and PAAm/PVP/EG organogel. (d_3) Relative resistance change curves of PAAm/PVP/EG organogel with different crosslinker contents. Reproduced from ref. 92 with permission from American Chemical Society, Copyright 2018.

a higher electrical conductivity at a higher temperature condition. As seen from Figure 22.10a$_2$, with the increase of temperature from 20 to 200 °C, the ionic conductivity increases gradually by >500% from 1.27×10^{-7} to 6.8×10^{-5} S cm^{-1}. This can be explained as the movement of polymer chains and ions being more intense at higher temperatures, leading to higher conductivity and easier ion transport.[34] The environmental stability of ICE in the open air is illustrated in Figure 22.10a$_3$, and we can see that the weight of ICE retained is almost constant at 25, 50, 100 °C about 4500 min. To verify the universality of the salt in polymer strategy, by replacing BA monomer with 2(2-ethoxyethoxy) ethyl acrylate (EOEOEA), poly(ethylene glycol) methyl ether acrylate (PEGMA), and vinylene carbonate (VC) respectively, the ionic conductivity of the as-prepared ICEs was greatly enhanced. Owing to the excellent performance of ICEs with high stability and ionic conductivity, Wang and coworkers reported a highly stretchable, environmentally stable single-electrode TENG with the ICE as electrode corresponding to a high stretchability of 1000% strain and transmittance of 91.5%.[90] Additionally, the ICE exhibited excellent thermal stability below 335 °C without obvious weight variation, avoiding the dehydration-induced performance degradation of PAAm hydrogel. As shown in Figure 22.10b$_1$, the ICE maintains a constant weight at 100 °C for 10 hours, while there is a 50% decrease in the weight of PAAm hydrogel. The ICE-based TENG exhibits a high stretchability up to 700% strain. To explore the environmental stability of ICE-based single-electrode TENG, open circuit voltages (V_{oc}) were systematically studied at different external temperatures. As displayed in Figure 22.10b$_2$, the output V_{oc} values of the ICE TENG are almost unchanged during the temperature ranging from −20 to 110 °C, indicating the remarkable environmental stability of ICE and ICE-based TENG.[90]

By replacing water solution with ethylene glycol (EG) as the organic solvent, similar to the preparation progress of PEDOT:PSS-PAAm hydrogel, researchers fabricated a strain-insensitive stretchable conductive PEDOT:PSS-PAAm organogel, as observed in Figure 22.10c$_1$.[91] The organogel exhibits excellent conductivity with strain–insensitive properties. Figure 22.10c$_2$ displays the optical images of the PEDOT:PSS-PAAm hydrogel and organogel films with side lengths of 1.0 cm at the initial state and after being dried in air for one day. It is found that the hydrogel was completely dried out and formed a hard bulk polymer, while the organogel almost maintained the initial state owing to the lack of evaporation of the EG solvent. Owing to the high electrical conductivity of PEDOT:PSS, the increase of PEDOT:PSS weight per cent will decrease the electrical resistance of the organogels with increasing electrical conductivity, as shown in Figure 22.10c$_3$.[91] According to the relative resistance variation at 100, 500 and 1000 cycles respectively, there is only a slight increase in electrical resistance, showing excellent cyclic stability and strain-insensitive performance. Through using EG as the solvent solution, Zhang *et al.* reported a stretchable and stable stain sensor based on double-network structural PAAm/PVP/EG organogel with PEGDA as the crosslinker, and the hybrid physically and chemically cross-linked double-networks enables

the organogel to be extraordinarily stretchable with a high tensile strain of 21 000%.[92] By incorporating graphene into EG organogel, the conductivity was greatly improved with high tensile strain as high as 10 800%, as seen from Figure 22.10d$_1$. Compared with PAAm/PVP/EG hydrogel with water as solvent, the PAAm/PVP/EG organogel exhibits high stability. Figure 22.10d$_2$ shows the relative weight change of the corresponding PAAm/PVP hydrogel and organogel in a vacuum chamber (0.09 atm, room temperature), where it is found that the relative weight of the PAAm/PVP/EG organogel was almost stable without obvious changes owing to the low vapor pressure of EG.[92] Through changing the crosslinker content in the synthetic process, the mechanical and electrical properties of PAAm/PVP/EG organogel can be adjusted. As illustrated in Figure 22.10d$_3$, the relative resistance change increases monotonically, and the increase of crosslinker content will decrease the tensile strain of PAAm/PVP/EG organogel. It is observed that there are two linear regions in resistance change of the sample with 0.25 wt% PEGDA400. In 0–9200% strain, the strain induced resistance change originates from the decrease of contact area between the adjacent graphene (contact-resistance effect). When the tensile strain exceeds 9200% strain, the quick increase in resistance mainly derives from the break in conductive graphene nanosheet–nanosheet connection channels (tunneling effect).[32,93]

22.4 Conclusions and Prospects

The rapid development of intrinsically stretchable electronic materials gradually enables the structure design, performance optimization and application of intrinsically stretchable electronic devices. Owing to the facile fabrication process, low manufacturing cost and mass production, the intrinsically stretchable conductive organic materials with excellent stretchability and electrical conductivity have played an important role in wearable electronics, e-skin, health monitoring, soft robotic and artificial muscle. In this chapter, we have reviewed the research development of intrinsically stretchable organic conductive materials in recent ten years. By choosing representative intrinsically stretchable organic conductive composites and polymers, we systematically discussed and summarized the structural design and performance optimization of diverse intrinsically stretchable conductive organic materials and potential applications in the stretchable electronics field.

Although the structure and performance of the above intrinsically stretchable conductive organic materials have been greatly improved, there are still many problems to be solved about the design and application of these materials. For example, for stretchable conductive organic composites, the mismatch of elastic modulus between the conductive active materials and flexible substrates, and the connection failure of the conductive network of active materials, will lead to a decline in mechanical and electrical properties of stretchable conductive organic composite materials, thus reducing the stability and service life of stretchable electronic devices. For stretchable

conductive polymer, the electrical conductivity is often relatively low as compared with stretchable metal conductors. Simultaneously making stretchable conductive polymers possess excellent mechanical and electrical properties is still a challenging research hotspot and difficulty.

At the same time, it is worth noting that stretchable electronics are in a broad market. The development of intrinsically stretchable organic electronic materials and devices will make the human–machine interaction and artificial intelligence in the Internet of Things (IOT) simple and efficient. Additionally, intrinsically stretchable organic electronic materials are expected to break through the inherent limitations of classical silicon electronics, and bring important strategic opportunities to provide fundamental and powerful support for the development of stretchable electronic devices in the future.

References

1. S. Hong, H. Lee, J. Lee, J. Kwon, S. Han, Y. D. Suh, H. Cho, J. Shin, J. Yeo and S. H. Ko, *Adv. Mater.*, 2015, **27**, 4744.
2. J. Liang, L. Li, D. Chen, T. Hajagos, Z. Ren, S. Y. Chou, W. Hu and Q. Pei, *Nat. Commun.*, 2015, **6**, 7647.
3. D. Zhang, K. Zhang, Y. Wang, Y. Wang and Y. Yang, *Nano Energy*, 2019, **56**, 25.
4. J. Xu, S. Wang, G.-J. N. Wang, C. Zhu, S. Luo, L. Jin, X. Gu, S. Chen, V. R. Feig, J. W. F. To, S. Rondeau-Gagné, J. Park, B. C. Schroeder, C. Lu, J. Y. Oh, Y. Wang, Y.-H. Kim, H. Yan, R. Sinclair, D. Zhou, G. Xue, B. Murmann, C. Linder, W. Cai, J. B. H. Tok, J. W. Chung and Z. Bao, *Science*, 2017, **355**, 59.
5. J. C. Lai, X. Y. Jia, D. P. Wang, Y. B. Deng, P. Zheng, C. H. Li, J. L. Zuo and Z. Bao, *Nat. Commun.*, 2019, **10**, 1164.
6. S. Wang, J. Xu, W. Wang, G.-J. N. Wang, R. Rastak, F. Molina-Lopez, J. W. Chung, S. Niu, V. R. Feig, J. Lopez, T. Lei, S.-K. Kwon, Y. Kim, A. M. Foudeh, A. Ehrlich, A. Gasperini, Y. Yun, B. Murmann, J. B. H. Tok and Z. Bao, *Nature*, 2018, **555**, 83.
7. J. Kang, D. Son, G.-J. N. Wang, Y. Liu, J. Lopez, Y. Kim, J. Y. Oh, T. Katsumata, J. Mun, Y. Lee, L. Jin, J. B. H. Tok and Z. Bao, *Adv. Mater.*, 2018, **30**, 1706846.
8. G. Schwartz, B. C. Tee, J. Mei, A. L. Appleton, D. H. Kim, H. Wang and Z. Bao, *Nat. Commun.*, 2013, **4**, 1859.
9. D. Zhang, Y. Song, L. Ping, S. Xu, D. Yang, Y. Wang and Y. Yang, *Nano Res.*, 2019, **12**, 2982.
10. E. Roh, B.-U. Hwang, D. Kim, B.-Y. Kim and N.-E. Lee, *ACS Nano*, 2015, **9**, 6252.
11. T. Wang, Y. Zhang, Q. Liu, W. Cheng, X. Wang, L. Pan, B. Xu and H. Xu, *Adv. Funct. Mater.*, 2018, **28**, 1705551.
12. H. Sun, Y. Zhao, C. Wang, K. Zhou, C. Yan, G. Zheng, J. Huang, K. Dai, C. Liu and C. Shen, *Nano Energy*, 2020, **76**, 105035.

13. K. Takei, W. Honda, S. Harada, T. Arie and S. Akita, *Adv. Healthcare Mater.*, 2015, **4**, 487.
14. I. del Agua, D. Mantione, U. Ismailov, A. Sanchez-Sanchez, N. Aramburu, G. G. Malliaras, D. Mecerreyes and E. Ismailova, *Adv. Mater. Technol.*, 2018, **3**, 1700322.
15. T. Q. Trung and N. E. Lee, *Adv. Mater.*, 2016, **28**, 4338.
16. B. Mosadegh, P. Polygerinos, C. Keplinger, S. Wennstedt, R. F. Shepherd, U. Gupta, J. Shim, K. Bertoldi, C. J. Walsh and G. M. Whitesides, *Adv. Funct. Mater.*, 2014, **24**, 2163.
17. I. Must, E. Sinibaldi and B. Mazzolai, *Nat. Commun.*, 2019, **10**, 344.
18. S. Palagi, A. G. Mark, S. Y. Reigh, K. Melde, T. Qiu, H. Zeng, C. Parmeggiani, D. Martella, A. Sanchez-Castillo, N. Kapernaum, F. Giesselmann, D. S. Wiersma, E. Lauga and P. Fischer, *Nat. Mater.*, 2016, **15**, 647.
19. S. M. Mirvakili and I. W. Hunter, *Adv. Mater.*, 2018, **30**, 1704407.
20. D. Chen and Q. Pei, *Chem. Rev.*, 2017, **117**, 11239.
21. M. Kanik, S. Orguc, G. Varnavides, J. Kim, T. Benavides, D. Gonzalez, T. Akintilo, C. C. Tasan, A. P. Chandrakasan and Y. Fink, *Science*, 2019, **365**, 145.
22. J. Mu, M. J. De Andrade, S. Fang, X. Wang, E. Gao, N. Li, S. H. Kim, H. Wang, C. Hou and Q. Zhang, *Science*, 2019, **365**, 150.
23. R. Ma, S.-Y. Chou, Y. Xie and Q. Pei, *Chem. Soc. Rev.*, 2019, **48**, 1741.
24. J. Kim, M. Lee, H. J. Shim, R. Ghaffari, H. R. Cho, D. Son, Y. H. Jung, M. Soh, C. Choi, S. Jung, K. Chu, D. Jeon, S. T. Lee, J. H. Kim, S. H. Choi, T. Hyeon and D. H. Kim, *Nat. Commun.*, 2014, **5**, 5747.
25. D.-Y. Khang, H. Jiang, Y. Huang and J. A. Rogers, *Science*, 2006, **311**, 208.
26. Y. Lee, V. T. Le, J. G. Kim, H. Kang, E. S. Kim, S. E. Ahn and D. Suh, *Adv. Funct. Mater.*, 2018, **28**, 1706007.
27. Z. Niu, H. Dong, B. Zhu, J. Li, H. H. Hng, W. Zhou, X. Chen and S. Xie, *Adv. Mater.*, 2013, **25**, 1058.
28. C. Chen, J. Cao, X. Wang, Q. Lu, M. Han, Q. Wang, H. Dai, Z. Niu, J. Chen and S. Xie, *Nano Energy*, 2017, **42**, 187.
29. Y. S. Guan, Z. Zhang, Y. Tang, J. Yin and S. Ren, *Adv. Mater.*, 2018, **30**, 1706390.
30. J. Li, S. Zhao, X. Zeng, W. Huang, Z. Gong, G. Zhang, R. Sun and C. P. Wong, *ACS Appl. Mater. Interfaces*, 2016, **8**, 18954.
31. S. Hong, J. Lee, K. Do, M. Lee, J. H. Kim, S. Lee and D.-H. Kim, *Adv. Funct. Mater.*, 2017, **27**, 1704353.
32. M. Amjadi, A. Pichitpajongkit, S. Lee, S. Ryu and I. Park, *ACS Nano*, 2014, **8**, 5154.
33. D. J. Lipomi, M. Vosgueritchian, B. C. K. Tee, S. L. Hellstrom, J. A. Lee, C. H. Fox and Z. Bao, *Nat. Nanotechnol.*, 2011, **6**, 788.
34. L. Shi, T. Zhu, G. Gao, X. Zhang, W. Wei, W. Liu and S. Ding, *Nat. Commun.*, 2018, **9**, 2630.
35. Y.-J. Liu, W.-T. Cao, M.-G. Ma and P. Wan, *ACS Appl. Mater. Interfaces*, 2017, **9**, 25559.

36. S. Y. Son, J. H. Kim, E. Song, K. Choi, J. Lee, K. Cho, T. S. Kim and T. Park, *Macromolecules*, 2018, **51**, 2572.
37. Y. Yang, S. Ding, T. Araki, J. Jiu, T. Sugahara, J. Wang, J. Vanfleteren, T. Sekitani and K. Suganuma, *Nano Res.*, 2016, **9**, 401.
38. B. W. An, E. J. Gwak, K. Kim, Y. C. Kim, J. Jang, J. Y. Kim and J. U. Park, *Nano Lett.*, 2016, **16**, 471.
39. J. Wu, H. Wang, Z. Su, M. Zhang, X. Hu, Y. Wang, Z. Wang, B. Zhong, W. Zhou, J. Liu and S. G. Xing, *ACS Appl. Mater. Interfaces*, 2017, **9**, 38745.
40. C. Pan, D. Liu, M. J. Ford and C. Majidi, *Adv. Mater. Technol.*, 2020, **5**, 2000754.
41. M. J. Ford, D. K. Patel, C. Pan, S. Bergbreiter and C. Majidi, *Adv. Mater.*, 2020, **32**, e2002929.
42. Y. Cheng, H. Zhang, R. Wang, X. Wang, H. Zhai, T. Wang, Q. Jin and J. Sun, *ACS Appl. Mater. Interfaces*, 2016, **8**, 32925.
43. J.-G. Lee, J.-H. Lee, S. An, D.-Y. Kim, T.-G. Kim, S. S. Al-Deyab, A. L. Yarin and S. S. Yoon, *J. Mater. Chem. A*, 2017, **5**, 6677.
44. S. Choi, J. Park, W. Hyun, J. Kim, J. Kim, Y. B. Lee, C. Song, H. J. Hwang, J. H. Kim and T. Hyeon, *ACS Nano*, 2015, **9**, 6626.
45. Z. Ma, S. Kang, J. Ma, L. Shao, A. Wei, C. Liang, J. Gu, B. Yang, D. Dong, L. Wei and Z. Ji, *ACS Nano*, 2019, **13**, 7578.
46. H. Kim, H. Lee, I. Ha, J. Jung, P. Won, H. Cho, J. Yeo, S. Hong, S. Han, J. Kwon, K.-J. Cho and S. H. Ko, *Adv. Funct. Mater.*, 2018, **28**, 1801847.
47. Z. Li, Z. Xu, Y. Liu, R. Wang and C. Gao, *Nat. Commun.*, 2016, **7**, 13684.
48. P. Liu, Y. Li, Y. Xu, L. Bao, L. Wang, J. Pan, Z. Zhang, X. Sun and H. Peng, *Small*, 2018, **14**, 1702926.
49. Y. Huang, Y. Ding, J. Bian, Y. Su, J. Zhou, Y. Duan and Z. Yin, *Nano Energy*, 2017, **40**, 432.
50. Y. Wang, Z. Yu, G. Mao, Y. Liu, G. Liu, J. Shang, S. Qu, Q. Chen and R.-W. Li, *Adv. Mater. Technol.*, 2019, **4**, 1800435.
51. M. D. Dickey, *Adv. Mater.*, 2017, **29**, 1606425.
52. T. K. Kim, J. K. Kim and O. C. Jeong, *Microelectron. Eng.*, 2011, **88**, 1982.
53. J. Li, S. Qi, J. Liang, L. Li, Y. Xiong, W. Hu and Q. Pei, *ACS Appl. Mater. Interfaces*, 2015, **7**, 14140.
54. S. Choi, S. I. Han, D. Jung, H. J. Hwang, C. Lim, S. Bae, O. K. Park, C. M. Tschabrunn, M. Lee, S. Y. Bae, J. W. Yu, J. H. Ryu, S. W. Lee, K. Park, P. M. Kang, W. B. Lee, R. Nezafat, T. Hyeon and D. H. Kim, *Nat. Nanotechnol.*, 2018, **13**, 1048.
55. J. Lee, S. Pyo, D. S. Kwon, E. Jo, W. Kim and J. Kim, *Small*, 2019, **15**, 1805120.
56. Z. Tang, S. Jia, F. Wang, C. Bian, Y. Chen, Y. Wang and B. Li, *ACS Appl. Mater. Interfaces*, 2018, **10**, 6624.
57. J. Z. Kovacs, *Compos. Sci. Technol.*, 2009, **69**, 1486.
58. Y. Cheng, R. Wang, J. Sun and L. Gao, *Adv. Mater.*, 2015, **27**, 7365.
59. A. H. Castro Neto, F. Guinea, N. M. R. Peres, K. S. Novoselov and A. K. Geim, *Rev. Mod. Phys.*, 2009, **81**, 109.
60. A. Geim and K. Novoselov, *Nat. Mater.*, 2007, **6**, 183.

61. K. Novoselov, A. Geim, S. Morozov, D. Jiang, Y. Zhang, S. Dubonos, I. Grigorieva and A. Firsov, *Science*, 2004, **306**, 666.
62. Y. Liu, W. Hao, H. Yao, S. Li, Y. Wu, J. Zhu and L. Jiang, *Adv. Mater.*, 2018, **30**, 1705377.
63. C. Yan, J. Wang, W. Kang, M. Cui, X. Wang, C. Y. Foo, K. J. Chee and P. S. Lee, *Adv. Mater.*, 2014, **26**, 2022.
64. W. Luo, J. Hayden, S.-H. Jang, Y. Wang, Y. Zhang, Y. Kuang, Y. Wang, Y. Zhou, G. W. Rubloff, C.-F. Lin and L. Hu, *Adv. Energy Mater.*, 2018, **8**, 1702615.
65. X. Zhao, D. Zhang, S. Xu, W. Qian, W. Han, Z. L. Wang and Y. Yang, *Nano Energy*, 2020, **75**, 104920.
66. D. Zhang, S. Xu, X. Zhao, W. Qian, C. R. Bowen and Y. Yang, *Adv. Funct. Mater.*, 2020, **30**, 1910809.
67. M. D. Dickey, *ACS Appl. Mater. Interfaces*, 2014, **6**, 18369.
68. S. Zhu, J. H. So, R. Mays, S. Desai, W. R. Barnes, B. Pourdeyhimi and M. D. Dickey, *Adv. Funct. Mater.*, 2013, **23**, 2308.
69. S. W. Jin, J. Park, S. Y. Hong, H. Park, Y. R. Jeong, J. Park, S. S. Lee and J. S. Ha, *Sci. Rep.*, 2015, **5**, 11695.
70. Q. Zhang, D. J. Roach, L. Geng, H. Chen, H. J. Qi and D. Fang, *Smart Mater. Struct.*, 2018, **27**, 035019.
71. D. J. Lipomi, J. A. Lee, M. Vosgueritchian, C. K. Tee, J. A. Bolander and Z. Bao, *Chem. Mater.*, 2012, **24**, 373.
72. J. Y. Oh, S. Kim, H. K. Baik and U. Jeong, *Adv. Mater.*, 2016, **28**, 4455.
73. Y. Wang, C. Zhu, R. Pfattner, H. Yan, L. Jin, S. Chen, F. Molina-Lopez, F. Lissel, J. Liu, N. I. Rabiah, Z. Chen, J. W. Chung, C. Linder, M. F. Toney, B. Murmann and Z. Bao, *Sci. Adv.*, 2017, **3**, e1602076.
74. Y. Ding, W. Xu, W. Wang, H. Fong and Z. Zhu, *ACS Appl. Mater. Interfaces*, 2017, **9**, 30014.
75. J. Rivnay, S. Inal, B. A. Collins, M. Sessolo, E. Stavrinidou, X. Strakosas, C. Tassone, D. M. Delongchamp and G. G. Malliaras, *Nat. Commun.*, 2016, **7**, 11287.
76. M. Jaymand, *Prog. Polym. Sci.*, 2013, **38**, 1287.
77. M. Ma, L. Guo, D. G. Anderson and R. Langer, *Science*, 2013, **339**, 186.
78. L. Pan, G. Yu, D. Zhai, H. R. Lee, W. Zhao, N. Liu, H. Wang, B. C. Tee, Y. Shi, Y. Cui and Z. Bao, *Proc. Natl. Acad. Sci. U. S. A.*, 2012, **24**, 9287.
79. G. Ge, Y. Zhang, J. Shao, W. Wang, W. Si, W. Huang and X. Dong, *Adv. Funct. Mater.*, 2018, **28**, 1802576.
80. Y. Ye, Y. Zhang, Y. Chen, X. Han and F. Jiang, *Adv. Funct. Mater.*, 2020, **30**, 2003430.
81. Q. Rong, W. Lei, L. Chen, Y. Yin, J. Zhou and M. Liu, *Angew. Chem., Int. Ed.*, 2017, **56**, 14159.
82. M. Hao, L. Li, S. Wang, F. Sun, Y. Bai, Z. Cao, C. Qu and T. Zhang, *Microsyst. Nanoeng.*, 2019, **5**, 9.
83. H. Yang, C. Li, J. Tang and Z. Suo, *ACS Appl. Bio Mater.*, 2019, **2**, 1781.

84. X. Yan, Z. Liu, Q. Zhang, J. Lopez, H. Wang, H.-C. Wu, S. Niu, H. Yan, S. Wang, T. Lei, J. Li, D. Qi, P. Huang, J. Huang, Y. Zhang, Y. Wang, G. Li, J. B. H. Tok, X. Chen and Z. Bao, *J. Am. Chem. Soc.*, 2018, **140**, 5280.
85. F. He, X. You, H. Gong, Y. Yang, T. Bai, W. Wang, W. Guo, X. Liu and M. Ye, *ACS Appl. Mater. Interfaces*, 2020, **12**, 6442.
86. X. Liang, H. Li, J. Dou, Q. Wang, W. He, C. Wang, D. Li, J.-M. Lin and Y. Zhang, *Adv. Mater.*, 2020, **32**, 2000165.
87. X. Peng, T. Liu, C. Jiao, Y. Wu, N. Chen and H. Wang, *J. Mater. Chem. B*, 2017, **5**, 7997.
88. K. Shi, Z. Liu, Y. Y. Wei, W. Wang, X. J. Ju, R. Xie and L. Y. Chu, *ACS Appl. Mater. Interfaces*, 2015, **7**, 27289.
89. B. Chen, W. Tang, T. Jiang, L. Zhu, X. Chen, C. He, L. Xu, H. Guo, P. Lin, D. Li, J. Shao and Z. L. Wang, *Nano Energy*, 2018, **45**, 380.
90. P. Zhang, Y. Chen, Z. H. Guo, W. Guo, X. Pu and Z. L. Wang, *Adv. Funct. Mater.*, 2020, **30**, 1909252.
91. Y. Y. Lee, H. Y. Kang, S. H. Gwon, G. M. Choi, S. M. Lim, J. Y. Sun and Y. C. Joo, *Adv. Mater.*, 2016, **28**, 1636.
92. H. Zhang, W. Niu and S. Zhang, *ACS Appl. Mater. Interfaces*, 2018, **10**, 32640.
93. P. Liu, W. Pan, Y. Liu, J. Liu, W. Xu, X. Guo, C. Liu, Y. Zhang, Y. Ge and Y. Huang, *Compos. Sci. Technol.*, 2018, **159**, 42.

CHAPTER 23

Materials Nanoarchitectonics Here, There, Everywhere: Looking Back and Leaping Forward

OMAR AZZARONI*[a], M. LORENA CORTEZ[a], MATÍAS RAFTI[a], WALDEMAR A. MARMISOLLÉ[a] AND KATSUHIKO ARIGA[b]

[a]Instituto de Investigaciones Fisicoquímicas Teóricas y Aplicadas (INIFTA), Departamento de Química, Facultad de Ciencias Exactas, Universidad Nacional de La Plata (UNLP), CONICET, Diagonal 113 y 64 (1900), La Plata, Argentina; [b]National Institute for Materials Science (NIMS), Tsukuba, Japan
*E-mail: azzaroni@inifta.unlp.edu.ar

23.1 Introduction

The design and elaboration of materials is the essence of technology, and has always been a key issue for the development of our societies and the advancement of mankind. In fact, the paramount relevance of materials is made clear from the naming of ages of civilizations – the stone, iron and bronze ages – with each new era being brought about by a new material. The emerging reality in these first decades of the twenty-first century is

Nanoscience & Nanotechnology Series No. 55
Concepts and Design of Materials Nanoarchitectonics
Edited by Omar Azzaroni and Katsuhiko Ariga

Published by the Royal Society of Chemistry, www.rsc.org

that our standards of living and economic and social progress are heavily reliant on more efficiently performing materials with properties superior to those of current – and hence aging – materials. This notion applies to a broad variety of technologies and applications including electronics, drug delivery, cancer diagnostics or alternative energy sources. Over the years, the search for fundamentally new materials with improved functional capabilities has led to a grand challenge: synthetic control at the "supramolecular" level.

Within this context, Aono coined the term "nanoarchitectonics" as a new conceptual framework in which nanoscale structural units are arranged into a configuration that creates novel materials through mutual interactions. As a result, materials nanoarchitectonics not only deals with the nanomaterial synthesis, but also with its nano-organization.

Achieving such an ambitious goal requires the harmonic integration of predesigned building blocks *via* adequate methods/techniques. In essence, the rational design of functional nanomaterials or nanostructures through nanoarchitectonics demands atomic/molecular manipulation of structures, manipulation of self-assembly properties, manipulation of chemical and physical characteristics and control over organization in the presence of external stimuli.

In this chapter, we identify key areas of materials science in which nanoarchitectonics concepts are increasingly pervading. The core concept of nanoarchitectonics is based on the controlled arrangement of structural nanoscale units, such as atoms, molecules and assemblies, to create a new class of materials for modern and emerging technological applications.

During the past decades, the creativity of chemists and materials scientists provided a means for developing a wide variety of materials with unprecedented functional properties. At this stage, we should bear in mind that one main focal point of chemistry is to rationally design molecular building blocks and nanomaterials entirely from scratch. Nowadays, the variety of available nanoscale objects prone to be used as building blocks of complex nanostructured systems is increasingly large. In this sense, practitioners or "nanoarchitects" willing to create a superstructure or hybrid assembly for a precise functional purpose should first ask themselves the following questions: What kind of building blocks do we need? What property or properties are we interested in? What kind of synergy can be expected, and how could it be enhanced? What is the best method to organize and assemble the selected building blocks?

Lastly, the ultimate goal of this final chapter is to provide some answers to the questions referred to above and to discuss current challenges and prospects. In doing this, they will be able to pinpoint those facets, elements and methods that render nanoarchitectonics a unique and versatile toolbox to achieve the actual molecular design of complex materials.

23.2 Building Blocks for Nanoarchitectonics – Important Emerging Actors for Relevant Applications

23.2.1 Polymer Brushes

Polymer brushes are macromolecular systems represented by polymer chains grafted or tethered to a solid substrate.[1] The increasing interest in polymer brushes as building blocks for nanoarchitectonics can be attributed to their flexibility to create tailored films displaying pseudo-3D spatial arrangements of functional units in which chemical composition can be manipulated with nanoscale precision[2] (see Figure 23.1). In this sense, interfacial nanoarchitectonics with polymer brushes has seen growing interest due to its potential to confer specific functions to a broad range of materials.[3] Polymer brushes offer a broad variety of resources to manipulate interfacial properties and gain molecular control over the synergistic combination of materials and devices for specific purposes.[4] This, in turn, has led to the rational integration of polymer brushes in a broad variety of nanoarchitectures resulting in devices with improved performance, lifetime and stability.

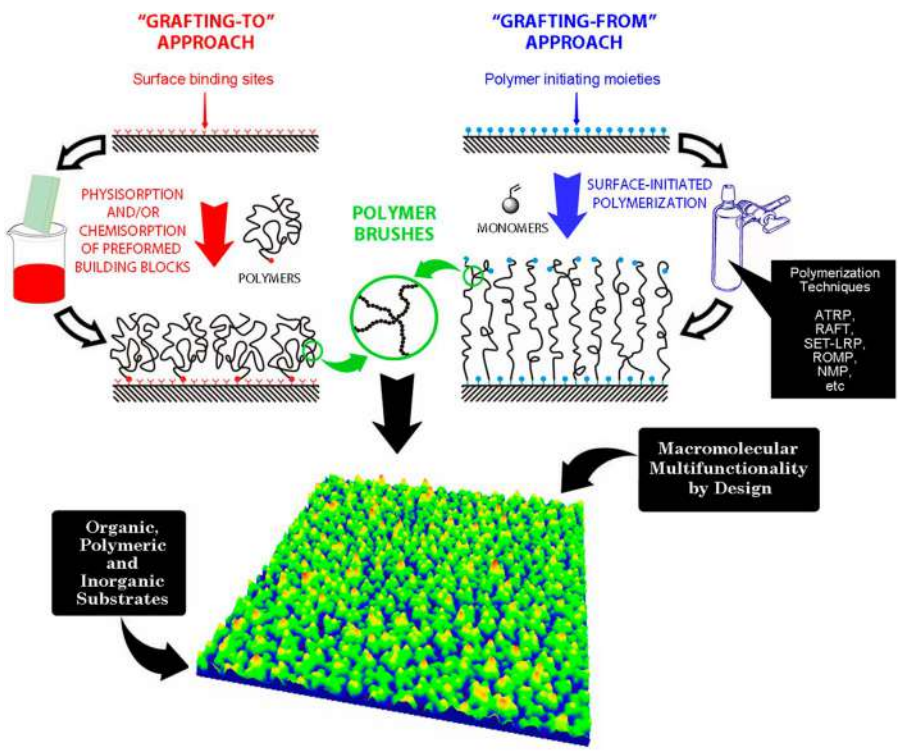

Figure 23.1 Chemical strategies for the modification of substrates with polymer brushes. Reproduced from ref. 2 with permission from John Wiley & Sons, Copyright © 2012 Wiley Periodicals, Inc.

Minko and co-workers employed polymer brush–enzyme hybrid interfacial architectures to create bioelectronic systems that allow biochemical processing of complex information.[5] Polymer brushes have been used as prominent building blocks to design biointerfaces and in particular in those areas concerning the control of bacterial and cell adhesion. For example, Okano and his collaborators developed switchable surfaces based on thermoresponsive poly(*N*-isopropylacrylamide) (PNIPAM) brushes to manipulate adhesion and detachment of cells from diverse substrates.[6] In a similar way, Ren *et al.*[7] employed poly(oligo(ethylene glycol) methacrylate-random-2-hydroxyethyl methacrylate) (poly(OEGMA-*r*-HEMA)) brushes combined with fibronectin (FN) and recombinant human bone morphogenetic protein-2 (rhBMP-2) to impart osteogenesis capacity to titanium-based surfaces. It has been also shown that the functionalization of poly(2-hydroxyethyl methacrylate) (PHEMA) or poly(poly(ethylene glycol) methacrylate) (PPEGMA) brushes with short peptide ligands promote the endothelialization of blood-contacting biomaterials.[8]

Surface modification of micro- and nanoparticles with functional polymer brushes has been extensively exploited as a versatile strategy to create functional, or even "smart", colloidal systems with tailorable dispersion properties. In these nanoarchitectures, the polymer brush confers environmental responsiveness towards variations in, *e.g.*, solvent nature, temperature, pH, or light. These hybrid nanoarchitectures have been increasingly used in diverse practical applications since an "ON/OFF" switch in interfacial properties can be prompted in the presence of specific stimuli. This nanoarchitectonic approach employing mixed brush-coated nanoparticles led to the creation of stimuli-responsive colloidal systems displaying a drastic switching of their colloidal properties upon external stimuli.[9]

In a similar vein, polymer brushes have been extensively used for the molecular design of substrates displaying switchable wettability. Polymer brushes are capable of drastic changes in their physicochemical properties in the presence of environmental chemical or physical stimuli, such as temperature, solvent, counterion nature or light, among others (see Figure 23.2). These remarkable characteristics of polymer brushes fostered the development

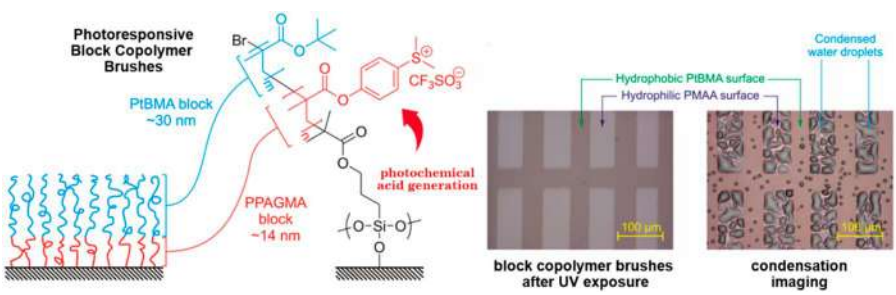

Figure 23.2 Light-responsive wettability using photoacid generators incorporated in polymer brushes. Reproduced from ref. 10 with permission from the Royal Society of Chemistry.

of numerous strategies to attain non-reversible and reversible control of wetting properties of a broad variety of substrates.[10–19]

In this context, these macromolecular architectures turned out to be outstanding building blocks to design chemically-modified electrodes as they can deliberately control the reactivity at the electrode solution/interface. Polymer brushes offer a versatile approach for the molecular design of electrode surfaces in which parameters such as porosity/permeability, environmental sensitivity and hydrophobicity can be controlled at will. Such control has a profound impact on relevant applications including electrocatalysis, electroanalysis, or electrochromics, among others.[20–22] As an example, the grafting of PMETAC brushes onto amine-appended polyaniline-modified electrodes allowed the reversible modulation or the electrochemical response by the presence of specific anions due to the occurrence of a blocking effect by the hydrophobic collapse on the polymer-solution interface[23] (see Figure 23.3).

The characteristics of polymer brushes have been deployed to improve the performance of organic electronic devices. Nanoscale interfacial phenomena play a key role in the regulation of processes taking place in these devices and, consequently, polymer brushes represent helpful tools to engineer interfacial and electronic properties of surfaces. One of the remarkable features of polymer brushes suitable for nanoarchitectonic interfacial design of organic electronic devices is the fact that polymer chains exhibit a high degree of perpendicular alignment with respect to the substrate that, in turn, leads to direct paths to the collection electrode. In the case of polymer brushes tethered to the anode of organic electronic devices, it has been demonstrated that charge-transporting polymer brushes exhibit an up to three orders of magnitude increase in current density normal to the substrate compared with a spin-coated film.[24] Polymer brushes have also been employed to manipulate the de Dirac point in graphene field-effect transistors by reversibly

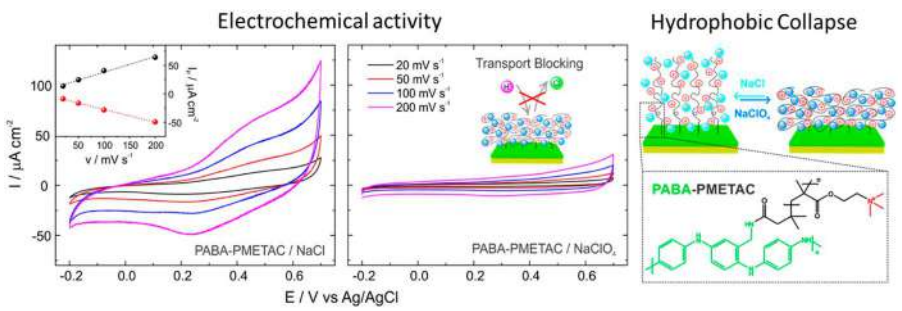

Figure 23.3 Voltammetric response of an amine-appended polyaniline (PABA) film electrode after grafting a PMETAC brush coating in the absence (left) and presence (center) of perchlorate anions in the electrolyte solution. The shut-down of the electroactivity is caused by the hydrophobic collapse induced by the strong interactions of perchlorate with quaternary ammonium moieties in the polymer brush (right). Reproduced from ref. 23 with permission from Elsevier, Copyright 2018.

controlling the charge density of the macromolecular layer in the presence of divalent ions (see Figure 23.4).[25]

Inorganic nanoparticle–polymer brush hybrids have been employed for the nanoarchitectonic design of thin film nanocomposites in which the unique properties of inorganic particles and the functional versatility of polymer brushes were exquisitely combined.[26]

Rational integration of nanoparticles inside polymer brushes boosts the synergy between these counterparts in order to maximize the catalytic, electronic or optical properties of the nanocomposite. For instance, nanoparticles at spherical brushes have been employed as excellent hosts for applications in catalysis.[27]

Another interesting application of polymer brushes is the selective molecular engineering of both outer and inner environments of mesoporous materials to translate biologically inspired concepts into the design of "active" nanosystems.[28–33] Along these lines, the use of responsive polymer brushes to create hybrid nanoarchitectures based on mesoporous materials has facilitated the development of gated molecular transport nanosystems and controlled delivery vehicles (see Figure 23.5).[34,35]

The modification of opal nanopores with polymer brushes has led to the rational design of "smart" colloidal membranes. Opals contain highly ordered arrays of 3D interconnected nanopores whose size can be controlled by changing the size of the silica spheres used to assemble the structure. The integration of polymer brushes into the interconnected pores endows the opal scaffold with built-in responses to multiple chemical and physical stimuli.[36,37] This interesting nanoarchitectonic strategy based on hybrid colloidal crystals has proved valuable in the construction of leak-free solid-state polymer electrolytes for application in lithium-ion rechargeable batteries.[38]

Likewise, the modification of ordered two-dimensional macroporous silicon membranes with anionic polyelectrolyte brushes gave rise to the development of novel proton-conducting membranes with enhanced transport properties.[39–41] Concomitantly, the modification of single solid-state

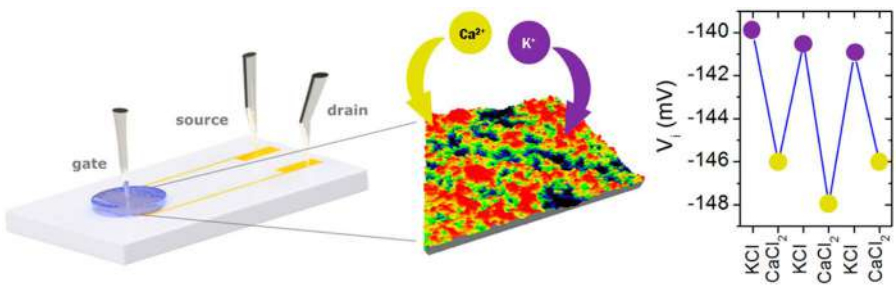

Figure 23.4 Reversible switching of the Dirac point in graphene field-effect transistors functionalized with polymer brushes bearing phosphate groups. Reproduced from ref. 25 with permission from American Chemical Society, Copyright 2019.

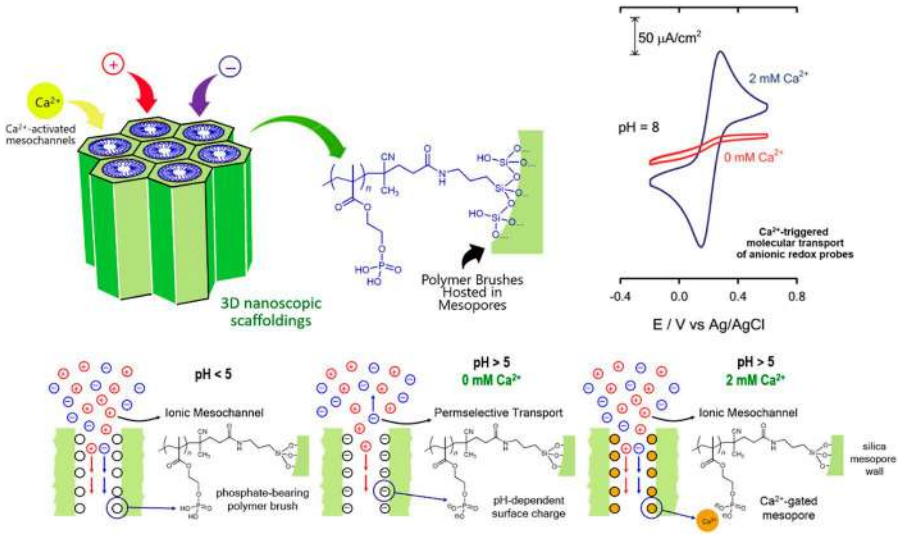

Figure 23.5 Construction of proton and calcium-gated ionic mesochannels through the modification of mesoporous thin films with phosphate-bearing polymer brushes. Reproduced from ref. 33 with permission from American Chemical Society, Copyright 2012.

nanopores with polymer brushes has been extensively explored as a strategy to create biomimetic nanofluidic elements with enhanced ion transport properties for potential applications in nanofluidic electronics, biosensing, separation, synthetic biology, and single-molecule manipulation.[42–45]

23.2.2 Metal–Organic Frameworks

Beginning with the earliest reported examples by Hoskins *et al.*,[46] the study of a new class of versatile porous materials known as metal–organic frameworks (MOFs) has become a field of research that expanded rapidly and constitutes now a prominent topic in the realm of materials science. This field has evolved from a combination of coordination chemistry, supramolecular chemistry and crystal engineering to the discovery of porous hybrid materials *via* the design and implementation of new synthetic strategies.[47] A wide range of new fascinating porous materials showing specific and unprecedented properties and functionalities are now emerging. This influx of notions and ideas lead to a *vertiginous rise in* the number of applications in which MOFs play a decisive role as nanoarchitectonic building blocks.[48]

Metal–organic frameworks are currently employed in diverse technological areas such as chiral separations, highly active catalysts, fuel gas storage and both detection and capture of hazardous agents.[49,50] The control of chemistry within confined nanoscale environments is an expanding platform technology for the future, which will be essential for energy and healthcare

applications. In this context, the nanoarchitectonic design of functional materials has never been more important.

The formation of aligned open channels decorated with metal centers turns MOFs into highly versatile platforms for catalysts as they integrate catalytic sites at specific locations within the frameworks. By and large, the nanoarchitectonic design of functional MOFs can be accomplished through two main strategies. One of them is to integrate building units equipped with specific active sites in their skeletons.[51] Another strategy relies on the pore surface engineering that enables post-synthetic integration of active sites onto the channel walls.[52] These two main strategies brought about remarkable progress in the use of MOF for multiple purposes.

The creativity of chemists and materials scientists provided different means of controlling the physical form of MOFs in order to create mesoscopic superstructures composed of nanocrystals as building blocks. These MOF architectures involve hollow capsules or microspheres, nanorods or nanofibers, thin films, membranes or patterns, and even three-dimensional (3D) architectures constituted of extended systems.[53]

The most impelling reason for the necessity of controlling the physical form of MOFs arises from the possibility of enhancing the functional performance by the selection and/or design of superstructures of the appropriate dimensionality. For example, 2D MOF nanosheets synthesized by using top-down methods, such as sonication exfoliation, or chemical exfoliation, and bottom-up methods, such as interfacial synthesis or surfactant-assisted synthesis have been successfully employed in energy conversion and storage, catalysis, sensors and biomedicine applications.[54]

Depending on the nature of the metal–organic framework, these materials can be employed as luminescent and photonic nanoarchitectures for sensing applications, including the detection of volatile organic compounds, ionic species and diverse environmental pollutants.[55]

MOF–enzyme hybrid nanoarchitectures[56] have shown unprecedented performance in terms of synergistic effects of enzymes loaded in porous supports in general. In several cases it has been observed that MOF–enzyme hybrids outperform the activity of the free enzyme even in *a priori* biologically incompatible conditions.

The formation of MOF–metal nanoparticle (MNP) nanohybrids resulted in interesting synergistic effects for enhanced catalysis.[57] The porosity of MOF architectures enables the confinement of small metal nanoparticles for improved catalytic performance in a broad scope of reactions. The synergy between the metal nanoparticles and the MOF arises from the delicate interplay between the active roles of both components. This implies that depending on the nanoarchitectonic design of the MOF-MNP hybrid different synergistic combinations can take place: (1) MNPs as active centers, stabilized by MOFs; (2) MNPs as active centers, with MOFs controlling size selectivity; (3) MNPs as active centers, and MOFs as pre-concentrating agents of gaseous reactants; (4) MNPs as active centers with MOFs regulating their electronic properties; (5) both MOFs and MNPs as active sites for tandem catalysis.

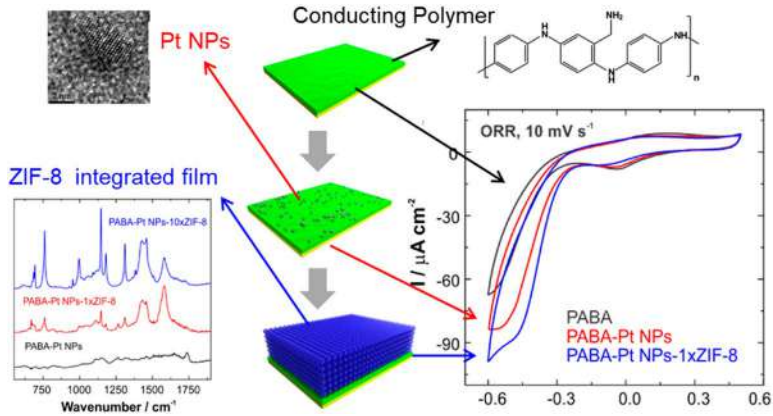

Figure 23.6 Sequential integration of an electroactive polymer thin film, *in situ* synthesis of Pt nanoparticles and deposition of a ZIF-8 coating for enhancing the oxygen reduction reaction in neutral pH solutions. Reproduced from ref. 63 with permission from American Chemical Society, Copyright 2018.

The development of new deposition strategies facilitated the progress in the nanoarchitectonic design of surface-supported metal–organic framework thin films.[58–60] By exerting better control over film thickness, homogeneity, morphology, and dimensions of metal–organic framework thin films,[61,62] the materials science community gained access to new opportunities in different application fields, such as photovoltaics, CO_2 reduction, energy storage, water splitting, electronic devices, and advanced membranes. One interesting example of the integration and/or attachment of MOF thin films onto electrode surfaces is the growth of ZIF-8 on conducting polymer films for enhancing the oxygen reduction reaction by O_2 pre-concentration within the porous structure[63] (see Figure 23.6). Devising new methods to anchor MOF on electrode surfaces has fostered the use of MOF thin films for solar energy conversion, field-effect transistors, supercapacitors or batteries.[64]

Nowadays, from the viewpoint of nanoarchitectonics, the main priorities of MOF research concentrate on the molecular design and synthesis of materials with optimized physical and chemical properties. Using suitable predesigned building blocks, the integration of specific interactions inside the framework can result in new nanomaterials with unprecedented properties suitable for their application in diverse technologies.

23.2.3 Mesoporous Materials

The importance and utility of mesoporous materials in nanoarchitectonics cannot be overestimated.[65] Ordered mesoporous materials derived from supramolecular templating exhibit high surface area and tailored pore sizes. Moreover, these pore surfaces can be further modified by organic,

organometallic or even biologically active functional groups. This enables the design and nanoconstruction of hybrid systems with distinct physical properties or chemical functions located in the framework walls, the pore surface, and the pore interior (see Figure 23.7).

The use of organic-inorganic mesoporous hybrid materials represents a creative nanoarchitectonic approach to design new materials for innovative applications.[66] All these applications exploit the versatility of sol–gel processes to generate materials with controllable mesoscale porosity and tunable chemical functionalities incorporated into well-defined ordered mesostructured frameworks. Due to the high flexibility of the synthesis, mesoporous materials have demonstrated high capability of integration in different processing technologies. This synthetic aspect has been an essential component of the successful use of mesoporous materials in multiple applications.[67]

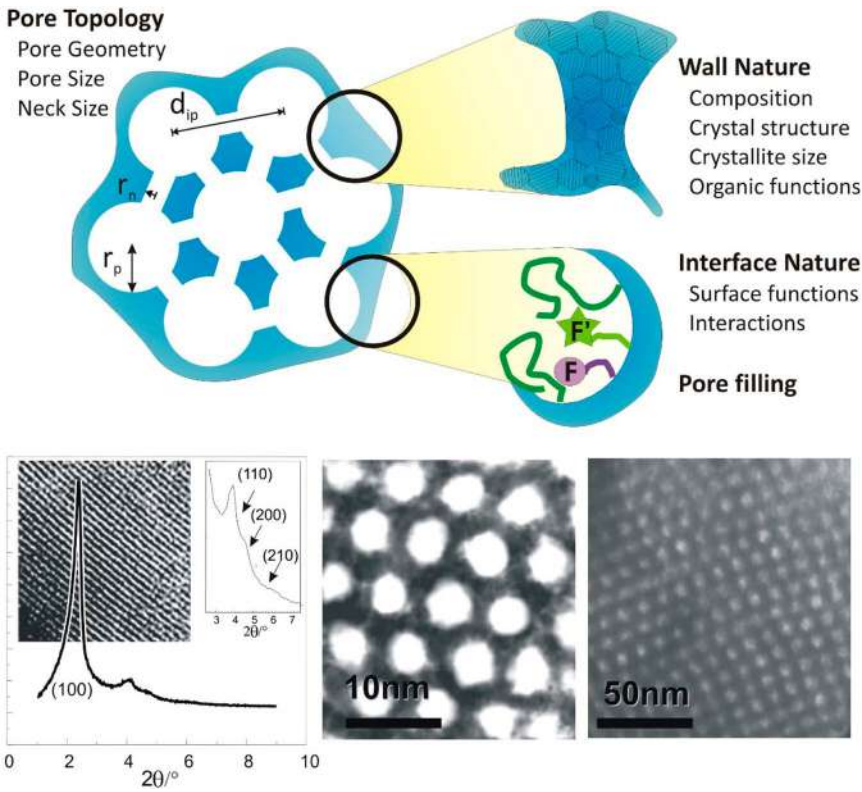

Figure 23.7 Top: Scheme of a mesoporous material and indication of the functional domains. Bottom: XRD diagram of MCM-41 silica. Insets show the channel-like structure observed by TEM (left). TEM images of the hexagonal pore structure of a CTAB-templated titania powder (center) and amino-functionalized zirconia thin film with cubic mesostructure (right). Reproduced from ref. 65b with permission from the Royal Society of Chemistry.

Mesoporous films have been employed in catalysis and photocatalysis, solar cells, ultra-low-k dielectric materials, low refractive index and thermal insulating films, electrochromic mesoporous films, photochromic applications, supercapacitors for energy storage, bioactive films, sensors, photonics, permselective membranes, electrode materials for lithium-ion batteries, gas sensing, adsorption and separation, among others.[68]

On the other hand, mesoporous silica nanoparticles with large surface areas and pore volumes have been extensively used as efficient carriers for various therapeutic agents.[69] The functionalization of these mesoporous particles with molecular, supramolecular or polymeric building blocks confers great versatility to the nanomaterial in order to perform drug delivery functions with enhanced control.

Supramolecular and polymeric building blocks offer the possibility of creating functional domains that, in turn, control the interactions operating within the restricted volume of the pore. From a synthetic viewpoint, this combination of "hard" and "soft" building blocks results in nanocomposite materials with tuneable functional domains ordered in space. From a nanoarchitectonic viewpoint, these nanocomposite materials are expected to exhibit new properties arising from the synergy of both kinds of components, and their spatial location.

At the same time, the "hybridization" of mesoporous materials with metal nanoparticles has vastly contributed to the field of catalysis due to the combination of high contact surface area and unique catalytic properties in the same material. Besides the large surface area, mesoporous materials are also able to provide a tailorable spatial confinement which is a critical issue in catalytic applications. This is an important functional aspect, as the mesoporous matrix facilitates the dispersion of the nanoparticles and prevents the nanoparticles from aggregating during the catalytic reaction. In addition, the physicochemical nature of the pore environment may offer diverse interactions with the immobilized nanoparticles and therefore modify their catalytic properties.

23.2.4 Colloidal Particles, Nanocrystals and Quantum Dots

Colloidal nanoparticles with controlled size, shape, and composition are quintessential building blocks in nanoarchitectonics.[70] Ordered assemblies of colloidal nanoparticles, or so-called artificial photonic crystals or "opals" exhibit collective electronic and optical properties highly suitable for diverse applications such as nanoelectronics and nanophotonics. Over recent years, a great deal of effort was put into the successful integration of colloidal nanoparticles into engineered battery electrodes, durable films/coatings, biomedical platforms, *etc.*[71] In all these cases, the use of nanoarchitectonic concepts was crucial to achieving surface functionality, reproducible assembly, mechanical robustness and patternability (when needed). Essential aspects related to size, shape, core/shell structure, surface chemistry are

critical to controlling the functional properties of colloidal nanoparticles and their assemblies.[72]

This explains, after all, why the materials science community (and especially those researchers involved in nanoarchitectonics) still devote research efforts to the development of new functionalization strategies to manipulate colloidal nanoparticles to achieve enhanced functions and properties. Another area of increasing interest is the manipulation of nanoparticle growth in order to control their assembly and interactions. These two aspects (nanoparticle functionalization and assembly) are critical to attaining large area integration of nanoparticle assemblies for additive manufacturing through patterning, nanoparticle printing or evaporation-induced self-assembly, among other techniques.[73]

In the specific case of semiconducting monodisperse shape-controlled nanocrystals, these nanomaterials are increasingly employed as nanoarchitectonic building blocks for the assembly of advanced thin films and devices. Significant strides in synthesis and purification of these materials facilitated the design of semiconductor nanoparticles (quantum dots) with tunable shapes, including spheres, rods, cubes, disks and octahedra, among others. Furthermore, depending on the synthetic procedure single phase nanocrystals or core–shell semiconducting heterostructures can be obtained. One of the most attractive features of nanocrystals and quantum dots is their tunable electronic, optical and magnetic properties, which allow them to confer specific functional characteristics to different assemblies and nanocomposites.

Nanocrystals can be assembled into single-component, binary or ternary superlattices providing a versatile nanoarchitectonic route to the production of multifunctional thin films. In fact, the modular assembly of these nanocrystals can enhance quantum phenomena as the interactions between the semiconducting particles allow new delocalized properties to emerge. The synergy arising from the electronic and optical coupling between nanocrystals is the key to the nanoarchitectonic design of artificial solids with tailorable 3D structure and optoelectronic properties suitable for different technological applications such as thin film transistors, thermo-electric materials or solution-processable photovoltaic devices.

23.2.5 Colloidal Supraparticles

The notion of creating designed materials *via* self-assembly of nanoscale blocks has gained considerable momentum over the last few years. The combination of supramolecular principles and nanoscopic structures is one of the primary essences of nanoarchitectonics and offers the possibility to create supraparticles using nanoparticles as functional and structural units (see Figure 23.8). Extensive work by numerous researchers in the last decade has demonstrated that the harmony between repulsive interactions and attractive noncovalent forces mediates the self-organization of nanoparticles and stabilizes discrete self-assembling mesoscopic supra-structures.

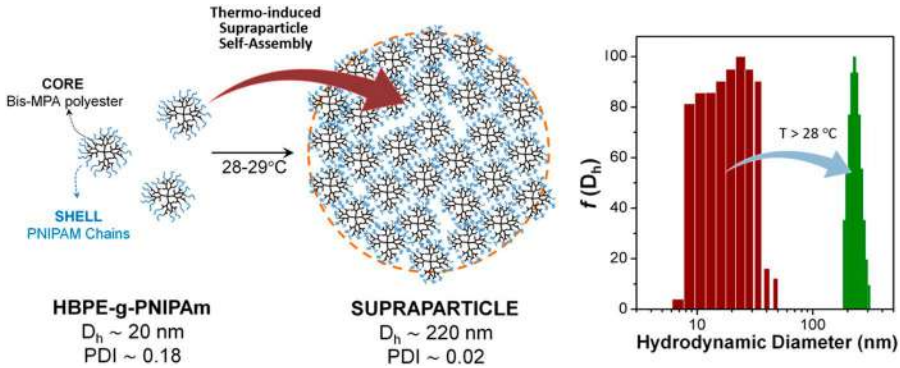

Figure 23.8 Self-assembly of thermoresponsive hyperbranched polymers into supraparticles. Reproduced from ref. 114 with permission from Elsevier, Copyright 2016.

These advances led to the rational design of supraparticles based on the self-limited assembly of nanoparticles. For example, the self-limiting self-assembly of non-uniform inorganic nanoparticles can lead to the formation of highly ordered 3D mesostructures.[74] This nanoarchitectonic strategy to create complex supra-structures has opened new horizons in materials science, especially if we consider that historically the formation of self-limiting nanostructures was almost an exclusive domain of biology.

We have already learned that nanoparticles represent a new generation of advanced materials exhibiting unique chemical and physical properties. However, when we enter into the realm of self-limited supraparticles, we realize that we can manipulate their collective properties by combining multiple components individually tailored for specific functions. As a result, this strategy offers unprecedented mesoscale compositional and structural control of self-limited colloidal materials, in a reproducible fashion, with enormous potential for scalability.

Supraparticles prepared from different materials such as metal or semiconductor nanoparticles, proteins and polymers (Figure 23.8) have been reported. By exploiting van der Waals attractions as the main driving force for spontaneous assembly, a variety of polydisperse nanoparticles (CdSe, CdS, ZnSe, PbS and Au/CdSe) were assembled in solution leading to colloidally stable monodisperse supraparticles.[75] Self-limited supraparticles have also been synthesized through more complex synthetic routes: seed-mediated,[76] sacrificial substrate,[77] thermal,[78] and other methods.[79] For example, semiconducting ZnSe nanoparticles can be spontaneously assembled *via* a high-temperature synthetic route, resulting in stable and monodisperse nanorod couples connected by twinning structures.

Over the last decade, a broad variety of supraparticles have been built using various nanomaterials and different synthetic approaches. This

ample repertoire of different kinds of supraparticle assemblies involves all-inorganic,[80,81] hybrid soft-inorganic[82,83] and all-organic systems.[84,85] Among them, a number of studies have focused on the construction of assemblies through van der Waals and electrostatic interactions due to the simplicity of this approach. However, recognition-driven assembly has also been employed as a nanoarchitectonic strategy to create bio-supraparticles with controlled size and composition. Stable enzymatic supraparticles were prepared through lectin– carbohydrate recognition-directed assembly of concanavalin A and glucose oxidase[86] (see Figure 23.9). The application of biospecific interactions mediated by DNA has been also explored for designing self-assembled self-limited superstructures. Within this framework, complementary nucleic acid sequences bound to different building blocks were self-assembled through DNA hybridization, thus resulting in precise

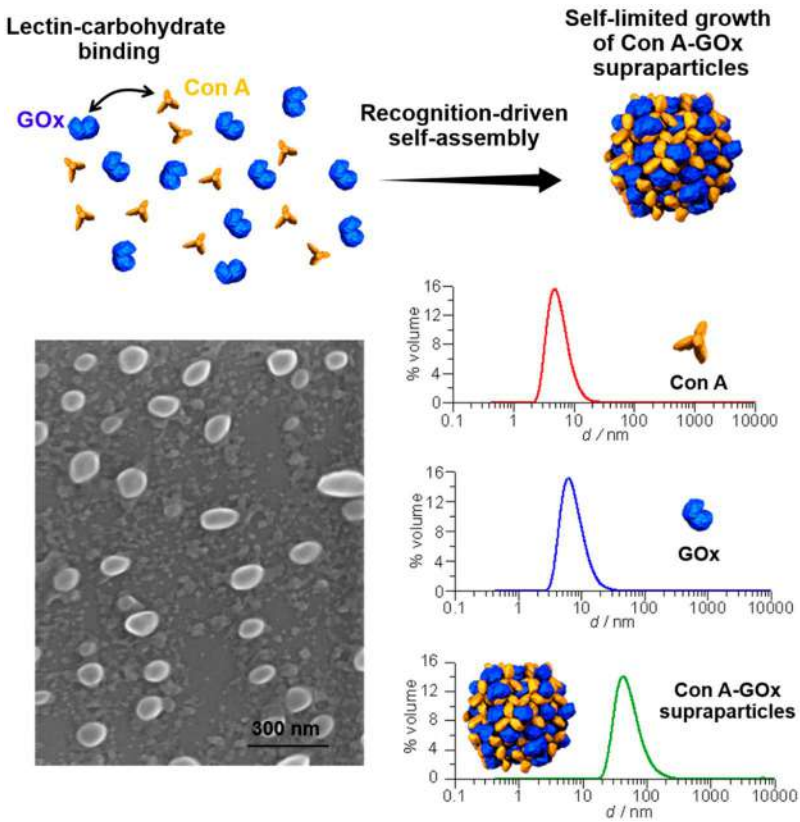

Figure 23.9 Recognition-driven assembly of self-limiting supramolecular enzymatic nanoparticles constituted of Concanavalin A (Con A) and glucose oxidase (GOx). Reproduced from ref. 86 with permission from the Royal Society of Chemistry.

and programmable control over the spatial assembly of nanoparticles.[87] These examples illustrate the ability of chemists and materials scientists to exert rational control over dimensions and functionality of complex colloidal materials that might provide exciting new opportunities in sensing, nanomedicine or catalysis, just to name a few examples.

23.2.6 Polyelectrolyte-surfactant Complexes

The formation of complexes of polyelectrolytes and oppositely charged surfactants represents a simple, but versatile strategy to create synthetic self-assembled polymeric systems.[88] The complexation process, also known as "ionic self-assembly" (ISA), is a reaction driven by electrostatic attraction between the polymer chain units and the surfactant ions. The ISA process is usually dominated by a cooperative binding mechanism in which the first complexed monomer units induce further binding along the polymer chain.

This strategy leads to the formation of polyelectrolyte-surfactant complexes in different scenarios. For example, complexes can take place at the air–water interface by spreading the amphiphile on an aqueous solution of the polyelectrolyte.[89] On the other hand, these polyelectrolyte-surfactant complexes can be prepared by simply mixing solutions of the two components in polar organic solvents. Such complexes combine in unique ways the properties of polyelectrolyte with those of low molecular weight amphiphiles. The polyelectrolyte components can provide, for instance, mechanical strength and thermal stability, while the surfactants retain their tendency to assemble in layered structures. They are able to form stable colloidal suspensions in water and they can be completely dissolved in organic solvent, allowing easier handling and a very stable structure after drying[90] (see Figure 23.10).

This supramolecular approach offers chemists and materials scientists a broad toolbox for creating new self-organized, hierarchically ordered functional materials, as it affords a truly vast parameter space for material design.[91] Along these lines, several research groups studied the incorporation of predefined functionalities within either the polyelectrolyte or the surfactant counterparts in order to attain self-assembled materials with specific functional features. In recent years, this type of supramolecular nanoarchitecture has been employed in the design of new electroactive materials. The use of sodium poly(styrenesulfonate) (PSS) complexed with n-alkyl (ferrocenylmethyl) ammonium bromide resulted in the formation of redox thin films with remarkable stability.[92] Similarly, redox-active mesomorphic complexes were obtained from the ISA of cationic polyferrocenylsilane polyelectrolytes and different anionic surfactants.[93] On the other hand, the combination of protonated amine-appended polyaniline with phosphate surfactants led to the formation of complexes by ISA, which could then be employed for the

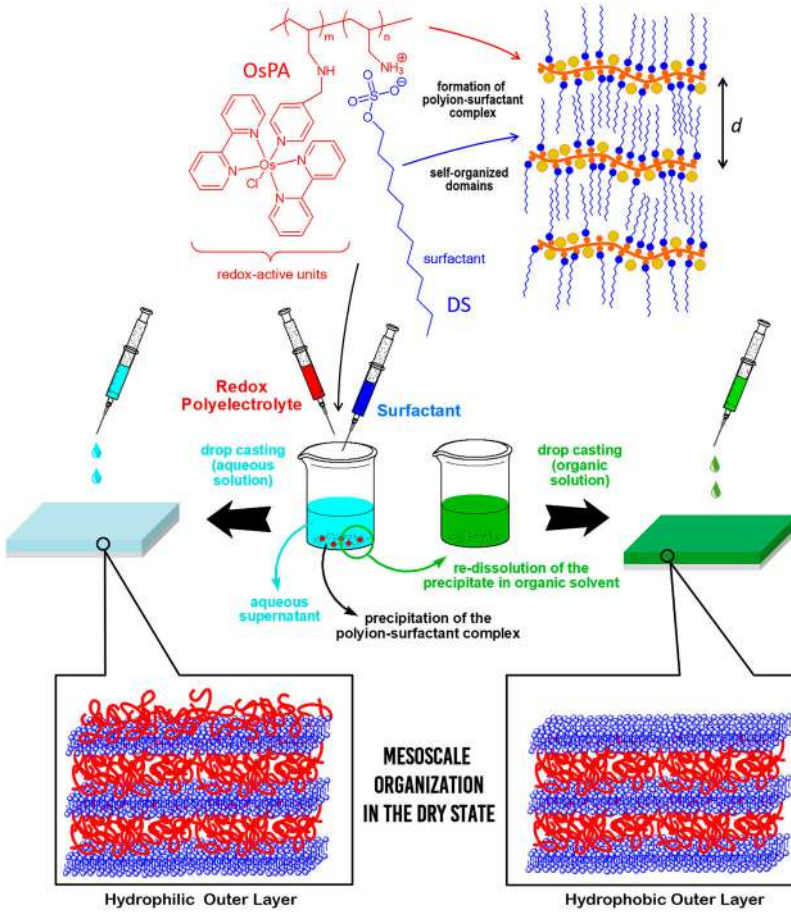

Figure 23.10 Assembly of mesoscale-organized polyion–surfactant complexes and subsequent formation of films *via* drop casting on solid substrates using aqueous or organic solvents. Reproduced from ref. 90 with permission from American Chemical Society, Copyright 2017.

construction of both meso-organized and electroactive nanofilms[94] (see Figure 23.11). The use of these supramolecular materials was then extended to the development of bioelectrochemical platforms integrating enzymes,[95] metal nanoparticles[96] or carbon nanotubes[97] within the self-assembled architecture. What is more, since recognition sites can be appended to the polyelectrolyte chain, the synergistic combination of ionic self-assembly and recognition-directed assembly[98] resulted in the creation of highly functional bioelectrochemical interfaces compatible with the supramolecular design of a wide variety of biosensing platforms.

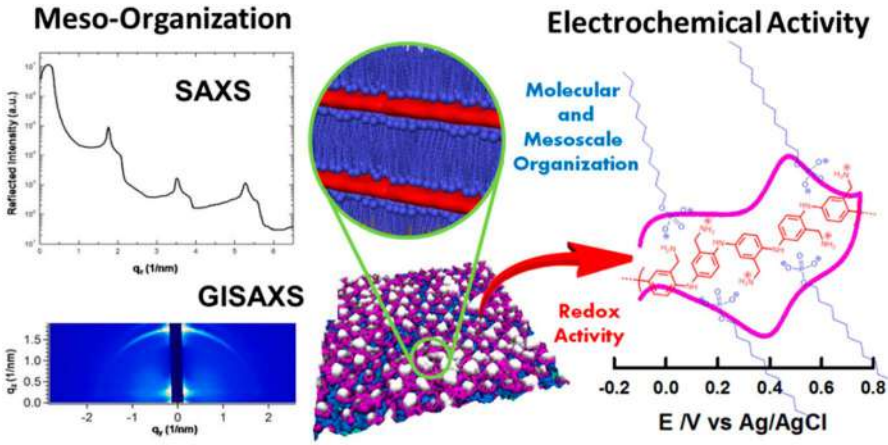

Figure 23.11 Meso-structure X-ray characterization and cyclic voltammetry response of nanofilms obtained by spin-coating of ionically self-assembled complexes of amine-appended polyaniline and phosphate-bearing surfactants. Reproduced from ref. 94 with permission from the Royal Society of Chemistry.

23.3 Nanoarchitectonics in Our Modern Societies – Health, Environment and Energy

23.3.1 Layer-by-layer Nanoarchitectonics for Clean Energy and Sustainable Environment

For developments of functional materials systems with high efficiencies, nanoarchitectonics efforts to precisely arrange component materials within materials structures would become key processes. One of the possible strategies to make structurally well-arranged functional structures is the fabrication of controlled layered structures by conventional technique, so-called alternate layer-by-layer (LbL) assembly.[99,100] In the following section, research examples on layer-by-layer nanoarchitectonics for clean energy and sustainable environment are introduced where basics of LbL assembly and application examples are described.

23.3.1.1 Basics of Layer-by-layer (LbL) Assembly

Before the 1990s, the self-assembled monolayer (SAM) technique and Langmuir–Blodgett (LB) method were recognized as representative methodologies to provide organized ultrathin films. The SAM method is an excellent method for providing organized monolayers that can be immobilized on surfaces. However, this method is mostly limited to the fabrication of a single monolayer on a solid surface and cannot be recognized as a general technique

for fabricating organized multilayers. In contrast, The LB technique is a powerful method in the preparation of multi-layered films. However, this method is applied mainly for lipid-like amphiphilic components. This method might not be applicable to a wide range of materials. Layer-by-layer (LbL) assembly was an emerging methodology after the 1990s to compensate for deficiencies in these traditional methods. The LbL method is a generally applicable simple method for fabricating multi-layered films through sequential layer-by-layer adsorption of unit layers. Especially, the LbL method allows many types of materials to be assembled. In addition, the processes of LbL assembly rely on very easy procedures and inexpensive apparatuses. Therefore, the LbL method has attracted attention as a more versatile fabrication method for multi-layer films[101–103] as compared with the SAM and LB methods.

As mentioned above, the LbL assembly method is applicable to a huge variety of components materials including conventional polymers (polyelectrolytes), functional polymers, inorganic substances, quantum and nanomaterials, molecular assemblies, biomaterials, viruses, and living cells (see Figure 23.12). Assembling functional components for energy and environmental uses into nanostructured assemblies is highly possible with LbL assembly. As shown below, electrostatic interactions between layered components are used as assembling driving forces in most cases. The other interactions such as hydrogen bonding, metal coordination, stereo-complex formation, charge transfer, supramolecular inclusion, biospecific interactions, covalent bonding, and electrochemical coupling can be included in the assembling processes of the LbL method. The required implementation of the LbL assembly is simple and inexpensive. In the LbL assembly, nano-level ultrathin films can be obtained only using beakers and tweezers while automatic dipping machines are also used. Another important feature of the LbL technique is the high amount of freedom to adjust layer structures both in the numbers of layers and layered sequences.

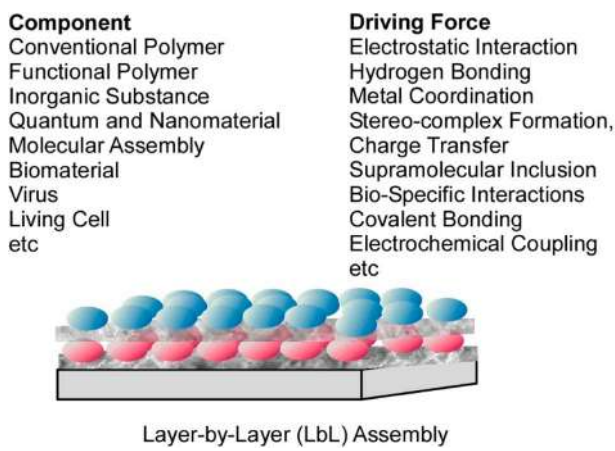

Figure 23.12 Versatile nature of the LbL assembly.

Typical procedures of the LbL assembly are illustrated in Figure 23.13 where LbL assembly of cationic polyelectrolytes and anionic particles by electrostatic interaction is described. In the illustrated example, the solid substrate has anionic charges on its surface. When the solid substrate is immersed into a solution containing a cationic polyelectrolyte, the cationic polyelectrolytes adsorb through electrostatic interaction. The adsorption of cationic polyelectrolytes onto the solid surface neutralizes the negative charges on the solid substrate. However, excess adsorption over a neutral point induces charge reversal and restructuration. These adsorption processes result in charge alteration to positive at the outermost surface of adsorbed layers on the solid surface. This excess adsorption is spontaneously saturated upon

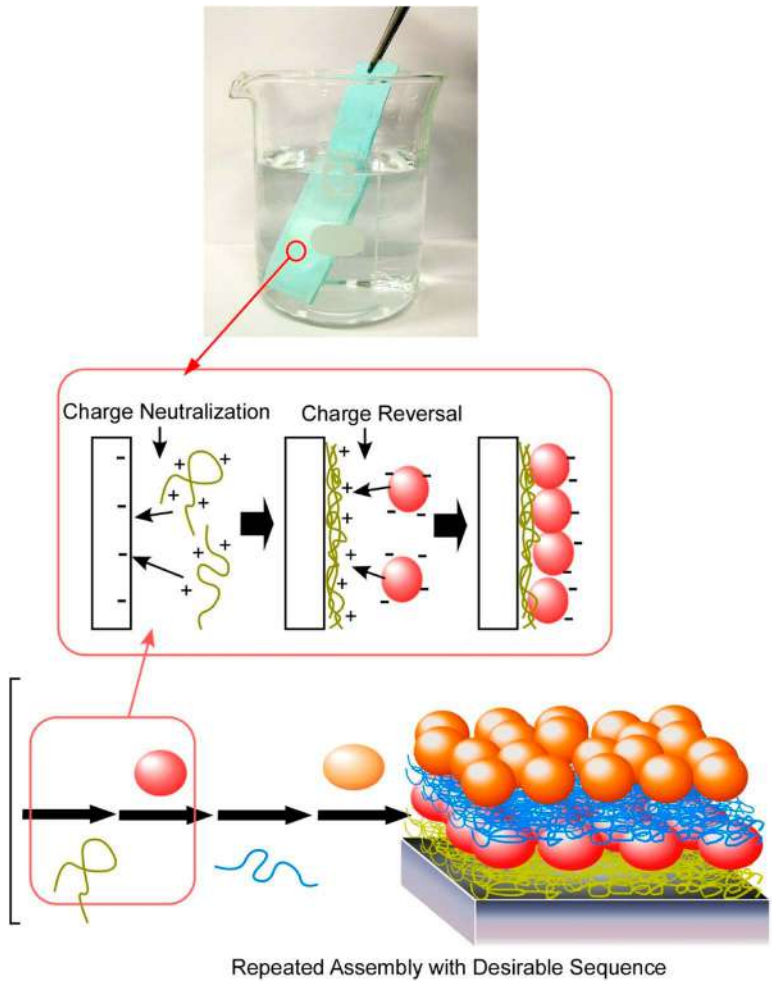

Figure 23.13 Typical procedure for LbL assembly.

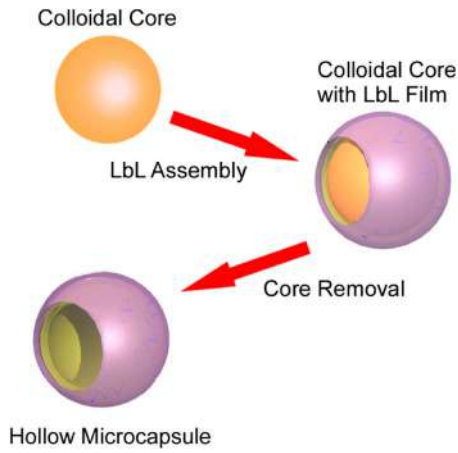

Figure 23.14 LbL assembly on a colloidal core for fabrication of hollow microcapsule.

unfavorable electrostatic repulsion at the surface area. The charge reversal allows anionic particles to be adsorbed on the surface of the polyelectrolyte layers when the covered solid substrate is immersed in a solution containing an anionic particle. Similarly to the previous step, charge neutralization and re-saturation result in formation of a negatively charged surface. Repeated alternate adsorption between the cationic polyelectrolyte and anionic particle becomes possible through this charge reversal process.

LbL films are not limited to being fabricated as flat films. It may be formulated into a variety of shapes such as microcapsules and tubes. LbL assembly into hollow microcapsules is one of the wise modifications of the conventional LbL method. As illustrated in Figure 23.14, LbL films are assembled sequentially on the colloidal core in a similar way to conventional LbL assemblies. Upon exposure of the particles to an appropriate solvent, the central particle core (sacrificial template) is dissolved, finally resulting in a hollow capsule. Ultrathin film kin layers of the hollow spheres are basically permeable for small molecules. Therefore, encapsulation and controlled release of important substances such as pharmaceutical drugs become possible using the LbL hollow capsules.

23.3.1.2 Application of Layer-by-layer (LbL) Assembly for Energy and Environment

Fabricated LbL structures have been used in various kinds of applications thanks to their high freedoms in component selection and structure designs. Some examples of applications of LbL assemblies are briefly shown below.

Marmisollé and co-workers demonstrate energy applications of LbL assemblies containing Pt nanoparticles (see Figure 23.15).[104] The use Pt nanoparticles

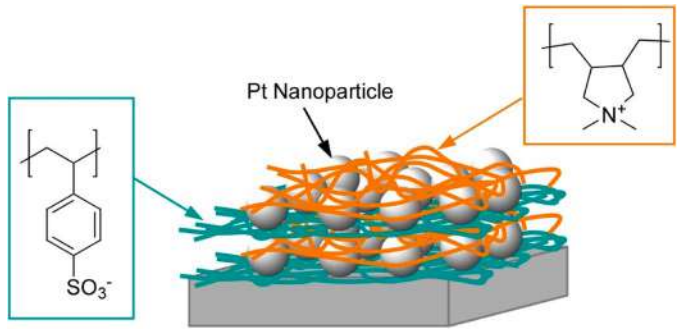

Figure 23.15 LbL assembly between polyelectrolyte-capped Pt nanoparticle and polyelectrolyte.

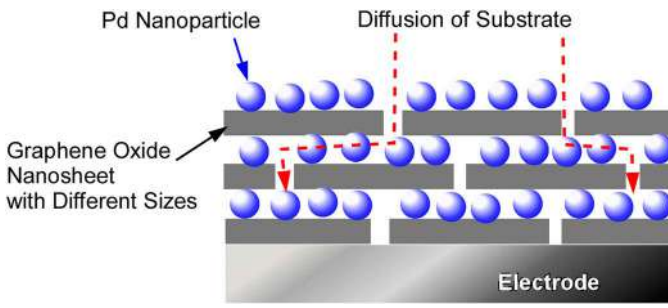

Figure 23.16 LbL assembly between graphene oxide nanosheets and Pd nanoparticle where the size of graphene oxide nanosheet influences substrate diffusion.

were first capped with poly(diallyldimethylammonium chloride) (cationic polyelectrolyte) and were then assembled with poly(sodium 4-styrenesulfonate) as an anionic polyelectrolyte in a layer-by-layer fashion. The Pl nanoparticles have high electrical connectivity that allows them to be implemented in electrochemical devices. The LbL films formed on graphite electrodes exhibited catalytic activities in H_2 production. Their electrical interconnections between the nanoparticles were effective for up to 20 layers of Pt nanoparticle-polyelectrolyte pairs. Stable arrays of well-dispersed electroactive Pt nanoparticles with a diameter of 2 nm can be easily obtained through the LbL process, which is advantageous for fabrications of energy conversion devices.

Regulation of the nanoarchitecture of the hybrid nanomaterials for electrodes is an important matter of their basic electrochemical application in future energy conversion and storage systems. Gu, Kim, and co-workers investigated the effects of diffusion and electron pathways on electrocatalytic activities of LbL films prepared with Pd nanoparticles and graphene oxide nanosheets with different lateral dimensions (see Figure 23.16).[105]

The maximum performance was observed for the LbL films with graphene oxide nanosheets in large lateral size in thinner films because of facile charge transfer in the thinner electrode films. Increased diffusion pathways in the LbL electrodes with smaller graphene oxide nanosheets exhibited the highest current density with higher mass loading in the thicker films. The obtained tortuous path effects of electrodes supported by graphene oxide nanosheets with different lateral sizes would provide novel insights and new design principles for electrode engineering. The versatility of the LbL method for nanoarchitecting three-dimensional electrodes is a key factor in future energy conversion. It also offers unique opportunities to understand the basic electrochemical kinetics of various electrode designs for storage systems.

An example shown in Figure 23.17 was used for facile detection of environmentally unfriendly toxic molecules as reported by Ji *et al.*[106] In this sensing system, a LbL assembled film of reduced graphene oxide and ionic liquids was immobilized on a mass-detective sensor device, a quartz crystal microbalance. Graphene oxide nanosheets were decomposed from graphite and reconstructed into hierarchical nanoarchitectures using the LbL method with reduction process. Graphene oxide nanosheets were first

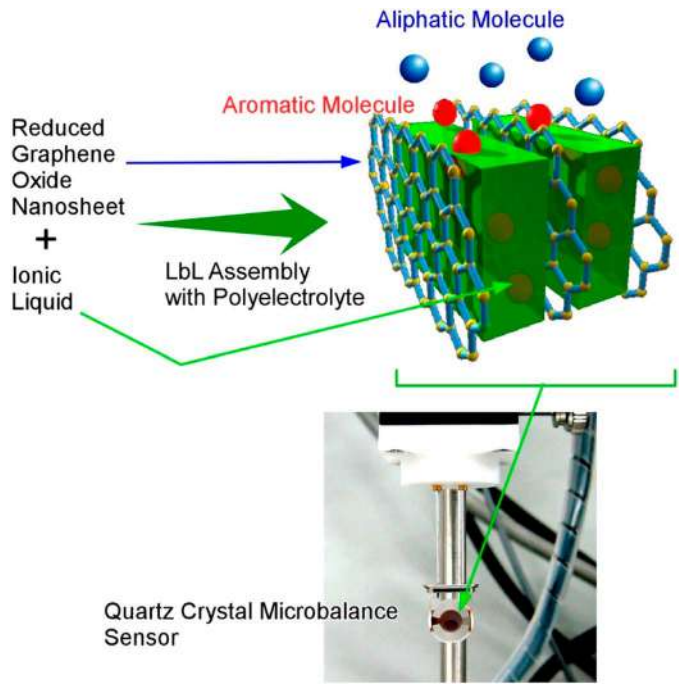

Figure 23.17 LbL assembly between reduced graphene oxide nanosheet and ionic liquid.

obtained by oxidization of graphite under acidic conditions. The resulting nanosheets were then reduced into reduced graphene nanosheets in water with the presence of ionic liquids, typically imidazolium salts. Composites between reduced nanosheets and ionic liquid behave as charge-decorated nanosheets that can be assembled into the LbL structures alternately with counter charged sodium polystyrene sulfonate on surfaces of quartz crystal microbalance electrodes. The fabricated sensor systems were subjected to the detection of target molecules in the gas phase. For example, aromatic gas substances such as benzene exhibited much higher sensitivity than aliphatic molecules probably because of their high affinities to π-electron-rich nanospaces between reduced graphene nanosheets with aromatic ionic liquids. These LbL based sensing systems can detect selectively environmentally toxic aromatic gas molecules.

Two-dimensional materials other than graphene and graphene oxide nanosheets have been used for environmental and bio-related applications. For example, transition metal dihalides such as MoS_2 nanosheets have sufficiently high biocompatibility for bio-related usages. Leong and co-workers demonstrated a cancer therapy application of LbL assembling layered composites of MoS_2 nanosheets and oligo-DNA.[107] MoS_2 nanosheets were first decorated with designed oligo-DNA fragments and can form multi-layer assembly only with complemental bridging DNA sequence. An anticancer drug, doxorubicin was then loaded into interlayer spaces in the LbL films. The used bridging DNA sequence has the role of DNA aptamer that is capable of strongly binding to ATP in cancer cells. Upon binding of the bridging DNA strands to ATP molecules, the LbL structures with MoS_2 nanosheets disassemble and release doxorubicin. This example demonstrated high potentials of the LbL assemblies of bio-decorated two-dimensional materials in biomedical applications.

As briefly exemplified in the above sections, the LbL assembling method with high versatility both in component and structural designs is advantageous for many kinds of applications including energy processes, detection of environmentally toxic substances, and cancer therapy. LbL nanoarchitectonics has become a powerful approach for clean energy and a sustainable environment.

23.3.2 Nanoarchitectonics for Biological and Medical Applications

It is no exaggeration to say that, in the last years, nanoarchitectonics has played a predominant role in the design and development of bio- and soft materials for innovative biological and medical applications. Some prominent examples include the development of multifunctional nanoprobes for biodiagnostics, advanced drug delivery systems or tailored biointerfaces for application in stem cell culture, tissue engineering, and regenerative medicine.

With these successes, nanoarchitectured bio- and soft materials are increasingly being considered as key elements in the construction of advanced biomedical devices and bioanalytical tools.

Numerous areas of medicine benefit from innovative features enabled by nanoarchitectonics. For instance, it has been demonstrated that the use of nanoarchitectured materials or surfaces to mimic naturally occurring structures can lead to optimal biological, physical, and mechanical characteristics of implants. The rational design of nanocoatings is critical to increase biocompatibility and thus improve integration with the surrounding tissues of a variety of medical implants. Examples can be found in cardiology (stent coating), orthopedics (coating on joint replacement implants) and dentistry (dental implants).[108]

A major issue in tissue engineering and regenerative medicine is the development of novel materials and surface coatings with mechanical and biological characteristics that enhance cell adhesion and promote long-term tissue regeneration. Cells must adhere well to scaffolds or to the surface of implants, prior to tissue regeneration. Cell spreading, migration, proliferation and even differentiation take place only after proper cell adhesion. In this regard, polyelectrolyte multilayers incorporating bioactive molecules and stimuli-sensitive building blocks are very appealing for the modulation of cell-surface interactions.[109]

Polyelectrolyte multilayers formed from assembled biopolyelectrolytes constitute a biocompatible cushion onto which proteins, peptides, and other biomolecules can be assembled, impacting cell functionalities; not only on cell adhesion but also on cell growth and migration. One of the benefits of polyelectrolyte multilayers is that their properties can be tuned by changing the conditions during the polyelectrolyte assembly or even by thermal treatment of the assembled film.[110,111]

Within this framework, a considerable amount of research has been focused on understanding and controlling the surface immobilization of biomolecules, in particular proteins, peptides, amino acids and nucleic acids. In biomedical diagnostics, the immobilization of biomolecules such as proteins, antibodies, peptides, nucleic acids, bacteria, and viruses onto colloidal particles, nanotubes or nanosheets is of paramount importance. In immunodiagnostic and specific nucleic acids isolation, the captured biomolecules should be adequately immobilized. This is a very critical point since further accessibility and activity of the fixed biomolecules could be affected. One of the fundamental challenges of biointerfacial nanoarchitectonics is to control the position and orientation of bioactive elements at interfaces. Biological molecules often adopt specific spatial configurations at interfaces, which are required to achieve proper physiological functions, like molecular recognition, catalysis and adhesion. In addition to that, we should bear in mind that surfaces and interfaces may induce misfolding and malfunction of biomolecules. Hence, understanding and manipulating biomolecule-interface interactions is essential for

nanoarchitectonics to create bio-composite and biomimetic materials, engineered biointerfaces or even design low-dimensional biomaterials. With this goal in mind, many researchers have explored novel functions by interfacing biomolecules with synthetic nanomaterials (quantum dots, carbon nanotubes, 2D nanomaterials, *etc.*) resulting in the self-assembly functional (static or dynamic) biohybrid nanostructures of high interest for biosensing, delivery and bioelectronic applications. Good examples of this nanoarchitectonic approach in action are DNA-templated nanostructures, peptide- and polypeptide-based self-assembled nanostructures, and stimuli-responsive biomolecular assemblies, among others.[112] Mastering self-assembly processes requires proper molecular design of the biomolecular and synthetic counterparts, and a synergistic set of interactions at the supramolecular level; this being a central aspect of nanoarchitectonics.

Biosensing is another area of biomedical engineering which is increasingly permeated by nanoarchitectonic concepts. In most cases, biosensors require precise chemical functionalization to confer specific features to the sensing surface/interface, such as predefined chemical reactivity, specific molecular recognition or antifouling properties. Consequently, tailoring the chemistry at the biosensing interface has a crucial role in obtaining the best selectivity and sensitivity. Let us take an example where we want to create a DNA-based biosensor. To achieve such a goal, we need to integrate biological probes on the sensing surface, we need to define the type of chemistry necessary to accomplish the chemical modification of the sensing surface, and we need to consider the antifouling properties of the sensing surface. In addition, we need to control the surface probe density in order to maximize the sensitivity. Hence, it is no wonder that the rational design of a biosensor involves a great deal of nanoarchitectonics concepts.

There is a growing need for reliable biosensing methods that can detect small molecules, DNA, RNA and proteins at very low concentrations (femtomolar range) from both human (*e.g.*, serum, saliva, urine) and environmental (*e.g.*, groundwater, air) samples. This need has led to the development of a broad variety of sensing nanodevices that incorporate unique interfacial nanostructures that can impart predefined physicochemical properties to enhance the sensing process. Examples of these "nanoarchitected" structures and devices include metal and semiconductor nanowires for electrochemical and electro-optical devices, graphene-based field-effect transistors, supramolecular assemblies for surface plasmon resonance, bioelectrochemical biosensors, and DNA nanostructures and hydrogels.

In therapeutic areas, nanoarchitectonics has been a key player in the advanced design of various kinds of colloidal particles that have been evaluated in different configurations. In recent years increasing interest has been given to the design, preparation and utilization of supramolecular capsules, biodegradable particles, ionically-crosslinked colloids, molecularly

imprinted polymeric nanoparticles and stimuli-responsive colloids, among other systems. These "nanoarchitectured" colloids were principally used as solid supports or micro-containers of active molecules (see Figure 23.18). Nowadays, the main objective in the therapeutic domain is the elaboration of new colloidal systems displaying enhanced targeting efficiency in order to reduce the therapeutic dose and minimize dose-related side effects. One possibility to face this problem is to go further into the integration of nanoarchitectonic concepts and notions into the molecular design of stimuli-responsive colloidal particles.

With this aim in mind, particular attention must be paid to the emerging field of supramolecular nanotheranostics. Theranostics involves the integration of therapeutic and diagnostic platforms to perform disease diagnosis and therapy simultaneously. Theranostic approaches have already been proposed for conditions like cancer, inflammatory diseases, and infections. However, the practical implementation of theranostics requires the "skills" of nanoarchitectonics to integrate various components along with customized therapeutic agents, to devise controlled-release mechanisms, and to design targeting strategies. For example, by the formation of host–guest complexes with macrocyclic hosts, anticancer drugs can be easily formulated to prepare nanomedicines showing satisfactory anti-tumor efficacy and reduced normal organ toxicity. In another example, a multiresponsive supramolecular theranostic nanoplatform based on supramolecular nanoparticles hosting glucose oxidase and insulin can accomplish concerted functions in the presence of glucose in order to release insulin only under hyperglycemic conditions[113] (see Figure 23.19).

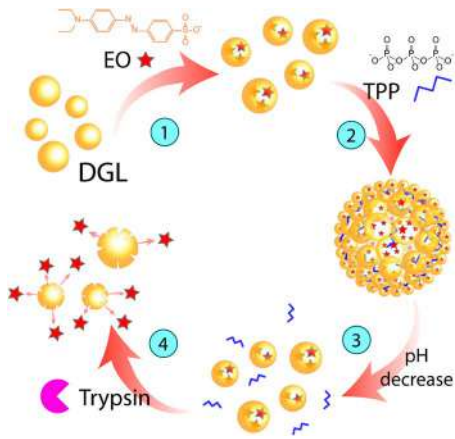

Figure 23.18 Self-assembled peptide dendrigraft supraparticles as pH/enzyme-triggered multistage drug release nanosystems. Reproduced from ref. 115 with permission from Elsevier, Copyright 2020.

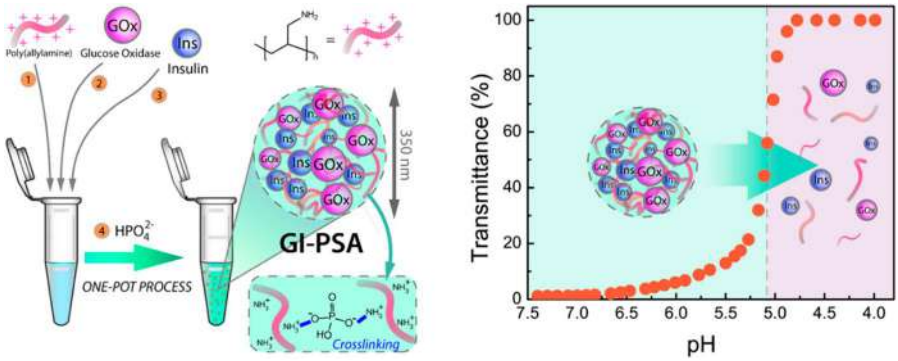

Figure 23.19 Poly(allylamine) cross-linking with phosphate anions and coimmobilization of GOx and insulin in a biomimetic polyamine-salt-aggregates (GI-PSA). Total transmittance at $\lambda = 580$ nm for a colloidal dispersion of GI-PSA *versus* pH. Reproduced from ref. 113 with permission from John Wiley & Sons, Copyright © 2019 Wiley-VCH Verlag GmbH & Co. KGaA, Weinheim.

23.4 Conclusions

In this chapter we have presented a series of iconic examples of physicochemical systems developed by the suitable integration of functional building blocks for a diversity of applications as an illustration of the vast universe of nanoarchitectonics.

At this point we would like to emphasize the importance of selecting adequate integration strategies, taking into account not only the nature of the building blocks but also the functional requirements imposed by the problems we are dealing with. Applications need for complex materials resulting from the assembly of building blocks with several roles, such as providing mechanical frameworks and stability, electrochemical connection, stimulus responsiveness or catalytic activity. The proper integration of the individual building blocks is essential for allowing these roles to operate and even being enhanced, yielding synergistic effects. Thus, the rational design and construction of complex nanoarchitectures requires the comprehension of the basis of the interactions between the individual building blocks and the evaluation of the suitability and compatibility of the different construction techniques with the nature and activity of the supramolecular entities.

Nanoarchitectonics is not really a new area but a change of perspective for looking at the material systems (particularly soft matter systems) as made of building blocks integrated by different strategies employing the variety of interactions between them. Facing the great variety of existing (and future) different molecular and supramolecular entities and great advances in the development and understanding of integration techniques, future solutions to real life problems in our societies seem to be limited just by our

creative mind. We hope this book, and particularly this chapter, stimulates the newcomers to look at material science problems through the lens of nanoarchitectonics.

Acknowledgements

This work was supported by the Consejo Nacional de Investigaciones Científicas y Técnicas (CONICET, Argentina) (Grant No. PIP 0370), Agencia Nacional de Promoción Científica y Tecnológica (ANPCyT) (PICT 2016-1680, 2017-1523), the Austrian Institute of Technology GmbH (AIT-CONICET Partner Group: "*Exploratory Research for Advanced Technologies in Supramolecular Materials Science*", Exp. 4947/11, Res. No. 3911, 28-12-2011), and Universidad Nacional de La Plata (UNLP). O.A., M.L.C., M.R. and W.A.M are staff members of CONICET.

References

1. *Polymer and Biopolymer Brushes: For Materials Science and Biotechnology*, ed. O. Azzaroni and I. Szleifer, John Wiley & Sons, Hoboken, 2018.
2. O. Azzaroni, *J. Polym. Sci., Part A: Polym. Chem.*, 2012, **50**, 3225.
3. J. O. Zoppe, N. C. Ataman, P. Mocny, J. Wang, J. Moraes and H. A. Klok, *Chem. Rev.*, 2017, **117**, 1105.
4. O. Azzaroni, S. E. Moya, A. A. Brown, Z. Zheng, E. Donath and W. T. S. Huck, *Adv. Funct. Mater.*, 2006, **16**, 1037.
5. T. K. Tam, J. Zhou, M. Pita, M. Ornatska, S. Minko and E. Katz, *J. Am. Chem. Soc.*, 2008, **130**, 10888–10889.
6. O. H. Kwon, A. Kikuchi, M. Yamato and T. Okano, *Biomaterials*, 2003, **24**, 1223–1232.
7. X. Ren, Y. Wu, Y. Cheng, H. Ma and S. Wei, *Langmuir*, 2011, **27**, 12069–12073.
8. S. Tugulu, P. Silacci, N. Stergiopulos and H.-A. Klok, *Biomaterials*, 2007, **28**, 2536–2546.
9. M. Motornov, Ro. Sheparovych, R. Lupitskyy, E. MacWilliams, O. Hoy, I. Luzinov and S. Minko, *Adv. Funct. Mater.*, 2007, **17**, 2307–2314.
10. A. A. Brown, O. Azzaroni, L. M. Fidalgo and W. T. S. Huck, *Soft Matter*, 2009, **5**, 2738–2745.
11. J. Cui, T. H. Nguyen, M. Ceolín, R. Berger, O. Azzaroni and A. del Campo, *Macromolecules*, 2012, **45**, 3213.
12. J. Cui, O. Azzaroni and A. del Campo, *Macromol. Rapid Commun.*, 2011, **32**, 1699.
13. T. A. García, C. A. Gervasi, M. J. Rodríguez Presa, J. I. Otamendi, S. E. Moya and O. Azzaroni, *J. Phys. Chem. C*, 2012, **116**, 13944.
14. O. Azzaroni, A. A. Brown and W. T. S. Huck, *Adv. Mater.*, 2007, **19**, 151.
15. O. Azzaroni, S. Moya, T. Farhan, A. A. Brown and W. T. S. Huck, *Macromolecules*, 2005, **38**, 10192.

16. S. Moya, O. Azzaroni, T. Farhan, V. L. Osborne and W. T. S. Huck, *Angew. Chem., Int. Ed.*, 2005, **44**, 4578.
17. N. Cheng, A. A. Brown, O. Azzaroni and W. T. S. Huck, *Macromolecules*, 2008, **41**, 6317.
18. A. A. Brown, O. Azzaroni and W. T. S. Huck, *Langmuir*, 2009, **25**, 1744.
19. O. Azzaroni, A. A. Brown and W. T. S. Huck, *Angew. Chem., Int. Ed.*, 2006, **45**, 1770.
20. J. M. Giussi, M. L. Cortez, W. A. Marmisollé and O. Azzaroni, *Chem. Soc. Rev.*, 2019, **48**, 814.
21. C.-H. Lin, W.-J. Chou and J.-T. Lee, *Macromol. Rapid Commun.*, 2012, **33**, 107.
22. E. Y. Choi, O. Azzaroni, N. Cheng, F. Zhou, T. Kelby and W. T. S. Huck, *Langmuir*, 2007, **23**, 10389.
23. G. E. Fenoy, J. M. Giussi, C. von Bilderling, E. M. Maza, L. I. Pietrasanta, W. Knoll, W. A. Marmisollé and O. Azzaroni, *J. Colloid Interface Sci.*, 2018, **518**, 92–101.
24. G. L. Whiting, H. J. Snaith, S. Khodabakhsh, J. W. Andreasen, D. W. Breiby, M. M. Nielsen, N. C. Greenham, R. H. Friend and W. T. S. Huck, *Nano Lett.*, 2006, **6**, 573–578.
25. E. Piccinini, C. Bliem, J. M. Giussi, W. Knoll and O. Azzaroni, *Langmuir*, 2019, **35**, 8038.
26. O. Azzaroni, A. A. Brown, N. Cheng, A. Wei, A. M. Jonas and W. T. S. Huck, *J. Mater. Chem.*, 2007, **17**, 3433.
27. (a) S. Wunder, F. Polzer, Y. Lu, Y. Mei and M. Ballauff, *J. Phys. Chem. C*, 2010, **114**, 8814–8820; (b) Y. Mei, Y. Lu, F. Polzer, M. Ballauff and M. Drechsler, *Chem. Mater.*, 2007, **19**, 1062–1069.
28. A. Calvo, B. Yameen, F. J. Williams, O. Azzaroni and G. J. A. A. Soler-Illia, *Chem. Commun.*, 2009, 2553.
29. A. Calvo, B. Yameen, F. J. Williams, G. J. A. A. Soler-Illia and O. Azzaroni, *J. Am. Chem. Soc.*, 2009, **131**, 10866.
30. A. Calvo, M. C. Fuertes, B. Yameen, F. J. Williams, O. Azzaroni and G. J. A. A. Soler-Illia, *Langmuir*, 2010, **26**, 5559.
31. A. Brunsen, A. Calvo, F. J. Williams, G. J. A. A. Soler-Illia and O. Azzaroni, *Langmuir*, 2011, **27**, 4328.
32. A. Brunsen, J. Cui, M. Ceolín, A. del Campo, G. J. A. A. Soler-Illia and O. Azzaroni, *Chem. Commun.*, 2012, **48**, 1422.
33. A. Brunsen, C. Díaz, L. I. Pietrasanta, B. Yameen, M. Ceolín, G. J. A. A. Soler-Illia and O. Azzaroni, *Langmuir*, 2012, **28**, 3583–3592.
34. E. Aznar, M. Oroval, L. Pascual, J. R. Murguía, R. Martinez-Mañez and F. Sancenon, *Chem. Rev.*, 2016, **116**, 561.
35. S. Alberti, G. J. A. A. Soler-Illia and O. Azzaroni, *Chem. Commun.*, 2015, **51**, 6050.
36. O. Schepelina and I. Zharov, *Langmuir*, 2006, **22**, 10523.
37. O. Schepelina and I. Zharov, *Langmuir*, 2007, **23**, 12704.
38. T. Sato, T. Morinaga, S. Marukane, T. Narutomi, T. Igarashi, Y. Kawano, K. Ohno, T. Fukuda and Y. Tsujii, *Adv. Mater.*, 2011, **23**, 4868–4872.

39. B. Yameen, A. Kaltbeitzel, G. Glasser, A. Langner, F. Muller, U. Gösele, W. Knoll and O. Azzaroni, *ACS Appl. Mater. Interfaces*, 2010, **2**, 279.
40. B. Yameen, A. Kaltbeitzel, A. Langer, F. Müller, U. Gösele, W. Knoll and O. Azzaroni, *Angew. Chem., Int. Ed.*, 2009, **48**, 3124.
41. B. Yameen, A. Kaltbeitzel, A. Langner, H. Duran, F. Müller, U. Gösele, O. Azzaroni and W. Knoll, *J. Am. Chem. Soc.*, 2008, **130**, 13140.
42. B. Yameen, M. Ali, R. Neumann, W. Ensinger, W. Knoll and O. Azzaroni, *J. Am. Chem. Soc.*, 2009, **131**, 2070.
43. B. Yameen, M. Ali, R. Neumann, W. Ensinger, W. Knoll and O. Azzaroni, *Small*, 2009, **5**, 1287.
44. B. Yameen, M. Ali, R. Neumann, W. Ensinger, W. Knoll and O. Azzaroni, *Nano Lett.*, 2009, **9**, 2788.
45. B. Yameen, M. Ali, R. Neumann, W. Ensinger, W. Knoll and O. Azzaroni, *Chem. Commun.*, 2010, **46**, 1908.
46. B. F. Hoskins and R. Robson, *J. Am. Chem. Soc.*, 1989, **111**(15), 5962–5964.
47. H. C. Zhou, J. R. Long and O. M. Yaghi, *Chem. Rev.*, 2012, **11**, 673.
48. C. Wang, X. Liu, N. K. Demir, J. P. Chen and K. Li, *Chem. Soc. Rev.*, 2016, **45**, 5107.
49. T. Zhang and W. Lin, *Chem. Soc. Rev.*, 2014, **43**, 5982.
50. J. E. Mondloch, M. J. Katz, W. C. Isley III, P. Ghosh, P. Liao, W. Bury, G. W. Wagner, M. G. Hall, J. B. DeCoste, G. W. Peterson, R. Q. Snurr, C. J. Cramer, J. T. Hupp and O. K. Farha, *Nat. Mater.*, 2015, **14**, 512–516.
51. Y. Gu, M. Huang, W. Zhang, M. A. Pearson and J. A. Johnson, *Angew. Chem., Int. Ed.*, 2019, **58**, 16676.
52. C. V. McGuire and R. S. Forgan, *Chem. Commun.*, 2015, **51**, 5199–5217.
53. S. Furukawa, J. Reboul, S. Diring, K. Sumida and S. Kitagawa, *Chem. Soc. Rev.*, 2014, **43**, 5700.
54. M. Zhao, Y. Huang, Y. Peng, Z. Huang, Q. Ma and H. Zhang, *Chem. Soc. Rev.*, 2018, **47**, 6267.
55. W. P. Lustig, S. Mukherjee, N. D. Rudd, A. V. Desai, J. Li and S. K. Ghosh, *Chem. Soc. Rev.*, 2017, **46**, 3242.
56. X. Lian, Y. Fang, E. Joseph, Q. Wang, J. Li, S. Banerjee, C. Lollar, X. Wang and H.-C. Zhou, *Chem. Soc. Rev.*, 2017, **46**, 3386.
57. Q. Yang, Q. Xu and H.-L. Jiang, *Chem. Soc. Rev.*, 2017, **46**, 4774.
58. J. Liu and C. Wöll, *Chem. Soc. Rev.*, 2017, **46**, 5730.
59. M. Rafti, J. A. Allegretto, G. M. Segovia, J. S. Tuninetti, J. M. Giussi, E. Bindini and O. Azzaroni, *Mater. Chem. Front.*, 2017, **1**, 2256.
60. J. S. Tuninetti, M. Rafti and O. Azzaroni, *RSC Adv.*, 2015, **5**, 73958.
61. J. S. Tuninetti, M. Rafti, A. Andrieu-Brunsen and O. Azzaroni, *Microporous Mesoporous Mater.*, 2016, **220**, 253.
62. G. M. Segovia, J. S. Tuninetti, S. Moya, A. S. Picco, M. R. Ceolín, O. Azzaroni and M. Rafti, *Mater. Today Chem.*, 2018, **8**, 29.
63. G. E. Fenoy, J. Scotto, J. Azcárate, M. Rafti, W. A. Marmisollé and O. Azzaroni, *ACS Appl. Energy Mater.*, 2018, **1**(10), 5428–5436.
64. P. Silva, S. M. F. Vilela, J. P. C. Tomé and F. A. Almeida Paz, *Chem. Soc. Rev.*, 2015, **44**, 6774.

65. (a) K. Ariga, A. Vinu, Y. Yamauchi, Q. Ji and J. P. Hill, *Bull. Chem. Soc. Jpn.*, 2012, **85**, 1; (b) G. J. A. A. Soler-Illia and O. Azzaroni, *Chem. Soc. Rev.*, 2011, **40**, 1107–1150.
66. C. Sanchez, B. Julián, P. Belleville and M. Popall, *J. Mater. Chem.*, 2005, **15**, 3559–3592.
67. P. Innocenzi and L. Malfatti, *Chem. Soc. Rev.*, 2013, **42**, 4198.
68. Y. Ren, Z. Ma and P. G. Bruce, *Chem. Soc. Rev.*, 2012, **41**, 4909–4927.
69. Z. Li, J. C. Barnes, A. Bosoy, J. Fraser Stoddart and J. I. Zink, *Chem. Soc. Rev.*, 2012, **41**, 2590.
70. G. Niu, A. Ruditskiy, M. Varac and Y. Xia, *Chem. Soc. Rev.*, 2015, **44**, 5806–5820.
71. (a) K. Wu and T. Lian, *Chem. Soc. Rev.*, 2016, **45**, 3781–3810; (b) T. Bollhorst, K. Rezwana and M. Maas, *Chem. Soc. Rev.*, 2017, **46**, 2091–2126; (c) S. Jiang, A. Van Dyk, A. Maurice, J. Bohling, D. Fasanoc and S. Brownell, *Chem. Soc. Rev.*, 2017, **46**, 3792–3807.
72. (a) X. Liu and M. T. Swihart, *Chem. Soc. Rev.*, 2014, **43**, 3908–3920; (b) H. Cong, B. Yu, J. Tang, Z. Lia and X. Liu, *Chem. Soc. Rev.*, 2013, **42**, 7774–7800.
73. (a) V. D. Ta, R. M. Carter, E. Esenturk, C. Connaughton, T. J. Wasley, J. Li, R. W. Kay, J. Stringer, P. J. Smith and J. D. Shephard, *Soft Matter*, 2016, **12**, 4530–4536; (b) M. Rosenberg, F. Dekker, J. G. Donaldson, A. P. Philipse and S. S. Kantorovich, *Soft Matter*, 2020, **16**, 4451–4461; (c) C. Karner, C. Dellago and E. Bianchi, *Soft Matter*, 2020, **16**, 2774–2785.
74. W. Ma, L. Xu, A. F. de Moura, X. Wu, H. Kuang, C. Xu and N. A. Kotov, *Chem. Rev.*, 2017, **117**(12), 8041–8093.
75. Y. Xia, T. D. Nguyen, M. Yang, B. Lee, A. Santos, P. Podsiadlo, Z. Tang, S. C. Glotzer and N. A. Kotov, *Nat. Nanotechnol.*, 2011, **6**, 580–587.
76. Q. Fu, Y. Sheng, H. Tang, Z. Zhu, M. Ruan, W. Xu, Y. Zhu and Z. Tang, *ACS Nano*, 2015, **9**, 172–179.
77. Y. Hu, Y. Liu and Y. Sun, *Adv. Funct. Mater.*, 2015, **25**, 1638–1647.
78. G. Jia, A. Sitt, G. B. Hitin, I. Hadar, Y. Bekenstein, Y. Amit, I. Popov and U. Banin, *Nat. Mater.*, 2014, **13**, 302–308.
79. T. Wang, X. Wang, D. LaMontagne, Z. Wang, Z. Wang and Y. C. Cao, *J. Am. Chem. Soc.*, 2012, **134**, 18225–18228.
80. G. Yang, H. Zhong, R. Liu, Y. Li and B. Zou, *Langmuir*, 2013, **29**, 1970–1976.
81. W. Zhang, J. Zheng, C. Tan, X. Lin, S. Hu, J. Chen, X. You and S. Li, *J. Mater. Chem. B*, 2015, **3**, 217–224.
82. J. I. Park, T. D. Nguyen, G. de Queiros Silveira, J. H. Bahng, S. Srivastava, G. Zhao, K. Sun, P. Zhang, S. C. Glotzer and N. A. Kotov, *Nat. Commun.*, 2014, **5**, 3593–3601.
83. S. T. Moerz, A. Kraegeloh, M. Chanana and T. Kraus, *ACS Nano*, 2015, **9**, 6696–6705.
84. C. Stoffelen and J. Huskens, *Chem. Commun.*, 2013, **49**, 6740–6742.
85. V. Liljestrom, J. Seitsonen and M. A. Kostiainen, *ACS Nano*, 2015, **9**, 11278–11285.

86. E. Piccinini, D. Pallarola, F. Battaglini and O. Azzaroni, *Chem. Commun.*, 2015, **51**, 14754–14757.
87. L. Y. T. Chou, K. Zagorovsky and W. C. W. Chan, *Nat. Nanotechnol.*, 2014, **9**, 148–155.
88. C. F. J. Faul and M. Antonietti, *Adv. Mater.*, 2003, **15**, 673.
89. W. J. Macknight, E. A. Ponomarenko and D. A. Tirrell, *Acc. Chem. Res.*, 1998, **31**, 781.
90. M. L. Cortez, M. Ceolín, J. L. Cuellar Camacho, E. Donath, S. Moya, F. Battaglini and O. Azzaroni, *ACS Appl. Mater. Interfaces*, 2017, **9**, 1119–1128.
91. M. R. Hammond and R. Mezzenga, *Soft Matter*, 2008, **4**, 952–961.
92. Z. Cheng, B. Ren, M. Gao, X. Liu and Z. Tong, *Macromolecules*, 2007, **40**, 7638.
93. R. Ahmed, M.-S. Hsiao, Y. Matsuura, N. Houbenov, C. F. J. Faul and I. Manners, *Soft Matter*, 2011, **7**, 10462.
94. A. Lorenzo, W. A. Marmisollé, E. M. Maza, M. Ceolín and O. Azzaroni, *Phys. Chem. Chem. Phys.*, 2018, **20**, 7570–7578.
95. (a) M. L. Cortez, A. Lorenzo, W. A. Marmisollé, C. von Bilderling, E. Maza, L. Pietrasanta, F. Battaglini, M. Ceolín and O. Azzaroni, *Soft Matter*, 2018, **14**, 1939; (b) M. L. Cortez, G. A. González, M. Ceolín, O. Azzaroni and F. Battaglini, *Electrochim. Acta*, 2014, **118**, 124; (c) M. L. Cortez, D. Pallarola, M. Ceolín, O. Azzaroni and F. Battaglini, *Anal. Chem.*, 2013, **85**, 2414; (d) M. L. Cortez, M. Ceolín, O. Azzaroni and F. Battaglini, *Bioelectrochemistry*, 2015, **105**, 117.
96. (a) M. L. Cortez, M. Ceolín, L. Cuellar Camacho, E. Donath, S. E. Moya, F. Battaglini and O. Azzaroni, *ACS Appl. Mater. Interfaces*, 2017, **9**, 1119; (b) M. L. Cortez, W. A. Marmisollé, D. Pallarola, L. I. Pietrasanta, D. H. Murgida, M. Ceolín, O. Azzaroni and F. Battaglini, *Chem. - Eur. J.*, 2014, **20**, 13366.
97. M. L. Cortez, M. Ceolín, O. Azzaroni and F. Battaglini, *Anal. Chem.*, 2011, **83**, 8011.
98. M. L. Cortez, D. Pallarola, M. Ceolín, O. Azzaroni and F. Battaglini, *Chem. Commun.*, 2012, **48**, 10868.
99. G. Decher, *Science*, 1997, **277**, 12.
100. F. Caruso, R. A. Caruso and H. Möhwald, *Science*, 1998, **282**, 1111.
101. K. Ariga, J. P. Hill and Q. Ji, *Phys. Chem. Chem. Phys.*, 2007, **9**, 2319.
102. K. Ariga, Y. Yamauchi, G. Rydzek, Q. Ji, Y. Yonamine, K. C.-W. Wu and J. P. Hill, *Chem. Lett.*, 2014, **43**, 36.
103. K. Ariga, E. Ahn, M. Park and B.-S. Kim, *Chem.–Asian J.*, 2019, **14**, 2553.
104. G. E. Fenoy, E. Maza, E. Zelaya, W. A. Marmisollé and O. Azzaroni, *Appl. Surf. Sci.*, 2017, **416**, 24.
105. M. Gu, J. Choi, T. Lee, M. Park, I.-S. Shin, J. Hong, H.-W. Lee and B.-S. Kim, *Nanoscale*, 2018, **10**, 16159.
106. Q. Ji, I. Honma, S.-M. Paek, M. Akada, J. P. Hill, A. Vinu and K. Ariga, *Angew. Chem., Int. Ed.*, 2010, **49**, 9737.

107. B. L. Li, M. I. Setyawati, L. Chen, J. Xie, K. Ariga, C.-T. Lim, S. Garaj and D. Tai Leong, *ACS Appl. Mater. Interfaces*, 2017, **9**, 15286.
108. *Layer-by-Layer Films for Biomedical Applications*, ed. C. Picart, F. Caruso and J.-C. Voegel, VCH-Wiley, Weinheim, 2015.
109. (a) T. Boudou, T. Crouzier, K. Ren, G. Blin and C. Picart, *Adv. Mater.*, 2010, **22**, 441; (b) C. Picart, *Curr. Med. Chem.*, 2008, **15**, 685.
110. (a) N. E. Muzzio, M. A. Pasquale, E. Diamanti, D. Gregurec, M. M. Moro, O. Azzaroni and S. Moya, *Mater. Sci. Eng., C*, 2017, **80**, 677; (b) E. Diamanti, N. Muzzio, D. Gregurec, J. Irigoyen, M. Pasquale, O. Azzaroni, M. Brinkmann and S. E. Moya, *Colloids Surf., B*, 2016, **145**, 328; (c) N. E. Muzzio, D. Gregurec, E. Diamanti, J. Irigoyen, M. A. Pasquale, O. Azzaroni and S. E. Moya, *Adv. Mater. Interfaces*, 2017, **4**, 1600126; (d) N. E. Muzzio, M. A. Pasquale, D. Gregurec, E. Diamanti, M. Kosutic, O. Azzaroni and S. E. Moya, *Macromol. Biosci.*, 2016, **16**, 482.
111. (a) N. E. Muzzio, M. A. Pasquale, X. Rios, O. Azzaroni, J. Llop and S. E. Moya, *Adv. Mater. Interfaces*, 2019, **6**, 1900008; (b) N. E. Muzzio, M. A. Pasquale, W. A. Marmisollé, C. von Bilderling, M. L. Cortez, L. I. Pietrasanta and O. Azzaroni, *Biomater. Sci.*, 2018, **6**, 2230; (c) N. E. Muzzio, M. A. Pasquale, S. E. Moya and O. Azzaroni, *Biointerphases*, 2017, **12**, 04E403.
112. Z. He, W. Jiang and C. A. Schalley, *Chem. Soc. Rev.*, 2015, **44**, 779–789.
113. M. L. Agazzi, S. E. Herrera, M. L. Cortez, W. A. Marmisollé, M. Tagliazucchi and O. Azzaroni, *Chem. - Eur. J.*, 2020, **26**, 2456–2463.
114. A. S. Picco, B. Yameen, W. Knoll, M. R. Ceolín and O. Azzaroni, *J. Colloid Interface Sci.*, 2016, **471**, 71–75.
115. M. L. Agazzi, S. E. Herrera, M. L. Cortez, W. A. Marmisollé and O. Azzaroni, *Colloids Surf., B*, 2020, **190**, 110895.

Subject Index